

W. J. Choyke  
H. Matsunami  
G. Pensl  
(Eds.)

# Silicon Carbide

Recent Major  
Advances

Volume I



Springer



## Advanced Texts in Physics

This program of advanced texts covers a broad spectrum of topics which are of current and emerging interest in physics. Each book provides a comprehensive and yet accessible introduction to a field at the forefront of modern research. As such, these texts are intended for senior undergraduate and graduate students at the MS and PhD level; however, research scientists seeking an introduction to particular areas of physics will also benefit from the titles in this collection.

Springer-Verlag Berlin  
Heidelberg GmbH

**Physics and Astronomy**



**ONLINE LIBRARY**

<http://www.springer.de>

W.J. Choyke H. Matsunami G. Pensl (Eds.)

---

# Silicon Carbide

Recent Major Advances

With 460 Figures and 82 Tables



Springer

## Professor Dr. W.J. Choyke

University of Pittsburgh, Department of Physics and Astronomy  
Pittsburgh, PA 15260, USA  
E-mail: choyke@imap.pitt.edu

## Professor Dr. H. Matsunami

Kyoto University, Department of Electronic Science and Engineering  
Yoshidahonmachi, Sakyo, Kyoto 606-8501, Japan  
E-mail: matsunam@kuee.kyoto-u.ac.jp

## Dr. G. Pensl

University of Erlangen–Nürnberg, Institute of Applied Physics  
Staudtstrasse 7/A3, 91058 Erlangen, Germany  
E-mail: gerhard.pensl@physik.uni-erlangen.de

### Library of Congress Cataloging-in-Publication Data

Silicon carbide : recent major advances / W.J. Choyke, H. Matsunami, G. Pensl (eds.).  
p. cm. – (Advanced texts in physics, ISSN 1439-2674)  
Includes bibliographic references and index.

ISBN 978-3-642-62333-2 ISBN 978-3-642-18870-1 (eBook)

DOI 10.1007/978-3-642-18870-1

1. Silicon carbide. I. Choyke, W. J. II. Matsunami, H. (Hiroyuki), 1939- III. Pensl, G. (Gerhard) IV. Series.  
QC611.8.S5S55 2004  
621.3815'2-dc22

2003059642

### ISSN 1439-2674

ISBN 978-3-642-62333-2

This work is subject to copyright. All rights are reserved, whether the whole or part of the material is concerned, specifically the rights of translation, reprinting, reuse of illustrations, recitation, broadcasting, reproduction on microfilm or in any other way, and storage in data banks. Duplication of this publication or parts thereof is permitted only under the provisions of the German Copyright Law of September 9, 1965, in its current version, and permission for use must always be obtained from Springer-Verlag. Violations are liable for prosecution under the German Copyright Law.

<http://www.springer.de>

© Springer-Verlag Berlin Heidelberg 2004

Originally published by Springer-Verlag Berlin Heidelberg New York in 2004  
Softcover reprint of the hardcover 1st edition 2004

The use of general descriptive names, registered names, trademarks, etc. in this publication does not imply, even in the absence of a specific statement, that such names are exempt from the relevant protective laws and regulations and therefore free for general use.

Typesetting: Data conversion using a Springer  $\text{\TeX}$  macro package

Production: PTP-Berlin, Protago-TeX-Production GmbH, Berlin

Cover design: *design & production* GmbH, Heidelberg

Printed on acid-free paper SPIN 10903216 57/3141/YU 5 4 3 2 1 0

# Preface

In 1997 we put out a two volume set entitled *SiC – A Review of Fundamental Questions and Applications to Current Device Technology*. Six years later we are here again with *Recent Major Advances in SiC*. The editors asked each other hard questions to justify asking colleagues all over the world to spend a lot of time and effort to put out yet another book. On examining the older work we found that many of the articles on fundamental issues were as good today as they were in 1997. However, some of the applied reports were now out of date, some of the experimental work requires considerable updating and theory has shifted from considerations of band structure to point defects. Nevertheless, we had to ask whether the admirable proceedings of both ICSCRM and ECSCRM did not serve to update the SiC community adequately. We concluded that the proceedings feature the latest results but cannot attempt to convey perspective and are not normally written in a transparent style. Secondly, while the proceedings of ICSCRM and ECSCRM are available to all participants of these congresses they are not generally available in libraries. Even colleagues who are active in the field but cannot always attend ICSCRM or ECSCRM do not have this valuable resource at hand. We concluded that if we could bring out *Recent Major Advances in SiC* in a timely fashion and at a price that all colleagues and students can afford then this effort would be justified. In Springer-Verlag we have found a publisher willing to bring out the book within less than a half year of the delivery of the manuscripts and in our authors we have found dedicated souls who not only worked hard to put pen to paper but undertook many of the tasks that in the past have been taken on by the book publisher. Furthermore, the time constraints that we placed on the authors were stringent by past standards. It was truly a labor of love since no one gets any remuneration. The community and certainly the editors owe each and every one of our contributors a debt of sincere gratitude!

The book is organized in very much the same way as our previous SiC I and SiC II. This was purposely done in order to emphasize the continuity with the older work and to avoid repetition wherever possible. We start with four papers on Theory, but the emphasis is on defects and nanostructures. Crystal growth comes next and we have three papers dealing with aspects of boule growth, three papers dealing with homoepitaxial film growth and a

contribution, which introduces the formation of SiC thin films by ion beam synthesis. New developments in surface and interface properties of SiC are covered next in a series of five papers. Not surprisingly, there is much new to tell in the realm of characterization and we include ten contributions in this section. The greatest effort in the last six years has been on the industrialization of SiC and this is reflected in the new depth and in some cases radical departure from the past, in four papers on processing and six papers on devices.

In closing the editors hope that this book will be a convenient guide to researchers and students for many years to come. Together with our previous volumes it should serve as a “friend” to have on one’s desk which one can consult with ease if issues arise which require a look into the literature of SiC. We believe that SiC is just beginning to approach its promise in many fields of human endeavor and we hope that this book will help bring this to reality in just a little less time.

It is with great pleasure that we thank Michael Krieger for his unswerving attention to solving the myriads of computer difficulties that we all encountered in bringing the writing of this book to closure. The efforts of Dr. Claus E. Ascheron and Ms. Adelheid Duhm of Springer-Verlag towards the realization of “Recent Advances in SiC” are greatly appreciated by the editors.

Pittsburgh, Kyoto and Erlangen,  
August 2003

*W.J. Choyke*  
*H. Matsunami*  
*G. Pensl*

# Contents

---

## Part I Theory

---

### Zero- and Two-Dimensional Native Defects

<i>F. Bechstedt, J. Furthmüller, U. Grossner, and C. Raffy</i> .....	3
1 Introduction .....	3
2 Computational Method .....	6
3 Zero-Dimensional Defects .....	7
3.1 Formation of Charged Vacancies and Antisites .....	7
3.2 Ionization Levels and Intravacancy Transitions .....	10
4 Two-Dimensional Defects .....	14
4.1 Tilt Boundaries .....	14
4.2 Boundaries Between Polytypes .....	17
4.3 Surface Influence on Defect Generation .....	21
5 Conclusion .....	22
References .....	22

### Defect Migration and Annealing Mechanisms

<i>M. Bockstedte, A. Mattausch, and O. Pankratov</i> .....	27
1 Introduction .....	27
2 First-Principles Calculation of Defects Properties .....	29
2.1 The First-Principles Method .....	29
2.2 Defect Abundance and Defect Formation Energy .....	29
2.3 Defect Migration: Migration Path and Energy Barriers .....	30
3 Hierarchy of Intrinsic Point Defects in SiC .....	31
3.1 Carbon and Silicon Vacancies .....	31
3.2 Vacancy-Antisite Complexes: The Metastability of the Silicon Vacancy .....	32
3.3 Silicon Interstitials .....	35
3.4 Carbon Interstitials .....	36
4 Interstitial Migration .....	37
4.1 Silicon Interstitials .....	37
4.2 Carbon Split-Interstitials .....	39

5	Vacancy Migration .....	41
5.1	Carbon and Silicon Vacancies .....	41
5.2	Transformation of $V_{Si}$ into $V_C-C_{Si}$ : Consequences for the Migration .....	42
6	Self and Dopant Diffusion .....	43
6.1	Self Diffusion .....	43
6.2	Dopant Diffusion .....	46
7	Annealing of Vacancies and Interstitials .....	47
7.1	Recombination of Vacancies and Interstitials .....	48
7.2	Hierarchy of Annealing Mechanisms .....	50
8	Conclusion .....	53
	References .....	54

## Hydrogen in SiC

	<i>P. Deák, A. Gali, and B. Aradi</i> .....	57
1	Introduction .....	57
1.1	Hydrogen Incorporation During CVD Growth of <i>p</i> -Type SiC ..	58
1.2	Diffusion of Hydrogen in SiC .....	58
1.3	Effect of Hydrogen on the Concentration of Carriers .....	59
1.4	Spectroscopic Fingerprints of Hydrogen-Related Defects .....	61
1.5	The Main Questions for Theory (in 1998) .....	61
2	Methods of Calculation .....	62
3	Results of Atomic Simulations .....	63
3.1	Hydrogen Related Defects .....	63
3.2	Hydrogen Incorporation Excluding Complexes with Dopants ..	66
3.3	Fast Diffusion of $H^+$ .....	71
3.4	Complexes of Hydrogen with <i>p</i> -Type Dopants .....	72
3.5	Effect of Complex Formation on Hydrogen Incorporation into <i>p</i> -Type Samples and on the Site Selection of Boron .....	73
3.6	Spectroscopic Fingerprints of H-Related Defects .....	75
4	What Have We Learned about Hydrogen in SiC from Theory and Experiments? .....	78
4.1	Incorporation of Hydrogen and Its Effect on the Free Carrier Concentration .....	78
4.2	Diffusion and Trapping of Hydrogen .....	79
4.3	Fingerprints of H-Related Defects .....	81
5	Conclusion .....	84
	References .....	85

## Electronic Properties of Stacking Faults and Thin Cubic Inclusions in SiC Polytypes

	<i>U. Lindefelt and H. Iwata</i> .....	89
1	Introduction .....	89
2	Structural Models .....	90

2.1	The Stacking Patterns Around Stacking Faults in the Most Common SiC Polytypes, and Their Specification ..	90
2.2	The Geometrical Structure of Cubic Polytype Inclusions in 4 <i>H</i> - and 6 <i>H</i> -SiC .....	94
3	Isolated SFs in 3 <i>C</i> -, 4 <i>H</i> -, 6 <i>H</i> - and 15 <i>R</i> -SiC .....	95
3.1	Tools for Characterization and Analysis of Wave Functions....	95
3.2	Band Structures .....	96
3.3	Strong and Weak Wave Function Localization .....	99
3.4	Strong Wave Function Localization and Quantum Confinement .....	103
3.5	Cases Where the SF Acts as a Quantum Barrier .....	105
3.6	Weak Localization .....	105
3.7	In-Plane Effective Masses for the Split-Off Bands and Modified Conduction Band Edges .....	106
3.8	Stacking Fault Energies.....	107
4	Thin Cubic Inclusions in 4 <i>H</i> - and 6 <i>H</i> -SiC .....	109
4.1	Band Structures .....	109
4.2	Strong Wave Function Localization and Quantum Confinement .....	110
4.3	Occurrence of Weak Localization and Wave Function Asymmetry .....	111
4.4	In-Plane Effective Masses in Cubic Inclusions .....	112
4.5	Successive Stacking Fault Energies Around Cubic Inclusions...	113
5	Experimental Observations Explained by the QW Action of SFs ....	114
5.1	Anomalous Resistivity Anisotropy in <i>n</i> -Type 4 <i>H</i> - and 6 <i>H</i> -SiC .....	114
5.2	Electrical Degradation of Bipolar Devices .....	114
5.3	Results from Luminescence Studies .....	115
5.4	Observation of the Occurrence of Double and Single SFs .....	116
	References .....	117

---

## Part II Crystal Growth

---

### Principles and Limitations of Numerical Simulation of SiC Boule Growth by Sublimation

	<i>M. Pons, R. Madar, and T. Billon</i> .....	121
1	Introduction .....	121
2	Modeling and Simulation of the Growth Procedure.....	122
2.1	Experimental Setup .....	122
2.2	State of the Art .....	122
2.3	Modeling and Databases .....	124
2.4	Selected Results in Heat and Mass Transfer .....	126
3	Conclusions .....	133
	References .....	134

**Defect Formation and Reduction During Bulk SiC Growth**

<i>N. Ohtani, M. Katsuno, T. Fujimoto, and H. Yashiro</i> .....	137
1 Introduction .....	137
2 Growth Along the $\langle 0001 \rangle$ $c$ -Axis Direction .....	138
2.1 Micropipes .....	138
2.2 Dislocations .....	145
2.3 Crystal Mosaicity (Domain Structure) .....	149
3 Growth Perpendicular to the $c$ -Axis Direction .....	153
3.1 Advantages over the Growth Along the $c$ -Axis .....	153
3.2 Dislocations and Crystal Mosaicity .....	154
3.3 Stacking Faults .....	156
4 Conclusion .....	160
References .....	160

**High Nitrogen Doping During Bulk Growth of SiC**

<i>H.-J. Rost, D. Schulz, and D. Siche</i> .....	163
1 Introduction .....	163
2 Nitrogen Incorporation .....	164
2.1 Influence of the Growth Temperature .....	166
2.2 Seed Orientation and Homogeneity .....	167
3 The Increase of Conductivity in 4H-SiC .....	169
4 Stacking Fault (SF) Formation .....	171
5 Wafer Properties .....	174
6 Conclusion .....	176
References .....	176

**Homoepitaxial and Heteroepitaxial Growth  
on Step-Free SiC Mesas**

<i>P.G. Neudeck and J.A. Powell</i> .....	179
1 Introduction .....	179
2 Background .....	179
2.1 Role of Steps and Terraces in Epitaxial Growth of SiC .....	181
2.2 Extended Defects in SiC Epilayers .....	183
2.3 Impact of Pre-Growth Surface Treatments on SiC Epitaxial Growth .....	184
3 Step-Free Basal Plane Mesa Formation .....	185
3.1 Process .....	185
3.2 Results .....	186
3.3 Impact on SiC Growth Understanding .....	188
4 Homoepitaxial Growth of Thin SiC Cantilevers .....	188
4.1 Growth Process and Results .....	188
4.2 Process Limitations and Further Optimization .....	192
5 Step-Free Surface Heteroepitaxy of 3C-SiC .....	193
5.1 Experimental Process Description .....	193
5.2 Experimental Results .....	194
5.3 Heteroepitaxial Growth and Defect Formation Model .....	197

6	Conclusion and Future Directions . . . . .	198
6.1	Summary of New Results and Understanding . . . . .	198
6.2	Major Material Issues for Further Study . . . . .	199
6.3	Future Device Applications . . . . .	199
6.4	Conclusion . . . . .	201
	References . . . . .	202

### **Low-Defect 3C-SiC Grown on Undulant-Si (001) Substrates**

<i>H. Nagasawa, K. Yagi, T. Kawahara, N. Hatta, G. Pensl,</i>		
<i>W.J. Choyke, T. Yamada, K.M. Itoh and A. Schöner . . . . .</i>		207
1	Introduction . . . . .	207
2	Mechanism of Generating Planar Defects at the 3C-SiC/Si Interface . . . . .	208
3	Principle of Planar Defect Reduction in 3C-SiC . . . . .	210
4	Experimental . . . . .	211
4.1	Preparation of Si Substrate . . . . .	211
4.2	3C-SiC Growth Process . . . . .	212
5	Effect of “Undulant-Si” on the Reduction of Planar Defects . . . . .	212
5.1	Morphologic Study . . . . .	212
5.2	Microscopic Observation Using TEM . . . . .	213
5.3	Mechanism for Reducing Planar Defects in 3C-SiC Grown on “Undulant-Si” . . . . .	216
6	Properties of 3C-SiC Grown on “Undulant-Si” . . . . .	217
6.1	Hall Effect Investigations . . . . .	217
6.2	Low Temperature Photoluminescence (LTPL) Measurements . .	218
6.3	Temperature Dependence of PL Spectra . . . . .	221
7	Properties of 3C-SiC Homoepitaxial Layer Grown on 3C-SiC Heteroepitaxial Layer on “Undulant-Si” . . . . .	223
7.1	Homoepitaxial Growth of 3C-SiC . . . . .	224
7.2	Deep Level Transient Spectroscopy (DLTS) Investigations . . . .	224
7.3	Interface State Density $D_{it}$ of $n$ - and $p$ -Type 3C-SiC MOS Capacitors . . . . .	225
8	Conclusion . . . . .	226
	References . . . . .	227

### **New Development in Hot Wall Vapor Phase Epitaxial Growth of Silicon Carbide**

<i>A. Schöner . . . . .</i>		229
1	Introduction . . . . .	229
1.1	Brief History on Vapor Phase Epitaxy of SiC . . . . .	229
1.2	Horizontal Hot Wall Reactor in General . . . . .	230
2	Homoepitaxial VPE-Growth of SiC . . . . .	231
2.1	Growth Process . . . . .	231
2.2	Substrate Preparation and Step-Controlled Epitaxy . . . . .	233
2.3	Site Competition Epitaxy . . . . .	233
2.4	Recent Growth Process Improvements . . . . .	234

3	New Generation of Hot Wall CVD Reactors . . . . .	238
3.1	Up-Scaling of the Standard Hot Wall VPE Reactor . . . . .	238
3.2	Reactor Design Improvements . . . . .	239
3.3	Hot Wall Reactor with Mechanical Rotation . . . . .	240
3.4	Multi Wafer Hot Wall Reactor . . . . .	247
4	Future Development . . . . .	248
5	Conclusion . . . . .	249
	References . . . . .	249

## **Formation of SiC Thin Films by Ion Beam Synthesis**

<i>J.K.N. Lindner</i> . . . . .	251
1 Introduction . . . . .	251
2 Fundamentals of Ion Beam Synthesis . . . . .	251
3 Basic Considerations on the IBS of SiC in Si . . . . .	254
4 Early Studies on the IBS of SiC . . . . .	256
5 Influence of Dose and Implantation Temperature . . . . .	260
6 The Annealed State . . . . .	265
7 SiC Thin Films at the Surface and Deep in the Si Substrate . . . . .	266
8 Multilayer Systems Including IBS Formed Buried SiC Layers . . . . .	267
8.1 SiC Layers Combined with SiO <sub>2</sub> . . . . .	267
8.2 Metallization of IBS Formed SiC Layers . . . . .	268
9 Applications of Buried SiC Layers . . . . .	269
9.1 IBIEC: Ion Beam Induced Epitaxial Crystallization of SiC . . . . .	269
9.2 Doping . . . . .	269
9.3 Optoelectronics . . . . .	270
9.4 Field Emission . . . . .	270
9.5 Large-Area Pseudosubstrates for Epilayer Growth . . . . .	271
9.6 Etch Stop Layers for Micromechanics . . . . .	271
9.7 Cantilever Beams . . . . .	272
9.8 Buried SiC Microstructures by MeV Ion Projection . . . . .	272
10 Conclusion . . . . .	273
References . . . . .	273

---

## **Part III Surface and Interface Properties**

---

### **Atomic Structure of SiC Surfaces**

<i>U. Starke</i> .....	281
1 Introduction .....	281
2 Crystal Structure and Surface Termination.....	283
2.1 Bulk Structure .....	283
2.2 Hexagonal Surfaces .....	285
2.3 Non-Basal Plane Surfaces .....	287
3 Experimental Methods .....	287
3.1 Preparation Procedures.....	287
3.2 Surface Analysis Techniques.....	288

4	Surface Reconstruction on SiC(0001) .....	289
4.1	Phase Diagram on SiC(0001) .....	289
4.2	Clean Surface Reconstructions .....	291
4.3	Epitaxial Systems and Adsorbates .....	300
5	Other Surface Orientations .....	305
5.1	Phase Diagram of the SiC(000 $\bar{1}$ )-Surface .....	305
5.2	A Complex (3 $\times$ 3) Reconstruction Phase on SiC(000 $\bar{1}$ ) .....	307
5.3	Atomic Structure of the (2 $\times$ 2) <sub>C</sub> -Phase on SiC(000 $\bar{1}$ ) .....	308
5.4	<i>a</i> -Planes and Diagonal Cuts Through the Hexagonal Unit Cell .....	309
6	Conclusion .....	309
	References .....	311

**The Continuum of Interface-Induced Gap States –  
The Unifying Concept of the Band Lineup  
at Semiconductor Interfaces – Application to Silicon Carbide**

	<i>W. Mönch</i> .....	317
1	Introduction .....	317
2	Experimental SiC Data Base .....	319
2.1	Barrier Heights of Laterally Homogeneous SiC Schottky Contacts .....	319
2.2	Valence-Band Offsets at SiC Heterostructures .....	327
3	IFIGS-and-Electronegativity Theory .....	329
4	Comparison of Experiment and Theory .....	331
4.1	IFIGS-and-Electronegativity Theory .....	331
4.2	Intrinsic Non-Uniformities in Schottky Contacts .....	336
4.3	Ab-Initio Theories .....	337
5	Conclusions .....	338
	References .....	339

**Contributions to the Density of Interface States  
in SiC MOS Structures**

	<i>V.V. Afanas'ev, F. Ciobanu, G. Pensl, and A. Stesmans</i> .....	343
1	Introduction .....	343
2	SiC/SiO <sub>2</sub> Interface State Spectrum .....	344
2.1	Energy Distribution .....	344
2.2	Sensitivity of $D_{it}$ to SiC Polytype .....	345
2.3	Sensitivity of $D_{it}$ to the Crystallographic Orientation of the SiC Surface .....	346
2.4	Effects of Annealing on $D_{it}$ .....	347
2.5	Thermally-Induced Interface Trap Generation .....	349
2.6	Injection-Induced SiC/SiO <sub>2</sub> Interface State Generation .....	350
3	Origin and Models of SiC/SiO <sub>2</sub> Interface States .....	352
3.1	Interface States in the Model System: (111)Si/SiO <sub>2</sub> .....	352
3.2	Dangling Bonds as SiC/SiO <sub>2</sub> Interface States? .....	355
3.3	Oxide-Related Traps .....	357

3.4	Hydrogen-Related States .....	357
3.5	Carbon Cluster Model of SiC/SiO <sub>2</sub> Interface States .....	358
3.6	Other SiC-Specific Contributions to $D_{it}$ .....	360
4	Alternative Insulators on SiC .....	362
5	Conclusions .....	365
	References .....	366

### Properties of Nitrided Oxides on SiC

<i>S. Dimitrijević, H.B. Harrison, P. Tanner, K.Y. Cheong, and J. Han</i> ...	373
1 Introduction .....	373
2 Growth of Nitrided Oxides .....	373
3 Physical Characterization .....	376
4 Interface and Near-Interface Defects .....	378
5 Characteristics of MOS Devices .....	381
6 Conclusions .....	385
References .....	385

### Hall Effect Studies of Electron Mobility and Trapping at the SiC/SiO<sub>2</sub> Interface

<i>N.S. Saks</i> .....	387
1 Introduction .....	387
2 Sample Design and Hall Measurements .....	388
2.1 Fabrication of Test Devices .....	388
2.2 Hall Bar Design .....	389
2.3 Hall Measurements .....	389
3 MOSFET Mobility .....	391
3.1 Comparison of Effective and Hall Mobility .....	391
3.2 Comparison of 4H- and 6H-SiC Mobility .....	394
3.3 Temperature Dependence .....	397
4 Using Hall Data to Calculate $D_{it}(E)$ .....	399
4.1 Alternative $D_{it}(E)$ Measurement Techniques .....	399
4.2 Hall Measurements of $D_{it}(E)$ .....	400
4.3 Hall Measurements of $D_{it}(E)$ in SiC .....	405
4.4 Temperature Dependence of $D_{it}(E)$ in 4H-SiC .....	407
References .....	409

---

## Part IV Characterization

---

### Optical Properties of SiC: 1997–2002

<i>W.J. Choyke and R.P. Devaty</i> .....	413
1 Introduction .....	413
2 Absorption Coefficient and Penetration Depth .....	413
3 Band Edge Absorption and Valence Band Splittings .....	417
4 Biedermann Absorption Bands in Nitrogen Doped SiC .....	418
5 Erbium .....	420

6	Intrinsic Defects . . . . .	421
6.1	The $D_I$ Defect . . . . .	422
6.2	The $D_{II}$ Defect . . . . .	424
6.3	The $E_A$ Spectrum . . . . .	426
7	Stacking Faults and Nano-Polytypes . . . . .	427
8	Optical Characterization of Wafers . . . . .	431
	References . . . . .	433

### **Cyclotron Resonance Studies of Effective Masses and Band Structure in SiC**

<i>N.T. Son, C. Persson, U. Lindefelt, W.M. Chen, B.K. Meyer, D.M. Hofmann, and E. Janzén . . . . .</i>		437
1	Introduction . . . . .	437
2	Band Structure and Effective Masses from Calculations . . . . .	439
2.1	Electronic Band Structure . . . . .	439
2.2	Effective Masses . . . . .	443
3	Band Structure and Effective Masses from ODCR Experiments . . . . .	447
3.1	4 <i>H</i> -SiC . . . . .	447
3.2	6 <i>H</i> -SiC . . . . .	452
3.3	Comparison Between Calculations and Experiments . . . . .	456
4	Conclusion . . . . .	457
	References . . . . .	458

### **Electronic Structure of Deep Defects in SiC**

<i>N.T. Son, Mt. Wagner, C.G. Hemmingsson, L. Storasta, B. Magnusson, W.M. Chen, S. Greulich-Weber, J.-M. Spaeth, and E. Janzén . . . . .</i>		461
1	Introduction . . . . .	461
2	Paramagnetic and Photoluminescence Centers . . . . .	463
2.1	Carbon Vacancy . . . . .	463
2.2	Silicon Antisite Related Defect . . . . .	465
2.3	Other EPR Centers in Irradiated <i>p</i> -Type SiC . . . . .	467
2.4	Si Vacancy Related Centers . . . . .	470
2.5	( $V_C$ -C <sub>Si</sub> ) Center . . . . .	473
2.6	Neutral Cr <sup>4+</sup> Center . . . . .	475
2.7	UD-1, UD-2 and UD-3 Centers . . . . .	477
3	DLTS of Intrinsic Defects . . . . .	480
4	Conclusion . . . . .	487
	References . . . . .	488

### **Phosphorus-Related Centers in SiC**

<i>M. Laube, F. Schmid, K. Semmelroth, G. Pensl, R.P. Devaty, W.J. Choyke, G. Wagner, and M. Maier . . . . .</i>		493
1	Introduction . . . . .	493
2	Doping of SiC with Phosphorus Donors . . . . .	493
3	Phosphorus Neutral Donor Bound Exciton Complex in 6 <i>H</i> -SiC . . . . .	495

4	IR Transmission Measurements on Phosphorus Donors in 6H-SiC . . .	499
5	Electrical Properties of P Donors . . . . .	502
6	Comparison of the Electrical Activation of Implanted P <sup>+</sup> - and N <sup>+</sup> -Ions . . . . .	507
7	Conclusion . . . . .	512
	References . . . . .	513

### **Hall Scattering Factor for Electrons and Holes in SiC**

	<i>F. Schmid, M. Krieger, M. Laube, G. Pensl, and G. Wagner</i> . . . . .	517
1	Analysis of Hall Effect Data . . . . .	517
2	Hall Scattering Factor . . . . .	522
3	Hall Scattering Factor for Electrons in 4H- and 6H-SiC . . . . .	523
4	Hall Scattering Factor for Holes in 4H- and 6H-SiC . . . . .	525
4.1	Determination of the Hall Scattering Factor of Holes in 4H- and 6H-SiC . . . . .	526
4.2	Test of the Hall Scattering Factor of Holes in 4H-SiC . . . . .	530
5	Conclusion . . . . .	534
	References . . . . .	535

### **Radiotracer Deep Level Transient Spectroscopy**

	<i>N. Achtziger and W. Witthuhn</i> . . . . .	537
1	Introduction . . . . .	537
2	Radiotracer Experiments in Semiconductors . . . . .	538
3	Radioactive Implantation: Requirements and Techniques . . . . .	539
4	Selected Aspects of Radiotracer Deep Level Transient Spectroscopy .	543
4.1	Deep Level Transient Spectroscopy (DLTS) . . . . .	543
4.2	Number of Isotopes Involved per Band Gap State . . . . .	544
4.3	Stability of the Initial Configuration . . . . .	545
4.4	Degree of Electrical Activation . . . . .	546
4.5	Decay-Induced Defects . . . . .	546
5	Deep Levels Detected by Radiotracer DLTS . . . . .	547
5.1	Deep Levels of Be, Zn, Cd . . . . .	548
5.2	Deep Levels of the Transition Metals Ti, Cr, and V . . . . .	549
5.3	Transition Metals Ta and W . . . . .	555
5.4	Deep Rare Earth Related Levels . . . . .	556
6	Summary and Conclusions . . . . .	557
	References . . . . .	559

### **Vacancy Defects Detected by Positron Annihilation**

	<i>A. Kawasuso, M. Weidner, F. Redmann, T. Frank, P. Sperr, G. Kögel, M. Yoshikawa, H. Itoh, R. Krause-Rehberg, W. Triftshäuser, and G. Pensl</i> . . . . .	563
1	Introduction . . . . .	563
2	Principle of Positron Annihilation . . . . .	563
3	Radiation-Induced Vacancy Defects in SiC . . . . .	565

3.1	Electron Irradiation .....	565
3.2	He Implantation .....	573
3.3	Polytype Dependent Vacancy Annealing .....	576
4	Correlation Between Positron Annihilation Centers and Electronic Energy Levels .....	576
5	Conclusion .....	581
	References .....	581

## **Characterization of Defects in SiC Crystals by Raman Scattering**

	<i>S. Nakashima and H. Harima</i> .....	585
1	Introduction .....	585
2	Detection of Defects by Raman Scattering .....	586
3	Detection of Stacking Faults in 4 <i>H</i> - and 6 <i>H</i> -SiC Using the (0001) Face .....	590
3.1	General Description on Detection of Defects .....	590
3.2	Case Studies of Defects in 4 <i>H</i> -SiC .....	591
4	Characterization of 3 <i>C</i> -SiC Epitaxial Films on Si .....	593
4.1	Stacking Faults in Epitaxial 3 <i>C</i> -SiC Layer .....	593
4.2	Defects in Heteroepitaxial Films .....	595
4.3	Defects in 3 <i>C</i> -SiC Homoepitaxial Films .....	596
4.4	Elimination of the Phonon Polariton Mode .....	596
4.5	Raman Intensity Profiles of SiC with Stacking Disorder .....	596
5	Raman Scattering Related to Damages and Impurities .....	597
6	Influence of Defects and Impurities on the Local Electronic Properties .....	598
6.1	Characterization of Electronic Properties by Raman Analysis ..	598
6.2	Changes in Electrical Properties by Defects .....	600
7	Conclusion .....	603
	References .....	604

## **Characterization of Low-Dimensional Structures in SiC Using Advanced Transmission Electron Microscopy**

	<i>U. Kaiser</i> .....	607
1	Introduction .....	607
2	Experimental .....	608
2.1	Lattice Parameter Determination Using TEM .....	608
2.2	Z-Contrast Imaging .....	609
2.3	ALCHEMI .....	610
2.4	Computation Techniques .....	610
2.5	TEM Sample Preparation .....	611
3	Applications of TEM Techniques to the Study of Low-Dimensional Structures .....	613
3.1	Lattice Parameters of Thin Cubic MBE-SiC Films and Quantum Well Structures .....	613

3.2	The Formation Process of Embedded Nanocrystals in Hexagonal SiC Created by Ion Implantation and Annealing.....	614
3.3	Properties of Embedded Nanocrystals Created after Er, Ge or Si Implantation-Annealing .....	617
4	Conclusion.....	625
	References .....	627

### **Synchrotron White Beam X-Ray Topography and High Resolution X-Ray Diffraction Studies of Defects in SiC Substrates, Epilayers and Device Structures**

	<i>M. Dudley, X. Huang, and W.M. Vetter</i> .....	629
1	Introduction .....	629
2	Back-Reflection Techniques .....	631
3	Transmission Topography Techniques .....	634
4	Characterization of SiC Heterostructures .....	638
5	Conclusions .....	646
	References .....	647

## **Part V Processing**

### **Ohmic Contacts for Power Devices on SiC**

	<i>S. Tanimoto, H. Okushi, and K. Arai</i> .....	651
1	Introduction .....	651
2	Critical Review of Ohmic Contacts on 4H-SiC .....	652
2.1	Contacts in the <i>n</i> -Type Region .....	652
2.2	Contacts in the <i>p</i> -Type Region .....	654
3	Contact Design for Practical Devices .....	654
3.1	Problems with Conventional Techniques .....	654
3.2	Preferred Contact Structure.....	657
4	Integration of Contacts into Vertical Power MOSFETs .....	658
4.1	Preliminary Study .....	658
4.2	Reliability of Contacts.....	661
4.3	Process Design and Fabrication of Power MOSFETs .....	664
5	Conclusion.....	666
	References .....	667

### **Micromachining of SiC**

	<i>C.A. Zorman and M. Mehregany</i> .....	671
1	Introduction .....	671
2	Thin Film Growth Processes for SiC MEMS .....	672
2.1	Single Crystal SiC .....	673
2.2	Polycrystalline SiC.....	674
2.3	Amorphous SiC .....	675

3	SiC Bulk Micromachining .....	676
4	SiC Micromolding .....	683
5	SiC Surface Micromachining .....	685
6	Wafer Bonding Techniques .....	690
7	Concluding Remarks .....	695
	References .....	695

### **Surface Preparation Techniques for SiC Wafers**

	<i>S. Monnoye, D. Turover, and P. Vicente</i> .....	699
1	Introduction .....	699
2	Preparation Techniques .....	699
2.1	Grinding/Lapping and Mechanical Polishing .....	699
2.2	Chemical Mechanical Polishing and Etching .....	700
2.3	Cleaning .....	702
3	Results .....	703
3.1	Polishing Results .....	703
3.2	Contamination Results .....	706
3.3	Impact of Surface Preparation on the Epitaxy and the Device Performances .....	706
3.4	Prospective .....	707
4	Conclusion .....	707
	References .....	708

### **Epitaxial Growth and Device Processing of SiC on Non-Basal Planes**

	<i>T. Kimoto, H. Yano, Y. Negoro, K. Hashimoto, and H. Matsunami</i> ...	711
1	Introduction .....	711
2	Non-Basal Planes in 4H-SiC .....	712
3	Chemical Vapor Deposition for Non-Basal Planes .....	713
3.1	Homoepitaxial Growth Process .....	713
3.2	Unintentionally Doped Epilayers .....	714
3.3	Nitrogen and Boron Doping .....	717
3.4	Structural Defects in 4H-SiC(11-20) Epilayers .....	719
3.5	Structural Defects in 4H-SiC(03-38) Epilayers .....	720
3.6	Effect of Structural Defects on Performance of Schottky Diodes .....	721
4	Device Processing .....	722
4.1	Phosphorus Ion Implantation and Implantation Damage Reduction .....	722
4.2	Performance of MOSFETs Fabricated on 4H-SiC(11-20) .....	725
4.3	MOS Interface Properties .....	727
5	Conclusions .....	730
	References .....	731

---

**Part VI Devices**


---

**SiC Power Bipolar Transistors and Thyristors**

<i>T.P. Chow, N. Ramungul, J. Fedison, and Y. Tang</i> .....	737
1 Introduction .....	737
2 Figures of Merit .....	738
3 Power Bipolar Transistors .....	742
3.1 Bipolar Junction Transistor (BJT)/Darlington Configuration ..	745
3.2 Bipolar-Mode JFET/ Static Induction Injected Accumulated FET (SIAFET) .....	748
3.3 Insulated-Gate Bipolar Transistor (IGBT) .....	749
3.4 MOS-Gated Bipolar Transistor (MGT) .....	752
3.5 Heterojunction Bipolar Transistor (HBT) .....	755
4 Power Thyristors .....	755
4.1 Silicon Controlled Rectifier (SCR) .....	755
4.2 Gate Turn-Off Thyristor (GTO) .....	756
4.3 Light Triggered Thyristor .....	760
4.4 Field-Controlled Thyristor .....	760
4.5 MOS-Gated Thyristors .....	762
5 Materials and Process Challenges .....	762
6 Conclusion .....	763
References .....	764

**High Voltage SiC Devices**

<i>Y. Sugawara</i> .....	769
1 Introduction .....	769
2 High Voltage 4H-SiC Diodes .....	770
2.1 5.0 kV 4H-SiC SBD [2] .....	770
2.2 3.7 kV 4H-SiC JBS Diode [4, 5] .....	771
2.3 6.2–19.3 kV 4H-SiC <i>pn</i> Diode [5, 6] .....	773
3 High Voltage 4H-SiC FETs .....	776
3.1 4.5 kV SIAFET [7] and 5.0 kV SEMOSFET [8] .....	776
3.2 5.3 kV SEJFET [9, 10] .....	777
4 High Voltage High Current SiC Module .....	779
4.1 Module Design and Fabrication .....	780
4.2 Diode Module Characteristics [13] .....	781
5 Conclusion .....	782
References .....	782

**Power MOSFETs in 4H-SiC: Device Design and Technology**

<i>A. Agarwal, S.-H. Ryu, and J. Palmour</i> .....	785
1 Introduction .....	785
2 Device Structures and Operation of Power MOSFETs .....	786
3 Design of the Drift Layer .....	788

3.1	Punch-Through Design .....	789
3.2	Non-Punch-Through Design .....	790
4	On-Resistance .....	791
4.1	Channel Resistance, $R_{ch}$ .....	791
4.2	JFET Region Resistance .....	792
4.3	Drift Layer Resistance .....	793
4.4	Optimization of the JFET Region .....	793
5	Reliability of the Gate Dielectric .....	795
5.1	On-State Under Positive Gate Bias .....	795
5.2	Off-State Under Negative Gate Bias .....	798
6	Design of the MOSFET Structure: Various Considerations .....	799
6.1	P-Well Design .....	801
6.2	Threshold Voltage .....	802
6.3	Cell Design .....	804
7	Process Integration .....	805
7.1	Fabrication Process Sequence .....	805
7.2	Processing Considerations .....	807
8	Results on 2.4 kV Design .....	808
	References .....	810

## **Normally-Off Accumulation-Mode Epi-Channel Field Effect Transistor**

<i>R.K. Malhan</i> .....	813
1 Introduction .....	813
2 Design of SiC Power MOSFETs .....	814
2.1 Accumulation-Mode SiC ECFET .....	814
2.2 Selection of SiC Polytype: Bulk Electron Mobility Anisotropy .	820
2.3 Selection of Crystal Plane: Channel Mobility Anisotropy .....	820
3 Key Device Processing Technologies .....	821
3.1 Quality of 4H-SiC Large Size Wafers .....	821
3.2 Thermally Oxidized SiO <sub>2</sub> /SiC MOS Interface .....	823
3.3 Selective Ion-Implantation Doping in SiC .....	826
4 Application of MOS Based Power Devices in HEV Inverters .....	832
5 Conclusions .....	835
References .....	835

## **Development of SiC Devices for Microwave and RF Power Amplifiers**

<i>E. Morvan, A. Kerlain, C. Dua, and C. Brylinski</i> .....	839
1 Introduction: At the End of the Feasibility Period .....	839
1.1 RF and Microwave Power: Switching vs. Analog .....	839
1.2 Wide Bandgap Semiconductors for Analog RF Power Applications: The Challenge of Thermal Management .....	840

1.3	The Small World of Analog Microwave Power .....	841
1.4	Troubles with Traps: The Importance of Getting “Clean” Material.....	842
1.5	Approaching the Market .....	843
2	Key Issues on the Way to SiC <i>RF</i> Power Device Industry.....	844
2.1	Device Topology .....	844
2.2	The Substrate Issue .....	846
2.3	Schottky Contacts for SiC Mesfet Gate .....	851
2.4	Transistor Design and Fabrication Process .....	856
2.5	Passivation .....	859
2.6	Chip Lay-Out .....	860
2.7	Packaging.....	861
3	Perspectives .....	864
3.1	Need for Better <i>RF</i> and Microwave Power Devices .....	864
3.2	Si and III-V Technologies Close to the Limit .....	865
3.3	Long Term Is Diamond and Related, for Sure .....	865
3.4	Minimum Time to Market for SiC and III-N Devices .....	865
3.5	III-N Devices Will Take It All... When They Arrive on the Market .....	865
3.6	To Go or Not to Go into the Industry of SiC <i>RF</i> Power Devices .....	866
	References .....	867

## **Advances in SiC Field Effect Gas Sensors**

	<i>A. Lloyd Spetz and S. Savage</i> .....	869
1	Introduction .....	869
2	Detection Mechanism of Field Effect Gas Sensors .....	870
2.1	Gas Sensing Principle .....	870
2.2	Selectivity at Different Temperatures .....	872
3	Field Effect Chemical Gas Sensor Devices.....	874
3.1	Capacitor Sensors.....	875
3.2	Schottky Sensors .....	876
3.3	Transistor Sensors .....	879
3.4	<i>p-n</i> Junction Diodes.....	880
4	Sensor Properties .....	880
4.1	Speed of Response .....	880
4.2	Long-Term Stability.....	883
5	Experimental .....	885
5.1	Sample Preparation .....	885
5.2	Mounting .....	885
5.3	Device Operation .....	886

6 Applications .....	886
6.1 Cylinder Specific Monitoring .....	887
6.2 Cold Start .....	887
6.3 NH <sub>3</sub> Sensor for Use in Selective Catalytic Reduction of Diesel Exhausts .....	888
6.4 Flue Gas Monitoring .....	890
7 Outlook and Conclusions .....	891
References .....	893
<b>Index</b> .....	897

# List of Contributors

## **N. Achtziger**

Friedrich-Schiller-Universität Jena,  
Institut für Festkörperphysik,  
Max – Wien – Platz 1,  
07743 Jena, Germany  
NorbertAchtziger@web.de

## **V.V. Afanas'ev**

Laboratory of Semiconductor  
Physics,  
Department of Physics  
and Astronomy,  
University of Leuven,  
Celestijnenlaan 200D,  
3001 Leuven, Belgium  
valeri.afanasiev@fys.  
kuleuven.ac.be

## **A. Agarwal**

Silicon Carbide Power Devices,  
Cree, Inc.,  
4600 Silicon Drive,  
Durham, NC 27703, USA  
Anant\_agarwal@cree.com

## **B. Aradi**

Department of Atomic Physics,  
Budapest University of Technology  
and Economics,  
Budapest, Budafoki út 8,  
1111, Hungary  
aradi@surphy.fat.bme.hu

## **K. Arai**

Power Electronics Research Center,  
National Institute of Advanced  
Industrial Science  
and Technology (AIST),  
AIST Tsukuba Central 2  
1-1-1, Umezono, Tsukuba,  
Ibaraki 305-8568, Japan  
*and*  
Ultra-Low-Loss Power Device  
Technology Research Body (UPR)  
arai-kazuo@aist.go.jp

## **F. Bechstedt**

Friedrich-Schiller-Universität Jena,  
Institut für Festkörpertheorie  
und Theoretische Optik,  
Max-Wien-Platz 1,  
07743 Jena, Germany  
bechsted@ifto.physik.  
uni-jena.de

## **T. Billon**

CEA-LETI,  
38054 Grenoble Cedex 9, France  
Thierry.Billon@cea.fr

## **M. Bockstedte**

Lehrstuhl für Theoretische  
Festkörperphysik,  
Universität Erlangen-Nürnberg,  
Staudtstrasse 7/B2,  
91058 Erlangen, Germany  
Michel.Bockstedte@physik.  
uni-erlangen.de

**C. Brylinski**

Thales Research and Technology,  
Domaine de Corbeville,  
91404 Orsay Cedex, France  
christian.brylinski@thales  
group.com

**W.M. Chen**

Department of Physics  
and Measurement Technology,  
Linköping University,  
581 83 Linköping, Sweden  
wmc@ifm.liu.se

**K.Y. Cheong**

School of Microelectronic  
Engineering,  
Griffith University,  
Nathan, Queensland 4111,  
Australia  
k.cheong@griffith.edu.au  
*and*  
School of Materials and  
Mineral Resources Engineering,  
University Sains Malaysia,  
Engineering Campus,  
14300 Nibong Tebal,  
Seberang Perai,  
Penang, Malaysia

**T.P. Chow**

Center for Power  
Electronics Systems  
Rensselaer Polytechnic Institute  
110 8th Street, CII 6015,  
Troy, NY 12180, USA  
chowt@rpi.edu

**W.J. Choyke**

University of Pittsburgh,  
Department of Physics  
and Astronomy,  
100 Allen Hall,  
Pittsburgh, PA 15260, USA  
choyke@imap.pitt.edu  
choyke+@pitt.edu

**F. Ciobanu**

Institute of Applied Physics,  
University of Erlangen-Nürnberg,  
Staudtstrasse 7 / A3  
91058 Erlangen, Germany  
Florin.Ciobanu@physik.  
uni-erlangen.de

**P. Deák**

Department of Atomic Physics,  
Budapest University of Technology  
and Economics,  
Budapest, Budafoki út 8,  
1111, Hungary  
p.deak@eik.bme.hu

**R.P. Devaty**

University of Pittsburgh,  
Department of Physics  
and Astronomy,  
100 Allen Hall,  
Pittsburgh, PA 15260, USA  
devaty@imap.pitt.edu

**S. Dimitrijević**

School of Microelectronic  
Engineering,  
Griffith University,  
Nathan, Queensland 4111,  
Australia  
s.dimitrijević@griffith.edu.au

**C. Dua**

Thales Research and Technology,  
Domaine de Corbeville,  
91404 Orsay Cedex, France  
christian.dua@thalesgroup.com

**M. Dudley**

Department of Materials Science  
and Engineering,  
State University of New York  
at Stony Brook,  
Stony Brook, NY 11974-2275, USA  
michael.dudley@sunysb.edu

**J. Fedison**

Semiconductor Technology  
Laboratory,  
GE Global Research Center,  
KW-C1327  
fedison@crd.ge.com

**T. Frank**

Institute of Applied Physics,  
University of Erlangen-Nürnberg,  
Staudtstrasse 7 / A3  
91058 Erlangen, Germany  
Thomas.Frank@physik.  
uni-erlangen.de

**J. Furthmüller**

Friedrich-Schiller-Universität Jena,  
Institut für Festkörpertheorie  
und Theoretische Optik,  
Max-Wien-Platz 1,  
07743 Jena, Germany  
furth@ifto.physik.uni-jena.de

**T. Fujimoto**

Nippon Steel Corporation,  
Advanced Technology Research  
Laboratories,  
20-1 Shintomi, Futtsu,  
Chiba 293-8511, Japan  
tfuji@re.nsc.co.jp

**Á. Gali**

Department of Atomic Physics,  
Budapest University of Technology  
and Economics,  
Budapest, Budafoki út 8,  
1111, Hungary  
agali@eik.bme.hu

**S. Greulich-Weber**

Fakultät für Naturwissenschaften,  
Physikdepartment,  
Universität Paderborn,  
33095 Paderborn,  
Germany  
siegmond@familie-weber-netz.de

**U. Grossner**

The University of Oslo,  
Fysisk Institutt,  
Postboks 1048 Blindern,  
0316 Oslo, Norway  
ulrike.grossner@fys.uio.no

**J. Han**

School of Microelectronic  
Engineering,  
Griffith University,  
Nathan, Queensland 4111,  
Australia  
j.han@griffith.edu.au

**H. Harima**

Department of Electronics  
and Information Science,  
Kyoto Institute of Technology,  
Matsugasaki, Sakyo-ku,  
Kyoto 606-8585, Japan  
harima@dj.kit.ac.jp

**H.B. Harrison**

School of Microelectronic  
Engineering,  
Griffith University,  
Nathan, Queensland 4111,  
Australia  
barry.harrison@griffith.edu.au

**K. Hashimoto**

Department of Electronic  
Engineering,  
Kyoto University,  
Yoshidahonmachi, Sakyo,  
Kyoto 606-8501, Japan  
k-hash@semicon.kuee.  
kyoto-u.ac.jp

**N. Hatta**

Hoya Advanced Semiconductor  
Technologies Co. Ltd.,  
1-17-16 Tanashioda, Sagamihara,  
Kanagawa 229-1125, Japan  
hatta@hast.co.jp

**C.G. Hemmingsson**

Department of Physics  
and Measurement Technology,  
Linköping University,  
581 83 Linköping, Sweden  
cah@ifm.liu.se

**D.M. Hofmann**

Physical Institute,  
University Giessen,  
Heinrich-Buff-Ring 16,  
35392 Giessen, Germany  
D.M.Hofmann@exp1.  
physik.uni-giessen.de

**X. Huang**

Department of Materials Science  
and Engineering,  
State University of New York  
at Stony Brook,  
Stony Brook, NY 11974-2275, USA  
xiahuang@ms.cc.sunysb.edu

**H. Itoh**

Japan Atomic Energy  
Research Institute,  
Watanuki, 1233, Takasaki,  
Gunma, 370-1292, Japan  
itohq@taka.jaeri.go.jp

**K.M. Itoh**

Department of Applied Physics  
and Physico-Informatics,  
Keio University, 3-14-1 Hiyoshi,  
Kohoku-ku, Yokohama 223-8522,  
Japan  
kitoh@appi.keio.ac.jp

**H. Iwata**

Department of Physics  
and Measurement Technology,  
Linköping University,  
581 83 Linköping, Sweden  
hisaomi@ifm.liu.se

**E. Janzén**

Department of Physics  
and Measurement Technology,  
Linköping University,  
581 83 Linköping, Sweden  
erj@ifm.liu.se

**U. Kaiser**

Friedrich-Schiller-Universität Jena,  
Institut für Festkörperphysik,  
Max-Wien-Platz 1,  
07743 Jena, Germany  
kaiser@pinet.uni-jena.de

**M. Katsuno**

Nippon Steel Corporation,  
Advanced Technology Research  
Laboratories,  
20-1 Shintomi, Futtsu,  
Chiba 293-8511, Japan  
katsuno@re.nsc.co.jp

**T. Kawahara**

Hoya Advanced Semiconductor  
Technologies Co. Ltd.,  
1-17-16 Tanashioda, Sagamihara,  
Kanagawa 229-1125, Japan  
kawahara@hast.co.jp

**A. Kawasuso**

Japan Atomic Energy  
Research Institute,  
Watanuki, 1233, Takasaki,  
Gunma, 370-1292, Japan  
ak@taka.jaeri.go.jp

**A. Kerlain**

Thales Research and Technology,  
 Domaine de Corbeville,  
 91404 Orsay Cedex, France  
[alexandre.kerlain@thalesgroup.com](mailto:alexandre.kerlain@thalesgroup.com)

**G. Kögel**

Universität der Bundeswehr  
 München,  
 85577 Neubiberg, Germany  
[gottfried.koegel@rz.unibw-muenchen.de](mailto:gottfried.koegel@rz.unibw-muenchen.de)

**R. Krause-Rehberg**

Martin-Luther-Universität,  
 Halle-Wittenberg,  
 Friedemann-Bach-Platz 6,  
 06108 Halle, Germany  
[krause@physik.uni-halle.de](mailto:krause@physik.uni-halle.de)

**M. Krieger**

Institute of Applied Physics,  
 University of Erlangen-Nürnberg,  
 Staudtstrasse 7 / A3  
 91058 Erlangen, Germany  
[Michael.Krieger@physik.uni-erlangen.de](mailto:Michael.Krieger@physik.uni-erlangen.de)

**T. Kimoto**

Department of Electronic  
 Engineering,  
 Kyoto University,  
 Yoshidahonmachi, Sakyo,  
 Kyoto 606-8501, Japan  
[kimoto@kuee.kyoto-u.ac.jp](mailto:kimoto@kuee.kyoto-u.ac.jp)

**M. Laube**

Institute of Applied Physics,  
 University of Erlangen-Nürnberg,  
 Staudtstrasse 7 / A3  
 91058 Erlangen, Germany  
[Michael.Laube@physik.uni-erlangen.de](mailto:Michael.Laube@physik.uni-erlangen.de)

**U. Lindefelt**

Department of Information  
 Technology and Media,  
 Mid-Sweden University,  
 85170 Sundsvall, Sweden  
[Ulf.Lindefelt@mh.se](mailto:Ulf.Lindefelt@mh.se)

**J.K.N. Lindner**

Institute of Physics,  
 University of Augsburg,  
 86135 Augsburg, Germany  
[lindner@physik.uni-augsburg.de](mailto:lindner@physik.uni-augsburg.de)

**A. Lloyd Spetz**

S-SENCE and Div.  
 of Applied Physics,  
 Linköping University,  
 581 83 Linköping, Sweden  
[asz@ifm.liu.se](mailto:asz@ifm.liu.se)

**R. Madar**

Institut National Polytechnique  
 de Grenoble,  
 LMGP-CNRS, BP 46,  
 38402, Saint Martin D'Hères,  
 France  
[Roland.Madar@inpg.fr](mailto:Roland.Madar@inpg.fr)

**B. Magnusson**

Department of Physics  
 and Measurement Technology,  
 Linköping University,  
 581 83 Linköping, Sweden  
[bjmag@ifm.liu.se](mailto:bjmag@ifm.liu.se)  
*and*  
 Okmetic AB  
 Hans Meijers väg 2,  
 583 30 Linköping, Sweden  
[bjorn.magnusson@okmetic.com](mailto:bjorn.magnusson@okmetic.com)

**M. Maier**

Fraunhofer Institut Angewandte  
 Festkörperphysik,  
 79109 Freiburg, Germany

**R.K. Malhan**

DENSO CORPORATION,  
Research Laboratories,  
500-1, Minamiyama, Komenoki-cho,  
Nisshin-shi, Aichi, 470-0111,  
Japan  
kumar@rlab.denso.co.jp  
Rajesh\_K\_Malhan@denso.co.jp

**H. Matsunami**

Department of Electronic  
Engineering,  
Kyoto University,  
Yoshidahonmachi, Sakyo,  
Kyoto 606-8501, Japan  
matsunam@kuee.kyoto-u.ac.jp

**A. Mattausch**

Lehrstuhl für Theoretische  
Festkörperphysik,  
Universität Erlangen-Nürnberg,  
Staudtstrasse 7/B2,  
91058 Erlangen, Germany  
Alexander.Mattausch@physik.  
uni-erlangen.de

**M. Mehregany**

Department of Electrical  
Engineering and Computer Science,  
Case Western Reserve University,  
409 Olin Building,  
10900 Euclid Ave.,  
Cleveland, Ohio 44106, USA  
mxm31@po.cwru.edu

**B.K. Meyer**

Physical Institute,  
University Giessen,  
Heinrich-Buff-Ring 16,  
35392 Giessen, Germany  
Bruno.K.Meyer@exp1.physik.  
uni-giessen.de

**W. Mönch**

Laboratorium für Festkörperphysik,  
Universität Duisburg-Essen,  
47048 Duisburg, Germany  
w.moench@uni-duisburg.de

**S. Monnoye**

NOVASIC, Savoie Technolac,  
L'arche no. 4,  
73375 Le Bourget du Lac, France

**E. Morvan**

Thales Research and Technology,  
Domaine de Corbeville,  
91404 Orsay Cedex, France  
erwan.morvan@thalesgroup.com

**H. Nagasawa**

Hoya Advanced Semiconductor  
Technologies Co. Ltd.,  
1-17-16 Tanashioda, Sagamihara,  
Kanagawa 229-1125, Japan  
nags@hast.co.jp

**S. Nakashima**

National Institute of Advanced  
Industrial Science and Technology,  
Power Electronics Research Center,  
1-1-1, Umezono, Tsukuba,  
Ibaraki 305-8568, Japan  
nakashima-s@aist.go.jp

**Y. Negoro**

Department of Electronic  
Engineering,  
Kyoto University,  
Yoshidahonmachi, Sakyo,  
Kyoto 606-8501, Japan  
negoro@semicon.kuee.  
kyoto-u.ac.jp

**P.G. Neudeck**

NASA Glenn Research Center,  
21000 Brookpark Rd., M.S. 77-1,  
Cleveland, OH 44135, USA  
Neudeck@nasa.gov  
[http://www.grc.nasa.gov/](http://www.grc.nasa.gov/WWW/SiC/SiC.html)  
[WWW/SiC/SiC.html](http://www.grc.nasa.gov/WWW/SiC/SiC.html)

**N. Ohtani**

Nippon Steel Corporation,  
Advanced Technology Research  
Laboratories,  
20-1 Shintomi, Futtsu,  
Chiba 293-8511, Japan  
ohtani@re.nsc.co.jp

**H. Okushi**

Diamond Research Center  
National Institute of Advanced  
Industrial Science  
and Technology (AIST),  
AIST Tsukuba Central 2  
1-1-1, Umezono, Tsukuba  
Ibaraki 305-8568, Japan  
*and*  
Ultra-Low-Loss Power Device  
Technology Research Body (UPR)  
h.okushi@aist.go.jp

**J. Palmour**

Silicon Carbide Power Devices,  
Cree, Inc.,  
4600 Silicon Drive,  
Durham, NC 27703, USA  
John.palmour@cree.com

**O. Pankratov**

Lehrstuhl für Theoretische  
Festkörperphysik,  
Universität Erlangen-Nürnberg,  
Staudtstrasse 7/B2,  
91058 Erlangen, Germany  
Oleg.Pankratov@physik.  
uni-erlangen.de

**G. Pensl**

Institute of Applied Physics,  
University of Erlangen-Nürnberg,  
Staudtstrasse 7 / A3  
91058 Erlangen, Germany  
Gerhard.Pensl@physik.  
uni-erlangen.de

**C. Persson**

Department of Physics  
and Measurement Technology,  
Linköping University,  
581 83 Linköping, Sweden  
*and*  
National Renewable Energy  
Laboratory,  
Golden, CO 80401, USA  
Clas.Persson@nrel.gov

**M. Pons**

Institut National Polytechnique  
de Grenoble,  
LTPCM-CNRS, BP 75,  
38402, Saint Martin D'Hères,  
France  
Michel.Pons@ltpcm.inpg.fr

**J.A. Powell**

Sest, Inc.,  
21000 Brookpark Rd., M.S. 77-1,  
Cleveland, OH 44135, USA  
J.A.Powell@grc.nasa.gov

**C. Raffy**

Friedrich-Schiller-Universität Jena,  
Institut für Festkörpertheorie  
und Theoretische Optik,  
Max-Wien-Platz 1,  
07743 Jena, Germany  
raffy@ifto.physik.uni-jena.de

**N. Ramungul**

nudjarin@ksc.th.com

**F. Redmann**

Martin-Luther-Universität,  
Halle-Wittenberg,  
Friedemann-Bach-Platz 6,  
06108 Halle, Germany  
frank.redmann@web.de

**H.-J. Rost**

Institut für Kristallzüchtung,  
Max-Born-Str. 2,  
12489 Berlin, Germany  
rost@ikz-berlin.de

**S.-H. Ryu**

Silicon Carbide Power Devices,  
Cree, Inc.,  
4600 Silicon Drive,  
Durham, NC 27703, USA  
sei-hyung\_ryu@cree.com

**N.S. Saks**

Code 6813,  
Naval Research Laboratory,  
4555 Overlook Ave.,  
Washington, D.C. 20375, USA  
saks@nrl.navy.mil

**S. Savage**

ACREO AB,  
Electrum 236,  
Isafjordsgatan 22,  
164 40 Kista, Sweden  
susan.savage@acreo.se

**A. Schöner**

ACREO AB,  
Electrum 236,  
Isafjordsgatan 22,  
164 40 Kista, Sweden  
Adolf.Schoner@acreo.se

**D. Schulz**

Institut für Kristallzüchtung,  
Max-Born-Str. 2,  
12489 Berlin, Germany  
dschulz@ikz-berlin.de

**F. Schmid**

Institute of Applied Physics,  
University of Erlangen-Nürnberg,  
Staudtstrasse 7 / A3  
91058 Erlangen, Germany  
Frank.Schmid@physik.  
uni-erlangen.de

**K. Semmelroth**

Institute of Applied Physics,  
University of Erlangen-Nürnberg,  
Staudtstrasse 7 / A3  
91058 Erlangen, Germany  
Kurt.Semmelroth@physik.  
uni-erlangen.de

**D. Siche**

Institut für Kristallzüchtung,  
Max-Born-Str. 2,  
12489 Berlin, Germany  
ds@ikz-berlin.de

**N.T. Son**

Department of Physics  
and Measurement Technology,  
Linköping University,  
581 83 Linköping, Sweden  
son@ifm.liu.se

**J.-M. Spaeth**

Fakultät für Naturwissenschaften,  
Physikdepartment,  
Universität Paderborn,  
33095 Paderborn, Germany  
spaeth@physik.upb.de

**P. Sperr**

Universität der Bundeswehr  
München,  
85577 Neubiberg, Germany  
Peter.Sperr@unibw-muenchen.de

**U. Starke**

Max-Planck-Institut  
für Festkörperforschung,  
Grenzflächenanalytik,  
Heisenbergstr. 1,  
70569 Stuttgart, Germany  
u.starke@fkf.mpg.de  
http://www.mpi-stuttgart.  
mpg.de/ga/

**A. Stesmans**

Laboratory of Semiconductor  
Physics,  
Department of Physics  
and Astronomy,  
University of Leuven,  
Celestijnenlaan 200D,  
3001 Leuven, Belgium  
andre.stesmans@fys.  
kuleuven.ac.be

**L. Storasta**

Department of Physics  
and Measurement Technology,  
Linköping University,  
581 83 Linköping, Sweden  
liust@ifm.liu.se

**Y. Sugawara**

The Kansai Electric  
Power Company, Inc.  
Power Engineering R&D Center  
Executive Researcher  
11-20 Nakoji, 3-Chome,  
Amagasaki, Hyogo,  
661-0974 Japan  
K467331@kepc.co.jp

**Y. Tang**

Rensselaer Polytechnic Institute,  
110 8th Street, CII 6015,  
Troy, NY 12180, USA  
tangy@rpi.edu

**S. Tanimoto**

Electronics and Information  
Technology Research Laboratory,  
Nissan Research Center, Nissan  
Motor Co., Ltd.,  
1, Natsushima-cho, Yokosuka,  
Kanagawa 237-8523, Japan  
*and*  
Ultra-Low-Loss Power Device  
Technology Research Body (UPR)  
s-tanimoto@mail.nissan.co.jp

**P. Tanner**

School of Microelectronic  
Engineering,  
Griffith University,  
Nathan, Queensland 4111,  
Australia  
p.tanner@griffith.edu.au

**W. Triftshäuser**

Universität der Bundeswehr  
München,  
85577 Neubiberg, Germany  
L21bMail@rz.unibw-muenchen.de

**D. Turover**

NOVASIC, Savoie Technolac,  
L'arche no. 4,  
73375 Le Bourget du Lac, France

**W.M. Vetter**

Department of Materials Science  
and Engineering,  
State University of New York  
at Stony Brook,  
Stony Brook, NY 11974-2275, USA  
wvetter@ms.cc.sunysb.edu

**P. Vicente**

NOVASIC, Savoie Technolac,  
L'arche no. 4,  
73375 Le Bourget du Lac, France

**G. Wagner**

Institute of Crystal Growth,  
Max-Born-Strasse 2,  
12489 Berlin, Germany

**M. Wagner**

Department of Physics  
and Measurement Technology,  
Linköping University,  
581 83 Linköping, Sweden  
matwa@ifm.liu.se

**M. Weidner**

Institute of Applied Physics,  
University of Erlangen-Nürnberg,  
Staudtstrasse 7 / A3  
91058 Erlangen, Germany  
Michael.Weidner@physik.  
uni-erlangen.de

**W. Witthuhn**

Friedrich-Schiller-Universität Jena,  
Institut für Festkörperphysik,  
Max-Wien-Platz 1,  
07743 Jena, Germany  
ofw@uni-jena.de

**K. Yagi**

Hoya Advanced Semiconductor  
Technologies Co. Ltd.,  
1-17-16 Tanashioda, Sagamihara,  
Kanagawa 229-1125, Japan  
yagi@hast.co.jp

**T. Yamada**

Department of Applied Physics  
and Physico-Informatics,  
Keio University, 3-14-1 Hiyoshi,  
Kohoku-ku, Yokohama 223-8522,  
Japan  
ytoshi@appi.keio.ac.jp

**H. Yano**

Graduate School  
of Materials Science,  
Nara Institute of Science  
and Technology,  
8916-5 Takayama, Ikoma,  
Nara 630-0101, Japan  
h-yano@ms.aist-nara.ac.jp

**H. Yashiro**

Nippon Steel Corporation,  
Advanced Technology Research  
Laboratories,  
20-1 Shintomi, Futtsu,  
Chiba 293-8511, Japan  
yashiro@re.nsc.co.jp

**M. Yoshikawa**

Japan Atomic Energy  
Research Institute,  
Watanuki, 1233, Takasaki,  
Gunma 370-1292, Japan  
htyskwm@taka.jaeri.go.jp

**C.A. Zorman**

Department of Electrical  
Engineering and Computer Science,  
Case Western Reserve University,  
712 Glennan Building,  
10900 Euclid Ave.,  
Cleveland, Ohio 44106, USA  
caz@po.cwru.edu

# Part I

## Theory

# Zero- and Two-Dimensional Native Defects

F. Bechstedt, J. Furthmüller, U. Grossner, and C. Raffy

## 1 Introduction

Silicon carbide (SiC) is a very promising material for semiconductor devices which have to work under extreme conditions, such as high temperature, high power, and high frequency. Because of the good thermal conductivity, the high radiation resistance, and the high breakdown voltage, SiC is well suited for demanding applications in harsh environments.

Defects and their complexes play an important role. This is not only true for the impurities used to dope the material. To a great extent the electrical and optical properties of SiC are governed by native defects, which also exhibit interesting physics of their own. Even though progress in crystal growth during the past years has been able to reduce imperfections in the SiC crystals, many properties of grown-in defects or those produced by irradiation damage during implantation of dopants are not well understood.

Because of their atomic character the most important native defects are zero-dimensional ones on a mesoscopic or macroscopic length scale. Defects of this type are vacancies, antisites, and eigeninterstitials or their small complexes. The monovacancies formed by nearest-neighbour atoms of empty silicon ( $V_{\text{Si}}$ ) or carbon ( $V_{\text{C}}$ ) lattice sites are prototypical examples in this respect. In SiC the situation is markedly different from that encountered in common semiconductors like silicon. Because of the stronger chemical bonding in this hard compound, the mobility of such point defects is remarkably reduced. They are thermally stable at room temperature, and far above [1]. In contrast to silicon, antisites, e.g. silicon antisites  $\text{Si}_{\text{C}}$ , also occur in the compound semiconductor SiC [2]. Interstitials are less likely for the same reason of strong bonding. The high thermal stability of a number of defect centers detected by photoluminescence (PL) [3, 4] may indicate more extended defects, e.g. simple examples such as a divacancy  $V_{\text{Si}}V_{\text{C}}$  formed by nearest-neighbour silicon ( $V_{\text{Si}}$ ) and carbon ( $V_{\text{C}}$ ) monovacancies [5].

A characteristic property of SiC is its polytypism. The compound exists in more than 200 different polytypes. The  $3C$ ,  $4H$ ,  $6H$  and  $15R$  structures are the most common polytypes [6]. The accompanying variation of the indirect fundamental gap between 2.39 eV ( $3C$ ) and 3.26 eV ( $4H$ ) [7] makes SiC also interesting for heterostructure devices, e.g. twinning superlattices [8, 9]. The polytypes differ in the stacking sequence of the hexagonally closed-

packed double layers of Si and C atoms along the cubic [111] or the hexagonal [0001] direction. Depending on the nearest-neighbour atom arrangement, the atomic sites in SiC crystals are classified to be cubic or hexagonal ones. The two extreme cases are purely cubic stacking (resulting in the zinc-blende ( $3C$ ) polytype) and purely hexagonal stacking (resulting in the wurtzite ( $2H$ ) polytype). Because of their importance for device applications, here we discuss mainly the  $3C$  and  $4H$  polytypes.

The native point defects can give rise to energy levels in the fundamental gap and, hence, exist in different charge states [10, 11]. The positions of the corresponding levels with respect to the band edges depend on the polytype. Consequently, they may influence the doping efficiency [12] but the strength of this effect depends on the polytype.

Strong indications for certain native defects or defect complexes come from characteristic sharp lines in PL spectra. One prototypical defect responsible for such emission lines in the low-temperature PL spectra is the so-called  $D_1$  center [13]. Its fingerprint is an efficient luminescence at a photon energy 0.35–0.45 eV below the excitonic gap independent of the polytype. The most important  $L_1$  line is followed by characteristic phonon-assisted structures [14]. It has been observed in different polytypes after irradiation [15]–[18], but also in as-grown material after quenching from growth temperature and epitaxial layers grown by chemical vapour deposition (CVD) or solid-source molecular beam epitaxy (MBE) [19]–[21]. In  $4H$ -SiC the  $L_1$  line appears at about 2.901 eV [16, 17], whereas  $3C$ -SiC shows this line at about 1.972 eV [22]. Other strong indications for a native defect, perhaps a silicon vacancy [23], are the characteristic PL bands with no-phonon lines at 1.121 eV in  $3C$ -SiC [24], 1.438 and 1.352 eV in  $4H$ -SiC [25, 26], or 1.433, 1.398, and 1.368 eV in  $6H$ -SiC [25, 26]. In contrast to the  $L_1$  lines, the positions of these PL bands depend only weakly on the polytype.

Stacking faults (SFs) and grain boundaries (GBs) are among the most important planar and, therefore, two-dimensional native defects in SiC. In a crystal with SFs, the various lattice planes are not stacked in the same way as in an ideal crystal, but certain lattice planes are twisted by an angle. Several types of SFs are discussed, for instance in the  $3C$  polytype intrinsic, extrinsic or twin stacking faults [27, 28]. The normal bond stacking in the cubic polytype and the stacking in the presence of an intrinsic or extrinsic SF are schematically indicated in Fig. 1. Because of the polytypism of silicon carbide, SiC crystals are known to contain SFs. The periodic combination of cubic and hexagonal stackings results in many polytypes [6, 31]. Grain boundaries occur in crystals which consist of two differently oriented crystal halves of the same polytype. A twin boundary is a lattice plane at which the two crystal halves meet. Particularly important are tilt boundaries, which involve a rotation about an axis in the plane of the interface [32]. If only one half of a stacking fault with the twisting of bonding tetrahedra in one bilayer is studied, one also speaks about a twin boundary [29, 30] between two crystal halves of the same polytype. In the case of SiC it is likely to consider such

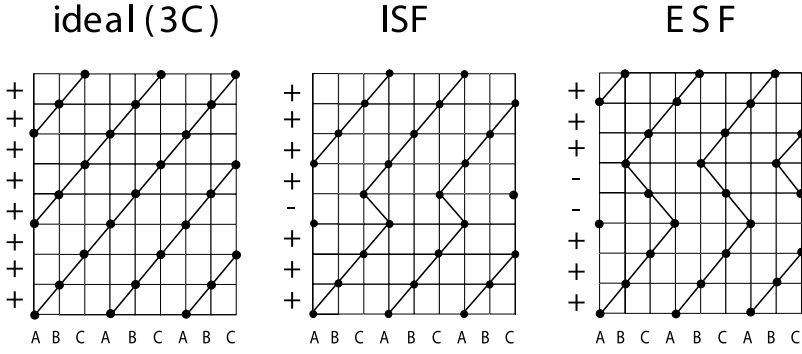


**Fig. 1.** Schematic representation of bilayer stacking in  $[111]$  direction in the  $3C$  polytype. The ideal stacking and the perturbation by an intrinsic stacking fault (ISF) or an extrinsic stacking fault (ESF) versus the positions A, B, and C of Si-C pairs (*dots*) in a  $(1\bar{1}0)$  plane are shown

interfaces also between two different polytypes. However, such an interface does not really represent a twin boundary. We will use the denotation as twist boundary to account for the fact that differently stacked (i.e., twisted) Si-C bilayers occur on both sides of the interface.

Two-dimensional native defects are usually regarded to cause deleterious electrical effects. In silicon, the extrinsic SFs [33] and the GBs [34] were shown to affect device performance by generating electronic states in the band gap, causing the segregation of impurities, or acting as electrical traps for charged carriers. In the case of SiC, the degradation of the electrical characteristics of bipolar devices has been related to stacking faults [35, 36]. Other studies of the SF impact on electronic devices [37] lead to the conclusion of deterioration under long time operation. First-principles studies [38] suggested that some SFs in  $3C$ -,  $4H$ -, and  $6H$ -SiC can be electrically active by introducing states in the gap below the conduction-band minimum (CBM). These findings correspond to the observation of electron states due to cubic inclusions in  $4H$ -SiC matrices [9]. In addition to the electronic properties [39] grain boundaries may also affect the mechanical properties by acting as initial zones of fracture with local stress concentration [40]. Corresponding tilt boundaries in cubic and hexagonal SiC have been observed by means of high-resolution transmission-electron microscopy (HRTEM) [41].

In the present chapter we discuss the relationship between energetics, geometry, and electronic states for native defects in  $3C$ - and  $4H$ -SiC. Mono-vacancies are considered as prototypical zero-dimensional defects, but anti-sites are also discussed. Particular stacking faults and grain boundaries are studied in the two-dimensional case. The computational method is described in Sect. 2. The following Sect. 3 is related to the formation of native point defects and the resulting electronic states. Studies of selected planar defects complete the chapter in Sect. 4. Finally, a brief summary is given.

## 2 Computational Method

The defect calculations are based on the density functional theory (DFT) [42] in the local density approximation (LDA) or in the local spin-density approximation (LSDA) [43]. Explicitly we use the Vienna Ab Initio Simulation Package (VASP) [44]. The interaction of the valence electrons with the atomic cores is treated by non-normconserving Vanderbilt pseudopotentials [45]. Their supersoftened form is especially important for the treatment of first-row elements such as C. It allows the restriction of the plane-wave expansion of the single-particle eigenfunctions to a cutoff energy of 13.4 Ry. This corresponds to about 55 plane waves per atom. Slightly larger cutoffs of 14.8 Ry are used for the planar defects. Exchange and correlation are described in the parameterization of Perdew and Zunger [46]. In order to avoid partial errors due to the use of frozen cores, nonlinear core corrections are included. For arbitrary spin polarization the correlation energy is interpolated between the nonpolarized and fully polarized case as for the exchange energy [47]. For the defect-free polytypes  $3C$  and  $4H$  the described method gives lattice constants slightly smaller than the experimental ones. The cubic lattice constant of the zinc-blende polytype with  $T_d^2$  symmetry amounts to  $a_0 = 4.332$  Å, whereas the two hexagonal lattice constants of  $4H$ -SiC ( $C_{6v}^4$ ) are  $a = 3.061$  Å and  $c = 10.013$  Å. The internal deformations of the bonding tetrahedra are small (see [48]). Without quasiparticle corrections [48, 49] DFT-LDA gives the values 1.33 eV ( $3C$ -SiC) and 2.23 eV ( $4H$ -SiC) for the energy gaps which are about 1 eV smaller than the experimental energies [7].

For the point defects extremely large supercells with 216 atoms ( $3C$ ) or 128 atoms ( $4H$ ) are used to avoid too strong defect-defect interactions and electrostatic effects. A heuristic approach of Makov and Payne for the error evaluation [50], which has been applied in recent studies by other authors [5, 51], is not used for interaction compensation. The total-energy minimization with respect to the atomic coordinates is performed by a conjugate-gradient technique [44]. Within the structural optimization a  $2 \times 2 \times 2$  special-point mesh [52] is used for the  $\mathbf{k}$ -space sampling. In order to describe excited defect states we take into account the constraint of a hole in the lowest  $a_1$ -derived single-particle defect state. However, the effects of the excitation as well as of the spin polarization are described restricting the sampling to the  $\Gamma$  point. The influence of unphysical  $\mathbf{k}$ -induced splittings and dispersions is suppressed in this way. Details of the computational method for point defects can be found in [10].

The planar defects are also modelled using a supercell approach [27, 39, 53]. In such a repeated-slab method usually two planar defects or interfaces are studied simultaneously. In the case of tilt boundaries inequivalent interfaces with respect to the cations and anions of the SiC compound are considered. Since the slabs contain a sufficient number of atomic layers or Si-C bilayers we apply planar  $\mathbf{k}$ -point sets. In the irreducible part of the two-dimensional Brillouin zone (BZ) usually 12 (3) special  $\mathbf{k}$ -points are used for

twist boundaries between polytypes (tilt boundaries between crystal halves of the same polytype). All atomic structures are fully optimized until the Hellmann-Feynman forces vanish. The repeated-slab approach and planar  $\mathbf{k}$ -point sets are also applied to study the surface influence on the stacking-fault formation [54].

### 3 Zero-Dimensional Defects

#### 3.1 Formation of Charged Vacancies and Antisites

First, we consider monovacancies  $V_X^q$  with  $X = \text{Si}$  or  $\text{C}$  in the charge state  $q = 2+, +, 0, -, 2-$ . Independent of the polytype,  $3C$  or  $4H$ , the ground state of a C-site vacancy generally exhibits a remarkable Jahn-Teller distortion apart from the double positively charged one. This can easily be explained for the cubic polytype [55]. However, disregarding the small deformations of the bonding tetrahedra, locally the same happens also in the  $4H$  case. There is a tendency for relaxation towards  $D_{2d}$  symmetry as a consequence of a pairing mode. The Si-dangling bonds of the C vacancy overlap partially. In addition to an inward (positively charged) or outward (negatively charged) breathing relaxation, the defect systems gain energy by formation of bonded pairs of first-nearest-neighbour atoms. This is demonstrated in Fig. 2. Lowering the local symmetry from  $T_d$  (which is locally also nearly valid in  $4H$ ) to  $D_{2d}$ , the threefold degenerate  $t_2$  defect level (without spin) splits into a lower  $b_2$  state and a higher twofold degenerate  $e$  state. This mechanism occurs for  $V_C^+$ ,  $V_C^0$ , and  $V_C^-$ . Further local symmetry reductions do not occur for  $V_C^{--}$ . In  $3C$  the additional electrons giving a nominal charging of the defect occupy conduction band states. Hence, negatively charged carbon vacancies do not exist in  $3C$ . However, they occur in the  $4H$  case with a wider energy gap. Additionally, the crystal-field splitting acts in the hexagonal polytype.

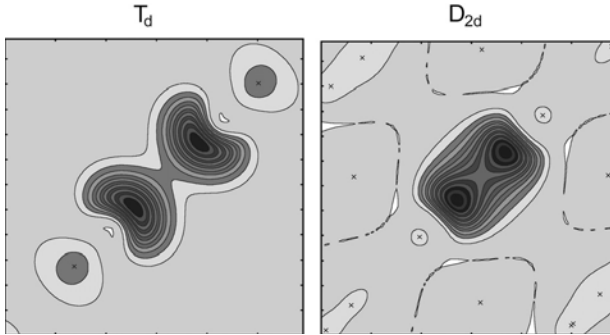


**Fig. 2.** Contour plot of the wave-function square of the highest occupied defect state of  $V_C^0$  in  $3C$ -SiC in a plane perpendicular to a cubic direction. Two local symmetries  $T_d$  and  $D_{2d}$  are allowed

$V_C^{++}$  exhibits a huge inward breathing mode, whereas  $V_C^0$  shows the mentioned pronounced pairing mechanism. The large geometrical changes in the  $V_C^0$  and  $V_C^{++}$  cases in comparison to the intermediate charge state  $q = +$  result in a negative  $U$  behaviour [56]. We calculate a Hubbard interaction  $U = E_{\text{tot}}(V_C^{++}) + E_{\text{tot}}(V_C^0) - 2E_{\text{tot}}(V_C^+) = -0.35$  eV [57]. Consequently, the single positively charged C vacancy should be unstable in the thermodynamic equilibrium. For 4H-SiC we calculate similar values  $U = -0.29$  and  $-0.24$  eV in dependence on the cubic ( $k$ ) or hexagonal ( $h$ ) lattice site [10]. In accordance with Fig. 1 the site character follows the stacking direction  $+$  or  $-$ . However, because of the larger energy gap of 4H also the double negatively charged vacancy can occur as a stable defect. As a consequence one observes a negative  $U$  behaviour with  $U = -0.29$  eV independent of the lattice site also for the defects with additional electrons.

The situation is quite different for the Si-site vacancies [10, 58]. Because of the strong localization of the C dangling bonds and the SiC lattice constant, only an outward breathing relaxation may occur [55]. The defect system can gain additional energy by a spin splitting of the  $t_2$  levels. In the case of the single positively charged, neutral and negatively charged Si-site vacancies, high-spin states are predicted independent of the polytype in agreement with Hund's rule. The total spins  $S = 0(V_{\text{Si}}^{++})$ ,  $1/2(V_{\text{Si}}^+)$ ,  $1(V_{\text{Si}}^0)$ ,  $3/2(V_{\text{Si}}^-)$ , and  $1(V_{\text{Si}}^{--})$  are obtained for the ground states [10, 57]. Meanwhile, there are doubts in the DFT-LSDA result of a  $^3T_1$  ground state for the neutral Si vacancy, at least in the 3C-SiC case [58]. More careful LSDA studies end with a mixed-spin state,  $^1E + ^3T_1$  [60]. However, because of principal limitations of the DFT-LSDA a pure spin multiplet  $^1E$  cannot be derived. Fortunately, despite of the spin problem the results for the atomic geometry and the energetics do not change very much. We estimate an energy difference between  $^1E$  and  $^3T_1$  of about 0.04 eV, which slightly increases after inclusion of gradient corrections in the exchange-correlation energy.

In the thermal equilibrium the concentrations of the defects are mainly determined by their formation energies  $\Omega_f(V_X^q)$ . We adopt the formalism of Zhang and Northrup [61]. One has

$$\Omega_f(V_X^q) = E_{\text{tot}}(V_X^q) - E_{\text{tot}}(\text{ideal}) + \mu_X + q(E_F + E_v), \quad (1)$$

for an  $X$ -site vacancy and

$$\Omega_f(C_{\text{Si}}^q) = E_{\text{tot}}(C_{\text{Si}}^q) - E_{\text{tot}}(\text{ideal}) + \mu_{\text{Si}} - \mu_{\text{C}} + q(E_F + E_v), \quad (2)$$

for a carbon antisite with the total energy  $E_{\text{tot}}$  (ideal) of the ideal SiC polytype and  $E_{\text{tot}}(V_X^q)$  or  $E_{\text{tot}}(C_{\text{Si}}^q)$  for the system with the point defect. All chemical potentials and heats of formation  $\Delta H_f$  are taken from total-energy ab initio calculations described in Sect. 2. The Fermi level  $E_F$  is allowed to vary in an interval defined by the experimental gap energy  $E_g$  [7]. In other words, the quasiparticle gap  $E_g$  is taken into account and the gap problem of the semiconductor physics using DFT-LDA or DFT-LSDA [49] is solved in

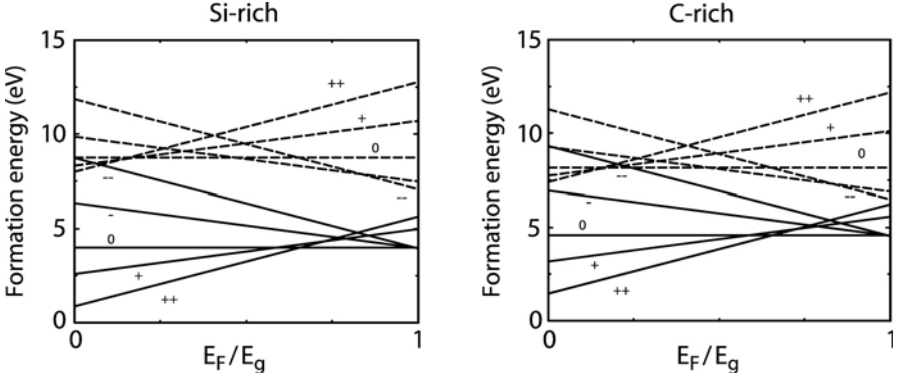


**Fig. 3.** Formation energies of C (*solid lines*) and Si (*dashed lines*) vacancies in 3C-SiC versus Fermi level position in the fundamental energy gap. The most extreme preparation conditions are considered, Si-rich:  $\mu_{\text{Si}} = \mu_{\text{Si}}^{\text{bulk}}$ ,  $\mu_{\text{C}} = \mu_{\text{C}}^{\text{bulk}} - \Delta H_{\text{f}}$  and C-rich:  $\mu_{\text{Si}} = \mu_{\text{Si}}^{\text{bulk}} - \Delta H_{\text{f}}$ ,  $\mu_{\text{C}} = \mu_{\text{C}}^{\text{bulk}}$

this way. More refined procedures, in which the overlap integrals of defect and band states determine how much of the total gap corrections contribute to a quasiparticle shift of a certain defect state [56], or direct self-energy calculations [62] are not considered here. The valence-band maximum (VBM)  $E_{\text{v}}$  is replaced by the corresponding Kohn-Sham eigenvalue. However, their values in supercells with different defects and different charge states are aligned using the average electrostatic potentials [10].

Results for monovacancies in 3C-SiC are presented in Fig. 3. The results for 4H-SiC are rather similar [10]. There is only a small difference of the vacancy formation at cubic or hexagonal sites. In general, the cubic sites are preferred for carbon vacancies. The most important change happens due to the increase of the energy gap by about 1 eV. The slopes in Fig. 3 indicate that in highly *n*-doped 4H crystals the negatively charged C vacancies should possess the lowest formation energies. The lowest formation energies (and, hence, highest defect concentrations) are found for  $V_{\text{C}}^{++}$  under *p*-type doping and both Si-rich and C-rich preparation conditions. That means that under equilibrium conditions in the *p*-type limit, the carbon vacancy is a double donor, regardless of stoichiometry [10, 12]. These findings may explain why as-grown cubic SiC is always weakly *n*-type as well as the lowered doping efficiency of acceptors [63]–[65]. It seems that 40–60% of Al acceptors are compensated in *p*-type epilayers [65].

The formation energies of carbon antisite defects in 3C-SiC are shown in Fig. 4. The underlying local symmetry is  $T_{\text{d}}$ . Test calculations employing starting configurations with  $D_{2\text{d}}$  or  $C_{3\text{v}}$  symmetry showed that the defect system relaxes into a  $T_{\text{d}}$  configuration. In contrast to these findings we expected a planar  $C_{3\text{v}}$  configuration of four carbon atoms with  $sp^2$  hybridization and an empty *p* dangling bond orbital. It turns out that the negatively charged

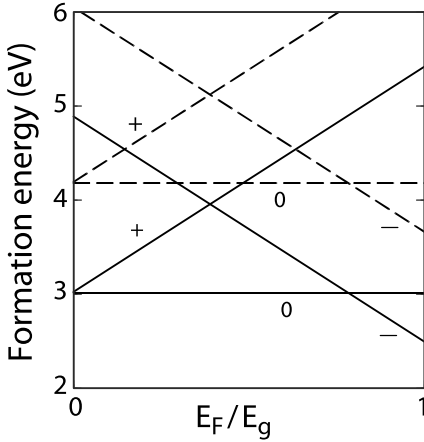


**Fig. 4.** Formation energies of  $C_{Si}^q$  antisites in 3C-SiC versus Fermi level position for two different preparation conditions. *Solid line: C-rich, dashed line: Si-rich*

carbon antisites  $C_{Si}^-$  have the lowest formation energy of all studied native defects in  $n$ -type 3C-SiC grown under C-rich conditions, in agreement with other published theoretical studies [11, 12]. However, the carbon antisite is not electrically active. It does not induce any state in the fundamental gap.

### 3.2 Ionization Levels and Intravacancy Transitions

The (donor-like) ionization levels  $(q - 1/q)$  of a defect are independent of the preparation conditions, i.e., the actual values of the chemical potentials of the species involved. They are defined as the positions of the Fermi level  $E_F$  at which the formation energy (1.1) or (1.2) of a defect in two different charge states  $q$  and  $q + 1$  or  $q - 1$  and  $q$  becomes equal in Figs. 3 or 4. One finds

$$\varepsilon(q + 1/q) = E_{\text{tot}}(V_X^{q+1}) - E_{\text{tot}}(V_X^q) - E_v \quad (3)$$

for the acceptor ionization levels with respect to the VBM,  $E_v$ , or

$$\tilde{\varepsilon}(q - 1/q) = E_c + E_{\text{tot}}(V_X^q) - E_{\text{tot}}(V_X^{q-1}) \quad (4)$$

for the donor ionization levels with respect to the CBM,  $E_c$ . It holds  $E_g = E_c - E_v$  for the fundamental energy gap and  $\tilde{\varepsilon}(q - 1/q) + \varepsilon(q/q - 1) = E_g$ . For instance, for  $q = -1$  the acceptor excitation energy  $\varepsilon(0/-)$  gives the energy being necessary to bring a single negatively charged vacancy into its neutral charge state. For  $q = 0$  the donor excitation energy  $\tilde{\varepsilon}(-/0)$  defines the energy that is needed to bring one electron from a  $t_2$ -derived single-particle vacancy level into the conduction band.

Results for the vacancy ionization levels are presented in Fig. 5 and Tables 1 and 2. The tables also contain results of Torpo et al. [51, 58] obtained using normconserving pseudopotentials, 128-atom supercells, and no Madelung corrections. The agreement of the theoretical results [10, 51, 58, 66]

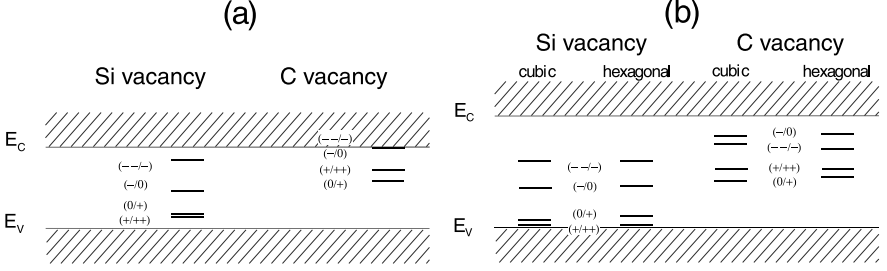


**Fig. 5.** Energy-level scheme for silicon and carbon vacancies in (a) 3C-SiC and (b) 4H-SiC

of different groups and using different numerical approaches is excellent. This holds in particular for the positively charged states in the lower part of the fundamental gap. The comparison of the level schemes in Fig. 5 for 3C-SiC (a) and 4H-SiC (b) indicates close similarities of the level schemes for a C-site or a Si-site vacancy if the VBM is taken as energy zero. The main variation is due to the wider energy gap in 4H. Deep midgap defect levels can more or less be used to align the band structures of 3C- and 4H-SiC according to the

**Table 1.** Ionization energies (in eV) of Si vacancies in 3C- and 4H-SiC with respect to the VBM (positively charged) or CBM (negatively charged). Values in parantheses from [48, 51]. In addition the position of the  $L_1$  line is given

Level	$k$ (3C)	$h$ (4H)	$k$ (4H)
(+ / + +)	0.34 (0.43)	0.08 (0.09)	0.06 (0.14)
(0 / +)	0.43 (0.50)	0.31 (0.27)	0.20 (0.18)
(- / 0)	1.28 (0.68)	1.98 (2.15)	2.07 (2.22)
(- - / -)	0.41 (0.02)	1.31 (1.58)	1.32 (1.56)
$L_1$	1.96 (1.89)	2.96 (3.00)	3.07 (3.09)

**Table 2.** Ionization energies (in eV) of C vacancies in 3C- and 4H-SiC with respect to the VBM (positively charged) or CBM (negatively charged). Values in parantheses from [48, 51]. Because of the negative- $U$  behaviour only the (0 / + +) and (- - / 0) levels are given in [51]

Level	$k$ (3C)	$h$ (4H)	$k$ (4H)
(+ / + +)	1.72	1.68	1.68
		(1.53)	(1.57)
(0 / +)	1.41	1.37	1.44
(- / 0)	unstable	0.65	0.52
		(0.82)	(0.63)
(- - / -)	unstable	0.84	0.81

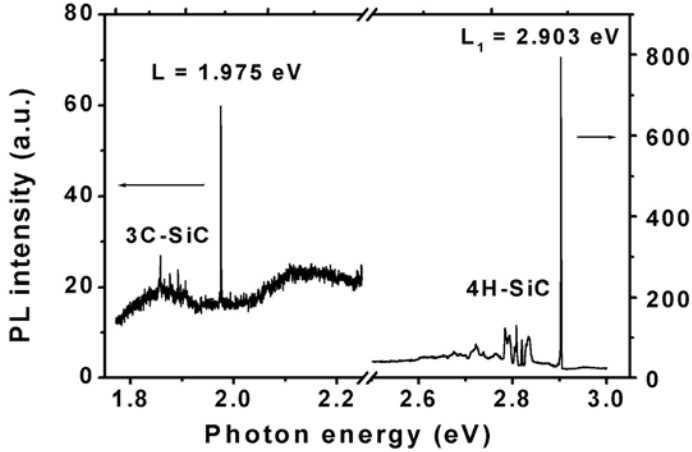


**Fig. 6.** Photoluminescence spectra of 4H- and 3C-SiC layers grown homoepitaxially by means of MBE. From [21]

Langer-Heinrich rule [67]. In the case of 4H-SiC the comparison of the level schemes for hexagonal ( $h$ ) and cubic ( $k$ ) sites only exhibits small differences. The variation of the level positions due to the site character is of the order of 0.1 eV or less.

Figure 6 presents the low-temperature PL spectra of 4H- and 3C-SiC layers grown by means of solid-source MBE [21]. They show the well-known emission lines of the  $D_1$  defect center, both the zero-phonon  $L_1$  line and the phonon replica. There are several indications that Si vacancies have to be taken into account for the explanation of the  $D_1$  center [13]. Carbon vacancy levels are too close to midgap positions. In the  $V_{Si}$  case, the corresponding optical emission energy can be related to a recombination of an electron in the CBM and a hole situated at the vacancy leaving back a neutral vacancy. Correspondingly, neglecting electron-hole binding energies and lattice-relaxation effects the donor ionization energy  $\varepsilon(0/+)$  (with respect to the CBM) is interpreted as  $L_1$  peak energy. The values in Tables 1 and 2 result using the experimental gaps  $E_g = 2.39$  eV (3C) and 3.27 eV (4H). The comparison with measured  $L_1$  line positions of about 1.98 eV (3C) and 2.90 eV (4H) shows that the donor ionization levels (0/+) of silicon vacancies in 3C and 4H (hexagonal site) nearly give the positions of the luminescence lines. Thereby, the binding energy of about 0.03–0.06 eV [16]–[18] of the bound exciton is neglected and an inaccuracy of about 0.1 eV of the theoretical level positions is taken into account. The advantage of this identification is the explanation of the polytype dependence of the  $L_1$  line and of the non-occurrence of a second line in 4H. The splitting of the two (0/+) energies of cubic and hexagonal sites is rather large, so that electron-hole pairs recombine via the lower-energy transition.

These results suggest the conclusion that a Si vacancy, or more strictly speaking a C dangling bond, is involved in the  $D_1$  center. There are also arguments against this interpretation. The Si vacancy formation energies are generally larger than that of C vacancies (cf. Fig. 3). However, the MBE growth of SiC [21] happens under conditions where the concentration of Si adatoms is nearly given by its equilibrium value. No accumulation of Si occurs on the growing SiC surface. On the other hand, desorption of carbon or carbon bearing species, such as  $\text{Si}_2\text{C}$  and  $\text{SiC}_2$ , can be neglected.

In addition, it has been suggested that Si vacancies are unstable in the thermodynamic equilibrium against a transformation into a defect complex according to  $V_{\text{Si}}^0 \rightarrow V_{\text{C}}^0 + C_{\text{Si}}^0$ , because of their larger formation energy in comparison to that of C vacancies [68]. However, there exists an energy barrier for this process of about 1.8 eV which is much higher than the thermal energy at a growth temperature of 1500 K (3C) or 1600 K (4H).

The question arises whether other PL lines, e.g. that at 1.35 and 1.44 eV in 4H [25, 26] or 1.12 eV in 3C [24], can be related to native defects like vacancies or not. To answer this question, we study the lowest intravacancy transition energies of Si vacancies in 3C- and 4H-SiC as total-energy differences  $\hbar\omega = E_{\text{tot}}(V_{\text{Si}}^q, \text{excited}) - E_{\text{tot}}(V_{\text{Si}}^q, \text{ground})$ . Thereby, the excited state is described using the constraint of a hole in the low-energy one-electron  $a_1$  defect state. Results are listed in Table 3. In the 3C case we also give transition energies that are corrected by about 0.15 or 0.35 eV, in order to account for the strong dispersion of the lowest  $a_1$  defect band [55]. Despite of the large supercells of 216 atoms, such a strong dispersion occurs due to the vacancy-vacancy interaction and the mixing with bulk-like contributions.

Interestingly all the intravacancy transition energies considered in Table 3 do not vary very much with the charge state of the vacancy  $V_{\text{Si}}^q$  and the

**Table 3.** Lowest intradefect transition energies (in eV) of  $V_{\text{Si}}^q$  in 3C- and 4H-SiC. The inequivalent lattice sites,  $k$  and  $h$ , are distinguished in 4H. In the 3C case the energies corrected by the strong  $\mathbf{k}$  dispersion of the  $a_1$  defect band are given in parentheses. In the 4H case the small perturbations of the hexagonal crystal field are ignored in comparison to the defect-induced geometry changes, and the localized defect states are locally still described as in the cubic polytype

Charge state $q$	Transition	3C ( $k$ )	4H ( $k$ )	4H ( $h$ )
+	$a_1^2 t_2^{\uparrow} \rightarrow a_1^{\downarrow} t_2^{\uparrow\uparrow}$	1.41 (1.06)	1.42	1.77
0	$a_1^2 t_2^{\uparrow\uparrow} \rightarrow a_1^{\downarrow} t_2^{\uparrow\uparrow\uparrow}$	1.42 (1.07)	1.44	1.82
−	$a_1^2 t_2^{\uparrow\uparrow\uparrow} \rightarrow a_1^{\uparrow} t_2^{\uparrow\uparrow\uparrow} t_2^{\downarrow}$	1.60 (1.40)	1.57	1.40
−−	$a_1^2 t_2^{\uparrow\uparrow\uparrow} t_2^{\downarrow} \rightarrow a_1^{\uparrow} t_2^{\uparrow\uparrow\uparrow} t_2^{\downarrow\downarrow}$	1.43 (1.23)	1.73	1.68

polytype of the host, in particular considering only cubic lattice sites. The reason is that the charge state  $q$  shifts both participating single-particle levels  $a_1$  and  $t_2$  in the same manner. The participating orbitals are combined by the same C hybrids in more or less the same distance. The large difference of the transition energies of  $3C$  and  $4H$  in the  $V_{\text{Si}}^{--}$  case is a consequence of the fact that in  $3C$  the  $t_2^\uparrow$  level lies above the conduction-band minimum. In  $4H$ -SiC the site dependence has to be taken into consideration. The transitions at hexagonal sites possess larger (smaller) energies for positively charged or neutral (negatively charged) Si vacancies than those at cubic sites.

The values in Table 3 approach the experimental findings [24]–[26]. Son et al. [24] relate the PL line at 1.12 eV in  $3C$  to a  $S = 1/2$  center, probably  $V_{\text{Si}}^+$ . We follow this interpretation, in particular because of the spin state. From the point of view of the energy, one cannot exclude  $V_{\text{Si}}^0$ . However, neither the spin  $S = 1$  nor the spin  $S = 0$  fits the PL experiments, in contrast to the corresponding vacancy in diamond [69]. The conclusions from the comparison are more vague in the case of  $4H$ , despite of the reduced dispersion of the lowest defect band as a consequence of the hexagonal crystal field. The transition energies 1.44 and 1.82 eV calculated without dispersion corrections for  $V_{\text{Si}}^0$  approach the positions of the two zero-phonon PL lines at 1.35 and 1.44 eV accompanied by a  $S = 1$  signal measured with optically detected magnetic resonance (ODMR) [25, 26]. However, such an interpretation is doubtful because of the spin state and the larger computed line splitting. Another possible explanation of the occurrence of two lines in  $4H$  may be related to the crystal-field splitting of the  $t_2^\uparrow$  level into  $a_1^\uparrow$  and  $e^\uparrow$  ones and not to the two inequivalent sites. Taking into account a dispersion correction of 0.31 eV also the transition in  $V_{\text{Si}}^{--}$  can be considered for the interpretation. Spin state and line splitting agree with the measurements. We mention that the high-spin state of the negatively charged  $V_{\text{Si}}^-$  predicted theoretically [10, 23, 58] has been confirmed recently by measurements of the electron paramagnetic resonance [70].

## 4 Two-Dimensional Defects

### 4.1 Tilt Boundaries

Planar defects – boundaries – may occur between crystal halves of the same or of different polytypes. Prototypical examples for the zinc-blende SiC are twin boundaries of the  $\Sigma 9$  type [71, 72]. In this notation, the intersection of the lattices of the two crystals is considered. The points common to both lattices form the Coincidence Site Lattice (CSL). The number 9 gives the ratio of the unit-cell volume of the CSL to that of the original lattice [73]. Two models [40, 72] have been proposed for the  $\Sigma 9\{221\}$  symmetrical coincidence boundary, in which the interface plane common to both  $3C$ -SiC grains is of a  $\{221\}$  type. For covalent Si and Ge semiconductors the glide-plane model has

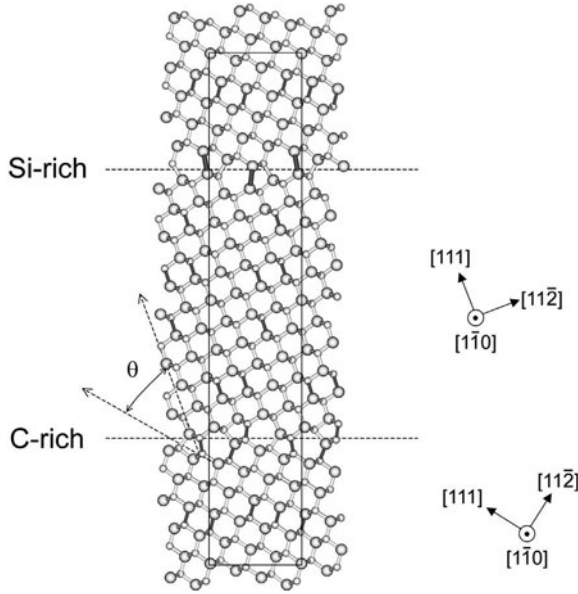


**Fig. 7.** Supercell to model Si-rich and C-rich  $\Sigma 9\{122\}$  boundaries in 3C-SiC within the glide-plane reconstruction. The Si atoms (*large circles*) and C-atoms (*small circles*) are projected along the  $[1\bar{1}0]$  axis. The tilt angle is indicated

been found to be more stable than the mirror-plane model [72]. The supercell in Fig. 7 represents the glide-plane model. The tilt angle between two cubic grains is  $\arccos(7/9)$ , i.e.,  $38.94^\circ$ . The supercell contains two boundaries with different local stoichiometry but the same number of Si and C atoms. Here supercells with 144 atoms are arranged in a simple orthorhombic Bravais lattice. The lattice constant of 5.2 nm in the direction perpendicular to the interfaces guarantees that the mutual interaction of the tilt boundaries is weak. Both the Si-rich and the C-rich interfaces consist of five- and seven-membered rings similar to the case of the  $\pi$ -bonded chain model of the  $2 \times 1$  reconstructed Si and Ge(111) surfaces [74]. The odd-membered ring structure allows to keep the fourfold coordination of the group-IV atoms.

As a consequence no dangling bonds occur in the twin interfaces. However, wrong (in the sense of the Si-C environment) Si-Si or C-C bonds dominate the corresponding Si-rich or C-rich interfaces. Because of the electron transfer from Si to C atoms in SiC, the Si-rich (C-rich) interface is called *p*-polar (*n*-polar). Each planar unit cell in an interface intersects two Si-Si or C-C bonds. One may also construct non-polar boundaries which contain both kinds of wrong bonds. Such non-polar interfaces seem to be observed in HRTEM of SiC films prepared by chemical vapour deposition (CVD) [40, 41]. However, they should be less stable than the polar ones [40]. The arrangement of the bonds in the tilt boundaries in odd-membered rings induces remarkable de-

viations of the bond angles from the ideal tetrahedron angle of  $109.47^\circ$  of about  $-20^\circ$  to  $+24^\circ$  [40, 41, 53]. The Si-Si wrong bonds at the interface have lengths rather similar to those in bulk Si. The bond lengths only deviate by about  $-2\%$  from the ideal value. In the C-C case and  $n$ -polar interfaces larger deviations of about  $5\%$  appear.

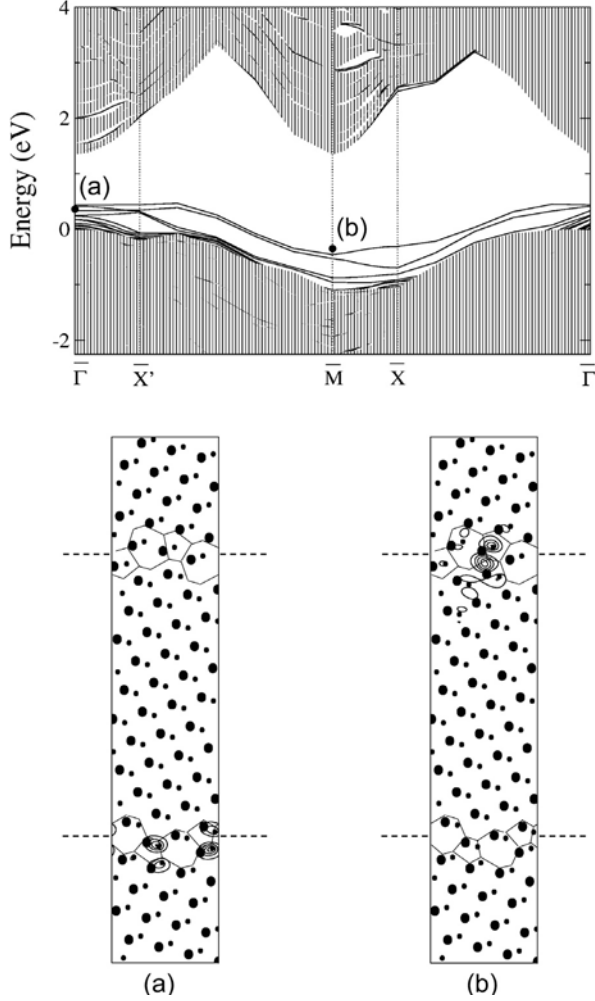


**Fig. 8.** Band structure (*upper part*) of the two  $\{221\}$  tilt boundaries (glide-plane model) versus the irreducible part of the corresponding two-dimensional BZ in DFT-LDA quality. The bulk band structure of 3C-SiC projected onto the planar BZ is shown as *hatched region*. The *lower part* of the figure represents the wave-function squares of the occupied interface states at (a)  $\bar{\Gamma}$  and (b)  $\bar{M}$ . *Larger (smaller) dots* indicate the Si (C) atoms in parallel (110) planes

The average value of the two interface or boundary energies amounts to  $\gamma = 1.60 \text{ J/m}^2$ . This value agrees well with that  $\gamma = 1.24 \text{ J/m}^2$  calculated by other authors [40, 41]. The positive value indicates that the formation of such a complicated interface requires some energy to generate the change of the bonding topology, the distortion of the tetrahedra and the slightly compressed Si-Si and stretched C-C bonds. The formation energy of a tilt boundary in cubic SiC amounts to 0.175 eV per interface atom. This value approaches the thermal energy  $k_B T = 0.15 \text{ eV}$  corresponding to the substrate temperature of about 1700 K in a CVD process and is much smaller than the thermal energy  $k_B T = 0.22 \text{ eV}$  being relevant for bulk growth at about 2500 K using a modified Lely method. This may explain why  $\{221\}$  tilt boundaries are observed in polycrystalline SiC [73] and even the occurrence of similar boundaries in hexagonal SiC [75].

The interface states accompanying the two  $\{221\}$  tilt boundaries are shown in Fig. 8 together with the bulk band structure of 3C-SiC projected onto the two-dimensional BZ. Occupied interface states occur in the lower part of the fundamental gap close to the VBM. The state at the  $\bar{\Gamma}$  point (denoted by “a”) being 0.2 eV above the VBM is localized at the C-rich boundary at Si-C bonds of the 5-fold rings as indicated by the corresponding wave-function square. The uppermost interface state at  $\bar{M}$  is localized at the Si-Si bonds of the Si-rich boundary. In pure or *n*-doped SiC these filled interface states should not drastically influence its electrical properties. However, the *p*-doping efficiency may be decreased. Shallow acceptors with levels only slightly above the VBM ( $< 0.4 \text{ eV}$ ) may be passivated by electronic states of the tilt boundaries.

## 4.2 Boundaries Between Polytypes

The significant polytypism of SiC is accompanied by a high probability for the appearance of SFs. Therefore the observation of twin boundaries, inclusions of stacking regions corresponding to another polytype, or the occurrence of extended SFs is likely. Such changes may happen along the normal stacking direction  $[111]$  (cubic) or  $[0001]$  (hexagonal). However, they may also be combined with a tilted boundary of the  $\{115\}$  type (cubic) or  $\{3\bar{3}02\}$  type (hexagonal). Here, we discuss as a prototype a  $\{111\}/\{0001\}$  interface between 3C-SiC and 2H-SiC. The wurtzite polytype 2H is considered to be a hexagonal model crystal instead of the more common 4H and 6H structures.

Still a supercell description is used (cf. Fig. 9). Again, the two interfaces are not symmetrically equivalent due to the polarity of the compound. The supercell consists of 24 Si-C bilayers, twelve with purely cubic stacking and the other twelve layers with purely hexagonal stacking. A total of 48 atoms belong to a supercell. The edge length of nearly 6 nm guarantees a weak interaction of the two interfaces. The resulting periodic structure represents a twinning superlattice  $(3C)_4(2H)_6$  [76], where the index gives the number of unit cells of the indicated polytype in a supercell. The system is slightly

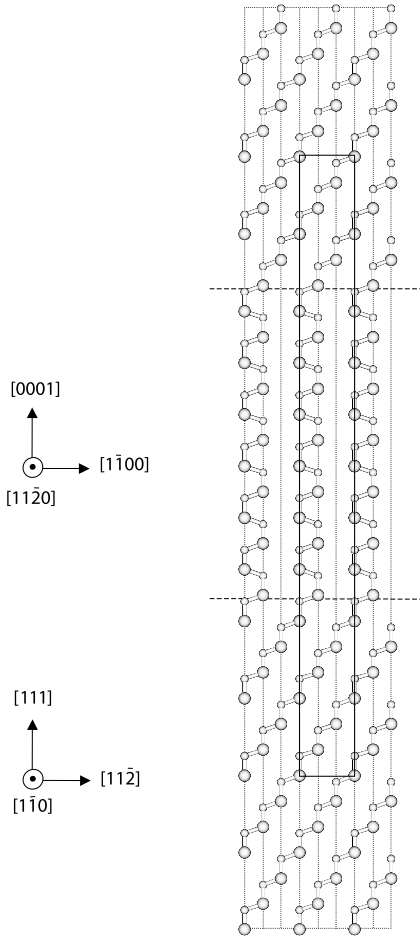


**Fig. 9.** Interface between zincblende and wurtzite SiC along the  $[111]/[0001]$  direction. The bond stacking is represented in a  $(11\bar{2}0)$  plane. The *rectangle* indicates the supercell. *Large (small) circles* stand for Si(C) atoms

biaxially strained and the interface bonds are relaxed to find the absolute minimum of the total energy. However, the effects of strain and relaxation on the electronic properties are negligible. The interface energy only amounts to  $\gamma = -1.12 \text{ mJ/m}^2$ . The negative value indicates an energetical favourization of the formation of such twin interfaces, in agreement with the fact that a mixed cubic/hexagonal stacking in the  $4H$  or  $6H$  polytypes is more favourable than a pure one in  $3C$  or  $2H$  [48, 77]. We mention that the absolute value of the interface energy is increased for smaller supercells as a consequence of the particle-in-a-box effect [39].

The electronic states of the twist boundaries (Fig. 9) are shown together with the projected bulk band structures of  $3C$ -SiC and  $2H$ -SiC in Fig. 10. There is only a tendency for rather shallow interface states. This is particularly true for the highest occupied interface states at  $\bar{\Gamma}$ . The wave-function

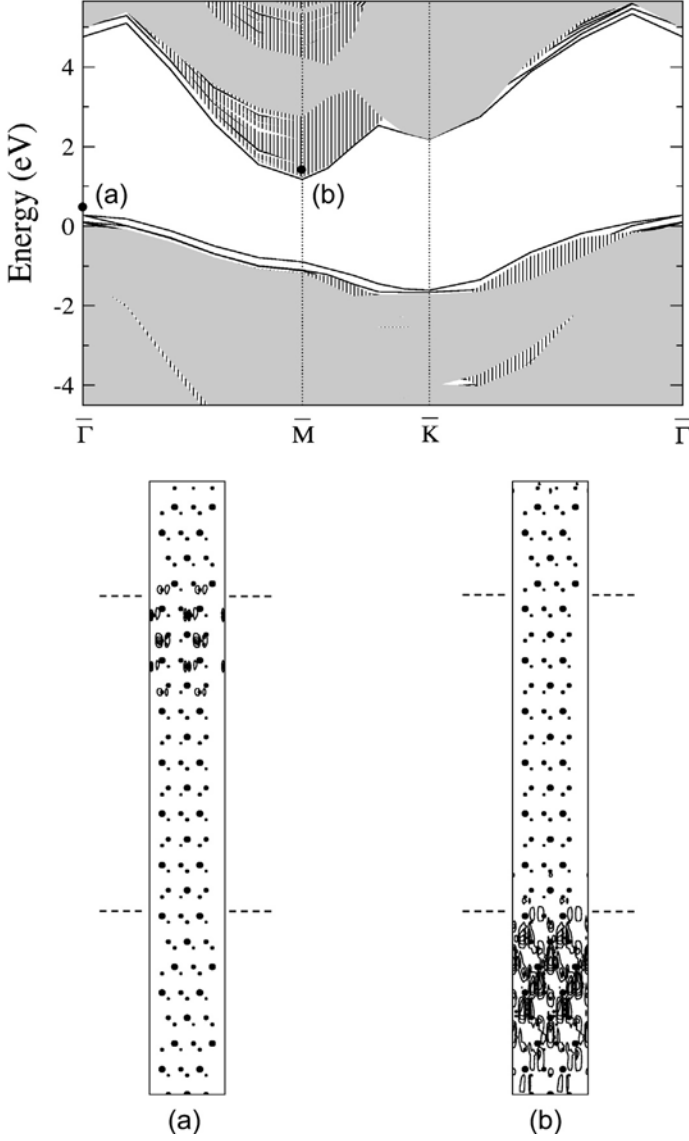


**Fig. 10.** Band structure of the  $\{111\}/\{0001\}$  twist boundaries between the polytypes 3C and 2H versus the two-dimensional hexagonal BZ in DFT-LDA quality (*upper part* of the figure). The *shaded region* represents the projected bulk band structure of 2H-SiC. The *hatched areas* indicate regions which are in addition allowed in 3C-SiC. The *lower part* of the figure represents the wave-function squares of the (a) highest occupied and (b) lowest empty interface state. *Larger (smaller) dots* denote the Si (C) atoms in parallel (11 $\bar{2}$ 0) planes

square (also Fig. 10) shows a localization of this state near the interface but slightly more at the  $2H$  side with a strong decay into the  $3C$  region. The lowest empty interface state at  $\bar{M}$  exhibits a much stronger localization on the  $3C$  side in agreement with the fact that the corresponding energies are close to midgap positions in  $2H$ -SiC. Our findings are obviously influenced by the type-II heterostructure character of the  $(3C)_4(2H)_6$  superlattice and the electric fields accompanying the spontaneous polarization field in the hexagonal crystal  $2H$ -SiC. According to the band discontinuities of  $\Delta E_c = 0.99$  eV and  $\Delta E_v = -0.13$  eV [48] the lowest electron wave functions should be localized in the  $3C$  regions, whereas the probability to find a hole should be larger in the  $2H$  stacking regions. This picture is interfered by the saw-tooth potential as a consequence of the spontaneous polarization field [9, 48].

The arrangement of the two twist boundaries in a superlattice allows two other interpretations. The results given in Fig. 10 remain valid for the discussion of thin inclusions of cubic  $3C$  layers which are embedded in a hexagonal  $4H$  matrix. Then, instead of the hatched conduction-band region of the projected  $3C$  band structure around  $\bar{M}$  in Fig. 10, two-dimensional bands appear. They are related to the fact that a  $3C$  layer embedded in a hexagonal matrix forms a deep quantum well for the movement of the electrons [9, 78, 79]. A corresponding band line-up is shown in Fig. 11. The spontaneous polarization in  $4H$  is taken into consideration. Another interpretation follows if the two twist boundaries come close to each other. Then a stacking fault appears. A SF in a hexagonal crystal represents an efficient trap for electrons [38, 79].

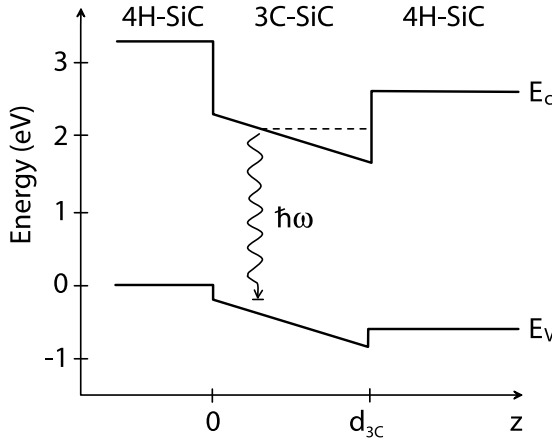


**Fig. 11.** Band-line up for a thin layered  $3C$  inclusion in a  $4H$  matrix (schematically). The spontaneous polarization field in the hexagonal crystal is considered

### 4.3 Surface Influence on Defect Generation

A growing surface influences the generation of planar defects beneath it. We study this effect in the case of a 3C-SiC crystal grown under Si-rich conditions. Prototypical two-dimensional defects are the intrinsic and extrinsic stacking faults, ISF and ESF (Fig. 1). The probability of their occurrence in thermodynamic equilibrium is studied in dependence on the depth beneath the surface. In Fig. 12 two Si-rich and Si-terminated SiC surfaces are considered with varying reconstruction and stoichiometry. The most Si-rich SiC(111) $3 \times 3$  surface consists of a Si tetramer on a twisted Si adlayer with clover-like rings [80, 81]. It corresponds to a Si coverage of  $\Theta = 13/9$ . Under less Si-rich conditions a  $\sqrt{3} \times \sqrt{3}$ R30° reconstruction exists for 4H(0001), 6H(0001), and 3C(111) surfaces. It is represented by a  $T_4$  adatom model [80, 82] and, hence, a  $\Theta = 1/3$  stoichiometry.

For both surfaces Fig. 12 demonstrates a remarkable dependence of the SF formation energy versus the depth beneath the surface. For SF positions directly below the surfaces the formation energies are positive, indicating that the formation of SFs is energetically unfavourable. For deeper bilayers beneath the surface, at least from the fourth bilayer, the formation energies become negative, indicating that the formation of mixed hexagonal and cubic bond stacking in 4H and 6H polytypes is energetically more favourable than the pure cubic stacking such as in the considered bulk case. Figure 12 leads to the conclusion that a surface stabilizes the cubic stacking in the first atomic layers in agreement with predictions based on model studies [83, 84]. The strength of this effect depends on the surface geometry and stoichiometry as well as on the type of the SF.

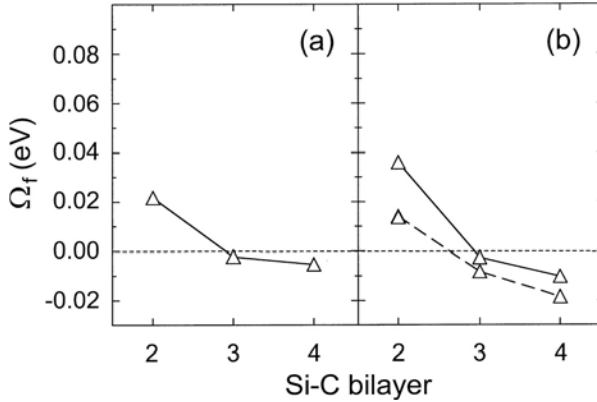


**Fig. 12.** Formation energy per  $1 \times 1$  surface unit cell area of a stacking fault in the surface region of cubic SiC versus SF location in a Si-C bilayer. ISF: *solid line*, ESF: *dashed line*. (a)  $3 \times 3$  surface, (b)  $(\sqrt{3} \times \sqrt{3})\text{R}30^\circ$  surface [54]

## 5 Conclusion

Also in the case of wide-band-gap semiconductors such as SiC *first-principles* calculations allow the description of geometric, thermodynamic and electronic properties of defects or defect complexes. In this review chapter this is mainly demonstrated for native defects. Monovacancies have been considered as prototypical zero-dimensional defects. However, to a certain extent also antisites and vacancy complexes have been discussed. We have shown that in the thermodynamic equilibrium the carbon vacancy should have the lowest formation energies in bulk SiC independent of the polytype. It forms a double donor which dramatically reduces the doping efficiency of acceptors such as Al atoms. The theory also allows the calculation of energies of optical transitions between bulk and vacancy states or excited and ground states of vacancies. We discussed their possible relationship to recent photoluminescence measurements. In the two-dimensional case examples for tilt and twist boundaries have been discussed. They give rise to completely empty or filled states in the fundamental gap close to the band edges of the ideal bulk. We show that the formation of two-dimensional defects depends on the thermal treatment and the growing surface.

## Acknowledgements

The work was financially supported by the Deutsche Forschungsgemeinschaft (SFB 196, Project A8) and the EU Research Training Network NANOPHASE (HPRN-CT-2000-00167).

## References

1. H. Itoh, N. Hayakawa, I. Nashiyama, and E. Sakuma: J. Appl. Phys. **66**, 4529 (1989)
2. N.T. Son, P.N. Hai, and E. Janzén: Phys. Rev. Lett. **87**, 045502 (2001)
3. H. Itoh, A. Kawasuso, T. Ohshima, M. Yoshikawa, I. Nashiyama, S. Tanigawa, S. Misawa, H. Okumura, and S. Yoshida: Phys. Stat. Sol. (b) **162**, 173 (1997)
4. E. Sörman, N.T. Son, W.M. Chen, O.Kordina, C. Hallin, and E. Janzén: Phys. Rev. B **61**, 2613 (2000)
5. L. Torpo, T.E.M. Staab, and R.M. Nieminen: Phys. Rev. B **65**, 085202 (2002)
6. N.W. Jepps and T.F. Page: Progr. Cryst. Growth Charact. **7**, 259 (1983)
7. W.J. Choyke, D.R. Hamilton, and L. Patrick: Phys. Rev. **133**, A1163 (1964)
8. F. Bechstedt and P. Käckell: Phys. Rev. Lett. **75**, 2180 (1995)
9. A. Fissel, U. Kaiser, B. Schröter, W. Richter, and F. Bechstedt: Appl. Surf. Sci. **184**, 37 (2001)
10. A. Zywiets, J. Furthmüller, and F. Bechstedt: Phys. Rev. B **59**, 15166 (1999)
11. L. Torpo, S. Pöykkö, and R.M. Nieminen: Phys. Rev. B **57**, 6243 (1998)
12. C. Wang, J. Bernholc, and R.F. Davis: Phys. Rev. B **38**, 12752 (1988)
13. J. Schneider and K. Maier: Physica B **185**, 199 (1993)

14. W.J. Choyke: in *The Physics and Chemistry of Carbides, Nitrides and Borides*, Vol. 185 of NATO Advanced Study Institute Series E: Applied Sciences, ed. by R. Freer (Kluwer Academic, Dordrecht, 1990), p. 563
15. V.V. Makarov: Sov. Phys. Solid State **13**, 1974 (1972)
16. Ch. Haberstroh, R. Helbig, and R.A. Stein: J. Appl. Phys. **76**, 509 (1994)
17. T. Egilsson, J.P. Bergmann, I.G. Ivanov, A. Henry, and E. Janzen: Phys. Rev. B **59**, 1956 (1999)
18. T. Egilsson, A. Henry, I.G. Ivanov, J.L. Lindström, and E. Janzen: Phys. Rev. B **59**, 8008 (1999)
19. T.A. Kenedy, J.A. Freitas, and S.G. Bishop: J. Appl. Phys. **68**, 6170 (1990)
20. K. Nishino, T. Kimoto, and H. Matsunami: Jpn. J. Appl. Phys. **34**, L1110 (1995)
21. A. Fissel, J. Furthmüller, W. Richter, and F. Bechstedt: Appl. Phys. Lett. **78**, 2512 (2001)
22. W.J. Choyke, Z.C. Fenc, and J.A. Powell: J. Appl. Phys. **64**, 3163 (1988)
23. A. Zywietz, J. Furthmüller, and F. Bechstedt: Phys. Rev. B **61**, 13655 (2000)
24. N.T. Son, E. Sörman, W.M. Chen, M. Singh, C. Hallin, O. Kordina, B. Mone-mar, and E. Janzen: J. Appl. Phys. **79**, 3784 (1996)
25. E. Sörman, N.T. Son, W.M. Chen, O. Kordina, C. Hallin, and E. Janzen: Phys. Rev. B **61**, 2613 (2000)
26. M. Wagner, B. Magnusson, W.M. Chen, E. Janzen, E. Sörman, C. Hallin, and J.L. Lindström: Phys. Rev. B **62**, 16555 (2000)
27. P. Käckell, J. Furthmüller, and F. Bechstedt: Phys. Rev. B **58**, 1326 (1998)
28. C. Raffy, J. Furthmüller, and F. Bechstedt: Phys. Rev. B **66**, 075201 (2002)
29. R.L. Headrick, B.E. Weir, J. Bevk, B.S. Freer, D.J. Eaglesham, and L.C. Feldman: Phys. Rev. Lett. **65**, 1128 (1990)
30. H. Hibino, K. Sumitomo, and T. Ogina: J. Vac. Sci. Technol. A **16**, 1934 (1998)
31. A.R. Verma and P. Krishna: *Polymorphism and Polytypism in Crystals* (Wiley, New York, 1966)
32. J. Hornstra: Physica **25**, 409 (1959)
33. O.L. Krivanek: Chemica Scripta **14**, 213 (1978–79)
34. C.R.M. Grovenor: J. Phys. C, Solid State Phys. **18**, 4079 (1985)
35. J.Q. Liu, M. Skowrowski, C. Hallin, R. Söderholm, and H. Lendemann: Appl. Phys. Lett. **80**, 749 (2002)
36. J.P. Bergman, H. Lendenmann, P.Å. Nilsson, U. Lindefelt, and P. Skytt: Materials Science Forum **353–356**, 299 (2001)
37. M.S. Miao, S. Limpijumnong, and W.R.L. Lambrecht: Appl. Phys. Lett. **79**, 4360 (2001)
38. H. Iwata, U. Lindefelt, S. Öberg, and P.R. Briddon: Phys. Rev. B **65**, 033203 (2001)
39. C. Raffy, J. Furthmüller, and F. Bechstedt: J. Phys. Condens. Matter **14**, 12725 (2002)
40. M. Kohyama: Phys. Rev. B **65**, 184107 (2002)
41. K. Tanaka and M. Kohyama: Philos. Mag. A **82**, 215 (2002)
42. P. Hohenberg and W. Kohn: Phys. Rev. **136**, B864 (1964)
43. W. Kohn and L.J. Sham: Phys. Rev. **140**, A1133 (1965)
44. G. Kresse and J. Furthmüller: Comput. Mater. Sci. **6**, 15 (1996); Phys. Rev. B **54**, 11169 (1996)
45. J. Furthmüller, P. Käckell, F. Bechstedt, and G. Kresse: Phys. Rev. B **61**, 4576 (2000)

46. J.P. Perdew and A. Zunger: Phys. Rev. B **23**, 5048 (1981)
47. U. von Barth and L. Hedin: J. Phys. C **5**, 1629 (1972)
48. F. Bechstedt, A. Zywietz, K. Karch, B. Adolph, K. Tenelsen, and J. Furthmüller: Phys. Stat. Sol. (b) **202**, 35 (1997)
49. B. Wenzien, P. Käckell, F. Bechstedt, and G. Cappellini: Phys. Rev. B **52**, 10897 (1995)
50. G. Makov and M.C. Payne: Phys. Rev. B **51**, 4014 (1995)
51. L. Torpo, M. Marlo, T.E.M. Staab, and R.M. Nieminen: J. Phys. Condens. Matter **13**, 6203 (2001)
52. H.J. Monkhorst and J.D. Pack: Phys. Rev. B **13**, 5188 (1976)
53. C. Raffy, J. Furthmüller and F. Bechstedt: unpublished
54. U. Grossner, A. Fissel, J. Furthmüller, W. Richter, and F. Bechstedt: Materials Science Forum **353–356**, 211 (2001)
55. A. Zywietz, J. Furthmüller, and F. Bechstedt: Phys. Stat. Sol. (b) **210**, 13 (1998)
56. G.A. Baraff and M. Schlüter: Phys. Rev. B **30**, 1853 (1984)
57. F. Bechstedt, A. Zywietz, and J. Furthmüller: Europhys. Lett. **44**, 309 (1998)
58. L. Torpo, R.M. Nieminen, K.E. Laasonen, and S. Pöykkö: Appl. Phys. Lett. **74**, 221 (1999)
59. P. Deak, J. Miro, A. Gali, L. Udvardi, and H. Overhof: Appl. Phys. Lett. **75**, 2103 (1999)
60. A. Zywietz, J. Furthmüller, and F. Bechstedt: Phys. Rev. B **62**, 6854 (2000)
61. S.B. Zhang and J.E. Northrup: Phys. Rev. Lett. **67**, 2339 (1991)
62. J. Furthmüller, G. Cappellini, H.-C. Weissker, and F. Bechstedt: Phys. Rev. B **66**, 045110 (2002)
63. H. Itoh, A. Kawasuro, T. Ohshima, M. Yoshikawa, I. Nashiyama, S. Tanigawa, S. Misawa, H. Okumura, and S. Yoshida: Phys. Stat. Sol. (a) **162**, 173 (1997)
64. H.J. Kim and R.F. Davis: J. Electrochem. Soc. **133**, 2350 (1986)
65. M. Yamanaka, H. Daimon, E. Sakuma, S. Misawa, and S. Yoshida: J. Appl. Phys. **61**, 599 (1987)
66. T. Wimbauer, B.K. Meyer, A. Hofstaetter, A.Scharmann, and H. Overhof: Phys. Rev. B **56**, 7384 (1997)
67. J.M. Langer and H. Heinrich: Phys. Rev. Lett. **55**, 1414 (1985)
68. E. Rauls, T. Lingner, Z. Hajnal, S. Greulich-Weber, T. Fraunheim, and J.-M. Spaeth: Phys. Stat. Sol. (b) **217**, R1 (2000)
69. G. Davies, S.C. Lawson, A.T. Collins, A. Mainwood, and S.J. Sharp: Phys. Rev. B **46**, 13157 (1992)
70. N. Mizuochi, S. Yamasaki, H. Takizawa, N. Morishita, T. Ohshima, H. Itoh, and J. Isoya: Phys. Rev. B **66**, 235202 (2002)
71. R.E. Thomson and D.J. Chadi: Phys. Rev. B **29**, 889 (1984)
72. D.P. DiVincenzo, O.L. Alerhand, M. Schlüter, and J.W. Wilkins: Phys. Rev. Lett. **56**, 1925 (1986)
73. M. Kohyama: Modelling Simul. Mater. Sci. Eng. **10**, R31 (2002)
74. K.C. Pandey: Phys. Rev. Lett. **47**, 1913 (1981)
75. E. Takuma and H. Ichinose: Mat. Res. Soc. Symp. Proc. **652**, Y10.5 (2001)
76. P. Käckell and F. Bechstedt: Appl. Surf. Sci. **104/105**, 490 (1996)
77. P. Käckell, B. Wenzien, and F. Bechstedt: Phys. Rev. B **50**, 17037 (1994)
78. F. Bechstedt, A. Fissel, U. Grossner, U. Kaiser, H.-C. Weissker, and W. Wesch: Materials Science Forum **389–393**, 737 (2002)

- 79. H. Iwata, U. Lindefelt, S. Öberg, and P.R. Briddon: Materials Science Forum **389–393**, 533 (2002); J. Appl. Phys. **93**, 1577 (2003)
- 80. J. Furthmüller, P. Käckell, F. Bechstedt, A. Fissel, K. Pfennighaus, B. Schröter, and W. Richter: J. Electronic Materials **27**, 848 (1998)
- 81. U. Starke, J. Schardt, J. Bernhardt, M. Franke, K. Reuter, H. Wedler, K. Heinz, J. Furthmüller, P. Käckell, and F. Bechstedt: Phys. Rev. Lett. **80**, 758 (1998)
- 82. J.E. Northrup and J. Neugebauer: Phys. Rev. B **52**, 17001 (1995)
- 83. V. Heine, C. Cheng, and R. Needs: J. Am. Soc. Ceram. **74**, 2630 (1991)
- 84. M.J. Rutter and V. Heine: J. Phys. Condens. Matter **9**, 8213 (1997)

# Defect Migration and Annealing Mechanisms

M. Bockstedte, A. Mattausch, and O. Pankratov

## 1 Introduction

The diffusion and the annealing of defects represent two fundamental mechanisms of mass transport and defect reactions in semiconductors including SiC. They play a pivotal role in the device processing, for instance in the ion-implantation. Ion-implantation is the main technology to produce doped regions. It provides spatially well-defined dopant-profiles that are required to separate regions of  $p$ - and  $n$ -type conductivity in modern devices. Yet, the implantation creates various defects in the crystal that affect the electron mobility. The subsequent annealing seeks to remove the implantation-induced defects and to achieve an electrical activation of the dopant. However, the heat treatment not only anneals unfavorable defects, it also invokes a dopant diffusion which broadens the previously implanted profiles. Understanding the annealing processes and the dopant diffusion is therefore pivotal for the success of a semiconductor material.

The dopant diffusion is tightly linked to the migration of intrinsic defects. Substitutional impurities are per se immobile. Mobile intrinsic defects, namely vacancies and interstitials, act as vehicles for the dopant migration. Two factors influence the dopant diffusion: the abundance of vacancies and interstitials, and the mobility of the vehicles. Indeed, an excess of mobile intrinsic defects generated by the implantation triggers an enhanced dopant diffusion, which severely affects the implanted dopant profiles. This has been recently observed for the  $p$ -type dopants boron [1]–[3] and aluminum [4].

The kinetic properties of vacancies and interstitials may be studied directly by monitoring the annealing of intrinsic defect-centers or by analyzing the self diffusion. For the first approach the identification of the corresponding defect-center is a prerequisite for the analysis. In electron spin resonance experiments (EPR), defect-centers were identified as isolated silicon vacancies in 3C- and 4H-SiC [5, 6] and as carbon vacancies in 4H- and 6H-SiC [7]–[9]. This identification was theoretically verified [6, 10, 11]. In positron-annihilation spectroscopy (PAS), defects related to silicon and carbon vacancies can be distinguished by a considerable difference in the positron lifetime [12, 13]. The annealing behavior of silicon and carbon vacancies studied by EPR and PAS in irradiated material also contains information on the kinetics of interstitials that may recombine with the vacancies. Characteristic

differences were found between carbon and silicon vacancies. The carbon vacancy anneals in a single annealing stage at around 500°C in irradiated SiC [7], while it persists annealing to 850°C in semi-insulating material [8, 14]. The silicon vacancy was found to anneal in several stages in irradiated SiC. In EPR experiments its signal eventually vanishes above 750°C. In PAS, centers related to silicon vacancies disappear after going through similar annealing stages as the silicon vacancy in EPR. They finally anneal above 1450°C.

In the analysis of the self diffusion, contributions by interstitials and vacancies may be separated, for instance, by a quantitative modeling of isotope diffusion profiles (e.g. [15]). The first quantitative experiments [16]–[18] on the self diffusion in 3C- and 4H-SiC reported large activation energies for both, the silicon and the carbon diffusion. The analysis could not unravel the underlying mechanisms. In particular, the contribution of interstitials and vacancies remains open.

A microscopic picture of defect migration and annealing is unlikely to be developed from experiments alone. Theoretical investigations are necessary to analyze the abundance of defects and their migration from a microscopic point of view. Microscopic models for experimentally observed defect-centers can be developed or verified by the calculation of local vibrational frequencies, hyperfine tensors or positron lifetimes.

The microscopic properties and the abundance of vacancies [6],[19]–[21], antisites [21]–[24], and interstitials [25]–[27] were investigated within the framework of density functional theory (DFT). An identification [6, 10, 11] of EPR-centers became possible by the calculation of hyperfine parameters. The evaluation of the positron lifetime [28, 29] for defects related to silicon and carbon vacancies supported the analysis of PAS experiments. Furthermore, a metastability of the silicon vacancy in *p*-type SiC was predicted theoretically [25, 30]. A carbon vacancy-antisite complex that evolves from the metastable silicon vacancy was later observed in annealed irradiated SiC [31]. The migration of intrinsic point defects was investigated by *ab initio* methods in 3C-SiC [11, 26] and by a DFT-based tight-binding scheme in 4H-SiC [32]. These investigations also included an analysis of the recombination of interstitials and vacancies. It is predicted that interstitials play an important role in diffusion processes. Their migration proceeds with lower barriers than the vacancy migration. In particular the metastability of the silicon vacancy in *p*-type material affects its participation in the defect kinetics. From the calculated barriers a hierarchy of annealing stages was derived that qualitatively agreed with the experimental findings.

The present article outlines the current achievements in the microscopic understanding of the diffusion and annealing of intrinsic point defects in SiC. First we briefly summarize the *ab initio* method. The abundance of the intrinsic defects and the relative importance of specific interstitial sites is discussed in the following section. In Sects. 3 and 4, the migration mechanisms of the interstitials and vacancies are analyzed. The analysis includes the metasta-

bility of the silicon vacancy and its consequences for the vacancy migration. The role of interstitials and vacancies in the self and dopant diffusion is outlined. Then we turn to the annealing mechanisms of vacancies. A summary concludes the paper.

## 2 First-Principles Calculation of Defects Properties

### 2.1 The First-Principles Method

The ground state properties and the migration of defects are described using the first principles plane-wave method implemented in the program package FHI96MD [33]. In this method, the defect is described within a large supercell containing 64 or 216 lattice sites for 3C-SiC and 128 lattice sites for 4H-SiC. The electronic structure of the system is obtained using the density functional theory (DFT) and the local density approximation (LDA) for the description of the exchange-correlation functional. All atomic positions are allowed to relax to minimize the total energy of the defect. For silicon and carbon, soft norm conserving pseudopotentials of the Troullier-Martins type [34] are employed. The carbon potential has been optimized to allow for a small plane wave basis set with an energy cut-off of 30 Ry. A special  $k$ -point sampling [35] with 8 special  $k$ -points in the Brillouin zone is used, except when Jahn-Teller distortions become important. The calculations then were pursued in 216 atom cell with the  $\Gamma$ -point only, thereby preserving the proper degeneracy of the defect levels. For charged defects we include Madelung corrections [36] to account for the electrostatic interaction of the defect with its periodic images and the neutralizing background charge.

### 2.2 Defect Abundance and Defect Formation Energy

In thermodynamic equilibrium, the abundance of a defect is given by the defect's formation energy. In SiC, the formation energy depends on the chemical environment that is expressed by a carbon and a silicon chemical potential  $\mu_C$  and  $\mu_{Si}$ . In equilibrium,  $\mu_C$  and  $\mu_{Si}$  are related to the chemical potential of SiC  $\mu_{SiC}$  by  $\mu_{SiC} = \mu_C + \mu_{Si}$ . Hence the formation energy is a function of only one chemical potential,  $\Delta\mu_{Si} = \mu_{Si} - \mu_{Si}^0$ , where  $\mu_{Si}^0$  refers to crystalline silicon. For charged defects also the doping conditions enter via the Fermi level  $\mu_F$ . As outlined in [37] and [38], the formation energy reads

$$E_f^q = E_D^q - (n_{Si} - n_C) \Delta\mu_{Si} + q\mu_F, \quad (1)$$

where  $q$  is the charge state of the defect, and  $n_{Si}$  and  $n_C$  are the number of silicon and carbon atoms in the super cell. The quantity  $E_D^q$  is given by

$$E_D^q = E_{D,cell}^q - n_C\mu_{SiC} - (n_{Si} - n_C)\mu_{Si}^0 + qE_V, \quad (2)$$

$E_{\text{D,cell}}^q$  is obtained from the total energy of the defect cell;  $\mu_{\text{SiC}}$  as well as  $\mu_{\text{Si}}^0$  are to a good approximation given by the total energy of the crystals;  $E_{\text{V}}$  is the position of the valence band edge that we use as a reference for  $\mu_{\text{F}}$ . In order to preserve the stability of SiC, the chemical potential  $\Delta\mu_{\text{Si}}$  may vary only within the bounds  $-H_{\text{f,SiC}} < \Delta\mu_{\text{Si}} < 0$ , where the heat of formation of SiC  $H_{\text{f,SiC}}$  amounts to 0.61 eV according to our results (experiment: 0.72 eV). The lower and upper limit corresponds to an excess of carbon (C-rich conditions) and silicon (Si-rich conditions), respectively.

The ionization levels of a defect correspond to the Fermi level positions at which it is favorable for the defect to alter its charge state. The ionization level is given by

$$\epsilon(q_2|q_1) = E_{\text{D}}^{q_2} - E_{\text{D}}^{q_1}, \quad (3)$$

where the ionization changes the charge state from  $q_1$  to  $q_2$ , usually by one electron. The transfer of a second electron has to overcome the additional electron-electron repulsion  $U$  and is typically unfavorable. However, an additional relaxation driven by a strong electron-phonon coupling may over-compensate the electron-electron repulsion. In such a situation the effective electron-electron interaction is attractive (negative- $U$ ) and the ionization level  $\epsilon(q|q-1)$  appears below  $\epsilon(q+1|q)$ . The ionization levels are not only important to understand the electrical activity of a defect. The charge state of a defect sometimes influences the migration and annealing of defects. Three aspects depend on the charge state: (i) the ground state configuration, (ii) the migration path, and (iii) the migration barrier. Instances for these aspects are the metastability of the silicon vacancy and the equilibrium sites of the silicon interstitial.

### 2.3 Defect Migration: Migration Path and Energy Barriers

The migration and annealing of defects is investigated by analyzing the migration paths and barriers of the mobile defects and the recombination of interstitials and vacancies. As emphasized above, this analysis has to account for all relevant charge states of the defect. The analysis includes the migration between the energetically most favorable sites and other intermediate configurations that are possibly visited during the migration. The migration path with the lowest migration barrier, that starts and finally ends at the energetically lowest sites, constitutes the migration mechanism. In our analysis we employed two standard methods, the ridge method [39] and the drag method (e.g. [40]). The ridge method implements an automated search for the saddle point between adjacent defect sites. In the drag method, the potential energy surface between the initial and final site is calculated for a relevant subset of atomic coordinates, while the other coordinates are allowed to relax. In this way the migrating defect is dragged from the initial to the final site and the migration barrier is obtained. The interstitial migration and the recombination of interstitials and vacancies were primarily investigated using the

ridge method. We resorted to the drag method for the analysis of the vacancy migration. During the vacancy migration, defect states disperse through the band gap and have to be properly occupied, which is difficult to accomplish in the automatic search.

### 3 Hierarchy of Intrinsic Point Defects in SiC

In this section we focus on the abundance of mobile intrinsic defects and their hierarchical ordering according to their relative importance. In the self and dopant diffusion this hierarchy is important, as the abundance of the mobile defects, besides their diffusivities, enters into the diffusion constants.

The following discussion briefly reports on the properties of vacancies and describes in more detail the vacancy-antisite complexes and the possible interstitial configurations. The vacancy-antisite complexes are relevant for the migration of the vacancies. In particular, the carbon vacancy-antisite complex is connected to the metastability of the silicon vacancy in *p*-type material. The silicon and carbon interstitial can exist at a number of different sites that are important for the migration.

#### 3.1 Carbon and Silicon Vacancies

The silicon and carbon vacancies were discussed in detail in the works of Zywietz et al. [19, 41, 42], Torpo et al. [20, 21] and Deák et al. [43]. The two vacancies possess a three-fold degenerate defect level in the band gap, which in *4H*-SiC is split by the lower crystal field into a non-degenerate and a doubly degenerate level. In case of the carbon vacancy ( $V_C$ ), its occupation invokes a considerable Jahn-Teller-distortion. In *3C*-SiC, the vacancy can exist in the charge states  $2^+$ ,  $1^+$  and neutral. The negative charge states  $1^-$  and  $2^-$  are only found in *4H*-SiC for a Fermi level above 2.0 eV. Our results for the ionization levels are given in Table 1. According to these results and the results of Zywietz et al., a negative- $U$  effect appears for the charge states

**Table 1.** Ionization levels of the mobile defects in *3C*-SiC in eV

	$\varepsilon(+ ++)$	$\varepsilon(0 +)$	$\varepsilon(- 0)$	$\varepsilon(- - -)$
$V_C$	1.29	1.14	2.69	2.04
$V_{Si}$	–	0.18	0.61	1.76
$V_C\text{-}C_{Si}$	1.24	1.79	2.19	–
$Si_{sp}\langle 110 \rangle$	0.4	1.1	–	–
$C_{sp}\langle 100 \rangle$	0.6	0.8	1.8	–
$C_{sp}Si\langle 100 \rangle$	0.4	0.7	1.9	2.3

$1^+$  and  $1^-$ . This effect is also found for the vacancy in  $4H$ -SiC using a special  $k$ -point sampling. However, the size of this effect is small when applying the Madelung corrections. We obtain a value of  $-0.15$  eV, which is comparable to the accuracy of our calculations. On the other hand, Torpo et al. ([21]) report the absence of the negative- $U$  using these corrections. Taking the uncertainty in the total energy of charged defects into account, we cannot exclude that the positive charge state is stable around a Fermi level of  $1.2$  eV. The recent identification of the EI5-center in  $4H$ -SiC [7, 11] as a positive carbon vacancy gives indication towards a stable positive vacancy and that the negative- $U$  may be artificial.

For the silicon vacancy ( $V_{\text{Si}}$ ) a relevant Jahn-Teller distortion is not observed in the DFT calculations. Instead, a high-spin state is predicted. This is consistent with the findings of EPR experiments [5, 6] for the ground state of  $V_{\text{Si}}^-$ . Our results and the results of Torpo et al. show that the vacancy exists in the charge states  $1^+$ ,  $0$ ,  $1^-$  and  $2^-$  in  $3C$ -SiC. Already in weakly doped  $p$ -type material, i.e. for a Fermi level above  $0.6$  eV, the vacancy becomes negative. In  $4H$ -SiC, also the charge states  $3^-$  and  $4^-$  are realized in  $n$ -type material.

### 3.2 Vacancy-Antisite Complexes: The Metastability of the Silicon Vacancy

The simplest vacancy-antisite complex is created by exchanging the position of the vacancy with one of its nearest neighbors. By this transformation the properties of the original vacancy dramatically change. It is transformed into a vacancy on the other sublattice and a neighboring antisite. The silicon vacancy-antisite complex, which is related to the carbon vacancy, is, according to our results in  $3C$ -SiC, unstable in all relevant charge states. The silicon vacancy and the carbon vacancy-antisite complex ( $V_{\text{C}}\text{-}C_{\text{Si}}$ ), on the other hand, are related to each other: in  $p$ -type material the  $V_{\text{C}}\text{-}C_{\text{Si}}$ -complex is energetically more favorable than the silicon vacancy, whereas in  $n$ -type material the silicon vacancy is the more stable configuration. This metastability of the silicon vacancy was discussed by Bockstedte et al. in  $3C$ -SiC [25] using an ab initio method and by Rauls et al. [30] for the neutral pair in  $4H$ -SiC using a DFT based tight binding method. The formation energy of  $V_{\text{Si}}$  and  $V_{\text{C}}\text{-}C_{\text{Si}}$  as a function of the Fermi level is plotted in Fig. 1 for  $3C$ - and  $4H$ -SiC. The comparison of the formation energies shows the large energy gain yielded by the transformation of  $V_{\text{Si}}$  into  $V_{\text{C}}\text{-}C_{\text{Si}}$ . The metastability is important for its migration and annealing properties. In the following, we discuss the origin of this metastability and the energetic aspects in more detail and turn to the kinetic aspects of the transformation in Sect. 5.2.

The metastability of the silicon vacancy has its origin in the bonding of the carbon neighbors surrounding the vacancy.  $V_{\text{Si}}$  possesses a threefold degenerate level within the band gap formed by four carbon dangling bonds. By its

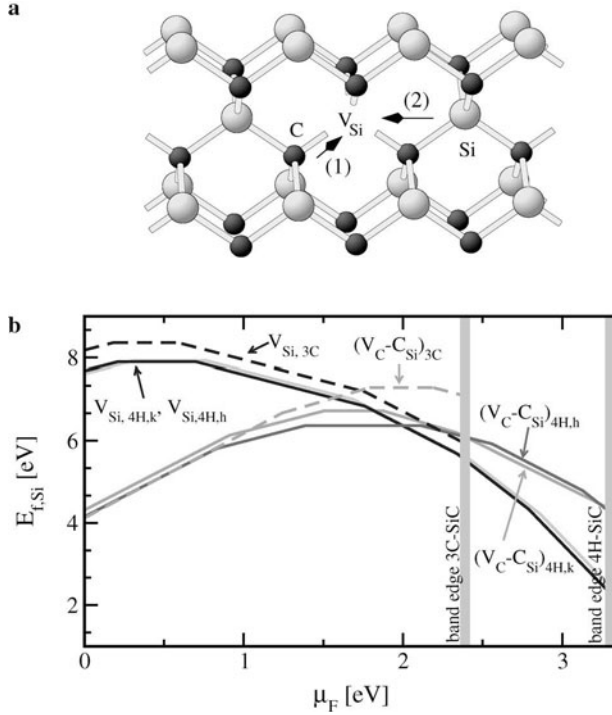


**Fig. 1.** Metastability of the silicon vacancy: (a) geometry of  $V_{Si}$ . The arrows indicate (1) the transformation of  $V_{Si}$  into  $V_C-C_{Si}$  and (2) the migration by second neighbor hops and (b) the formation energy of the silicon vacancy and the carbon vacancy-antisite complex as function of the Fermi level  $\mu_F$  for Si-rich conditions in 3C-SiC and 4H-SiC. The cubic and the hexagonal complexes are indicated by the subscripts  $k$  and  $h$ , respectively (cf. text)

transformation into the carbon vacancy-antisite complex three silicon dangling bonds and only one carbon dangling bond at the antisite are generated. These dangling bonds form a non-degenerate defect state mainly localized at the carbon dangling bond and a two-fold degenerate state comprised of the three silicon dangling bonds within the band gap. The creation of the carbon dangling bonds is energetically more costly than the silicon dangling bonds of the carbon vacancy, as a comparison of the formation energies in Figs. 2 and 3 shows. Therefore also the carbon vacancy-antisite complex is energetically more favorable than the silicon vacancy, when the defects are positively charged or neutral. However, the two defect levels of the carbon vacancy-antisite complex lie above the levels of the silicon vacancy. This observation implies that (i) the charge states of  $V_{Si}$  and  $V_C-C_{Si}$  are different for a given  $\mu_F$ , and (ii) with the successive occupation of the defect levels, the energy of  $V_C-C_{Si}$  rises faster than that of  $V_{Si}$ . Due to these facts it is pos-

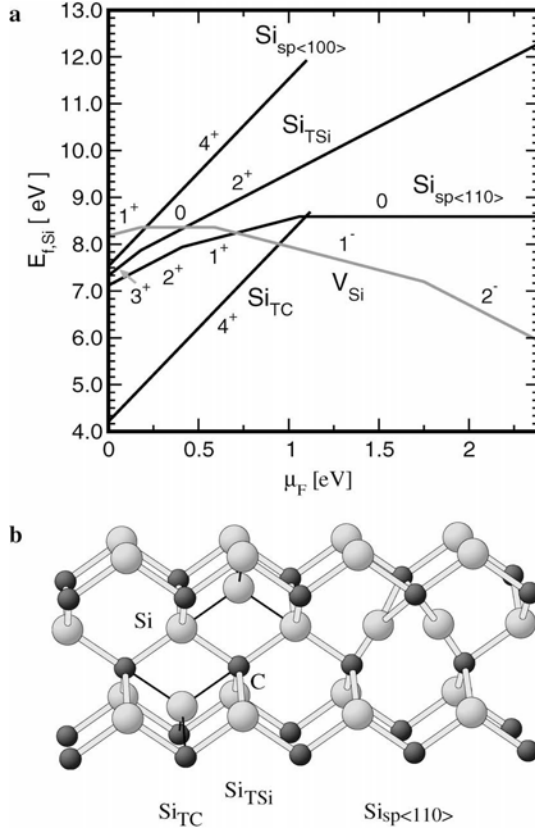


**Fig. 2.** Silicon interstitials: (a) formation energies of silicon interstitials and the silicon vacancy for Si-rich material, (b) geometry of the tetrahedrally coordinated interstitials and the  $\langle 110 \rangle$ -oriented split-interstitial

sible that the silicon vacancy becomes more stable in *n*-type material than the carbon vacancy-antisite complex. The vacancy-antisite complex is found in the charge states  $2^+$  through  $2^-$  in *3C*- and *4H*-SiC. Its ionization levels (cf. Table 1) lie above the corresponding levels of the silicon vacancy. The stabilization of the silicon vacancy over the vacancy-antisite complex occurs for a Fermi level above 1.7 eV, when the vacancy-antisite complex is neutral and the silicon vacancy is negative. As Fig. 1b shows, the properties of the defect in *3C*-SiC and *4H*-SiC are similar. In *4H*-SiC, several configurations of the complex exist, which are distinguished by the occupation of cubic or hexagonal lattice sites and the orientation of the complex with respect to the *c*-axis. In Fig. 1b, we have considered complexes oriented parallel to the *c*-axis with the vacancy and the antisite occupying either cubic or hexagonal sites.

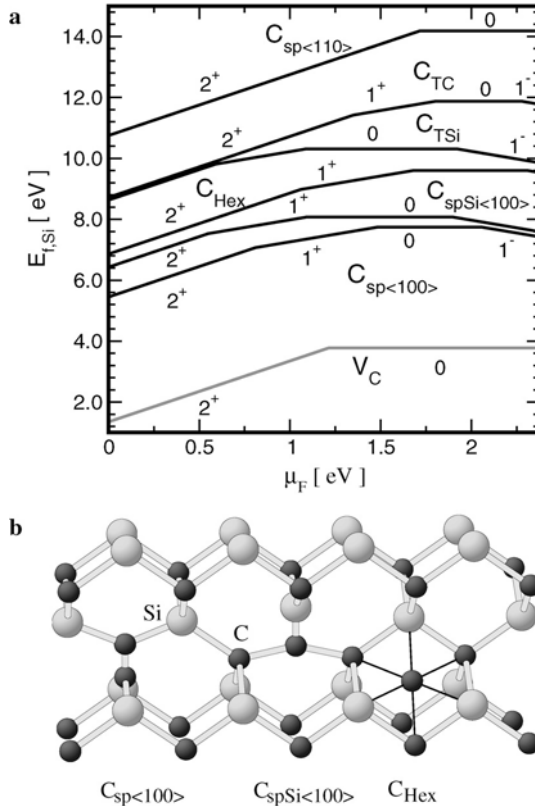


**Fig. 3.** Carbon interstitials: (a) formation energy of the carbon interstitials and the carbon vacancy for Si-rich material and (b) the  $\langle 100 \rangle$ -oriented split-interstitials at the carbon and silicon site and the hexagonal interstitial

### 3.3 Silicon Interstitials

Several different interstitial sites exist in cubic SiC as depicted in Fig. 2a,b besides tetrahedrally coordinated sites with either four carbon or silicon neighbors and hexagonal sites, bond-centered interstitials and split-interstitials may exist. The bond centered interstitial is located at the bond of two lattice atoms. In a split-interstitial, the silicon atom shares a site with a lattice atom forming a dumbbell-like atom pair. This atom pair is primarily oriented along the  $\langle 100 \rangle$ - or  $\langle 110 \rangle$ -directions. The realization of the tetrahedral, hexagonal and bond centered sites were first investigated using ab initio methods by Wang et al. [44] and later studied together with the split-interstitial sites by Bockstedte and Pankratov [25], and Mattausch et al. [26]. The latter investigation showed that the hexagonal and bond-center sites are unstable. Based on a comparison of the formation energies of the interstitial sites, it was found

that two different sites dominate: the tetrahedrally carbon coordinated interstitial ( $\text{Si}_{\text{TC}}$ ) and the  $\langle 110 \rangle$ -oriented split-interstitial ( $\text{Si}_{\text{sp}\langle 110 \rangle}$ ).

In  $p$ -type material, the tetrahedrally carbon coordinated site  $\text{Si}_{\text{TC}}$  is the most favorable site. The interstitial does not possess deep levels in the band gap. The interstitial silicon atom therefore donates its electrons to conduction band states. By the interaction with its carbon neighbors and a polarization of the surrounding bonds, the silicon atom is efficiently neutralized. As discussed in [38], polarization induced levels occur just below the conduction band edge. Due to their extended nature, an accurate treatment of these states is not possible. As the analysis indicated, the ionization levels are located above the mid gap (in Fig. 2a the formation energy of  $\text{Si}_{\text{TC}}$  is therefore not plotted above mid-gap).

In  $n$ -type material the split-interstitial  $\text{Si}_{\text{sp}\langle 110 \rangle}$  dominates over all other interstitial sites. This dominance is observed already for a mid-gap Fermi level, corresponding to intrinsic conditions. The interstitial has deep levels in the band gap arising from the  $sp^2$ -like bonding of the silicon atoms with their carbon neighbors. According to our results for the ionization levels,  $\text{Si}_{\text{sp}\langle 110 \rangle}$  is neutral for a Fermi level above mid-gap and positive below.

The other interstitial configurations have higher formation energies and are hardly relevant. In the migration of the two dominating sites they may act as intermediate sites, in particular for  $\text{Si}_{\text{TC}}$ . The electronic structure of these interstitials is discussed in detail in [38]. Here we also note that the silicon vacancy is less abundant than the silicon interstitial in  $p$ -type material. Only the carbon vacancy-antisite complex has a comparable formation energy. This situation changes in compensated and  $n$ -type material.

The silicon interstitials in  $4H$ -SiC have not been investigated in detail so far. Besides the interstitial sites discussed for  $3C$ -SiC, additional sites known from the hexagonal wurzite structure ( $2H$ -SiC) appear: a site where the interstitial has simultaneously four silicon and carbon neighbors and an open cage formed by the hexagonal rings of two adjacent lattice planes. For the interstitial sites with cubic surrounding we expect similar properties as in  $3C$ -SiC. The properties of the interstitial sites related to the hexagonal environment still needs to be investigated. Yet, we presume that the migration barriers are similar to those in the cubic arrangement.

### 3.4 Carbon Interstitials

Similar sites are available for the carbon interstitials as for the silicon interstitials. The detailed analysis [25, 27, 38] of the interstitial sites in  $3C$ -SiC shows that the carbon split-interstitial at the carbon and the silicon site with  $\langle 100 \rangle$ -orientation are the most abundant sites  $3C$ -SiC (cf. Fig. 3). The split-interstitial at the carbon site ( $\text{C}_{\text{sp}\langle 100 \rangle}$ ) is for all doping conditions energetically lower than that at the silicon site ( $\text{C}_{\text{spSi}\langle 100 \rangle}$ ). The next important site is the hexagonal site ( $\text{C}_{\text{Hex}}$ ). The tetrahedral sites and the  $\langle 110 \rangle$ -oriented split-interstitial site are less favorable.

The carbon split-interstitial  $C_{\text{sp}\langle 100 \rangle}$  has a doubly degenerate defect state within the band gap. The state derives from a  $sp^2$ -like hybridization of the carbon-orbitals and the dangling bonds of the four silicon neighbors. On the carbon atoms it is dominated by the  $p$ -orbital oriented perpendicular to the bonds of the carbon atom with its two silicon neighbors. In the charge state  $2^+$ , the degenerate defect state is not occupied and the symmetry of  $C_{\text{sp}\langle 100 \rangle}$  is  $D_{2d}$ . In the charge state  $1^+$ , a Jahn-Teller distortion moves the silicon neighbors out of the (110)-plane and reduces the symmetry to  $D_2$ . It is driven by a rehybridization of the carbon  $p$ -orbitals which now can participate in the bonds with the silicon neighbors. In the neutral and negative charge states also a tilt of the dumbbell with respect to the  $\langle 100 \rangle$ -direction is observed. According to our results for the ionization levels (cf. Table 1), the positive charge states  $2^+$  are  $1^+$  relevant for  $C_{\text{sp}\langle 100 \rangle}$  in  $p$ -type material. Only in  $n$ -type material, i.e. for  $\mu_F > 1.8$  eV, the interstitial is negative. The split-interstitial at the silicon site  $C_{\text{spSi}\langle 100 \rangle}$  has only non-degenerate states within the band gap. Therefore, it maintains its  $C_{2v}$ -symmetry and the orientation of the dumbbell when the defect states are occupied.  $C_{\text{spSi}\langle 100 \rangle}$  is realized in the charge states  $2^+$  through  $2^-$ . The energy difference between the  $C_{\text{spSi}\langle 100 \rangle}$ -site and the more stable  $C_{\text{sp}\langle 100 \rangle}$ -site is at most 0.9 eV, therefore this site is relevant for the migration of  $C_{\text{sp}\langle 100 \rangle}$ .

The lattice distortion introduced by the split-interstitials  $C_{\text{sp}\langle 100 \rangle}$  and  $C_{\text{spSi}\langle 100 \rangle}$  is essentially restricted to the surrounding neighbors. Hence, we expect similar properties also in other polytypes. Our recent results for  $C_{\text{sp}\langle 100 \rangle}$  and  $C_{\text{spSi}\langle 100 \rangle}$  in  $4H$ -SiC [38] essentially confirm this expectation. However, the hybridization of the defect states in  $4H$ -SiC differs from our findings in  $3C$ -SiC. This slightly affects the orientation of the pair and the bond distances. Due to the larger band gap of this polytype, also  $C_{\text{sp}\langle 100 \rangle}^{2-}$  becomes a stable charge state in  $n$ -type material. The neutral interstitials  $C_{\text{sp}\langle 100 \rangle}$  and  $C_{\text{spSi}\langle 100 \rangle}$  were investigated by Rauls et al. [32] before. Within their DFT-based tight-binding approach  $C_{\text{sp}\langle 100 \rangle}$  and  $C_{\text{spSi}\langle 100 \rangle}$  were found to be stable. Yet, a larger energy difference between  $C_{\text{sp}\langle 100 \rangle}$  and  $C_{\text{spSi}\langle 100 \rangle}$  were obtained. As argued there, this finding could depend on the employed tight-binding parameterization.

## 4 Interstitial Migration

### 4.1 Silicon Interstitials

The migration path of the silicon interstitial starts and ends at the energetically most stable site. In  $3C$ -SiC, these sites are the tetrahedral interstitial  $\text{Si}_{\text{TC}}$  in  $p$ -type material and the split-interstitial  $\text{Si}_{\text{sp}\langle 110 \rangle}$  for intrinsic conditions and in  $n$ -type material. In the following, we discuss the most relevant migration paths for the two interstitials. Examples for these paths are sketched in Fig. 4a,b. A summary of the migration paths and barriers is given in Table 2.

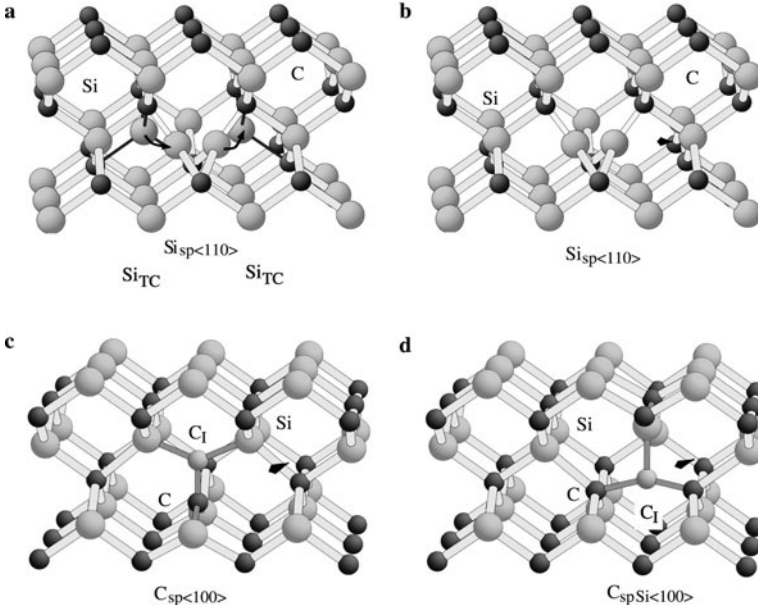


**Fig. 4.** Migration of silicon and carbon interstitials: (a) migration of the  $Si_{TC}$ -interstitial via the split-interstitial  $Si_{sp<110>}$ , (b) migration of  $Si_{sp<110>}$  between adjacent lattice sites, (c) second neighbor hop of the carbon split-interstitial  $C_{sp<100>}$ , (d) nearest neighbor hop of the split-interstitial between silicon and carbon sites. In (a) the initial, intermediate, and final site and the motion of the Si-atoms is indicated. In (b), (c), and (d) the initial site and the hopping direction are shown

**Table 2.** Silicon interstitials: migration barriers in eV for the dominant migration paths

	$Si_{TC}^{4+} \leftrightarrow Si_{TC}^{4+}$	$Si_{TC}^{4+} \leftrightarrow Si_{sp<110>}^{4+}$	$Si_{TC}^{4+} \leftrightarrow Si_{TSi}^{4+}$
1 $\rightarrow$ 2	3.5	3.4	3.5
2 $\rightarrow$ 1	0.03	0.05	0.3
	$Si_{sp<110>}^+ \leftrightarrow Si_{sp<110>}^+$	$Si_{sp<110>}^0 \leftrightarrow Si_{sp<110>}^0$	$Si_{sp<110>}^0 \leftrightarrow Si_{sp<1-10>}^0$
1 $\leftrightarrow$ 2	1.0	1.4	1.3

In *p*-type material, the migration path connects adjacent  $Si_{TC}$ -sites. Such carbon-coordinated tetrahedral sites are found in the  $\langle 100 \rangle$ -direction and the  $\langle 110 \rangle$ -direction. In the  $\langle 110 \rangle$ -direction, the  $Si_{TC}$ -sites are connected via a tetrahedrally silicon coordinated site. Along the  $\langle 100 \rangle$ -direction, a silicon-lattice atom hinders a direct motion of the interstitial to the next  $Si_{TC}$ -site. From this observation two migration mechanisms become plausible: (a) direct migration through the interstitial region via the silicon coordinated

site  $\text{Si}_{\text{TSi}}$  and (b) the migration via the split-interstitials  $\text{Si}_{\text{sp}\langle 100 \rangle}$  or  $\text{Si}_{\text{sp}\langle 110 \rangle}$  as intermediate sites.

The direct migration path leads along the  $\langle 111 \rangle$ -direction through the hexagonal ring to the next  $\text{Si}_{\text{TSi}}$ -site with a barrier of 3.5 eV. From the  $\text{Si}_{\text{TSi}}$ -site, the interstitial could continue in the  $\langle 110 \rangle$ -direction or change its direction to reach one of the other three surrounding  $\text{Si}_{\text{TC}}$ -sites. The barrier for the migration from the  $\text{Si}_{\text{TSi}}$ -site to the  $\text{Si}_{\text{TC}}$ -site amounts to 0.3 eV. Since at the  $\text{Si}_{\text{TSi}}$ -site the charge state  $4^+$  is not the ground state, a charge transfer may alter the charge state with some probability. Then the migration could alternatively continue via the  $\langle 110 \rangle$ -oriented split-interstitial with a low barrier. However, this route is not very likely as the  $\text{Si}_{\text{TSi}}$ -interstitial with an even lower barrier would move towards an adjacent  $\text{Si}_{\text{TC}}$ -site.

The migration of  $\text{Si}_{\text{TC}}$  via the split-interstitial sites proceeds by a hop towards one of the neighboring silicon lattice sites. By this hop, the lattice atom is displaced from its site, thus creating either a  $\langle 100 \rangle$ - or  $\langle 110 \rangle$ -oriented split-interstitial ( $\text{Si}_{\text{sp}\langle 100 \rangle}$  or  $\text{Si}_{\text{sp}\langle 110 \rangle}$ ). This displaced atom then may continue towards the adjacent  $\text{Si}_{\text{TC}}$ -site as depicted in Fig. 4a. In case of the  $\text{Si}_{\text{sp}\langle 110 \rangle}$ -site, the migration could also proceed with the initial silicon atom to a different  $\text{Si}_{\text{TC}}$ -site. As for  $\text{Si}_{\text{TSi}}$ , the charge state  $4^+$  is not the equilibrium charge state of  $\text{Si}_{\text{sp}\langle 110 \rangle}$ . However, since we have found very low barriers for leaving the split-interstitial sites, we expect that the migration continues without altering the charge state at this site. The migration barriers amount to 3.4 eV ( $\text{Si}_{\text{sp}\langle 110 \rangle}$ ) and 3.5 eV ( $\text{Si}_{\text{sp}\langle 100 \rangle}$ ). Within the accuracy of the calculation, the migration via the direct or the kick-out path is equally likely.

For intrinsic conditions and in  $n$ -type material the silicon interstitial migrates as a neutral split-interstitial  $\text{Si}_{\text{sp}\langle 110 \rangle}$ . As depicted in Fig. 4b, one of the silicon atoms of the interstitial configuration hops along the  $\langle 110 \rangle$ -direction towards the next silicon lattice site. In this manner it displaces the silicon atom at this site and thus forms a new split-interstitial. The migration barrier for this path amounts to 1.4 eV. The direction of the migration by this hop is determined by the orientation of the silicon pair. The pair can change its orientation for example from  $\langle 110 \rangle$ -direction to the  $\langle 1\bar{1}0 \rangle$ -direction by turning around the  $\langle 001 \rangle$ -axis. The barrier for this turn amounts to 1.3 eV. This enables an isotropic migration of the split-interstitial.

## 4.2 Carbon Split-Interstitials

The carbon split-interstitial  $\text{C}_{\text{sp}\langle 100 \rangle}$  is the most stable carbon interstitial. The migration of the carbon interstitial thus proceeds between adjacent  $\text{C}_{\text{sp}\langle 100 \rangle}$ -sites. The energetically lowest intermediate-site for the migration is the  $\text{C}_{\text{spSi}\langle 100 \rangle}$ -sites. Two migration mechanisms exploit this fact: (i) the second neighbor hop of one carbon atom ( $\text{C}_I$  in Fig. 4c) in the  $\langle 110 \rangle$ -direction to the next carbon site as indicated in Fig. 4c and (ii) the consecutive nearest neighbor hops between neighboring carbon and silicon sites in the sequence  $\text{C}_{\text{sp}\langle 100 \rangle} \rightarrow \text{C}_{\text{spSi}\langle 100 \rangle} \rightarrow \text{C}_{\text{sp}\langle 100 \rangle}$  (the last hop is indicated in Fig. 4d)

**Table 3.** Carbon split-interstitial: migration barriers in eV for the nearest and second neighbor hop in 3C-SiC. The last column refers to the values in 4H-SiC of Ref. [38]

				2 <sup>+</sup>	1 <sup>+</sup>	0	1 <sup>-</sup>	4H,0
C <sub>sp&lt;100&gt;</sub>	↔	C <sub>sp&lt;100&gt;</sub>		1.4	0.9	0.5	0.6	2.9
C <sub>sp&lt;100&gt;</sub>	→	C <sub>spSi&lt;100&gt;</sub>		1.7	0.9	0.5	0.7	–
C <sub>spSi&lt;100&gt;</sub>	→	C <sub>sp&lt;100&gt;</sub>		0.7	0.2	0.2	0.1	–

In both cases, the hop in the (110)-direction induces a rotation of the carbon pair and a displacement of the silicon-neighbor next to the hopping carbon atom basically in the (001)-direction. To avoid strained bonds the motion of the involved atoms is not restricted to the (1-10)-plane alone. We have calculated the barriers for the migration of C<sub>sp<100></sub><sup>2+</sup>, C<sub>sp<100></sub><sup>+</sup> and C<sub>sp<100></sub><sup>0</sup>, and C<sub>sp<100></sub><sup>-</sup>. The results are listed in Table 3. For the migration by second neighbor hops and via C<sub>spSi<100></sub>-sites, similar barriers are found. Hence both mechanisms are equally likely. Significantly lower barriers are found for C<sub>sp<100></sub><sup>0</sup> than for C<sub>sp<100></sub><sup>2+</sup> and C<sub>sp<100></sub><sup>-</sup>. This shows that in compensated material the split-interstitial is far more mobile than in *p*-type material.

A migration of the split-interstitial via the hexagonal site, the tetrahedral site, or the <110>-oriented split-interstitial is unlikely. The energy difference between C<sub>sp<100></sub> and the hexagonal site in the charge state 2<sup>+</sup> is slightly lower than the migration barrier of C<sub>sp<100></sub> and exceeds it in the positive and neutral charge states. Assuming similar barriers as for the second neighbor hop, we expect that a migration via the hexagonal site contributes little to the migration of C<sub>sp<100></sub>. The tetrahedral sites and the <110>-oriented split-interstitial have a much higher energy than C<sub>sp<100></sub> and are therefore not relevant.

In 4H-SiC, Rauls et al. [32] have analyzed the migration of C<sub>sp<100></sub> via second neighbor hops for the neutral charge state. The migration in this polytype is not isotropic, as at hexagonal and cubic sites different arrangements of the second neighbor sites are found. This affects the barrier heights differently in each possible direction. A lowest migration barrier of 2.9 eV was determined in their calculations for the migration along the (0001)-direction. This migration barrier is much higher than our result. The difference to our result is consistent with their finding of the much larger energy difference between the C<sub>sp<100></sub>-site and the C<sub>spSi<100></sub>-site that, as stated there, may be related to the tight binding parameterization. Other results for the migration barriers in 4H-SiC are to our knowledge not available.

## 5 Vacancy Migration

### 5.1 Carbon and Silicon Vacancies

The migration of the vacancies can proceed by hops of neighboring atoms into the vacancy, whereby the vacancy moves to the lattice site of the hopping atom. Such hops are primarily performed by the nearest neighbor and the second neighbor of the vacancy, as sketched in Fig. 1a for the silicon vacancy. Apparently, the nearest neighbor hop transforms the vacancy into a vacancy-antisite complex. In the case of the carbon vacancy such a complex is unstable. Hence, a migration via second neighbor hops is a more likely scenario. In the case of the silicon vacancy, the nearest neighbor hop transforms the vacancy into the more stable vacancy-antisite complex. However, a further transformation of the carbon vacancy-antisite complex by a consecutive nearest neighbor hop is not possible. The  $V_{\text{Si-SiC-C}_{\text{Si}}}$ -complex that would result from such a transformation is unstable in all relevant charge states. Hence, a migration mechanism solely based on nearest neighbor hops is not possible. A migration of the silicon vacancy by second neighbor hops should prevail. Yet, except for  $n$ -type material, where the silicon vacancy is stable, the effect of the metastability has to be taken into account. We defer this discussion to the next section and concentrate on the migration by second neighbor hops first.

Our analysis of the second neighbor hop in  $3C\text{-SiC}$ , including its migration path and the calculation of the migration barriers using the drag method is detailed in [38]. Here we basically outline the results for the migration barriers we have tabulated in Table 4. For the carbon vacancy, we find a strong dependence of the migration on the charge state. The migration of  $V_{\text{C}}^{2+}$  proceeds with a barrier of 5 eV in  $p$ -type material. In  $n$ -type material, bonding states are occupied at the transition state, which reduces the barrier of the neutral vacancy to 3.5 eV. The migration for intrinsic conditions may proceed in the positive charge state with a barrier between these two extremes. For the silicon vacancy, the barriers of the second neighbor hop are affected to

**Table 4.** Carbon and silicon vacancies: energy barriers in eV for the migration of  $V_{\text{C}}$  and  $V_{\text{Si}}$  by second neighbor hops and for the transformation of  $V_{\text{Si}}$  into  $V_{\text{C-C}_{\text{Si}}}$  for the relevant charge states in  $3C\text{-SiC}$ . The last column refers to the values in  $4H\text{-SiC}$  of Ref. [38]

		$2^+$	$1^+$	0	$1^-$	$2^-$	$4H, 0$
$V_{\text{C}}$	$\leftrightarrow V_{\text{C}}$	5.2	4.1	3.5	–	–	5.2
$V_{\text{Si}}$	$\leftrightarrow V_{\text{Si}}$	–	3.6	3.4	3.2	2.4	4.8
$V_{\text{Si}}$	$\rightarrow V_{\text{C-C}_{\text{Si}}}$	–	1.9	2.4	2.5	2.7	1.7
$V_{\text{C-C}_{\text{Si}}}$	$\rightarrow V_{\text{Si}}$	6.1	4.2	3.5	2.4	–	

a smaller extend by the charge state. In  $p$ -type and compensated material values between 3.2 eV and 3.6 eV are found. Only the migration of  $V_{\text{Si}}^{2-}$  in  $n$ -type material proceeds with a smaller barrier of 2.4 eV. However, a transformation into the more stable vacancy-antisite complex for a Fermi level below 1.7 eV affects the migration of the silicon vacancy. Only in  $n$ -type material the migration may proceed freely.

## 5.2 Transformation of $V_{\text{Si}}$ into $V_{\text{C-CSi}}$ : Consequences for the Migration

The discussion in the previous section has shown that the silicon vacancy and vacancy-antisite complex  $V_{\text{C-CSi}}$  can transform into each other. In  $p$ -type and compensated material  $V_{\text{C-CSi}}$  is the stable configuration. When the two configurations are in thermodynamic equilibrium, the kinetics of the metastability-induced transformation does not interfere with the migration of the silicon vacancy. The kinetics of the transformation may become important if the barriers involved in the vacancy migration and the metastability-induced transformation differ significantly. Then, the timescale and the temperature may play an important role. A comparison of the barriers of these processes is also important for the annealing mechanisms of the vacancy.

As above, we refer the reader to [38] for a detailed description of the mechanism and the calculation of the energy barriers. The results for the transformation barriers of  $V_{\text{Si}}$  into  $V_{\text{C-CSi}}$  and for the reverse process are summarized in Table 4. The charge state that is relevant during the transformation is determined by the charge state at the initial site. We assume that the charge state is preserved during the process. Yet, this is not the preferred charge state of the final configuration. Eventually, the equilibrium charge state is obtained at the final configuration by exchanging electrons with other defects, the valence or conduction band. This applies also for the transformations  $V_{\text{Si}}^{2-} \rightarrow (V_{\text{C-CSi}})^{2-}$  and  $(V_{\text{C-CSi}})^{2+} \rightarrow V_{\text{Si}}^{2+}$ , where  $(V_{\text{C-CSi}})^{1-}$  and for example  $V_{\text{Si}}^{1+}$  are the preferred charge states.

The metastability of the vacancy in  $p$ -type material and its stabilization in  $n$ -type material is accompanied by a pronounced variation of the transformation barriers with the charge state. In  $p$ -type and compensated material, the transformation  $V_{\text{Si}} \rightarrow V_{\text{C-CSi}}$  has a much lower barrier (between 1.9 eV and 2.5 eV) than the reverse process  $V_{\text{C-CSi}} \rightarrow V_{\text{Si}}$  (6.1 eV for  $\mu_{\text{F}} < 1.24$  eV, and between 4.2 eV and 3.5 eV for  $1.24 \text{ eV} < \mu_{\text{F}} < 2.19$  eV). The first process is thus more likely than the second. Only for  $\mu_{\text{F}} > 2.19$  eV, where  $(V_{\text{C-CSi}})^{1-}$  is stable, the transformation  $V_{\text{Si}}^{2-} \rightarrow (V_{\text{C-CSi}})^{2-}$  has a lower probability than the reverse process  $(V_{\text{C-CSi}})^{1-} \rightarrow V_{\text{Si}}^{1-}$ .

For the migration of  $V_{\text{Si}}$  the energy barrier is higher than the transformation barrier for  $V_{\text{Si}} \rightarrow V_{\text{C-CSi}}$  except for  $V_{\text{Si}}^{2-}$ , i.e. when  $\mu_{\text{F}} > 1.76$  eV. Thus kinetic effects may become important at low and moderate temperatures, when the metastability-induced transformation is thermally activated, but

not the reverse transformation and the vacancy migration. Then the transformation of the vacancy into the vacancy-antisite complex efficiently diminishes its concentration and prevents its migration. Only at higher temperatures, when the reverse transformation  $V_C-C_{Si} \rightarrow V_{Si}$  is sufficiently activated, a migration via the silicon vacancy, now acting as an intermediate site, should be observed. The effective barrier for the process is given by the difference of the formation energies  $E_f^{V_{Si}}$  and  $E_f^{V_C-C_{Si}}$  and the migration barrier of the vacancy  $E_m^{V_{Si}}$

$$E_{m,eff}^{V_C-C_{Si}} = E_f^{V_{Si}} - E_f^{V_C-C_{Si}} + E_m^{V_{Si}}. \quad (4)$$

In *p*-type material,  $E_{m,eff}^{V_C-C_{Si}}$  amounts to 7.7 eV and drops to 4.3 eV for  $\mu_F = 1.2$  eV. Yet, equilibrium has to be maintained between the two defects. This implies that the transformation with a barrier of 6.1 eV has to be activated for  $\mu_F < 1.24$  eV. For a Fermi level above mid-gap, this activation barrier becomes much lower and this criterion is no longer critical. An effective barrier of 3.2 eV still has to be surmounted at  $\mu_F = 1.76$  eV, where  $V_{Si}$  becomes stable.

Besides the migration via a metastable silicon vacancy, a dissociation of the vacancy-antisite complex may lead to a migration of the carbon vacancy away from the antisite at the expense of the binding energy. Using the migration barrier for the vacancy in *p*-type material plus the binding energy of 1 eV, we arrive at an estimate of 6.2 eV and 4.5 eV for the dissociation of  $(V_C-C_{Si})^{2+}$  and  $(V_C-C_{Si})^0$ , respectively. Only in *p*-type and compensated material ( $\mu_F < 1.24$  eV), the dissociation has a similar probability as the transformation  $(V_C-C_{Si}) \rightarrow V_{Si}$ , followed by a vacancy migration.

We have not investigated the transformation barriers in 4*H*-SiC. Rauls et al. [30] have investigated the neutral case. They obtained a transformation barrier of 1.7 eV, which is in agreement with our results in 3*C*-SiC. Therefore we expect similar properties of this transformation in relation to the vacancy migration and a possible dissociation of the carbon vacancy-antisite complex in *p*-type and compensated material.

## 6 Self and Dopant Diffusion

The availability of vacancies or interstitials is crucial for their contribution to self and dopant diffusion besides the migration rates of individual lattice atoms or mobile dopant-vacancy complexes and dopant interstitials. In the following discussion we outline the interplay of these two factors, namely the abundance and the mobility, for the self diffusion. We also discuss the dopant-diffusion in the context of the vacancy and interstitial migration.

### 6.1 Self Diffusion

The self diffusion constants  $D_{Si}$  and  $D_C$  of silicon and carbon atoms are obtained from contributions of different migration mechanisms, in particular

from the vacancies  $V_{\text{Si}}$ ,  $V_{\text{C}}$  and the interstitials  $\text{Si}_{\text{TC}}$ ,  $\text{Si}_{\text{sp}\langle 110 \rangle}$ , and  $\text{C}_{\text{sp}\langle 100 \rangle}$ . For example, the carbon self diffusion constant reads

$$D_{\text{C}} = D_{V_{\text{C}}} + D_{\text{CI}} + \Sigma_i D_i, \quad (5)$$

where  $D_{V_{\text{C}}}$  and  $D_{\text{CI}}$  denote the diffusion constants of  $V_{\text{C}}$  and  $\text{C}_{\text{sp}\langle 100 \rangle}$ , respectively. The third term in (5) stands for contribution of other possible mechanisms such as the migration along extended defects, which we do not consider here. In thermodynamic equilibrium, the contribution of vacancy and interstitial related mechanisms is described by a prefactor  $D_0$  and an activation energy  $Q$

$$D = D_0 \exp(-Q/kT), \quad (6)$$

where  $k$  is the Boltzmann constant and  $T$  the temperature. The activation energy  $Q$  accounts for the concentration of the mobile defect, as described by the formation energy  $E_{\text{f}}^q(\Delta\mu_{\text{Si}}, \mu_{\text{F}})$  in (1) and its migration with a migration barrier  $E_{\text{m}}^q$

$$Q = E_{\text{f}}^q(\Delta\mu_{\text{Si}}, \mu_{\text{F}}) + E_{\text{m}}^q. \quad (7)$$

According to (1), the formation energy depends on the chemical environment through the chemical potential  $\Delta\mu_{\text{Si}}$  and on the doping conditions through the Fermi level  $\mu_{\text{F}}$ . This expresses the fact that in a carbon-rich environment, for instance, carbon interstitials and silicon vacancies have a higher abundance than in silicon-rich environment. Hence, also the activation energy will depend on the chemical environment and the doping conditions, which also enter via the charge state dependence of the migration barrier. According to (1), the formation energy linearly depends on  $\mu_{\text{F}}$  for a given charge state  $q$ , which translates into the same linear dependence of the activation energy. This so called Fermi level effect has to be taken into account when comparing activation energies measured in different samples [45].

In Tables 5 and 6 we have compiled the activation energies of the contributions by vacancies and interstitials to the carbon and silicon self diffusion. The activation energy for each charge state is listed in three different ways. In the second column  $Q$  is listed as derived from (1) and (7). In the following two columns this expression is evaluated for the relevant range of  $\mu_{\text{F}}$ . Whereas the third column accounts for Si-rich conditions, i.e.  $\Delta\mu_{\text{Si}} = 0$ , the fourth column accounts for C-rich conditions, i.e.  $\Delta\mu_{\text{Si}} = -H_{\text{f,SiC}}$ . A comparison of the activation energies for vacancies and interstitials reveals the dominant contributions to self diffusion.

Our results indicate that the carbon self diffusion is mediated to similar extend by carbon vacancies and carbon split-interstitials. In Si-rich material, no clear dominance exists. In C-rich material a preference for a split-interstitial mediated carbon diffusion is observed. The silicon self diffusion is clearly dominated by silicon interstitials ( $\text{Si}_{\text{TC}}^{4+}$ ) in Si- or C-rich  $p$ -type material, i.e. for  $\mu_{\text{F}} < 0.8$  eV. The contribution of the silicon vacancy for  $\mu_{\text{F}} > 0.8$  eV is restricted to conditions where an equilibrium between the vacancy and the

**Table 5.** Carbon self diffusion: activation energies for vacancy and interstitial mediated diffusion. The activation energy is listed as an explicit function of  $\mu_F$  and  $\Delta\mu_{Si}$  as obtained from (1) and (7). In columns 3 and 4, the ranges of the activation energy corresponding to the range of  $\mu_F$ , in which the defect is stable, are given for Si-rich and C-rich conditions.  $E_C$  denotes the conduction band edge

Defect	$Q(\Delta\mu_{\text{Si}}, \mu_F)$ [eV]							$\mu_F$ [eV]
	Explicit				Si-rich	C-rich	Range	
$V_C^{2+}$	6.6 eV	+	$2\mu_F$	−	$\Delta\mu_{\text{Si}}$	6.6–9.0	7.2–9.6	0.0–1.2
$V_C^0$	7.3 eV	+		−	$\Delta\mu_{\text{Si}}$	7.3	7.9	1.2– $E_C$
$C_{\text{sp}(100)}^{2+}$	6.7 eV	+	$2\mu_F$	−	$\Delta\mu_{\text{Si}}$	6.7–7.8	6.1–7.2	0.0–0.6
$C_{\text{sp}(100)}^{1+}$	6.6 eV	+	$\mu_F$	−	$\Delta\mu_{\text{Si}}$	7.2–7.9	6.6–7.3	0.6–0.8
$C_{\text{sp}(100)}^0$	7.2 eV	+		−	$\Delta\mu_{\text{Si}}$	7.2	6.6	0.8–1.8
$C_{\text{sp}(100)}^-$	9.1 eV	−	$\mu_F$	−	$\Delta\mu_{\text{Si}}$	7.3–6.7	6.7–6.1	1.8– $E_C$

**Table 6.** Silicon self diffusion: activation energies for vacancy and interstitial mediated diffusion. The activation energy is listed as an explicit function of  $\mu_F$  and  $\Delta\mu_{Si}$  as obtained from (1) and (7). In columns 3 and 4, the ranges of the activation energy corresponding to the range of  $\mu_F$ , in which the defect is stable, are given for Si-rich and C-rich conditions.  $E_C$  denotes the conduction band edge

Defect	$Q(\Delta\mu_{\text{Si}}, \mu_{\text{F}})$ [eV]							$\mu_{\text{F}}$ [eV]
	Explicit					Si-rich	C-rich	Range
$V_{\text{Si}}^-$	12.2 eV	−	$\mu_{\text{F}}$	+	$\Delta\mu_{\text{Si}}$	11.6–10.4	11.0–9.8	0.6–1.8
$V_{\text{Si}}^{2-}$	13.1 eV	−	$2\mu_{\text{F}}$	+	$\Delta\mu_{\text{Si}}$	9.6–7.7	9.0–7.1	1.8– $E_{\text{C}}$
$\text{Si}_{\text{TC}}^{4+}$	7.7 eV	+	$4\mu_{\text{F}}$	−	$\Delta\mu_{\text{Si}}$	7.8–12.6	8.4–13.2	0.0–1.2
$\text{Si}_{\text{sp}(110)}^0$	9.9 eV	−	$\Delta\mu_{\text{Si}}$			9.9	10.5	1.1– $E_{\text{C}}$

vacancy-antisite complex is maintained. In compensated and  $n$ -type material, the silicon split-interstitial is the relevant interstitial site. This interstitial dominates the silicon diffusion in Si-rich material for  $\mu_F < 1.8$  eV. Above this value for  $\mu_F$  the abundance of  $V_{Si}^{2-}$  increases and compensates for the barrier of the vacancy migration. The vacancy mediated diffusion thereby becomes the leading mechanism in  $n$ -type material. In C-rich material and for  $\mu_F > 0.8$  eV, the silicon vacancy clearly dominates the self diffusion, except for intrinsic conditions where the split-interstitial and the vacancy contribute to a similar extent.

The carbon and silicon self diffusion in  $3C$ - and  $4H$ -SiC were investigated by Hong et al. [16, 18] and Hon et al. [17] by a tracer method. The activation energies were determined for nominally undoped poly-crystalline  $3C$ -SiC as well as for intrinsic and  $n$ -type  $4H$ -SiC. It was not stated whether Si-rich or

C-rich conditions applied to the experiments. In 3C-SiC an activation energy of  $9.45 \text{ eV} \pm 0.05 \text{ eV}$  was found for the silicon self diffusion. Assuming that the Fermi level in the undoped experimental samples was positioned at or above mid-gap, the experimental activation energy is in good agreement with our values found for  $\text{Si}_{\text{sp}\langle 110 \rangle}$  in Si-rich material (9.9 eV) and in C-rich material, where the values range between 9.8 eV and 10.5 eV (depending on  $\mu_F$ ). For the carbon self diffusion in polycrystalline 3C-SiC, the experimental activation energy amounted to  $8.72 \text{ eV} \pm 0.14 \text{ eV}$ . This result has to be compared with our values in Si-rich material of about 7.2 eV ( $\text{C}_{\text{sp}\langle 100 \rangle}^0$  or  $\text{V}_C^0$ ) and in C-rich material of 6.6 eV for the diffusion mediated by  $\text{C}_{\text{sp}\langle 100 \rangle}$ . The discrepancy of 1.7 eV–2 eV cannot be explained by the uncertainty in the chemical potential  $\Delta\mu_{\text{Si}}$  and the Fermi level  $\mu_F$ . Only if we assume that  $\text{V}_C^{2+}$  mediates the diffusion and the contribution of interstitials is suppressed the calculated activation energy agrees with the experimental value. Here the polycrystalline nature of the material may have affected the defect equilibrium.

Even though our results for the self diffusion are obtained for 3C-SiC, with some limitations these results should also apply for the self diffusion in 4H-SiC. This expectation is based on two observations: (i) the formation energy of vacancies and carbon interstitials typically vary by less than 1 eV between different polytypes and (ii) the migration mechanisms are similar in 3C- and 4H-SiC. The main differences lie in the existence of additional sites for the silicon interstitials in the hexagonal polytypes and the larger band gap. However, the self diffusion experiments in intrinsic and *n*-type 4H-SiC resulted in different activation energies than in polycrystalline 3C-SiC. For the carbon self diffusion  $7.14 \text{ eV} \pm 0.05 \text{ eV}$  (intrinsic material) and  $8.20 \text{ eV} \pm 0.08 \text{ eV}$  (*n*-type material) were obtained by the analysis. The silicon self diffusion was described by  $7.22 \text{ eV} \pm 0.07 \text{ eV}$  (intrinsic material) and  $8.18 \text{ eV} \pm 0.10 \text{ eV}$  (*n*-type material). In the light of our expectation, the large difference between the experimental values in undoped 3C-SiC and intrinsic 4H-SiC are not explained by uncertainties in the chemical potential or by Fermi level effects. Here we note that the investigation of the aluminum- and boron-diffusion in 4H-SiC [2, 45] indicate to a slower silicon self diffusion than observed in the tracer diffusion experiments of Hong et al. [16, 18] and Hon et al. [17].

## 6.2 Dopant Diffusion

The dopant diffusion necessarily involves the mobile dopant-vacancy complexes or the mobile dopant interstitials. A prerequisite for both mechanisms is the presence of mobile intrinsic defects. Therefore, our understanding of the vacancy and interstitial migration allows us to draw a few general conclusions for the dopant migration.

The dopant diffusion based on silicon vacancies in *p*-type material has to be considered in the light of the metastability of the silicon vacancy. A nearest or second neighbor complex with the silicon vacancy may be affected

by a similar metastability. This is indeed the case for boron [47]. The nearest neighbor complex of boron with  $V_{Si}$  is almost unstable in  $p$ -type material. Similarly large barriers are found for the reverse transformation as for the transformation  $V_C-C_{Si} \rightarrow V_{Si}$ . The complex is therefore rather immobile. A migration mechanism based on silicon vacancies thus seems not likely for  $p$ -type dopants. It is available for  $n$ -type dopants, where the vacancy is stable. A migration mechanism based on carbon vacancies is affected by the large migration barrier of the carbon vacancy itself. In case of boron, an even larger migration barrier was found for the second neighbor complex  $B_C-V_C$  as for the carbon vacancy.

Interstitials may thus play an important role in the dopant diffusion. Silicon interstitials are clearly relevant in  $p$ -type material. Only in  $n$ -type material the silicon vacancy is stable and may be more relevant than the silicon split-interstitial due to its larger equilibrium abundance. Carbon interstitials most likely counterbalance their low equilibrium abundance by their high mobility. The key to an interstitial-mediated dopant diffusion, hence, are the properties of the dopant-interstitial itself. In case of boron, we found that the dominant interstitial sites are the carbon coordinated tetrahedral site and the hexagonal site. The kick-out reactions by silicon or carbon interstitials have similar or even lower barriers than the interstitial migration. It is accompanied by a large energy gain. Thus the interstitial is stabilized by a considerable kick-in barrier, which is larger than the barrier for the migration between the interstitial sites.

These qualitative considerations support the conclusions recently drawn by Konstantinov [46], Bracht et al. [2] and Janson et al. [3] from their analysis of the diffusion of the  $p$ -type dopants aluminum and boron. The quantitative modeling of the diffusion profiles attributed the migration to a kick-out mechanism based on silicon interstitials. The earlier assumption [48] of a vacancy mediated boron diffusion was not confirmed.

## 7 Annealing of Vacancies and Interstitials

During the processing of a semiconductor device, intrinsic defects are generated in excess. The subsequent annealing seeks to reduce these defects to an inevitable abundance determined by the defect equilibrium. The success depends on the defects produced and the temperatures applied during the annealing. Here the mobile defects, namely vacancies and interstitials, play a pivotal role. Their annealing properties are central to the annealing of other immobile defects that may be diminished by reacting with or separating into vacancies and interstitials. The principal annealing mechanisms of vacancies and interstitials are (i) the out-diffusion to the surface, (ii) the diffusion to extended defects, and (iii) the recombination of vacancies with interstitials. The relevance of these mechanisms depends on the kind of the damage introduced into the material. In particular, the vacancy-interstitial recombination

becomes relevant only when vacancies and interstitials are present to a similar extent. This is the case in irradiated SiC, which has been studied extensively in order to identify intrinsic defect centers and their annealing properties. In the following, we focus on the vacancy-interstitial recombination. Based on the findings, we discuss then a hierarchy of annealing processes for vacancies and interstitials.

### 7.1 Recombination of Vacancies and Interstitials

Depending on the separation of the vacancy and the interstitial, their recombination essentially proceeds in two steps; (i) diffusion limited motion of the vacancy and interstitial towards one another and (ii) the recombination of the pair by a direct hop of the interstitial into the vacancy. The first step is diffusion-limited and is described by the migration barrier of either the interstitial or the vacancy. This barrier is modified by the mutual interaction. An understanding of the final step requires an analysis of closeby Frenkel-pairs, which we give in the following paragraphs.

For the direct recombination of carbon interstitials and vacancies in 3C-SiC, we have considered the Frenkel-pairs where the interstitial is located at the nearest and second neighbor site to the vacancy,  $C_{spSi(100)}-V_C$  and  $C_{sp(100)}-V_C$ . These Frenkel pairs are depicted in Fig. 5a. Besides the displayed nearest neighbor pair, the pair with an opposite orientation of the carbon-silicon dumb bell was considered. This pair turned out to be unstable and recombined without a barrier. The stable nearest neighbor pair  $C_{spSi(100)}-V_C$  exists in the charge states  $2^+$  through  $1^-$  with the ionization levels  $\epsilon(+|++) = 0.4$  eV,  $\epsilon(0|+) = 0.7$  eV, and  $\epsilon(-|0) = 1.8$  eV. The recombination of the pair was investigated [11] using the ridge method. It turned out that at the transition state the defect wave functions remained localized. The defect levels merged with the valence band states only after the transition state was passed. For the positive charge state we therefore expect that the pair is neutralized at the end of the recombination. The recombination barriers for

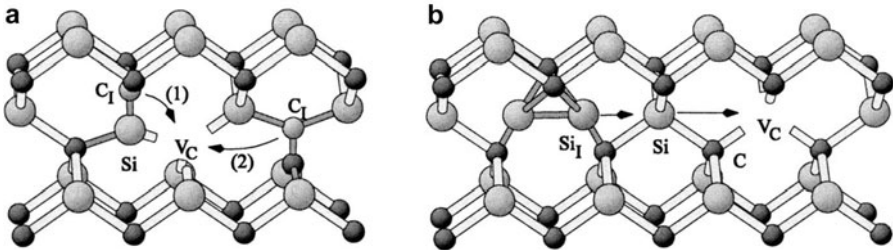


**Fig. 5.** Recombination of interstitials and vacancies: (a) recombination of the  $C_{spSi(100)}-V_C$  pair by a nearest-neighbor hop (1) and recombination of the  $C_{sp(100)}-V_C$  pair by a second neighbor hop (2) and (b) recombination of the fourth-neighbor  $Si_{sp(110)}-V_{Si}$  pair by a kick-out of the second neighbor silicon into the vacancy

**Table 7.** Recombination of Frenkel pairs: Energy barriers in eV for the relevant charge states in  $3C$ -SiC. The geometry of the Frenkel pairs is displayed in Fig. 5. The last column refers to values in  $4H$ -SiC of [32]

	$2^+$	$1^+$	0	$4H,0$
$C_{\text{sp}\langle 100 \rangle}-V_C$	1.0	0.5	0.4	0.5
$C_{\text{spSi}\langle 100 \rangle}-V_C$	1.2	1.2	1.4	
$Si_{\text{sp}\langle 110 \rangle}-V_{Si}$	0.0	$\sim 0.2$	0.2	

the pair are listed in Table 7. The values vary between 1.2 eV for the positive Frenkel-pairs and 1.4 eV for the neutral pair. In case of the negative pair, which is only relevant in  $n$ -type material, the extra electron is donated to the conduction band. The treatment of this case involves the electron transfer and is beyond the scope of our methods.

The recombination of the Frenkel pair  $C_{\text{sp}\langle 100 \rangle}-V_C$  proceeds by a second neighbor hop as indicated in Fig. 5a. In this hop, the carbon atom that has a common neighbor with the vacancy performs the recombination. As for the nearest neighbor Frenkel-pair the charge states  $2^+$  through  $1^-$  are realized with ionization levels at  $\epsilon(+|++) = 0.8$  eV,  $\epsilon(0|+) = 1.1$  eV, and  $\epsilon(-|0) = 1.9$  eV. For this Frenkel pair we found lower recombination barriers as for  $C_{\text{spSi}\langle 100 \rangle}-V_C$ . The values listed in Table 7 show that  $(C_{\text{sp}\langle 100 \rangle}-V_C)^+$  and  $(C_{\text{sp}\langle 100 \rangle}-V_C)^0$  recombine with a barrier of only 0.4 eV and 0.5 eV. These barriers are lower than the migration barriers of the split-interstitial. Using the DFT-based tight-binding method, Rauls et al. [32] obtained a barrier of 0.5 eV for the recombination of the neutral second neighbor pair  $C_{\text{sp}\langle 100 \rangle}-V_C$  in  $4H$ -SiC. This finding indicates that similar mechanisms are operative in both polytypes.

For both Frenkel pairs, we have found a sizeable binding energy, which indicates an attractive interaction. The value depends on the charge state of the pair and amounts to 2 eV–4 eV for  $C_{\text{spSi}\langle 100 \rangle}-V_C$  and about 1.0 eV for  $C_{\text{sp}\langle 100 \rangle}-V_C$ . Note that for a Fermi level above 0.8 eV either the carbon split-interstitial or the carbon vacancy is neutral, thus the diffusion of the interstitial towards the vacancy is not hindered by a long-range repulsive electrostatic interaction.

The recombination of silicon vacancies and silicon interstitials proceeds via  $Si_{TC}$ -sites in  $p$ -type material and via  $Si_{\text{sp}\langle 110 \rangle}$ -sites in compensated and  $n$ -type material. The only stable Frenkel-pair with a tetrahedral interstitial ( $Si_{TC}$  or  $Si_{TSi}$ ) we have found is the pair in which the  $Si_{TC}$ -interstitial binds to one of the carbon neighbors of the silicon vacancy. The pair is positively charged in  $p$ -type material and neutral in intrinsic material. With a high probability an antistructure pair, i.e. a complex of a silicon and carbon antisite, evolves from this Frenkel-pair. The barrier for this process amounts to 3.5 eV and 2.6 eV for the positive and neutral pair, respectively. When

the silicon interstitial reaches other tetrahedral sites in the vicinity of the vacancy, a barrier-less recombination is observed. Thus in *p*-type material the vacancy-interstitial recombination is essentially limited by the diffusion of the interstitial towards the vacancy with a migration barrier of about 3.5 eV.

Our analysis of Frenkel pairs with a silicon split-interstitial showed that second neighbor pairs are unstable. Stable pairs result when the interstitial occupies a third or fourth neighbor site of the vacancy. Here we consider in more detail the recombination of the fourth neighbor pair that is depicted in Fig. 5b. The pair exists in the charge states  $1^+$  through  $2^-$ , with ionization levels at  $\epsilon(0|+) = 1.3$  eV,  $\epsilon(-|0) = 1.8$  eV and  $\epsilon(- - |-) = 2.3$  eV. In the charge state  $2^+$  the pair is unstable (for  $\mu_F$  below 0.5 eV). For the neutral pair we have obtained a very low recombination barrier of only 0.2 eV. The recombination process proceeds as indicated by arrows in Fig. 5b: the silicon interstitial hops towards the second neighbor site displacing the silicon atom of that site towards the vacancy. This atom is only loosely bound and recombines immediately with the vacancy. For the third neighbor and other orientations of the split-interstitial we also expect recombination barriers much lower than the migration barrier of the split-interstitial. This expectation is mainly based on the instability of the second neighbor pair.

Also the recombination of carbon vacancies with silicon interstitials or of silicon vacancies with carbon interstitials is possible. By these recombination processes antisites are created. Such vacancy-interstitial pairs most likely evolve from the implantation damage by a diffusion of the interstitial. Rauls et al. [32] have considered such a recombination of the silicon vacancy with a carbon interstitial. A moderate barrier of 1.1 eV was obtained, which is similar to the diffusion limited recombination of the vacancy with the silicon interstitial.

## 7.2 Hierarchy of Annealing Mechanisms

A hierarchy of annealing mechanisms is discussed in the following for the silicon and carbon vacancy. This hierarchy is based on the results for the defect migration, the metastability of the silicon vacancy and the recombination of vacancies and interstitials and focuses on the energy barriers of these processes (cf. Tables 2, 4 and 7). The central point is the observation that interstitials in SiC have lower migration barriers than vacancies. Thus the mobility of interstitials plays an important role in the early stages of the annealing, in particular at low temperatures.

The findings for the silicon interstitial and the silicon vacancy suggest different hierarchies for *p*-type, compensated and *n*-type material. In *p*-type material, the metastability-induced transformation of the silicon vacancy is activated at lower temperatures than the migration of the Si<sub>TC</sub>-interstitial. As already discussed, the majority of silicon vacancies is converted into vacancy-antisite complexes at low and moderate temperatures. Its concentration inevitably drops below its detection limit in the experiment. Instead, signatures

related to  $V_C-C_{Si}$  should appear. An annealing based on the recombination of Frenkel pairs is thus unlikely. Further annealing now concerns the vacancy-antisite complex. A recombination of  $Si_{TC}$  and  $V_C-C_{Si}$  becomes possible once the migration of  $Si_{TC}$  is activated. This recombination most likely yields anti-structure pairs. The dissociation of the vacancy-antisite complex or its diffusion to sinks occurs with much larger barriers and is therefore only activated at much higher temperatures.

In compensated material, the  $Si_{sp(110)}$ -interstitial becomes relevant. The silicon vacancy is still metastable for  $\mu_F < 1.7$  eV. Since the barrier of interstitial migration is now much lower than that of the metastability-induced transformation, the Frenkel-pair recombination is activated at lower temperatures than the transformation-induced annealing of the vacancy. In particular, Frenkel-pairs with a small separation between the vacancy and the interstitial recombine, before the diffusion-limited recombination sets in. The diffusion of the  $V_C-C_{Si}$  to sinks, such as extended defects, is associated with the largest barrier and therefore constitutes the final annealing stage. In  $n$ -type material, the silicon vacancy is no longer metastable. Since its migration barrier is still higher (at least in  $3C-SiC$ ) than that of the silicon interstitials, we expect that the recombination process is activated before the diffusion of the vacancy and its recombination with sinks.

Experimentally, the annealing of the silicon vacancy and related centers were studied by spin resonance experiments [5, 31] and positron annihilation spectroscopy [12, 13, 49, 50]. Itoh et al. [5] observed the annealing of the T1-center in irradiated  $p$ -type and  $n$ -type  $3C-SiC$  by EPR and found three annealing stages at 150°C, 350°C and 750°C. For the last annealing stage an activation energy of 2.2 eV was deduced. The center was shown to be a negative silicon vacancy [5, 6, 11], which may exist only for  $0.6 \text{ eV} < \mu_F < 1.8 \text{ eV}$ . In the irradiated material, the Fermi level is most likely trapped by defect levels around mid gap. Thus according to our hierarchy, these annealing stages can be interpreted in terms of the recombination of closeby Frenkel pairs, followed by the diffusion-limited recombination and finally the vanishing of the T1-signal by the metastability induced transformation into a carbon vacancy-antisite complex. The activation energy deduced for this last annealing stage is in excellent agreement with our value for the transformation barrier of  $V_{Si}^-$  of 2.5 eV. The vacancy-antisite complex is not paramagnetic for a mid-gap Fermi level in  $3C-SiC$  and thus cannot be detected by direct EPR experiments. Recently, a defect center was observed by Lingner et al. [31] using MCDA detected EPR in irradiated  $6H-SiC$ . Based on their theoretical analysis, the center was identified as a carbon vacancy-antisite complex. It was observed only in material annealed above the annealing temperature of the silicon vacancy. An EPR-center with a similar  $g$ -tensor and finestructure constant  $D$  was observed by ODMR experiments [51] in electron irradiated nominally undoped  $3C-SiC$  (L3-center). This center, which has trigonal symmetry was observed after annealing the samples above 750°C and is related

to a photoluminescence band in the near mid gap region. The similarity suggests the carbon vacancy-antisite complex as a common model for the centers in  $3C$ - and  $6H$ -SiC. This observation of the carbon vacancy-antisite complex underlines our interpretation of the annealing stages reported by Itoh et al. for the T1-center. The PAS experiments of Kawasuso et al. [12] in  $6H$ -SiC show similar annealing stages for silicon vacancy-related defects up to  $750^{\circ}\text{C}$ , where the T1-center disappears. Above this temperature, a silicon vacancy-related component was still observed until it finally annealed at  $1400^{\circ}\text{C}$ . This was explained by the formation and annealing of vacancy-nitrogen complexes. The explanation assumes that the nitrogen concentration exceeds the vacancy concentration in the irradiated material. The onset of the vacancy migration may explain this process, provided the  $n$ -type character of the material remained unaffected by the irradiation. On the other hand, an interstitial-mediated nitrogen diffusion could also account for the complex-formation.

An annealing of the carbon vacancy by two processes follows from the analysis of our calculations: the annealing by an interstitial-vacancy recombination and the migration of vacancies to sinks. Since the migration of interstitials and the recombination of Frenkel pairs have much lower barriers, this annealing mechanism is activated before the migration of the carbon vacancy. This hierarchy is essentially independent of the doping conditions, except for  $p$ -type material ( $\mu_F < 0.7$  eV), where a coulomb repulsion between the positively charged interstitial and the vacancy could hinder a recombination process.

Experimentally, the annealing of carbon vacancy-related centers has been studied by EPR [7] and PAS [12, 13, 49]. In irradiated  $4H$ -SiC, Son et al. [7] observed the EPR-center EI5 that was identified as the positive carbon vacancy at the cubic lattice site [11]. The signature of this center completely vanishes above  $500^{\circ}\text{C}$ . A similar annealing temperature was deduced from the PAS experiments in irradiated material. This low annealing temperature indicates that a large fraction of the carbon vacancies anneals by a recombination with interstitials. The vacancies that escaped the Frenkel-pair recombination should anneal only at significantly higher temperatures. Such an annealing stage is not observed in irradiated material. Yet, it may be the only relevant stage when the excess of vacancies outnumbers the available interstitials by far. For example, EPR experiments [8, 14] in as grown semiinsulating material report a much larger thermal stability of the carbon vacancy than in irradiated material. The vacancy was found to persist thermal annealing up to  $850^{\circ}\text{C}$ . Since the carbon interstitials have a much lower abundance than vacancies in this case, an annealing of the vacancy by recombination with carbon interstitials is not possible. The out-diffusion of the vacancy (or its diffusion to other sinks) is the only available annealing mechanism in this case.

## 8 Conclusion

A picture of the defect migration and the annealing mechanisms has been devised that emerged from theoretical investigations based on ab initio methods within the framework of DFT. The investigation of the microscopic structure and the abundance of the mobile intrinsic defects, their migration mechanisms and the recombination of vacancies with interstitials contribute to this microscopic picture. A strong influence of the doping conditions is reported for the mobile silicon defects. Among the silicon interstitials, the tetrahedrally carbon-coordinated interstitial and the split-interstitial  $\text{Si}_{\text{sp}\langle 110 \rangle}$  are the relevant interstitials in *p*-type, and in compensated or *n*-type SiC, respectively. A metastability of the silicon vacancy occurs in *p*-type and compensated material which transforms the vacancy to a more stable carbon vacancy-antisite complex. This has strong implications for the diffusion mediated by the mobile silicon defects and the annealing of silicon vacancies and interstitials: (i) the interstitial migration in *p*-type material proceeds with higher barriers than in compensated and *n*-type material, and (ii) the silicon vacancy becomes unavailable on behalf of the kinetic aspects of the transformation. The central result is the finding that the interstitials are more mobile than the vacancies.

The importance of interstitials and vacancies in the self and dopant diffusion is influenced by two factors: their abundance and their diffusivity. The discussion of these two factors showed that in most cases the interstitials play a significant role in the dopant and self diffusion. One example is the dominance of silicon interstitials in the silicon self diffusion in *p*-type material. In case of the carbon interstitials, their lower abundance compared to the carbon vacancy may be even overcompensated by their higher mobility. For the dopant diffusion, similar qualitative conclusions were drawn and outlined for the case of boron, for which theoretical investigations indicate an important role of the interstitial mediated diffusion.

A hierarchy of annealing mechanisms for the carbon and silicon vacancies is derived. This hierarchy predicts that the recombination of vacancies with interstitials is activated before the diffusion of vacancies to sinks. The metastability-induced transformation of the silicon vacancy into a carbon vacancy-antisite complex in *p*-type and compensated material constitutes an important annealing mechanism. In the hierarchy of annealing mechanisms, the metastability-induced transformation follows the recombination of silicon vacancies and interstitials in compensated material. The hierarchy of annealing mechanisms is in qualitative agreement with the annealing stages observed in recent experiments for defect centers identified as silicon and carbon vacancies.

## Acknowledgements

We acknowledge fruitful discussions with Dr. Pensl, who has initiated this project. The support of this work by the Deutsche Forschungsgemeinschaft through SFB 292 and the SiC-Researchgroup is gratefully acknowledged.

## References

1. M. Laube, G. Pensl, and H. Itoh: Appl. Phys. Lett. **74**, 2292 (1999)
2. H. Bracht, N. A. Stolwijk, M. Laube, and G. Pensl: Appl. Phys. Lett. **77**, 3188 (2000)
3. M.S. Janson et al.: Appl. Phys. Lett. **76**, 1434 (2000)
4. I.O. Usov et al.: J. Appl. Phys. **86**, 6039 (1999)
5. H. Itoh et al.: Phys. Stat. Sol. (a) **162**, 173 (1997)
6. T. Wimbauer et al.: Phys. Rev. B **56**, 7384 (1997)
7. N.T. Son, P.N. Hai, and E. Janzén: Phys. Rev. B **63**, 201201 (2001)
8. V.V. Konovalov et al.: Physica B **308–310**, 671 (2001)
9. V.Y. Bratus et al.: Physica B **309–310**, 621 (2001)
10. T.T. Petrenko, T.L. Petrenko, V.Y. Bratus, and J.L. Monge, Physica B **308–310**, 637 (2001)
11. M. Bockstedte, M. Heid, A. Mattausch, and O. Pankratov: Mater. Sci. Forum **389–393**, 471 (2002); M. Bockstedte, M. Heid, and O. Pankratov: Phys. Rev. B. **67**, 193102 (2003)
12. A. Kawasuso, H. Itoh, S. Okada, and H. Okumura: J. Appl. Phys. **80**, 5639 (1996)
13. G. Brauer et al.: Phys. Rev. B **54**, 3084 (1996)
14. M.E. Zvanut and V.V. Konovalov: Appl. Phys. Lett. **80**, 410 (2002)
15. L. Wang et al.: Phys. Rev. Lett. **76**, 2342 (1996)
16. J.D. Hong, M.D. Hon, and R.F. Davis: Ceram. Internat. **5**, 155 (1979)
17. M.H. Hon, R.F. Davis, and D.E. Newbury: J. Mater. Sci. **15**, 2073 (1980)
18. J.D. Hong, R.F. Davis, and D.E. Newbury: J. Mater. Sci. **16**, 2485 (1981)
19. A. Zywiets, J. Furthmüller, and F. Bechstedt: Phys. Rev. B **59**, 15166 (1999)
20. L. Torpo and R.M. Nieminen: Appl. Phys. Lett. **74**, 221 (1999)
21. L. Torpo, M. Marlo, T.E.M. Staab, and R.M. Nieminen: J. Phys. Cond. Matt. **13**, 6203 (2001)
22. L. Torpo, S. Pöykkö, and R.M. Nieminen: Phys. Rev. B **57**, 6243 (1998)
23. E. Rauls et al.: Mater. Sci. Forum **353–356**, 435 (2001)
24. T.A.G. Eberlein et al.: Phys. Rev. B **65**, 184108 (2002)
25. M. Bockstedte and O. Pankratov: Mater. Sci. Forum **338–342**, 949 (2000)
26. A. Mattausch, M. Bockstedte, and O. Pankratov: Mater. Sci. Forum **353–356**, 323 (2001)
27. F. Gao, E.J. Bylaska, W.J. Weber, and L.R. Corrales: Phys. Rev. B **64**, 245208 (2001)
28. G. Brauer et al.: Phys. Rev. B **54**, 2512 (1996)
29. T.E.M. Staab, L.M. Torpo, M.J. Puska, and R.M. Nieminen: Mater. Sci. Forum **353–356**, 533 (2001)
30. E. Rauls et al.: Phys. Stat. Sol. (b) **217**, R1 (2000)

31. T. Lingner et al.: Phys. Rev. B **64**, 245212 (2001)
32. E. Rauls, T.E.M. Staab, Z. Hajnal, and T. Frauenheim: Physica B **308–310**, 645 (2001)
33. M. Bockstedte and M. Scheffler: Z. Phys. Chem. **200**, 195 (1997)
34. N. Troullier and J.L. Martins: Phys. Rev. B **43**, 1993 (1991)
35. H.J. Monkhorst and J.D. Pack: Phys. Rev. B **13**, 5188 (1976)
36. G. Makov and M.C. Payne: Phys. Rev. B **51**, 4014 (1995)
37. A. Fukumoto: Phys. Rev. B **53**, 4458 (1996)
38. M. Bockstedte, M. Heid, A. Mattausch, and O. Pankratov: Mater. Sci. Forum **433–436**, 471 (2003); M. Bockstedte, A. Mattausch, and O. Pankratov: unpublished
39. I.V. Ionova and E.A. Carter: J. Chem. Phys. **98**, 6377 (1993)
40. M. Bockstedte, A. Kley, J. Neugebauer, and M. Scheffler: Comp. Phys. Comm. **200**, 107 (1997)
41. A. Zywietz, J. Furthmüller, and F. Bechstedt: Phys. Rev. B **61**, 13655 (2000)
42. A. Zywietz, J. Furthmüller, and F. Bechstedt: Phys. Rev. B **62**, 6854 (2000)
43. P. Deák et al.: Appl. Phys. Lett. **75**, 2103 (1999)
44. C. Wang, J. Bernholc, and R.F. Davis: Phys. Rev. B **38**, 12752 (1988)
45. T.Y. Tan et al.: J. Appl. Phys. **72**, 5206 (1992)
46. A.O. Konstantinov: Sov. Phys. Semicond. **26**, 151 (1992)
47. M. Bockstedte, A. Mattausch, and O. Pankratov: Mater. Sci. Forum **353–356**, 447 (2001)
48. E.N. Mokhov, E.E. Goncharov, and G.G. Ryabova: Sov. Phys. Semicond. **18**, 27 (1984)
49. A. Polity, S. Huth, and M. Lausmann: Phys. Rev. B **59**, 10603 (1999)
50. A. Kawasuso et al.: J. Appl. Phys. **90**, 3377 (2001)
51. N.T. Son et al.: Phys. Rev. B **55**, 2863 (1997)

# Hydrogen in SiC

P. Deák, A. Gali, and B. Aradi

## 1 Introduction

Hydrogen is one of the most common impurities in electronics technology with profound and very versatile influence on the electronic characteristics of the semiconductor material. It is of special importance in the case of SiC. Due to the difficulties with bulk crystal growth and diffusion doping, in-growth doped homoepitaxial layers prepared by chemical vapor deposition (CVD) play a crucial role in device processing. Hydrogen is, of course, a natural contaminant of such layers. Even though consequences of this fact have been anticipated, at the time of writing the most recent comprehensive review [1] about state of the art in SiC research, the information about the properties and effects of hydrogen was scarce and not well understood.

Atomistic theoretical modeling at quantum mechanical level can provide information about the stable forms of an impurity, the possible complexes it can form with intrinsic defects and dopants, and about the energetics of these complexes, allowing conclusions to be drawn regarding the conditions under which the complexes are formed. Various properties of defects, observable in electric, optical and magnetic resonance spectroscopy, can also be predicted. Even if the data supplied by model calculations are only approximate, they can guide the identification of the fingerprints of a given impurity in the spectra and can help to understand the mechanisms by which it influences the concentration and lifetime of free carriers. Therefore, in 1998, we decided to start a systematic study of hydrogen in SiC, using first principles methods. This work is not finished yet (notably donor + hydrogen complexes still have to be considered) but it seems to be reasonable to summarize our results in parallel with what is known from experiments. As we will show, the “interactive” use of theoretical and experimental results advanced our knowledge about hydrogen in SiC a great deal, even though a lot remains to be done with the latter to verify the predictions of the former. Obviously, future advances in the methodology of theory will help to increase the accuracy of the predictions, too, and even resolve some controversies stemming from the errors today’s theoretical tools suffer from.

This paper is organized as follows. First, in this introductory section, we summarize the knowledge about hydrogen in SiC, gathered up to the time we have started our studies (shortly after the appearance of [1]). In Sect. 2, we

describe the applied theoretical methods, and then, in Sect. 3 we summarize our results regarding hydrogen. Finally, in Sect. 4, we try to draw conclusions about what can be known today about the behavior of hydrogen in SiC in light of our results *and* those of new experiments.

### 1.1 Hydrogen Incorporation During CVD Growth of *p*-Type SiC

Since doping utilizes the competition of dopants and host atoms for a given site in the crystal [2], hydrogen entering the race for the free valences of a vacancy may influence doping efficiencies. Monitoring a hydrogen-related photoluminescence (PL) center [3, 4] (assigned tentatively to a H atom trapped in a silicon vacancy, see later) it was proven that hydrogen enters together with boron in boron-doped CVD grown epitaxial 6H-SiC layers. The correlation of increasing H-related PL intensity with increasing *p*-type doping, as well as secondary ion mass spectroscopy (SIMS) measurements, showing correlation between the hydrogen and boron concentrations, suggested that the hydrogen incorporation is directly proportional to the amount of boron in the SiC epilayer [5, 6]. After an  $\sim 1700^\circ\text{C}$  anneal for 0.5 h in argon, the SIMS measurements showed that the hydrogen diffused out of the samples, while the capacitance-voltage (*C-V*) curves indicated a three to fourfold increase in the net carrier concentration. This could be interpreted as, prior to the anneal, hydrogen had been passivating the acceptors [5, 7]. It was found, by varying the Si/C ratio during the CVD growth, that boron prefers the silicon site versus the carbon site [5]. Larkin speculated [7] that – based on the non-polar covalent radii – boron (without hydrogen) should have substituted carbon – in direct conflict with the experimental evidence. However, assuming that boron and hydrogen were incorporated together, the size of a B-H species could have required incorporation onto the silicon site, as indeed observed.

No evidence for donor passivation was found in these experiments [5, 6], nevertheless, hydrogen was observed by nuclear reaction analysis and infrared absorption measurements in *n*-type epitaxial layers [8].

### 1.2 Diffusion of Hydrogen in SiC

Svensson and co-workers implanted *n*-type 6H-SiC substrates by hydrogen [9]. It was found that during anneals at temperatures between  $750$  and  $850^\circ\text{C}$ , H migrated within the implanted region and gradually decorated defects generated by the implantation. These H-related defect complexes were stable up to  $\sim 900^\circ\text{C}$ , after which an out-diffusion of hydrogen was observed. Later, epitaxial layers of low doped 4H-SiC were implanted with  $20\text{ keV } ^2\text{H}^+$  ions to a dose of  $10^{15}\text{ cm}^{-2}$ . The samples were subsequently annealed at temperatures ranging from  $1040$  to  $1135^\circ\text{C}$  [10]. SIMS was used to obtain the depth

profiles of deuterium. Assuming that hydrogen migrated rapidly and became trapped and de-trapped at implantation-induced defects, a dissociation energy between 3.5 and 4.9 eV was estimated as the rate limiting step [9, 10]. Since the hydrogen-related PL center (mentioned above) annealed out in this temperature range [11], the dominant trap for hydrogen was associated with the silicon vacancy.

Causey et al. studied H diffusion by measuring the release rate of gaseous tritium ( $^3\text{H}$ ) during thermal annealing of different SiC materials hydrogenated by recoil injected  $^3\text{H}$  [12]. For highly Al-doped monocrystalline 6H-SiC they obtained an activation energy of  $(1.5 \pm 0.2)$  eV for diffusion, while the corresponding values for unintentionally doped material were typically 1 eV higher [12].

The SIMS depth profile of low doped epitaxial SiC samples (see Sect. 1.3.3), implanted with  $^2\text{H}^+$  at low energy (300 eV/atom), showed that – compared to high-energy implantation [13] – hydrogen was mobile even at surprisingly low temperatures (from 300 K), presumably because of the drastically reduced implantation damage [14]. It was found that hydrogen diffused on a  $\mu\text{m}$  scale in  $p$ -type SiC, whereas no such effect was found in  $n$ -type samples.

### 1.3 Effect of Hydrogen on the Concentration of Carriers

The effect of hydrogen on the electric properties was investigated by intentionally introducing hydrogen into SiC with high temperature – high pressure annealing in  $\text{H}_2$ , or with low temperature – low pressure H-plasma treatment, or through hydrogen implantation.

#### 1.3.1 $\text{H}_2$ Annealing of SiC

6H-SiC bulk material was annealed in ultra pure  $\text{H}_2$  gas at 10 bar between 1500–1700°C for 10–20 hours [15]. Al-doped  $p$ -type ( $[p] \sim 10^{17} \text{ cm}^{-3}$ ) and nitrogen doped  $n^+$ - ( $[n] \sim 10^{19} \text{ cm}^{-3}$ ) and  $n$ -type ( $[n] \sim 10^{17} \text{ cm}^{-3}$ ) samples were investigated by electron paramagnetic resonance (EPR) and Hall effect measurements [15, 16]. The EPR signal of Al dropped by 68% and that of the residual boron also diminished significantly upon hydrogenation. At the same time, the Hall measurements showed a 80% loss in the hole concentration indicating passivation of the acceptors by hydrogen [15]. It has been shown that up to 90% of the acceptors (B and Al) can be passivated by this hydrogenation method [17]. In N-doped samples it was found that after hydrogenation the  $n$ -type sample did not show a decrease in the EPR signal of N, within the experimental accuracy (2%), while the intensity dropped by 75% in the heavily doped  $n^+$ -sample. The  $n$ -type wafer was then annealed again at 500°C for 30 hours without the presence of hydrogen, after which a drop of 65% in the EPR signal of N donors was measured. This observation was interpreted as hydrogen having been present in the  $n$ -type sample

as well but that hydrogen-donor binding reaction was thermodynamically or kinetically impeded [16]. This was supported by SIMS measurements: the hydrogenation setup of [15] was filled with  $D_2$  instead of  $H_2$ , and  $n^+$ - and  $n$ -SiC wafers were annealed under the same pressure and temperatures as in the case of  $H_2$ . It was found that, in fact, the penetration depth and the detected amount of D were higher in  $n$ - than in  $n^+$ -type material. It was speculated that with the Fermi-level higher in  $n^+$ , the hydrogen was negatively charged and could easily be trapped by ionized nitrogen donors while, at the lower Fermi-level positions in the  $n$ -type samples, hydrogen could have been neutral, binding less easily to the positively charged N donors. That could have also been the reason why hydrogen was less mobile in  $n^+$ - than in  $n$ -type material. Nevertheless, no H-related local vibration modes have been found in  $n^+$ -type samples [17]. (It has to be noted that the investigated samples were quite opaque in the infrared range where such modes might be expected.)

### 1.3.2 Hydrogen-Plasma Annealing

Hydrogen-plasma anneal of  $p$ -type  $6H$ -SiC epilayers (doped with Al to  $[p] \sim 10^{18} \text{ cm}^{-3}$ ) at low temperature ( $250^\circ\text{C}$ ) for 3 h caused passivation of the acceptors [18]. Monitoring the EPR signal of Al and B before and after hydrogenation, a decrease of 22% and 18% has been observed. Since a post-anneal at  $500^\circ\text{C}$  for 80 min. decreased the intensity of the EPR lines further, passivation due to dopant-hydrogen complex formation seemed more likely than carrier trapping in defects created by the plasma. Exposing  $n$ - and  $p$ -type SiC substrates (doping level:  $7 \times 10^{17} \text{ cm}^{-3}$ ) to a deuterium plasma at  $300^\circ\text{C}$ , the passivation was much more prevalent in  $p$ -type than in  $n$ -type samples. Reactivation of passivated B acceptors occurred at  $700^\circ\text{C}$  [19, 20]. After exposure to an Ar plasma  $n$ -type samples also showed loss of carrier concentration [20], indicating that the change in the carrier concentration after plasma annealing can also be due to carrier trapping in intrinsic defects. Konstantinov and co-workers studied  $n$ -type SiC exposed to a hydrogen plasma [21] at 0.1 torr, in the range  $300$ – $700^\circ\text{C}$ . The carrier concentration profile as monitored by  $C$ - $V$  measurements on a Schottky-contact showed that the hydrogen plasma led to the formation of a high-resistance layer at the surface of the crystal, with a characteristic typical of structures with a space-charge-limited current. Since Ar plasma treatments achieved the same effect, this was regarded as evidence that the plasma treatment created intrinsic trapping centers.

### 1.3.3 Low Energy Implantation of Hydrogen

Low energy (300 eV per atom) ion implantation of deuterium was performed to investigate the mobility (see Sect. 1.2) and the passivating effect of hydrogen in epitaxial  $4H$ -, and  $6H$ -SiC [14]. The  $^2H_2^+$  depth profile was analyzed by SIMS, the electrical properties measured by  $C$ - $V$  profiling and admittance spectroscopy. The samples were slightly doped ( $5$ – $10 \times 10^{15} \text{ cm}^{-3}$ )  $n$ -

and *p*-type epitaxial layers on heavily doped substrates of the same type. No evidence for an influence of the polytype was found. SIMS showed that the concentration ratio of Al to B varied between 1:1 and 2:1 in the epilayer of *p*-type samples. It was found that in *p*-type SiC hydrogen passivated both boron and aluminum. Up to at least 465 K, the passivation was strong (>90%) and affected both types of acceptors, whereas at 680 K boron was passivated preferentially and a net acceptor concentration remained due to aluminum. A partial reactivation of passivated acceptors was achieved by post-implantation annealing between 530 and 600 K, indicating the dissociation of an Al-H complex in this temperature range [22]. In *n*-type SiC, no electric effects or incorporation on a  $\mu\text{m}$  scale was detected [14].

A substantial decrease of the free carrier concentration after H-implantation into heavily doped *n*-type ( $\sim 10^{19} \text{ cm}^{-3}$ ) 4*H*-SiC was reported based on spectroscopic ellipsometry studies [23], however, that was attributed to electron traps created during implantation.

#### 1.4 Spectroscopic Fingerprints of Hydrogen-Related Defects

For several decades the only direct evidence for the existence of a hydrogen-related defect in SiC was a low temperature PL center. Bands arising as phonon replica due to local modes at 2962, 2977, 2988  $\text{cm}^{-1}$  in 6*H*-, and 2959, 2985  $\text{cm}^{-1}$  in 4*H*-SiC after  $\text{H}^+$  implantation of *p*-type material grown in C-rich environment were interpreted as C-H stretch modes due to H in silicon vacancies at different inequivalent sites [3, 4]. A decrease in the PL intensity of these C-H lines at around 1000°C was reported [11]. Later this PL center has also been found in as-grown slightly *p*-type SiC epilayers [24].

6*H*-SiC *n*-type CVD epilayers ( $[n] \sim 10^{15}\text{--}10^{16} \text{ cm}^{-3}$ ) irradiated by 2 MeV-electrons and implanted by 300 keV-deuterium ions were investigated by deep level transient spectroscopy (DLTS) [25]. Six occupation levels were found ranging from  $E_C\text{--}0.87$  up to  $E_C\text{--}0.34$  eV (where  $E_C$  is the conduction band minimum) but the intensities were the same in electron-irradiated and deuterium implanted samples [25]. The conclusion was that none of the observed DLTS centers were hydrogen related. However, it should be noted that the CVD epilayers might have had a higher hydrogen content in the first place than that introduced by the implantation.

No EPR signals related to H has been observed either, but muon spin resonance experiments indicated Mu (an analogue of the H atom made of a muon and an electron) to be at tetrahedral interstitial site (see [26] and references therein).

#### 1.5 The Main Questions for Theory (in 1998)

It was clear from the experiments that hydrogen was present in as-grown *p*-type CVD epilayers. Its significant effect on the carrier concentration seemed likely to stem from complex formation with the acceptors, leading to their

passivation. The process for both the passivation and the reactivation seemed to be different for boron and aluminum. In contrast to *p*-type samples, little evidence of hydrogen incorporation into as-grown *n*-type SiC was found. Apparently, hydrogen plasma treatments at relatively low temperatures were also able to achieve passivation of *p*-type material only, while their effect on *n*-type samples was mainly the creation of trapping centers. High temperature – high pressure annealing in H<sub>2</sub> was capable to hydrogenate both type of samples but hydrogen passivation was less effective in *n*-type ones. Also, the mobility of hydrogen appeared to be higher in *p*-type than in *n*-type material, unless intrinsic defects (created by the radiation damage) served as traps. Except for a PL center assigned to a hydrogen atom trapped in a silicon vacancy ( $V_{\text{Si}}$ ), no spectroscopic fingerprints of hydrogen related defects were found, despite of the obvious presence of H in all these *p*-type and in some of the *n*-type samples.

Therefore, the most intriguing question was that what were the dominant hydrogen defects in SiC and where should they show up in optical (PL, IR, Raman), electric (DLTS) and magnetic resonance spectra. The primary target of our investigations was, therefore, to find the stable forms of one- and two-hydrogen defects and calculate their measurable properties. The only theoretical studies we were aware of in SiC had considered hydrogen solely as an isolated interstitial in the neutral charge state, using a molecular cluster model [27, 28]. The equilibrium position of H<sup>0</sup> in 3C-SiC was found at the tetrahedral interstitial site in the cage of the less electronegative atoms, Si (at  $T_{\text{Si}}$ ). In 6H-SiC the most stable configuration for the interstitial hydrogen was found at the *R*-site. We have considered interstitial and “substitutional” (i.e. vacancy-trapped) H and H<sub>2</sub>. (Since self-interstitials anneal out at lower temperatures, we neglected their interaction with H).

After establishing the relative stability of the different configurations of hydrogen defects, we could hope to find explanation to the observed dependence of hydrogen incorporation on the level of doping. In order to understand the anomalies found in dopant passivation, first of all the Fermi-level dependence of the charge state and mobility of hydrogen had to be investigated. Obviously, the interaction of hydrogen with the dopants had to be studied as well, in order to understand the dependence of the mechanism of passivation on the type of the dopants.

## 2 Methods of Calculation

In the following we briefly state the parameters of the calculations we carried out on hydrogen related defects. Models of defect complexes have been studied in a supercell geometry. Energy and wave function related results quoted for 3C-SiC and for 4H-SiC refer to calculations on 128- and 96-atom cells, respectively. Local vibration modes (LVM) were obtained in a 64-atom 3C-SiC supercell. The isolated defects levels were reconstructed by fitting the

obtained dispersion of the defect levels in a tight binding scheme, with the isolated defect level as parameter. The total energy was corrected according to the occupation of the defect levels. In calculation of the total energy of charged defects no correction was applied. With the cell sizes used here, a monopole correction [29] for singly charged defects would be about 0.2 eV, which is comparable with other error sources in the calculation. Due to the uncertainties [30] in correcting higher charge states, we have rather refrained from discussing them. Brillouin-zone summations were usually carried out on a  $2 \times 2 \times 2$  Monkhorst-Pack scheme [31]. (In case of 3C-SiC, sometimes the  $3 \times 3 \times 3$  scheme was necessary to explicitly include the band edge states.) The  $\Gamma$ -point approximation was used in vibration calculations.

The quantum mechanical problems were solved in the framework of the density functional theory (DFT [32, 33]) in the local density approximation (LDA), using the functional of Perdew and Zunger [34]. For calculating defect properties related to total and one-electron energies we have used a plane wave basis (with a cut-off of 36 Ry) in conjunction with Troullier-Martins [38] norm-conserving pseudopotentials, applying the FHI98MD code [39]. The position of the defect levels (and, consequently, the total energy) has been modified [35] by shifting them proportional to their overlap with the conduction band states of the perfect crystal. (A correct gap and appropriate defect levels can be obtained in a self-consistent way by mixing exact exchange with the DFT method [36, 37]. We have used the CRYSTAL98 code for such calculations to check on the one-electron level positions.) The local vibration modes were determined for the 3C-polytype by using the supercell version of the AIMPRO code [40] which utilizes the same LDA functional as FHI98MD but with norm conserving Bachelet-Hamman-Schlüter pseudopotentials [41]. We have used an optimized basis with four *s*- and four *p*-type Gaussians for each Si or C atom while two *s* and *p* Gaussians were included for hydrogen atoms. In addition, an *s*-type Gaussian was put at each bond center to simulate the effect of polarization functions. Hyperfine tensors of paramagnetic defects were determined using the CRYSTAL98 [42] code in spin-polarized 96-atom supercell calculations, where the first neighbors of the defect were handled with a 6-21G\* all-electron basis, while the rest with a compatible 21G\* basis and Durrand-Barthelat type pseudopotentials [43].

## 3 Results of Atomic Simulations

### 3.1 Hydrogen Related Defects

To understand how a given impurity appears in the observed spectra of a semiconductor, one has to investigate the energetics of the various defects it may form. Knowing the equilibrium total energies of the stable complexes makes it possible to estimate the dependence of their relative concentration on the experimental conditions (assuming equilibrium). Therefore, first we

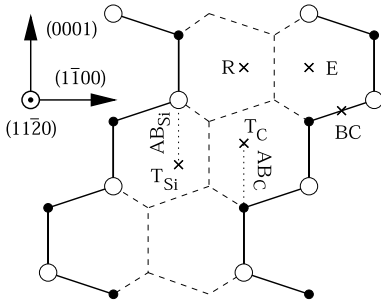


**Fig. 1.** Interstitial sites in 4H-SiC. Black and white circles represent C and Si atoms, respectively

present a short summary of our results regarding the most basic hydrogen-related defects: interstitial and “substitutional” (i.e., vacancy-trapped) H and H<sub>2</sub>. For the 3C polytype a detailed description of the various configurations can be found in [44]. The data given here relate to 4H-SiC (unless otherwise noted) and (except for interstitial H and the acceptor-hydrogen complexes) *have not been published before*. Note, that most of the configurations are very similar in the two polytypes; we mention differences only when they are significant.

Interstitial atomic hydrogen in the positive charge state is in equilibrium at an antibonding site (see Fig. 1) binding to a carbon atom ( $C_{3v}$  symmetry). The bond between that C atom and its Si neighbor along the symmetry axis is greatly weakened, and the C–H bond is quite strong, as if the hydrogen would be the forth neighbor of the carbon atom. In the 4H-polytype (unlike in 3C-SiC, see [44]) both the neutral and the negatively charged hydrogen atom select an antibonding position behind a silicon atom, near to the *T* or *R* site ( $C_{3v}$  symmetry). However, interstitial hydrogen is a “negative U” defect, i.e., the neutral charge state is less stable in equilibrium than the charged states at any position of the Fermi-level. The (+/−) occupation level is at  $E_V + 2.2$  eV, where  $E_V$  is the top of the valence band [45].

The hydrogen molecule is most stable at the *R* site with the bond parallel to the *c*-axis of the crystal. Figure 2 shows the relative energy per hydrogen atom for the possible interstitial defects as a function of the Fermi-level position.

The molecule is energetically preferred over H<sup>+</sup> if  $E_F > E_V + 0.8$  eV and it is always more stable than H<sup>−</sup>. (The molecule is more stable in 4H-SiC than in 3C because of the larger open space available around the *R* site.) Note, however, that except for Fermi-level positions around the (+/−) occupation level, most of the hydrogen atoms in the crystal have the same charge and so they repel each other. Therefore, molecule formation is hindered. (As we shall see, incorporation of H<sub>2</sub> into the crystal is mostly also unlikely under equilibrium conditions.)

A hydrogen atom, captured in a silicon vacancy, saturates one of the four carbon dangling bonds and a strong C–H bond is formed. (Similarly

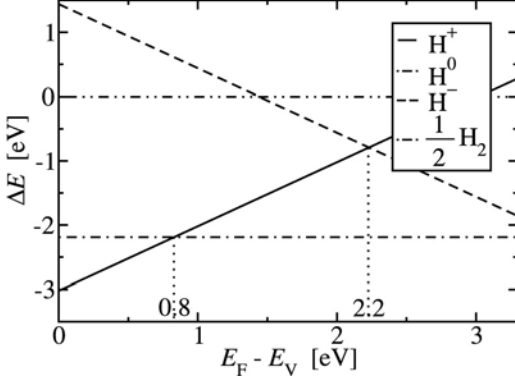


**Fig. 2.** Relative stability of the interstitial hydrogen defects in 4H-SiC

to 3C-SiC, the silicon vacancy shows almost no reconstruction in 4H either, due to the localized nature of the carbon dangling bonds, which prevents the formation of long bonds between the other carbon atoms around the vacancy. Therefore the symmetry of the complex is nearly  $C_{3v}$ .) Considering the calculated (0/−) occupation level of the silicon vacancy and the (+/−) occupation level of interstitial hydrogen, it follows that they are attracted to each other if the Fermi-level is between  $E_V + 0.5$  and  $E_V + 2.2$  eV. Both  $V_{Si}$  and  $(V_{Si} + H)$  become doubly negative already in moderately  $n$ -type samples (both can be more negative in strongly  $n$ -doped material), so the binding energy of the complex can be calculated as:

$$p\text{-type: } V_{Si}^- + H^+ \xrightarrow{[3.1 \text{ eV} + (E_F - E_V)]} (V_{Si} + H)^- + h^+, \quad (1)$$

$$n\text{-type: } V_{Si}^{2-} + H^+ \xrightarrow{[3.1 \text{ eV} + (E_F - E_V)]} (V_{Si} + H)^{2-} + h^+, \quad (2)$$

where  $h^+$  is a free hole created in the process. The first reaction holds for  $E_F \geq E_V + 0.5$  eV (when  $V_{Si}$  becomes negative), i.e. the minimal energy gain is 3.6 eV. The calculated (−/2−) occupation level for the vacancy is at  $E_F \approx E_V + 1.3$  eV, so the lowest energy gain upon the second reaction is about 4.4 eV. (Note that a charge correction may shift the (−/2−) occupation level up.)

A second hydrogen atom can also be trapped in the vacancy where it saturates another dangling bond. The binding energy is

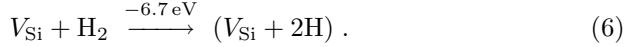
$$p\text{-type: } (V_{Si} + H)^- + H^+ \xrightarrow{[2.6 \text{ eV} + (E_F - E_V)]} (V_{Si} + 2H)^- + h^+, \quad (3)$$

$$n\text{-type: } (V_{Si} + H)^{2-} + H^+ \xrightarrow{[2.6 \text{ eV} + (E_F - E_V)]} (V_{Si} + 2H)^{2-} + h^+. \quad (4)$$

However, as long as  $[V_{Si}] > [H]$ , the monohydrid is preferentially formed because the disproportionation reaction is exothermic. In  $p$ -type material

$$2 \times (V_{Si} + H)^- \xrightarrow{+0.4 \text{ eV}} (V_{Si} + 2H)^- + V_{Si}^-. \quad (5)$$

For Fermi-level positions above  $E_V + 0.5$  eV the  $(V_{\text{Si}} + 2\text{H})$  complex also becomes negative, so it can attract further hydrogen atoms but, similarly to the  $n = 2$  case,  $(V_{\text{Si}} + n\text{H}) + (n - 1)V_{\text{Si}}$  is increasingly less stable than  $n(V_{\text{Si}} + \text{H})$  for  $n = 3, 4$  as well (see [44]). It is interesting to note, however, that



Therefore, molecules will be captured and dissociated by silicon vacancies.

The dangling  $sp^3$  hybrids of the Si atoms around  $V_C$  can easily make long bonds (across an unrelaxed distance of about 3.1 Å), causing a considerable Jahn-Teller distortion, resulting in  $C_{1h}$  symmetry in  $4H\text{-SiC}$  ( $D_{2d}$  in  $3C\text{-SiC}$ ). The  $(0/-)$  occupation level of the carbon vacancy lies at  $E_V + 2.3$  eV. That is very close to the  $(+/-)$  occupation level of interstitial H, thus  $V_C$  and H will practically never attract each other. Since the  $(+/0)$  occupation level of  $V_C$  is at  $E_V + 1.8$  eV, there is just a 0.4 eV window for the Fermi-level where there is no repulsion. In case a hydrogen gets trapped in a carbon vacancy, a stable complex is formed with the hydrogen in a symmetric position between two silicon neighbors of the vacancy (forming a puckered three-center bond with them:  $C_{1h}$  symmetry in  $4H\text{-SiC}$  ( $C_{2v}$  in  $3C\text{-SiC}$ ) [46]. A second hydrogen in the vacancy forms another three-center bond with the two other silicon atoms. (This configuration has  $C_{1h}$  symmetry in the hexagonal and  $D_2$  symmetry in the cubic polytype.) Calculations, similar to those above, show that the binding energy of H to  $V_C$  is significantly ( $\sim 2$  eV) lower than in the case of the silicon vacancy. So, if both types of vacancies are present in sufficient concentration, interstitial hydrogen prefers complex formation with  $V_{\text{Si}}$  over  $V_C$  both kinetically and thermodynamically under equilibrium conditions.

### 3.2 Hydrogen Incorporation Excluding Complexes with Dopants

For calculating the amount of hydrogen incorporated into SiC under various conditions, we have to assume that the crystal is in thermal equilibrium with the hydrogen gas contained in the surrounding ambient. As mentioned in the introduction, hydrogen can be incorporated into SiC by implantation, during CVD growth, with H-plasma treatment or by annealing in hydrogen gas. Implantation is definitively not an equilibrium process, and practically any amount of hydrogen can enter the crystal. The post-implantation heat treatment acts to restore equilibrium conditions but metastable species, created during irradiation or in the early stages of annealing, may survive even long-term, high-temperature heat treatments. The calculated relative stabilities of the various hydrogen related defects – as outlined in the previous subsection – may help to guess the dominating species.

Strictly speaking, CVD is no equilibrium process either, but under stationary growth conditions the assumption of the thermal equilibrium between the hydrogen content of the reactive gas mixture and the growing crystal is

acceptable. The concentration of the incorporated hydrogen can be obtained by using the formation energies of the hydrogen related defects in the crystal. These are calculated for each defect as the total energy  $E_{\text{tot}}$  of the supercell containing the defect minus the chemical potential of the constituents:

$$E_{\text{form}} = E_{\text{tot}} - \sum n_i \mu_i + q E_F \quad (7)$$

where  $n_i$  is the number of atoms of type  $i$  in the supercell and  $\mu_i$  is their chemical potential in the gas,  $q$  is the charge of the defect and  $E_F$  is the Fermi energy (the chemical potential of electrons) in the doped crystal. The chemical potentials of C and Si are connected ( $\mu_{\text{Si}} + \mu_{\text{C}} = \mu_{\text{SiC}}$ ) and are theoretically limited, on the one hand, by bulk silicon formation (extreme Si-rich conditions,  $\mu_{\text{Si}} = \mu_{\text{Si}}^{\text{bulk}}$ ) and, on the other hand, by bulk graphite formation (extreme C-rich conditions,  $\mu_{\text{C}} = \mu_{\text{C}}^{\text{bulk}}$ ). To calculate the actual chemical potential of the atoms in the reactive gas mixture is beyond our possibilities. Therefore, in the following, we will use these extremes as the limit of Si- or C-rich growth conditions. It should be kept in mind, however, that these are far out from what is practically applied in growth experiments. (Who would want to grow Si or graphite instead of SiC?)

The gas mixture used in CVD consists mainly of  $\text{H}_2$  molecules (the carrier gas). We found, however, that the chance for incorporation of molecules into the crystal is minuscule under the investigated circumstances – it is the atomic hydrogen content of the mixture which is responsible for the hydrogen defects in the crystal. The chemical potential for atomic hydrogen is calculated, assuming an ideal monatomic gas [44, 47], as a function of the temperature and pressure. While the effect of temperature is crucial in the gas phase, it is usually neglected in the crystal, and the concentration of a given defect can be approximated in the form of

$$N_i = N_i^0 \frac{g_i \exp\left(\frac{E_{\text{form}}(i)}{kT}\right)}{1 + \sum_j g_j \exp\left(\frac{E_{\text{form}}(j)}{kT}\right)} \quad (8)$$

where  $T$  is the temperature,  $k$  is the Boltzmann constant,  $N_i^0$  is the number of possible sites in the crystal for the given defect,  $g_i$  is the statistical weight of the electron configurations, and the sum goes over all defects, which occupy the same lattice site. This approximation is valid in the low concentration limit, where there is no interaction between the defects and, therefore, the concentration of each defect can be calculated independent of the others.

Many of the defects (and, of course, the dopants) can be charged, depending on the position of the Fermi level, which is – in turn – determined by their charge and concentration. Therefore, the concentrations have to be calculated self-consistently with the neutrality condition for the semiconductor, assuming a given concentration of dopants. As mentioned in Sect. 2, only singly charged states have been considered here. This might cause some

underestimation in the total hydrogen content in case of very high doping as will be discussed. (The concentrations published for 3C-SiC [44, 45] are based on formation energies with no charge correction, so the data given for higher charge states there are suspect to strong overestimations.)

In a first step, excluding complexes of hydrogen with the dopants (and neglecting self-interstitial + hydrogen complexes) we have considered only interstitial hydrogen and vacancy + hydrogen complexes as the possible forms of hydrogen incorporation during growth. As mentioned above, the calculations predicted negligible incorporation of hydrogen if only the  $H_2$  gas was considered in the environment. Due to dissociation of the molecules at the temperature of growth and – more importantly – due to the reactions at or near the crystal surface, about 1% of the hydrogen could be atomic. Therefore, to simulate the effect of that we have assumed equilibrium between the crystal and an atomic hydrogen gas of a (partial) pressure of 0.01 atm, at the typical CVD growth temperature of 1500°C. (Boron acceptors and extreme C-rich growth conditions, and nitrogen donors and extreme Si-rich conditions were assumed for  $p$ -type and  $n$ -type material, respectively.) The results are shown in Fig. 3. Except for heavy  $n$ -doping, the only hydrogen defect present is the positively charged interstitial atomic hydrogen,  $H^+$ , the amount of which follows the  $p$ -type dopant concentration, lagging behind by 2–3 orders of magnitude. (This is in contradiction with the experimental finding in B-doped samples, where an almost equal concentration of hydrogen with that of boron was observed. Obviously, the discrepancy must originate from the

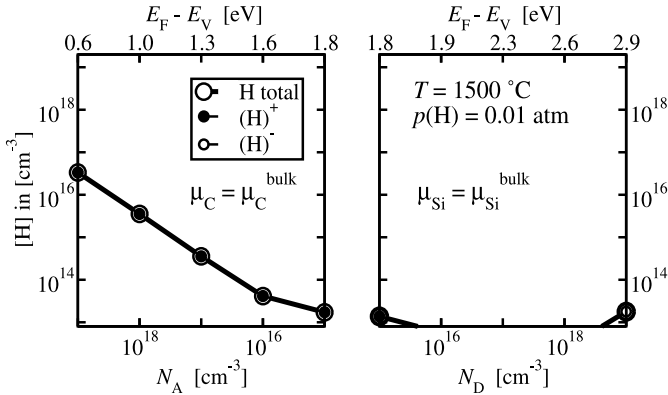


**Fig. 3.** Concentration of hydrogen related defects in 4H-SiC. The crystal is assumed to be in equilibrium with 0.01 atm atomic hydrogen gas at 1500°C. The chemical potentials of Si and C are assumed to take their extremal values in the  $n$ - and  $p$ -type case, respectively.  $N_A$  and  $N_D$  are the concentrations of the boron acceptors and nitrogen donors, respectively, and  $E_F - E_V$  is the position of the Fermi level relative to the valence band edge. The conditions assumed here may give an estimate for the incorporation during CVD except for the fact that dopant-hydrogen complexes were not considered here

interaction of B with H. If, as assumed, they are incorporated together, the difference should be made up by B + H complexes, which have not been considered here so far.) In heavily  $n$ -type samples some  $H^-$  may appear. The dominating form of hydrogen in  $n$ -type material should be the higher negative charge states of  $(V_{Si} + 2H)$  complex (excluded from our present concentration calculation). Including  $(V_{Si} + 2H)^{2-}$  in the calculation without charge correction would give a maximum of  $\sim 10^{16} \text{ cm}^{-3}$  but, at this temperature, the expected error should amount to about 2 orders of magnitude overestimation.  $(V_{Si} + H)^{3-}$  may, however reach concentrations comparable to those of the dopants for very heavy  $n$ -type doping.

Among the post growth hydrogenation methods, H-plasma treatments around  $300^\circ\text{C}$  appear to be the most popular. This is no equilibrium process either but an estimation about the hydrogen incorporation can be given assuming the crystal to be in equilibrium with an amount of atomic hydrogen corresponding to that in a hydrogen plasma, typically 0.03 atm. Obviously, at such a low temperature, hydrogen molecules are much more stable than H atoms in equilibrium, so molecule formation has to be excluded. (In reality this is prevented by the energy supplied to the plasma.) The results shown in Fig. 4 indicate that this hydrogenation method is very effective. The amount of  $H^+$  is almost equal to the dopant concentration in  $p$ -type samples leading to almost complete compensation of the acceptors. The calculations also predict the concentration of  $(V_{Si} + 2H)^-$  complexes, created by the plasma treatment, to be near the dopant concentration in  $n$ -type material. Together

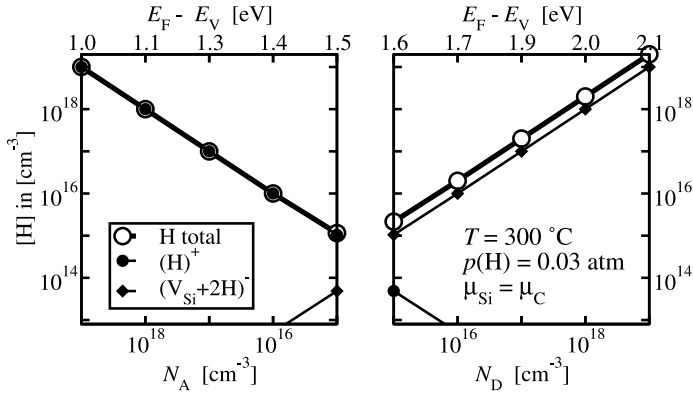


**Fig. 4.** Concentration of hydrogen related defects in 4H-SiC. The crystal is assumed to be in equilibrium with 0.03 atm atomic hydrogen gas at  $300^\circ\text{C}$ . The chemical potentials of Si and C are assumed to be equal.  $N_A$  and  $N_D$  are the concentrations of the boron acceptors and nitrogen donors, respectively, and  $E_F - E_V$  is the position of the Fermi level relative to the valence band edge. The conditions assumed here may give an estimate for hydrogen incorporation during low temperature H-plasma treatment except for the fact that dopant-hydrogen complexes were not considered here

with higher charge states of silicon vacancy + hydrogen complexes, these would lead to elimination of the free carriers by trapping.

Hydrogenation was also attempted by high temperature – high pressure annealing in  $H_2$ . Here the assumption of equilibrium between the gas and the crystal is completely justified. We have carried out the calculations for the experimental conditions,  $1700^\circ\text{C}$  and 10 atm [15], but found very little hydrogen incorporation if only assuming  $H_2$  to be present. However, a considerable amount of the molecules should be dissociated at this temperature. Repeating the calculation at the same temperature but with 1 atm atomic H, instead, we obtained the results shown in Fig. 5. Again,  $H^+$  is the dominant species in  $p$ -type material, its concentration approaching that of the dopant at lower levels of doping but about an order of magnitude less in the heavy doping limit. In  $n$ -type SiC, the amount of  $H^-$  becomes higher than that of  $H^+$  as the Fermi level passes the  $(+/-)$  occupation level of hydrogen.  $(V_{\text{Si}} + 2H)^-$  also appears and higher charge states of silicon vacancy + hydrogen complexes may even have larger concentrations. For  $n$ -type doping between  $10^{17}$  and  $10^{18} \text{ cm}^{-3}$ ,  $H^-$  and  $H^+$  coexists and molecules may form.

As mentioned in the introduction of this subsection, our method of estimating the concentrations is valid in the low concentration limit of each species, i.e., interaction between them is excluded. Therefore, the calculated concentration of  $H_2$  refers only to those molecules which are incorporated as such in the first place. Since that requires the incorporation of two hydrogen atoms at the same time, the formation energy is much higher than the one needed for one hydrogen atom (the formation energy of one H atom is

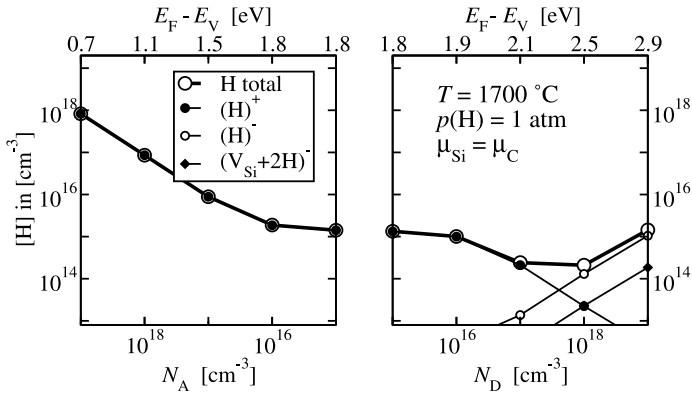


**Fig. 5.** Concentration of hydrogen related defects in 4H-SiC. The crystal is assumed to be in equilibrium with 1 atm atomic hydrogen gas at  $1700^\circ\text{C}$ . The chemical potentials of Si and C are assumed to be equal.  $N_A$  and  $N_D$  are the concentrations of the boron acceptors and nitrogen donors, respectively, and  $E_F - E_V$  is the position of the Fermi level relative to the valence band edge. The conditions assumed here may give an estimate for hydrogen incorporation during high temperature annealing except for the fact that dopant-hydrogen complexes were not considered here

higher than half of the binding energy between two H atoms in a molecule in the crystal). Therefore, the directly incorporated  $\text{H}_2$  concentration remains always very low. In contrast, in  $V_{\text{Si}} + 2\text{H}$ , the binding energy of the C–H bonds makes up for the incorporation of the second hydrogen in the vacancy.

We would like to emphasize again that the concentrations given here are estimates about the direct (and independent) incorporation of the various forms of hydrogen defects under the assumption of equilibrium with an atomic hydrogen gas (at different temperatures and pressures) and serve only as a semi-quantitative guide to the real situations (CVD-growth, H-plasma treatment, high  $T$  – high  $p$  annealing in  $\text{H}_2$ ), which they simulate. The total hydrogen concentration for heavy doping might be enhanced by the higher charge states of the vacancy + hydrogen defects (not considered here), especially in the  $n$ -type case. Still, as we will discuss in Sect. 4, our findings can very well be used to interpret the available results on hydrogen incorporation into SiC.

### 3.3 Fast Diffusion of $\text{H}^+$

Hydrogen related complexes, other than the ones created during growth or by hydrogenation, can form, in principle, if the binding energy of the constituents (two H atoms, a vacancy plus hydrogen atoms, etc.) is negative, provided the constituents do not repel each other, given their equilibrium charge states for the actual Fermi-level position. The necessary condition for the actual formation is, however, a sufficient mobility of hydrogen. The same holds for the post-implantation anneals. In a molecular cluster model of  $4H\text{-SiC}$ , the diffusion of a neutral hydrogen atom has been calculated to be 0.7 eV [48]. Unfortunately, the neutral charge state appears to be irrelevant due to the negative  $U$  character of hydrogen. The mobile species should be  $\text{H}^+$ , the equilibrium configuration of which is at the antibonding site behind a carbon atom (unlike for  $\text{H}^0$ ), on a mirror plane to the  $c$ -axis of the crystal. The C–H bond points toward either an interstitial  $T$  or an  $R$  site (see Fig. 1). Since the direction orthogonal to this plane is a channel direction, it seems plausible to assume that moving  $\text{H}^+$  along this direction will have the lowest migration barrier. We fixed the coordinate of  $\text{H}^+$  along the channel direction at different points and allowed the system to find its minimal energy by relaxing the hydrogen orthogonal to the channel direction and the surrounding atoms in every direction [49]. The results of the calculations show that  $\text{H}^+$  moves along oscillating between the two sides of the channel (see Fig. 6).

We found the highest barrier along this path to be 0.4 eV which is, therefore, an upper bound for the activation energy of  $\text{H}^+$  migration. Taken into consideration, that the zero point vibration energy of  $\text{H}^+$  in the equilibrium state is 0.27 eV, at annealing temperatures around 1500°C ( $kT = 0.15$  eV)  $\text{H}^+$  should diffuse almost freely in the lattice, unless it is trapped by another hydrogen, or by dopants, or by vacancies.

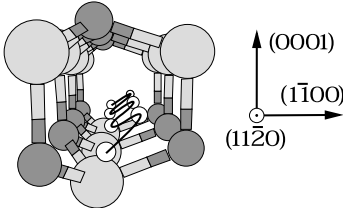


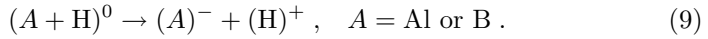
**Fig. 6.** The path of hydrogen diffusion along the channel direction. *Dark grey, light grey and white atoms represent C, Si, and H atoms, respectively*

As described in the preceding subsections, silicon vacancies are expected to be the major traps for  $\text{H}^+$ . In case of trapping, the energy to activate diffusion is the dissociation energy of the  $V_{\text{Si}} + \text{H}$  complex. That can be estimated as the sum of the negative of the binding energy and the diffusion barrier for  $\text{H}^+$  migration. Using (1–4), the dissociation energy can be estimated, in  $p$ -type and weakly  $n$ -type material to be between about 4.0 and 5.3 eV from  $(V_{\text{Si}} + \text{H})$ , or 3.5–4.8 eV from  $(V_{\text{Si}} + 2\text{H})$  depending on the Fermi-level position during annealing. (The upper limit was taken at  $E_V + 1.8$  eV.)

### 3.4 Complexes of Hydrogen with $p$ -Type Dopants

The very mobile  $\text{H}^+$ , which is the dominating form of hydrogen in  $p$ -type SiC, can easily be captured by the ionized acceptors ( $A^-$ ). Therefore, the formation of electrically inactive  $A^-\text{H}^+$  complexes is likely. Experimental findings indicated that this might, indeed, be the case. Therefore, we have investigated the interaction of boron and aluminum with hydrogen in  $4H$ -SiC [45],[50]–[54]. In  $4H$ -SiC there are two inequivalent substitutional sites in both sublattices, but our investigations showed no significant difference between them, as far as the complex formation is concerned. As it turned out, the most stable configurations are determined by simple rules. First of all, hydrogen always binds to the carbon sublattice (which is negatively charged), i.e., to a carbon neighbor if the acceptor sits on a Si site and to the acceptor, if it sits on a C site. In the case of  $\text{B}_{\text{Si}}$ , the small size of the B atom and the flexibility of the carbon bond angles make a  $\text{B}_{\text{Si}} + \text{H}_{\text{BC}}$  complex with  $\text{B}_{\text{Si}}\text{--H--C}$  bonding the most stable one (C being pushed toward the plane of its Si neighbors). This is followed in energy by  $\text{B}_{\text{Si}} + \text{H}_{\text{AB}(\text{C})}$  with a difference of approximately 1 eV. The larger Al atom makes an  $\text{Al}_{\text{Si}} + \text{H}_{\text{AB}(\text{C})}$  complex with  $\text{Al}_{\text{Si}}\text{--C--H}$  bonding more stable than  $\text{Al}_{\text{Si}} + \text{H}_{\text{BC}}$  by 0.3 eV. When the acceptors are on the carbon site, the rigidity of the Si bond angles precludes the bond centered position for H (the Si atom is hard to push toward the plane of its C neighbors), and the most stable configurations are  $\text{B}_{\text{C}} + \text{H}_{\text{AB}(\text{B})}$  and  $\text{Al}_{\text{C}} + \text{H}_{\text{AB}(\text{Al})}$  with a  $\text{H--A}_{\text{C}}\text{--Si}$  bonding.

The complex formation with hydrogen passivates both boron and aluminum, i.e., the arising complexes have no level in the gap and cannot become charged. Reactivation of the acceptor requires the dissociation of these complexes according to the reaction



The binding energy of the (neutral) complex with respect to the isolated (charged) constituents can be estimated by subtracting the sum of the total energies of a supercell containing  $A^-$  and a supercell containing  $H^+$  from the sum of the total energies of a supercell containing a neutral  $A + H$  complex and of a perfect supercell. Due to the different bonding configurations in the most stable forms, the calculated binding energies for the  $B_{\text{Si}} + H_{\text{BC}}$  and the  $Al_{\text{Si}} + H_{\text{AB(C)}}$  complexes are significantly different,  $-1.6$  and  $-0.7$  eV, respectively [50]. It should be noted, that the reaction (9) compares energies of two charged species with a neutral one. The error committed in the energy calculation of charged supercells is independent of the sign of the charge and can be estimated in this case to be about 0.2 eV/cell [51]. Therefore, a better estimate for the binding energies would be  $-2.0$  and  $-1.1$  eV for  $B + H$  and  $Al + H$ , respectively.

The dissociation reaction (9) requires that the more mobile constituent,  $H^+$ , be moved away from the acceptor. Therefore, the activation energy (i.e. the energy of reactivating the acceptor) is approximately the sum of the negative of the binding energy of the complex and of the migration barrier for  $H^+$ . (The barrier height for the first step in the dissociation process might be affected somewhat by the presence of the acceptor.) Using our calculated barrier for the  $H^+$  migration with the estimates for the binding energies we obtain a dissociation energy of 2.4 and 1.5 eV for  $B + H$  and  $Al + H$ , respectively. These should also be the effective activation energies for hydrogen diffusion in B- and Al-doped samples if no vacancies are present.

### 3.5 Effect of Complex Formation on Hydrogen Incorporation into *p*-Type Samples and on the Site Selection of Boron

If stable complexes of the acceptors with hydrogen exist, they can also form during in-growth doping of CVD layers. Therefore, it is interesting to investigate how the possibility of complex formation influences the incorporation of hydrogen during CVD growth. Also, in-growth doping utilizes the site competition technique, which may be influenced by the effect of hydrogen.

In order to investigate the incorporation of the dopants *and* hydrogen, one needs to calculate the formation energies  $E_{\text{form}}$  of the complexes (see (7)), calculated with respect to a  $\mu_{\text{H}}$  corresponding to – as before – the atomic H content (about 0.01 atm) of the reactive gas mixture. The calculation of the chemical potential of the acceptor atoms is difficult. One should take into account that in the gas phase the precursor molecules of the dopants ( $B_2H_6$  or  $Al(CH_3)_3$ ) dissociate. Using standard heat of formation data the dissociation leading to a BH (AlH) molecule requires 1.2 eV (0.7 eV) less energy than dissociation leading to free B (Al) atoms. Therefore, BH and AlH are definitely present in the gas phase. If these molecules are incorporated into

the crystal, the acceptor-hydrogen complex may form in the first place, depending on how their formation energy compares with that of the isolated acceptor. Calculating this difference does not require the chemical potential of the acceptor atoms. The results [51, 52] show that isolated aluminum is more stable than the  $(\text{Al}_{\text{Si}} + \text{H}_{\text{AB}(\text{C})})$  complex for any CVD growth temperature. Therefore, Al is incorporated as isolated substitutional acceptor, and the amount of incorporated hydrogen depends on the Al concentration only through the doping effect of the latter as described in Sect. 3.2, i.e.,  $[\text{H}]$  should be about 2–3 orders of magnitude less than  $[\text{Al}]$ .

In contrast to aluminum, due to the higher binding energy between B and H, the formation energy difference between  $\text{B}_{\text{Si}}$  and  $(\text{B}_{\text{Si}} + \text{H}_{\text{BC}})$  is positive in the whole temperature range, indicating that the incorporation of the B + H complex is favored over the isolated B atom. Therefore, boron and hydrogen gets incorporated together, in equal amounts [51, 53, 54], in agreement with the observations.

One has, of course, also take into account that B can occupy the carbon site in the lattice as well. (In case of Al, the energy difference between the two sites is much too high.) Since the site selection of boron can be influenced by tuning the Si/C ratio in the gas phase, we investigated the formation energy difference between the two sites for B and for the B + H complex in dependence of the Si/C ratio. Except for extreme Si-rich conditions,  $\text{B}_{\text{Si}} + \text{H}$  is favored over  $\text{B}_{\text{C}} + \text{H}$ , and except for extreme C-rich conditions,  $\text{B}_{\text{C}}$  is favored over  $\text{B}_{\text{Si}}$ . We remind the reader that these theoretical extremes are set by bulk silicon and graphite formation, so normal growth conditions are well away from these limits. Therefore, under realistic CVD conditions (where hydrogen is abundant)  $\text{B}_{\text{Si}} + \text{H}$  is formed. In contrast, in situations like implantation, where there is no hydrogen present during B incorporation,  $\text{B}_{\text{C}}$  should be the dominant form of boron. Comparing the stability ranges of these two complexes in dependence of the Si/C ratio and the temperature shows that except of very extreme Si-rich conditions or very high temperatures,  $\text{B}_{\text{Si}} + \text{H}$  is more likely, i.e., boron incorporation onto the Si site, together with hydrogen is preferred if H is present at all.

Accepting the proposal of [60] to assign the deep boron acceptor to  $\text{B}_{\text{C}}$ , it becomes clear why the concentration of deep boron acceptors was so low in CVD layers grown even in Si-rich conditions at 1350°C as reported in [55] while high concentration of deep boron acceptors could be achieved in implanted samples [56]. It is the effect of hydrogen during in-growth doping which makes the boron select the silicon site and produce the shallower acceptor center. If hydrogen is present, boron is incorporated together with a hydrogen atom, preferentially onto the Si site as an electrically inactive complex. Given the binding energy of the complex, some of them can dissociate during the growth process. However, for the B atom to change site would then require more than 4 eV [57]. Therefore, it is activated as a shallow acceptor. In case of implantation, boron is introduced without hydrogen, and

in course of the heat treatment selects the C site (unless B is co-implanted with C [58]), becoming activated as a deep acceptor.

Since H is incorporated together with B in CVD growth,  $[H] \sim [B]$  in such samples. Since the B + H complexes may dissociate during the growth in a non-equilibrium process, it is difficult to say, how much is in B + H complexes, and how much is interstitial.

In case of post-growth hydrogenation, the formation of acceptor-hydrogen complexes has little influence on the total amount of incorporated hydrogen concentration,  $[H]$ . As shown in Fig. 4, H-plasma treatment of *p*-type SiC would result in  $[H]$  about equal to the acceptor concentration,  $[A]$ , even without complex formation. If the latter is taken into account, what is gained in “passivating” H atoms, is lost in number of active acceptors, lifting the Fermi-level, and diminishing the number of “compensating” free  $H^+$ . In case of high- $T$ , high- $p$  anneal in  $H_2$ , (where  $[H] \ll [A]$ , otherwise) the A-H complexes can increase  $[H]$ . However, although the binding energy lowers the formation energy with respect to interstitial H, the acceptor concentration is orders of magnitude lower than that of the interstitial site (prefactor in (8)), so the increase in  $[H]$  is not more than 50% even for the highest doping concentration in Fig. 5.

### 3.6 Spectroscopic Fingerprints of H-Related Defects

Occupation levels have already been mentioned in the preceding subsections. Figure 7 shows the summary of the calculated  $+0/-$  occupation levels for interstitial H and for the  $V + nH$  defects, for comparison with DLTS experiments. (As mentioned before, our experience, since the publication of our work on hydrogen in 3C-SiC [44], showed that for higher charge states the charge correction cannot be neglected but also that the usually applied monopole correction leads to serious overcorrection. Therefore, in the time being we do not venture to predict occupation levels involving higher charge states, and advise caution with respect to such data published in our papers on 3C-SiC. In the case of the  $(+0)$  and  $(0/-)$  occupation levels the error

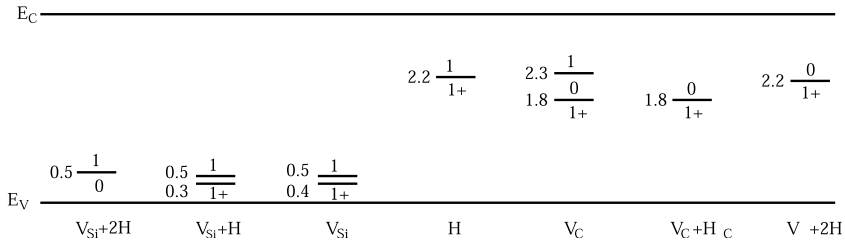


**Fig. 7.** The calculated occupation levels for various H-related defects in 4H-SiC. The energies are given in eV with respect to the valence band. (Only singly charged states have been considered)

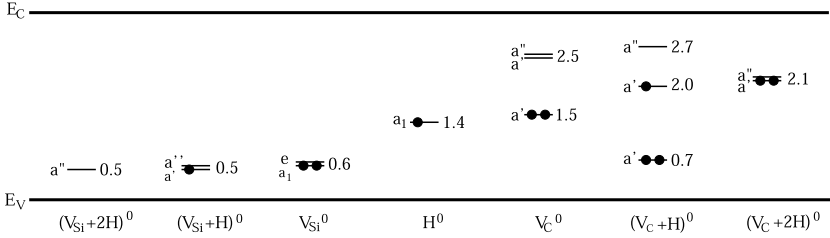


**Fig. 8.** The calculated one-electron levels for neutral H-related defects in 4H-SiC. The energies are given in eV with respect to the valence band

due to the lack of charge correction is much smaller and – considering other error sources – we expect the given values to be accurate within 0.2 eV. In case of the (+/–) occupation level the charge corrections cancel each other.) As can be seen from the figure, all  $V_{Si}$  related defects have similar occupation levels near the valence band, acting as traps in  $n$ -type material.  $V_C$  related defects have occupation levels closer to the conduction band and are amphoteric, similar to interstitial hydrogen. (Note that the positive charge state of  $V_{Si} + 2H$  and the negative charge state of  $V_C + H$  and  $V_C + 2H$  may exist but have not been calculated yet). The acceptor + hydrogen complexes are electrically inactive.

The electronic transition energies detected in optical spectroscopy (absorption, PL and PL excitation, or optically detected magnetic resonance, ODMR) can be related, to a good approximation, to the relative positions of the one electron levels. Figure 8 shows our calculated one-electron level positions in the neutral charge state of the defects. Here we expect an accuracy within about 0.1 eV. (Note: sometimes, e.g., in case of  $D^+A^-$  recombination detected by PL, the relevant one-electron levels are those of the charged states. Those, however, cannot be calculated reliably because of the problem with charge in supercell calculations.)

Local vibration modes (LVM) of the defects can also be calculated – including the effect of isotope substitution – to help the assignment of observed vibration bands in IR, Raman and PL spectroscopy. The expected accuracy is about  $\pm 30 \text{ cm}^{-1}$ , so it makes no sense to try to reproduce site- or polytype-dependent effects. Therefore, vibration calculations have been carried out in 3C-SiC only. In the simple case of the C–H stretching mode vibration in  $V_{Si} + H$ , even anharmonicity effects could be taken into account and an anharmonicity parameter of 14.4 meV was obtained [59]. The results in the harmonic approximation are summarized in Table 1.

Electron magnetic resonance experiments give usually the most important cues to set up models for various defect centers. The quantity, calculation can provide, to check upon the models by comparison with experimental data is the hyperfine (hf) tensor. Using the CRYSTAL98 code with all electron basis for the immediate neighbors of the defects and a valence basis for the rest

**Table 1.** Vibration frequencies for hydrogen related defects in silicon carbide. The frequencies had been calculated in 3C-SiC in the quasi-harmonic approximation and are given in  $\text{cm}^{-1}$ . Columns H-H, H-D and D-D indicate the number of H atoms substituted by D

Defect	Mode	H-H	H-D	D-D
$(\text{H})^+$	stretching	2747		
$(\text{H})^-$	stretching	1268		
$(\text{H}_2)^0 \text{ }^{(a)}$	stretching	3452		
$(V_{\text{Si}} + \text{H})^0$	stretching	2961	2170	
$(V_{\text{Si}} + 2\text{H})^0$	symmetric	3051	3014	2229
	asymmetric	2999	2206	2200
$(V_{\text{C}} + \text{H})^0$	asymmetric	1570		
	symmetric	991		
$(V_{\text{C}} + \text{H})^+$	asymmetric	1770		
	symmetric	1189		
$(V_{\text{C}} + 2\text{H})^0$	symmetric	1332	1177	952
	asymmetric	976	975	730
	asymmetric	976	797	730
$(V_{\text{C}} + 2\text{H})^+$	asymmetric	1279		
	asymmetric	1271		
	symmetric	1000		
$(B_{\text{Si}} + \text{H})^0$	stretching	3114		
$(Al_{\text{Si}} + \text{H})^0$	stretching	2908		

<sup>(a)</sup> Note that the  $\text{H}_2$  vibration in 4H-SiC may be considerably higher around the higher due to the larger open space around the  $R$  site

in a 96-atom 4H-SiC supercell, we have attempted to calculate the hf tensor for the hydrogen related defects in their paramagnetic state. The lack of reconstruction in case of  $V_{\text{Si}}$  causes the vacancy related defect states to be rather delocalized, therefore, the accuracy of the calculated hf tensors for the various paramagnetic states of  $V_{\text{Si}}$  itself turned out to be pure with this approximation. (Calculations with all electron basis for the second neighbors are under way but they are very time consuming.) In contrast, for the case of the more localized defect states in  $V_{\text{C}}$  the results are rather reasonable in comparison with values published in the literature [79]. Therefore, Table 2 in Sect. 4.3 gives the principal values of the calculated hf tensors for  $V_{\text{C}}$ ,  $(V_{\text{C}} + \text{H})$  and  $(V_{\text{C}} + 2\text{H})$  in the appropriate spin states [78].

**Table 2.** The calculated principal values of the hyperfine tensor (MHz) of defects at the  $k$ -site compared to the EI1 center [84] in  $4H$ -SiC and to the T5 center in parentheses [77] in  $3C$ -SiC. The calculations were carried out at the  $k$  site. The spin density is localized on two silicon atoms in EI1 ( $C_{1h}$  symmetry) while on four equivalent Si atoms in T5 ( $D_2$  symmetry). Si(1) is on the  $c$ -axis, Si(2) is in the mirror plane while Si(3) and Si(4) are equivalent in  $C_{1h}$  symmetry. H(1) binds to Si(1) and Si(2) while H(2) binds to Si(3) and Si(4)

Atom	$(V_C)^-$	$(V_C + H)^0$	$(V_C + 2H)^+$	$(V_C + 2H)^+$	Experiment
$^1\text{H}(1)$		-42.3	-23.7	-56.7	
		-43.8	-21.6	-51.6	
		13.5	-2.4	-1.5	
$^1\text{H}(2)$			-33.0	-57.0	
			-0.6	-2.1	
			-31.5	51.3	
$^{29}\text{Si}(1)$	-138.8	-151.7	-63.0	-173.3	60.6(41.1)
	-141.5	-152.9	-63.6	-175.1	70.2(41.4)
	-180.5	-243.1	-101.3	-270.4	85.7(56.7)
$^{29}\text{Si}(2)$	-157.7	-284.2	-112.4	-288.4	70.2
	-123.5	-182.0	-67.2	-187.7	67.8
	-120.8	-181.1	-66.6	-185.9	57.0
$^{29}\text{Si}(3,4)$	-11.1	2.1	-89.3	-178.4	
	-13.8	3.9	-148.7	-279.4	
	-12.6	1.2	-90.2	-180.2	

## 4 What Have We Learned about Hydrogen in SiC from Theory and Experiments?

### 4.1 Incorporation of Hydrogen and Its Effect on the Free Carrier Concentration

Our calculations have verified the assumption of Larkin [7] about hydrogen being incorporated together with boron during CVD growth and influencing the site selection of the latter in favor of the Si site. In addition, accepting the suggested assignment of  $B_{\text{Si}}$  to the shallow, and  $B_{\text{C}}$  to the deep boron acceptor center [60], our results can explain the experimental findings regarding the relative abundance of them in growth or in implantation. More recent experiments have also proven that boron carries hydrogen into the crystal. Samples with a low level of boron doping have been prepared in a nominally hydrogen-free environment [61]. After the ion bombardment of a SIMS measurement, the PL signal assigned to the  $V_{\text{Si}} + \text{H}$  center has appeared. According to our prediction, the amount of hydrogen is comparable to the amount of the acceptors only in B-doped as-grown CVD samples. In case of

Al-doping (where the Al and H incorporation is independent), the hydrogen concentration,  $[H]$ , is 2–3 orders of magnitude lower (depending on doping level) than that of  $[Al]$  (see Fig. 3). This prediction has been experimentally confirmed [62]. Our results indicated hydrogen incorporation to be negligible in as-grown  $n$ -type epilayers explaining why no passivation of been found [5].

According to our calculations – and in agreement with [22, 63, 64] – the dominating form of hydrogen in  $p$ -type samples is the mobile interstitial  $H^+$ , which can be easily introduced by H-plasma treatment at low temperature with  $[H^+]$  close to that of the acceptor concentration (see Fig. 4). That explains the high level of compensation in hydrogenated  $p$ -type samples [18]–[20],[64]. In contrast, the dominant hydrogen defect in  $n$ -type samples is the electron trap  $V_{Si} + 2H$ , which diminishes the free carrier concentration by trapping just the same way as pure  $V_{Si}$  (created during, e.g. Ar-plasma treatment) does – again in agreement with observations [19]–[21],[23]. A recent experiment [65] also confirmed our interpretation. H-plasma treatment of samples coated with a thin Ni or Pt film showed complete passivation of  $p$ -type samples, while no loss of carrier concentration was observed in  $n$ -type ones up to 800°C. The metal coating protects the samples from vacancy formation but  $H^+$  can easily penetrate it. The only successful way to achieve hydrogen passivation of  $n$ -type samples so far was annealing at high temperature in high pressure hydrogen gas. Our calculations indicate (see Fig. 5) that in such cases the concentration of interstitial H- may be higher than that of  $V_{Si} + 2H$ , and could, indeed, cause donor passivation. (Although our results simulating the effect of such treatments still did not show  $[H^-]$  to be comparable with  $[N]$ .) The lower passivation rate found in  $n$ - vs.  $n^+$ -samples – despite the higher amount of H detected by SIMS in the former [15] – can be explained by the higher likelihood of molecule formation in the  $10^{17}$ – $10^{18}$  doping range.

## 4.2 Diffusion and Trapping of Hydrogen

Many experiments monitoring the hydrogen diffusion profiles in  $p$ -type material have established that hydrogen must be rather mobile unless the level of radiation damage is high [14, 22, 62, 63, 66, 68]. The very low diffusion barrier we find for  $H^+$ , 0.4 eV, is in line with that.

In  $n$ -type material the hydrogen diffusion is slow, even if little damage was created [14]. According to our results, hydrogen forms molecules in moderately doped  $n$ -type samples, when the Fermi energy is around  $E_V + 2.2$  eV (for a doping level around few times  $10^{17}$  cm $^{-3}$ ). These are much less mobile than  $H^+$ . Also, the dominant hydrogen-defects, created by hydrogenation other than high temperature annealing, are the silicon vacancy + hydrogen complexes in which hydrogen is tightly bonded.

H-implantation at high energy creates radiation damage. Self-interstitials are expected to anneal out relatively early, so the dominant traps for hydrogen in such cases are vacancies. We have shown that the binding energy

of hydrogen is significantly ( $\sim 2$  eV) higher to  $V_{\text{Si}}$  than to  $V_{\text{C}}$ . The calculated dissociation energy of  $\text{H}^+$  is between about 4.0 and 5.3 eV from  $V_{\text{Si}}$  + H, and about 3.5–4.8 eV from  $V_{\text{Si}}$  + 2H (depending on the position of the Fermi-level). This is in fair agreement with range 3.5–4.9 eV, found experimentally [9, 10]. Hydrogen atoms in the silicon vacancy passivate the dangling bonds one by one. According to theory,  $V_{\text{Si}}$  can accommodate four H atoms, which would passivate the hole trap activity completely. To achieve that, however,  $[\text{H}] > [V_{\text{Si}}]$  is needed, because the disproportional distribution of hydrogen among the vacancies is energetically not favored. It should be noted that  $V_{\text{C}}$  and H never attract each other. (Except for Fermi-level positions between  $E_{\text{V}} + 1.8$  eV and 2.2 eV, there is even repulsion). Therefore, even if the irradiation energy is between the displacement limits of the two sublattices, the chances for hydrogen getting trapped in  $V_{\text{C}}$  are meager.

$\text{H}_2$  molecules, even when they may be formed at all, have a binding energy of about  $-1$  eV, corresponding roughly to a dissociation energy of about 1.4 eV. Therefore, in the absence of silicon vacancies, the major trap for hydrogen are the dopants. Our calculated dissociation energies for B + H and Al + H complexes, 2.4 and 1.5 eV agree nicely with the observed acceptor reactivation energies of 2.5 and 1.6 eV [68]. They also agree with the observed activation energies of hydrogen migration in Al-doped and in unintentionally, i.e., B-doped samples [12], confirming that in defect-free *p*-type material the acceptors limit the hydrogen diffusion.

The B + H and Al + H complexes were found to be electrically inactive. Therefore, besides compensation, the observed loss of free holes after  $\text{H}_2$  annealing, H-plasma treatment low energy H-implantation [14]–[16],[18]–[22] could have occurred also due to passivation by complex formation, as indicated by the loss of the acceptor related EPR (electron paramagnetic resonance) signal [15, 18]. Since the ionized acceptors and  $\text{H}^+$  are electrically attracted to each other, and the latter is very mobile, this seems very likely. More recent experiments [62]–[69],[71], especially the one reported in [64] seem to prove that, indeed, that is the case. In the latter, a Schottky-diode was prepared from Al-doped ( $4 \times 10^{17} \text{ cm}^{-3}$ ) bulk 6H-SiC material by electron beam evaporation of a ruthenium contact. Hydrogen was introduced by a dc hydrogen plasma through the contact in order to reduce the near-surface damage and accumulation of near-surface hydrogen. The diffusion of  $\text{H}^+$  could be enhanced by reverse bias annealing. After passivation, *C-V* measurements showed that the reactivation kinetics was a first order process, and the obtained dissociation energy (1.5 eV) was very close to the values in [12, 68]. The passivation – reactivation process was reversible (without switching on the H-plasma again), proving that the reactivation did not occur by out-diffusion of H (as would be the case for mere compensation). It should be noted that our calculations also predict a metastable, electrically inactive Al + H configuration, only about 0.3 eV higher in energy, than the

stable one. This might explain some uncertainties in the observed effective diffusion activation energy of hydrogen in Al-doped samples [66, 69].

Existence of a metastable Al + H complex has been suggested based on experiments as well. Al-doped ( $1-8 \times 10^{16} \text{ cm}^{-3}$ ) 6H-epilayers were subjected to a hydrogen plasma and changes in both the H- and the Al-related PL lines were monitored [70]–[72]. Upon hydrogenation the well-known PL-center, related to  $V_{\text{Si}} + \text{H}$  [3, 4] have appeared, together with a strong reduction in the intensity of the Al-BE (bound exciton) line. The latter indicates that – besides the creation of  $V_{\text{Si}} + \text{H}$  defects – apparently electrically inactive Al + H complexes have been formed as well. The passivation was, however, not complete. Prolonged excitation with above band gap light caused a gradual reduction and finally a complete disappearance of the Al-BE emission during the measurement. (After annealing the hydrogen out at 1100°C, the recovery of the Al-BE PL line was complete, and no light-induced quenching could be observed anymore.) It was, therefore, assumed [71] that an electrically active metastable Al + H complex exists which is transformed into the electrically inactive configuration due to optical excitation. We have not been able to find electrically active complexes of Al and H. Considering the fast diffusion of  $\text{H}^+$ , which at elevated temperatures could even be athermal, it seems likely that the additional passivation occurred due to the heating effect of the high intensity illumination by the formation of further Al + H complexes.

We have not as yet investigated donor + hydrogen complexes but our results so far indicate that they are difficult to form because it is difficult to get mobile hydrogen into *n*-type SiC. Upon plasma treatment the total hydrogen concentration may reach that of the donors but it is present in the form of  $V_{\text{Si}} + 2\text{H}$  complexes. Hydrogen implantation of *n*-type samples should primarily create  $V_{\text{Si}} + \text{H}$ . These defects can also cause loss in the carrier concentration by electron trapping. Further measurements on H-plasma treated *n*-type samples would be necessary.

### 4.3 Fingerprints of H-Related Defects

The knowledge obtained about the stable hydrogen related defects and about the conditions of their formation explains the scarcity of direct spectroscopic evidence of hydrogen in SiC. Hydrogen is easily captured by vacancies and dopants, thus the observation of interstitial hydrogen can only be expected under special circumstances in high quality crystals. Although, for  $E_{\text{F}} > E_{\text{V}} + 0.8 \text{ eV}$ ,  $\text{H}_2$  is the stable species (see Fig. 2) with a characteristic LVM around  $3452 \text{ cm}^{-1}$  (see Table 1), molecule formation can only be expected around the (+/–) occupation level of interstitial atomic hydrogen at  $E_{\text{F}} = E_{\text{V}} + 2.2 \text{ eV}$ . Unfortunately, in this range of doping (except for implantation which would also create vacancies) only high temperature annealing in high pressure hydrogen gas seemed to be able to produce an observable amount of hydrogen but no Raman measurements were performed on those samples. The dominant interstitial hydrogen defect is  $\text{H}^+$  at the  $\text{AB}_{\text{C}}$  site, with a

characteristic LVM at  $2747\text{ cm}^{-1}$ . In principle, a measurable amount of  $\text{H}^+$  could be created by H-plasma treatment (especially through a protecting metal coating) in  $p$ -type samples, but dissociation of acceptor + hydrogen complexes has to be achieved without loss of hydrogen from the sample. (Since the activation energy for diffusion is much less than the binding energy to the acceptor, this should be difficult but, obviously possible in  $p$ -type samples [64].) In fact, a hydrogen related LVM near the predicted one has been observed in  $6H$ -SiC epilayers with  $[\text{H}] \sim 10^{20}\text{ cm}^{-3}$  [73] but definite assignment to  $\text{H}^+$  was not possible. We expect that low-energy implantation (below the displacement threshold of the Si sublattice) could also create a sufficient surplus of interstitial  $\text{H}^+$  in moderately  $p$ -type material.

From acceptor ( $A$ ) passivation studies it is clear that  $A + \text{H}$  complexes can be created in detectable amount but, being electrically inactive, they could only be seen in infrared absorption ( $IR$ ) or Raman spectroscopy. The characteristic LVMs were calculated to be  $3114$  and  $2908\text{ cm}^{-1}$  for  $\text{B}_{\text{Si}} + \text{H}_{\text{BC}}$  and  $\text{Al}_{\text{Si}} + \text{H}_{\text{AB(C)}}$ , respectively. In [17] no such vibration could be detected. We note, though that according to our estimation (see Fig. 3), the expected amount of  $\text{Al} + \text{H}$  complexes in those samples with  $\sim 10^{17}\text{ cm}^{-3}$  Al-doping could have been a few times  $10^{15}\text{ cm}^{-3}$  – difficult to see in rather opaque material. IR measurements in H-plasma treated highly doped material could be more successful. In boron and hydrogen implanted SiC samples a PL center, called  $\text{BH}^0$ , was found with two vibrational side bands at  $86$  and  $118\text{ meV}$  [74]. We have found two LVMs at  $82$  and  $84\text{ meV}$ , and one at  $116\text{ meV}$  for the  $\text{B}_{\text{Si}} + \text{H}_{\text{BC}}$  defect, and no gap modes have been found for  $\text{Al}_{\text{Si}} + \text{H}_{\text{AB(C)}}$ . Based on that it would be tempting to identify the  $\text{BH}^0$  center with  $\text{B}_{\text{Si}} + \text{H}_{\text{BC}}$  complex, however, the  $\text{B}_{\text{Si}} + \text{H}_{\text{BC}}$  stretch mode around  $386\text{ meV}$  ( $3114\text{ cm}^{-1}$ ) was not detected, and binding of an exciton to an electrically inactive defect is questionable. Further investigation (including B and H isotope substitution) is needed to clarify the nature of  $\text{BH}^0$  PL center.

The hydrogen concentration can be best increased by implantation but at the cost of creating vacancies. Since hydrogen trapping in silicon vacancies is preferred both kinetically and thermodynamically,  $V_{\text{Si}} + \text{H}$  complexes should be dominant.  $V_{\text{Si}} + n\text{H}$  complexes with  $n > 1$  should appear only if  $[V_{\text{Si}}] < [\text{H}]$  (or in H-plasma treated samples, see Fig. 4). As mentioned in the introduction, the only H-related defect observed by spectroscopy was, indeed, the PL center associated with  $V_{\text{Si}} + \text{H}$ , based on the vibrational sidebands due to the stretch mode of a C–H bond [3, 4]. The calculated LVM (in  $3C$ -SiC),  $2961\text{ cm}^{-1}$  (see Table 1) is well within the range observed for the various sites in the hexagonal polytypes between  $2959$  and  $2988\text{ cm}^{-1}$ . Recently, with improved methods in crystal growth, ion implantation, and spectroscopy, these spectra were revisited in  $6H$ -SiC [75]. Besides the known lines, new peaks have also been found. These were associated with the overtones of the C–H stretch mode [59, 75] based on agreement with theoretical calculation regarding its anharmonicity. It was found that the PL peaks ap-

peared only in moderately *p*-type samples and not in *n*- or heavily *p*-type ones. Assuming that the exciton is captured by the neutral defect, our results for the occupation levels (see Fig. 7) can explain this, namely  $V_{\text{Si}} + \text{H}$  in 4*H*-SiC is neutral only when the Fermi-level is between  $E_{\text{V}} + 0.3$  and 0.5 eV. (In 3*C*-SiC  $E_{\text{V}} + 0.3$  and 0.7 were obtained.) These occupation levels should be observable by DLTS.

Hydrogen related defects remain elusive for magnetic resonance spectroscopy. Interstitial hydrogen and dopant + hydrogen complexes are diamagnetic, therefore, only vacancy + hydrogen complexes have a chance for detection. EPR studies after wet oxidation showed an EPR signal which could be attributed to a defect in the SiC crystal, involving a carbon dangling bond, but not identical with the known  $V_{\text{Si}}$  signatures [76]. The difference between the annealing characteristics of the center in Al-doped and unintentionally, i.e., boron-doped samples was reminiscent to the behavior of hydrogen [9, 10, 12] so the disappearance of the signal was attributed to hydrogen diffusion. The observed activation energy, 4.0 eV, was well in the range we have obtained for the binding energy of H to a carbon dangling bond in the  $V_{\text{Si}} + \text{H}$  complex (see Sect. 3.1). Unfortunately, due to the lack of hyperfine data, no identification of this observed EPR center is as yet possible. The calculation of the hyperfine tensor for  $V_{\text{Si}} + n\text{H}$  complexes are under way.

The formation of  $V_{\text{C}} + \text{H}$  complexes requires very special circumstances. Low-energy electron-irradiation of samples with Fermi-level between  $E_{\text{V}} + 1.8$  and 2.2 eV during irradiation could, in principle produce them, provided the H-content was originally sufficiently high. LVMS related to  $V_{\text{C}} + n\text{H}$  defects are given in Table 1, while the calculated principal values of the hyperfine tensor in paramagnetic states can be seen in Table 2.

An EPR center, called T5, with  $D_2$  symmetry has been observed in boron-doped electron irradiated CVD layers of 3*C*-SiC and associated with  $V_{\text{C}}^+$  [77]. The EPR signal could not be detected in similar samples if they were even weakly *n*-type. This was interpreted as loss of the paramagnetic state due to an occupation level at midgap. Both the latter assumption and the observed symmetry contradict theoretical results on  $V_{\text{C}}$  [44]. Since the  $(V_{\text{C}} + 2\text{H})^+$  complex did possess  $D_2$  symmetry, and it could be expected to occur only after irradiating *p*-type material, we suggested it as the real origin of the T5 center. This had a special importance, since the T5 center could be annealed out around 200°C with an activation energy of 1.45 eV. Assuming that to be characteristic for  $V_{\text{C}}$  diffusion, meant that  $V_{\text{C}}$  could be removed by low temperature annealing. This is at odds with results of positron annihilation studies [82]. Later EPR work [83] in electron-irradiated hexagonal material identified the so-called EI5 as the fingerprint of  $V_{\text{C}}$ . Our calculations as well as that of [60, 79] confirm the assignment. At the same time the EI1 center [78] of 4*H*-SiC showed characteristics very similar to that of T5 in 3*C*-SiC. Therefore, EI1 and related centers have been tentatively assigned to  $V_{\text{C}} +$

$n\text{H}$  complexes [84], assuming that the low activation energy is connected with hydrogen diffusion. Recently, however, the calculation of the hyperfine tensor became possible for us and the calculated values have not confirmed the assignment [78]. The positively charged carbon (split) interstitial (sharing a carbon lattice site with another carbon atom in a similar configuration as the  $V_{\text{C}} + 2\text{H}$  complex) appears to be a better candidate [78, 80, 81], although C-related hyperfine interaction could not be found yet.

## 5 Conclusion

Although, at present, few of the possible hydrogen defects have been experimentally observed, most of the technologically important effects of hydrogen (passivation of  $p$ -type material by complex formation with  $\text{H}^+$  and its influence on the site competition doping, as well as passivation of  $n$ -type material by carrier trapping in  $V_{\text{Si}} + n\text{H}$  defects) are by now understood. Since the dissociation energy of hydrogen from vacancies is comparable to the migration barriers of vacancy motion, it would be interesting to study the effect of hydrogen on the annealing kinetics of vacancies. This is even more true for self-interstitials. The complex formation of hydrogen with donors is rarely observed, mainly because the low concentration and low mobility of hydrogen in most  $n$ -type samples. Still, theoretical studies may reveal some surprises even there. Another subject not studied so far is the formation of larger aggregates of hydrogen (e.g. platelets), which have been observed in other semiconductors and might have technological importance for SiC as well. We hope to cover these problems in the near future. We also expect progress in the calculation of the energy of higher charge states of defects which may correct some of the results reported here.

## Note

The authors of this paper are subject of scientometric evaluation in their country. This publication contains new results but is not carried by the Citation Index. Therefore, you are kindly requested to give an e-mail notification to the address [p.deak@eik.bme.hu](mailto:p.deak@eik.bme.hu) whenever you refer to this work.

## Acknowledgement

We are greatly indebted to our experimentator partners, W.J. Choyke and R.P. Devaty (U. Pittsburgh), E. Janzén and N.T. Son (Linköping U.; cooperation supported by the IVA-MTA Grant Nr. 36), A.W.R. Leitch (U. Port Elisabeth; cooperation supported by the SA-Hungary S&T Grant Nr. 7/98) and J. v. Bardeleben (U. Paris 6&7) for their guidance in our studies and for the computer capacity they provided for us (through the Pittsburgh Supercomputer Grants Nr. PHY970006P and PHY010001P, the Swedish National

Supercomputer Grant Nr. 2000018 and at the computer center in Paris). We are also grateful to J.E. Lowther (U. Witwatersrand) and M. Bockstedte (U. Erlangen) for many useful advices in computational methodology. The support of the Hungarian grants OTKA T-034397 and F-038357 are appreciated.

## References

1. *Fundamental Questions and Applications of SiC*, ed. by W.J. Choyke, H. Matsunami, and G. Pensl (Wiley-VCH, Berlin 1997), special issue of Phys. Stat. Sol. (a) **162** and (b) **202** (1997)
2. D.J. Larkin, P.G. Neudeck, J.A. Powell, and L.G. Matus: Appl. Phys. Lett. **65**, 1659 (1994)
3. W.J. Choyke and L. Patrick: Phys. Rev. Lett. **29**, 355 (1972)
4. W.J. Choyke, L. Patrick, and P.J. Dean: Phys. Rev. B **9**, 3214 (1974)
5. D.J. Larkin, S.G. Sridhara, R.P. Devaty, and W.J. Choyke: J. Electronic. Mater. **24**, 289 (1995)
6. A. Schöner, K. Rottner, N. Nordell, M.K. Linnarson, C. Peppermüller, and R. Helbig: Diamond Relat. Mater. **6**, 1293 (1997)
7. D.J. Larkin: Phys. Stat. Sol. (b) **202**, 305 (1997)
8. J. Portman, C. Haug, R. Brenn, J. Schneider, K. Rottner, and R. Helbig: Nucl. Instrum. Methods Phys. Res. B **155**, 132 (1999)
9. M.K. Linnarson, J.P. Doyle, and B.G. Svensson: in *III-Nitride, SiC and Diamond Materials for Electronic Devices*, ed. by D. Gaskill, C.D. Brandt, and R.J. Nemanich, Mat. Res. Soc. Symp. Proc. No. 423 (Material Research Society, Pittsburgh, 1996), p. 635
10. M. Janson, M.K. Linnarson, A. Hallén, and B.G. Svensson: in *Hydrogen in Semiconductors and Metals*, ed. by R.G. Leisure, Mater. Res. Symp. Proc. No. 513 (Material Research Society, Warrendale, 1998), p. 439
11. L. Patrick and W.J. Choyke: Phys. Rev. B **8**, 1660 (1973)
12. R.A. Causey, J.D. Fowler, C. Revenbakht, T.S. Elleman, and K. Verhese: J. Am. Ceram. Soc. **61**, 221 (1978)
13. M.K. Linnarson, M. Janson, and B.G. Svensson: Phys. Status Solidi B **210**, 395 (1998)
14. N. Achtziger, J. Gillenberger, W. Witthuhn, M.K. Linnarson, M. Janson, and B.G. Svensson: Appl. Phys. Lett. **73**, 945 (1998)
15. F. Gendron, L.M. Porter, C. Porte, and E. Bringuier: Appl. Phys. Lett. **67**, 1253 (1995)
16. B. Theys, F. Gendron, C. Porte, E. Bringuier, and C. Dolin: J. Appl. Phys. **82**, 6346 (1997)
17. B. Clerjaud, F. Gendron, C. Porte, and W. Wilkening: Solid State Commun. **93**, 463 (1995)
18. G.J. Gerardi, E.H. Pointdexter, and D.J. Keeble: Appl. Spectrosc. **50**, 1428 (1996)
19. F. Ren, J.M. Grow, M. Bhaskaran, R.G. Wilson, and S.J. Pearton: J. Electron. Mater. **26**, 198 (1996)

20. G. McDaniel, J.W. Lee, E.S. Lambers, S.J. Pearton, P.H. Holloway, F. Ren, J.M. Grow, M. Bashkaran, and R.G. Wilson: *J. Vac. Sci. Technol. A* **15**, 885 (1997)
21. A.O. Konstantinov, N.S. Konstantinova, O.I. Kon'kov, E.I. Terukov, and P.A. Ivanov: *Fiz. Tekh. Poluprovodn. (Semiconductors* **28**, 209 (1994))
22. N. Achtziger, C. Hülsen, W. Witthuhn, M.K. Linnarson, M. Janson, and B.G. Svensson: *Phys. Status Solidi B* **210**, 395 (1998)
23. T.E. Tiwald, J.A. Woollam, S. Zollner, J. Christiansen, R.B. Gregory, T. Wetheroth, S.R. Wilson, and A.R. Powell: *Phys. Rev. B* **60**, 11464 (1999)
24. L.L. Clemen, W.J. Choyke, A.A. Burk, Jr., D.J. Larkin and J.A. Powell: *Silicon Carbide and Related Materials*, Proc. 5th Intl. Conf., Institute of Physics Conf. Series, No. 137 (Bristol, United Kingdom: IOP Publishing, 1993), p. 227
25. M.O. Aboelfotoh and J.P. Doyle: *Phys. Rev. B* **59**, 10823 (1999)
26. S.K. Estreicher: *Mater. Sci. Forum* **148–149**, 349 (1994)
27. C.H. Chu and S.K. Estreicher: *Phys. Rev. B* **42**, 9486 (1990)
28. M.A. Roberson, and S.K. Estreicher: *Phys. Rev. B* **44**, 10578 (1991)
29. G. Makov and M.C. Payne: *Phys. Rev. B* **51**, 4014 (1995)
30. P. Deák, U. Gerstmann, R. Rurali, and B. Aradi: to be published
31. H.J. Monkhorst and J.K. Pack: *Phys. Rev. B* **13**, 5188 (1976)
32. P. Hohenberg and W. Kohn: *Phys. Rev.* **136**, 864B
33. W. Kohn and L.J. Sham: *Phys. Rev.* **140**, A1133 (1965)
34. J.P. Perdew and A. Zunger: *Phys. Rev. B* **23**, 5048 (1981)
35. G.A. Baraff and M. Schlüter: *Phys. Rev. B* **30**, 1853 (1984)
36. M. Städele, M. Moukara, J.A. Majewski, P. Vogl, and A. Görling: *Phys. Rev. B* **59**, 10031 (1999)
37. R. Dovesi, R. Orlando, C. Roetti, C. Pisani, and V.R. Saunders: in *Computer Simulation of Materials at Atomic Level*, Vol. 217 of *Phys. Stat. Sol. (b)*, ed. by P. Deák, Th. Frauenheim, and M.R. Pederson (VILEY-VCH, Berlin, 2000), p. 63
38. N. Troullier and J.L. Martins: *Phys. Rev. B* **43**, 1993 (1991)
39. M. Bockstedte, A. Kley, J. Neugebauer, and M. Scheffler: *Comput. Phys. Commun.* **107**, 187 (1997)
40. R. Jones: *Philos. Trans. R. Soc. London, Ser. A* **341**, 351 (1992)
41. G.B. Bachelet, D.R. Hamann, and M. Schlüter: *Phys. Rev. B* **26**, 4199 (1982)
42. V.R. Saunders, R. Dovesi, C. Roetti, M. Caus, N.M. Harrison, R. Orlando, and C.M. Zicovich-Wilson: *CRYSTAL'98 User's Manual* (University of Torino, Torino 1998)
43. P. Durrand and J.C. Barthelat: *Theor. Chim. Acta* **38**, 283 (1975)
44. B. Aradi, A. Gali, P. Deák, J.E. Lowther, N.T. Son, E. Jánzén, and W.J. Choyke: *Phys. Rev. B* **63**, 245202 (2001)
45. P. Deák, A. Gali, and B. Aradi: in *European Conference on SiC and Related Materials 2000*, ed. by G. Pensl, D. Stephani, and M. Hundhausen, *Mater. Sci. Forum* **353–356** (Trans. Tech. Publ., Switzerland, 2001) p. 421.
46. A. Gali, B. Aradi, P. Deák, W.J. Choyke, and N.T. Son: *Phys. Rev. Lett.* **84** 4929 (2000)
47. J.E. Northrup, R.D. Felice, and J. Neugebauer: *Phys. Rev. B* **56**, R4325 (1997)
48. M. Kaukonen, C.J. Fall, P.R. Briddon, R. Jones: unpublished
49. B. Aradi, A. Gali, P. Deák: to be published
50. B. Aradi, A. Gali, P. Deák, N.T. Son, and E. Jánzén: *Physica B* **308–310**, 722 (2001)

51. P. Deák, B. Aradi, A. Gali, and U. Gerstmann: Phys. Stat. Sol. (b) **235**, 139 (2003)
52. B. Aradi, P. Deák, N.T. Son, E. Janzén, W.J. Choyke, and R.P. Devaty: Appl. Phys. Lett. **79**, 2746 (2001)
53. P. Deák, B. Aradi, and A. Gali: J. Phys. Condens. Matter **13**, 11607 (2001)
54. B. Aradi, A. Gali, P. Deák, N.T. Son, and E. Janzén: in *International Conference on Silicon Carbide and Related Materials*, ed. by S. Yoshida, S. Nishino, H. Harima, and T. Kimoto, Mater. Sci. Forum **389–393** (Trans. Tech. Publ., Switzerland, 2002), p. 561
55. S.G. Sridhara, L.L. Clemen, R.P. Devaty, W.J. Choyke, D.J. Larkin, H.S. Kong, T. Troffer, and G. Pensl: J. Appl. Phys. **83**, 7909 (1998)
56. M. Gong, C. V. Reddy, C.D. Beling, S. Fung, G. Brauer, H. Wirth, and W. Skrupa: Appl. Phys. Lett. **72**, 2739 (1998)
57. B. Aradi, A. Gali, P. Deák, E. Rauls, Th. Frauenheim, and N.T. Son: *ibid.* [45], p. 455
58. H. Itoh, T. Troffer, C. Peppermüller, and G. Pensl: Appl. Phys. Lett. **73**, 1427 (1998)
59. A. Gali, B. Aradi, D. Heringer, W.J. Choyke, R.P. Devaty, and S. Bai: Appl. Phys. Lett. **80**, 237 (2002)
60. T.T. Petrenko, T.L. Petrenko, V.Y. Bratus and J.L. Monge: Physica B **308–310**, 637 (2001)
61. A. Henry, B. Magnusson, M.K. Linnarsson, A. Ellison, M. Syväjärvi, R. Yakimova, and E. Janzén: *ibid.* [45], p. 373
62. M.K. Linnarson, U. Forsberg, M.S. Janson, E. Janzén, and B.G. Svensson: *ibid.* [54], p. 565
63. M.S. Janson, M.K. Linnarson, A. Hallén, B.G. Svensson, N. Nordell, and S. Karlsson: Phys. Rev. B **61**, 7195 (2000)
64. M.E. Samiji, A. Venter, M.C. Wagener, and A.W.R. Leitch: J. Phys. Condens. Matter **13**, 9011 (2001)
65. M.K. Linnarson, A.L. Spetz, M.S. Janson, L.G. Ekdahl, S. Karlsson, A. Schöner, I. Lundström, and B.G. Svensson: in *International Conference on SiC and Related Materials*, ed. by J.C.H. Carter, R.P. Devaty, and G.S. Roher, Mater. Sci. Forum **338–342** (Trans. Tech. Publ., Switzerland, 2000), p. 937
66. C. Hülsen, N. Achtziger, U. Resilöhner, and W. Witthuhn: in *International Conference on Silicon Carbide and Related Materials*, ed. by C.H. Carter, R.P. Devaty, and G.S. Roher, Mater. Sci. Forum **338–342** (Trans. Tech. Publ., Switzerland, 2000), p. 929
67. M.S. Janson, A. Hallén, M.K. Linnarson, N. Nordell, S. Karlsson, and B.G. Svensson: *ibid.* [45], p. 353
68. M.S. Janson, A. Hallén, M.K. Linnarson, and B.G. Svensson: Phys. Rev. B **64**, 195202 (2001)
69. C. Hülsen, N. Achtziger, J. Herold, and W. Witthuhn: *ibid.* [45], p. 331
70. Y. Koshka and M. Mazzola: *ibid.* [54], p. 609
71. Y. Koshka and M.S. Mazzola: Appl. Phys. Lett. **79**, 752 (2001)
72. Y. Koshka and M.S. Mazzola: in *European Conference on Silicon Carbide and Related Materials 2002*, Mater. Sci. Forum in print
73. K. Rottner and R. Helbig: Appl. Phys. A **59**, 427 (1994)
74. C. Peppermüller, R. Helbig, K. Rottner, and A. Schöner: Appl. Phys. Lett. **70**, 1014 (1997)

75. W.J. Choyke, R.P. Devaty, S. Bai, A. Gali, P. Deák, and G. Pensl: *ibid.* [54], p. 585
76. P.J. Macfarlane and M.E. Zvanut: *J. Appl. Phys.* **88**, 4122 (2000)
77. H. Itoh, A. Kawasuso, T. Oshima, M. Yoshikawa, I. Nashiyama, S. Tanigawa, S. Misawa, H. Okumura, and S. Yoshida: *Phys. Stat. Sol. (a)* **162**, 173 (1997)
78. A. Gali, P. Deák, N.T. Son, and E. Janzén: in *European Conference on Silicon Carbide and Related Materials 2002*, Mater. Sci. Forum, in print
79. M. Bockstedte, M. Heid, A. Mattausch, and O. Pankratov: *ibid.* [54], p. 471
80. M. Bockstedte, M. Heid, A. Mattausch, and O. Pankratov: *ibid.* [78]
81. T. Petrenko, T. Petrenko, and V. Bratus': to be published
82. A. Kawasyuso, H. Itoh, and S. Okada: *J. Appl. Phys.* **80**, 5639 (1996)
83. N.T. Son, P.N. Hai, and E. Janzén: *Phys. Rev. B* **63**, 201201 (2001)
84. N.T. Son, W.M. Chen, J.L. Lindström, B. Monemar, and E. Janzén: *Mater. Sci. Eng. B* **61–62**, 202 (1999)

# Electronic Properties of Stacking Faults and Thin Cubic Inclusions in SiC Polytypes

U. Lindefelt and H. Iwata

## 1 Introduction

The ability of SiC to crystallize in many different polytypes still remains a mystery. The distance over which an often complicated stacking order repeats ranges from around 10 Å in 4H-SiC to several hundred Å in the largest polytypes. The mechanism behind such a long-range correlation is difficult to imagine, and intuitively deviations from perfect stacking order, i.e., the occurrence of stacking faults (SF), should be quite common.

SFs can appear not only during crystal growth at high temperatures, but also in the crystalline material at lower temperatures. In this case, partial dislocations are set into motion to relieve stress, leaving a faulted area (SF ribbon) between the leading and trailing partials. The width of this SF ribbon depends on the SF energy, i.e., the energy per unit area required to create a SF, with small SF energies leading to wide SF ribbons. In SiC, one often observes quite broad SF ribbons, which is thus consistent with the observed small SF energies.

At temperatures as low as room temperature, a very large resolved stress, of the order GPa and more, is usually required to cause partial dislocation motion in SiC. In other words, stress alone is generally too low to cause SF expansion in SiC at room temperature, and if SFs are to expand at such temperatures some other mechanism is required.

It was recently discovered [1] that *pin* diodes manufactured from 4H-SiC gradually degraded in the sense that the voltage drop across the diode, for a constant current, gradually increased with the time of operation. The increase in voltage drop, compared to its ideal value (around 3.4 V at a current density of 100 A/cm<sup>2</sup>) was typically in the range from several mV to several tenths of a volt, even up to more than 1 V in some cases. It was also realized [1, 2] that this electrical degradation was associated with the expansion of SFs across the active regions of the device, despite the low temperatures. Although the physical mechanisms for SF expansion at low temperatures have not been investigated in detail in connection with diode degradation, the most likely cause is electron-hole recombination enhanced dislocation motion [3]–[5].

Thus, SFs may appear in many different situations. The work described in this chapter started in order to bridge a logical gap: even if SFs *appear* in connection with diode degradation, do they really *cause* degradation? If

not, getting rid of SFs need not solve the problem. If they do cause degradation, how does it work? This chapter is a review of the work leading to a rather complete understanding of the basic physics involved in SF-induced diode degradation. It is based on several articles [6]–[12] whose aim was not only to understand the degradation problem, but later also to increase our understanding of SFs and cubic inclusions in SiC polytypes in general.

## 2 Structural Models

### 2.1 The Stacking Patterns Around Stacking Faults in the Most Common SiC Polytypes, and Their Specification

In this chapter we will consider SFs that are introduced by partial dislocation glide in the basal (0001) plane, which is orthogonal to the hexagonal  $c$ -axis. In 3C-SiC, this plane corresponds to the (111)-plane. If  $a$  denotes the lattice constant in the basal plane, a complete dislocation with Burgers vector  $(a/3)\langle 2\bar{1}\bar{1}0 \rangle$  can dissociate into two partial dislocations:

$$(a/3)\langle 2\bar{1}\bar{1}0 \rangle \rightarrow (a/3)\langle 1\bar{1}00 \rangle + (a/3)\langle 10\bar{1}0 \rangle . \quad (1)$$

Each partial corresponds to a slip of the upper part of the crystal relative to the lower part by a non-primitive translation vector. After the passage of the leading partial, a SF has been created between the two partials (the SF ribbon).

As will be seen below, there generally exist many different types of intrinsic SFs in each polytype. To facilitate the discussion of SFs we need a notation system that uniquely specifies each one of them, and which at the same time can help visualize and interpret the local stacking order. No such system seems to exist. Therefore, this section is largely devoted to the introduction and description of a convenient system of notation. We will also analyse the number of different intrinsic SFs possible in each polytype.

When discussing stacking orders in SiC polytypes it has become customary to use the classical ABC-notation. In connection with SFs and polytype inclusions we find it much more convenient to use the Hägg notation and the related Zhdanov notation. It may even be that the inconvenient notation system used so far has contributed to the confusion and erroneous statements regarding the number of inequivalent SFs that are possible in different polytypes. In the Hägg notation, the stacking orders AB, BC and CA are all denoted  $+$  (to the ‘right’, cf. Fig. 1), and the reverse stacking orders BA, AC, CB are all denoted  $-$  (to the ‘left’). The crystal structures for 3C-, 2H-, 4H-, 6H-, and 15R-SiC are then represented by a repetition of  $(+++)$ ,  $(+-)$ ,  $(++--)$ ,  $(+++-)$ , and  $(+++-)(+++-)(+++-) = (+++-)_3$ , respectively. The Zhdanov notation is a further simplification of this notation, and consists of a sequence of integers in which the first integer denotes

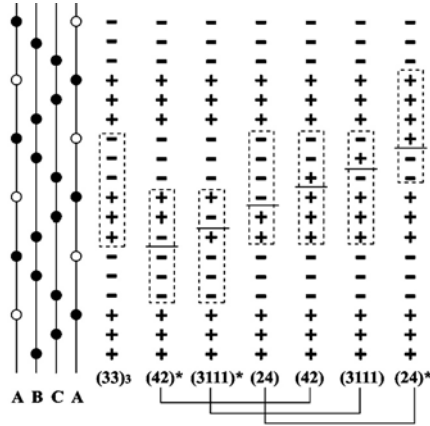


**Fig. 1.** (*left*) Stacking sequences as viewed from the  $[11\bar{2}0]$ -direction in three unit cells of perfect  $6H$ -SiC  $((33)_3)$  and different kinds of SFs expressed in the Hägg notation (and arranged in columns). The *rectangles* show different choices of unit cells, and below each column the stacking sequence within each unit cell is expressed in the Zhdanov notation. SFs which are equivalent by symmetry are indicated by *connecting lines* at the *bottom*. The *horizontal solid lines* inside each unit cell indicate the location of the SF plane. To the *left* is the Hägg sequence for perfect  $6H$ -SiC translated into the conventional ABC-notation (*solid circles*). *Open circles* indicate the positions of bi-layers coming from neighbouring cells

the number of consecutive plus signs, the second the number of consecutive minus signs, the third the number of consecutive plus signs again, etc. Thus, the five polytypes can be denoted (3), (11), (22), (33), and  $(32)_3$ . As a further extension of this notation, we will write for instance  $(33)^*$  to denote a sequence  $(---++)$  starting with a *minus* sign. Note that a starred sequence corresponds to rotating the crystal  $180^\circ$  around the hexagonal  $c$ -axis, i.e., watching the crystal from ‘the other side’. Furthermore, we shall use the term *hexagonal turn* to denote a change of sign in the Hägg sequence.

In Fig. 1 we analyse the different SFs that can appear in  $6H$ -SiC using this notation. The important point to note is that a moving partial dislocation changes a plus (minus) sign immediately above the glide plane into a minus (plus) sign, leaving *all* the other signs in the Hägg sequence unaltered. We start by letting a partial pass at a hexagonal turn  $\dots(+++---)|(+++---)\dots$  in perfect (33), where  $|$  denotes the slip plane, resulting in  $\dots(+++---)|(-++---)\dots$ . In the faulted unit cell this is denoted  $(123)^*$ , or, to be more specific,  $\dots(33)(123)^*(33)\dots$ . By choosing another and perfectly equivalent unit cell (see Fig. 1), we can regard this as  $\dots(33)^*(42)^*(33)^*\dots$  since infinite sequences of (33) and  $(33)^*$  both represent  $6H$ -SiC. We can thus, instead of  $SF(123)^*$ , use the notation  $SF(42)^*$  to identify this SF, keeping in mind that  $(42)^*$  refers to the starred environment  $(33)^*$  in the sense just indicated. There are five more possible

glide planes within a unit cell of  $6H$ -SiC. With the choice of unit cells indicated in Fig. 1, we thus get at most six different SFs in  $6H$ -SiC, which we can denote  $SF(42)^*$ ,  $SF(3111)^*$ ,  $SF(24)$ ,  $SF(42)$ ,  $SF(3111)$ , and  $SF(24)^*$  with the convention that a starred SF refers to a starred environment, e.g.,  $SF(3111)^*$  corresponds to  $\dots(33)^*(3111)^*(33)^*\dots$ .

We will now see that the symmetry of the crystal reduces the number of nonequivalent SFs in  $6H$ -SiC to three. Take, for instance, the stacking sequence for  $SF(42)^*$ . Making a  $180^\circ$  rotation around the hexagonal  $c$ -axis corresponds to interchanging plus- and minus signs. Apart from a translation by  $c/2$ , which is of no consequence in an infinite crystal, the resulting stacking sequence is the same as that for  $SF(42)$ . Thus,  $SF(42)^*$  is just  $SF(42)$  seen by an observer on ‘the other side’ of the crystal. Since the two observers are watching the same piece of material, we conclude that  $SF(42)^*$  and  $SF(42)$  are equivalent. The same argument applies to  $SF(3111)^*$  compared to  $SF(3111)$ , and to  $SF(24)^*$  compared to  $SF(24)$ . Thus, there can at most be three different inequivalent types of SFs in  $6H$ -SiC:  $SF(42)$ ,  $SF(24)$  and  $SF(3111)$ . Furthermore, there are no symmetry operations in the space group ( $C_{6v}^4$ ) of  $6H$ -SiC which transform one of these SFs into another. We then conclude that there are exactly three types of inequivalent SFs in  $6H$ -SiC. Using the same kind of arguments we find two different types of SFs in  $4H$ -SiC, which we denote  $SF(31)$  and  $SF(13)$ , and, of course, only one type of SF in  $3C$ -SiC, denoted  $SF(111)$ .

Note that the sum of the integers in the parenthesis specifying a SF in each case equals the integer in the Ramsdell notation specifying the polytype of the host material containing the SF, so there is no need to specify the host polytype explicitly. Furthermore, we note that the number of different SFs in each polytype coincides with the number of different energy levels associated with a given defect state. For instance, it is well known that substitutional N in SiC gives rise to one, two and three different donor levels in  $3C$ -,  $4H$ - and  $6H$ -SiC, respectively, corresponding to the different planes in which the N atom can be present.

There is one more important comment to make about the notation system used here. As specified so far, our SF notation is not unique. This is because  $SF(31)$  and  $SF(13)$ , and similarly  $SF(42)$  and  $SF(24)$ , are related through an interchange of Si and C atoms. For instance, interchanging Si and C atoms in  $SF(31)$  transforms it into  $SF(13)$ . To make the notation unique we have to specify the relative positions of the Si and C atoms. We use the convention that each bi-layer consists of a C atom on *top* of a Si atom, i.e., a vector from a Si atom to its partner C atom in each bi-layer is in the *positive*  $c$ -direction.

Figure 2 shows a unit cell and the different SFs in  $15R$ -SiC. This polytype is represented by an infinite sequence of  $(32)_3$ , or by  $(23)^*_3$ . Clearly there can be no basic difference between SFs in different subcells  $(32)$  (which are actually rhombohedral unit cells), so there are no more than five different types of SFs in  $15R$ -SiC. Above or below each stacking sequence in Fig. 2 we show the full Zhdanov sequence within a (hexagonal) unit cell. To simplify this

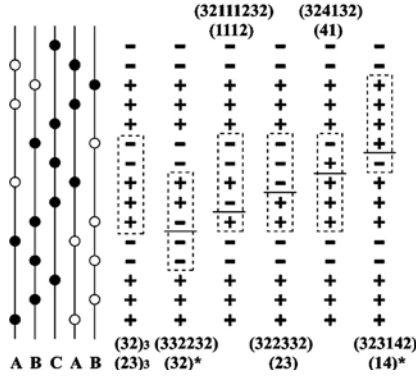


**Fig. 2.** (*right*) Stacking sequences as viewed from the  $[11\bar{2}0]$ -direction in one hexagonal unit cell of perfect  $15R$ -SiC  $((32)_3)$  and different kinds of SFs expressed in the Hägg notation (and arranged in columns). The *rectangles* show different choices of subcells (rhombohedral unit cells). *Above* or *below* each column, the stacking sequence is expressed in the Zhdanov notation, both inside a hexagonal unit cell and inside a subcell. The *horizontal solid lines* inside each cell indicate the location of the SF plane. To the *left* is the Hägg sequence for perfect  $15R$ -SiC translated into the conventional ABC-notation (*solid circles*). *Open circles* indicate the positions of bi-layers coming from neighbouring cells

notation we can specify the stacking sequences only inside the rhombohedral unit cells indicated in the figure. In this simplification, SFs marked with a star, like SF(32)\*, are to be thought of as representing  $\dots(23)^*(32)^*(23)^*\dots$ , i.e., in a starred environment, while SFs with no star, like SF(41), represents  $\dots(32)(41)(32)\dots$ , i.e., in an unstarred environment. Note that in the starred environment, the Zhdanov integers change places compared to the unstarred counterpart, or, more generally in larger polytypes, are obtained after one cyclic permutation. With this convention we can specify the SFs as SF(41), SF(14)\*, SF(23), SF(32)\* and SF(1112). Of these SF(41) and SF(14)\* are expected to have similar properties since both contain a 4-step leg between hexagonal turns. Similarly for SF(23) and SF(32)\*, which both contain neighbouring pairs of 2- and 3-step legs, while SF(1112) locally shows a more  $2H$ -like (zig-zag) stacking sequence. Since, unlike the hexagonal polytypes,  $15R$ -SiC does not have a  $180^\circ$  symmetry rotation around the  $c$ -axis (hexagonal or triclinic), SFs like SF(23) and SF(32)\* are not related by spatial symmetry. They do, however, transform into one another under an interchange of Si and C atoms, as do also SF(41) and SF(14)\*, so again we use the same convention as earlier regarding the relative positions of the Si and C atoms to make the notation unique. Note also that if  $15R$ -SiC is regarded as  $(23)_3$  instead of  $(32)_3$  as assumed here, the starred SFs become unstarred and vice versa.

The layer sequences for the various SFs in  $3C$ -,  $4H$ -, and  $6H$ -SiC are illustrated later in connection with the SF wave functions (see Figs. 8–13).

## 2.2 The Geometrical Structure of Cubic Polytype Inclusions in 4H- and 6H-SiC

Stacking faults in neighbouring (0001) planes can give rise to 3C-like cubic inclusions, i.e., layers having a straight 3C-like stacking sequence. This is illustrated for 4H-SiC in Fig. 3. Starting from 1SF(31) and aiming in each step to maximize the length of the 3C-like (straight) stacking sequence, one can obtain the inclusions 2SF(62), 3SF(71) and 4SF(10,2), where the integer in front of ‘SF’ denotes the number of SFs used to produce the inclusion. Note the relatively large increase in the length of the 3C-like (cubic) sequence when going from an odd to an even number of SFs. In 6H-SiC, the corresponding cubic inclusions are 1SF(42), 2SF(51), 3SF(93), and 4SF(10,2). In this case the relatively large increase in the width of the inclusion is in every third step.

In Fig. 3 we chose to insert additional SFs only along the positive  $c$ -direction (‘up’). There are, of course, other choices that can be made and which can take place in nature. For a more systematic study of these possibilities, see [10]. The 3C-like inclusions corresponding to those in Fig. 3 are illustrated more clearly in Fig. 4.

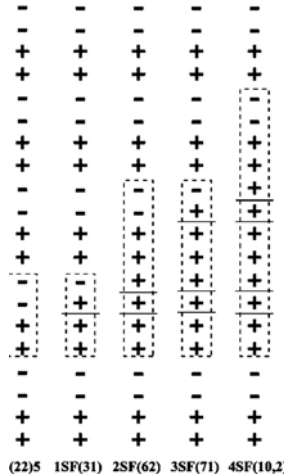


**Fig. 3.** (*left*) Stacking sequences as viewed from the  $[11\bar{2}0]$ -direction in five unit cells of perfect 4H-SiC  $((22)_5)$  and different kinds of cubic inclusions expressed in the Hägg notation (and arranged in columns). Below each column the stacking sequence within the cell indicated by a *rectangle* is expressed in the Zhdanov notation. *Horizontal solid lines* indicate the locations of SFs

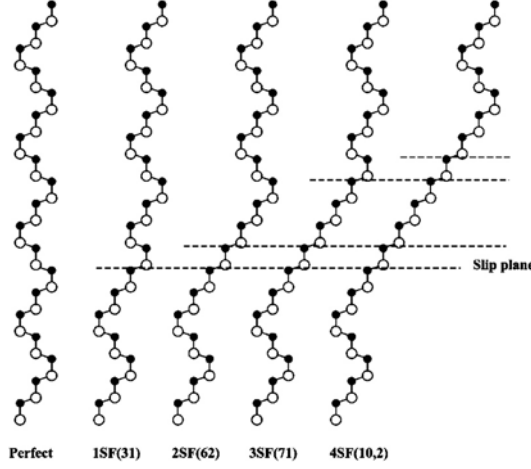


**Fig. 4.** (*right*) Atomic models of stacking sequences as viewed from the  $[11\bar{2}0]$ -direction for some cubic inclusions in  $4H$ -SiC. The *horizontal lines* denote different slip planes, and *solid (open) circles* represent C (Si) atoms

### 3 Isolated SFs in $3C$ -, $4H$ -, $6H$ - and $15R$ -SiC

The computational method we have used is a state-of-the-art local density method, applied to a supercell geometry with typically 96 or 120 atoms per supercell depending on the polytype and property being investigated. For more details about the method we refer to [12] and references therein.

#### 3.1 Tools for Characterization and Analysis of Wave Functions

The basic output from the calculations are total energies, band structure energies and wave functions. To simplify the inspection of the wave functions, we will not plot the wave functions themselves, but rather the projected probability distribution

$$f_{\alpha}(z) = \int \int |\Psi_{\alpha}(x, y, z)|^2 dx dy , \quad (2)$$

where  $\Psi_{\alpha}$  is the wave function for a state  $\alpha$  which corresponds to a certain band with index  $n$  and wave vector  $\mathbf{k}$  in the Brillouin zone. For each value of  $z$  along the crystal  $c$ -direction, the integration is performed in a basal plane within the supercell. The projected probability distribution  $f_{\alpha}(z)$  is simply the probability to find an electron occupying the given state  $\alpha$  at a certain distance  $z$  away from the SF plane.

As a simple measure of the degree of wave function localization in the direction perpendicular to the SF plane we use the localization parameter  $w_\alpha$ , defined as the distance within which the truncated normalization integral

$$I_\alpha(z) = \int^z f_\alpha(z') dz' \quad (3)$$

increases from 10% to 90%. In (3) the integration starts at the bottom of the supercell.

### 3.2 Band Structures

We will start by considering SFs in  $4H$ -SiC. In Figs. 5a–c are shown the 96-atom supercell Kohn-Sham band structures along the closed path  $\Gamma$ -M-K- $\Gamma$  in the Brillouin zone for the perfect crystal and for crystals containing SF(31) and SF(13). The most striking feature in the fundamental band gap region is the appearance of a split-off band about 0.22 eV (0.18 eV) below the bottom of conduction band at M for SF(31) (SF(13)). On the other hand, the top of the valence band shows no similar features. We also note similar split-off bands in local band gaps in the Brillouin zone. Similar results were obtained by Miao et al. [13] for one of the SFs in  $4H$ -SiC.

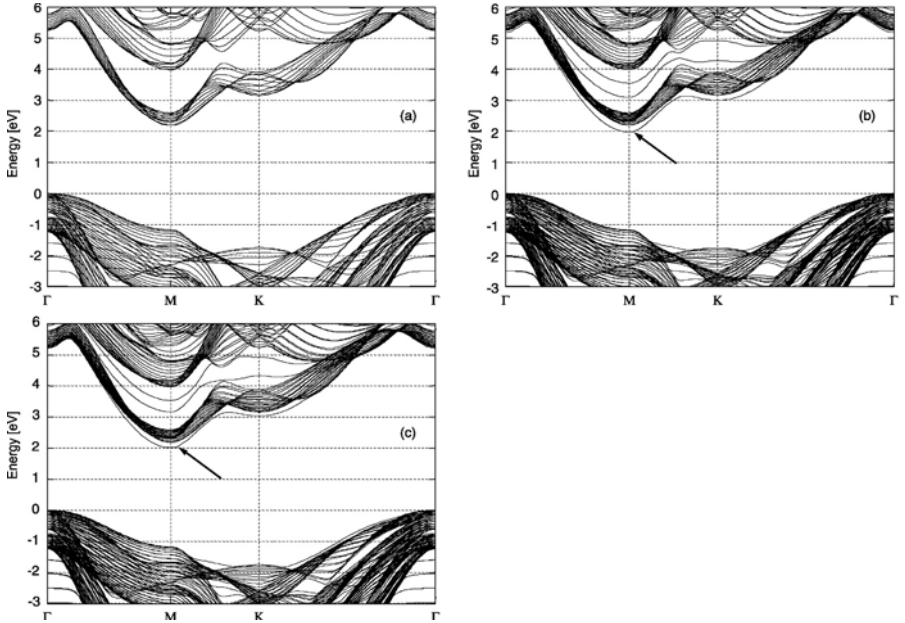


**Fig. 5.** Kohn-Sham band structure for 96 atom supercells for (a) perfect  $4H$ -SiC, (b) with SF(31) and (c) with SF(13). The arrows point at the split-off bands below the conduction band caused by the SF

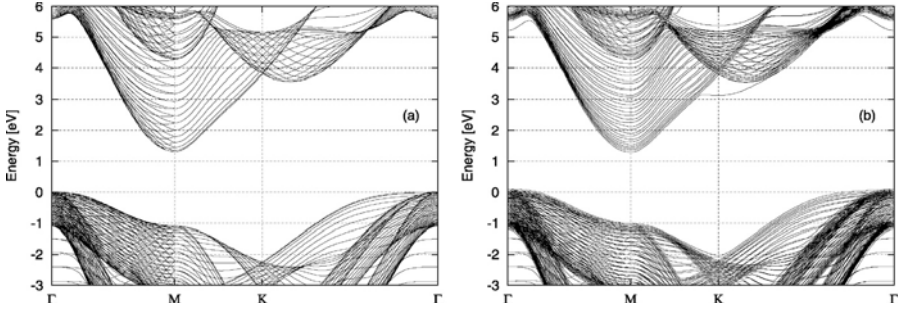


**Fig. 6.** Kohn-Sham band structure for 96 atom supercells for (a) perfect 3C-SiC and (b) with SF(111)

In contrast to the situation for 4H-SiC, no clearly split-off bands in the vicinity of the fundamental band gap for SF(111) in 3C-SiC can be seen (Fig. 6). However, around the K-point, which is the point where 2H-SiC has its conduction band minimum, there are clear signs of band split-off. This is probably related to the fact that SF(111) introduces two hexagonal turns in neighbouring planes, i.e., SF(111) introduces locally a 2H-like zig-zag pattern in the stacking sequence.

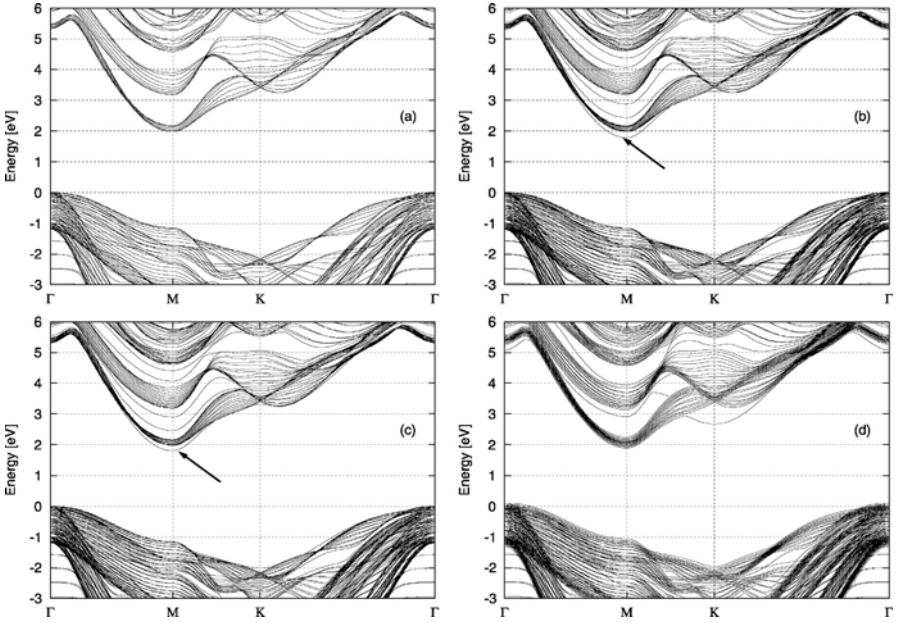


**Fig. 7.** Kohn-Sham band structure for 96 atom supercells for (a) perfect 6H-SiC, (b) with SF(42), (c) with SF(24), and (d) with SF(3111). The arrows point at the split-off band caused by the SF

In  $6H$ -SiC (Fig. 7) the situation seems to be a mixture of that for  $4H$ - and for  $3C$ -SiC. SF(42) and SF(24) both give rise to clearly split-off states in the fundamental band gap at M, 0.19 eV and 0.17 eV below the conduction band minimum, respectively, whereas for SF(3111) there are no clearly split-off bands in the vicinity of the fundamental band gap. Just like SF(111), however, SF(3111) causes a band split-off at the bottom of the conduction band around K. This is again consistent with the  $2H$ -like zig-zag pattern associated with SF(3111). No clear split-off occurs around the valence band maximum.

The band structures for the five different SFs in  $15R$ -SiC are qualitatively very-similar to those already shown for the other polytypes, and will therefore only be summarized here. There are clearly split-off bands 0.16 eV and 0.11 eV below the conduction band minimum at M for SF(41) and SF(14)\*, respectively, but not for the other SFs. As expected, SF(1112) causes a clear split-off at the lowest conduction band at K, but not at M. Finally, for SF(23) and SF(32)\*, no clearly split-off states in the band gap appear.

The energies of the split-off states below the conduction band minimum at M for all the polytypes are summarized in Table 1, together with other information and characteristic features that will be discussed below.

**Table 1.** Electronic structure data for different SFs in four different polytypes.  $E_B$  is the energy of the split-off band minimum below the conduction band minimum, with  $\sim 0$  indicating cases where no clearly split-off states are seen.  $w_B$ ,  $w_C$ , and  $w_V$  are the localization parameters for the minimum of the split-off band, for the weakly localized near-band-edge state just below the bottom of the extended state at the conduction band minimum, and for the weakly localized near-band-edge state just above the top of the extended state at the valence band maximum, respectively.  $E_{QW}$  and  $w_{QW}$  are the energy and wave function localization parameters obtained using the simple QW model as described in the main text

Polytype	Type of SF	$E_B$ [eV]	$w_B$ [ $\text{\AA}$ ]	$w_C/w_V$ [ $\text{\AA}$ ]	$E_{QW}$ [eV]	$w_{QW}$ [ $\text{\AA}$ ]
$3C$	SF(111)	$\sim 0$		30/18		
$4H$	SF(31)	-0.22	7.2	-/-	-0.24	6.1
	SF(13)	-0.18	8.6	-/28	-0.24	6.1
$6H$	SF(42)	-0.19	8.0	-/-	-0.22	6.5
	SF(3111)	$\sim 0$		15/15		
	SF(24)	-0.17	9.5	-/28	-0.22	6.5
$15R$	SF(32)*	$\sim 0$		-/-		
	SF(1112)	$\sim 0$		23/18		
	SF(23)	$\sim 0$		-/35		
	SF(41)	-0.16	8.3	-/-	-0.22	6.5
	SF(14)*	-0.11	9.8	-/28	-0.22	6.5

From these results the following rules seem to emerge: (1) Clearly split-off band states below the overall bottom of the conduction band (at M) are created if and only if the length of the longest cubic ‘leg’ in the stacking sequence has increased. (2) No clear split-off takes place at the top of the valence band in any case. (3) Clear conduction band split-off at K occurs if the number of hexagonal turns in the local stacking sequence has increased.

### 3.3 Strong and Weak Wave Function Localization

In order to reveal more about the electronic structure of the SFs, we shall now study the wave functions for various states. Again we will start with 4H-SiC and show in Fig. 8  $f_\alpha(z)$  for the bottom of the conduction band, for the split-off band below the bottom of the conduction band at M, and for the top of the valence band in the case SF(31). The wave function for the split-off band (Fig. 8b) exhibits very *strong localization* around the SF plane with localization  $w = 7.2 \text{ \AA}$ , whereas the wave functions for both the top of the valence band and the bottom of the conduction band are still

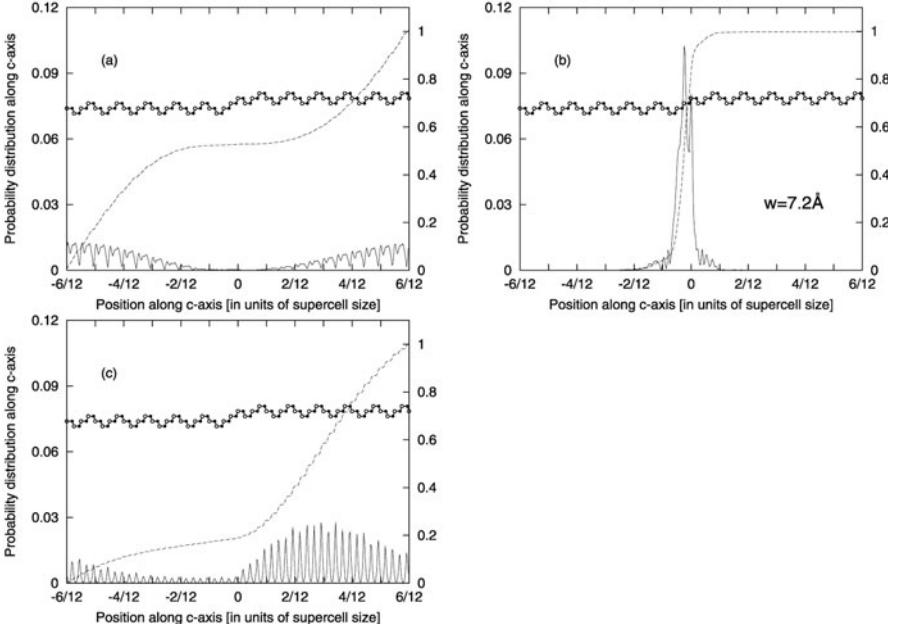


**Fig. 8.** The projected probability distribution (2) (*left-hand scale, solid line*) and the truncated normalization integral (3) (*right-hand scale, dashed line*), within a 96 atom supercell, for (a) the bottom of the conduction band, (b) the split-off band at M and (c) the top of the valence band in 4H-SiC containing SF(31). Also shown are the stacking sequence and the degree of localization ( $w$ ) for localized states

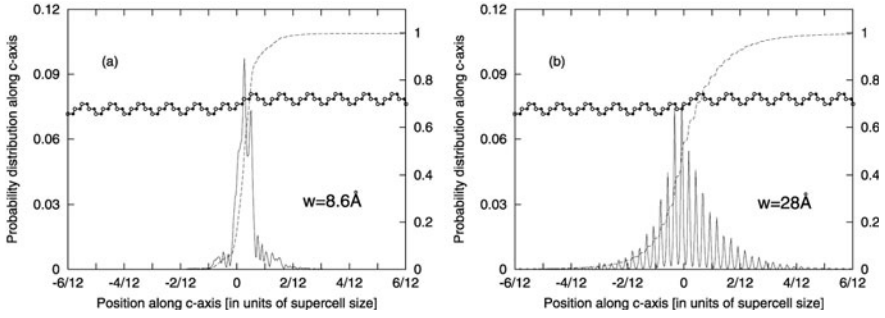


**Fig. 9.** Same as Fig. 8b,c but for SF(13)

delocalized, band-like states extending throughout the supercell along the  $c$ -direction. (This is, of course, the reason why we identify the latter states as valence band and conduction band states, respectively.) Thus, without the occurrence of broken or strongly distorted bonds, which usually result in gap states and wave function localization in connection with intrinsic defects and surfaces, *a SF in 4H-SiC also leads to a localized SF band in which the electron has a strongly enhanced probability to be in the immediate vicinity of the SF plane.* Of course, in contrast to the case of localized point defect states, this is only a one-dimensional localization, since an electron in the bound SF state is free to move along the SF plane with an effective mass corresponding to the inverse of the curvature of the split-off band in Fig. 5b (see Sect. 3.7). It is important to note that the wave function is to a large extent localized within the elongated cubic ‘leg’ associated with the SF. In the next section we will discuss this one-dimensional localization in more detail.

The projected probability distributions for SF(13) are shown in Fig. 9. For the conduction band minimum at M,  $f_\alpha(z)$  looks almost identical to that

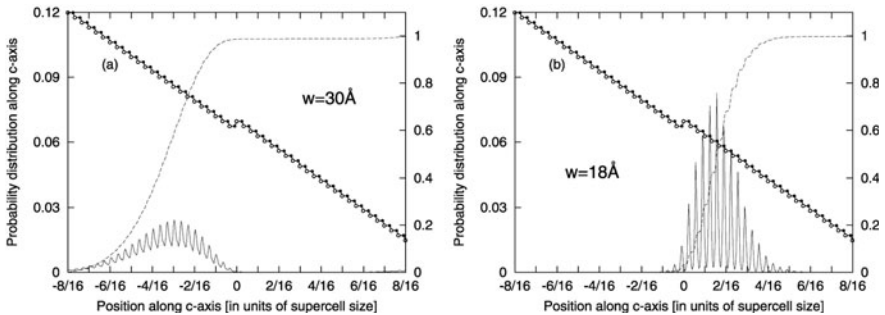


**Fig. 10.** The projected probability distribution (*left-hand scale*) and the truncated normalization integral (*right-hand scale*), within a 96 atom supercell, for (a) the bottom of the conduction band and (b) the top of the valence band in 3C-SiC with a SF

for SF(31) and is therefore not shown again. The localized SF state 0.18 eV below the conduction band minimum ( $E_C$ ) also has a projected probability distribution which is very similar to that for SF(31), whereas it looks different for the highest valence state. In fact, the probability distribution in Fig. 9b has the appearance of a localized state (in one dimension), essentially localized around the SF, but with a localization  $w \approx 28$  Å, which is much larger than for the bound SF state at ( $E_C - 0.18$ ) eV for which  $w \approx 8.6$  Å (see Table 1). Furthermore, this highest energy valence state lies very close in energy (typically a few meV) to other (extended) valence band states, with no clear signs of split-off. We refer to the type of localization seen in this state as *weak localization*.

In 3C-SiC the projected probability distributions for the lowest conduction state and highest valence state for SF(111) are shown in Fig. 10. Even though they are very close in energy to the delocalized band states in their respective bands, they are surprisingly localized, in particular the valence state with localization  $w \approx 18$  Å. We also observe that they have most of their wave functions in the 3C host region outside the thin 2H-like stacking sequence, and, which is perhaps more mysterious, with amplitudes almost exclusively

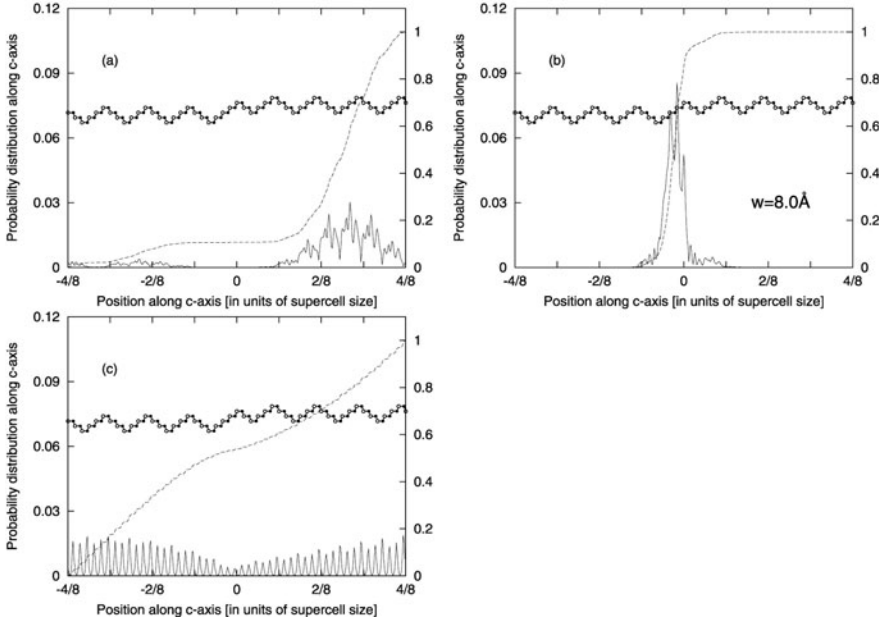


**Fig. 11.** The projected probability distribution (*left-hand scale*) and the truncated normalization integral (*right-hand scale*), within a 96 atom supercell, for (a) the bottom of the conduction band, (b) the split-off band at M and (c) the top of the valence band in 6H-SiC containing SF(42)

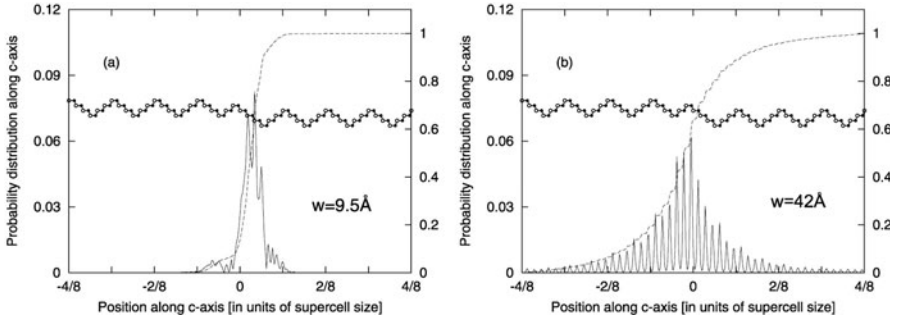


**Fig. 12.** Same as Fig. 11b,c but for SF(24)

on *different sides* of the SF. We refer to the latter feature as (conduction and valence band) *wave function segregation*.

For the three different SFs SF(42), SF(24) and SF(3111) in 6H-SiC,  $f_\alpha(z)$  for the bottom of the conduction band, for the split-off band at M below the bottom of the conduction band, and for the uppermost valence state are shown in Figs. 11–13. Similar to SF(31) and SF(13) in 4H-SiC, the projected probability distributions for the states at the bottom of the conduction band at M in 6H-SiC look almost the same for the cases SF(42) and SF(24). Like for the band structures, the wave functions for the SFs in 6H-SiC show characteristics which are a mixture of those in 4H- and 3C-SiC. We find band states with strong localization for SF(42) and SF(24) (like for SF(31) and SF(13)), with weak localization at the valence band edge for SF(24) (like for SF(13)), and with wave function segregation of the conduction and valence band edges for SF(3111) (like for SF(111)). In 15R-SiC the projected probability distributions are qualitatively very similar to those already shown for

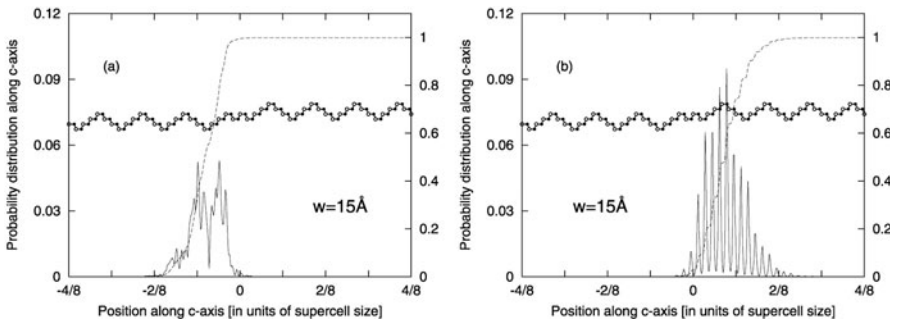


**Fig. 13.** The projected probability distribution (*left-hand scale*) and the truncated normalization integral (*right-hand scale*), within a 96 atom supercell, for (a) the bottom of the conduction band (b) the top of the valence band in 6H-SiC containing SF(3111)

the other polytypes and we will therefore only summarize the results: SF(41) is similar to SF(42) and SF(31) but with split-off band localization 8.3 Å, SF(14)\* is similar to SF(24) and SF(13) but with split-off band localization 9.8 Å, SF(1112) is similar to SF(3111) and SF(111) but with segregated conduction and valence band edge localizations 23 Å and 18 Å, respectively, SF(23) is similar to SF(24) and SF(13) at the valence band edge but with a localization 35 Å, and SF(32)\* is similar to SF(42) and SF(31) in the sense that none of these give rise to band edge localization.

All these results concerning wave function localization are also summarized in Table 1. From these results the following pattern emerges: (1) The clearly split-off states below the overall bottom of the conduction band (at M) are strongly localized (with localization less than 10 Å) and bound in the direction perpendicular to the SF plane. (2) Weak localization of bound near valence band edge states can take place. (3) Weak localization near the conduction band edge takes place only in the form of wave function segregation (of conduction and valence band edge states), and occurs if and only if the SF corresponds to an increase in the number of local hexagonal turns.

### 3.4 Strong Wave Function Localization and Quantum Confinement

The question arises what is causing the strong localization of the clearly split-off states. It is well understood that heavily deformed, broken or chemically perturbed bonds around point defects (regarded as a zero-dimensional defect) can give rise to gap states and three-dimensional localization of the wave function. Two-dimensional localization around dislocations (a one-dimensional defect) and one-dimensional localization in the vicinity of surfaces (regarded as a two-dimensional defect) can also be understood in terms of deformed or broken bonds, but requires interaction between individual atomic sites along the dislocation line or surface to account for the lower dimension of the localization. In the case of SFs, however, strongly perturbed bonds are not involved in an obvious way like for a surface, since the crystal retains its perfect structure (apart from a very small relaxation of the lattice which is irrelevant for this discussion) on either side of the SF plane.

We noted earlier that the strongly localized wave functions associated with a SF have most of their amplitude in the region where the cubic stacking sequence is elongated relative to the perfect crystal. It has been found [14, 15] that for a 3C/4H-SiC interface, for instance, the conduction band offset is around 1 eV, with the conduction band for 3C-SiC being below that for 4H-SiC, whereas the corresponding valence band offset is much smaller. Therefore, if there are elongated 3C-like regions in a faulted 4H-SiC crystal, one could argue that the conduction band electrons tend to be attracted to such a region with a locally lower conduction band. Since 3C-SiC is the polytype with the smallest band gap, and the valence band offset between

**Table 2.** Valence and conduction band offsets,  $\Delta E_V(nH/3C) = E_V(nH) - E_V(3C)$  and  $\Delta E_C(nH/3C) = E_C(nH) - E_C(3C)$ , respectively, for interfaces between three different hexagonal SiC polytypes ( $n = 2, 4$ , and  $6$ ) and  $3C$ -SiC, and between  $15R$ - and  $3C$ -SiC. The valence band offsets have been determined from the calculated value  $\Delta E_V(2H/3C) = 0.13$  eV [14, 15, 18] and assuming that they are proportional to the degree of hexagonality, as suggested in [18]. The conduction band offsets are obtained using the values  $E_G(3C) = 2.4$  eV,  $E_G(2H) = 3.3$  eV,  $E_G(4H) = 3.2$  eV, and  $E_G(6H) \approx E_G(15R) = 3.0$  eV. By taking appropriate differences, the band edge offsets between the hexagonal polytypes can be estimated, neglecting interface-dependent charge rearrangement effects

	$2H/3C$	$4H/3C$	$6H/3C$	$15R/3C$
$\Delta E_V$ (eV)	0.13	0.07	0.04	0.05
$\Delta E_C$ (eV)	1.03	0.87	0.64	0.65

$3C$ -SiC and other polytypes seems to be small,  $3C$ -like regions in *all* polytypes should give rise to locally lower conduction bands. We have therefore suggested [6, 7] that one could regard the SF as giving rise to a thin electron-attractive quantum-well (QW), and that *the one-dimensional localization can be understood as a QW confinement effect*. This can be considered as a limiting case of two or more SFs in neighbouring glide planes, leading to  $3C$ -like inclusions (to be discussed in more detail in Sect. 4), in which case an interpretation in terms of QWs is more obvious and straightforward.

We can check whether this interpretation in terms of a thin QW is realistic and possibly lend further support to it by estimating the binding energy and wave function localization using a simple one-dimensional theory for quantum square wells [12, 16]. Since the lattice constant  $c$  for  $4H$ -SiC, for instance, is close to  $10$  Å, it is reasonable to assume a QW width of  $5$  Å for both SF(31) and SF(13). Assuming a QW depth of  $0.87$  eV (i.e., the conduction band offset  $\Delta E_C(4H/3C)$  from Table 2), and the effective mass  $0.3$  (in units of the free electron mass), which is the effective mass for  $3C$ -SiC in the  $[111]$ -direction calculated from the effective mass components in [17], the QW model results in one bound state with binding energy  $0.24$  eV and wave (envelope) function localization  $w = 6.1$  Å. In the cases of SF(42) and SF(24) in  $6H$ -SiC, we have used a QW depth of  $0.64$  eV (Table 2) and a QW width of  $7.0$  Å, resulting in one bound state with energy  $0.22$  eV below the conduction band minimum, with localization  $w \approx 6.5$  Å. These results are reproduced in Table 1 for comparison with the results from the supercell calculations. The close agreement suggests that the QW interpretation is indeed realistic, and supports the idea that the one-dimensional localization can be understood as a QW confinement effect.

A similar estimate for SF(41) and SF(14)\* in  $15R$ -SiC using the estimated conduction band offset in Table 2 and a QW width  $7.0$  Å (the same as for SF(42) and SF(24)) gives a binding energy which is in less good agreement

with the supercell results (see Table 1), but we still feel that the conclusion about a QW confinement effect is basically correct. Of course, the simple square shape of the QW potential used here to interpret the numerical results is chosen only because of its analytical simplicity. It has been shown both in [15] and [18] that a  $2H/3C$  interface induces a dipole moment in the vicinity of the interface. We therefore also expect a dipole moment at a  $4H/3C$ ,  $6H/3C$  or  $15R/3C$  interface, since the dipole moment in principle originates from the hexagonal or rhombohedral symmetry. The electric field associated with such a dipole moment can change the electrostatic potential, leading to a potential shape that is different from a simple square well. But even though this model is simple and crude, both with respect to the shape, the width and the depth of the QW, we think the arguments above do indeed suggest that SF(31) and SF(13) in  $4H$ -SiC, SF(42) and SF(24) in  $6H$ -SiC, and SF(41) and SF(14)\* in  $15R$ -SiC, are each associated with a QW of some shape, and that a QW model offers a helpful and reasonable description of the SF results.

### 3.5 Cases Where the SF Acts as a Quantum Barrier

We have seen earlier that SF(111), SF(3111) and SF(1112) are similar in the sense that none of them gives rise to clearly split-off states with strong localization. A glance at the stacking sequences leads to the impression that, just like SF(31), SF(13), SF(42), SF(24), SF(41), and SF(14)\* lead to local  $3C$ -like structures, SF(111), SF(3111) and SF(1112) locally resemble  $2H$ -like regions.  $2H$ -SiC is the polytype with the largest band gap, and from Table 2 we infer that, in analogy with  $3C$ -like QWs, these thin  $2H$ -like regions should act as quantum barriers, explaining the absence of bound band states in the fundamental band gap below the conduction band. A partial justification of this interpretation is offered by the result that SF(111), SF(3111) and SF(1112) all give rise to a clearly split-off band below the bottom of the conduction band at K, which is where  $2H$ -SiC has its conduction band minimum, hence lowering the local conduction band minimum at K relative to that at M.

### 3.6 Weak Localization

Unfortunately space does not permit a discussion of the mechanisms behind the weak localization and the (conduction and valence band) wave function segregation observed among Figs. 8–13 and Table 1. This issue was discussed in [12], where it was found that the underlying cause is the pyroelectric nature of the non-cubic polytypes, i.e., the existence of electric dipole moments (spontaneous polarization) associated with the hexagonal turns and an accompanying depolarization field. Briefly, for the polytypes considered here, a SF can either displace a hexagonal turn in the positive  $c$ -direction (as in

e.g. SF(31)), in the negative  $c$ -direction (e.g. SF(13)), or add hexagonal turns (e.g. SF(3111)). This creates a local attractive potential perturbation, a local repulsive perturbation, and a perturbation which is attractive on one side of the SF and repulsive on the other, respectively. It is the effects of these perturbations which show up as weak localization and wave function segregation in the band edge wave functions. This feature also explains the different energies for the clearly split-off bands for different types of SFs in a given polytype [12].

### 3.7 In-Plane Effective Masses for the Split-Off Bands and Modified Conduction Band Edges

We have seen that the electrons occupying the clearly split-off states are bound in the [0001] direction, but still free to move in the (0001) plane, i.e., along the planar QW. To get some insight into the dynamical properties of such electrons moving along the planar QW we have calculated (Table 3) their effective mass components for the in-plane motion. For comparison, we also show the planar effective mass components for the lowest (extended) conduction band in both the perfect and faulted crystals. From Table 3 we conclude that:

1. The effective masses in the lowest (extended) conduction band are essentially unaffected by the SF.
2. The effective mass components in the MK-direction in the Brillouin zone for an electron in the strongly localized, quantum confined band states are essentially the same as in 3C-SiC.

**Table 3.** Effective mass components (in units of the free electron mass) around the M-point along the two Brillouin zone directions M- $\Gamma$  and M-K for the strongly localized split-off band (SOB) and for the extended states forming the conduction band minimum (CB). The masses for the partner SFs SF(13), SF(24) and SF(14)\* in the polytypes 4H, 6H and 15R, respectively, are the same as those shown within the numerical accuracy. For comparison, the in-plane effective mass components for perfect 3C-SiC are  $m_{M\Gamma} = 0.42$  and  $m_{MK} = 0.23$

		4H		6H		15R	
		Perfect	SF(31)	Perfect	SF(42)	Perfect	SF(41)
SOB	M- $\Gamma$		0.74		0.65		0.66
	M-K		0.22		0.22		0.23
CB	M- $\Gamma$	0.59	0.60	0.76	0.76	0.65	0.67
	M-K	0.29	0.29	0.26	0.26	0.23	0.22

3. The effective masses for SF(31) and SF(13) in  $4H$ -SiC are practically the same, and this is also true for SF(42) and SF(24) in  $6H$ -SiC, and for SF(41) and SF(14)\* in  $15R$ -SiC.
4. The effective mass components  $m_{\text{MT}}$  in the MT-direction are clearly larger for the quantum confined states than in  $3C$ -SiC.

The components  $m_{\text{MT}}$  for SF(31) and SF(13) are larger than for SF(42) and SF(24), whereas the latter are almost the same as for SF(41) and SF(14)\*. We shall see later (Sect. 4.4) that this effective mass component decreases as the thickness of the  $3C$ -like inclusion increases, and the presently stated result may thus be related to the fact that SF(31) and SF(13) have shorter cubic ‘legs’ in the stacking sequence than have SF(42), SF(24), SF(41) and SF(14)\*.

### 3.8 Stacking Fault Energies

From a practical point of view, one of the reasons for studying SFs in SiC is their small SF energies  $\gamma$ , defined as  $\gamma = (E(\text{faulted}) - E(\text{perfect}))/A$ , where  $A$  is the SF area,  $E(\text{faulted})$  is the total energy of the faulted portion of the crystal with a SF and  $E(\text{perfect})$  is the total energy of the same portion of the perfect crystal. For instance, the SF energy in  $6H$ -SiC is around 3 mJ/m<sup>2</sup> and around 15 mJ/m<sup>2</sup> in  $4H$ -SiC [19, 20], compared to 280 mJ/m<sup>2</sup> in diamond [21], 55 mJ/m<sup>2</sup> in Si, and 45 mJ/m<sup>2</sup> in GaAs (see [19] and references therein). In crystals where the SF energy is large, perfect dislocations tend not to split up into partial dislocations to any appreciable extent, since the effective pulling force acting on the trailing partial from the leading partial, given by  $\gamma/b$  where  $b$  is the length of the Burgers vector, is large. In SiC, however, where  $\gamma$  is relatively small, the area between the leading and trailing partials (i.e., the area containing a SF and showing up as a SF ribbon) can become large without requiring too much energy, and thereby influence the properties of the crystal substantially.

Direct calculations of the SF energy are computationally quite demanding. There is, however, a very elegant method for calculating SF energies, known as the ANNNI (axial next nearest neighbour Ising) model [19, 22, 23]. It requires only the total energy per primitive unit cell for a few (usually four) *unfaulted* polytypes to give the SF energy in any polytype. As with most models, however, it is very difficult to assess its accuracy. It is therefore of value to compare the predictions of the ANNNI model with those of a first-principles calculation.

In Table 4 we show the SF energies calculated with the supercell method and with the ANNNI model. The supercell calculations were performed in two different ways, one in which all atoms were held in their ideal positions (without ISR, i.e., without intra-supercell relaxation) and the other with full relaxation of all atoms in the supercell (with ISR). The ANNNI model calculations were based on the following inter-layer interaction parameters (in eV):  $J_1 = 1.9097$ ,  $J_2 = -2.3059$ ,  $J_3 = -0.3959$  [7].

**Table 4.** Theoretical and experimental SF energies  $\gamma$  (in mJ/m<sup>2</sup>) for four different SiC polytypes. ISR means ‘intra-supercell relaxation’ and is defined in the main text. Experimental values are from [19]

Polytype	Type of SF	$\gamma$ (without ISR)	$\gamma$ (with ISR)	$\gamma$ (ANNNI)	$\gamma$ (exp.)
3C-SiC	SF(111)	-1.71	-2.70	-6.27	—
4H-SiC	SF(31)	17.7	18.4	18.3	14.7 $\pm$ 2.5
	SF(13)	18.1	18.7	18.3	14.7 $\pm$ 2.5
6H-SiC	SF(42)	3.1	1.35	3.14	2.9 $\pm$ 0.6
	SF(3111)	40.1	38.4	36.6	—
	SF(24)	3.35	1.63	3.14	2.9 $\pm$ 0.6
15R-SiC	SF(32)*	0.03	—	0	—
	SF(1112)	38.7	—	38.7	—
	SF(23)	0.1	—	0	—
	SF(41)	20.8	—	21.4	—
	SF(14)*	20.7	—	21.4	—

We note the following characteristics:

1. The ANNNI model and the supercell calculations are in very good agreement for the non-cubic polytypes.
2. The effects of intra-supercell relaxation are less than 2 mJ/m<sup>2</sup>.
3. The agreement with experimental results is good in the few cases where such results are available.
4. The ANNNI model can not distinguish between SFs related through an interchange of Si and C atoms, thus giving the same SF energies for SF(31) and SF(13), SF(42) and (24), and SF(41) and SF(14)\*.
5. The SF energies for the SFs increasing the number of hexagonal turns in 6H- and 15R-SiC are clearly higher than the SF energies for the other SFs belonging to the same polytype. Thus, unless there is a preference as to in which glide plane partial dislocations are nucleated, these types of SFs should be relatively rare if created after growth.
6. The SF energy for the SF in 3C-SiC is negative, both in the supercell calculations and in the ANNNI model. The same result has been obtained by others [24].

The result in (6) may appear puzzling in view of the fact that 3C-SiC is regarded as a stable polytype [25]. One must be aware, however, that the calculation of SF energies corresponds to two points on an energy vs. configuration diagram, with no information whatsoever about possible energy barriers the system must overcome to change configuration.

## 4 Thin Cubic Inclusions in 4*H*- and 6*H*-SiC

With thin cubic inclusions in these polytypes we mean cases where one of the cubic ‘legs’ in the stacking sequence has increased by two or a few steps (bi-layers) compared to the perfect crystal. Here we will consider the cubic inclusions 2SF(62), 3SF(71) and 4SF(10,2) in 4*H*-SiC (cf. Fig. 4), and 2SF(51), 3SF(93) and 4SF(10,2) in 6*H*-SiC. The formation of thin cubic inclusions has been observed in highly doped *n*-type 4*H*-SiC epilayers [26]–[30] and will be discussed further in Sect. 5.4.

### 4.1 Band Structures

In Fig. 14 we show how the band structure along the closed path  $\Gamma$ –M–K– $\Gamma$  in the Brillouin zone changes as two, three, and four SFs in neighbouring planes are introduced, converting a part of the 4*H*-SiC crystal into a 3*C*-like region. From Fig. 14 we see that as the cubic inclusion becomes broader, the split-off band moves further down in the band gap. For the broadest cubic inclusion considered here (4SF(10,2) in Fig. 14d) a second split-off band can be clearly seen, but is actually present also in the case of 3SF(71) (Fig. 14c).

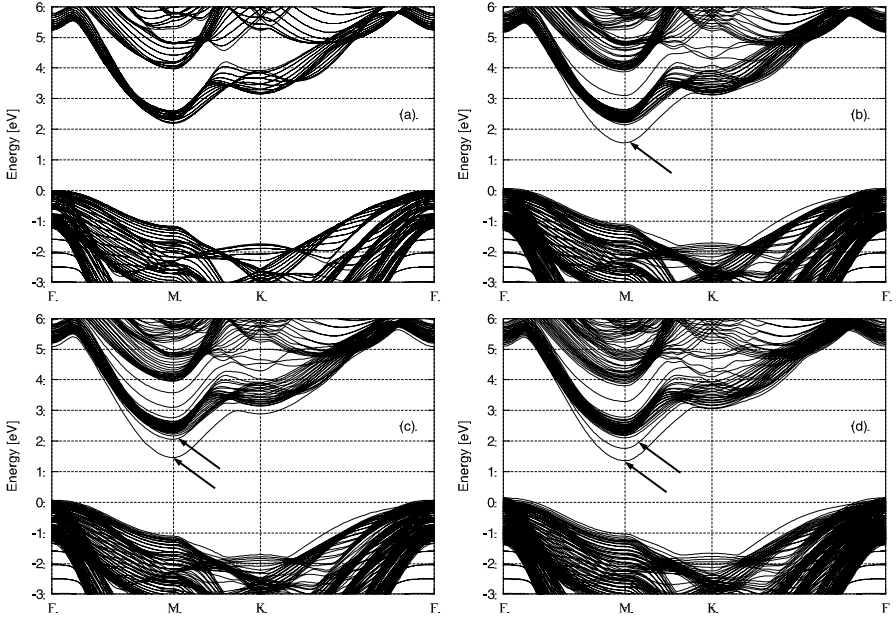


**Fig. 14.** Band structure of (a) perfect 4*H*-SiC, (b) 4*H*-SiC with 2SF(62), (c) 4*H*-SiC with 3SF(71), and (d) 4*H*-SiC with 4SF(10,2). The arrows point at the bands which have been split-off from the conduction bands into the band gap due to the narrow cubic inclusion

**Table 5.** The lowest ( $n = 1$ ) and second lowest ( $n = 2$ ) bound state energy  $E_B$  inside various cubic inclusions in  $4H$ - and  $6H$ -SiC as obtained from the supercell calculations and from a simple rectangular QW model. The last column shows the width of the QW model potential, whose depth was assumed to be 0.87 eV and 0.64 eV in  $4H$ - and  $6H$ -SiC, respectively, and with an effective mass equal to 0.3 free electron masses

Polytype	Type of inclusion	$E_B(\text{supercell})$ [eV]		$E_B(\text{QW})$ [eV]		Width [Å]
		$n = 1$	$n = 2$	$n = 1$	$n = 2$	
$4H$ -SiC	2SF(62)	-0.60	—	-0.58	—	12.5
	3SF(71)	-0.71	-0.11	-0.63	-0.08	15.0
	4SF(10,2)	-0.75	-0.35	-0.73	-0.36	22.5
$6H$ -SiC	2SF(51)	-0.35	—	-0.32	—	10.0
	3SF(93)	-0.49	-0.06	-0.49	-0.12	20.0
	4SF(10,2)	-0.55	-0.17	-0.52	-0.18	22.5

The numerical values of the energies of the split-off bands at the M-point are summarized in Table 5 both for  $4H$ - and  $6H$ -SiC, together with the results from the simple rectangular QW model [16].

In the QW model the depths of the QW potentials and the effective mass were assumed to be the same as in the case of isolated SFs. The agreement between the two methods is seen to be very good, even though the QW model in comparison with the ab initio supercell method is exceedingly simple. Here one can really talk about having done things the hard way!

## 4.2 Strong Wave Function Localization and Quantum Confinement

The conclusion that the split-off bands are 2-dimensional QW bands is even further strengthened by the close agreement between the split-off wave functions from the supercell calculations (see Figs. 15–17 for the cases 2SF(62), 3SF(71) and 4SF(10,2) in  $4H$ -SiC) with those from the simple rectangular QW model [10]. In view of these results for thin cubic inclusions, where the intuitively quite obvious explanation concerning the split-off bands in terms of a planar QW is definitely quantitatively supported, one can regard the QW interpretation of the split-off bands in the case of isolated SFs as a limiting case of the same physical mechanisms, although this interpretation is no doubt much less obvious in the latter case.

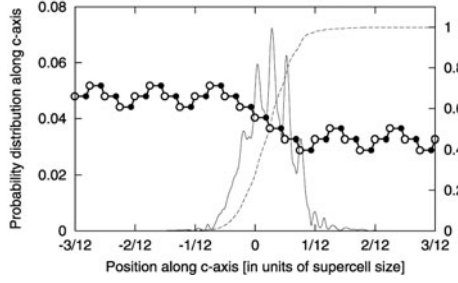


**Fig. 15.** The projected probability distribution (2) (*left-hand scale*) and the truncated normalization integral (3) (*right-hand scale*) for the minimum of the split-off band in the case 2SF(62) in 4H-SiC. Also shown is a portion of the stacking sequence

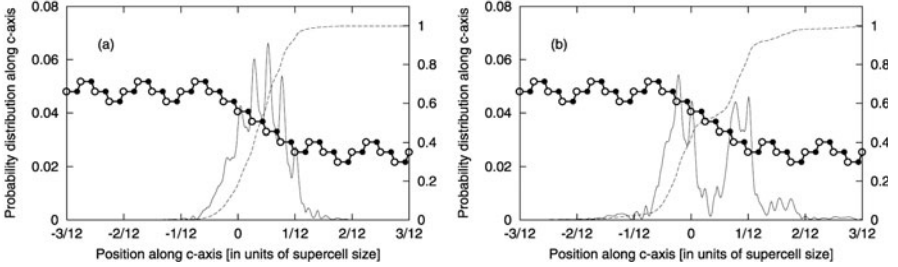


**Fig. 16.** Same as Fig. 15 but for (a) the lowest ( $n = 1$ ) and (b) second lowest ( $n = 2$ ) split-off band for 3SF(71) in 4H-SiC

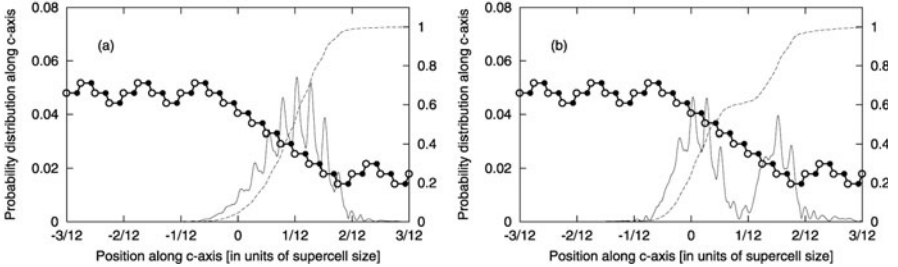


**Fig. 17.** Same as Fig. 15 but for (a) the lowest ( $n = 1$ ) and (b) second lowest ( $n = 2$ ) split-off band for 4SF(10,2) in 4H-SiC

### 4.3 Occurrence of Weak Localization and Wave Function Asymmetry

As in the case of isolated SFs, SF-induced changes in the spontaneous polarization lead to wave function segregation also in the case of cubic inclusions [10]. In the isolated SF case, wave function segregation can be related to the creation of additional hexagonal turns [12], whereas in the cubic inclusion

case, wave function segregation (which is of the opposite type) can be related to the annihilation of hexagonal turns. In [10] it was furthermore concluded that the clear asymmetry in the probability distribution for the strongly localized states, in the sense that the QW wave functions inside the inclusion are displaced towards the upper part of the cubic stacking sequence (to the right in Figs. 15–17), is also related to this change in spontaneous polarization, which causes a tilt of the QW potential with lower energy towards the right in Figs. 15–17 than towards the left.

#### 4.4 In-Plane Effective Masses in Cubic Inclusions

The calculated effective masses of electrons inside cubic inclusions in  $4H$ - and  $6H$ -SiC for motion along the M- $\Gamma$  and M-K directions in the Brillouin zone, are shown in Table 6. The most notable features are:

1. The mass component along M- $\Gamma$  for the lowest subband decreases steadily as the width of the inclusion increases.
2. For the widest inclusion studied here (with a width around 22.5 Å for 4SF(10,2)), the effective mass component for the lowest subband is still about 25% above its infinite-width value 0.42.
3. The mass component along M-K is essentially independent of the width of the QW and very close to its value in 3C-SiC.

**Table 6.** Effective masses (in units of the free electron mass) for motion parallel with the basal plane for electrons occupying the bottom of the lowest ( $n = 1$ ) and second lowest ( $n = 2$ ) sub-band at M inside some cubic inclusions, and for two isolated SFs. For comparison, the in-plane effective mass components for perfect 3C-SiC are  $m_{M\Gamma} = 0.42$  and  $m_{MK} = 0.23$

Polytype	Type of inclusion	$n = 1$		$n = 2$	
		M- $\Gamma$	M-K	M- $\Gamma$	M-K
$4H$ -SiC	1SF(31)	0.74	0.22	–	–
	2SF(62)	0.60	0.22	–	–
	3SF(71)	0.60	0.22	0.59	0.21
	4SF(10,2)	0.56	0.23	0.65	0.21
$6H$ -SiC	1SF(42)	0.65	0.22	–	–
	2SF(51)	0.63	0.22	–	–
	3SF(93)	0.57	0.23	0.69	0.22
	4SF(10,2)	0.56	0.23	0.66	0.21

#### 4.5 Successive Stacking Fault Energies Around Cubic Inclusions

With successive SF energies  $\gamma_p$  we shall mean  $\gamma_p = (E(p) - E(p-1))/A$ , where  $A$  is the SF area,  $E(p)$  is the total energy of the faulted portion of the crystal with  $p$  SFs in neighbouring planes ( $p$ SF) and  $E(0)$  is the total energy of the same portion of the perfect crystal. Table 7 shows the successive SF energies  $\gamma_p$ ,  $p = 2, 3$  and 4, for cubic inclusions in  $4H$ - and  $6H$ -SiC. For convenience we have also included  $\gamma_1(4H\text{-SiC})$  and  $\gamma_1(6H\text{-SiC})$  from Table 4. We observe that

1. In  $4H$ -SiC,  $\gamma_2$  is almost a factor 4 *smaller* than  $\gamma_1$  (using the values from the supercell calculation). Thus, barring too high energy barriers between the different configurations (i.e., too high Peierls barriers for partial dislocation motion), there should be a tendency for 1SF(31) (a single SF) to transform into 2SF(62) (a double SF). Similarly, if 3SF(71) is created, 4SF(10,2) could form with relative ease.
2. In  $6H$ -SiC, the situation is reversed in the sense that  $\gamma_2$  is almost a factor 7 *larger* than  $\gamma_1$ . Thus, single SFs should dominate over double SFs in this polytype.
3. The ANNNI model agrees well with the supercell calculations.

In Sect. 5.4 we shall discuss items (1) and (2) in the light of experimental observations.

The low value of  $\gamma_2$  relative to  $\gamma_1$  in  $4H$ -SiC can of course be regarded as a SF-SF interaction effect: it is seen from Fig. 4 that the second SF in 2SF(62) is introduced in the plane adjacent to the SF plane in 1SF(31). The relation between 3SF(71) and 4SF(10,2) is similar. However, 3SF(71) is obtained from 2SF(62) by skipping two glide planes before the third SF is introduced. This reduces the SF-SF interaction, leading to a value of  $\gamma_3$  which is rather close to  $\gamma_1$ . The same argument can be applied to  $6H$ -SiC. In this

**Table 7.** SF energies  $\gamma_p$  (in mJ/m<sup>2</sup>) for successive SFs in neighbouring basal planes leading to cubic inclusions in  $4H$ - and  $6H$ -SiC (without ISR)

Polytype	Transformation		$p$	$\gamma_p$ (supercell)	$\gamma_p$ (ANNNI)
$4H$ -SiC	Perfect	→ 1SF(31)	1	17.7	18.3
	1SF(31)	→ 2SF(62)	2	4.7	3.1
	2SF(62)	→ 3SF(71)	3	20.3	21.5
	3SF(71)	→ 4SF(10,2)	4	5.4	3.1
$6H$ -SiC	Perfect	→ 1SF(42)	1	3.1	3.1
	1SF(42)	→ 2SF(51)	2	21.0	21.4
	2SF(51)	→ 3SF(93)	3	6.4	6.3
	3SF(93)	→ 4SF(10,2)	4	3.8	3.1

polytype 4SF(10,2) is obtained from 3SF(93) by skipping three glide planes relative to the previously inserted SF plane. This reduced SF-SF interaction brings  $\gamma_4$  close to  $\gamma_1$ .

## 5 Experimental Observations Explained by the QW Action of SFs

### 5.1 Anomalous Resistivity Anisotropy in *n*-Type 4*H*- and 6*H*-SiC

By growing 4*H*- and 6*H*-SiC crystals using different growth directions, Takahashi et al. [31] produced crystals containing a high density of SFs and measured the resistivity in directions essentially perpendicular and parallel to the SF plane, both in *n*-type and *p*-type samples. It was found that the resistivity perpendicular to the SF in *n*-type samples of both 4*H* and 6*H* polytypes was much larger than the resistivity along the SF plane provided the temperature was not too high. This anisotropy was much too large to be explained by the normal bulk resistivity anisotropy [32]–[34], which is mainly caused by the anisotropy of the electron effective mass [35, 36]. On the other hand, no corresponding resistivity anomaly was found in *p*-type samples even though the density of SFs in these samples were as large as in the *n*-type samples. The authors could not find a proper explanation of these results.

This resistivity anomaly, and its restriction to *n*-type samples only, can easily be explained in terms of our results suggesting a QW action of the SFs. In *n*-type samples, electrons are trapped by the strongly localized SF band states around 0.2 eV below the conduction band, and they will essentially remain there provided the temperature is not high enough to excite them to the conduction band. Due to the strong localization in the *c*-direction, the electron transport along this direction (perpendicular to the SF plane) is obstructed, whereas the electrons are free to move in the SF plane with the effective masses shown in Table 3. In *p*-type samples, the Fermi level is well below the localized SF band at  $(E_C - 0.2)$  eV, which is therefore not affecting the current transport. The weakly localized states in the immediate vicinity of the valence band maximum are very close in energy to the extended band states, and therefore do not cause abnormal resistivity anisotropy unless the temperature is very low.

### 5.2 Electrical Degradation of Bipolar Devices

We mentioned in the Introduction that electrical degradation of bipolar 4*H*-SiC devices (diodes) coincided with the observation of SFs in the active regions of the device. This can be explained by the following arguments. Electrons injected into the base region of, for instance, a pin-diode containing SFs, are captured by the bound, strongly localized QW states around the

SF, tending to make the SF negatively charged. To screen out the increase in negative charge density, holes are also attracted to the SF region. This enhanced local concentration of electrons and holes will increase the probability for electron-hole recombination, leading to a reduction of the electron and hole lifetimes, and hinder electrons and holes from moving freely in the device. This will impede the normal build-up of an electron-hole plasma, and consequently obstruct the normal conductivity modulation, causing an increased voltage drop across the device.

An interesting question is what is causing the expansion of the SFs. This has not been investigated in detail, but it could be noticed that apart from stress, which is generally too low to cause partial dislocation motion around room temperature in SiC, recombination enhanced dislocation motion [4, 5] is most likely involved [3]. In this case, electrons and holes injected into the base region from the emitters recombine in the vicinity of the leading partial, which probably has created recombination levels in the band gap. If this recombination is radiationless, an energy of approximately the band gap, or a considerable fraction thereof, can be released for each recombining electron-hole pair in the form of phonons. This energy can then be available for double kink formation and migration, pushing the dislocation over the energy barriers associated with the dislocation motion.

Today the electrical degradation problem is a serious obstacle for the development of bipolar SiC technology. The results and conclusions presented here imply that bipolar device technology in all hexagonal and rhombohedral polytypes are likely to suffer to some degree from the same electrical degradation problem as found for 4H-SiC devices, until the expansion of SFs can be controlled or minimized, if not completely avoided. However, for non-cubic polytypes with band gaps not too different from 3C-SiC (e.g. those with small hexagonality), the QW capture effect may not be essential and in practice permit sufficiently stable devices. For unipolar SiC devices of all polytypes, and for bipolar 3C-SiC devices, no such degradation problems are expected at present.

### 5.3 Results from Luminescence Studies

Bergman et al. [37] and Sridhara et al. [38] have observed low temperature photoluminescence (PL) peaks around 425 nm (2.92 eV) in electrically degraded 4H-SiC diodes with developed SFs. The emission was observed from the entire SF area. Although all details in the PL spectrum are presently not understood, it is thought to be due to the recombination of excitons whose electron states are formed from the bottom of the split-off band at M, 0.2–0.3 eV below the conduction band minimum.

Room temperature electroluminescence from entire SFs in degraded diodes have also been reported [3], and reveal radiative transitions with photon energies around 2.8 eV. This was interpreted as transitions from the strongly

localized QW-like states 0.2–0.3 eV below the conduction band minimum to the top of the valence band.

PL peaks around 510 nm (2.43 eV) have also been observed in 4*H*-SiC [39]. Similarly, Skromme et al. [40] have observed PL peaks at around 510 nm, which they suggested came from a cubic environment. These peaks have tentatively been assigned by Bergman as coming from a double SF, since, according to our calculations, the double SF 2SF(62) in 4*H*-SiC has a QW-like level approximately 0.6 eV below the conduction band minimum.

#### 5.4 Observation of the Occurrence of Double and Single SFs

It has been reported recently [27, 28] that double SFs (2SF(62)) were generated in *n*-type 4*H*-SiC samples after annealing at 1150°C for 90 minutes in argon gas. The samples, which were SF free before the anneal, were highly N-doped to a concentration about  $3 \times 10^{19} \text{ cm}^{-3}$ , and the density of double SFs was as high as 50–80  $\mu\text{m}^{-1}$ , corresponding to a distance between faults of about 12–20 unit cells of 4*H*-SiC. In this case there should be no electron-hole plasma that can drive the SF expansion. Nor were there any obvious sources of stress. So why are SFs generated, and why are double SFs generated instead of single SFs?

An interesting mechanism for SF expansion, which does not require electron-hole recombination or large stress, has been suggested by Miao et al. [13]. It assumes an *n*-type sample with the electrons being excited into the conduction band. If we take isolated SFs in 4*H*-SiC as an example, each electron can gain about 0.2 eV by making a transition from the conduction band into the strongly localized SF state. If the energy that can be released in this way exceeds the energy required to locally expand the SF sufficiently much to create the localized state, the system can gain energy and the SF can thus expand.

To explain the formation of double SFs Liu et al. [28] and Kuhr et al. [27] suggested a mechanism, which is the same as that proposed by Miao et al., except that they suggested that the conduction band electrons instead induce a double SF. In fact, creation of single SFs only by this mechanism in 4*H*-SiC does not seem very likely. In 4*H*-SiC the SF energy for creation of the first SF is around 15 mJ/m<sup>2</sup>. Suppose that the around 0.2 eV gain in electronic energy is sufficient to overcome the SF energy to create a single SF. Then it seems plausible that creating a second nearby SF, which only requires about 5 mJ/m<sup>2</sup> (Table 7) would also take place since the additional gain in electronic energy is even larger, namely  $(0.6 - 0.2) \text{ eV} = 0.4 \text{ eV}$ , where 0.6 eV is the QW energy level in the case of 2SF(62) (Table 5). The 2.5 eV photon peak observed in [29, 30] fits very well with transitions from this QW-like level to the top of the valence band.

This mechanism for doping-induced creation of SFs has been investigated in more detail and with more formal rigour in [27]. It was also found that in 6*H*-SiC, the mechanism produces only single SFs, as in the original suggestion

by Miao et. al. The reason is basically that in this polytype the SF energy for the first SF is around  $3 \text{ mJ/m}^2$ , creating a QW level at around  $0.18 \text{ eV}$ , whereas the formation of a second nearby SF requires much more energy, namely around  $21 \text{ mJ/m}^2$  (Table 7), but gives an additional contribution from the electronic transitions to the QW level of only  $(0.35 - 0.18) \text{ eV} = 0.17 \text{ eV}$ . This conclusion [27] is in agreement with experimental observations [41].

## Acknowledgement

The authors gratefully acknowledge financial support from ABB Group Services Center, Corporate Research, Sweden, and from the Swedish Foundation for Strategic Research (SSF). We also thank the National Supercomputer Center (NSC), Sweden, for ample supercomputer time.

## References

1. J.P. Bergman, H. Lendenmann, P.-Å. Nilsson, U. Lindefelt, and P. Skytt: *Mater. Sci. Forum* **353–356**, 299 (2001)
2. J.Q. Liu, M. Skowronski, C. Hallin, R. Söderholm, and H. Lendenmann: *Appl. Phys. Lett.* **80**, 749 (2002)
3. A. Galeckas, J. Linnros, and P. Pirouz: *Appl. Phys. Lett.* **81**, 883 (2002)
4. K. Maeda and S. Takeuchi: in *Dislocations in Solids* **10** (eds. F.R.N. Nabarro and M.S. Duesbery), North Holland Publishing Co., Amsterdam, 443 (1996)
5. J.D. Weeks, J.C. Tully, and L.C. Kimerling: *Phys. Rev. B* **12**, 3286 (1975)
6. H. Iwata, U. Lindefelt, S. Öberg, and P.R. Briddon: *Phys. Rev. B* **65**, 033203 (2002)
7. H. Iwata, U. Lindefelt, S. Öberg, and P.R. Briddon: *Mater. Sci. Forum* **389–393**, 529 (2002); *ibid.* 439; *ibid.* 533
8. H. Iwata, U. Lindefelt, S. Öberg, and P.R. Briddon: *J. Phys. Condens. Matter* **14**, 12733 (2002)
9. H. Iwata, U. Lindefelt, S. Öberg, and P.R. Briddon: in *Proceedings of the European Conference on Silicon Carbide and Related Materials* (ECSCRM2002) (eds. W.J. Choyke, G. Pensl, H. Matsunami), Trans. Tech. Publications (2003), four articles to appear
10. H. Iwata, U. Lindefelt, S. Öberg, and P.R. Briddon: *J. Appl. Phys.* **93**, 1577 (2003)
11. U. Lindefelt, H. Iwata, S. Öberg, and P.R. Briddon: in *Proceedings of the European Conference on Silicon Carbide and Related Materials* (ECSCRM2002) (eds. W.J. Choyke, G. Pensl, H. Matsunami), Trans. Tech. Publications (2003), to appear
12. U. Lindefelt, H. Iwata, S. Öberg, and P.R. Briddon: *Phys. Rev. B* **67**, 155204 (2003)
13. M.S. Miao, S. Limpijumnong, and W. Lambrecht: *Appl. Phys. Lett.* **79**, 4360 (2001)
14. F. Bechstedt and P. Käckel: *Phys. Rev. Lett.* **75**, 2180 (1995)
15. F. Bechstedt, P. Käckel, A. Zywiets, K. Karch, B. Adolph, K. Tenelsen, and J. Furthmüller: *Phys. Stat. Sol. (b)* **202**, 35 (1997)

16. G. Bastard: in *Wave Mechanics Applied to Semiconductor Heterostructures*. Monographies de Physique, les Edition de Physique, Avenue de Hoggar, Zone Industrielle de Courtaboeuf, 91944 Les Ulis Cedex, France (1992)
17. C. Persson and U. Lindefelt: J. Appl. Phys. **82**, 5496 (1997)
18. A. Qteish, V. Heine, and R.J. Needs: Phys. Rev. B **45**, 6376 (1992); *ibid.* 6534
19. M.H. Hong, A.V. Samant, and P. Pirouz: Phil. Mag. A **80**, 919 (2000)
20. K. Maeda, K. Suzuki, S. Fujita, M. Ichihara, and S. Hyodo: Phil. Mag. A **57**, 573 (1988)
21. P. Pirouz, D.J.H. Cockayne, N.S. Sumida, P. Hissch, and A.R. Lang: Proc. R. Soc. London Ser. A **386**, 241 (1983)
22. P.J.H. Denteneer: Mat. Res. Soc. Symp. Proc. **141**, 343 (1989)
23. C. Cheng, R.J. Needs, and V. Heine: J. Phys. C **21**, 1049 (1988)
24. P. Käckel, J. Furthmüller, and F. Bechstedt: Phys. Rev. B **58**, 1326 (1998)
25. W.J. Choyke: private communication
26. S. Bai, G. Wagner, E. Shishkin, W.J. Choyke, R.P. Devaty, M. Zhang, P. Pirouz, and T. Kimoto: Mater. Sci. Forum **389–393**, 589 (2002)
27. T.A. Kuhr, J.Q. Liu, H.J. Chung, and M. Skowronski: J. Appl. Phys. **92**, 5863 (2002)
28. J.Q. Liu, H.J. Chung, T. Kuhr, Q. Li, and M. Skowronski: Appl. Phys. Lett. **80**, 2111 (2002)
29. R.S. Okojie, M. Xhang, P. Pirouz, S.T. Tumakha, G. Jessen, and L.J. Brillson: Appl. Phys. Lett. **79**, 3056 (2001)
30. R.S. Okojie, M. Xhang, P. Pirouz, S. Tumakha, G. Jessen, and L.J. Brillson: Mater. Sci. Forum **389–393**, 451 (2002)
31. J. Takahashi, N. Ohtani, M. Katsuno, and S. Shinoyama: J. Cryst. Growth **181**, 229 (1997); Mater. Sci. Forum **264–268**, 25 (1998)
32. U. Lindefelt: J. Appl. Phys. **76**, 4164 (1994)
33. W.J. Schaffer, G.H. Negley, K.G. Irvine, and J.W. Palmour: Mater. Res. Soc. Symp. Proc. **339**, 595 (1994)
34. M. Schadt, G. Pensl, R.P. Devaty, W.J. Choyke, R. Stein, and D. Stephani: Appl. Phys. Lett. **65**, 3120 (1994)
35. H. Iwata, K.M. Itoh, and G. Pensl: J. Appl. Phys. **88**, 1956 (2000)
36. H. Iwata and K.M. Itoh: J. Appl. Phys. **89**, 6228 (2001)
37. J.P. Bergman, H. Jakobsson, L. Storasta, F.H.C. Carlsson, B. Magnusson, S. Sridhara, G. Pozina, H. Lendenmann, and E. Janzén: Mater. Sci. Forum **389–393**, 9 (2002)
38. S.G. Sridhara, F.H.C. Carlsson, J.P. Bergman, and E. Janzén: Appl. Phys. Lett. **79**, 3944 (2001)
39. J. P. Bergman: private communication
40. B. J. Skromme, K. Palle, C.D. Poweleit, L.R. Bryant, W.M. Vetter, M. Dudley, K. Moore, and T. Gehoski: Mater. Sci. Forum **389–393**, 455 (2002)
41. M. Skowronski: private communication

## Part II

### Crystal Growth

# Principles and Limitations of Numerical Simulation of SiC Boule Growth by Sublimation

M. Pons, R. Madar, and T. Billon

## 1 Introduction

To overcome some of the problems in SiC crystal growth, modeling can now be considered as a reliable engineering tool in research, development and production of electronic materials. There is a multitude of physical phenomena in the sublimation growth process. Only a partial modeling of the whole process can be made even by the most ambitious researcher. The main objective is to reach an accurate understanding of heat and mass transfer. It could lead to “better” material or more “efficient” production processes. The purpose of modeling should not be the model itself, but to provide tools for the development of the process. In this sense, if it is easy to reach a consensus on the meaning of better and efficient in the fabrication of materials, the role of process modeling in achieving these goals, in contributing to them is not easily identifiable (S. Motakef, Cape Simulation Inc., <http://www.capesim.com>). In the sublimation process, there is no direct way to control the behavior of individual species and therefore the growth process can be influenced through macroscopic parameters, such as thermal environment, mass transport and chemical composition and reactivity. Firstly, modeling gives an insight on what is actually happening in the system. Secondly, it helps in evaluating new systems without the need of building them.

Numerical simulation is now the most prevailing technique for the solution of macroscopic governing equations. The popularity of this approach comes from the fact that calculations can be performed for complex geometries and multi-physics and multi-scale phenomena can be solved.

This approach is often limited due to a poor understanding of fundamental physics or to the complexity of the system. Direct numerical simulation might not be possible. The main limitation in SiC crystal growth modeling is the accurate knowledge of physical, thermal, radiative, chemical and electrical data for the different components of the reactor. This is the weakest link in developing completely predictive models. In addition, the link between the thermochemical history of the grown material and its structure and defects still needs further development and input of experimental data [1]. Despite these limitations, numerical modeling is sufficiently mature to support effective optimization of SiC growth conditions. The key of success is the combined

use of simulation, experiments and characterization with “daily interaction”. It is the goal of this paper to show that modeling and simulation can now be considered as characterization tools in SiC technology.

## 2 Modeling and Simulation of the Growth Procedure

### 2.1 Experimental Setup

In 1978 Tairov and Tsvetkov introduced a modification of the Lely’s method of crystal growth [2]. In order to control the polytype of the crystals produced by spontaneous nucleation on the graphite walls, they introduced a SiC single crystal seed in the growth cavity. Physical vapor transport is driven by the temperature gradient between the powdered source and the surface of the seed (Fig. 1).

Generally, the powder is placed in the lower half of a graphite crucible and the single crystal seed is stuck on the graphite lid with carbonized sugar or graphite glue. The main interest in this growth method is that it allows obtaining several circular single crystalline slices from the same ingot, as in the case of silicon crystal growth.

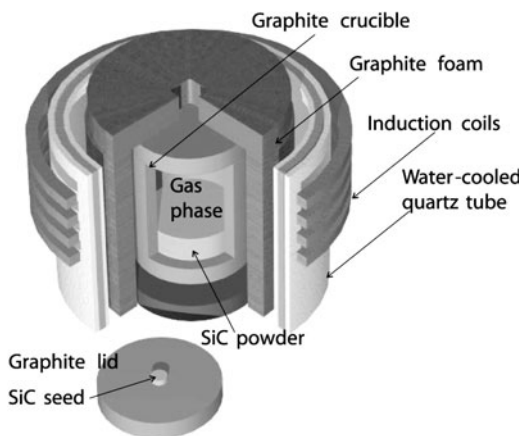


**Fig. 1.** Schematic representation of the reactor and graphite lid

### 2.2 State of the Art

It is obvious that improvement in SiC growth technology occurs through extensive experimentation. However the advances made in process modeling as well as in the various tools of numerical simulation proves their effectiveness in so far as the help with the understanding of problems and with the design of equipment. This effort was initially motivated by the need for a better

knowledge of the local temperature range in the cavity. The main contribution of this activity is to make visual the history of the growth and to convey complex and highly coupled phenomena to common knowledge. This is a further help to the experimentation.

Heat transfer phenomena include conduction, convection, radiation, heating through induction as well as the latent heat of sublimation and condensation on the gas-solid interface. Since the first publications in this research field [3]–[6], the models, the databases were refined and the experimental verification of numerous hypotheses was confirmed. A lot of advances have been made in the last five years period along several routes. The majority of published results are based on 2-dimensional modeling of heat transfer [7]–[41]. Useful set of data can be found [4, 27]. Transient numerical results on the evolution of heat transfer during the growth process have been recently studied to refine the knowledge of the evolution of important growth parameters [37]. Models including the semi-transparency of the growing boule were introduced by Klein et al. [27] to improve the accuracy of the simulation approach. Inverse modeling was also applied to the optimization of the shape of the crucible [33].

The modeling and the simulation of heat transfer is not sufficient to determine the rate of growth and the shape of the crystal. Mass transfer models must therefore be coupled with the preceding as well as with thermodynamic and kinetic databases [11, 14]. During the last five years, modeling of mass transfer was performed to understand macroscopic growth phenomena and to provide simultaneous control of many factors like (i) the SiC powder sublimation and the growth rate on the seed, (ii) the shape of SiC boule during growth [9, 11, 17, 19, 38], (iii) silicon and graphite inclusion in the crystal [8, 26, 38], (iv) the influence of source powder evolution [8, 31, 38, 39], (v) the influence of Stefan flow due to intense sublimation and condensation [9, 35]. Many attempts to relate thermal and concentration macroscopic fields to crystal properties and defect occurrence were proposed. As an example, it was demonstrated that minor modifications in the reactive cavity were part of the many causes of the creation of defaults during growth [8],[24]–[26], that frequently, the requirements for controlling the different factors are in contradiction with each other [8, 13].

Finally, the more recent modeling development was based on the integration of the thermoelastic stress due to temperature gradient in the growing crystal and to its shape. It was shown that the magnitude of shear stress and the Von Mises stress can provide guidelines to understand the distribution of dislocations [22]–[25],[38]–[41].

One of the weak points in regard to realistic modeling of PVT growth is the accurate description of mass transfer and chemical reactions within the SiC powder provoking a change in fluxes of Si and C containing species [31, 38].

All along the development of these models, comparison with experimental growth results, in situ visualization techniques with X-Ray [42, 43], measurements of high temperature properties [44] were performed for the validation and the improvement of the predictive capabilities of the simulation results.

We are primarily interested in SiC ingots grown by the modified Lely method with graphite walls for the reactive cavity. Similar procedures are also operational. These use tantalum walls or short distances between the powder and the seed (sandwich sublimation method) [45]–[47].

First of all, the different models and the database sets will be described. They will be applied to a standard configuration in order to visualize the different macroscopic fields.

In the second part, the influence of the geometric modifications on the thermal history of the cavity will be discussed. The first series of simulations will be carried out at the beginning of growth. The growth of ingots of 8 to 10 mm provokes geometric modifications that are not insignificant in view of the dimensions of the reaction cavity (15 to 20 mm). The modifications of the local thermal field in the cavity will then be presented as a function of the stage of crystal growth. Finally, more advanced modeling and simulation of mass transfer and reactivity will be discussed as well as new modeling development.

### 2.3 Modeling and Databases

In the course of the development of bulk growth processes, increased attention was paid to crucible design and optimization of the thermal and concentration profiles in the growth cavity. There is no way to control the behavior of individual species and therefore the growth process can only be influenced through macroscopic mechanisms, such as thermal environment, mass transport and chemical reactions.

In our group, for two-dimensional axisymmetric geometry, a software package has been initially built from commercial and in-house software packages [4, 7]. The current knowledge of thermal, electrical and chemical databases is also inserted. Other software packages like CFDACE<sup>1</sup> or Virtual Reactor<sup>2</sup> [30] are available for this specific problem and can be easily used. Equations describing heat and mass transfer have been already published [4, 27, 28].

---

<sup>1</sup> CFDACE is a product of CFD Research Corporation, 215 Wyan Drive, Huntsville, AL 35805, USA, <http://www.cfdrc.com>

<sup>2</sup> Virtual Reactor and Global heat transfer are products of Soft Impact, P.O. Box 33, Engelsa pr. 27 194156 Saint-Petersburg, Russia <http://www.softimpact.ru>

### 2.3.1 Thermodynamic Modeling

The thermodynamic calculations were carried out by minimization of the total free energy of the Si-C-Ar system in the temperature range 2300–3000 K. A self-consistent set of data was generated for the gaseous molecules from a literature review, measurements and heat capacity and entropy calculations using recent results on molecular structures, vibrational frequencies and electronic spectra. Nine gaseous species in addition to argon ( $\text{Si}_1$ ,  $\text{Si}_2$ ,  $\text{Si}_3$ ,  $\text{C}_1$ ,  $\text{C}_2$ ,  $\text{C}_3$ ,  $\text{SiC}$ ,  $\text{Si}_2\text{C}$ ,  $\text{SiC}_2$ ) and three condensed phases ( $\text{SiC}$ ,  $\text{Si}$  and  $\text{C}$  graphite) were considered [7, 11]. The parameters introduced in the calculations were the temperature, the crucible volume and the initial quantities of argon and solid silicon carbide at the source. Calculations show that only three species are of importance:  $\text{Si}_1$ ,  $\text{Si}_2\text{C}$ ,  $\text{SiC}_2$ .

### 2.3.2 Gas and Surface Chemistry

A comprehensive capability must be available to simulate multi-step gas and surface chemistry. Large sets of multi-step reactions or thermodynamic equilibrium must be handled in the code. The surface chemistry is treated by doing a complete reaction-diffusion balance at the surface to obtain the surface concentration of species. The heat release from the gas/surface reactions is included in the model.

The use of local thermodynamic equilibrium (LTE) assumes infinite length or time scale. We have checked that mass transport computations linked with LTE can give the trends in the crystal shape and on the influence of pressure, but with too high absolute growth rate. High temperature spectrometry

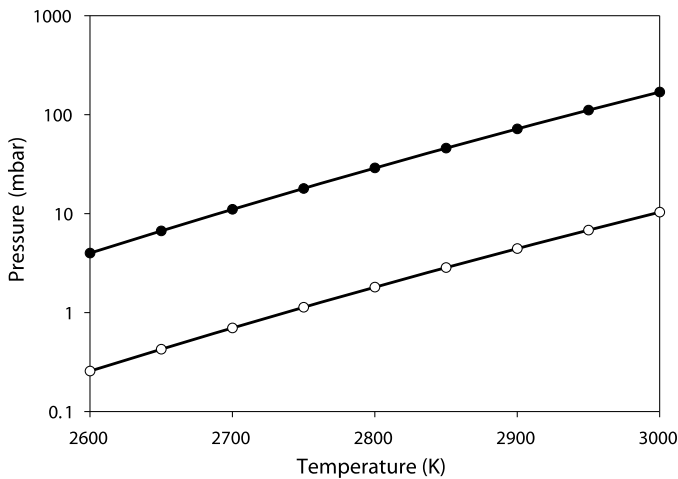


**Fig. 2.** Total pressure of reactive gas species over solid SiC as a function of temperature with (○) and without (●) evaporation coefficients [14, 48]

(2000–2300 K) was used to evaluate sublimation coefficients [14]. It is clear that the chemical system does not reach thermodynamic equilibrium. One order of magnitude has been measured between equilibrium partial pressure and measured pressure (Fig. 2). These data are now included in the models to compute the growth rates and crystal shapes [48].

### 2.3.3 Induction Heating and Temperature Distribution

Electromagnetodynamics must be coupled with heat transfer, especially radiative heat transfer within the growth cavity. The radiation model is tightly coupled to the fluid transport, conjugate heat transfer and chemistry models to ensure energy conservation.

These calculations make use of a materials database which include the electrical and the thermal conductivity of crucible and insulation material, the source and the boule material properties, the gas species and associated reactivity data, the induction frequency and the current density. The current database has been partially validated with external and indirect measurements. A precise knowledge of the thermophysical properties of the component materials of the reactor as well as the powder, single- and poly-crystal forms of SiC are essential for obtaining realistic results [20].

### 2.3.4 Multicomponent Fluid Transport

The fluid transport model is based on the low pressure kinetic theory of gases. Transport coefficients such as viscosity, conductivity, specific heat, diffusivity and thermodiffusion coefficients are calculated as local functions of temperature, pressure and composition. The Stefan-Maxwell formulation for diffusive transport ensures complete mass conservation of all species in the system. The transport database is interactive with the calculations and comes from the kinetic theory of gases.

For the modified-Lely method with graphite crucible, within the range of investigated experimental parameters, it was found that the natural convective transport of heat and of chemical species (buoyancy effects) can be neglected when compared to diffusive transport and heat conduction and radiation.

## 2.4 Selected Results in Heat and Mass Transfer

### 2.4.1 Overview

A generic representation of the different macroscopic fields is presented in Fig. 3. Magnetic vector potential contours for five turns of coil and frequency of 120 kHz are shown in Fig. 3a. A large amount of energy is absorbed by the susceptor (Fig. 3b) within a thin skin depth. A temperature field

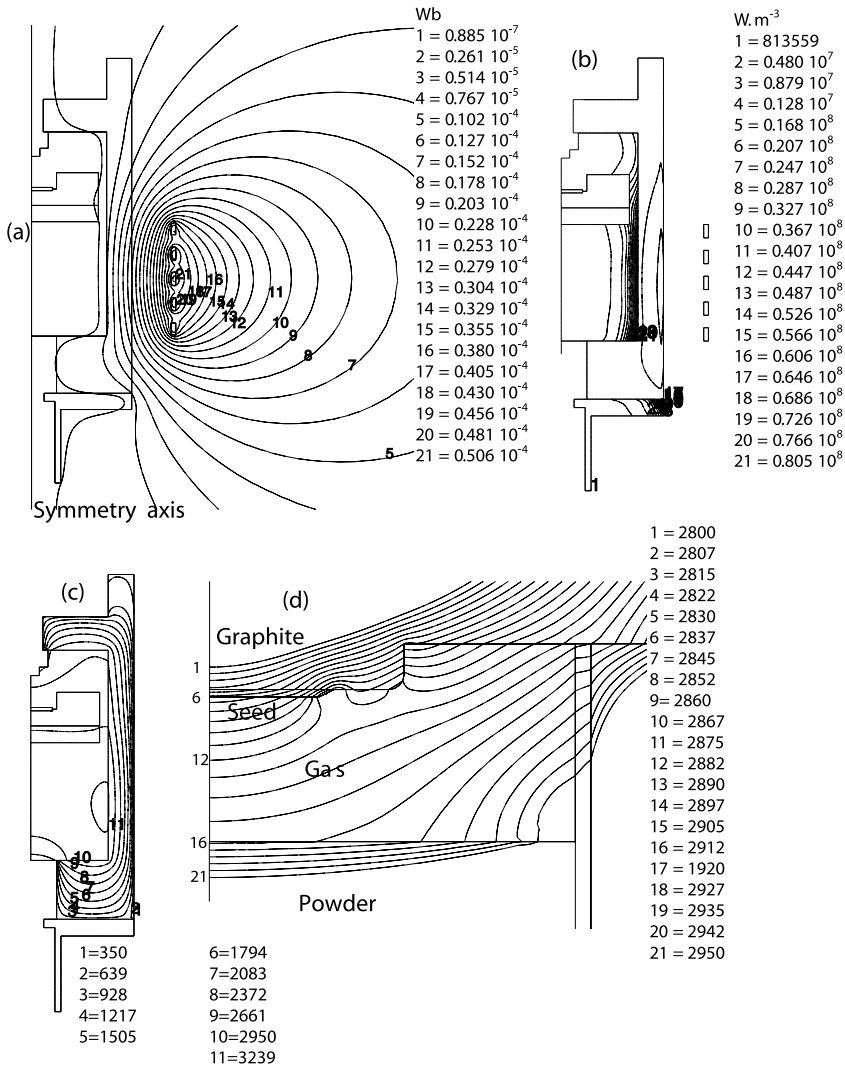


**Fig. 3.** Half-right part of the axisymmetric reactor: (a) Potential vector, (b) Joule losses, (c) temperature field, (d) temperature field in the cavity ( $T$  in K) ( $f = 120$  kHz) adapted from [7]

is established inside the crucible (Fig. 3c). A thermal gradient of less than  $80 \text{ Kcm}^{-1}$  is typical (see zoom in Fig. 3d).

The value of the growth rate is determined by the growth temperature, the total pressure in the system, the temperature difference between the surfaces of source and seed and the seed-source distance. It is important to note, at this stage, that the challenge is to control small temperature differences (less

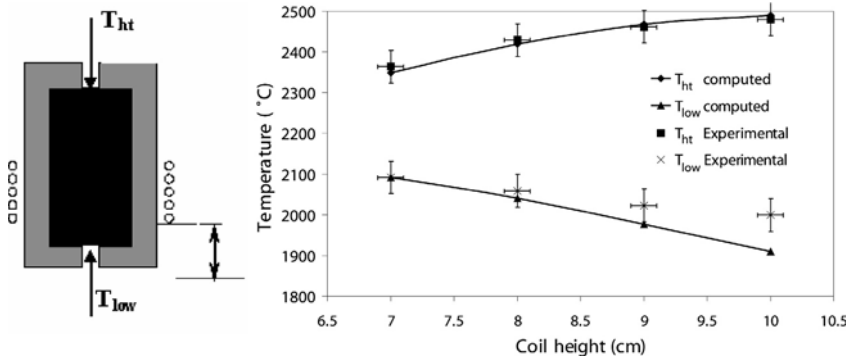


**Fig. 4.** Comparison of experimental and computed results as a function of coil position [49]

than 100 K) in the gas cavity, as compared to the total temperature difference (about 2500 K).

This kind of simulation was validated by changing frequency, current and coil position (Fig. 4). The numerical tool seems able to give guidelines for a better control of the temperature field in the cavity. More refined models of heat transfer were recently published [27, 33, 37].

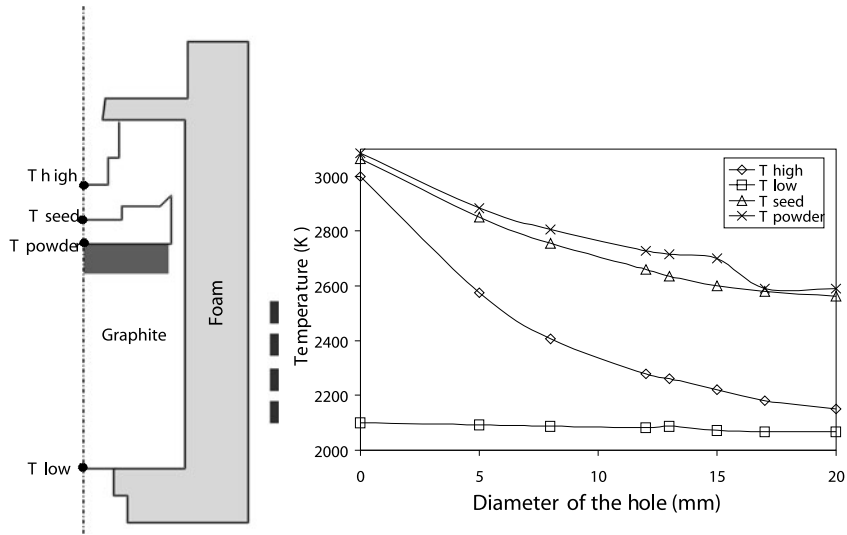


**Fig. 5.** Influence of the diameter of the hole used for pyrometric measurements on the calculated temperature of the different parts of the reactor along the symmetry axis [49]

### 2.4.2 Heat Transfer: Influence of the Diameter of Pyrometric Holes

The next example deals with the ability of the simulation tools to predict the influence of any modification of the crucible design on the thermal field inside the reaction chamber. We will discuss one example, the influence of the modification in the size of the hole on the graphite lid (Fig. 5). The simulation of the variation of the axial temperature as function of the diameter of the hole at the backside of the seed crystal is also shown. The thermal gradient can be strongly increased by increasing the diameter of the hole and consequently the thermal stress level [41]. We shall discuss after what are the implications of such modifications.

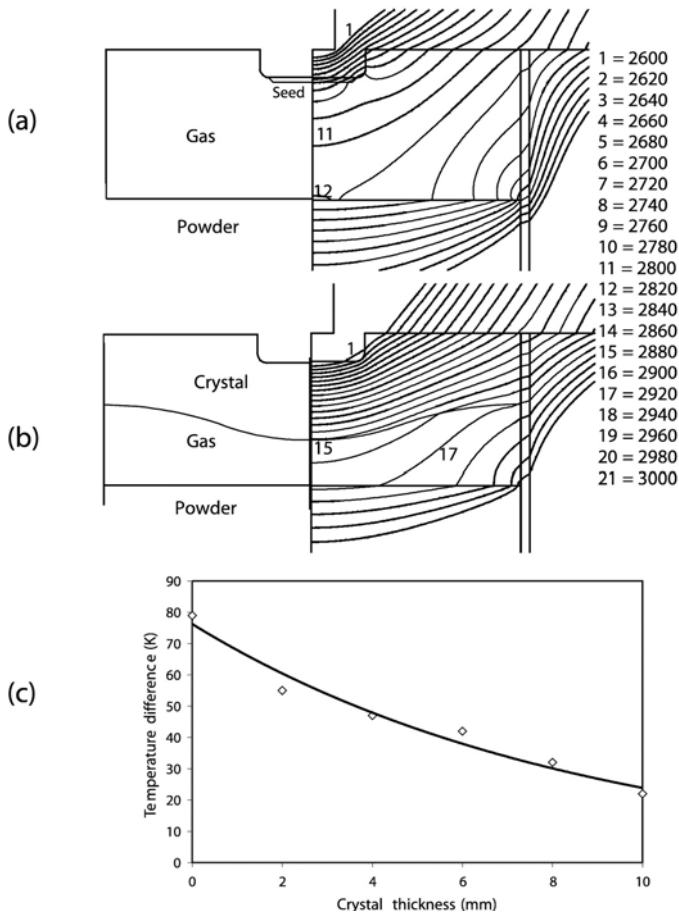


**Fig. 6.** Influence of the crystal thickness on the thermal field and on the axial temperature difference in the cavity [49]

2.4.3 Heat Transfer: Influence of the Growing Crystal

Many simulations have been performed at the beginning of the growth process. Nevertheless, it is also important to simulate the evolution of the temperature field as the growth proceeds. In fact, during the growth process, the distance between the crystal and the powder varies. The shape of the reaction chamber is modified and the variation of the electrical and thermal conductivities of the SiC powder due to its sintering and graphitization must be taken into account [39]. An example of the evolution of the thermal field inside the reaction chamber as the crystal grows is given in Fig. 6. When the length of the boule increases, the radiative transfer inside the crucible leads to lower values of axial and radial temperature differences. The exact knowledge of this evolution is of importance for further discussions about the modeling of crystal shape [17]–[19], stress pattern, defect, dislocation and micropipe density [22]–[25],[38]–[41].

2.4.4 Influence of the Insulation

A graphite foam is always used around the crucible to ensure a good thermal insulation. Some experiments have been conducted with two different insulating foam thicknesses. The standard process with a large foam thickness leads to 4H polytype growth on 4H. Processes that have been carried out with a reduced foam thickness have led to crystals which initially grow with the 4H polytype and then switch to the 6H polytype (Fig. 7). Heat transfer simulation predicts a decrease of the radial temperature difference along the seed (30 mm in diameter) of about 30% when the thickness of the insulation

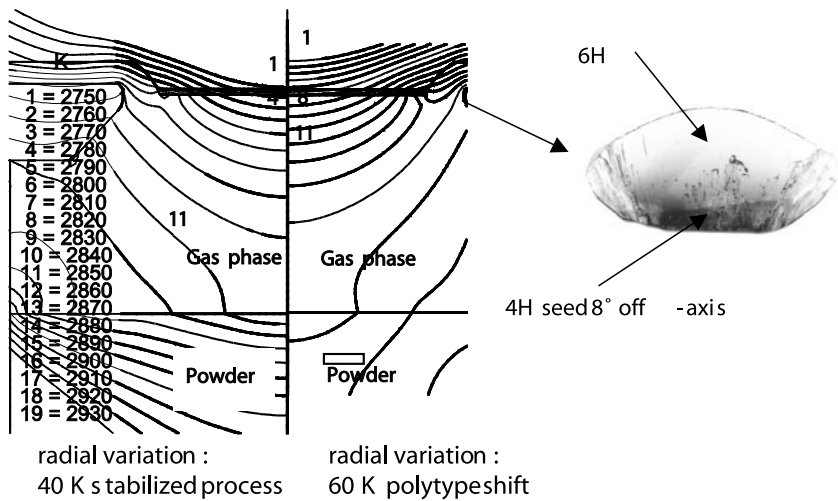
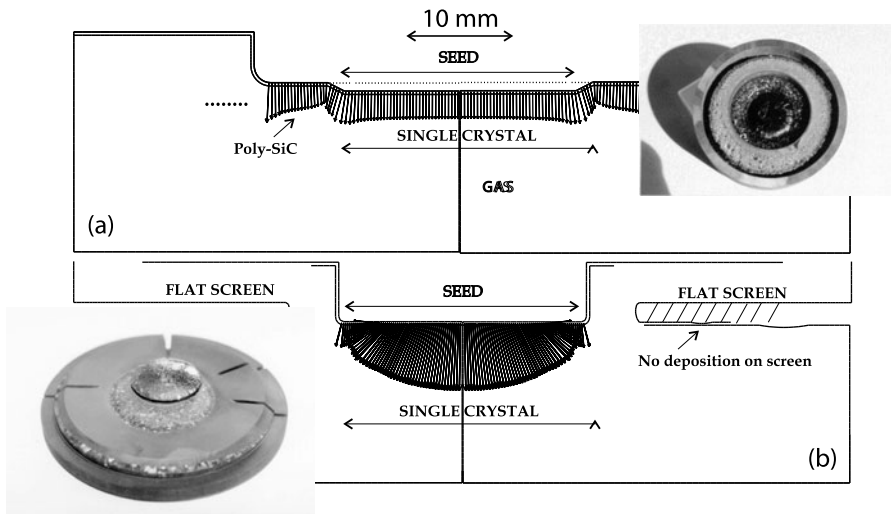


Fig. 7. Influence of the foam thickness on heat transfer [26]

is increased. It drops from 60 K with a poor insulation to 40 K. These results indicate that a small increase of the radial temperature difference (in comparison with the working temperature) is sufficient to change the growth mode and strongly deteriorate the material.

#### 2.4.5 Geometry Modification and Crystal Shape

Some years ago, with seeds of 20 mm, two different configurations of the cavity were studied, a standard configuration (Fig. 8a) and a configuration with a flat screen acting as a radiation shield (Fig. 8b) [7]. It could be advantageous for the growth of SiC crystals to prevent the formation of SiC deposits on the crucible around the seed. To provide this, it is necessary to establish a temperature field on the surface of the crucible which is everywhere higher than the temperature of the surface of the growing crystal. This provides material transport predominantly to the seed. A flat screen allows crystal growth while avoiding poly-SiC growth. Mass transport modeling shows that no deposition occurs on the screen. The crystal grows with free boundaries. But, after an initial enlargement, the ingot diameter progressively decreases. The screen becomes too far from the growing interface to ensure the same conditions as in the first growth stages. This geometry allows the growth without poly-SiC but is inadequate to ensure a long-lasting enlargement due to changes in the thermal and fluxes fields during growth.



**Fig. 8.** Initial growth flux for (a) a standard configuration and (b) a configuration with a flat screen inserted in the cavity [7]

### 2.4.6 Influence of Argon Dilution

In addition to temperature, the partial pressures of argon and reactive species are among the process key parameters. It was simulated that for an argon pressure of 3 Torr (3.99 mbar), the crystal is convex (Fig. 9) and its shape more sensitive to the temperature field. When the argon pressure is increased to 7 Torr (9.3 mbar), i.e. the dilution of reactive species is increased, the growth rate decreases and the shape less sensitive to the temperature field (the same for both cases at the beginning of the process). This example shows that it is possible to understand and quantify the final shape of the ingot [17, 19, 24, 39]. Generally, flat ingots are less subject to crack and a process less sensitive to variations of the temperature field is preferred.

These heat and mass transfer simulations may allow minimizing design problems and completing the experimental and characterization approaches. But, many technological problems as for example seed attachment, powder transformation [8, 31, 38, 39], insulation aging and quality are not yet described by simulation.

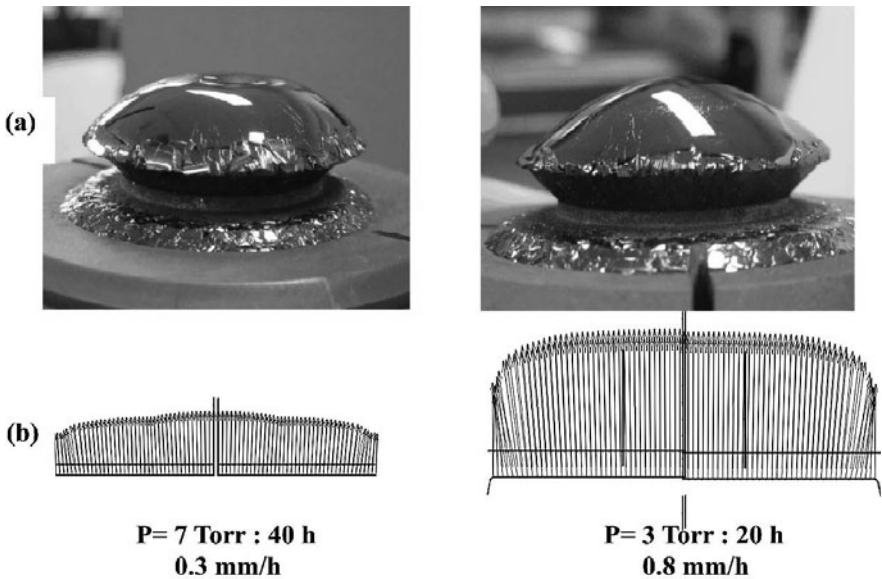


**Fig. 9.** Influence of the argon pressure on the final shape of the crystal: (a) growth experiments, (b) simulation results of the reactive flux

### 2.4.7 Scaling up of the Reactor

With heat transfer simulation, a design for the scaling up of the previous reactor can be proposed to keep similar temperature distributions. The pedestal supporting the seed is changed from 30 to 50 mm and all dimensions of the

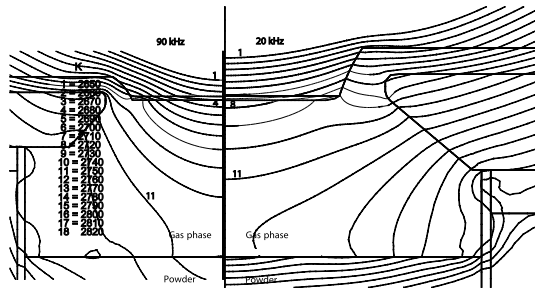


**Fig. 10.** Influence of frequency heating on the scale up of the reactor

different parts of the reactor were increased. It is possible by changing frequency to obtain a temperature distribution in the cavity of the scale up (right of Fig. 10) similar to that of the standard reactor (left of Fig. 10). This kind of quantification does not give all the keys to succeed but may allow minimizing design problems [21].

#### 2.4.8 Model Development

The present development of the simulation tools is now focused on the prediction of dislocation formation [22]–[25],[38]–[41]. Thermoelastic stresses are considered to be one of the reasons for the formation of crystalline defects (dislocations, micropipes). All thermoelasticity and plasticity [1] data are not available to implement the model of dislocation generation and multiplication already used for silicon. Experiments and measurements analysis have to be scheduled. However, with simple models, it was shown that the calculated stresses exceed considerably the critical resolved shear stress in SiC which represents an indicator for the start of plastic deformation, i.e., formation of dislocations. This indicates that the observed dislocation network should be partly caused by thermal stresses. The thermoelastic approach can be used to correlate the temperature field in the growing crystal, its shape and the spatial distribution of dislocations.

These first results show that a careful control of the shape of the boule is needed to control the temperature gradient and the subsequent stress field.

### 3 Conclusions

It is not possible to build a single model that can capture the physics and chemistry of silicon carbide growth processes that covers all time and length scales. Different types of models can be proposed, each one appropriate to a specific range, each one giving insight. The sublimation process is difficult to control. Minor geometric or experimental parameters variations considerably modify the growth of the boule. The combination of experimental and

simulation approaches is powerful to delimit material science problems from process problems and to pave the route of the future virtual prototyping of such reactors.

From a macroscopic point of view, numerical modeling is becoming mature to support effective optimization of SiC growth conditions. Present capabilities include simulation of heat and mass transfer and thermal stresses. These tools can now be used as a characterization technique for the visualization of the different fields in this “black box” process and to help process engineers in decision making. The uncertainties in material properties and data on growth kinetics limit the predictive capabilities of the numerical tool but are not sufficiently high to inhibit comparison with experimental results.

## Acknowledgements

The authors acknowledge Drs Karpov and Makarov from Soft Impact, Dr. Nishisawa from AIST Japan, Dr. Hofmann from Erlangen University, and all colleagues involved in this research area for fruitful discussions and exchanges of information in the past years.

## References

1. S.Y. Karpov, A.V. Kulik, M.S. Ramm, Y.N. Makarov: Mater. Sci. Forum, to be published (2003)
2. Y.M. Tairov, V.F. Tsvetkov: J. Cryst. Growth, **43**, 208 (1978)
3. D. Hofmann, M. Heinze, A. Winnaker, F. Durst, L. Kadinski, P. Kaufmann, Y.N. Makarov, M. Schäfer: J. Cryst. Growth **146**, 214 (1995)
4. M. Pons, E. Blanquet, J.M. Dedulle, I. Garcon, R. Madar, C. Bernard: J. Electrochem. Soc. **143**, 3727(1996)
5. S.Y. Karpov, Y.N. Makarov, M.S. Ramm: Phys. Stat. Sol. (b) **202**, 201 (1997)
6. P. Råback: *Modeling of the sublimation growth of silicon carbide crystals*, PhD thesis (Helsinki University of Technology, 1999)
7. M. Pons, M. Anikin, K. Chourou, J.M. Dedulle, R. Madar, E. Blanquet, A. Pisch, C. Bernard, P. Grosse, C. Faure, G. Basset, Y. Grange: Mat. Sci. Engng. B **30**, 18(1999)
8. D. Hofmann, M. Bickermann, R. Eckstein, M. Kölbl, S.G. Müller, E. Schmitt, A. Weber, A. Winnacker: J. Cryst. Growth **198–199**, 1005 (1999)
9. M.S. Ramm, E.N. Mokhov, S.E. Demina, M.G. Ramm, A.D. Roenkov, Y.A. Vodakov, A.S. Segal, A.N. Vorob'ev, S.Y. Karpov, A.V. Kulik, Y.N. Makarov: Mat. Sci. Eng. B **61–62**, 107 (1999)
10. D.D. Avrov, A.S. Bakin, S.I. Dorozhkin, V.P. Rastegaev, Y.M. Tairov: J. Cryst. Growth **198–199**, 1011 (1999)
11. A. Pisch, E. Blanquet, M. Pons, C. Bernard, M. Anikin, J.M. Dedulle, R. Madar: J. Phys. IV (Proceedings) **9**, 213 (1999)
12. P. Råback, R. Nieminen, R. Yakimova, M. Tuominen, E. Janzen: Mat. Sci. Forum **264–268**, 65 (1998)

13. K. Chourou, M. Anikin, J.M. Bluet, J.M. Dedulle, R. Madar, M. Pons, E. Blanquet, C. Bernard, P. Grosse, C. Faure, G. Basset, Y. Grange: *Mat. Sci. Eng. B* **61–62**, 82 (1999)
14. A. Pisch, A.M. Ferrara, C. Chatillon, E. Blanquet, M. Pons, C. Bernard, M. Anikin, R. Madar: *Mat. Sci. Forum* **338–342**, 91 (2000)
15. R.H. Ma, Q.S. Chen, H. Zhang, V. Prasad, C.M. Balkas, N.K. Yushin: *J. Cryst. Growth* **211**, 352 (2000)
16. M. Selder, L. Kadinski, F. Durst, T. Straubinger, D. Hofmann, P. Wellmann: *Mat. Sci. Forum* **338–342**, 31 (2000)
17. M. Selder, L. Kadinski, Y.N. Makarov, F. Durst, P. Wellmann, T. Straubinger, D. Hofmann, S. Karpov, M. Ramm: *J. Cryst. Growth* **211**, 333 (2000)
18. R.H. Ma, Q.S. Chen, H. Zhang, V. Prasad, C.M. Balkas, N.K. Yushin: *J. Cryst. Growth* **211**, 352 (2000)
19. S. Nishizawa, Y. Kitou, W. Bahng, N. Oyanagi, M.N. Khan, K. Arai: *Mat. Sci. Forum* **338–342**, 99 (2000)
20. S.G. Muller, R.C. Glass, H.M. Hobgood, V.F. Tsvetkov, M. Brady, D. Henshall, J.R. Jenny, D. Malta, C.H. Carter: *J. Cryst. Growth* **211**, 325 (2000)
21. M.S. Ramm, A.V. Kulik, I.A. Zhmakin, S.Y. Karpov, O.V. Bord, S.E. Demina, Y.N. Makarov: *Mat. Res. Soc. Symp. Proc.* **616**, 227 (2000)
22. I.A. Zhmakin, A.V. Kulik, S. Karpov, S.E. Demina, M.S. Ramm, Y.N. Makarov: *Diamond Rel. Mat.* **9**, 446 (2000)
23. M. Selder, L. Kadinski, F. Durst, D. Hofmann: *J. Cryst. Growth* **226**, 501 (2001)
24. M. Pons, C. Moulin, J.M. Dedulle, A. Pisch, B. Pelissier, E. Blanquet, M. Anikin, E. Pernot, R. Madar, C. Bernard, C. Faure, T. Billon, G. Feuillet: *Mat. Res. Soc. Symp. Proc.* **640**, H1.4-1 (2001)
25. D. Hofmann, M. Bickermann, D. Ebling, B. Epelbaum, L. Kadinski, M. Selder, T. Straubinger, R. Weingaertner, P. Wellmann, A. Winnacker: *Mat. Res. Soc. Symp. Proc.* **640**, H1.1 (2001)
26. C. Moulin, M. Pons, A. Pisch, P. Grosse, C. Faure, A. Basset, G. Basset, A. Passero, T. Billon, B. Pelissier, M. Anikin, E. Pernot, P. Pernot Rejmankova, R. Madar: *Mat. Sci. Forum* **353–356**, 7 (2001)
27. O. Klein, P. Philip, J. Sprekels, K. Wilmanski: *J. Cryst. Growth* **222**, 832 (2001)
28. Q.S. Chen, H. Zhang, V. Prasad: *J. Cryst. Growth* **230**, 239 (2001)
29. R.H. Ma, Q.S. Chen, H. Zhang, V. Prasad, C.M. Balkas, N.K. Yushin, S. Wang: *J. Cryst. Growth* **224**, 101 (2001)
30. M.V. Bogdanov, A.O. Galyukov, S.Y. Karpov, A.V. Kulik, S.K. Kochuguev, D. Ofengeim, A.V. Tsiryulnikov, M.S. Ramm, A.I. Zhmakin, Y.N. Makarov: *J. Crystal Growth* **225**, 307 (2001)
31. P.J. Wellmann, D. Hofmann, L. Kadinski, M. Selder, T.L. Straubinger, A. Winnacker: *J. Cryst. Growth* **225**, 312 (2001)
32. R. Yakimova, M. Syvajarvi, J.M. Dedulle, M. Pons, E. Janzen: *Proceedings First International Conference on Microgravity Research Applications in Physical Sciences*, Biotechnol (SP-454) ESA, Noordwijk, Netherlands **1**, 381 (2001)
33. A.V. Kulik, S.E. Demina, S.K. Kochuguev, D.K. Ofengeim, S.Y. Karpov, A.N. Vorob'ev, V. Bogdanov, M.S. Ramm, A.I. Zhmakin, A.A. Alonso, S.G. Gurevich, Y.N. Makarov: *Mat. Res. Soc. Symp.* **640**, 6-1 (2001)
34. S. Nishizawa, T. Kato, N. Oyanagi, K. Arai: *Mat. Sci. Forum* **389–393**, 43 (2002)

35. K. Böttcher, D. Schulz: *J. Cryst. Growth* **237–239**, 1196 (2002)
36. M. Schäfer, I. Teschauer, L. Kadinski, M. Selder: *Comp. Mat. Sci.* **24**, 409 (2002)
37. O. Klein, P. Philip: *J. Cryst. Growth* **247**, 219 (2003)
38. M.V. Bogdanov, S.E. Demina, S.Y. Karpov, M.S. Ramm, Y.N. Makarov: *Cryst. Res. Technol.* **38**, 237 (2003)
39. M.V. Bogdanov, S.E. Demina, S.Y. Karpov, A.V. Kulik, D.K. Ofengeim, M.S. Ramm, E.N. Mokhov, A.D. Roenkov, Y.N. Vodakov, Y.N. Makarov, H. Heleva: *Mat. Res. Soc. Symp.* **742**, 1–3 (2003)
40. D.I. Cherednichenko, R.V. Drachev, I.I. Khlebnikov, X. Deng, T.S. Sudarshan: *Mat. Res. Soc. Symp.* **742**, 2–18 (2003)
41. R.H. Ma, H. Zhang, S. Ha, M. Skowronski: *J. Cryst. Growth* **252**, 523 (2003)
42. N. Oyanagi, S. Nishizawa, T. Kato, H. Yamaguchi, K. Arai: *Mat. Sci. Forum* **338–342**, 75 (2000)
43. P.J. Wellmann, M. Bickermann, D. Hofmann, L. Kadinski, M. Selder, T.L. Straubinger, A. Winnaker: *J. Cryst. Growth* **216**, 263 (2000)
44. S.G. Muller, R. Eckstein, J. Fricke, D. Hofmann, R. Hofmann, R. Horn, H. Mehling, O. Nilsson: *Mat. Sci. Forum* **264–268**, 623 (1998)
45. Y.E. Egorov, A.O. Galyukov, S.G. Gurevich, Y.N. Makarov, E.N. Mokhov, M.G. Ramm, M.S. Ramm, A.D. Roenkov, A.S. Segal, Y.A. Vodakov, A.N. Vorob'ev, A.I. Zhmakin: *Mat. Sci. Forum* **264–268**, 61 (1998)
46. S.Y. Karpov, A.V. Kulik, I.A. Zhmakin, Y.N. Makarov, E.N. Mokhov, M.G. Ramm, M.S. Ramm, A.D. Roenkov, Y.A. Vodakov: *J. Crystal Growth* **211**, 347 (2000)
47. A.S. Segal, A.N. Vorob'ev, S.Y. Karpov, E.N. Mokhov, M.G. Ramm, M.S. Ramm, A.D. Roenkov, Y.A. Vodakov, Y.N. Makarov: *J. Cryst. Growth* **208**, 431 (2000)
48. A. Pisch, E. Blanquet, M. Pons, C. Bernard, J.M. Dedulle, R. Madar: *Mat. Sci. Forum* **353–356**, 61 (2001)
49. R. Madar, M. Pons, J.M. Dedulle, E. Blanquet, A. Pisch, P. Grosse, C. Faure, M. Anikin, C. Bernard: *Mat. Sci. Forum* **338–342**, 25 (2000)

# Defect Formation and Reduction During Bulk SiC Growth

N. Ohtani, M. Katsuno, T. Fujimoto, and H. Yashiro

## 1 Introduction

The development of silicon carbide (SiC) bulk crystal growth technology in the last decade has brought about tremendous progress in the techniques of growing large high-quality SiC bulk crystals. SiC crystals up to four inches in diameter have been successfully demonstrated, and three-inch SiC substrates have already been brought to market. However, the commercialization of SiC devices is still largely limited due to relatively high density of structural defects in SiC bulk crystals, and thus it is abundantly clear that the further successful development of SiC semiconductor technology relies on achieving an understanding of the defect formation processes during SiC bulk crystal growth. This paper aims to describe the current understanding of defect formation during SiC bulk crystal growth, and it also tries to provide strategies to reduce the crystallographic defects in SiC bulk crystals.

The first part of this paper deals with the seeded physical vapor transport (PVT) growth of bulk SiC single crystals in the conventional  $\langle 0001 \rangle$   $c$ -axis direction. One of the major problems with SiC bulk crystals grown along the  $c$ -axis is “micropipe” defects. Over the past several years, a significant reduction in micropipe density has been achieved and SiC substrates with a micropipe density of less than a few tens per square centimeters have been commercially available. However, micropipes are still a major obstacle limiting the widespread use of SiC devices, and thus understanding of the origin of micropipes is of the utmost importance to extend the successful application of SiC technology. In addition, the investigation of structural defects other than micropipes, such as dislocations and crystal mosaicity (domain structure), is at an even earlier stage and thus little is known about the origins of these defects. In the first part of this paper, we discuss the causes and formation mechanisms of micropipes, dislocations and mosaicity in bulk SiC crystals and try to relate the obtained knowledge to reduction of these crystallographic defects.

The second part of this paper concentrates on the PVT growth of bulk SiC crystals perpendicular to the  $c$ -axis. Many aspects are different between the growth parallel and perpendicular to the  $c$ -axis. The types and distribution of crystallographic defects in SiC crystals grown in the  $[1\bar{1}00]$  and  $[11\bar{2}0]$  directions are largely different from those of crystals grown along the

*c*-axis. A major advantage of these growth directions is that the growth prevents micropipe formation. However, the growth instead tends to yield a large number of basal plane stacking faults in SiC crystals. It was found that the density of the stacking faults largely depends on the crystal growth direction and polytype. Based on these results, we discuss the defect formation process during growth in the  $[1\bar{1}00]$  and  $[11\bar{2}0]$  directions and demonstrate successful reduction of stacking fault density in SiC bulk crystals.

## 2 Growth Along the $\langle 0001 \rangle$ *c*-Axis Direction

### 2.1 Micropipes

#### 2.1.1 General Features

Micropipes are hollow tubes penetrating SiC single crystals along their *c*-axis and very often occur in PVT grown SiC crystals. They are interpreted in the framework of Frank's model of hollow core dislocations [1]. Frank predicted that a dislocation whose Burgers vector exceeds a critical value should have a hollow tube at the core. By balancing the elastic dislocation strain energy released by the formation of a hollow core against the energy of the free surface, Frank showed that for isotropic linear elasticity and a cylindrical core, the equilibrium core radius  $r$  is

$$r = \frac{\mu b^2}{8\pi\gamma}, \quad (1)$$

where  $\gamma$  is the surface energy,  $\mu$  is the shear modulus and  $b$  is the Burgers vector.

Figure 1 shows an atomic force microscope (AFM) image of the (0001)Si surface of 6H-SiC, where a spiral step ending at a micropipe is visible. The almost archimedean circular spiral step is characterized by a large step height

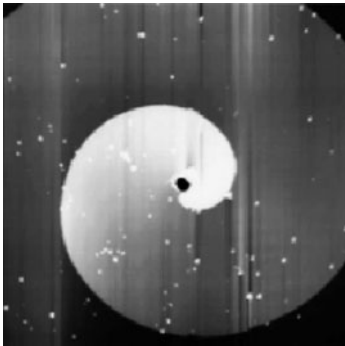


**Fig. 1.** AFM image of a growth spiral due to a micropipe on the 6H-SiC(0001)Si surface. The scanning size was  $40\text{ }\mu\text{m} \times 40\text{ }\mu\text{m}$ , and the step height was 13.5 nm, which is nine times the *c* lattice parameter of 6H-SiC

(13.5 nm corresponding to nine times the unit  $c$  lattice parameter of 6H-SiC) due to the large Burgers vector of the micropipe.

Micropipes in PVT grown SiC crystals were first recognized as fatal defects by Koga et al. [2] in 1992. Koga et al. fabricated blue light-emitting diodes (LEDs) using PVT grown SiC crystals and found that the leakage current in blue LEDs was caused by hollow tube defects penetrating the entire crystals along the  $c$ -axis. They also reported that micropipes cause large hexagonal etch pits on the etched (0001)Si surface. Micropipes are replicated into the device epitaxial layers and become a critical defect for SiC devices [3].

Several groups have confirmed that the Frank relationship (1) between the radius and the Burgers vector of hollow core dislocation is approximately established for micropipes in SiC crystals, corroborating the assumption that micropipes are hollow core dislocations. Heindl et al. [4] measured the radii of micropipes on the (0001) surface of PVT grown 6H-SiC crystals and the step height of the accompanying growth spirals by AFM. Assuming that the obtained step height is equal to the Burgers vector, i.e. that micropipes are pure screw dislocations, they fitted Frank's theory of hollow core dislocations to the obtained experimental results as modified with regard to kinetic effects by Cabrera and Levine [5], and calculated the values for surface energy and supersaturation near the emergence point of a micropipe.

Based on their detailed AFM studies of micropipes, Heindl et al. [6] argued the dislocation content of micropipes. They discussed the obtained surface energy for the inner surface of micropipes and found that it appears too small and physically unreasonable. They claimed that micropipes are mixed-type dislocations and not pure screw dislocations, and that the apparent small surface energy for the inner surface of micropipes resulted from the underestimate of the Burgers vector of micropipes, which occurs when the edge components of micropipes do not contribute to the surface step height. On the other hand, Huang et al. [7], using synchrotron white beam X-ray topography (SWBXT), provided evidence that micropipes are pure screw dislocations with a large Burgers vector. They analyzed a series of micropipe images in comparison with the corresponding simulated images and concluded that micropipes are pure screw dislocations. Using the same technique combined with scanning electron microscopy (SEM), they also revealed that the magnitude of the Burgers vector of micropipes in 6H- and 4H-SiC crystals are several times the unit  $c$  lattice parameter, while no discernible hollow cores are detected for elementary  $c$  screw dislocations for 6H-SiC and for elementary  $c$  and  $2c$  screw dislocations for 4H-SiC, respectively [8].

PVT grown SiC bulk crystals contain micropipe defects of typically  $\sim 10^2 \text{ cm}^{-2}$ , and several empirically determined characteristics have been reported. The micropipe formation has been related to the purity of the starting SiC source material [2], and the generation and propagation of micropipes are also sensitive to specific seeding techniques employed and to growth parameters, such as pressure and temperature. Micropipes appear to originate

in the vicinity of the seed crystal, lie generally along the growth direction, and are often associated with low angle grain boundaries [9].

An important aspect of micropipes is that while they are forming during growth, simultaneous processes also occur which reduce their concentration, such as dissociation, coalescence, recombination and transformation [10, 11]. These processes are largely controlled by growth kinetics rather than equilibrium thermodynamics, and many of them are believed to be surface-mediated processes [12]. In principle, a dislocation with a Burgers vector  $\mathbf{b} = n\mathbf{c}$  ( $\mathbf{c}$  being the smallest translation vector) is energetically unfavorable compared to the distribution of  $n$  elementary dislocations with a Burgers vector  $\mathbf{c}$ . The fact that micropipes appear stable and propagate in the crystal implies that a large kinetic energy barrier exists to nucleate a dislocation in SiC crystals adjacent to the micropipe [13].

### 2.1.2 Causes of Micropipes

Several possible causes for the formation of micropipes exist, and are categorized into three groups: (1) thermodynamic, (2) kinetic, and (3) technological causes [14, 15]. For example, the thermodynamic causes include thermoelastic stress due to non-uniform heating, while the kinetic causes are related to the nucleation process and growth surface morphology. In all these cases, one must also consider the technological aspects, such as the seed surface preparation and contamination of the growth system.

Schulze et al. [15] demonstrated micropipe-free growth of 6H-SiC bulk crystals on a micropipe-free Lely platelet (seed crystal) and indicated that the thermal gradient inside the growth crucible is a relevant process parameter for micropipe-free crystal growth. They supposed that the low thermal gradient ( $\leq 5$  K/cm) resulted in near-thermal equilibrium growth conditions, which largely suppressed improper nucleation processes. Under these growth conditions, the achievable growth rate was limited to be less than 0.27 mm/h.

Tsvetkov et al. cited evidence pointing to nucleation of micropipes occurring as a result of growth instabilities that lead to the formation of secondary phase precipitates such as graphite particles and silicon droplets [14]. This was later borne out by the observation of Glass et al. [10], who observed micropipes in SiC crystals that were associated with graphite particles and silicon droplets. They have ascribed the causes of graphite particles and Si droplets, which have lead to micropipe streaming in the crystals, to a technological issue and growth instabilities, respectively.

Another example of a cause of micropipe formation is illustrated in Fig. 2. The figure shows an optical micrograph of a 6H-SiC crystal vertically sliced along the  $c$ -axis growth direction, where polytype instabilities (15R-SiC polytype inclusions) cause micropipes. They are visible as vertical line defects in the micrograph, and a multitude of micropipes emerge slightly above the non-basal plane interfaces between the 6H and 15R polytypes. Different polytypes

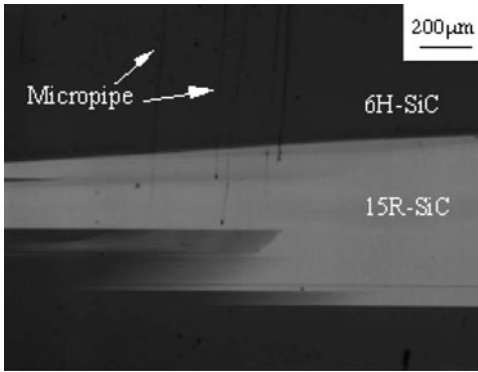


**Fig. 2.** Longitudinally sliced 6H-SiC crystal along the growth direction, showing a multitude of micropipes emerging at the polytypic boundaries between 6H and 15R

possess different stacking sequences along the  $c$ -axis and thus cause a disregistry in the atomic bonding when they have a non-basal plane interface. This disregistry and associated large localized strains are relieved by the formation of micropipes at the interface.

### 2.1.3 Micropipe Formation Models

To date, several models have been proposed to elucidate the formation mechanism of micropipes [16]–[21]. They are classified into two groups: one is mechanisms that generate depressions or voids at the growing surface, which subsequently or almost simultaneously attract dislocations to stabilize voids (hollow cores) during growth; and the other is mechanisms that lead to an extremely large Burgers vector and the hollow core is a consequence of the energy reduction according to Frank's theory.

Giocondi et al. [17] proposed a surface depression model that tried to explain an accumulation of elementary  $c$  screw dislocations via the formation of a surface depression surrounded by a macrostep at the growing surface. Macrosteps, which are very often observed on the SiC{0001} surface, sweep up screw dislocations during growth by shifting their emergence points in the direction of motion. Once the macrostep stops at an obstacle, e.g. secondary phase precipitate, it bows around the obstacle, reunifies and moves further as a reformed complete macrostep. Consequently, the obstacle is surrounded by a macrostep forming a depression, into which the screw dislocations have been collected.

On the other hand, a mechanism that leads to a dislocation with an extremely large Burgers vector was elucidated by Pirouz [18]. He pointed out that the twist-type misorientation existing in SiC crystals plays a major role in the micropipe formation. PVT grown SiC crystals have a mosaic structure, with all the domains having a strong [0001] texture. The boundaries among these domains may have both the tilt and twist nature of misorientation, and a small twist misorientation between the adjacent domains is accommodated by arrays of screw dislocations lying on the boundary plane. Pirouz

considered a triple junction of such twist-type low angle grain boundaries, and that at the triple junction, there will be a screw dislocation with  $\mathbf{b} = 3\mathbf{c}$  when all the twist boundaries are in the same sense. Since the magnitude of the Burgers vector of the  $\mathbf{b} = 3\mathbf{c}$  screw dislocation exceeds the critical value (2–3 nm) for the dislocation core to be empty, this junction dislocation will become a hollow core dislocation (micropipe). This relatively small micropipe will further attract elementary  $c$  screw dislocations, by the image force mechanism [18], to become a larger diameter micropipe.

Ohtani et al. [20] recently proposed a different story for micropipe formation, i.e. a surface step model for the micropipe formation in SiC crystals, taking into account several important aspects experimentally observed for micropipe formation. Micropipes are very often observed at the foreign polytype and/or secondary phase inclusions during growth, where high density elementary  $c$  screw dislocations are introduced and the spiral steps emanating from them are very closely located and interact with each other. The model assumes that the strong repulsive interaction between these steps [22] coalesces the underlying elementary  $c$  screw dislocations through the energetic bunching of the spiral steps.

It was found that there exists a strong repulsive elastic (long-range) interaction between the unit cell size steps on the SiC{0001} surface [22]. The elastic repulsive force (per unit step length) between steps at the surface of an isotropic solid is proportional to the square of the step height and the surface tension at the step (step stiffness) [23]. For SiC{0001}, the height of steps is often as large as the  $c$  lattice parameter (1.512 nm for 6H-SiC and 1.005 nm for 4H-SiC) [12], so that the step repulsive interaction is enhanced by one to two orders of magnitude compared to those on Si(111) and Si(001). Furthermore, SiC{0001} has proved to have considerable resistance to chemical attack or oxidation, which implies that a highly stable step structure with a large stiffness is established on the SiC{0001} surface.

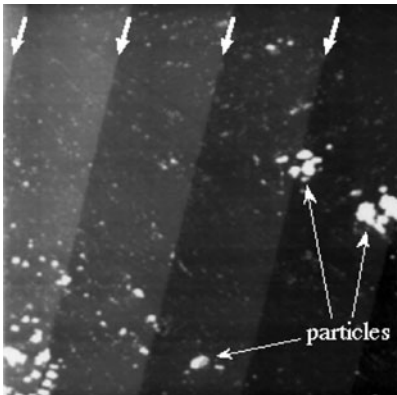


**Fig. 3.** 5  $\mu\text{m} \times 5 \mu\text{m}$  AFM image of the stepped structure of the 6H-SiC(0001)Si surface. Small protrusions observed on the entire surface are foreign particles that adhered to the surface after growth. The step down direction is from the *upper left to the lower right*. Steps of a height equal to the unit  $c$  lattice parameter (1.512 nm) were regularly arranged; the positions of the steps are indicated by *short arrows*

Figure 3 shows an AFM image of extremely regularly arranged surface steps on the  $6H$ -SiC(0001) surface where the observed area was  $5\text{ }\mu\text{m} \times 5\text{ }\mu\text{m}$ . The height of the observed steps is equal to the unit  $c$  lattice parameter of  $6H$ -SiC. The edges of steps are fairly straight and the local distribution of distances between the steps is extremely uniform, which is a clear manifestation of the strong repulsive interaction between steps on the SiC(0001) surface [22].

For simplicity, two elementary  $c$  screw dislocations having the same sign Burgers vector are considered (the discussions below can be extended to include the cases that involve more than two screw dislocations). Each screw dislocation provides a spiral step of unit cell height as denoted by  $A$  and  $B$  in Fig. 4a. If the dislocations are placed very close together, the spiral steps are intermixed and arranged alternately, as schematically illustrated in Fig. 4a. In this step system, steps  $A$  and  $B$  interact via the strong repulsive force between them, and this repulsive interaction induces the energetic bunching of steps  $A$  and  $B$ .

In general, coalescence of steps, i.e. step bunching, costs more energy than an equivalent height of a distribution of isolated steps. However, when the steps are located close to each other (Fig. 4b), this energy is outweighed by the decrease in step repulsive energy since the coalescence of steps  $A$  and  $B$  increases the average separation between the steps (Fig. 4c).

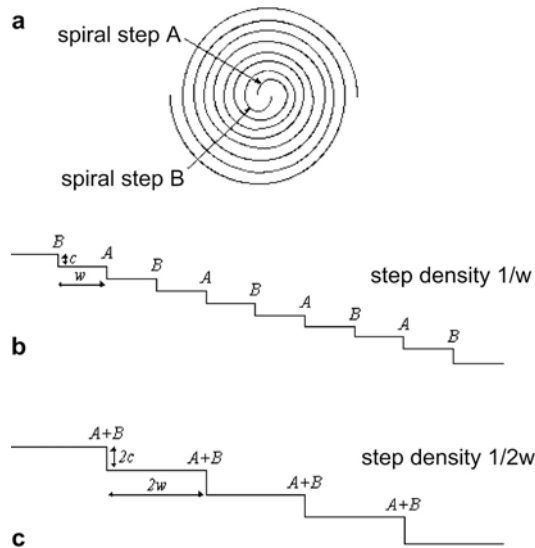


**Fig. 4.** Schematic diagrams of (a) the intermixed growth spirals from two adjacent screw dislocations with the same-sign Burgers vector, and a step train comprising alternately arranged steps  $A$  and  $B$  (b) before and (c) after the energetic step bunching

The energetic bunching of spiral steps drives the coalescence of the two adjacent screw dislocations at their centers, giving rise to a screw dislocation with a Burgers vector  $\mathbf{b} = 2\mathbf{c}$ . It should be noted that the coalescence of dislocations only occurs via the crystal growth process, and thus the parts of the screw dislocations already existing in the crystal before the spiral steps are bunched are never coalesced.

It is obvious that the coalescence of dislocations occurs at the cost of bulk elastic energy. In terms of energetics, the energy gain by the coalescence of spiral steps needs to overcome the energy cost due to the elastic strains to form a screw dislocation having a twice larger Burgers vector  $\mathbf{b} = 2\mathbf{c}$  (super screw dislocation). This condition is satisfied at the initial stage of coalescence, since the coalesced length of dislocations is small; the coalescence is limited to a near surface region. When the growth proceeds and the coalesced length of dislocations becomes larger, the energy cost due to the elastic strains tends to be greater than the energy gain due to the reduced step repulsive energy. At this stage, however, the core substance is evaporated, releasing the large elastic strains at the core, and this hollow core formation further stabilizes the super screw dislocation (micropipe) and kinetically prevents it from dissociating.

#### 2.1.4 Micropipe Dissociation and Reduction

As discussed above, there exists a large kinetic energy barrier against micropipes being dissociated; however there is a significant suggestion that this kinetic barrier can be reduced by optimizing the growth conditions, and micropipes are dissociated [24]. For example, a micropipe can be dissociated into a micropipe with a slightly smaller Burgers vector *plus* one elementary  $c$  screw dislocation as schematically shown in Fig. 5. It is worth noting that this dissociation process only occurs during crystal growth and cannot be

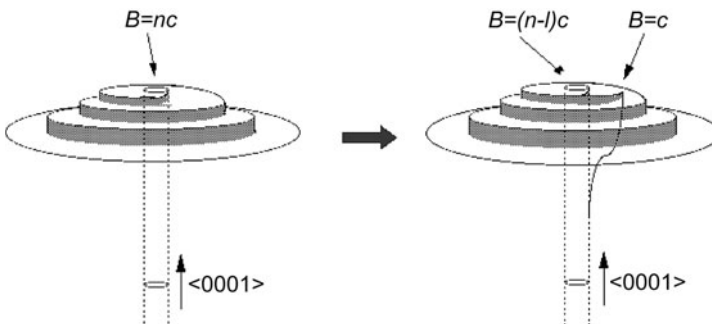


**Fig. 5.** Schematic drawing of micropipe dissociation process, where a micropipe is dissociated into a micropipe with a slightly smaller Burgers vector *plus* one elementary  $c$  screw dislocation

driven by post-growth processes such as annealing [20]. In this respect, micropipe dissociation is assumed to be a surface-mediated process, and the spiral growth mechanism on the SiC{0001} surface plays an important role in the dissociation process of micropipes.

The lateral advance of multiple unit cell height spiral steps emanating from micropipes during growth would become unstable under the optimized growth conditions. The changes in growth conditions may affect the growth kinetics and also the characteristics of spiral steps, such as step energy and stiffness. The unstable multiple unit cell height spiral steps are transformed into fully or partially dissociated spiral steps, which leads to full or partial dissociation of micropipes located at their centers, as illustrated in Fig. 5.

Recently Kamata et al. reported that a similar dissociation process of micropipes occurs during SiC homoepitaxial thin film growth by chemical vapor deposition (CVD) [25]. They conducted deliberate etching experiments and defect analysis to conclude that micropipes are structurally transformed into several closed-core elementary *c* screw dislocations during CVD thin film growth of SiC. The probability of micropipe dissociation increased from around 1% to 98% as the C/Si ratio of the reactant gasses for CVD growth decreased from 0.9 to 0.6 [26]. They discussed the dissociation mechanism of micropipes during CVD growth and claimed the importance of the step-flow growth mode and also the curvature of steps that are pinned at micropipes. Their results clearly suggested that the C/Si gas ratio during CVD growth influences the micropipe dissociation process through the modification of the growth kinetics (spiral growth *versus* step-flow growth) and the characteristics of surface steps.

Recent advances in the PVT growth technique have made possible a highly-controlled growth process of SiC bulk crystals and allowed us to achieve a reproducible crystal growth under the optimized growth conditions, which has led to a continuous reduction in micropipe density over the past several years, and recent demonstration of low micropipe density ( $1\text{--}10\text{ cm}^{-2}$ ) SiC substrates [27, 28].

## 2.2 Dislocations

### 2.2.1 Grown-in Type Dislocations

As described in the previous section, a significant reduction in micropipe density has been successfully demonstrated by several groups. However, while the micropipe density is decreasing, SiC device commercialization is still largely limited by the presence of crystallographic defects other than micropipes. In particular, dislocations are another critical defect for the implementation of high blocking voltage ( $\geq 2000\text{ V}$ ) SiC devices [29]. In this section, we overview several dislocation processes occurring during growth and/or post-growth of hexagonal SiC bulk crystals.

Grown-in type dislocations in SiC bulk crystals have been studied by several authors [13, 16, 19, 30]. Dudley et al. have tried to explain the nucleation of screw dislocations at the SiC bulk growth by considering the lateral growth over secondary phase precipitates on the growing surface [19]. When the surface precipitate is overgrown, the growth fronts may meet at the precipitate and coalesce with misalignment under the influence of small stresses. In order to accommodate this misalignment, screw dislocations of opposite signs are created, which have Burgers vector magnitudes equal to the magnitude of the misalignment. Their model is based on the observation of micropipes (super screw dislocations) often originating at secondary phase inclusions in PVT grown SiC crystals.

Threading edge dislocations are present in SiC crystals with a density between  $10^3$  to  $10^5$   $\text{cm}^{-2}$  and frequently appear in arrays corresponding to low angle grain boundaries. Takahashi et al. investigated the dislocation structure of 6H-SiC crystals grown in the  $[000\bar{1}]$  direction by X-ray topography [13]. They found that the growth inherited the defects existing in the seed crystal and also introduced, at the initial stage of growth, an additional high density of threading dislocations extending along the  $\langle 0001 \rangle$  growth direction. Both screw and edge-type threading dislocations were introduced at the foreign polytype inclusions during growth, where non-basal plane interfaces between different polytypes contain crystallographic imperfections that are a serious cause of grown-in dislocations.

Defect formation at the initial stage of PVT growth of SiC has been deliberately examined by Sanchez et al. using transmission electron microscopy (TEM), AFM, X-ray topography and defect selective etching [30]. They observed the formation of basal plane stacking faults at the initial stage of growth, with densities showing a good correlation with the threading dislocation density. Threading screw dislocations tended to form in pairs with opposite Burgers vectors, and these results bear out the pair generation model of screw dislocations by Dudley et al. [19]. Sanchez et al. [30] also showed pair generation of edge dislocations at the stacking faults nucleated at the initial stage of growth. If partial dislocations encompassing the stacking faults are Shockley type, then resulting threading dislocations would have an edge character. Frank type partial dislocations would result in screw type threading dislocations. The stacking fault formation was attributed to nucleation of two-dimensional (2D) islands on the surface of seed crystal, and the density of threading dislocations markedly decreased as the growth rate decreased and at growth on the off-oriented seed crystal.

All the above results combine to clearly indicate that grown-in type dislocations are a major source of threading dislocations in PVT grown SiC bulk crystals. Most of them propagate from a seed crystal and are caused by secondary phase and/or foreign polytype inclusions and stacking fault formation due to 2D nucleation process. The nucleation density of threading dislocations largely depends on the crystal growth conditions.

Grown-in type basal plane dislocations were investigated by Wang et al. [31] using SWBXT. They have revealed a basal plane dislocation network in PVT grown SiC crystals. Transmission topographs clearly revealed a number of glide dislocations, connecting or emanating from micropipes, which consist of a dislocation network lying in the (0001) basal plane. Wang et al. argued the relationship between micropipes and the glide dislocations on the basal plane. Micropipes running along the growth direction always intersect the growth front, a free surface, and the image force due to the existence of the free surface, then, can provide a significant shear stress along the basal plane because of the large magnitude of the Burgers vector of micropipes. This shear stress may in turn generate glide dislocations with much smaller Burgers vectors on the basal plane *via* Frank-Read type mechanism of dislocation multiplication. These basal plane dislocations would be weakly dissociated into Shockley type partial dislocations on the (0001) basal plane, and a large difference between the mobilities of the dissociated Si core and C core partial dislocations has been reported [32]

### 2.2.2 Stress-Induced Dislocations

Generally, the distribution of dislocations in a semiconductor crystal is well correlated with the distribution of thermal stress within the crystal induced by non-uniform temperature distribution during post-solidification cooling. For hexagonal SiC crystals, the basal plane (0001)(11 $\bar{2}$ 0) glide system is most easily activated. Fujita et al. studied the deformation behavior of 6H-SiC single crystals up to 1600°C and determined two critical stresses as a function of temperature [33]. One is the critical shear stress resolved to the basal plane. The other is the critical normal stress exerted on the crystal to activate the prism plane slip system. The two critical stresses differ significantly and the latter is about 30 times greater than the former. This is due to a large Peierls energy for the prism plane slip in hexagonal SiC.

Both the basal plane slip and prism plane slip bands have been observed in PVT grown SiC crystals by Ha and co-workers [34, 35]. Ha et al. observed arrays or bands of oval-shaped etch pits on the etched vicinal (0001)Si surface of PVT grown 4H-SiC crystals [34]. The characteristic oval shape is due to the shallow angle between a dislocation line confined in the basal plane and an off-cut wafer surface. The long axis of an etch pit is approximately parallel to the corresponding dislocation line. The arrays were aligned parallel to each other and perpendicular to the off-cut direction, and based on the characteristic distribution, they were interpreted as the basal plane slip bands due to high-temperature deformation during the growth or post-growth processes; thermoelastic stress was proposed as a plausible cause of the deformation. Ha et al. have also experimentally confirmed prismatic slip bands in PVT grown SiC crystals [35]. They observed rows of etch pits extending along the  $\langle 11\bar{2}0 \rangle$  directions on the etched (0001) surface in vicinity of micropipes, mis-oriented grains and polytypic inclusions at the periphery of the crystals. The

rows of etch pits correspond to arrays of threading dislocations approximately extending along the  $c$ -axis, and formed a band configuration which is characteristics to slip band dislocations induced by generation and multiplication of dislocations under thermal stress.

The presence of thermoelastic stress during PVT growth of SiC crystals has been modeled by several research groups [36]–[39]. If a crystal is grown along the  $c$ -axis in the growth apparatus with cylindrical symmetry, the stress distribution is going to be axisymmetric. Numerical modeling revealed that the magnitude and distribution of thermoelastic stress during SiC bulk growth largely depend on the boundary conditions that the grown crystal experiences during growth [39]. The density of basal plane slip bands observed by Ha et al. was well correlated with the calculated shear stress distribution across the wafer [34]. Furthermore, Hobgood et al. reported that the radial distribution of  $\langle 0001 \rangle$  threading dislocations across a PVT grown 6H-SiC wafer was also well correlated with radial distribution of the resolved shear stress in the  $(0001)\langle 11\bar{2}0 \rangle$  glide system [37]. They measured distributions of shallow etch pit density on the etched  $(0001)$  6H-SiC wafer surface and found that the radial distribution of etch pits across the wafer diameter exhibited a characteristic W-pattern. This spatial variation is consistent with predictions of the radial dependence in resolved shear stress stemming from excess thermoelastic stresses during growth. However, the above result naturally raised a question why there was a good correlation between the  $\langle 0001 \rangle$  threading dislocation density and the stress distribution in the  $(0001)\langle 11\bar{2}0 \rangle$  glide system. The next section discusses a possible explanation to this question.

### 2.2.3 Dislocation Conversion

A newly revealed dislocation conversion process during SiC crystal growth has recently been reported by Ha et al. [40]. They have observed that during CVD epitaxial growth of SiC, basal plane dislocations in the substrates convert into threading edge dislocations in the epilayers [40]. The conversion was interpreted as a result of the image force effect in the epilayer between flowing growth steps and basal plane dislocations. A majority of basal plane dislocations in the substrates (both in the slip bands and background) were converted into threading edge dislocations in the subsequently grown epilayers.

It should be noted that this mechanism can be operative in PVT growth of SiC bulk crystals and can increase the threading edge dislocation density. The conditions similar to the epitaxial growth on a vicinal substrate are also established for PVT growth of SiC bulk crystals, where the growth front is domed (curved). Basal plane dislocations existing in bulk SiC crystals bend toward the  $c$ -axis direction during growth by the interaction with the growing curved surface and are structurally converted into threading edge dislocations approximately extending along the  $c$ -axis.

As described in Sect. 2.2.1, most threading dislocations extending along the  $\langle 0001 \rangle$  growth direction observed in PVT grown SiC bulk crystals are likely to be grown-in type dislocations; however the dislocation conversion could be another major source of threading dislocations. If significant portions of basal plane slip band dislocations are converted into threading edge dislocations, it reasonably corroborates the observation of the W-pattern distribution of etch pits due to the threading dislocations described in Sect. 2.2.2.

## 2.3 Crystal Mosaicity (Domain Structure)

### 2.3.1 General Features

Crystal mosaicity (domain structure) is commonly observed in the PVT grown bulk SiC single crystals produced to date. The crystals typically contain slightly misoriented domains bordered by regions of high dislocation density. These domains are fully replicated into the device epitaxial layers by a thin film growth process, and consequently the mosaicity of the substrate has a major impact on the performance of SiC devices made on it. The mosaicity in SiC single crystal wafers was first reported by Glass et al. [41]. They examined commercially available 6H-SiC substrates by high-resolution X-ray diffractometry (HRXRD) and reciprocal space mapping, and the results indicated a presence of domain structure in SiC crystals, with varying domain densities. The X-ray diffraction curves obtained from the substrates showed multiple peaks distributed over several hundred arcseconds, while a single diffraction peak with a full width at half maximum (FWHM) of 15 arcsec was obtained for Lely platelets grown *via* the non-seeded sublimation process. They ascribed this difference to a lower growth temperature and higher degree of supersaturation in PVT (seeded sublimation) growth process than in the Lely (non-seeded sublimation) growth process; these growth conditions are expected to increase the nucleation density on the growing surface. Following work by Glass et al. [41], Tuominen et al. [42] conducted a series of X-ray rocking curve measurements for commercial 4H-SiC substrates by varying the beam spot size for a constant 0004 reflection and changing the order of reflection at a constant beam spot size. They obtained very similar results to those for 6H-SiC substrates reported by Glass et al.

Ellison et al. [43] studied the relationship between the warpage and mosaic structure of SiC substrates. They found that the warpage of SiC substrates results from a convolution of the surface preparation and intrinsic properties inherited from the bulk growth process. A high defect content present in the substrates easily enables them to deform plastically (crystal bending). The warpage of SiC wafers severely hampers the full wafer processing of micron or sub-micron optical lithography patterning, and the final quality of SiC epilayers is also expected to be influenced by the crystal bending of the underlying substrates.

### 2.3.2 Causes of Mosaicity

Several causes and mechanisms of the misoriented domain formation in PVT grown SiC crystals have been proposed and discussed. Glass et al. [41] found that the micropipe density was approximately consistent with the number of multiple peaks or the magnitude of broadening of X-ray rocking curves (over several hundred arcseconds), and thus suggested the possibility that micropipes are the main cause of the mosaicity in PVT grown bulk SiC crystals. More recently, Pirouz [18] discussed the dislocation systems lying on a prism plane, e.g.,  $\{11\bar{2}0\}$  or  $\{1\bar{1}00\}$  plane. As discussed in Sect. 2.2.2,  $\{11\bar{2}0\}$  and  $\{1\bar{1}00\}$  are not usually activated to be a slip plane in hexagonal SiC polytypes, even though the low angle grain boundaries commonly observed in PVT grown SiC crystals lie in the  $\{11\bar{2}0\}$  plane, which implies that the dislocations comprising the low angle grain boundaries are not introduced by thermal stress after growth, and that they are grown-in type dislocations and rather introduced during growth by the growth process itself. Pirouz [18] and Glass et al. [10] claimed that the strong  $[0001]$  texture in PVT grown SiC crystals originates in a spiral growth mechanism. The interaction between two growth spirals can be assumed to result in low angle grain boundaries due to twist misorientation between the two growth spirals.

Recently, Katsuno et al. [44] revealed that micropipes and elementary  $c$  closed-core screw dislocations only slightly affect the shape of the X-ray rocking curves. The rocking curves obtained from regions that contained micropipes (density  $\sim 200\text{--}600\text{ cm}^{-2}$ ) and/or elementary  $c$  closed-core screw dislocations (density  $\sim 2 \times 10^4\text{ cm}^{-2}$ ) showed a relatively narrow single diffraction peak with an FWHM of 13–27 arcsec. The width of the rocking curves slightly increased with the increase of micropipe density. However, even for crystal areas with a micropipe density of  $600\text{ cm}^{-2}$ , the width remained less than 30 arcsec and the rocking curves did not show multiple peaks. These results preclude the possibility of micropipes being the cause of the strong (0001) mosaicity present in SiC bulk crystals.

Katsuno et al. [45] found that PVT grown SiC crystals have a strong  $[0001]$  texture around etch pit rows due to edge dislocation walls aligned along  $\langle 1\bar{1}00 \rangle$  directions. Figure 6 shows the 0006 X-ray rocking curves obtained from a region that accommodated two parallel etch pit rows (coupled low angle grain boundaries) with the incident plane (a) parallel and (b) perpendicular to the etch pit rows. The rocking curve with the incident plane parallel to the boundaries shows a narrow single diffraction peak (Fig. 6a), while the one with the incident plane perpendicular to the boundaries shows a much broader peak (40–80 arcsec), often splitting into multiple peaks as shown in Fig. 6b. Based on these results, Katsuno et al. concluded that the tilting of the (0001) lattice plane has a rotation axis parallel to both the boundary plane and the (0001) basal plane, which is quite contradictory to the twist misorientation due to the growth spiral interaction modeled by Glass et al.

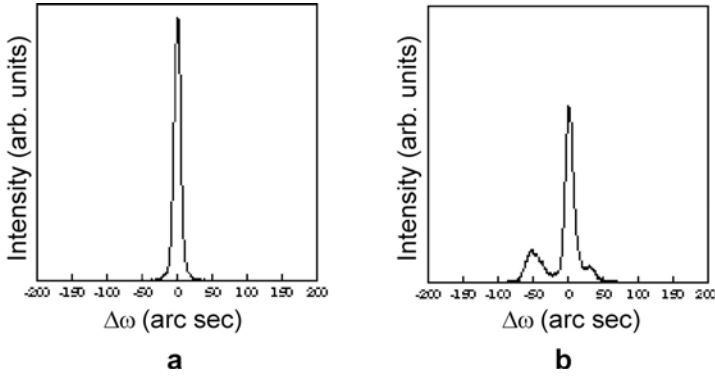


**Fig. 6.** 0006 X-ray rocking curves obtained from two parallel etch pit rows with the incident plane (a) parallel and (b) perpendicular to the etch pit rows

[10] and Pirouz [18]. The twist misorientation causes the tilting of the (0001) basal plane with a rotation axis perpendicular to the boundary plane.

The tilting of the (0001) basal plane of SiC bulk crystals has been discussed by Katsuno et al. [45] and Ha et al. [34]. Katsuno et al. [45] have attributed the tilting of the (0001) basal plane to the inclination of the boundary dislocations from the  $c$ -axis. The polygonization of edge dislocations along  $\langle 1\bar{1}00 \rangle$  directions requires glide and climb motions of the dislocations. The glide and climb of dislocations are temperature-activated processes [46], and thus they most probably occur during growth. In the course of these motions, the edge dislocations predominantly lie along the  $c$ -axis but often jog toward  $\langle 1\bar{1}00 \rangle$  directions due to the climb motion. It is assumed that these jogs virtually bend the edge dislocations at the grain boundary from the  $c$ -axis and bring about a tilting of the (0001) basal plane around it. Such a jog structure of boundary dislocations was recently observed by Hong et al. using TEM [47]

Ha et al. have recently proposed a different model for the origin of the tilting of the (0001) basal plane in SiC crystals [34]. They observed an abrupt change in the population of basal plane dislocations across a grown-in polygonized domain wall. The domain wall is composed of threading dislocations of pure edge type, forming a prism-plane-tilt boundary in a low energy configuration. The strain field around domain wall dislocations can act as an obstacle to the movement of basal plane dislocations. Basal plane dislocations approaching the domain wall experience a repulsive force, which is proportional to the threading dislocation density comprising the wall. The piled-up basal plane dislocations are parallel to the wall and are of pure edge type. The distribution of these piled-up basal plane dislocations results in a basal-plane-tilt across the domain wall. Consequently the piled-up of basal plane dislocations creates mixed-tilt (containing both basal-plane-tilt and prism-plane-tilt) low angle grain boundaries in SiC crystals.

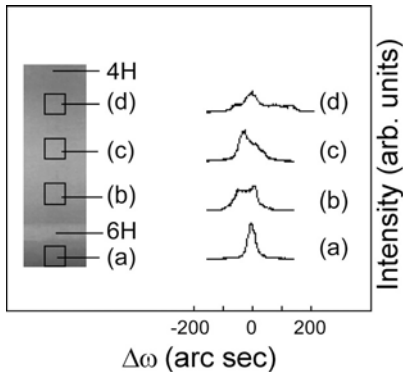


**Fig. 7.** Evolution of the crystal mosaicity during crystal growth in the  $[000\bar{1}]$  direction after polytype instabilities occurred. The  $11\bar{2}0$  X-ray rocking curves with the incident plane perpendicular to the growth direction were acquired at the points along the growth direction (a) before polytype instabilities occurred, (b) 1 mm, (c) 3 mm and (d) 5 mm from foreign polytype inclusion. The *inset figure* is a photo of polytype-mixed  $4H$ -SiC crystal

One of the major causes of the domain formation in PVT grown SiC crystals is the inclusion of foreign polytypes during growth [48]. Figure 7 shows the evolution of mosaicity (prism-plane-tilt) in a  $4H$ -SiC crystal during growth after polytype instabilities at the near seed regions. The  $11\bar{2}0$  X-ray rocking curve with the incident plane perpendicular to the growth direction becomes broader and splits into multiple peaks as the scan goes far from the foreign polytype inclusion along the growth direction. The polytypic inclusion would result in stresses due to the differences in the lattice constant and the coefficient of thermal expansion [50] between different polytypes. During growth, the stresses are released by the introduction of dislocations, which are further activated to glide and climb in the crystals to minimize their total strain energy by aligning themselves along  $\langle 1\bar{1}00 \rangle$ , forming low angle grain boundaries.

### 2.3.3 Reduction of Mosaicity

An important aspect of the low angle grain boundaries is that they are not uniformly distributed, and most often occur at the peripheral regions of crystal [45, 49]. Figure 8 shows the etched  $(0001)Si$  surfaces of the central and peripheral regions of a  $6H$ -SiC wafer. As seen in the figure, the central region of the wafer appears free of low angle grain boundaries, while the peripheral region often contains polygonized low angle grain boundaries.

Powell et al. [51] analyzed SiC wafers by crossed polarizer imaging and found that the wafers had three distinct regions: (i) the central region free of contrast, (ii) the cross-hatched region (contrasts due to localized strain fields at low angle grain boundaries) surrounding the central area and (iii) the wafer rind, composed of polycrystalline SiC. They claimed that, to expand the central region of a better crystallinity, a high degree of control of both the transient and continuous thermal profiles is required. To achieve this, they employed a numerical modeling of the heat dissipation and flow in the growth reactor and developed an optimal design and growth process

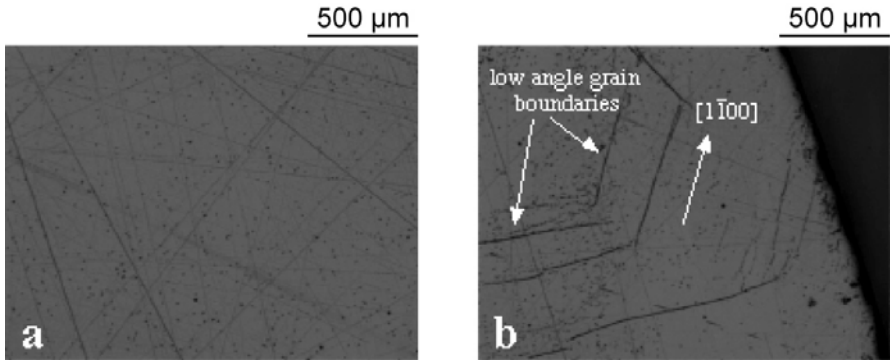


**Fig. 8.** Etch pit features on the (0001)Si surface of a 6H-SiC wafer: (a) the central and (b) the peripheral regions. The central region appears free of low angle grain boundaries, while the peripheral region contains polygonized low angle grain boundaries

for the single crystal area expansion. Hofmann et al. [52] also pointed out the critical role of the numerical growth process analysis. After adjustment of heating distribution and modification of the thermal insulation, they successfully achieved the reduction of stress variations due to low angle grain boundaries.

Optimized crucible design and growth processes have been pursued to minimize the undesirable temperature gradients existing in SiC crystals during growth, with the aid of the numerical simulation of temperature profile inside the crucible (for a recent review of the numerical simulation of SiC bulk crystal growth see the contribution by M. Pons et al. in this book). This effort has recently led to the demonstration of a low crystal mosaicity two-inch 4H-SiC wafer [53], which shows a series of single diffraction peaks of X-ray rocking curve across the wafer, as narrow as a few tens of arcseconds, indicating that the wafer possesses a low crystal mosaicity.

### 3 Growth Perpendicular to the $c$ -Axis Direction

#### 3.1 Advantages over the Growth Along the $c$ -Axis

Recently a drastic improvement in the channel mobility has been demonstrated for SiC MOSFETs on the (11 $\bar{2}$ 0) surface [54, 55]. SiC MOSFETs on the (11 $\bar{2}$ 0) surface showed a markedly enhanced channel mobility compared to that of the conventional MOSFETs fabricated on the (0001) surface. Some additional advantageous characteristics have also emerged about thin film epitaxy [56] and ion implantation [57] for the SiC(11 $\bar{2}$ 0) surface, and these outstanding achievements have naturally spurred interest in bulk crystal growth in the [11 $\bar{2}$ 0] direction. Bulk crystal growth in this direction is

essential for the fabrication of SiC( $1\bar{1}20$ ) substrates having a large diameter and reasonable uniformity of doping concentration.

A major advantage of growth perpendicular to the  $c$ -axis is micropipe suppression. Takahashi et al. proved that micropipes can be eliminated in SiC crystals grown in the  $[1\bar{1}00]$  and the  $[11\bar{2}0]$  directions [58, 59], which are naturally favored growth directions in the Acheson and Lely growth processes. They ascribed the micropipe suppression to the different strain relaxation mechanism in the growth perpendicular to the  $c$ -axis. Strain relaxation (defect formation) processes depend on the crystal growth direction and differ largely between the crystals grown along the  $c$ -axis and perpendicular to the  $c$ -axis [13].

Another advantage of growth in the  $[1\bar{1}00]$  and the  $[11\bar{2}0]$  directions is polytype control [59]. The polytypic structure of the grown crystal perfectly succeeds that of the seed crystal in the  $[1\bar{1}00]$  and  $[11\bar{2}0]$  growth:  $6H$  always grows on a  $6H$  part of the seed, and  $4H$  always grows on a  $4H$  part of the seed crystal, independently of the growth conditions such as the growth temperature and Ar pressure. These results are reasonably understood from the fact that the information on the stacking sequence of atomic layers appears on the  $(1\bar{1}00)$  and the  $(11\bar{2}0)$  growing surfaces.

### 3.2 Dislocations and Crystal Mosaicity

The dislocation structure and crystal mosaicity of SiC bulk crystals grown in the  $[1\bar{1}00]$  and  $[11\bar{2}0]$  directions have been reported by Takahashi et al. [13] and Katsuno et al. [48]. Takahashi et al. [13] investigated the dislocation structure of  $6H$ -SiC crystals grown in the  $[1\bar{1}00]$  direction by X-ray topography, HRXRD and defect selective etching. They revealed that the crystal does not contain defects having displacements along the  $[1\bar{1}00]$  growth direction, such as screw dislocations, and that a number of edge dislocations with a  $1/3\langle 11\bar{2}0 \rangle$  Burgers vector are introduced at the initial stage of growth and extend along the  $[1\bar{1}00]$  growth direction. They also measured X-ray rocking curves from a  $\{0001\}$  wafer vertically sliced along the  $[1\bar{1}00]$  growth direction and showed that the rocking curves exhibited an anisotropic behavior. The rocking curve with incident plane parallel to the  $[1\bar{1}00]$  growth direction showed a narrow single symmetrical peak with a FWHM of 20 arcsec, which is as good as that for high-quality Lely platelets, and as the wafer was scanned along the growth direction, the rocking curve hardly changed for the peak position and FWHM. On the other hand, the rocking curve showed split peaks by about 200 arcsec when the X-ray incident plane was perpendicular to the growth direction. Takahashi et al. [13] attributed this anisotropic behavior of X-ray rocking curves to the existence of low angle tilt grain boundaries (edge dislocation walls) extending in the  $[1\bar{1}00]$ - $\langle 0001 \rangle$  plane, which provided a tilt around the growth direction.

Recently Katsuno et al. [48] re-examined the above interpretation and obtained similar results to those of Takahashi et al. [13] for  $4H$ -SiC crystals

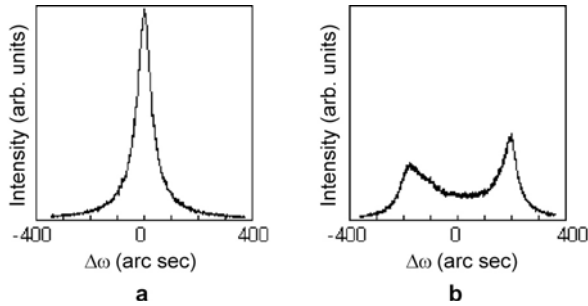


**Fig. 9.** 0004 X-ray rocking curves acquired from a (0001) wafer vertically sliced from a  $[11\bar{2}0]$  grown 4H-SiC crystal. The incident plane was (a) parallel and (b) perpendicular to the  $[11\bar{2}0]$  growth direction

grown in the  $[11\bar{2}0]$  direction; a  $\{0001\}$  wafer vertically sliced along the  $[11\bar{2}0]$  growth direction showed anisotropic X-ray rocking curves. Figure 9 shows the results of the X-ray rocking curve measurements. The incident plane of diffraction was chosen either (a) parallel or (b) perpendicular to the  $[11\bar{2}0]$  growth direction. The rocking curve with the incident plane parallel to the growth direction (Fig. 9a) shows a single diffraction peak with a FWHM of 60 arcsec, and the peak position and FWHM hardly changed for the wafer scans along the growth direction. On the other hand, the rocking curve with the incident plane perpendicular to the growth direction shows split peaks by about 350 arcsec (Fig. 9b). The positions and separation of these split peaks slightly varied for scans across the wafer. These results suggested that the crystal contained domains separated by low angle tilt grain boundaries extending in the  $[11\bar{2}0]$ - $\langle 0001 \rangle$  lattice plane.

They also examined a horizontally sliced  $(11\bar{2}0)$  wafer from a 4H-SiC crystal grown in the  $[11\bar{2}0]$  direction, where the rocking curves were measured with the incident plane parallel to  $\langle 0001 \rangle$  and  $[1\bar{1}00]$ . For both diffraction geometries, the rocking curves showed a narrow single symmetrical peak with FWHM of 20–30 arcsec, indicative of very small mosaicity in the  $(11\bar{2}0)$  lattice plane.

In their experiments, a seed crystal prepared from a 4H-SiC crystal grown in the  $[000\bar{1}]$  direction was used. The seed crystal did not have the kind of anisotropic mosaicity in the (0001) lattice plane that they have observed in the  $[11\bar{2}0]$  grown crystal, and thus the observed (0001) mosaicity in the  $[11\bar{2}0]$  grown crystal was caused by the growth process itself. It was also revealed that the mosaic structure abruptly changed between the seed and grown crystals; the anisotropic mosaicity in the (0001) lattice plane almost fully evolved after crystal growth of about 1 mm in length from the seed and grown crystal interface.

The anisotropic mosaicity in the (0001) lattice plane is assumed to stem from rearrangement of basal plane dislocations. They are directed approxi-

mately along the  $[11\bar{2}0]$  growth direction and arrayed in the  $\langle 0001 \rangle$  direction during growth. The basal plane dislocations are mainly inherited from the seed crystal and also often introduced by improper surface preparation of seed crystal [60]. The glide and climb motions of the basal plane dislocations are even more highly activated during growth, compared to the  $\langle 0001 \rangle$  threading edge dislocations, since the Peierls energy is minimum for the basal plane glide. The observed drastic change in the mosaic structure between the seed and the grown crystals would result from these fast rearrangement processes of the basal plane dislocations.

### 3.3 Stacking Faults

#### 3.3.1 General Features

Micropipe formation is fully suppressed by growth perpendicular to the  $c$ -axis. At the same time, however, the growth brings about another problem, which is the stacking fault formation during growth. Takahashi et al. observed linear etch pits extending along  $\langle 11\bar{2}0 \rangle$  on the etched  $(1\bar{1}00)$  surface of a  $[1\bar{1}00]$  grown  $6H$ -SiC crystal [61]. By a direct comparison with X-ray topographs, they concluded that the etch pits are caused by the stacking faults in the basal plane.

Figure 10 shows (a) a high-resolution transmission electron microscope (HRTEM) image of a stacking fault in a  $6H$ -SiC  $[1\bar{1}00]$  grown crystal and (b) a corresponding schematic stacking sequence of Si-C bilayers along the  $c$ -axis. In Fig. 10a, the dot images correspond to Si-C pairs and the alternate bright and dark bands correspond to the ACB:ABC stacking sequence; each comprises three Si-C double layers. A slightly thicker dark band, indicated

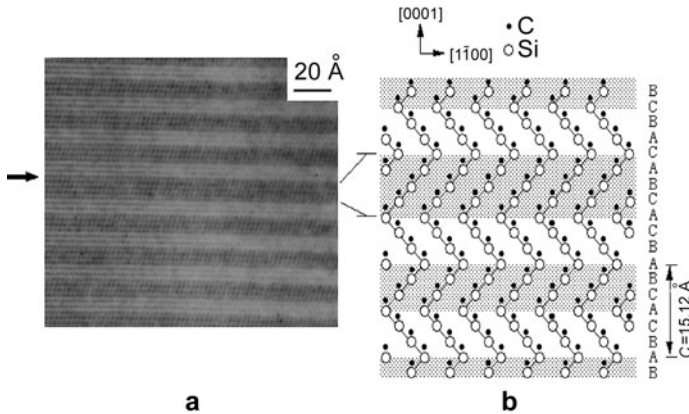


**Fig. 10.** (a) HRTEM micrograph of stacking fault in a  $6H$   $[1\bar{1}00]$  grown crystal, and (b) a corresponding schematic stacking sequence of Si-C bilayers along the  $c$ -axis

by an arrow, can be seen in the middle of the figure. The band consists of four Si-C double layers and the local stacking sequence is ACB:ACA:BCB, which represents an extrinsic type stacking fault. HRTEM observations over a reasonable number of specimens revealed that most of the stacking faults are produced by an excess or lack of single Si-C double layer.

The stacking fault density increases as growth proceeds. Once the stacking faults are generated, they proceed to grow and are not terminated. Stacking faults are hardly observed in the  $\langle 0001 \rangle$  grown seed crystal, and there are also very few stacking faults introduced at the interface between the seed and the grown crystals, implying that the stacking fault formation occurs throughout the entire growth process rather than at the initial stage of growth.

Stacking fault formation strongly depends on the crystal growth direction and grown polytype [61]. In particular, the  $6H$   $[1\bar{1}00]$  grown crystal contains a large number of stacking faults, with densities at least 10 times higher than those for the  $6H$   $[11\bar{2}0]$  grown crystal and  $10^3$  times higher than those for the  $6H$   $[000\bar{1}]$  grown crystal. By contrast, for  $4H$ -SiC, the  $[1\bar{1}00]$  and  $[11\bar{2}0]$  grown crystals have similar densities of stacking faults, though both still contain a higher density of stacking faults than the  $4H$   $[000\bar{1}]$  grown crystal.

### 3.3.2 Formation Model of Stacking Faults

Based on the results described in Sect. 3.3.1, Takahashi et al. have ascribed a major cause of stacking fault formation to the SiC growth kinetics on the  $(1\bar{1}00)$  surface [61], where fluctuation of the bonding configuration of Si-C tetrahedral on the  $(1\bar{1}00)$  growing crystal surface causes stacking faults. The  $6H$ -SiC  $(1\bar{1}00)$  surface is assumed to comprise  $(1\bar{1}02)$  and  $(1\bar{1}0\bar{2})$  microfacets of three Si-C double layers, which are alternately arranged in the  $\langle 0001 \rangle$  direction. When the nucleation occurs on the microfacet, there are two possible bonding configurations, i.e. staggered and eclipsed bonding configurations of Si-C tetrahedra. The two configurations have a small energy difference [62], and thus while the staggered configuration is the most favorable in terms of bulk total energy, the eclipsed bonding configuration is also kinetically established during growth. Stacking faults are caused by this kinetically-induced misarrangement of surface adatoms. When a bilayer island with the eclipsed bonding configuration nucleates on the microfacet, it brings about regions of disregistry at the microfacet boundaries. Stacking fault formation may relax this disregistry and relieve the associated large localized strains at the boundaries.

The difference between  $6H$   $(1\bar{1}00)$  and  $4H$   $(1\bar{1}00)$  is the width of microfacets; narrower microfacets on  $4H$   $(1\bar{1}00)$ . This causes a large difference in the nucleation behavior of surface adatoms, i.e., they more frequently nucleate at the microfacet boundaries. When a bilayer island nucleates over the microfacet boundary, the bond configuration is uniquely determined, and regions of disregistry do not happen.

The surface kinetics model proposed by Takahashi et al. [61] well accounts for the observed dependence of stacking fault density on the crystal growth direction and the polytype of grown crystals;  $4H$ -SiC crystals grown on the  $(11\bar{2}0)$  surface exhibit a lowest stacking fault density. Stacking fault density, however, is still high compared to the crystals grown on the  $(000\bar{1})$  surface.

A similar mechanism to that on the  $(1\bar{1}00)$  surface is proposed for the stacking fault formation on the  $(11\bar{2}0)$  growing surface [63], where occurrences result from the formation of the  $(10\bar{1}0)$  and  $(01\bar{1}0)$  facets on the  $(11\bar{2}0)$  growing surface. The  $(10\bar{1}0)$  and  $(01\bar{1}0)$  facets are likely to be kinetically induced on the  $(11\bar{2}0)$  growing surface since they are singular surfaces closest to  $(11\bar{2}0)$  ( $30^\circ$  inclined from  $(11\bar{2}0)$ ) and have a lower surface energy compared to  $(11\bar{2}0)$ . On these  $(10\bar{1}0)$  and  $(01\bar{1}0)$  facets, stacking fault formation occurs in the same manner as on the  $(1\bar{1}00)$  surface.

### 3.3.3 Reduction of Stacking Faults

Recently it was found that an introduction of an off-angle at the  $(11\bar{2}0)$  crystal growth surface would be a successful strategy to prevent stacking fault formation [63]. The effect of off-angle growth on stacking fault formation is

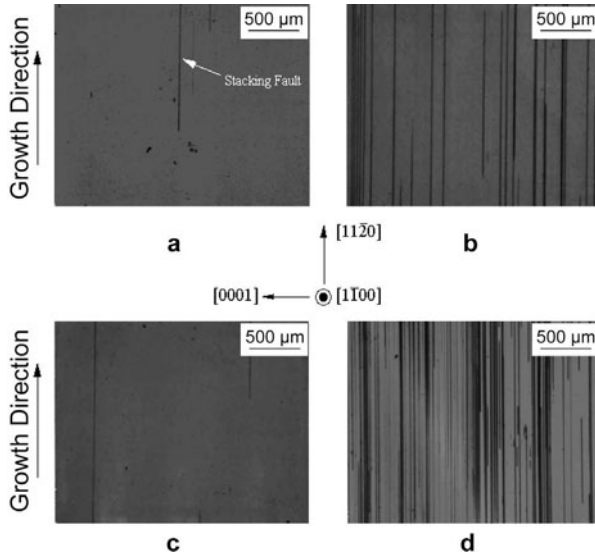


**Fig. 11.** Etched  $(1\bar{1}00)$  surface of wafers vertically sliced along the growth direction from  $4H$ -SiC crystals grown in the  $[11\bar{2}0]$  direction on a well-oriented seed crystal; (a) the near seed crystal and (b) the near top growth surface regions. (c) and (d) show the near top growth surface regions of  $4H$ -SiC crystals grown on a  $10^\circ$  off-oriented seed crystal from the  $(11\bar{2}0)$  surface toward (c)  $[0001]\text{Si}$  and (d)  $[1\bar{1}00]$ , respectively

illustrated in Fig. 11. Figures 11a,b show the etched ( $1\bar{1}00$ ) surfaces of wafer vertically sliced along the growth direction from a 4H-SiC crystal grown on a well-oriented ( $11\bar{2}0$ ) seed crystal. The figures correspond to (a) the near seed crystal and (b) the near top growth surface regions, respectively. The observed linear etch pits extending along the growth direction were caused by the stacking faults in the basal plane. As shown in Fig. 11b, a number of stacking faults were introduced during growth on a well-oriented ( $11\bar{2}0$ ) seed crystal. The etch pits were barely observed in the near seed crystal region (Fig. 11a) and the etch pit density gradually increased along the growth direction. The stacking fault density at the near top growth surface region, which had the highest stacking fault density, was typically  $100\text{--}150\text{ cm}^{-1}$ .

The results for the growth on off-oriented ( $11\bar{2}0$ ) seed crystals toward  $[0001]\text{Si}$  and  $[1\bar{1}00]$  are shown in Figs. 11c,d; both figures correspond to the near top growth surface regions of the crystals. The degree of off-orientation was  $10^\circ$  from the ( $11\bar{2}0$ ) surface for both crystals. The growth conditions were the same as in Fig. 11b with the exception of the off-orientation of the seed crystal. As seen in Fig. 11c, very few stacking faults were detected for the growth on a ( $11\bar{2}0$ ) seed crystal  $10^\circ$  off-oriented toward  $[0001]\text{Si}$ .

4H-SiC crystals were also grown on a ( $11\bar{2}0$ ) seed crystal off-oriented toward  $[000\bar{1}]\text{C}$ , and this growth similarly resulted in the reduction of stacking fault density. On the other hand, no such reduction was observed for the growth on a ( $11\bar{2}0$ ) seed crystal off-oriented toward  $[1\bar{1}00]$ . The stacking fault density rather increased when the seed crystal was off-oriented toward  $[1\bar{1}00]$  (Fig. 11d).

The dependence of stacking fault density on the degree of off-orientation is summarized in Fig. 12, where the stacking fault density is plotted against the degree of off-orientation from the ( $11\bar{2}0$ ) seed crystal surface. As seen in the figure, the stacking fault density rapidly decreases as the off-orientation

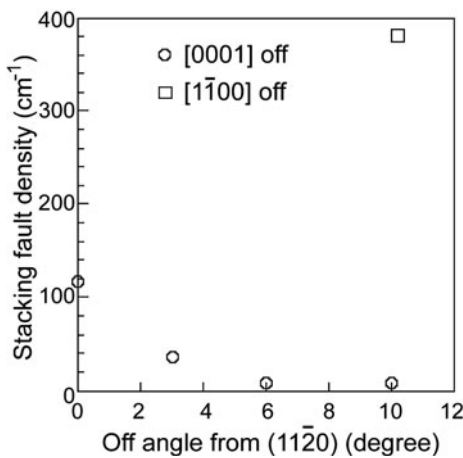


**Fig. 12.** Dependence of stacking fault density on the degree of off-orientation from the ( $11\bar{2}0$ ) seed crystal surface toward  $[0001]\text{Si}$  and  $[1\bar{1}00]$ . The stacking fault density was measured at the near top growth surface region

toward  $[0001]\text{Si}$  is increased. Although the average stacking fault density was  $10\text{ cm}^{-1}$  for the crystal grown on a  $10^\circ$  off-oriented seed crystal, which was estimated at the near top growth surface region, significant portions of the grown crystal were free of stacking faults.

The introduction of the off-orientation of seed crystal toward  $\langle 0001 \rangle$  is assumed to prevent the  $(10\bar{1}0)$  and  $(01\bar{1}0)$  facet formation through modification of the surface growth kinetics and suppress the stacking fault formation. The fact that off-orientation toward  $[1\bar{1}00]$  increases the stacking fault density lends support to this assumption.

## 4 Conclusion

The recent studies of defect formation during PVT growth of hexagonal SiC bulk crystals have been overviewed. The defects commonly observed in PVT grown SiC bulk crystals, such as micropipes, dislocations, mosaicity and stacking faults, have been discussed in terms of their origins and formation mechanisms. These crystallographic defects have been extensively investigated over the past several years and their densities have been significantly reduced. Nevertheless, there still remains increasing demand for SiC bulk crystals with better crystalline quality. Further deeper understanding of the crystal growth process and the defect formation mechanism is required to implement SiC crystals with increased diameter and higher crystallographic perfection.

## Acknowledgement

This work was partly conducted under the management of the R&D Association for Future Electron Devices (FED) as part of the Ministry of Economy, Trade and Industry (METI) New Sunshine (NSS) program (R&D of Ultra-Low-Loss Power Device Technologies) supported by the New Energy and Industrial Technology Development Organization (NEDO).

## References

1. F.C. Frank: *Acta. Cryst.* **4**, 497 (1951)
2. K. Koga, Y. Fujikawa, Y. Ueda, T. Yamaguchi: *Amorphous and Crystalline Silicon Carbide IV*, Springer Proceedings in Physics, Vol. 71, ed. by C.Y. Yang, M.M. Rahman, G.L. Harris (Springer-Verlag, Berlin, Germany, 1992) p. 96
3. P.G. Neudeck, J.A. Powell: *IEEE Electron Device Lett.* **15**, 63 (1994)
4. J. Heindl, W. Dorsch, R. Eckstein, D. Hofmann, T. Marek, S.G. Müller, H.P. Strunk, A. Winnacker: *J. Cryst. Growth* **179**, 510 (1997)
5. N. Cabrera, M.M. Levine: *Phil. Mag.* **1**, 450 (1956)
6. J. Heindl, W. Dorsch, H.P. Strunk, S.G. Müller, R. Eckstein, D. Hofmann, A. Winnacker: *Phys. Rev. Lett.* **80**, 740 (1998)

7. X.R. Huang, M. Dudley, W.M. Vetter, W. Huang, S. Wang, C.H. Carter, Jr.: Appl. Phys. Lett. **74**, 353 (1999)
8. W. Si, M. Dudley, R. Glass, V. Tsvetkov, C.H. Carter, Jr.: Mater. Sci. Forum **264-268**, 429 (1998)
9. H.M. Hobgood, D.L. Barrett, J.P. McHugh, R.C. Clarke, S. Sriram, A.A. Burk, J. Gregg, C.D. Brandt, R.H. Hopkins, W.J. Choyke: J. Cryst. Growth **137**, 181 (1993)
10. R.C. Glass, D. Henshall, V.F. Tsvetkov, C.H. Carter, Jr.: phys. stat. sol. (b) **202**, 149 (1997)
11. N. Ohtani, J. Takahashi, M. Katsuno, H. Yashiro, M. Kanaya: Mater. Res. Soc. Symp. Proc. **510**, 37 (1998)
12. N. Ohtani, M. Katsuno, T. Aigo, T. Fujimoto, H. Tsuge, H. Yashiro, M. Kanaya: J. Cryst. Growth **210**, 613 (2000)
13. J. Takahashi, N. Ohtani, M. Kanaya: J. Cryst. Growth **167**, 596 (1996)
14. V.F. Tsvetkov, S.T. Allen, H.S. Kong, C.H. Carter, Jr.: Inst. Phys. Conf. Ser. **142**, 17-22 (1996)
15. N. Schulze, D.L. Barrett, G. Pensl: Appl. Phys. Lett. **72**, 1632 (1998)
16. J. Heindl, H.P. Strunk, V.D. Heydemann, G. Pensl: phys. stat. sol. (a) **162**, 251 (1997)
17. J. Giocondi, G.S. Rohrer, M. Skowronski, V. Balakrishna, G. Augustine, H.M. Hobgood, R.H. Hopkins: J. Cryst. Growth **181**, 351 (1997)
18. P. Pirouz: Phil. Mag. A **78**, 727 (1998)
19. M. Dudley, X.R. Huang, W. Huang, A. Powell, S. Wang, P. Neudeck, M. Skowronski: Appl. Phys. Lett. **75**, 784 (1999)
20. N. Ohtani, M. Katsuno, T. Fujimoto, T. Aigo, H. Yashiro: J. Cryst. Growth **226**, 254 (2001)
21. S. Mahajan: Appl. Phys. Lett. **80**, 4321 (2002)
22. N. Ohtani, M. Katsuno, J. Takahashi, H. Yashiro, M. Kanaya: Phys. Rev. B **59**, 4592 (1999)
23. V.I. Marchenko, A.Y. Parshin: Sov. Phys. JETP **52**, 129 (1980)
24. N. Ohtani, J. Takahashi, M. Katsuno, H. Yashiro, M. Kanaya: Electron. and Commun. in Japan, Part **2**, 81, 8 (1998)
25. I. Kamata, H. Tsuchida, T. Jikimoto, K. Izumi: Jpn. J. Appl. Phys. **39**, 6496 (2000)
26. I. Kamata, H. Tsuchida, T. Jikimoto, K. Izumi: Jpn. J. Appl. Phys. **41**, L1137 (2002)
27. St.G. Müller, M.F. Brady, W.H. Brixius, G. Fechko, R.C. Glass, D. Henshall, H.McD. Hobgood, J.R. Jenny, R. Leonard, D. Malta, A. Powell, V.F. Tsvetkov, S. Allen, J. Palmour, C.H. Carter, Jr.: Mater. Sci. Forum **389-393**, 23 (2002)
28. N. Ohtani, T. Fujimoto, M. Katsuno, T. Aigo, H. Yashiro: Mater. Sci. Forum **389-393**, 29 (2002)
29. Q. Wahab, A. Ellison, C. Hallin, A. Henry, J.Di Persio, R. Martinez, E. Janzén: Mater. Sci. Forum **338-342**, 1175 (2000)
30. E.K. Sanchez, J.Q. Liu, M.De. Graef, M. Skowronski, W.M. Vetter, M. Dudley: J. Appl. Phys. **91**, 1143 (2002)
31. S. Wang, M. Dudley, C.H. Carter, Jr., D. Asbury, C. Fazi: Mater. Res. Soc. Symp. Proc. **307**, 249 (1993)
32. X.J. Ning, N. Huvey, P. Pirouz: J. Am. Ceram. Soc. **80**, 1645 (1997)
33. S. Fujita, K. Maeda, S. Hyodo: Phil. Mag. A **55**, 203 (1987)
34. S. Ha, M. Skowronski, W.M. Vetter, M. Dudley: J. Appl. Phys. **92**, 778 (2002)

35. S. Ha, N.T. Nuhfer, G.S. Rohrer, M.De Graef, M. Skowronski: J. Electron. Mater. **29**, L5 (2000)
36. S. Ha, G.S. Rohrer, M. Skowronski, V.D. Heydemann, D.W. Snyder: Mater. Sci. Forum **338–342**, 67 (2000)
37. D. Hobgood, M. Brady, W. Brixius, G. Fechko, R. Glass, D. Henshall, J. Jenny, R. Leonard, D. Malta, St.G. Müller, V. Tsvetkov, C.H. Carter, Jr.: Mater. Sci. Forum **338–342**, 3 (2000)
38. M. Selder, L. Kadinski, F. Durst, D. Hofmann: J. Cryst. Growth **226**, 501 (2001)
39. R. Ma, H. Zhang, V. Prasad, M. Dudley: Cryst. Growth & Design **2**, 213 (2002)
40. S. Ha, P. Mieszkowski, M. Skowronski, L.B. Rowland: J. Cryst. Growth **244**, 257 (2002)
41. R.C. Glass, L.O. Kjellberg, V.F. Tsvetkov, J.E. Sundgren, E. Janzén: J. Cryst. Growth **132**, 504 (1993)
42. M. Tuominen, R. Yakimova, R.C. Glass, T. Tuomi, E. Janzén: J. Cryst. Growth **144**, 267 (1994)
43. A. Ellison, H. Radamson, M. Tuominen, S. Milita, C. Hallin, A. Henry, O. Korcina, T. Tuomi, R. Yakimova, R. Madar, E. Janzén: Diamond Relat. Mater. **6**, 1369 (1997)
44. M. Katsuno, N. Ohtani, T. Aigo, H. Yashiro, M. Kanaya: Mater. Sci. Forum **338–342**, 493 (2000)
45. M. Katsuno, N. Ohtani, T. Aigo, T. Fujimoto, H. Tsuge, H. Yashiro, M. Kanaya: J. Cryst. Growth **216**, 256 (2000)
46. K. Maeda, K. Suzuki, S. Fujita, M. Ichihara, S. Hyodo: Phil. Mag. A **57**, 573 (1988)
47. M.H. Hong, P. Pirouz: to be published in J. Electron. Mater.
48. M. Katsuno, N. Ohtani, T. Fujimoto, T. Aigo, H. Yashiro: Mater. Sci. Forum **389–393**, 55 (2002)
49. H. Yamaguchi, S. Nishizawa, W. Bang, K. Fukuda, S. Yoshida, K. Arai, Y. Takano: Mater. Sci. Eng B **61–62**, 221 (1999)
50. Z. Li, R.C. Bradt: J. Appl. Phys. **60**, 612 (1986)
51. A.R. Powell, S. Wang, G. Fechko, G.R. Brandes: Mater. Sci. Forum **264–268**, 13 (1998)
52. D. Hofmann, R. Eckstein, M. Kölbl, Y. Makarov, St.G. Müller, E. Schmitt, A. Winnacker, R. Rupp, R. Stein, J. Völkl: J. Cryst. Growth **174**, 669 (1997)
53. N. Ohtani, T. Fujimoto, M. Katsuno, H. Yashiro: *SiC Power Materials and Devices*, ed. by Z.C. Feng (Springer-Verlag, Berlin, Germany, 2003)
54. H. Yano, T. Hirao, T. Kimoto, H. Matsunami, K. Asano, Y. Sugawara: Mater. Sci. Forum **338–342**, 1105 (2000)
55. J. Senzaki, K. Fukuda, K. Kojima, S. Harada, R. Kosugi, S. Suzuki, T. Suzuki, K. Arai: Mater. Sci. Forum **389–393**, 1061 (2002)
56. Z.Y. Chen, T. Kimoto, H. Matsunami: Jpn. J. Appl. Phys., Part **2**, 38, L1375 (1999)
57. M. Satoh: Mater. Sci. Forum **389–393**, 773 (2002)
58. J. Takahashi, M. Kanaya, T. Hoshino: Inst. Phys. Conf. Ser. **137**, 13 (1994)
59. J. Takahashi, N. Ohtani: phys. stat. sol. (b) **202**, 163 (1997)
60. J. Takahashi, M. Kanaya, Y. Fujiwara: J. Cryst. Growth **135**, 61 (1994)
61. J. Takahashi, N. Ohtani, M. Katsuno, S. Shinoyama: J. Cryst. Growth **181**, 229 (1997)
62. V. Heine, C. Cheng, R.J. Needs: J. Am. Ceram. Soc. **74**, 2630 (1991)
63. N. Ohtani, M. Katsuno, T. Fujimoto: Jpn. J. Appl. Phys. **42**, L277 (2003)

# High Nitrogen Doping During Bulk Growth of SiC

H.-J. Rost, D. Schulz, and D. Siche

## 1 Introduction

Nitrogen is the most important shallow donor impurity in SiC and the ionization energy is lower in the  $4H$  polytype compared to  $6H$ -SiC. Dependent on the lattice site the activation energy is in the 60 meV range for the hexagonal site and is twice as high for the cubic site [2]–[5]. Highly conducting  $4H$ -SiC substrates of high crystalline quality are one of the most important prerequisites for power electronic devices. The specific resistance should be as low as possible and  $n$ -type resistivities lower than 10 m $\Omega$ cm have been reported for both  $6H$ - and  $4H$ -SiC [1].

Usually nitrogen is incorporated via implantation or during crystal growth, since reasonable diffusion rates can only be achieved at rather high temperatures. On the other hand, annealing at temperatures between 1300°C and 1750°C is required after implantation due to high subsurface damage [6]–[8]. Consequently, most often nitrogen or nitrogen containing gases are used for the doping process during growth. The nitrogen doping during chemical vapor deposition (CVD) and the dependence on input C/Si ratio, growth temperature and process pressure have been investigated in detail by different groups [2, 9, 10]. The site-competition principles are met at C/Si ratios higher than 0.3, whereas the nitrogen doping becomes less sensitive to the C/Si ratio on both the Si- and the C-terminated faces at C/Si ratios below 0.3 [9]. The nitrogen incorporation during high temperature-CVD (HTCVD) in a chimney reactor is of great interest with regard to bulk growth due to comparable growth rates. Thermal activation energies of the nitrogen incorporation of 200 kcal/mol for the Si-face and 108 kcal/mol for the C-face of  $4H$ -SiC samples were obtained [11]. It was also found, that the total pressure has a strong effect on the nitrogen incorporation efficiency, allowing lower doping at the lower pressure [12]. Epitaxial layers can also be grown by a closed space sublimation method and data on the nitrogen doping have been compiled [13].

In sublimation grown crystals nitrogen is the most abundant background impurity. Most of the crucible parts are commonly made of graphite and therefore an almost infinite source of adsorbed nitrogen. Intentional doping is used for the preparation of highly conductive substrates. A special application of nitrogen during bulk crystal growth is the use as interface marker.

Either the nitrogen supply is interrupted or its partial pressure is increased for a certain time period resulting in a marking of the growth interface. By means of these doping marks the time dependence of the growth rate and the interface shape can be investigated. The slope of the nitrogen concentration increase from background level to the maximum value remains almost unchanged during growth, because within one crystal the first doping mark has been found to be as sharp as the last one. Therefore, nitrogen diffusion should be negligible in the crystal.

In this work different aspects of nitrogen doping during bulk crystal growth of  $4H$ - and  $6H$ -SiC by the modified Lely method as well as effects on the crystal properties will be discussed. Sublimation growth of  $4H$ -SiC can only be performed on the C-terminated seed face and the range of suitable growth parameters is much smaller than for  $6H$ -SiC. Therefore, the limits of growth parameters are rather narrow. In general, only high quality crystals (micropipe density  $< 100 \text{ cm}^{-2}$ ) have been taken into consideration for the present analysis.

## 2 Nitrogen Incorporation

Nitrogen can be easily introduced into the crystal during sublimation growth using a controlled  $\text{N}_2$  gas flow. This allows to adjust the donor concentration above the background  $n$ -type doping level which is defined by outgassing of  $\text{N}_2$  embedded in the graphite of the growth chamber. Using electrical characterization and X-ray investigations Lely concluded, that nitrogen is incorporated at carbon sites into the growing crystal [14]. This was confirmed by electron spin resonance studies a few years later and up to date there is no evidence of any other occupancy [15]. According to these investigations nitrogen substitutes uniformly into the inequivalent carbon sites.

The incorporation kinetics have been studied in terms of several growth parameters. It was found that the growth rate hardly influences the doping concentration, indicating that nitrogen incorporation is not kinetically limited at typical growth rates (0.41–1.1 mm/h). Furthermore, the incorporation is not limited by the gas flow into the chamber, it is solely determined by the partial pressure  $p_{\text{N}_2}$ . On the other hand, surface polarity and polytype were found to influence the nitrogen incorporation kinetics at the growth front. By optimizing the growth conditions, bulk resistivities as low as  $5.3 \text{ m}\Omega\text{cm}$  were obtained for  $4H$ -SiC [18].

In Fig. 1 the increase of the nitrogen concentration  $[\text{N}]$  with increasing nitrogen to argon ratio is shown. Basically, the nitrogen concentration is higher in C-face grown SiC compared to Si-face grown crystals and the ratio  $[\text{N}]_{6H}/[\text{N}]_{4H}$  is greater than unity, which will be discussed later. In addition,  $[\text{N}]$  tends to saturate at a certain  $\text{N}_2/\text{Ar}$  level. The difference in the absolute nitrogen concentration in  $6H$ -SiC is most probably due to the growth

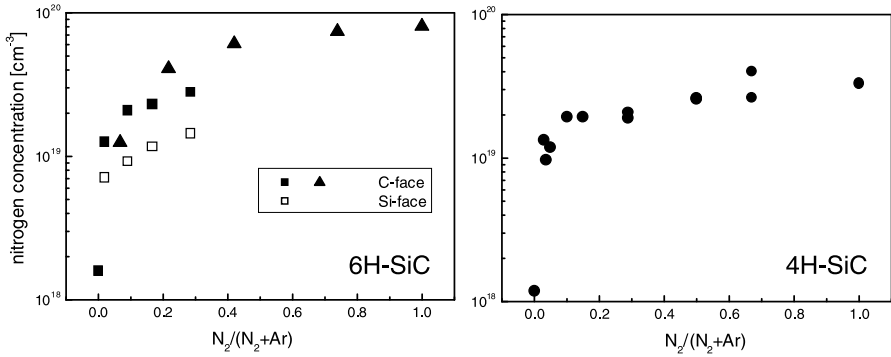


**Fig. 1.** Nitrogen concentration versus nitrogen to argon ratio (*squares*: [16], *triangles*: [17])

conditions used by both authors. For 4H-SiC commonly a lower growth temperature is applied.

An attempt for the phenomenological description of the impurity incorporation mechanism was made by using a adsorption-desorption model [19]. A Langmuir isotherm type equation

$$[N] = (K \cdot p)^x / (1 + K \cdot p)^x \quad (1)$$

( $p$ : pressure,  $K$ : ratio between adsorption and desorption rate,  $x$ : exponent) can be fitted to the data. The exponent is set either to unity or to 1/2, the latter being valid for taking dissociation into account. The analysis for 6H-SiC reveals, that  $[N]$  is not proportional to the square root of  $p_{N_2}$  [20]. Data are given in Table 1.

A kinetic parameter  $K$  larger than unity implies, that the adsorption rate is higher than the desorption rate. This corresponds to the use of nitrogen for the marking of the growth interface. Nitrogen is easily incorporated into the growing crystal and the desorption is suppressed. Furthermore, the large relative error in case of the Langmuir isotherm with dissociation leads to the assumption, that the nitrogen incorporation is a non-dissociative process, as far as the Langmuir theory is concerned. This seems to be in contradiction to

**Table 1.** Kinetic parameter  $K$  for non-dissociative ( $x = 1$ ) and dissociative case [16]

Orientation	$K$		$x$
C-face	36.2	$\pm 9.6$	1
	2.5	$\pm 0.9$	0.5
Si-face	46.7	$\pm 17.2$	1
	2.9	$\pm 1.3$	0.5

**Table 2.** Available data concerning nitrogen solubility

Polytype	Temperature K	Solubility limit $\text{cm}^{-3}$	Resistivity $\text{m}\Omega\text{cm}$	Method/Remark	Ref.
	1660	$2 \cdot 10^{20}$		SIMS	[21]
	1873	$3 \cdot 10^{19}$		Hall-effect	[22]
	2023	$> 1 \cdot 10^{20}$		Hall-effect	[23]
	2723	$2.6 \cdot 10^{20}$		mass spectr.	[23]
4H	2373–2523	$4 \cdot 10^{19}$	4.5	SIMS/eddy current	[24]
4H		$5 \cdot 10^{19}$	7.0	SIMS/4point probe	[25]
4H	2348	$3 \cdot 10^{19}$		SIMS	[26]
4H			2.8		[27]
6H			1.6		[27]
4H-C	2503	$1.1 \cdot 10^{20}$	5.3	SIMS/Hall-effect	[18]
6H-C	2553	$2 \cdot 10^{20}$	7.6		[18]
4H-C	2503–2553	$3.5 \cdot 10^{19}$		SIMS/Hall-effect	[19]
6H-C	2503–2553	$8 \cdot 10^{19}$			[19]
4H+6H		$3 \cdot 10^{19}$			[28]
4H		$2.5 \cdot 10^{19}$			[29]
4H		$3 \cdot 10^{19}$			[30]
6H		$> 1 \cdot 10^{20}$			[31]
4H+6H		$6 \cdot 10^{20}$			[32]

the fact, that molecular nitrogen has never been detected in silicon carbide so far.

The solubility limit for nitrogen can be gathered from various analyses, but the data deviate strongly caused by different growth conditions. A compilation is shown in Table 2. Since mostly no information is given about growth parameters and crystal quality, the direct comparison is rather complicated.

In contrast to the modified Lely method, where the nitrogen containing gas has to diffuse through porous media, an increased incorporation was achieved by the use of a modified growth configuration. An additional nitrogen gas flow through a graphite pipe, mounted in the source region, was adjusted [31]. In comparison with the conventional sublimation the carrier concentration was significantly higher,  $n > 1 \cdot 10^{20} \text{ cm}^{-3}$  instead of  $1 \cdot 10^{19} \text{ cm}^{-3}$ .

## 2.1 Influence of the Growth Temperature

There is only limited information available about the temperature dependence of the nitrogen incorporation for the modified Lely method. Commonly it is assumed, that with increasing growth temperature the nitrogen concentration decreases [27].

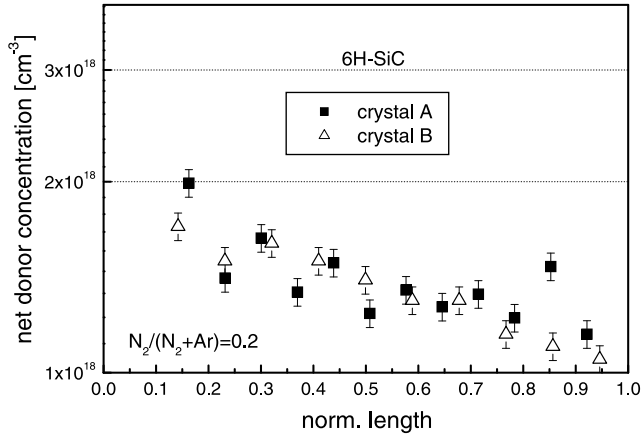


**Fig. 2.** Axial distribution of nitrogen versus normalized length, *C-V* measurements

The axial nitrogen distribution of two 6*H*-SiC crystals is shown in Fig. 2. Crystal A was grown at a constant control temperature, whereas for crystal B the temperature was varied. Following five temperature steps, crystal B was grown at  $-40$ ,  $-20$ ,  $\pm 0$ ,  $+20$  and  $+40$  K with respect to the temperature of crystal A. Although in both crystals a slight [N] decrease is observed with increasing crystal length, the difference in nitrogen concentration is rather small and certainly within the measurement error. Only in the last grown crystal part a higher growth temperature results in a somewhat lower nitrogen concentration. One has to keep in mind, that by changing the growth temperature the growth rate also changes. Therefore a separation of influencing parameters is often limited.

## 2.2 Seed Orientation and Homogeneity

As already shown, the nitrogen incorporation is also influenced by the seed orientation. In both polytypes, 4*H*- and 6*H*-SiC, the highest concentration is observed in C-face grown crystals (Fig. 3). Because nitrogen competes for the carbon lattice site, the concentration is expected to be higher in (0001)C grown crystals and was found to be about twice as high compared to (0001)Si in 6*H*-SiC.

Nitrogen incorporation on the Si-face agrees well with the site-competition model, while it is more complex on the C-face [9]. The difference in surface morphology between the polar faces is assumed to be the determining factor, because the [N] is almost insensitive to the C/Si ratio during growth on the C-face.

Usually bulk crystal growth is performed on slightly off-oriented seeds. This off-orientation is in the range of  $2^\circ$ – $8^\circ$  from the basal plane for 6*H*- and 4*H*-SiC respectively. Since the basal plane incorporates more nitrogen

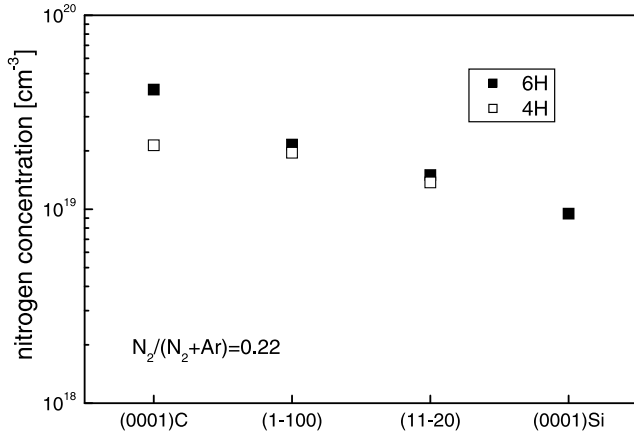


**Fig. 3.** Nitrogen concentration versus seed surface orientation [17]

than any other crystallographic plane it can be recognized as a region of higher absorption. In Fig. 4 the ratio between  $[N]$  of the facet area and the concentration in the non-facetted area for  $4H$ -SiC grown on off-oriented seeds is shown. In unintentionally doped crystals this ratio does not exceed a factor of two and is rapidly decreasing with doping. Already at 15% nitrogen in the growth ambient ( $[N] > 10^{19} \text{ cm}^{-3}$ ) the nitrogen concentration in the  $c$ -plane is only slightly above the average  $[N]$  of the wafer.

The fact, that on the C-face of  $6H$ -SiC more nitrogen is incorporated than of  $4H$ -SiC, can not be explained by the site-competition model. With

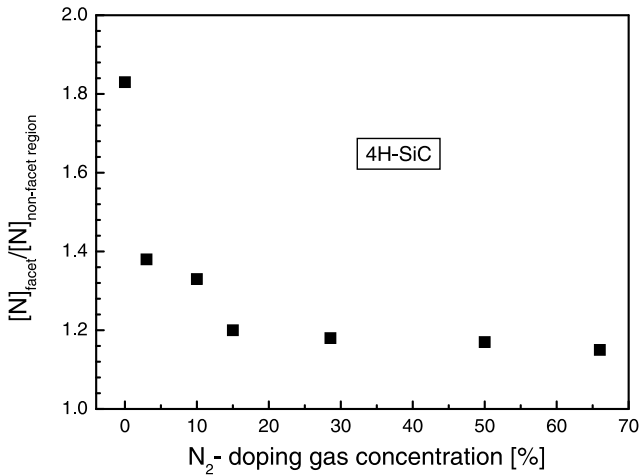


**Fig. 4.** Ratio of  $[N]$  in the facetted region to that outside versus the  $N_2$  concentration in the gas

regard to the structural properties the polytypes only differ in the stacking sequence and therefore the surface atomic arrangement should be similar. However, the surface morphology is rather different even in unintentionally doped crystals. Investigating the morphology of 6H-SiC Ohtani et al. found a different behavior of the (0001)Si face compared to the (0001)C face [33]. Whereas step height and distance remained unchanged when intentional nitrogen doping was applied on the Si-face, there was a strong increase observed on the C-face up to ten times the unit cell height and a macrostep spacing in the micrometer range. Furthermore, the macrosteps meandered and were directed along the  $\langle 1\bar{1}00 \rangle$  directions.

A strong influence of nitrogen on the growth morphology is also observed on 4H-SiC crystals grown on  $8^\circ$  off-oriented substrates. Growth defects can be reduced during sublimation growth by the use of nitrogen [34]. In addition, the macrostep height is reduced upon nitrogen doping not only on the (0001)C-plane but also in the off-orientation area of flat crystal interfaces. Consequently, in case of 4H-SiC the effect of polytype stabilization by nitrogen is rather due to a change in surface morphology than to the influence of nitrogen on the C/Si ratio in front of the interface. Since nitrogen replaces for the carbon atom, the C/Si ratio should increase in the vapor phase, but according to the experiments no evidence has been found. The transformation of 4H-SiC to other polytypes has been mostly observed on the c-plane.

Moreover, the higher nucleation rate on the C-face can be attributed to a lower surface diffusion length of adatoms. This is one reason for polytype instabilities in 4H-SiC sublimation growth. Information about the stacking sequence could be lost due to 2D nucleation on large terraces between neighboring steps. The addition of nitrogen may increase the adatom mobility and hence migration to steps is preferred to nucleation.

### 3 The Increase of Conductivity in 4H-SiC

For substrates of low resistivity it is of special interest to explore the electrical and structural crystal properties in the range of high N doping levels above  $10^{19} \text{ cm}^{-3}$ . Therefore, 4H-SiC single crystals of 35 mm in diameter with an average length of about 12 mm were grown on off-oriented (0001)C 4H-SiC seeds in the temperature range from 2100 to 2250°C. The nitrogen was mixed to the argon growth atmosphere in the composition range from 0 to 100%. For a first series of crystals the doping gas was added to a constant carrier gas flow, whereas for a second one the total gas flow remained constant.

SIMS was used to determine the chemically incorporated nitrogen concentration. The electrical properties were investigated at room temperature (*RT*) by capacitance-voltage (*CV*), Hall effect and conductivity as well as contactless eddy current measurements. Furthermore, the crystals were characterized by *RT*-photoluminescence (PL) recorded for wavelengths from 350

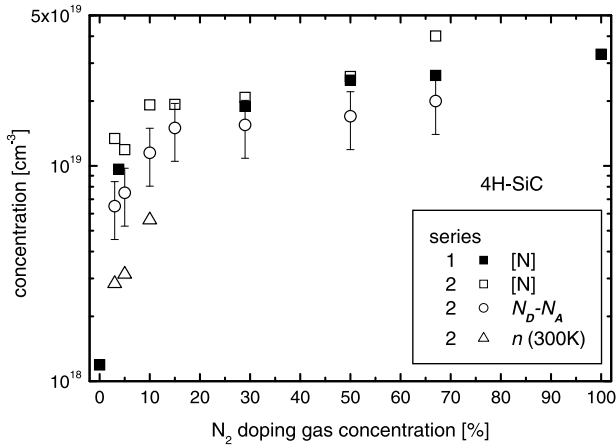


**Fig. 5.** Chemical nitrogen ( $[N]$ ), net doping ( $N_D - N_A$ ) and charge carrier concentration ( $n$ ) at  $RT$  in nitrogen doped crystals outside the growth facet

to 800 nm and scanning electron microscopy (SEM) combined with cathodoluminescence (CL) and the selected area channeling pattern technique.

As a result the influence of the total gas amount on the doping behavior could be neglected. Furthermore, it was found that the unintentional nitrogen doping was in the range of  $10^{16}$ – $10^{18}$   $\text{cm}^{-3}$  due to the memory effect. Already some percent of  $N_2$  in Ar increases this level to about  $10^{19}$   $\text{cm}^{-3}$ . At higher  $N_2$  concentrations in the atmosphere, the crystals seem to be saturated with  $[N] \approx 4 \cdot 10^{19}$   $\text{cm}^{-3}$ .

In Fig. 5 these results are compared with the net donor concentration (CV) and the electron concentration (Hall effect) at  $RT$  [24]. The CV method was limited to concentrations below  $1.5 \cdot 10^{19}$   $\text{cm}^{-3}$ . The blocking current through the Schottky contacts became too high at higher doping level (tunnel effect) and resulted in contact problems. The deviations between the CV- and the Hall effect parameters are due to the incomplete donor ionization at  $RT$ . More interesting is the feature that the chemical nitrogen concentration generally exceeds the net donor concentration. The concentration of compensating acceptor impurities like [B] and [Al] was measured in the range of  $10^{16}$   $\text{cm}^{-3}$  and therefore, it cannot be responsible for this deviation. Reasons may be the increased probability that nitrogen atoms occupy other than carbon sites as well as to form complexes. The expected decrease of the resistivity with increasing nitrogen concentration is shown in Fig. 6. Values as low as 4.5 m $\Omega\text{cm}$  are achieved for growth in pure nitrogen atmosphere. Some of the differences between the two doping series may be explained by an inhomogeneous distribution of grown-in crystal defects resulting in different average resistivities. Measurements of the Hall mobility which were only possible for low  $N_2$  doping concentrations up to 10% (measurement of volt-

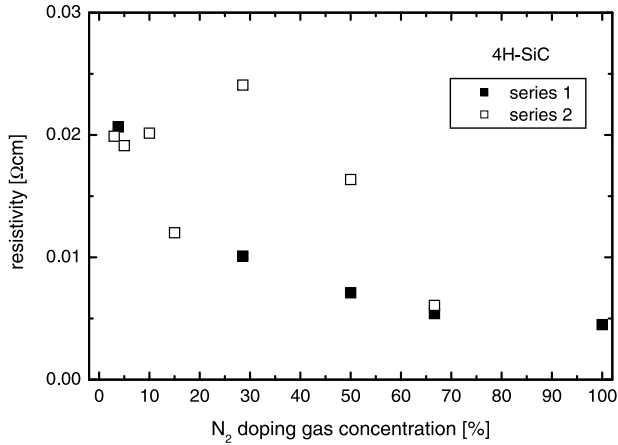


**Fig. 6.** Resistivities obtained for different N<sub>2</sub> doping gas concentrations (contactless eddy current measurements)

age drops at low resistive samples was crucial) show a strong decrease from nearly 600 cm<sup>2</sup>/Vs (“undoped”) to values between 50 and 100 cm<sup>2</sup>/Vs.

Already some percent of N<sub>2</sub> in argon increase the nitrogen level to about 10<sup>19</sup> cm<sup>-3</sup>, the saturation seems to be at [N] ≈ 4 · 10<sup>19</sup> cm<sup>-3</sup> (corresponding to 4.5 mΩcm). Generally, the net donor concentration is less than the chemical nitrogen concentration. The reason is not yet understood.

## 4 Stacking Fault (SF) Formation

Recently, the formation of stacking faults has been reported, which sometimes resulted in a polytype transformation from 4H to 3C, induced by oxidation of *n*<sup>+</sup>-4H-SiC crystals [35]–[37] or by annealing in argon gas [38]. In highly doped ([N] = 1.7 · 10<sup>19</sup> cm<sup>-3</sup>) 4H-SiC-CVD layers single and multiple SF layers are formed during dry thermal oxidation at 1150°C. Stacking faults on neighboring (0001) planes form bands of the 3C polytype. It was suggested that this polytype transformation may be the result of nucleation and propagation of 1/3(10 $\bar{1}$ 0) Shockley partial dislocations on basal planes. They may relieve the strain produced by the stresses due to heavy doping [36, 37]. The induced strain in 4H-SiC crystals, nitrogen doped up to a concentration of 2.5 · 10<sup>19</sup> cm<sup>-3</sup>, was explained with the assumption, that nitrogen atoms affect the inter-planar spacing [29]. As [N] increases, the lattice parameter decreases.

Nearly 35 SF/μm were formed during annealing of *n*<sup>+</sup>-type CVD grown layers at 1150°C for 90 min in argon gas. All stacking faults terminated at the substrate/layer interface. Point defect coalescence was excluded as a fault formation mechanism [38].

The spontaneous formation of stacking faults in highly doped  $4H$ -SiC during annealing was also studied by Kuhr et al. [30]. In wafers with  $[N] = 3 \cdot 10^{19} \text{ cm}^{-3}$  a density of 80 SF/ $\mu\text{m}$  was observed after annealing at  $1150^\circ\text{C}$  for 90 min. Double layer Shockley faults were formed by shear on two neighboring basal planes. If the SF is defined by the dissociation of a perfect dislocation into two partials, separated by a SF, than one partial can be defined as leading and one as trailing with respect to the shear direction. At temperatures below  $1100^\circ\text{C}$  the trailing partial dislocation is immobile, above  $1100^\circ\text{C}$  it is mobile and can follow the leading partial dislocation. The width of stacking fault ribbons is expected to be narrow ( $< 70 \text{ nm}$ ).

Obviously, such structural deterioration of the substrates must be avoided. Concerning the prevention of SF formation near growth temperature two ideas were discussed [30]:

- the hexagonal stacking sequence is more stable than the cubic one at higher temperatures,
- double layer faults could be formed, but there are no nucleation sites available.

A comparison between Ar and  $\text{N}_2$  for high temperature treatment of  $4H$ -SiC substrates resulted in a stable surface for nitrogen ambient at  $1650^\circ\text{C}$  and a strongly degraded surface at  $1900^\circ\text{C}$  compared to the use of argon at this higher temperature. On the other hand Ar causes at  $1650^\circ\text{C}$  a rough surface by step bunching. At low pressure the higher the temperature the more pronounced the step bunching is. A Gibbs free energy calculation resulted in  $\text{C}_2\text{N}_2$  and not  $\text{Si}_2\text{C}$  as the most abundant carbon containing gas species [39]. A rough surface could provide nucleation sites for SF formation.

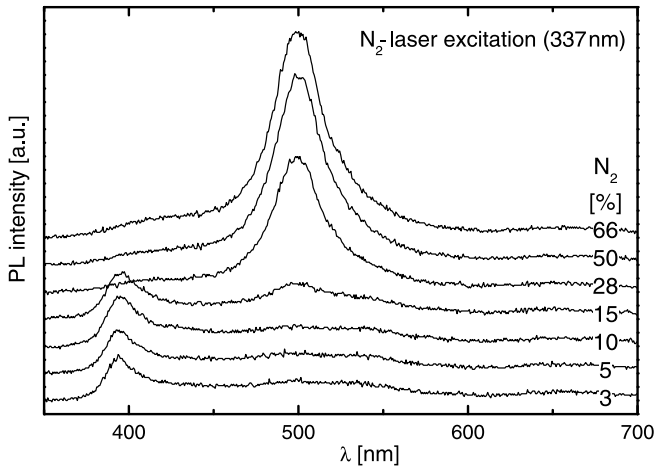


**Fig. 7.** *RT*-photoluminescence spectra in dependence on the  $\text{N}_2$  doping gas concentration

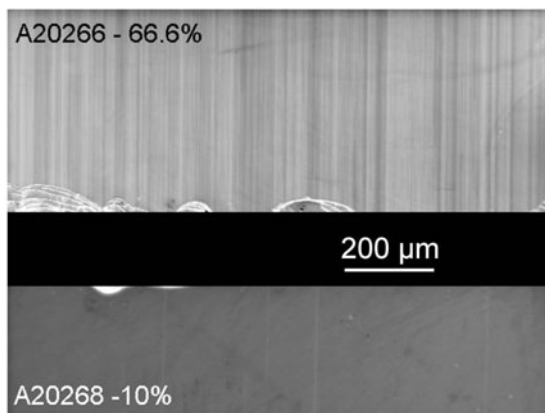


**Fig. 8.** Scanning electron microscopy images (SE mode) of the off-oriented wafer surfaces of two differently  $N_2$  doped crystals

In this work  $4H$ -SiC single crystals of different  $[N]$  have been grown by sublimation. After wet oxidation wafers were investigated to find a compromise between structural perfection and high electrical conductivity [24].

In the  $RT$ -photoluminescence spectra the bandgap emission (394 nm) decreases whereas the intensity of a PL band at about 500 nm increases in crystals with  $[N] > 2 \cdot 10^{19} \text{ cm}^{-3}$  (Fig. 7,  $N_2$  doping gas concentration of 28%). This behavior correlates well with the observed increase of the wafer warp starting at the same concentration range. In order to investigate this effect in more detail two samples from crystals grown with different  $N_2$  doping gas concentrations (10% and 66.6%) having different PL peak intensities were analyzed by SEM. Using the secondary electron (SE) mode, the images of the wafer surfaces, presented in Fig. 8, show different densities of stripes between both samples. The direction of the stripes is found to be parallel to the growth steps. Due to the off-orientation we observe at the wafer surface the intersecting lines of planar defects being parallel to the basal plane. The stripes are not homogeneously distributed across the investigated sample areas and their density is directly related to the nitrogen concentration. Within one sample, the highest stripe density is always observed in the region of the growth facet.  $RT$ -cathodoluminescence measurements showed that the stripes are associated with the luminescence band at 500 nm whereas outside the stripes the 394 nm band, characteristic of the  $4H$  polytype, dominates. Although electron channeling patterns of areas of high planar defect density are blurred, they indicate only the  $4H$  polytype (Fig. 9). Obviously, there is no complete polytype transformation.

Referring to the investigations on structural defects in  $4H$ -SiC crystals of low  $n$ -type resistivity of the authors, mentioned at the beginning of this chapter, we assume the formation of double stacking faults in our crystals. The

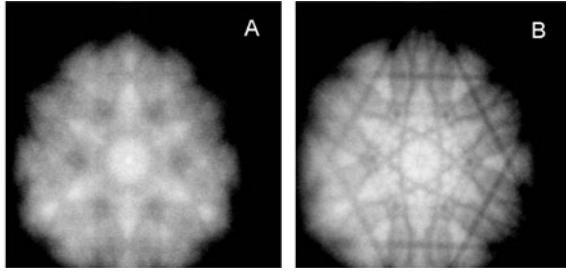


**Fig. 9.** Selected area channeling pattern (stripe density: (A) high; (B) low)

faults could be generated by gliding of partial dislocations on basal planes. Liu et al. observed exclusively double stacking faults spontaneously generated in heavily nitrogen doped  $4H$ -SiC [40]. Therefore, each fault consists of only six bilayers stacked in a cubic sequence. Furthermore, it was proposed that the stacking faults act as quantum wells. Calculations have shown, that localized trenches in the conduction band are formed and electrons occupying these trenches can lower their energy by nearly 600 meV [41]. This could explain the PL band at 500 nm instead of the 541 nm peak which is characteristic of pure  $3C$ -SiC. The high  $RT$ -PL intensities of the 500 nm bands observed in our crystals support this idea. Since the stacking fault formation seems to be spontaneously driven for nitrogen concentrations in crystals exceeding about  $2 \cdot 10^{19} \text{ cm}^{-3}$ , the usefulness of higher doping for  $4H$ -SiC substrates appears to be fundamentally questionable.

## 5 Wafer Properties

The influence of the nitrogen doping on the mechanical wafer properties was of special interest. Geometrical parameters of polished wafers have been estimated using a surface profiler. The investigated wafers were cut at similar axial positions in the different crystals. After the mechanical treatment the wafer warp is in the range of 10–20  $\mu\text{m}$  up to a nitrogen concentration in the gas of about 30% and is strongly increasing at higher concentrations by a factor of 3–4 (Fig. 10). The stacking fault formation starts in the same doping region ( $[N] > 2 \cdot 10^{19} \text{ cm}^{-3}$  in the crystal or 28% in the gas) like the increase of the macroscopic wafer warp. There seems to be a maximum in wafer warp in the range of 60–80%  $\text{N}_2$  in the gas.

The roughness  $R_z$  versus  $\text{N}_2$  doping gas concentration is shown in Fig. 11. There was no significant dependence, but a slight trend to higher values has been found. The differences between both series reflect an improved wafer technology.

Searching for the mechanism of warp generation the ratio of the nitrogen concentration in the faceted region to the concentration outside this region

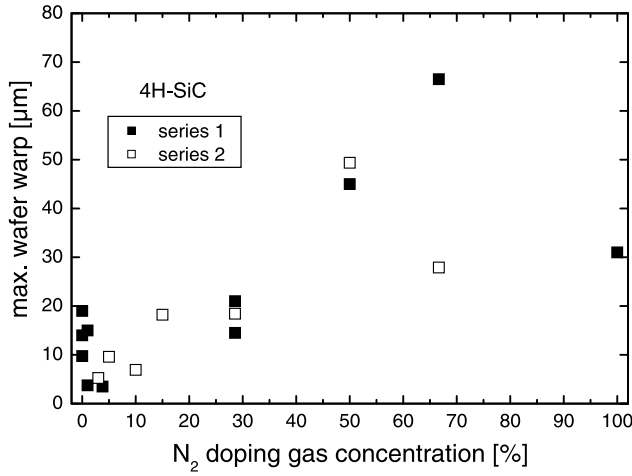


**Fig. 10.** Maximum wafer warp vs. N<sub>2</sub> doping gas concentration

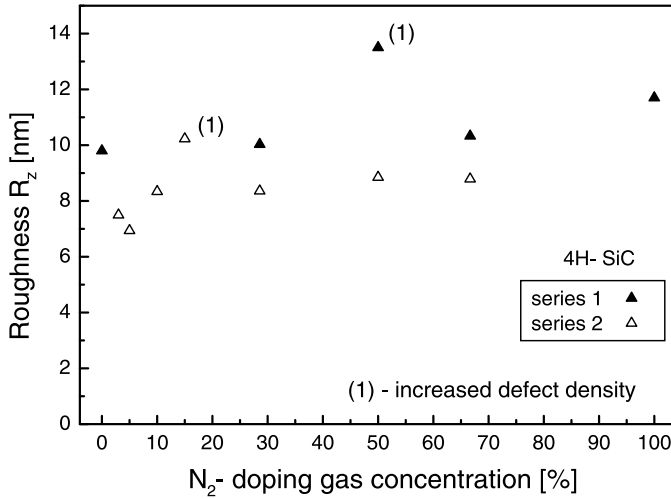


**Fig. 11.** Roughness  $R_z$  versus N<sub>2</sub> doping gas concentration on the polished C-side

is shown vs. the N<sub>2</sub> concentration in the gas (Fig. 4). The ratio decreases and therefore, it can hardly be responsible for the increased wafer warp. Beside the difference in these two regions the doping is homogeneously and it is not understood what the warp mechanism is.

## 6 Conclusion

Nitrogen doping during bulk single crystal growth of SiC has been studied in order to evaluate the ratio between low electrical resistivities desired by device manufacturers and the influence of a high doping level on the crystal quality. Different interconnected growth parameters affecting the nitrogen incorporation complicate the statement of an actual solubility limit as far as high quality crystal growth is concerned. The microscopic mechanism has to be studied in more detail in order to completely understand the incorporation of nitrogen.

In 6H-SiC the highest nitrogen concentration (up to  $1 \cdot 10^{20} \text{ cm}^{-3}$ ) is observed when growing on the (0001)C face. In 4H-SiC a maximum nitrogen concentration of  $\approx 4 \cdot 10^{19} \text{ cm}^{-3}$  has been achieved. In addition, the difference between values measured by SIMS (chemically incorporated) and electrical characterization suggests, that not only carbon sites are occupied by nitrogen atoms and/or complexes are formed.

The formation of stacking faults in highly doped 4H-SiC is observed. These stacking faults lead to characteristic *RT*-photoluminescence spectra at about 500 nm. An increase of the wafer warp with increasing  $[N]$  has been measured and starts to become significant at the same nitrogen doping level of  $\approx 2 \cdot 10^{19} \text{ cm}^{-3}$ . Thermal treatment seems to be a key factor in controlling the stacking fault formation.

## Acknowledgement

The authors would like to acknowledge the support by the Bundesministerium für Bildung und Forschung under the project number 01BM071 and by SiCrystal AG.

## References

1. N. Ohtani, J. Takahashi, M. Katsuno, H. Yashiro, M. Kanaya: Electronics and Communications In Japan, Part 2, **81**, 8 (1998)
2. T. Kimoto, A. Itoh, H. Matsunami, S.G. Sridhara, L.L. Clemen, R.P. Devaty, W.J. Choyke, T. Dalibor, C. Peppermüller, G. Pensl: Appl. Phys. Lett. **67**, 2833 (1995)
3. R.P. Devaty, W.J. Choyke: Phys. Status Solidi A **162**, 5 (1997)
4. H. Matsuura, T. Kimoto, H. Matsunami: Jap. J. Appl. Phys. **38**, 4013 (1999)
5. C.Q. Chen, J. Zeman, F. Engelbrecht, C. Peppermüller, R. Helbig, Z.H. Chen, G. Martinez: J. Appl. Phys. **87**, 3800 (2000)
6. T. Kimoto, N. Inoue, H. Matsunami: Phys. Status Solidi A **162**, 263 (1997)
7. D. Dwight, M.V. Rao, O.W. Holland, G. Kelner, P.H. Chi, J. Kretchmer, M. Ghezzi: J. Appl. Phys. **82**, 5327 (1997)
8. M.A. Capano, J.A. Cooper, M.R. Melloch, A. Saxler, W.C. Mitchel: J. Appl. Phys. **87**, 8773 (2000)

9. D.J. Larkin: Phys. Status Solidi B **202**, 305 (1997)
10. I. Pintilie, L. Pintilie, K. Irmscher, B. Thomas: Mater. Sci. Forum **433–436**, 463 (2003)
11. J. Zhang, A. Ellison, A. Henry, M.K. Linnarsson, E. Janzen: Mater. Sci. Engineer. B **61–62**, 151 (1999)
12. J. Zhang, A. Ellison, A. Henry, M.K. Linnarsson, E. Janzen: J. Cryst. Growth **226**, 267 (2001)
13. Y.A. Vodakov, E.N. Mokhov, M.G. Ramm, A.D. Roenkov: in *Springer Proceedings In Physics*; Vol. 56, ed. by G.L. Harris, M.G. Spencer, and C.Y. Yang (1992), p. 329
14. J.A. Lely: Berichte der Deutschen Keramischen Gesellschaft e.V. **32**, 229 (1955)
15. H.H. Woodbury, G.W. Ludwig: Phys. Rev. **124**, 1083 (1961)
16. D. Schulz: PhD Thesis, Brandenburgische Technische Universität Cottbus, 2001
17. N. Ohtani, M. Katsuno, J. Takahashi, H. Yashiro, M. Kanaya, S. Shinoyama: Mater. Sci. Forum **264–268**, 49 (1998)
18. K. Onoue, T. Nishikawa, M. Katsuno, N. Ohtani, H. Yashiro, M. Kanaya: Jap. J. Appl. Phys. **35**, 2240 (1996)
19. N. Ohtani, M. Katsuno, J. Takahashi, H. Yashiro, M. Kanaya: J. Appl. Phys. **83**, 4487 (1998)
20. D. Schulz, K. Irmscher, J. Dolle, W. Eiserbeck, T. Müller, H.-J. Rost, D. Siche, G. Wagner, J. Wollweber: Mater. Sci. Forum **338–342**, 87 (2000)
21. H.J. Kim, J.A. Edmond, J. Ryu, H. Kong, C.H. Carter Jr., J.T. Glass, R.F. Davis: in *1st International SAMPE Electronic Conference* (Santa Clara, 1987), p. 370
22. S. Karman: PhD Thesis, Friedrich-Alexander-Universität Erlangen-Nürnberg, 1992
23. Y.A. Vodakov, E.N. Mokhov: in *Silicon Carbide 1973*, ed. by R.C. Marshall, J.W. Faust Jr., and C.E. Ryan (University of South Carolina Press, 1973), p. 508
24. H.-J. Rost, K. Irmscher, D. Siche, D. Schulz, J. Wollweber: Mater. Sci. Forum **433–436**, 91 (2003)
25. G. Augustine, H.M. Hobgood, V. Balakrishna, G. Dunne, R.H. Hopkins: Phys. Status Solidi B **202**, 145 (1997)
26. R.R. Ciechonski, R. Yakimova, M. Syväjärvi, E. Janzen: Mater. Sci. Forum **433–436**, 75 (2003)
27. R.C. Glass, D. Henshall, V.F. Tsvetkov, C.H. Carter Jr.: Phys. Status Solidi B **202**, 149 (1997)
28. D. Hofmann, M. Bickermann, R. Eckstein, M. Kölbl, S.G. Müller, E. Schmitt, A. Weber, A. Winnacker: J. Cryst. Growth **198/199**, 1005 (1999)
29. H. Jacobson, J. Birch, U. Lindefelt, C. Hallin, A. Henry, R. Yakimova, E. Janzén: Mater. Sci. Forum **433–436**, 269 (2003)
30. T. Kuhr, J.Q. Liu, H.J. Chung, M. Skowronski: J. Appl. Phys. **92**, 5863 (2002)
31. T.L. Straubinger, P.J. Wellmann, A. Winnacker: Mater. Sci. Forum **353–356**, 33 (2001)
32. Y.A. Vodakov, A.D. Rodenkov, M.G. Ramm, E.N. Mokhov, Y.N. Makarov: Phys. Status Solidi B **202**, 177 (1997)
33. N. Ohtani, M. Katsuno, T. Aigo, H. Yashiro, M. Kanaya: Mater. Sci. Forum **338–342**, 379 (2000)
34. D. Schulz, M. Lechner, H.-J. Rost, D. Siche, J. Wollweber: Mater. Sci. Forum **433–436**, 17 (2003)

35. B.J. Skromme, K. Palle, C.D. Poweleit, L.R. Bryant, W.M. Vetter, M. Dudley, K. Moore, T. Gehoski: Mater. Sci. Forum **389–393**, 455 (2002)
36. R.S. Okojie, M. Xhang, P. Pirouz, S. Tumakha, G. Jessen, L.J. Brillson: Appl. Phys. Lett. **79**, 3056 (2001)
37. R.S. Okojie, M. Xhang, P. Pirouz, S. Tumakha, G. Jessen, L.J. Brillson: Mater. Sci. Forum **389–393**, 451 (2002)
38. H.J. Chung, J.Q. Liu, A. Henry, M. Skowronski: Mater. Sci. Forum **433–436**, 253 (2003)
39. G. Younes, G. Ferro, C. Jacquier, J. Dazord, Y. Monteil: Mater. Sci. Forum **433–436**, 119 (2003)
40. J.Q. Liu, H.J. Chung, T. Kuhr, Q. Li, M. Skowronski: Appl. Phys. Lett. **80**, 2111 (2002)
41. H. Iwata, U. Lindefelt, S. Öberg, P.R. Briddon: J. Phys. Condens. Matter **14**, 12733 (2002)

# Homoepitaxial and Heteroepitaxial Growth on Step-Free SiC Mesas

P.G. Neudeck and J.A. Powell

## 1 Introduction

Presently, SiC devices are implemented in homoepitaxial films grown on large 4*H*- and 6*H*-SiC wafers cut from large SiC boules and with surfaces polished 3°–8° *off-axis* from the (0001) basal plane. This conventional approach has been largely unable to prevent many substrate crystal defects from propagating into SiC epilayers where they have been shown to harm the performance of the electronic devices. Furthermore, this approach has also not supported the implementation of potentially useful SiC heterojunction devices.

This article describes recent advancements in SiC epitaxial growth that begin to overcome the above shortcomings for arrays of mesas patterned into commercial nearly *on-axis* SiC wafers. These advancements are largely based upon properly controlling the SiC growth surface step structure to a degree not possible with off-axis wafer polish. First, we show that atomic-scale surface steps can be completely eliminated from 4*H*- and 6*H*-SiC mesas via on-axis homoepitaxial step-flow growth, forming (0001) basal plane surfaces (up to 0.4 mm × 0.4 mm) far larger than previously attained or thought possible. Step-free surface areas are then extended by growth of thin lateral cantilevers from the mesa tops. These lateral cantilevers enable substrate defects to be controllably reduced and relocated in homoepitaxial films in a manner not possible with conventional off-axis SiC growth. Finally, growth of vastly improved 3*C*-SiC was achieved on 4*H*-SiC and 6*H*-SiC mesas using a newly developed step-free surface heteroepitaxy process. The new growth developments described in this article should enable a variety of improved homojunction and heterojunction silicon carbide electronic devices.

## 2 Background

In order to appreciate the progress described in the remainder of this article, the relevant background and state of prior understanding of SiC epitaxial growth on conventional SiC wafers cut to within 10 degrees of the (0001) plane is briefly reviewed in this section. Herein, any wafer surface within 0.5° of the basal plane shall be called *on-axis*. The topic of SiC epitaxial growth and film defects on non-SiC substrates (such as silicon) and on non-standard

SiC surface orientations, such as  $(1\bar{1}00)$ ,  $(11\bar{2}0)$ , and  $(03\bar{3}8)$  is beyond the scope of this article [1, 2].

There are many possible different crystal structures (i.e., polytypes) for SiC, each of which has its own set of semiconductor properties. As better described in [3], the crystal structure of each polytype is described by a repeated stacking sequence of tetrahedrally bonded Si-C bilayers. The atoms in any bilayer can take on one of three positions (labeled as “A”, “B”, or “C”) relative to other bilayers in the lattice. The cross-sectional structure and associated bilayer stacking sequences of the most commonly produced polytypes are shown in Fig. 1.  $3C$ -SiC is the only SiC polytype with a cubic crystal structure, and thus is the only SiC polytype with four geometrically equivalent  $\langle 111 \rangle$  stacking directions. There are two rotational variants of  $3C$ -SiC, denoted as  $3C(I)$  and  $3C(II)$ , that are related to each other by a  $180^\circ$  rotation about a stacking direction. The other SiC polytypes have only one stacking direction, the  $\langle 0001 \rangle$  crystallographic  $c$ -axis. The close-packed planes normal to the stacking directions (i.e.,  $\{111\}$  for  $3C$ -SiC and  $\{0001\}$  for the

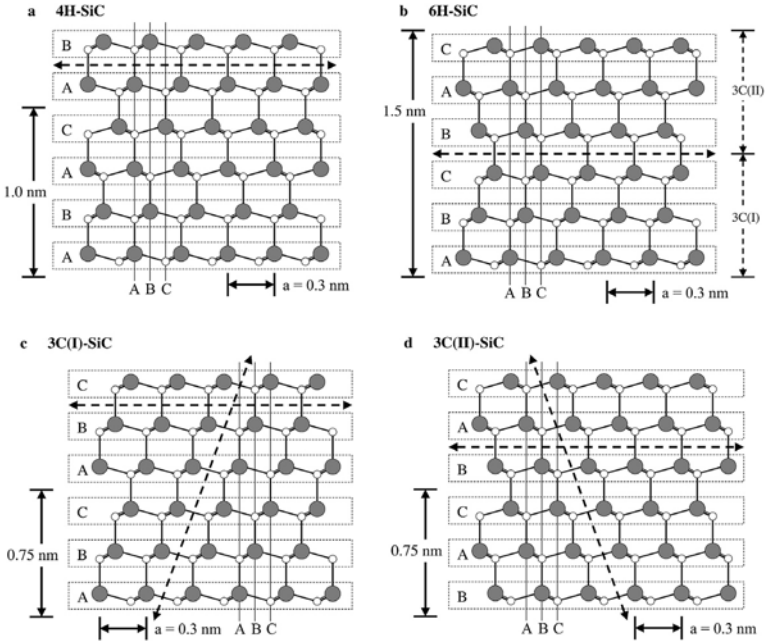


**Fig. 1.** Crystal structure of major SiC polytypes projected onto  $(11\bar{2}0)$  or  $(110)$  planes. The bilayer stacking sequence,  $c$ -axis stacking repeat height, in-plane lattice parameter ( $a = 0.3$  nm), and corresponding lateral positions of silicon (dark) atoms are illustrated. The  $\{0001\}$  basal plane for  $4H$ -SiC and  $6H$ -SiC and two of the four equivalent  $\{111\}$  planes for  $3C$ -SiC are illustrated by the dashed lines

other SiC polytypes) have the lowest defect propagation energies, and are thus most favorable for dislocation defect propagation [3, 4].

Most SiC electronic devices realized to date are fabricated in well-controlled homoepitaxial layers grown on top of commercial 4H- and 6H-SiC wafers cut from large boules. To date, 3C-SiC crystals have suffered from excessive densities of extended crystallographic defects, which has largely rendered them unsuitable for the realization of beneficial semiconductor electronics compared to silicon or 4H- or 6H-SiC. The chemical vapor deposition (CVD) technique is widely accepted as offering the most promise for well-controlled homoepitaxial growth required for mass-production of most SiC electronic devices. There are many variations of SiC CVD epitaxial growth, and many rely on heating a 4H- or 6H-SiC substrate to growth temperatures of around 1300°C to 1600°C in the presence of flowing silicon (often SiH<sub>4</sub>) and carbon (often C<sub>3</sub>H<sub>8</sub>) containing gas species in a carrier gas (often H<sub>2</sub>) at various pressures near or below atmospheric pressure [5]–[10].

## 2.1 Role of Steps and Terraces in Epitaxial Growth of SiC

Control of crystal polytype and minimization of extended crystal defects (i.e., dislocations) during SiC epitaxial growth is necessary for the manufacture of reproducible SiC electronic devices. The microscopic structure and growth evolution of the SiC epitaxial growth surface has a large impact on polytype and quality of the grown SiC crystal.

Figure 2 shows a simplistic microscopic depiction of a SiC growth surface, which is prepared by polishing the surface of a SiC wafer cut from a large boule to within 10° of parallel to the (0001) crystallographic basal plane. Due to the off-cut angle (i.e., tilt angle) of the surface polish, the growth surfaces have atomic scale steps separated by basal plane terraces, as schematically depicted in Fig. 2. Single crystal growth usually takes place when gas source molecules are chemisorbed onto the crystal growth surface in a weakly bound highly mobile state. The adsorbed molecules diffuse across the wafer surface

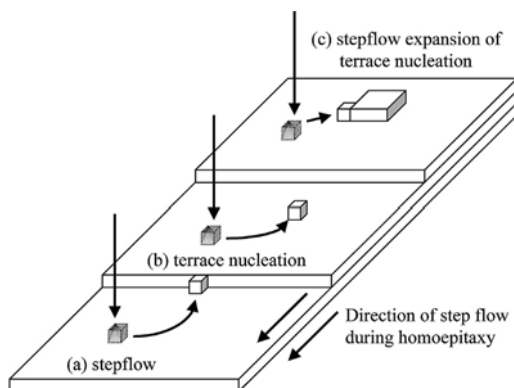


**Fig. 2.** Simplified schematic illustration of steps and adatoms on SiC epitaxial growth surface

until they reach a favorable bonding site, where they are then incorporated into the crystal. The favorable bonding site is often a step or defect on the crystal surface. Instead of growing in monolayers (e.g., a silicon monolayer growing followed by a carbon monolayer), the CVD epitaxial growth of SiC is observed to proceed via lateral extension of bilayers, or as multiple bilayers [9, 11, 12]. Step heights observed on all as-CVD-grown SiC surfaces are multiples of 0.25 nm, the height of a single Si-C bilayer. The tetrahedral bonding configuration of SiC supports lateral stepflow growth of bilayers across the crystallographic basal plane during CVD growth. The tetrahedral bonding of SiC is such that the step edge has a higher bond density available to facilitate reactant incorporation into the crystal (i.e., growth) than the top surface of a basal plane terrace.

### 2.1.1 Stepflow Growth of Homoepitaxial 4*H*- and 6*H*-SiC

Presently, all SiC devices are implemented in homoepitaxial films of the 4*H*- and 6*H*-SiC polytypes grown on commercial SiC wafers with surfaces polished 3° to 8° off the (0001) basal plane. This off-axis polish provides a high density of steps so that step-controlled epitaxy can be used to grow 6*H*-SiC and 4*H*-SiC homoepilayers [5, 7, 13]. The high step density and small terrace width ensures migration of mobile surface-adsorbed growth adatoms to step edges where they incorporate into the crystal, as depicted on terrace (a) of Fig. 2. Thus, homoepitaxy of 4*H*-SiC or 6*H*-SiC is kinetically controlled growth, in that it relies on lateral bilayer expansion (i.e., lateral stepflow) from substrate step edges for growth and structural stacking replication.

### 2.1.2 Terrace Nucleation of Heteroepitaxial 3*C*-SiC

It is well known that 3*C*-SiC layers, usually with many extended crystal defects, can be nucleated and grown on 6*H*-SiC or 4*H*-SiC “on-axis” wafers, in which the wafer surface is polished to within a few tenths of a degree of being parallel to the crystallographic (0001) basal plane [7, 9, 13, 14]. Such a low polish angle greatly increases the length of terraces (i.e., distance between steps) on the growth surface (Fig. 2). The nucleation of 3*C*-SiC occurs in epitaxial growth situations where growth reactants adsorbed onto the substrate surface two-dimensionally (2D) nucleate and incorporate into the crystal on top of basal plane terraces between the steps. Such nucleation, schematically depicted on terrace (b) of Fig. 2, occurs when adsorbed surface adatom diffusion length becomes small (i.e., surface adatom mobility is low) compared to average terrace length (i.e., distance between steps). The sides of terrace nucleated islands form additional steps (i.e., favorable adatom bonding sites) on the growth surface, so that islands can stepflow expand as depicted on terrace (c) of Fig. 2.

The fact that 2D terrace nucleation consistently produces the 3*C* polytype in conventional SiC CVD epitaxy processes suggests that the cubic bilayer

stacking sequence is thermodynamically preferred for standard SiC epitaxial growth conditions. Some prior works, such as Fig. 3 of [7], suggest that either rotational variant of 3C-SiC (3C(I) or 3C(II)) could nucleate on the same (0001) 4H- or 6H-SiC basal plane terrace.

## 2.2 Extended Defects in SiC Epilayers

### 2.2.1 Defects in 4H- and 6H-SiC Homoepilayers

There are numerous extended crystallographic defects found in 4H- and 6H-SiC homoepitaxial layers. Many of these defects originate in the initial substrate and propagate into the epilayers during growth [10],[15]–[18]. Axial screw dislocations (SD's) have the most impact on the homoepitaxial growth described in this article. Axial screw dislocations, both hollow core micropipes (with large dislocation Burgers vectors) and closed-core screw dislocations (with small dislocation Burgers vectors), are examples of extended defects that originate in the substrate and propagate along the crystallographic  $c$ -axis through SiC epilayers to adversely affect many SiC electronic devices [10],[17],[19]–[22]. The self-replicating structural nature of screw dislocations assists the growth of many crystals, including 4H- and 6H-SiC  $c$ -axis boules, by providing a continual spiral pattern of new growth steps on the crystal surface [3, 23, 24]. Thus, screw dislocation growth spirals lead to the formation of hexagonal growth hillocks in 4H- and 6H-SiC homoepilayers grown on substrates with surface angles of less than a degree [3, 9, 11]. However, it is important to note that growth of conventional off-axis 4H- and 6H-SiC homoepilayers is dominated by steps supplied by the relatively high wafer miscut angle, so that steps provided by screw dislocations have only a small localized impact on the morphology (formation of a small surface pit) of standard SiC epilayers used for present-day SiC electronic devices [25].

### 2.2.2 Defects in 3C-SiC Heteroepilayers

As discussed above in Sect. 2.1.2, terrace nucleation and growth of 3C-SiC becomes much more probable when SiC epitaxy is carried out on low offcut angle (0001) 4H- or 6H-SiC substrates. The resulting 3C-SiC heteroepitaxial films have a (111) surface orientation, and were (prior to work reviewed in the present article) known to contain high densities of extended crystallographic defects that rendered them unsuitable for most electronic device applications [3, 7]. The two major defects observed in previous 3C-SiC films on (0001) 4H- and 6H-SiC substrates are double-positioning boundary (DPB) defects and stacking fault (SF) defects [7, 14, 26].

As illustrated in Fig. 3a, DPB defects are essentially a boundary where opposite rotational variants of 3C-SiC meet. A DPB defect can be created when islands of the two different rotational variants of 3C-SiC (i.e., 3C(I) and 3C(II) of Fig. 1) nucleate at separate locations on a 4H- or 6H-SiC substrate

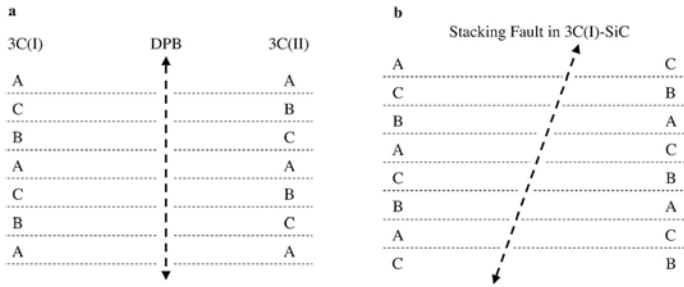


**Fig. 3.** Examples of discontinuous bilayer stacking associated with (a) double-positioning boundary (DPB) defect, and (b) stacking fault (SF) in 3C-SiC

and then laterally coalesce [7, 13]. Stacking faults are planar defects that are essentially a disruption (or misalignment) of the same cubic stacking, as simplistically illustrated in Fig. 3b. Stacking fault defects propagate along the  $\{111\}$  planes. As noted previously, the  $\{111\}$  planes in 3C-SiC and the (0001) plane in hexagonal SiC polytypes are the lowest energy fault planes, so that most movement of dislocations takes place along these crystal planes [3, 4, 27].

### 2.2.3 Role of Steps in Heteroepitaxial Film Defects

Several previous works have indicated that atomic-scale steps in the surface of a 6H-SiC or 4H-SiC substrate are one source of defects in heteroepitaxial films grown thereon. In the case of Group III-nitride (III-N) growth on hexagonal SiC substrates, recent studies have shown that many dislocations propagating from the substrate/epilayer interface originate at atomic-scale steps that are left behind on the substrate surface prior to epitaxial growth [28]. The step-related epitaxial film defects have been shown to arise even when III-N growth is carried out on well-ordered 6H-SiC terraces with *c*-axis unit repeat height (i.e., 1.5 nm for 6H-SiC) step heights defined by in-situ pre-growth etching [29, 30]. Similar observations have also been reported for heteroepitaxial 3C-SiC films grown on 6H-SiC substrates [7, 12, 13]. Thus, these works allude to step-free SiC surfaces as being highly beneficial for realizing improved heteroepitaxial films.

### 2.3 Impact of Pre-Growth Surface Treatments on SiC Epitaxial Growth

Previous works have established surface defects and morphology as important factors in on-axis epitaxial SiC growth. In growth of 3C-SiC on as-grown 6H-SiC Lely substrates it was found that surface contamination played a role in the formation of DPB's in the 3C-SiC films [31]. Subsequently, both 6H-SiC and 3C-SiC epitaxial films were grown on nearly on-axis (about 0.2° tilt angle) commercial SiC wafers [14]. It was found that, if the 6H-SiC substrate

was subjected to a HCl etch at 1375°C, homoepitaxial 6H films could be grown at 1450°C over large areas (several mm across) without 3C-SiC inclusions. It was also found that by intentionally damaging the substrate at a specific location, 3C-SiC films with reduced DPB density could be grown. It was concluded that the HCl etch at intermediate temperatures was very effective in removing surface damage due to wafer polishing and surface contamination. A growth model was proposed wherein the 3C terrace nucleation was facilitated by dislocations and surface contamination, and not a result of insufficient surface mobility of precursor adatoms.

In further growth studies, 1 mm square growth mesas were cut into the surfaces of nearly on-axis 6H-SiC substrates [32, 33]. Following etching and growth, some of these mesas yielded 3C-SiC heterofilms and some mesas yielded 6H-SiC homofilms. In most cases the 3C-SiC films nucleated at a corner of a mesa and then grew laterally across the mesa. It was suggested that in the early stages of growth a locally atomically flat 6H-SiC region forms at the uppermost atomic layer of the mesa, and that this region becomes a preferred site for terrace nucleation of 3C-SiC. Most 3C-SiC mesa films grown by this technique were free of DPB's with a reduced incidence of stacking faults. Diodes fabricated from these films exhibited the best blocking characteristics ever reported for 3C-SiC, but the remaining defects nevertheless rendered them significantly inferior to the 6H-SiC diodes in other 1 mm square regions of the same wafer [34].

### 3 Step-Free Basal Plane Mesa Formation

#### 3.1 Process

As discussed in Sect. 2.3, on-axis homoepitaxy of (0001) 4H- and 6H-SiC is possible when proper pre-growth surface treatment and epitaxial growth conditions are employed. In the absence of terrace nucleation of 3C-SiC, kinetic dominated homoepitaxial growth occurs from screw dislocation step spirals. By etching a pattern of deep trenches into an on-axis SiC wafer surface to form mesas prior to epitaxial growth, some surface regions without screw dislocations can be isolated from the kinetic growth steps produced by screw dislocations.

The process schematically depicted in Fig. 4 has enabled the realization of large (up to 0.4 mm × 0.4 mm) (0001) basal plane surfaces completely free of bilayer steps on top of 4H- and 6H-SiC mesas [35, 36]. Figure 4a depicts the mesa cross-section and initial (due to unavoidable polish error) surface steps prior to epitaxial growth. Figure 4b depicts the mesa after pure stepflow homoepitaxy grows all initial surface steps over to the edge of the mesa, leaving behind a perfectly flat (0001) basal plane top surface that is completely free of atomic steps (i.e., is a single large terrace). For simplicity, growth that occurs on the mesa sidewall and bottom of the trenches is not

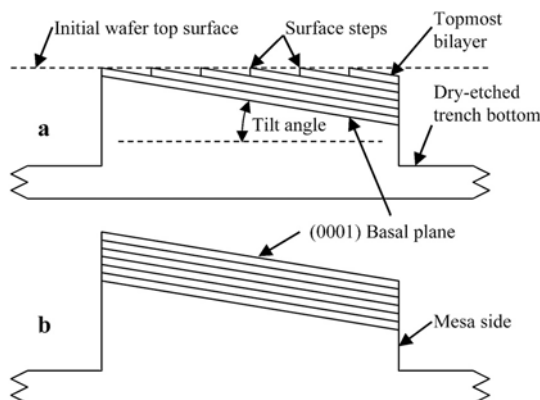


**Fig. 4.** Simplified cross-sectional depiction of process for realizing step-free SiC mesas. Bilayers and surface step structure of mesa (a) before growth and (b) following stepflow homoepitaxy without terrace nucleation or screw dislocation [35]

shown in Fig. 4b. The growth process, more fully described in [35], consisted of (1) an in-situ  $\text{H}_2$  etch for 5 minutes at 1600–1650°C at a pressure of 100–200 mbar followed by (2) growth using  $\text{SiH}_4$  (2.7 cm<sup>3</sup>/min) and  $\text{C}_3\text{H}_8$  (0.3 cm<sup>3</sup>/min) in  $\text{H}_2$  (total flow 4400 cm<sup>3</sup>/min) at 1600–1650°C at a pressure of 200 mbar. It should be noted that the uncoated graphite in the reactor supplies additional carbon to the growth environment, as we have observed some SiC growth in this reactor configuration even when  $\text{C}_3\text{H}_8$  gas flows are reduced to zero. As discussed in Sect. 2.3, the in-situ etch crucially removes surface damage and contamination that could otherwise lead to undesired terrace nucleation of 3C-SiC during the initial stages of epitaxial growth. For 4H-SiC epilayers grown on 8° off-axis wafers in these reactor conditions, 2 μm/hour growth rates were obtained.

### 3.2 Results

Following growth, numerous mesas on over a dozen wafer samples have been characterized by differential interference contrast (DIC) optical microscopy and atomic force microscopy (AFM). The typical findings can be summarized by comparing two adjacent mesas shown in the DIC optical micrographs of Fig. 5. The left mesa of the Fig. 5 micrograph has an optically featureless top surface. A 50 μm × 50 μm AFM scan, one of 16 taken to span the entire top surface area of the left mesa, is shown in Fig. 6a [35]. Despite some particulate contamination, no atomic steps were revealed in AFM scans of the entire left mesa. In contrast, a hexagonal growth hillock due to a screw dislocation is readily apparent in the optical micrograph of the right Fig. 5 mesa. The AFM scan measured at the center of the hexagonal growth hillock, shown in Fig. 6b, reveals organized growth steps (0.5 nm and 1.0 nm high)

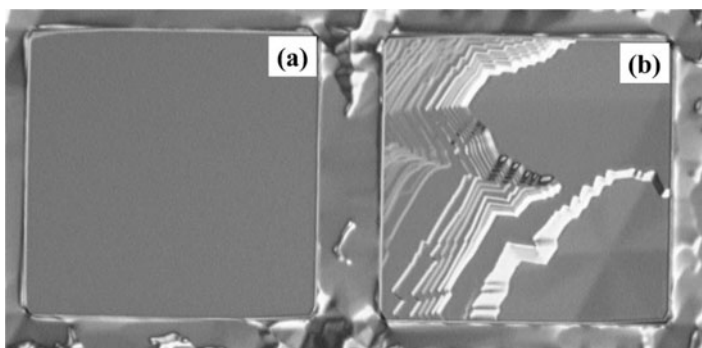


**Fig. 5.** DIC optical micrographs of two  $200\ \mu\text{m} \times 200\ \mu\text{m}$  mesas following homoepitaxial growth. Mesa (a) formed a step-free surface, while mesa (b) exhibits bunched steps and a hexagonal growth hillock from a screw dislocation in the lower right of the mesa [35]

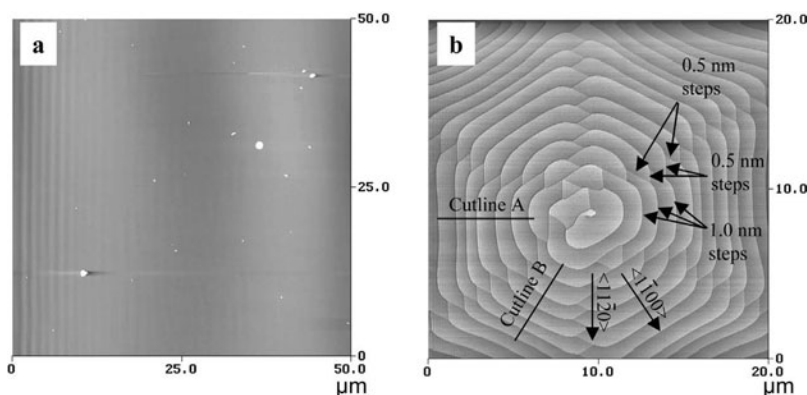


**Fig. 6.** AFM measurements recorded on mesas shown in Fig. 5. Mesa (a) exhibiting no steps, and peak of hexagonal hillock of mesa (b) [35]

emanating from an elementary screw dislocation (i.e., screw dislocation with Burgers vector equal to the  $1.0\ \text{nm}$  stacking repeat height of  $4H\text{-SiC}$ ). The interleaved step pattern of Fig. 6b evolves due to the anisotropic bonding of  $4H\text{-SiC}$  bilayers as a function of crystallographic direction [9, 11].

The primary factor limiting the size and yield of step-free surfaces produced in these experiments was the presence of screw dislocations in the substrates. As with the example mesas illustrated in Figs. 5 and 6, mesas with screw dislocations were identifiable using DIC optical microscopy due to the presence of hexagonal growth hillocks. Over 90% of mesas that failed to become step-free following epitaxial growth contained at least one screw dislocation. Wafers with regions of relatively low substrate screw dislocation density enabled the realization of some  $0.4\ \text{mm} \times 0.4\ \text{mm}$  (the largest mesa size patterned) step-free surfaces. The mesa film polytypes were spa-

tially mapped by both thermal oxidation color mapping and X-ray topography [26, 37]. Over 90% of mesa tops in wafer central regions maintained the  $4H$ -SiC polytype, exhibiting no evidence of  $3C$ -SiC nucleation.

### 3.3 Impact on SiC Growth Understanding

The above experiments show that (0001) basal plane surfaces several hundred micrometers in dimension can be homoepitaxially grown on  $4H$ - and  $6H$ -SiC mesas without screw dislocations. These results could not have been achieved without complete suppression of  $3C$ -SiC terrace nucleation on mesas during growth. The suppression of  $3C$ -SiC nucleation over *tenth-millimeter* scale terrace dimensions during SiC epitaxial growth had never previously been demonstrated, especially at growth temperatures below  $1700^{\circ}\text{C}$ . In fact, the above experimental results are quantitatively inconsistent with the previous experimental SiC growth nucleation studies at Kyoto University [7, 38]. However, the Kyoto studies failed to employ important pre-growth etching processes discussed above in Sect. 2.3. As discussed in Sect. 2.3, proper surface preparation, pre-growth etching, and growth procedures are crucial toward preventing terrace nucleation to obtain high-quality stepflow homoepitaxial film growth on low offcut angle (0001) surfaces. Following publication of our recent studies described in this section, the Kyoto group has subsequently adopted and further investigated in-situ pre-growth etching to also obtain high quality homoepitaxial growth while suppressing terrace nucleation on low-offcut angle substrates [39].

The above experiments also show that once a step-free surface is established, homoepitaxial growth up the crystallographic  $c$ -axis direction completely ceases. Therefore, the above experiments in forming step-free mesas are a confirmation that well-ordered homoepitaxial growth of hexagonal SiC polytypes in the crystallographic  $c$ -axis direction cannot be carried out without screw dislocations providing new growth steps. However, where screw dislocations are present, these experiments demonstrate that homoepitaxial growth of  $4H$ - and  $6H$ -SiC can be carried out at substrate surface miscut angles as low as zero degrees (i.e., perfectly on-axis) at  $1600$ – $1650^{\circ}\text{C}$  growth temperatures.

## 4 Homoepitaxial Growth of Thin SiC Cantilevers

### 4.1 Growth Process and Results

Continued epitaxial growth of a screw-dislocation-free mesa following achievement of a step-free surface leads to the formation of thin lateral cantilevers that extend the step-free surface area from the top edge of the mesa side-walls [40, 41]. By selecting a proper pre-growth mesa shape and crystallographic orientation, the rate of cantilever growth can be greatly enhanced in a “web growth” process that has been used to enlarge step-free surface areas and overgrow and laterally relocate micropipes and screw dislocations.

#### 4.1.1 General Growth Properties

The cantilevered web growth process is briefly illustrated in Figs. 7–10. The specific experimental processes employed were identical to those stated in Sect. 3.1, except for the fact that more complex mesa shapes and longer epitaxial growth times were sometimes employed [40]. Figure 7 shows a schematic cross-section of cantilever formation as a mesa (already rendered step-free as depicted in Fig. 4b) is subjected to additional growth time with terrace nucleation remaining completely suppressed. Growth adatoms, harvested by the step-free surface, migrate to the mesa edges where the more favorable sidewall bonding leads to incorporation into the crystal near the top of the mesa sidewall. This leads to the growth of thin cantilevers, on the order of one to two micrometers in thickness, that seamlessly extend the step-free top surface area of a mesa. As depicted in Fig. 7, growth on the underside of the thin cantilevers is not uniform, partially due to mesa sidewall growth steps. It is important to note that almost no cantilevering is observed when the pre-growth mesas contain substrate screw dislocations, due to the previously discussed fact that screw dislocations provide steps for vertical (instead of lateral) growth of such mesas.

Figures 8 and 9 illustrate that the lateral propagation of the step-free cantilevered surface is significantly affected by pre-growth mesa shape and crystallographic orientation. The highest lateral expansion rates of thin cantilevers were observed to occur at the inside concave corners of mesas. When complete spanning of the interiors of V's (Fig. 8) and other (Fig. 9) non-hollow mesa shapes by thin cantilevers was achieved, step-free surfaces with significantly enlarged surface area over the pre-growth mesa area were formed. As such growth loosely resembles the webbed feet of a duck, we refer to such interior-corner enhanced cantilevered growth as *cantilevered web growth*. The thin cantilevers exhibit  $\{1\bar{1}00\}$  growth facet formation typical of hexagonal polytype SiC crystals. Some lateral enlargement of the mesa support structure takes place during the web growth process. Non-uniform underside growth is evident in the interference fringes seen in the cantilevered regions shown in the Figs. 8 and 9 optical micrographs.

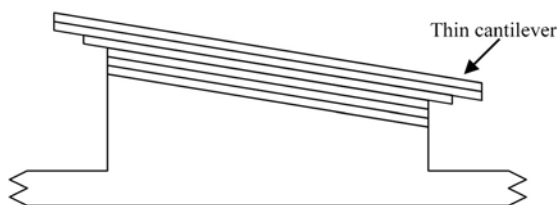


**Fig. 7.** Simplified cross-sectional illustration of cantilever growth at the top edges of a step-free mesa

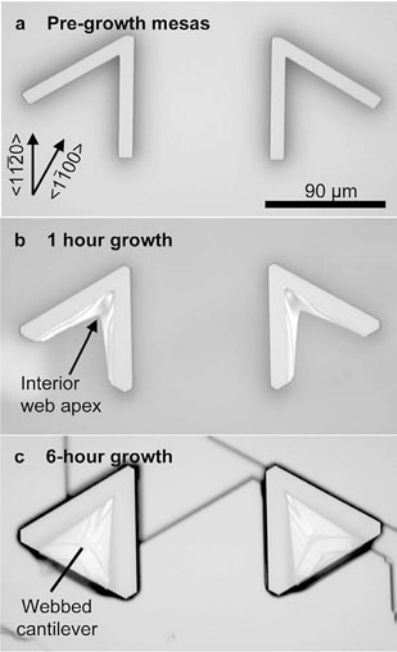


**Fig. 8.** Optical micrographs illustrating thin webbed cantilever formation on a V-shaped pre-growth mesa [40]

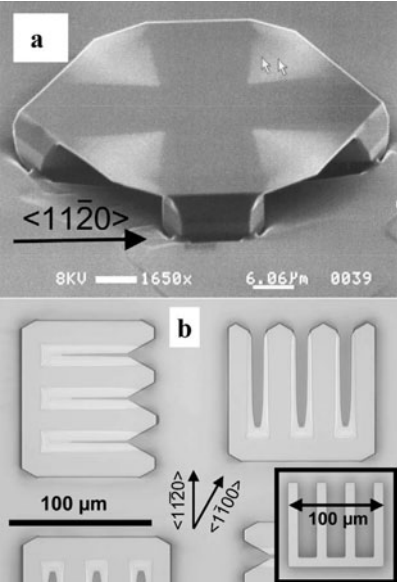


**Fig. 9.** Thin lateral cantilevers grown from (a) plus-shaped pre-growth mesa and (b) comb-shaped (*inset*) pre-growth mesas [40]

### 4.1.2 Cantilever Coalescence

It is important to note that when thin cantilevers from separated pre-growth mesa shapes (such as side-by-side rectangles) converged during growth, imperfect coalescence was almost always observed [40]. In order for a step-free surface to be realized following growth, mesas must have continuous top surface shapes that (like the V-shape of Fig. 8a) promote a progressive zippering of thin cantilevers from opposite arms. Using a much larger multi-armed pre-growth mesa shape that promoted zipper-like cantilever coalescence, webbed surfaces as large as  $1 \times 10^{-3} \text{ cm}^2$  were achieved, representing a more than 4-fold enlargement from pre-growth mesa surface area. As discussed below in Section 4.1.4 and in [42], dislocations were sometimes observed to form when cantilevers from the same mesa shape coalesced down to a point from more than two sides.

### 4.1.3 Dislocation Reduction Properties

Because the crystal structure of the thin cantilevers is established laterally from the mesa sidewalls, cantilevered films can successfully overgrow substrate regions with dislocations, including axial screw dislocations. Detailed analysis of cantilevered web films formed directly over axial screw dislocations show that these defects are completely absent from the cantilevered material [40, 41]. For example, the webbing of the rightside mesa of Fig. 8c resides directly over a micropipe (screw dislocation), yet its surface was measured by AFM to be completely free of any atomic steps (in stark contrast to the screw dislocation steps shown in Fig. 6b). In addition, recent defect-preferential etching studies (using molten potassium hydroxide) of thin cantilevered webs failed to reveal any etch pits in properly coalesced web film regions, despite the fact that hexagonal etch pits due to non-screw dislocations were observed in adjoining pre-growth mesa regions [42].

### 4.1.4 Lateral Relocation of Screw Dislocations

In contrast to open pre-growth mesa surface shapes (such as the V-shape of Fig. 8a), homoepitaxial web growth can also be applied to mesa surface shapes that form enclosed hollow geometries. An example of an enclosed hollow pre-growth mesa geometry is shown in the upper right inset of Fig. 10, wherein the raised pregrowth mesa surface forms six triangular hollow trench regions in the interior [42]. By carrying out web growth on such a structure until webbed cantilevers coalesce in the middle of each triangular hollow region forming a complete roof, substrate screw dislocations that reside within each hollow region can be laterally relocated and combined to the central point of final cantilevered film coalescence. Figure 10 shows an optical micrograph of a mesa following complete webbed cantilever coalescence. Most of the optical features in the webbed regions arise from non-uniform growth on the undersides of

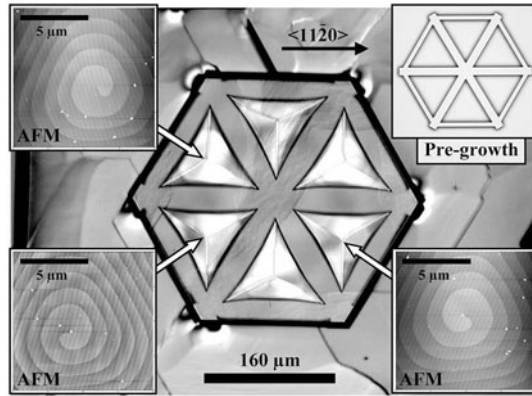


**Fig. 10.** Optical micrograph of spoked hexagonal mesa following web growth that completely overgrew six enclosed triangular trench regions. The AFM insets show the three screw dislocation growth spirals that formed exactly where roof closures occurred [42]

the cantilevers [40]. AFM measurements revealed that three elementary screw dislocation growth spirals, each shown in AFM insets of Fig. 10, formed in the film roof at three respective points of film coalescence. For reasons that are not yet understood, these growth spirals lack the interleaving step pattern observed Fig. 6b. No other growth spirals were observed elsewhere on the mesa surface, even over the pre-growth mesa and the other three cantilever coalescence points.

The above results clearly demonstrate that coalesced web growth from hollow enclosed mesa shapes can produce screw dislocations in predictable lateral locations. The point of final coalescence can be designed into the pre-growth mesa pattern using a basic understanding of the cantilever growth and faceting behavior of SiC as a function of crystallographic direction. Following coalescence, the preplaced screw dislocation can then provide steps for *c*-axis growth of on-axis homoepilayers on top of the mesa structure. Devices fabricated on top of such mesas can then be patterned to avoid the pre-placed screw dislocations.

## 4.2 Process Limitations and Further Optimization

It is important to note that uncontrolled material growth in the trench regions, (visible in Figs. 8–10) can rise up to interfere with laterally expanding cantilevers whose growth is confined along the (0001) basal plane. The merging of webs with trench growth actually limited the step-free yield of the largest webbed surfaces produced during initial experiments [40]. However, trench growth can be selectively prevented in a more optimized process using patterned growth masking techniques [43, 44].

A more fundamental limitation of the homoepitaxial SiC web growth process is the fact that almost no cantilevering occurs when pre-growth mesas contain substrate screw dislocations, due to the previously discussed fact that screw dislocations provide steps for vertical growth of such mesas. Pre-growth mesa shapes with long narrow fingers joined on one end (such as the comb shape of Fig. 9b) can be employed to maximize the webbing area while minimizing the chances that a pre-growth mesa will undesirably contain a screw dislocation. Such pre-growth mesa designs may require longer lateral cantilever extensions (i.e., growth of more material) in order to achieve a completely webbed structure. Higher temperature CVD epitaxial techniques should enable increased growth rate and surface adatom mobility favorable to realizing larger step-free webbed cantilevers [8]. The degree to which these goals can be achieved, coupled with the substrate screw dislocation density, will determine practical limits as to the size of step-free surfaces that can be realized using further optimizations of the SiC web growth process.

## 5 Step-Free Surface Heteroepitaxy of 3C-SiC

For many years researchers have attempted to grow 3C-SiC heteroepitaxial films of sufficient quality to better enable high-performance wide bandgap electronic devices. However, all previous efforts resulted in 3C-SiC with too many extended crystal defects to be useful for important electronic applications. In this section, we describe a step-free surface heteroepitaxy technique that has reproducibly grown high-quality 3C-SiC on step-free 4H- and 6H-SiC mesa surfaces [45, 46].

### 5.1 Experimental Process Description

The step-free surface heteroepitaxy process starts by first etching mesas and growing step-free 4H- and 6H-SiC surfaces using the same procedures described above in Sect. 3 and 4. Once homoepitaxial growth has achieved step-free mesas, heteroepitaxial nucleation and growth of 3C-SiC is then initiated in a controlled manner in-situ by lowering the growth temperature. As previously discussed in Sect. 2.1, the decreased growth temperature decreases surface adatom mobility, thereby increasing the chances (rate) of 2D

**Table 1.** Experimental 3C-SiC Initial Nucleation Processes [46]

Sample	Temperature profile (from 1620°C)	SF density
A	Ramp down 190° over 5 min.	$> 10^4/\text{cm}^2$
B	Ramp down 120° over 5 min.	0
C	Ramp down 190° over 60 min.	0

terrace nucleation that initiates 3C-SiC growth on the (0001) basal plane surface. Temperature decreases to achieve nucleation were carried out with well-controlled ramps to avoid rapid thermal and chemical transient effects. The specifics of the 3C film nucleation and growth temperature ramps are given in Table 1.

## 5.2 Experimental Results

Following epitaxial growth, films were characterized initially by DIC optical microscopy and AFM. Samples were dry thermally oxidized for 5 hours at 1150°C to color-map film polytype and reveal DPB and SF defects [26]. Detailed polytype mapping of some samples was carried out using X-ray topography. Substrate defects (e.g., screw dislocations) in the substrate were mapped using the backreflection geometry, while forward-reflection geometry was used to spatially map 3C(I) and 3C(II) heteroepilayers [37]. High-resolution X-ray diffractometry (HRXRD) was employed to measure substrate and film lattice parameters [47, 48]. A few 3C mesas were also studied by high-resolution cross-sectional transmission electron microscopy (HRX-TEM) and molten potassium hydroxide (KOH) etching [45].

### 5.2.1 Defective 3C Films on Mesas with Screw Dislocations

Figure 11 shows an optical micrograph typical of many 3C-SiC heterofilms that were grown on the top of 4H- or 6H-SiC substrate mesas *that contained a screw dislocation*. The defect-enhanced oxidation reveals an abundance of both DPB and SF defects that arose due to the fact that the 3C-SiC film was nucleated on a stepped 4H-SiC surface (due to growth steps provided by the screw dislocation), instead of on a step-free surface. The region of lighter oxide color denotes a region of 4H-SiC, and the peak of a hexagonal screw

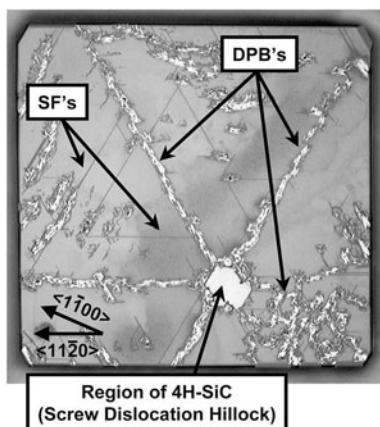


**Fig. 11.** Optical micrograph of 200  $\mu\text{m} \times$  200  $\mu\text{m}$  oxidized mesa showing defective 3C-SiC film (darker oxide) nucleated on 4H-SiC mesa *with steps* from a screw dislocation

dislocation resides roughly at the center of this region.  $3C$ -SiC, denoted by the darker (thicker) oxide color, surrounds the screw dislocation. As more thoroughly described in [37], a mixed polytype structure of this kind is anticipated when nucleation and growth of  $3C$ -SiC competes with stepflow growth from screw dislocations.

The typical defect structure observed in the  $3C$ -SiC surrounding the screw dislocation is extremely noteworthy. In addition to numerous stacking faults, DPB defects surround the screw dislocation, roughly corresponding to the  $\langle 11\bar{2}0 \rangle$  directions of the underlying  $4H$ -SiC. This defect structure indicates that opposite rotations of  $3C$ -SiC were nucleated roughly every  $60^\circ$  surrounding the screw dislocation. As described in [9, 11], the stacking termination of step terraces interleaved around a  $4H$ -SiC screw dislocation (such as shown in Fig. 6b) alternates between AB and AC every  $60^\circ$  surrounding the screw. Thus, the Fig. 11 defect structure supports a terrace nucleation model in which the initial  $3C$ -SiC bilayers that nucleate on a terrace acquire the stacking that continues the local cubic stacking established by the topmost two bilayers [12, 36, 49]. For example, if terraces along cutline A of Fig. 6b ended with AB stacking (B being the topmost bilayer), 2D nucleation would yield  $3C(I)$  with ABC stacking. Terrace nucleation along cutline B would then result in  $3C(II)$ . Thus, in the absence of kinetic “step-flow” polytype control, experimental evidence indicates that there is a strong thermodynamic driving force for new bilayers to continue the local cubic stacking of the immediately underlying bilayers.

### 5.2.2 $3C$ -SiC Films on Step-Free Mesas

Consistent with the thermodynamic cubic stacking nucleation model discussed in the preceding section, DPB defects were experimentally eliminated from almost all  $3C$ -SiC heterofilms nucleated on step-free  $4H$ - and  $6H$ -SiC mesas. Figure 12 shows data typical of the screw-dislocation-free mesas on sample B of Table 1. In contrast to the defects readily apparent in Fig. 11, the Fig. 12 optical micrograph of the oxidized mesa reveals that no DPB's and no SF's intersect the film surface. The HRXTEM from an SF-free mesa

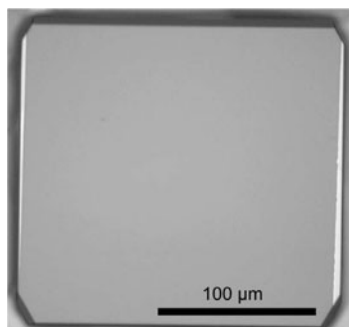


**Fig. 12.** Optical micrograph of oxidized  $200\ \mu\text{m} \times 200\ \mu\text{m}$   $3C$ -SiC heterofilm nucleated on a *step-free*  $4H$ -SiC mesa. No SF's and no DPB's are observed [46]

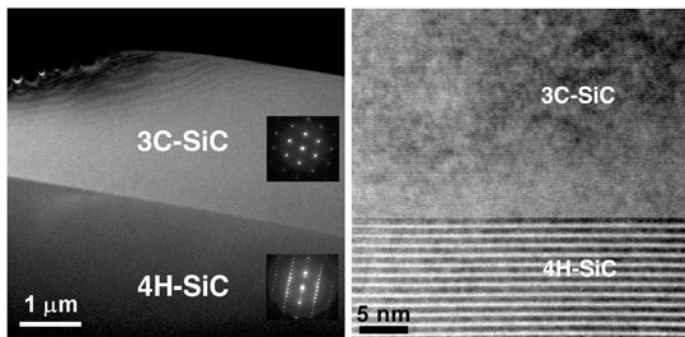


**Fig. 13.** HRXTEM of SF-free 3C-SiC heterofilm on 4H-SiC mesa (*left*) at low magnification and (*right*) high magnification. No defects and no stacking disorder were observed in the 3C heterofilm, and the 3C/4H interface was atomically flat with no steps observed [45]

(on sample C of Table 1) shown in Fig. 13 also indicates a structurally perfect 3C-SiC film with no defects and no stacking disorder detected within the field of view. The lack of any stacking disorder throughout the thickness of the 3C-SiC film is consistent with the thermodynamic model for continuation of local cubic bilayer stacking in growing layers. The apparent 3C/4H interface was perfectly flat and atomically abrupt with no evidence of growth steps and/or dislocations. Spatial mapping of the sample by X-ray topography confirmed that only one phase of 3C-SiC (either variant I or variant II) was present on each screw-dislocation-free mesa, and that no other polytypes grew to a detectable extent [48]. Single Si-C bilayer height (0.25 nm) steps were observed on all 3C-SiC mesa films studied by AFM.

While the step-free surface successfully eliminated DPB defects, the SF content of 3C-SiC films varied greatly as a function of the heterogrowth initiation process [46]. The data of Table 1 indicates a correlation between the in-situ temperature rampdown parameters and the SF-content of the resulting 3C-SiC mesa films. In particular, 3C-SiC films that were nucleated by more rapid temperature decreases (such as sample A of Table 1) exhibited 3C-SiC mesas with a high incidence of stacking fault defects. In contrast, 3C-SiC films nucleated by more gradual temperature decreases (such as samples B and C of Table 1) exhibited high SF-free mesa yields, over 60% on screw dislocation free mesas. The 3C-SiC films subjected to low growth temperatures (i.e., high nucleation rates) after an initial thickness of 3C-SiC had been slowly nucleated (such as sample C) did not exhibit SF's on the majority of screw dislocation free mesas.

Defect preferential etching of 3C-SiC heterofilm mesas (using molten KOH) indicate the possible presence of additional dislocation defects in 3C-SiC films besides DPB's and SF's previously revealed by thermal oxidation [45]. Most  $200\text{ }\mu\text{m} \times 200\text{ }\mu\text{m}$  mesas free of DBP and SF defects typically ex-

hibited 1 to 5 isolated triangular etch pits, which is comparable to (hexagonal-shaped) etch pit densities reported for commercial *4H*- and *6H*-SiC homoepilayers [15]. *3C*-SiC mesas that contained SF and DPB defects typically exhibited at least an order of magnitude higher triangular etch pit density than SF-free mesas. These etch pits remain a subject for further investigation.

The *3C*-SiC mesa heterofilms have also been studied by HRXRD [47, 48]. The measurements distinctly resolve a *3C*-SiC epilayer peak and a *4H*-SiC substrate peak, definitively indicating a difference in lattice constants (both *a* and *c* parameters) for the two materials in the mesa heterostructure. The higher quality *3C*-SiC films exhibited comparable FWHM as the *4H*- or *6H*-SiC substrate and no measurable rotational misorientation with the substrate lattice. In-plane substrate/epilayer lattice constant mismatch ( $\Delta a/a$  range of 0.02% to 0.09%) was observed on all samples indicating that some in-plane lattice mismatch strain relief occurred in the *3C* film. Meanwhile, the measured out-of-plane lattice constant difference  $\Delta c/c$  was  $-0.13\%$  to  $-0.15\%$  for *3C* on *4H* and around  $-0.092\%$  for *3C* on *6H*. The *3C*-SiC films are not fully relaxed, as the HRXRD measured *3C* lattice constants slightly deviated from those of the ideal cubic structure. In particular, the measured *3C* heterofilm lattice is slightly compressed along the in-plane direction and slightly elongated along the out-of-plane direction.

### 5.3 Heteroepitaxial Growth and Defect Formation Model

As discussed in Sect. 2.2, the probability (and rate) of 2D terrace nucleation of *3C*-SiC increases as growth temperature decreases due to decreased adatom surface mobility. Once a *3C*-SiC island nucleates, it then laterally expands via step-flow as depicted for terrace (c) of Fig. 2. Faster temperature drops increase the probability that multiple *3C*-SiC islands will be nucleated on a relatively large step-free *4H/6H* surface, as the resulting fast increase in nucleation rate leaves less time for new islands to enlarge via stepflow before additional islands nucleate elsewhere on the surface. In contrast, more gradual temperature drops provide more time for stepflow expansion of an initial island before other islands are nucleated on the step-free *4H/6H* surface.

Based upon the above, we have hypothesized that the more gradual nucleation temperature ramps permit *3C*-SiC heteroepitaxial growth to initiate from a single *3C*-SiC island, which subsequently expands laterally via stepflow to cover the entire *4H* (or *6H*) mesa before nucleation of a second *3C*-SiC island can occur elsewhere on the *4H* (or *6H*) mesa surface [46, 49]. This growth model conversely suggests that stacking faults arise when multiple *3C* islands terrace nucleate on a single mesa, laterally expand (via stepflow) across the step-free hexagonal-SiC growth surface, and coalesce in a defective manner. Coalescence-related stacking faults have been previously observed in other heteroepitaxial material systems [50, 51]. However, after an initial thickness of *3C*-SiC has been grown via low (i.e., single-island) terrace nucleation conditions, the film quality (i.e., SF-density) does not degrade when

the temperature is lowered to increase terrace nucleation probability (such as sample C of Table 1). Therefore, the experimental results indicate that a key mechanism promoting stacking fault formation is only present when the initial bilayers of the 3C-SiC heterofilm are grown. We have also proposed that a possible driving force for the defective 3C island coalescence is strain, which is largest at the substrate/film heterointerface, and/or strain relief effects that arise from in-plane lattice mismatch between the 3C-SiC film and the step-free 4H (or 6H) mesa [46, 49].

## 6 Conclusion and Future Directions

### 6.1 Summary of New Results and Understanding

The work reviewed in this article demonstrates that device-sized step-free surfaces can be homoepitaxially grown on the hexagonal polytypes of SiC. Growth of such surfaces was accomplished on trench-isolated screw-dislocation-free mesa regions of nearly on-axis wafers by carrying out stepflow homoepitaxial growth with 2D nucleation completely suppressed. The complete suppression of terrace nucleation across terrace widths of hundreds of micrometers had never been demonstrated in SiC prior to this work. The fact that *c*-axis growth became completely arrested (following step-free surface formation) on screw-dislocation free mesas confirms that these defects are necessary step-sources for *c*-axis growth of hexagonal SiC polytypes.

Continued homoepitaxial growth on 4H- or 6H-SiC step-free mesas (with terrace nucleation still suppressed) resulted in evolution of thin lateral cantilevers emanating from mesa tops that seamlessly extended the step-free surface area. The rate of cantilever expansion was observed to depend upon pre-growth mesa shape and crystallographic orientation. The highest cantilever extension rates were observed at the inside corners of concave pre-growth mesa shapes, leading to a process we have named cantilevered web-growth. Thin webbed cantilevers demonstrated the ability to successfully enlarge the step-free surface area directly over micropipes and closed-core screw dislocations. Defect-preferential molten KOH etching failed to reveal hexagonal etch pits on properly coalesced webbed cantilevers. Substrate screw dislocations enclosed by hollow pre-growth mesa shapes were laterally confined in the cantilever films to the point where cantilevers converged to form a complete roof over each hollow region. The screw dislocations with lateral position determined by the final convergence points can then be used to provide new growth steps necessary for growth of an 4H- or 6H-SiC epitaxial layer with lower screw dislocation density than the substrate.

The step-free surface heteroepitaxy growth process has achieved 3C-SiC mesa films completely free of double positioning boundary and stacking fault defects. This process is based upon the initial 2D terrace nucleation and lateral expansion of a single island of 3C-SiC on the step-free (0001) 4H-SiC (or

6H-SiC) mesa surface. Our experimental results indicate that extremely high 3C-SiC film quality was achieved, despite the fact that substrate/film lattice mismatch stress was not fully relieved. The experiments also indicate that terrace-nucleated SiC bilayers will continue the local cubic stacking structure of the immediately underlying bilayer pair.

## 6.2 Major Material Issues for Further Study

The new fundamental SiC growth understanding gained in these initial studies naturally raise a variety of important follow-up questions for future investigation. For example, quantitative limits of terrace nucleation suppression have not yet been explored as a function of wider ranging growth conditions and larger mesa sizes. In addition, none of the growth processes described in this article have been carried out on carbon-face (000 $\bar{1}$ ) wafers. The impact of intentional film doping (both *n*-type and *p*-type) on both step-free surface formation and subsequent 3C-SiC film growth must also be explored. Also, the durability of 3C-SiC films subjected to various processes (such as ion implantation and high temperature annealing) is also a major materials question remaining to be investigated.

## 6.3 Future Device Applications

The crystal growth processes described in this article lay a unique foundation for the experimental realization of a variety of novel prototype device structures. In addition to being an ideal surface upon which to construct atomic-scale nanostructures, the perfectly flat SiC surfaces should also enable better fundamental understanding of SiC interfaces and surfaces.

### 6.3.1 4H/6H-SiC Devices

The perfectly on-axis step-free 4H- and 6H-SiC surfaces are structurally and chemically different from the stepped surface structure of conventional off-axis SiC. The flat surfaces should enable the experimental formation and study of nearly ideal metal-semiconductor Schottky barriers with atomic smoothness and interfacial abruptness over the entire contact area. Such contacts are likely to exhibit less barrier inhomogeneity than those exhibited by off-axis SiC Schottky contacts. Similarly, it seems possible that higher quality inversion-channel MOSFET devices might be realized using such surfaces [52, 53].

The lateral growth techniques described in Sect. 4 offer some interesting new structures and/or benefits to 4H- and 6H-SiC devices. The ability demonstrated in Sect. 4 to reduce and/or relocate dislocations in webbed films could improve the reproducibility, performance, and leakage properties of junctions used for switching or photodetection. In particular, small-area

devices could be fabricated in etch-pit free regions of the crystal, and their electrical performance and reliability compared to devices in bulk crystal regions known to contain defects. The cantilevered geometry also makes it possible to implement lateral SiC device geometries with active areas free of substrate parasitics. In addition, the cantilevers may also be useful in the realization of new single-crystal  $4H/6H$  microelectromechanical device structures, such as accelerometers and pressure sensors for harsh environment applications.

### 6.3.2 3C-SiC Devices

Almost all previous 3C-SiC electronic devices have been realized using inferior crystals with high densities of extended crystallographic defects. This has generally resulted in poor electrical characteristics of 3C-SiC diodes and transistors compared to similar devices implemented in silicon,  $4H$ -SiC, and  $6H$ -SiC. For example, experimental 3C-SiC  $pn$  junctions are unable to support high electric fields without excessive leakage through the crystallographic defects [34].

Now that device-sized regions of low-defect 3C-SiC can be realized (as described above in Sect. 5), the further exploration of potentially important electrical device benefits of 3C-SiC is warranted. For example, 3C-SiC MOSFET's have recently demonstrated much higher inversion channel mobilities than those demonstrated in  $4H$ -SiC MOSFET's [54]. This mobility advantage is believed to arise from the fact that the lower 3C-SiC conduction band energy removes the high density of interface states known to exist close the conduction bands of  $4H$ - and  $6H$ -SiC [55]–[57]. The reduction of interface states should enable a reduction in surface-related generation and recombination phenomenon known to affect bipolar junctions and MOS charge storage (i.e., non-volatile random access memories) and transfer (charge coupled) devices [58]–[62]. In addition, the oxide-semiconductor conduction band potential barrier is close to 0.8 eV higher for 3C-SiC than for  $4H$ -SiC, which should reduce field-assisted carrier tunneling harmful to oxide reliability [55, 63].

The wide 3.2 eV bandgap of  $4H$ -SiC enables high breakdown field beneficial for high voltage power device off-state blocking properties. However,  $4H$ -SiC bipolar power devices must overcome the associated higher built-in potential of the  $pn$  junction before high on-state current density is achieved, which leads to undesired on-state power losses. Therefore, even though the breakdown field of 3C-SiC is somewhat less than  $4H$ -SiC, the lower (by nearly a volt)  $pn$  junction turn-on voltage (due to 2.3 eV bandgap) offers interesting bipolar power device design tradeoffs versus  $4H$ -SiC bipolar devices, and far superior current density performance compared to silicon. Recently, stacking faults have been observed to degrade the operational properties of  $4H$ -SiC bipolar devices [18]. In addition, thermal processing has also been shown to induce stacking faults into heavily doped  $4H$ -SiC epilayers [64]. The faults

that form have been shown to be localized transformations of hexagonal-stacked bilayers towards cubic stacking structure [64, 65]. By starting with a SiC crystal structure that is entirely cubic, this degradation mechanism might be absent from 3C-SiC bipolar device structures. A high quality 3C/4H-SiC heterojunction, such as the one shown in Fig. 13, should enable beneficial SiC/SiC heterojunction devices to be realized, including heterojunction bipolar transistors and high electron mobility field-effect transistors [66].

The 3C-SiC step-free surface heteroepitaxy process demonstrated in Sect. 5 should enable experimental exploration of all these potential benefits in small-area prototype device structures. If experimental studies validate sufficient electrical device benefits, further scale-up development of 3C-SiC crystal growth should be pursued.

### 6.3.3 III-N Growth and Devices

On-axis hexagonal SiC substrates are often used for the growth of heteroepitaxial Group III-nitride (III-N) devices used in short-wavelength light emitting diodes, lasers, and heterojunction radio frequency transistors [67]. These devices typically contain numerous extended crystal defects that originate at the substrate/epilayer interface and harm the performance and reliability of III-N devices [28]. In particular, previous works indicate that many of these defects correspond to the locations of steps on the SiC growth surface, even in cases where pre-growth etching produces well-ordered surface steps [30]. By carrying out III-N growth on step-free SiC surfaces, interface-step-related defects are eliminated, which should result in some improvement in III-N film quality.

## 6.4 Conclusion

This article has described significant new understanding and approaches to SiC homoepitaxial and heteroepitaxial growth using on-axis (0001) 4H- and 6H-SiC mesa surfaces. These advancements demonstrate far better control of the SiC growth surface structure and epitaxial film defect structure than previous SiC growth approaches. The superior films should enable a variety of improved small-area devices to be demonstrated in the near future. With further upscaling and process improvements, the demonstrated growth principles may potentially displace conventionally-grown SiC materials in a variety of applications.

## Acknowledgements

The authors are most grateful to the following people for their contributions to the works reviewed in this article: A. Trunek, D. Spry, G. Beheim, P. Abel, L. Matus, R. Hoffman, Jr., D. Larkin, E. Benevise, B. Osborn,

J. Heisler, D. Androjna, L. Keys, R. Okojie, M. Mrdenovich, S. Elder, J. Krotine, C. Blaha, P. Lampard and G. Hunter at NASA Glenn Research Center; M. Dudley, X. Huang and W. Vetter at State University of New York at Stony Brook, M. Skowronski, T. Kuhr and J. Liu at Carnegie Mellon University. This work was primarily funded and carried out at NASA Glenn Research Center under the Aerospace Propulsion and Power Program.

## References

1. T. Kimoto, T. Yamamoto, Z.Y. Chen et al.: in *Silicon Carbide and Related Materials 1999*, ed. by C.H. Carter, Jr., R.P. Devaty, and G.S. Rohrer, Mat. Sci. Forum (Trans Tech Publications, Switzerland, 2000), Vol. **338–342**, p. 189
2. T. Kimoto, S. Nakazawa, K. Fujihira et al.: in *Silicon Carbide and Related Materials 2001*, ed. by S. Yoshida, S. Nishino, H. Harima et al., Mat. Sci. Forum (Trans Tech Publications, Switzerland, 2002), Vol. **389–393**, p. 165
3. J.A. Powell, P. Pirouz, and W.J. Choyke: in *Semiconductor Interfaces, Microstructures, and Devices: Properties and Applications*, ed. by Zhe Chuan Feng (Institute of Physics Publishing, Bristol, United Kingdom, 1993), p. 257
4. M.H. Hong, A.V. Samant, and P. Pirouz: *Philos. Mag.* **80** (4), 919 (2000)
5. J.A. Powell, D.J. Larkin, L.G. Matus et al.: *Appl. Phys. Lett.* **56** (15), 1442 (1990)
6. A.A. Burk, Jr. and L.B. Rowland: *Phys. Status Solidi B* **202** (1), 263 (1997)
7. T. Kimoto, A. Itoh, and H. Matsunami: *Phys. Status Solidi B* **202** (1), 247 (1997)
8. O. Kordina, C. Hallin, A. Henry et al.: *Phys. Status Solidi B* **202** (1), 321 (1997)
9. J.A. Powell and D.J. Larkin: *Phys. Status Solidi B* **202** (1), 529 (1997)
10. A.R. Powell and L.B. Rowland: *Proc. IEEE* **90** (6), 942 (2002)
11. J.A. Powell, D.J. Larkin, P.B. Abel et al.: in *Silicon Carbide and Related Materials 1995*, ed. by S. Nakashima, H. Matsunami, S. Yoshida et al., IOP Conf. Series (Institute of Physics Publishing, Bristol, UK, 1996), no. **142**, p. 77
12. S. Tyc: in *Silicon Carbide and Related Materials: Proceedings of the Fifth International Conference*, ed. by M. Spencer, R. Devaty, J. Edmond et al., IOP Conf. Series (Institute of Physics Publishing, Bristol, United Kingdom, 1994), no. **137**, p. 333
13. H. Matsunami, K. Shibahara, N. Kuroda et al.: in *Amorphous and Crystalline Silicon Carbide*, ed. by G.L. Harris and C.Y.-W. Yang, Springer Proc. Phys. (Springer-Verlag, Berlin, Heidelberg, 1989), Vol. **34**, p. 34
14. J.A. Powell, J.B. Petit, J.H. Edgar et al.: *Appl. Phys. Lett.* **59** (3), 333 (1991)
15. S. Ha, P. Mieszkowski, M. Skowronski et al.: *J. Cryst. Growth* **244** (3–4), 257 (2002)
16. S. Wang, M. Dudley, C.H. Carter, Jr. et al.: in *Diamond, SiC and Nitride Wide Bandgap Semiconductors*, ed. by C.H. Carter, Jr., G. Gildenblat, S. Nakamura et al., MRS Symp. Proc. (Materials Research Society, Pittsburgh, PA, 1994), Vol. **339**, p. 735
17. P.G. Neudeck: in *Silicon Carbide and Related Materials 1999*, ed. by C.H. Carter, Jr., R.P. Devaty, and G.S. Rohrer, Mat. Sci. Forum (Trans Tech Publications, Switzerland, 2000), Vol. **338–342**, p. 469

18. H. Lendenmann, F. Dahlquist, J.P. Bergman et al.: in *Silicon Carbide and Related Materials 2001*, ed. by S. Yoshida, S. Nishino, H. Harima et al., Mat. Sci. Forum (Trans Tech Publications, Switzerland, 2002), Vol. **389–393**, p. 389
19. W. Si, M. Dudley, R. Glass et al.: J. Electronic Materials **26** (3), 128 (1997)
20. W. Si, M. Dudley, H.S. Kong et al.: J. Electronic Materials **26** (3), 151 (1997)
21. P.G. Neudeck and J.A. Powell: IEEE Electron Device Lett. **15** (2), 63 (1994)
22. P.G. Neudeck, W. Huang, and M. Dudley: Solid-State Electron. **42** (12), 2157 (1998)
23. J. Giocondi, G. Rohrer, M. Skowronski et al.: J. Cryst. Growth **181** (4), 351 (1997)
24. R.C. Glass, D. Henshall, V.F. Tsvetkov et al.: Phys. Status Solidi B **202** (1), 149 (1997)
25. P.G. Neudeck, M.A. Kuczmarski, M. Dudley et al.: in *Wide-Bandgap Electronic Devices*, ed. by R.J. Shul, F. Ren, M. Murakami et al., MRS Symp. Proc. (Materials Research Society, Warrendale, PA, 2000), Vol. **622**, p. T1.2.1
26. J.A. Powell, J.B. Petit, J.H. Edgar et al.: Appl. Phys. Lett. **59** (2), 183 (1991)
27. P. Pirouz: Solid State Phenomena **56**, 107 (1997)
28. S. Tanaka, R.S. Kern, and R.F. Davis: Appl. Phys. Lett. **66** (1), 37 (1995)
29. S. Nakamura, T. Kimoto, H. Matsunami et al.: Appl. Phys. Lett. **76** (23), 3412 (2000)
30. S. Yamada, J. Kato, S. Tanaka et al.: presented at the Fall 2000 Materials Research Society Meeting, Boston, MA, 2000 (unpublished)
31. J.A. Powell, D.J. Larkin, L.G. Matus et al.: Appl. Phys. Lett. **56** (14), 1353 (1990)
32. D.J. Larkin and J.A. Powell: U.S. Patent No. 5,363,800 (1994)
33. J.A. Powell, J.B. Petit, L.G. Matus et al.: in *Amorphous and Crystalline Silicon Carbide III*, ed. by G.L. Harris, M.G. Spencer, and C.Y. Yang, Springer Proc. Phys. (Springer-Verlag, Berlin-Heidelberg, 1992), Vol. **56**, p. 313
34. P.G. Neudeck, D.J. Larkin, J.E. Starr et al.: IEEE Trans. Electron Devices. **41** (5), 826 (1994)
35. J. Powell, P. Neudeck, A. Trunek et al.: Appl. Phys. Lett. **77** (10), 1449 (2000)
36. J.A. Powell, D.J. Larkin, P.G. Neudeck, and L.G. Matus: U.S. Patent No. 5,915,194 (1999)
37. M. Dudley, W.M. Vetter, and P.G. Neudeck: J. Cryst. Growth **240** (1–2), 22 (2002)
38. T. Kimoto and H. Matsunami: J. Appl. Phys. **78** (5), 3132 (1995)
39. S. Nakamura, T. Kimoto, and H. Matsunami: in *Silicon Carbide and Related Materials, 2002*, Mat. Sci. Forum (Trans Tech Publications, Switzerland, 2003), Vol. **433–436**, p. 149
40. P.G. Neudeck, J.A. Powell, G.M. Beheim et al.: J. Appl. Phys. **92** (5), 2391 (2002)
41. P.G. Neudeck, J.A. Powell, A. Trunek et al.: in *Silicon Carbide and Related Materials 2001*, ed. by S. Yoshida, S. Nishino, H. Harima et al., Mat. Sci. Forum (Trans Tech Publications, Switzerland, 2002), Vol. **389–393**, p. 251
42. P.G. Neudeck, D.J. Spry, A.J. Trunek et al.: in *Silicon Carbide 2002–Materials, Processing and Devices*, ed. by S.E. Saddow, D.J. Larkin, N.S. Saks et al., MRS Symp. Proc. (Materials Research Society, Warrendale, PA, 2003), Vol. **742**, p. K5.2.1
43. Y. Khlebnikov, I. Khlebnikov, M. Parker et al.: J. Cryst. Growth **233**, 112 (2001)

44. E. Eshun, C. Taylor, M.G. Spencer et al.: in *Wide-Bandgap Semiconductors for High Power, High Frequency and High Temperature Applications, 1999*, ed. by S.C. Binari, A.A. Burk, M.R. Melloch et al., MRS Symp. Proc. (Materials Research Society, Warrendale, PA, 1999), Vol. **572**, p. 173
45. P.G. Neudeck, J.A. Powell, D.J. Spry et al.: in *Silicon Carbide and Related Materials, 2002*, Mat. Sci. Forum (Trans Tech Publications, Switzerland, 2003), Vol. **433–436**, p. 213
46. P.G. Neudeck, J.A. Powell, A.J. Trunek et al.: in *Silicon Carbide and Related Materials 2001*, ed. by S. Yoshida, S. Nishino, H. Harima et al., Mat. Sci. Forum (Trans Tech Publications, Switzerland, 2002), Vol. **389–393**, p. 311
47. X. Huang, M. Dudley, P.G. Neudeck et al.: in *Silicon Carbide 2002 – Materials, Processing and Devices*, ed. by S.E. Saddow, D.J. Larkin, N.S. Saks et al., MRS Symp. Proc. (Materials Research Society, Warrendale, PA, 2003), Vol. **742**, p. K3.8.1
48. M. Dudley, X. Huang, W.M. Vetter, and P.G. Neudeck: in *Silicon Carbide and Related Materials, 2002*, Mat. Sci. Forum (Trans Tech Publications, Switzerland, 2003), Vol. **433–436**, p. 247
49. J.A. Powell and P.G. Neudeck: U.S. Patent No. 6,488,771 B1 (2002)
50. J.W. Matthews: Philos. Mag. **4**, 1017 (1959)
51. J.W. Matthews: Philos. Mag. **6**, 915 (1961)
52. S. Bai, Y. Ke, Y. Shishkin et al.: in *Silicon Carbide 2002 – Materials, Processing and Devices*, ed. by S.E. Saddow, D.J. Larkin, N.S. Saks et al., MRS Symp. Proc. (Materials Research Society, Warrendale, PA, 2003), Vol. **742**, p. K3.1.1
53. M. Bhatnagar, B.J. Baliga, H.R. Kirk et al.: IEEE Trans. Electron Devices **43** (1), 150 (1996)
54. J. Wan, M.A. Capano, M.R. Melloch et al.: IEEE Electron Device Lett. **23** (8), 482 (2002)
55. V.V. Afanasev, M. Bassler, G. Pensl et al.: Phys. Status Solidi A **162** (1), 321 (1997)
56. J.R. Williams, G. Y. Chung, C.C. Tin et al.: in *Silicon Carbide – Materials, Processing, and Devices*, ed. by A. Agarwal, M. Skowronski, J.A. Cooper, Jr. et al., MRS Symp. Proc. (Materials Research Society, Warrendale, PA, 2001), Vol. **640**, p. H3.5.1
57. R. Schörner, P. Friedrichs, D. Peters et al.: IEEE Electron Device Lett. **20** (5), 241 (1999)
58. A. Agarwal, S.-H. Ryu, C. Capell et al.: in *Silicon Carbide 2002 – Materials, Processing and Devices*, ed. by S.E. Saddow, D.J. Larkin, N.S. Saks et al., MRS Symp. Proc. (Materials Research Society, Warrendale, PA, 2003), Vol. **742**, p. K7.3.1
59. P.A. Ivanov, M.E. Levinshtein, S.L. Rumyantsev et al.: Solid-State Electron. **46** (4), 567 (2002)
60. P.G. Neudeck: J. Electronic Materials **27** (4), 317 (1998)
61. S. Dimitrijevic, K.Y. Cheong, J. Han et al.: Appl. Phys. Lett. **80** (18), 3421 (2002)
62. S.T. Sheppard, M.R. Melloch, and J.A. Cooper, Jr.: IEEE Electron Device Lett. **17** (1), 4 (1996)
63. A.K. Agarwal, S. Seshadri, and L.B. Rowland: IEEE Electron Device Lett. **18** (12), 592 (1997)

- 64. R.S. Okojie, M. Xhang, P. Pirouz et al.: Appl. Phys. Lett. **79** (19), 3056 (2001)
- 65. M. Skowronski, J.Q. Liu, W.M. Vetter et al.: J. Appl. Phys. **92** (8), 4699 (2002)
- 66. G. Gao, J. Sterner, and H. Morkoc: IEEE Trans. Electron Devices **41** (7), 1092 (1994)
- 67. S.J. Pearton, J.C. Zolper, R.J. Shul et al.: J. of Appl. Phys. **86** (1), 1 (1999)

# Low-Defect 3C-SiC Grown on Undulant-Si (001) Substrates

H. Nagasawa, K. Yagi, T. Kawahara, N. Hatta, G. Pensl, W.J. Choyke, T. Yamada, K.M. Itoh and A. Schöner

## 1 Introduction

Attempts to grow mono-crystalline cubic silicon carbide (3C-SiC) have been made using vapor phase hetero-epitaxial growth with Si [1], TiC [2], and sapphire [3] as substrates, and with bulk growth [4] using the sublimation method. In 1983, Nishino et al. reported hetero-epitaxial growth of 3C-SiC on a carbonized Si(001) surface [5]. Since then, 3C-SiC heteroepitaxy on Si substrate using the CVD or MBE methods has been studied intensively, because it has been proved that using Si as a substrate facilitates the upsizing of SiC, while reducing manufacturing costs, and that carbonization of the Si surface significantly improves the reproducibility of the 3C-SiC grown on it.

However, the development of semiconductor devices using 3C-SiC is still lagging behind those using 4H-SiC or 6H-SiC. One reason is that the growth rate of the CVD method commonly used for the hetero-epitaxial growth of 3C-SiC is too slow to obtain free-standing substrates, which need to be at least 100  $\mu\text{m}$  thick to have sufficient mechanical strength to endure the device fabrication process. Another major reason is that device performance using 3C-SiC is degraded by high-density planar defects that are generated at the interface between 3C-SiC and the Si substrate due to the large lattice mismatch.

In 2002, Nagasawa et al. reported a new technique to reduce planar defects in 3C-SiC that involved growing 3C-SiC on “undulant-Si” with slopes oriented in the [110]- and  $\bar{1}\bar{1}0$ -directions [6]. In this paper, we first review the mechanism for reducing planar defects on “undulant-Si”. This mechanism is verified by morphologic and microscopic observations. Then, the electrical and optical properties of low-defect 3C-SiC grown on “undulant-Si” observed by Hall effect measurements and low temperature photoluminescence (LTPL) are described. Finally, the feasibility of using 3C-SiC as a substrate for semiconductor devices is examined by growing additional homo-epitaxial layers on it, and measuring their properties using deep level transient spectroscopy (DLTS) and conductive technique.

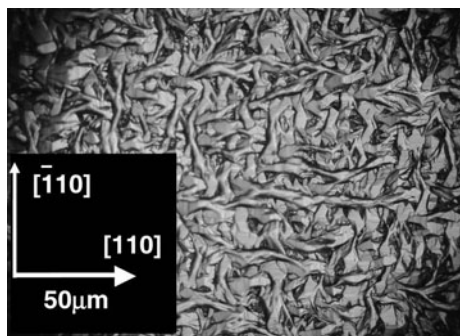
## 2 Mechanism of Generating Planar Defects at the 3C-SiC/Si Interface

The planar defects that occur at the 3C-SiC/Si(001) interface can be classified into two groups: anti-phase boundary (APB) and stacking fault (SF).

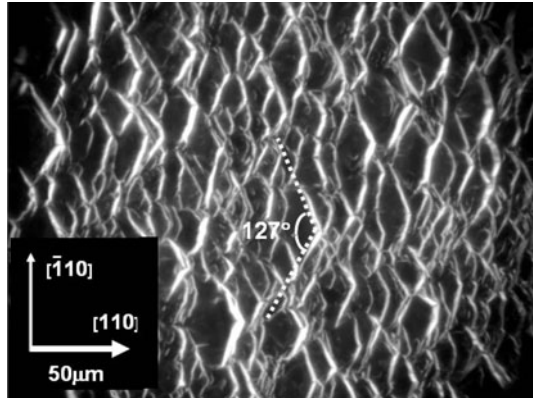
APBs are generated because the polar faces of 3C-SiC (Si- and C-faces) must be aligned with the non-polar face of the Si substrate. For example, in the growth of 3C-SiC on Si(001) substrate, multinucleation of 3C-SiC is caused by spontaneous nucleation during the carbonization process before the growth process occurs [7]. Since 3C-SiC is grown on Si epitaxially, the {111}-planes of 3C-SiC must be absolutely parallel with {111}-planes of Si. The {111}-planes of Si are all equivalent, while those of 3C-SiC are inequivalent and classified as Si- or C-faces. Accordingly, in the multinucleation of 3C-SiC, Si-face and C-face are simultaneously aligned in a specific [111]-direction. With the growth of 3C-SiC, nuclei with different polar face orientations grow horizontally and combine each other forming APBs.

Figure 1 shows an optical microscope image of 3C-SiC grown epitaxially on Si(001) (hereafter referred to as “just-Si”). The surface of the 3C-SiC shows a mosaic pattern, resulting from the horizontal and vertical domains crossing at right angles. The observed shape of these domains implies the direction of their polar faces; the C-face, which has a lower surface energy, grew faster than the Si-face [8], indicating that the long side of the domain corresponds to the Si-face, and the short side corresponds to the C-face. Therefore, the boundary between domains with different long-side directions corresponds to an APB.

To eliminate APBs, it is necessary to orient a specific polar face in the desired direction. The simplest method for manipulating polar faces is to use a Si(001) surface with a 2~4° off-angle in the [110]-direction as the substrate



**Fig. 1.** Optical microscope image of 3C-SiC surface grown on “just-Si” substrate. The surface of the 3C-SiC shows a mosaic pattern, resulting from the horizontal and vertical domains crossing at right angles. The boundary between domains with different long-side directions corresponds to an APB



**Fig. 2.** Optical microscope image of 3C-SiC surface grown on “off-Si” substrate. Steps of  $127^\circ$ , that deformed from the (111) Si-face, are observed on the 3C-SiC surface. These step edges are all oriented in the  $[110]$ -direction, indicating that the Si-face of 3C-SiC is aligned with Si(111)-plane, and the APBs have vanished

(“off-Si” substrate) [9]. Figure 2 shows the surface of 3C-SiC grown on “off-Si”. In contrast to the mosaic structure observed in Fig. 1, steps of  $127^\circ$  are observed on the 3C-SiC surface grown on “off-Si”. The edges of these steps consist of (311) and (131) facets deformed from the (111)Si-face [6]. These step edges are all oriented in the  $[110]$ -direction, indicating that the Si-face of 3C-SiC is aligned with the Si(111)-plane, and the APBs have vanished.

In the  $(\bar{1}10)$  cross-section of the 3C-SiC grown on “off-Si” observed by a transmission electron microscope (TEM), however, SFs parallel to the  $(\bar{1}\bar{1}1)$ -plane are observed as inclined lines (Fig. 3). The SFs are generated to relax the lattice mismatch of 19.7% at the 3C-SiC/Si interface. For example, defin-

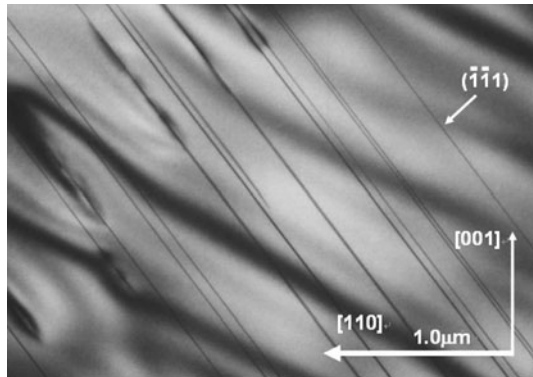


**Fig. 3.** TEM image of  $(\bar{1}10)$  cross-section of 3C-SiC grown on “off-Si” substrate. SFs parallel to the  $(\bar{1}\bar{1}1)$ -plane are observed as inclined lines

ing the stacking sequence of Si-C pairs in 3C-SiC as ABCABCABC along the  $[111]$ -direction (where A, B, and C denote the three inequivalent layers), if extra Si-C layers along the  $(111)$ -plane are generated at each fifth layer in order to minimize the number of dangling bonds at the SiC/Si interface, the stacking sequence changes to ABCA**C**BCA**B**ABCA**B**, and hexagonal sites (underlined characters) inevitably occur to sandwich the extra layers (boldface). As the stacking sequence in the  $\langle 111 \rangle$ -directions is always exposed on the  $(001)$  surface, the structure of hexagonal sites generated at the interfaces is perpetuated in the epitaxial 3C-SiC layer forming planar SFs along the  $\{111\}$ -planes. Since SFs propagate along the four equivalent  $\{111\}$ -planes of Si, the SF density decreases as the 3C-SiC thickness increases by combining of counter-SFs when “just-Si” is used as a substrate. On “off-Si” substrate, the steps on the surface oriented in the  $[110]$ -direction predominantly terminate SF propagation in the  $(111)$ -plane, but there are no steps in the  $[\bar{1}\bar{1}0]$ -direction to terminate SF propagation in the  $(\bar{1}\bar{1}1)$ -plane. Finally, the propagating direction of SFs is limited in the  $(\bar{1}\bar{1}1)$ -plane [10]. As a result, as long as “off-Si” is used as the substrate, SF density cannot be reduced as the thickness of 3C-SiC increases.

### 3 Principle of Planar Defect Reduction in 3C-SiC

Based on the above discussion, an effective means of eliminating APBs and SFs was devised [6]. APBs can be obliterated effectively by orienting the specific polar face in the desired direction based on the inclination of the substrate surface. However, in order to maintain the reduction mechanism of SF by combining SFs, the SF collimation in the  $(\bar{1}\bar{1}1)$ -plane that was observed on “off-Si” must be avoided. In other words, to effectively eliminate SFs, the SFs must be arranged so that their configurations are symmetric. An effective way to satisfy these requirements is to make many undulations with inclinations in the  $[110]$ - and  $[\bar{1}\bar{1}0]$ -directions on the Si(001) surface before growing the 3C-SiC. In this paper, this Si(001) substrate is referred to as an “undulant-Si” substrate. Figure 4 illustrates “undulant-Si”. On the surface of the “undulant-Si”, ridges extend in the  $[\bar{1}\bar{1}0]$ -direction, and slopes inclined toward the  $[110]$ - and  $[\bar{1}\bar{1}0]$ -directions cover the entire surface.

The “undulant-Si” reduces planar defects in the following manner. Initially, the Si-face of 3C-SiC is oriented in the  $[111]$ - and  $[\bar{1}\bar{1}1]$ -directions uniformly, and APBs therefore vanish on the slope of the “undulant-Si” in a manner similar to that seen with “off-Si”. SFs still propagate along the  $\{111\}$ -planes after the APBs vanish. Unlike “off-Si”, however, the SFs are arranged symmetrically, so that they annihilate as they connect with each other. Therefore, the SF density decreases as the SiC thickness increases.

To maximize the effect of “undulant-Si” in reducing planar defects, it is preferable that (1) the undulations formed on the Si(001) substrate are

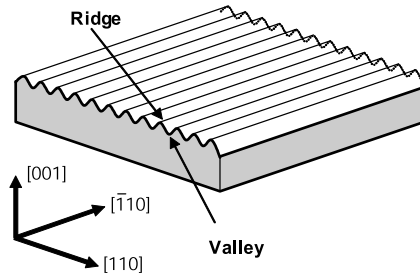


**Fig. 4.** Schematic structure of the surface of “undulant-Si”. Ridges extend in the  $[1\bar{1}0]$ -direction, and slopes inclined toward the  $[110]$ - and  $[1\bar{1}0]$ -directions cover the entire surface

continuous, because APBs will occur in any flat regions on the “undulant-Si”, as in “just-Si”; and (2) the inclination of the undulations is  $2 \sim 4^\circ$ , similar to that in “off-Si”. If the inclinations are too small, the orientation of the SiC polar faces cannot be manipulated, since it is influenced by the initial misorientation of the Si substrate, and if the inclinations are too large, the probability of generating a stacking fault at a SiC/Si interface is increased considerably.

## 4 Experimental

This section describes the fabrication of “undulant-Si” and growth of thick 3C-SiC layer on it using an example.

### 4.1 Preparation of Si Substrate

First, the entire surface of “just-Si” is pushed against a  $15\text{-}\mu\text{m}$  diamond slurry at a load of  $0.1\text{ kg}\cdot\text{cm}^{-2}$ , and moved back and forth in the  $[1\bar{1}0]$ -direction to form scratches on the surface of the Si(001) (scratching process). The scratching process forms countless continuous scratches roughly paralleling the  $[1\bar{1}0]$ -direction. Then, dry oxidation at 1373 K for 5 h is used to remove crystal defects introduced on the surface of the Si substrate by the scratching process, which forms an oxidized layer about 200-nm thick on the defective surface. Finally, the substrate is etched in 5% HF solution for 10 min to completely remove the oxidized layer, and the “undulant-Si” surface is exposed. Figure 5 is an atomic force microscope (AFM) image of the surface of “undulant-Si” fabricated using this processes. The figure shows continuous undulations with ridges roughly paralleling the  $[1\bar{1}0]$ -direction formed on the Si substrate. The interval between adjacent ridges is 400–700 nm, and the difference between ridges and valleys is 7–26 nm.

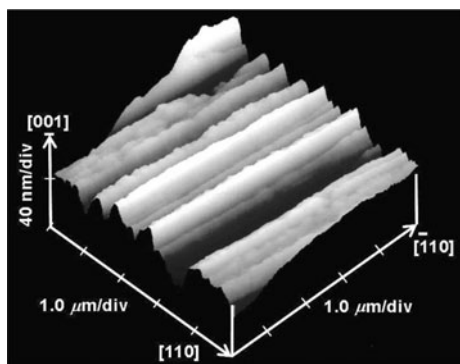


**Fig. 5.** AFM image of “undulant-Si” surface: Continuous undulations with ridges almost parallel to the  $[1\bar{1}0]$ -direction are formed on the Si substrate. The interval between adjacent ridges is 400–700 nm, and the difference between ridges and valley is 7–26 nm

## 4.2 3C-SiC Growth Process

A cold-wall-type low-pressure reactor is used to produce 3C-SiC epitaxial growth on “undulant-Si”. The substrate is heated in the reactor from room temperature to 1623 K while introducing 10 sccm  $C_2H_2$  and 100 sccm  $H_2$  in order to prevent thermal roughening of the Si surface. Carbonization covers the surface of the substrate with a 3C-SiC layer about 10 nm thick during the heating process, and the undulating structure is conserved. Then, while keeping the substrate temperature at 1623 K, 3C-SiC is grown on the “undulant-Si” using 50 sccm  $SiH_2Cl_2$ , 10 sccm  $C_2H_2$ , and 100 sccm  $H_2$ . The pressure in the reactor during this carbonization and growth process is kept at 13.3 Pa. The growth rate of 3C-SiC under these conditions is approximately  $40 \mu m \cdot h^{-1}$ , which is comparable to the growth rate using the sublimation method ( $30 \mu m \cdot h^{-1}$ ), as reported by Virgil et al. [4]. After growth for 5 h, a 3C-SiC layer about 200  $\mu m$  thick forms on the “undulant-Si”.

## 5 Effect of “Undulant-Si” on the Reduction of Planar Defects

### 5.1 Morphologic Study

The surface of 3C-SiC grown on “undulant-Si” is mirror-like, unlike the surfaces formed on “just-Si” and “off-Si”. Figure 6 shows an optical microscope image of a 3C-SiC surface grown on “undulant-Si”. The mosaic patterns observed on 3C-SiC grown on “just-Si” are not seen in this figure. This indicates that APBs are eliminated by growing 3C-SiC on “undulant-Si”. The AFM image of the surface (Fig. 7) shows that the 3C-SiC surface is much

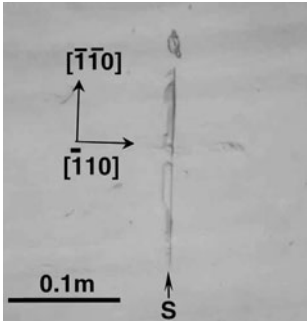


**Fig. 6.** Optical microscope image of 3C-SiC surface grown on “undulant-Si” substrate. The mosaic patterns observed on 3C-SiC grown on “just-Si” are not seen. Suggesting the elimination of APBs. However, the intersection of SF at the (001) surface forms a groove, indicated as “S”, along the [110]-direction due to the higher surface energy of Si-face

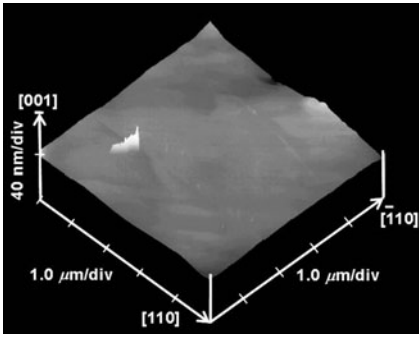


**Fig. 7.** AFM image of 3C-SiC surface grown on “undulant-Si” substrate. The surface of 3C-SiC is much smoother than the surface of “undulant-Si” before the 3C-SiC growth

smoother than the surface of the “undulant-Si”. These results corroborate that the growth rate in the [110]- and  $\bar{1}\bar{1}0$ -directions (lateral growth rate of the Si-face exposed on the side of undulations) is faster than that in the [001]-direction (vertical to the surface). It is thought that APBs are generated during the carbonization process even though “undulant-Si” is used as a substrate. However, the Si-face is oriented in the [111]- and  $\bar{1}\bar{1}1$ -directions as a result of the slope of the undulations, and the APBs vanish with SiC growth. The steps consisting of the Si-face then inevitably grow horizontally on each slope of the undulations [6]. Unlike “off-Si”, on “undulant-Si” the densities of the steps growing in the [110]- and  $\bar{1}\bar{1}0$ -directions are equal. Therefore, on “undulant-Si”, the counter steps combine to produce the mirror-like 3C-SiC surface as seen in Fig. 6 and Fig. 7.

## 5.2 Microscopic Observation Using TEM

Figure 8 is a TEM image of a cross-section of 3C-SiC grown on “undulant-Si”. Figure 8a is a TEM image of the (110) cross-section. Unlike the case of “off-Si” (Fig. 3), SFs parallel to the  $\bar{1}\bar{1}1$ - and  $\bar{1}\bar{1}1$ -planes are observed in the same field of view. The SF density observed in Fig. 8 is lower than that in Fig. 3. By contrast, in the TEM image of the  $\bar{1}\bar{1}0$  cross-section shown in Fig. 8b, SFs are observed as trapezoidal horizontal stripes, but are not observed as

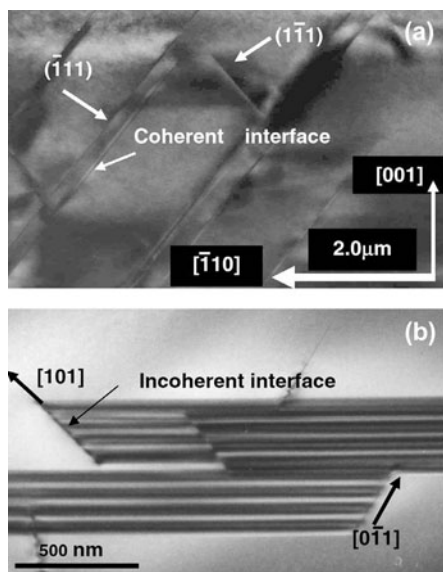


**Fig. 8.** Cross-sectional TEM images of 3C-SiC grown on “undulant-Si” substrate: (a) at the (110) cross-section; (b) at the  $(\bar{1}10)$  cross-section. SFs parallel to the  $(\bar{1}11)$ - and  $(1\bar{1}1)$ -planes are observed in the same field of view. However, at the  $(\bar{1}10)$  cross section, SFs are observed as trapezoidal horizontal stripes, but are not observed as inclined lines parallel to the (111)- or  $(\bar{1}11)$ -plane

inclined lines parallel to the (111)- or  $(\bar{1}11)$ -planes. Therefore, the planar defects remaining in the 3C-SiC grown on “undulant-Si” are plate-like SF regions, whose coherent interfaces are aligned in the  $(\bar{1}11)$ - or  $(1\bar{1}1)$ -planes.

As the SF observed in Fig. 8 corresponds to the region rotated 60 degrees around the  $[\bar{1}11]$  or  $[1\bar{1}1]$  axes with respect to the surrounding crystal lattice, it exposes the Si-face on the (001) surface, which should be a non-polar face as illustrated in Fig. 9 [6]. In fact, the intersection of SF with the (001) surface, which is indicated as “S1” or “S2” in Fig. 9, forms a groove (indicated by “S” in Fig. 6) along the  $[110]$ -direction due to the higher surface energy of Si-face.

Once a plate-like SF is generated parallel to the  $\{111\}$ -plane of the 3C-SiC, the edge of the SF inevitably forms incoherent interfaces. These incoherent interfaces can be observed as edges in the  $\langle 110 \rangle$ -directions in Fig. 8b. Since these incoherent interfaces are equivalent to the section of the SFs on the (001) surface due to the three-fold symmetry of 3C-SiC around the  $\langle 111 \rangle$  axes, they correspond to the Si-face [11]. Figure 10a illustrates the three-dimensional structure of the SFs remaining in 3C-SiC grown on “undulant-Si”. The SFs orient their coherent interfaces along the  $(\bar{1}11)$ - or  $(1\bar{1}1)$ -planes exposing Si-face on the (001) surface, and align their incoherent interfaces (E1, E2: Si-polar interfaces) to the  $[101]$ ,  $[0\bar{1}1]$ , or  $[\bar{1}01]$ ,  $[011]$ -directions.

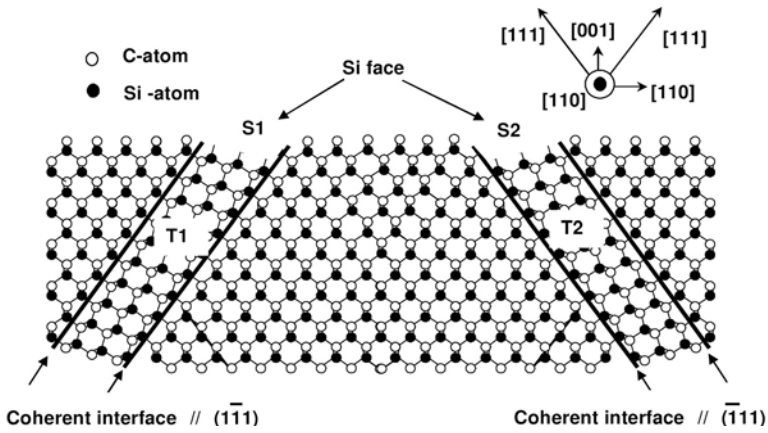


**Fig. 9.** Schematic lattice image of (110) cross-section for 3C-SiC grown on “undulant-Si”. The planar defects remaining in the 3C-SiC grown on “undulant-Si” are plate-like SF regions indexed as T1 and T2, whose coherent interfaces are aligned in the  $(\bar{1}11)$  or  $(1\bar{1}1)$  planes. The SF exposes the Si-face (S1, S2) on the (001) surface

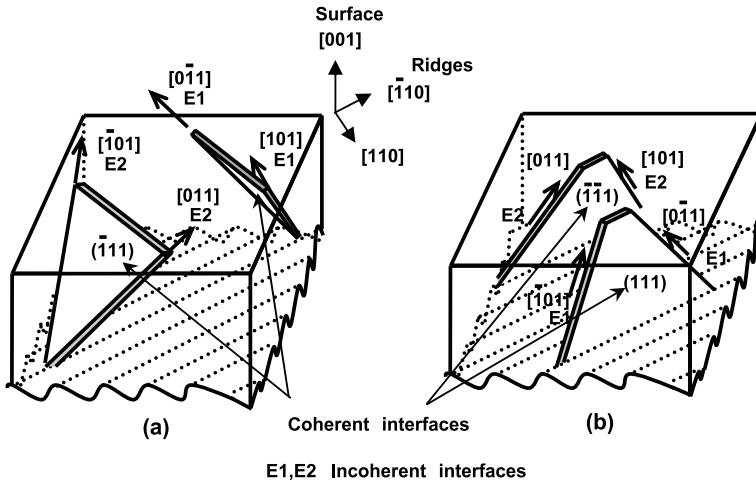


**Fig. 10.** Schematic structure of SFs in 3C-SiC grown on “undulant-Si”: (a) SFs parallel to the  $(\bar{1}11)$ - or  $(1\bar{1}1)$ -planes. The SFs orient their coherent interfaces along the  $(\bar{1}11)$ - or  $(1\bar{1}1)$ -planes exposing Si-face on the surface, and align their incoherent interfaces (E1, E2) to the [101],  $[0\bar{1}1]$ , or  $[\bar{1}01]$ , [011]-directions; (b) SFs parallel to the (111)- or  $(\bar{1}11)$ -planes

### 5.3 Mechanism for Reducing Planar Defects in 3C-SiC Grown on “Undulant-Si”

From the above discussion, the mechanism leading to the reduction of planar defects in 3C-SiC when grown on “undulant-Si” is described in the following paragraph.

During the initial 3C-SiC growth, APBs generated during the carbonization process vanish due to the control of the orientation of polar faces on the slope of the “undulant-Si”. Then, the SFs along the (111)- or ( $\bar{1}\bar{1}\bar{1}$ )-planes are eliminated via a self-vanishing process. Since the propagation of incoherent boundaries (Si-polar interface) along the  $[\bar{1}01]$ ,  $[0\bar{1}1]$  or  $[101]$ ,  $[011]$ -directions reduces the SFs along the (111)- or ( $\bar{1}\bar{1}\bar{1}$ )-planes, they vanish as the 3C-SiC thickness increases, as shown in Fig. 10b.

By contrast, SFs parallel to the ( $\bar{1}11$ )- or ( $1\bar{1}\bar{1}$ )-planes align their incoherent interfaces in the  $[101]$ ,  $[0\bar{1}1]$  or  $[\bar{1}01]$ ,  $[011]$ -directions, so that they expand as the SiC thickness increases. However, unlike the case of “off-Si” substrate, density of SF paralleling ( $\bar{1}11$ ) plane is quite similar to that of SF paralleling ( $1\bar{1}\bar{1}$ ) plane in order to maintain a SF termination process shown in Fig. 11 [6]. Figure 11 is an optical microscope image of a (110) cleaved cross-section of 3C-SiC grown on “undulant-Si”. In this figure, SFs are observed as rather bright inclined lines, and it is obvious that a SF parallel to the ( $1\bar{1}\bar{1}$ )-plane (L1) is terminated by a counter SF (L2).

Since the probability of SF termination is inversely proportional to the SiC thickness, SFs parallel to the ( $\bar{1}11$ )- or ( $1\bar{1}\bar{1}$ )-planes decrease more slowly than SFs parallel to the ( $\bar{1}\bar{1}\bar{1}$ )- or (111)-planes. Therefore, SFs parallel to the ( $\bar{1}11$ )- and ( $1\bar{1}\bar{1}$ )-planes are observed as residual defects even when the 3C-SiC thickness exceeds 200  $\mu\text{m}$ .

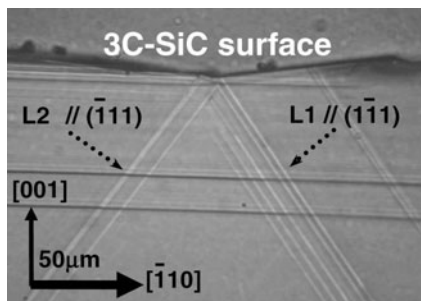


**Fig. 11.** Optical microscope image at (110) cleaved cross section of 3C-SiC grown on “undulant-Si”: SFs are observed as rather bright inclined lines, and it is obvious that one SF parallel to the ( $1\bar{1}\bar{1}$ )-plane (L1) is terminated by the counter SF (L2)

## 6 Properties of 3C-SiC Grown on “Undulant-Si”

This section describes the electrical and optical properties of the low-defect 3C-SiC layer grown on “undulant-Si” observed by Hall effect measurements and low temperature photoluminescence (LTPL).

### 6.1 Hall Effect Investigations

Hall effect measurements in a Hall-bar configuration as schematically shown in Fig. 12 allow the determination of the electron mobility and resistivity in a specific direction. Sample 1 and sample 2 have their longest edge in  $[\bar{1}10]$ - and  $[110]$ -direction, respectively. Prior to the sample fabrication, “undulant-Si” under the grown 3C-SiC was selectively removed to exclude undesirable contribution of Si on the measurements of Hall effect.

The applied magnetic field was oriented perpendicular to the large surface of the sample. The free electron concentration  $n$  as a function of the reciprocal temperature is displayed in Fig. 13a. The course of  $n(1/T)$  is identical for both samples. The freeze-out of nitrogen donors dominates in the temperature range from 200 K to 100 K. Below 100 K the slope of the  $n(1/T)$ -curve becomes flatter with decreasing temperature caused by an increasing influence of conduction in an impurity band. The dashed curve represents a least-squares-fit of the neutrality equation to the experimental data in the freeze-out region. From the fit, the following defect parameters are determined:

ionization energy of nitrogen donors	$\Delta E(N)$	$= 47 \text{ meV},$
concentration of nitrogen donors	$N(N)$	$= 4 \times 10^{15} \text{ cm}^{-3},$
concentration of compensation	$N(\text{comp})$	$= 1 \times 10^{15} \text{ cm}^{-3}.$

The Hall mobility of electrons is revealed in Fig. 13b. It shows an anisotropy parallel ( $[\bar{1}10]$ -direction) and perpendicular ( $[110]$ -direction) to the undulation ridges over the complete investigated temperature range. In  $[110]$ -direction, the electron mobility is higher by a factor of approximately four and reaches a maximum value of  $300 \text{ cm}^2 \cdot \text{V}^{-1} \text{s}^{-1}$  at 55 K. As a consequence, also the resistivity shows an anisotropy (see Fig. 13c). In the temperature range from 500 K to 100 K, the resistivity decreases. At low temperatures ( $T < 100 \text{ K}$ ), the resistivity increases again; in this region, it is dominated by conduction in an impurity band [12].

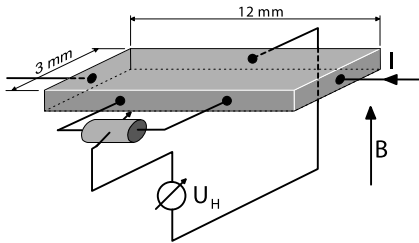


**Fig. 12.** Scheme of the Hall bar configuration used for the determination of the anisotropy of the electrical properties

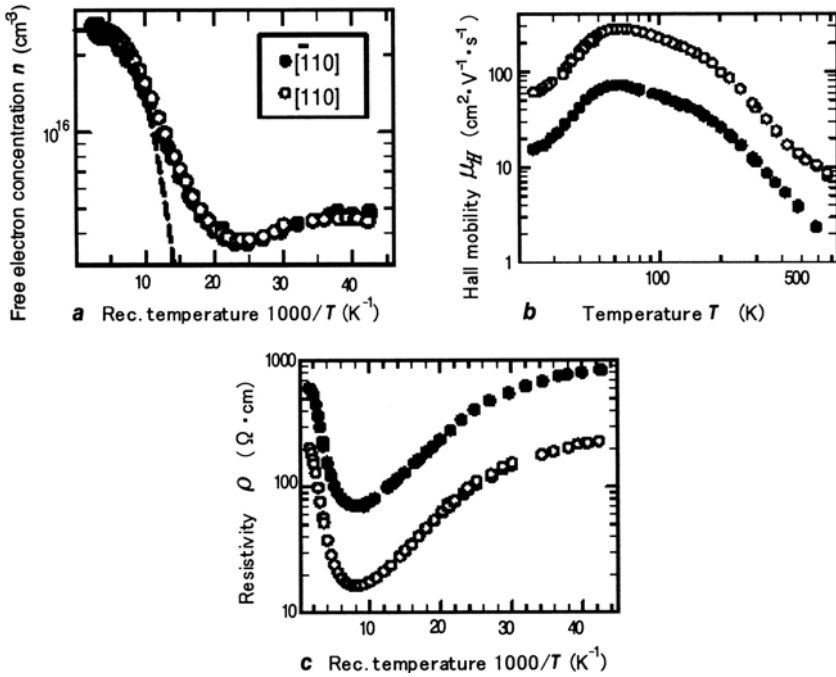


**Fig. 13.** Hall effect results taken on samples 1 and 2 with their longest edges aligned in  $[110]$ - and  $[1\bar{1}0]$ -direction, respectively: (a) free electron concentration  $n$  versus reciprocal temperature, (b) electron Hall mobility  $\mu_H$  versus temperature, (c) resistivity  $\rho$  versus reciprocal temperature

The anisotropy in the electrical properties of the 3C-SiC is probably caused by extended crystal defects [13, 14], e.g. residual SFs along  $(\bar{1}11)$ - or  $(1\bar{1}1)$ -planes as observed in Figs. 6 and 8. Such residual SFs force the lattice atoms from their equilibrium positions leading to deviations from the periodicity and as a consequence to an additional scattering process of the electrons. In addition in the strain field of the coherent and incoherent interfaces of SFs, charged extrinsic atoms may be captured forming a potential barrier. Both effects hinder the motion of electrons in the  $[\bar{1}10]$ -direction and result in the observed increase of the resistivity.

This anisotropy may degrade the performance of 3C-SiC power devices such as MOSFET's. We, therefore, have to eliminate the residual SFs along  $(\bar{1}11)$ - or  $(1\bar{1}1)$ -planes, which are responsible for the observed degradation effect.

## 6.2 Low Temperature Photoluminescence (LTPL) Measurements

In order to give further insight into defect centers and their depth distribution in the 3C-SiC layer, LTPL was carried out. The LTPL measurements were performed on a large, 219  $\mu\text{m}$  thick 3C-SiC layer cut into a number of pieces.

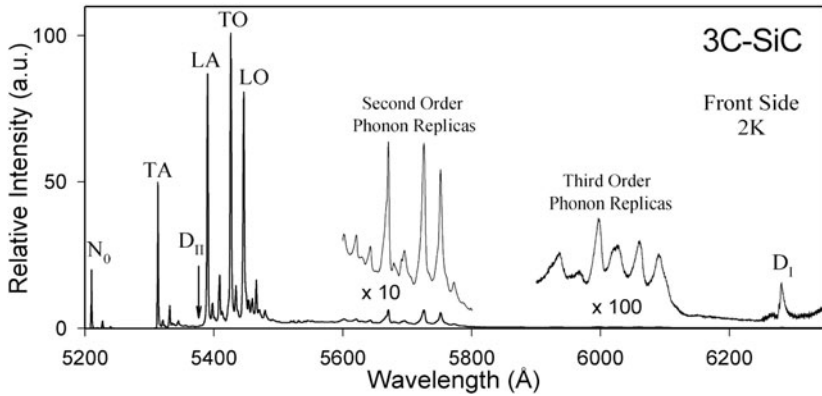


**Fig. 14.** 2 K spectrum of the “front” side of a 219  $\mu\text{m}$  thick 3C-SiC film removed from “undulant-Si”.  $N_0$  is the no-phonon line of the exciton bound to the neutral nitrogen donor and TA, LA, TO, and LO are first order phonon replicas.  $D_{II}$  and  $D_I$  are the two most common intrinsic defects seen in SiC by means of optical experiments

The samples were irradiated with a 30 mW He-Cd laser (325 nm) at 2 K and we measured the 3C-SiC front surface whilst still on the (001) Si substrate. Subsequently the 3C-SiC layer was removed from the substrate and one then could measure both the front and back surfaces of the free standing 3C-SiC layer. In Fig. 14 only the spectrum from the front side of the 3C-SiC layer is shown. We then thinned down the 3C-SiC layer from the back side, or substrate side, until samples of 205  $\mu\text{m}$ , 150  $\mu\text{m}$  and 110  $\mu\text{m}$  were obtained. All these samples were then spectrally examined from front and back.

Returning to Fig. 14 we see a global picture of the 2 K, 3C-SiC LTPL spectrum measured from the front of the 219  $\mu\text{m}$  thick film after removal from the “undulant-Si”. The most notable features are marked as follows:  $N_0$  is the nitrogen no-phonon line at 5210 Å,  $D_{II}$  is an intrinsic defect whose no-phonon line is at 5373 Å, TA, LA, TO, LO are the first order phonon replicas of  $N_0$ , the ranges of the second and third order phonon replicas of  $N_0$  are marked, and lastly we indicate  $D_I$ , at 6279 Å, the most common intrinsic defect in SiC observed by means of optical experiments.

On Fig. 15 one sees a normalized and expanded view of the  $N_0$  lines measured from the “back” of the samples for all the thicknesses of our 3C-SiC layer. The authors did not interpret the nature of the small high energy satellite on the high energy side of  $N_0$ . The largest stress shift towards lower energies is seen for the 219  $\mu\text{m}$  film. It is about 1 meV which is smaller than the 4 meV to 7 meV shifts towards lower energy observed from the front of thin (10  $\mu\text{m}$ ) CVD films of 3C-SiC grown on (001) Si by J.A. Powell [15].

Figure 16 shows the diminution of the  $D_{II}$  defect no phonon line measured from the “back” with thinning of the 3C-SiC layer. The  $D_{II}$  defect was reported 30 years ago [16], but its very nature is still the subject of active

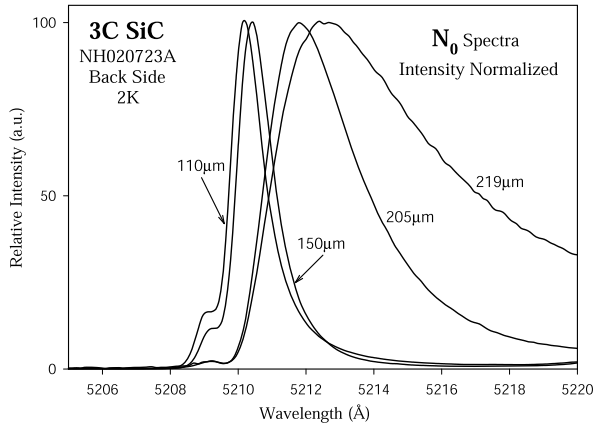


**Fig. 15.** The  $N_0$  line as measured from the “back” of the sample. The sample was successively thinned to 205  $\mu\text{m}$ , 150  $\mu\text{m}$ , and 110  $\mu\text{m}$

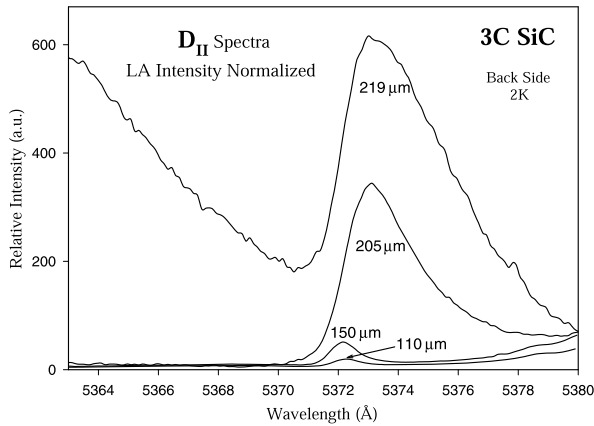


**Fig. 16.** The  $D_{II}$  no-phonon line, where the LA phonon replica is normalized such as to show the relative strength of the  $D_{II}$  line as material is removed from the “back” of the sample

theoretical investigation. It is certainly a carbon related complex but the final verdict is not yet in. Normally, this defect is observed in heavily implanted samples subsequent to high temperature annealing. It has been reported once before in 3C-SiC grown on “undulant-Si” [17].

Figure 17 shows the normalized  $D_I$  defect spectrum measured on the “back” side as a function of SiC thickness.  $D_I$  is the most common intrinsic defect in SiC observed by means of optical experiments. It was first described in 3C-SiC in 1971 [18]. It is seen that the line marked L of the 219  $\mu\text{m}$  layer is shifted slightly (1 meV) towards lower energy and is much broader than the line at 110  $\mu\text{m}$ . This shift is quite similar to the measured red shift of the  $N_0$

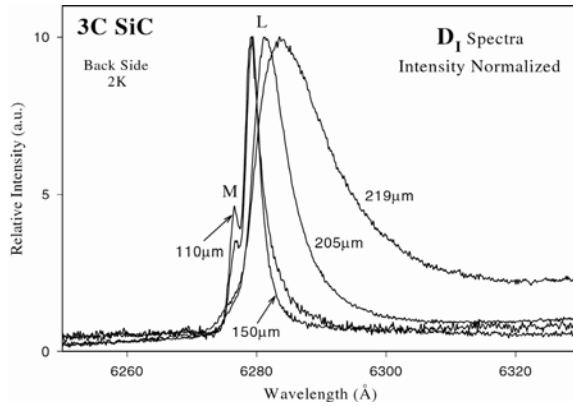


**Fig. 17.** The  $D_I$  no-phonon line, measured from the “back” of the sample with intensities being normalized. As the sample is thinned to 150  $\mu\text{m}$  the  $D_I$  line becomes sharp enough to reveal an excited state M of the L line

no-phonon line. For the 110  $\mu\text{m}$  film, the L line of the  $D_I$  center has a high energy satellite (an excited state) marked M using the notation of [18]. Since 1971 there has been a spate of papers which have attempted to pinpoint the nature of this defect center in SiC. The model that is currently most accepted is the “pseudo donor” model [19]. Recent theoretical calculations attribute the  $D_I$  defect center to the neutral anti-site pair [20]. The film stress relief is relatively minor and hence the sharpening of the L line in Fig. 17, as we remove material from the substrate side, is likely a sign of defect reduction.

### 6.3 Temperature Dependence of PL Spectra

To evaluate the crystalline quality of 3C-SiC by observing the temperature dependence of free-exciton (FE) luminescence, PL measurements were performed at various temperatures between 3 and 50 K for a 205- $\mu\text{m}$ -thick, free-standing 3C-SiC layer. The front of the sample was excited by the 476 nm line from a 25 mW Ar ion laser in order to avoid the unwanted overlap of PL features with the second order Raman peaks of 3C-SiC. The penetration depth of 476 nm at room temperature is 83  $\mu\text{m}$  [15].

Figure 18 shows the temperature dependence of the PL spectra. FE luminescence is clearly observed above 15 K, while the nitrogen-bound exciton feature disappears [21, 22]. Since 3C-SiC is an indirect semiconductor, the decay must be accompanied by the emission of the momentum-conserving phonon, i.e., TA, TO, LA, and LO at the conduction band minimum.

The luminescence intensity depends on the temperature, intensity of excitation, and concentration and capture cross-sections of neutral nitrogen impurities and defects. FE luminescence is usually observed at low temperatures in high purity material. Figure 18 shows the weak features of TA and TO

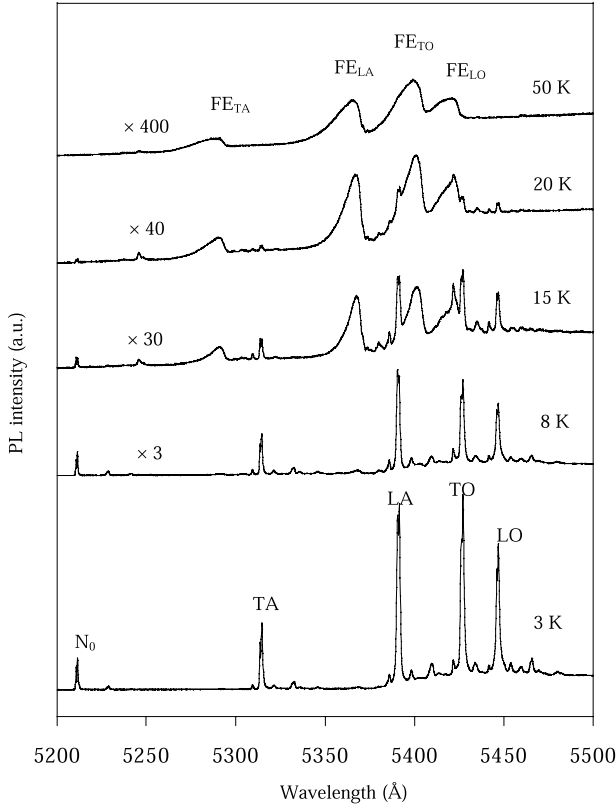


**Fig. 18.** Temperature dependence of FE luminescence for 3C-SiC grown on “undulant Si” substrate. FE indicates a luminescence related to free exciton recombination and the subscripts associated with FE denote related phonons

phonon replicas of FE. These observations indicate that the 3C-SiC grown on “undulant-Si” has a very low defect density and nitrogen concentration (we estimate the impurity concentration to be approximately  $10^{15} \text{ cm}^{-3}$ ). Although the “back” side has many defects, the front side is high quality due to the reduction of planar defects by the mechanism described in the preceding section. At higher temperatures, the nitrogen BE luminescence disappears, as shown in Fig. 18 because the excitons bound to nitrogen donors are released.

Therefore, excitons move freely at higher temperatures, i.e., FE emission dominates the PL features. The temperature dependence of the FE luminescence agrees well with that reported for high-quality 3C-SiC [21, 22]. One difference is the temperature at which the intensity of the FE luminescence is strongest. In our case, it was around 20 K, while it was higher in previous reports (50 K [21] and 70 K [22]). Thermal quenching of FE is associated with the exciton binding energy [21].

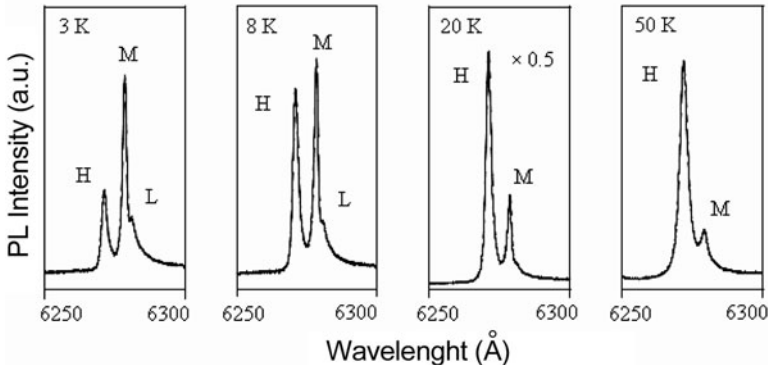


**Fig. 19.** Temperature dependence of  $D_I$  defect luminescence for 3C-SiC grown on “undulant Si” substrate. H, M and L indicate peaks associated with the no-phonon lines of  $D_I$  defect. Around 20 K,  $D_I$  luminescence takes the maximum intensity. Temperature dependence of  $D_I$  defect is similar to the previous report [18]

The lower maximum temperature of FE may be due to interference with the  $D_I$  defect, whose presence becomes clearer at high temperatures, as shown in Fig. 19. The  $D_I$  defect band in Fig. 19 resembles the spectra reported for ion-implanted samples [18]. Strong evidence of H and M bands, and weak L bands, is observed at 3 K. The L spectrum disappears at around 8 K and the relative intensity of H and M changes at above 8 K. However, the features of the  $D_I$  defect remain evident up to 50 K, i.e.,  $D_I$  defects are likely responsible for the thermal quenching of FE luminescence above 20 K seen in our samples via the efficient capturing of free excitons.

Although a  $D_I$  band is observed, FE luminescence, which is a good measure of the crystalline quality of samples, is observed at higher temperatures. These results are remarkable, considering that the 3C-SiC layer was grown heteroepitaxially directly on Si.

## 7 Properties of 3C-SiC Homoepitaxial Layer Grown on 3C-SiC Heteroepitaxial Layer on “Undulant-Si”

For the fabrication of electronic devices using thick 3C-SiC layers grown on “undulant-Si”, additional thin, high quality *n*- or *p*-type 3C-SiC homoepilayers have to be grown on them, which serve as a “substrate”. In this section, at first, the homoepitaxial growth process of such additional epilayers is described. Then the electrical quality of the homo-epilayers is investigated by DLTS measurements. Finally, differently processed 3C-SiC MOS capacitors are fabricated using the homo-epilayer and the density of interface states is determined by the conductance technique.

## 7.1 Homoepitaxial Growth of 3C-SiC

The homoepitaxial growth of 3C-SiC was performed on the 3C-SiC layer grown on the “undulant-Si” substrates in a hot wall reactor for chemical vapor deposition (CVD), described more in detail elsewhere [23, 24]. The “undulant-Si” substrate under the 3C-SiC was removed prior to the homoepitaxial growth in order to avoid melting of Si at growth temperature above the melting point of Si (1683 K). The reactor includes mechanical substrate rotation for increased uniformity of the epilayer doping concentration and thickness. The homoepitaxial 3C-SiC growth was done with parameters similar to the conditions for growth on 6H-SiC substrates. The growth temperatures were between 1773 K and 1873 K and the reactor pressure was set to 20 000 Pa. Silane ( $\text{SiH}_4$ ) and propane ( $\text{C}_3\text{H}_8$ ) was used as growth precursors and palladium cell purified hydrogen as the carrier gas. Nitrogen gas and trimethylaluminum (TMA) were employed to achieve *n*- and *p*-type conductivity, respectively. The net doping concentrations in the *n*-layers, determined by capacitance-voltage (*C-V*) measurements, were in the mid  $10^{16} \text{ cm}^{-3}$  range and the net doping concentrations in the *p*-layers were in the mid  $10^{17} \text{ cm}^{-3}$  range.

## 7.2 Deep Level Transient Spectroscopy (DLTS) Investigations

DLTS measurements taken on gold Schottky contacts were conducted to check whether energetically deep traps are incorporated in these epilayers. The dashed line in Fig. 20 is the result of a DLTS analysis of an *n*-type 3C-SiC epilayer (concentration of nitrogen donors =  $2 \times 10^{16} \text{ cm}^{-3}$ ). The deposited 3C-SiC epilayer reveals a high electrical quality; no traps are observable within the detection limit of  $1 \times 10^{11} \text{ cm}^{-3}$ . Subsequently this sample

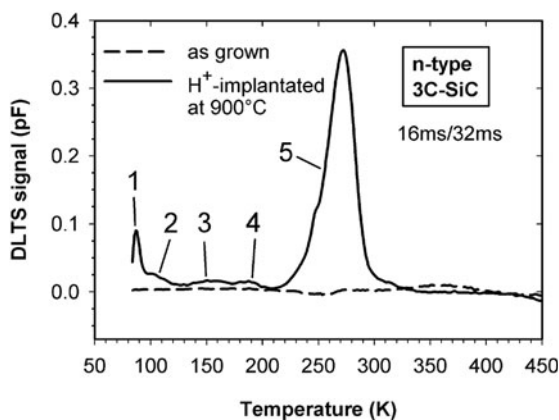


**Fig. 20.** DLTS spectra taken on an as-grown and  $\text{H}^+$ -implanted *n*-type 3C-SiC homo-epilayer

has been implanted with a hydrogen-box-profile (mean  $H^+$ -concentration =  $1 \times 10^{15} \text{ cm}^{-3}$ , depth  $d = 1.6 \text{ }\mu\text{m}$ ) at 1173 K. The solid DLTS spectrum in Fig. 20 is taken subsequent to the  $H^+$ -implantation. Five traps are generated; their parameters are:

$$\begin{aligned} \text{trap 1: } \Delta E(1) &= 150 \text{ meV} & N(1) &= 3 \times 10^{14} \text{ cm}^{-3}, \\ \text{trap 2: } \Delta E(2) &= 165 \text{ meV} & N(2) &= 7 \times 10^{13} \text{ cm}^{-3}, \\ \text{trap 3: } \Delta E(3) &= 180 \text{ meV} & N(3) &= 5 \times 10^{13} \text{ cm}^{-3}, \\ \text{trap 4: } \Delta E(4) &= 470 \text{ meV} & N(4) &= 8 \times 10^{13} \text{ cm}^{-3}, \\ \text{trap 5: } \Delta E(5) &= 590 \text{ meV} & N(5) &= 3 \times 10^{15} \text{ cm}^{-3}. \end{aligned}$$

Chemical composition and microstructure of these defects are not yet identified; the ionization energy of trap 3 is close to the ionization energy of the  $Z_1/Z_2$ -center observed in 4H- and 6H-SiC.

### 7.3 Interface State Density $D_{it}$ of $n$ - and $p$ -Type 3C-SiC MOS Capacitors

Differently processed 3C-SiC MOS capacitors (see Table 1) were fabricated and the density of interface states was determined by the conductance technique. The gate oxide was grown in nominally dry  $O_2$  at 1393 K for 1 h followed by a post-oxidation anneal at the same temperature [25]. In Fig. 21, the interface state density ( $D_{it}$ ) is compared for three 3C-SiC MOS capacitors.  $D_{it}$  can be reduced, when the standard RCA clean of the sample surface is combined with an UV ( $h\nu \geq 6 \text{ eV}$ ) ozone treatment (see samples #1 and #2) and when an additional  $n$ -type 3C-SiC epilayer is grown on the substrate (sample #3). In Fig. 22,  $D_{it}$  of an  $n$ -type (sample #3)/ $p$ -type (sample #4) 3C-SiC MOS capacitor is depicted. Close below the conduction band edge,

**Table 1.** Processing steps applied to the investigated  $n$ -/ $p$ -type 3C-SiC MOS capacitors

3C-SiC sample no.	Conductivity type	Processing		
		additional 3C-SiC epilayer	RCA- preclean	additional ozone- preclean
# 1	$n$ (substrate)	no	yes	no
# 2	$n$ (substrate)	no	yes	yes
# 3	$n$ (substrate) + $n$ (epi)	yes	yes	yes
# 4	$n$ (substrate) + $p$ (epi)	yes	yes	yes

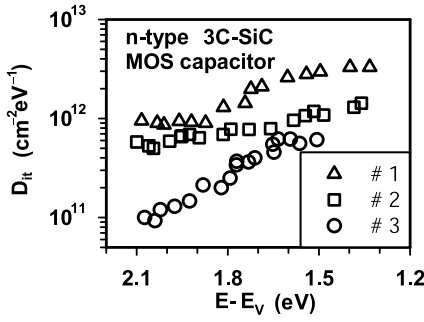


Fig. 21. Interface state density  $D_{it}$  as a function of energy for differently processed  $n$ -type 3C-SiC MOS structure

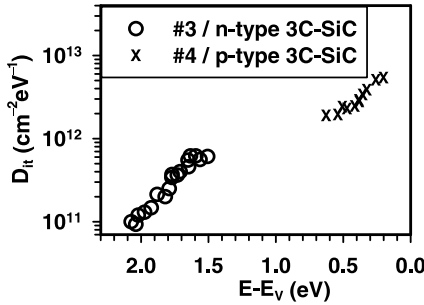


Fig. 22. Interface state density  $D_{it}$  as a function of energy for an identically processed  $n$ - and  $p$ -type 3C-SiC MOS structure

the density of interface states  $D_{it}$  reaches values of  $10^{11} \text{ cm}^{-2} \text{ eV}^{-1}$ ; such values are about two orders of magnitude lower than comparable values for the 4H-SiC polytype. In the lower half of the band gap,  $D_{it}$  of 3C- and 4H-SiC MOS capacitors result in largely the same values.

## 8 Conclusion

This paper describes a technique for fabricating low-defect “bulk 3C-SiC” by the hetero-epitaxial growth of 3C-SiC on “undulant-Si”. During initial 3C-SiC growth, anti-phase boundaries are eliminated on each slope. As the 3C-SiC grows thicker, stacking faults in the  $(\bar{1}11)$ - or  $(1\bar{1}1)$ -planes are annihilated as they combine with counter-stacking faults, while those parallel to  $(111)$  or  $(\bar{1}\bar{1}\bar{1})$  self-vanish. The advantages of this technique are that the orientation of the polar face is controlled on the non-polar Si substrate, and the annihilation and self-vanishing of SFs are brought about concurrently.

The electrical properties of the low-defect 3C-SiC layer grown on “undulant-Si” were investigated by Hall effect measurements. The least-squares-fitting of temperature dependence of free electron concentration revealed the defect parameters as follows: Ionization energy of nitrogen donors = 47 meV, concentration of nitrogen donors =  $4 \times 10^{15} \text{ cm}^{-3}$ , and concentration of compensation =  $1 \times 10^{15} \text{ cm}^{-3}$ . The Hall mobility of electrons shows in the

[110]-direction is higher than that in the  $\bar{[110]}$ -direction by a factor of approximately four and reaches a maximum value of  $300 \text{ cm}^2\text{V}^{-1}\text{s}^{-1}$  at 55 K. The residual stacking faults along the  $(\bar{1}11)$ - or  $(1\bar{1}\bar{1})$ -planes are thought as an origin of the anisotropic electron mobility.

We have measured LTPL spectra of 3C-SiC grown on “undulant-Si” as a function of the removal of 3C-SiC material from the backside, which originally faced the substrate. There is a maximum stress shift of 1 meV to a lower energy for the  $N_0$  line, as well as the L line of the  $D_I$  center, and a somewhat smaller shift (0.4 meV) for the no-phonon line of the  $D_{II}$  center. The diminution of the defect centers,  $D_I$  and  $D_{II}$ , as we remove material from the backside is consistent with mechanism for the reduction of planar defects by “undulant-Si”. The FE luminescence at the front side depends on the measurement temperature. Although a  $D_I$  band is observed, FE luminescence is observed at higher temperatures of up to 50 K, suggesting good crystalline quality.

The additional homo-epilayers were grown on the thick 3C-SiC hetero-epilayers grown on “undulant-Si” substrate. The deposited 3C-SiC homo-epilayer reveals a high electrical quality; no deep-level traps are observable within the detection limit of  $1 \times 10^{11} \text{ cm}^{-3}$ . However, traps are generated by  $H^+$ -implantations. Differently processed 3C-SiC MOS capacitors were fabricated using the homo-epilayer and  $D_{it}$  was determined by the conductance technique.  $D_{it}$  can be reduced, when the standard RCA clean of the sample surface is combined with an UV ( $h\nu \geq 6 \text{ eV}$ ) ozone treatment and when an additional  $n$ -type 3C-SiC epilayer is grown on the substrate. Close below the conduction band edge, the  $D_{it}$  reaches values of  $10^{11} \text{ cm}^{-2}\text{eV}^{-1}$ ; such values are about two orders of magnitude lower than comparable values for the 4H-SiC polytype.

## Acknowledgements

The authors thank F. Ciobanu, M. Krieger, F. Schmid and M. Weidner for the electrical characterization of the 3C-SiC samples.

## References

1. H. Matsunami, S. Nishino, H. Ono: IEEE Trans. Elect. Devices **ED-38**, 1235 (1981)
2. F.R. Chien, S.R. Nutt, J.M. Carulli, Jr., N. Bunchan, C.P. Beetz, Jr., W.S. Yoo: J. Mater. Res. **9**, 2086 (1994)
3. X. Tang, K.G. Irvine, Z. Ping, M.G. Spencer: Mater. Sci. Eng. B **11**, 39 (1992)
4. B. Virgil, F. Konjit, M.G. Spencer: Appl. Phys. Lett. **62**, 1919 (1993)
5. S. Nishino, J.A. Powell, W. Will: Appl. Phys. Lett. **42**, 460 (1983)
6. H. Nagasawa, K. Yagi, T. Kawahara: J. Cryst. Growth **237-239**, 1244 (2002)
7. H. Nagasawa, K. Yagi: Phys. Stat. Solidi (b) **202**, 335 (1997)

8. E. Pearson, T. Takai, T. Halicioglu, W.A. Tiller: J. Cryst. Growth **70**, 33 (1984)
9. K. Shibahara, S. Hishino, H. Matsunami: J. Cryst. Growth **78**, 538 (1986)
10. H. Nagasawa, K. Yagi, T. Kawahara, N. Hatta: to be published in: Proceed. of the MRS Fall Meeting (2002), Symposium K.
11. H. Nagasawa, T. Kawahara, K. Yagi: Matr. Sci. Forum **389–393**, 319 (2002)
12. K. Seeger: *Semiconductor Physics* (Springer Verlag, Berlin, 1985), p. 207
13. R.M. Broudy: Adv. Phys. **12**, 135 (1963)
14. J.H.P. van Weeren, R. Struikmans, J. Blok: phys. stat. sol. **19**, K107 (1967)
15. W.J. Choyke, Z.C. Feng, J.A. Powell: J. Appl. Phys. **64**, 3163 (1988)
16. L. Patrick, W.J. Choyke: J. Phys. Chem. Solids **34**, 565 (1973)
17. T. Yamada and K.M. Itoh: Mater. Sci. Forum **389–393**, 675 (2002)
18. W.J. Choyke, L. Patrick: Phys. Rev. B **4**, 1843 (1971)
19. L. Storasta, F.H.C. Carlsson, S.G. Sridhara, J.P. Bergman, A. Henry, T. Egilsson, A. Hallén, E. Janzén: Appl. Phys. Lett. **78**, 46 (2001)
20. A. Gali, P. Deák, E. Rauls, N.T. Son, I.G. Ivanov, E. Janzén, W.J. Choyke: submitted to Phys. Rev. B (2002)
21. M. Ikeda, H. Matsumani: Phys. Stat. Solidi A **30** 657 (1980)
22. K. Nishino, T. Kimoto, H. Matsunami: Jpn. J. Appl. Phys. **36**, 6405 (1997)
23. A. Schöner, A. Konstantinov, S. Karlsson, R. Berge: Mater. Sci. Forum **389–393**, 187 (2002)
24. See Chap. “New Developments in Hot Wall CVD Growth of SiC” of this book
25. F. Ciobanu, G. Pensl, H. Nagasawa, A. Schöner, S. Dimitrijević, K.-Y. Cheong, V.V. Afanas’ev, G. Wagner: Proceedings of the 4th European Conference on Silicon Carbide and Related Materials, Linköping, 2002

# New Development in Hot Wall Vapor Phase Epitaxial Growth of Silicon Carbide

A. Schöner

## 1 Introduction

### 1.1 Brief History on Vapor Phase Epitaxy of SiC

The progress in performance of devices made from Silicon Carbide (SiC) is to a large extent related to the quality and the size improvements in bulk material growth and homoepitaxial growth. Homoepitaxial growth of SiC by vapor phase epitaxy (VPE) was started in the mid 1980th due to unsatisfactory results in epilayer quality by growth techniques such as liquid phase epitaxy and close space sublimation. The first VPE-reactors for SiC were former gallium-arsenide reactors converted to meet the requirements for the growth of SiC. Figure 1 shows the schematic drawing of such a converted VPE-reactor. The heating of the substrate and the reactive gases was provided by high purity graphite susceptors, which were heated up to the growth temperature of about 1500°C by round or pancake like *RF*-coils. Because of the high temperatures SiC is grown, special care had to be taken to protect the quartz tube from being overheated, especially on the bottom side, where the susceptor is closest to the quartz. The thermal insulation of the susceptor was provided by graphite felt or highly reflective graphite layers deposited on additional quartz tubes. The reactor quartz tube was cooled by

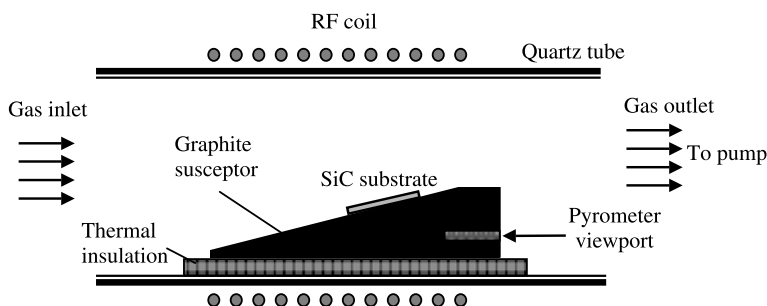


**Fig. 1.** Schematic drawing of a horizontal cold wall VPE-reactor for the epitaxial growth of SiC. The SiC substrate is placed on a high purity graphite susceptor, which is thermally insulated from the quartz tube and is heated up to the growth temperature by the *RF*-coil

either water or air. Hence, the surrounding quartz tube walls were several hundred degrees colder than substrate and susceptor. This reactor type with cold sidewalls was called horizontal cold wall reactor.

The first VPE-reactors for SiC were mainly designed for growth on small wafers ( $< 1''$  diameter), but their use was extremely important to investigate specific aspects of SiC epitaxial growth including dopant incorporation in dependence on the carbon to silicon ratio in the gas phase, dependence of the growth rate on the silicon content, and growth precursor depletion over the wafer.

The growth on larger diameter wafers has set high demands for the temperature homogeneity in VPE-reactors. To achieve uniform epilayers required an improved reactor design. Special care needed to be taken to provide uniform temperature distributions on the substrate surface and in the gas phase. In the beginning of the 1990th, a reactor concept was designed at the University of Linköping, Sweden, which applied heating of the growth cell and the reactive gases on the four surrounding sides of the susceptor. This horizontal concept for SiC homoepitaxy was called hot wall reactor [1]. Today, the horizontal hot wall reactor is the most advanced and developed machine for homoepitaxial growth of SiC. It is commercially available in single- and multi-wafer configuration for R&D and production purposes, respectively.

Besides the horizontal concept, vertical hot wall reactors have been developed [2]. The vertical reactors are designed for higher temperatures up to  $2000^{\circ}\text{C}$  and have an increased growth rate compared with the horizontal hot wall machines. The high temperature VPE-reactors can be either used for homoepitaxial growth or bulk growth. Despite the extensive capabilities of these vertical machines, the focus of this chapter will be the horizontal hot wall reactors, because of their potential for increased yield of SiC device processing and production due to the introduction of substrate rotation.

## 1.2 Horizontal Hot Wall Reactor in General

Figure 2 shows the schematic drawing of a horizontal hot wall reactor for homoepitaxy of SiC. The susceptor is made of high purity graphite with an inner cell of rectangular cross section for placing the substrate wafer. The susceptor is surrounded by graphite felt for thermal insulation and placed inside an air-cooled quartz tube. The hot wall reactor concept minimizes the radiation losses and limits them to the entrance and exit parts of the reactor inner cell. It provides inside the susceptor a region with at least 2 inch diameter around the temperature maximum with a temperature uniformity of better than  $\pm 10^{\circ}\text{C}$ . The substrate is placed in a recess of the wafer carrier plate. The carrier plate is loaded from the downstream side into the reactor. A stop in the end of the susceptor makes sure that 2 inch substrates are always placed at the same position in the inner cell.

Different shapes of the inner cell were tried during the development of the hot wall reactor. Today's design of the hot wall reactor inner cell has an

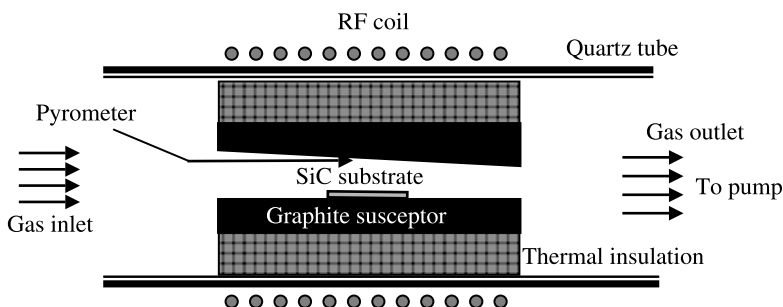


**Fig. 2.** Schematic drawing of a horizontal hot wall reactor for the homoepitaxy of SiC. The substrate is placed inside a rectangular inner cell with an inclined ceiling and heating is provided by the four surrounding *RF*-heated sidewalls

inclined ceiling to increase the gas velocity over the wafer. The increased gas velocity avoids the depletion of the reactive gas species in order to grow uniform layers. The growth temperature is measured by an optical pyrometer at the ceiling as illustrated in Fig. 2. The pyrometer is adjusted to the temperature maximum above the substrate wafer and is calibrated by melting silicon on the wafer carrier plate. Additional calibration points using materials with melting point close to the temperature of the homoepitaxial growth can be of interest, if a more accurate pyrometer calibration is desired.

## 2 Homoepitaxial VPE-Growth of SiC

### 2.1 Growth Process

The homoepitaxial VPE-growth process for SiC is basically similar for the different cold wall and hot wall reactor concepts. An illustration of the typical growth process for SiC homoepitaxy is shown in Fig. 3. The growth process employs high purity precursor gases, which are introduced into the reactor inner cell together with a carrier gas. The introduced gases are heated up to the growth temperature and the chemical reactions take place in the gas phase and at the surface of the substrate wafer.

The VPE-growth of SiC consists basically of the following processes:

- (1) Transport of the reactive gases from the inlet to the reactor inner cell,
- (2) cracking of the precursor gas molecules,
- (3) diffusion of silicon and carbon containing species to the surface,
- (4) adsorption of silicon and carbon containing species at the surface,
- (5) desorption and evaporation of silicon and carbon from the surface,
- (6) surface diffusion of adsorbed species,
- (7) incorporation of adsorbed species into the growing crystal, preferably at steps or defect sites.

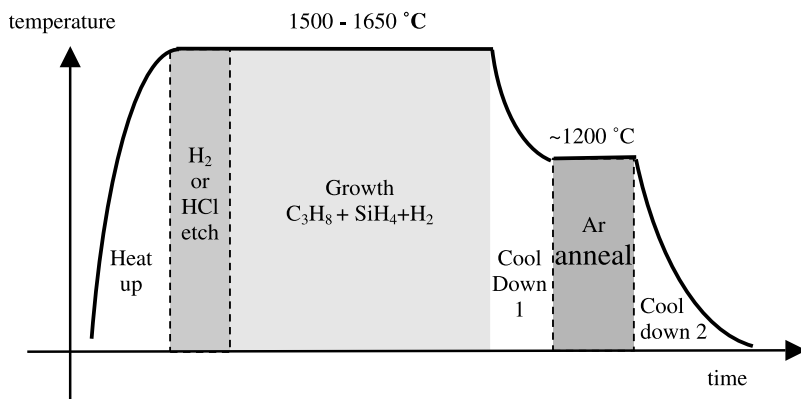


**Fig. 3.** Typical VPE growth process for homoepitaxy of SiC with silane ( $\text{SiH}_4$ ) and propane ( $\text{C}_3\text{H}_8$ ) as growth precursors in hydrogen carrier gas. The argon anneal is optional and sometimes used to activate acceptor dopants

The adsorption (4), surface diffusion (6), and incorporation of silicon and carbon containing species (7) contribute mainly to the deposition of SiC. Desorption and evaporation (5) of silicon and carbon from the surface can be regarded as etching. If the deposition dominates over the etching, thin SiC films are grown on the substrate. The growth rate of the film depends on which of the above listed processes is the limiting one and on the ratio of deposition rate to etch rate. Both, the growth limiting process and the rate ratio of deposition to etching are strongly dependent on the temperature and the supplied gas flows.

Standard VPE-processes in a horizontal hot wall reactor employ growth temperatures between  $1500^\circ\text{C}$  and  $1650^\circ\text{C}$ . The total pressure in the reactor varies from 100 hPa to 500 hPa, controlled by a throttle valve and a process dry pump. The most commonly used precursors for silicon and carbon are silane ( $\text{SiH}_4$ ) and propane ( $\text{C}_3\text{H}_8$ ). Hydrocarbons such as methane ( $\text{CH}_4$ ) and ethane ( $\text{C}_2\text{H}_6$ ) were investigated as alternative carbon precursors [3]. In addition, precursors containing silicon as well as carbon atoms were studied intensively for the heteroepitaxial growth of cubic 3C-SiC on silicon. Hydrogen purified through heated palladium cells is commonly used as carrier gas. The hydrogen flows ranges from 10 slm (standard liter per minute) up to 70 slm, depending on the size of the reactor inner cell. Nitrogen ( $\text{N}_2$ ) gas and trimethylaluminum (TMA,  $(\text{CH}_3)_3\text{Al}$ ) are employed for donor and acceptor doping, respectively. Nitrogen donors occupy preferentially carbon lattice sites, whereas aluminum because of its size is incorporated on silicon lattice sites. The doping concentration ranges achieved in horizontal hot wall reactors are for nitrogen from below  $1 \cdot 10^{14} \text{ cm}^{-3}$  up to  $1 \cdot 10^{20} \text{ cm}^{-3}$  and for aluminum from about  $1 \cdot 10^{15} \text{ cm}^{-3}$  up to  $1 \cdot 10^{21} \text{ cm}^{-3}$ . It should be avoided that epilayers with high and low doping concentrations have to be grown

in the same reactor cell, or at least not with the same susceptor. Especially aluminum causes severe memory effects and aluminum concentrations below  $5 \cdot 10^{16} \text{ cm}^{-3}$  are difficult to achieve for at least one hour of growth time after high doped *p*-type layers have been grown.

## 2.2 Substrate Preparation and Step-Controlled Epitaxy

Very important for the quality of the growing epilayer is the initial substrate surface. Today, chemical-mechanical polishing is applied to achieve mirror-like surfaces and excellent surface roughness [4]. In-situ etching by the hydrogen carrier gas at the growth temperatures removes the damage remaining from the polishing. Alternatively, adding a small amount of hydrogen chloride (HCl) to the hydrogen carrier gas during the etching step improves further the surface and reduces unwanted defect nucleation centers [5]. The etching step is very important to prepare the substrate for the SiC growth process. It can vary with the reactor design and the growth process, and has to be carefully investigated for new reactor designs and processes.

One of the breakthroughs in SiC epitaxy was the discovery of the so called step-controlled epitaxy [6]. Growing epilayers on on-axis substrates resulted in polycrystalline SiC films due to spontaneous nucleation and island growth. The information on the stacking sequence of silicon-carbon bi-layers is not transferred to the growing layer. The growing islands are mostly of 3C-SiC polytype, the most stable SiC crystal configuration at the VPE growth temperatures. In step-controlled epitaxy, the replication of the polytype is achieved by orienting the wafer surface with a small off-angle towards the *c*-plane. This off-angle cut results in a large amount of atomic steps at the surface, which are then preferred adsorption and incorporation centers for the growth species. The steps contain the information on the stacking sequence and this stacking sequence is thus transferred to the growing layer. The off-angle for the surface orientation has to be chosen in that way, that the remaining terraces between the steps are small enough to prevent spontaneous nucleation. In addition, the mobility of the surface diffusion for the adsorbed species should be high enough, so that the adsorbed species are able to reach the step sites. The SiC growth should only occur at the steps. The standard angle for the Si-face off-axis cut was determined to  $3.5^\circ$  and  $8^\circ$  towards  $\langle 11\text{-}20 \rangle$  for 6H-SiC and 4H-SiC, respectively.

## 2.3 Site Competition Epitaxy

In the mid 1990th, the discovery of the site competition epitaxy [7], which explains the dependence of the doping atom incorporation on the ratio of available silicon and carbon atoms (C/Si-ratio) in the gas phase, provided an explanation for the observation of unexpectedly high content of acceptor species in epilayers grown in horizontal hot wall reactors. The high content

of acceptor species was often observed in reactors used for growth of both *n*-type and *p*-type epilayers. But high acceptor background was even found in reactors used only for the growth of *n*-type epilayers. In this case the source was mainly residual boron in the susceptor graphite material. The acceptor background was especially disturbing during the growth of thick, low concentration *n*-type, high carrier lifetime epilayers for high voltage applications. The thick, low doped *n*-type epilayers were usually grown with no intentional doping supplied and residual nitrogen in the reactor was used as the doping source. Long growth runs resulted sometimes in a change of the conductivity type due to with time faster decreasing supply of background nitrogen compared with e.g. the boron coming from the susceptor walls.

The reason for the “easy” incorporation of acceptor dopants was found to be again the susceptor graphite acting as an additional carbon source. The graphite susceptor delivers through evaporation and the attack from the hydrogen carrier gas so much carbon to the gas phase that the growth was carried out always under carbon rich conditions [8]. In some cases it was even possible to grow without any carbon precursor, achieving good quality SiC layers. With site competition epitaxy it was observed, that the shallow acceptor dopants aluminum and boron, which are incorporated on silicon lattice sites, are preferred build into the crystal under carbon rich conditions. Therefore, to reduce the acceptor background, a solution had to be found to prevent the evaporation of carbon from the graphite susceptor. Thermally stable coating of the susceptor by polycrystalline SiC was one of the solutions and is still used in many reactor designs. Today, also tantalum carbide coating is investigated as an alternative to the SiC coating [9]. Using coated susceptors was and is the only way to achieve control over the C/Si-ratio in hot wall reactors. With coated susceptors, site-competition epitaxy could be applied to reduce the background doping and create thick, low doped layers of homogeneous conductivity type.

Furthermore, the control of the C/Si-ratio is important to achieve sharp dopant transitions between layers with opposite conductivity type [10, 11]. Together with stopping the growth for some minutes at the growth temperature and etching the wafer during the stop time slightly by the hydrogen carrier gas, an interface sharpness of below 20 nm between *p*-type and *n*-type layers can be achieved.

## 2.4 Recent Growth Process Improvements

### 2.4.1 Carrier Gas Mixture of Hydrogen and Argon

Hydrogen is normally the preferred carrier gas due to the relatively easy way of purifying it with heated palladium cells. Hydrogen exists mainly as H<sub>2</sub> molecules, but at the growth temperatures of 1500°C to 1650°C the hydrogen molecules are partly decomposed and highly reactive hydrogen atoms participate in the growth process. These reactive hydrogen atoms etch the

substrate surface during the growth and increase the surface mobility of the reactive species, which leads to a reduced formation of defects and 3C-SiC inclusions. Hence, atomic hydrogen has a positive effect on the growing surface and on the layer quality. But atomic hydrogen reacts not only with the substrate surface. Also the reactor graphite parts are attacked by atomic hydrogen and mainly methane is formed. Even the coating, including SiC coating, is attacked during the growth. In addition, hydrogen has a high cooling efficiency and is affecting the temperature distribution inside the susceptor cell, especially on the gas entrance side (see also Fig. 4).

To reduce the negative effect of hydrogen on the reactor parts and the temperature distribution, and at the same time preserve the positive effect on the epilayer growth, carrier gas mixtures of purified hydrogen and argon have been investigated. The experiments were done in a standard horizontal hot wall reactor with silane and propane as the reactive gases, keeping the total carrier gas flow constant at 50 slm, the reactor pressure at 250 hPa, the C/Si-

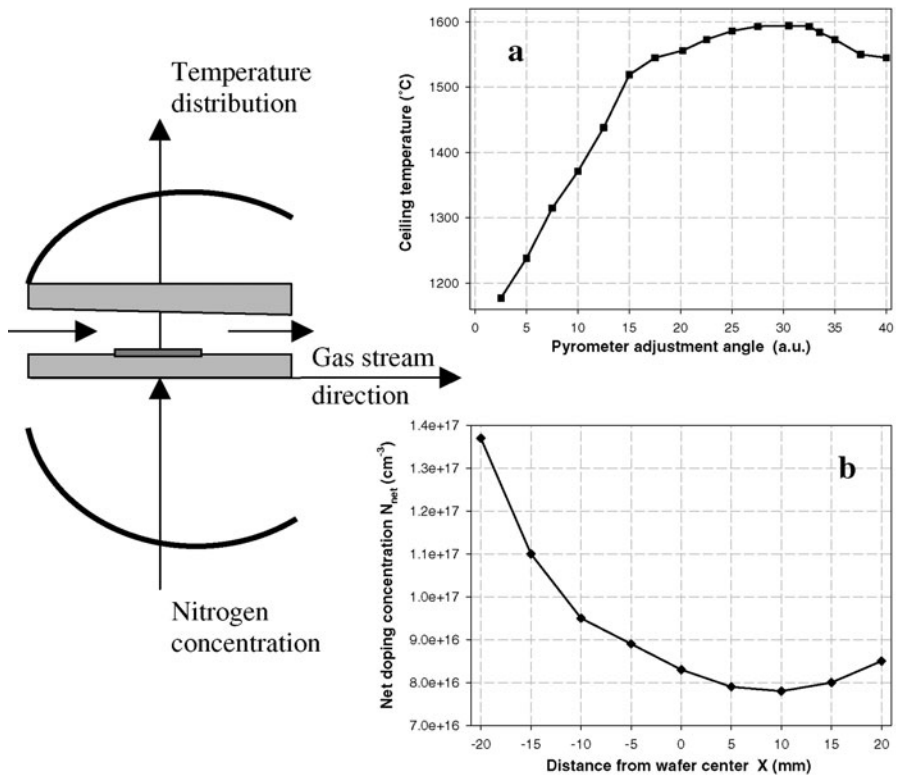


**Fig. 4.** Temperature distribution (a) and variation of the net doping concentration (b) obtained by *C-V* of a nitrogen-doped epilayer in gas stream direction of a standard horizontal hot wall reactor

ratio at 1.5 and the silane flow at 7.5 sccm. The Argon content of the carrier gas was varied from 0% to 30%. It was observed that thickness and doping uniformity of the grown layers were significantly improved by using a carrier gas mixture of hydrogen and argon. The maximum variation over mean values were decreased from 21% to 12% and from 54% to 22% for epilayer thickness and doping concentration, respectively. The uniformity values are calculated for 2 inch wafers with an edge exclusion of 5 mm. An uniformity improvement was achieved up to the argon content of about 15% to 20%. For argon contents above 20% no significant further improvement in layer uniformity was observed. The layer uniformity improvement is attributed to the lower cooling efficiency of the hydrogen-argon carrier gas mixture compared with a pure hydrogen carrier gas, resulting in a more homogeneous temperature distribution, especially in the upstream part of the susceptor.

The drawback in using hydrogen-argon mixtures as carrier gas is the reduction in growth rate, which is caused most probably by a reduced diffusivity of reactants through the carrier gas combined with a reduced cooling of the growing surface. The reduced cooling results in an enhanced evaporation of the adsorbed growth species. In the experiments mentioned above, the growth rate was almost linearly reduced from 2.4  $\mu\text{m}/\text{h}$  at no argon content to 2.2  $\mu\text{m}/\text{h}$  at an argon content of 30%. At this medium growth rate range each added percentage of argon to the hydrogen carrier gas was reducing the growth rate by about 10 nm/h. The reduced growth rate for the hydrogen-argon carrier gas mixture is an additional indication for the decreased cooling efficiency and therefore the increased temperature at the growing surface.

As mentioned above, carrier gas mixtures of hydrogen and argon are useful to improve the layer uniformity, but the growth rate is reduced. The layer uniformity is especially important for high frequency devices such as bipolar transistors and MESFETs. These high frequency devices consist of thin, precisely doped layers as the active region of the device. The layer thickness is in the order of 100 nm to 1  $\mu\text{m}$ . Hence the growth rate reduction by using hydrogen-argon carrier gas mixtures does not play a significant role. The gain in device yield and performance due to improved layer homogeneity is by far more important than the extra time needed for the growth.

#### 2.4.2 Silicon Droplets

As mentioned in Sect. 2.2, the in-situ etch before the actual growth is crucial for the homoepitaxial SiC growth process and has been studied carefully [5, 13]. The etching process consists mainly of the formation of hydrocarbons through reaction of the hydrogen carrier gas with the surface carbon and the evaporation of silicon. It was found that at pressures above 100 hPa a pure hydrogen etch removes carbon from the SiC surface by forming hydrocarbons and the silicon evaporation becomes the limiting process for the etch. The remaining silicon on the surface can form silicon droplets, which act as nucleation centers for defects. A similar effect occurs under silicon

rich growth conditions (C/Si-ratio below 1). Under these growth conditions, substrate defects such as micropipes and dislocations can act as nucleation centers for the formation of silicon droplets. The result is a high number of crystal defects and the deterioration of the epilayer surface morphology.

Several ways were found to avoid the silicon droplet formation. The heating and etching process should be done at low pressure, preferably below 100 hPa, where the hydrocarbon formation and not the silicon evaporation is the limiting process for the in-situ etch. If a pressure below 100 hPa cannot be achieved during the heating, then reducing the hydrocarbon formation rate or increasing the silicon evaporation rate are further possibilities. The addition of HCl to the carrier gas increases the silicon evaporation due to the reaction of Si and Cl atoms. A surplus of silicon at the surface is avoided. On the other hand, adding propane during the heat-up phase of the growth run reduces the hydrocarbon formation and the SiC surface is stabilized. It allows the controlled etching as a well defined step in the growth process by reducing the uncontrolled etching during the heat-up phase to a minimum. The epitaxial re-growth on processed or implanted structures, which imply that the surface etching before the growth has to be minimized, becomes possible.

#### **2.4.3 Micropipe Closing and Dissociation into Screw Dislocations**

One of the application areas for SiC is high power electronics. High-voltage devices processed on the (0001)-face (Si-face) of SiC were investigated with respect to the influence of extended crystal defects on the device performance [14]. It was found that the so called micropipes, hollow cores associated with “super screw” dislocations, severely affect the blocking characteristic of high-voltage devices in a negative way. Devices containing micropipes in the active area sustained lower blocking voltages than devices without micropipes. On the other hand, high-voltage blocking devices should also be able to carry high current in forward direction, which implies a larger device area. To increase the blocking and current handling capability of SiC power devices, the micropipe density in the material had to be reduced. In recent years, tremendous progress was made in sublimation bulk growth to reduce the micropipe density to values below 1 per  $\text{cm}^2$  and there are substrates available with micropipe free areas of 1  $\text{cm}^2$  and more [15]–[17].

Recently, progress has been made in developing homoepitaxial VPE-growth processes with closing or dissociating effect on micropipes [18, 19]. It was found that under Si-rich conditions (C/Si-ratio below 1) micropipes transform into elementary screw dislocations and the hollow cores are no longer observed in micrographs taken after molten KOH etching. Depth analysis showed that most micropipes were closed in the initial stage of the epitaxial growth process. Epitaxial material with micropipes dissociated into closed core screw dislocations was tested under high-voltage operation [19]. Nickel

Schottky barrier diodes were processed using about 20  $\mu\text{m}$  thick 4H-SiC epilayers and investigated with respect to breakdown voltage. The Schottky barrier diodes, which included a dissociated micropipe in the contact area, withstood breakdown voltages up to 1000 V, where the Schottky diodes with micropipes propagated from the substrate resulted in poor blocking characteristics and breakdown voltages less than 400 V. The observation of micropipe closing in VPE encourages the use of advanced buffer layer techniques for the fabrication of SiC power devices to improve the device yield and performance significantly.

### 3 New Generation of Hot Wall CVD Reactors

#### 3.1 Up-Scaling of the Standard Hot Wall VPE Reactor

In recent years, the substrate diameter for SiC wafers was steadily increased and 3 inch diameter substrates are now available in production. 4 inch substrates are demonstrated in R&D. As device concepts are being more and more commercialized, the minimum wafer size for cost efficient device production is 4 inch. With 4 inch diameter wafers, existing foundries for device production could be used to a large extend and the initial investment for mass production of SiC devices could be reduced. One device manufacturing process, which is normally not available in semiconductor processing foundries, is VPE for SiC. For the production of SiC epilayers, multi-wafer reactors have been developed and are commercially available. Multi wafer reactors will be discussed in Sect. 3.4.

Scaling up the substrates to larger diameter implies also that the wafer handling capability of epitaxial machines are increased. But just scaling up the reactor chamber, to be able to place large diameter wafers in there, does not necessarily give the desired results. If for example the up-scaling of the standard hot wall reactor, described in Sect. 1.2, is not carefully designed, then unwanted variations of the epilayer thickness and doping concentration over the wafer are detected. Especially in carrier gas stream direction, U-shape nitrogen doping profiles are observed with the doping concentration at the wafer edges up to the factor 2 to 3 higher than in the wafer center. The main reason for the ununiformity in gas stream direction is the temperature inhomogeneity. From experiments, investigating the nitrogen incorporation in dependence of the growth temperature, it is known that the nitrogen concentration is decreasing with increasing temperature. The observed U-shape nitrogen distribution can therefore be regarded as a measure of the temperature profile over the substrate. The temperature distribution in gas stream direction observed by scanning the measurement spot of an optical pyrometer over the inner cell ceiling and the observed variation in the net doping concentration of a nitrogen doped epilayer are shown in Fig. 4.

The lower temperatures at the upstream and downstream side of the susceptor inner cell are mainly due to radiation losses. At the upstream side, the susceptor is even cooled by the hydrogen carrier gas. Both effects contribute to a bell-like temperature distribution as shown in Fig. 4 and the temperature variation over the substrate the gas heating zone at the upstream side of the susceptor should be sufficiently long to heat the gases to the growth temperature and the process conditions like carrier gas flow and reactor pressure should be optimized for each reactor design separately.

Perpendicular to the carrier gas stream direction the ununiformity in doping concentration is not as large as in gas stream direction due to the symmetric heating of the reactor cell in this direction and the laminar carrier gas flow conditions. The temperature variation perpendicular to the gas stream direction is in the order of 5 to 10°C and the thickness and doping uniformities are about 5% and 15%, respectively.

### 3.2 Reactor Design Improvements

In the horizontal hot wall reactor described in Sect. 1.2, the only not actively heated sides are the gas entrance and exit part of the susceptor. Due to radiation losses at these sides, the temperature can be 100°C to 300°C lower than in the susceptor center, depending on the reactor design and geometry (see also Fig. 4). Additional graphite insulation covering the entrance and exit sides of the susceptor limit the radiation losses. However, the hydrogen carrier gas attacks the graphite insulation. Dust particles are created and are transported to the wafer surface, where they are overgrown during the run. An unwanted deterioration of the surface morphology is observed. Combining the additional radiation shield with a gas liner made from coated graphite, to streamline the gases into the reaction cell, avoids that particles are reaching the wafer surface.

The liner acts also as a pre-heating zone for the gases, which is important to avoid disturbances in the temperature profile over the substrate. In addition to the radiation losses the entrance part of the susceptor is cooled through the carrier gas. Depending on the size of the inner cell, carrier gas flow rates of 10 slm to 70 slm are typically used. If the carrier gas flow rate is too high for the size of the inner cell and/or if the heating zone is too short, cold carrier gas reaches the growth area and disturbs the temperature homogeneity over the wafer. To avoid that cold carrier gas reaches the growth zone, heating of the supplied gases can be provided by either additional *RF*-coils or a *RF*-coil with larger number of turns, where the spacing between the turns can be individually adjusted. In that way the *RF*-heating is tailored to achieve very uniform temperature distribution over a wide area inside the susceptor.

For some device structures, the requirements for doping and thickness uniformity are so extreme, that an improved reactor design and a uniform

temperature distribution is not sufficient. Instabilities in the gas composition and the flow dynamics can still introduce inhomogeneities in the growth. To overcome the effect of these instabilities, substrate rotation is introduced into the reactor design. There are two ways of introducing substrate rotation, mechanical rotation driven by a motor and gas foil rotation (GFR). Both techniques will be subject of the next sections.

### 3.3 Hot Wall Reactor with Mechanical Rotation

#### 3.3.1 Reactor Design

The design for a horizontal hot wall reactor with mechanical substrate rotation was demonstrated in [12]. Figure 5 shows the schematic drawing of the reactor design and the upstream side of the reactor in operation.

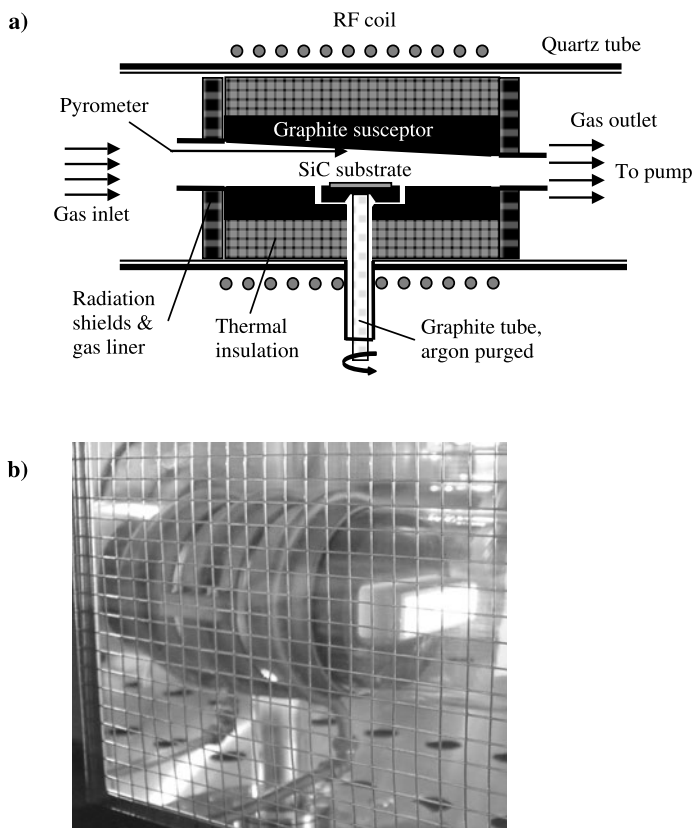


**Fig. 5.** Horizontal hot wall reactor with mechanical substrate rotation. (a) Schematic drawing; (b) picture of the upstream part (gas entrance side) in operation

horizontal hot wall reactors, the susceptor is *RF*-heated and consists of SiC coated graphite surrounded by graphite felt insulation. The susceptor contains a recess in the middle of the bottom part for the rotating wafer carrier disc. The rotation of the wafer carrier is carried out by a coated graphite tube, which rotates motor driven with the rotation speed of about 60 rpm. This coated graphite tube is fed through a third flans of the quartz tube, through the bottom part of the graphite insulation, and through the bottom of the susceptor into the reactor inner cell. The design of the rotation part was done in that way that the temperature distribution and the susceptor heating as well as the laminar gas flow conditions are not significantly disturbed. In addition, the rotation part is purged with argon to avoid hydrogen attacking the rotating graphite tube.

The wafer carrier disc is loaded into the reactor from the downstream side with a transport fork. To pick up the wafer carrier from the fork, the rotating graphite tube is movable also in vertical direction. The wafer carrier is designed for 2 inch substrates and consists of tantalum carbide (TaC) coated graphite to avoid deposition of SiC on the wafer backside. Such deposition takes place in conventional SiC VPE reactors employing SiC coated susceptors or wafer carriers through sublimation of the SiC coating to the wafer backside.

The growth temperature in hot wall reactors is often controlled by optical pyrometers measuring the temperature in a hole in the susceptor. In the reactor with mechanical rotation the temperature is measured at the inclined ceiling of the susceptor above the carrier disc. The pyrometer is adjusted to measure at the maximum ceiling temperature. The carrier disc is probably not actively heated by the *RF*-field, but mainly through the radiation from the susceptor and the contact with the hot gases. It is expected that the substrate temperature is slightly lower than the ceiling temperature measured by the pyrometer. The temperature difference is not very big as crystal quality and surface morphology of the grown layers are comparable with epilayers grown in horizontal hot wall reactors without substrate rotation.

### 3.3.2 *C-V* Characterization of Epilayer Thickness and Doping Concentration Uniformity

The most interesting properties to characterize for epilayers grown in the horizontal hot wall reactor with substrate rotation are the uniformities of the layer thickness and doping concentration. Different optical techniques like Fourier infrared spectroscopy and low temperature photoluminescence, and electrical techniques like capacitance-voltage (*C-V*) and Hall effect measurements can be used to determine either layer thickness or doping concentration, or both at the same time. In this section, the possibilities of *C-V* measurements to investigate epilayer thickness and doping concentration together will be discussed.

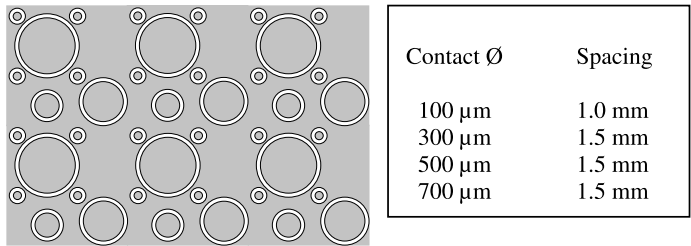


**Fig. 6.** Mask layout for the processing of metal Schottky barrier contacts by lithography. The mask is mainly used for  $C$ - $V$  characterization of the electrical properties of epilayers

For the  $C$ - $V$  measurements titanium or nickel Schottky barrier contacts with diameters 100 μm, 300 μm, 500 μm, and 700 μm were evaporated and lithographically structured. The used mask has 1.5 mm spacing between two contacts of the same size, except for the 100 μm Schottky contacts, where the spacing is 750 μm (Fig. 6). Hence, about 800 to 1000 Schottky contacts of each size are possible to place on a 2 inch diameter wafer. The remaining surface area is also covered with metal, leaving 50 μm spacing to the Schottky contacts. The large area contact forms the ground contact for the  $C$ - $V$  measurements.

To create the doping concentration and the layer thickness map, the Schottky devices are measured by  $C$ - $V$  in a semi-automatic probe station and then analyzed with respect to the doping depth profile. The  $C$ - $V$  technique is useful up to doping concentrations of about  $5 \cdot 10^{18} \text{ cm}^{-3}$ . For doping concentrations in the range from  $1 \cdot 10^{17} \text{ cm}^{-3}$  to  $5 \cdot 10^{18} \text{ cm}^{-3}$  small device structures ( $\emptyset$  100 μm to 300 μm) have to be used to avoid wrong results due to leaky devices.

For a given doping concentration, the layer thickness must be adjusted carefully to be able to determine it from  $C$ - $V$ . The layer thickness has to be decreased with increasing doping concentration as shown in Fig. 7. The equation to calculate the maximum thickness possible to detect with  $C$ - $V$  is shown in the inset of Fig. 7. If the substrate doping concentration differs at least the factor 5 from the epilayer doping concentration, but is of the same conductivity type, then the transition epilayer to substrate can be observed in  $C$ - $V$  measurements with applied reverse bias voltages up to 100 V. When a highly doped substrate is reached, the capacitance becomes constant and decreases no longer with increasing reverse bias voltage. The epilayer thickness can then be calculated by multiplying the dielectric constant for SiC with the device area and divide it by the constant value of the capacitance.

The  $C$ - $V$  results for layer thickness and doping concentration should be occasionally checked with other methods. Doping depth profiles can also be obtained from secondary ion mass spectrometry (SIMS). The epilayer thickness and concentration determined from  $C$ - $V$  and SIMS should agree within

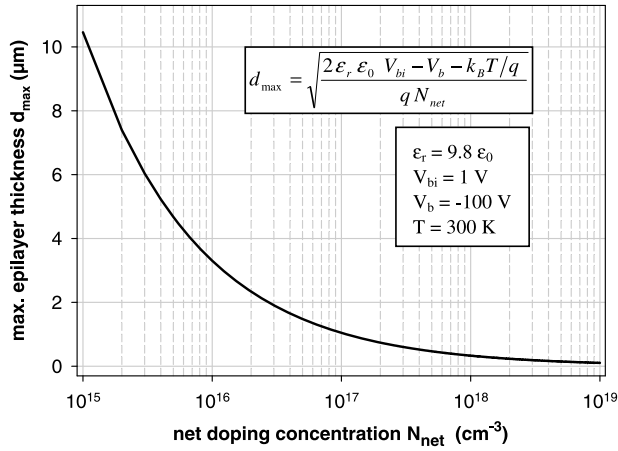


**Fig. 7.** Maximum thickness  $d_{\max}$  of epilayers to be detected with  $C$ - $V$  as a function of the epilayers net doping  $N_{\text{net}}$ .  $\epsilon_r \epsilon_0$  is the dielectric constant for SiC,  $V_{bi}$  the Schottky barrier height,  $V_b$  the bias voltage,  $k_B$  the Boltzmann constant,  $T$  the temperature, and  $q$  the electron charge

the accuracy of these measurement methods. An agreement of the results from SIMS and  $C$ - $V$  indicates that the concentration of compensating impurities and defects is small in the investigated layers.

### 3.3.3 Uniformity of the Epilayer Thickness

The thickness uniformity of epilayers grown in the reactor with wafer rotation is excellent with a typical standard deviation over mean value of around 0.5% and a maximum thickness variation over mean value of around 2.0%, when excluding 5 mm at the wafer edges (Fig. 8). Compared with a standard hot wall reactor these thickness uniformity values are about the factor 3 to 5 better. It was found that the achieved thickness uniformity is almost independent on the employed growth conditions and on the carrier gas, and on the conductivity type of the grown epilayer.

In addition to the excellent thickness uniformity, the reactor with substrate rotation showed an increased growth rate compared to the standard horizontal hot wall reactor. Using the same precursor flow rates and the same growth temperature in both reactor types, the growth rate was around the factor 1.5 to 2 higher in the reactor with substrate rotation. As the growth rate goes down with increasing temperature and constant silane flow rate, the higher growth rate in the reactor with rotation results most likely from a lower substrate temperature due to the difference in heating of the wafer carrier and the different coating of the wafer carrier. The heat transport between the SiC substrate and the SiC coating used in the standard hot wall

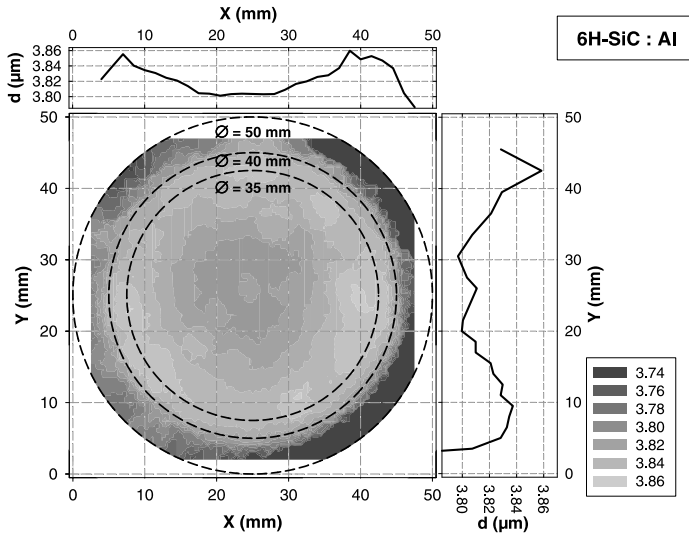


**Fig. 8.** Thickness uniformity of a *p*-type 6H-SiC epilayer grown in a hot wall reactor with substrate rotation using silane, propane, and TMA as growth precursors and hydrogen as carrier gas. The standard deviation over mean value is 0.4% and the maximum variation over mean value is 2.2% with an edge exclusion of 5 mm (circle diameter 40 mm)

reactor is most likely better than between the SiC substrate and the TaC coating used for the wafer carrier disc in the reactor with rotation.

The thickness map from epilayers grown in the reactor with rotation has a minimum in the center of the wafer and the thickness increases slowly towards the wafer edge (Fig. 8). The increase in thickness is due to a decrease in temperature. The distribution is circular symmetric as expected from the growth with substrate rotation. A decrease of the thickness is observed at the wafer edges, which is probably caused by an artifact of the *C-V* measurements. An increased number of defects are usually observed at the wafer edge causing the Schottky devices to be leaky. The capacitance measured on leaky Schottky devices is typically higher than for good blocking devices, resulting in a lower calculated thickness.

### 3.3.4 Uniformity of the Epilayer Doping Concentration

For SiC devices such as high frequency devices, the requirements in doping uniformity are stronger than achievable with the standard horizontal hot wall reactor. Substrate rotation has to be introduced in the reactor design. Figure 9 shows the doping uniformity map of an aluminum doped *p*-type 6H-SiC epilayer grown in the horizontal hot wall reactor with mechanical substrate rotation. The growth temperature was 1600°C, the C/Si-ratio 1.5, the carrier gas flow rate 35 slm, and the reactor pressure 200 hPa. The net doping

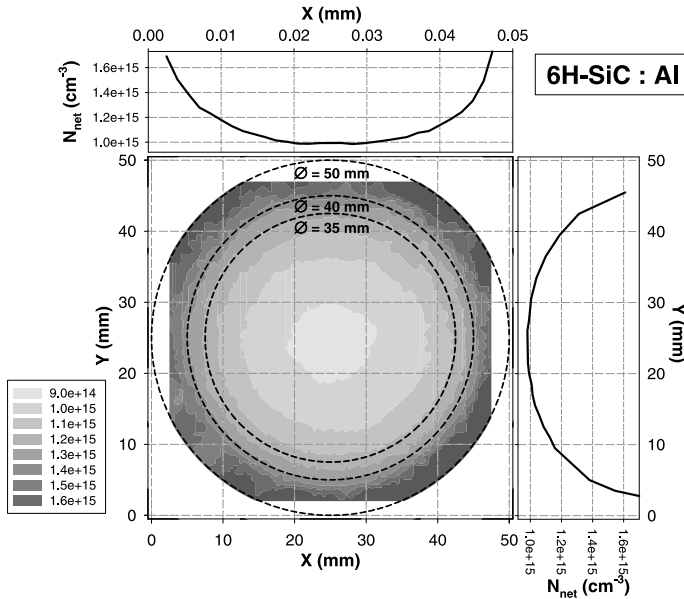


**Fig. 9.** Doping concentration uniformity of a *p*-type 6H-SiC epilayer grown in a hot wall reactor with substrate rotation using silane, propane, and TMA as the growth precursors and hydrogen as the carrier gas. The standard deviation over mean value is 9.5% and the maximum variation over mean value is 57.8% with an edge exclusion of 5 mm (circle diameter 40 mm)

concentration as obtained by the *C-V* characterization was  $1 \cdot 10^{15} \text{ cm}^{-3}$  in the wafer center. As seen in Fig. 9, the net doping concentration has a minimum in the wafer center and increases towards the wafer edges. This circular symmetric concentration distribution is typically observed in epilayers grown in the reactor with mechanical substrate rotation and does not depend on the conductivity type or the doping concentration. Excluding 5 mm at the wafer edge, the standard deviation over mean value is around 10% and the maximum variation over mean value is around 60%.

The increase of the doping concentration towards the wafer edges is to some extent coming from a decrease in the temperature, especially in the upstream part of the susceptor inner cell. But the steep increase of the doping concentration at the wafer edges is most likely overestimated due to poor blocking Schottky devices. The capacitance of poor blocking Schottky devices is typically higher than for good blocking devices, which leads to an overestimation of the calculated doping concentration.

The distribution of the epilayer doping concentration becomes more uniform with increasing dopant concentration, indicating a decreasing influence of the temperature inhomogeneity on the growing layer. Figure 10 shows the results from *C-V* mapping of an *n*-type 4H-SiC epilayer, doped to

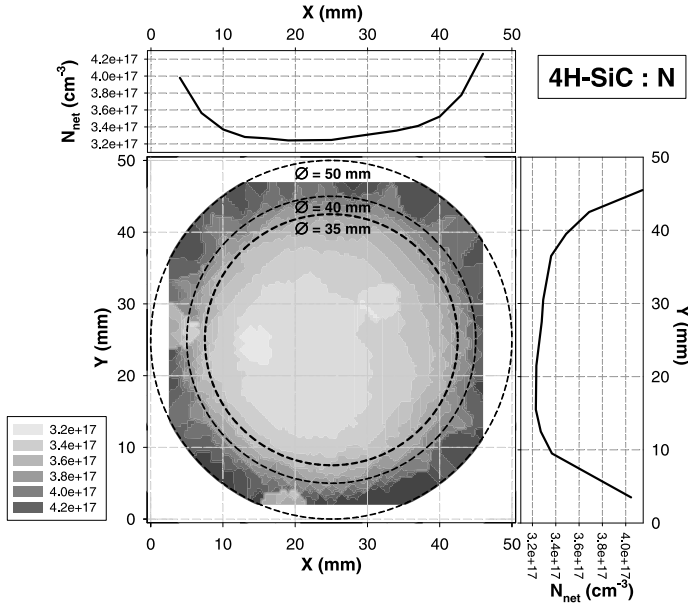


**Fig. 10.** Doping concentration uniformity of an *n*-type 4H-SiC epilayer grown in the hot wall reactor with substrate rotation using silane, propane, and nitrogen gas as growth precursors and hydrogen as the carrier gas. The standard deviation over mean value is 6.1% and the maximum variation over mean value is 36.3% with an edge exclusion of 5 mm (circle with diameter 40 mm)

$3.5 \cdot 10^{17} \text{ cm}^{-3}$  with nitrogen. In this case, the standard variation over mean value is about 6% and the maximum variation over mean value about 35% with 5 mm edge exclusion. Again, the doping concentration is circular symmetric and lowest in the wafer center. It increases towards the wafer edges due to the decrease in temperature.

Previously we reported unexpectedly high doping ununiformities for epilayers grown in the reactor with rotation, when hydrogen was employed as carrier gas and the epilayers were doped in the order of  $1 \cdot 10^{16} \text{ cm}^{-3}$  and below [12]. Adjusting the temperature uniformity over the wafer by reducing the hydrogen carrier gas flow rate from 40 slm to 35 slm and the total pressure in the reactor from 250 hPa to 200 hPa resulted in a significant improvement with respect to doping uniformity also for the concentration range below  $1 \cdot 10^{16} \text{ cm}^{-3}$ . The results are similar to the reported growth employing the carrier gas mixture of 85% hydrogen and 15% argon. It is expected that adding argon to the carrier gas could further improve the homogeneity of epilayers grown in the reactor with mechanical substrate rotation for the doping concentration range below  $1 \cdot 10^{16} \text{ cm}^{-3}$ .

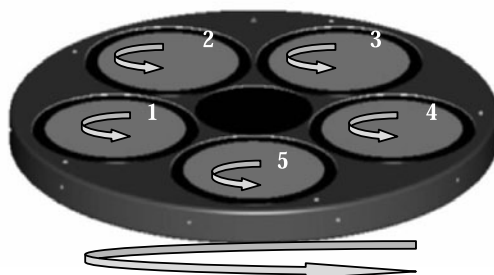
### 3.4 Multi Wafer Hot Wall Reactor

As the commercialization of SiC devices is proceeding, special attention has to be laid on the larger scale production of SiC epilayers. The development of multi-wafer VPE-reactors has already been on-going for several years. Recently, the multi wafer hot wall VPE-reactor with planetary rotation was introduced for the homoepitaxial growth of SiC [20]. The planetary hot wall reactor is one of the most promising machines for industrial production of homogeneous epitaxial SiC layers.

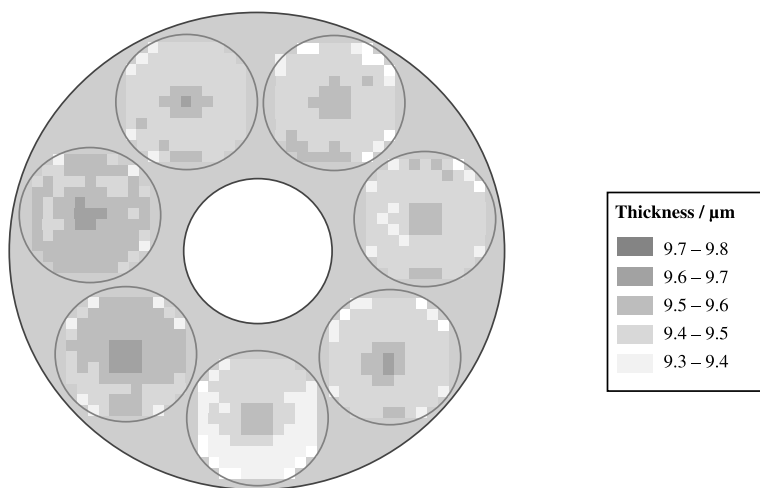
The multi wafer hot wall reactor features planetary rotation including the main rotation of the susceptor plate and the individual gas foil rotation of each of the substrate wafers. An important improvement to earlier versions of the planetary reactor for SiC is the possibility to independently heat the susceptor and the reactor ceiling by separately controlled *RF*-coils. The reactor was designed with the help of extensive simulation and modeling analysis [21], to understand basic features of the SiC homoepitaxial growth process and to demonstrate the capability of the planetary hot wall concept. The capability of the planetary reactor is to grow simultaneously on  $7 \times 2$  inch or  $5 \times 3$  inch wafers with a growth rate up to at least  $10 \mu\text{m/h}$ . Figure 11 illustrates the basic principle of the planetary rotation for a  $5 \times 3$  inch wafer configuration.

Figure 12 shows the thickness uniformity of seven 2 inch *4H*-SiC epilayers grown in the same run of the planetary hot wall reactor. The intra-wafer uniformity and the wafer-to-wafer uniformity of the epilayer thickness are better than 1%.

The planetary reactor concept is employed for many different material systems, including III-V and III-N compound semiconductors. The concept has proven to be very flexible and today production machines for  $15 \times 2$  inch up to  $5 \times 10$  inch wafers are available for the MOVPE growth of compound semiconductors. It is expected, that the hot wall planetary reactor concept



**Fig. 11.** Planetary rotation principle in the  $5 \times 3$  inch wafer configuration featuring a main rotation of the susceptor and individual rotation of the wafer carriers (satellites) using the patented Gas-Foil-Rotation<sup>®</sup> technique (courtesy of Epigress AB)



**Fig. 12.** Thickness uniformity of 4H-SiC epilayers grown in the planetary hot wall reactor with  $7 \times 2$  inch wafer configuration. The intra-wafer thickness uniformity for a  $9.5 \mu\text{m}$  thick epilayer is  $\sigma/\text{mean} = 0.4\text{--}0.6\%$ . The wafer-to-wafer variation of the thickness uniformity is calculated to  $(\text{max-min})/\text{mean} = \pm 0.6\%$  (courtesy of Epigress AB)

can also be scaled up for SiC substrate diameters of 6 inch, 8 inch or more. Multi wafer 6 inch or 8 inch machines will be very big and the *RF*-power handling will probably be the limitation for the amount of wafers, which can be grown at the same time at the high growth temperatures of up to  $1600^\circ\text{C}$  or  $1700^\circ\text{C}$ .

## 4 Future Development

The currently available SiC VPE hot wall reactors will probably be state of the art for several years, especially as the progress in increasing the diameter of SiC substrates is comparably slow. This progress in substrate diameter increase will determine the time, when new VPE machines for SiC have to be developed. Wafers with diameter 2 inch and 3 inch are the present state of the art substrates. But the near future will probably see 4 inch substrates as the standard size. In the far future, 6 inch wafers will become available, too. Substrate sizes up to 6 inch are still possible to be handled in the present hot wall epitaxy machines. Despite the sufficient wafer size handling capability of the available hot wall reactors, there is still room for further development and improvements in for example reducing the epitaxy process induced defects or developing advanced techniques to overcome limitations of the substrate quality and the surface preparation. The started investigations on simulating growth kinetics and chemical reactions in the gas phase and on the substrate

surface [22], in addition to calculations of the temperature distribution and the flow dynamics, will further increase the knowledge and understanding of the SiC VPE-process. Modifications of the growth reactor systems will be made in line with the progress in understanding further the SiC homoepitaxial growth process. The steadily increasing simulation possibilities regarding computer power and software development will help to accomplish the complex simulation tasks.

## 5 Conclusion

During the last 5 to 10 years, considerable improvements in the understanding of the SiC VPE-process and in the development of the SiC VPE-growth machines have been made. Today the most used reactor concept for SiC VPE growth is the hot wall concept and state of the art of these hot wall machines are the reactors with rotation. The superiority of the hot wall concept for SiC VPE growth lies in the achievable high growth rates, the low defect density, and the thermal management of the whole reactor inner cell. Temperature profiles can be adjusted very uniform in a wide area of the susceptor, allowing multiple wafer growth. The epilayers grown in hot wall reactors, especially in the reactors with rotation, consist of very uniform layers in thickness and doping with low defect density and excellent surface morphology. The growth processes for the hot wall VPE machines are basically understood and are well characterized, but there are still possibilities for improvements, especially as growth on non-standard faces of SiC become more and more interesting for device processing. In addition, with the presently available multi wafer hot wall reactors, cost effective large scale production of epitaxial structures are possible.

## Acknowledgements

The author greatly thank the Epigress AB in Lund, Sweden and the SiC group at Acreo AB in Kista, Sweden for their help and contributions to the development of Acreo's hot wall reactor for SiC homoepitaxial growth.

## References

1. O. Kordina, C. Hallin, A. Henry, J.P. Bergman, I. Ivanov, A. Ellison, N.T. Son, E. Janzén: *Phys. Stat. Sol. (b)* **202**, 321–334 (1997)
2. A. Ellison, J. Zhang, A. Henry, E. Janzén: *J. Cryst. Growth* **236**, 225–238 (2002)
3. C. Hallin, I.G. Ivanov, T. Egilsson, A. Henry, O. Kordina, E. Janzén: *J. Cryst. Growth* **183**, 162–174 (1998)

4. S.E. Sadow, T.E. Shattner, J. Brown, L. Grazulis, K. Mahalingam, G. Landis, R. Bertke, W.C. Mitchel: *J. Electr. Mat.* Vol. **30**, 228–234 (2001)
5. A.A. Burk, L.B. Rowland: *J. Cryst. Growth* **167**, 586–595 (1996)
6. T. Kimoto, A. Itoh, H. Matsunami: *Phys. Stat. Sol. (b)* **202**, 247–262 (1997)
7. D.J. Larkin: *Phys. Stat. Sol. (b)* **202**, 305–320 (1997)
8. K. Rottner, R. Helbig: *J. Cryst. Growth* **144**, 258–266 (1994)
9. B. Landini: *J. Electr. Mat.* **29** (3), 384–390 (2000)
10. N. Nordell, A. Schöner, M.K. Linnarsson: *J. Electr. Mat.* Vol. **26**, 187–192 (1997)
11. S. Karlsson, N. Nordell, F. Spadafora, M. Linnarsson: *Mat. Science & Engineering B* **61–62**, 143–146 (1999)
12. A. Schöner, A. Konstantinov, S. Karlsson, R. Berge: *Mat. Science Forum* **389–393**, 187–190 (2002)
13. C. Hallin, F. Owman, P. Mårtensson, A. Ellison, A. Konstantinov, O. Kordina, E. Janzén: *J. Cryst. Growth* **181**, 241–253 (1997)
14. P.G. Neudeck, J.A. Powell: *IEEE Electron Device Letters* **15**, 63–65 (1994)
15. N. Schulze, D.L. Barrett, G. Pensl, S. Rohmfeld, M. Hundhausen: *Mat. Science & Engineering B* **61–62**, 44–47 (1999)
16. S.G. Müller, R.C. Glass, H.M. Hobgood, V.F. Tsvetkov, M. Brady, D. Henshall, J.R. Jenny, D. Malta, C.H. Carter Jr.: *J. Cryst. Growth* **211**, 325–332 (2000)
17. R. Yakimova, E. Janzén: *Diamond and Related Materials* **9**, 432–438 (2000)
18. I. Kamata, H. Tsuchida, T. Jikimoto, K. Izumi: *Jpn. J. Appl. Phys.* **39**, 6496–6500 (2000)
19. I. Kamata, H. Tsuchida, T. Jikimoto, K. Izumi: *Jpn. J. Appl. Phys.* **40**, L1012–L1014 (2001)
20. F. Wischmeyer, K. Christiansen, C. Hecht, R. Berge, D. Stephani, H. Jürgensen: presented at the International Conference on SiC and Related Materials, Tsukuba, Japan (2001)
21. A.N. Vorob'ev, A.K. Semennikov, A.I. Zhmakin, Y.N. Makarov, M. Dauelsberg, F. Wischmeyer, M. Heuken, H. Jürgensen: *Mat. Science Forum* **353–356**, 103–106 (2001)
22. J. Mézière, E. Blanquet, M. Pons, J.M. Dedulle, P. Ferret, L. Di Cioccio, T. Billon: *Mat. Res. Soc. Symp. Proc.* **742** (2003)

# Formation of SiC Thin Films by Ion Beam Synthesis

J.K.N. Lindner

## 1 Introduction

Ion beam synthesis (IBS) is a promising technique for forming homogeneous, stoichiometric, large-area thin films of epitaxial 3C-SiC within or on a silicon wafer. Although well-known in silicon device technology as a technique to form buried SiO<sub>2</sub> or metal silicide layers, the IBS technique has only recently attracted larger interest as a means of creating buried or near-surface SiC films. In this chapter the major recent achievements will be reviewed, our present understanding of the temperature and dose dependence of the mechanisms involved in the IBS of SiC will be summarized, the characteristics of IBS formed layers will be described and first applications of such SiC layers will be compiled. As the IBS technique has not been described in the preceding *Silicon Carbide* volumes [1], the review will start with a brief description of the basics of the IBS technique and a short chronological summary of early observations. The presentation will be limited to the use of directed ion beams with energies of some keV to few MeV and will not include beam assisted deposition techniques.

## 2 Fundamentals of Ion Beam Synthesis

Ion beam synthesis has been successfully applied to create homogeneous films consisting of one to four atomic species forming an elemental layer, an alloy or a compound. The either amorphous, polycrystalline or single-crystalline thin films are usually formed in a two-step process: a high-dose implantation to roughly adjust the chemical composition of a near-surface region and a subsequent annealing step to redistribute the implanted atoms from a more or less Gaussian depth distribution into a box-like depth profile corresponding to a homogeneous layer. The annealing step also serves to reduce the density of lattice defects in the synthesized layer and its vicinity. In most materials systems investigated so far, the piling-up of the depth distribution of implanted atoms during annealing has been attributed to the Ostwald ripening of precipitates, i.e. the growth of larger precipitates near the ion profile peak at the expense of dissolving smaller ones in the wings of the depth distribution, driven by the minimization of the systems total interfacial energy. Therefore

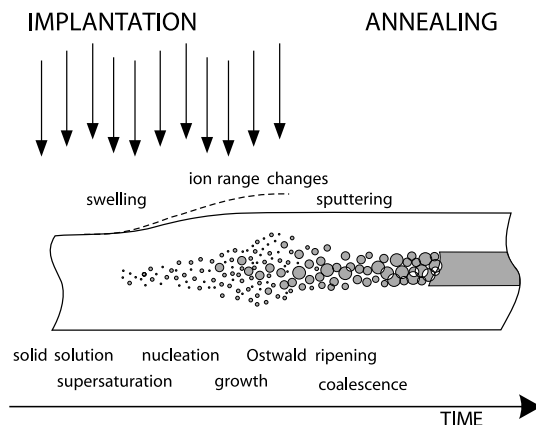


**Fig. 1.** Phenomena occurring during the ion beam synthesis of layers

it is clear today that the depth and size distribution of all crystalline and amorphous phases in the as-implanted state has a large impact on the desired redistribution of implanted atoms during annealing; together with the defect distribution, it sets the starting conditions for the diffusive redistribution of atoms during the anneal. The major processes playing a role in usual IBS are sketched in Fig. 1, even though this picture has to be slightly modified (for the precipitate size distribution) in the case of SiC layer synthesis in silicon, as we will see later.

High-dose implantation usually leads to a supersaturation of the implanted atomic species followed by the nucleation, growth and coalescence of precipitates, in particular at the peak of the ion profile. Either during implantation or during the post-implantation anneal Ostwald ripening causes a coarsening of the impurity size distribution. Under ideal conditions, this results in the growth of just one precipitate, the buried layer. The transport of implanted impurity atoms from the profile wings towards the centre may be supported by snow plough effects, which may occur if the peak of the ion distribution is located within a buried amorphous layer and the annealing step causes crystallization of this zone.

The depth position of the ion beam synthesized layer can be adjusted by means of the ion energy. For a reliable prediction of ion ranges, typical high-dose effects such as sputter erosion of the surface, changes of the ion ranges due to composition dependent stopping power changes and swelling effects have to be taken into account. In addition, diffusive redistribution of implanted atoms during implantation – in some cases mediated by the implantation induced lattice defects – may influence the ion profile and thus the resulting layer position. Owing to these effects, a reliable prediction of high-dose ion profiles is presently not available and properties such as the stoichiometry dose  $D_s$ , i.e. the dose  $D$  at which the desired stoichiometric com-

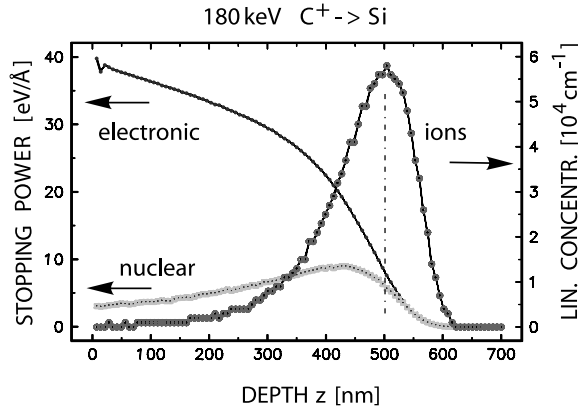


**Fig. 2.** TRIM92 [2] simulation of the ion range and stopping power profiles for a 180 keV  $C^+$  implantation into silicon

position is reached at the profile peak, must be determined experimentally. For a rough estimation neglecting high-dose effects, the peak concentration  $c_{\max}$  can be calculated as

$$c_{\max}(D) = \frac{D\zeta_{\max}}{D\zeta_{\max} + \rho_t}, \quad (1)$$

where  $\zeta_{\max}$  is the linear concentration at the profile peak easily obtainable from static Monte-Carlo ion range simulations, as shown in Fig. 2, and  $\rho_t$  is

**Table 1.** TRIM92 simulated carbon profile parameters and resulting IBS properties

Energy [keV]	$R_{\max}$ [nm]	$\zeta_{\max}$ [ $10^4 \text{ cm}^{-1}$ ]	FWHM [nm]	$D_s$ [ $10^{17} \text{ C/cm}^2$ ]	$d(D_s)$ [nm]	$c_{\max}$ ( $5e17 \text{ C/cm}^2$ )	$c_{\max}$ ( $1e18 \text{ C/cm}^2$ )
20	69	16.7	56	2.9	60	0.63	0.78
30	100	12.8	74	3.8	78	0.57	0.73
40	133	10.8	87	4.5	93	0.53	0.69
65	206	8.24	109	5.9	121	0.46	0.63
100	313	7.02	128	6.9	142	0.42	0.59
125	376	6.41	140	7.5	156	0.40	0.57
150	437	6.00	148	8.0	167	0.38	0.55
180	500	5.68	150	8.5	176	0.37	0.54
200	547	5.50	158	8.8	182	0.36	0.53
300	745	5.13	172	9.4	195	0.35	0.52

$R_{\max}$  (depth of maximum carbon concentration),  $\zeta_{\max}$  (linear concentration at the profile peak), FWHM (full width at half maximum) and estimated stoichiometry doses  $D_s$ , layer thicknesses  $d$  and peak concentrations  $c_{\max}$  for doses of  $5 \times 10^{17}$  and  $1 \times 10^{18} \text{ C/cm}^2$ . It should be noted that – owing to differences in the stopping powers implemented – the moments of TRIM simulated ion range profiles may depend to a great extent on the program version used and resulting deviations in calculated stoichiometry doses  $D_s$  may be as high as 10%.

the atomic density of the (Si) target. The SiC stoichiometry dose  $D_s$  ( $c_{\max} = 0.5$ ) follows from (1), and the maximum layer thickness  $d(D_s)$  at this dose from

$$d(D_s) = D_s/\rho_C \quad (2)$$

with  $\rho_C$  being the atomic carbon density of SiC of  $4.83 \times 10^{22}$  C/cm<sup>3</sup>. With (2), a dose of  $1 \times 10^{17}$  C/cm<sup>2</sup> corresponds to a SiC layer thickness of 20.7 nm. For the energy range most frequently considered in the literature on the IBS of SiC, stoichiometry doses and resulting layer thicknesses calculated on the basis of static TRIM92 Monte-Carlo simulations and (1,2) are compiled in Table 1.

### 3 Basic Considerations on the IBS of SiC in Si

One should expect SiC precipitate formation at doses considerably below the stoichiometry doses of some  $10^{17}$  C/cm<sup>2</sup> tabulated here, as the room temperature solid solubility extrapolatable from the high-temperature ( $> 1050^\circ\text{C}$ ) data of Bean and Newman [3] is negligible:

$$C_s^{\text{eq}} = 4 \times 10^{24} \exp(-2.3 \text{ eV}/k_B T) \text{ cm}^{-3}, \quad (3)$$

with  $k_B T$  the product of Boltzmann's constant and the absolute temperature.

The diffusivity  $D_C$  of the mostly substitutionally incorporated [4] carbon in the silicon lattice has been determined [5] to be

$$D_C = 1.9 \exp(-3.2 \text{ eV}/k_B T) \text{ cm}^2 \text{ s}^{-1}. \quad (4)$$

There is experimental evidence that carbon diffusion is enhanced in the presence of a silicon self-interstitial supersaturation [6, 7], and as the carbon diffusion is significantly faster than Si self-diffusion, it is assumed that the carbon diffusion mechanism involves either the formation of a highly mobile carbon/Si self-interstitial complex (CSi<sub>i</sub>) according to



where  $C_s$  is a substitutional carbon atom and  $\text{Si}_i$  is a silicon self-interstitial, or that a kick-out of substitutional carbon by a silicon self-interstitial takes place, according to



where  $\text{C}_i$  denotes a highly mobile carbon interstitial atom. For high temperatures, the former mechanism is believed to dominate the carbon diffusion, and a diffusivity of

$$D_i = 4.4 \exp(-0.88 \text{ eV}/k_B T) \text{ cm}^2 \text{ s}^{-1}, \quad (7)$$

is estimated for this ( $\text{CSi}_i$ ) complex [8]. The carbon diffusion, the formation of ( $\text{CSi}_i$ ) complexes, their agglomeration and finally the nucleation of SiC precipitates are thus governed by the supersaturation of silicon self-interstitials, which in turn is determined by the presence of other lattice defects, such as point defect clusters, stacking faults, dislocations or amorphous Si inclusions or  $\text{SiO}_2$  precipitates. For a recent overview of various effects caused by the interaction of carbon atoms with Si point defects, the reader is referred to the comprehensive review of Skorupa and Yankov [9].

In all recent studies on the IBS of SiC in silicon, the formation of 3C-SiC is observed. Therefore, the structural data of 3C-SiC and crystalline silicon (c-Si) are compared in Table 2. The lattice mismatch of 3C-SiC and c-Si amounts to 19.7%. Thus 5 lattice spacings of 3C-SiC almost exactly match 4 lattice spacings of silicon, assuming a small residual strain of the silicon matrix by 0.36%.

The Si atomic densities of crystalline Si and SiC (all polytypes) are nearly identical. Therefore, the transformation of silicon into unstrained and stoichiometric SiC is accompanied by only a small increase of the specific volume of Si atoms by 3.5%. Thus, either Si interstitial  $\text{Si}_i$  formation, or target swelling, or a mixture of both has to be expected as a result of a transformation from c-Si to SiC. Both effects are, however, expected to be small (Table 2). Swelling should be much larger, if amorphous  $\text{Si}_{1-x}\text{C}_x$  layers are formed, since the amorphization of SiC leads to a density reduction from 3.214 to 2.6–2.9 g/cm<sup>3</sup> [10, 11].

**Table 2.** Structural quantities of crystalline Si and 3C-SiC and expected volumetric changes resulting from a c-Si to c-SiC conversion

	c-Si	3C-SiC
Lattice constant at $RT$	5.4301 Å	4.3596 Å
Mean thermal expansion coefficient (25–1000°C)	$3.8 \times 10^{-6}/\text{K}$	$4.8 \times 10^{-6}/\text{K}$
Lattice mismatch at $RT$		19.7%
Mass density	2.321 g/cm <sup>3</sup>	3.214 g/cm <sup>3</sup>
Si atomic density $\rho_{\text{Si}}$	$5 \times 10^{22}$ Si/cm <sup>3</sup>	$4.83 \times 10^{22}$ Si/cm <sup>3</sup>
C atomic density $\rho_{\text{C}}$		$4.83 \times 10^{22}$ C/cm <sup>3</sup>
Si volume increase		3.57%
Swelling per $10^{17}$ C/cm <sup>2</sup>		0.70 nm
Si interstitials per $10^{17}$ C/cm <sup>2</sup>		$3.5 \times 10^{15}$ Si/cm <sup>2</sup>

## 4 Early Studies on the IBS of SiC

First attempts to form buried SiC layers in silicon by high-dose carbon implantation and annealing have been reported since the early 1970s [12]–[22], and were triggered by the difficulties encountered in fabricating the material by other methods [12]. Borders, Picraux, and Beezhold observed after room-temperature 200 keV  $C^+$  implantation ( $D = 1 \times 10^{17} \text{ C/cm}^2$ ,  $j_i = 1 \text{ } \mu\text{A/cm}^2$ ) into  $p$ -type silicon strong broad-band absorption in infrared transmission spectra around  $700\text{--}725 \text{ cm}^{-1}$ , later assigned to the formation of disordered Si-C bonds. A shift of the absorption band to  $800 \text{ cm}^{-1}$  and a considerable decrease in the peak width was observed upon annealing at  $850 \pm 25^\circ\text{C}$ , indicating crystallization of SiC. RBS measurements showed a 10 at.% carbon concentration peak at a depth of 600 nm after implantation. After annealing at  $800^\circ\text{C}$ , the carbon distribution had spread and a carbon profile peak could no longer be detected.

Rothmund and Fritzsche [15] performed overstoichiometric, multiple-energy (15–70 keV) implantations into  $n$ -type Si(111) wafers at current densities  $j_i$  of  $10 \text{ } \mu\text{A/cm}^2$  and at nominally  $RT$ , aiming to achieve a broad overstoichiometric layer ( $> 10^{23} \text{ C/cm}^3$ ) of homogeneous composition.  $IR$  absorption confirms Si-C bond formation in the as-implanted state and the onset of crystallization above  $800^\circ\text{C}$ . Further  $IR$  peak narrowing interpreted as bond reformation was observed up to the highest annealing temperature of  $1300^\circ\text{C}$ . The carbide layers showed a low resistivity ( $10^{-2}$  to  $10^{-3} \text{ } \Omega\text{cm}$ ), rectifying characteristics and a photovoltaic effect. Electron diffraction studies failed to identify  $3C$ -SiC, but patterns resembling those of diamond and a cubic form of graphite were revealed.

Edelman et al. [16, 23] studied the influence of the target temperature on the structure of 40 keV  $C^+$  ion implanted Si(100) and Si(111) by  $IR$  spectroscopy and transmission electron microscopy (TEM) for a fixed dose of  $D = 1 \times 10^{18} \text{ C/cm}^2$ . For target temperatures  $T_i$  between  $RT$  and  $500^\circ\text{C}$  they found amorphous material, at temperatures of  $600^\circ\text{C}$  and above increasingly single-crystalline  $3C$ -SiC. After annealing of low-temperature samples, up to  $1300^\circ\text{C}$  poly- $3C$ -SiC [23] was obtained;  $1100^\circ\text{C}$  annealing of samples implanted at  $600^\circ\text{C}$  leads to layers with single-crystalline portions [16].

Akimchenko et al. [17, 18, 24, 25] confirm for stoichiometrically at  $RT$  implanted silicon (40 and 70 keV  $C^+$  ions) the crystallization induced  $IR$  peak shift at 700 to  $1100^\circ\text{C}$ , the rectifying behaviour of SiC/Si samples and the photovoltaic effect. Interestingly, for temperatures of 700 and  $900^\circ\text{C}$  the authors observe a strong dependence of the degree of crystallization on the substrate orientation, the differences vanishing upon annealing at  $1100^\circ\text{C}$ . The conduction of layers is  $n$ -type, irrespective of that of the silicon substrate.

Kimura et al. performed  $C^+$  implantations into Si(100) wafers at nominally  $RT$  [19] and  $300$  and  $600^\circ\text{C}$  [20], using energies of 50–200 keV, doses of  $2 - 20 \times 10^{17} \text{ C/cm}^2$  and current densities of  $4 \text{ } \mu\text{A/cm}^2$ . A detailed evaluation of  $IR$  absorption spectra for 100 keV implants with doses of 6 and

$8 \times 10^{17} \text{ C/cm}^2$  reveals that after 0.5 h at  $900^\circ\text{C}$ , 40–50% of implanted carbon atoms are incorporated into 3C-SiC lattice bonds. This portion  $\gamma$  linearly increases with annealing temperature up to 70–80% at  $1200^\circ\text{C}$ , the portion being consistently higher for the smaller dose [19]–[21] (corresponding to a carbon peak concentration of about 43 at.%). For far overstoichiometric doses ( $> 1.2 \times 10^{18} \text{ C/cm}^2$ ) it is assumed that carbon clusters are formed, which do not contribute to SiC formation upon annealing at temperatures up to  $1200^\circ\text{C}$ . The portion  $\gamma$  is observed to increase with increasing target temperature [20], and it is expected that elevated implantation temperatures therefore will reduce the temperature required for the formation of homogeneous layers in the annealing step. AES depth profiling for the smaller dose shows an unexpectedly broad Gaussian carbon depth distribution which does not significantly change upon 0.5 h/ $1100^\circ\text{C}$  annealing. Electron diffraction studies for as-implanted samples ( $T_i = RT$ , dose unknown) indicate the presence of 2H-SiC with few portions of 3C-SiC and mainly polycrystalline 3C-SiC after annealing for 0.5 h at  $1100^\circ\text{C}$ .

Kroko et al. [22] find evidence from XRD measurements that either oriented 3C-SiC or nH-SiC or a mixture of both is formed in float-zone (FZ) or Czochralski-grown silicon and silicon-on-sapphire wafers upon carbon implantation at energies of 125–180 keV ( $T_i = 450\text{--}650^\circ\text{C}$ ,  $j_i = 30\text{--}40 \mu\text{A/cm}^2$ ). The authors measured sputtering yields between 0 and 1 atom/ion depending on implantation temperature and attributed the differences to differences in the crystallinity of the sample surface regions.

Stimulated by the success of IBS in forming buried homogeneous  $\text{SiO}_2$  and  $\text{Si}_3\text{N}_4$  layers in silicon, a large number of investigations on the IBS of SiC layers was initiated since the second half of the 1980s. The formation of  $\text{SiO}_2$ ,  $\text{Si}_3\text{N}_4$  and SiC layers in silicon after 200 keV implantations at about  $500^\circ\text{C}$  with doses of  $2 - 18 \times 10^{17}/\text{cm}^2$  and annealing for several hours at  $1200^\circ\text{C}$  was compared in [26]. Assuming that super-stoichiometric implantations will result in the formation of stoichiometric compound layers, samples with the highest doses were annealed, since this was successful in the case of  $\text{O}^+$  and  $\text{N}^+$  implantations. No evidence was found, however, for SiC layer formation ( $D = 1.4 \times 10^{18} \text{ C/cm}^2$ ). The different behaviour was attributed to the differences in the enthalpy of formation  $\Delta H_f$  of  $-200$ ,  $-180$ , and  $-27 \text{ kcal mol}^{-1}$  for  $\text{SiO}_2$ ,  $\text{Si}_3\text{N}_4$  and SiC, respectively. It was concluded that higher annealing temperatures or longer annealing times are required.

Consequently, annealing conditions of 1.5 h/ $1405^\circ\text{C}$  and 20 h/ $1300^\circ\text{C}$  were used in the following studies [27]–[30], and for the first time, buried homogeneous and stoichiometric SiC layers in Si(100) were obtained by the Surrey University group and partners [27, 28] ( $E = 200 \text{ keV}$ ,  $D = 9.5 \times 10^{17}/\text{cm}^2$ ,  $T_i \approx 550^\circ\text{C}$  obtained by beam heating,  $t_a = 1.5 \text{ h}$ ,  $T_a = 1405^\circ\text{C}$ ). XTEM investigations reveal that layer formation starts from a complicated seven-layer system in the as-implanted state, involving a defective Si top layer, followed by a laminar layer, an amorphous layer, a layer of polycrystalline 3C-SiC,

a further amorphous layer, a crystalline but damaged Si layer and the substrate. The origin of this layer system was not investigated, but the temperature dependence of the thickness of individual sublayers was estimated for temperatures of 500–800°C [29, 30] and the as-implanted structure was described in detail in [31]. The 3C-SiC layer obtained after 1405°C annealing was found to be subdivided into a polycrystalline upper part and an epitaxial lower part, separated by a silicon-rich central region containing poly-Si and silicon twins. The Si top layer was observed to be single-crystalline with isolated, oriented SiC precipitates. A high density of large SiC precipitates next to the upper interface of the buried SiC layer is observed in samples annealed for 20 h at 1300°C [29, 30], causing moderate slopes in Rutherford backscattering spectroscopy (RBS) random and channeling profiles instead of the desired step-like shape. A major difficulty of synthesizing SiC layers, compared to the relatively easy IBS of SiO<sub>2</sub> layers, is attributed [31] to the comparatively high stability of such SiC precipitates in silicon and the relatively slow carbon diffusion. This difficulty was reflected by the extremely high temperatures (1405°C) required in the annealing step close to the melting temperature of silicon (1423°C), which made the IBS of SiC layers in silicon rather unattractive for applications.

In order to overcome the need for extreme annealing conditions necessary to achieve homogeneous stoichiometric layers, Martin et al. [32] used 15  $\mu\text{A}/\text{cm}^2$  triple-energy implantations (180–90 keV) with stoichiometric doses at a constant target temperature as high as 860°C, which unlike in most earlier studies, was achieved by external heating. RBS measurements revealed a buried SiC layer with a Si-to-C ratio of 1.0–1.3 and compositionally graded transitions to the Si-rich surface layer and the substrate. IR absorption and XRD spectra showed the presence of crystalline cubic SiC and seemingly a minor portion of a hexagonal SiC phase. XTEM investigations revealed that the nearly-stoichiometric region consisted of 3C-SiC grains with sizes of less than 15 nm, each being heavily twinned (up to third order) about a unique [111] axis. As no amorphous or polycrystalline regions were identified, twinning was considered to be the main limiting factor in the IBS of SiC layers.

Higher annealing temperatures are expected to be tolerable if sapphire substrates are used instead of silicon. High-temperature implantations at 900–1000°C into silicon-on-sapphire wafers [33, 34], however, showed that usable annealing temperatures were limited to 1300°C. Resulting SiC layers were described as being composed of 3C-SiC-nanocrystallites embedded in a heteroepitaxial SiC matrix.

In 1994, Lindner et al. [35] demonstrated that homogeneous, stoichiometric buried 3C-SiC layers with sharp interfaces can be formed in silicon (100) and (111) using “reasonably low” annealing temperatures of 1250°C, if in the implantation step the stoichiometry dose is not exceeded. Abrupt interfaces were observed both in RBS spectra (Fig. 3) and in cross-sectional

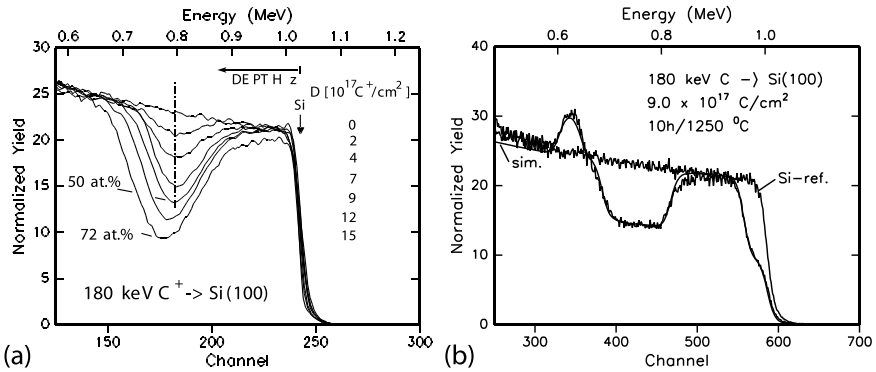


**Fig. 3.** (a) 1.8 He<sup>+</sup> RBS profiles of 180 keV C<sup>+</sup> implanted Si(100), showing the evolution with increasing dose. Only slight changes of the profile shape are visible upon exceeding the stoichiometry dose. (b) RBS spectrum [35] of a buried SiC layer in Si(100), obtained by a 180 keV C<sup>+</sup> implantation into Si ( $D = 9 \times 10^{17}$  C/cm<sup>2</sup>,  $T_i = 330$ – $440^\circ\text{C}$  by beam heating,  $j_i = 11$   $\mu\text{A}/\text{cm}^2$ ) and subsequent annealing for 10 h at  $1250^\circ\text{C}$  in Ar. A homogeneous, stoichiometric and epitaxial 3C-SiC layer of 174 nm thickness has developed from a previously Gaussian carbon depth distribution (a), causing the rectangular dip in the spectrum at channel no. 400–460. A little carbon is present (chn. no. 470–500) near the sharp upper SiC/Si interface. A 92 nm thick SiO<sub>2</sub> surface layer (chn. no. 560–580) has formed due to residual oxygen in the annealing atmosphere. The surface O signal is visible near channel no. 350. The spectrum of an unimplanted silicon reference sample and a simulated spectrum are overlaid for comparison

TEM images. The layers (described below in more detail) give rise to electron diffraction patterns and XRD pole figures of almost perfect single-crystalline material. The presence of an upper dose limit in the IBS of homogeneous SiC layer was confirmed [36] and its origin seems to be clear from *IR* [20, 37] and Raman [37] measurements, indicating the formation of stable graphitic clusters at concentrations exceeding 53–55 at.% of carbon. In addition it was shown [38] that isotropic tensile strain ( $< 1.4\%$ ) in the SiC phase builds up during implantation and is significantly reduced at doses below the stoichiometry dose, presumably due to the beginning coalescence of SiC precipitates. Strain values are in reasonable agreement to data reported by Frangis et al. [39], evaluating high-resolution TEM Moiré fringes of SiC precipitates formed during substoichiometric implantations at  $950^\circ\text{C}$ . A further reduction of strain occurs upon annealing [38].

While the first homogeneous SiC layers were formed with keV carbon ions, it was subsequently shown that carbon profile pile-up can also be obtained in MeV carbon implanted silicon using this annealing temperature, resulting in a deeply buried stoichiometric layer with sharp interfaces [40, 41]. These results have stimulated a series of further systematic studies, mostly devoted to a better understanding of the layer formation mechanisms, the reproduction

of results at constant target temperatures obtained by resistive heating, and the application of such layers for various purposes. These investigations will be reviewed in the following.

## 5 Influence of Dose and Implantation Temperature

The formation of well-defined epitaxial SiC layers by annealing of high-dose carbon implanted Si in [35] was observed to start from an intriguing as-implanted state [35, 41, 42]. The as-implanted structure of such samples implanted under beam heating conditions (330–440°C) can be described as a more or less box-like density distribution of quite equally sized (3–5 nm diameter), oriented SiC precipitates, forming a dense precipitate layer sandwiched between the crystalline silicon (c-Si) bulk and a c-Si top layer with significantly reduced precipitate density (Fig. 4). The precipitates are of the 3C polytype and are aligned such that all lattice planes of SiC are parallel to corresponding (*hkl*) lattice planes of the c-Si top layer and the substrate [35],[41]–[44]. Two thin amorphous interfacial layers free of precipitates are observed between the buried SiC precipitate layer and the surrounding c-Si matrix. This unexpected structure has evoked a number of questions:

- Why are the precipitates preferably observed in a limited depth interval?
- Why are they almost equally sized?
- Why are they oriented, even though there are the amorphous interfacial layers?
- Why does amorphization occur at these implantation conditions?

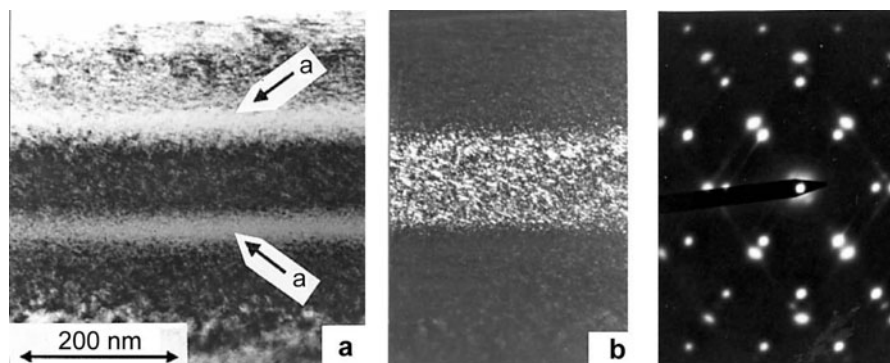


**Fig. 4.** XTEM bright-field image (a), SiC(111) dark-field image (b), and selected area diffraction pattern (c) of Si(111) implanted with  $9 \times 10^{17}$  C/cm<sup>2</sup> [42]. The box-like depth distribution of epitaxially aligned SiC precipitates (b), sandwiched between two thin amorphous stripes (marked in (a) as “a”) is a good starting point for the formation of a continuous SiC layer with sharp interfaces during annealing

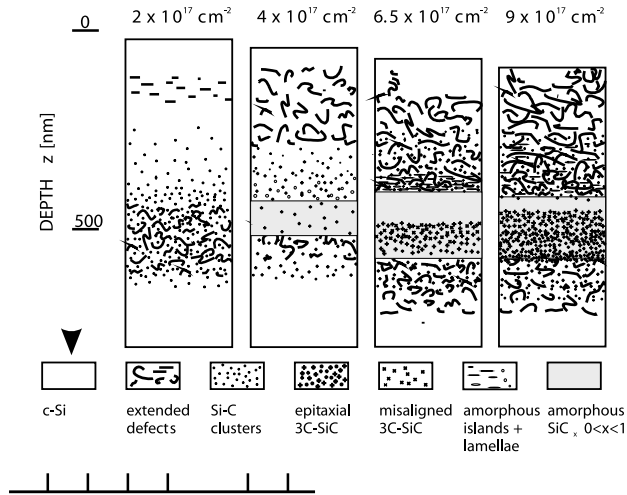


**Fig. 5.** Structural evolution of Si(100) implanted with 180 keV  $C^+$  ions for doses of  $2 - 9 \times 10^{17} \text{ C/cm}^2$  at  $335\text{--}385^\circ\text{C}$  [45], as observed by cross-section TEM. In order to account for the sputtering effect, the schematic structure plots are shifted in depth

The answer to some of these questions has been found by extended cross-sectional TEM (XTEM) studies of the structural evolution of samples as a function of dose [45]. It was observed (Fig. 5) that formation of crystalline SiC precipitates occurs only at doses exceeding  $2 - 4 \times 10^{17} \text{ C/cm}^2$ , i.e. far above the extrapolated solid solubility of carbon in silicon (Sect. 2). At doses beneath the nucleation dose, XTEM dark-field images of c-Si regions showed small (1.5 nm diameter) point shaped contrast regions, which were interpreted [45] as carbon containing interstitial atom clusters (see below). At doses between  $4$  and  $9 \times 10^{17} \text{ C/cm}^2$  nm-sized, epitaxially oriented 3C-SiC precipitates were found in crystalline silicon regions, with their size being almost identical, nearly independent of the depth and dose. With increasing dose, it was mainly the density of precipitates which increases, as long as the Si lattice preserves its crystallinity. Amorphization of the silicon host lattice, occurring at doses above  $4 \times 10^{17} \text{ C/cm}^2$  in the depth range between nuclear stopping power and ion profile maximum, leads to depth zones with a strongly decreased density of oriented crystalline SiC precipitates. This means that irradiation induced destruction of crystalline precipitates takes place, and it is correlated to the amorphization observed to occur during high-dose carbon implantation at elevated temperatures. Thus it was concluded that both the irradiation induced formation and destruction of SiC precipitates contribute to the generation of a nearly box-shaped precipitate density distribution at doses near the stoichiometry dose. Consequently, it was shown to be possible to tailor the density-vs-depth distribution of equally sized precipitates by

exploiting the ballistic destruction of SiC nano-crystallites [46]. However, prolonged ion irradiation of amorphized regions was observed also to lead to beam induced nucleation and growth of larger, randomly oriented SiC crystallites in the amorphous matrix. Thus, overly broad amorphous zones need to be avoided in the as-implanted state in order to obtain completely epitaxial 3C-SiC layers after annealing.

Since the various mechanisms involved with high-dose carbon implantations in silicon strongly depend on the implantation temperature, the structure in the as-implanted state and thus the structure after annealing do as well. The mechanisms contributing to the complicated as-implanted structure required for the IBS of SiC layers have been described in some detail in [47]. An overview is displayed in Fig. 6. The solid line represents the critical dose for amorphization as a function of implantation temperature, roughly estimated from the few data available for an implantation energy of 180 keV, a constant beam current density of  $10 \mu\text{A}/\text{cm}^2$  and FZ-silicon.

Due to the low mass of carbon ions, the collision cascades triggered by  $\text{C}^+$  ions are not expected to be strong enough to cause amorphization of pure c-Si at temperatures above  $130^\circ\text{C}$  [47]. However, amorphization is observed up to temperatures of  $500^\circ\text{C}$  [46]. This amorphization occurs in a dose region where the carbon concentration profile peak reaches more than about 17 at.% carbon. In addition, at high temperatures, the amorphization is observed to set in at the depth of carbon profile maximum, rather than at the depth of the nuclear stopping power maximum [46] where it would be expected for the case of normal, “ballistic” amorphization. Thus, this high-temperature amorphization is mediated by high carbon concentrations and is therefore termed “carbon induced amorphization” (Fig. 6).

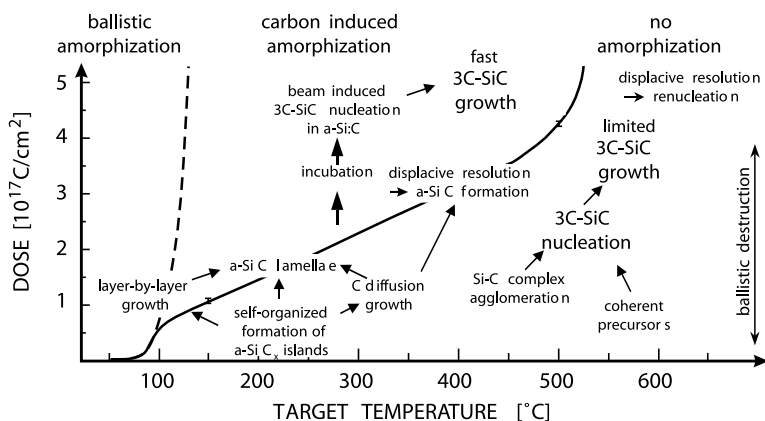


**Fig. 6.** Overview of the mechanisms contributing to the formation of crystalline and amorphous phases in Si(100) implanted with 180 keV  $\text{C}^+$  ions at  $10 \mu\text{A}/\text{cm}^2$ , displayed as a function of dose and target temperature. For explanations see text

The low temperature region (150–350°C) of this “carbon induced amorphization” has recently been studied in detail [48, 49]. It was observed that a self-organized arrangement of amorphous, spherical or lamella-shaped carbon-rich inclusions (Fig. 6) takes place at the upper interface of buried amorphous layers formed in this regime of implantation parameters (schematically indicated also in Fig. 5). The formation of the typically 3 nm large precipitates has been interpreted in terms of a supersaturation of silicon with carbon atoms and the large energy barrier involved with the formation of crystalline 3C-SiC precipitates, caused by the large 3C-SiC/c-Si interfacial energy [50] owing to the 20% lattice misfit. To circumvent this energy barrier, the system is believed to decompose by forming amorphous carbon-rich precipitates.

At temperatures of 200°C and above (Fig. 6), crystallization of randomly oriented 3C-SiC precipitates is observed in the amorphous phase. As thermal crystallization temperatures are significantly higher (see Sect. 3), beam induced nucleation must be responsible for this effect. Beam induced nucleation of crystalline SiC has been clearly demonstrated also for pulsed high-current density carbon implantations using a MEVVA ion source [51]. Once nucleation of SiC crystals has taken place, further growth is obviously facilitated in the amorphous surrounding, as these crystallites are observed to be generally larger than those in a crystalline matrix ([45] and refs.).

Nucleation of 3C-SiC in c-Si requires more elevated temperatures to be effective (Fig. 6). In FZ silicon implanted at 500°C with  $8.5 \times 10^{17}$  C/cm<sup>2</sup>, oriented 3C-SiC precipitates with 5 nm diameter were visible by their Moiré contrast fringes in high-resolution XTEM at the peak of the carbon concentration [52]. In those sample regions where SiC crystallites were absent, a cloud-like contrast was superimposed to the otherwise undisturbed lattice image of c-Si. The same observation was done in far substoichiometrically carbon implanted silicon (room temperature implantation) after annealing at temperatures below 850°C [53, 54]. The cloudy contrasts were interpreted as agglomerates of Si-C dimers sharing Si lattice sites. Thus, nucleation of SiC in c-Si is preceded by the formation of a precursor, and these precursors are sufficiently large to be detected by high-resolution TEM, because of the large critical nucleation radius for SiC resulting from the large 3C-SiC/c-Si interfacial energy. (It might be interesting to note that very similar “dark contrasts” were also observed at the first few nearest surface atomic layers of c-Si wafers after a short time exposure to a flux of carbon atoms, as it is used in the silicon surface carbonization step for the solid state molecular beam epitaxy of SiC surface layers on c-Si [55].) Another nucleation path (Fig. 6) for crystalline SiC via the formation of coherent carbon rich clusters, as it has been proposed in [56], might occur at very high temperatures and small concentrations, but is assumed to be less dominant under the conditions used for the IBS of SiC layers. It should also be noted that precipitates in CZ-Si [43]

tend to be larger than those in FZ-Si [52], probably due to the influence of oxygen [57].

Growth of SiC precipitates in c-Si is notoriously slow and even during stoichiometric implantations at temperatures of 600°C the precipitate diameters reach only 5 nm [46]. Therefore it was proposed that displacive precipitate resolution caused by the collision cascades of impinging ions may play a significant role for the size evolution of the precipitate ensembles [58]. In order to estimate the strength of such an effect *in the absence of any precipitate regrowth mechanism*, a simple model was suggested, giving rise to an exponential decay of the number of carbon atoms in a precipitate with increasing dose. Using atomic displacement probabilities derived from Monte-Carlo simulations, a dose of few  $10^{16}$  ions/cm<sup>2</sup> was estimated to be sufficient enough to destroy a precipitate with an initial diameter of a few nm [58]. The ballistic destruction of 4–5 nm sized SiC precipitates in c-Si was recently confirmed [59, 60] by a two-beam experiment, where a C<sup>+</sup> ion beam is used to create precipitates at 450°C and a Si<sup>+</sup> ion beam is employed to either simultaneously or subsequently destroy the particles. The experiments indicate, too, that the regrowth of precipitates may depend on the local concentration of open volume defects (facilitating regrowth) and Si self-interstitials (promoting the demigration of carbon atoms). Summarizing the consequences of ballistic destruction, it seems to be obvious that the observable ensemble of precipitates results from a dynamic or quasi-equilibrium of precipitate formation, destruction and regrowth. It is a dynamic equilibrium, since the total number of carbon atoms involved in the competing processes of course increases with dose.

When the density of simultaneously dissolvable precipitates becomes sufficiently high, the amount of carbon atoms which is released from the precipitated phase into the host matrix may exceed a threshold concentration at which an amorphous phase becomes more favourable. This is believed to be the origin of the “carbon induced amorphization” [46] at intermediate temperatures (Fig. 6). It explains why 3C-SiC precipitates which were formed at a certain depth position at a lower dose disappear at higher doses [45], along with the amorphization of the c-Si surrounding of SiC precipitates. Thin amorphous seams around SiC precipitates have occasionally been found also in [43]. Recently, using a sophisticated high-resolution TEM technique, amorphous inclusions that coalesce to form the thin amorphous interfacial layers surrounding the dense precipitate layer (see Fig. 4) have been shown to be neighbored by crystalline SiC remainders [61], supporting the idea that carbon induced amorphization at high temperatures (400–500°C) is related to the ballistic destruction of precipitates.

The as-implanted structure shown in Fig. 4, which is favorable for the IBS of buried single-crystalline SiC layers, can be achieved by adjusting the implantation temperature such that nucleation of 3C-SiC precipitates occurs in a c-Si surrounding and a limited carbon induced amorphization takes place.

For beam current densities of  $\sim 10 \mu\text{A}/\text{cm}^2$  typical for medium current implanters this is the case at  $450\text{--}500^\circ\text{C}$  [52]. Slightly improved results have been obtained using a (non-optimized) two-temperature implantation technique [46], where a distribution of oriented SiC precipitates is created first by implanting a large fraction of carbon ions at  $500^\circ\text{C}$  and the amorphous seams are formed in a second step by implanting a minor fraction of carbon at a reduced target temperature.

## 6 The Annealed State

Annealing of stoichiometrically implanted samples for some hours at  $1200^\circ\text{C}$  in Ar atmosphere leads to some pile-up of the carbon depth distribution, but really box-like profiles have been obtained only for temperatures of  $1250^\circ\text{C}$  [35]. Carbon profile pile-up has recently also been reported after 15 min electron beam annealing at  $1150^\circ\text{C}$  [62] and  $1250^\circ\text{C}$  [63] in vacuum.

While box-like distributions were achieved independently of the target temperature for  $400^\circ\text{C} \leq T_i \leq 600^\circ\text{C}$ , the internal structure of layers and the abruptness of the interfaces after 5 h at  $1250^\circ\text{C}$  annealing in Ar significantly depends on  $T_i$  [64, 46]. The stronger amorphization at lower temperatures followed by beam induced formation of large misoriented SiC crystallites leads to buried SiC layers, which have an upper polycrystalline and a lower single crystalline part. Their interfaces to the top Si layer and the substrate are sharp. Even lower implantation temperatures would lead to completely polycrystalline SiC layers [65]. In contrast, completely single-crystalline SiC layers are obtained at  $T_i = 600^\circ\text{C}$  [46], however, with comparatively rough interfaces resulting from the presence of large tails in the precipitate density profile in the as-implanted state. Implantation temperatures of  $850\text{--}950^\circ\text{C}$  lead to dendritic growth of larger precipitates and thus to even more rugged interfaces already in the as-implanted state [66, 39]. A good compromise was the use of an intermediate temperature of  $500^\circ\text{C}$  [64], but single-crystalline layers with even sharper interfaces were achieved at  $450^\circ\text{C}$  [46]. Figure 7 shows the X-ray diffraction pole figure of such a layer, as well as the RBS profile and corresponding XTEM images of a 155 nm thick 3C-SiC layer covered with 290 nm c-Si (with a low density of residual SiC precipitates) and a 75 nm  $\text{SiO}_2$  passivation layer grown during annealing to protect the surface. The electron diffraction pattern (inset) in Fig. 7 shows pairs of spots resulting from the lattice planes of 3C-SiC in perfect alignment with those of the c-Si in the top layer and substrate. The contrasts within the SiC layer are mostly due a high density of planar defects on  $\{111\}$  planes, as determined from high-resolution images.

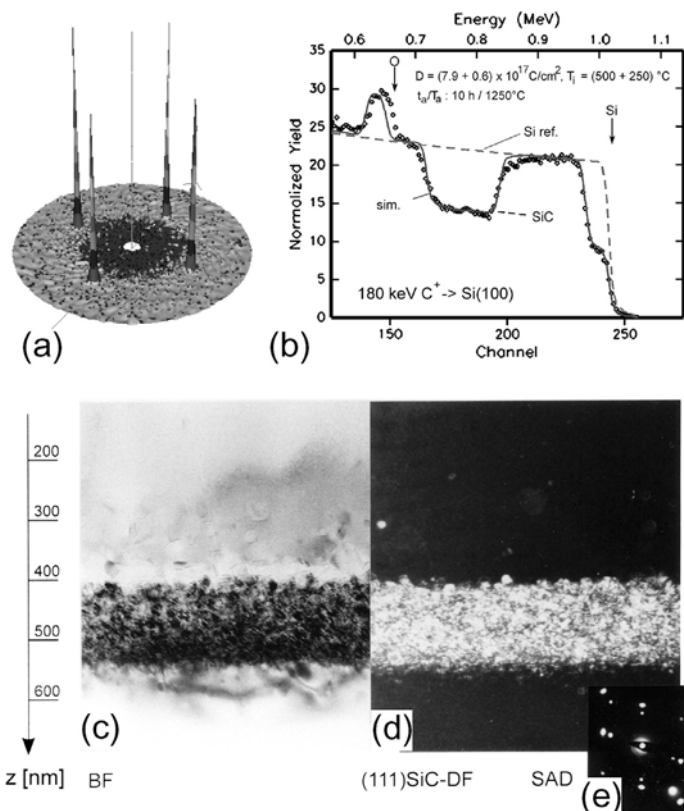


**Fig. 7.** IBS formed 3C-SiC layers in Si(100). (a) XRD pole figure showing the four {111} poles of single-crystalline 3C-SiC [61]. (b) RBS profile demonstrating a rectangular carbon profile, obtained using the two-temperature technique [46]. (c) XTEM bright-field and (d) SiC (111) dark-field images of the layer in (b), and corresponding electron diffraction pattern (e)

## 7 SiC Thin Films at the Surface and Deep in the Si Substrate

The presentation above has focused on the formation of well-defined, homogeneous, stoichiometric, single-crystalline SiC films buried few hundred nanometers beneath the surface. It is obvious that compositionally graded (containing either Si or graphitic inclusions) and polycrystalline (e.g. [65]) SiC films can be formed, too. For the sake of completeness it should be mentioned that attempts have also been made to achieve deeply buried SiC layers using MeV ion beams [35, 40, 41, 67, 68], deeply buried SiC microstructures [69, 70] using an MeV ion beam projector, or SiC films at the surface. For the latter purpose a variety of techniques has been employed, including conven-

tional implantation with energies of a few 10 keV [36, 62, 63], fast implantation also at a few 10 keV with a MEVVA ion source [51],[71]–[79] or with a MEVVA ion source coupled with a plasma lens [80], or with a supersonic C<sub>60</sub> beam [81]. As a general note, SiC film formation then is obviously affected by the free surface, allowing for e.g. needle-like precipitate growth [76], and by the presence of impurities during the annealing [62, 63].

## 8 Multilayer Systems Including IBS Formed Buried SiC Layers

### 8.1 SiC Layers Combined with SiO<sub>2</sub>

A limited number of studies [82]–[84] has so far addressed the ion beam synthesis of buried SiC layers in the top layer of a Si/SiO<sub>2</sub>/Si SIMOX layer system. These studies cover a range of target temperatures of 400–1030°C and, taken altogether, give a conclusive picture of the main effects occurring upon high-dose carbon implantation into such silicon-on-insulator layer systems.

The use of SIMOX layer systems as a target material for the IBS of buried SiC layers is interesting for a number of reasons, including the study of interactions of carbon with oxygen, silicon oxide and Si/SiO<sub>2</sub> interfaces and including the electrical insulation of a possible electronic high-temperature device in the SiC layer from carriers thermally generated in the silicon bulk [82]–[84]. As an alternative approach to the IBS of SiC layers in SIMOX wafers, the IBS of SiC layers followed by oxidation of the Si top layer and subsequent bonding to an oxidised Si wafer followed by an etch-back step was recently demonstrated to be a successful technique of forming SiC/SiO<sub>2</sub>/Si layer systems [85].

Experiments in [83] with ion energies from 90–120 keV and target temperatures of 400–600°C demonstrate that a careful tuning of overlayer thickness, ion energy and dose results in the formation of a Si/SiC/SiO<sub>2</sub>/Si layer system. Depending on the implantation conditions, in particular the dose and energy, Si/SiC/Si/SiO<sub>2</sub>/Si layer systems can also be formed, where the thermally stable Si intermediate layer between the SiC and SiO<sub>2</sub> layers can be as thin as 7 nm. The structural properties of the SiC layers are comparable to those obtained in pure Si wafers under equivalent conditions. Carbon concentrations of up to at least 38 at.% can be incorporated into SiO<sub>2</sub>, leading to amorphous SiO<sub>x</sub>C<sub>y</sub> layers which are stable against thermal carbon loss at temperatures up to 1250°C.

In principle, SiC layer formation using implantation temperatures of 400–600°C is little affected by the presence of a deeper buried SiO<sub>2</sub> layer. The interaction of carbon with Si/SiO<sub>2</sub> interfaces however is prominent at the higher implantation temperatures used in [84, 86]. Si/SiO<sub>2</sub> interfaces are then

observed to be preferred formation sites for SiC, enabling the formation of a few nm thin interfacial 3C-SiC layers. Ion beam mediated carbon diffusion to the surface of silicon crystals and outdiffusion out of buried SiO<sub>2</sub> layers are also observed at temperatures of 750°C and above.

## 8.2 Metallization of IBS Formed SiC Layers

Two sorts of experiments have so far been performed to create a metallic layer directly contacting an IBS formed SiC layer: (a) Conversion of the silicon top layer into a metal silicide, and (b) direct metal ion implantations into an IBS formed SiC layer at the surface (see overview in [87]).

180 keV Ti<sup>+</sup> implantation at 500°C was used to convert the Si top layer into a well-conductive textured C54-TiSi<sub>2</sub> film [88]–[90]. To achieve a complete conversion of the top layer without an intermediate Si rich region, the metal ion dose must be sufficiently high. However, at overly high doses, where in the as-implanted state metal rich silicides are formed in the Si top layer, degradation of the 150 nm thin buried SiC layer occurs. This layer degradation consists in the formation of crack-like macrodefects [90] – probably caused by the large differences in thermal expansion coefficients – followed by the outdiffusion of Si atoms towards the Si top layer and the indiffusion of metal atoms towards the lower SiC/Si interface. The former effect is visible [88] by the formation of large cavities at the lower SiC/Si interface and is assumed to be due to differences in the formation enthalpy of titanium silicides, favouring the TiSi<sub>2</sub> phase and thus causing strong Si updiffusion. Similar solid state reactions have also be observed upon Mo<sup>+</sup> implantations

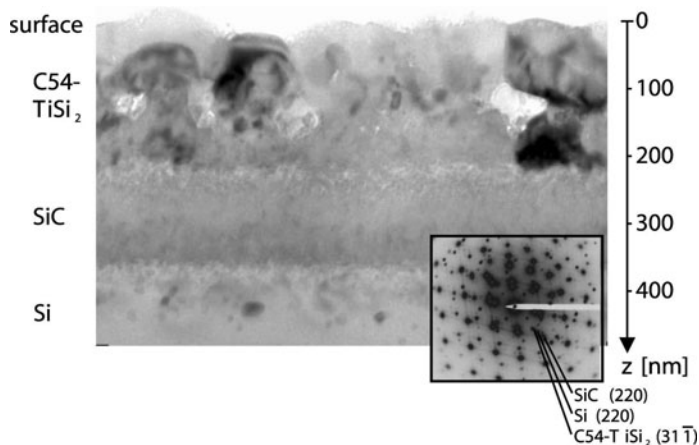


**Fig. 8.** Metal disilicide film contacting a buried 3C-SiC layer on Si(100). The silicide film was formed by implantation of Ti ions into the Si top layer of a Si/SiC/Si layer system [89]

into IBS formed SiC films with the Si-top layer wet-chemically stripped-off before  $\text{Mo}^+$  implantation [89], or after  $\text{W}^+$  implantations into as-implanted SiC surface layers [91]. Layer degradation can be completely avoided by adjusting the Ti dose in a way that taking into account the temperature dependent sputtering rates [90], at the end of implantation the ratio of metal to silicon atoms is 1:2. In this case  $\text{TiSi}_2$  layers in direct contact to the buried SiC layer have been achieved (Fig. 8), which are thermally stable up to  $900^\circ\text{C}$  or higher and which show electrical conductivities close to values reported for thick silicide films. Presently investigations are underway exploring the metallization of IBS formed SiC films using Ni implantation [87].

## 9 Applications of Buried SiC Layers

The application of ion beam synthesized SiC layers in silicon and SIMOX structures is only just beginning. Layers have been used to study both fundamental and technological questions (sometimes replacing bulk wafers simply for economic reasons), and they have been applied to create some new devices in microelectronics and micromechanics. A promising application is the use as a large-area pseudosubstrate for epilayer growth. Thus, the range of possible applications is very broad, as will be seen in the following brief summary of most important examples.

### 9.1 IBIEC: Ion Beam Induced Epitaxial Crystallization of SiC

In order to investigate the ion beam induced epitaxial crystallization (IBIEC) effect [92], homogeneous buried SiC layers were selectively amorphized with a two-step procedure, (a) irradiation with MeV  $\text{Si}^+$  ions to achieve amorphization of the SiC layer and surrounding Si and (b) subsequent thermal recrystallization of the surrounding a-Si at temperatures far below the recrystallization temperature of a-SiC. It was shown that upon an additional MeV ion irradiation of such an a-SiC film sandwiched between two c-Si layers, IBIEC occurs from both interfaces and leads to an epitaxial recrystallization of 3C-SiC at temperatures ( $600^\circ\text{C}$ ) significantly reduced compared to purely thermal recrystallization [92].

### 9.2 Doping

Comparatively little is known so far about the electrical properties of IBS formed SiC films. In [93], two approaches have been studied to form  $n$ -type doped SiC layers, (a)  $\text{N}^+$  implantation into IBS formed layers, and (b) pre-doping of the Si wafer by  $\text{N}^+$  or  $\text{P}^+$  implantation prior to IBS. The latter technique succeeds to create  $n$ -type conduction, even though the electrical activation is limited (carrier concentration  $6 \times 10^{17} \text{ cm}^{-3}$ ). However, remarkable carrier mobilities of  $600\text{--}800 \text{ cm}^2/\text{Vs}$  were achieved.

### 9.3 Optoelectronics

A first optoelectronic device application of IBS formed near surface SiC films was published recently by Li et al. [94]. They implanted 50 keV  $C^+$  ions with a dose of  $2 \times 10^{17}$  C/cm<sup>2</sup> into *p*-type boron doped Si(100) and performed 1 h annealing in N<sub>2</sub> atmosphere to achieve precipitation of SiC. According to Li et al., the dose of  $2 \times 10^{17}$  C/cm<sup>2</sup> is sufficient enough to form a continuous SiC layer at this energy and the annealing conditions used. The samples were subsequently anodized in a HF:C<sub>2</sub>H<sub>5</sub>OH=2:1 solution in order to create a porous structure consisting of 150 nm porous SiC on top of 1  $\mu$ m porous Si. Devices were made by adding a semitransparent Au front side and an Al back side contact. These structures were observed to have rectifying properties. Under forward bias conditions (positive voltage applied to the Al contact), stable, repeatable and uniform emission of light is obtained at voltages of 10 to 30 V, and this electroluminescence is reported to be clearly visible by eye at room temperature in the dark. The emitted light contains two spectral components, a blue peak from the porous SiC (480 nm) and a larger green peak from porous Si (560 nm), generated by the radiative recombination of carriers injected from the *p*-type Si substrate into the porous layers. It is anticipated that the blue emission component and the threshold voltage for electroluminescence can be optimized by means of the implantation, annealing and anodization parameters.

### 9.4 Field Emission

The fabrication of electron field emitters from near surface SiC films on silicon formed by overstoichiometric ( $1 \times 10^{18}$  C/cm<sup>2</sup>) MEVVA implantation of 35 keV  $C^+$  ions and subsequent annealing has been reported in [76]. The implantation leads to sputter saturated, near stoichiometric SiC<sub>x</sub> surface films. Annealing for 2 h in nitrogen atmosphere at 1200°C results in the growth of SiC protrusions extending approximately 40 nm out of the surface, as demonstrated by atomic force microscopy (AFM). The occurrence of these protrusions is correlated with the observation of electron field emission at turn-on fields as low as 1V/ $\mu$ m when a voltage is applied in UHV between the layer and a copper anode (turn-on current density defined as 1  $\mu$ A/cm<sup>2</sup>). Fowler-Nordheim tunnelling was clearly demonstrated and the field enhancement and turn-on voltages were observed to be correlated to the dose dependent aspect ratio of SiC protrusions found at the surface. A second emission mechanism originates from local fluctuations in the composition of these surface layers, as was demonstrated by conductive AFM measurements [95]. Emission properties can be further improved by turning the IBS-SiC layer into a SiC/WC nano-composit by an additional W<sup>+</sup> implantation [96]. Thus SiC<sub>x</sub> surface layers have application potential for Si-based flat emitter displays.

## 9.5 Large-Area Pseudosubstrates for Epilayer Growth

The IBS technique can be quite easily scaled up to large wafer sizes. Homogeneous 3C-SiC films of 75 and 100 mm diameter have already been formed in the authors lab. Large-area, single-crystalline SiC layers on top of a silicon wafer constitute an attractive substrate for the homo- or heteroepitaxial growth of thicker layers of SiC, GaN, AlN or diamond on top. In fact it has already been demonstrated that the nucleation density of CVD diamond films can be enhanced using IBS-SiC substrates [97] and that homoepitaxial CVD growth of SiC on IBS formed 3C-SiC is possible without the need of any further carbonization step [98]. In principle, SiC surface layers could be achieved by using carbon ion energies around 35 keV as in the field emission studies mentioned above. The surface protrusions which are beneficial for the local field enhancement, however, need to be avoided if an IBS formed SiC layer is to be used as a pseudosubstrate for epigrowth. Therefore, and since the Si top layers form a protective coating during the necessary high-temperature annealing step, we focused our efforts on the development of a technique to remove the Si top layer rather than trying to optimize the IBS of SiC surface layers. Our earlier attempts to remove the Si top layer by selectively etching or polishing off the Si surface layer never led to convincing results. In particular, attempts using Si etching with HF/HNO<sub>3</sub> or KOH solutions always produced rough and disordered surfaces, probably due to redeposition effects in the chemical bath. Also in [98] difficulties with the Si top layer removal were conceded, and it appears that similar effects also occurred in the other work [99, 100], describing unexpectedly high carbon concentrations at the surface of etched samples. Potassium contaminations were reported in early attempts to reveal buried SiC rich zones by etching in KOH [101]. We now have found a simple technique to solve this problem and create large-area, clean SiC surfaces with 2 nm RMS roughness [102].

## 9.6 Etch Stop Layers for Micromechanics

The excellent chemical resistivity of SiC against all kinds of etchants can be exploited to fabricate buried etch stop layers for the micro-machining of silicon [100, 101]. Etch stop layers of 120 nm thickness and with a surface roughness of 6–7 nm RMS were produced [100] by implanting 300 keV C<sup>+</sup> ions with a substoichiometric dose of  $5 \times 10^{17}$  C/cm<sup>2</sup> into silicon at a temperature of 500°C, followed by annealing for 10 h at 1150°C. The layers show complete resistance against etching from the front and the back when exposed for 1 h to tetramethylammonium hydroxide (TMAH) at 80°C, an unisotropic etchant which is CMOS process compatible. The small strain in particular of annealed films enabled the fabrication of micromechanical structures with high planarity. The layers produced are described as being superior compared to those obtained by implantation of B, Ge, Ne, Ar, and Si as regards their thermal stability, dose efficiency and layer roughness.

## 9.7 Cantilever Beams

The mechanical properties of buried SiC layers were studied using a cantilever technique [103]. To this end, 300 nm thick cantilever beams were formed by a combination of lithographic patterning, reactive ion etching through the buried SiC layer and anisotropic etching of the surrounding silicon with the SiC layer acting as an etch stop. Using such structures and a self-developed AFM technique, the Young's modulus of IBS formed SiC was determined to be  $470 \pm 10$  GPa, which is well within the spread of data (350–650 GPa) found in the literature for SiC synthesized by different methods [103].

## 9.8 Buried SiC Microstructures by MeV Ion Projection

In order to exploit the mechanical hardness and chemical inertness of SiC in micromechanics and biomedicine, attempts have been made [69, 70] to create small structures of SiC (instead of entire layers) by directly writing with a MeV  $C^+$  ion beam through a stencil mask using an ion projection system. This system [104] allows for a demagnified projection of a mask pattern onto the target, while the mask is not in contact with the target. Thus implantations can be performed at high implantation temperatures. The main advantage is the short time in the order of a few minutes which is required to fabricate a microstructure. An example of an overstoichiometrically implanted microstructure is shown in Fig. 9. It can be clearly observed using Nomarski interference contrast microscopy, which is sensitive to surface curvatures of a sample. The surface curvature could be shown to result from swelling of the buried SiC microstructure due to the formation of a carbon-rich (up to 70 at.% carbon) internal layer [69]. Swelling was avoided at substoichiometric doses [70].

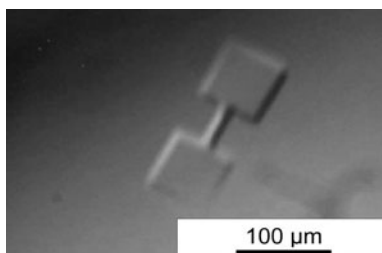


**Fig. 9.** Nomarski interference contrast micrograph of a buried SiC microstructure [69]

## 10 Conclusion

Ion beam synthesis (IBS) has become an attractive technique for forming thin, homogeneous layers of 3C-SiC within or on Si(100) and Si(111) wafers. A significantly improved understanding of the basic physical mechanisms involved in the IBS of SiC layers has been achieved in the last few years. Thus, by means of the precisely and reproducibly adjustable implantation parameters, the properties of SiC films can be precisely adjusted. Both single crystalline and polycrystalline layers can be made; buried amorphous stoichiometric SiC layers within c-Si have been achieved by an additional implantation. The ease with which ion beam techniques can be scaled up to large wafer sizes has helped to form homogeneous layers with up to 100 mm diameter, and further upscaling should be just as simple. Buried SiC layers have already been combined with insulating SiO<sub>2</sub> and conductive transition metal silicide/carbide layers. Even though there is still room for structural improvements of the layers, and our present knowledge of the electrical characteristics is still limited, some first applications in micro- and vacuum-electronics, in micromechanics and as pseudosubstrates have been successfully tested and further applications are clearly foreseeable.

## Acknowledgement

Various contributions of M. Häberlen, W. Attenberger, S. Wenzel, M. Schmid, B. Stritzker, W. Reiber, W. Brückner and D. Donimierski (University of Augsburg), as well as of S.P. Wong (Chinese University of Hong Kong), A. Rosenauer (University of Karlsruhe), S. Kubsky (University P. et M. Curie, Paris) and A. Schertel (FEI GmbH) are gratefully acknowledged. Part of this work has been supported by a Germany-Hong Kong Joint Research Scheme of the DAAD of Germany and the RGC of Hong Kong.

## References

1. *Silicon Carbide, A Review of Fundamental Questions and Applications to Current Device Technology*, Vol. I and II, ed. by W.J. Choyke, H. Matsunami, G. Pensl (Akademie Verlag, Berlin, 1997)
2. J.F. Ziegler, J.P. Biersack, and U. Littmark: in *The Stopping and Range of Ions in Matter*, Vol. 1, ed. by J.F. Ziegler (Pergamon Press, New York, 1985)
3. A.R. Bean and R.C. Newman: *J. Phys. Chem. Solids* **32**, 1211 (1971)
4. R.C. Newman: *Mater. Res. Soc. Symp. Proc. Vol. 59*, 403 (1986), and refs.
5. R.C. Newman and J. Wakefield: *J. Phys. Chem. Solids* **19**, 230 (1961)
6. J.P. Kalejs, L.A. Ladd, and U. Gösele: *Appl. Phys. Lett.* **45**, 268 (1984)
7. L.A. Ladd, J.P. Kalejs, and U. Gösele: *Mater. Res. Soc. Symp. Proc. Vol. 36*, 89 (1985)
8. U. Gösele: *Mater. Res. Soc. Symp. Proc. Vol. 59*, 419 (1986)
9. W. Skorupa and R.A. Yankov: *Mater. Chem. and Phys.* **44**, 101 (1996)

10. L.L. Horton, J. Bentley, L. Romana, A. Perez, C.J. McHargue, and J.C. McCallum: Nucl. Instr. and Meth. B **65**, 345 (1992)
11. W. Skorupa, V. Heera, Y. Pacaud, and H. Weishart: in *New Trends in Ion Beam Processing of Materials*, Europ. Mater. Res. Soc. Symp. Proc. **65**, Part 1, ed. by F. Priolo, J.K.N. Lindner, A. Nylandsted Larsen, and J.M. Poate (Elsevier, Amsterdam, 1997) pp. 114
12. J.A. Borders, S.T. Picraux, and W. Beezhold: Appl. Phys. Lett. **18**, 509 (1971)
13. J.A. Borders and W. Beezhold: in *Ion Implantation in Semiconductors*, ed. by I. Ruge and J. Graul (Springer, Berlin, 1971) pp. 241
14. E.K. Baranova, K.D. Demakov, K.V. Starinin, L.N. Strel'tsov, and I. Khaibulin: Dokl. Akad. Nauk SSSR **200**, 869 (1971)
15. W. Rothmund and C.R. Fritzsche: J. Electrochem. Soc. **121**, 587 (1974)
16. F.L. Edelman, O.N. Kuznetsov, L.V. Lezheiko, and E.V. Lubopytova: Radiat. Eff. **29**, 13 (1976)
17. I.P. Akimchenko, Kh.R. Kazdaev, I.A. Kamenskikh, and V.V. Krasnopevtsev: Sov. Phys. Semicond. **13**, 219 (1979)
18. I.P. Akimchenko, K.V. Kiseleva, V.V. Krasnopevtsev, Yu.V. Milyutin, A.G. Turyanskii (Touyansky), and V.S. Vavilov: Radiat. Eff. **33**, 75 (1977)
19. T. Kimura, S. Kagiya, and S. Yugo: Thin Solid Films **81**, 319 (1981)
20. T. Kimura, S. Kagiya, and S. Yugo: Thin Solid Films **94**, 191 (1982)
21. T. Kimura, S. Yugo, S.B. Zhou, and Y. Adachi: Nucl. Instr. and Meth. B **39**, 238 (1989)
22. L. Kroko, I. Golecki, and H.L. Glass: Mater. Res. Soc. Symp. Proc. Vol. **45**, 323 (1985)
23. N.N. Gerasimenko, O.N. Kuznetsov, L.V. Lezheiko, and E.V. Lubopytova, L.S. Smirnov, and F.L. Edelman: Mikroelektronika **3**, 467 (1974); L.V. Lezheiko and E.V. Lubopytova: Sov. Phys. Semicond. **10**, 1039 (1976)
24. I.P. Akimchenko, K.V. Kiseleva, V.V. Krasnopevtsev, A.G. Tourganski, and V.S. Vavilov: Radiat. Eff. **48**, 7 (1980)
25. I.P. Akimchenko, Kh.R. Kazdaev, and V.V. Krasnopevtsev: Sov. Phys. Semicond. **11**, 1149 (1977)
26. K.J. Reeson, P.L.F. Hemment, R.F. Peart, C.D. Meekison, C. Marsh, G.R. Booker, R.J. Chater, J.A. Kilner, and J. Davis: Radiat. Eff. **99**, 71 (1986)
27. K.J. Reeson, P.L.F. Hemment, J. Stoemenos, J.R. Davis, and G.K. Celler: Inst. Phys. Conf. Ser. **87**, 472 (1987)
28. K.J. Reeson, P.L.F. Hemment, J. Stoemenos, J.R. Davis, and G.K. Celler: Appl. Phys. Lett. **51**, 2242 (1987)
29. K.J. Reeson, P.L.F. Hemment, J. Stoemenos, J.R. Davis, and G.K. Celler: Mater. Res. Soc. Symp. Proc. Vol. **107**, 473 (1988)
30. K.G. Stephens, K.J. Reeson, B.J. Sealy, R.M. Gwilliam, and P.L.F. Hemment: Nucl. Instr. and Meth. B **50**, 368 (1990)
31. K.J. Reeson, J. Stoemenos, P.L.F. Hemment: Thin Solid Films **191**, 147 (1990)
32. P. Martin, B. Daudin, M. Dupuy, A. Ermolieff, M. Olivier, A.M. Papon, and G. Rolland: J. Appl. Phys. **67**, 2908 (1990)
33. G. Derst, S. Kalbitzer, G. Krötz, and G. Müller: Mater. Sci. and Eng. B **11**, 79 (1992)
34. A. Battaglia, G. Derst, and S. Kalbitzer: Nucl. Instr. and Meth. B **80/81**, 915 (1993)

35. J.K.N. Lindner, A. Frohnwieser, B. Rauschenbach, and B. Stritzker: Fall Meeting of the Materials Research Society, Boston, USA (1994), Mater. Res. Soc. Symp. Proc. Vol. **354**, 171 (1995)
36. L. Simon, J. Fauré, A. Mesli, T. Heiser, J.J. Grob, and J.L. Balladore: Nucl. Instr. and Meth. B **112**, 325 (1996)
37. L. Calcagno, G. Compagnini, M.G. Grimaldi, G. Foti, and P. Musumeci: Nucl. Instr. and Meth. B **120**, 121 (1996)
38. U. Preckwinkel, J.K.N. Lindner, B. Rauschenbach, and B. Stritzker: Nucl. Instr. and Meth. B **120**, 125 (1996)
39. N. Frangis, A. Nejim, P.L.F. Hemment, J. Stoemenos, and J. Van Landuyt: Nucl. Instr. and Meth. B **112**, 330 (1996)
40. J.K.N. Lindner, B. Götz, A. Frohnwieser, and B. Stritzker: Mater. Res. Soc. Symp. Proc. Vol. **396**, 877 (1996)
41. J.K.N. Lindner, K. Volz, U. Preckwinkel, B. Götz, A. Frohnwieser, B. Rauschenbach, and B. Stritzker: Materials Chemistry and Physics **46**, 147 (1996)
42. J.K.N. Lindner, K. Volz, and B. Stritzker: Inst. Phys. Conf. Ser. **142**, 145 (1996)
43. A. Romano-Rodríguez, C. Serre, L. Calvo-Barrio, A. Pérez-Rodríguez, J.R. Morante, R. Kögler, and W. Skorupa: Mater. Sci. and Eng. B **36**, 282 (1996)
44. Details of the alignment of precipitates as a function of Ti in: F. Eichhorn, N. Schell, A. Mücklich, H. Metzger, W. Matz, R. Kögler: J. Appl. Phys. **91**, 1287 (2002)
45. J.K.N. Lindner, K. Volz, and B. Stritzker: Mater. Res. Soc. Symp. Proc. **438**, 289 (1997) and **439**, 173 (1997)
46. J.K.N. Lindner and B. Stritzker: Nucl. Instr. and Meth. B **147**, 249 (1999)
47. J.K.N. Lindner: Nucl. Instr. and Meth. B **178**, 44 (2001)
48. J.K.N. Lindner, M. Häberlen, M. Schmid, W. Attenberger, and B. Stritzker: Nucl. Instr. and Meth. B **186**, 206 (2002)
49. M. Häberlen, J.K.N. Lindner, B. Stritzker: Nucl. Instr. and Meth. B, in the press
50. W.J. Taylor, T.Y. Tan, and U. Gösele: Appl. Phys. Lett. **62**, 3336 (1993)
51. Dihu Chen, W.Y. Cheung, and S.P. Wong: Nucl. Instr. and Meth. B **148**, 589 (1999)
52. J.K.N. Lindner and B. Stritzker: Nucl. Instr. and Meth. B **148**, 528 (1999)
53. P. Werner, R. Koegler, W. Skorupa, and D. Eichler: in *Proc. 11th Int. Conf. on Ion Implantation Technology*, ed. by E. Ishidida, S. Banerjee, S. Mehta, T.C. Smith, M. Current, L. Larson, A. Tasch, T. Romig (Austin, TX, USA, June 16–21, 1996) pp. 675
54. P. Werner, S. Eichler, G. Mariani, R. Koegler, and W. Skorupa: Appl. Phys. Lett. **70**, 252 (1997)
55. W. Attenberger, J.K.N. Lindner, B. Stritzker, V. Cimalla, and J. Pezoldt: unpublished
56. J.W. Strane, H.J. Stein, S.R. Lee, S.T. Picraux, J.K. Watanabe, and J.W. Mayer: J. Appl. Phys. **76**, 3656 (1994)
57. V.V. Artamonov, M.Ya. Valakh, N.I. Klyui, V.P. Melnik, A.B. Romanyuk, B.N. Romanyuk, and V.A. Yuhimchuk: Nucl. Instr. and Meth. B **147**, 256 (1999)
58. J.K.N. Lindner, K. Volz, and B. Stritzker: Inst. Phys. Conf. Ser. **142**, 145 (1996)

59. R. Kögler F. Eichhorn, J.R. Kaschny, A. Mücklich, H. Reuther, W. Skorupa, C. Serre, A. Perez-Rodriguez: Appl. Phys. A (2002), publ. online on Dec. 17 (2002)
60. R. Kögler, F. Eichhorn, A. Mücklich, H. Reuther, V. Heera, W. Skorupa, J.K.N. Lindner: presented at IBMM 2002, Kobe, Japan, submitted to Nucl. Instr. and Meth. B.
61. J.K.N. Lindner: accepted for publ. in Appl. Phys. A (2002)
62. E.Theossdossiu, H. Baumann, K. Bethge: J. Appl. Phys. **86**, 4703 (1999)
63. E.Theossdossiu, H. Baumann, E.K. Polychroniadis, K. Bethge: Nucl. Instr. and Meth. B **161–163**, 941 (2000)
64. J.K.N. Lindner, W. Reiber, and B. Stritzker: Materials Science Forum Vols. **264–268**, 215 (1998)
65. C. Serre, A. Pérez-Rodríguez, A. Romano-Rodríguez, J.R. Morante, R. Kögler, and W. Skorupa: J. Appl. Phys. **77**, 2978 (1995)
66. A. Nejim, P.L.F. Hemment, and J. Stoemenos: Appl. Phys. Lett. **66**, 2646 (1995)
67. A. Chayahara, M. Kiuchi, Y. Horino, K. Fujii, and M. Satou: Jpn. J. Appl. Phys. **31**, 139 (1992)
68. A. Chayahara, M. Kiuchi, A. Kinomura, Y. Mokuno, Y. Horino, and K. Fujii: Jpn. J. Appl. Phys. **32**, L1286 (1993)
69. S. Kubsky, J.K.N. Lindner, and A. Schertel: accepted for publ. in: Surface Science (2002)
70. J.K.N. Lindner, S. Kubsky, and A. Schertel: accep. for publ. in Thin Solid Films (2002)
71. S.P. Wong, L.C. Ho, D. Chen, W.S. Guo, H.Yan, and R.W.M. Kwok: Mater. Res. Soc. Symp. Proc. Vol. **438**, 277 (1997); and Mater. Res. Soc. Symp. Proc. Vol. **439**, 167 (1997)
72. H. Yan, R.W.M. Kwok, and S.P. Wong: Appl. Surf. Sci. **92**, 61 (1996)
73. H. Yan, R.W.M. Kwok, and S.P. Wong: Diamond and Rel. Mat. **5**, 556 (1996)
74. S.P. Wong, D. Chen, L.C. Ho, H.Yan, and R.W.M. Kwok: Nucl. Instr. and Meth. B **140**, 70 (1998)
75. W. Wu, D.H. Chen, W.Y. Cheung, J.B. Xu, S.P. Wong, R.W.M. Kwok, and I.H. Wilson: Appl. Phys. A **66**, S539 (1998)
76. D. Chen, S.P. Wong, W.Y. Cheung, W.Wu, E.Z. Luo, J.B. Xu, I.H. Wilson, and R.W.M. Kwok: Appl. Phys. Lett. **72**, 1926 (1998)
77. S. Yang, D. Chen, H. Li, Y. Zhang, D. Mo, S.P. Wong: Sol. State Com. **116**, 177 (2000)
78. H. Yan, B. Wang, X. Song, G. Chen, S.P. Wong, R.W.M. Kwok: Thin Solid Films **368**, 241 (2000)
79. H. Yan, B. Wang, X.M. Song, L.W. Tan, S.J. Zhang, G.H. Chen, S.P. Wong, R.W.M. Kwok, L.W.M. Lau: Diamond and Related Materials **9**, 1795 (2000)
80. A.A. Goncharov, I.M. Protsenko, G.Yu. Yushkov, O.R. Monteiro, I.G. Brown: Surface and Coatings Technolgy **128–129**, 15 (2000)
81. L. Aversa, R. Verucchi, G. Ciullo, L. Ferrari, P. Moras, M. Pedio, A. Pesci, S. Iannotta: Appl. Surf. Sci. **184**, 350 (2001)
82. A. Nejim, P.L. Hemment, J. Stoemenos: Nucl. Instr. and Meth. B **120**, 129 (1996)
83. B. Götz, J.K.N. Lindner, B. Stritzker: Nucl. Instr. and Meth. B **127/128**, 333 (1997)

84. R. Koegler, H. Reuther, M. Voelskow, W. Skorupa, A. Romano-Rodriguez, A. Perez-Rodriguez, C. Serre, L. Calvo-Barrio, J.R. Morante: *Proc. 11th Int. Conf. on Ion Implantation Technology*, ed. by E. Ishidida, S. Banerjee, S. Mehta, T.C. Smith, M. Current, L. Larson, A. Tasch, T. Romig (IEEE, New York, 1997) pp. 709
85. C. Serre, A. Romano-Rodríguez, A. Pérez-Rodríguez, J.R. Morante, L. Fonseca, M.C. Acero, R. Kögler, W. Skorupa: *Sensors and Actuators* **74**, 169 (1999)
86. J. Stoemenos, A. Garcia, B. Aspar, J. Margail: *J. Electrochem. Soc.* **142**, 1248 (1995)
87. J.K.N. Lindner, W.M. Tsang, B. Stritzker, and S.P. Wong: submitted to *Proc. of 7th Int. Conf. on the Appl. of Accelerators in Research and Industry*, CAARI 2002, Denton, TX, USA, Nov. 2002
88. J.K.N. Lindner, S. Wenzel, B. Stritzker: *Mater. Res. Soc. Symp. Proc. Vol.* **622**, T8.4.1–T8.4.6 (2001)
89. J.K.N. Lindner, S. Wenzel, B. Stritzker: *Nucl. Instr. and Meth. B* **175–177**, 324 (2001)
90. J.K.N. Lindner, S. Wenzel, B. Stritzker: *Appl. Surf. Science* **184**, 299 (2001)
91. J.K.N. Lindner, W.M. Tsang, S.P. Wong, J.B. Xu, I.H. Wilson: *Thin Solid Films* **427**, 417 (2003)
92. K. Volz, J.K.N. Lindner, B. Stritzker: *Nucl. Instr. and Meth. B* **120**, 133 (1996)
93. C. Serre, D. Panknin, A. Perez-Rodriguez, A. Romano-Rodriguez, J.R. Morante, R. Kögler, W. Skorupa, J. Esteve, M.C. Acero: *Appl. Surface Science* **184**, 367 (2001)
94. N.-S. Li, X.-H. Wu, L.-S. Liao, X.-M. Bao: *Nucl. Instr. and Meth. B* **142**, 308 (1998)
95. W.M. Tsang, S.P. Wong, J.K.N. Lindner: *Appl. Phys. Lett.* (2002)
96. W.M. Tsang, S.P. Wong, and J.K.N. Lindner: MRS Fall Meeting 2002, accepted for publ. in *Mater. Res. Soc. Symp. Proc.* (2002)
97. W. von Münch and S. Wiebach: *Diamond and Rel. Mat.* **3**, 500 (1994)
98. A. Romano-Rodríguez, A. Pérez-Rodríguez, C. Serre, J.R. Morante, J. Esteve, M.C. Acero, R. Kögler, W. Skorupa, M. Östling, N. Nordell, S. Karlsson, J. van Landuyt: *Materials Science Forum* **338–342**, (2000) pp. 309
99. K. Higashi, H. Shirakura, M. Kitahara, T. Inada: presented at the Int. Conf. on Ion Beam Modifications in Materials 96 in Canberra, Australia
100. C. Serre, A. Pérez-Rodríguez, A. Romano-Rodríguez, L. Calvo-Barrio, J.R. Morante, J. Esteve, M.C. Acero, W. Skorupa, R. Kögler: *J. Electrochem. Soc.* **144**, 2211 (1997)
101. D. Fröse, D. Kollwe, W. von Münch: *Nucl. Instr. Meth. B* **64**, 760 (1992)
102. W. Attenberger, J.K.N. Lindner, B. Stritzker: patents pending
103. C. Serre, A. Pérez-Rodríguez, J.R. Morante, P. Gorostizas, J. Esteve: *Sensors and Actuators* **74**, 134 (1999)
104. J. Meijer, A. Stephan: *Microelec. Eng.* **41–42**, 257 (1998)

## Surface and Interface Properties

# Atomic Structure of SiC Surfaces

U. Starke

## 1 Introduction

With its specific physical properties silicon carbide promises to allow the development of electronic devices that can not be made from silicon or III-V compound semiconductors. This is in several aspects due to the superior electronic parameters of SiC compared to those materials and promises to facilitate high power, high frequency and high temperature device applications. Considerable effort has been seen in recent years to improve the material properties of SiC wafers for an industrial device production. However, the quality of substrate material available is still by far below that of common silicon wafers and crystals. A high defect density, grain boundaries, large voids in the material which develop around screw dislocations – so-called micropipes – are defects that are still difficult to control in the industrial production of crystalline SiC material suitable for a commercial utilization of its promising properties.

One of the most puzzling physical properties of SiC is its crystal structure itself. It exists in many crystal modifications, called polytypes. These polytypes are distinguished by just the vertical stacking of SiC bilayers with an otherwise identical bond coordination [1]. Yet, the electronic band gap of different polytypes varies from 2.4 eV to 3.3 eV [2, 3]. In principle, this would offer the unique possibility to fabricate layered structures of periodically changing band gap, i.e. electronic heterostructures without any strain caused by a varying lattice parameter in the different components. However, the development of a specific polytype cannot be controlled well enough during practical growth processes. In fact, the quality of single crystalline *homopolytype* material as substrate for device production is often limited due to grains of a different polytype. Bulk growth requires a seed crystal that in most cases determines the structure of the material obtained. Nevertheless, temperature and material supply during growth have a considerable impact on the result achieved [4]. Most growth experiments and processes are carried out on the basal plane of the material. However, growth of homoepitaxial films by chemical vapor deposition (CVD) or molecular beam epitaxy (MBE) requires in particular so-called off-axis substrates. These are samples with the surface cut slightly tilted, away from the intended growth direction (*c*-axis) in order to reproduce the substrate polytype at the steps on the surface.

Nevertheless, the growth parameters and the resulting stoichiometry of the reactor environment again strongly influence the quality of such homoepitaxial films. As mentioned above, with the different band gaps of different polytypes [2] and their lattice parameters parallel to the hexagonal bilayers being practically equal, the development of strain free heterostructures composed from different polytypes appears feasible. For this kind of application one needs to switch between different polytypes during growth and obtain sharp, well defined polytype interfaces, which of course requires flat surfaces during growth.

A different, yet similarly important aspect for the successful use of SiC in device production is the generation of oxide films. In particular, for MOSFET devices and passivation layers a low defect density is essential both in the oxide layer itself and at the SiC/SiO<sub>2</sub> interface. However, state of the art SiC/oxide interfaces suffer from high electronic interface trap densities ( $D_{it}$ ) in the energy gap which at least in part is caused by stoichiometric defects in an interface region of several atomic layer thickness. This is in spite of the fact that the SiC and SiO<sub>2</sub> lattice parameters match within only 5% supposedly allowing for an epitaxial SiC/SiO<sub>2</sub> interface. For Si where the misfit is about 25% the electronic quality of the substrate-oxide interface is by far superior to that for SiC [5].

Metal films on SiC are important in two aspects, on the one hand simply for electrical connection, on the other hand and more sophisticated, for the development of Schottky devices. The latter Schottky aspect is covered by a separate contribution in this review issue by Mönch [6]. The electric interconnect aspect has been dealt with in numerous papers and reviews. However, detailed investigation on an atomic level of the deposition of ultrathin metal layers and their initial interaction with the SiC surface are scarce.

These technological issues listed above, namely material growth, oxide generation and epitaxial metal layers are ultimately related to the properties of the substrate surface. As mentioned, most growth processes have been carried out on the basal plane surfaces of SiC. On these surfaces a large variety of surface phases with different lateral periodicities have been observed depending on the actual stoichiometry of the preparation conditions [7, 8]. On the nominally Si terminated (0001) surface the stable phases have been described first by Kaplan [9]. The atomic structure of these phases has been analyzed by low-energy electron diffraction (LEED) in combination with other techniques [7, 10, 11]. In addition, several other phases have been reported on SiC(0001) which, however, are apparently all metastable [11]. On the nominally C terminated face, the SiC(000 $\bar{1}$ ) surface, the phase development has also been established recently [8] and a structure analysis been carried out [12]. In addition, well ordered epitaxial oxide layers were discovered on both faces [13, 14] and their atomic structure was determined.

The present article illuminates recent advances in the understanding of the structure of such phases and their relation to certain growth modes [15]–

[17] following up a previous review [18] within a SiC review volume [19]. After the introduction the paper reviews the crystal structure and its implication to basal plane surfaces as well as other orientations. The theoretical and experimental methods used in the course of the investigations are discussed including the preparation procedures. In the main sections the paper describes the phase development on both basal plane surfaces, i.e. the Si and the C face, as well as the first investigations dealing with the so-called *a*-planes perpendicular to the basal plane. The atomic structure of the phases as revealed by surface crystallography is covered both with respect to the atomic geometry of the reconstruction pattern as well as to the bilayer stacking in the topmost region of the surface. Both *ex situ* phases with ordered and disordered oxygen coverage and phases prepared in ultra-high vacuum (UHV) by annealing and exposure to silicon will be touched. Hydrogen and oxygen covered surfaces, adsorption of metals and III-group elements as well as other orientations are discussed. A summary concludes the paper.

## 2 Crystal Structure and Surface Termination

The complicated crystal structure of SiC in combination with the different polytypes has serious implications on the structure and properties of its surfaces. On basal plane surfaces this influences the layer stacking and causes polytype dependent step structures. On surfaces perpendicular or diagonal to the basal planes the stacking sequence is directly exposed on an atomic level.

### 2.1 Bulk Structure

Silicon carbide is composed of carbon and silicon in a stoichiometric ratio of 1:1. Each atom is bonded to four atoms of the respective other element in tetrahedral configuration. The basic building block of SiC is a hexagonal bilayer with alternating site occupation in which each element is exclusively positioned in one of the two (upper or lower) sublayers, cf. Fig. 1a. In perpendicular direction these bilayers are stacked on top of each other. The tetrahedral Si-C bonds may be continued in two orientations different by  $60^\circ$  as depicted in Fig. 1b,c by an atomic model and pyramids representing individual  $\text{SiC}_4$  tetrahedra. Accordingly, consecutive bilayers can also be stacked in two different mutual orientations, i.e. either identical or rotated by  $60^\circ$  with respect to each other. In SiC the orientation of adjacent bilayers is practically degenerate energetically [20] which leads to many different crystal structures of different stacking sequence, the so-called *polytypes*. The zinc blende structure contains bilayers all stacked in the same orientation and is displayed in Fig. 2a. This structure has cubic symmetry and resembles the diamond lattice except for the alternating chemical site occupation. The contrasting extreme with adjacent bilayers rotated by  $60^\circ$  with respect to each

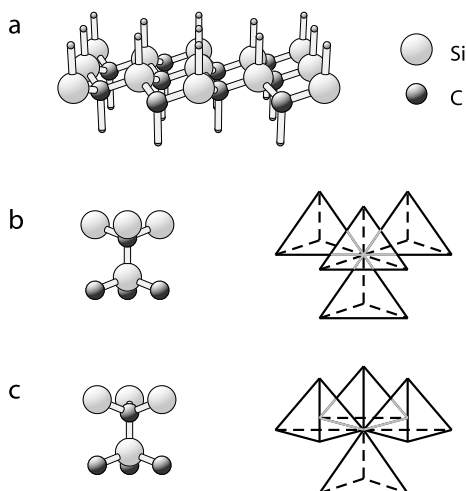


**Fig. 1.** Atomic structure of SiC: (a) Hexagonal bilayer with Si and C in alternating tetrahedrally coordinated sites, (b) Si-C tetrahedra bonded in identical orientation and (c) rotated with respect to each other

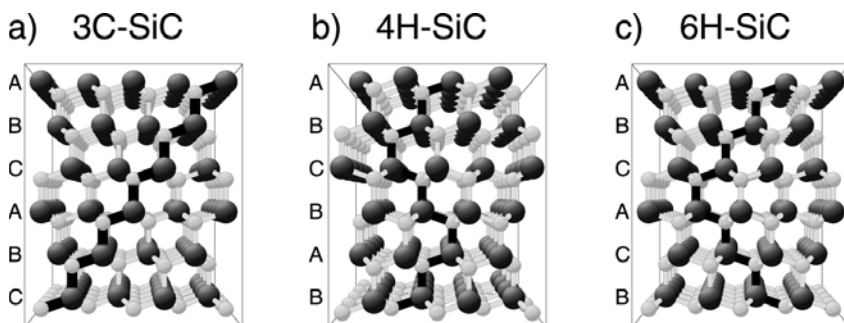


**Fig. 2.** Crystal structure of different SiC polytypes displayed parallel to the  $(11\bar{2}0)$  plane: (a) Zinc blende structure (cubic 3C-SiC), (b) hexagonal 4H-SiC and (c) hexagonal 6H-SiC. The layer orientation and stacking sequence are indicated by the enhanced (*thick black line*) Si-C bond train parallel to the  $(11\bar{2}0)$  projection plane

other corresponds to the hexagonal wurtzite structure. These two polytypes occur in ZnS and several III-V compound semiconductors. In SiC, however, the Wurtzite structure is not stable. Yet, as mentioned, many other combinations of layer orientations are found to represent stable crystal structures. In those cases the unit cell consists of consecutive stacks of identically oriented bilayers which in turn are rotated with respect to each other. As the two simplest arrangements of this kind we can envisage lattices containing stacks of two or three bilayers which in fact both represent very common

SiC polytypes. Figure 2b,c show the corresponding crystal structures. For all three polytypes the varying bilayer orientation is depicted by the bond train parallel to the  $(11\bar{2}0)$  plane drawn as a thick dark line. More than 100 other polytypes have been identified with unit cells extending more than 1000 Å along the  $c$ -axis.

SiC in cubic crystal structure is often called  $\beta$ -SiC whilst all other configurations, hexagonal and rhombohedral structures, are referred to as  $\alpha$ -SiC. For a more differentiated description of the latter configurations a short form of indexing SiC polytypes is commonly used which is based on the choice of a hexagonal unit cell regardless of the actual lattice symmetry: The structures are identified by the number of bilayers within this hexagonal unit cell and a letter indicating the true lattice symmetry. Correspondingly, the Cubic structure with 3 bilayers per unit cell is called 3C-SiC, the two Hexagonal structures shown in Fig. 2b,c with 4 and 6 bilayers per unit cell are named 4H-SiC and 6H-SiC, respectively. In the further course of the paper we will use an even more exact notation of the bilayer stacking sequence which was first introduced by Ramsdell [21]. The notation is particularly useful to describe the stacking sequence at the surface when indicating the layers from top to bottom. Each bilayer is indicated by a letter according to the lateral position of its upper atoms with respect to a reference layer. The reference layer which we choose to be the topmost bilayer of the surface is represented by the letter A. In the next bilayer which gets the letter B the upper atoms are directly below the lower atoms of the reference layer. Any further bilayer is indicated A or B if its upper atoms are below the upper or the lower atoms of the reference layer, respectively. If the upper atoms of a bilayer are below the hexagonal hollow of the reference layer it is indicated C. Although the letter itself does not indicate the rotational orientation of the individual bilayer we can draw the actual stacking sequence from the letter combination. A sequence of three different letters indicates identically oriented bilayers, i.e. a cubic type of stacking. A repetition within three letters indicates a mutual rotation, i.e. a hexagonal type of stacking. This Ramsdell type notation can be seen in Fig. 2 where the corresponding letter combination is included for the different polytypes.

## 2.2 Hexagonal Surfaces

Parallel to the hexagonal bilayers a silicon carbide sample develops polar surfaces, the so-called hexagonal or basal plane surfaces. If we assume a truncation by a complete bilayer which would have only one dangling bond per unit cell, these surfaces are nominally terminated by either silicon or carbon. Accordingly, they are usually denoted *Si face* or *C face*, respectively. Crystallographically, the *Si face* is indicated as SiC(0001) while the *C face* corresponds to the SiC(000 $\bar{1}$ ) surface. At these hexagonal surfaces different polytypes naturally will display their different stacking sequences in deeper layers. However, even for a single polytype different configurations may be

present for the actual terminating layer sequence. Intuitively, one might assume a full unit cell as drawn in Fig. 2 as surface termination for the different polytypes. Yet, of course, any other layer in the sequence of the unit cell might be the topmost layer at the surface. For simplicity the discussion in this paragraph is restricted to bulk truncated surfaces thus neglecting a possible reduction of dangling bonds by reconstruction or even a layer reorientation. Then, for a  $6H$ -SiC surface six different surface terminating layer sequences are feasible. We have three configurations with a different number of identically oriented bilayers at the very top of the surface which are drawn in Fig. 3. In the Ramsdell type notation these configurations correspond to the letter combinations (ABCACB)A..., (BCACBA)B... and (CACBAB)C... which for shortness we denote S3, S2 and S1, respectively, indicating the number of identically oriented bilayers at the surface before the occurrence of a bilayer rotation (see the enhanced bond train parallel to the  $(11\bar{2}0)$  plane depicting the stacking sequence in Fig. 3). Due to a glide plane symmetry in hexagonal polytypes the three remaining configurations (ACBABC)A..., (CBABCA)C... and (BABAC)B... have the same structure as those discussed before except for a  $60^\circ$  rotation of the whole semi-infinite crystal. Consequently, we denote those S3\*, S2\* and S1\*. Similarly, for bulk truncated surfaces of  $4H$ -SiC, we should expect S2, S1, S2\* and S1\* terminations.

Of course, a bulk truncated crystal would be energetically unfavorable as it contains one dangling bond per atom in the topmost atomic layer (upper half of a bilayer). Therefore we have to expect a different structure in real-

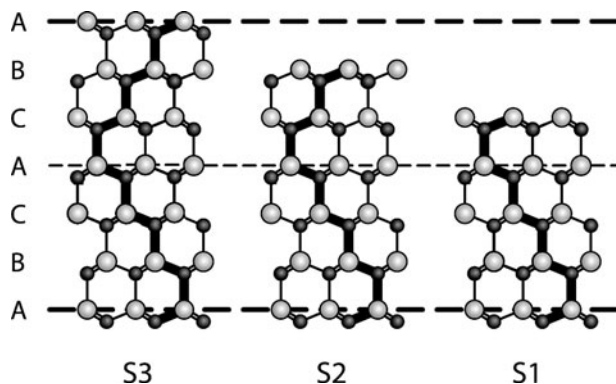


**Fig. 3.** Surface termination layer sequences on  $6H$ -SiC(0001): Configurations S3, S2 and S1, differing by and denoted according to the number of identically oriented bilayers directly at the surface. The layer orientation and stacking sequence are indicated by the enhanced Si-C bond train parallel to the  $(11\bar{2}0)$  projection plane and by the Ramsdell type notation. In the plot, large light spheres correspond to Si atoms, small dark spheres to C atoms. Long bonds drawn within the projection plane represent single bonds, shorter double lines indicate two bonds directed by  $60^\circ$  into and out of the plane

ity, e.g. adatoms saturating the dangling bonds or more or less complicated reconstruction patterns. The most feasible adatom positions in saturation or reconstruction structures on the hexagonal bilayer surface are three high symmetry sites, which one usually denotes according to position and coordination number. The two different possible threefold hollow adatom positions are commonly denoted  $T4$  for on Top of an underlying second layer atom, thus effectively 4-fold coordinated, and  $H3$  for true Hollow site and 3-fold coordinated. A single 1-fold coordinated bond representing a Top site is called  $T1$ . Certainly, adlayers and adatom clusters are also possible and will indeed be encountered in the course of this article.

## 2.3 Non-Basal Plane Surfaces

A high symmetry surface of  $\beta$ -SiC which has been investigated intensively is the (100) orientation (see [22, 23] in the previous SiC review book [19], recent reviews [24, 25] or [26]). This surface displays two-fold symmetry similar to the Si(100) surface, except that subsequent layers are either Si or C. Thus, the surface is of polar nature.

Recently, on hexagonal polytypes several non-basal plane surface orientations have attracted interest due to the possibility of faster growth rates for bulk material and homoepitaxial films. The orientation mainly investigated so far is along the so-called a-plane or crystallographically SiC(11 $\bar{2}$ 0) [27, 28]. Its surface termination is non-polar and to some extent similar to the (110) surface of cubic material ( $\beta$ -SiC). Very recently, Kimoto et al. also investigated growth on SiC(03 $\bar{3}$ 8) substrates whose surface represents a diagonal plane through the hexagonal unit cell that to some extent is comparable to the (100) face in cubic crystals [28, 29].

# 3 Experimental Methods

## 3.1 Preparation Procedures

Scratches from cutting and polishing on the surface of SiC samples cannot be removed as usual in surface experiments by sputter/anneal cycles in UHV owing to the different vapor pressure of Si and C. Si loss during recrystallization at elevated temperatures of the sputter-damaged layers inevitably leads to a carbonization of the surface. Instead many researchers perform an ex situ preparation consisting of thermal oxidation and etching in hydrofluoric acid to remove the damaged layers of the sample. One method often applied is known as RCA procedure [30]. This typically leads to a (1 $\times$ 1) LEED pattern with some diffuse background, indicating an inhomogeneous, ill-defined surface. The surface structure of several such samples was determined as unreconstructed SiC bilayers covered by disordered submonolayers of oxygen or hydrogen [7],[18],[31]–[35]. A detailed compilation of ex situ chemical

treatment recipes, in vacuo annealing and Si deposition methods has been given in the previous review [18]. A much more successful method to obtain well defined surfaces is the preparation by ex situ hydrogen treatment which etches and removes SiC material: This method has first been reported to yield flat surfaces with a  $(1\times 1)$  pattern [36] from which then the various surface reconstructions can be generated. However, it was soon found that samples annealed to  $1500^\circ\text{C}$  under continuous  $\text{H}_2$  gas flow at atmospheric pressure display a  $(\sqrt{3}\times\sqrt{3})\text{R}30^\circ$  LEED pattern in UHV with bright and sharp spots and practically no background on surfaces of both polarities [13, 14]. About one monolayer of oxygen is present in these phases as determined by electron spectroscopy which also indicates a  $\text{SiO}_2$  type bonding in this layer. The atomic structure of these surfaces is described in Sect. 4.3. Absolutely clean, bulk truncated and hydrogen terminated surfaces can be obtained by eliminating the residual oxygen and water from the preparation process. This was shown by Sieber et al. using extra hydrogen purification and UHV conditions for the hydrogen treatment [37, 38].

For the experiments discussed in this article, SiC samples obtained from different sources including pieces of bulk grown wafers and epitaxial layers grown by chemical vapor deposition were prepared ex situ by hydrogen treatment. For the  $(3\times 3)$  phase a 3C-SiC(111) film grown on Si(111) was used which was just cleaned by organic solvents. In UHV the samples could be heated by electron bombardment and cooled to liquid nitrogen temperature. From an electron beam evaporator the surface could be exposed to Si flux during the heating procedure [7].

### 3.2 Surface Analysis Techniques

The experiments carried out in the author's group were performed in a stainless steel UHV chamber equipped with a sample introduction stage, a scanning tunneling microscope (STM), a 4-grid backview LEED optics and a  $150^\circ$  spherical sector analyzer for Auger electron spectroscopy (AES) [39]. Additional X-ray photoelectron spectroscopy (XPS) experiments were performed in a different UHV chamber [40]. STM and AES provide direct experimental information about the atomic arrangement in the topmost surface layer and the surface stoichiometry. XPS and AES reveal additional information about the chemical coordination of surface and subsurface atoms of the different elements. For LEED analyses spot intensity  $I(E)$ -spectra were measured using a computer controlled, video based data acquisition system [41]. The atomic geometries of the different surface phases were determined using full dynamical LEED intensity calculations together with the tensor LEED perturbation method [41]–[43]. An automated search algorithm [44] guided by the Pendry  $R$ -factor  $R_p$  [45] identified the best-fit structure including the relative weights of domains exhibiting different surface layer stacking. A holographic interpretation of the LEED spot intensities directly provided partial structural models in some cases [12, 46]. Further surface science techniques discussed in

this article include Synchrotron based photoelectron spectroscopy (PES) of core levels (sometimes called CLPS) and of valence states as well as its angular resolved detection (ARPES) for analysis of the electronic band structure. Valence band spectroscopy can also be performed using an ultra-violet light source (UPS and ARUPS). The unoccupied electronic bands are analyzed by momentum resolved inverse photoelectron spectroscopy (KRIPES) which is also described as Bremsstrahlung isochromate spectroscopy (BIS). For crystallographic analysis X-ray diffraction (XRD) was used in one case. Furthermore electron energy loss spectroscopy (EELS) was used to investigate electronic and high-resolution EELS (HREELS) to investigate vibrational properties. For the vibrational analysis also (Fourier transform) infrared absorption spectroscopy (FTIR or IRAS) has been employed. As further structurally sensitive technique ion scattering spectroscopy (ISS) is used. Depending on their detailed experimental setup authors speak of medium ion scattering spectroscopy (MEIS) or coaxial impact-collision ion scattering spectroscopy (CAICISS). A variety of the STM technique is the ballistic electron emission microscope (BEEM) which is used for spatially resolved measurements of metal-semiconductor barrier heights. Detailed information about these techniques can be found e.g. in the books by Lüth [47] or Woodruff [48] and references given there (see also the previous review [18]). In addition theoretical investigations of SiC surfaces will be discussed that use ab initio calculations using density functional theory (DFT) (see e.g. [22]) as well as quantum chemical methods [49].

## 4 Surface Reconstruction on SiC(0001)

The SiC(0001) face is the most extensively investigated surface of SiC. Accordingly, the composition dependent phase diagram is well established. The atomic and electronic structure of the reconstructed phases have been analyzed and are reviewed in the following.

### 4.1 Phase Diagram on SiC(0001)

Starting from an ex situ prepared sample of atomically well defined structure a variety of surface phases can be prepared in UHV. Different series of phases exist on the two hexagonal orientations, i.e. (0001) and (000 $\bar{1}$ ), of which we first discuss the Si face. Figure 4 depicts the development of the individual structures dependent on annealing temperature and additional Si deposition [7, 50]. Higher temperatures yield carbon rich phases eventually leading to graphitic overlayers [51]. Higher Si supply leads to Si rich phases, in the extreme even a Si(111) like film develops with the (7 $\times$ 7) reconstruction visible and a high step density due to the epitaxial mismatch [52]. The phase transformations are reversible. Three well ordered phases are observed with periodicities of (3 $\times$ 3), ( $\sqrt{3}\times\sqrt{3}$ )R30° and (6 $\sqrt{3}\times$ 6 $\sqrt{3}$ )R30° in

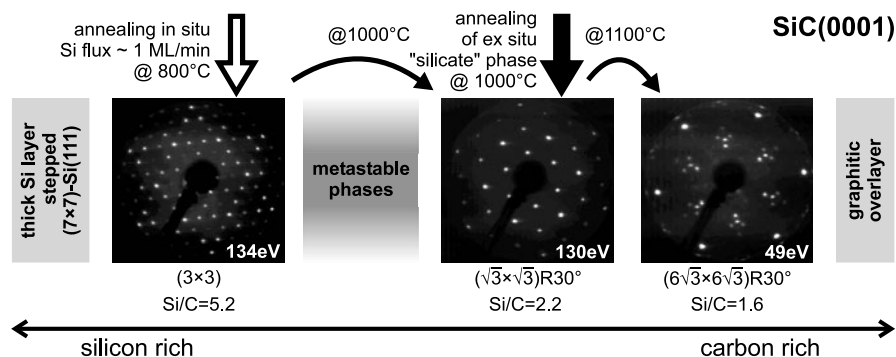


**Fig. 4.** LEED patterns of in situ prepared phases on the hexagonal SiC(0001) surface with preparation conditions, stoichiometry, surface periodicity and primary LEED energy indicated. Arrows indicate phases emerging from Si deposition (*open*) or annealing of ex situ samples (*filled*). See text for more details

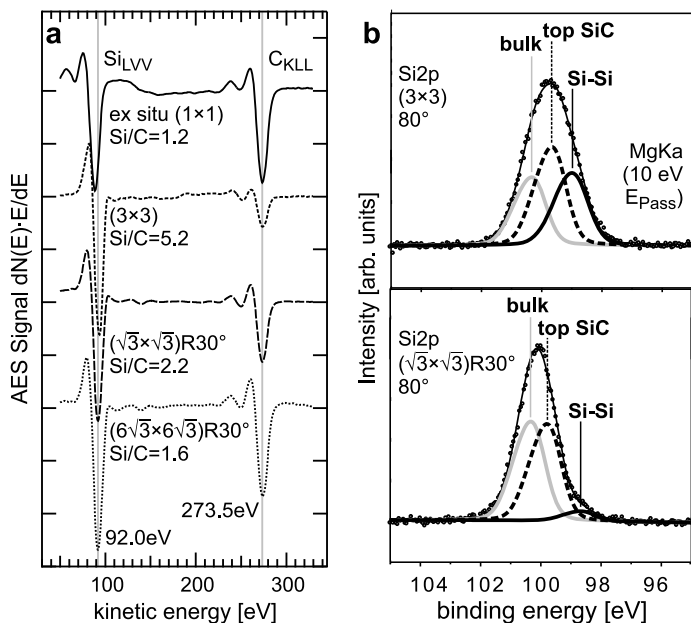


**Fig. 5.** Electron spectroscopy data for SiC(0001) surface phases: (a) Differentiated Auger electron spectra and peak-to-peak intensities of a chemically prepared (1×1) sample and the ordered (3×3), ( $\sqrt{3}\times\sqrt{3}$ )R30° and ( $6\sqrt{3}\times6\sqrt{3}$ )R30° phases. (b) XPS Si2p intensity for the (3×3) phase (*upper panel*) and for the ( $\sqrt{3}\times\sqrt{3}$ )R30° phase (*lower panel*). Bulk and surface shifted components are fitted into the surface sensitive 80° emission angle XPS data

order of decreasing Si content. Composition and chemical nature of the different phases were investigated by electron spectroscopy. Figure 5a shows AES differentiated intensities ( $dN(E) \cdot E/dE$ ) for the three ordered phases together with a chemically prepared  $(1 \times 1)$  sample. Figure 5b shows XPS data for the  $(3 \times 3)$  and the  $(\sqrt{3} \times \sqrt{3})R30^\circ$  phase. The photoelectrons were detected with  $80^\circ$  emission angle for enhanced surface sensitivity. Figure 4 notes the Si:C composition as determined from AES (peak-to-peak ratios taken from Fig. 5a) and the surface periodicity for each phase [7, 50]. Large arrows in the figure in addition indicate the phases emerging from annealing with Si flux or of ex situ prepared samples (hydrogen etched or HF cleaned). STM images of the three ordered phases were compiled in a previous review [7]. The phase diagram of SiC(0001) has been investigated repeatedly by numerous groups corroborating the observation of the three stable phases noted above [53]–[58]. A region of coexisting metastable phases is encountered upon annealing the most Si rich structure,  $(3 \times 3)$ , before the next stable structure,  $(\sqrt{3} \times \sqrt{3})R30^\circ$  is reached [11, 59]. Only a  $(6 \times 6)$  phase on SiC(0001) seems to be homogeneously developing in this range under certain conditions [55, 57, 60] contradicting earlier reports of  $(2\sqrt{3} \times 2\sqrt{3})R30^\circ$ ,  $(2\sqrt{3} \times 6\sqrt{3})R30^\circ$ ,  $(2 \times 3)$ ,  $(9 \times 9)$  [52, 61], a  $(2\sqrt{3} \times 2\sqrt{13})R30^\circ$  [62] and others. Such phases appear only in small patches always mixed with other phases [11]. A more detailed discussion of the metastable phase regime will be published shortly [63].

## 4.2 Clean Surface Reconstructions

### 4.2.1 $(3 \times 3)$ -SiC(0001): Dangling Bond Saturation and Growth

On the Si rich side of the phase diagram on SiC(0001) the  $(3 \times 3)$  phase represents the first ordered phase. It is prepared by annealing at  $800$ – $850^\circ\text{C}$  under simultaneous Si deposition [9]. On the  $3C$ -SiC(111)/Si(111) sample which was used in the initial experiments to analyze this structure [10], it develops by heating alone, presumably by silicon diffusion through defects in the heteroepitaxial film. The reconstruction geometry, however, is the same for  $3C$ -,  $4H$ - and  $6H$ -SiC [64]. The surface is covered by a Si adlayer as indicated by AES [7, 9] and XPS [40]. AES (cf. Fig. 5a) shows a strong Si enrichment and also an energy shift of the Si peak indicating a layer containing Si-Si bonds on top of the SiC substrate. Kaplan in addition detected the Si surface plasmon using EELS [9]. In Fig. 5b showing XPS spectra for the  $(3 \times 3)$  phase in comparison to those of the  $(\sqrt{3} \times \sqrt{3})R30^\circ$  phase this is even more clearly visible. In the surface sensitive experimental geometry of  $80^\circ$  emission angle two shifted surface components are evident that may be correlated to the topmost SiC layer (S1) and the additional Si layer (S2) [40].

The initial believe was that the Si adlayer of the  $(3 \times 3)$  phase would represent a variant of the dimer-adatom-stacking-fault (DAS) type reconstruction known from  $(7 \times 7)$ -Si(111) [9]. As such the surface unit cell would contain

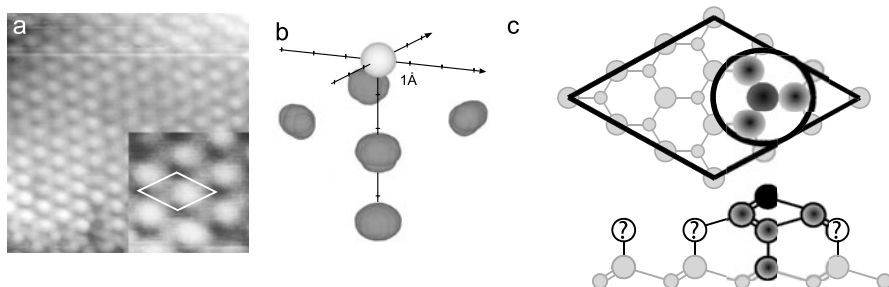


**Fig. 6.** Experimental information for the  $(3\times 3)$  phase: (a) Topographic STM image ( $112\text{ \AA} \times 112\text{ \AA}$ ) with the unit cell indicated in the *zoomed inset* ( $27\text{ \AA} \times 27\text{ \AA}$ ). (b) 3D image of the holographic reconstruction showing the local adcluster environment (*dark spheres*) of the topmost single adatom (*light sphere*) down to the fourth layer. (c) Partial model from STM and LEED holography

two adatoms and one cornerhole. However, STM images reveal the presence of only one prominent (adatom like) structure per unit cell [7, 65] as depicted in Fig. 6a, which led to the proposal of another variant of the DAS model with only one adatom and two cornerholes in the Si layer [65] as well as a simple Si tetramer model [66]. However, a holographic interpretation of the experimental LEED data [67, 68] cannot be correlated to these models. The holographic reconstruction shows the surrounding of the adatom and reveals its position to be on top of a trimer of atoms which in turn sits above two deeper atoms as shown in Fig. 6b. Thus, the adatom effectively occupies a  $T_4$  site. The three atoms forming the hollow site are positioned in a plane  $1.3\text{ \AA}$  below the adatom, the additional atom another  $1.3\text{ \AA}$  below this plane and the fifth atom resolved another  $2\text{ \AA}$  below, which would fit to the spacing between the Si adlayer and the SiC substrate [46, 69]. This partial model covers a considerable part of the  $(3\times 3)$  unit cell as shown in Fig. 6c and invalidates the models discussed above. In particular, a detailed analysis of the holography process rules out the presence of cornerholes (i.e. requires the “questioned” atom in Fig. 6c) as well as the single tetramer geometry [69]. The unresolved rest of the unit cell and the detailed positions of the atoms on the surface were determined by both quantitative LEED structure analysis and DFT calculations [10, 64, 70]. The optimized model contains and corroborates all features drawn from the experimental evidence, i.e. the  $T_4$  adatom position, and the presence of a Si adlayer that in turn is covering the topmost SiC substrate bilayer. A strong rotation (“twist”) of  $9^\circ \pm 2^\circ$  within the adlayer (cf. Fig. 7a) is observed which results in displacements of up to  $0.74\text{ \AA}$ . As a consequence the epitaxial mismatch of the Si adlayer to the SiC substrate is relieved and the interatomic distances within the adlayer are between  $2.31\text{ \AA}$  and  $2.35\text{ \AA}$ , i.e. close to the value of  $2.35\text{ \AA}$  for an ideal Si-Si bond length. In addition as shown in Fig. 7b all atoms are situated in a single layer being three-fold coordinated to their Si neighbors with  $120^\circ$  bond an-

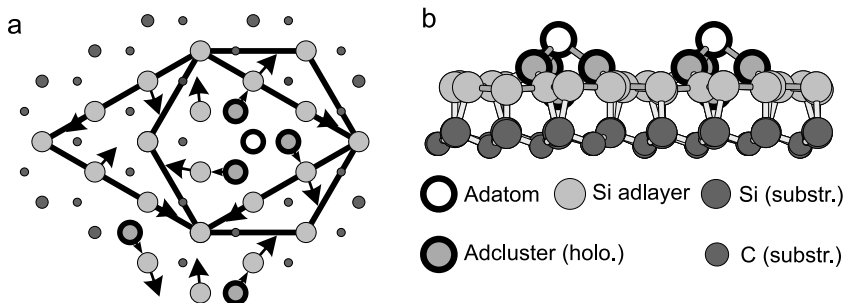


**Fig. 7.** (a) The SiC(0001)-(3 × 3) structure in top view: Lateral relaxations within the silicon adlayer (*light and dark shaded atoms*) and of the trimer (*light shaded, thick contour*) supporting the adatom (*open circle, thick contour*) are indicated with respect to the ideal positions in the topmost SiC bilayer. (b) Side view along the (1120) projection. The *open circle* indicates the adatom, *dark shading* indicates the atoms revealed by LEED holography. Lateral and vertical displacements within the Si adlayer and the SiC substrate bilayer are drawn on scale

gles and one-fold coordinated to the Si atoms of the substrate bilayer. Thus, these Si atoms are effectively  $sp^2$ -hybridized and their four bonds fully saturated. The only and single remaining dangling bond per unit cell is located at the Si adatom. A quantum chemical calculation subsequently carried out has confirmed the *twist* model as the only energetically feasible among those proposed for the (3 × 3) [71].

The high degree of bond saturation caused by the (3 × 3) reconstruction (actually better than in the case of the (7 × 7)-Si(111)) provides a very effective passivation of the surface which explains the good homoepitaxial growth possible under Si rich growth conditions in CVD and MBE [72]–[74]: A successful growth process in this manner requires the substrate to be cut slightly tilted with respect to the basal plane, i.e. in a so-called *off-axis* orientation. On such a substrate with the (3 × 3) phase present, the surface passivation leads to a high mobility of incoming particles such that they can diffuse along the terraces and attach themselves to a step. The new material continues the periodic structure of the bilayer and thus reproduces the stacking sequence of the substrate which is exposed and interrupted at the steps. So, a step flow growth mode is established that leads to a *homo-polytype* epitaxy.

#### 4.2.2 ( $\sqrt{3} \times \sqrt{3}$ )R30°-SiC(0001): Si Adatoms and SiC Layer Stacking Rearrangement

Annealing the (3 × 3)-SiC(0001) structure at 1000°C for 30 min leads to a ( $\sqrt{3} \times \sqrt{3}$ )R30° phase [7, 9]. This phase has been found already in earlier SiC surface investigations [75]–[77] since it can also be obtained by heating the ex situ prepared samples at 950–1000°C [39, 78] (cf. Fig. 4). It should be noted that this (in situ prepared) ( $\sqrt{3} \times \sqrt{3}$ )R30° phase is clearly distinguishable by

AES and LEED  $I(E)$ -spectra from the (ex situ prepared) silicate structure of the same periodicity which is discussed in Sect. 4.3. The remainder of the present paragraph concerns the (in situ prepared)  $(\sqrt{3}\times\sqrt{3})R30^\circ$  phase. Besides the above two methods, the phase can, in addition, be prepared starting from any surface phase by annealing at 1000–1100°C under simultaneous Si deposition. However, the difficult balance between Si desorption and deposition makes this third preparation method rather delicate and the phase often fails to develop in perfect order.

The phase has been subject to a long and controversial debate with respect to its crystallographic as well as electronic properties. For its atomic structure a number of models have been proposed based on different experimental observations. First of all, the composition of the phase was debated: Carbon rich [79]–[83] as well as Si rich [7, 9, 84, 85] surfaces were reported. Secondly, different STM studies revealed contradicting atomic corrugation patterns. Yet, the bias dependent images reported by Li et al. [52] could not be confirmed by other groups [7, 78, 86], who found a single protrusion per  $(\sqrt{3}\times\sqrt{3})R30^\circ$  unit cell independent of the tunneling bias. The latter situation favors a simple adatom structure. However, from STM it is not possible *a priori* to distinguish between the two three-fold hollow positions  $T4$  and  $H3$  (cf. Sect. 2.2) as well as the chemical nature of the adatom. Figure 8a shows four different models (each in one of the grey shaded unit cells). The  $T4$  site is shown in the top left cell, the  $H3$  site in the top right cell.

Several theoretical groups using ab initio DFT calculations indeed predicted a Si adatom on top of the SiC substrate in a  $T4$  position [22],[87]–

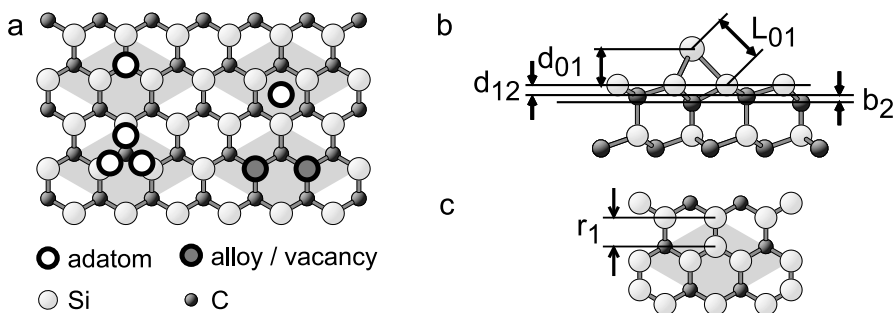


**Fig. 8.** (a) Top view of different models for the  $(\sqrt{3}\times\sqrt{3})R30^\circ$  phase discussed in the literature. Each model is drawn within one of the grey shaded unit cells. Models from left to right, top: Adatom in  $T4$ , and in  $H3$  position, respectively (representing Si or C atoms); bottom: Adatom trimer in  $T4$  position, and vacancy or substitutional alloy model. (b) The  $T4$  Si adatom structure for the  $(\sqrt{3}\times\sqrt{3})R30^\circ$  phase on SiC(0001) displayed in a side view projection along the  $[11\bar{2}0]$  direction. Geometry parameters as given in Table 1 are indicated. (c) Top view with the (planar component of the) Si-C bond  $r_1$  within the first bilayer indicated. The lateral displacement  $\Delta r_1$  of the substrate Si atoms is given in the table

[89] although a quantum chemical approach favored a  $C_3$  cluster [49] or  $C_6$  rings [90] as shown at the bottom left in the figure. Li et al. from their STM experiments even proposed a vacancy or alloy model [52] as shown in the bottom right. Further confusion came with the observation of two surface shifted components for both Si and C in PES [80, 81] which could not be correlated to a simple adatom model. Note, that one of the C components observed could later be attributed to carbon species from residual gas adsorption [40] thus resolving this contradiction. The most severe doubts about this model, however, came from investigations of the electronic structure where the absence of electronic states in the vicinity of the Fermi level was observed. Instead, in ARPES a filled surface state was found about  $1.2 \pm 0.1$  eV below  $E_F$  [91]. KRIPES detected an unoccupied state about  $1.1 \pm 0.05$  eV above  $E_F$  [53]. These surprising results were later confirmed by other groups [56, 92]. From the above DFT calculations, instead, a surface state that originates from the half filled dangling bonds was predicted to cross the Fermi level as one would also naively assume from simple electron counting. So, a crystallographic analysis was indeed called for.

One might assume that the different experimental findings and as such the model confusion could be caused by the different possible preparation procedures for the  $(\sqrt{3} \times \sqrt{3})R30^\circ$  phase. However, the LEED intensities for the three methods, i.e.  $I(E)$ -spectra, are very similar indicating structural similarity of the underlying surface [18]. The fractional order spots in particular are practically identical which means that the reconstruction geometry is the same. (There are residual differences in the integer order spots which will be discussed in the next paragraph.) For a  $4H$ -SiC(0001) sample the quantitative LEED analysis found a reconstruction geometry characterized by a single Si adatom in  $T_4$  position on top of a SiC substrate bilayer [11] as shown in Fig. 8b. The same result was retrieved for a  $6H$ -SiC sample [60]. The main reconstruction parameters, i.e. adatom layer spacing  $d_{01}$ , substrate bilayer thickness  $d_{12}$ , buckling  $b_2$  and lateral displacement  $\Delta r_1$  below the adatom as well as the resulting Si-Si bond length  $L_{01}$  of the adatom (cf. Fig. 8b,c) compare very well for the differently prepared surfaces and also for the different polytypes. Variations are below our approximate error margin determined by the  $R$ -factor variance of  $\pm 0.05$  Å. The values are listed in Table 1 and compared to the earlier DFT calculations [22, 87, 88] showing a remarkable agreement. Results from recent XRD work which confirmed the  $T_4$ -site Si-adatom model [93] are also included. This latter method, unfortunately, cannot resolve the vertical reconstruction geometry within the bilayer ( $d_{12}$  and buckling  $b_2$ ) and also shows slight deviations from LEED and DFT. A recent investigation of the  $(\sqrt{3} \times \sqrt{3})R30^\circ$  phase by CAICISS retrieved the same model. However, the adatom height (the only parameter given) appears to be underestimated by this method with  $1.5 \text{ Å} \pm 0.2 \text{ Å}$ , although with a large error margin [94]. The unambiguous crystallographic analysis with the result of a simple Si adatom structure corroborates the theoretical model

**Table 1.** Structural parameters as defined in Fig. 8b,c determined for the  $(\sqrt{3}\times\sqrt{3})R30^\circ$  superstructure by LEED (error limits about  $\pm 0.05 \text{ \AA}$ ), DFT and XRD

Parameters	From LEED	From DFT		From XRD
	[11]	[87]	[22]	[93]
$d_{01} \text{ (\AA)}$	1.77	1.75	1.71	1.61
$d_{12} \text{ (\AA)}$	0.58	0.57	0.54	–
$b_2 \text{ (\AA)}$	0.34	0.22	0.25	–
$\Delta r_1 \text{ (\AA)}$	–0.06	–0.06	–0.08	–0.12
$L_{01} \text{ (\AA)}$	2.46	2.42	2.41	2.31

from DFT and as such the explanation based on this model of the electronic surface gap observed experimentally to be caused by electron correlation (see below).

While in neither DFT nor XRD investigations the surface terminating stacking sequence was investigated, the LEED analysis finds significant differences in this respect for the three preparation methods. These stacking differences reflect the subtle deviations mentioned above in the  $I(E)$ -spectra for the three recipes [11]. An inclusion of S3 stacking domains (cf. Fig. 3), i.e. a deviation from the bulk termination of the  $4H$ -SiC substrate, is needed to achieve good fit agreement. The ratio of S3 domains in the best-fit model depends on the amount of Si present in the preparation procedure, as listed in Table 2. The most Si rich situation, i.e. annealing the  $(3\times 3)$ -phase, yields 65% S3 domains in contrast to annealing the ex situ sample which yields 75% S2 and practically no S3. The result from annealing in Si flux lies somewhere in between [11, 59]. The chemical environment obviously is a trigger parameter for the stacking sequence, as derived from recent oxygen adsorption/desorption experiments [60]. A Si rich situation enhances cubic type stacking, while more oxygen has the reverse influence. A more detailed publication on this issue is in preparation [95]. The mechanism of this stacking rearrangement in the Si rich preparation process can be understood from comparison to the ex situ silicate phase on  $4H$ -SiC(0001), where S2 is the

**Table 2.** Weights of domains with different surface terminating stacking sequences and Pendry  $R$ -factors derived for the optimized geometries of the three differently prepared  $(\sqrt{3}\times\sqrt{3})R30^\circ$  structures on  $4H$ -SiC(0001)

Preparation method	Pendry $R$ -factor	Surface stacking		
		S1	S2	S3
Annealing ex situ sample	0.13	15%	75%	10%
Direct prep. in Si-flux	0.13	15%	50%	35%
Annealing $(3 \times 3)$ phase	0.11	15%	20%	65%

dominant surface stacking sequence [13, 59]. Thus, the predominant S3 stacking in the  $(\sqrt{3}\times\sqrt{3})R30^\circ$  phase cannot be caused by a re-orientation of the topmost layer but only by the attachment of an additional bilayer in “cubic” orientation. The source of the additional bilayer is the material transport during the transition stage between the  $(3\times 3)$  and the  $(\sqrt{3}\times\sqrt{3})R30^\circ$  phase where a severe roughening of the surface is observed in STM accompanied by an inhomogeneous mixture of metastable structures with varying periodicities as also seen in LEED [11, 59]. Very recently, a stacking rearrangement has also been found upon annealing of hydrogen terminated 6H-SiC(0001) samples [96] (see Sect. 4.3).

Two theoretical investigations using DFT looked into the phenomenon of the surface layer stacking on SiC(0001) following up the pioneering work by Heine et al. [20, 97]. The energetic balance of different surface stackings (within and outside the polytype bulk sequence) was calculated, and a preference for a “cubic” stacking determined [98, 99]. Thus, it appears that from an energy equilibrium point of view, the stacking transformation observed experimentally can be understood. However, the apparent influence of the chemical environment still represents a puzzle. Nevertheless, recently growth experiments were reported where indeed 3C layers could be produced onto hexagonal polytypes [100]–[102].

With the Si adatom model established for the  $(\sqrt{3}\times\sqrt{3})R30^\circ$  and the twist model for the  $(3\times 3)$  phase, the surface shifted components observed in XPS could be compared and assigned (cf. Fig. 5b). According to the intensities from the  $(\sqrt{3}\times\sqrt{3})R30^\circ$  phase, the S1 component was assigned to the Si atoms of the topmost SiC bilayer, the S2 component to the Si adatom. Since their energetic position is the same for the two phases, the S1 component should represent the SiC bilayer also in the  $(3\times 3)$  phase. Accordingly, the S2 component, which is considerably broadened in the  $(3\times 3)$  phase is attributed to the Si adlayer and adcluster. The intensities of this component compared for the two phases agree well to the Si amount in the two models [40]. The above assignment was carried out using non-monochromatized MgK $\alpha$  radiation. A parallel synchrotron radiation core level PES study provided a better energy resolution [103]. In that study a much higher relative intensity and a slightly larger energy shift was found for S1 (SS2 in their nomenclature). As a consequence, this component was assigned to the Si adlayer and trimer and the very small S2 (their SS1) was attributed to the Si adatom [103]. However, a topmost bilayer component was found also in synchrotron experiments on the  $(\sqrt{3}\times\sqrt{3})R30^\circ$  phase [81] with an energy shift comparable to the S1 (SS2) component. The  $(3\times 3)$  phase data of ref. [103] are unfortunately not compared to a  $(\sqrt{3}\times\sqrt{3})R30^\circ$  phase and a bilayer component was not considered. It appears, therefore, that the core level assignment for the  $(3\times 3)$  phase is still under debate. Note also recent theoretical work where even the experimental assignment for the  $(\sqrt{3}\times\sqrt{3})R30^\circ$  phase is questioned [104].

### 4.2.3 Adatom Rings in the $(6\sqrt{3}\times 6\sqrt{3})R30^\circ$ Reconstruction of SiC(0001)

The  $(\sqrt{3}\times\sqrt{3})R30^\circ$  structure can be gradually transformed to the strongly silicon depleted  $(6\sqrt{3}\times 6\sqrt{3})R30^\circ$  phase by prolonged heating to  $1100^\circ$ . The transformation can be monitored by the appearance of additional spots in the vicinity of the  $(\frac{1}{3}\frac{1}{3})$  spot as well as around the integer order spots as shown in Fig. 4 (right LEED pattern). Upon completion of the transformation the  $(\frac{1}{3}\frac{1}{3})$  superstructure spots disappear. Although their distance corresponds to  $\frac{1}{6}$  of the reciprocal unit vector, the remaining spots in the vicinity of the  $(\frac{1}{3}\frac{1}{3})$  spot position are clearly not on a  $(6\times 6)$  grid as demonstrated by the lines drawn onto those spots in Fig. 9a. The lines do not coincide with those spots emerging around the integer order position. The complete set of LEED spots can only be arranged on a  $(6\sqrt{3}\times 6\sqrt{3})R30^\circ$  grid. Yet, using STM only an apparent “ $(6\times 6)$ ” corrugation is found for most tunneling conditions (cf. Fig. 9b with a  $(6\times 6)$  unit cell included) [7]. As mentioned above this led to

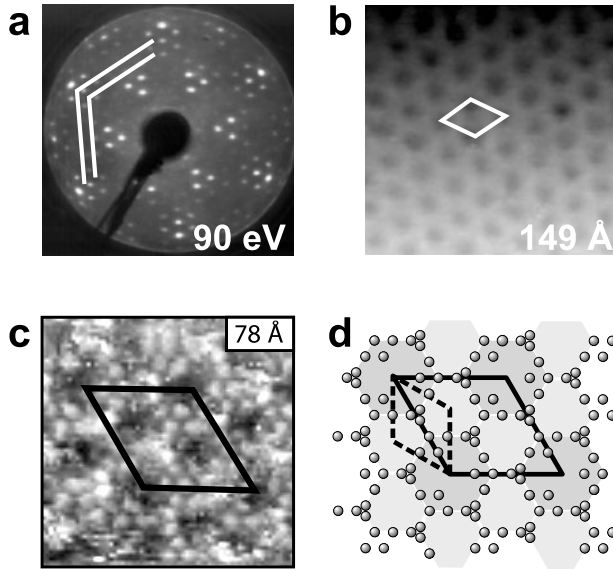


**Fig. 9.** LEED and STM data obtained from the  $(6\sqrt{3}\times 6\sqrt{3})R30^\circ$  phase: (a) LEED pattern at 90 eV. Lines are drawn through the spots around the  $(\frac{1}{3}\frac{1}{3})$  position for comparison with the spot positions around the  $(10)$  position. (b) STM image at  $U_{\text{tip}} = 1.95$  V showing a  $(6\times 6)$  corrugation ( $(6\times 6)$  unit cell included). (c) Atomically resolved STM image at  $U_{\text{tip}} = 0.2$  V, showing rings of adatoms of two different sizes ( $(6\sqrt{3}\times 6\sqrt{3})R30^\circ$  unit cell included). (d) Model drawn with the ring atoms showing one larger (*dark shading*) and two smaller (*lighter shading*) rings in approximate  $(6\times 6)$  distance, together forming the true  $(6\sqrt{3}\times 6\sqrt{3})R30^\circ$  unit cell (both unit cells included)

the proposal of a stable  $(6\times 6)$  phase on hexagonal SiC surfaces. Based on a Fourier-transform analysis the apparent inconsistency between LEED and STM results was interpreted by the coexistence of a  $(6\times 6)$  and an incommensurate  $(\sqrt{2.1}\times\sqrt{2.1})R30^\circ$  phase by Owman and Mårtensson [105]. However, using very small tunneling voltages one can observe the true  $(6\sqrt{3}\times 6\sqrt{3})R30^\circ$  structure. In Fig. 9c an atomically resolved image acquired under such conditions is shown with the unit cell compatible to the LEED pattern indicated by the black line [50]. Individual atoms can be identified forming ring-like structures that indeed are arranged in a quasi  $(6\times 6)$  periodicity. Yet, the size of adjacent rings differs slightly, and three atomic bumps within the rings are only present in every third, namely the larger ring. In panel (d) of the figure the rings with their different size and the three additional atoms are sketched together with unit cells according to a  $(6\times 6)$  and a  $(6\sqrt{3}\times 6\sqrt{3})R30^\circ$  periodicity. The atoms individually imaged by STM on the ring boundary are arranged in rows and diamonds of  $\sqrt{3} \cdot a_0 = 5.33 \text{ \AA}$  distances. So possibly the  $(6\sqrt{3}\times 6\sqrt{3})R30^\circ$  structure also contains atoms in three-fold bonding sites, similar to the  $(\sqrt{3}\times\sqrt{3})R30^\circ$ , although the stoichiometry is very different. However, at the joint of three rings the atoms appear to have  $a_0 = 3.08 \text{ \AA}$  distance. The ring arrangement in a quasi  $(6\times 6)$  periodicity presumably leads to a kinematic suppression of two out of three spots and the " $\frac{1}{6}$ " mutual distance of the remaining spots as seen in the LEED pattern. Thus, this phase has true  $(6\sqrt{3}\times 6\sqrt{3})R30^\circ$  periodicity and its very complex structure is only partially resolved up to now.

#### 4.2.4 Electronic Structure

For both Si terminated reconstruction phases on SiC(0001), namely the  $(3\times 3)$  and the  $(\sqrt{3}\times\sqrt{3})R30^\circ$  the above mentioned phenomenon of an electronic surface gap was observed by spectroscopic measurements of the occupied and unoccupied states [53, 56, 91, 92, 106], which as noted can not be explained in a one-electron picture. For the  $(\sqrt{3}\times\sqrt{3})R30^\circ$  phase a theoretical interpretation of this effect as a metal-insulator transition was given by Northrup and Neugebauer [107] who considered large electron correlation effects using a Mott-Hubbard type interaction. Their corresponding DFT calculations were based on the  $T_4$ -site Si-adatom model. In that sense this explanation is corroborated by the crystallographic results. The intra-atomic coulomb interaction energy (the so-called Hubbard  $U$  parameter) found upon slightly different calculational details varies from 1.6 eV to 2.1 eV [92],[107]–[109]. These values compare well to those extracted from experiments [53, 56, 91, 92] of 2.0–2.2 eV. Spectroscopic STM investigations could confirm these results on an atomic level [86]. For the  $(3\times 3)$  phase the effect was also seen in the experiment [56, 106, 110]. In this case the Hubbard  $U$  is smaller, i.e. about 1.0 eV, corresponding to the larger screening by the Si adlayer. Theoretical treatment confirms the value with about 1.1 eV [92, 111]. Interestingly, such a surface gap appears to be present on many other SiC surface phases as well.

For instance on the silicate surface on SiC(000 $\bar{1}$ ), which is discussed in more detail in the next paragraph, a band splitting was found. The experimental value of  $U \geq 1.4$  eV [112] correlates well to calculations with  $U = 1.2$  eV [113], while on SiC(0001) only a theoretical value  $U = 1.8$  eV is available [113]. On hydrogen terminated unreconstructed SiC surfaces of both orientations (see also below), Sieber et al. [37] discovered dangling bond states below the Fermi energy upon photon induced dehydrogenation. These findings were also interpreted in the Mott-Hubbard picture. Recently, the surface band splitting for the two clean phases, (3 $\times$ 3) and Si adatom ( $\sqrt{3}\times\sqrt{3}$ )R30°, was investigated by EELS [58]. Energy loss features observed are interpreted as direct electronic transitions between the occupied and empty surface states. The values are in good agreement to the above findings [58].

### 4.3 Epitaxial Systems and Adsorbates

In Sect. 3.1 the ex situ treatment with hydrogen was noted to result in well defined, ordered SiC surfaces. Two types of surface structures have been observed depending on the experimental details of the preparation, one is terminated by an ordered oxide layer, the other by dangling bond saturation with hydrogen.

#### 4.3.1 Silicate Layers

The oxide terminated phases which exist on both faces, i.e. SiC(0001) and SiC(000 $\bar{1}$ ), have been analyzed crystallographically. Both the ( $\sqrt{3}\times\sqrt{3}$ )R30° LEED pattern with its  $I(E)$  spectra and the oxygen related features in AES are stable against annealing up to 1000°C. Thus, the reconstruction patterns (on both surfaces) necessarily include oxygen. The atomic arrangement was determined by LEED structure analyses as a Si<sub>2</sub>O<sub>3</sub> compound layer above an otherwise bulk-truncated crystal with Pendry  $R$ -factors of 0.20 for the 4H-SiC(0001) and 0.14 for the 6H-SiC(000 $\bar{1}$ ) surface indicating the good fit agreement. As shown in Fig. 10a the layer consists of a honeycomb-like arranged sublayer of two Si atoms per ( $\sqrt{3}\times\sqrt{3}$ )R30° unit cell connected by an overlayer of two-fold coordinated oxygen atoms. This *silicate* like layer is directly connected to the topmost SiC bilayer by a Si-C bond (panel b) on SiC(000 $\bar{1}$ ) while on SiC(0001) a linear Si-O-Si bridge mediates the contact (panel c) [13, 14, 114]. On both surface orientations the oxygen atoms saturate all bonds of the silicate adlayer, only one of the three Si or C atoms per unit cell in the topmost substrate bilayer is not fully saturated and has only threefold coordination. Hydrogen has been found on these remaining substrate atoms at lower temperatures which desorbs at around 600°C [115]. The almost perfect bond saturation explains the stability of the structures against exposure to air ambient.

An idea about the origin of the silicate adlayer reconstruction can be drawn from recent experiments by Sieber et al. [38] who performed an in

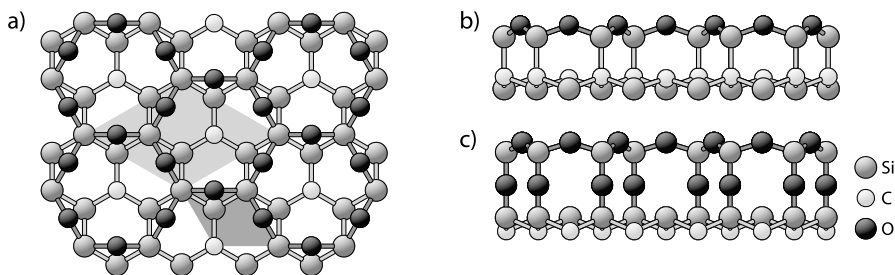


**Fig. 10.** (a) Top view of the oxide structure on  $\text{SiC}(000\bar{1})$ . The  $\text{Si}_2\text{O}_3$  silicate adlayer consists of a honeycomb structure with Si–O–Si bonds. In the center of the hexagons one carbon atom of the topmost substrate bilayer is visible (*dark shaded area* indicates the  $(1\times 1)$ -, *light shaded* the  $(\sqrt{3}\times\sqrt{3})\text{R}30^\circ$ -unit cell). (b) Side view projection of (a) along the  $(01\bar{1}0)$  direction. (c) Equivalent side view of the oxide structure on  $\text{SiC}(0001)$ . Linear Si–O–Si bonds connect the silicate layer and the SiC substrate

situ ultra pure hydrogen preparation procedure and found no oxygen on the surface (see below). This indicates that residual oxygen present in the ex situ procedure may be responsible for the silicate development. The oxidation obviously proceeds on a faster time scale than the etching process as it has also been found on diamond surfaces [116]. The hydrogen treatment, however, is necessary for the  $(\sqrt{3}\times\sqrt{3})\text{R}30^\circ$  periodicity to develop, otherwise the latter should have been also observed in earlier investigations of ex situ prepared surfaces. In case the initial order would be absent, the oxygen adsorption and reaction would proceed statistically on all available sites, and a  $(1\times 1)$  lattice gas disorder would develop. The lack of such an ordered seed may even be one of the reasons for the poor electronic quality of thermally oxidized layers on SiC. The high interface state density has been attributed to disordered species between the SiC substrate and the oxide layer [117]–[120]. However, the structure of the ordered adlayer being remarkably similar to that of bulk  $\text{SiO}_2$  certainly is intuitive, leading to the speculation that it might serve as seed to deposit thicker oxide films. Indeed, the lateral unit vector of the  $(\sqrt{3}\times\sqrt{3})\text{R}30^\circ$  periodic lattice matches that of bulk  $\text{SiO}_2$  within 95%. The only difference between the silicate monolayers on SiC and the bulk structure of a high temperature  $\text{SiO}_2$  phase known as  $\beta$ -tridymite is the position of the Si atoms. In the bulk structure a silicate layer consists of three sublayers with the Si atoms alternatingly positioned below and above the oxygen atoms. Hypothetically, the silicate adlayer found on SiC can be transformed into this structure simply by shifting one of the two Si atoms in the unit cell upwards into this upper Si sublayer position [13].

### 4.3.2 Etching and Oxidation

In the ex situ preparation of SiC samples hydrogen at atmospheric pressures is used in order to remove SiC material by etching. On a different pressure scale, namely under UHV conditions, hydrogen can also be used to etch the in situ phases on SiC(0001). All studies discussed here used thermally (at a hot Tungsten filament) dissociated hydrogen. Exposures are noted in units of Langmuir (L). Van Elsbergen et al. observed the conversion of the  $(3\times 3)$  and the  $(\sqrt{3}\times\sqrt{3})R30^\circ$  phase to a  $(1\times 1)$  periodic structure upon long exposures to hydrogen (3000 L and 300 L, respectively) [121]. The initial reaction at lower exposure has been monitored using vibrational spectroscopy (HREELS) [40, 122]: Tautz et al. [40] observed a Si-H vibration on both phases after exposure at room temperature (*RT*). A slight difference in the stretching mode energy by 1.7 meV indicates a stiffer bond in the case of the  $(3\times 3)$  phase reflecting its Si enriched adlayer. For the  $(3\times 3)$  also a larger intensity is observed as compared to the  $(\sqrt{3}\times\sqrt{3})R30^\circ$  phase after similar exposures of 100 L for both phases. That shows that the hydrogen not only bonds to the adatom but also to Si in the adlayer in the case of the  $(3\times 3)$ . At these exposures (at *RT*) the LEED pattern becomes more diffuse, however, the reconstruction periodicity is maintained for both phases [40]. Using STM, this complex reaction behaviour on the  $(3\times 3)$  phase could be demonstrated on an atomic level. Different changes in the adatom appearance were interpreted as Si displacement by C, formation of vacancy defects and adatom removal. At higher dosage a disintegration of the underlying layers was observed [123]. At a temperature of 320 K the  $(3\times 3)$  LEED pattern weakens starting from 5 L exposure [122]. Note, that deuterium was used in that study for a better distinction from residual hydrogen. At 50 L the LEED pattern disappears and the Si/C ratio in AES decreases with the Si adlayer related features fading in the Si peak. At 320 K the etching process proceeds through the Si adlayer with D attacking the substrate (C-D vibrations). However, at 180 K this is not the case as also indicated by higher deuteride species ( $\text{SiD}_2$ ,  $\text{SiD}_3$ ) [122]. From these studies, it appears that the hydrogen interaction switches from a mere surface reaction to bulk etching just above room temperature. For the  $(\sqrt{3}\times\sqrt{3})R30^\circ$  phase a CAICISS study determined a saturation coverage for hydrogen exposure at *RT* with about 1.7 monolayers (ML) [124].

As noted in the introduction, the oxidation of SiC surfaces is important in connection with the generation of well defined  $\text{SiO}_2$  layer on SiC. For a better understanding of the processes involved in the device related technological processes of oxidation or oxide deposition, a variety of studies have been devoted to the initial interaction of oxygen with the well defined in situ prepared SiC surface phases [79, 125, 126]. In recent experiments the surfaces were exposed to molecular oxygen under UHV conditions at *RT* and elevated temperatures. In the regime of low doses of only a few L of  $\text{O}_2$  the two phases show marked differences: On the  $(3\times 3)$  phase the oxide incorporation takes place by interaction of individual molecules at randomly distributed

sites [127]. In STM one apparently observes only the electronic effect of a subsurface incorporation of oxygen atoms. It influences the appearance of adatoms always in three neighboring ( $3\times 3$ ) unit cells. The Si oxidation states in XPS and Si-O-Si vibrations found in IRAS indicate an immediate oxidation within the Si adlayer in the middle between three adatoms rather than an attack of the Si adatoms themselves. [127, 128]. A polytype dependence was found, with larger amounts of oxide products having higher oxidation states for the  $6H$ -SiC(0001) surface, while mixed oxides including carbon species (Si-O-C) are the dominant oxide products for the  $4H$  polytype surface. The oxidation rate is improved at increased surface temperatures. In all cases, the oxygen uptake remains significantly larger for the  $6H$  polytype when compared to  $4H$ -SiC [129].

The oxidation reaction on the  $(\sqrt{3}\times\sqrt{3})R30^\circ$  phase was investigated at elevated temperatures and small  $O_2$  doses (0.05–0.26 L) using STM [130]. At  $500^\circ\text{C}$  the initial interaction (0.05 L  $O_2$ ) is isotropic with isolated, randomly chosen sites attacked. At higher doses (0.15 L) the reaction becomes anisotropic with etch lines developing. At higher temperatures ( $700^\circ\text{C}$ ) the anisotropy of the reaction is observed immediately. The etch pattern changes from one-dimensional (lines) at 0.05 L to line triangles and two-dimensionally etched patches at 0.26 L. Intact  $(\sqrt{3}\times\sqrt{3})R30^\circ$  patches enclosed by etch lines are observed to be likely to assume adatom positions which are out-of-phase to the neighboring area (anti-phase domains). In the two-dimensional etch patches the underlying substrate bilayer can be imaged with the atoms in their  $(1\times 1)$  arrangement [130]. The picture is completed by PES and MEIS investigations for oxidation between  $RT$  and  $800^\circ\text{C}$  [131, 132]. At  $RT$  early saturation is observed [131, 132] with the saturation coverage specified by MEIS at 1.07 ML of oxygen upon exposure to 10 L [131]. The oxide regime in the PES  $Si2p$  line is dominated by the  $Si^{1+}$  component, and the Si adatom related surface state disappears [131, 132]. This is interpreted such that at  $RT$  mainly the adatoms are oxidized and only 10–15% of the oxygen atoms are inserted into Si-C bonds [131]. At  $500^\circ\text{C}$ , the reaction proceeds into the subsurface region with  $SiC_xO_y$  species observed in PES. Here, a saturation coverage of 1.8 ML (upon 100 L  $O_2$ ) is determined [131]. At even higher temperatures ( $800^\circ\text{C}$ ) saturation is not observed, the oxidation proceeds even after  $10^6$  L exposure [133]. The  $Si^{4+}$  component of the  $Si2p$  peak which is about equal in intensity to the  $Si^{1+}$  component below 1000 L rises at higher exposures and/or higher oxygen pressure (here approx.  $10^{-3}$  torr). Above  $10^5$  L the  $Si^{4+}$  component dominates. However, the  $Si^{1+}$  state persists indicating a coexistence of bulk oxide and a near surface suboxide in this regime [132]. Note, that on the SiC(0001) surface a different suboxide is detected with a  $Si^{2+}$  oxidation state [132]. The electronic properties resulting from high pressure oxidation yet starting from a well defined  $(\sqrt{3}\times\sqrt{3})R30^\circ$  structure were investigated by UPS and XPS [134, 135]. Atomic level experimental and theoretical investigations are now also focussing on the structural interface properties upon high pressure oxidation [136]–[142].

### 4.3.3 Hydrogen Termination

A well defined hydrogen termination of both basal plane surfaces, SiC(0001) and SiC(000 $\bar{1}$ ) has been achieved by a thermal treatment in ultra pure hydrogen [37, 38],[143]–[145]. The 6H-SiC samples used were heated for 20 min at 1000°C in 10<sup>5</sup> Pa of ultrapure hydrogen. After this preparation they were transferred under UHV conditions into the analysis chamber. On both faces a sharp, low background (1×1) LEED pattern was observed, indicative of an unreconstructed surface. This could be confirmed by XPS and synchrotron based core level spectroscopy of the Si2*p* and C1*s* photoemission peaks: In addition to the SiC bulk components only one chemically shifted component was found for each orientation, i.e. corresponding to C<sub>3</sub>SiH on SiC(0001) and Si<sub>3</sub>CH on SiC(000 $\bar{1}$ ), respectively. In vibrational spectroscopy using FTIR sharp Si-H stretching modes were observed with the polarization dependence clearly indicating monohydride Si-H bonds in surface normal direction. Practically no multihydride and oxygen related species were present, so that the surface could be identified as full hydrogen saturated, unreconstructed (1×1) phase [38]. Additionally, a splitting of the Si-H stretching mode observed on the Si face could be identified as originating from different surface stacking terminations by comparison of a 6H-SiC(0001) and a 3C-SiC(111) sample [96]. The hydrogenated surfaces are passivated chemically and electronically. The oxygen uptake is less than 1% of a monolayer after 2 days air exposure without any sign of Si-O or C-O bond formation. No pinning of the Fermi level is observed [38]. Photon induced desorption of hydrogen from these surfaces due to high doses of synchrotron radiation leads to hydrogen-free and (1×1)-surfaces with dangling bonds states within the fundamental band gap below  $E_F$  [37]. It should be noted that the Si-H stretching vibrations had been previously observed in FTIR after ex situ hydrogen treatment, yet, those surfaces were not oxygen free [146].

### 4.3.4 Epitaxial Metal Films

The technological importance of metal deposition on SiC is clearly immense, and the electrical properties of such films have been investigated extensively (see the review by Mönch [6] within this review book). Surprisingly, the structure of thin metal film surfaces and interfaces on SiC has been investigated only scarcely. A few STM studies partly combined with electron spectroscopies were published investigating morphology, growth mechanism of evaporated metals starting on well defined SiC(0001) phases, ( $\sqrt{3}\times\sqrt{3}$ )R30° or (3×3). Ti was actually investigated on the Si- and C-face and ordered superstructures observed [147]. For Co, Ag and Ni more or less inhomogeneous films were reported with clustering of the thin metal layers [148, 149, 150]. The detailed atomic structure of the films could not be determined. For Pd the reaction with the SiC substrate was investigated using LEED, UPS and XPS. For thin metal films a silicide reaction was observed. Thicker material

deposition resulted in epitaxial Pd films [151]. The electric contact properties of the metal-semiconductor interface can be spatially analyzed using the BEEM technique. This was carried out for Pd and Pt [152]. For Au on SiC, the Schottky barrier height was studied using PES [153]. The atomic structure of several III-group elements was investigated using DFT. Stability, reconstruction, and surface electronic states were analyzed [154]. For these elements, however, experimental surface analyses have not been reported.

## 5 Other Surface Orientations

The majority of surface related investigations on SiC have been carried out on SiC(0001) and  $\beta$ -SiC(001). The former surface orientation was reviewed in the previous sections. Since a discussion of the latter would go beyond the scope of this review and in addition exceed the space available here, the reader is referred to recent reviews [22]–[25] and e.g. [26]. Less intensively looked at is the carbon terminated basal plane surface, i.e. SiC(000 $\bar{1}$ ) and the recently more popular (11 $\bar{2}$ 0) and (03 $\bar{3}$ 8) surfaces, which are treated in the following section.

### 5.1 Phase Diagram of the SiC(000 $\bar{1}$ )-Surface

The SiC(000 $\bar{1}$ ) surface as alternative to SiC(0001) for device fabrication possesses distinctly different growth behavior and oxidation rates. Also the electric properties of metal/SiC(000 $\bar{1}$ ) interfaces are different from those on SiC(0001). The stable surface phases are again dependent on the Si:C composition. An overview over the different phases found in a variety of investigations [9, 66, 75, 76, 79, 155] was compiled in [18]. A complete phase diagram, however, was drawn only recently. Structure and composition of the stable phases were investigated by STM, LEED and AES [8]. Figure 11 displays those phases in order of their appearance upon annealing with the Si:C composition indicated by the AES peak-to-peak ratios as obtained from the experimental data (cf. [8]). It should be noted that the phase diagram contains two (2 $\times$ 2) phases. For clarity, they are denoted (2 $\times$ 2)<sub>Si</sub> and (2 $\times$ 2)<sub>C</sub> according to their more or less Si rich composition. Large arrows in the figure again indicate the phases emerging from annealing with Si flux (open arrow) or of ex situ prepared samples (filled arrow). Annealing the silicate or a HF treated phase leads to the (3 $\times$ 3) phase, the (2 $\times$ 2)<sub>Si</sub> phase can only be prepared with additional Si deposition. A region of metastable phases is found in LEED between the (2 $\times$ 2)<sub>Si</sub> and the (3 $\times$ 3) phase. During the transformation from the (3 $\times$ 3) to the (2 $\times$ 2)<sub>C</sub> phase, the surface traverses a phase coexistence regime. The stoichiometry values determined for those two phases should be considered with caution due to slightly different peak shapes but also in view of the coexistence, since the (2 $\times$ 2)<sub>C</sub> phase can only be prepared

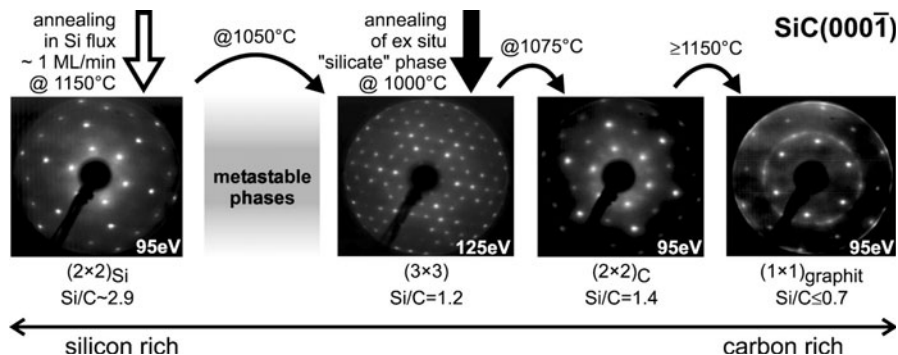


**Fig. 11.** Stable, clean, well ordered, in situ prepared surface phases on SiC(000 $\bar{1}$ ) identified by sharp LEED patterns. Preparation conditions, stoichiometry, surface periodicity and primary LEED energy are indicated. *Arrows* indicate phases emerging from Si deposition (*open*) or annealing of ex situ samples (*filled*). See text for more details

alone when it is already starting to degrade [156]. Yet, from the preparation cycle it seems clear that the  $(3 \times 3)$  phase contains more Si than the  $(2 \times 2)_C$ . In analogy to SiC(0001) annealing to higher temperature leads to a graphitic phase with a  $(1 \times 1)$  LEED pattern with extra diffraction rings consistent with the graphite lattice parameter and typical graphite like features in the carbon Auger peak. The phase diagram can be traversed repeatedly by preparation of the  $(2 \times 2)_{Si}$  phase by Si deposition [8]. The major part of this phase diagram was also found by a parallel investigation except for the Si rich  $(2 \times 2)_{Si}$  [157]. Using KRIPEs that work also confirms the graphitic nature of the carbon rich “ $(1 \times 1)$ ” phase. The  $(3 \times 3)$  phase has been reported by several groups [66, 75, 76, 79], [158]–[161]. A  $(2 \times 2)$  phase was also mentioned by van Bommel et al. [75]. The  $(2 \times 2)_{Si}$  found on the very Si rich side of the phase diagram has not been clearly identified in other investigations, however, Hoster et al. [159] found chains of atoms in local  $(2 \times 2)$  arrangement in STM upon Si deposition. From the preparation conditions one might suspect that the  $(2 \times 2)$  phase reported by Li et al. [160] is in fact identical to the present  $(2 \times 2)_{Si}$ . Except for its Si enrichment further information about the  $(2 \times 2)_{Si}$  has not been reported. Structural information about the  $(3 \times 3)$  and the  $(2 \times 2)_C$  are reviewed in the following. Other phases are apparently not stable since they could not be prepared repeatedly [160]. Observations of a reported  $(\sqrt{3} \times \sqrt{3})R30^\circ$  phase [9, 66] should probably be attributed to the silicate phase. Superstructures previously investigated by theory [89, 163] are not found in the experimental phase diagram, so that no comparison is possible.

## 5.2 A Complex $(3\times 3)$ Reconstruction Phase on SiC(000 $\bar{1}$ )

As noted above, a  $(3\times 3)$  phase has been reported by various authors upon different preparation procedures. The phase has been prepared by annealing ex situ prepared samples, by annealing the  $(2\times 2)_{\text{Si}}$  on the Si rich side in the phase diagram (Fig. 11) or by annealing after Si deposition. The composition determined in the respective experiments are not always coincident. However, at least the former two preparation methods (indicated in Fig. 11) yield identical structures as deduced from AES intensities, LEED  $I(E)$ -spectra and STM. The AES intensities indicate a Si:C composition at the surface, that is relatively close to the bulk stoichiometry. STM images show that its atomic structure is rather complex. The STM appearance changes dramatically upon bias reversal as demonstrated in Fig. 12. While in the empty state image (right) only one bright spot per unit cell is observed, the filled states (left) show a diamond like arrangement of four protrusions within the  $(3\times 3)$  unit cell. In addition, a domain boundary between two out-of phase  $(3\times 3)$  patches as indicated by the arrow in the right panel displays a non-trivial atomic structure. These STM images were first observed by Hoster et al. [159] together with LEED patterns with spot intensities identical to the present data [8]. Their preparation was according to the third method. Interestingly, in contrast to the structural identity to the phase originating from annealing an ex situ sample, the stoichiometry as derived from AES (Si:C  $\approx 6$ ) is drastically different. Hollering, upon annealing after Si deposition also obtained a Si rich  $(3\times 3)$  surface with Si surface components found in core level PES [162]. On the other hand, Johansson et al. after annealing an ex situ prepared sample also found a  $(3\times 3)$  phase of approximate bulk stoichiometry, yet with core level shifts in the C1s peak [158]. Based on the

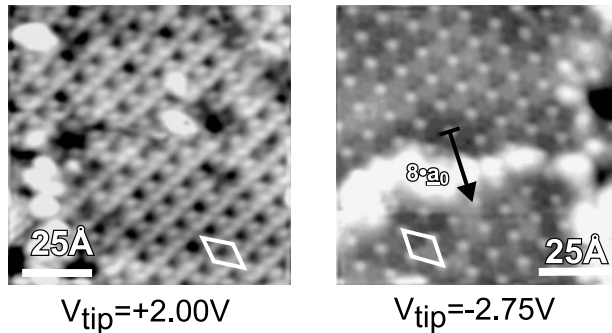


**Fig. 12.** STM images of the  $(3\times 3)$  phase acquired for filled (*left*) and empty (*right*) states. Besides the different appearance of the surface for opposite tunneling bias the atomic arrangement in the vicinity of the antiphase domain boundary as indicated by the *black arrow* in the right panel ( $8\cdot a_0$  instead of  $9\cdot a_0$  between bright  $(3\times 3)$  periodic spots in the image) is heavily distorted. The  $(3\times 3)$  unit cell is indicated by the *white diamond*

STM images Hoster et al. [159] proposed a model for the  $(3\times 3)$  phase which, however, has not been tested and confirmed by crystallographic methods. It should be noted, that the same type of STM images (Fig. 12) were observed by Li et al. [160]. Their superperiodicity assignment as  $(2\sqrt{3}\times 2\sqrt{3})$ , however, must be questioned in view of the other experiments.

So, in view of these contradicting results, it is not clear whether one of two  $(3\times 3)$  phases exist on  $\text{SiC}(000\bar{1})$ . While electron spectroscopy indicates different surface compositions and bonding situations resulting from the different preparations, the STM results clearly point towards one phase emerging from all three preparation methods.

### 5.3 Atomic Structure of the $(2\times 2)_C$ -Phase on $\text{SiC}(000\bar{1})$

A  $(2\times 2)$  LEED pattern on a hexagonal surface is not an unambiguous indication for a  $(2\times 2)$  periodicity of the superstructure. Three domains of a  $(2\times 1)$  structure rotated by  $60^\circ$  with respect to each other would yield the same LEED pattern. By the STM image shown in Fig. 13a, however, the  $(2\times 2)$  periodicity is settled. The individual protrusions visible there have the corresponding  $6.2 \text{ \AA}$  lateral distance. In addition, the STM data show the typical signature of a simple adatom structure [8, 12]: Independent of the tunneling direction and voltage the vicinity of the adatom vacancy which is indicated by the arrow as well as the anti-phase boundaries (vertical bar) are completely undistorted. The AES data indicate a nearly bulk-like stoichiometry [8]. A holographic interpretation of the LEED intensities reveals the adatom site configuration [164]. In contrast to the  $(\sqrt{3}\times\sqrt{3})R30^\circ$ -periodic adatom phase on  $\text{SiC}(0001)$ , here an  $H3$  site is occupied, i.e. the adatom is positioned above the hexagonal space in the topmost bilayer (Fig. 13b,c). It should be noted that the holographic reconstruction shows a superposition of two 3-fold sites mutually rotated by  $60^\circ$  resulting from the presence of  $S_n$  and  $S_n^*$  domains on the hexagonal sample (see Sect. 2.2). The detailed reconstruction geometry and the surface stacking is determined by LEED crystallography [12]:

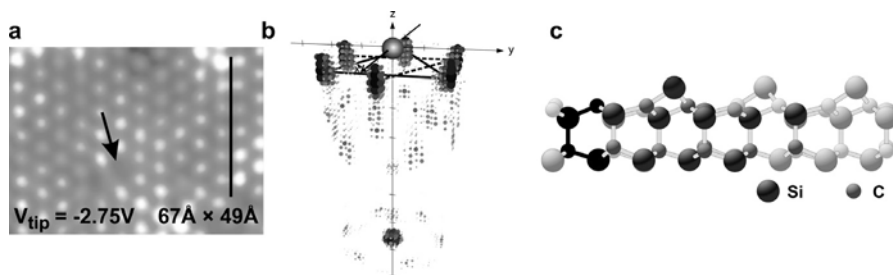


**Fig. 13.** (a) STM image of the  $(2\times 2)_C$  phase on  $\text{SiC}(000\bar{1})$ . An adatom vacancy is indicated by the *arrow*, an anti-phase domain boundary by the *vertical line*. (b) Holographic reconstruction of the adatom site from LEED raw intensities. (c) Best-fit structural model in side view

Noteworthy, the S1 stacking dominates the surface by 60% (6*H*-SiC) which also contrasts the  $(\sqrt{3}\times\sqrt{3})\text{R}30^\circ\text{-SiC}(0001)$  structure. Yet, also here this S1 dominance is not found in the silicate phase and only driven by the reconstruction [114, 156]. The reconstruction is a simple Si adatom structure in *H*3 sites with an adatom layer spacing  $d_{01} = 1.07 \text{ \AA}$  resulting in a Si-C bond length of  $L_{01} = 1.95 \text{ \AA}$  which is very close to the bulk value (1.89  $\text{\AA}$ ). The adatoms induce buckling displacements in the first substrate bilayer of 0.22  $\text{\AA}$  (C sublayer) and 0.20  $\text{\AA}$  (Si sublayer) and further reconstructions in deeper layers [60]. A respective side view of an S1 domain is shown in Fig. 13c.

Comparison of the results on the  $(\sqrt{3}\times\sqrt{3})\text{R}30^\circ\text{-SiC}(0001)$  and  $(2\times 2)_\text{C}\text{-SiC}(000\bar{1})$  structures indicates another possibility to influence the stacking at SiC surfaces in addition to controlling the chemical environment during preparation. The S3 surface termination found on 4*H*-SiC(0001) could serve as seed for the development of a different polytype such as 3*C*- or 6*H*-SiC, or the S1 stacking on SiC(000 $\bar{1}$ ) could induce growth of hexagonally stacked slabs.

#### 5.4 $\alpha$ -Planes and Diagonal Cuts Through the Hexagonal Unit Cell

As noted in Sect. 2.3 non-basal plane surface orientations of hexagonal polytypes have been used for growth experiments of bulk material and homoepitaxial films. SiC(11 $\bar{2}$ 0) and SiC(03 $\bar{3}$ 8) have evolved as promising substrate orientations [27]–[29]. Another, also interesting orientation is the (10 $\bar{1}$ 0) surface even though it seems not as well suited for growth purposes. Interestingly, the actual atomic structure of these surfaces is practically unknown. For the (11 $\bar{2}$ 0) and (10 $\bar{1}$ 0) LEED patterns were published after UHV based SiH<sub>4</sub> cleaning to remove the surface oxide. The surfaces appear well ordered and unreconstructed [165]. Further structural information can be gained from theoretical investigations [166]–[168], also for SiC(11 $\bar{2}$ 0) and SiC(10 $\bar{1}$ 0): There are several possibilities of bulk truncated surface arrangements on these surfaces partly due to the elongated unit cell of the higher hexagonal polytypes (4*H*, 6*H*). However, from energy minimization calculations it seems that the surface would prefer an extra Si termination with a superperiodicity, i.e. a reconstruction, that was not observed in the experiment. For SiC(03 $\bar{3}$ 8) no surface investigation has been reported neither experimentally nor theoretically.

## 6 Conclusion

In this article the atomic structure of SiC surfaces was reviewed. For both hexagonal SiC surfaces the phase diagram was discussed including well ordered and metastable structures. The detailed geometry of several phases has been resolved. Often, there exists a direct relevancy to the technological application of SiC in electronic devices. The  $(3\times 3)$  phase on SiC(0001) prepared in

UHV by annealing under simultaneous deposition of Si is well saturated and facilitates step flow growth for homoepitaxial and *homo-polytype* CVD and MBE layers. The structure analysis of the in situ prepared  $(\sqrt{3}\times\sqrt{3})R30^\circ$ -SiC(0001) phase determined the  $T_4$ -site Si-adatom reconstruction and revealed a dependence of the surface terminating stacking sequence on the chemical environment. By carefully controlling the preparation procedure, a cubic surface stacking sequence can be induced that breaks the periodic stacking of the substrate polytype. Thus, a change of polytypes might be induced during growth possibly allowing the development of polytype heterojunctions and periodic heterostructures. The unit cell assignment of the carbon rich phase on SiC(0001) was confirmed as  $(6\sqrt{3}\times6\sqrt{3})R30^\circ$  by LEED and STM. The  $(6\sqrt{3}\times6\sqrt{3})R30^\circ$  cell contains three atomic rings of slightly different size which are arranged in a quasi “ $(6\times6)$ ” pattern. On SiC(0001) the  $(2\times2)_C$  phase represents a Si adatom reconstruction. However, in complete contrast to the  $(\sqrt{3}\times\sqrt{3})R30^\circ$ -SiC(0001) phase, here the adatom sits in the true  $H3$  hollow site and the reconstruction induces a preference for hexagonal surface stacking termination. A well ordered  $\text{Si}_2\text{O}_3$  film can be generated by an ex situ hydrogen etching treatment of the SiC samples prior to their introduction into the UHV chamber. This silicate monolayer might represent a perfect seeding layer for the deposition of well ordered thick  $\text{SiO}_2$  films, thus overcoming the difficulties imposed by the poor quality of the SiC-oxide interface conventionally obtained by thermal oxidation. Surfaces treated by ultrapure hydrogen were found to be solely hydrogen terminated on an otherwise bulk truncated surface. Monitoring hydrogen and oxygen etching in UHV on an atomic level reveals complicated reaction pathways that seem to be dependent on the reconstruction phase and on surface orientation and polytype. Future SiC surface investigations may focus on the complicated structure of the non-basal plane surfaces  $(11\bar{2}0)$  and  $(03\bar{3}8)$ , as well as on questions related to adsorption and epitaxial films of metals, dopants and surfactants. Further effort will be necessary to understand the etching and oxidation processes on an atomic level. In summary, a strong relevancy of detailed structural properties of surface phases for growth and other technological applications has been demonstrated that can only be understood when the structure is analyzed in detail as carried out in the presented examples by a combination of experimental surface science techniques and theoretical investigations.

## Acknowledgements

This work was supported by the Deutsche Forschungsgemeinschaft through SFB 292. I would like to thank several colleagues for making available their manuscripts prior to publication. The enormous number of publications on the issue of SiC surfaces makes it inevitable that some work may have been overlooked or some trend may be under-represented in this article.

## References

1. R. Verma and P. Krishna: *Polymorphism and Polytypism in Crystals* (Wiley, New York, 1966)
2. W.J. Choyke, D.R. Hamilton and L. Patrick: Phys. Rev. **133**, A1163 (1964)
3. G.L. Harris (ed.): "Properties of Silicon Carbide", in *EMIS Datareviews Series*, No. 13 (Inspec, London, 1995)
4. N. Schulze, D. Barret and G. Pensl: phys. stat. sol. (a) **178**, 645 (2000)
5. J.A. Cooper, Jr.: phys. stat. sol. (a) **162**, 305 (1997)
6. W. Mönch: this volume (2003)
7. U. Starke, J. Schardt and M. Franke: Appl. Phys. A **65**, 587 (1997)
8. J. Bernhardt, M. Nerding, U. Starke and K. Heinz: Mat. Sci. Eng. B **61-62**, 207 (1999)
9. R. Kaplan: Surf. Sci. **215**, 111 (1989)
10. U. Starke, J. Schardt, J. Bernhardt, M. Franke, K. Reuter, H. Wedler, K. Heinz, J. Furthmüller, P. Käckell and F. Bechstedt: Phys. Rev. Lett. **80**, 758 (1998)
11. U. Starke, J. Schardt, J. Bernhardt, M. Franke and K. Heinz: Phys. Rev. Lett. **82**, 2107 (1999)
12. A. Seubert, J. Bernhardt, M. Nerding, U. Starke and K. Heinz: Surf. Sci. **454-456**, 45 (2000)
13. J. Bernhardt, J. Schardt, U. Starke and K. Heinz: Appl. Phys. Lett. **74**, 1084 (1999)
14. U. Starke, J. Schardt, J. Bernhardt and K. Heinz: J. Vac. Sci. Technol. A **17**, 1688 (1999)
15. U. Starke, J. Bernhardt, J. Schardt and K. Heinz: Surf. Rev. and Lett. **6**, 1129 (1999)
16. U. Starke: Mat. Sci. Forum **353-356**, 205 (2001)
17. K. Heinz, U. Starke, J. Bernhardt and J. Schardt: Appl. Surf. Sci. **162-163**, 9 (2000)
18. U. Starke: phys. stat. sol. (b) **202**, 475 (1997)
19. Phys. stat. sol. (b) Vol. **202** (1997)
20. V. Heine, C. Cheng and R.J. Needs: J. Am. Ceram. Soc. **74**, 2630 (1991)
21. L.S. Ramsdell: Am. Mineralogist **32**, 64 (1947)
22. J. Pollmann, P. Krüger and M. Sabisch: Phys. stat. sol. (b) **202**, 421 (1997)
23. V.M. Bermudez: Phys. stat. sol. (b) **202**, 447 (1997)
24. P. Soukiassian: Mat. Sci. Eng. B **61-2**, 506 (1999)
25. A. Catallani, G. Galli: Prog. Surf. Sci. **69**, 101 (2002)
26. H.W. Yeom: Surf. Sci. **433-435**, 392 (1999)
27. H. Yano, T. Hirao, T. Kimoto, H. Matsunami, K. Asano and Y. Sugawara: IEEE Electron Device Lett. **20** 611 (1999)
28. T. Kimoto, K. Hashimoto, K. Fujihira, K. Danno, S. Nakamura, Y. Negoro and H. Matsunami: MRS proceedings **742**, K1.1 (2003)
29. T. Hirao, H. Yano, T. Kimoto, H. Matsunami and H. Shiomi: Mater. Sci. Forum **389-393**, 1065 (2002)
30. W. Kern and D.A. Puotinen: RCA Rev. **31**, 187 (1970)
31. J. Schardt, Ch. Bram, S. Müller, U. Starke, K. Heinz and K. Müller: Surf. Sci. **337**, 232 (1995)

32. U. Starke, J. Bernhardt, M. Franke, J. Schardt and K. Heinz: *Diam. Rel. Mat.* **6**, 1349 (1997)
33. J. Schardt, J. Bernhardt, U. Starke and K. Heinz: *Surf. Rev. and Lett.* **5**, 181 (1998)
34. M. Hollering, J. Bernhardt, J. Schardt, A. Ziegler, R. Graupner, B. Mattern, A.P.J. Stampfl, U. Starke, K. Heinz and L. Ley: *Phys. Rev. B* **58**, 4992 (1998)
35. J. Schardt, J. Bernhardt, M. Franke, U. Starke and K. Heinz: *Mat. Sci. Forum* **264–268**, 343 (1998)
36. F. Owman, C. Hallin, P. Martensson and E. Janzen: *J. Cryst. Growth* **167**, 391 (1996)
37. N. Sieber, T. Seyller, L. Ley, M. Polcik, D. James, J.D. Riley and R.C.G. Leckey: *Mat. Sci. Forum* **389–393**, 713 (2002)
38. N. Sieber, B. F. Mantel, T. Seyller, J. Ristein, L. Ley, T. Heller, D.R. Batchelor and D. Schmeisser: *Appl. Phys. Lett.* **78**, 1216 (2001)
39. U. Starke, Ch. Bram, P.-R. Steiner, W. Hartner, L. Hammer, K. Heinz and K. Müller: *Appl. Surf. Sci.* **89**, 175 (1995)
40. F.S. Tautz, S. Sloboshanin, U. Starke and J.A. Schaefer: *Surf. Sci. Lett.* **470**, L25 (2000)
41. K. Heinz: *Rep. Prog. Phys.* **58**, 637 (1995)
42. P.J. Rous: *Prog. Surf. Sci.* **39**, 3 (1992)
43. K. Heinz, R. Döll and M. Kottcke: *Surf. Rev. Lett.* **3**, 1651 (1996)
44. M. Kottcke and K. Heinz: *Surf. Sci.* **376**, 352 (1997)
45. J.B. Pendry: *J. Phys. C* **13**, 937 (1980)
46. K. Reuter, J. Bernhardt, H. Wedler, J. Schardt, U. Starke and K. Heinz: *Phys. Rev. Lett.* **79**, 4818 (1997)
47. H. Lüth: *Surfaces and interfaces of solids* (Springer, Berlin, 2001)
48. D.P. Woodruff, T.A. Delchar: *Modern techniques of surface science* (University Press, Cambridge, 1994)
49. P. Badziag: *Surf. Sci.* **337**, 1 (1995)
50. U. Starke, M. Franke, J. Bernhardt, J. Schardt, K. Reuter and K. Heinz: *Mat. Sci. Forum*, **264–268**, 321 (1998)
51. I. Forbeaux, J.M. Themlin, A. Charrier, F. Thibaudau and J.M. Debever: *Appl. Surf. Sci.* **162**, 406 (2000)
52. L. Li, Y. Hasegawa, T. Sakurai and I.S.T. Tsong: *J. Appl. Phys.* **80**, 2524 (1996)
53. J.-M. Themlin, I. Forbeaux, V. Langlais, H. Belkhir and J.-M. Debever: *Europhys. Lett.* **39**, 61 (1997)
54. X.N. Xie and K.P. Loh: *Appl. Phys. Lett.* **77**, 3361 (2000)
55. X.N. Nie, H.Q. Wang, A.T.S. Wee and K.P. Loh: *Surf. Sci.* **478**, 57 (2001)
56. C. Benesch, M. Fartmann and H. Merz: *Phys. Rev. B* **64**, 205314 (2001)
57. W.J. Ong, E.S. Tok, H. Xu and A.T.S. Wee: *Appl. Phys. Lett.* **80**, 3406 (2002)
58. J.R. Ahn, S.S. Lee, N.D. Kim, C.G. Hwang, J.H. Min and J.W. Chung: *Surf. Sci.* **516**, L529 (2002)
59. U. Starke, J. Bernhardt, J. Schardt, A. Seubert and K. Heinz: *Mat. Sci. Forum* **338–342**, 341 (2000)
60. J. Bernhardt: PhD thesis, Univ. Erlangen (2001)
61. L. Li and T. Sakurai: in *Advances in Scanning Probe Microscopy*, ed. by T. Sakurai and Y. Watanabe (Springer, Berlin, 2000) p. 65
62. M. Naitoh, J. Takami, S. Nishigaki and N. Toyama: *Appl. Phys. Lett.* **75**, 650 (1999)

63. J. Bernhardt, M. Franke, U. Starke and K. Heinz: to be published
64. J. Schardt, J. Bernhardt, U. Starke and K. Heinz: *Phys. Rev. B* **62**, 10335 (2000)
65. M.A. Kulakov, G. Henn and B. Bullemer: *Surf. Sci.* **346**, 49 (1996)
66. L. Li and I.S.T. Tsong: *Surf. Sci.* **351**, 141 (1996)
67. D.K. Saldin and P.L. De Andres: *Phys. Rev. Lett.* **64**, 1270 (1990)
68. K. Heinz, U. Starke and J. Bernhardt: *Prog. Surf. Sci.* **64**, 163 (2000)
69. K. Reuter, J. Schardt, J. Bernhardt, H. Wedler, U. Starke and K. Heinz: *Phys. Rev. B* **58**, 10806 (1998)
70. J. Furthmüller, P. Käckell, F. Bechstedt, A. Fissel, K. Pfenninghaus, B. Schröter and W. Richter: *J. Electron. Mater.* **27**, 848 (1998)
71. P. Badziag: *Surf. Sci.* **404**, 822 (1998)
72. T. Kimoto, A. Itoh, H. Matsunami and T. Okano: *J. Appl. Phys.* **81**, 3494 (1997)
73. S. Tanaka, R.S. Kern and R.F. Davis: *Appl. Phys. Lett.* **65**, 2851 (1994)
74. A. Fissel, B. Schröter and W. Richter: *Appl. Phys. Lett.* **66**, 3182 (1995)
75. A.J. Van Bommel, J.E. Crombeen and A. Van Tooren: *Surf. Sci.* **48**, 463 (1975)
76. S. Nakanishi, H. Tokutaka, K. Nishimori, S. Kishida and N. Ishihara: *Appl. Surf. Sci.* **41–42**, 44 (1989)
77. V. van Elsbergen, T.U. Kampen and W. Mönch: *Surf. Sci.* **365**, 443 (1996)
78. F. Owman and P. Mårtensson: *Surf. Sci. Lett.* **330**, L639 (1995)
79. V.M. Bermudez: *Appl. Surf. Sci.* **84**, 45 (1995)
80. L.I. Johansson, F. Owman and P. Martensson: *Surf. Sci. Lett.* **360**, L483 (1996)
81. L.I. Johansson, F. Owman and P. Martensson: *Phys. Rev. B* **53**, 13793 (1996)
82. T. Tsukamoto, M. Hirai, M. Kusaka, M. Iwami, T. Ozawa, T. Nagamura and T. Nakata: *Appl. Surf. Sci.* **114**, 467 (1997)
83. T. Tsukamoto, M. Hirai, M. Kusaka, M. Iwami, T. Ozawa, T. Nagamura and T. Nakata: *Surf. Sci.* **371**, 316 (1997)
84. T. Jikimoto, T. Tsukamoto, A. Kinoshita, Y. Satoh, M. Hirai, M. Kusaka, M. Iwami and T. Nakata: *Appl. Surf. Sci.* **117**, 794 (1997)
85. R. Gunnella, J.Y. Veuillen, A. Berthet and T.A.N. Tan: *Surf. Rev. Lett.* **5**, 187 (1998)
86. V. Ramachandran and R.M. Feenstra: *Phys. Rev. Lett.* **82**, 1000 (1999)
87. J.E. Northrup and J. Neugebauer: *Phys. Rev. B* **52**, R17001 (1995)
88. F. Bechstedt, P. Käckell, A. Zywietz, K. Karch, B. Adolph, K. Tenelsen and J. Furthmüller: *Phys. stat. sol. (b)* **202**, 35 (1997)
89. M. Sabisch, P. Krüger and J. Pollmann: *Phys. Rev. B* **55**, 10561 (1997)
90. P. Badziag: *Surf. Sci.* **413**, 502 (1998)
91. L.I. Johansson, F. Owman and P. Martensson: *Surf. Sci. Lett.* **360**, L478 (1996)
92. J. Furthmüller, F. Bechstedt, H. Husken, B. Schröter and W. Richter: *Phys. Rev. B*, **58**, 13712 (1998)
93. A. Coati, M. Sauvage-Simkin, Y. Garreau, R. Pinchaux, T. Argunova and K. Aïd: *Phys. Rev. B* **59**, 12224 (1999)
94. T. Fujino, T. Fuse, J.T. Ryu, K. Inudzuka, Y. Yamazaki, M. Katayama and K. Oura: *Jpn. J. Appl. Phys.* **39**, 6412 (2000)
95. J. Bernhardt, A. Seubert, J. Schardt, U. Starke and K. Heinz: to be published

96. N. Sieber, T. Stark, T. Seyller, L. Ley, C. A. Zorman and M. Mehregany: *Appl. Phys. Lett.* **80** 4726 (2002); *Appl. Phys. Lett.* **81** 1534 (2002)
97. M.J. Rutter and V. Heine: *J. Phys. CM* **9**, 8213 (1997)
98. U. Grossner, A. Fissel, J. Furthmüller, W. Richter and F. Bechstedt: *Mat. Sci. Forum* **353–353**, 211 (2000)
99. M.C. Righi, C.A. Pignedoli, G. Borghi, R. Di Felice, C.M. Bertoni and A. Catellani: *Phys. Rev. B* **66**, 45320 (2002)
100. A. Fissel, U. Kaiser, B. Schröter, W. Richter and F. Bechstedt: *Appl. Surf. Sci.* **184**, 37 (2001)
101. A. Fissel: *J. Cryst. Growth* **227**, 805 (2001)
102. M. Diani, L. Simon, L. Kubler, D. Auber, I. Matko, B. Chenevier, R. Madar and M. Audier: *J. Cryst. Growth* **235**, 95 (2002)
103. F. Amy, P. Soukiasian, Y.K. Hwu and C. Brylinski: *Surf. Sci.* **464**, L691 (2000)
104. G. Santoro, S. Scandolo and E. Tosatti: *Surf. Sci.* **454**, 534 (2000)
105. F. Owman and P. Mårtensson: *Surf. Sci.* **369**, 126 (1996)
106. L.S.O. Johansson, L. Duda, M. Laurenzis, M. Krieffewirth and B. Reihl: *Surf. Sci.* **445**, 109 (2000)
107. J.E. Northrup and J. Neugebauer: *Phys. Rev. B* **57**, R4230 (1998)
108. M. Rohlfing and J. Pollmann: *Phys. Rev. Lett.* **84**, 135 (2000)
109. V.I. Anisimov, A.E. Bedin, M.A. Korotin, G. Santoro, S. Scandolo and E. Tosatti: *Phys. Rev. B* **61**, 1752 (2000)
110. V.A. Gasparov, M. Riehl-Chudoba, B. Schröter and W. Richter: *Europhys. Lett.* **51**, 527 (2000)
111. R. Rohlfing: *Appl. Phys. A* **72**, 413 (2000)
112. M. Hollering, F. Maier, N. Sieber, M. Stammer, J. Ristein, L. Ley, A.P.J. Stampfl, J.D. Riley, R.C.G. Leckey, F.P. Leisenberger and F.P. Netzer: *Surf. Sci.* **442**, 531 (1999)
113. W.C. Lu, P. Krüger and J. Pollmann: *Phys. Rev. B* **61**, 13737 (2000)
114. J. Bernhardt, J. Schardt, U. Starke and K. Heinz: *Mat. Sci. Forum* **338–342**, 383 (2000)
115. N. Sieber, M. Hollering, J. Ristein and L. Ley: *Mat. Sci. Forum* **338–342** 391 (2000)
116. U. Köhler: priv. communication
117. V.V. Afanasev, M. Bassler, G. Pensl, M.J. Schulz and E. Stein von Kamienski: *J. Appl. Phys.* **79**, 3108 (1996)
118. B. Hornetz, H.-J. Michel and J. Halbritter: *J. Mater. Res.* **9**, 3088 (1994)
119. C. Öneby and C.G. Pantano: *J. Vac. Sci. Technol. A* **15**, 1097 (1997)
120. A. Gözl, G. Lucovsky, K. Koh, D. Wolfe, H. Niimi and H. Kurz: *J. Vac. Sci. Technol. B* **15**, 1097 (1997)
121. V. van Elsbergen, O. Janzen and W. Mönch: *Mat. Sci. Eng. B* **46**, 366 (1997)
122. C. R. Stoldt, C. Carraro and R. Maboudian: *Surf. Sci.* **466**, 66 (2000)
123. J. Takami, M. Naitoh, I. Yokoh, S. Nishigaki and N. Toyama: *Surf. Sci.* **482**, 359 (2001).
124. T. Fujino, T. Fuse, J.T. Ryu, K. Inudzuka, Y. Yamazaki, M. Katayama and K. Oura: *Appl. Surf. Sci.* **169**, 113 (2001)
125. L. Muehlhoff, M.J. Bozack, W.J. Choyke and J.T. Jates, Jr.: *J. Appl. Phys.* **60**, 2558 (1986)
126. J.M. Powers and G.A. Somorjai: *Surf. Sci.* **244**, 39 (1991)

127. F. Amy, H. Enriquez, P. Soukiassian, P.F. Storino, Y.J. Chabal, A.J. Mayne, G. Dujardin, Y.K. Hwu and C. Brylinski: *Phys. Rev. Lett.* **86**, 4342 (2001)
128. F. Amy, P. Soukiassian, Y.K. Hwu and C. Brylinski: *Appl. Phys. Lett.* **75**, 3360 (1999)
129. F. Amy, P. Soukiassian, Y.K. Hwu and C. Brylinski: *Phys. Rev. B* **65**, 165323 (2002)
130. O. Kubo, T. Kobayashi, N. Yamaoka, S. Itou, M. Katayama, K. Oura and H. Ohkado: *Appl. Phys. Lett.* **80**, 4330 (2002)
131. Y. Hoshino, T. Nishimura, T. Yoneda, K. Ogawa, H. Namba and Y. Kido: *Surf. Sci.* **505**, 234 (2002)
132. C. Virojanadara and L.I. Johansson: *Surf. Sci.* **505**, 358 (2002)
133. C. Virojanadara and L.I. Johansson: *Surf. Sci.* **472**, L145 (2001)
134. L. Simon, L. Kubler, A. Ermoloeff and T. Billon: *Phys. Rev. B* **60**, 5673 (1999)
135. M.L. O'Brien, C. Koitzsch and R.J. Nemanich: *J. Vac. Sci. Technol. B* **18**, 1776 (2000)
136. S.W. Wang, M. Di Ventura, S.G. Kim and S.T. Pantelides: *Phys. Rev. Lett.* **86**, 5946 (2001)
137. S.T. Pantelides, G. Duscher, M. Di Ventura, R. Buczko, K. McDonald, M.B. Huang, R.A. Weller, I. Baumvol, F.C. Stedile, C. Radtke, S.J. Pennycook, G. Chung, C.C. Tin, J.R. Williams, J.H. Won and L.C. Feldman: *Mat. Sci. Forum* **338–343**, 1133 (2000)
138. R. Buczko, S.J. Pennycook and S.T. Pantelides: *Phys. Rev. Lett.* **84**, 943 (2000)
139. M. Di Ventura and S.T. Pantelides: *Phys. Rev. Lett.* **83**, 1624 (1999)
140. G.G. Jernigan, R.E. Stahlbush, M.K. Das, J.A. Cooper and L.A. Lipkin: *Appl. Phys. Lett.* **74**, 1448 (1999)
141. K. McDonald, L.C. Feldman, R.A. Weller, G.Y. Chung, C.C. Tin and J.R. Williams: *Journ. Appl. Phys.* **93**, 2257 (2003)
142. J.R. Williams, G.Y. Chung, C.C. Tin, K. McDonald, D. Farmer, R.K. Chanana, R.A. Weller, S.T. Pantelides, O.W. Holland, M.K. Das and L.C. Feldman: *Mat. Sci. Forum* **389–393**, 967 (2002)
143. N. Sieber, B.F. Mantel, T. Seyller, J. Ristein and L. Ley: *Diam. Rel. Mat.* **10**, 1291 (2001)
144. N. Sieber, T. Seyller, B.F. Mantel, J. Ristein and L. Ley: *Mat. Sci. Forum* **353–356**, 223 (2001)
145. N. Sieber, T. Seyller, R. Graupner, L. Ley, R.P. Mikalo, P. Hoffmann, D. Batchelor and D. Schmeisser: *Mat. Sci. Forum* **389–393**, 717 (2002)
146. H. Tsuchida, I. Kamata, and K. Izumi: *Jpn. J. Appl. Phys. Part 2*, **36**, L699 (1997)
147. L. Li and I.S.T. Tsong: *Surf. Sci.* **364**, 54 (1996)
148. M. Hirai, Y. Marumoto, M. Kusaka, M. Iwami, T. Ozawa, T. Nagamura and T. Nakata: *Appl. Surf. Sci.* **114**, 360 (1997)
149. O. Kubo, T. Harada, T. Kobayashi, J.T. Ryu, M. Katayama and K. Oura: *Jap. Journ. Appl. Phys. Part 1* **39**, 4343 (2000)
150. M. Iwami, N. Hattori, T. Fujimoto, M. Hirai, M. Kusaka, T. Morii, H. Watabe and M. Watanabe: *Surf. Rev. and Lett.* **7**, 679 (2000)
151. J.Y. Veuillen, T.A.N. Tan, I. Tsiaoussis, N. Frangis, M. Brunel and R. Gunnella: *Diam. Rel. Mat.* **8**, 352 (1999)
152. H.J. Im, B. Kaczer, J.P. Pelz, S. Limpijumnong, W.R.L. Lambrecht and W.J. Choyke: *Journ. of Elec. Mat.* **27**, 345 (1998)

153. C. Virojanadara, R.A. Glans, T. Balasubramanian, L.I. Johansson, E.B. Macak, Q. Wahab and L.D. Madsen: *Journ. Elec. Mat.* **31**, 1353 (2002)
154. U. Grossner, J. Furthmüller and F. Bechstedt: *Phys. Rev. B* **64**16, 165308 (2001)
155. L. Muehlhoff, W.J. Choyke, M.J. Bozack and J.T. Jates, Jr.: *J. Appl. Phys.* **60**, 2842 (1986)
156. J. Bernhardt, A. Seubert, M. Nerding, U. Starke and K. Heinz: *Mat. Sci. Forum* **338-342**, 345 (2000)
157. I. Forbeaux, J.M. Themlin and J.M. Debever: *Surf. Sci.* **442**, 9 (1999)
158. L.I. Johansson, P.A. Glans and N. Hellgren: *Surf. Sci.* **405**, 288 (1998)
159. H.E. Hoster, M.A. Kulakov and B. Bullemer: *Surf. Sci.* **382**, L658 (1997)
160. L. Li, Y. Hasegawa, I.S.T. Tsong and T. Sakurai: *Journ. de Physique IV* **6**, 167 (1996)
161. M. Hollering, B. Mattern, F. Maier, L. Ley, A.P.J. Stampfl, J. Xue, J.D. Riley and R.C.G. Leckey: *Mat. Sci. Forum* **264-268**, 331 (1998)
162. M. Hollering: Thesis, Universität Erlangen-Nürnberg (2000)
163. P. Badziag: *Surf. Sci.* **236**, 48 (1990)
164. A. Seubert, D.K. Saldin, J. Bernhardt, U. Starke and K. Heinz: *J. Phys. Condens. Mat.* **12**, 5527 (2000)
165. S.W. King, R.S. Kern, M.C. Benjamin, J.P. Barnak, R.J. Nemanich and R.F. Davis: *J. Electrochem. Soc.* **146**, 3448 (1999)
166. E. Rauls, J. Elsner, R. Gutierrez and T. Frauenheim: *Solid State Commun.* **111**, 459 (1999)
167. E. Rauls, Z. Hajnal, P. Deak and T. Frauenheim: *Mat. Sci. Forum* **338-342**, 365 (2000)
168. E. Rauls, Z. Hajnal, P. Deak and T. Frauenheim: *Phys. Rev. B* **64**, 245323 (2001)

# The Continuum of Interface-Induced Gap States – The Unifying Concept of the Band Lineup at Semiconductor Interfaces – Application to Silicon Carbide

W. Mönch

## 1 Introduction

In one of his pioneering articles, Schottky [1] described the many thorny roundabout routes which finally ended in his *Semiconductor Theory of the Blocking Layer* [2] at metal-semiconductor or, as they are called to honor his many basic contributions to this field, Schottky contacts. The ensuing endeavors for a physical understanding of the mechanisms which determine the barrier heights in Schottky contacts were again fraught with difficulties. Heine [3] further developed Bardeen's basic concept [4] of interface states at metal-semiconductor interfaces. He noted that *for energies in the semiconductor band gap the volume states of the metal have tails in the semiconductor*. Tejedor and Flores [5] applied this idea to semiconductor heterostructures where for energies in the band-edge discontinuities the volume states of the one semiconductor tunnel in the other one.

The continua of interface-induced gap states (IFIGS), as they were called later, are an *intrinsic* property of the semiconductors and they are the *fundamental* mechanism that determines both the barrier heights of Schottky contacts and the band offsets of heterostructures. The IFIGS derive from the valence- and conduction-band states of the semiconductor. They will carry a net charge the sign of which depends on the Fermi-level position relative to their branch point where their character changes from predominantly valence-band- or donor-like to mostly conduction-band- or acceptor-like. Hence, the IFIGS give rise to intrinsic interface dipoles. Both Schottky barrier heights and band offsets in heterostructures thus divide up into a zero-charge-transfer term and a dipole contribution.

From a more chemical point of view, these interface dipoles are attributed to the partial ionic character of the covalent bonds between atoms right at the interface. In generalizing Pauling's electronegativity concept [6], the charge transfer at semiconductor interfaces is described by the difference of the electronegativities of the atoms involved. In combining the physical IFIGS and the chemical electronegativity concept the dipole contributions of the Schottky barrier-heights as well as of the heterostructure band-offsets vary proportional to the difference of the electronegativities of the metal and the semiconductor and of the two semiconductors, respectively, which are forming the contact.

While the theoreticians appreciated Heine's IFIGS concept at once the experimentalists adopted it very slowly. One of the reasons was that the theoretical IFIGS lines marked upper limits of the barrier heights of real Schottky contacts only [7, 8]. Schmitsdorf et al. [9] resolved this dilemma in their experimental studies of Ag/*n*-Si(111) contacts. They observed a linear decrease of the effective barrier heights with increasing ideality factors which they determined from the current-voltage or  $I/V$  characteristics of their diodes. Such a behavior is observed with all Schottky contacts investigated so far. Schmitsdorf et al. attributed this correlation to the existence of patches with decreased barrier heights and lateral dimensions smaller than the depletion layer width. Most importantly, they concluded that the barrier heights of the laterally homogeneous contacts are obtained from plots of effective barrier heights versus the ideality factors by extrapolation to the ideality factor that is determined by the image-force- or Schottky effect [10] only.

Ballistic-electron-emission microscopy (BEEM), which was invented by Kaiser and Bell [11], makes it possible to measure nm-scale distributions of the local barrier heights of Schottky contacts. Such histograms are well approximated by Gaussian functions. Their maxima represent the barrier height of the laterally homogeneous area surrounding the nm-scale patches with reduced or increased barrier height.

The barrier heights of laterally homogeneous Schottky contacts evaluated from the linear correlation between effective barrier heights and ideality factors and from BEEM barrier-height distributions are identical within the margins of experimental error. Mönch [12, 13] plotted the barrier heights of laterally homogeneous Si, GaN, GaP, GaAs, ZnSe and 3C-, 6H-, and 4H-SiC contacts versus the difference of the metal and the semiconductor electronegativities and found excellent agreement with the predictions of the IFIGS-and-electronegativity theory.

The IFIGS dipole term or, in other words, the difference of the metal and semiconductor electronegativities determines the dependence of the barrier heights of Schottky contacts with different metals on one and the same semiconductor. The electronegativities of the semiconductors are equal to within 10% since the elements which constitute the semiconductors are all placed in the middle of the Periodic Table of the Elements. Hence, the IFIGS dipole term of semiconductor heterostructures will be small and may be neglected [14]. The valence-band offsets of lattice-matched and non-polar and of metamorphic heterostructures should thus equal the difference of the branch-point energies of the semiconductors in contact.

## 2 Experimental SiC Data Base

### 2.1 Barrier Heights of Laterally Homogeneous SiC Schottky Contacts

#### 2.1.1 $I/V$ Characteristics

The current transport in real Schottky contacts occurs via thermionic emission and the current-voltage characteristics may be written as

$$I = AA_R^* T^2 \exp(-\Phi_{\text{Bn}}^{\text{eff}}/k_B T) \exp(e_0 V_c / nk_B T) [1 - \exp(-e_0 V_c / k_B T)] , \quad (1)$$

where  $A$  is the diode area,  $A_R^*$  is the effective Richardson constant of the semiconductor, and  $T$ ,  $k_B$ , and  $e_0$  are the temperature, Boltzmann's constant, and the electronic charge, respectively. The externally applied bias  $V_a$  divides up into a voltage drop  $V_c$  across the depletion layer of the Schottky contact and an  $IR$  drop at the series resistance  $R_s$  of the diode, i.e.,  $V_c = V_a - IR_s$ . For *ideal*, i.e., intimate, abrupt, defect-free, and, above all, laterally homogeneous Schottky contacts the effective zero-bias barrier height  $\Phi_{\text{Bn}}^{\text{eff}}$  equals the difference  $\Phi_{\text{Bn}}^{\text{hom}} - \delta\Phi_{\text{if}}^0$  between the homogeneous barrier height and the zero-bias image-force lowering. The ideality factor  $n$  describes the voltage dependence of the barrier height. For *real* diodes one finds  $n > n_{\text{if}}$  or, in other words, the ideality factors are generally larger than the ideality factor  $n_{\text{if}}$  which is determined by the image-force effect only.

The effective barrier heights and the ideality factors of real Schottky diodes fabricated under experimentally identical conditions vary from one specimen to the next. However, the effective barrier heights become smaller as the ideality factors increase. As an example, Fig. 1 displays  $\Phi_{\text{Bn}}^{\text{eff}} - n$  data

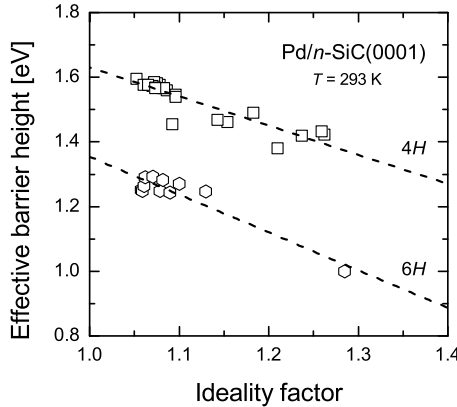


**Fig. 1.** Effective barrier heights versus ideality factors determined from  $I/V$  curves of Pd/ $n$ -4H-SiC(0001) and Pd/ $n$ -6H-SiC(0001) contacts at room temperature. The dashed lines are linear least-squares fits to the data. Data from Im et al. [15]

of Pd contacts on  $n$ -4H-SiC(0001) and  $n$ -6H-SiC(0001) substrates [15]. The dashed lines are linear least-squares fits to the data points.

Schmitsdorf et al. [9] observed such a linear  $\Phi_{\text{Bn}}^{\text{eff}} - n$  correlation with Ag/ $n$ -Si(111) contacts and formulated the dependence of the effective barrier heights on the ideality factors as

$$\Phi_{\text{Bn}}^{\text{eff}} = \Phi_{\text{Bn}}^{\text{nif}} - \varphi_{\text{p}}(n - n_{\text{if}}), \quad (2)$$

where  $\Phi_{\text{Bn}}^{\text{nif}}$  is the barrier height at the ideality factor  $n_{\text{if}}$ . Several conclusions may be drawn from this relation. First, the  $\Phi_{\text{Bn}}^{\text{eff}} - n$  correlation evidences that more than just one physical mechanism determines the barrier heights of real Schottky contacts. Second, the extrapolation of  $\Phi_{\text{Bn}}^{\text{eff}}$  versus  $n$  curves to  $n_{\text{if}}$  leaves all mechanisms out of consideration which cause a larger bias-dependence of the barrier height than the image-force effect itself. Third, the extrapolated barrier heights  $\Phi_{\text{Bn}}^{\text{nif}}$  equal the zero-bias barrier height  $\Phi_{\text{Bn}}^{\text{hom}} - \delta\Phi_{\text{if}}^0$

**Table 1.** Barrier heights of laterally homogeneous SiC Schottky contacts obtained by linear extrapolation of  $\Phi_{\text{B}}^{\text{eff}}$  versus  $n$  curves to  $n_{\text{if}}$ , from histograms of BEEM barrier heights, and by internal and external photoemission spectroscopy

Substrate	Orientation	Metal	Method	$\Phi_{\text{Bn}}^{\text{hom}}$ [eV]	Reference
3C-SiC	(001)	Au	$I/V$	0.84*	Constantinidis et al. [25]
4H-SiC	(0001)	Cs	PES	1.00	van Elsbergen [26]
	(0001)	Ti	$I/V$	1.26	Defives et al. [27]
	(0001)	Ti	$I/V$	1.14	Skromme et al. [24]
	(0001)	Ni	$I/V$	1.57*	Khemka et al. [28], Schoen et al. [29]
	(0001)	Ni	$I/V$	1.60	Skromme et al. [23]
6H-SiC	(-1-210)	Mo	IPEYS	1.66	Bai et al. [30]
	(0001)	Pd	$I/V$	1.63*	Im et al. [15]
	(0001)	Pt	$I/V$	1.68*	Im et al. [15]
	(0001)	Pt	$I/V$	1.63	Skromme et al. [23]
	(1-100)	Pt	IPEYS	1.62	Shigiltchoff et al. [31]
	(0001)	Cs	PES	0.74	van Elsbergen et al. [32]
	(0001)	Cu	$I/V$	1.26	Suezaki et al. [33]
	(000-1)	Ti	$I/V$	1.11*	Shigiltchoff et al. [34]
	(000-1)	Ti	$I/V$	1.095	Bai et al. [30]
	(0001)	Pd	$I/V$	1.35*	Im et al. [15]
	(0001)	Pd	BEEM	1.30	
	(0001)	Pd	$I/V$	1.24	Im et al. [21]
	(0001)	Pd	BEEM	1.25	
	(0001)	Pt	$I/V$	1.31*	Im et al. [15]
	(0001)	Pt	BEEM	1.30	
	(0001)	Pt	IPEYS	1.38	Shigiltchoff et al. [31]

\* Data obtained by extrapolation to  $n = 1$ .

of the laterally homogeneous contact. Table 1 summarizes barrier heights of laterally homogeneous SiC Schottky contacts which were determined by extrapolation of  $\Phi_{\text{Bn}}^{\text{eff}} - n$  curves to  $n_{\text{if}}$ .

The two extrapolated barrier heights  $\Phi_{\text{Bn}}^{\text{uf}}$  of the data plotted in Fig. 1 differ by  $0.28 \pm 0.14$  eV. Within the margins of experimental error this value equals the difference of the band gaps of the two polytypes  $4H$  and  $6H$ . Hence, Pd/ $p$ -SiC contacts would have identical barrier heights irrespective of the specific polytype.

Patches of reduced barrier height with lateral dimensions smaller than the depletion layer width which are embedded in large areas of laterally homogeneous barrier height are the only model known that explains a lowering of effective barrier heights with increasing ideality factors. In their phenomenological studies of such patchy Schottky contacts, Freeouf et al. [16, 17] found the potential distribution to show a saddle point *in front* of such nm-size patches of reduced barrier height. Figure 2 explains this behavior. In front of, for example, circular patches, the barrier height right at the saddle point is lowered with respect to the laterally homogeneous barrier height  $\Phi_{\text{Bn}}^{\text{hom}}$  of the embedding area by [18]

$$\delta\Phi_{\pi}^{\text{sad}} = \gamma_{\pi} [(\Phi_{\text{Bn}}^{\text{hom}} - W_{\text{n}} - e_0 V_{\text{c}}) k_{\text{B}} T / L_{\text{D}}^2]^{1/3}, \quad (3)$$

where  $W_{\text{n}} = W_{\text{cb}} - W_{\text{F}}$  and  $L_{\text{D}}$  are the energy distance from the Fermi level to the conduction-band edge in the bulk and the Debye length of the semiconductor, respectively. The saddle-point barrier height is determined by the patch parameter

$$\gamma_{\pi} = 3 (\Delta_{\pi} R_{\pi}^2 / 4)^{1/3}, \quad (4)$$

where  $R_{\pi}$  is the radius and  $\Delta_{\pi}$  the barrier-height reduction of the patch.

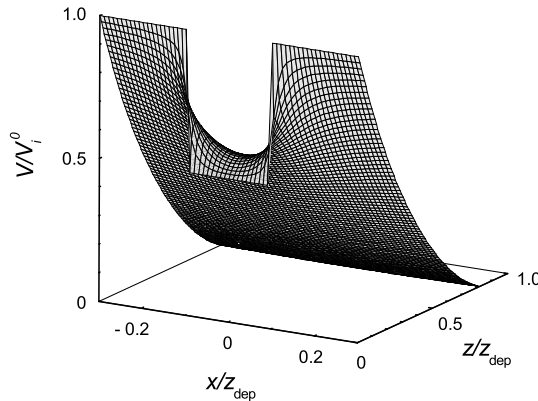


**Fig. 2.** Calculated potential distribution underneath a patch embedded in a region of larger interface band-bending or, what is the same, larger barrier height

Equation (3) shows that the saddle-point barrier height strongly depends on the voltage drop  $V_c$  across the depletion layer. Already Freeouf et al. [16, 17] simulated the current transport in such patchy Schottky contacts and found a reduction of the effective barrier height and a correlated increase of the ideality factor as they reduced the lateral dimensions of the patches. However, they missed to note that the barrier heights of the laterally homogeneous contacts may be obtained from  $\Phi_{\text{Bn}}^{\text{eff}}$  versus  $n$  plots by extrapolation to  $n_{\text{if}}$ . It remained to Schmitsdorf et al. [9] to draw this conclusion.

### 2.1.2 BEEM

Ballistic-electron-emission microscopy (BEEM) [11], is *the* experimental tool for measuring spatial variations of the barrier height on the nm-scale [19]. A tip injects almost monoenergetic electrons into the metal film which will reach the semiconductor as ballistic electrons provided they lose no energy on their way through the metal. Hence, the collector current  $I_{\text{coll}}$  is expected to set in when the ballistic electrons surpass the metal-semiconductor barrier, i.e., if the voltage  $V_{\text{tip}}$  applied between tip and metal film exceeds the *local* potential barrier  $\Phi_{\text{Bn}}^{\text{loc}}(z)/e_0$ . Bell and Kaiser [20] derived the square-law

$$I_{\text{coll}}(z) = R^* I_{\text{tip}} [e_0 V_{\text{tip}} - \Phi_{\text{Bn}}^{\text{loc}}(z)]^2 \quad (5)$$

of the BEEM  $I_{\text{coll}}/V_{\text{tip}}$  characteristics where  $I_{\text{tip}}$  is the injected tunnel current. BEEM measures *local* barrier heights, i.e., the saddle-point barrier heights in front of nm-size patches rather than their lower barrier heights right at the interface.

Im et al. [21] investigated Pd/*n*-6H-SiC(0001) contacts. With some of their diodes they *simultaneously* measured their conventional  $I/V$  curves and BEEM  $I_{\text{coll}}(z)/V_{\text{tip}}$  characteristics at 800 different locations over the surfaces, each separated by at least 30 nm. From fits of the thermionic-emission relation (1) to the  $I/V$  curves of the *macroscopic* diodes and of the Bell-Kaiser square-law (5) to the *nanoscopic*  $I_{\text{coll}}(z)/V_{\text{tip}}$  characteristics, they determined the effective barrier heights and ideality factors and the local BEEM barrier heights, respectively. Figure 3 displays BEEM barrier-heights distributions of two of their diodes, a “good” and a “bad” one. They are distinguished by their ideality factors, 1.06 and 1.49, which are close to and much larger than  $n_{\text{if}} = 1.01$ . Most remarkably, the two BEEM barrier height distributions are essentially identical. As usual, they are well described by Gaussian distributions. Their center values and standard deviations are 1.271 eV and 29 meV and 1.268 eV and 33 meV, respectively. The standard deviations are slightly larger than the margins of experimental error of the individual BEEM values, approximately 20 meV.

Their findings led Im et al. [21] to conclude that there exist two types of patches, intrinsic and extrinsic ones. Im et al. assumed the intrinsic patches to occupy a fractional area  $C_{i\pi}$  of the diode and the distribution function

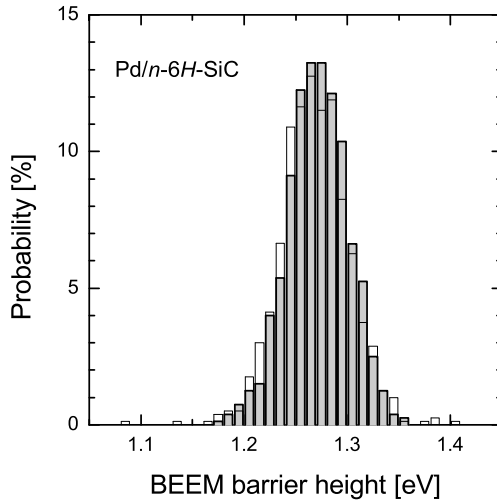


**Fig. 3.** Histograms of BEEM barrier heights of a “good” (*gray solid bars*) and a “bad” Pd/*n*-6H-SiC(0001) diode (*empty bars*) as determined by fitting 800 BEEM spectra each using the Bell-Kaiser square-law (5). Data from Im et al. [21]

of their patch parameters  $\gamma_{i\pi}$  to be Gaussian with the standard variation  $\sigma_{i\gamma}$ . The distribution of the saddle-point or, what is the same, of the local BEEM barrier-heights will be a Gaussian function too. It is centered at the barrier height  $\Phi_{\text{Bn}}^{\text{hom}}$  of the embedding area  $(1 - C_{i\pi})A$  and has the standard deviation [21]

$$\sigma_{i\pi} = [(\Phi_{\text{Bn}}^{\text{hom}} - W_n) N_d / \varepsilon_b \varepsilon_0]^{1/3} \sigma_{i\gamma}, \quad (6)$$

where  $N_d$  and  $\varepsilon_b$  are the bulk donor density and the static dielectric constant of the semiconductor, respectively, and  $\varepsilon_0$  is the permittivity of vacuum. The model barrier-height distribution of the entire diode may then be written as

$$P_{\text{mod}}^{i\pi}(\Phi_{\text{Bn}}^{\text{BEEM}}) = \frac{C_{i\pi}}{\sqrt{2\pi}\sigma_{i\pi}} \exp\left(-\frac{(\Phi_{\text{Bn}}^{\text{BEEM}} - \Phi_{\text{Bn}}^{\text{hom}})^2}{2\sigma_{i\pi}^2}\right) + (1 - C_{i\pi}) \delta_D(\Phi_{\text{Bn}}^{\text{BEEM}} - \Phi_{\text{Bn}}^{\text{hom}}), \quad (7)$$

where the Dirac  $\delta_D(\Phi_{\text{Bn}}^{\text{BEEM}} - \Phi_{\text{Bn}}^{\text{hom}})$  describes the laterally homogeneous area of the diode. Figure 4 explains this model. The overall standard deviation of the model barrier height-distribution is then given by

$$\sigma_{\text{mod}}^{i\pi} = \sqrt{C_{i\pi}} \sigma_{i\pi} = \sqrt{C_{i\pi}} [(\Phi_{\text{Bn}}^{\text{hom}} - W_n) N_d / \varepsilon_b \varepsilon_0]^{1/3}. \quad (8)$$

Unfortunately, no experimental data of SiC Schottky diodes are available to test (8). However, Morgan et al. [22] measured BEEM barrier-height distributions of gold Schottky diodes prepared on differently doped *n*-Si(001) wafers. Figure 5 displays their results. The experimental data are again ex-

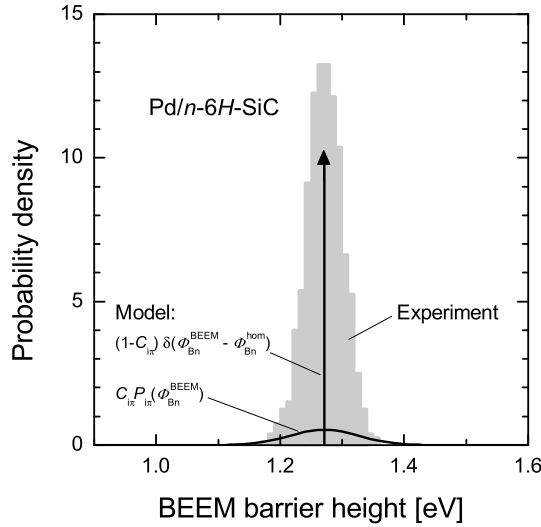


**Fig. 4.** Gaussian and Dirac  $\delta$ -function distributions of barrier heights of intrinsic patches and of the embedding area, respectively, of a model diode and histogram of experimental BEEM barrier heights of a real Pd/*n*-6H-SiC(0001) diode (same data as in Fig. 3). The model parameters are  $\phi_{Bn}^{hom} = 1.271$  eV,  $C_{i\pi} = 0.107$ ,  $\sigma_{i\pi} = 1.03 \times 10^{-4} \text{ eV}^{1/3} \text{ cm}^{2/3}$ , and  $\rho_{i\pi} = 6 \times 10^9 \text{ cm}^{-2}$

cellently fitted by Gaussian functions and their standard deviations increase as the doping level becomes larger. Figure 6 shows the standard deviations of the barrier-height distributions given in Fig. 5 as a function of the donor density of the Si wafers. The dashed line is a linear least-squares fit to the data points. Its slope parameter of  $0.34 \pm 0.09$  excellently confirms the exponent predicted by (8).

Im et al. [21] derived an area density  $\rho_{i\pi} \approx 5 \times 10^9 \text{ cm}^{-2}$ , a fractional coverage  $C_{i\pi} \approx 0.05$ , and a standard variation  $\sigma_{i\pi} = \langle \gamma_{i\pi} \rangle \approx 1 \times 10^{-4} \text{ eV}^{1/3} \text{ cm}^{2/3}$  for the intrinsic patches at the interfaces of their Pd/*n*-6H-SiC diodes. A possible physical explanation of the nature if these intrinsic patches is discussed in Sect. 4.2.

Not only Im et al. [21] but also Skromme et al. [23] concluded the existence of a few gross defects of extrinsic nature which determine the properties of “bad” diodes with ideality factors much larger than  $n_{if}$ . The possible nature of such extrinsic patches may vary widely and their occurrence will strongly depend on fabrication details of each individual diode even if they are prepared under experimentally identical conditions. Such few extrinsic patches will easily escape detection by BEEM. The only well-documented example are interfacial dislocations at CoSi<sub>2</sub>/*n*-Si(001) contacts investigated by Siringhaus et al. [24].

Table 1 shows barrier heights of laterally homogeneous SiC Schottky contacts determined from BEEM barrier-height distributions.

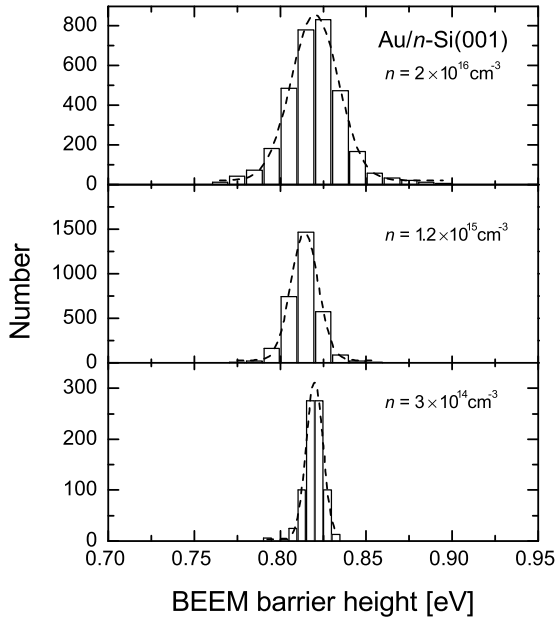


**Fig. 5.** Histograms of BEEM barrier heights on Au/*n*-Si(001) contacts with different donor densities of the silicon substrates. The *dashed lines* are Gaussian least-squares fits to the data. The centers and the standard deviations of the three Gaussians are  $0.820 \pm 0.0003$  eV and  $0.014 \pm 0.0002$  eV,  $0.814 \pm 0.0002$  eV and  $0.008 \pm 0.0001$  eV, and  $0.820 \pm 0.0001$  eV and  $0.005 \pm 0.0001$  eV, respectively. Data from Morgan et al. [22]

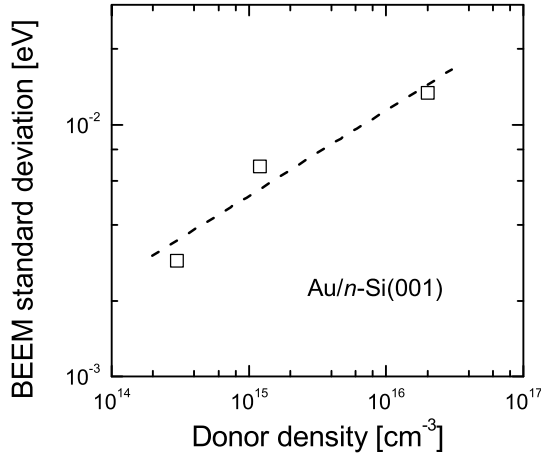


**Fig. 6.** Standard deviations of the Gaussian fits to the BEEM barrier-height histograms of Fig. 5 as a function of the donor density. The *dashed line* is a linear least-squares fit

### 2.1.3 Internal Photoemission Yield Spectroscopy

Metal-semiconductor contacts show a photoelectric response to optical radiation with photon energies smaller than the width of the bulk band gap. This effect is caused by internal photoemission of electrons from the metal over the interfacial barrier into the conduction band of the semiconductor and is another technique for determining barrier heights in Schottky contacts. Internal photoemission yield spectroscopy or, for short, IPEYS and ballistic-electron-emission spectroscopy are similar in that hot electrons are injected from the metal across the interface. Hence, the same arguments as in the derivation of the BEEM collector current apply for IPEYS and above a threshold value the flux of the photoinjected electrons will vary quadratically as a function of the photon energy  $\hbar\omega$ . The yield of the photoinjected electrons depends on the photon energy as

$$Y(\hbar\omega) \propto (\hbar\omega - \Phi_{\text{Bn}}^{\text{IPEYS}})^2 / \hbar\omega. \quad (9)$$

Patches only cover a small portion of metal-semiconductor interfaces so that the threshold energy  $\Phi_{\text{Bn}}^{\text{IPEYS}}$  will equal the barrier height  $\Phi_{\text{Bn}}^{\text{hom}}$  of the laterally homogeneous part of the contact minus the image-force lowering  $\delta\Phi_{\text{if}}^0$ .

The experimental  $[Y(\hbar\omega) \cdot \hbar\omega]^{1/2}$  data deviate towards larger values slightly below and above the threshold. This behavior is caused by the shape of the Fermi-Dirac distribution function at finite temperatures and by the existence of patches with barrier heights smaller and larger than  $\Phi_{\text{Bn}}^{\text{hom}}$ .

Table 1 displays barrier heights of laterally homogeneous SiC Schottky contacts as determined by extrapolation of  $[Y(\hbar\omega) \cdot \hbar\omega]^{1/2}$  curves to zero yield.

### 2.1.4 Photoemission Spectroscopy

Photoemission spectroscopy may be used to study the band bending at surfaces and interfaces. The depth resolution of photoemission spectroscopy depends on the escape depth of the photoemitted electrons. The escape depth varies between approximately 0.4 and 30 nm at 60 and 1000 eV, respectively. Hence, photoemission spectroscopy as a probe of metal-semiconductor interfaces is limited to metal films the thickness of which does not exceed 1 to 4 nm. Most metals show island rather than layer-by-layer growth on semiconductor surfaces. However, cesium wets SiC as other semiconductor surfaces and already during the formation of the second cesium layer a metallic Fermi edge develops at the high-energy termination of the energy distribution curve (EDC) of the photoemitted electrons and the work function assumes the value characteristic of cesium metal [26, 32]. The difference of the ionization energy  $I(\Theta_{\text{Cs}}) = W_{\text{vac}} - W_{\text{vi}}$  and of the work function  $\Phi(\Theta_{\text{Cs}}) = W_{\text{vac}} - W_{\text{F}}$ , both measured as a function of the cesium coverage  $\Theta_{\text{Cs}}$ , gives the energy position  $W_{\text{F}} - W_{\text{vi}}$  of the Fermi level above the valence-band top right at the surface or

the interface or, in other words, the surface and the interface band-bending, respectively. The ionization energy equals the difference  $\hbar\omega - W_{\text{EDC}}$  of the energy of the exciting photons and the width of the EDC of the photoelectrons while the work function may be determined using a Kelvin probe.

Table 1 displays the barrier heights of laterally homogeneous Cs contacts on the two SiC polytypes  $6H$  and  $4H$  which were obtained by simultaneous PES and Kelvin-probe measurements.

## 2.2 Valence-Band Offsets at SiC Heterostructures

### 2.2.1 X-Ray Photoemission Spectroscopy

Semiconductors generally grow layer-by-layer, at least initially. Hence, core-level photoemission spectroscopy is one of the most reliable tools for determining the band-structure lineup at semiconductor heterostructures. The valence-band offset may be obtained from the energy positions of core-level lines in X-ray photoelectron spectra (XPS) recorded with bulk samples of the semiconductors in contact and with the interface itself [35]. Since the escape depths of the photoelectrons are in the order of 2 nm only, one of the two semiconductors has to be sufficiently thin. This condition is easily met when heterostructures are grown by molecular beam epitaxy (MBE) and XPS spectra are recorded during growth interrupts. The valence-band discontinuity results as

$$\begin{aligned} \Delta W_v = W_{\text{vir}} - W_{\text{vil}} = W_{\text{ir}}(nl) - W_{\text{il}}(\tilde{n}\tilde{l}) \\ + [W_{\text{vbr}} - W_{\text{br}}(nl)] - [W_{\text{vbl}} - W_{\text{bl}}(\tilde{n}\tilde{l})] , \end{aligned} \quad (10)$$

**Table 2.** Valence-band offsets of SiC heterostructures with group-III nitrides

SiC Poly-type	Orientation	Semiconductor	Method	$\Delta W_v$ [eV]	Reference
$6H$	(0001)	AlN	XPS	1.4 $\pm$ 0.3	King et al. [36]
	(0001)	AlN	XPS	1.6 $\pm$ 0.1	Rizzi et al. [37]
	(0001)	AlN	XPS	1.45 $\pm$ 0.1	King et al. [38]
	(0001)*	AlN	XPS	1.15 $\pm$ 0.1	
	(0001)	AlN	XPS	0.95 $\pm$ 0.1	
	(000-1)**	AlN	XPS	0.85 $\pm$ 0.1	
	(1-100)	AlN	XPS	0.65 $\pm$ 0.1	
	(0001)	GaN	XPS	0.9 $\pm$ 0.1	Rizzi et al. [37]
$3C$	(111)-1 $\times$ 1	GaN	XPS	0.5 $\pm$ 0.1	King et al. [39]
	(111)-3 $\times$ 3	GaN	XPS	0.8 $\pm$ 0.1	

\*  $(\sqrt{3} \times \sqrt{3})R30^\circ$  on- and off-axis, \*\* off-axis

where  $(nl)$  and  $(\tilde{n}\tilde{l})$  denote the core levels of the semiconductors on the right, r, and the left side, l, of the interface, respectively. Subscripts i and b characterize interface and bulk properties, respectively. The energy difference  $W_{ir}(nl) - W_{il}(\tilde{n}\tilde{l})$  between the core levels of the two semiconductors is determined from EDCs of photoelectrons recorded during MBE growth of the heterostructure. The energy positions  $W_{vbr} - W_{br}(nl)$  and  $W_{vbl} - W_{bl}(\tilde{n}\tilde{l})$  of the core levels relative to the valence-band maxima in each of the two semiconductors are evaluated separately.

Table 2 shows valence-band offsets of SiC heterostructures with group-III nitrides which were determined by core-level X-ray photoemission spectroscopy.

### 2.2.2 Internal Photoemission Yield Spectroscopy

Another widely used technique for determining band offsets in heterostructures is internal photoemission yield spectroscopy. The evaluation of the IPEYS signals is the same as described in Sect. 2.1.3. Generally, more than one interface-related threshold energy is observed with semiconductor heterostructures. If, for example, one of the semiconductors is doped  $n$ -type then electrons may be excited not only from its valence but also from its conduction band across the interface into the conduction band of the other semiconductor. The corresponding two threshold energies will differ by the width of the band gap of the  $n$ -type emitter and the second threshold equals the conduction-band discontinuity of the heterostructure. Valence-band offsets

**Table 3.** Valence-band offsets at semiconductor-SiO<sub>2</sub> interfaces

Semiconductor	Orientation	$\Delta W_v$ [eV]	Reference
3C-SiC	(001)	$2.95 \pm 0.1$	Afanas'ev et al. [40]
4H-SiC	(0001)	$2.95 \pm 0.1$	Afanas'ev & Stresmans [41]
6H-SiC	(0001)	$2.95 \pm 0.1$	
15R-SiC		$2.95 \pm 0.1$	
Si	—	4.45	Williams [42]
	(111)	$4.5 \pm 0.1$	Grunthaner & Grunthaner [43]
	(001)	$4.3 \pm 0.1$	Himpsel et al. [44]
	(001)	$4.53 \pm 0.1$	Afanas'ev et al. [40]
	(001)	4.49	Alay & Hirose [45]
	(111)	4.36	
	(001)	$4.54 \pm 0.06$	Keister et al. [46]
	(111)	$4.35 \pm 0.06$	
	(111)	$4.42 \pm 0.01$	Hirose et al. [47]
	(111)	$4.62 \pm 0.01$	
ZnS	(111)	$2.8 \pm 0.2$	Ban et al. [48]
CdTe	(111)	$4.7 \pm 0.2$	

of heterostructures between  $\text{SiO}_2$  and the  $3C$ ,  $6H$ ,  $4H$ , and  $15R$ -SiC polytypes which were determined by internal photoemission yield spectroscopy are displayed in Table 3.

### 3 IFIGS-and-Electronegativity Theory

Because of the quantum-mechanical tunnel effect, the wave functions of bulk electrons decay exponentially into vacuum at surfaces or, more generally speaking, at solid-vacuum interfaces. In energy regions of Schottky contacts and of semiconductor heterostructures where occupied band states overlap a band gap the wave functions of these electrons will behave the same in that they tail across the interface into the corresponding semiconductor. The virtual gap states (ViGS) of the complex band structure of the semiconductor determine this tailing behavior. Figure 7 schematically explains both effects. These interface-induced gap states or, for short, IFIGS are an intrinsic property of the semiconductor. For the band-structure lineup at semiconductor interfaces only the IFIGS within the gap between the top valence and the conduction band are of importance since the energy position of the Fermi level determines their charging state.

The IFIGS are made up of valence- and conduction-band states of the semiconductor. Their net charge depends on the energy position of the Fermi level relative to their branch point where their character changes from predominantly donor- or valence-band- to mostly acceptor- or conduction-band-like. The band-structure lineup at semiconductor interfaces is thus described by a zero-charge-transfer term and an electric-dipole contribution.

The charge transfer at semiconductor interfaces may be easily estimated by applying Pauling's description of the partial ionic character of covalent bonds by the difference of the electronegativities of the atoms involved. The combination of the physical IFIGS and the chemical electronegativity concept

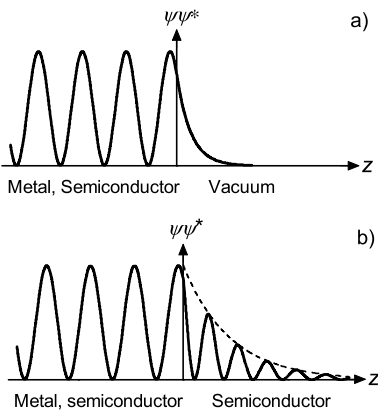


**Fig. 7.** Wave-function tails at surfaces (a) and at semiconductor interfaces in energy regions where occupied states overlap a band gap (b)

yields the barrier heights of ideal  $p$ -type Schottky contacts to vary as

$$\Phi_{\text{Bp}} = \Phi_{\text{bp}}^{\text{p}} - S_X (X_{\text{m}} - X_{\text{s}}) \quad (11)$$

and the valence-band offsets of ideal semiconductor heterostructures to vary as

$$\Delta W_{\text{v}} = \Phi_{\text{bpr}}^{\text{p}} - \Phi_{\text{bpl}}^{\text{p}} + D_X (X_{\text{sr}} - X_{\text{sl}}) , \quad (12)$$

where  $\Phi_{\text{bp}}^{\text{p}} = W_{\text{bp}} - W_{\text{v}}(\Gamma)$  is the energy distance from the valence-band maximum to the branch point of the IFIGS or the  $p$ -type branch-point energy and  $X_{\text{m}}$  and  $X_{\text{s}}$  are the electronegativities of metals and semiconductors, respectively. The subscripts r and l stand for the right and the left side, respectively, of heterostructures. The slope parameters  $S_X$  and  $D_X$  are explained at the end of this section.

The IFIGS derive from the virtual gap states of the complex band structure of the semiconductor. Their branch point is an average property of the semiconductor. Baldereschi's concept [49] of mean-value  $k$ -points in the Brillouin zone avoids the extensive computations required for calculations of branch points. At the mean-value  $k$ -point, the separation between the valence and the conduction band indeed equals the average or dielectric band gap [50]

$$W_{\text{dg}} = \hbar\omega_{\text{p}} / \sqrt{\varepsilon_{\infty} - 1} , \quad (13)$$

where  $\hbar\omega_{\text{p}}$  is the plasmon energy of the bulk valence electrons and  $\varepsilon_{\infty}$  is the optical dielectric constant [51]. Mönch [50] plotted the theoretical branch-point energies  $W_{\text{bp}} - W_{\text{v}}(\underline{k}_{\text{mv}}) = \Phi_{\text{bp}}^{\text{p}} + [W_{\text{v}}(\Gamma) - W_{\text{v}}(\underline{k}_{\text{mv}})]_{\text{ETB}}$  at the mean-value  $k$ -point  $\underline{k}_{\text{mv}}$  versus the width of the dielectric band gaps of 15 different elemental and compound semiconductors. He took the branch-point energies  $\Phi_{\text{bp}}^{\text{p}} = W_{\text{bp}} - W_{\text{v}}(\Gamma)$  which had been computed by Tersoff [52] and calculated the energy dispersions  $[W_{\text{v}}(\Gamma) - W_{\text{v}}(\underline{k}_{\text{mv}})]_{\text{ETB}}$  of the top valence band in the empirical tight-binding approximation. A linear least-squares fit to the data yielded [50]

$$\Phi_{\text{bp}}^{\text{p}} = 0.449 \cdot W_{\text{dg}} - [W_{\text{v}}(\Gamma) - W_{\text{v}}(\underline{k}_{\text{mv}})]_{\text{ETB}} . \quad (14)$$

The IFIGS branch points are thus slightly below the middle of the band gap at the mean-value  $k$ -point. The same result is well-known for the ViGS of one-dimensional linear chains. For silicon carbide (14) gives the branch-point energy  $\Phi_{\text{bp}}^{\text{p}} = 1.44$  eV.

A simple phenomenological model of Schottky contacts with a continuum of interface states of constant density of states  $D_{\text{is}}$  across the semiconductor band gap yields the slope parameter [53, 54]

$$S_X = A_X / [1 + (e_0^2 / \varepsilon_{\text{i}} \varepsilon_0) D_{\text{is}} \delta_{\text{is}}] , \quad (15)$$

where  $\varepsilon_{\text{i}}$  is an interface dielectric-constant. The parameter  $A_X$  depends on the electronegativity scale chosen and amounts to 0.86 eV/Miedema-unit

and 1.79 eV/Pauling-unit. The extension  $\delta_{\text{is}}$  of the interface states is approximated by their charge decay-length  $1/2q_{\text{is}}$ . For one-dimensional linear chains, both the density of states and the charge decay-lengths of their ViGS vary inversely proportional to the width of their band gaps. In view of the relations (13) and (15), Mönch [54] plotted theoretical values  $(e_0^2/\varepsilon_0) D_{\text{gs}}^{\text{mi}}/2q_{\text{gs}}^{\text{mi}}$  of metal-induced gap states (MIGS), as the IFIGS in Schottky contacts are traditionally called, versus the optical susceptibility  $\varepsilon_\infty - 1$ . A least-squares fit to the data points yielded a quadratic dependence, and relation (15) was rewritten as

$$A_X/S_X - 1 = 0.29 \cdot (\varepsilon_\infty - 1)^2, \quad (16)$$

where the reasonable assumption  $\varepsilon_i \approx 3$  was made. For silicon carbide (16) gives the slope parameter  $S_X = 0.24$  eV/Miedema-unit.

To a first approximation, the slope parameter  $D_X$  of heterostructures may be equated with the slope parameter  $S_X$  of Schottky contacts since the IFIGS determine the intrinsic dipole contributions to both the valence-band offsets and the barrier heights. Furthermore, the elements forming semiconductors are all found in the center columns of the Periodic Table of the Elements. Therefore, their electronegativities are almost equal so that the dipole term  $D_X \cdot (X_{\text{sr}} - X_{\text{sl}})$  in (12) will be small and may be neglected. Consequently, (12) reduces to

$$\Delta W_v \cong \Phi_{\text{bpr}}^{\text{p}} - \Phi_{\text{bpl}}^{\text{p}} \quad (17)$$

for practical purposes.

## 4 Comparison of Experiment and Theory

### 4.1 IFIGS-and-Electronegativity Theory

#### 4.1.1 SiC Schottky Contacts

The experimental barrier heights of intimate, abrupt, clean, and laterally homogeneous Schottky contacts on the three SiC polytypes  $3C$ ,  $6H$ , and  $4H$  are plotted versus the difference of the Miedema electronegativities of the metals and SiC in Fig. 8. Miedema's electronegativities are preferred since they were derived from properties of metal alloys and intermetallic compounds while Pauling considered covalent bonds in small molecules. For  $n$ -type Schottky contacts (11) has to be replaced by

$$\Phi_{\text{Bn}}^{\text{hom}} = \Phi_{\text{bp}}^{\text{n}} + S_X(X_{\text{m}} - X_{\text{SiC}}), \quad (18)$$

where the energy position of the branch point relative to the conduction band minimum is given by

$$\Phi_{\text{bp}}^{\text{n}} = W_{\text{c}} - W_{\text{bp}} = W_{\text{g}} - \Phi_{\text{bp}}^{\text{p}} \quad (19)$$

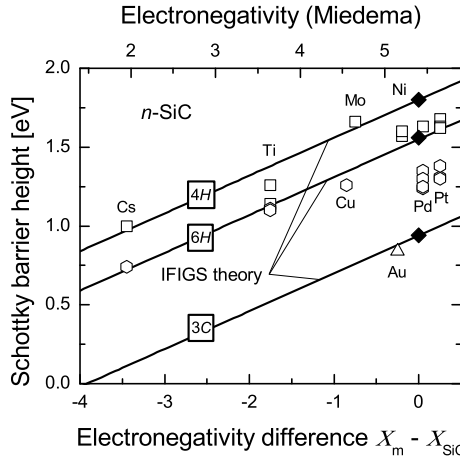


**Fig. 8.** Experimental barrier heights of laterally homogeneous *n*-type 3C-, 6H-, and 4H-SiC Schottky contacts versus the difference of the Miedema electronegativities of the metal and silicon carbide. The  $\Delta$ ,  $\square$ , and  $\circ$  symbols differentiate the data of 3C-, 4H-, and 6H-SiC Schottky contacts, respectively, as compiled in Table 1. The solid IFIGS lines are drawn with  $\Phi_{\text{bp}}^{\text{p}} = 1.44$  eV of cubic 3C-SiC [50], the respective band gaps of the polytypes, and  $S_X = 0.24$  eV/Miedema-unit (see text)

and  $W_g$  is the width of the fundamental band gap. The ETB matrix elements used in calculating the valence-band dispersion in (14) were evaluated for cubic zincblende-structure semiconductors so that the theoretical  $\Phi_{\text{bp}}^{\text{p}}$  value of 1.44 eV first of all applies to 3C-SiC. The three IFIGS lines in Fig. 8 were drawn with the assumption that the energy position  $\Phi_{\text{bp}}^{\text{p}} = W_{\text{bp}} - W_v(\Gamma)$  of the branch point relative to the valence-band maximum is the same irrespective of the specific polytype considered. Obviously, the IFIGS lines quantitatively explain the experimental barrier heights of laterally homogeneous metal contacts on *n*-type 3C-, 6H-, and 4H-SiC although the barrier heights of the Pd- and Pt/6H-SiC contacts are by approximately 100 meV smaller than theoretically predicted.<sup>1</sup>

The assumption of identical branch-point energies  $\Phi_{\text{bp}}^{\text{p}}$  for the three SiC polytypes is further illustrated by Fig. 9 which displays *p*-type barrier heights  $\Phi_{\text{Bp}}^{\text{hom}} = W_g - \Phi_{\text{Bn}}^{\text{hom}}$  as a function of the electronegativity difference  $X_m - X_{\text{SiC}}$ . They were obtained by converting the experimental *n*-type barrier heights by using the band gaps of the respective polytypes. The data points excellently agree with the line which the IFIGS-and-electronegativity theory first of all predicts for 3C-SiC Schottky contacts. A similar conclusion was reached for 2H-GaN Schottky contacts. Again, the branch-point energy calculated for the cubic zincblende-structure compound explains the experimental bar-

<sup>1</sup> Mönch [55] reached this conclusion already from barrier heights of single but laterally inhomogeneous Schottky contacts on 3C- and 6H-SiC.

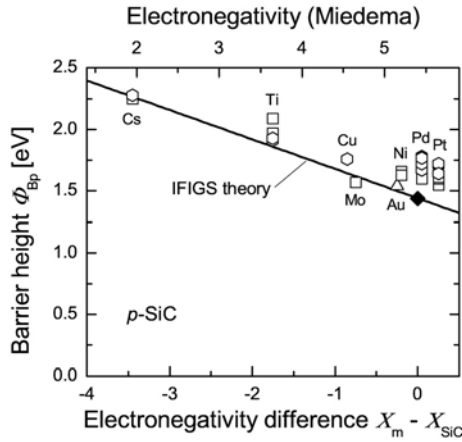


**Fig. 9.** Barrier heights of laterally homogeneous *p*-type 3*C*-, 6*H*-, and 4*H*-SiC Schottky contacts versus the difference of the Miedema electronegativities of the metal and silicon carbide. The experimental *n*-type data shown in Fig. 8 were converted using the respective band gaps of the polytypes. The  $\Delta$ ,  $\square$ , and  $\circ$  symbols differentiate 3*C*-, 6*H*-, and 4*H*-SiC Schottky contacts, respectively. The IFIGS line is drawn with  $\Phi_{bp}^p = 1.44$  eV of cubic 3*C*-SiC and  $S_X = 0.24$  eV/Miedema-unit

rier heights of Schottky contacts on hexagonal wurtzite-structure GaN [56]. In view of (17) this means that the valence-band offsets of 3*C*/2*H* homo-structures of SiC and GaN but also of 3*C*/6*H*, 3*C*/4*H*, and 4*H*/6*H* SiC interfaces should be zero or at least very small. Density-functional calculations within the local-density approximation using *ab-initio* pseudopotentials indeed produced valence-band offsets of approximately 50 meV not only for 3*C*/2*H* homo-structures of SiC, AlN, GaN, and Cd chalcogenides [57]–[63] but also of 3*C*/6*H*, 3*C*/4*H*, and 4*H*/6*H* SiC homo-junctions [58]. The conduction-band offsets then account for the band gap differences. The environment of the atoms in the cubic and the hexagonal lattice structure differs only beyond the nearest neighbors. Binggeli et al. [62] now argue that the bonding orbitals are highly localized on the anions and, consequently, the valence-band states are almost the same irrespective of the lattice structure. The conduction states, on the other hand, are more delocalized and, hence, are quite sensitive to the bonding geometry beyond of the nearest-neighbor shell. The dielectric band gap, on the other hand, has the same width irrespective of the polytype and, to a first approximation, the *p*-type branch-point energies should be almost identical for all polytypes.

#### 4.1.2 SiC Heterostructures

Nonpolar and lattice-matched epitaxial semiconductor heterostructures are the most simple examples for an analysis of valence-band offsets. They are well described by the IFIGS relation (17), see, for example, Mönch [13]. How-

ever, the band-structure lineup at semiconductor heterostructures is also affected by mechanisms other than the intrinsic IFIGS. There are two extrinsic effects which are of main importance.

First, intermixing will occur at polar interfaces of heterovalent heterostructures such as, for example,  $C^{II}A^{VI}/C^{III}A^V$  or  $C^{IV}A^{IV}/C^{III}A^V$ . This is to avoid macroscopic electric fields across the heterostructure. The resulting extrinsic electric-dipoles right at the interface will reduce or increase the band offset observed with the respective non-polar heterostructure by up to some tenths of an eV.

Second, the lattice parameters of the semiconductors generally differ. Lattice-mismatch will cause tetragonal distortions right at the interface of such pseudomorphic heterostructures even if they are isovalent. The valence-band offsets of lattice-matched heterostructures are insensitive to hydrostatic pressure. However, the uniaxial lattice strain in pseudomorphic heterostructures causes their valence-band offsets to decrease almost linearly as a function of the lattice strain  $(a_{||} - a_0)/a_0$  where  $a_{||}$  is the lattice parameter parallel to the interface. If the strain energy becomes too large in lattice-mismatched heterostructures then the strain is relieved by misfit dislocations. The band-structure lineups at such fully relaxed or metamorphic interfaces are again well described by the IFIGS relation (17). Figure 10 displays data of ZnTe/CdTe, Si/Ge, GaN/GaAs, ZnS/Ge, and GaN/AlN heterostructures, some typical examples of metamorphic structures. While the other semiconductors show cubic zincblende or diamond structure, the group-III nitrides GaN and AlN exhibit the hexagonal wurtzite lattice. As for the 3C-, 6H- and 4H-SiC polytypes, the barrier heights of 2H-GaN Schottky contacts are also well described by the branch-point energy calculated for the cubic

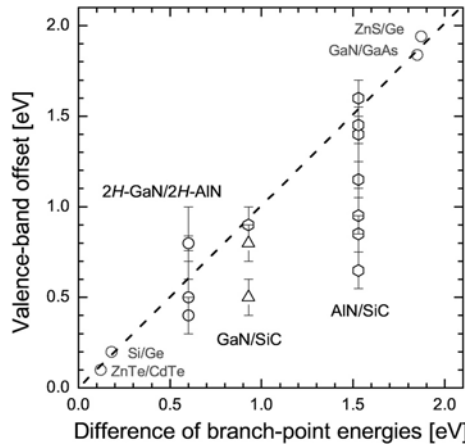


**Fig. 10.** Valence-band offsets of metamorphic heterostructures versus difference of IFIGS branch-point energies. Data from Table 3 and from Martin et al. [64], King et al. [65], and Rizzi et al. [37] for 2H-GaN/2H-AlN

zincblende-structure modification. Hence, it is no surprise that within the margins of experimental error the valence-band offsets of the isovalent  $2H$ -GaN/ $2H$ -AlN heterostructures [37, 64, 65] agree with the difference of the  $p$ -type branch-point energies of 2.97 and 2.37 eV calculated for the respective cubic  $3C$  modifications of AlN and GaN, respectively.

Figure 10 also displays the experimental valence-band offsets of AlN- and GaN/SiC heterostructures given in Table 2 as a function of the difference of the respective  $p$ -type branch-point energies. For SiC again the value calculated for the  $3C$  polytype, 1.44 eV, is taken. The AlN/ $6H$ -SiC and the GaN/ $3C$ -SiC data clearly demonstrate a strong influence of both the orientation and the clean-surface structure of the SiC substrates used on the valence-band offsets. Most probably extrinsic interface dipoles are responsible for the differences. However, no quantitative estimates are possible since neither the geometrical nor the chemical structures right at the interfaces are known. But nevertheless, the valence-band offsets of GaN/ $3C$ -SiC(111) and GaN/ $6H$ -SiC(0001) as well as of AlN/ $6H$ -SiC(0001) interfaces are well explained by the difference of the respective IFIGS branch-point energies.

#### 4.1.3 Insulator-SiC Interfaces

Insulators may be considered as semiconductors with large band gaps. Hence, the band-structure lineup at metal- and semiconductor-insulator interfaces is described by the IFIGS theory as well. Afanas'ev et al. [40] and Afanas'ev and Stesmans [41] determined the valence-band offsets at interfaces between SiO<sub>2</sub> overlayers and  $3C$ -,  $6H$ -,  $4H$ -, as well as  $15R$ -SiC by using internal photoemission yield spectroscopy. Their data are listed in Table 3. In agreement with what was observed with SiC heterostructures they observed the same value, 2.95 eV, of the valence-band offsets with the four different polytypes. This finding again supports the conclusion that the  $p$ -type branch-point energy of the IFIGS is the same for all SiC polytypes.

Unfortunately, the branch-point energy in the ViGS continuum of the complex SiO<sub>2</sub> band structure has not been calculated. However, it may be estimated from experimental data. Experimental valence-band offsets are not only available for the four different SiO<sub>2</sub>/SiC interfaces mentioned but also for Si-, ZnS-, and CdTe/SiO<sub>2</sub>. The respective data are also given in Table 3. In Fig. 11 these experimental data are plotted versus the  $p$ -type branch-point energy of the respective semiconductor. Only the SiO<sub>2</sub>/CdTe data point deviates from the general trend that the valence-band-offset becomes smaller with increasing branch-point energy of the respective semiconductor. The dashed line is the linear least-squares fit

$$\Delta W_v = (4.84 \pm 0.08) - (1.2 \pm 0.08) \cdot \Phi_{\text{bps}}^p \text{ eV} \quad (20)$$

to the data points where the CdTe/SiO<sub>2</sub> result is not considered. The sign of the slope parameter, which is slightly larger than one, indicates that the

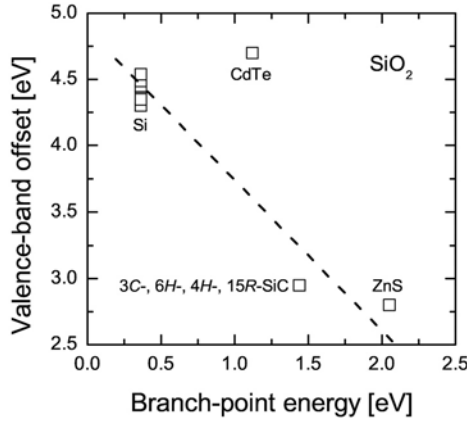


**Fig. 11.** Valence-band offsets at semiconductor-SiO<sub>2</sub> interfaces versus branch-point energies of the semiconductors. Data from Table 3. The *dashed line* is a linear least-squares fit

valence-band maximum of SiO<sub>2</sub> is lower in energy than the valence-band maxima of the semiconductors. If the dipole term  $D_X(X_{\text{SiO}_2} - X_s)$  in (12) is neglected then the *p*-type branch-point energy of SiO<sub>2</sub> is estimated as approximately 4.8 eV.

## 4.2 Intrinsic Non-Uniformities in Schottky Contacts

The conventional model of space-charge layers assumes a uniform distribution of charge. However, already Schottky [66] and Bethe [67] pointed out that the random distribution of the ionized donors and acceptors will most likely cause spatial fluctuations of the barrier height. Boudville and McGill [68] and then Bondarenko et al. [69] considered non-uniformly distributed impurities in depletion layers. Their calculations indeed showed potential fluctuations superimposed on the quadratic potential distribution that is characteristic of the usual jellium model of the space charge. For a donor density of  $3 \times 10^{15} \text{ cm}^{-3}$ , the donor density of the SiC wafers used by Im et al. [21] in their BEEM studies of Pd/*n*-6H-SiC(0001) contacts, these intrinsic potential fluctuations  $\langle V_i \rangle$  are estimated as approximately 50 meV. From their simultaneous conventional *I/V* and BEEM  $I_{\text{coll}}/V_{\text{tip}}$  studies of their contacts Im et al. [21] estimated that intrinsic patches of reduced barrier height should cover approximately 5% of the total diode area with an area density of  $5 \times 10^9 \text{ cm}^{-2}$ . These values correspond to an average patch radius  $\langle R_{i\pi} \rangle$  of approximately 18 nm. Using these values, relation (4) then yields an average patch parameter  $\langle \gamma_{i\pi} \rangle = 3(e_0 \langle V_i \rangle \langle R_{i\pi} \rangle^2 / 4)^{1/3}$  of  $\approx 1.03 \times 10^{-4} \text{ eV}^{1/3} \text{ cm}^{2/3}$ . This estimate surprisingly agrees with the value of  $1 \times 10^{-4} \text{ eV}^{1/3} \text{ cm}^{2/3}$  evaluated by Im et al. [21] for their Pd/*n*-6H-SiC(0001) diodes. Hence, the potential fluctuations

caused by the random distribution of the ionized donors might explain the intrinsic lateral inhomogeneities of the barrier heights of Pd/*n*-6H-SiC(0001) Schottky contacts.

### 4.3 Ab-Initio Theories

#### 4.3.1 SiC Schottky Barrier Heights

The local-density approximation to the density-functional theory or, for short, LDA-DFT is a most powerful and widely used tool for studies of ground-state properties of solids. However, such calculations notoriously underestimate the widths of the fundamental band gaps. This dilemma was overcome by the so called GW approximation for the electron self-energy. For SiC the respective GW shift of the valence-band maximum was estimated as approximately 0.78 eV to lower energies.

Hoekstra and Kohayama [70] and Kohayama and Hoekstra [71] applied LDA-DFT theory using *ab initio* pseudopotentials to Al- and Ti/3C-SiC interfaces. Depending on whether the SiC substrates were assumed to be C- or Si-terminated, they obtained barrier heights of 0.08 and 0.85 eV for Al- and of 0.22 and 0.5 eV for Ti/*p*-3C-SiC. Even if the GW correction of 0.78 eV is applied *a posteriori* the GW-LDA-DFT barrier heights of the Ti contacts are by far smaller than what is observed experimentally. The GW correction only brings the barrier height at Si-terminated Al/*p*-3C-SiC interfaces close to the experimental data of the other SiC Schottky contacts which are excellently explained by the IFIGS-and-electronegativity theory, see Fig. 9. Similar discrepancies are found for Schottky contacts on other semiconductors. Even if the respective GW correction is applied *a posteriori* the LDA-DFT barrier heights of Al-, Ag-, and Au/*p*-3C-GaN [72, 73] are smaller by approximately 0.6 eV than the experimental values which are also well explained by the IFIGS-and-electronegativity theory.

#### 4.3.2 SiC Heterostructures

In complete contrast to Schottky barrier heights, *ab initio* LDA-DFT calculations yield valence-band offsets of heterostructures which are much closer to both the experimental data and the results of the IFIGS theory. Binggeli et al. [62], Städele et al. [74], Majewski et al. [75], Agrawal et al. [76], and Laridjani et al. [77] calculated valence-band offsets of AlN- and GaN/SiC heterostructures. Figure 12 displays their data. C<sup>III</sup>A<sup>V</sup>/C<sup>IV</sup>A<sup>IV</sup> heterostructures are heterovalent and, therefore, 3C-(110) interfaces are non-polar while 3C-(111), 3C-(001), and 2H-(0001) heterostructures will be polar. Most remarkably, the LDA-DFT valence-band offsets at non-polar and pseudomorphic AlN- and GaN/3C-SiC(110) heterostructures deviate by only  $\approx 0.1$  and  $\approx -0.4$  eV, respectively, from the values predicted by the IFIGS theory. For GaN/3C-SiC(110) interfaces, approximately 0.14 eV of this difference might

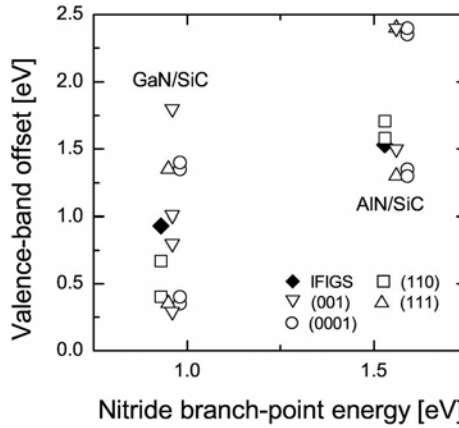


**Fig. 12.** Valence-band offsets of GaN- and AlN/SiC heterostructures calculated using *ab initio* LDA-DF theory [62],[74]–[77] and predicted by the IFIGS theory

be attributed to the 3% lattice mismatch.  $C^{III}-C^{IV}$  and  $A^V-A^{IV}$  intermixing will avoid charging of polar interfaces. The correlated electric dipoles, however, will increase and reduce, respectively, the valence-band offsets with regard to the value observed with the non-polar interface. The LDA-DFT calculations considered a 50% intermixing in the atomic layers right at the interface. For one and the same polar interface, the different LDA-DFT valence-band discontinuities are generally quite close. However, the scatter of the GaN/SiC data is somewhat larger. The difference between the  $C^{III}-C^{IV}$  and  $A^V-A^{IV}$  intermixed interfaces amounts to approximately 1 eV irrespective of whether AlN or GaN is considered. A simple point-charge model easily explains this observation by the only slight difference between the electronegativities of Al and Ga. Most importantly, the *ab-initio* valence-band offsets of the  $2H$ -(0001) and the  $3C$ -(111) interfaces turned out to be equal. However, for a direct comparison of the experimental and the LDA-DFT valence-band offsets a more detailed characterization of the geometrical structure and the chemical composition at the heteropolar III-N/SiC interfaces is highly desirable.

## 5 Conclusions

In energy regions where occupied band states on one side overlap a band gap on the other side of a semiconductor interface the quantum-mechanical tunnel effect causes the wave functions of the conduction- or valence-band electrons to tail across the interface. These intrinsic interface-induced gap states or IFIGS determine the band lineup at ideal semiconductor interfaces and, as to be expected, SiC behaves like all other semiconductors in that the IFIGS-and-electronegativity theory quantitatively describes both the barrier heights

of SiC Schottky contacts and the valence-band offsets of SiC heterostructures. An essential for the comparison of experimental data and theoretical predictions is that experimental data are available for ideal interfaces. In the past, many of such tests failed since real interfaces, and this is especially true for Schottky contacts, contain defects of various origin. However, this article demonstrates that well-prepared and well-characterized interfaces and carefully chosen experimental methods combined with an elaborate analysis of the measured data make it possible to find agreement between experimental data obtained with *real* samples and results of calculations assuming *ideal* interfaces, even for such a delicate material as SiC.

**Note added in proof:** Quite recently, Aboelfotoh et al. [78] studied Ti, Ni, Cu, and Au contacts on 6H-SiC doped both *n*- and *p*-type. They measured  $C/V$ ,  $I/V$ , and IPEYS characteristics of their diodes and determined the corresponding flat-band, effective, and IPEYS barrier heights, respectively. Most importantly, the IPEYS barrier heights of their Schottky contacts on *p*-6H-SiC substrates confirm the trend of the hypothetical *p*-type barrier heights which are displayed in Fig. 9 and which were obtained by conversion of the *n*-type barrier heights shown in Fig. 8.

## References

1. W. Schottky: Z. Physik **113**, 367 (1939)
2. W. Schottky: Naturwissenschaften **26**, 843 (1938)
3. V. Heine: Phys. Rev. **138** A1689 (1965)
4. J. Bardeen: Phys. Rev. **71**, 717 (1947)
5. C. Tejedor and F. Flores: J. Phys. C **11**, L19 (1978)
6. L.N. Pauling: *The Nature of the Chemical Bond* (Cornell Univ., Ithaca, NY, 1939)
7. W. Mönch: Phys. Rev. Lett. **58**, 1260 (1987)
8. W. Mönch: Phys. Rev. B **37**, 7129 (1988)
9. R. Schmitsdorf, T.U. Kampen, and W. Mönch: Surf. Sci. **324**, 249 (1995)
10. W. Schottky: Physik. Zeitschr. **15**, 872 (1914)
11. W.J. Kaiser and L.D. Bell: Phys. Rev. Lett. **60**, 1406 (1988)
12. W. Mönch: J. Vac. Sci. Technol. B **17**, 1867 (1999)
13. W. Mönch: *Semiconductor Surfaces and Interfaces*, 3rd ed. (Springer, Berlin, 2001)
14. W. Mönch: in *Festkörperprobleme* (Adv. Solid State Physics) Vol. 26, ed. by P. Grosse (Vieweg, Braunschweig, 1986), p. 67
15. H.-J. Im, B. Kaczer, J.P. Pelz, and W.J. Choyke: Appl. Phys. Lett. **72**, 839 (1998) and private communication
16. J.L. Freeouf, T.N. Jackson, S.E. Laux, and J.M. Woodall: Appl. Phys. Lett. **40**, 634 (1982)
17. J.L. Freeouf, T.N. Jackson, S.E. Laux, and J.M. Woodall: J. Vac. Sci. Technol. B **21**, 570 (1982)
18. R.T. Tung: Phys. Rev. B **45**, 13509 (1992)

19. A.E. Fowell, R.H. Williams, B.E. Richardson, and T.-H. Shen: *Semicond. Sci. Technol.* **5**, 348 (1990)
20. L.D. Bell and W.J. Kaiser: *Phys. Rev. Lett.* **61**, 2368 (1988)
21. H.-J. Im, Y. Ding, J.P. Pelz, and W.J. Choyke: *Phys. Rev. B* **64**, 075310 (2001)
22. B.A. Morgan, K.M. Ring, K.L. Kavanagh, A.A. Talin, R.S. Williams, T. Yasuda, T. Yasui, and Y. Segawa: *J. Appl. Phys.* **79**, 1532 (1996)
23. B.J. Skromme, E. Luckowski, K. Moore, M. Bhatnagar, C.E. Weitzel, T. Gehoski, and D. Ganser: *J. Electron. Mater.* **29**, 376 (2000)
24. H. Sirringhaus, T. Meyer, E.Y. Lee, and H. von Känel: *Phys. Rev. B* **53**, 15944 (1996)
25. G. Constantinidis, J. Kuzmic, K. Michelakis, and K. Tsagaraki: *Solid-State Electron.* **42**, 253 (1998)
26. V. van Elsbergen: *Untersuchungen an reinen und Adsorbat-bedeckten SiC-Oberflächen und Charakterisierung von Metall-SiC-Grenzflächen*; Dissertation (Universität Duisburg, 1998)
27. D. Defives, O. Noblanc, C. Dua, C. Brylinski, M. Barthula, and F. Meyer: *Mater. Sci. Engin. B* **61**, 395 (1999)
28. V. Khemka, T.P. Chow, and R.J. Gutman: *J. Electron Mater.* **27**, 1128 (1998)
29. K.J. Schoen, J.M. Woodall, J.A. Cooper, and M.R. Melloch: *IEEE Trans. ED-* **45**, 1595 (1998)
30. S. Bai, Y. Ke, Y. Shishkin, O. Shigiltchoff, R.P. Devaty, W.J. Choyke, D. Strauch, B. Stojetz, B. Dorner, D. Hobgood, J. Serrano, M. Cardona, H. Nagasawa, T. Kimoto, and L.M. Porter: *Mat. Res. Soc. Symp. Proc.* in print
31. O. Shigiltchoff, T. Kimoto, D. Hobgood, P.G. Neudeck, L.M. Porter, R.P. Devaty, and W.J. Choyke: *Mater. Sci. Forum* **389–393**, 921 (2002)
32. V. van Elsbergen, T.U. Kampen, and W. Mönch: *J. Appl. Phys.* **79**, 316 (1996)
33. T. Suezaki, K. Kawahito, T. Hatayama, Y. Uraoka, and T. Fuyuki: *Jpn. J. Appl. Phys.* **40**, L43 (2001)
34. O. Shigiltchoff, S. Bai, R.P. Devaty, W.J. Choyke, T. Kimoto, D. Hobgood, P.G. Neudeck, and L.M. Porter: *Mater. Sci. Forum* in print
35. R.W. Grant, J.R. Waldrop, and E.A. Kraut: *Phys. Rev. Lett.* **40**, 656 (1978)
36. S.W. King, M.C. Benjamin, R.J. Nemanich, R.F. Davis, and W.R.L. Lambrecht: *Mat. Res. Soc. Symp. Proc.* **395**, 375 (1996)
37. A. Rizzi, R. Lantier, F. Monti, H. Lüth, F. Della Sala, A. Di Carlo, and P. Lugli: *J. Vac. Sci. Technol. B* **17**, 1674 (1999)
38. S.W. King, R.F. Davis, C. Ronning, M.C. Benjamin, and R.J. Nemanich: *J. Appl. Phys.* **86**, 4483 (1999)
39. S.W. King, R.F. Davis, C. Ronning, and R.J. Nemanich: *J. Electron. Mater.* **28**, L34 (1999)
40. V.V. Afanas'ev, M. Bassler, G. Pensl, M.J. Schulz, and E. Stein von Kamienski: *J. Appl. Phys.* **79**, 3108 (1996)
41. V.V. Afanas'ev and A. Stesmans: *Appl. Phys. Lett.* **77**, 2024 (2000)
42. R. Williams: *Phys. Rev.* **140**, A569 (1965)
43. F.J. Grunthaner and P.J. Grunthaner: *Mater. Sci. Rep.* **1**, 65 (1986)
44. F.J. Himpsel, F.R. McFeely, A., Taleb-Ibrahimi, J.A. Yarmoff, and G. Hollinger: *Phys. Rev. B* **38**, 6084 (1988)
45. J.L. Alay and M. Hirose: *J. Appl. Phys.* **81**, 1606 (1997)
46. J.W. Keister, J.E. Rowe, J.J. Kolodziej, H. Niimi, T.E. Madey, and G. Lucovsky: *J. Vac. Sci. Technol. B* **17**, 1831 (1999)

47. K. Hirose, K. Sakano, H. Nohira, and T. Hattori: Phys. Rev. B **64**, 155325 (2001)
48. D. Ban, J. Xue, and R. Fang: J. Vac. Sci. Technol. B **16**, 989 (1998)
49. A. Baldereschi: Phys. Rev. B **7**, 5212 (1973)
50. W. Mönch: J. Appl. Phys. **80**, 5076 (1996)
51. D.R. Penn: Phys. Rev. **128**, 2093 (1962)
52. J. Tersoff: J. Vac. Sci. Technol. B **4**, 1066 (1986)
53. A.M. Cowley and S.M. Sze: J. Appl. Phys. **36**, 3212 (1965)
54. W. Mönch: Appl. Surf. Sci. **92**, 367 (1996)
55. W. Mönch: in *Control of Semiconductor Interfaces*, ed. by I. Ohdomari, M. Oshima, and A. Hiraki (Elsevier, Amsterdam, 1994), p. 169
56. T.U. Kampen and W. Mönch: Appl. Surf. Sci. **117/118**, 388 (1997)
57. A. Qteish, V. Heine, and R.J. Needs: Phys. Rev. B **45**, 6534 (1992)
58. P. Käckell, B. Wenzien and F. Bechstedt: Phys. Rev. B **50**, 10761 (1994)
59. S. Ke, J. Zi, K. Zhang, and X. Xie: Phys. Rev. B **54**, 8789 (1996)
60. C. Stampfl and C.G. Van de Walle: Phys. Rev. B **57**, R15052 (1998)
61. J.A. Majewski and P. Vogl: MRS Internet J. Nitride Semicond. Res. **3**, 21 (1998)
62. N. Binggeli, P. Ferrara, and A. Baldereschi: Phys. Rev. B **63**, 245306 (2001)
63. S.-H. Wei and S.B. Zhang: Phys. Rev. B **62**, 6944 (2000)
64. G. Martin, S.C. Strite, A. Botchkarev, A. Agarwal, A. Rockett, W.R.L. Lambrecht, B. Segall, and H. Morkoç: Appl. Phys. Lett. **65**, 610 (1994)
65. S.W. King, C. Ronning, R.F. Davis, M.C. Benjamin and R.J. Nemanich: J. Appl. Phys. **84**, 2086 (1998)
66. W. Schottky: Z. Physik **118**, 539 (1942)
67. H.A. Bethe: MIT Radiation Lab. Rep. 43–12 (1942)
68. W.J. Boudville and T.C. McGill: J. Vac. Sci. Technol. B **3**, 1192 (1985)
69. V.B. Bondarenko, Yu.A. Kudinov, S.G. Ershov, and V.V. Korablev: Semiconductors **32**, 495 (1998)
70. J. Hoekstra and M. Kohyama: Phys. Rev. B **57**, 2334 (1998)
71. M. Kohyama and J. Hoekstra: Phys. Rev. B **61**, 2672 (1998)
72. S. Picozzi, A. Continenza, G. Satta, S. Massidda, and A.J. Freeman: Phys. Rev. B **61**, 16736 (2000)
73. S. Picozzi, G. Profeta, A. Continenza, S. Massidda, and A.J. Freeman: Phys. Rev. B **65**, 165316 (2002)
74. M. Städele, J.A. Majewski, and P. Vogl: Phys. Rev. B **56**, 6911 (1997)
75. J.A. Majewski, M. Städele, and P. Vogl: Mat. Res. Soc. Symp. Proc. **449**, 917 (1997)
76. B.K. Agrawal, S. Agrawal, R. Srivastava, and P. Srivastava: Physica E **11**, 27 (2001)
77. M.R. Laridjani, P. Masri, and J.A. Majewski: Mat. Res. Soc. Symp. Proc. **639**, G11.34 (2001)
78. M.O. Aboelfotoh, C. Fröjdh, and C.S. Peterson: Phys. Rev. B **97**, 075312 (2003)

# Contributions to the Density of Interface States in SiC MOS Structures

V.V. Afanas'ev, F. Ciobanu, G. Pensl, and A. Stesmans

## 1 Introduction

Development of metal-oxide-semiconductor (MOS) technology for silicon carbide has attracted great attention because of the unique physical, chemical and, in particular, electronic properties of various crystallographic modifications (polytypes) of SiC, promising substantial advantages as compared to the conventional Si-based MOS devices [1]–[6]. The most important features of SiC are the wide band gap (from 2.38 eV for 3C-SiC to 3.26 eV for 4H-SiC, [7]), the high critical electric field, the high saturation electron velocity, and the high thermal conductivity [1, 2]. These properties potentially allow operation of SiC devices under conditions at which silicon electronics fails, thus extending the application area of semiconductor devices to higher voltages, higher power levels, higher temperatures, and higher frequencies. As compared to other wide-band gap semiconductors, SiC additionally has a significant advantage related to the possibility to grow insulating SiO<sub>2</sub> overlayers by simple thermal oxidation, naturally leading to the MOS device configuration. Albeit fabricated in recent years by many groups, SiC MOS field-effect transistors have yet not met the expectations. Their failure is largely related to the greatly enhanced density of imperfections at the SiO<sub>2</sub>/SiC interface [8, 9], which not only degrade the device performance but also cause reliability problems related to the anticipated extreme operating conditions [10]. Thus, reduction of the SiO<sub>2</sub>/SiC interface defect density becomes a key issue in the development of SiC MOS technology. Experience gained over the last years indicates that the standard ways to reduce the density of electrically harmful defects such as passivation with hydrogen known from the Si MOS processing, fail for the SiO<sub>2</sub>/SiC structures. This has evoked research efforts aimed at better understanding of the defect nature in the oxidized SiC, which is needed to find technologically feasible methods to eliminate and/or passivate the defect sites.

In the present work, we will analyze possible reasons for the enhanced defect density in the as-prepared SiO<sub>2</sub>/SiC structures as compared to the oxidized Si. This will be done by comparing the SiC/SiO<sub>2</sub> interface state spectrum to the much better studied case of Si/SiO<sub>2</sub> in order to reveal similar and dissimilar contributions to the observed imperfection density. Next, the interface defects specific for the oxidized SiC will be associated with the

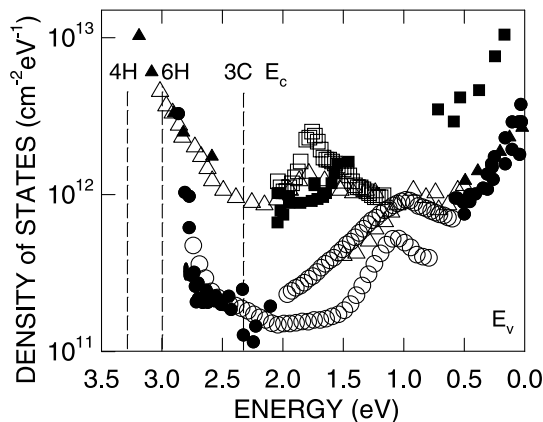


**Fig. 1.** Interface state density  $D_{it}$  as a function of energy for 3C- (squares), 6H- (circles), and 4H- (triangles) SiC/SiO<sub>2</sub> MOS structures determined by admittance spectroscopy (filled symbols) and by constant capacitance deep level transient spectroscopy (open symbols). The zero point of the energy scale corresponds to the top of the SiC valence band. The dashed lines indicate the energy position of the conduction band edge of the investigated SiC polytypes

particular chemical, structural, and electronic features of SiC. We will also consider the highly efficient SiC/SiO<sub>2</sub> interface defect generation observed upon injection of electrons and holes into the oxide [11, 12] pertinent to the understanding of the hot-carrier reliability problems in SiC MOS electronics. The latter may pose limits to the operational range of device parameters, reducing the benefits provided by the intrinsic SiC properties and forcing one to search for an alternative insulating material for SiC [13]–[17]. High-permittivity insulators are currently under development for advanced Si MOS devices [18], and some perspectives of their application in the SiC MOS technology will also be addressed.

## 2 SiC/SiO<sub>2</sub> Interface State Spectrum

### 2.1 Energy Distribution

The enhanced density of electrically active imperfections at the interface between SiC and SiO<sub>2</sub> as compared to Si/SiO<sub>2</sub> is a combined result of the wider semiconductor bandgap and more numerous electrically active states. The key information is provided by the analysis of the energy ( $E$ ) distribution of the SiC/oxide interface states ( $D_{it}$ ) across the SiC band gap. The typical result obtained using the combination of admittance spectroscopy (AS) at variable temperature and the constant capacitance deep level transient spectroscopy (CC-DLTS) is shown in Fig. 1. The figure presents the  $D_{it}(E)$  distributions of SiC MOS structures obtained by oxidation of Si faces of the three most

common SiC polytype crystals (3C-, 6H-, and 4H-, both of *n*- and *p*-type conductivity) in dry O<sub>2</sub> [8]. It is seen that for all the polytypes  $D_{it}$  remains above  $10^{11} \text{ cm}^{-2} \text{ eV}^{-1}$  over the entire SiC band gap energy range. Moreover, one can notice two regions with particularly high  $D_{it}$ :

- in the lower half of the SiC band gap  $D_{it}$ , is in the range of  $10^{12} \text{ cm}^{-2} \text{ eV}^{-1}$ ;
- in the vicinity of conduction band edge, particularly in 4H-SiC,  $D_{it}$  approaches  $10^{13} \text{ cm}^{-2} \text{ eV}^{-1}$ .

These observations are well supported by results obtained by other techniques. For instance, the capacitance-voltage (*C-V*) measurements indicate that *p*-type SiC MOS structures show much higher  $D_{it}$  in the vicinity of the Fermi level than the *n*-type ones [8],[19]–[22], with a considerable density of positive charge, suggesting the predominantly donor character of these defects. The positive charging initially led to the hypothesis that this portion of the SiC/SiO<sub>2</sub> interface state spectrum is associated with Al dopants typically used as acceptor impurities in SiC [19]. However, these states were also observed in *n*-type samples using the internal electron photoemission (IPE) technique [8] and in samples with Al replaced by B acceptors which are known to be unharmed, at least in the Si/SiO<sub>2</sub> entity [23]. Moreover, overcompensation of Al-doped *p*-SiC into *n*-type SiC by nitrogen ion implantation results in a similar interface quality as encountered in Al-free *n*-type SiC MOS structures [24]. These observations led to the conclusion that Al can be rehabilitated and safely used in the SiC MOS technology.

Concerning the high density of interface states observed near the conduction band of 4H-SiC, and, with a lower density, in 6H-SiC/SiO<sub>2</sub>, there is also a good agreement between different analyzing methods: the low-temperature *C-V* analysis [25, 26], the thermally-stimulated capacitance [25, 27] and current [28] techniques indicate a high  $D_{it}$  near the SiC conduction band edge. Worth mentioning here is that this portion of the  $D_{it}$  spectrum is not observed in 3C-SiC MOS structures [29]. The latter suggests the relationship of these interface traps either to a particular energy range or, else, to the particular SiC polytype. It is interesting to add here the results of recent Hall effect measurements indicating that the spectral density of these imperfections in the vicinity of the 4H-SiC conduction band edge even approaches  $10^{14} \text{ cm}^{-2} \text{ eV}^{-1}$  [30, 31].

## 2.2 Sensitivity of $D_{it}$ to SiC Polytype

The impact of the SiC polytype on the quality of its interface with native oxide was analyzed in several studies before [8],[22],[32]–[34]. Direct comparison between  $D_{it}$  close to the SiC valence band for the Si-faces of two hexagonal polytypes (6H and 4H) shows that, here, the difference is marginal [8, 22, 32, 33] suggesting that the size of the SiC elemental unit has little effect on the interface trap density. By contrast, when looking at  $D_{it}$  in the upper part of the SiC band gap, a considerably higher defect density is systematically observed in 4H-SiC than in 6H-SiC MOS samples (cf. Fig. 1)

[22, 25, 30, 31]. One also may notice from Fig. 1 that  $D_{it}$  in the central portion of the band gap is higher in the oxidized  $4H$ -SiC than in  $6H$ -SiC. Thus, as one more result, there is no direct relationship between the defects responsible for the enhanced interface state density in the upper and lower parts of the SiC band gap.

With respect to the cubic  $3C$ -SiC, there is a considerable spread in the literature data concerning interface state and fixed charge densities [8],[19],[35]–[42]. This might indicate that the quality of the interface depends strongly on the quality of the starting SiC epi-layer. Recent results suggest that  $D_{it}$  near the valence band of  $3C$ -SiC can be reduced to the low  $10^{12} \text{ cm}^{-2} \text{ eV}^{-1}$  range by improved epi-layer growth and proper pre-oxidation surface preparation, i.e. it becomes comparable to that of  $4H$ -SiC [29]. At the same time, the interface state density near the conduction band of  $3C$ -SiC appears to be in the range of  $10^{11} \text{ cm}^{-2} \text{ eV}^{-1}$ , which is at least one order of magnitude lower than in  $4H$ -SiC [29]. The latter can be associated with an approximately  $\approx 1 \text{ eV}$  decrease in the SiC conduction band energy in the  $3C$  polytypes as compared to  $4H$ -SiC which shifts the semiconductor Fermi level towards the energy range of the low  $D_{it}$  values (cf. Fig. 1). A similar trend is also observed when comparing the oxidized  $4H$ -SiC to another polytype with a narrower band gap, like  $15R$ -SiC: It appears that, for the same kind of technological processing, the  $15R$ -SiC/SiO<sub>2</sub> MOS structures exhibit higher surface electron mobility than  $4H$ -SiC MOS transistors [43, 44].

### 2.3 Sensitivity of $D_{it}$ to the Crystallographic Orientation of the SiC Surface

The general trend of the occurrence of a higher density of traps and charges at the C-face of hexagonal SiC ( $6H$ -,  $4H$ -polytypes) than at the Si-face is long known [8, 45, 46].  $D_{it}$  also increases with increasing crystal surface misalignment angle from the (0001) plane (Si face), which is explained by a higher defect density at the SiC surfaces with an orientation different from (0001) [47]. Indeed, MOS structures fabricated on other faces of  $6H$ -SiC, like (11 $\bar{2}$ 0) and (1 $\bar{1}$ 00), exhibit much enhanced interface state densities in the lower portion of the SiC band gap [8, 48, 49] which was associated with the higher availability of carbon atoms at these SiC surface planes [8].

For SiC/SiO<sub>2</sub> interface states with energy levels close to the SiC conduction band edge, the interface state density is reported to be lower at the (0001) plane (Si-face) of  $6H$ -SiC than for the (11 $\bar{2}$ 0) one [50]. However, in another hexagonal polytype,  $4H$ -SiC,  $D_{it}$  on (11 $\bar{2}$ 0) appears to be reproducibly lower than on the Si-face [50]–[52] resulting in much improved surface electron mobility [51, 52]. The same trend was also demonstrated recently for a (03 $\bar{3}$ 8) surface of  $4H$ -SiC [53]. This different behavior of SiC/SiO<sub>2</sub> interface states in the lower and upper parts of the  $4H$ -SiC band gap suggests again, a different nature of defects responsible for these two portions of the  $D_{it}$  distribution.

## 2.4 Effects of Annealing on $D_{it}$

In an attempt to reduce the interface state density, numerous annealing studies were performed during the last decade. They can be divided in three groups on the basis of the chemical mechanism behind particular thermal treatment.

First, the conventional for Si technology post-oxidation anneal (POA) in non-oxidizing ambient [54, 55] was applied to SiC/SiO<sub>2</sub> to reduce the fixed charge density. In *n*-type 6H-SiC samples the high-temperature POA in Ar is reported to significantly improve the interface quality [56]. However, only a weak, if any improvement at all, is seen in other non-oxidizing gases like He or N<sub>2</sub>, leading to the suspicion that the success of Ar might have been due to residual H<sub>2</sub>O content [57].

Second, the attempts to passivate defects in 6H-, 4H-SiC/SiO<sub>2</sub> by attaching hydrogen to them have shown that only a weak improvement can be achieved by POA in H<sub>2</sub> at temperatures typical for Si (350–450°C) [8, 33, 34, 58]. With increasing temperature of the hydrogen anneal up to 1000°C, a limited  $D_{it}$  reduction is observed in the *n*-type 6H- and 4H-SiC/SiO<sub>2</sub> [8, 34, 59], but not in the *p*-type samples [8, 33, 34]. This affirms the different chemical behavior of the interface states located close to the conduction and valence band edges of SiC. A negative impact of POA in H<sub>2</sub> consists in the generation of a considerable density of positive charge, particularly pronounced in the *p*-type samples [8, 58, 60]. This charge, also observed in Si/SiO<sub>2</sub>, is associated with bonding of protons in the near-interface layer of SiO<sub>2</sub> [60].

A more significant impact of hydrogen on  $D_{it}$  is observed when it is introduced from an oxygen-containing source (H<sub>2</sub>/O<sub>2</sub> mixture, H<sub>2</sub>O) which strongly decreases  $D_{it}$  in the lower part of the SiC band gap [61]. However, analysis of the  $D_{it}$  distribution across the *entire* SiC band gap reveals that this kind of POA greatly enhances the density of interface states near the conduction band of SiC, particularly in 4H-SiC [22, 25, 62]. These effects are illustrated by the *C-V* and conductance curves shown in Fig. 2 for two types of oxides grown on 4H-SiC at the same temperature [62]. One can notice, for instance, that the difference between flat band voltages in the *n*- and *p*-type SiC MOS capacitors in Fig. 2a, which gives an integral of interface state distribution across the entire SiC band gap, is even increased by wet oxidation. This is primarily due to the considerable increase in the  $D_{it}$  near the SiC conduction band edge observed in the *n*-type samples that overcompensates the reduction of  $D_{it}$  in the lower part of the SiC band gap observed in the *p*-MOS capacitors. This is revealed by the corresponding increase/reduction of peaks in the conductance-voltage curves shown in Fig. 2b.

The reason for the opposite action of wet oxidation on *p*- and *n*-type 4H-SiC/SiO<sub>2</sub> samples is revealed by the IPE spectra shown in Fig. 3. The major impact of wet oxidation is seen to be an approximately  $\sim 10$ -fold increase of the IPE yield in the low-energy emission band starting at  $\Phi_1$ , which cor-

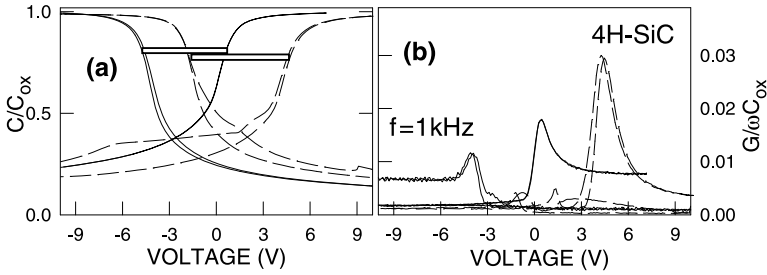


**Fig. 2.** Normalized 1 kHz capacitance (a) and ac conductance (b) as a function of voltage for *n*- and *p*-type 4*H*-SiC MOS structures with 50 nm thick SiO<sub>2</sub> layers grown at 1120°C in dry O<sub>2</sub> (solid lines) or in Ar+H<sub>2</sub>O (dashed lines)

responds to the excitation of electrons from the SiC conduction band [63]. As the total electron density at the SiC surface remains the same (it is determined by the strength of the applied electric field), the yield rise suggests an increase in the probability of electron escape, which means that electrons are excited not only from the SiC conduction band but also from some other states. The IPE yield drop at  $h\nu = E_g$  observed in dry 4*H*-SiC/SiO<sub>2</sub> is due to the onset of electron-electron scattering in SiC [63, 64]. Its absence in the wet oxidized 4*H*-SiC/SiO<sub>2</sub> case suggests that in these samples electrons are emitted from oxide traps close to the SiC/oxide interface rather than from the SiC crystal. Apparently, the wet oxidation results in the generation of

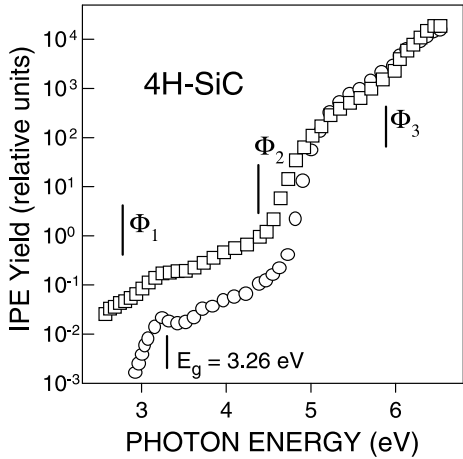


**Fig. 3.** Spectral dependences of the IPE yield for *n*-type 4*H*-SiC MOS structures with 50 nm thick oxide grown at 1120°C in dry O<sub>2</sub> (○) or in Ar+H<sub>2</sub>O (□). The curves were measured with an electric field strength in SiO<sub>2</sub> of 2 MV/cm. The SiC band gap value and the spectral thresholds of electron transitions from various states are indicated in the figure

oxide acceptor-type defects near the conduction band of SiC. They compensate the positive charge of donor states with energy levels in the lower part of the SiC band gap. The latter remain nearly unaffected by the wet oxidation process: The IPE yield in the defect-related emission band  $\Phi_2$  is unchanged within the measurement accuracy. The apparent  $D_{it}$  reduction suggested by the conductance data in Fig. 2b may be caused by Coulomb attraction between the donor and acceptor states which would shift the energy levels of donors deeper into SiC band gap. The observed strong enhancement in the density of SiC/SiO<sub>2</sub> acceptor states upon hydrogen/re-oxidation processing may prevent from using this method in the MOS transistor fabrication because it impairs the electron mobility at the SiC/SiO<sub>2</sub> interface [22].

A third group of treatments concerns direct growth or POA nitridation of oxide in nitric gases (NO, N<sub>2</sub>O, NH<sub>3</sub>). As first exposed by measurements of lower density of slow traps on *n*-type NO-treated NO-treated 6H-SiC/SiO<sub>2</sub> [65], it was found afterwards that the nitridation in NO appears to improve significantly the electrical properties of the 4H-SiC/SiO<sub>2</sub> interface as well [66]–[69], which is affirmed by independent experiments [70]. In contrast to other POA treatments, nitridation allows to reduce  $D_{it}$  both in the upper and lower parts of the 4H-SiC band gap, albeit to a different extent [71]. Nitridation in N<sub>2</sub>O and NH<sub>3</sub> provides only a limited improvement [65, 69, 72, 73]. The mechanism of nitrogen impact is likely to be complex [69], and its analysis is beyond the scope of this review.

## 2.5 Thermally-Induced Interface Trap Generation

In the course of device processing, thermal oxidation represents one of the first steps. Hereupon the SiO<sub>2</sub>/SiC structure may be subjected to various supplemental thermal steps such as treatments aimed at activation of doping impurities, formation of Ohmic contacts, etc. This additional processing, however, ensue also a negative effect on the electrical properties of the SiC/SiO<sub>2</sub> interface and result in the generation of additional defects. As a first indication of this problem, annealing of the poly-Si gate electrode deposited on *p*-type 6H-SiC/SiO<sub>2</sub> at  $T > 800^\circ\text{C}$  was found to increase the interface state density [4], which was ascribed to the influence of thermally-induced strain [74]. A very similar effect, though, was reported for the bare oxide samples annealed at  $1000^\circ\text{C}$  in order to obtain Ohmic contacts [75], suggesting involvement a chemical factor, e.g., hydrogen-related species, in the defect generation.

As discussed in the previous section, annealing in hydrogen appears to be only marginally efficient in improving the electrical behavior of SiC/SiO<sub>2</sub> interfaces. So far, the only observed benign effect of such a treatment is partial passivation of interface states produced by radiation in a sputtering metalization process [33]. At  $T > 500^\circ\text{C}$ , annealing in hydrogen leads to positive charge buildup at the interfaces of both *n*- and *p*-type SiC with SiO<sub>2</sub> [58, 60]. Taking into account that formation of a H-induced positively charged state

may be involved into a bond rupture process both at the interface [76] and in the SiO<sub>2</sub> layer itself [77, 78], it is well possible that the presence of H accounts for the SiO<sub>2</sub>/SiC interface state generation upon annealing.

The malignant damaging effect of protons is further revealed by degradation of the SiC/SiO<sub>2</sub> interface (in terms of the fixed charge and interface state density) under negative bias-temperature stress. It appears that at  $T > 250^\circ\text{C}$  a large density of interface states is generated under negative electric field in the oxide as compared to the thermal treatment without field application [79]. As the charge density of electrons or holes injected into the oxide is still very low ( $< 10^{-7} \text{ C/cm}^2$ ), the degradation is likely to involve formation (injection) of another charged particle – a proton. A similar conclusion can be drawn from the instability of  $C$ - $V$  curves in  $p$ -type  $6H$ -SiC MOS capacitors [80]. The scenario involving a proton was considered earlier for the bias-temperature instability of Si/SiO<sub>2</sub> structures [81, 82]. Both for oxidized Si and SiC the degradation is enhanced on  $p$ -type crystals and in water-containing oxides, which points towards a common mechanism.

## 2.6 Injection-Induced SiC/SiO<sub>2</sub> Interface State Generation

Injection of mobile charge carriers (electrons and holes) in oxides grown on SiC may be more efficient than the hot-electron injection in Si/SiO<sub>2</sub> structures for two reasons. First, the electric fields in SiC based devices are much higher than in silicon based ones [1, 83]. Second, electrons with an energy of about 3 eV, which is sufficient for injection into the oxide, will have a large mean free path with respect to electron-electron scattering because the SiC band gap width is larger than the SiC/SiO<sub>2</sub> interface barrier height. The presence of high-energy electrons in SiC is affirmed by efficient field emission of electrons from SiC  $p$ - $n$  junctions into vacuum [84]. Moreover, as the device operation temperature increases, the effective interfacial barrier becomes lower [83, 85] leading to a further increase of the electron emission rate.

It has been reported previously that injection of electrons into the oxides grown on SiC results in the generation of interface states [11, 12, 56, 86]. Noteworthy here is that the charge trapping in the oxide itself remains similar to that in the SiO<sub>2</sub> layers grown on Si indicating a predominantly interface-controlled degradation mechanism. The electron injection results in the generation of both donors and acceptors, which leads to a net positive charge in  $p$ -type and to a negative charge in  $n$ -type samples. The kinetics of the interface state trapped charge are compared in Fig. 4 for three SiC polytypes ( $4H$ ,  $6H$ ,  $3C$ ). They reveal two important features:

- the density of interfacial acceptors may be considerably higher than that of donors;
- there is a strong influence of the SiC polytype on the degradation process:  $4H$ -SiC samples show much more defects than  $6H$ - or  $3C$ -SiC MOS structures.

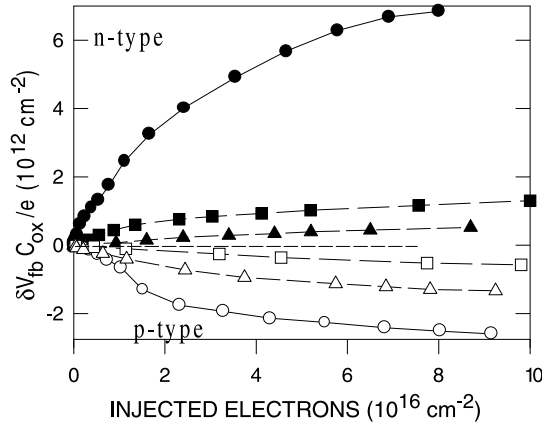


**Fig. 4.** Density of charge trapped at the interface derived from the hysteresis of  $C$ - $V$  curves as a function of the injected electron flux in  $p$ - (*open symbols*) and  $n$ -type (*filled symbols*) SiC MOS structures with approx. 100 nm thick oxides grown on 4H- (*circles*), 6H- (*squares*) and 3C-SiC (*triangles*)

In addition, the generation of SiC/SiO<sub>2</sub> interface acceptors appears to be correlated with the presence of C at the interface [11], suggesting (trans)formation of C-related defects during charge injection into the oxide.

Injection of holes into the oxide results in a further acceleration of SiC/SiO<sub>2</sub> interface state generation [12, 86]. In addition, the injected holes generate a positive charge related to their trapping in the oxide itself [87], which, however, shows no immediate correlation with the generation of interface traps [12]. Moreover, pre-injection of holes into the oxide is found to accelerate the interface state generation during subsequent electron injection. A possible explanation of these effects includes the interaction of holes with hydrogen-terminated bonds at the SiC/SiO<sub>2</sub> interface or generation of defects by atomic hydrogen released during the charge injection into the oxide. Involvement of hydrogen is suggested by the close values of the SiC/SiO<sub>2</sub> interface state generation cross section and that of electron capture by H-containing defects in SiO<sub>2</sub> [78].

The SiC MOS degradation caused by injection of electrons and holes is not only significantly enhanced as compared to Si MOS samples but also results in defects more stable than Si/SiO<sub>2</sub> interface states [11, 86]. This is shown in Fig. 5 which demonstrates the effect of an anneal in vacuum on injection-degraded 6H- and 4H-SiC/SiO<sub>2</sub> interfaces. Also shown is the effect of a 30 min annealing at 400°C in pure H<sub>2</sub>, exhibiting some impact. These results indicate that an efficient inactivation/elimination of the defects at 400°C cannot be reached neither in vacuum nor in hydrogen. This suggests that the generated states may be related to some stable bonding configurations of interfacial atoms and thus explain the enhanced SiO<sub>2</sub>/SiC interface state

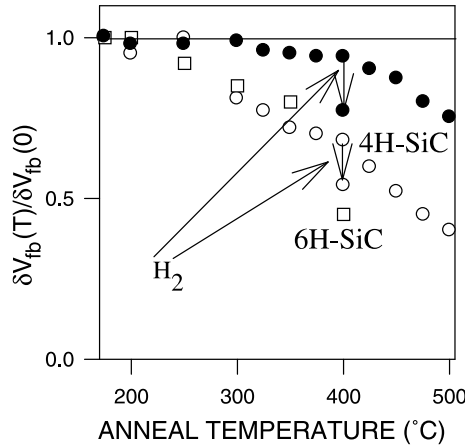


**Fig. 5.** Fraction of interface states in  $p$ - ( $\circ$ ) and  $n$ -type ( $\bullet$ ) 4H-SiC and  $n$ -type 6H-SiC ( $\square$ ) MOS structures remaining at the interfaces (degraded by injection of  $10^{17}$  e/cm $^2$ ) after 30 min annealing in vacuum at the indicated temperature. The arrows indicate the effect of 30 min anneal in pure  $H_2$  at 400 $^\circ\text{C}$

density observed when using electron-beam evaporation or sputtering of a metal [33]. Clearly, generation of such stable defects poses a serious threat to the device reliability.

### 3 Origin and Models of SiC/SiO $_2$ Interface States

#### 3.1 Interface States in the Model System: (111)Si/SiO $_2$

In order to understand to what extent the above described SiC/SiO $_2$  interface state spectrum can be associated with contributions of already known defects, it is useful to compare it with the  $D_{it}$  distributions observed at the well studied (111)Si/SiO $_2$  interface which is structurally isomorphic to the oxidized (0001) surface (Si-face) of hexagonal SiC. Three atomically different types of interface states have been isolated so far in thermal (111)Si/SiO $_2$ :

First, electron spin resonance (ESR) spectroscopy revealed the presence at the (111)Si/SiO $_2$  interface of unpaired electrons in the unsaturated  $sp^3$ -hybridized orbitals of the surface Si atoms (so-called  $P_b$  centers) [88, 89]. These defects, commonly referred as “dangling bonds” at the interface, provide a dominant contribution to the  $D_{it}$  in the form of two characteristic peaks corresponding to (+/0) and (0/−) transitions of the amphoteric  $P_b$  centers [90]. The two  $D_{it}$  peaks, about 0.2–0.3 eV width at half height, are positioned approximately symmetrically with respect to the Si band gap edges and are split by 0.4–0.5 eV. The density of  $P_b$  centers per unit interface area is in the range of  $10^{12}$  cm $^{-2}$ , with the “natural” density observed upon

standard thermal oxidation as  $\approx 5 \times 10^{12} \text{ cm}^{-2}$  [91]. It can be enhanced by post-oxidation annealing in an O-free ambient at  $T > 640^\circ\text{C}$  [92]. Annealing in hydrogen further enhances the  $P_b$  density up to values as high as  $\approx 3 \times 10^{13} \text{ cm}^{-2}$  for  $T \geq 800^\circ\text{C}$  [93]. The low-temperature oxidation of (111)Si leads to higher  $P_b$  densities as compared to their “natural” number [94] underlining that  $P_b$ s represent imperfections related to the structural mismatch between Si and  $\text{SiO}_2$  [91].

The important property of  $P_b$  centers consists in their interaction with hydrogen, often referred to as the passivation phenomenon [95]–[97]. It consists in saturation of the “dangling bond” with a H atom leading to elimination of the  $P_b$ -related  $D_{it}$  peaks from the silicon band gap and results in a structureless background interface state spectrum of  $D_{it}$  in the range of  $10^{10} \text{ cm}^{-2} \text{ eV}^{-1}$ . In this way the post-oxidation hydrogen passivation allows to reach the device-grade oxide/semiconductor interface. The reverse process, depassivation, may occur if the interface is treated thermally in a H-free ambient at  $T \geq 500^\circ\text{C}$  [96], or is exposed to electrical stressing [98, 99], ionizing radiation [100] or even to atomic H [101]. In this case, the resulting  $D_{it}$  distribution shows the same characteristic two-peak structure as outlined above.

Second, there are acceptor-type interface states energetically located slightly above the Si conduction band edge as revealed by photon-stimulated electron tunneling (PST) [102, 103]. These states are observed universally in oxidized Si and SiC, suggesting their relationship to an intrinsic oxide defect [103]. Their energy levels determined from both PST and photoionization experiments appears to be at 2.8 eV below the  $\text{SiO}_2$  conduction band bottom [103, 104], i.e., at  $\approx 0.35 \text{ eV}$  above the Si conduction band edge for zero electric field at the interface. As no ESR signal, which might allow atomic identification of these states, is yet detected from the 2.8 eV defect, its structure remains unknown. The enhanced density of the 2.8 eV deep centers observed in Si-rich buried [105] and deposited  $\text{SiO}_2$  layers [104] suggests their possible relationship to some form of excess silicon. As a close energy level is observed for an electron (3.1 eV below the  $\text{SiO}_2$  conduction band edge) in the H-terminated O-vacancy in  $\text{SiO}_2$  [106], some configuration of Si-H bonding seems to be a feasible candidate for the 2.8 eV states. As an alternative one might consider other diamagnetic forms of excess Si in  $\text{SiO}_2$  like the two-fold coordinated Si atom [107] or the Si-Si link in the oxide near its interface with Si [108].

In contrast to the  $P_b$  centers and the 2.8-eV defects, which are present already in the as-oxidized Si/ $\text{SiO}_2$ , the third type of the defects is reproducibly observed only after degrading action, like hot-carrier stressing or irradiation [109, 110]. It represents a broad peak centered at 0.25 eV above the silicon mid gap point, which corresponds to the 0/+ transition of these interface donors with the areal defect densities reaching  $10^{13} \text{ cm}^{-2} \text{ eV}^{-1}$  [111, 112]. No corresponding acceptor-type peak is observed in the lower part of the

Si band gap. The origin of these degradation induced donor states can be traced down to incorporation of some hydrogen-related species near the interface [112, 113]. As the exposure of Si/SiO<sub>2</sub> to atomic hydrogen appears to be sufficient to produce these defects [111], some bonded state of H is suspected to be at its atomic core. Experimental arguments favoring bonding of H to the lone-pair electrons of a bridging O atom in SiO<sub>2</sub>, possibly under strain, have been presented [113, 114] but solid proof for this model is not available yet. These H-induced donors anneal slowly already at room temperature [112], which may explain the complex picture of  $D_{it}$  re-distribution after electrical stressing or irradiation [115], while their generation is completely suppressed for  $T > 150^\circ\text{C}$ .

Hydrogen is also capable of generating thermally stable positively charged states. For instance, it can be trapped in SiO<sub>2</sub> when incorporated in form of a proton directly implanted into SiO<sub>2</sub> [116] or, else, split from an O<sub>3</sub>≡Si-H fragment, leaving a neutral ESR-active O<sub>3</sub>≡Si• defect ( $E'$ -center) behind [117]. In both cases, the positive charge is related to proton trapping and appears to be stable up to at least 180°C with an activation energy for annealing out of  $\approx 1.7$  eV [77]. Even more stable positive centers were reported after annealing of (111)Si/SiO<sub>2</sub> in H<sub>2</sub> at  $T > 500^\circ\text{C}$  [60, 118]. The binding energy of the proton in this configuration exceeds 2 eV [60] which is close to that of the bond of H with a surface Si atom [96, 97]. All together, the observations of different H-induced positive charges at the (111)Si/SiO<sub>2</sub> interface indicate that H<sup>+</sup> can be trapped by a variety of network sites of SiO<sub>2</sub> yielding donor states with different binding energies and with different 0/+ transition energies. Depending on the energy position of the re-charging level with respect

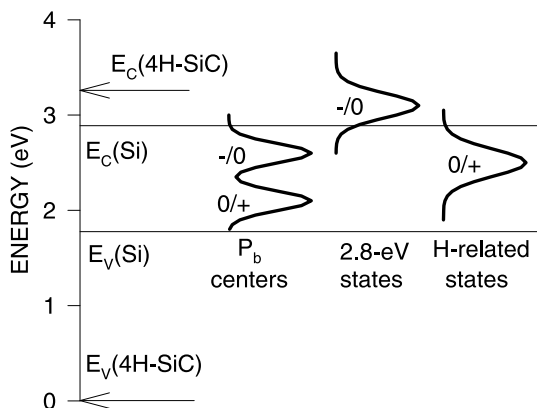


**Fig. 6.** Scheme of identified contributions to the (111)Si/SiO<sub>2</sub>  $D_{it}$ : amphoteric  $P_b$  centers, acceptor-type 2.8-eV states related to the oxygen-deficiency centers in oxide and hydrogen-related interface donor states. The band gap edges position is shown for both Si and 4H-SiC with the zero of energy scale placed at the SiC valence band top

to the conduction band edge of the semiconductor substrate, one can observe the trapped H either as a donor-type interface state or, if the level lies well above the Si conduction band edge, as a fixed positive charge.

Obviously, one can find other components of the Si/SiO<sub>2</sub> interface state spectrum [119] but their identification remains, at best, tentative. Only the three above discussed kinds of interface states have been solidly attributed to certain atomic configurations. Their contributions to the energy distribution of (111)Si/SiO<sub>2</sub> interface states are illustrated in Fig. 6. To give an impression regarding the possible effect of these imperfections on  $D_{it}$  of the SiC/SiO<sub>2</sub> interface, the Si band gap is positioned within the 4H-SiC one according to the measured barrier heights [63].

### 3.2 Dangling Bonds as SiC/SiO<sub>2</sub> Interface States?

On the basis of the structural similarities between the (111)Si/SiO<sub>2</sub> and (0001)SiC/SiO<sub>2</sub> interface one could speculate that in both cases  $P_b$ -like dangling bond centers will provide the dominant contribution to  $D_{it}$ . Though it has been many times repeated in the literature, it should be realized that validation of such hypothesis will require an experimental backing equally solid as in the case of (111)SiO<sub>2</sub>. As indicated in the previous section,  $P_b$  centers (dangling Si bonds) in standard (111)Si/SiO<sub>2</sub> can be distinguished from other contributions to  $D_{it}$  on the basis of three features:

- Observation of an ESR signal typical for dangling bonds of Si or C surface atoms, with an areal density of unpaired electrons corresponding to that of interface states;
- An amphoteric electrical behavior with a peak-type  $D_{it}$  distribution. The latter is suggestive for a defect geometry well defined by the crystalline substrate;
- A passivation-depassivation behavior with respect to hydrogen.

When looking at the available ESR data on SiC/SiO<sub>2</sub> interfaces, two types of dangling bond centers can be distinguished: First, there is a nearly isotropic (with respect to magnet angle) signal at  $g = 2.0027$ – $2.0030$  observed both in cubic and hexagonal SiC [87, 120] of properties similar to the ESR spectrum stemming from unpaired electrons in a-C:H [121]–[123] or in irradiated diamond [124]. Accordingly, it is ascribed to the dangling bond of a carbon atom, possibly in an amorphous surrounding [87]. At least in 3C-SiC, the density of these centers is in the range of the low  $10^{12}$  cm<sup>-2</sup>, which agrees with the integral of the  $D_{it}$  distribution (cf. Fig. 1). Second, there are two recent reports on anisotropic ESR lines in the  $p$ -type 4H-SiC/SiO<sub>2</sub> [125] and in the nano-porous oxidized  $n$ -type 6H-SiC [126]. Both centers show the same  $C_{3v}$  symmetry as the  $P_b$  center, but their spectroscopic parameters are reported to be significantly different. Also, it remains unclear where these centers are located: For instance, the use of double side polished 4H-SiC

substrates with (0001) surface orientation (Si-face) [125] automatically implies that the backside represents an inequivalent C-face. In absence of clear etch-off experiment data, one cannot conclude from what face the signal in the oxidized SiC does originate. Nevertheless, this summary of the ESR data clearly shows that dangling bond centers, probably of several types, can be present in the SiC/SiO<sub>2</sub>. The point now is to evaluate their contribution to  $D_{it}$ .

When looking at the  $D_{it}$  distributions shown in Fig. 1, one may notice that they are generally asymmetric, with a higher density of donor states in the lower part of the SiC band gap than that of acceptor states in the upper part. Moreover as already mentioned, the technologically induced variations in the density of the SiC/SiO<sub>2</sub> donors and acceptors are generally *not correlated*, which must be the case, though, should they stem from the *same amphoteric defect*. It may be added that featureless  $D_{it}$  spectra reported in the literature indicate that there is no peak-type  $D_{it}$  distribution typical for dangling bond defects in registry with a rigid semiconductor crystal. Therefore, it was concluded that the  $P_b$ -type dangling bond centers cannot account for the observed  $D_{it}$  at SiC/SiO<sub>2</sub> interfaces [8, 62, 127].

The impact of hydrogen annealing on  $D_{it}$  in as-oxidized SiC/SiO<sub>2</sub> structures has been discussed in Sect. 2.4. It also suggests a qualitatively different passivation behavior of traps at Si/SiO<sub>2</sub> and SiC/SiO<sub>2</sub> interfaces, which is inconsistent with the dominance of defects of the same type. The remarkable thermal stability of SiC/SiO<sub>2</sub> interface states indicates a high energy barrier for their annealing or passivation. The latter suggests that either the dominant contributions to  $D_{it}$  at the SiC/SiO<sub>2</sub> interface are provided by defects related to saturated atomic configurations or, else, there may be a strong atomic relaxation in the fragments containing an unpaired electron. In any case, these states cannot be described with the concept of a “dangling bond” as the latter would require from the defect atom to preserve largely the same orbital hybridization as the “normally-bonded” atoms at the interface.

However, there is a component of the SiC/SiO<sub>2</sub> interface state spectrum, which has properties closely resembling those of the  $P_b$ -type centers. Namely, the traps generated upon electron/hole injection or irradiation in MOS structures fabricated on hexagonal SiC polytypes exhibit a portion of deep interface states with nearly the same density of interface donors in  $p$ -type and acceptors in  $n$ -type SiC (cf. Fig. 4 in [12]). Moreover, there is a clear impact of hydrogen on the annealing of injection-induced traps (as shown in Fig. 5) observed in the same temperature range as for dangling bonds in Si/SiO<sub>2</sub> ( $\approx 400^\circ\text{C}$ ). Finally, the energy distribution of these defects in the lower part of the SiC band gap has a peak-type form as can be evaluated from the differences observed in  $D_{it}$  between irradiated and subsequently annealed  $p$ -type 6H- and 4H-SiC MOS structures (cf. Figs. 8, 10 and 12 in [33]). It is likely then that the dangling bond defects are present at SiC/SiO<sub>2</sub> interfaces but they are well passivated during capacitor processing and give no immediate contribution to the measured  $D_{it}$ .

### 3.3 Oxide-Related Traps

The wider band gap of SiC than that of Si may entail some oxide defects, which do not act as interface traps in Si/SiO<sub>2</sub>, to behave as SiC/SiO<sub>2</sub> interface states. This might happen if their energy levels enter the energy range corresponding to the semiconductor band gap. Using the barriers determined at the interfaces between Si and SiC with SiO<sub>2</sub> [63, 128] one can point at two energy ranges of interest.

First, the traps with levels close to (or slightly above) the conduction band edge of Si may contribute to  $D_{it}$  at the 6H-SiC/SiO<sub>2</sub> and, particularly, 4H-SiC/SiO<sub>2</sub> interfaces. As already discussed in Sect. 3.1, there are acceptor type electron states at 2.8 eV below the SiO<sub>2</sub> conduction band edge, which are observed by photon-stimulated electron tunneling in the oxides both on Si and SiC [103]. This led to the hypothesis [8], supported by later experimental results [25] that high  $D_{it}$  values near the SiC conduction band edge in 4H-SiC MOS structures may be caused by intrinsic oxide defects. The major features observed of the shallow SiC/SiO<sub>2</sub> interface states are consistent with this model. Among others it qualitatively explains the observed  $D_{it}$  reduction with increasing conduction band offset at the interface, i.e., in the SiC polytype row 4H → 6H → 15R → 3C. The considerable density of slow traps and the energy spread of defect states in this spectral range also indicate that they may be located at some distance from the SiC crystal, i.e., in the oxide layer. Finally, the high thermal stability of these defects is consistent with the observed one of acceptor-type traps in SiC/SiO<sub>2</sub>.

Second, addressing the donor-type traps in the lower part of the SiC bandgap (cf. Fig. 1), one might recall several theoretical works which place in this energy range the levels corresponding to the 0/+ transition for O-vacancy related centers [129, 130]. ESR performed in 3C-SiC/SiO<sub>2</sub> clearly shows that the  $E'$ -centers (O<sub>3</sub>≡Si• entity in SiO<sub>2</sub>, where the dot symbolizes an unpaired electron) originating from O-deficiency centers in SiO<sub>2</sub>, are present in the oxide. Therefore, one could expect a contribution of oxygen vacancies to  $D_{it}$  at the SiC/SiO<sub>2</sub> interface in the lower part of the SiC bandgap. However, annealing in O-free ambient which is known to introduce oxygen deficiency centers, including the  $E'$ -center precursors, appears not to significantly degrade SiC/oxide  $D_{it}$ . Rather, an improvement of the interface properties is often reported [56]. These results suggest that through intrinsic SiO<sub>2</sub> defects could partly contribute to  $D_{it}$  in the lower part of the SiC band gap, but they are unlikely to be dominant.

### 3.4 Hydrogen-Related States

Analysis of hydrogen-related interface states and charges near the Si/SiO<sub>2</sub> interface (cf. Sect. 3.1) strongly suggests that their electrical appearance is determined by trapping of atomic H or protons in the oxide and their subsequent electronic exchange with the semiconductor substrate. Assuming that

the structure is similar for the oxides grown on Si and SiC in the same temperature range, one might expect that trapping of hydrogen, well established in Si/SiO<sub>2</sub> structures, will also occur in the SiC/SiO<sub>2</sub> structures. Indeed, all the H-related charge states discussed in Sect. 3.1 for Si/SiO<sub>2</sub> are also observed in SiC MOS structures. This concerns:

- H-related donor states observed after charge injection into the oxide [87];
- positive charges caused by injected holes [87] or protons in SiO<sub>2</sub> [77];
- positive charge related to bias-temperature stressing of MOS capacitors [79];
- fixed positive charges observed in Si/SiO<sub>2</sub> and SiC/SiO<sub>2</sub> entities after high temperature annealing in hydrogen [60].

There are, however, differences in the electrical and annealing behavior of the H-induced interface donor states related to the different energy position of the band gap edges in Si and SiC relative the interface trap level(s) [87]: These states are generated in significantly different densities in SiC MOS capacitors of different semiconductor conductivity type. Their annealing behavior (determined by trapping of an electron from the substrate [113]) is strongly sensitive to the SiC polytype. Similar polytype-related peculiarities associated with the difference in energy of the SiC conduction band edge are also observed in the density of fixed positive charge observed after high-temperature annealing in hydrogen [60]. Nevertheless, we may conclude that the general picture of H-induced SiC/SiO<sub>2</sub> interface states shows strong resemblance to Si/SiO<sub>2</sub> defects of the same origin.

### 3.5 Carbon Cluster Model of SiC/SiO<sub>2</sub> Interface States

The enhanced SiC/SiO<sub>2</sub>  $D_{it}$  may not only be related to the contribution of states known from Si/SiO<sub>2</sub> studies but may also result from the involvement of new, SiC-specific factors. For instance, as already indicated, even within the energy range corresponding to the Si band gap, the SiC/SiO<sub>2</sub> interface exhibits a much enhanced  $D_{it}$  (cf. Fig. 1). On the basis of the observed trend of an enhanced interface state density on faces of SiC with a larger density of C atoms [8, 63], and significant reduction of  $D_{it}$  by anti-carbon pre-oxidation processing [131], a relationship between the elemental carbon content and  $D_{it}$  of the SiC/SiO<sub>2</sub> interface was suggested [8, 63, 132]. Additionally, it appears that the energy levels of donor-type SiC/SiO<sub>2</sub> interface states in the lower part of the SiC bandgap are the same as those of the upper valence states in wide-bandgap hydrogenated amorphous carbon (a-C:H) [8, 63, 123] suggesting that both originate from the same electron states. In a-C:H, the filled upper states are related to  $\pi$ -orbitals in  $sp^2$ -bonded clusters imbedded in a matrix of predominantly  $sp^3$ -bonded carbon of wide band gap [133]–[136]. Therefore, the  $sp^2$ -bonded C clusters at the interface between SiC and SiO<sub>2</sub> were suggested to represent an important source of interface traps [8, 9, 57, 132, 137].

Since then numerous experimental results appeared in the literature demonstrating clustering of elemental carbon at thermally grown SiC/SiO<sub>2</sub> interfaces and its relationship to the interface state density. Among them, we may mention

- Observation of excess carbon at the 6H-SiC/SiO<sub>2</sub> interfaces using angle resolved X-ray photoelectron spectroscopy and its correlation with  $D_{it}$  [138];
- Atomic-force microscopy observations of C-related particles after removal of the thermal oxide from SiC [58, 139];
- Observation by transmission electron microscopy/energy loss spectroscopy of carbon particles at the SiC/SiO<sub>2</sub> interfaces [140];
- ESR observations of paramagnetic centers related to dangling bonds of C atoms in a surrounding similar to that in amorphous carbon [87, 120].

The potential contribution of  $sp^2$ -bonded carbon clusters to  $D_{it}$  of the SiC/SiO<sub>2</sub> interface can be evaluated using IPE results at the energy position of the filled and empty states relative to the SiO<sub>2</sub> conduction band edge at SiC/SiO<sub>2</sub> and a-C:H/SiO<sub>2</sub> interfaces [8]. The *small clusters*, which have a large band gap width of about 3 eV, will have the top filled  $\pi$ -states located at 4.6 eV below the SiO<sub>2</sub> conduction band, i.e. at 1.4 eV above the valence band of SiC as shown in Fig. 7. When emitting electrons into  $p$ -type SiC, these states will become positively charged. In communication with  $n$ -type SiC, they will retain neutrality because the conduction band of C cluster lies well above the conduction band of any of the SiC polytypes. This donor-type behavior and the inferred of  $+/0$  transition energy are in agreement with the properties of donor states observed at SiC/SiO<sub>2</sub> interfaces (cf. Fig. 1).

*Large clusters*, in which a graphite-like electron state spectrum is developed, will provide a continuous  $D_{it}$  spectrum. The graphite Fermi level lies

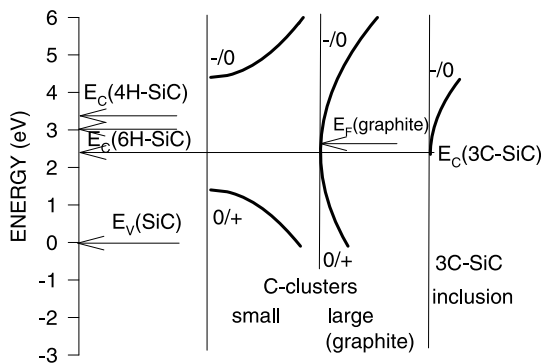


**Fig. 7.** Scheme of SiC-specific contributions to the SiC/SiO<sub>2</sub> interface state density:  $\pi$ -bonded carbon clusters, small and large (graphite-like), and inclusions of the narrow-band gap 3C-SiC polytype. The energy scale origin is taken at the upper SiC valence band edge

energetically at 3.6 eV below the SiO<sub>2</sub> conduction band edge [123], i.e. 2.4 eV above the upper SiC valence band edge. The latter means that in the *n*-type samples of all SiC polytypes, except of 3C-SiC, these clusters will trap an electron yielding a negative charge (cf. Fig. 7). Particularly for 4H-SiC, the small  $\pi$ - $\pi^*$  splitting ( $\approx 1$  eV) observed in the narrow band gap a-C:H layers [123] may give rise to a high  $D_{it}$  near the conduction band. Thus, the contribution of large C clusters is capable of explaining the acceptor-type SiC/SiO<sub>2</sub>  $D_{it}$  in the upper part of the SiC band gap.

It is easy to see from Fig. 7 that combination of contributions to  $D_{it}$  originating from the small and large carbon clusters allows one to reproduce the experimentally observed  $D_{it}$  shown in Fig. 1. At the same time, the known stability of  $\pi$ -bonded carbon compounds against oxidation, interaction with hydrogen, and thermal decomposition may explain the experimentally observed remarkable resistance of SiC/SiO<sub>2</sub> interface traps against post-oxidation processing.

The formation of elemental C clusters during oxidation of SiC may be explained by the oxidation-induced disordering of the semiconductor surface (the “boiling layer” model [141]). Recently, ion scattering studies revealed signs of such disordering in the oxidized 4H-SiC [142] suggesting the possibility of replacing Si atoms in the SiC bi-layer by carbons [143]. This automatically yields an elemental C-cluster, which, taking into account the possibility of asymmetric relaxation in the formed C<sub>4</sub> tetrahedrons, can create *sp*<sup>2</sup>-bonded fragments of carbon atom chains. Further growth of the cluster is possible due to a continuous supply of carbon from the SiC substrate during the oxide growth. Therefore, one might expect that increasing the initial C concentration (which determines the density of the carbon nucleation sites) and the duration of oxidation will result in a higher  $D_{it}$ . Indeed, well in line with this, there are indications of reduced elemental C content [144] and improved electrical properties [145] in SiC/SiO<sub>2</sub> structures with thin thermal oxides.

### 3.6 Other SiC-Specific Contributions to $D_{it}$

In addition to the formation of elemental carbon, the supply of C from SiC crystals may potentially lead to an enhanced density of oxide defects. For instance, carbon has been shown to promote SiO<sub>2</sub> reduction resulting in the generation of oxygen deficiency related oxide traps [146, 147]. However, there is, to our knowledge, no solid proof so far that the oxides thermally grown on SiC are more defective than those grown on Si. The ESR analysis of defects in the oxide grown on SiC shows that the density of  $E'$ -centers ( $O_3 \equiv Si\bullet$  entity in SiO<sub>2</sub>) is comparable to that found in Si/SiO<sub>2</sub> structures [87]. Also other impurities from SiC crystals could potentially be incorporated into the oxide and/or to the interface and result in a degradation of their electrical properties. Though one cannot exclude this possibility *a priori*, the impurity

mechanism cannot explain the differences observed between  $D_{it}$  values measured for different SiC polytypes (cf. Fig. 1). Therefore, the effect of oxide contamination is unlikely to dominate the interface trap generation.

What could appear to be a more feasible model for the interface state generation, is an oxidation-induced polytype transformation in SiC. It has been observed recently that  $4H$ -SiC is partially transformed into  $3C$ -SiC upon thermal oxidation [148]. Taking into account that  $3C$ -SiC has a band gap width of approx.  $\approx 1$  eV smaller than the “host”  $4H$ -SiC and approximately the same energy position of the valence band edge [63], such transformation would lead to an interface state spectrum with continuous  $D_{it}$  down to 1 eV below the  $4H$ -SiC conduction band edge as indicated in Fig. 7. Indeed a high density of  $4H$ -SiC/SiO<sub>2</sub> interface traps is seen to be distributed in the energy range between the conduction band edges of  $4H$ - and  $3C$ -SiC as shown in Fig. 1. No such effect is seen in  $6H$ -SiC MOS structures, which are not prone to the polytype transition. Worth to notice here is that the interface states related to  $3C$ -SiC inclusions lead to hopping-type electron transport near  $4H$ -SiC/SiO<sub>2</sub> interfaces [149], which would agree with experimentally observed thermally activated electron transport in the surface channel of  $4H$ -SiC MOS transistors [51]. However, there are several problems in assigning the high  $D_{it}$  near the conduction band edge of  $4H$ -SiC to inclusions of  $3C$ -SiC. First, the IPE suggests that no measurable decrease in the  $4H$ -SiC volume fraction is observed upon oxidation at temperature as high as 1300°C [64], while the effect observed in [148] may be due to the extremely high concentration of nitrogen dopants in the studied epilayers. Second,  $3C$ -SiC related states are physically located inside the semiconductor and thus must represent fast interface states. These would be unable to retain electrons after trapping them at 77 K, as observed experimentally. Therefore, it seems unlikely that the  $4H \rightarrow 3C$  transition can significantly contribute to the interface trap generation.

The continuum of shallow interface states and, related to this, the observed thermal activation of electron transport, were also ascribed to a structural disorder at the SiC/SiO<sub>2</sub> interfaces [150]. Though the structural analysis of SiC/SiO<sub>2</sub> suggests the possibility of such a disorder [142], this hypothesis is hardly capable of explaining the differences observed between the  $D_{it}$  of different polytypes of SiC (Fig. 1) because the degree of disorder must be nearly polytype-insensitive. Would one consider disorder as a perturbation to the SiC periodic crystal potential, a comparable tail-like  $D_{it}$  should tail off from the conduction and valence band edges down the gap in all the polytypes, which is not the case. Rather, the disorder may be treated in terms of structural defects both in SiC and SiO<sub>2</sub> or “normally absent” chemical bonds like C-C ones in a carbon cluster. In this case the impact of disorder on the  $D_{it}$  spectrum will be an increased contribution of one of the discussed imperfections.

4 Alternative Insulators on SiC

The problems associated with SiO<sub>2</sub>-based gate insulation for SiC, including a high interface state density and insufficient stability of the oxide's electrical properties at elevated temperatures and in high electric fields, has inspired researchers to evaluate the possibility of the application of other insulators. Several attempts were made to use Al-based insulating materials, like AlN and Al<sub>2</sub>O<sub>3</sub>, as a replacement for SiO<sub>2</sub> [13]–[16],[151]. It appears, however, that they provide no substantial improvements as compared to silicon dioxide, and suffer both from the high interface state density and substantial leakage current. The latter suggests that the deposited Al nitride and Al oxide films cannot provide an interface energy barrier sufficiently high to block electron/hole injection because both of them have a band gap width only slightly exceeding 6 eV [152]–[154].

Substantial technological developments related to the perspectives of metal oxide applications in Si MOS electronics [18] has made possible the well controlled growth of other metal oxides on semiconductor substrates. Using the experimentally determined band gap values and barrier heights for electrons/holes at the interfaces of different insulators with silicon [154]–[159], the expected band offsets between these insulating oxides and SiC polytypes can be calculated, if assuming the absence of substantial interface dipoles [17]. The results are listed in Table 1 both for the “classical” SiO<sub>2</sub> and three metal oxides: Al<sub>2</sub>O<sub>3</sub>, ZrO<sub>2</sub> and HfO<sub>2</sub>. It is immediately clear that all the alternative insulating materials have greatly reduced valence band offsets at the interfaces with SiC as compared to SiO<sub>2</sub>. This means that the barrier height for hole emission from SiC is low and, under negative bias conditions, large leak-

**Table 1.** Conduction and valence band offsets  $\Delta E_C$  and  $\Delta E_V$ , at the interfaces of Si and SiC with different insulators

Insulator	SiO <sub>2</sub>	Al <sub>2</sub> O <sub>3</sub>	ZrO <sub>2</sub>	HfO <sub>2</sub>
$E_g$ (eV)	<b>8.9</b>	<b>6.2</b>	<b>5.4</b>	<b>5.6/5.9</b>
Semi-conductor	$\Delta E_C/\Delta E_V$ [eV]	$\Delta E_C/\Delta E_V$ [eV]	$\Delta E_C/\Delta E_V$ [eV]	$\Delta E_C/\Delta E_V$ [eV]
Si	<b>3.1/4.7</b>	<b>2.1/3.0</b>	<b>2.0/2.3</b>	<b>2.0/2.5</b>
3C-SiC	<b>3.6/2.9</b>	2.6/1.2	2.5/0.5	2.5/0.7
15R-SiC	<b>3.0/2.9</b>	2.0/1.2	1.9/0.5	1.9/0.7
6H-SiC	<b>2.95/2.9</b>	1.95/1.2	1.85/0.5	1.85/0.7
4H-SiC	<b>2.7/2.9</b>	1.7/1.2	1.6/0.5	1.6/0.7

<sup>a</sup> Bold numbers indicate experimental band gap and band offset values determined by internal electron photoemission spectroscopy

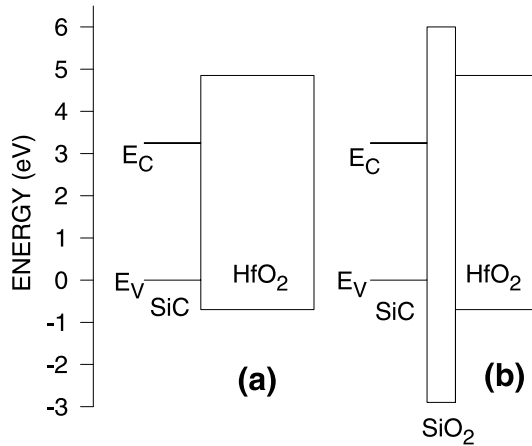


**Fig. 8.** Energy band diagram of the  $4H$ -SiC/HfO<sub>2</sub> (a) and  $4H$ -SiC/SiO<sub>2</sub>/HfO<sub>2</sub> (b) interfaces inferred from IPE experiments on the SiC/SiO<sub>2</sub>, Si/SiO<sub>2</sub>, and Si/HfO<sub>2</sub> interfaces. The zero of the energy scale is taken at the upper silicon carbide valence band edge

age currents will be observed in the MOS capacitors explaining the above mentioned literature results.

A possible solution of the problems related to the low valence band offset consists of the insertion of a thin layer of the classical wide-band gap insulator SiO<sub>2</sub> between SiC and the metal oxide [17] as depicted in Fig. 8. This would result in a significant suppression of the hole tunneling rate, both because of the enhanced SiC/SiO<sub>2</sub> barrier height [128] and the high effective mass of holes in SiO<sub>2</sub> [160]. One may also expect an improvement of the SiC/insulator interface properties because, as already mentioned, ultrathin native oxides on SiC do exhibit superior electrical properties as compared to thicker ones [17]. At the same time, it is experimentally observed that the interface barrier height corresponding to SiO<sub>2</sub> is maintained in oxides as thin as  $\approx 1$  nm [155], which would make it sufficient to (pre)grow only a few nm of SiO<sub>2</sub> on SiC.

This approach to insulator formation on SiC has been tested recently using HfO<sub>2</sub> deposition at 400°C from the nitrato precursor Hf(NO<sub>3</sub>)<sub>4</sub> [161]. The latter was chosen because it contains no carbon which might degrade the interface quality. Moreover, there is no hydrogen-containing species which could damage the thin SiO<sub>2</sub> interlayer [162] grown on SiC prior to the HfO<sub>2</sub> deposition. The successful suppression of hole injection into the insulator is revealed by current-voltage curves as shown in Fig. 9 for (0001) $4H$ -SiC/3 nm SiO<sub>2</sub>/20 nm HfO<sub>2</sub>/Au MOS capacitors without and with high-temperature post-deposition anneal. It is seen that despite of the large difference in barrier heights for electrons and holes at the SiC/HfO<sub>2</sub> interface (cf. Fig. 8a) no enhanced hole injection is observed in SiC-based MOS capacitors with SiO<sub>2</sub> interlayer. By contrast, large leakage currents are observed in the structures

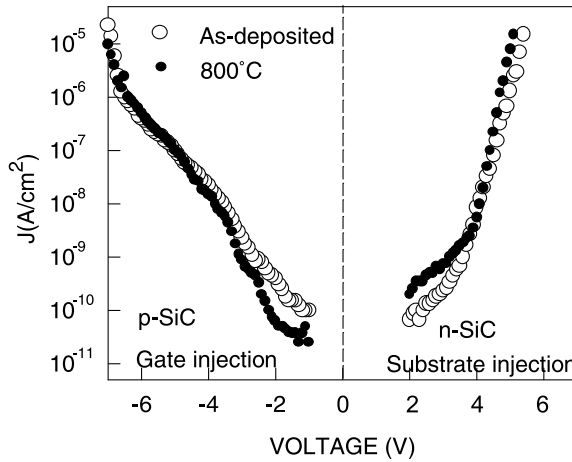


**Fig. 9.** Current-voltage curves of *n*- and *p*-type 4*H*-SiC MOS capacitors with an insulating stack of 3 nm SiO<sub>2</sub> and 20 nm HfO<sub>2</sub> without (○) and with (●) a 10 min post-deposition anneal at 800°C in 5% O<sub>2</sub> + N<sub>2</sub>

with HfO<sub>2</sub> insulator deposited immediately on the clean SiC surface (curves not shown).

The benign effect of incorporating a thin SiO<sub>2</sub> interlayer is further supported by the *C-V* analysis of SiC/insulator interface properties. In Fig. 10 the *C-V* curves for both *n*- and *p*-type samples obtained by depositing 20 nm HfO<sub>2</sub> onto differently prepared (0001)4*H*-SiC surfaces are compared. In the first case (solid lines), the oxide was deposited onto a clean SiC surface, where the by-products of Hf precursor decomposition (NO, NO<sub>2</sub>) are allowed to oxidize it at the temperature of deposition (400°C). In the case of a Si substrate, such a procedure yields a 1.5–2 nm thick silicon oxynitride layer [163]. It is seen that in the case of SiC the interface appears to be highly defective with a large density of charges present both in *n*- and *p*-type samples and a high density of leakage current. In the second case (*C-V* curves shown by dashed lines), prior to the HfO<sub>2</sub> deposition, the SiC surface was oxidized at room temperature by exposure to UV radiation and ozone [131]. This oxidation at low temperature is also seen to result in poor interface properties. Only in the case of high temperature (1000°C) oxidation, a high quality interface is attained as indicated by the dotted *C-V* curves. Remarkable is the 3 V difference in the flat band voltages measured between the *n*- and *p*-type MOS capacitor; it corresponds to an interface state density in the range of 10<sup>11</sup> cm<sup>-2</sup> eV<sup>-1</sup>, suggesting improved electrical properties of the 4*H*-SiC/SiO<sub>2</sub> interface as compared to the thicker (50–100 nm) oxides (cf. Fig. 1). Comparison between low-temperature UV/ozone grown and thermally grown oxides on SiC indicates that only the last ones are capable of providing an interface with a semiconductor of acceptable electrical quality.

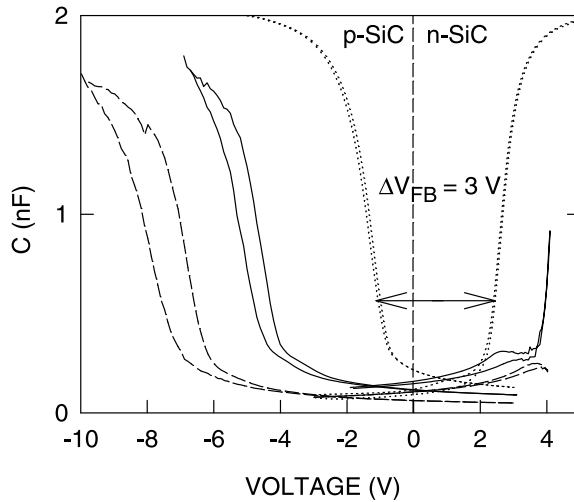


**Fig. 10.** 10 kHz  $C$ - $V$  curves of 3 kinds of  $n$ - and  $p$ -type  $4H$ -SiC MOS capacitors combining 20 nm thick  $\text{HfO}_2$  with three different types of Si dioxide interlayers: Si dioxide grown at  $400^\circ\text{C}$  in NO and  $\text{N}_2\text{O}$  by-products during  $\text{HfO}_2$  deposition on a clean SiC surface (*solid lines*), oxide grown at room temperature by exposure to UV radiation and ozone (*dashed lines*), and 3 nm thick thermally grown at  $1000^\circ\text{C}$   $\text{SiO}_2$  (*dotted lines*).  $C$ - $V$  traces are shown for both directions of the voltage sweep

Therefore, the already discussed contributions to the SiC/ $\text{SiO}_2$  interface state density are likely to remain important issues, even when attempting to apply an alternative insulating material to SiC.

## 5 Conclusions

The reviewed results on the properties of SiC/ $\text{SiO}_2$  interface states allow identification of the most important contributions to the  $D_{\text{it}}$  spectrum. In as-oxidized SiC/ $\text{SiO}_2$ , the interface state density is dominated by carbon-cluster related centers responsible both for the donor states in the lower part of the SiC band gap and for a continuum of states in the central part of the band gap. The acceptor-type defects in the upper part of the band gap in the case of hexagonal SiC polytypes are likely related to intrinsic oxide defects correlated with an O-deficiency, but atomic identification is still lacking. The dominant contributions to the interface states observed after degradation of the SiC/ $\text{SiO}_2$  interface can be associated with amphoteric dangling bond centers, H-related interface donor states and with the modification of C-cluster states. The latter may also be related to the impact of hydrogenic species on the SiC/ $\text{SiO}_2$  interface.

Any possible improvement of the properties of the SiC/ $\text{SiO}_2$  interface must address all the indicated components of  $D_{\text{it}}$ . Taking into account the

different origin of the observed imperfections, it is unlikely that one "magic" technological step will be sufficient to entirely resolve the problem, if such a recipe would exist at all. Rather, one may look for the combination of methods which permit simultaneous reduction of different groups of interface defects. Most promising approaches, partially discussed in the present work, include the combination of ultrathin thermal oxide on SiC with a deposited insulating layer of another type, nitridation of the interfacial oxide and optimal choice of the SiC polytype. In this way, one may hope to reach the desired SiC/SiO<sub>2</sub> interface quality.

## References

1. M. Ruff, H. Mitlehner, and R. Helbig: IEEE Trans. Electron Devices **ED-41**, 1040 (1994)
2. H. Morçoç, S. Strite, G.B. Gao, M.E. Lin, B. Sverdlov, and M. Burns: J. Appl. Phys. **76**, 1363 (1994)
3. J.A. Cooper, Jr.: Phys. Status Solidi **A162**, 305 (1997)
4. M.R. Melloch and J.A. Cooper, Jr.: MRS Bull. **22**, 42 (1997)
5. H. Matsunami: Mater. Sci. Forum **389-393**, 3 (2002)
6. J.A. Cooper, Jr.: Mater. Sci. Forum **389-393**, 15 (2002)
7. See, e.g., W.J. Choyke: in *The Physics and Chemistry of Carbides, Nitrides, and Borides*, ed. by R. Freer, NATO ASI Series Vol. 185 (Kluwer, Dordrecht, the Netherlands, 1990) p. 653
8. V.V. Afanas'ev, M. Bassler, G. Pensl, and M.J. Schulz: Phys. Status Solidi **A 162**, 321 (1997)
9. V.V. Afanas'ev: Microelectron. Eng. **48**, 241 (1999)
10. M.M. Maranovski and J.A. Cooper, Jr.: IEEE Trans. Electron Devices **ED-46**, 520 (2000)
11. V.V. Afanas'ev, A. Stesmans, M. Bassler, G. Pensl, M.J. Schulz and C.I. Harris: J. Appl. Phys. **55**, 8292 (1999)
12. V.V. Afanas'ev and A. Stesmans: Mater. Sci. Eng. B **71**, 309 (2000)
13. C.I. Harris, M.O. Aboelfotoh, R.S. Kern, S. Tanaka, and R.F. Davis: Inst. Phys. Conf. Ser. **142**, 777 (1996)
14. C.-M. Zetterling, M. Östling, N. Nordell, O. Schön, and M. Deschler: Appl. Phys. Lett. **70**, 3549 (1997)
15. L. Lipkin and J. Palmour: IEEE Trans. Electron Devices **ED-46**, 525 (1999)
16. H.R. Lazar, V. Misra, R.S. Johnson, and G. Lucovsky: Appl. Phys. Lett. **79**, 973 (2001)
17. V.V. Afanas'ev, M. Bassler, G. Pensl, and A. Stesmans: Mater. Sci. Forum **389-393**, 961 (2002)
18. G.D. Wilk, R.M. Wallace, and J.M. Anthony: J. Appl. Phys. **89**, 5243 (2001)
19. M. Shinohara, M. Yamanaka, S. Misawa, H. Okumura, and S. Yoshida: Jap. J. Appl. Phys. **30**, 240 (1991)
20. D.M. Brown, M. Ghezzo, J. Ketchmer, E. Downey, J. Pimbley, and J. Palmour: IEEE Trans. Electron Devices **ED-41**, 618 (1994)
21. D. Alok, P.K. McLarty, and B.J. Baliga: Appl. Phys. Lett. **65**, 2177 (1994)

22. H. Yano, F. Katafuchi, T. Kimoto, and H. Matsunami: IEEE Trans. Electron Devices **ED-46**, 504 (1999)
23. J.N. Shenoy, G.L. Chindalore, M.R. Melloch, J.A. Cooper, Jr., J.W. Palmour, and K.G. Irvine: J. Electron. Mater. **24**, 303 (1995)
24. M. Bassler, V.V. Afanas'ev, and G. Pensl: Mater. Sci. Forum **264-268**, 861 (1998)
25. V.V. Afanas'ev, A. Stesmans, M. Bassler, G. Pensl, and M.J. Schulz: Appl. Phys. Lett. **76**, 336 (2000)
26. N.S. Saks, S.S. Mani, and A.K. Agarwal: Appl. Phys. Lett. **76**, 2250 (2000)
27. M. Bassler, V.V. Afanas'ev, G. Pensl, and M.J. Schulz: Mater. Sci. Forum **338**, 1065 (2000)
28. H.Ö. Olafsson, E.Ö. Sveinbjornsson, T.E. Rudenko, V.I. Kilchytska, I.P. Tyagulski, and I.N. Osiyuk: Mater. Sci. Forum **389-393**, 1001 (2002)
29. F. Ciobanu, G. Pensl, H. Nagasawa, A. Schöner, S. Dimitrijevic, K.-Y. Cheong, V.V. Afanas'ev, and G. Wagner: Mater. Sci. Forum **433-436**, 551 (2003)
30. N.S. Saks, M.G. Ancona, and R.W. Rendell: Appl. Phys. Lett. **80**, 3219 (2002)
31. M.K. Das, G.Y. Chung, J.R. Williams, N.S. Saks, L.A. Lipkin, and J.W. Palmour: Mater. Sci. Forum, **389-393**, 981 (2002)
32. J.N. Shenoy, J.A. Cooper, Jr., and M.R. Melloch: Appl. Phys. Lett. **68**, 803 (1996)
33. J. Campi, Y. Shi, Y. Luo, F. Yan, and J.H. Zhao: IEEE Trans. Electron Devices **ED-46**, 511 (1999)
34. P. Friedrichs, E.P. Burt, and R. Schorner: J. Appl. Phys. **79**, 7814 (1996)
35. K. Shibahara, S. Nishini, and H. Matsunami: Jap. J. Appl. Phys. **23**, L862 (1984)
36. R.E. Avila, J.J. Kopanski, and C.D. Fung: Appl. Phys. Lett. **49**, 334 (1986)
37. M.I. Chaudhry and W.B. Berry: J. Mater. Res. **4**, 1491 (1989)
38. S.M. Tang, W.B. Berry, R. Kwor, M.V. Zeller, and L.G. Matus: J. Electrochem. Soc. **137**, 221 (1990)
39. S. Zaima, K. Onoda, Y. Koide, and S. Yasuda: J. Appl. Phys. **68**, 6304 (1990)
40. M.I. Chaudry: J. Appl. Phys. **69**, 7319 (1991)
41. M. Yoshikawa, H. Itoh, Y. Morita, I. Nashiyama, S. Misawa, H. Okumura, and S. Yoshida: J. Appl. Phys. **70**, 1309 (1991)
42. C. Raynaud, J.-L. Autran, J.-B. Briot, B. Balland, N. Becourt, and C. Jausaud: J. Electrochem. Soc. **142**, 282 (1995)
43. R. Schorner, P. Friedrichs, D. Peters, and D. Stephani: IEEE Electron Device Lett. **20**, 241 (1999)
44. H. Yano, T. Kimoto, H. Matsunami, M. Bassler, and G. Pensl: Mater. Sci. Forum **338**, 1109 (2000)
45. C.-M. Zetterling and M. Östling: Physica Scripta **T54**, 291 (1994)
46. K. Fukuda, W.J. Cho, K. Arai, S. Suzuki, J. Senzaki, and T. Tanaka: Appl. Phys. Lett. **77**, 866 (2000)
47. F. Lanois, D. Planson, P. Lassagne, C. Raynaud, and E. Bano: Mater. Sci. Forum, **264-268**, 1029 (1998)
48. J.N. Shenoy, M.K. Das, G.L. Chindalore, J.A. Cooper, Jr., M.R. Melloch, J.W. Palmour, and K.G. Irvine: Inst. Phys. Conf. Ser. **142**, 745 (1996)
49. J.N. Shenoy, M.K. Das, J.A. Cooper, Jr., M.R. Melloch, and J.W. Palmour: J. Appl. Phys. **79**, 3042 (1996)
50. H. Yano, T. Kimoto, and H. Matsunami: Appl. Phys. Lett. **81**, 301 (2002)

51. H. Yano, T. Hirao, T. Kimoto, and H. Matsunami: Appl. Phys. Lett. **78**, 374 (2001)
52. K. Fukuda, J. Senzaki, M. Kushibe, K. Kijima, R. Kosugi, S. Suzuki, S. Harada, T. Suzuki, T. Tanaka, and K. Arai: Mater. Sci. Forum **389–393**, 1057 (2002)
53. T. Hirao, Y. Yano, T. Kimoto, H. Matsunami, and H. Shiomi: Mater. Sci. Forum **389–393**, 1065 (2002)
54. E.A. Irene: J. Electrochem. Soc. **125**, 1708 (1978)
55. J.M. Gibson and D.W. Dong: J. Electrochem. Soc. **127**, 2722 (1980)
56. E.G. Stein von Kamienski, F. Portheine, J. Stein, A. Golz, and H. Kurz: J. Appl. Phys. **79**, 2529 (1996)
57. C.I. Harris and V.V. Afanas'ev: Microelectron. Eng. **36**, 167 (1997)
58. V.V. Afanas'ev, A. Stesmans, and C.I. Harris: Mater. Sci. Forum **264–268**, 857 (1998)
59. K. Fukuda, S. Suzuki, T. Tanaka, and K. Arai: Appl. Phys. Lett. **76**, 1585 (2000)
60. V.V. Afanas'ev and A. Stesmans: Phys. Rev. Lett. **80**, 5176 (1998)
61. L.A. Lipkin and J.A. Palmour: J. Electron. Mater. **25**, 909 (1996)
62. V.V. Afanas'ev: Microelectron. Eng. **48**, 241 (1999)
63. V.V. Afanas'ev, M. Bassler, G. Pensl, M.J. Schulz, and E. Stein von Kamienski: J. Appl. Phys. **79**, 3108 (1996)
64. V.V. Afanas'ev and A. Stesmans: Mater. Sci. Eng. B, in print
65. H.F. Li, S. Dimitrijević, H.B. Harrison, and D. Sweatman: Appl. Phys. Lett. **70**, 2028 (1997)
66. H.F. Li, S. Dimitrijević, D. Sweatman, and H.B. Harrison: J. Electron. Mater. **29**, 1027 (2000)
67. P. Jamet and S. Dimitrijević: Appl. Phys. Lett. **79**, 323 (2001)
68. P. Jamet, S. Dimitrijević, and P. Tanner: J. Appl. Phys. **90**, 5058 (2001)
69. R. Schorner, P. Friedrichs, D. Peters, D. Stephani, S. Dimitrijević, and P. Jamet: Appl. Phys. Lett. **80**, 4253 (2002)
70. G.Y. Chung, C.C. Tin, J.R. Williams, K. McDonald, M. DiVentra, S.T. Pantelides, L.C. Feldman, and R.A. Weller: Appl. Phys. Lett. **76**, 1713 (2000)
71. V.V. Afanas'ev, A. Stesmans, F. Ciobanu, G. Pensl, K.Y. Cheong, and S. Dimitrijević: Appl. Phys. Lett. **82**, 568 (2003)
72. P.T. Lai, S. Chakraborty, C.L. Chan, and Y.C. Cheng: Appl. Phys. Lett. **76**, 3744 (2000)
73. G.Y. Chung, C.C. Tin, J.R. Williams, K. McDonald, M. DiVentra, S.T. Pantelides, L.C. Feldman, and R.A. Weller: Appl. Phys. Lett. **77**, 3601 (2000)
74. W. Xie, J.N. Shenoy, S.T. Sheppard, M.R. Melloch, and J.A. Cooper, Jr.: Appl. Phys. Lett. **68**, 2231 (1996)
75. K. Ueno: Mater. Sci. Forum **264–268**, 845 (1998)
76. V.V. Afanas'ev and A. Stesmans: Phys. Rev. B **60**, 5506 (1999)
77. V.V. Afanas'ev, F. Ciobanu, G. Pensl, and A. Stesmans: Solid State Electron. **46**, 1815 (2002)
78. V.V. Afanas'ev, J.M.M. de Nijs, P. Balk, and A. Stesmans: J. Appl. Phys. **78**, 6481 (1995)
79. M. Bassler, V.V. Afanas'ev, G. Pensl, and M. Schulz: Microelectron. Eng. **48**, 257 (1999)
80. N. Yamada, H. Fuma, and H. Tadano: Inst. Phys. Conf. Ser. **142**, 737 (1996)

81. C.E. Blat, E.H. Nicollian, and E.H. Poindexter: J. Appl. Phys. **69**, 1712 (1991)
82. G.J. Gerardi, E.H. Poindexter, M. Harmatz, W.L. Warren, E.H. Nicollian, and A.H. Edwards: J. Electrochem. Soc. **138**, 3765 (1991)
83. A.K. Agarwal, S. Seshardi, and L.B. Rowland: IEEE Electron Dev. Lett. **18**, 592 (1997)
84. L. Patrick and W.J. Choyke: Phys. Rev. Lett. **2**, 48 (1959)
85. E. Bano, T. Ouisse, P. Lassagne, T. Billon, and C. Jaussaud: Inst. Phys. Conf. Ser. **142**, 733 (1996)
86. V.V. Afanas'ev, M. Bassler, G. Pensl, and M.J. Schulz: Microelectron. Eng. **28**, 197 (1995)
87. V.V. Afanas'ev and A. Stesmans: Appl. Phys. Lett. **69**, 2252 (1996)
88. E.H. Poindexter: Semicond. Sci. Technol. **4**, 961 (1989)
89. C.R. Helms and E.H. Poindexter: Rep. Prog. Phys. **57**, 791 (1994)
90. M.J. Uren, J.H. Stathis, and E. Cartier: J. Appl. Phys. **80**, 3915 (1996)
91. A. Stesmans: Phys. Rev. B **48**, 2418 (1993)
92. A. Stesmans and V.V. Afanas'ev: Phys. Rev. B **54**, R11 129 (1996)
93. A. Stesmans and V.V. Afanas'ev: Appl. Phys. Lett. **72**, 2271 (1998)
94. A. Stesmans and V.V. Afanas'ev, Appl. Phys. Lett. **77**, 1469 (2000)
95. K.L. Brower: Phys. Rev. B **38**, 9657 (1988)
96. K.L. Brower: Phys. Rev. B **42**, 3444 (1990)
97. For review of recent data see, e.g., A.L. Stesmans: in *Defects in SiO<sub>2</sub> and Related Dielectrics: Science and Technology*, ed. by G. Paccioni, L. Skuja, and D.L. Griscom. NATO ASI Series II Vol. 2 (Kluwer, Dordrecht, the Netherlands, 2000), p. 529
98. J.H. Stathis: Microelectron. Eng. **22**, 191 (1993)
99. J.W. Gabrys, P.M. Lenahan, and W. Weber: Microelectron. Eng. **22**, 273 (1993)
100. P.M. Lenahan and P.V. Dressendorfer: Appl. Phys. Lett. **44**, 86 (1984)
101. J.H. Stathis and E. Cartier: Phys. Rev. Lett. **72**, 2745 (1994)
102. V.V. Afanas'ev and A. Stesmans: J. Phys: Condens. Matter **9**, L55 (1997)
103. V.V. Afanas'ev and A. Stesmans: Phys. Rev. Lett. **78**, 2437 (1997)
104. V.V. Afanas'ev and A. Stesmans: Microelectron. Eng. **36**, 149 (1997)
105. V.V. Afanas'ev and A. Stesmans: Appl. Phys. Lett. **70**, 1260 (1997)
106. V.V. Afanas'ev and A. Stesmans: Appl. Phys. Lett. **71**, 3844 (1997)
107. L. Skuja: J. Non-Cryst. Solids **239**, 16 (1998)
108. G. Pacchioni and G. Ierano: Phys. Rev. B **57**, 818 (1998)
109. C.T. Sah, J.Y.C. Sun, and J.J.T. Tzou: J. Appl. Phys. **53**, 8886 (1982)
110. C.T. Sah, J.Y.C. Sun, and J.J.T. Tzou: J. Appl. Phys. **54**, 5864 (1983)
111. E. Cartier and J.H. Stathis: Microelectron. Eng. **28**, 3 (1995)
112. C.T. Sah, J.Y.C. Sun, and J.J.T. Tzou: J. Appl. Phys. **55**, 1525 (1984)
113. J.M.M. de Nijs, K.G. Druif, V.V. Afanas'ev, E. van der Drift, and P. Balk: Appl. Phys. Lett. **65**, 2428 (1994)
114. J.M.M. de Nijs, K.G. Druif, P. Balk, and V.V. Afanas'ev: in *Fundamental Aspects of Ultrathin Dielectrics on Si-Based Devices: Towards an Atomic-Scale Understanding*, ed. by A.Ya. Vul'. NATO ASI Series III Vol. 47 (Kluwer, Dordrecht, the Netherlands, 1998), p. 425
115. T.P. Ma: Microelectron. Eng. **22**, 197 (1993)
116. V.V. Afanas'ev, G.J. Adriaenssens, and A. Stesmans: Microelectron. Eng. **59**, 85 (2001)

117. V.V. Afanas'ev and A. Stesmans: *Europhys. Lett.* **53**, 233 (2001)
118. V.V. Afanas'ev and A. Stesmans: *Appl. Phys. Lett.* **72**, 79 (1998)
119. See, e.g., Y.C. Cheng: *Progr. Surf. Sci.* **8**, 181 (1977)
120. P.J. Macfarlane and M.E. Zvanut: *J. Appl. Phys.* **88**, 4122 (2000)
121. S.P. Wong, S. Peng, N. Ke, and P. Li: *Nucl. Instr. Methods* **80/81**, 1494 (1995)
122. Y. Bounouh, L. Chaded, A. Sadki, M.L. Theye, C. Cardinaud, M. Zarrbian, H.J. von Bardeleben, K. Zellama, J. Cernogora, and J.-L. Fave: *Diamond Relat. Mater.* **4**, 492 (1995)
123. V.V. Afanas'ev, A. Stesmans, and M.O. Andersson: *Phys. Rev. B* **54**, 10820 (1996)
124. Y. Mori, Y. Show, M. Deguchi, H. Yagi, H. Yagyu, N. Eimori, T. Okada, A. Hatta, K. Nishimura, M. Kitabatake, T. Ito, T. Hirao, T. Izumi, T. Sasaki, and A. Hiraki: *Jpn. J. Appl. Phys.* **32**, L987 (1993)
125. J. Isoya, R. Kosugi, K. Fukuda, and S. Yamasaki: *Mater. Sci. Forum* **389–393**, 1025 (2002)
126. H.J. von Bardeleben, J.L. Cantin, S.E. Saddow, and M. Mynbaeva: *Mater. Sci. Forum* **433–436**, 459 (2002)
127. V.V. Afanas'ev, A. Stesmans, M. Bassler, G. Pensl, and M.J. Schulz: *Appl. Phys. Lett.* **78**, 4043 (2001)
128. V.V. Afanas'ev and A. Stesmans: *Appl. Phys. Lett.* **77**, 2024 (2000)
129. A. Chu and W.B. Fowler: *Phys. Rev. B* **41**, 5061 (1990)
130. K.C. Snyder and W.B. Fowler: *Phys. Rev. B* **48**, 13238 (1993)
131. V.V. Afanas'ev, A. Stesmans, M. Bassler, G. Pensl, M.J. Schulz and C.I. Harris: *Appl. Phys. Lett.* **68**, 2141 (1996)
132. G. Pensl, V.V. Afanas'ev, M. Bassler, M. Schadt, T. Troffer, J. Heindl, H.P. Strunk, M. Maier, and W.J. Choyke: *Inst. Phys. Conf. Ser.* **142**, 275 (1996)
133. J. Robertson: *Adv. Phys.* **35**, 317 (1984)
134. D.D. Dasgupta, F. Demichelis, C.F. Pirri, and A. Tagliaferro: *Phys. Rev. B* **43**, 2131 (1991)
135. C.H. Lee, W.R.L. Lambrecht, B. Segall, P.C. Kelires, Th. Frauenheim, and U. Stephan: *Phys. Rev. B* **49**, 11 448 (1994)
136. J. Robertson: *Diamond Relat. Mater.* **4**, 297 (1995)
137. M. Bassler, G. Pensl, and V.V. Afanas'ev: *Diamond Relat. Mater.* **6**, 1472 (1997)
138. V.K. Vathuya, D.N. Wang, and M.H. White: *Appl. Phys. Lett.* **73**, 2161 (1998)
139. A. Koh, A. Kestle, C. Wright, S.P. Wilks, P.A. Mawby, and W.R. Bowen: *Appl. Surf. Sci.* **174**, 210 (2001)
140. K.C. Chang, T. Nuhfer, L.M. Porter, and Q. Wahab: *Appl. Phys. Lett.* **77**, 2186 (2000)
141. C.J. Sofield and A.M. Stoneham: *Semicond. Sci. Technol.* **10**, 215 (1995)
142. D.J. Hayton, T.E. Jenkins, P. Bailey, and T.C.Q. Noakes: *Semicond. Sci. Technol.* **17**, L29 (2002)
143. P. Martensson, F. Owman, and L.I. Johansson: *Phys. Status Solidi B* **202**, 501 (1997)
144. L. Simon, L. Kubler, A. Ermolieff, and T. Billon: *Phys. Rev. B* **60**, 5673 (1999)
145. V.V. Afanas'ev, M. Bassler, G. Pensl, and A. Stesmans: *Mater. Sci. Forum* **389–393**, 961 (2002)
146. A.G. Revesz, G.A. Brown, and H.L. Hughes: *Mater. Res. Soc. Symp. Proc.* **244**, 555 (1993)

147. S.I. Raider: *Microelectron. Eng.* **22**, 29 (1993)
148. R.S. Okojie, M. Xhang, P. Pirous, S. Tumakha, G. Jessen, and L.J. Brillson: *Appl. Phys. Lett.* **79**, 3056 (2001)
149. A.O. Konstantinov, Q. Wahab, C. Hallin, C.I. Harris, and B. Pecz: *Mater. Sci. Forum* **264–268**, 1025 (1998)
150. T. Ouisse: *Phys. Status Solidi (a)* **169**, 339 (1997)
151. N. Onojima, J. Suda, and H. Matsunami: *Appl. Phys. Lett.* **80**, 76 (2002)
152. W.M. Wim, E.J. Stofko, P.J. Zanzucchi, J.I. Pankove, M. Ettenberg, and S.L. Gilbert: *J. Appl. Phys.* **44**, 292 (1973)
153. P.B. Perry and R.F. Rutz: *Appl. Phys. Lett.* **33**, 319 (1978)
154. V.V. Afanas'ev, A. Stesmans, B.J. Mrstik, and C. Zhao: *Appl. Phys. Lett.* **81**, 1678 (2002)
155. V.V. Afanas'ev, M. Houssa, A. Stesmans, and M.M. Heyns: *Appl. Phys. Lett.* **78**, 3073 (2001)
156. V.V. Afanas'ev, M. Houssa, A. Stesmans, and M.M. Heyns: *J. Appl. Phys.* **91**, 3079 (2002)
157. V.V. Afanas'ev, M. Houssa, A. Stesmans, G.J. Adriaenssens, and M.M. Heyns: *J. Non-Cryst. Solids* **303**, 69 (2002)
158. V.V. Afanas'ev, A. Stesmans, F. Chen, X. Shi, and S.A. Campbell: *Appl. Phys. Lett.* **81**, 1053 (2002)
159. V.V. Afanas'ev, A. Stesmans, and W. Tsai: *Appl. Phys. Lett.* **82**, 245 (2003)
160. See, e.g., J.R. Chelikovsky and M. Schlüter: *Phys. Rev. B* **15**, 4020 (1977)
161. V.V. Afanas'ev, A. Stesmans, F. Chen, S.A. Campbell, and R. Smith: *Appl. Phys. Lett.* **82**, 922 (2003)
162. F.J. Feigl, D.R. Young, D.J. DiMaria, S. Lai, and J. Calise: *J. Appl. Phys.* **52**, 5665 (1981)
163. S.A. Campbell, T.Z. Ma, R. Smith, W.L. Gladfelter, and F. Chen: *Microelectron. Eng.* **59**, 361 (2001)

# Properties of Nitrided Oxides on SiC

S. Dimitrijević, H.B. Harrison, P. Tanner, K.Y. Cheong, and J. Han

## 1 Introduction

If there is a singular property of silicon that has contributed to its success as a semiconductor material, it is the native oxide,  $\text{SiO}_2$ . This oxide can be thermally grown to form an effective insulating layer as part of the gate in a metal-oxide-semiconductor field-effect transistor (MOSFET) structure. Silicon Carbide also has the ability to grow a similar oxide, and when combined with the bulk properties of wide bandgap, high thermal conductivity and extremely low intrinsic free carrier concentration, will lead to an enormous number of applications. This means that as far as the gate oxide is concerned SiC can be processed in much the same way as Si, the exception being that the processing temperatures are generally higher.

A major obstacle to the formation of a high quality oxide on SiC is the role that carbon plays during the oxide growth. Thermal oxidation in a wet or dry atmosphere results in residual carbon in the oxide layer and carbon clusters at the oxide-SiC interface. It has been found that oxidation or post oxidation annealing in a nitrogen-containing atmosphere has two beneficial effects – enhanced removal of carbon, and passivation of silicon dangling bonds [1]. The most effective gases in achieving this effect have been nitric oxide (NO) and nitrous oxide ( $\text{N}_2\text{O}$ ).

This chapter reviews the recent results on nitrided oxides on SiC. Initially, the various growth techniques are reviewed and compared to show the steps that gave the best result. Then the properties deduced from physical characterization of nitrided oxides are discussed to reveal the way nitrogen is bonded in the oxide and at the interface. The role that nitrogen plays in the removal of carbon during oxidation is also examined. This is followed by a discussion of interface and near-interface traps measured by a range of electrical techniques. Finally, benefits of nitridation of gate oxides used to form MOSFET's and charge storage devices are discussed.

## 2 Growth of Nitrided Oxides

The quality of oxides on SiC, and the beneficial effects on the near surface bulk properties, has been steadily improving as more is discovered about the growth kinetics and interface reactions. Early attempts to nitride the oxide

**Table 1.** Historical comparison of various nitridation techniques and their effects on electrical properties

Process	Effect on oxide quality	References
Annealing in N <sub>2</sub> O	Deterioration of electrical properties	[2, 3]
Annealing in NO (thin oxides, no epi layer)	Improvements in electrical properties	[4, 5]
Direct growth in N <sub>2</sub> O	Improvement in electrical properties	[6, 7]
Direct growth in NO	Shown as the best process in terms of interfacial properties and oxide reliability	6H-SiC: [9] 4H-SiC: [10]
Diluted N <sub>2</sub> O	Good oxide reliability; comparable to NO-grown	[1]
High-temperature growth in N <sub>2</sub> O (> 1200°C)	Reduce interface states and increase MOSFET electron mobility	[8]
Jet vapour deposition (JVD)	Reduced $D_{it}$ in upper half of energy gap. Reduced sub-oxides and dangling bonds at interface	[11]
NO/O <sub>2</sub> /NO sandwich process	MOSFETs with low field mobility = 48 cm <sup>2</sup> /Vs; $D_{it} = 3 \times 10^{11}$ cm <sup>-2</sup> eV <sup>-1</sup> ; oxide breakdown = 9 MV/cm	[13, 14]
Nitrogen radical treatment	Improved field effect mobility in 4H- and 6H-SiC	[12]

by annealing in N<sub>2</sub>O were not very successful, resulting in a deterioration of electrical properties [2, 3]. However more recently, the use of NO and different N<sub>2</sub>O processes has produced a significant improvement in both the bulk oxide and oxide-SiC interface quality. Table 1 summarizes the historical evolution of the nitridation process.

It was found by a number of research groups that annealing of dry oxides in NO reduces interface traps and improves oxide reliability, while similar annealing in N<sub>2</sub>O has a deleterious effect. These early results were performed on thin oxides on bulk SiC without epi-layers [4, 5]. On the other hand, direct growth of the oxide in N<sub>2</sub>O has proven beneficial as N<sub>2</sub>O breaks down into O<sub>2</sub>, N<sub>2</sub> and NO at the oxidation temperature [6, 7], particularly above 1200°C [8]. It has been proposed that in an N<sub>2</sub>O ambient, there exists two competing

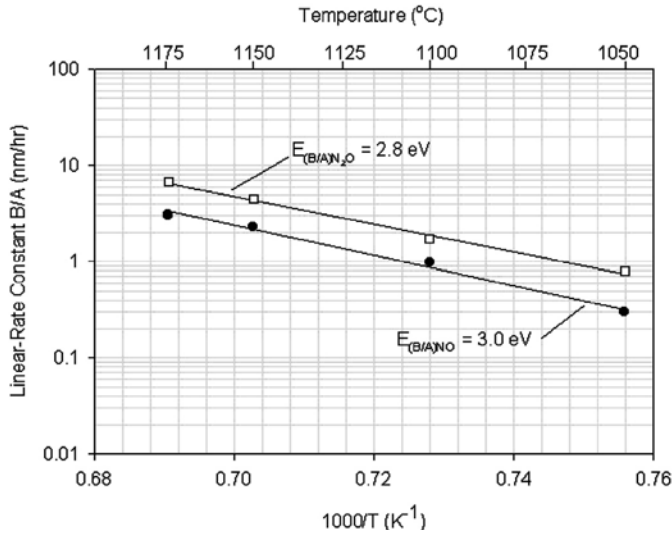


**Fig. 1.** Arrhenius plots for linear oxide growth in NO and N<sub>2</sub>O and the extracted activation energies [1]

processes: oxidation via O<sub>2</sub> producing carbon buildup and nitridation via NO assisting in carbon removal [1]. The optimum oxidation process appears to occur when the kinetics for carbon removal are just sufficient to keep pace with carbon generation which is linked to the oxidation rate. The best results on interface quality and oxide reliability to date have been from direct oxide growth in NO, both for 6H-SiC [9] and 4H-SiC [10]. Due to the very slow growth rate of the oxide in NO (5 hours at 1175°C to grow 16 nm), there is sufficient time for the nitrogen to remove excess carbon. This slow growth rate and the toxic nature of 100% NO means the process may not be desirable for industrial use. If NO presence during the oxide growth is desirable, then the question is what minimum level is required for efficient nitridation of the interface and carbon removal. Fortunately, dilution of N<sub>2</sub>O in nitrogen to achieve the desired amount of NO has been found to produce good results [1]. Figure 1 compares the linear growth rate constants for oxide growth in 100% NO and N<sub>2</sub>O, with the calculated activation energies of 3.0 eV and 2.8 eV respectively.

As well as conventional thermal oxide growth, a number of other methods have provided workable gate oxides on SiC. Jet vapor deposition (JVD) of oxide-nitride-oxide stacks on an ultra-thin nitride produced improved interface properties and evidence of nitrogen at the interface and possible N-C bonding [11]. Interface state densities near the conduction band were reduced to below 10<sup>12</sup> cm<sup>-2</sup> eV<sup>-1</sup>. In another case, dry oxides were exposed to nitrogen radicals generated by remote plasma and the resulting MOSFETs showed improved channel mobility [12]. To overcome the low growth rate of oxide in

NO, the so-called “sandwich process” was used, consisting of an initial growth period in NO followed by the main growth in dry oxygen, and then completed with an NO anneal. This process produced a MOSFET low field electron mobility of  $48 \text{ cm}^2/\text{Vs}$ , low interface state densities, and a dielectric breakdown field strength of  $9 \text{ MV/cm}$  [13, 14].

### 3 Physical Characterization

With the vastly different growth kinetics of thermal oxides on SiC compared to Si, it is important to determine the amount of nitrogen and its distribution relative to the interface. In the Si case,  $\text{Si}\equiv\text{N}$  bonds passivate the dangling Si bonds. Figure 2 compares the SIMS profiles of nitrogen and oxygen through the oxide-semiconductor interface of both Si and SiC samples nitrided in NO. The nitrogen distribution relative to the interface is exactly the same in both cases, but the percentage of N in SiC is greatly reduced [15].

The question then is how the nitrogen is bonded at the oxide-SiC interface. Figure 3 compares XPS spectra for Si  $2p$  at the interface of argon and NO annealed dry oxides on  $4H$ -SiC samples [16]. The argon annealed sample has a broader and more complex peak than the NO annealed sample. A similar difference was also seen in the oxygen and carbon peaks. This indicates that NO annealing of the oxide creates a cleaner interface with less sub-oxides

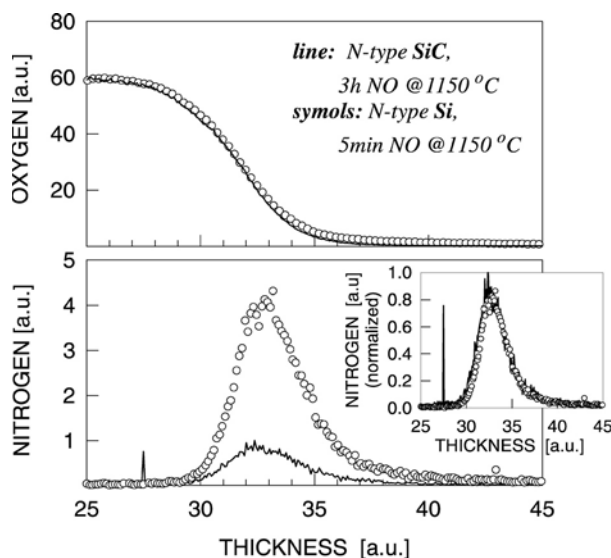


**Fig. 2.** Normalized SIMS profiles of oxygen (*top*) and nitrogen (*bottom*) in nitrided oxides on Si (*symbols*) and SiC (*lines*). The nitrogen peak shape and position are the same relative to the oxygen profiles [15]

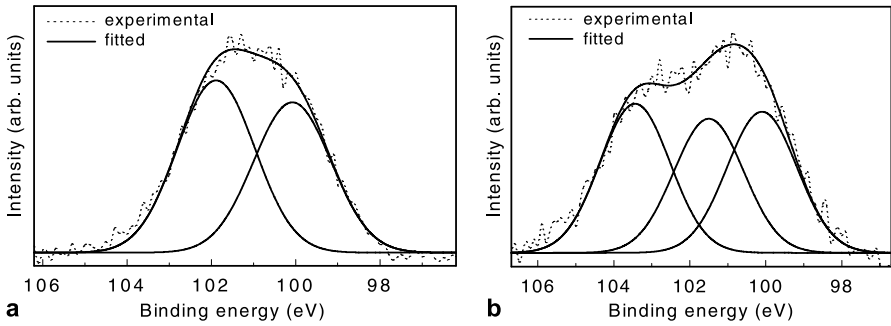


**Fig. 3.** (a) Si 2p XPS spectrum at the NO annealed SiO<sub>2</sub>/SiC interface. (b) Si 2p XPS spectrum at the Ar annealed SiO<sub>2</sub>/SiC interface [16]

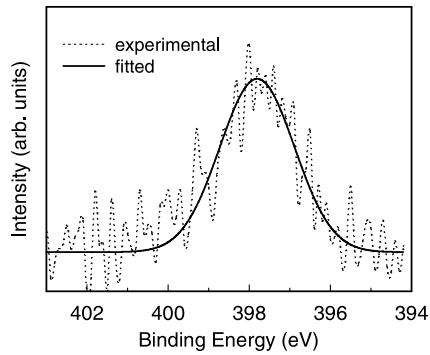


**Fig. 4.** N 1s XPS spectrum at the interface of NO annealed sample, N-1 is the spectrum for Si $\equiv$ N [16]

compared to annealing in an inert gas such as argon. There is also evidence that Si $\equiv$ N bonding occurs at the interface in NO annealed oxides on SiC, as demonstrated in Fig. 4 which shows the N 1s peak at 397.8 eV. This is very close to the energy of the Si $\equiv$ N bonding in silicon nitride.

Another physical effect of nitridation is smoothing of the interface, as shown in the atomic force microscope images of Fig. 5. Removal of the dry oxide and nitrided oxide layers revealed a significantly smoother SiC surface in the nitrided case, with a mean square roughness of 0.1322 nm compared to 0.5778 nm for the dry oxide [14]. This is thought to be due to the more efficient carbon removal during oxide growth in the nitrided case and hence reduced formation of carbon clusters at the interface.

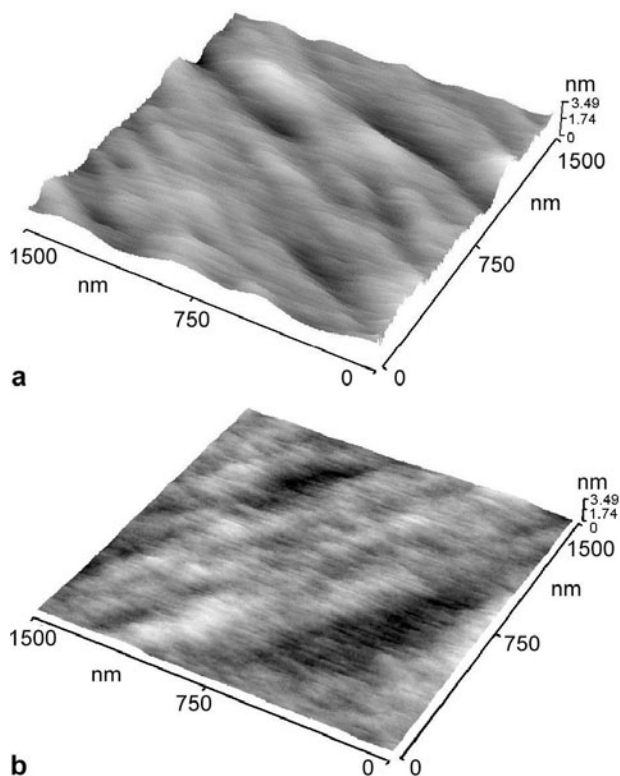


**Fig. 5.** AFM topography for (a) dry oxide and (b) nitrided oxide. The root-mean-square roughness are 0.5778 nm and 0.1322 nm, respectively

## 4 Interface and Near-Interface Defects

Having discussed the physical effects of nitridation on the oxide-SiC interface, we now look at the benefits to the electrical properties of the oxide and its interface with SiC. A major hurdle to be overcome in the development of a viable SiC MOSFET is the reduced channel mobility caused by high densities of interface and near-interface traps. As the different polytypes have differing energy gaps, the energy level of traps with respect to the energy gap means they are electrically active in some polytypes but not in others [17]. For instance, traps with energies just below the conduction band of 4H-SiC are not active in the case of 3C-SiC as they are placed above the conduction band edge, as shown in Fig. 6 [18].

Various studies have linked certain physical defects to the energy location of traps in the energy gap. Traps in the lower half of the energy gap are thought to be related to carbon compounds [19]. Near to the conduction band of 4H-SiC, high densities of predominantly near-interface traps are thought to be responsible for the poor inversion layer mobility in lateral MOSFETs

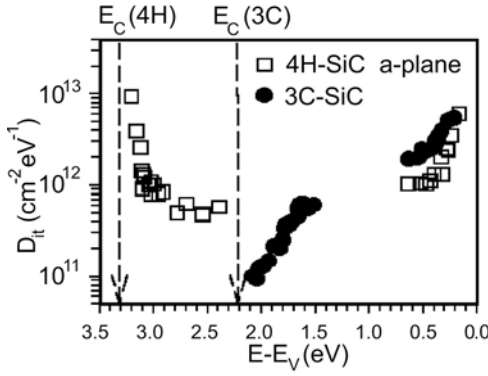


**Fig. 6.** Interface-trap density,  $D_{it}$  as a function of energy for identically processed 3C (001)-/4H (11-20)-SiC MOS capacitors [18]

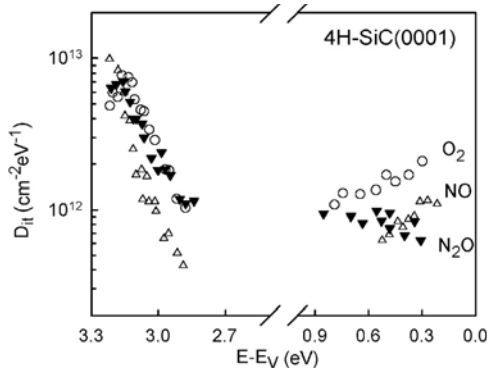


**Fig. 7.** Energy distribution of 4H-SiC/SiO<sub>2</sub> interface states obtained from ac conductance measurements on samples with oxides grown at 1300°C in dry O<sub>2</sub> (●) or 10% N<sub>2</sub>O (▼), and at 1175°C in NO (△) [20]

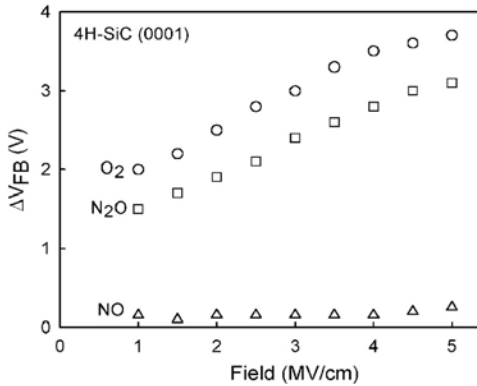


**Fig. 8.** Shift of the flatband voltage observed when lowering the temperature from 300 to 77 K in the  $n$ -type 4H-SiC MOS capacitors with  $\approx 20$ -nm thick oxides grown at 1300°C in dry O<sub>2</sub> (○) or in O<sub>2</sub> + 10% N<sub>2</sub>O (□), and at 1175°C in NO (△) as a function of maximum accumulation electric field strength. The  $V_{FB}$  values were taken when sweeping the voltage from accumulation to depletion [20]

when standard wet and dry oxidation processes are used. Afanas'ev et al. studied NO and N<sub>2</sub>O nitrided oxides on 4H-SiC and the effects on fast and slow interface traps [20]. They found that fast interface traps were reduced over the entire energy gap in both cases, due to removal of carbon clusters, as seen in Fig. 7.

The major effect of NO-nitridation was seen to be the reduction in very slow traps in the oxide near the interface. Figure 8 shows this result as a shift in the flatband voltage of a MOS capacitor after being held in strong accumulation [20].

This is in agreement with the results of a separate study using the slow trap profiling technique to measure traps with slow response times [21]. Figure 9 compares wet and NO-nitrided oxides, with the wet oxide having a band of slow traps at around 0.2 eV below the 4H-SiC conduction band as evidenced by a broad, slow response peak at 0 V, while in the nitrided case these are not evident.

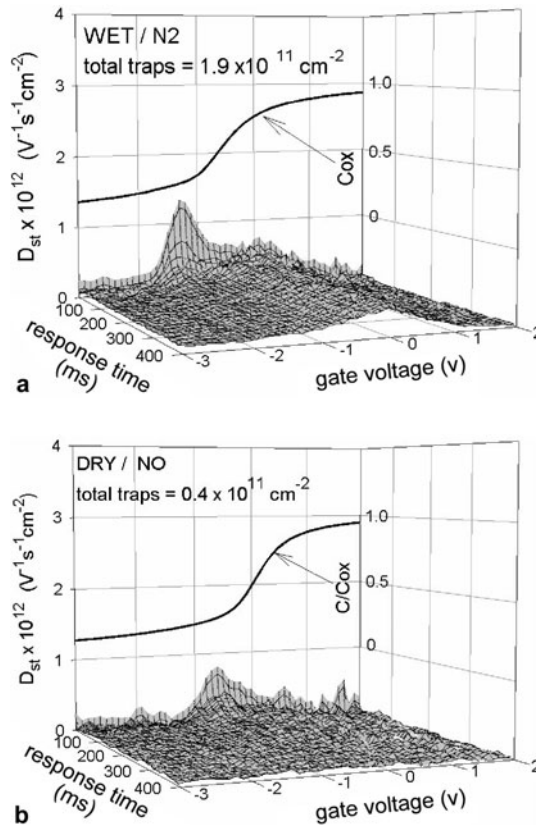


**Fig. 9.** Slow Trap Profiles of (a) wet oxide and (b) NO-annealed dry oxide on 4H-SiC. The slow response peak around 0 V in (a) is due to near interface traps located at 0.2 eV below the conduction band edge [21]

## 5 Characteristics of MOS Devices

Many studies have shown that nitrided gate oxides produce superior MOSFET characteristics, such as lower on resistance as a consequence of improved channel mobility, higher gate breakdown voltages, and more practical threshold voltages. In the case of inversion-type MOSFETs on 4H-SiC, Das et al. showed that NO-nitridation resulted in a four fold decrease in both fixed oxide charge and interface traps in the nitrided oxide compared to a dry oxidation followed by a low temperature wet anneal, as seen in Fig. 10 [22]. The nitridation process produced a low field electron mobility of  $28 \text{ cm}^2/\text{Vs}$ , was uniform across the wafer, independent of channel orientation in the *c*-plane, and only slightly reduced due to the presence of an ion implanted *p*-well.

The output characteristic of a 4H-SiC enhancement mode *n*-channel MOSFET fabricated by Schorner et al. with a NO-nitrided gate oxide are

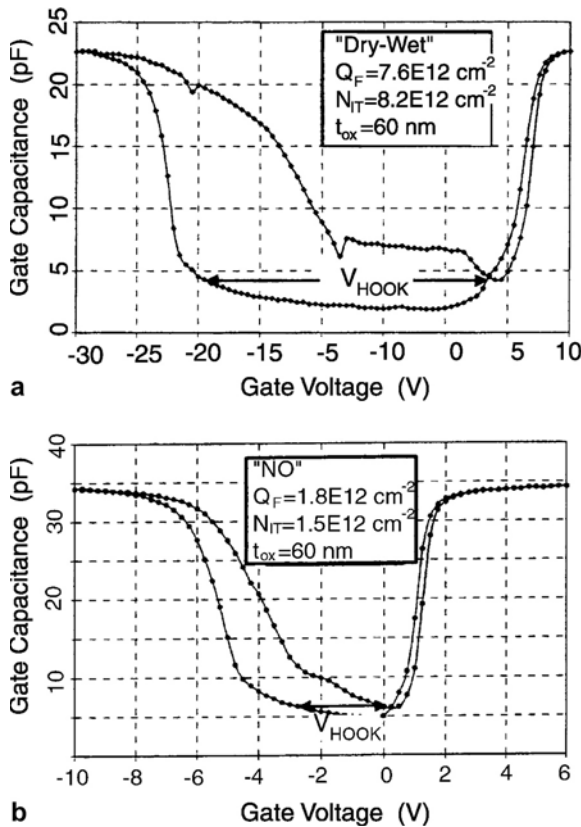


**Fig. 10.** Capacitance-Voltage measurements on (a) "Dry-Wet" MOSFET and (b) "NO" MOSFET showing the reduced interface charges and trapping due to the post-oxidation NO annealing [22]

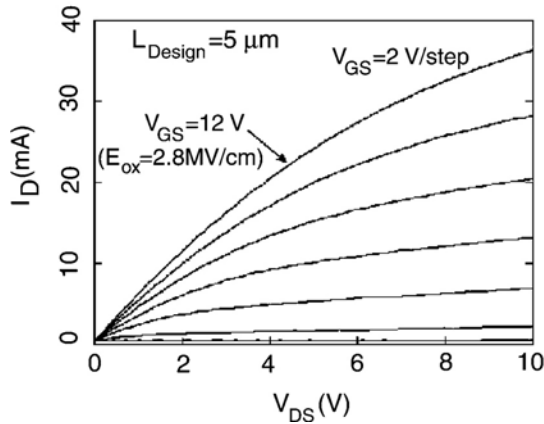


**Fig. 11.** Output characteristic of a 4H-SiC enhancement mode *n*-channel MOSFET with a designed length of 5  $\mu$ m (substrate doping  $N_A - N_D = 6 \times 10^{14}$  cm $^{-3}$ ) [13]

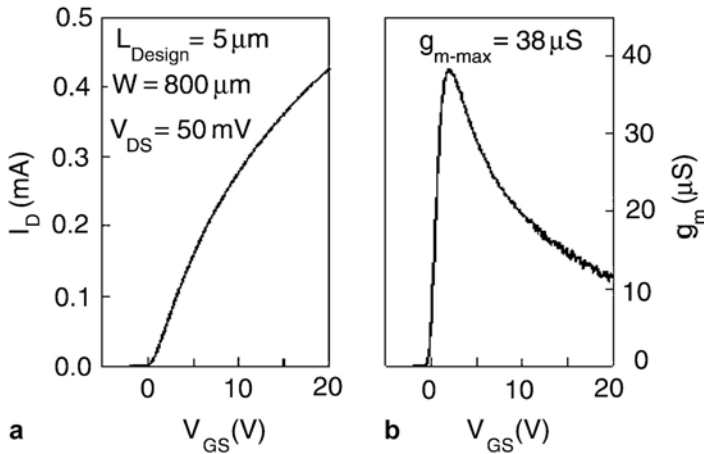


**Fig. 12.** (a) Transfer characteristics of the 4H-SiC enhancement-mode *n*-channel MOSFET and (b) the corresponding transconductance [13]

shown in Fig. 11 [13]. The transfer characteristics appear in Fig. 12, and from this were extracted values for low field mobility of 48 cm $^2$ /Vs, and threshold voltage of 0.6 V [13].

Similar result was obtained by Chung et al. in a study of NO-annealing of various gate oxidation processes on 4H-SiC [23, 24]. The nitridation process resulted in an eight fold decrease in interface traps near the conduction band edge and a ten fold increase in field effect channel mobility to a value of 35 cm $^2$ /Vs. Nitridation was also seen to produce a lower temperature dependence of the field effect mobility and a significantly reduced threshold voltage shift at higher temperatures. Another problem affecting the long term stabil-

ity of MOSFETs has been the barrier height lowering seen at the oxide-SiC interface. Yet it has been shown that NO annealed oxides produce electron injection barrier heights close to the theoretical value [25].

As well as MOSFETs for power and high frequency applications, the idea of using SiC MOS capacitors as charge-storage elements in nonvolatile memory devices has been investigated. In standard silicon memory, the deep-depletion capacitance level can be defined as the logic 1 level, whereas the inversion capacitance level can be defined as the logic 0 level. Given that the inversion capacitance is the value in thermal equilibrium, the charge-retention time of a MOS capacitor used as a memory element is determined by how long it takes for the capacitance to change from the deep depletion to the inversion state. Because of the wide bandgap the thermal generation process in SiC is extremely slow. Consequently, it should be possible to achieve very long charge-retention times at room temperature. In order to accelerate the thermal generation process, measurements were conducted at high temperature, and charge-retention times at room temperature extracted from an Arrhenius-type temperature dependence plot [26]–[28].

It was demonstrated that MOS capacitors with thermally grown dry oxides prevent their use as memory elements due to charge leakage through the gate oxide and poor quality of the passivating oxide-SiC interface that facilitates fast surface generation [27]. Due to these issues, the first SiC-based nonvolatile memory element was fabricated in an *n-p-n* structure [29, 30]. By using a nitrided SiO<sub>2</sub>-SiC interface, both the charge leakage and carrier-generation rate can be reduced to an acceptable level. Figure 13 shows charge-retention times using MOS capacitors on 4H- and 6H-SiC produced by two different nitridation techniques, i.e. *sandwich* process (100% NO/dry O<sub>2</sub>/100%NO) and high-temperature diluted-N<sub>2</sub>O process. In the case of 4H-SiC, room temperature retention times were  $1.49 \times 10^{10}$  years for the *sandwich* process and  $1.5 \times 10^9$  years for the dilute N<sub>2</sub>O process. The *sandwich* process on 6H-SiC produced a lower value of  $8 \times 10^5$  years. As these results illustrate, the charge-retention time is strongly affected by the interface-trap density ( $D_{it}$ ), where the mid-gap interface traps are the most active.

Another major benefit of an improved interface and oxide quality through nitridation is the improved reliability and long term stability of devices. Li demonstrated a dramatic improvement in the immunity of NO-nitrided oxides to highfield stress and high temperature negative-bias stress compared to inert gas annealed oxides [32]. N<sub>2</sub>O nitridation was shown to produce similar benefits, even when diluted 10% in nitrogen [1]. Figure 14 compares the flatband voltage shift of a dry oxide to that of oxides grown or annealed in N<sub>2</sub>O of various dilutions. An oxide grown in 10% N<sub>2</sub>O at 1175°C was shown to have the best immunity to high-field stress.

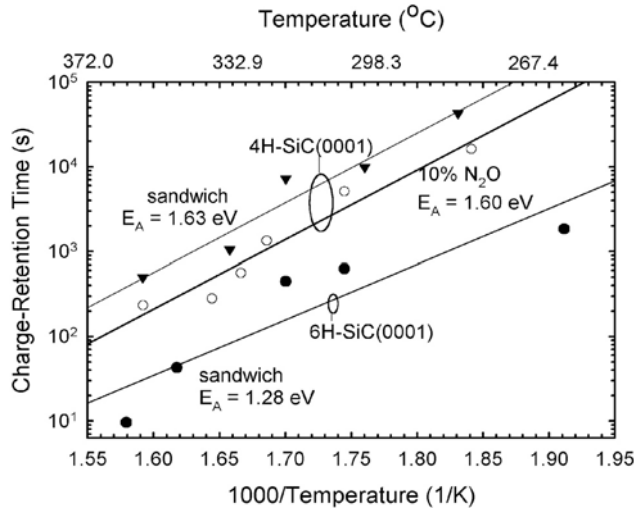


**Fig. 13.** Arrhenius plots for charge-retention time for MOS capacitors on 4*H*- and 6*H*-SiC as a function of temperature for gate oxides grown in different processes. 4*H*-SiC, *sandwich* process, (▼); 4*H*-SiC, high temperature 10% NO, (○); 6*H*-SiC, *sandwich* process, (●)

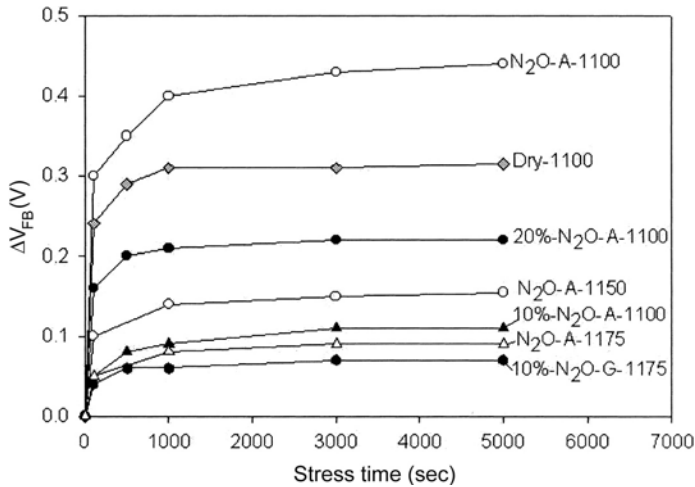


**Fig. 14.** Flatband shifts during high-field stressing of oxide samples related to the N<sub>2</sub>O process optimization: dry oxides (DRY-1100) annealed in either 10% (10% N<sub>2</sub>O-A-1100), 20% (20% N<sub>2</sub>O-A-1100) or 100% N<sub>2</sub>O (N<sub>2</sub>O-A-1100), dry oxides annealed at higher temperatures, 1150°C (N<sub>2</sub>O-A-1150) and 1175°C (N<sub>2</sub>O-A-1175), and oxide grown directly in 10% N<sub>2</sub>O at 1175°C for 6 hours (10%-N<sub>2</sub>O-1175) [1]

## 6 Conclusions

There is a growing body of evidence that many of the problems associated with producing high quality oxides on SiC can be overcome through various nitridation techniques. Oxide growth or annealing in the presence of nitric oxide appears to be the most effective method to enhance carbon removal and incorporate nitrogen at the interface, thereby lowering interface trap densities and improving dielectric strength and reliability. This in turn translates to improved low-field mobility and lower threshold voltages in MOSFET devices. While NO may not be the best option for industry, the more benign N<sub>2</sub>O or diluted N<sub>2</sub>O can also be used to produce device quality gate oxides.

In addition to the extensive work being done on SiC MOSFET development, investigations have begun on using the very desirable properties of SiC in charge storage devices for future non-volatile memory. To date, nitrided oxides on SiC show charge retention times far exceeding currently available silicon technology.

## References

1. P. Jamet, S. Dimitrijević, P. Tanner: J. Appl. Phys. **90**, 5058 (2001)
2. R.C. De Meo, T.K. Wang, T.P. Chow, D.M. Brown, L.G. Matus: Inst. Phys. Conf. Ser. No 137, pp. 321–323 (1993)
3. R.C. De Meo, T.K. Wang, T.P. Chow, D.M. Brown, L.G. Matus: J. Electrochem. Soc. **141**, L150 (1994)
4. S. Dimitrijević, H.F. Li, H.B. Harrison, D. Sweatman: IEEE Electron Dev. Lett. **18**, 175 (1997)
5. H.F. Li, S. Dimitrijević, H.B. Harrison, D. Sweatman: Appl. Phys. Lett. **70** 2028 (1997)
6. P.T. Lai, J.P. Xu, Y.C. Cheng: IEEE Trans. Electron Dev. **46**, 2311 (1999)
7. J.P. Xu, P.T. Lai, C.L. Chan, B. Li B, Y.C. Cheng: IEEE Electron Dev. Lett. **21**, 298 (2000)
8. L.A. Lipkin, M.K. Das, J.W. Palmour: Mater. Sci. Forum **389–393**, 985 (2002)
9. S. Chakraborty, P.T. Lai, P.C.K. Kwok: Microelectron. Reliab. **42**, 455 (2002)
10. P. Jamet, S. Dimitrijević: Appl. Phys. Lett. **79**, 323 (2001)
11. X.W. Wang, H.M. Bu, B.L. Laube, C. Caragianis-Broadbridge, T.P. Ma: Mater. Sci. Forum **389–393**, 993 (2002)
12. H. Yano, Y. Maeyama, Y. Furumoto, T. Hatayama, Y. Uraoka, T. Fuyuki: to be published in Mater. Sci. Forum
13. R. Schörner, P. Friedrichs, D. Peters, D. Stephani, S. Dimitrijević, P. Jamet: Appl. Phys. Lett. **80**, 4253 (2002)
14. K.Y. Cheong, S. Dimitrijević, J. Han: to be published in Mater. Sci. Forum
15. P. Tanner, S. Dimitrijević, H.F. Li, D. Sweatman, K.E. Prince, H.B. Harrison: J. Electron. Mater. **28**, 109 (1999)
16. H.F. Li, S. Dimitrijević, D. Sweatman, H.B. Harrison, P. Tanner, B. Feil: J. Appl. Phys. **86**, 4316 (1999)
17. R. Schörner, P. Friedrichs, D. Peters, D. Stephani: IEEE Electron Dev. Lett. **20**, 241 (1999)

18. F. Ciobanu, G. Pensl, H. Nagasawa, A. Schöner, S. Dimitrijević, K.Y. Cheong, V.V. Afanas'ev, G. Wagner: to be published in *Mater. Sci. Forum*
19. M. Bassler, G. Pensl, V. Afanas'ev: *Diamond and Related Materials* **6**, 147 (1997)
20. V.V. Afanas'ev, A. Stesmans, F. Ciobanu, G. Pensl, K.Y. Cheong, S. Dimitrijević: Mechanism responsible for improvement of 4H-SiC/SiO<sub>2</sub> interface properties by nitridation, *Appl. Phys. Lett.* **82**(4), 568–570 (2003)
21. P. Jamet, S. Dimitrijević, P. Tanner: *Mater. Sci. Forum* **389–393**, 973 (2002)
22. M.K. Das, G.Y. Chung, J.R. Williams, N.S. Saks, L.A. Lipkin, J.W. Palmour: *Mater. Sci. Forum* **389–393**, 981 (2002)
23. G.Y. Chung, C.C. Tin, J.R. Williams, K. McDonald, R.K. Chanana, R.A. Weller, S.T. Pantelides, L.C. Feldman, O.W. Holland, M.K. Das, J.W. Palmour: *IEEE Electron Dev. Lett.* **22**, 176 (2001)
24. G.Y. Chung, J.R. Williams, C.C. Tin, K. McDonald, D. Farmer, R.K. Chanana, S.T. Pantelides, O.W. Holland, L.C. Feldman: *Appl. Surf. Sci.* **184**, 399 (2001)
25. H. Li, S. Dimitrijević, D. Sweatman, H.B. Harrison: *Microelectron. Reliab.* **40**, 283 (2000)
26. K.Y. Cheong, S. Dimitrijević: *IEEE Electron Dev. Lett.* **23**, 404 (2002)
27. S. Dimitrijević, K.Y. Cheong, J. Han, H.B. Harrison: *Appl. Phys. Lett.* **80**, (2002)
28. K.Y. Cheong, S. Dimitrijević, J. Han: to be published in *Proceedings of 3rd International Conference on Recent Advances in Materials, Minerals, and Environment*
29. C.T. Gardner, J.A. Cooper Jr, M.R. Melloch, J.W. Palmour, C.H. Carter Jr.: *Appl. Phys. Lett.* **61**, 1185 (1992)
30. Y. Wang, J.A. Cooper Jr, M.R. Melloch, S.T. Sheppard, J.W. Palmour, L.A. Lipkin: *J. Electron. Mater.* **25**, 899 (1996)
31. W. Xie, J.A. Cooper Jr, M.R. Melloch, J.W. Palmour, C.H. Carter Jr.: *IEEE Electron. Dev. Lett.* **15**, 212 (1994)
32. H.F. Li, S. Dimitrijević, H.B. Harrison: *IEEE Electron Dev. Lett.* **19**, 279 (1998)

# Hall Effect Studies of Electron Mobility and Trapping at the SiC/SiO<sub>2</sub> Interface

N.S. Saks

## 1 Introduction

SiC is an attractive semiconductor for fabricating high power metal-oxide-semiconductor (MOS) devices because of its high breakdown field and high thermal conductivity. In addition, like silicon, SiC has a natural advantage for fabricating MOS devices because high quality SiO<sub>2</sub> for gate insulators can be thermally grown directly on the SiC in an oxidizing ambient. Despite these potential advantages, experimental SiC MOS devices today have poor performance and abnormally low conductance. This is particularly a problem in 4H- compared to 6H-SiC, although 4H is the preferred polytype for power devices because of its higher electron mobility. It was proposed initially that the low conductance arises from extreme SiC surface roughness [1] or segregation of aluminum dopant atoms at the SiC/SiO<sub>2</sub> interface from the *p*-type SiC substrate [2, 3]. It is generally recognized now that the low conductance is actually due to a high density of electron traps  $D_{it}$  at the SiC/SiO<sub>2</sub> interface [1, 4, 5]. These traps reduce the conductance by two approximately equal effects: (1) many electrons are trapped by the defects and are not free to contribute to the drain current, and (2) the mobility of the remaining free electrons is reduced by Coulomb scattering from all the trapped electrons. The traps are believed to arise from two physical mechanisms: near-interfacial traps in the oxide caused by oxygen deficiencies, and clusters of graphite-like excess carbon at the interface released by the oxidation process [4].

In *silicon* MOS devices, the electron mobility and scattering processes are typically studied by analyzing the drain-to-source current  $I_{ds}$  in MOSFETs as a function of gate voltage and temperature [6]. The mobility determined in this way is an *effective* mobility which does not take the effects of electron trapping in the MOS inversion layer into account. In typical silicon MOS devices,  $D_{it}$  is relatively low ( $\approx 10^{10} - 10^{11}$  traps/cm<sup>2</sup>-eV), trapping is small, and the effective mobility is approximately equal to the actual mobility of the electrons. However, in SiC MOS devices, trap densities are typically several orders of magnitude higher, and the measured effective mobility is quite different from the actual mobility due to trapping effects.

Due to these problems, it is desirable to directly measure the electron mobility in SiC MOS inversion layers. This can be accomplished using the Hall effect. Data will be presented here showing effective and Hall mobilities

in 4H- and 6H-SiC inversion layers. These results demonstrate that the actual inversion (Hall) mobility can be as much as a factor of ten higher than the effective mobility in some SiC devices. The Hall measurements and samples are described in some detail here because Hall effect measurements on MOS inversion layers, although not new, are somewhat unusual.

Improved accuracy in determining the inversion mobility is not the only advantage to using Hall data. In the Hall measurement, two independent parameters are obtained: the Hall mobility, as discussed, and  $n_{\text{inv}}$ , the density of electrons in the inversion layer of an  $n$ -channel MOSFET. Given  $n_{\text{inv}}$  as a function of gate voltage  $V_g$  and the samples' physical parameters, we demonstrate how to calculate the density of interface traps as a function of energy  $D_{\text{it}}(E)$ . This is a major advantage because  $D_{\text{it}}(E)$  can therefore be measured in the actual device structure. It is also possible to calculate the total number of electrons trapped at each gate voltage  $n_t(V_g)$ . Using  $n_t(V_g)$ , it is possible to study the effects of Coulomb scattering by trapped electrons on the inversion layer mobility, which is the dominant mechanism reducing the mobility in SiC MOS devices [7]. Thus a variety of important inversion layer phenomena can be calculated from Hall effect data.

## 2 Sample Design and Hall Measurements

### 2.1 Fabrication of Test Devices

The experimental devices used in this paper are MOS Hall bars fabricated on 4H- and 6H-SiC. Since MOS Hall bars are essentially MOSFETs with taps on the sides, these Hall test devices can be fabricated on the same wafers as  $n$ -channel MOSFETs. Most Hall samples studied here were fabricated by the author and co-workers as test devices for lateral RESURF power LDMOSFETs [8]–[11]. Other Hall devices were fabricated as part of a DMOS power FET development program [12, 13]. In [8]–[11], a typical process sequence was as follows: non-self-aligned MOS devices were fabricated on lightly doped  $p$ -type ( $1 \times 10^{15} - 2 \times 10^{16}/\text{cm}^3$ ) epitaxial layers grown on heavily-doped  $P^+$  wafers cut from sublimation-grown 6H- and 4H-SiC purchased from Cree, Inc. Heavily-doped  $N^+$  source and drains were implanted with nitrogen at 600°C at multiple implant energies to obtain “box” profiles. After implantation, the thick  $\text{SiO}_2$  implant mask was stripped and the implants were annealed in an SiC pillbox in Ar for  $\sim 1/2$  hr at 1300–1500°C. Hall studies of implanted layers from this process show good activation of the implanted nitrogen [14]. After a standard RCA clean, gate oxides were grown in a wet ambient at 1100°C for  $\sim 3$  hrs, resulting in typical gate oxide thickness of  $\sim 3.0$ – $3.5$  nm. Phosphorus-doped poly-silicon was used for the gate metal. For contacts to the  $N^+$  SiC, a thin ( $\sim 80$  nm) nickel layer was deposited and patterned by lift-off. The nickel was rapid thermal annealed at 800°C for  $\sim 3$  min to form nickel silicide contacts. These contacts are ohmic

with reasonably low contact resistivity ( $0.5 - 10 \times 10^{-4}$  ohm-cm<sup>2</sup>). After deposition of an inter-level dielectric, aluminum was deposited and patterned for interconnects and bond pads.

## 2.2 Hall Bar Design

In order to obtain Hall effect data, special Hall devices must be designed and fabricated. An example of a bridge-type MOS Hall bar design is shown in Fig. 1. A heavily doped N<sup>+</sup> source and drain are provided at the ends of the bar, and two symmetric pairs of N<sup>+</sup> voltage taps are provided along the length. The distance  $L$  between the taps must be large compared to the width  $W$  [15]. A typical Hall bar geometry here is 162  $\mu\text{m}$  (end-to-end) with a width  $W$  of 20  $\mu\text{m}$ . Van de Pauw devices [15] have also been used in this work.

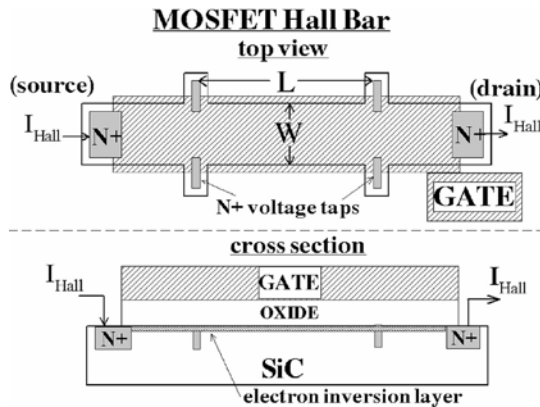


**Fig. 1.** Drawing of MOS Hall Bar (not to scale). Plan view (*top*); cross-section (*bottom*). The Hall current flows in the electron inversion layer from source to drain. A magnetic field  $B$  is applied perpendicular to the plane of the gate during the Hall measurement

## 2.3 Hall Measurements

In operation, a positive voltage  $V_g$  is applied to the MOSFET gate which establishes an inversion layer at the SiC/SiO<sub>2</sub> interface. With the source grounded and a small voltage  $V_d$  applied to the drain, a current  $I_{\text{Hall}}$  flows from source to drain. The voltage difference between the two taps separated by  $L$  is measured, from which the sheet resistance of the inversion layer  $\rho_s$  is calculated from  $I_{\text{Hall}}$  and  $V_d$ . A magnetic field  $B$  is then applied perpendicular to the plane of the gate and a Hall voltage  $V_{\text{Hall}}$  is measured between two taps on opposite sides of the bar. The free electron density in the inversion layer,

$n_{\text{inv}}$ , is calculated from  $V_{\text{Hall}}$ . The Hall mobility  $\mu_{\text{Hall}}$  is then calculated from  $n_{\text{inv}}$  and  $\rho_s$  [15]. Multiple Hall measurements are required to obtain  $n_{\text{inv}}(V_g)$  and  $\rho_s(V_g)$  which are strongly dependent on  $V_g$ .

Obtaining reliable, reproducible Hall data from SiC MOS devices can be difficult due to the low SiC inversion mobilities. Low-resistance  $N^+$  ohmic contacts are used to minimize undesired voltage drops and to reduce noise. High impedance ( $> 10^{12}$  ohm), low noise, OPA627 voltage follower op-amp buffers are used to minimize loading and noise when measuring potentials at the voltage taps. Noise is also minimized by using voltmeter integration times synched to the 60 Hz power line and by averaging multiple ( $\sim 100$ ) measurements. *DC* voltage offsets at the taps are removed by reversing the Hall current.  $V_{\text{Hall}}$  can be just a few microvolts in low mobility samples, so very low noise ( $< \sim 0.5$   $\mu\text{V}$ ) is required.

Obtaining accurate Hall data is particularly difficult when the MOSFET is biased below threshold. In this case, it is necessary to keep  $V_d$  small ( $V_d \leq kT/q \cong 25$  mV at 300 K) in order to maintain a uniform inversion layer and to insure linear dependence of  $I_{\text{Hall}}$  on  $V_d$ . This was satisfied here by using  $V_d = 1$ –10 mV (only for  $V_g$  below threshold). At these low values of  $V_d$ ,  $I_{\text{Hall}}$  is also very small, so all extraneous leakage currents in the sample and wiring must be carefully eliminated.

A Hall scattering factor  $r_{\text{Hall}}$  of 1.00 was assumed here for inversion electrons in both 4H- and 6H-SiC. This is a critical assumption because the value of  $r_{\text{Hall}}$  directly affects the calculation of both  $\mu_{\text{eff}}$  and  $n_{\text{inv}}$ . Experimental measurements show that  $\sim 0.9 \leq r_{\text{Hall}} \leq \sim 1.0$  between 200 and 300 K for bulk

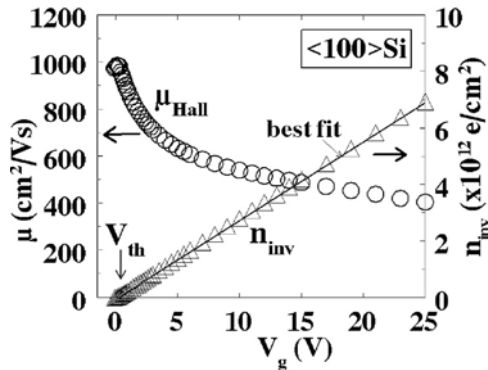


**Fig. 2.** Example of Hall mobility  $\mu_{\text{Hall}}$  and free electron density  $n_{\text{inv}}$  in a reference silicon  $\langle 100 \rangle$  MOS inversion layer.  $n_{\text{inv}}$  increases linearly with applied  $V_g$  as predicted by (2) assuming no electron trapping at the interface. The threshold voltage  $V_{\text{th}}$  is determined from the intercept of the straight line best fit to  $n_{\text{inv}}$  with the  $x$ -axis.  $\mu_{\text{Hall}}$  decreases with increasing  $V_g$  due to increased scattering by surface phonons [17]

electrons in SiC [16], but there is no known measurement for electrons in SiC inversion layers.

The SiC MOS samples were die-bonded in 28-pin ceramic dual-in-line packages. The packages were mounted on a temperature-controlled cold finger in a vacuum system capable of stabilized temperatures between 77 and 600 K using liquid nitrogen cooling. An electro-magnet was used to provide a magnetic field of 5.0 kgauss for the Hall measurements.

In order to evaluate our Hall apparatus and analysis procedures, Hall measurements were first obtained on *silicon*  $\langle 100 \rangle$  MOS devices with low trap density (mid-gap  $D_{it} \approx 4 \times 10^{10}$  traps/cm<sup>2</sup>-eV). Results are shown in Fig. 2. Experimental values for the Hall mobility  $\mu_{\text{Hall}}$  and the free electron inversion layer density  $n_{\text{inv}}$  were obtained at each value of  $V_g$ . These Hall data show typical behavior for silicon inversion layers:  $\mu_{\text{Hall}}$  decreases with increasing  $V_g$ , primarily due to increasing scattering by surface phonons [17].  $n_{\text{inv}}$  increases linearly with  $V_g$ , as shown by the straight line which is a best fit to the data [18]. An accurate value for the threshold voltage  $V_{\text{th}}$  can be found from the intercept of this straight line with the  $x$ -axis. As will be shown later, this behavior is *not* typical of SiC inversion layers.

### 3 MOSFET Mobility

#### 3.1 Comparison of Effective and Hall Mobility

A common and simple technique for measuring MOSFET inversion layer mobility  $\mu$  is to measure the drain current  $I_d$  as a function of the gate voltage  $V_g$  in the linear regime, i.e., at low drain voltages  $V_d$  ( $\leq 0.10$  V).  $I_d$  is given by:

$$I_d = q(W/L)\mu n_{\text{inv}}V_d \quad (1)$$

where  $L$  and  $W$  are the geometric length and width of the FET, respectively, and  $n_{\text{inv}}$  is the density of free electrons in the MOS inversion layer which contribute to the current [6]. The *total* number of electrons electro-statically induced at the interface by applying  $V_g$  can be expressed by the “strong inversion” approximation:

$$n_{\text{total}} \cong C_{\text{ox}}(V_g - V_{\text{th}})/q, \quad (2)$$

where  $C_{\text{ox}}$  is the capacitance of the gate oxide per unit area [6]. In the absence of electron trapping at the interface, the density of free electrons will be the same as the total electron density, or  $n_{\text{inv}} = n_{\text{total}}$ . An excellent fit of a straight line to  $n_{\text{inv}}$  data is obtained for the silicon device in Fig. 2, and the slope of the straight line nearly equals  $C_{\text{ox}}/q$ , as predicted by (2). Assuming that  $n_{\text{inv}} = n_{\text{total}}$  and substituting (2) into (1) we obtain:

$$I_d = (W/L)\mu C_{\text{ox}}(V_g - V_{\text{th}})V_d. \quad (3)$$

Solving (3) for the mobility yields:

$$\mu = \mu_{\text{eff}} \equiv (L/W)(I_d/V_d)/\{C_{\text{ox}}(V_g - V_{\text{th}})\} \quad (4)$$

where  $\mu_{\text{eff}}$  in (4) is the effective mobility [17].  $\mu_{\text{eff}}$  is widely used in silicon MOSFETs to characterize the average inversion layer mobility. However, this approach is really proper only if electron trapping is negligible. When electron trapping is *not* negligible,  $n_{\text{inv}} \neq n_{\text{total}}$ , and  $\mu_{\text{eff}}$  is not equal to the mobility of the transporting electrons. However,  $\mu_{\text{eff}}$  is still useful in a practical sense because it can be used to calculate  $I_d$  in a MOSFET using (3).

Typical  $I_d$ - $V_g$  characteristics for 4H- and 6H-SiC MOSFETs are shown in Fig. 3 using log and linear scales (Figs. 3a and b, respectively). For the 6H-SiC device, there is a sharp, near-exponential turn-on at threshold. A straight line appears to provide a good fit to the experimental data above threshold in the linear plot (see Fig. 3b). From this fit,  $V_{\text{th}}$  is found from the intercept of the straight line with the  $x$ -axis, while  $\mu_{\text{eff}}$  is calculated from the slope of the straight line and (3). This approach *appears* to provide accurate values for both  $V_{\text{th}}$  and  $\mu_{\text{eff}}$  in this 6H device because a good straight line fit is obtained. However, as will be discussed below, this is not correct.

On the other hand, the 4H device displays a high threshold and non-exponential turn-on in Fig. 3. This indicates a high density of trapped electrons. It is not possible to fit a straight line to the 4H data in Fig. 3b, since

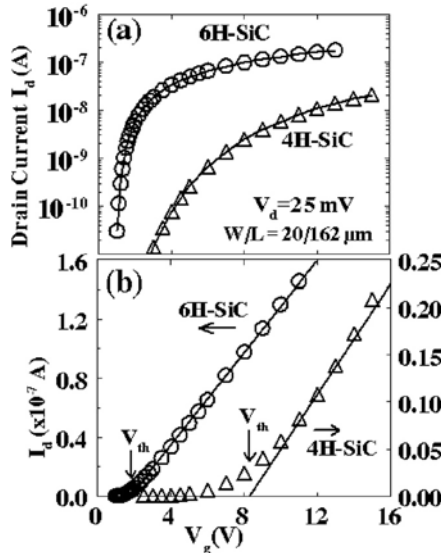


**Fig. 3.** Drain current  $I_d$  vs.  $V_g$  in 6H- and 4H-SiC MOS Hall bars with  $W/L = 20/162 \text{ } \mu\text{m}$  and  $V_d = 0.025 \text{ V}$ . (a) Log scale; (b) linear scale. The 6H characteristic appears “normal”:  $I_d$  increases exponentially below  $V_{\text{th}}$  and linearly above  $V_{\text{th}}$ . The 4H device displays neither characteristic and has an anomalously high  $V_{\text{th}}$

the slope of the fitted line depends on which data one chooses to fit. These results indicate that unique values for  $V_{th}$  and  $\mu_{eff}$  cannot be found for the  $4H$  device by this approach.

Although the results in Fig. 3 suggest that the standard approach for determining  $\mu_{eff}$  and  $V_{th}$  works satisfactorily at least for the  $6H$  device (but not  $4H$ ), this conclusion is incorrect. In Fig. 4, a comparison is made between  $\mu_{eff}$  and the Hall mobility  $\mu_{Hall}$  for the same  $6H$ -SiC device shown in Fig. 3. Data from the silicon device in Fig. 2 are also shown in Fig. 4 for comparison. The data in Fig. 4 are plotted as a function of  $V_g/t_{ox}$  rather than  $V_g$ , to simplify comparisons among samples with different gate oxide thickness  $t_{ox}$ . In Fig. 4a,  $\mu_{eff}$  and  $\mu_{Hall}$  are shown for both devices. The mobility in the  $6H$ -SiC device is roughly ten times smaller than in the silicon device. Part of this reduction is due to the lower bulk electron mobility in  $6H$ -SiC ( $\sim 390$  vs.  $\sim 1200$   $\text{cm}^2/\text{Vs}$  for  $N_d = 1 \times 10^{16} \text{ cm}^{-3}$ , respectively [19]). The  $6H$  mobility is also reduced by increased scattering from a high density of trapped electrons. The key point is that, in the silicon device, where the interface trap density is low, agreement between  $\mu_{Hall}$  and  $\mu_{eff}$  is quite good, within about 5%. For the  $6H$ -SiC device,  $\mu_{eff}$  is significantly smaller than  $\mu_{Hall}$ , and  $\mu_{eff}$  is

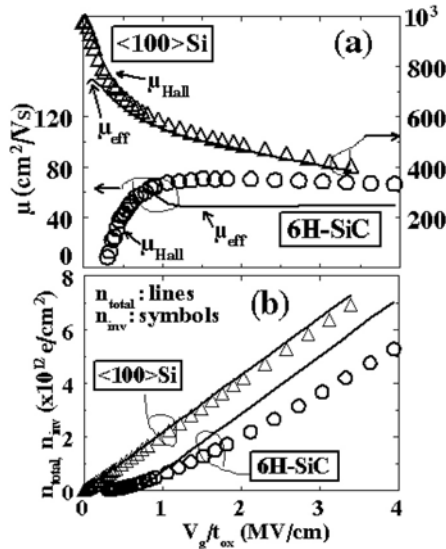


**Fig. 4.** (a) Comparison between effective mobility  $\mu_{eff}$  (solid lines) and Hall mobility  $\mu_{Hall}$  (symbols) in silicon and  $6H$ -SiC inversion layers as a function of  $V_g/t_{ox}$ . In the silicon device,  $\mu_{eff}$  and  $\mu_{Hall}$  are in good agreement, indicating minimal electron trapping. Agreement between  $\mu_{eff}$  and  $\mu_{Hall}$  in the  $6H$ -SiC device is poor, indicating higher electron trapping. (b) Comparison between calculated  $n_{total}$  (lines) and measured  $n_{inv}$  (symbols) in the same two devices. In the silicon device,  $n_{inv}$  and  $n_{total}$  are nearly the same. In  $6H$ -SiC, agreement between  $n_{total}$  and  $n_{inv}$  is poor, indicating high electron trapping

especially inaccurate near  $V_{th}$ . Also, in the  $6H$  device,  $\mu_{Hall}$  falls at low  $V_g$  below threshold. This behavior is real and is not an artifact, but the same behavior is not observed in  $\mu_{eff}$ .

The free and total inversion layer electron densities,  $n_{inv}$  and  $n_{total}$ , are shown in Fig. 4b for the same two samples.  $n_{inv}$  is obtained from experimental Hall data, whereas  $n_{total}$  is calculated from the “strong inversion” approximation (2). (Note that  $n_{total}$  in the silicon sample in Fig. 4b is not the same as the straight line in Fig. 2 which is merely a best fit to the same  $n_{inv}$  data.) In the silicon device, agreement between  $n_{inv}$  and  $n_{total}$  is quite good. However, in the  $6H$ -SiC device,  $n_{inv}$  is clearly considerably smaller than  $n_{total}$ . In both samples,  $n_{inv}$  is less than  $n_{total}$  due to trapping of electrons at the semiconductor/SiO<sub>2</sub> interface. From this difference, about 25% of  $n_{total}$  appears to be trapped in the  $6H$ -SiC sample, whereas only about 5% of  $n_{total}$  is trapped in the silicon device.

### 3.2 Comparison of $4H$ - and $6H$ -SiC Mobility

A comparison between experimental  $\mu_{eff}$  and  $\mu_{Hall}$  data from  $6H$ - and  $4H$ -SiC MOS Hall bars is shown in Fig. 5. As in Fig. 4, these data are plotted as a function of  $V_g/t_{ox}$  rather than  $V_g$  to normalize differences in gate oxide thickness. In Fig. 5, the gate oxides for both SiC polytypes were grown at the same time in the same process lot. The measured inversion layer mobilities in both polytypes are well below their bulk mobilities as shown in the figure. In  $4H$ -SiC, the bulk mobility is about two times higher than  $6H$ , but the experimental inversion layer mobilities are considerably lower than  $6H$  as is often observed [5, 20]. This result is consistent with the much higher  $D_{it}$  typically

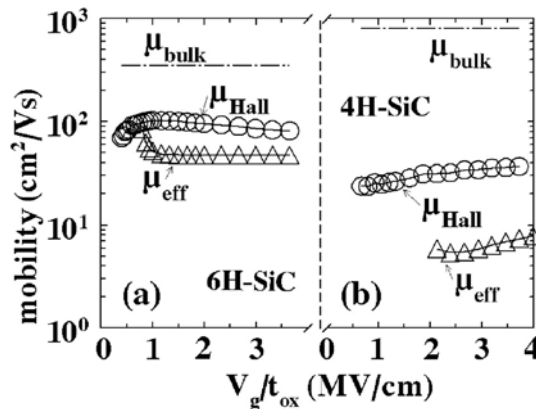


**Fig. 5.** Comparison of mobilities in (a)  $6H$ -SiC and (b)  $4H$ -SiC as a function of  $V_g/t_{ox}$ . The inversion layer mobilities  $\mu_{eff}$  and  $\mu_{Hall}$  are considerably smaller than the bulk mobility  $\mu_{bulk}$  in both polytypes, particularly in  $4H$ -SiC.  $\mu_{eff}$  is always smaller than  $\mu_{Hall}$  in both samples

found in  $4H$  samples [4, 5, 20]. Since the oxides were grown simultaneously, this result is apparently a fundamental property of oxides grown on the two polytype surfaces. Note that  $\mu_{\text{eff}}$  is roughly 5 times smaller than  $\mu_{\text{Hall}}$  in the  $4H$  sample, which highlights the significant difference between  $\mu_{\text{eff}}$  and the actual electron mobility.

Experimental measurements of  $\mu_{\text{eff}}$  and  $n_{\text{total}}$  require an accurate value for  $V_{\text{th}}$  (see (2)–(4)). However, in SiC samples with high  $D_{\text{it}}$ , and particularly in  $4H$ -SiC as shown in Fig. 3, it isn't possible to define a reliable value of  $V_{\text{th}}$  due to the rounded shape of the  $I_{\text{d}}\text{-}V_{\text{g}}$  curves. Therefore, experimental values of  $\mu_{\text{eff}}$  and  $n_{\text{total}}$  in SiC have a large source of error from this uncertainty in  $V_{\text{th}}$ .

Due to the difficulty of defining  $V_{\text{th}}$ , an alternate method for displaying these experimental data is to use the field-effect mobility  $\mu_{\text{FE}}$  rather than  $\mu_{\text{eff}}$ . By taking the derivative of  $I_{\text{d}}$  with respect to  $V_{\text{g}}$  in (3), it can be shown that:

$$\partial I_{\text{d}}/\partial V_{\text{g}} = (W/L)\mu C_{\text{ox}}V_{\text{d}} \Rightarrow \mu_{\text{FE}} \equiv \mu = (\partial I_{\text{d}}/\partial V_{\text{g}})/[(W/L)C_{\text{ox}}V_{\text{d}}] . \quad (5)$$

Likewise, by taking the derivative of  $n_{\text{total}}$  with respect to  $V_{\text{g}}$  in (2), we obtain:

$$\partial n_{\text{total}}/\partial V_{\text{g}} = C_{\text{ox}}/q . \quad (6)$$

Note that  $\mu_{\text{FE}}$  and  $\partial n_{\text{total}}/\partial V_{\text{g}}$  do not depend on  $V_{\text{th}}$ , and therefore have no error associated with guesstimating its value.  $\mu_{\text{FE}}$  is the mobility associated with incremental electrons added to the inversion layer when  $V_{\text{g}}$  is increased to  $(V_{\text{g}} + \partial V_{\text{g}})$ , whereas both  $\mu_{\text{Hall}}(V_{\text{g}})$  and  $\mu_{\text{eff}}(V_{\text{g}})$  represent *averages* for all electrons in the inversion layer.

Results for  $\mu_{\text{FE}}$  and  $\partial n_{\text{inv}}/\partial V_{\text{g}}$  for  $6H$ - and  $4H$ -SiC samples are shown in Figs. 6 and 7, respectively. To be consistent, experimental values for  $\mu_{\text{FE}}(V_{\text{g}})$  calculated from  $I_{\text{d}}\text{-}V_{\text{g}}$  data are compared with the differential Hall mobility  $\mu_{\text{Hall,FE}}$  associated with an incremental change in the electron density  $\partial n_{\text{inv}}$ :

$$\mu_{\text{Hall,FE}}(V_{\text{g}}) \equiv \{\mu_{\text{Hall}}(V_{\text{g}} + \partial V_{\text{g}})n_{\text{inv}}(V_{\text{g}} + \partial V_{\text{g}}) - \mu_{\text{Hall}}(V_{\text{g}})n_{\text{inv}}(V_{\text{g}})\} / \{n_{\text{inv}}(V_{\text{g}} + \partial V_{\text{g}}) - n_{\text{inv}}(V_{\text{g}})\} . \quad (7)$$

In the  $6H$ -SiC device in Fig. 6a,  $\mu_{\text{FE}}$  and  $\mu_{\text{Hall,FE}}$  are quite different near threshold, but the two mobilities equalize at high  $V_{\text{g}}$ . Likewise, as shown in Fig. 6b,  $\partial n_{\text{inv}}/\partial V_{\text{g}}$  calculated from experimental Hall data is well below the maximum possible value  $C_{\text{ox}}/q$  (6) near threshold, but ultimately  $\partial n_{\text{inv}}/\partial V_{\text{g}}$  approaches  $C_{\text{ox}}/q$  at high  $V_{\text{g}}$ . As  $V_{\text{g}}$  increases, both  $n_{\text{total}}$  and  $n_{\text{inv}}$  increase. The data in Fig. 6b show that the rates of increase in  $n_{\text{total}}$  and  $n_{\text{inv}}$  equalize at high  $V_{\text{g}}$ . This result shows that the *relative* effect of trapping becomes smaller for incrementally added electrons as  $V_{\text{g}}$  increases, but it is not clear why this happens. These data can be used to calculate the trap density  $D_{\text{it}}(E)$  as will be discussed below in Sect. 4.2.

The same comparison of mobility and free electron density data is shown for a  $4H$ -SiC MOS sample in Fig. 7. In this case,  $\mu_{\text{FE}}$  in Fig. 7a is considerably

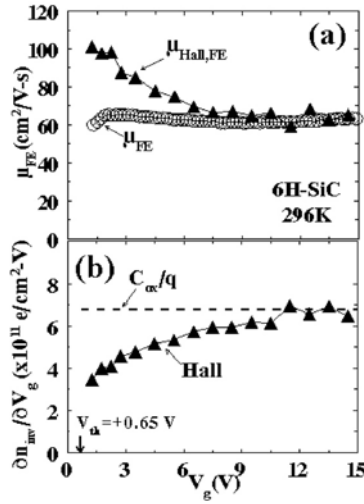


**Fig. 6.** (a) Comparison of field effect mobilities obtained from  $I_d$ - $V_g$  data ( $\mu_{FE}$ ) vs. Hall data ( $\mu_{FE,Hall}$ ) in a 6H-SiC inversion layer.  $\mu_{FE,Hall}$  is considerably higher than  $\mu_{FE}$  near threshold but similar values are obtained at high  $V_g$ . (b) Change in  $n_{inv}$  with  $V_g$  ( $\partial n_{inv}/\partial V_g$ ) from Hall experiments compared to maximum possible  $\partial n_{inv}/\partial V_g = C_{ox}/q$  (6) which would be obtained without trapping, in the same 6H-SiC sample. The effect of trapping is large near threshold but is reduced at high  $V_g$

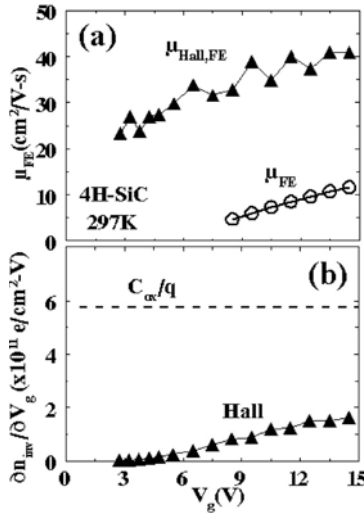


**Fig. 7.** Same plot as Fig. 6 for a 4H-SiC sample.  $\mu_{FE} \ll \mu_{FE,Hall}$  and  $\partial n_{inv}/\partial V_g \ll C_{ox}/q$ , indicating severe electron trapping at the SiC/SiO<sub>2</sub> interface

smaller than  $\mu_{\text{Hall,FE}}$  and never approaches the Hall mobility even at the highest values of  $V_g$ . Likewise,  $\partial n_{\text{inv}}/\partial V_g$  from the Hall data is considerably smaller than  $C_{\text{ox}}/q$  and never approaches it even at the highest values of  $V_g$  (Fig. 7b). It is clear from these large discrepancies that electron trapping at the SiC/SiO<sub>2</sub> interface is much higher in this 4H sample than in the 6H sample. Again, the gate oxides for these two samples from the same process lot were grown under identical conditions.

One surprising feature of the data in Figs. 6a and 7a is that the incremental Hall mobility  $\mu_{\text{Hall,FE}}$  *decreases* with increasing  $V_g$  in the 6H device but *increases* in the 4H device. In silicon MOS devices, the inversion mobilities  $\mu_{\text{eff}}$  and  $\mu_{\text{FE}}$  usually decrease with increasing  $V_g$  due to increased scattering by surface phonons [17]. Thus, the behavior of the 6H sample appears qualitatively similar to silicon. The unusual behavior of mobility in the 4H sample is presumably the result of extreme trapping and scattering in the 4H-SiC inversion layer [7].

### 3.3 Temperature Dependence

The experimental temperature dependence of  $\mu_{\text{Hall}}$  in typical 4H- and 6H-SiC inversion layers is shown in Fig. 8. Surprisingly, the qualitative temperature-dependent behavior is quite different in the two SiC polytypes.

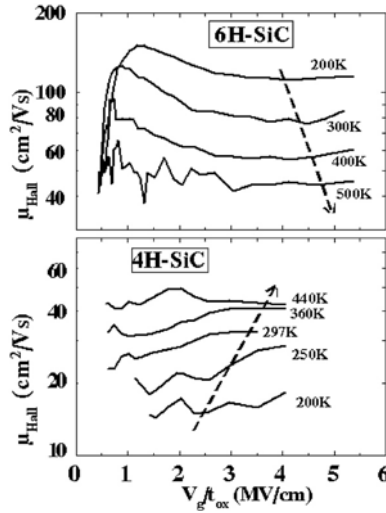


**Fig. 8.** The temperature dependence of  $\mu_{\text{Hall}}$  in typical 6H- and 4H-SiC electron inversion layers as a function of  $V_g/t_{\text{ox}}$ .  $\mu_{\text{Hall}}$  *decreases* with increasing temperature in 6H (similar to silicon) but *increases* with temperature in 4H. This qualitative difference is probably related to the higher electron trapping and scattering at the 4H-SiC/SiO<sub>2</sub> interface [7]

The mobility *decreases* with increasing temperature in *6H*, whereas it *increases* in *4H*. The *6H* temperature dependence is qualitatively consistent with the behavior of silicon inversion layers, which is believed to arise from the temperature dependence of surface phonon scattering [17]. The cause of the opposite temperature dependence in the *4H* sample is unclear, but is likely related to the much higher density of trapped electrons in *4H*. A similar increasing mobility with increasing temperature has been reported previously for *effective* mobilities measured on low-mobility inversion layers in *4H*-SiC MOSFETs [21, 22]. It was proposed that this behavior is caused by thermally activated hopping of inversion electrons [21]–[23]. Alternatively, it may arise from the temperature dependence of Coulomb scattering by trapped electrons in *4H* inversion layers [7].

The temperature dependence of  $\partial n_{\text{inv}}/\partial V_g$  is shown in Fig. 9 for the same two SiC samples as in Fig. 8. The behavior of  $\partial n_{\text{inv}}/\partial V_g$  is similar in both polytypes:  $\partial n_{\text{inv}}/\partial V_g$  increases with increasing  $V_g$  and it also increases with temperature. In the *6H*-SiC sample,  $\partial n_{\text{inv}}/\partial V_g$  gradually approaches the maximum theoretical value in the absence of electron trapping ( $= C_{\text{ox}}/q$ ) at high temperatures and high  $V_g$ . Results for the *6H* sample near 300 K are qualitatively similar to previous data in Fig. 6b for a *6H* sample from a different wafer from the same process lot. The differences in these two samples apparently arise just from uncontrolled wafer-to-wafer variations. In the *4H* device,  $\partial n_{\text{inv}}/\partial V_g$  is less than 40% of  $C_{\text{ox}}/q$  even at high temperatures and high gate biases.

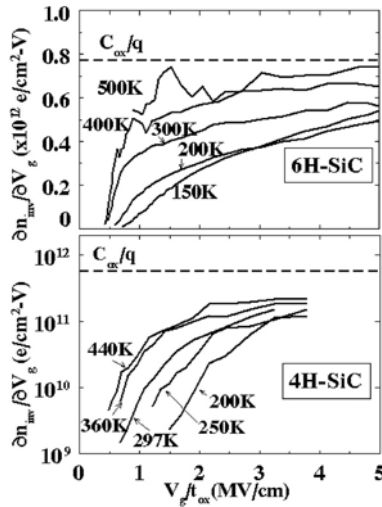


**Fig. 9.** Temperature dependence of  $\partial n_{\text{inv}}/\partial V_g$  for the same two samples in Fig. 8.  $\partial n_{\text{inv}}/\partial V_g$  increases with increasing temperature but is always less than  $C_{\text{ox}}/q$  in both samples

In summary, the dependencies of  $\mu_{\text{Hall}}$  and  $n_{\text{inv}}$  on gate voltage and temperature in  $6H$ -SiC inversion layers appear qualitatively similar to well-known results reported for silicon. However, in  $4H$ -SiC, these dependencies differ qualitatively and quantitatively. These differences are believed to arise from the much higher level of electron trapping in  $4H$  compared to  $6H$ . Even in the  $6H$  sample,  $\partial n_{\text{inv}}/\partial V_g$  is considerably smaller than  $C_{\text{ox}}/q$ , indicating that there are significant trapping effects in  $6H$  which cannot be ignored at any temperature.

## 4 Using Hall Data to Calculate $D_{\text{it}}(E)$

In order to understand the behavior of  $\mu_{\text{Hall}}$  and  $n_{\text{inv}}$  in these SiC MOS devices, knowledge of  $D_{\text{it}}(E)$  is required. In Sect. 4.1, conventional techniques for measuring  $D_{\text{it}}(E)$  and their drawbacks for use in SiC devices will be described. In Sect. 4.2, a technique using Hall data to obtain  $D_{\text{it}}(E)$  will be described. In Sect. 4.3, experimental  $D_{\text{it}}(E)$  results for  $4H$ - and  $6H$ -SiC devices using this Hall technique will be presented.

### 4.1 Alternative $D_{\text{it}}(E)$ Measurement Techniques

There are many techniques for measuring  $D_{\text{it}}(E)$  in MOS devices such as quasistatic capacitance-voltage ( $C$ - $V$ ) [24],  $AC$  conductance [25], and charge-pumping [26]. However, SiC has several properties which make it difficult to implement these standardized techniques. Because of its relatively wide bandgap (3.0 and 3.3 eV for  $6H$  and  $4H$ -SiC, respectively, vs. 1.1 eV for silicon), trapped carriers further than  $\sim 0.5$  eV from either SiC band edge have very long emission times at 300 K. Consequently, deep interface states in SiC are often not in equilibrium with the applied gate bias, which prevents implementation of quasi-static  $C$ - $V$  measurements at 300 K. This effect can be minimized by measuring at high temperatures ( $\sim 300^\circ\text{C}$ ), but present-technology SiC MOS capacitors tend to permanently degrade at high temperatures due to unknown causes.

$AC$  conductance measurements of  $D_{\text{it}}(E)$  are obtained from MOS  $C$ - $V$  data. For  $n$ -channel MOSFETs, the traps of interest are electron traps near the conduction band edge, which requires  $C$ - $V$  data from  $n$ -type substrates. However,  $n$ -channel MOSFETs are fabricated on  $p$ -type substrates, so MOS test capacitors for  $C$ - $V$  measurements must be fabricated on separate  $n$ -type test wafers. This is a significant drawback.  $D_{\text{it}}(E)$  is not necessarily the same on different  $n$ - and  $p$ -type wafers, even if the fabrication process is identical.  $AC$  conductance also has the disadvantage of being insensitive to “slow” traps with long capture and emission times. These near-interfacial slow traps probably represent a significant fraction of the traps in current SiC MOS devices [4]. This is unlike a typical silicon MOS device where slow traps account

for less than  $\sim 10\%$  of all traps [27]. Thus, although  $AC$  conductance is currently widely used to measure  $D_{it}(E)$  in SiC, these measurements probably significantly undercount the actual trap densities.

Charge pumping measurements use short gate length MOSFETs, so fabrication of separate test wafers is not required. However, charge pumping requires rapid lateral transport of electrons in the inversion layer, and fast capture of electrons at the traps [26]. In SiC MOS devices, minority carrier transport is slow due to the low electron inversion mobility, and fast capture is not possible at slow traps which usually have very small capture cross sections [27].

## 4.2 Hall Measurements of $D_{it}(E)$

### 4.2.1 Background

Due to difficulties in implementing standard techniques for measuring  $D_{it}(E)$  as just discussed, the use of Hall measurements to obtain  $D_{it}(E)$  will be described in this section. This approach has the disadvantage that special MOS Hall devices must be designed. Once this is done, however, the MOS Hall devices can be fabricated on the same wafers as other lateral MOSFETs without requiring any changes in the fabrication process. Furthermore, because it is a static measurement, the Hall technique is less susceptible to problems with non-equilibrium capture and emission of carriers at the traps.

Analysis of Hall data to obtain  $D_{it}(E)$ , was first discussed early in the development of silicon MOS devices in a classic paper on MOS inversion layers by Fang and Fowler [28]. However, their approach was not widely adopted because of its poor sensitivity (see below). This is a distinct disadvantage for silicon MOS devices which typically have low trap densities ( $D_{it} = \sim 0.1 - 5 \times 10^{10}$  traps/cm<sup>2</sup>-eV). In SiC MOS devices with high trap densities, two groups have recently demonstrated that this Hall technique can be used advantageously to determine  $D_{it}(E)$  [11, 29].

### 4.2.2 Analysis Technique

In order to perform MOS calculations to determine parameters such as  $D_{it}(E)$ , it is critical to know the surface potential  $\phi_s$  which corresponds to each applied gate voltage  $V_g$ . However, calculation of  $\phi_s$  is difficult when there is a high density of trapped electrons  $n_t$  at the interface. Because  $n_t$  is unknown, since it is the quantity to be determined, there is no way to calculate  $\phi_s$  from  $I_d$ - $V_g$  data alone. In the Hall technique,  $\phi_s$  is determined from an independent measured parameter,  $n_{inv}$ . This approach works because  $\phi_s$  can be calculated directly from  $n_{inv}$ , independently of the amounts of  $n_t$  and oxide charge [11, 28, 29]. This is the key insight on which this measurement technique is based.

In the Hall measurements, an independent experimental value for  $n_{\text{inv}}$  is obtained at each  $V_g$ . The analysis to find  $D_{\text{it}}(E)$  proceeds as follows: (a)  $\phi_s$  is determined by solving the semiconductor space charge (Poisson) equation at each value of  $n_{\text{inv}}(V_g)$ . (b) A *theoretical* value for  $V_g$  corresponding to each value of  $\phi_s$  is calculated using the electric fields in the semiconductor calculated in part (a) assuming no interface traps and zero oxide charge. (c) The change in the number of trapped electrons  $\Delta n_t$  between two successive values of applied gate voltage is calculated from the difference between theoretical and experimental values of  $\Delta V_g$  (see later discussion which describes this step in detail). (d) The trap density  $D_{\text{it}}$  between adjacent values of  $\phi_s$  is then calculated using  $D_{\text{it}}$  (at trap energy  $E_t = \phi_s$ ) =  $\Delta n_t / \Delta \phi_s$  [28].

This same fundamental approach is followed here and in [28, 29], but different approaches are used to calculate  $\phi_s$  from  $n_{\text{inv}}$  in step (a). In [28],  $\phi_s$  was determined using the simplifying assumption of strong inversion above threshold  $V_{\text{th}}$ , i.e., assuming that  $n_{\text{inv}} = n_{\text{total}}$  (2). In the presence of strong electron trapping, this assumption is incorrect as discussed previously. Furthermore, this approximation fails completely for  $V_g \leq V_{\text{th}}$ . In comparison, Arnold and Alok [29] find  $\phi_s$  using an accurate analytic solution to the space charge equations which is not subject to these limitations.

In this work,  $\phi_s$  is found by numerical solution of the space charge equations [11]. Using this approach, it is not necessary to establish a value for  $V_{\text{th}}$ , and  $\phi_s$  can be obtained accurately throughout the entire range of  $n_{\text{inv}}$ , even below threshold. Using Mathcad 2001 software, numerical solutions for  $\phi_s$  for  $\sim 30$   $n_{\text{inv}}$  data points are calculated in about 30 seconds using a desktop PC [30]. A further advantage to using a numerical solution is that details of the calculation can be modified more easily. For example, Fermi-Dirac (FD) statistics were used for all calculations here for improved accuracy close to  $E_c$  [11]. Results for FD statistics were verified to be identical to Boltzman statistics at energies more than  $\sim 0.05$  eV below  $E_c$  at 300 K. A second change currently being implemented is the use of non-uniform  $p$ -type substrate doping, which is desired for samples with  $n$ -type surface implants which has been shown to improve mobility [31]. These changes would be difficult to implement using an analytic solution for  $\phi_s$ .

Many SiC physical constants and sample parameters are required for these numerical calculations. Values for SiC physical constants such as density of states in the conduction band, carrier effective masses, etc., were obtained primarily from [32, 33]. The two main required sample parameters are oxide thickness  $t_{\text{ox}}$  and substrate doping  $N_A$ . Because these parameters can vary significantly across a processed wafer,  $N_A$  and  $t_{\text{ox}}$  were measured individually on each Hall bar chip using adjacent large area ( $1.6 \times 10^{-3}$  cm<sup>2</sup>) MOS capacitors. Calculated  $D_{\text{it}}(E)$  values are found to be quite sensitive to the value used for  $t_{\text{ox}}$ , especially at high values of  $V_g$  where the electric field across the oxide, and resulting oxide voltage drop, are high. The calculated  $D_{\text{it}}(E)$  is not particularly sensitive to the value of  $N_A$ , at least for the relatively low doping densities in the samples studied here.

### 4.2.3 Example Data Analysis

An example of the 4-step analysis performed on a 6H-SiC sample is illustrated in Figs. 10 and 11. In step (a),  $\phi_s(V_g)$  is calculated for each  $n_{\text{inv}}$  data point as discussed above. The result is shown by the “experiment” curve in Fig. 10. The “theory” curve in Fig. 10 is calculated in step (b) from known sample parameters assuming no trapping. In order to plot both curves in the same figure, the “theory” curve is equated to the data curve at the most negative value of  $V_g$ . However, any reference value could have been used because, in the next step, only *changes* in each curve are used, so the absolute position of the curves is unimportant.

Next, in step (c), the change in gate voltage  $\Delta V_g$  required to obtain a given change in  $\phi_s$  is calculated for both curves. An example is demonstrated graphically in Fig. 10 for a change in  $\phi_s$  from  $-0.1$  to  $-0.05$  eV. Values for  $V_{g,\text{exp}}$  and  $V_{g,\text{th}}$  calculated for this change for experiment and theory, respectively, are shown in the figure. Note that the experimental  $V_g$  is always larger than the theoretical  $V_g$ . This occurs because the electric field in the oxide, and therefore the voltage drop across the oxide, increase when electron trapping exists at the interface. Thus  $\Delta V_{g,\text{exp}}$  must be greater than  $\Delta V_{g,\text{th}}$  which is calculated assuming no charge trapping. In Fig. 10, a relatively large step,  $\Delta\phi_s = 0.05$  eV, is used for the purpose of illustration. In practice, smaller changes are calculated using adjacent experimental data points.

Values for  $\Delta V_{g,\text{exp}}$  and  $\Delta V_{g,\text{th}}$  calculated as shown in Fig. 10 are shown in Fig. 11 as a function of  $\phi_s$ . The experimental  $\Delta V_{g,\text{exp}}$  just represents the steps in gate voltage applied during the Hall measurements. These start out as relatively small 0.1 V steps near threshold and increase in 0.2, 0.5, and 1.0 V increments as the inversion layer becomes more conductive and the

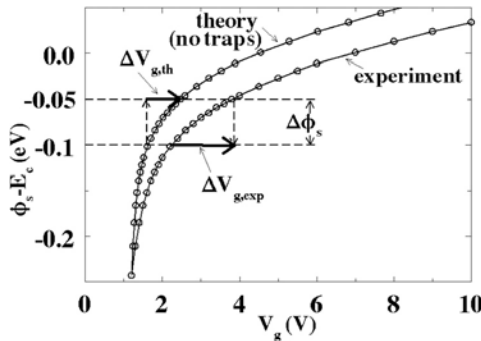


**Fig. 10.** Example of data analysis to calculate  $D_{\text{it}}(E)$  from Hall data in a 6H-SiC MOS Hall bar. “Experiment” curve shows  $\phi_s$  calculated from  $n_{\text{inv}}(V_g)$  (see text). “Theory” curve shows  $\phi_s$  calculated from theory assuming no trapping. The *heavy arrows* represent the changes in  $V_g$  required to produce a change in  $\phi_s$  from  $-0.10$  to  $-0.05$  eV in each curve.  $\Delta V_g$  is always larger in the “experiment” curve due to trapping

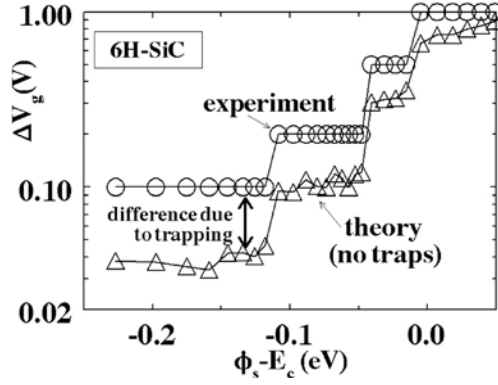


**Fig. 11.** Hall data analysis to calculate  $D_{it}(E)$  (continued from Fig. 10). Step (c): changes in  $V_g$  required to obtain a fixed change in  $\phi_s$  are calculated from the “experiment” and “theory” curves in Fig. 10. The change in the number of trapped electrons  $\Delta n_t$  is calculated at each  $\phi_s$  from the difference between the two curves. In step (d),  $D_{it}(E)$  is calculated from  $D_{it}(E) = \Delta n_t / \Delta \phi_s$  (see text)

percentage change in  $n_{inv}$  becomes smaller. Figure 11 clearly shows that the theoretical  $\Delta V_{g,th}$  calculated without trapping is always smaller than the experimental  $\Delta V_g$ . In step (c) of the analysis, the change in the number of trapped electrons  $\Delta n_t$  at a given value of  $\phi_s$  is then calculated from the difference between the two  $\Delta V_g$  curves using  $\Delta n_t(\phi_s) = C_{ox} (\Delta V_{g,exp} - \Delta V_{g,th}) / q$ . The relatively large difference between  $\Delta V_{g,exp}$  and  $\Delta V_{g,th}$  in Fig. 11 (note that the  $y$ -axis in this figure is a log scale) shows that the amount of trapping  $\Delta n_t$ , and ultimately the trap density  $D_{it}(E)$ , can be calculated with good accuracy in this 6H-SiC sample using Hall data. This difference becomes small only at the highest values of  $\phi_s$  and  $n_{inv}$ , at which point the resolution and accuracy of this technique becomes poor.

Finally, in step (d) of the analysis,  $D_{it}(E)$  (at trap energy  $E_t = \phi_s$ ) is calculated from  $\Delta n_t / \Delta \phi_s$ . A rough value for the limiting resolution of this calculation can be obtained by assuming a resolution in  $(\Delta V_{g,exp} - \Delta V_{g,th})$  of  $\sim 5$  mV for a 10 mV change in  $\phi_s$ . For a 30 nm gate oxide, this results in a resolution in  $D_{it}$  of  $\sim 3.5 \times 10^{11}$  traps/cm<sup>2</sup>-eV. This resolution is quite poor compared to standard techniques for silicon MOS samples [24]–[26]. However, as will be shown below, this resolution is adequate for the high- $D_{it}$  SiC samples measured here.

#### 4.2.4 Comparing $C$ - $V$ and Hall $D_{it}(E)$ in Silicon

In order to evaluate the accuracy of Hall  $D_{it}(E)$  analysis, these measurements were compared with standard  $C$ - $V$  measurements on a *silicon*  $\langle 100 \rangle$  reference MOS Hall bar ( $t_{ox} = 7.38 \times 10^{-6}$  cm,  $N_A = 1.6 \times 10^{15}$ /cm<sup>3</sup>) as shown in Fig. 12. A large area ( $1 \times 10^{-3}$  cm<sup>2</sup>) Hall bar was used to obtain accurate

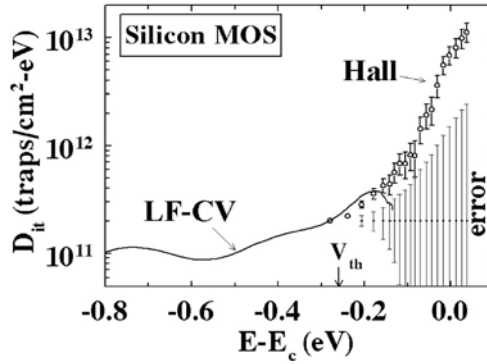


**Fig. 12.** Comparison of  $D_{it}(E)$  from quasi-static  $C$ - $V$  (solid line) and Hall measurements (open circles) on the same silicon MOS Hall bar. Agreement between the two measurements is quite good where the two measurements overlap ( $\sim -0.3$  to  $-0.15$  eV). Error bars show the relative (heavy bars) and absolute (light bars) errors calculated for  $\pm 2\%$  variation in oxide thickness

$C$ - $V$  and Hall data on the exact same device. The device was irradiated to 200 krad to produce a high trap density to allow accurate Hall measurements of  $D_{it}$ . The sample was annealed for about 6 months after irradiation to allow time-dependent annealing effects to subside. A silicon device was used in this experiment in order to be able to use quasi-static  $C$ - $V$  measurements to obtain reference  $D_{it}(E)$  values [24]. (As discussed above, obtaining useful quasi-static  $C$ - $V$  data from SiC is difficult at 300 K due to its wide bandgap.) Silicon band parameters for the Hall calculations were obtained from [6].

For the  $C$ - $V$  data, the MOS gate to substrate capacitance was measured at low frequency (1.0 Hz). In order to obtain equilibrium minority carrier response without using extremely low ramp rates, all  $N^+$  taps on the Hall bar were electrically shorted to the  $p$ -type substrate [34]. This supplies electrons without delay to the inversion layer. Standard quasi-static  $C$ - $V$  analysis [24] was then employed to calculate  $D_{it}(E)$  throughout the silicon band gap as shown by the solid line in Fig. 12. The quasi-static  $D_{it}(E)$  in this sample is roughly flat in the center of the gap, with a gentle rise towards the conduction band edge  $E_c$ . Although quasi-static  $D_{it}(E)$  results are generally accurate in the center of the band-gap, it is well-known that large errors occur approaching the band edges [35]. Consequently, the quasi-static  $D_{it}(E)$  curve in Fig. 12 is truncated at  $\sim -0.15$  eV where errors become large.

Hall effect measurements on the same silicon device are also shown in Fig. 12. Using the Hall effect,  $D_{it}(E)$  can only be measured when the MOS device is inverted, so the minimum energy of the Hall data is limited to  $\sim -0.3$  eV below  $E_c$  at 300 K. Agreement between the two techniques is quite good in the relatively small region of overlap which demonstrates the accuracy of the Hall data. Due to the relatively small overlap region, an attempt was made on this sample to push the Hall measurements of  $D_{it}$  as

deep into the bandgap as possible. This is the reason that high impedance buffers, low leakage samples, and sub-threshold measurements with low  $V_d$  are all required as discussed above in Sect. 2.3.

Above  $-0.2$  eV, the Hall data in Fig. 12 show that  $D_{it}(E)$  increases exponentially with energy approaching  $E_c$ . Similar exponential dependences of  $D_{it}(E)$  near  $E_c$  have been reported previously in silicon MOS devices [36, 37]. These states are sometimes characterized as “band-tail” states which arise due to “mild disorder” at the Si/SiO<sub>2</sub> interface [37].

The largest source of error in the Hall measurement is likely due to the error in determining  $t_{ox}$ . Error bars for the Hall data in Fig. 12 are plotted for a variation of  $\pm 2\%$  in  $t_{ox}$  (roughly equal to the uncertainty in  $t_{ox}$  in this sample). The error is small at  $E_t = -0.3$  eV, but it increases dramatically approaching  $E_c$ . However, the actual  $D_{it}(E)$  also increases rapidly approaching  $E_c$ , so that the *relative* error in  $D_{it}$  remains approximately constant in this particular sample. This is shown by the heavy error bars on the Hall  $D_{it}(E)$  data.

### 4.3 Hall Measurements of $D_{it}(E)$ in SiC

Experimental Hall measurements of  $D_{it}(E)$  in a 4H-SiC MOS sample are shown in Fig. 13. For comparison,  $D_{it}$  measurements from  $C$ - $V$  data from a large-area ( $100 \times 100 \mu\text{m}$ ) MOSFET are also shown in Fig. 13 [9]. This MOSFET is from a different wafer, but the same process lot, as the Hall sample (the fabrication process for these two wafers is described in detail in [8, 9, 38, 39] and Sect. 2.1). The  $C$ - $V$  data were obtained using a modified Gray-Brown analysis of threshold voltage shifts in the MOSFET as a function of temperature [9]. Agreement between the two techniques is good except for an unexplained anomaly in the  $C$ - $V$  data near  $E_t \approx -0.15$  eV. The

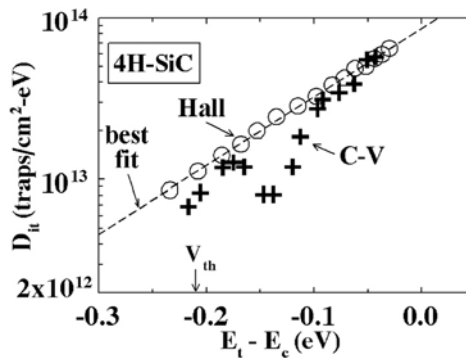


**Fig. 13.** Comparison of  $D_{it}(E)$  from low-frequency  $C$ - $V$  [9] and Hall measurements on devices from the different wafers. Reasonably good agreement is obtained. The *dashed line* is a best fit to the Hall data, showing that  $D_{it}(E)$  increases exponentially with energy

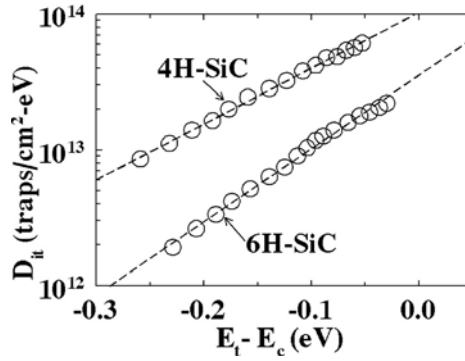


**Fig. 14.** Comparison of  $D_{it}(E)$  calculated from Hall data for 4H- and 6H-SiC MOS samples whose oxides were grown at the same time.  $D_{it}(E)$  is much higher in the 4H sample. The *dashed lines* are best fits to the two curves.  $D_{it}(E)$  increases exponentially with energy in both polytypes, but with slightly different slopes

Hall data show relatively little noise/scatter compared to the  $C$ - $V$  data. The Hall  $D_{it}(E)$  increases approximately exponentially with trap energy between threshold and  $E_C$ , which is consistent with many previously reported results [1, 4, 5, 9]. The exponential nature of the increase is demonstrated by the straight line in Fig. 13 which is a best fit to the Hall data.

Hall measurements of  $D_{it}(E)$  in 4H- and 6H-SiC samples are compared in Fig. 14, using the same 4H data from Fig. 13. These two wafers were processed identically in the same process lot with oxides grown simultaneously by a wet pyrogenic oxidation at 1100°C for 3 hours [10].  $D_{it}(E)$  is significantly higher in the 4H sample compared to 6H by a factor of about five. This result is consistent with many previous results [1, 5, 29] in samples where no special oxidation techniques were employed to reduce  $D_{it}$ .  $D_{it}(E)$  increases exponentially with energy in both samples, as shown by the dashed straight lines in the figure. The rate of increase in  $D_{it}(E)$  is higher in the 6H sample by  $\sim 30\%$ . This result is reproducible for the limited number of SiC samples studied to date.

An exponential increase in  $D_{it}$  near  $E_c$  is also observed in silicon (see Fig. 12 and related discussion). By analogy, this suggests that band-tail states could be the cause of the exponential behavior in both silicon and SiC. Any successful model describing the physical origin of interface traps at the SiC/SiO<sub>2</sub> interface must explain this exponential dependence.

New oxidation techniques have recently been developed which significantly reduce  $D_{it}(E)$  in 4H-SiC MOS devices [40, 41]. These techniques involve the incorporation of nitrogen in the oxide at or near the SiC/SiO<sub>2</sub> interface. In Fig. 15,  $D_{it}(E)$  results from the “as-grown” 4H-SiC oxide in Figs. 13 and 14 are compared with an NO-annealed oxide on 4H. This NO-annealed oxide was fabricated as a test oxide for a SiC power DiMOSFET [12].  $D_{it}(E)$  measurements in this NO-annealed sample are limited to energies

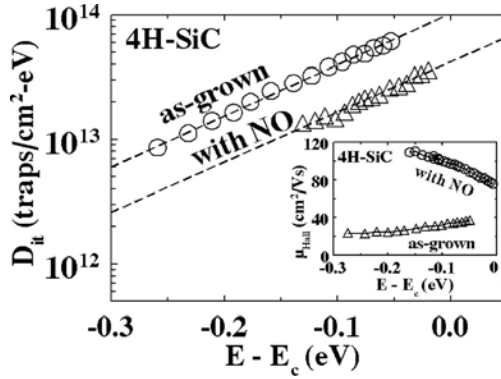


**Fig. 15.** Comparison of  $D_{it}(E)$  calculated from Hall data for two 4H-SiC MOS samples with and without an anneal in NO to reduce  $D_{it}$ . Dashed lines show straight line best fits to the Hall data.  $D_{it}(E)$  is smaller in sample with NO anneal. Inset shows that the Hall mobility in the same two samples is considerably higher in the NO-annealed, low- $D_{it}$  sample

above  $-0.15$  eV because of the high DC leakage current in this sample. This comparison between NO-annealed and non-NO-annealed samples is clearly not ideal because the two samples are from different process lots fabricated at different institutions. Despite this limitation,  $D_{it}(E)$  is significantly smaller by a factor of  $\sim 2.3$  in the NO-annealed sample, while the slopes are almost identical. NO-annealing can reduce  $D_{it}$  by as much as a factor of  $\sim 5$  or more [42]. The inset in the Fig. 15 shows the significant improvement in Hall mobility in these same samples due to the NO-anneal [13].

#### 4.4 Temperature Dependence of $D_{it}(E)$ in 4H-SiC

In Figs. 12–15,  $D_{it}(E)$  has been obtained by analyzing room temperature Hall data. This analysis method can be extended to cover a wide range of measurement temperatures. The temperature dependence of the various SiC constants used in the analysis must of course be accounted for. In this work, a temperature coefficient of  $-3.3 \times 10^{-4}$  eV/K is used for the temperature dependence of the 6H and 4H-SiC bandgaps [43]. The temperature dependences of other parameters are obtained from [32]. A value for  $r_{Hall}$  of 1.00 is assumed throughout the temperature range. This rough assumption for  $r_{Hall}$  is probably one of the more significant sources of error in the temperature dependent analysis.

Analysis of Hall data over the temperature range from 150–400 K for an NO-annealed 4H-SiC sample is shown in Fig. 16. As the temperature is reduced, the surface fermi level  $\phi_s$  is forced higher in the bandgap towards  $E_c$  at constant  $n_{inv}$ . Consequently, measurement energies are closer to  $E_c$  at low temperatures, and further from  $E_c$  at high temperatures. In this particular

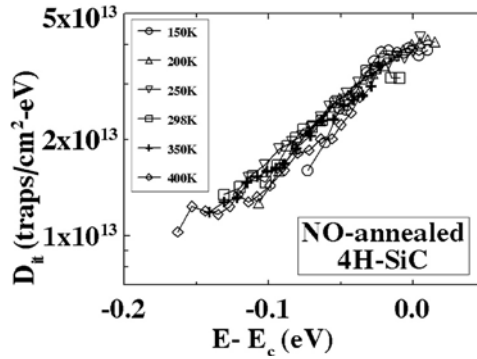


**Fig. 16.**  $D_{it}(E)$  calculated from Hall data for an NO-annealed 4H-SiC sample (from Fig. 15) as a function of measurement temperature from 150–400K. The  $D_{it}(E)$  curves are nearly independent of temperature

sample, increasing leakage currents at high temperatures limit the maximum measurement temperature to  $\sim 500$  K. In addition, the Hall measurements generally tend to become excessively noisy at high temperatures (for example, see the high noise level in the 6H-SiC sample in Fig. 8 at 500 K.). The source of the high noise is not known. Despite these measurement problems, it appears that  $D_{it}(E)$  is essentially temperature independent in Fig. 16 within experimental error.

#### 4.4.1 Summary and Conclusions

The *effective* mobility of electrons in MOS inversion layers can be determined simply by measuring the drain-to-source current in a MOSFET using (1)–(4). In *silicon* MOSFETs, this is a satisfactory approach because the effective mobility is essentially equal to the actual electron mobility because there is minimal electron trapping at the Si/SiO<sub>2</sub> interface. Thus, in silicon MOS devices, just about all of the electrons which are electro-statically induced at the Si/SiO<sub>2</sub> interface are free carriers and are able to contribute to the MOSFET source-to-drain current.

This is emphatically not the situation in SiC MOS devices. Due to high levels of electron trapping at the SiC/SiO<sub>2</sub> interface in current state-of-the-art devices, the density of free electrons in inversion layers is considerably smaller than the total density of electrons induced at the interface, as shown by experimental data in Figs. 4–7. These data show the necessity of using Hall data to de-convolute the relative contributions of the electron mobility and the free electron density to the conductivity of a SiC MOS inversion layer.

The use of Hall data also provides a powerful tool to analyze inversion layer behavior in SiC MOS devices. As demonstrated in this paper,  $D_{it}(E)$  can be calculated directly from  $n_{inv}(V_g)$  Hall data. In the future, these data

will be useful for studying electron scattering in SiC inversion layers in order to understand why electron mobility is so low. Initial attempts to model electron scattering behavior using Hall data have recently been presented [7, 29]. These papers concluded that, as expected, the dominant electron scattering mechanism is excessive scattering from all the trapped electrons at the interface, which causes the low electron mobilities. Future measurements of  $D_{it}(E)$  may also lead to better understanding of the source(s) of the high densities of traps and defects at the SiC/SiO<sub>2</sub> interface.

## Acknowledgements

The author would like to thank many colleagues who aided in the fabrication of devices for these experiments, including A. Agarwal, S.S. Mani, V.S. Hegde, V. Vathulya, and M.H. White. The author would also like to thank S.-H. Ryu and M. Das for providing additional Hall devices, and R. Rendell and M. Ancona for the software programming required to implement the Hall  $D_{it}(E)$  analysis.

## References

1. M.K. Das, B. S. Um, and J.A. Cooper: Jr., Mat. Sci. Forum **338–342**, 1069 (2000)
2. S. Sridevan, P.K. McLarty, and B.J. Baliga: IEEE Elec. Dev. Letts. **17**, 136 (1996)
3. D.M. Brown, E., Downey, M. Ghezzi, J. Kretchmer, V. Krishnamurthy, W. Hennessy, and G. Michon: Solid-State Electronics **39**, 1531 (1996)
4. V.V. Afanasev, M.Bassler, G.Pensl, and M.Schulz: Phys. Stat. Sol. A **162**, 321 (1997)
5. R. Schorner, P. Friedrichs, and D. Peters: IEEE Trans. Electron Dev. **46**, 533 (1999)
6. S.M. Sze: *Physics of Semiconductors*, 2nd ed. (John Wiley & Sons, New York, NY., 1981) Chap. 8
7. N.S. Saks: Mat. Res. Soc. Symp. Proc. **742**, 233 (2003)
8. A.K. Agarwal, N.S. Saks, S.S. Mani, V.S. Hegde, and P.A. Sanger: Mat. Sci. Forum **338–342**, 1307 (2000)
9. N.S. Saks, S.S. Mani, and A.K. Agarwal: Appl. Phys. Letts. **76**, 2250 (2000)
10. N.S. Saks and A.K. Agarwal: Appl. Phys. Letts. **77**, 3281 (2000)
11. N.S. Saks, M.G. Ancona, and R.W. Rendell: Appl. Phys. Letts. **80**, 3219 (2002)
12. S.-H. Ryu, A. Agarwal, J. Richmond, J. Palmour, N.S. Saks, and J. Williams: Electron Dev. Letts. **23**, 321 (2002)
13. M.K. Das, G.Y. Chung, J.R. Williams, N.S. Saks, L.A. Lipkin, and J.W. Palmour: Mat. Sci. Forum **389–393**, 981 (2002)
14. N.S. Saks, A.K. Agarwal, S.S. Mani, and V.S. Hegde: Appl. Phys. Letts. **76**, 1896 (2000); also, N.S. Saks, S-H Ryu, and A.V. Suvorov: Appl. Phys. Lett. **81**, 4958 (2002)

15. D.K. Schroder: *Semiconductor Material and Device Characterization* (John Wiley & Sons, New York, N.Y., 1990) Chap. 5
16. G. Rutsch, R.P. Devaty, W.J. Choyke D.W. Langer, and L.B. Rowland: *J. Appl. Phys.* **84**, 2062 (1998)
17. S.C. Sun and J.D. Plummer: *IEEE Trans. Electron Dev.* **ED-27**, 1497 (1980)
18. H. Sakaki. K. Hoh, and T. Sugano: *IEEE Trans. Electron Dev.* **ED-17**, 892 (1970)
19. W.J. Schaffer, G.H. Negley, K.G. Irvine, and J.W. Palmour: *Mat. Res. Soc. Symp.* **339**, 595 (1994)
20. H. Yano, T. Kimoto, H. Matsunami, M. Bassler, and G. Pensl: *Mat. Sci. Forum* **338-342**, 1109 (2000)
21. D.M. Brown, M. Downey, M. Ghezzi, J. Kretchmer, V. Krishnamurthy, W. Hennessy, and G. Michon: *Solid-State Electronics* **39**, 1531 (1996)
22. E. Bano, T. Ouisse, S.P. Scharnholtz, A. Golz, and E.G. von Kamienski: *Electronics Letts.* **33**, 243 (1997)
23. T. Ouisse: *Phys. Stat. Sol. A* **162**, 339 (1997)
24. M. Kuhn: *Solid-State Electronics* **13**, 873 (1970)
25. E.H.Nicollian and A.Goetzberger: *The Bell System Technical Journal* **46**, 1055 (1967)
26. G. Groeseneken, H.E. Maes, N. Beltran, and R.F. DeKeersmaecker: *IEEE Trans. Electron Dev.* **ED-31**, 42 (1984)
27. M.J. Uren, S. Collins, and M.J. Kirton: *Appl. Phys. Letts.* **54**, 1448 (1989)
28. F.F. Fang and A.B. Fowler: *Phys. Rev.* **169**, 619 (1968)
29. E. Arnold and D. Alok: *IEEE Trans. Electron Dev.* **48**, 1870 (2001)
30. Mathsoft, Inc., 201 Broadway, Cambridge, MA., 02139 ([www.mathsoft.com](http://www.mathsoft.com))
31. K. Ueno and T. Oikawa: *IEEE Electron Dev. Letts.* **20**, 624 (1999)
32. M. Schadt, G. Pensl, R.P. Devaty, W.J. Choyke, R. Stein, and D. Stephani: *Appl. Phys. Letts.* **65**, 3120 (1994)
33. M. Bakowski, U. Gustafsson, and U. Lindfeldt: *Phys. Stat. Sol. A* **162**, 421 (1997)
34. H.S. Haddara and M. El-Sayed: *Solid-State Electronics* **31**, 1289 (1988)
35. G. Declerck, R. Van Overstraeten, and G. Broux: *Solid-State Electron* **16**, 1451 (1973)
36. H. Deuling, E. Klausmann, and A. Goetzberger: *Solid-State Electron.* **15**, 559 (1972)
37. C. Svensson: *The Si-SiO<sub>2</sub> System*, ed. by P. Balk (Elsevier Science Publishing, New York, NY, 1988) Chap. 5, pp. 235-6
38. N.S. Saks, S.S. Mani, A.K. Agarwal, and M.G. Ancona: *IEEE Electron Dev. Letts.* **20**, 431 (1999)
39. N.S.Saks, S.S.Mani, A.K.Agarwal, and V.S.Hegde: *Mat. Sci. Forum* **338-342**, 737 (2000)
40. H.F. Li, S. Dimitrijević, H.B. Harrison, D. Sweatman, and P.T. Turner: *Mat. Sci. Forum* **264-268**, 869 (1998)
41. G.Y. Chung, C.C. Tin, J.R. Williams, K. McDonald, M. DiVentra, S.T. Pantelides, L.C. Feldman, and R.A. Weller: *Appl. Phys. Letts.* **76**, 1713 (2000)
42. L.A. Lipkin, M.K. Das, and J.W. Palmour: *Mat. Sci. Forum* **389-393**, 985 (2002)
43. *Properties of Silicon Carbide*, emis datareview series number 13, INSPEC, ed. by G.L. Harris (London, UK, 1995) Chap. 3.3, Y. Yoshida, p. 74

## Part IV

### Characterization

# Optical Properties of SiC: 1997–2002

W.J. Choyke and R.P. Devaty

## 1 Introduction

Our charge for this article was to bring the reader up-to-date with respect to our bird's eye view of the optical properties of SiC in Vol. II of SiC [1] published in 1997. It is with great pleasure that we discovered a treasure trove of new material which has emerged since 1997. The downside is that we can cover only a small fraction of the new material due to the severe space limitations. It was decided that topics would be chosen which appear to be of greatest interest to the theorists and experimentalists in the SiC Community.

## 2 Absorption Coefficient and Penetration Depth

Normally, ultra-violet lasers are used for optical excitation across the bandgap in the low temperature photoluminescence (LTPL) characterization of SiC boules grown wafers and epitaxial films.

At present lasers with wavelengths from 356.4 nm to 244 nm are used for this purpose. Hence, it is important to have reliable values of the absorption coefficients available for at least the commonly used polytypes 3C, 6H and 4H-SiC. For thin epitaxial films especially, one must know the penetration depth of the laser excitation in order to be aware of spurious effects from lower lying films or the substrate. Even then, as will be discussed later, LTPL signals may be seen from depths deeper than one would expect from the penetration of the laser excitation.

In [2] room temperature values of the absorption coefficient are given for 3C, 6H, and 4H-SiC in the wavelength range from 390.0 nm to 296.8 nm. By using the measured shift of the bandgap from 300 K to 2 K an estimate is made of the absorption coefficients at 2 K. It should be noted that this estimate can be further improved by taking into account the additional absorption due to phonon absorption at 300 K. However, this is not likely to be a large correction in this temperature interval [3]. In Table 1 we give the absorption coefficients in  $\text{cm}^{-1}$  for 3C, 6H and 4H-SiC at seven common laser wavelengths. On Fig. 1a comparison of the square root of the absorption coefficient at 300 K from 390.0 nm to 296.8 nm is given. Unfortunately, to date no precise values of the absorption coefficients are available below

**Table 1.** Absorption coefficients for 3*C*, 6*H* and 4*H*-SiC at seven common laser wave-lengths

Wave-length [nm]	Laser	3 <i>C</i>	6 <i>H</i>	4 <i>H</i>
		300 K/2 K (est.) $\alpha$ [cm <sup>-1</sup> ]	300 K/2 K (est.) $\alpha$ [cm <sup>-1</sup> ]	300 K/2 K (est.) $\alpha$ [cm <sup>-1</sup> ]
325.0	He-Cd	3660/3480	2300/2160	1330/1190
333.6	Ar <sup>+</sup> Ion	3190/3030	1760/1640	900/780
337.1	N <sub>2</sub> gas	2970/2860	1600/1480	730/630
351.1	Ar <sup>+</sup> Ion	2260/2160	1060/960	290/230
354.0	He-Cd	2160/2070	960/870	230/170
355.0	3×Q/Nd:YAG	2120/2030	930/840	210/160
356.4	Kr <sup>+</sup>	2070/1980	900/810	200/140

296.8 nm but very crude estimates for all three polytypes may be obtained by extrapolating the data in Fig. 1 to the quadrupled Nd-YAG laser wavelength at 266.0 nm ( $\alpha \sim 10^4$  cm<sup>-1</sup>) and the frequency doubled argon ion laser at 244.0 nm ( $\alpha \sim 2 \times 10^4$  cm<sup>-1</sup>).

For a given thickness of epitaxial film one would think that the knowledge of the absorption coefficient at the excitation wavelength of the laser would be sufficient to guarantee that spurious signals from the substrate or other underlying epitaxial films could be avoided. Unfortunately, more caution is required! It has been observed by several groups in recent years that broad

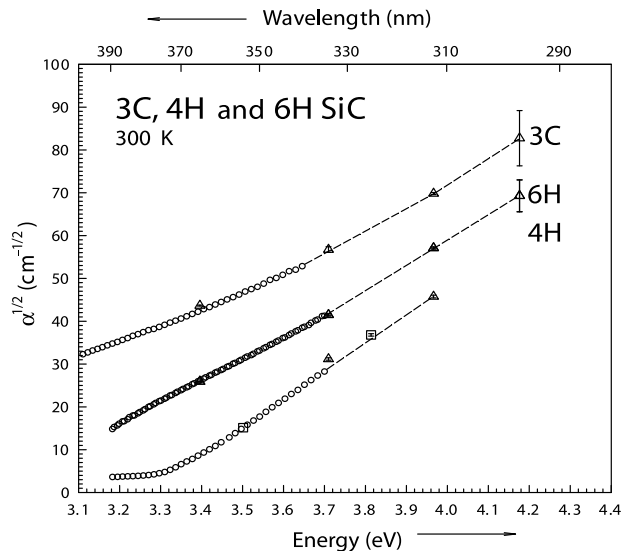


**Fig. 1.** A comparison of the square root of the absorption coefficients of 3*C*, 6*H* and 4*H*-SiC as a function of wavelength at 300 K

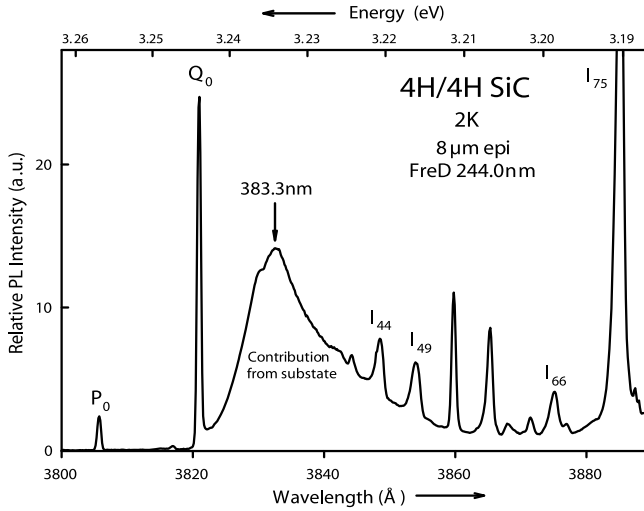


**Fig. 2.** 2 K photoluminescence of a very pure 8  $\mu\text{m}$  thick 4H-SiC epi film on a heavily doped *n*-type substrate. The band with a peak at 383.3 nm is a contribution of the *substrate* despite the fact that the 244.0 nm excitation is absorbed in the first micron of the epi film

structure from the substrate is easily apparent in low temperature photoluminescence (LTPL) spectra taken from high purity epitaxial films deposited on heavily doped substrates. It appears that other energy transport mechanisms come into play which enable the excitation to penetrate far deeper into the sample than one would have supposed from the knowledge of the absorption coefficient. This issue has been clarified in three important papers by A. Henry and collaborators [4]–[6]. We show in Fig. 2 one of our 2 K bandedge LTPL spectra from a very pure, 8  $\mu\text{m}$  thick film deposited on a heavily doped substrate and excited with 244.0 nm laser light. The 8  $\mu\text{m}$  thickness of the epitaxial film is many times greater than the penetration depth of the laser light. Nevertheless, we see a broad band feature extending from 382.2 nm to 386.0 nm. Such a broad feature is not normally seen in very pure 4H-SiC. This spurious band is now recognized as coming from the heavily doped *n*-type substrate upon which the epitaxial film was grown. In Fig. 3a and b we reproduce data taken from [6] to show the evolution of a nitrogen band in three 4H-SiC:N substrates doped from  $2.5 \times 10^{18} \text{ cm}^{-3}$  to  $1 \times 10^{19} \text{ cm}^{-3}$  as well as the evolution of a similar broad band in heavily *p*-type doped 4H-SiC:Al samples. The mechanism which permits this light “leakage” from the substrate is under current study. In ultra pure Ge [7] the diffusion length for free excitons at low temperature is measured to be about 1000  $\mu\text{m}$  and in ultra pure Si it is estimated in [8] to be about 150  $\mu\text{m}$ . Although the binding energies of the SiC free excitons in 3C, 6H and 4H-SiC are still under discussion at this time one can nevertheless be fairly sure that

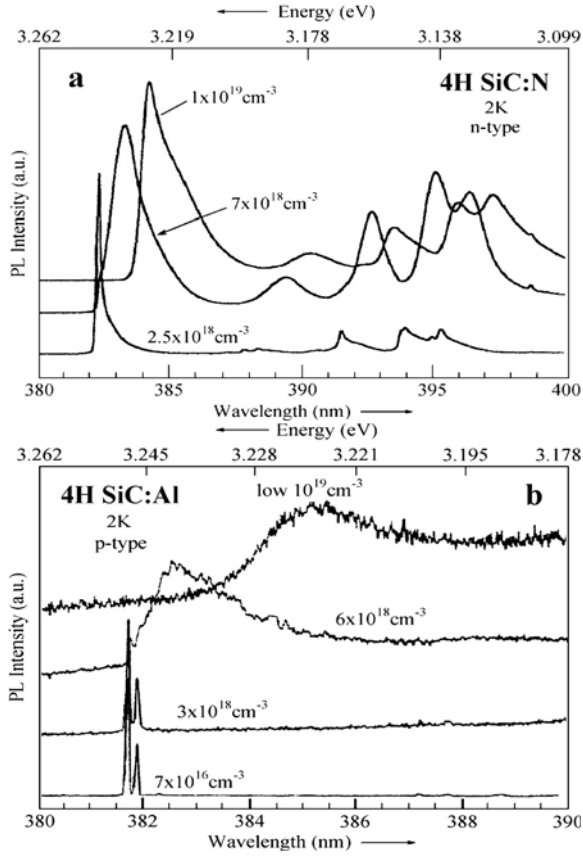


**Fig. 3.** LTPL spectra of heavily doped (a) *n*- and (b) *p*-type 4*H*-SiC. The data are taken from [6]. These broad bands are often seen in LTPL spectra of pure epitaxial films even though the absorption coefficient at the wavelength of the exciting laser light should guarantee that a minimal amount of such substrate light emerges from the sample

the binding energies are larger than for Ge and Si. Hence, it is not unreasonable to assume that in the highest purity but somewhat defect ridden epitaxial films of 4*H*-SiC currently available, the diffusion lengths of the free excitons may be 50  $\mu\text{m}$  or more.

Above 300 K there is some recent data for 4*H* and 6*H*-SiC [9]. These authors give the absorption coefficient for 4*H* and 6*H*-SiC boule wafer material from 300 K to 650 K. They also measure the absorption coefficient of pure thick epitaxial 4*H*-SiC in the same temperature range. A comparison is made for the absorption coefficient (300 K to 650 K) for 4*H*-SiC measured with  $\vec{E} \parallel \hat{c}$  in the wafer material and for the 4*H*-SiC epitaxial film with  $\vec{E} \perp \hat{c}$ , where  $\hat{c}$  denotes the crystal *c*-axis.

### 3 Band Edge Absorption and Valence Band Splittings

The band structure near the top of the valence bands at (or very near) the point  $\Gamma$  at the center of the Brillouin zone determines the properties of the holes, including their effective mass parameters. In 3C-SiC the highest valence bands are separated by a small spin-orbit splitting, with a measured value of about 10 meV. The valence bands of the hexagonal and rhombohedral polytypes are split due to both spin-orbit and crystal-field interactions, so that there are three closely spaced bands.

The measurement of these splittings by optical absorption is facilitated by the use of modulation spectroscopy to enhance the weak features associated with phonon assisted creation of intrinsic excitons in these indirect gap semiconductors. We measure the wavelength derivative of the absorption coefficient by wavelength modulated spectroscopy using a sensitive, stable system [10]–[12] based on a double grating monochromator. Spectra are obtained for both polarizations  $\vec{E} \perp \hat{c}$  and  $\vec{E} \parallel \hat{c}$  using specially prepared boule pieces as samples.

The spin-orbit splitting  $\Delta_{SO}$  is the energy separation of the topmost valence bands (Fig. 4). The spectra show doublets due to phonon assisted free exciton absorption involving holes from the top two valence bands. The en-

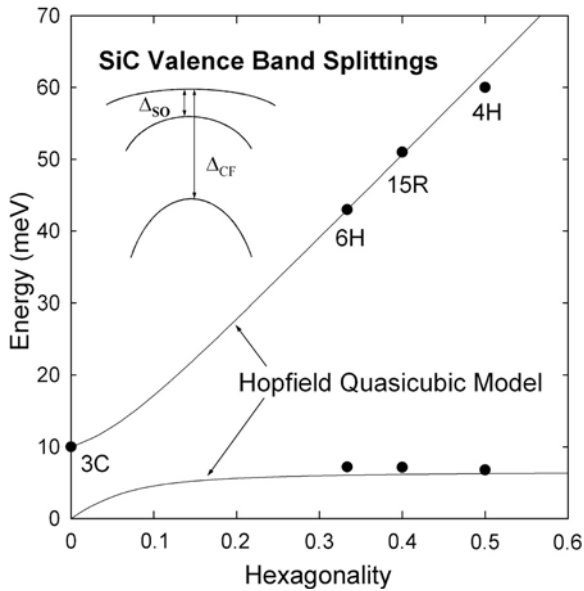


**Fig. 4.** Measured spin-orbit and crystal-field splittings for SiC polytypes (*solid circles*). The curves are calculated using Hopfield's quasicubic model. The hexagonality scale is defined in the text. The *inset* schematically defines the valence band splittings

ergy separations of these doublets are averaged to obtain an estimate of  $\Delta_{\text{SO}}$  with an uncertainty of a few tenths of a meV. There is an unknown, presumably small, correction because the binding energies of excitons having holes from one or the other of the two bands are different.

The crystal-field splitting  $\Delta_{\text{CF}}$  is defined in the inset on Fig. 4. It does not have such a clear cut signature in the spectra, so the assignments, which were made using spectra taken in both polarizations with the assistance of selection rules obtained using group theory, are less certain. Details are discussed in the references [12, 13].

Figure 4 shows the measured valence band splittings [10]–[13] as a function of polytype hexagonality, defined as the ratio of hexagonal sublattice sites to the sum of the hexagonal and quasicubic sublattice sites. The Si sublattice, for example, comprises all of the sites occupied by Si atoms in a perfect SiC crystal. The solid lines are calculated using Hopfield's quasicubic model [14]. This model is an approximation having only two parameters, whereas three parameters are permitted according to symmetry arguments, to describe the splittings of the valence band at the  $\Gamma$  point. The parameters are expressed as spin-orbit and crystal-field interaction energies  $\delta_{\text{SO}}$  and  $\delta_{\text{CF}}$ , respectively. We set  $\delta_{\text{SO}} = 10$  meV to agree with the measured spin-orbit splitting of 3C-SiC [15]. The parameter  $\delta_{\text{CF}}$  is varied. It is converted to hexagonality by dividing by 117. This factor is chosen so that the calculated curve agrees reasonably well with the measured crystal-field splittings. This choice corresponds to a crystal-field splitting of about 120 meV at hexagonality 1.0 (2H-SiC). The plot illustrates the strong mixing of spin-orbit and crystal-field interactions near hexagonality 0.1, so that the point corresponding to the spin-orbit splitting in 3C-SiC is on the same curve as the crystal-field splittings of the noncubic polytypes. According to this model, the spin-orbit splitting shows little dependence on hexagonality beyond about 0.3, and asymptotically approaches the value  $2\delta_{\text{SO}}/3$ . While the calculated  $\delta_{\text{SO}}$  slowly increases with hexagonality over most of the range, the measured values show a small decrease with increasing hexagonality. A possible explanation is proposed in [13]. The measured splittings can be used as input to band structure calculations, or they can serve as reality checks. Band structure calculations predict a linear dependence of  $\Delta_{\text{CF}}$  on hexagonality in agreement with the behavior of the data. The agreement with the calculations of Lambrecht et al. [16] is quite good.

## 4 Biedermann Absorption Bands in Nitrogen Doped SiC

Strong, polarized absorption bands below the band edge in highly nitrogen doped (estimated on the order of  $5 \times 10^{18} \text{ cm}^{-3}$ ) 4H, 6H, 8H and 15R-SiC were measured by Biedermann [17], who proposed that they are associated with transitions from the conduction band minima to higher conduction bands. It is also possible that the donor states are involved in the transitions.

These bands are responsible for the colors of nitrogen doped SiC crystals. Recent experimental and theoretical work has led to an improved understanding of these bands. On the experimental side, the availability of large, moderately doped ( $n \sim 10^{17} - 10^{18} \text{ cm}^{-3}$ ) boule samples of 4H and 6H-SiC has made possible a careful study [18] of the absorption. Spectra measured in both polarizations  $\vec{E} \parallel \hat{c}$  and  $\vec{E} \perp \hat{c}$  were reported over a temperature range from 2 K to room temperature. Based on band structure calculations [19, 20], it is now possible to assign the observed peaks to specific interconduction band transitions. To account for the width of the bands in Biedermann's spectra, Limpijumnong et al. [19] proposed that the  $\Delta k = 0$  selection rule is broken in highly doped material due to band tailing and mixing of states near the bottom of the conduction band with the shallow nitrogen donor states. They estimated  $\delta k \sim 0.1(2\pi/a)$ , where  $a$  is the lattice constant, and calculated the density of states of each conduction band for states within a sphere of radius  $\delta k$  in  $k$  space about the minimum of the lowest conduction band. They compare the shapes of the calculated densities of states of the final state conduction bands with Biedermann's spectra, taking into account the polarization selection rules. The recently measured spectra [18] feature narrower bands with a wealth of detail. These spectra show not only shifts of peaks but the appearance and disappearance of peaks as the temperature ranges from room temperature down to liquid helium temperature. It is not possible to explain all these observations by considering band-to-band transitions alone. Sridhara et al. [18] proposed the participation of shallow nitrogen donor states and donor induced resonances below the final state conduction band, most prominently for  $\vec{E} \parallel \hat{c}$  spectra at low temperature. The shallower, hexagonal sublattice site nitrogen donors are thought to make the dominant contributions, while the deeper quasicubic nitrogen donors are not observed due to smaller absorption cross sections associated with tighter binding.

Figure 5 shows  $\vec{E} \parallel \hat{c}$  and  $\vec{E} \perp \hat{c}$  absorption spectra of moderately nitrogen doped 4H-SiC at room temperature and above. These spectra were obtained using the same sample as those reported in Figs. 3 and 4 of [18], but have not previously been published. The reader is warned that all measurements of the absorption coefficient are challenging and not to take the numerical values too seriously. Therefore, we have labeled the vertical axes using arbitrary units rather than  $\text{cm}^{-1}$ . Also, the offsets from zero and relative offsets between spectra should not be taken too seriously. At these temperatures, most of the details that are described by the interpretation discussed above have disappeared, leaving asymmetric bands for both polarizations. With increasing temperature, the bands broaden and the peaks shift to lower energy. Since these are inter-conduction band transitions, there is no reason to expect that the temperature dependent shifts should be the same as the temperature dependence of the indirect band gap. In fact, the temperature shifts are considerably smaller than that of the band gap.

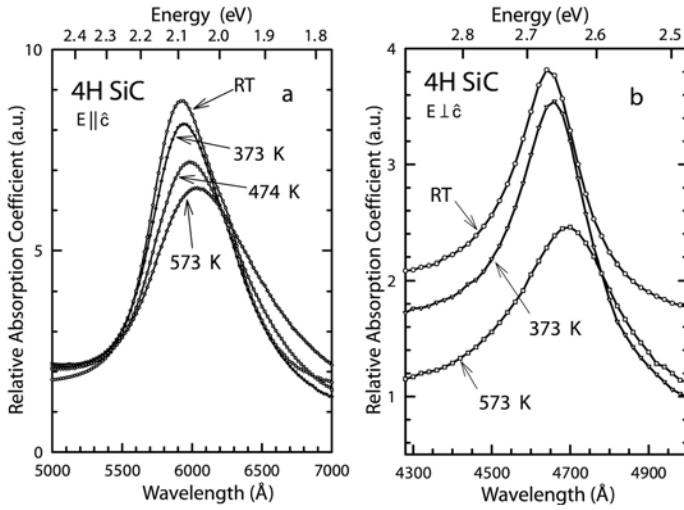


**Fig. 5.** Below band gap absorption bands of nitrogen doped 4H-SiC measured at and above room temperature (*RT*): (a) polarization  $\vec{E} \parallel \hat{c}$ , (b)  $\vec{E} \perp \hat{c}$

The Biedermann absorption bands have practical importance. As an example, Weingärtner et al. [21] and Wellmann et al. [22] recently calibrated the below bandgap absorption coefficients of *n*-type 4H, 6H and 15R-SiC at selected wavelengths to the free carrier concentration using Hall effect measurements on the same samples and applied the calibration to wafer mapping. The method is non-contact, rapid, and can be applied at room temperature, but the wafers must be polished on both sides. They claim an accuracy of 15–20% and a useful free carrier concentration range of approximately  $1 \times 10^{17}$ – $1 \times 10^{19} \text{ cm}^{-3}$ .

## 5 Erbium

Optical characterization of Erbium in SiC was surveyed in [1]. A number of papers have been published since that time that discuss various aspects of Erbium in SiC [23]–[32]. Prior to the experiments discussed in [28], doping of SiC with Erbium was obtained by relatively low energy ion implantation with Er concentrations in excess of  $10^{19} \text{ cm}^{-3}$ . The resulting Er doped layers were very shallow, of the order of 100 nm thick, and consequently good signals could only be observed for very highly doped samples. At such high concentrations of Erbium the temperature dependence of the  $\text{Er}^{3+}$  integrated luminescence intensity (1.49  $\mu\text{m}$ –1.64  $\mu\text{m}$ ) is more or less constant from 2 K to 400 K in 6H and 4H-SiC and then drops off steeply towards higher temperatures. In the experiments described in [28], chemical vapor deposition

(CVD) grown epitaxial films of  $4H$  and  $6H$ -SiC doped with nitrogen in the range from  $3 \times 10^{14} \text{ cm}^{-3}$  to  $1 \times 10^{16} \text{ cm}^{-3}$  were doped with Erbium by multiple implantations of 2.5, 4.0, 6.0, 8.5, 11.5 and 15 MeV at room temperature. A quasi-rectangular depth profile of Er in the depth interval 0.3  $\mu\text{m}$  to 2.5  $\mu\text{m}$  was achieved and then the samples were annealed at 1500°C. For such relatively thick Er doped regions it was possible to obtain good integrated luminescence signals for concentrations as low as  $5 \times 10^{15} \text{ cm}^{-3}$ . The temperature variation of the integrated luminescence intensity is now completely different from what it was for the highly doped samples and what has been observed in most semiconductors, highly doped with Erbium. At 2 K for the dilutely doped  $4H$  and  $6H$ -SiC samples the Er signal is now very small. It rises rapidly until 77 K and then remains roughly constant to above room temperature and then thermally quenches in the normal manner.

A detailed model consistent with these new results was not presented, but it was suggested that if one assumes that the energy transfer to the  $\text{Er}^{3+}$  proceeds via the shallow nitrogen donor to a defect associated with the Erbium implantation, then it is quite plausible that this process is governed by a barrier between the donor and the defect. At high doping levels the close proximity of the donor and Erbium atoms effectively wipes out this barrier even at 2 K. At much lower Erbium concentrations, below  $1 \times 10^{17} \text{ cm}^{-3}$ , the average donor-defect separation becomes such that at 2 K the energy transport is effectively controlled by a barrier which is function of separation. New deep level transient spectroscopy (DLTS) results presented in [30] show that the defects generated in  $n$ -type SiC by the Erbium implantation are not associated with the Erbium. On the other hand, defects generated by Erbium implantation in  $p$ -type SiC can be identified with defects specific to Erbium. LTPL spectra shown in [30] give evidence for the fact that the  $\text{Er}^{3+}$  spectrum is only seen in  $n$ -type SiC. The authors of [30] suggest that the excitation of the  $\text{Er}^{3+}$  4f electrons may occur through the collapse of a donor bound exciton at one of the well known damage centers in the top half of the bandgap rather than at an Erbium related defect. It is currently not known whether the Erbium related defects in the lower half of the bandgap play any role in the energy transfer to the  $\text{Er}^{3+}$ , 4f electrons.

## 6 Intrinsic Defects

Intrinsic defects introduced during growth or processing steps such as ion implantation and annealing can have important detrimental effects on the electronic properties of device material, e.g., carrier lifetimes. Mid-gap levels in particular can be lifetime limiters.

We cannot review even in the most perfunctory fashion the progress that has been made between 1997 and 2002 based on optical studies of intrinsic defects. Rather, we shall focus on three defects: the long-known  $\text{D}_1$  and

$D_{II}$  centers that persist after anneals up to 1700°C, and the more recently classified  $E_A$  spectrum, also known as the “alphabet lines.”

In the early work in the 1970’s, proposals for the structures of defects responsible for the  $D_I$  and  $D_{II}$  spectra were inferred based on clues gleaned from experiment. Now theorists perform modern ab initio density functional calculations on proposed defect structures. The most useful data from optical experiments available for comparison with theory are the vibrational replicas due to local modes in photoluminescence spectra.

## 6.1 The $D_I$ Defect

Although the  $D_I$  photoluminescence (PL) spectrum was discovered and thoroughly investigated in a number of SiC polytypes in the 1970’s, particularly by the Westinghouse group and in the Soviet Union, much has been learned since 1997. Egilsson et al. [33, 34] studied the  $D_I$  bound exciton spectrum in 4H and 3C-SiC and proposed that the defect is a pseudo-donor. Some of the results that we summarize here have been known for a long time, but are mentioned here as background to the model. Only a single  $D_I$  spectrum, characterized by a sharp no-phonon line  $L_1$  at low temperature and its vibrational replicas, is observed in 4H-SiC [35]. Two spectra might be expected based on the number of inequivalent sublattice sites. Photoluminescence time decay measurements yield long lifetimes, consistent with an isoelectronic defect. If the defect carries an electron or hole in addition to binding the exciton, it would be possible for nonradiative Auger processes to compete with radiative recombination, thus limiting the lifetime. With increasing temperature, excited state no-phonon lines  $M_1$  and  $H_1$  appear along with their phonon replicas.  $M_1$  and  $H_1$  are stronger than  $L_1$ , suggesting that  $L_1$  is a forbidden transition. Studies of the temperature dependence reveal that  $M_1$  and  $H_1$  thermalize with  $L_1$ . The  $D_I$  spectrum quenches at temperatures between 100 K and 250 K. The activation energy of about 57 meV is much less than the exciton binding energies of  $M_1$  and  $H_1$ , which are approximately 356 and 353 meV, respectively. The interpretation is that either the electron or the hole, whichever is more weakly bound, detaches from the complex during thermal quenching. In photoluminescence excitation spectroscopy (PLE), the excitation wavelength is scanned while the photoluminescence (PL) over a selected band, typically a PL line, is monitored. The PLE spectrum shows peaks at the wavelengths of absorption lines that are coupled to the monitored luminescence. From PLE on  $D_I$  in 4H-SiC, the  $L_1$  line is connected to  $M_1$ ,  $H_1$  and a weak line  $N_1$  on the high energy side of  $M_1$ . In addition, a series of sharp lines associated with excited states of the bound exciton is observed in the range 45 to 65 meV above  $L_1$ . These lines can be classified into groups of up to four lines, and are interpreted as due to a series of hydrogenic excited states. A fit based on the simple hydrogenic effective mass theory leads to a binding energy of 62 meV and an isotropic effective mass consistent with an estimate based on the measured electron effective masses in 4H-SiC. Egilsson

et al. [35] also performed a fit based on Faulkner's model [36], which applies if the electron pocket is an ellipsoid with uniaxial symmetry. The binding energy is comparable to the dissociation energy (thermal quenching), suggesting that the electron is the weakly bound particle. Based on these experimental observations and interpretations, Egilsson et al. [33]–[35] proposed that  $D_I$  behaves as a pseudodonor. In this model, the  $D_I$  defect in its neutral state has a strong hole-attractive potential. When the crystal is excited, the center can capture a hole, which is bound strongly. The positively charged defect can then bind an electron hydrogenically. The electron behaves analogously to the electron in a shallow hydrogenic donor, hence the name pseudo-donor. Photon emission returns the defect to its initial neutral state. Storasta et al. [37] estimated that the binding energy of a hole to the defect is about 343 meV and suggested that there should be a hole trap separated from the top of the valence band by approximately this energy.

Magneto-optics provides further details about the electronic structure of a defect. Dean et al. [38] performed Zeeman spectroscopy on  $D_I$  in  $6H$ -SiC and suggested a model based on J-J coupling to explain their data. However, the applicability of a J-J model can be questioned [34]. Egilsson et al. [39] reported Zeeman spectra of  $D_I$  in  $3C$  and  $4H$ -SiC in magnetic fields up to 5 T and proposed a new model that seems to take into account the important interactions necessary to explain the spectra. The model can be presented as a hierarchy of interactions of decreasing strength. The bound exciton complex consists of an electron and a hole bound to a neutral defect. The hole is assumed  $p$ -like, with orbital angular momentum quantum number  $L_h = 1$  and spin  $S_h = 1/2$ . In the case of  $4H$ -SiC, the crystal field splitting of the valence band, about 43 meV (see Sect. 3), exceeds the energy spread of the  $D_I$  no phonon lines, which is about 10 meV. The crystal field split valence band is excluded by retaining only the  $M_L = \pm 1$  states, where the axis of quantization is the crystal  $c$ -axis. (However, note that the binding energy of the hole to the complex greatly exceeds the crystal field splitting.) For the electron, there are three equivalent conduction band minima for both  $3C$  and  $4H$ -SiC, so valley orbit splitting is expected. The nature of the splitting depends on the site symmetry of the defect, which is not known. For example, in  $4H$ -SiC, a substitutional effective mass like donor with  $C_{3v}$  symmetry has  $A$  (singlet) and  $E$  (doublet) valley orbit levels. The model of Egilsson et al. is essentially spherical in nature and makes no explicit mention of site. They consider two valley orbit levels, each presumably a singlet. The valley orbit levels are treated independently in the remainder of the hierarchy. Each valley orbit level is treated as an electron with  $L_e = 0$  and  $S_e = 1/2$ . Next in the hierarchy are the electron-hole exchange coupling  $\vec{S}_e \cdot \vec{S}_h$  and the hole spin orbit coupling  $\vec{S}_h \cdot \vec{L}_h$ . The two "spin Hamiltonians" for the bound exciton (to treat the electron in each of two valley orbit levels) include exchange and spin orbit couplings, and the Zeeman effect. The parameters are adjusted to fit the Zeeman "fan diagram". What is learned from this analysis? First, the

fits indicate that the spin orbit coupling is weak, consistent with a strongly bound hole. The success of the model suggests that site symmetry does not play an important role, and no clues about the site symmetry or structure of the  $D_I$  defect are obtained. If  $D_I$  consists of more than one primary defect, this work provides no evidence for spectral differences related to orientation or inequivalent sites. Chen et al. [40] measured Zeeman spectra of  $D_I$  in  $4H$ -SiC, using magnetic fields up to 23 T in both Faraday and Voigt configurations, and also measured the polarization of the lines.

What is the defect responsible for the  $D_I$  spectrum? At this time there is no definitive answer. Eberlein et al. [41] recently speculated that  $D_I$  might be a nearest neighbor antisite pair.

## 6.2 The $D_{II}$ Defect

Sridhara et al. [42] observed new low temperature photoluminescence spectra in ion implanted and annealed  $4H$  and  $6H$ -SiC epilayers. These spectra persist after anneals in argon up to 1700°C. The same spectrum was observed in  $6H$ -SiC implanted with five different ions, and in  $4H$ -SiC implanted with eight different ions. The logical conclusions are that the defect must be intrinsic and most likely is a complex. The vibrational replicas include two local modes in the phonon gap and a number of local vibrational modes (LVM's) beyond the lattice limit of about 120 meV. The spectra called  $D_{II}$ , previously observed in  $3C$  [43] and  $15R$ -SiC [44], are very similar. In fact, the energies of five of the prominent high energy LVM's are common to  $3C$ ,  $4H$  and  $6H$ -SiC. Therefore, these new spectra are identified as  $D_{II}$ . The primary purpose of reference [42] was to warn the reader against blindly associating new spectra produced by ion implantation and annealing with the particular ion. Sridhara et al. [42] observed the  $D_{II}$  spectrum in  $4H$ -SiC epilayers co-implanted with boron and carbon, but not in samples co-implanted with boron and silicon. This result indicates that carbon plays a role in the structure of  $D_{II}$ .

A good deal is known about the  $D_{II}$  spectrum in  $4H$  [42, 45] and  $6H$  [42, 46] SiC. We shall discuss the  $6H$ -SiC spectrum. Figure 6 shows a  $6H$ -SiC spectrum taken at 7 K [42]. Generally the clearest  $D_{II}$  spectra are obtained above 2 K so that the overlapping nitrogen bound exciton spectra are thermally quenched. At 7 K four no-phonon lines appear, labeled  $d^1$  through  $d^4$ . At least seven additional excited states appear with increasing temperature [46]. The exciton binding energies to the defect are not very large; the greatest is 78.7 meV for line  $d^4$ . The lowest energy line  $d^4$  quenches near 20 K, while the entire spectrum disappears near 80 K with activation energy 69 meV. Sridhara et al. [46] suggest that the early quenching of  $d^4$  indicates that it is a forbidden transition. The decay times of the no-phonon lines are long, indicating that Auger processes do not participate and therefore the defect is isoelectronic. Since the activation energy for thermal quenching and the exciton binding energies are comparable in magnitude, it is not likely that one of the electronic particles is much more strongly bound, as is the case for

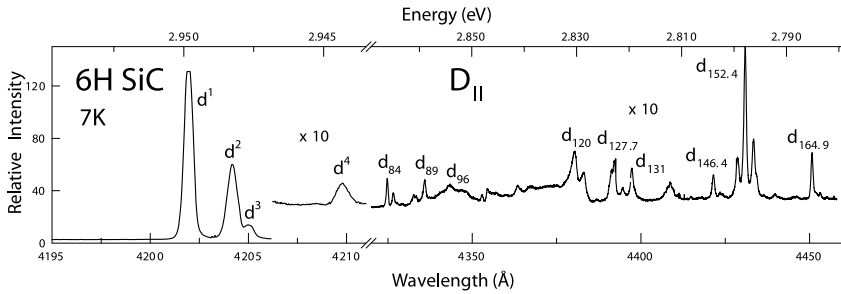


**Fig. 6.**  $D_{II}$  photoluminescence spectrum of 6H-SiC measured at  $T = 7$  K. No phonon lines are labeled  $d^1$  through  $d^4$ . The rest of the labels mark vibrational replicas, where the subscript is the phonon energy in meV. Five prominent local vibrational modes beyond the lattice limit of approximately 120 meV are highlighted in bold

the  $D_I$  center. Sridhara et al. [46] observed shifts but no splitting of the  $D_{II}$  no-phonon lines for a sample placed under stress by mounting it to a holder using glue. Zeeman spectroscopy reveals that some of the no-phonon lines shift, but no splitting of lines is observed in magnetic fields up to 5 T, suggesting that the transitions are singlet-to-singlet. Similar observations apply to the  $D_{II}$  spectrum in 4H-SiC [42, 45].

Theorists are able to calculate the energies of the local vibrational modes of proposed models of the  $D_{II}$  center for comparison with experiment. It is important to note that the tabulated five local modes above the lattice maximum [42] are common to 3C, 4H and 6H-SiC, but additional high energy modes are also observed. Models with one or more C-C bonds are considered as candidates for  $D_{II}$  because diamond-like C-C bonds are seemingly the only way to obtain high energy local modes for an intrinsic defect. Mattausch et al. [47, 48] performed ab initio density functional calculations on clusters of 3C and 4H-SiC for four defects based on interstitial carbon (notation for 3C-SiC): the carbon antisite  $C_{Si}$ , the carbon split interstitial  $C_{sp\langle 100 \rangle}$  (two carbons at a carbon site, with the C-C bond along a  $\langle 100 \rangle$  direction), the carbon-silicon split interstitial  $C_{sp,Si\langle 100 \rangle}$  (a carbon and a silicon on a silicon site, connected by a bond along a  $\langle 100 \rangle$  direction), and the carbon split interstitial-antisite complex  $C_{sp,C_{Si}\langle 100 \rangle}$  (two carbon atoms on a silicon site). Only the last model, the di-carbon antisite, has two LVM's in the phonon gap and five modes beyond the lattice maximum, which are in "reasonable agreement" with the measured values. The calculated formation energy is comparable to those of the C split interstitials, suggesting that this defect can appear in significant concentrations, and its binding energy is compatible with stability up to high temperatures. Figure 7 shows a schematic of the structure of the di-carbon antisite in the 3C-SiC lattice, with local symmetry  $D_{2d}$ . On a qualitative level, each of the two antisite carbon atoms can be regarded as having three bonds with adjacent carbons in a plane, consistent

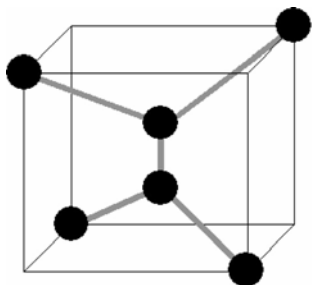


**Fig. 7.** Schematic diagram of a possible structure for the di-carbon antisite in 3C-SiC. The *black spheres* represent carbon atoms. The two C atoms in the interior replace a Si atom in the perfect lattice. Note the five C-C bonds

with  $sp^2$  hybridization. However, there is a  $90^\circ$  twist between the two planes of three carbon atoms, so that the “ $\pi$ -bond” is highly distorted. Depending on its charge state, levels in the gap may be occupied, leading to Jahn-Teller distortion to  $C_{2v}$  symmetry. The calculated levels in the gap have not been related to the photoluminescence spectrum, nor has the spectrum been associated with specific charge states. Mattausch et al. [47] propose that the di-carbon antisite is formed via the combination of two mobile carbon split interstitials and a Si vacancy.

Koshka and Melnychuk [49] investigated the depth distribution of the  $D_I$  and  $D_{II}$  defects in nitrogen implanted and annealed 6H-SiC homoepitaxial layers. The depth dependence was determined by measuring photoluminescence spectra after successive reactive ion etching steps. They observe  $D_{II}$  photoluminescence within the penetration range of the ion implantation, but see  $D_I$  photoluminescence from depths beyond this range. They suggest that the defects responsible for the formation of  $D_{II}$  do not diffuse significant distances on the scale of resolution of this experiment (about  $0.1\ \mu\text{m}$ ).

### 6.3 The $E_A$ Spectrum

It has long been known that after implantation with ions, neutrons or electrons the near band edge photoluminescence (free excitons, donor and acceptor bound excitons) vanishes or is greatly reduced, while a forest of lines can appear at longer wavelengths. The damage spectra evolve with annealing, and after annealing at sufficiently high temperature we are left with the persistent  $D_I$  and  $D_{II}$  spectra and some recovery of the near band edge emission. The complex spectra that appear after irradiation and their evolution with annealing have not been studied in detail until recently. Electron irradiation is particularly convenient for this purpose because it can introduce defects homogeneously throughout a sample with relatively low damage to the crystal.

Egilsson et al. [50] investigated a spectrum that appears in 4H-SiC after room temperature irradiation by 2 MeV electrons. Although the spectrum appears in both  $n$ - and  $p$ -type material, it is strongest in epilayers with low residual doping. Very little happens due to annealing below  $750^\circ\text{C}$ . Annealing

stages above 750°C lead to reduction of the lower energy lines and enhancement of many of the higher energy lines. After annealing at 1500°C, only the D<sub>1</sub> spectrum remains. At least forty no phonon lines appear in the  $E_A$  spectrum over the range 2.8–2.9 eV (4415–4265 Å), including excited states that appear at temperatures above 2 K. Most of the lines are polarized  $\vec{E} \perp \hat{c}$ . The spectrum begins to quench at 100 K. Based on photoluminescence excitation spectroscopy, the spectra can be classified into twelve groups each containing two to four lines. The groups were named with letters a, b, c, ...l starting at the lowest energy, with subscripts to distinguish the members of the group. Due to this choice of notation, this spectrum is sometimes called the “alphabet lines”. It is proposed that each group is associated with a distinct isoelectronic defect. The defects are thought to be isoelectronic because the photoluminescence decay times are long. Also, the lowest energy line in a group has relatively low oscillator strength indicating that it is a forbidden transition, a common occurrence for isoelectronic defects. The Zeeman splitting [51] of the line d<sup>1</sup> is similar to D<sub>1</sub> in 4H and 6H-SiC, whereas the Zeeman spectrum of line c<sup>1</sup> shows no dependence on the orientation of the magnetic field relative to the crystal *c*-axis or evidence for zero field splittings. This result illustrates that all twelve groups do not show the same behavior.

Steeds et al. [52] varied the energy of the irradiating electrons using an electron microscope. Based in part on the appearance of the  $E_A$  spectrum, they argue that the threshold energies for displacement of C and Si atoms are about 90 keV and 225–250 keV, respectively. Sridhara et al. [53] continued this work and showed that the  $E_A$  lines created using 200 keV and 300 keV electrons are no different, except in relative intensity, indicating that the centers are related to C rather than to Si.

Eberlein et al. [41] used the results of cluster calculations on defect models to argue that the centers responsible for the  $E_A$  spectrum are Si antisites perturbed by nearby defects such as C antisites. According to their results, a neutral Si antisite can trap a hole. However, the C antisite has no occupied levels within the bandgap of 4H-SiC. The level of the hole trap is shallower for a Si<sub>C</sub>-C<sub>Si</sub> pair than for an isolated Si antisite. They also propose a process for the formation of antisite pairs.

## 7 Stacking Faults and Nano-Polytypes

In a series of papers [54]–[56] the effects of long term forward voltage operation on 4H-SiC *pn* junctions was elucidated. After electrically stressing the diodes for long periods of time an increase in forward voltage drop was observed. Characterization of these diodes with cathodoluminescence, photoluminescence lifetime mapping and synchrotron white beam X-ray topography showed newly created defects which could be correlated with the softening of the forward characteristics.

The structural defects were interpreted to be stacking faults in the  $4H$ -SiC basal plane. These features were observed to be acting as recombination centers which reduced the intensity of the luminescence and lifetime of the material in the regions identified with the increase of the static forward voltage drop in the  $4H$ -SiC  $pn$  diodes. In [56] the authors show a new and previously unreported set of luminescence lines associated with the entire stacking fault area in their stressed diode samples. They show photoluminescence spectra from 2 K to 250 K in the region from 415 to 440 nm. It was suggested that these stacking faults give rise to local potential fluctuations corresponding to a reduction in bandgap. This potential is imagined to attract and bind carriers and excitons which then recombine with phonon participation. The stacking fault has a two dimensional extension which resembles a quantum well like structure.

Following up on the observations of the relation between stacking faults and associated low temperature recombination radiation the authors of [57] made a careful study of spectra associated with stacking faults in thick and very pure  $4H$ -SiC epitaxial films grown in hot-wall CVD reactors. Low temperature photoluminescence (LTPL), optical lifetime measurements and electron microscopy were used in these studies. A series of LTPL lines in the range from 410 nm to 432.5 nm, not ordinarily seen in pure  $4H$ -SiC spectra, was clearly identified with a stacking fault region in the sample under study. These lines are similar to the ones reported in [56]. A more detailed look at the additional features that are seen in the regions of these samples correlated with stacking faults reveals a surprising wealth of additional LTPL lines. All the epitaxial  $4H$ -SiC films investigated were extremely pure ( $n$ -type low  $10^{13} \text{ cm}^{-3}$  to low  $10^{14} \text{ cm}^{-3}$ ) and hence the intrinsic exciton peaks dominate the  $4H$ -SiC bandedge spectrum. In Fig. 8 we see two sets of lines that are normally not present in the LTPL spectrum of  $4H$ -SiC. A close inspection reveals that they are two sets of the familiar intrinsic exciton phonon replicas and using the 75 meV free exciton phonon replica as the reference in both spectra one obtains,  $E_{GX}$ , the exciton band gaps to be 3.030 eV and 2.977 eV. These gaps are close to the normal values of  $E_{GX}$  at 2 K for  $6H$ -SiC and  $15R$ -SiC, respectively. On Fig. 9 we have three more such intrinsic exciton spectra with exciton gaps of 2.931 eV, 2.863 eV and 2.797 eV. These spectra are assigned to  $21R$  SiC,  $8H$  SiC and the third one is somewhat uncertain but could be  $10H$ -SiC. In Fig. 10 we attempt to pull together the information presently known about imbedded nanopolytypes which was published in [57] and has subsequently been added to in our Laboratory. In Fig. 10 we plot  $E_{GX}$  as a function of hexagonality. It has been shown in the past that  $E_{GX}$  values for a number of polytypes lie on a straight line which connects  $3C$ -SiC (0.0 hexagonality) with  $4H$ -SiC (0.5 hexagonality). However,  $15R$ -SiC (0.4 hexagonality) and  $2H$ -SiC (1.0 hexagonality) are known not to lie on this line. The arrows on Fig. 10 point to the energy positions on the "polytype line" for the observed values of these nano-polytypes embedded in  $4H$ -SiC

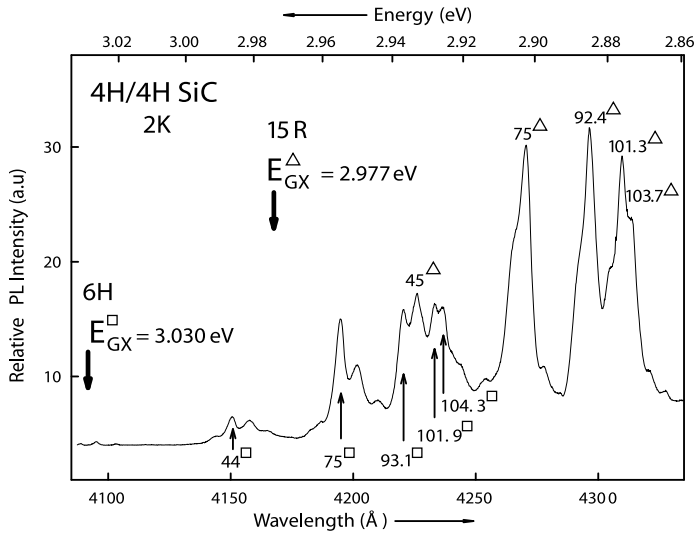


**Fig. 8.** Free exciton phonon replica spectra with exciton bandgaps of 3.030 eV and 2.977 eV embedded in a 4H-SiC epitaxial film. The phonon replica lines are given in meV

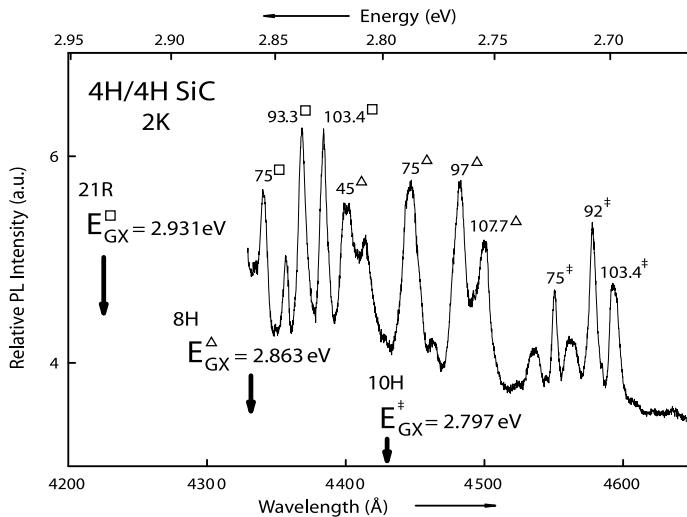


**Fig. 9.** Free exciton phonon replica spectra with exciton bandgaps of 2.931 eV, 2.863 eV and 2.797 eV embedded in a 4H-SiC epitaxial film. The phonon replica lines are given in meV

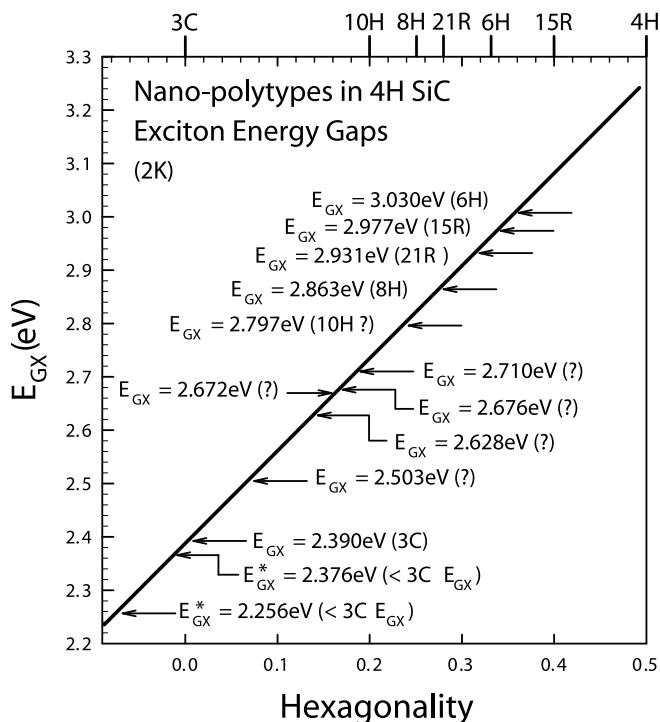


**Fig. 10.** A plot of exciton energy gaps  $E_{GX}$  as a function of hexagonality for nano-polytypes of SiC embedded in 4H-SiC. The solid line is a segment of a line connecting  $E_{GX}$  of bulk 3C-SiC (zero hexagonality) with  $E_{GX}$  of bulk 4H-SiC. This straight-line relationship is known to deviate for  $E_{GX}$  of bulk 15R-SiC and 2H-SiC. The arrows point to the  $E_{GX}$  values of the embedded nano-polytypes found primarily in 4H-SiC grown in hot-wall CVD reactors. A question mark means that the polytype assignment is either somewhat uncertain or actually unknown

epitaxial films. The observed gaps are consistent with the hexagonality of 6H, 21R, 8H and likely the 10H polytypes of SiC. Five lower energy values of  $E_{GX}$  which have been observed are designated with question marks since no reliable correlation exists between hexagonality and exciton bandgap. Three exciton energy gap values related to 3C-SiC are shown. One has the normal exciton energy band gap value and is likely from a large 3C inclusion in the sample. However, two spectra yield bandgaps below the normal 3C exciton energy gap value. This shows that there is a considerable red shift associated with these 3C nano-polytypes. It has been shown in [58] that spontaneous polarization is an important effect for hexagonal SiC and in [59] that multi-quantum well structures of 4H and 3C-SiC can show a red shift in the 3C-SiC luminescence due to spontaneous polarization of as much as 170 meV. This is consistent with the “starred” energy gaps shown for two of the 3C-SiC nano-

polytypes in Fig. 10. A detailed theoretical article by Lindefelt and Iwata at pp. 89 of this volume considers the electronic properties of stacking faults and thin cubic inclusions in SiC polytypes.

## 8 Optical Characterization of Wafers

Optical lifetime measurements which can be applied to wafers were treated extensively in [60] and the reader is urged to consult this paper preparatory to reading this section. We now survey optical techniques published since 1997 and which are finding utility in the field.

Non-destructive thickness determinations of low doped smooth epitaxial films deposited on heavily doped wafers may be obtained by means of room temperature infrared reflectance measurements [61, 62]. Interference fringes are obtained and by comparing the measured reflectance spectra to calculated spectra, highly accurate estimates can be obtained for the thicknesses of the epi films. The origin of the interference fringes comes from the difference in free carrier concentrations between the heavily doped substrate and the epi film. A sufficiently highly doped substrate will have an optical index of refraction which is sufficiently different from the epi film so that over a certain wavelength region clear interference fringes appear and can easily be measured. From these measurements thickness contour maps of  $4H$  and  $6H$ -SiC epi films have been generated.

In [63] micro Fourier transform infrared (FTIR) instrumentation has been used to determine the spatial distribution of the carrier concentration and mobility in SiC wafers. Measurements are made at room temperature in the reststrahlen region for  $4H$  and  $6H$ -SiC. The carrier concentration and mobility are derived from reflectance spectra based on the dielectric function of phonons and plasmons. This method was tried out on both intentionally inhomogeneously doped  $n$ -type wafers as well as commercial wafers. Electron concentration and mobility maps obtained from the optical data are shown for  $4H$  and  $6H$ -SiC wafers.

A room temperature photoluminescence (PL) scanning apparatus is reported in [64] which uses a frequency doubled argon ion laser at 244 nm for the excitation of the wafer surface. The spatial resolution is 1  $\mu\text{m}$  and an area of  $10 \times 10 \text{ cm}^2$  can be scanned with a spectral resolution of 1 nm in the range from 0.3  $\mu\text{m}$  to 1.7  $\mu\text{m}$ . Micropipes have been revealed with this apparatus without the need to etch the sample. The authors show that the effect of non-radiative traps around dislocations yields a loss of PL signal in those regions. By measuring the integrated PL intensity at 392 nm for  $4H$ -SiC, the integrated intensity at 423 nm for  $6H$ -SiC and the integrated intensity at 520 nm for  $3C$ -SiC, a wafer map is generated which will indicate polytype inclusions in large diameter wafers. Polytype maps have been generated on two inch wafers with a spatial resolution of 200  $\mu\text{m}$ .

Room temperature mapping of the luminescence decay of lightly doped *n*-type 4*H*-SiC was reported in [65]. Excitation in this apparatus is by means of a quadrupled Nd:YAG laser at 266 nm. The spot size that is attainable with this arrangement is  $10 \times 15 \mu\text{m}^2$ . No spectral selection of the PL light is used and the shortest decay time that is measurable is 12 ns. An assumption is made that there is a single exponential decay time. Large differences of the decay time were observed as intensity coded squares across a Cree epilayer with 50  $\mu\text{m}$  thickness and a doping level of  $7.5 \times 10^{14} \text{ cm}^{-3}$ .

Characterization of bulk and epitaxial two inch wafers of 4*H*-SiC is demonstrated in [66]. Here the wafers are placed in the bath of a cryostat which is mounted on a movable support. The luminescence excitation is either from a frequency doubled argon ion laser at 244 nm or an  $\text{Ar}^+$  laser at 351 nm. Detection is by an ultraviolet (UV) sensitive charge coupled device (CCD) array. Different positions on the wafer are accessed by letting a stepping motor run the movable support from grid point to grid point. Spectra are recorded for a 20 nm region appropriate for 4*H*, 6*H* and 15*R*-SiC. It is shown how different calibration methods may be used to generate doping maps in a variety of doping regimes. The dynamic range possible for nitrogen doping concentration using this technique extends from a low of  $10^{14} \text{ cm}^{-3}$  to a high of  $10^{19} \text{ cm}^{-3}$ .

Tajima et al. [67] have recently developed a room temperature photoluminescence mapping system applicable to 300 mm silicon-on insulator (SOI) wafers. In [68] Professor Tajima informs us that this system is currently being re-engineered for use with large SiC wafers. For this reason it is interesting here to call attention to the capabilities of this system for photoluminescence mapping of SOI wafers with 300 mm diameters:

- (a) UV, visible and near infrared excitation capability,
- (b) Monochromatic detection of the photoluminescence from 800 nm to 1700 nm for bandedge and deep level emissions, and
- (c) Macroscopic mapping of a full 300 mm diameter wafer and microscopic mapping of selected regions with a maximum resolution of 1  $\mu\text{m}$ .

Presumably, in the new SiC system the range of wavelength will be expanded down to 244 nm or 266 nm. As production of large diameter wafers of 4*H* and 6*H*-SiC with and without epilayers steadily increases, such a rapid optical characterization device will find great utility.

## Acknowledgements

We wish to thank ONR (grant N00014-01-1-0028) and NASA (grant NAG3-2538) for partial support of this work. We thank Song Bai for assistance in preparing the figures.

## References

1. R.P. Devaty and W.J. Choyke: in *Silicon Carbide*, Vol. II, ed. by W.J. Choyke, Hiroyuki Matsunami and Gerhard Pensl, (WILEY-VCH, Berlin, 1997), pp. 5–38
2. S.G. Sridhara, T.J. Eperjesi, R.P. Devaty and W.J. Choyke: *Mater. Sci. Eng. B* **61–62**, 229 (1999)
3. T.P. McLean: *Progress in Semiconductors*, Vol **5** (1960) pp. 66–70
4. A. Henry, I.G. Ivanov, A. Ellison and E. Janzén: *Mater. Sci. Eng. B* **61–62**, 234 (1999)
5. U. Forsberg, A. Henry, M.K. Linnarsson and E. Janzén: *Mater. Sci. Forum* **338–342**, 619 (2000)
6. A. Henry, A. Ellison, U. Forsberg, B. Magnusson, G. Pozina and E. Janzén: *Mater. Sci. Forum* **389–393**, 593 (2002)
7. Ya.E. Pokrovskii and K.I. Svistunova: *Sov. Phys.-Solid State* **13**, 1241 (1971)
8. G. Davies: *Physics Reports* **176**, 96 (1989)
9. A. Galeckas, V. Grivickas, V. Bikbajevs, J. Linnros and P. Grivickas: *Phys. Stat. Sol. (a)* **191**, 613 (2002)
10. R.P. Devaty, W.J. Choyke, S.G. Sridhara, L.L. Clemen, D.G. Nizhner, D.J. Larkin, T. Troffer, G. Pensl, T. Kimoto and H.S. Kong: *Mater. Sci. Forum* **264–268**, 455 (1998)
11. W.J. Choyke, R.P. Devaty and S.G. Sridhara: *Physica Scripta T* **79**, 9 (1999)
12. S.G. Sridhara, S. Bai, O. Shigiltchoff, R.P. Devaty and W.J. Choyke: *Mater. Sci. Forum* **338–342**, 567 (2000)
13. R.P. Devaty, S. Bai, W.J. Choyke, D. Hobgood and D.J. Larkin: *Mater. Sci. Forum* **353–356**, 357 (2001)
14. J.J. Hopfield: *J. Phys. Chem. Solids* **15**, 97 (1960)
15. R.G. Humphreys, D. Bimberg and W.J. Choyke: *Solid State Commun.* **39**, 163 (1981)
16. W.R.L. Lambrecht, S. Limpijumnong, S.N. Rashkeev and B. Segall: *Phys. Stat. Sol. (b)* **202**, 5 (1997)
17. E. Biedermann: *Solid State Commun.* **3**, 343 (1965)
18. S.G. Sridhara, S. Bai, O. Shigiltchoff, R.P. Devaty and W.J. Choyke: *Mater. Sci. Forum* **338–342**, 551 (2000)
19. S. Limpijumnong, W.R.L. Lambrecht, S.N. Rashkeev and B. Segall: *Phys. Rev. B* **59**, 12890 (1999)
20. W.R.L. Lambrecht, S. Limpijumnong, S. Rashkeev and B. Segall: *Mater. Sci. Forum* **338–342**, 545 (2000)
21. R. Weingärtner, P.J. Wellmann, M. Bickermann, D. Hofmann, T.L. Straubinger and A. Winnacker: *Appl. Phys. Lett.* **80**, 70 (2002)
22. P.J. Wellmann, R. Weingärtner, M. Bickermann, T.L. Straubinger and A. Winnacker: *Mater. Sci. Eng. B* **91–92**, 75 (2002)
23. S.-I Uekusa, K. Awahara and M. Kumagai: *Mater. Sci. Forum* **264–268**, 505 (1998)
24. A. Kozanecki, C. Jeynes, B.J. Sealy, W. Jantsch, S. Lanzerstorfer, W. Heiß and G. Precht: *Mater. Sci. Forum* **264–268**, 501 (1998)
25. K. Awahara, S. Uekusa, T. Goto, T. Kobayashi and M. Kumagai: *Nucl. Inst. Meth. B* **148**, 507 (1999)

26. A. Kozanecki, C. Jeynes, N.P. Barradas, B.J. Sealy and W. Jantsch: Nucl. Inst. Meth. B **148**, 512 (1999)
27. A. Kozanecki, C. Jeynes, B.J. Sealy and A. Nejim: Nucl. Inst. Meth. B **136–138**, 1272 (1998)
28. Y. Shishkin, W.J. Choyke, R.P. Devaty, N. Achtziger, Th. Opfermann and W. Witthuhn: Mater. Sci. Forum **338–342**, 639 (2000)
29. R.A. Babunts, V.A. Vetrov, I.V. Il'in, E.N. Mokhov, N.G. Romanov, V.A. Khramtsov and P.G. Baranov: Phys. Solid State **42**, 829 (2000)
30. O. Klettke, S.A. Reshanov, G. Pensl, Y. Shishkin, R.P. Devaty and W.J. Choyke: Physica B **308–310**, 687 (2001)
31. U. Kaiser, D.A. Muller, J.L. Grazul, A. Chuvilin and M. Kawasaki: Mater. Sci. Forum **433–436**, 487 (2003)
32. G. Pasold, F. Albrecht, J. Grillenberger, U. Grossner, C. Hülsen, R. Sielemenn and W. Witthuhn: Proc. of ECSCRM'2002, to be published in Mater. Sci. Forum (2003)
33. T. Egilsson, J.P. Bergman, I.G. Ivanov, A. Henry and E. Janzén: Phys. Stat. Sol. B **210**, 337 (1998)
34. T. Egilsson, J.P. Bergman, I.G. Ivanov, A. Henry and E. Janzén: Phys. Rev. B **59**, 1956 (1999)
35. T. Egilsson, I.G. Ivanov, A. Henry and E. Janzén: Mater. Sci. Forum **338–342**, 647 (2000)
36. R.A. Faulkner: Phys. Rev. **184**, 713 (1969)
37. L. Storasta, F.H.C. Carlsson, S.G. Sridhara, J.P. Bergman, A. Henry, T. Egilsson, A. Hallén and E. Janzén: Appl. Phys. Lett. **78**, 46 (2001)
38. P.J. Dean, D. Bimberg and W.J. Choyke: in *Proc. Int. Conf. on Defects and Radiation Effects in Semiconductors*, IOP Conf. Proc. No. 46 (Institute of Physics and Physical Society, London, 1979), p. 447
39. T. Egilsson, I.G. Ivanov, A. Henry and E. Janzén: Physica B **273–274**, 677 (1999)
40. C.Q. Chen, R. Helbig, R. Winkler, A. Wyszomolek and M. Potemski: Mater. Sci. Forum **353–356**, 361 (2001)
41. T.A.G. Eberlein, C.J. Fall, R. Jones, P.R. Briddon and S. Öberg: Phys. Rev. B **65**, 184108 (2002)
42. S.G. Sridhara, D.G. Nizhner, R.P. Devaty, W.J. Choyke, T. Dalibor, G. Pensl and T. Kimoto: Mater. Sci. Forum **264–268**, 493 (1998)
43. L. Patrick and W.J. Choyke: J. Phys. Chem. Solids **34**, 565 (1973)
44. W.J. Choyke and L. Patrick: Inst. Phys. Conf. Ser. No. 16, 218 (1972)
45. A. Henry, T. Egilsson, I.G. Ivanov, C.I. Harris, S. Savage and E. Janzén: Mater. Sci. Forum **264–268**, 497 (1998)
46. S.G. Sridhara, F.H.C. Carlsson, J.P. Bergman, A. Henry and E. Janzén: Mater. Sci. Forum **353–356**, 377 (2001)
47. A. Mattausch, M. Bockstedte and O. Pankratov: Physica B **308–310**, 656 (2001)
48. A. Mattausch, M. Bockstedte and O. Pankratov: Mater. Sci. Forum **389–393**, 481 (2002)
49. Y. Koshka and G. Melnychuk: Mater. Sci. Forum **389–393**, 513 (2002)
50. T. Egilsson, A. Henry, I.G. Ivanov, J.L. Lindström and E. Janzén: Phys. Rev. B **59**, 8008 (1999)
51. T. Egilsson, A. Henry, I.G. Ivanov, J.L. Lindström and E. Janzén: Mater. Sci. Forum **264–268**, 477 (1998)

52. J.W. Steeds, F. Carosella, G.A. Evans, M.M. Ismail, L.R. Danks and W. Voegeli: *Mater. Sci. Forum* **353–356**, 381 (2001)
53. S.G. Sridhara, P.O.Å. Persson, F.H.C. Carlsson, J.P. Bergman, E. Janzén, G. Evans and J.W. Steeds: *Mat. Res. Soc. Symp. Vol.* **640**, H6.5.1 (2001)
54. J.P. Bergman, H. Lendenmann, P.Å. Nilsson, U. Lindefelt and P. Skytt: *Mater. Sci. Forum* **353–356**, 299, (2001)
55. H. Lendenmann, F. Dahlquist, N. Johansson, R. Söderholm, P.Å. Nilsson, J.P. Bergman and P. Skytt: *Mater. Sci. Forum* **353–356**, 727 (2001)
56. J.P. Bergman, L. Storasta, F.H.C. Carlsson, S. Sridhara, B. Magnusson and E. Janzén: *Physica B* **308–310**, 675 (2001)
57. S. Bai, G. Wagner, E. Shishkin, W.J. Choyke, R.P. Devaty, M. Zhang, P. Pirouz and T. Kimoto: *Mater. Sci. Forum* **389–393**, 589 (2002)
58. A. Qteish, Volker Heine and R.J. Needs: *Phys. Rev. B* **45**, 6534 (1992)
59. A. Fissel, U. Kaiser, B. Schröter, W. Richter and F. Bechstedt: *Appl. Surf. Sci.* **184**, 37 (2001)
60. J.P. Bergman, O. Kordina and E. Janzén: *Silicon Carbide*, Vol. II, ed. by W.J. Choyke, H. Matsunami and G. Pensl (Wiley-VCH, Berlin, 1997), pp. 65–77
61. M.F. MacMillan, A. Henry and E. Janzén: *J. Electron. Mater.* **27**, 300 (1998)
62. M.F. MacMillan, P.O. Narfgren, A. Henry and E. Janzén: *Mater. Sci. Forum* **264–268**, 645 (1998)
63. H. Yaguchi, K. Narita, Y. Hijikata, S. Yoshida, S. Nakashima and N. Oyanagi: *Mater. Sci. Forum* **389–393**, 621 (2002)
64. L. Masarotto, J.M. Bluet and G. Guillot: *Mater. Sci. Forum* **389–393**, 601 (2002)
65. K. Schneider and R. Helbig: *Mater. Sci. Forum* **389–393**, 605 (2002)
66. A. Henry, A. Ellison, U. Forsberg, B. Magnusson, G. Pozina and E. Janzén: *Mater. Sci. Forum* **389–393**, 593 (2002)
67. Michio Tajima, Zhiqiang Li and Ryosuko Shimidzu: *Jpn. J. Appl. Phys.* **41**, L28 (2002)
68. Michio Tajima: private communication (2003)

# Cyclotron Resonance Studies of Effective Masses and Band Structure in SiC

N.T. Son, C. Persson, U. Lindefelt, W.M. Chen, B.K. Meyer,  
D.M. Hofmann, and E. Janzén

## 1 Introduction

Many fundamental physical properties of semiconductors are governed by the structure of the energy bands. Electrons in the conduction band (CB) or holes in the valence band (VB) have an effective mass  $m_e^*$  or  $m_h^*$ , respectively, which is usually anisotropic depending on the shape of the corresponding bands. Effective masses can be calculated from the curvature of the energy bands or can be experimentally determined through their correlation with other parameters in processes involving the transport of electrons and/or holes. In the 1960s Hall effect and infrared Faraday rotation [1, 2] were used to determine electron effective masses in *6H*- and *15R*-SiC. Other experimental methods such as Zeeman splitting of photoluminescence lines, magnetoresistance, infrared light reflection, and far-infrared absorption [3]–[8] were also employed to study electron effective masses in common polytypes. In those experiments, effective mass values were determined rather indirectly via other parameters using theoretical models. The lack of reliable experimental data due to low crystalline quality of the *6H*- and *15R*-SiC in those days together with the use of an over-simplified effective mass model have resulted in largely scattered values of the effective masses.

The most direct method for determination of effective masses is cyclotron resonance (CR). The first successful electron CR experiment in SiC was performed by Kaplan et al. [9] in the *3C* polytype. The results were later on confirmed by Kono et al. [10] and also by theoretical calculations [11]–[18]. In the high-frequency CR studies [10], Kono et al. also observed a broad peak in transmission spectra performed at a wavelength of 119  $\mu\text{m}$  in *p*-type *3C*-SiC. The peak corresponds to an effective mass of 0.45  $m_0$  ( $m_0$  is the mass of the free electrons) and was interpreted as a CR of the light hole of the degenerate valence band. Even at such high frequencies, the resolution was still not enough to provide reliable data. This value is quite different from the value of hole effective masses obtained by different theoretical calculations [13]–[17],[19]. For *3C*-SiC, CR experiments using far-infrared radiation have successfully determined the electron effective masses [9]. For the hexagonal polytypes, conventional CR experiments were not able to detect any well-defined CR signal from either electrons or holes. The reason is due to too low carrier mobility in the material, especially in the substrates, which

often have much higher concentrations of impurities and defects compared to epitaxial layers grown by chemical vapour deposition (CVD). The scattering by impurities and defects reduces the carrier momentum relaxation time  $\tau$ . Because of this, the requirement for obtaining a well-defined cyclotron resonance,  $\omega_c \tau > 1$  ( $\omega_c$  is the cyclotron resonance angular frequency), could not be satisfied and hence the CR feature is not distinguishable from the background signal. There are two ways to fulfil this requirement. The first approach is to increase  $\omega_c$  by performing the CR experiments at higher frequencies using far-infrared radiation as has been successfully demonstrated in the CR studies of 3C-SiC [9, 10]. However, no such CR study has been reported for hexagonal polytypes so far. The second approach is to increase  $\tau$ . Since the relaxation time  $\tau$  is governed by carrier scattering processes, it can be increased by using samples of high crystal quality and low impurity concentration and/or by photo-neutralization of ionized scattering centers. High purity samples are essential, especially for CR experiments performed at low frequency radiation in the microwave (MW) frequency range. This approach is carried out by using optical detection of cyclotron resonance (ODCR), which was first used by Baranov et al. [20] in germanium. In the ODCR experiments, the effect of carriers under cyclotron resonance conditions on radiative carrier recombination as monitored by photoluminescence (PL) is measured, instead of a direct detection of the absorption of the electromagnetic radiation as is done in the conventional CR measurements. The mechanism for ODCR of electrons in 4H- and 6H-SiC has been suggested as due to a lattice heating effect [21]. This optical excitation and detection allows one to select only PL emissions of interested spectral regions in the pure epitaxial layers to avoid the influence from high-doped substrates. General aspects of cyclotron resonance have been described in our previous review [22].

ODCR experiments [23, 24] have been used to determine the electron effective masses in 4H-SiC. The obtained values [24] are in excellent agreement with theoretical calculations [12],[14]–[18],[25]. For the 6H polytype, due to poor resolution (very broad ODCR signals), the anisotropy of electron effective masses in 6H-SiC has not been resolved. So far, only two components, one along the  $c$ -axis (the longitudinal mass  $m_{e\parallel}$ ) and the other – the average effective mass value in the basal plane (the transverse mass  $m_{e\perp}$ ) – have been determined [26]. The results are also in agreement with calculations [14]–[17], but a large uncertainty in the experimental data still remains. The anisotropy of the electron effective mass tensor observed by ODCR [26] could explain the sizable anisotropy of the electron Hall mobility in 6H-SiC as measured by Hall effect [27, 28]. Recently, based on the Boltzmann transport equation and using the average in-plane mass determined by ODCR [26] at low temperatures to fit the anisotropy of the electron Hall mobility [27, 28], Iwata [29] was able to obtain the electron-effective-mass tensor with principal mass values in good agreement with theoretical calculations [14]–[18],[25]. However, the

fits used the transverse mass value [26]  $m_{e\perp} = 0.42m_0$ , which is about 15% smaller than the more reliable value [51]  $m_{e\perp} = 0.485m_0$  with assuming the relaxation time and electron scattering are isotropic. However, it is not clear if this assumption is relevant for the hexagonal SiC crystal, especially with the presence of structural defects, such as micropipes, stacking faults and dislocations, point defects and impurities. The model was suggested [29] to be more suitable for the high temperature region, where the phonon-scattering processes become dominant compared to the scattering by impurities. As will be seen later, however, the lowest CB in 6H-SiC is very flat along the ML-line [16] and has a curvature (effective mass) that should be strongly  $\mathbf{k}$ -dependent. Therefore, in the high temperature region the electrons in this band occupy a relatively large portion of the Brillouin zone (BZ), and the whole concept of a  $\mathbf{k}$ -independent electron effective mass in 6H-SiC becomes questionable.

The purpose of this paper is to review the current status of cyclotron resonance studies in SiC. Section 2 gives a brief description of the latest picture of the band structure and the effective masses in cubic and hexagonal SiC obtained from first-principles relativistic calculations. ODCR studies of hole and electron effective masses in 4H- and 6H-SiC are presented in Sect. 3.

## 2 Band Structure and Effective Masses from Calculations

The present theoretical study of the electronic structure and the effective masses of SiC is based on the local density approximation (LDA), employing a first-principles full-potential linearized augmented plane wave (FPLAPW) method [30]. The spin-orbit interaction is treated variationally outside the self-consistency loop (see [15]–[17] for more details). The point-group notation [31] of the irreducible representations  $\Gamma_{d(s)}$  of double- and single-groups depends for certain  $\mathbf{k}$ -points lying on the BZ surface on the choice of atomic positions. In this work, a Si atom is positioned at  $(2/3, 1/3, 0)$  in 2H-SiC, in units of the primitive vectors, and at  $(0, 0, 0)$  in 3C-, 4H-, and 6H-SiC.

### 2.1 Electronic Band Structure

The LDA electronic band structures of cubic  $(T_d^2)3C$ -SiC and of hexagonal  $(C_{6v}^4) 2H$ -,  $4H$ -, and  $6H$ -SiC are presented in Fig. 1, where the  $\mathbf{k}$ -point labelling is defined by Fig. 2. With the quasi-particle (QP) model by Bechstedt and del Sole [32] we correct the LDA band-gap energies with a constant energy shift  $\Delta_g$ . The correction is based on the difference in zero-temperature self-energies obtained from the LDA and the GW approximation [32]. The LDA+QP fundamental band-gaps are  $E_g + \Delta_g = 2.46, 3.28, 3.35$ , and  $3.10$  eV, for 3C-, 2H-, 4H-, and 6H-SiC, respectively, which are very close to measured

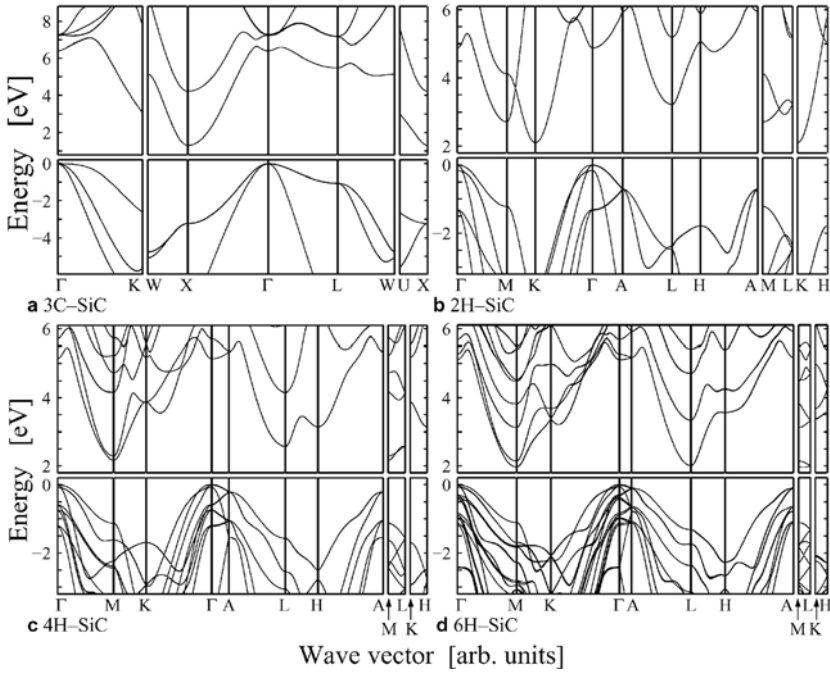


**Fig. 1.** Electronic band structure near the energy gap of 3C-, 2H-, 4H-, and 6H-SiC. Note that the LDA band-gap energies have not been corrected, and that most part of the forbidden band gap is not shown

values (Table 1). It is seen from Table 1 that  $\Delta_g$  is essentially independent of polytype, which means that for these polytypes LDA gives the correct band gap variation.

Whereas both Si and diamond have their CB minima along the  $\Delta$ -line, the lowest CB minimum of 3C-SiC is located at the X-point (with  $D_{2d}$  point-group symmetry). Also the second minimum is at the X-point, and the energy difference between the two minima is [16]  $E(X_{c6(1)} - X_{c7(4)}) = 2.92$  eV. The

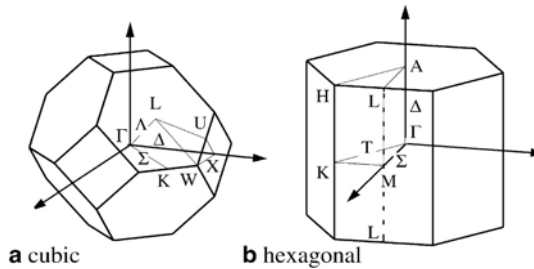


**Fig. 2.** Brillouin zones of (a) cubic 3C-SiC and (b) hexagonal SiC structures

**Table 1.** Lattice constants  $a$  and  $c/p$  (in units of Å), where  $p$  is the number of hexagonal bilayers ( $p = 2, 4, 6$  for  $2H$ -,  $4H$ -, and  $6H$ -SiC). Fundamental band-gap energy  $E_g$  (in eV) with and without QP correction  $\Delta_g$ . The crystal-field  $\Delta_{cf}$  and spin-orbit  $\Delta_{so}$  split-off energies

		Ref.	3C-SiC	2H-SiC	4H-SiC	6H-SiC
$a$	LDA		4.343	3.061	3.067	3.080
	Expt.	[33]	4.360	3.076	3.073	3.081
$c/p$	LDA			2.517	2.508	2.519
	Expt.	[33]		2.524	2.513	2.520
CB min.	LDA/Expt.	[33]–[36]	X	K	M	U
$E_g$	LDA		1.30	2.13	2.18	1.97
$E_g + \Delta_g$	LDA+QP		2.46	3.28	3.35	3.10
	Expt.	[33]	2.40	3.33	3.29	3.10
$\Delta_{cf}$				131	50	38
$\Delta_{so}$	LDA		14.5	8.8	8.4	8.1
	Expt.	[37, 38]	10			7

measured value is 3.1 eV [39]. In  $2H$ -SiC, the lowest CB minimum is at the K-point ( $C_{3v}$  symmetry), whereas the CB minimum of  $4H$ -SiC is at the M-point ( $C_{2v}$  symmetry) and of  $6H$ -SiC along the ML-line (also  $C_{2v}$  symmetry).

Thus,  $2H$ -SiC has two,  $4H$ -SiC has three and  $6H$ -SiC has six equivalent minima in the first BZ. The second lowest CB minimum is located at the M-point for all three hexagonal SiC polytypes and consequently in  $4H$ -SiC, like in  $3C$ -SiC, there can be direct transitions between the two minima. The energy difference between the two lowest minima is small in  $4H$ -SiC [ $E(M_{c5(1)} - M_{c5(4)}) = 0.12$  eV], which is close to the optical phonon energies of 0.10–0.12 eV [40]. The second band will therefore influence the electronic transport properties at high temperatures and/or when high electric fields are applied. In  $2H$ -SiC ( $6H$ -SiC) the second minimum is 0.60 (1.16) eV above the lowest CB minimum.

The lowest CB of  $6H$ -SiC is very flat along the ML-line (Fig. 3). The difference in energy between the minimum and the M- (L-) point is only 5.3 (45.6) meV. Since the minimum is not at a symmetry point, the band has a double-well-like nature (a “camel’s back”) along the LML-line with M as a saddle point. Therefore, drift of electrons can easily occur between the two close-lying minima at applied electric field, which will have a direct consequence on the electronic transport. The non-parabolic curvature along the ML-line can be described by the polynomial:

$$\varepsilon_{c1}(k_{\parallel}) = \varepsilon_{c1}(\mathbf{k}_M) - (a_1 k_{\parallel})^2 + (a_2 k_{\parallel})^4 - (a_3 k_{\parallel})^6, \quad (1)$$

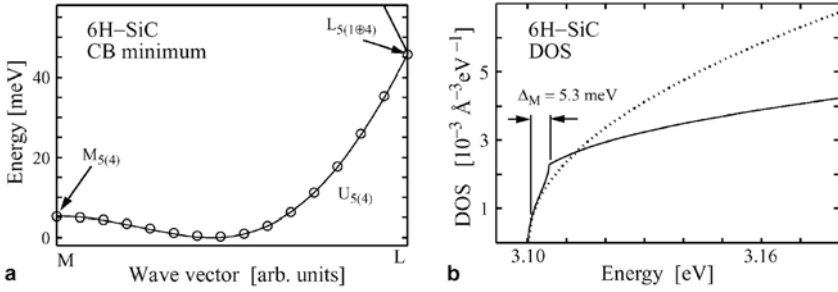


**Fig. 3.** (a) The shape of the lowest CB in 6H-SiC along the ML line. *Open circles* show the fitted polynomial of (1). (b) Density-of-states of the CB [41]. *Dotted line* represents a parabolic approximation of the CB minimum

with the fitted parameters  $a_1 = 1.102 \text{ \AA}(\text{eV})^{1/2}$ ,  $a_2 = 2.980 \text{ \AA}(\text{eV})^{1/4}$ , and  $a_3 = 2.961 \text{ \AA}(\text{eV})^{1/6}$ . Figure 4 shows how the constant energy surface turns from a double-well into a more ellipsoidal shaped minimum as the energy increases. A strong effect on the electronic mobility due this non-parabolicity has been seen in recent Monte Carlo studies of SiC based MESFETs by Bertilsson et al. [42].

In order to investigate if the ML curvature changes with temperature or pressure, we have performed a LDA calculation with the lattice constants  $a = 3.089 \text{ \AA}$  and  $c/p = 2.528 \text{ \AA}$ , which represent the crystal at the temperature  $\sim 700 \text{ K}$ . The CB minimum was almost unaffected by this change in volume. However, a many-particle calculation of doping-induced effects in SiC [18] shows that band filling ( $n_e \sim 10^{19} \text{ cm}^{-3}$ ) of the CB strongly modifies the band curvature, whereas the electron-optical phonon coupling has only a relatively small affect.

Despite similar values of the calculated lattice constants and band-gap energies between different authors [11]–[17],[19],[25], the calculated values of the crystal field splittings for hexagonal polytypes are significantly different. The present values are  $\Delta_{\text{cf}} = 131, 50$ , and  $38 \text{ meV}$  for 2H-, 4H-, and 6H-SiC, respectively [17]. Other calculated values are 132, 66, and  $46 \text{ meV}$  by

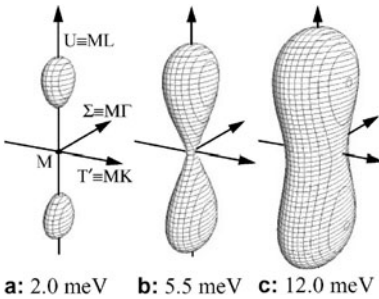


**Fig. 4.** Constant energy surfaces  $E(\mathbf{k})$  of the double-well-like CB minimum in 6H-SiC for the energies  $E(\mathbf{k}) =$  (a) 2.0, (b) 5.5, and (c) 12.0 meV referred to the conduction-band minimum (see also Fig. 3)

Lambrech et al. [14], and 97, 56, and 36 meV by Käckel et al. [19]. The reason for this deviation is the different internal positions of the hexagonal layers [17]. Changing the internal lattice parameter in  $2H$ -SiC by 0.2% changes  $\Delta_{\text{cf}}$  by as much as  $\sim 22\%$ , whereas the affects on the hole effective masses are almost negligible [17]. Experimental  $\Delta_{\text{cf}}$  values for the  $4H$  [43] and  $6H$  [44] polytype are  $\sim 60$  meV and 42–44 meV, respectively.

## 2.2 Effective Masses

The effective mass tensor  $m(\mathbf{k})$  is defined as  $1/m(\mathbf{k})_{ij} = \pm \partial^2 E(\mathbf{k}) / \hbar^2 \partial k_i \partial k_j$ , where  $+$ ( $-$ ) stands for electrons (holes). We determine the effective masses in the three principal directions directly from the FPLAPW electronic energies. Although the Si-C bonds in SiC are covalent, carbon atoms are more electronegative than silicon atoms and hence the material is partly ionic. Therefore, when vibrating, the longitudinal optical (LO) phonons will build up an electric field along the direction of vibration. This field will interact with electrons and holes (known as the polaron effect), resulting in a change in the effective masses. The polaron mass  $m_p$  can be estimated from the energy of the LO phonon,  $\hbar\omega_{\text{LO}}$ , and the dielectric constants  $\kappa_0$  and  $\kappa_\infty$ , assuming non-degenerate bands, harmonic oscillation of the ions, interactions only with long wavelength phonons (with constant  $\omega_{\text{LO}}$ ), and the effective mass approximation [18, 33, 45, 46]:

$$m_p = m \cdot \frac{1 - 0.0008\alpha^2}{1 - \alpha/6 + 0.0034\alpha^2} \approx m \cdot (1 - \alpha/6)^{-1}, \quad (2)$$

where the Fröhlich constant  $\alpha$  is defined as:

$$\alpha = \frac{e^2 \sqrt{2m\omega_{\text{LO}}/\hbar}}{8\pi\kappa_0\hbar\omega_{\text{LO}}} \left( \frac{1}{\kappa_\infty} - \frac{1}{\kappa_0} \right). \quad (3)$$

Experimental values of the crystal parameters are  $\hbar\omega_{\text{L}} = 121$  meV,  $\kappa_0 = 9.72$ , and  $\kappa_\infty = 6.52$  for  $3C$ -SiC and  $\hbar\omega_{\text{LO}} = 120$  meV,  $\kappa_{0,\perp} = 9.66$ ,  $\kappa_{0,\parallel} = 10.03$ ,  $\kappa_{\infty,\perp} = 6.52$ , and  $\kappa_{\infty,\parallel} = 6.70$  for  $6H$ -SiC [33, 47]. For  $2H$ - and  $4H$ -SiC we use the parameters of  $6H$ -SiC since infrared optical properties are similar for the hexagonal polytypes [33, 48].

The location of the minimum determines if the masses can be anisotropic or not.  $2H$ -SiC has therefore isotropic transverse masses, whereas the other investigated minima of  $\alpha$ -SiC show strong anisotropy. We present our calculated LDA electron effective masses of the lowest and the second lowest conduction band minima in Table 2. Most calculations [11]–[17],[19],[25] yield similar values of the electron effective masses. One exception is the longitudinal mass in  $6H$ -SiC. For instance, early QP calculations by Wenzien et al. [12] located the  $6H$ -SiC minimum at the M-point, which resulted in a very small mass value:  $m_{\text{ML}} = 0.51m_0$ . Their corresponding LDA value was

**Table 2.** The electron effective masses and corresponding polaron masses  $m_p$  of the two lowest CB minima. a, b, and c are from [12, 13, 25], respectively. The subscripts on the effective masses denote the  $\mathbf{k}$ -space direction of the mass-tensor

Polytype	Effective mass ( $m_0$ )	First minimum		Second minimum		
		This work	Other calc.	This work		
		$m$	$m_p$	$m$	$m$	$m_p$
3C-SiC	$m_{\parallel}$	0.68	0.73	$0.67^a, 0.60^b$	1.00	1.10
	$m_{\perp}$	0.23	0.24	$0.24^a, 0.29^b$	0.25	0.26
2H-SiC	$m_{\parallel}$	0.26	0.27	$0.25^a, 0.27^c$	$m_{\text{ML}}$	1.07
	$m_{\perp}$	0.43	0.46	$0.43^a, 0.45^c$	$m_{\text{M}\Gamma}$	0.96
					$m_{\text{MK}}$	0.14
4H-SiC	$m_{\text{ML}}$	0.31	0.33	$0.19^b, 0.31^c$	0.71	0.77
	$m_{\text{M}\Gamma}$	0.57	0.61	$0.60^b, 0.58^c$	0.78	0.85
	$m_{\text{MK}}$	0.28	0.29	$0.28^b, 0.28^c$	0.16	0.17
6H-SiC	$m_{\text{ML}}$	1.83	2.07	$0.51^b, 1.42^c$	0.56	0.60
	$m_{\text{M}\Gamma}$	0.75	0.81	$0.71^b, 0.77^c$	1.08	1.19
	$m_{\text{MK}}$	0.24	0.25	$0.30^b, 0.24^c$	0.17	0.18

$m_{\text{ML}} = 1.95m_0$ . It was suggested by Lambrecht et al. [25] that renormalization due to the polaron effects could be the reason for the deviation between their calculated results ( $m_{\text{ML}} = 1.42m_0$ ) and the early measurement ( $2.0m_0$ ) by Son et al. [26]. Although, the polaron coupling is strong in 6H-SiC, this effect alone is too small to explain the deviation. We conclude that the very flat and non-parabolic CB in combination with its sensitivity to band filling requires a careful theoretical analysis in order to compare calculated and experimental results.

In order to calculate the hole effective masses, it is crucial to include the spin-orbit interaction (Fig. 5). The reason for the very strong effect on the masses even in relatively light materials, like SiC, is the splitting of the VB degeneracy caused by the spin-orbit interaction ( $\Gamma_5 \otimes D_{1/2} \Rightarrow \Gamma_7 \oplus \Gamma_8$  in  $T_d$  symmetry). The spin-orbit interaction thus changes the symmetry of the eigenfunctions in the vicinity of the maximum [15], and consequently it also changes the curvatures of the bands. The spin-orbit split-off energy in 3C-SiC is calculated to be  $\Delta_{\text{so}} = 14.5$  meV, which is larger than the experimental value of about 10 meV [37, 38]. The LDA split-off energies of 2H-, 4H-, and 6H-SiC are very similar:  $\Delta_{\text{so}} = 8.8, 8.6,$  and  $8.5$  meV, respectively. A measured value of  $\sim 7$  meV for 6H-SiC has been reported by Humphreys et al. [38]. The constant energy surfaces of the three uppermost VBs in 3C-SiC are shown in Fig. 6a, both without and with spin-orbit interaction included. The very noticeable protuberance in the  $\Sigma$  direction for the  $hh$ -band implies an extremely large hole effective mass of  $m_{\text{TK}} = 15.0m_0$ , which is reduced

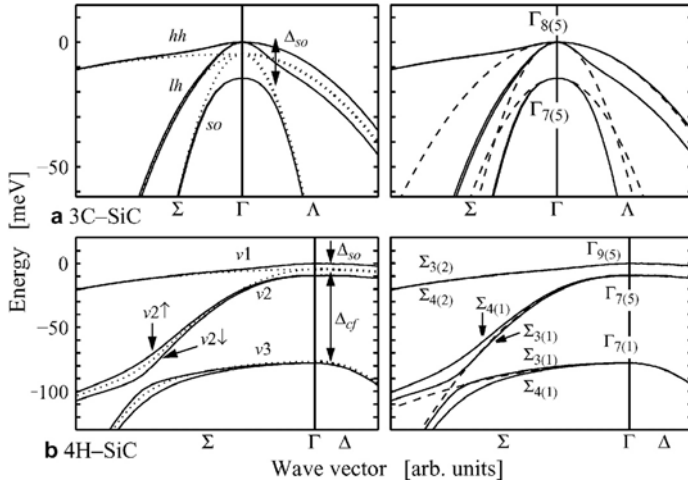


**Fig. 5.** The VB maximum of (a) 3C-SiC and (b) 4H-SiC. We show 10% of the total length to the BZ boundary. The solid (dotted) lines represent LDA calculations with (without) spin-orbit coupling. The dashed lines depict the curvatures from the  $k \cdot p$  parameterization of (4) and (6). 2H- and 6H-SiC look very similar to 4H-SiC

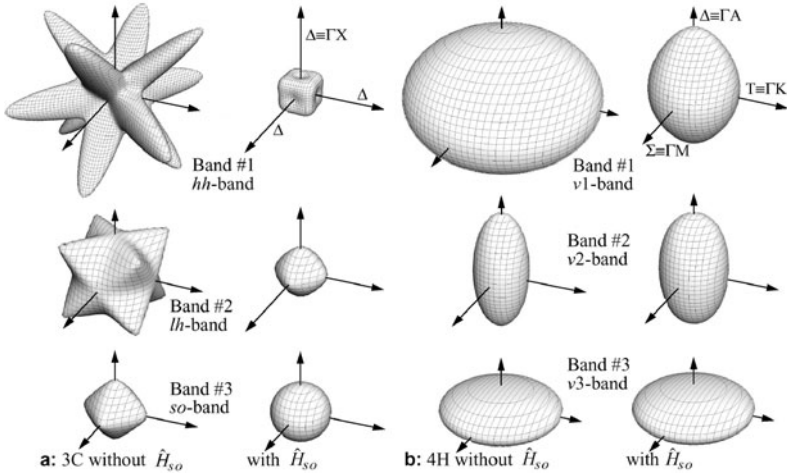


**Fig. 6.** Constant energy surfaces around  $\Gamma$  for the three uppermost VBs in (a) 3C- and (b) 4H-SiC (1 and 4 meV below each VB maximum, respectively) without and with spin-orbit interaction ( $\hat{H}_{so}$ )

to  $1.32 m_0$  when spin-orbit interaction is taken into account. The effective masses in the  $\Delta$  and  $\Lambda$  directions remain essentially unchanged. Moreover, the so-band becomes spherical. The three uppermost VBs of 3C-SiC can be parametrized according to the  $\mathbf{k} \cdot \mathbf{p}$  approximation [16]:

$$\begin{aligned}\varepsilon_{hh,th}(\mathbf{k}) &= \frac{\hbar^2 k^2}{2m_0} \left( A \pm \sqrt{B^2 + C^2 f(\theta, \varphi)} \right), \\ \varepsilon_{so}(\mathbf{k}) &= -\Delta_{so} + \frac{\hbar^2}{2m_0} A k^2,\end{aligned}\quad (4)$$

where  $f(\theta, \varphi) = \sin^4 \theta \cos^2 \varphi \sin^2 \varphi + \sin^2 \theta \cos^2 \theta$ . The spin-split is small (see Fig. 5), and the above parametrization assumes equal spin-up- and spin-down-like states  $[\varepsilon_{j\uparrow}(\mathbf{k}) = \varepsilon_{j\downarrow}(\mathbf{k})]$ . The parameters for 3C-SiC are  $A = -1.96$ ,  $|B| = 0.30$ , and  $|C| = 2.27$ .

The hole effective masses depend strongly on  $\mathbf{k}$ -direction. An average mass value can be obtained by integrating over angles [16].

$$\begin{aligned}m_{hh,th}^{\text{ave}} &= -m_0 \left( A \pm I_\alpha \cdot \sqrt{B^2 + C^2 \alpha} \right)^{-1}, \quad \text{where} \\ I_\alpha &= \frac{1}{4\pi} \int_0^{2\pi} \int_0^\pi \sqrt{1 + \frac{C^2(f(\theta, \varphi) - \alpha)}{B^2 + C^2 \alpha}} \sin(\theta) d\theta d\varphi.\end{aligned}\quad (5)$$

By custom, (5) has been used with  $I_\alpha = 1$  and  $\alpha = 1/6$ , derived by Lax and Mavroides [49]. However, a Taylor expansion of  $I_\alpha$  reveals [16] that better accuracy is obtained with  $I_\alpha = 1$  and  $\alpha = 1/5$ .

Also in the hexagonal SiC polytypes the spin-orbit interaction affects the VB maximum. Fig. 6b shows the constant energy surfaces for 4H-SiC. Parameterization of the three uppermost VBs can be done with  $\mathbf{k} \cdot \mathbf{p}$  expressions, valid for wurtzite structures if the crystal-field splitting is sufficiently large [16]:

$$\begin{aligned}\varepsilon_{v1,v2}(\mathbf{k}) &= -\frac{\Delta_{so}}{2} + \frac{\hbar^2}{2m_0} \left( ck_{\parallel}^2 + dk_{\perp}^2 \pm \sqrt{\frac{m_0^2 \Delta_{so}^2}{\hbar^4} + (d'' k_{\perp}^2)^2} \right), \\ \varepsilon_{v3}(\mathbf{k}) &= -\frac{\Delta_{so}}{2} - \Delta_{cf} - \frac{\hbar^2 k_{\parallel}^2}{2m_{\parallel}} - \frac{\hbar^2 k_{\perp}^2}{2m_{\perp}}.\end{aligned}\quad (6)$$

The longitudinal and transverse hole masses for the two uppermost bands are obtained as  $m_{\parallel} = -m_0/c$  and  $m_{\perp} = -m_0/d$ . The parameter  $d''$  is found to be 1.33, 1.39, and 1.41 for 2H-, 4H-, and 6H-SiC, respectively. The transverse mass for the first (second) VB is decreased (increased) by a factor of about 5 (2) when the spin-orbit interaction is included. The third VB is not affected by the spin-orbit interaction in the vicinity of the  $\Gamma$ -point, but in the  $\Sigma$  direction the spin-split is strong when the split-off band and the crystal-field split band interact (see Fig. 5).

**Table 3.** Hole effective masses calculated with spin-orbit interaction

Poly-type	Hole mass $m_0$	Band # 1		Band # 2		Band # 3	
		This work	[13, 14]	This work	[13, 14]	This work	[13, 14]
3C-SiC	$m_{\Gamma X} = m_{[100]}$	0.59	0.59 <sup>a</sup>	0.43	0.43 <sup>a</sup>		
	$m_{\Gamma K} = m_{[110]}$	1.32	1.35 <sup>a</sup>	0.31	0.34 <sup>a</sup>	0.51	0.50 <sup>a</sup>
	$m_{\Gamma L} = m_{[111]}$	1.64	1.68 <sup>a</sup>	0.30	0.32 <sup>a</sup>		
	$m^{\text{ave}}$	1.11		0.33		0.51	
2H-SiC	$m_{\parallel}$	1.55	1.52 <sup>b</sup>	1.52	1.51 <sup>b</sup>	0.20	0.21 <sup>b</sup>
	$m_{\perp}$	0.59	0.61 <sup>b</sup>	0.56	0.61 <sup>b</sup>	1.51	1.35 <sup>b</sup>
4H-SiC	$m_{\parallel}$	1.62	1.60 <sup>b</sup>	1.42	1.55 <sup>b</sup>	0.21	0.21 <sup>b</sup>
	$m_{\perp}$	0.61	0.62 <sup>b</sup>	0.58	0.62 <sup>b</sup>	1.46	1.58 <sup>b</sup>
6H-SiC	$m_{\parallel}$	1.65	1.67 <sup>b</sup>	1.35	1.56 <sup>b</sup>	0.21	0.21 <sup>b</sup>
	$m_{\perp}$	0.60	0.62 <sup>b</sup>	0.58	0.62 <sup>b</sup>	1.49	1.58 <sup>b</sup>

<sup>a</sup> from [13], <sup>b</sup> from [14]

The LDA hole effective masses for the four polytypes are presented in Table 3. It is noticeable that the hole effective masses for all three bands are similar in the hexagonal SiC polytypes. This indicates that the three polytypes should have comparable hole mobilities.

### 3 Band Structure and Effective Masses from ODCR Experiments

#### 3.1 4H-SiC

Electron effective masses in 4H-SiC have been reliably determined both theoretically and experimentally before, and the results have been described in our previous review [22]. Hole effective masses have also been calculated before [12]–[16],[18], but experimentally determined only very recently [50]. Therefore, in this section we will focus only on recent and new ODCR experiments.

In order to observe ODCR of holes, the concentration of acceptors in the samples must reach a certain level. With the sensitivity of optical detection, the acceptor concentration may need to be above  $10^{13} \text{ cm}^{-3}$ . Nowadays, available *p*-type SiC crystals are often compensated due to residual N donors. For investigation of hole effective masses we used *n*-type 4H-SiC epitaxial layers grown by hot-wall CVD with the N concentration of  $\sim 1 \times 10^{14} \text{ cm}^{-3}$  and Al concentration of  $\sim 5 \times 10^{13} \text{ cm}^{-3}$ . The substrates were removed by polishing and the thickness of these free-standing layers is about 80  $\mu\text{m}$ .

The ODCR measurements were performed on a modified Bruker ER-200D X-band ( $\sim 9.23 \text{ GHz}$ ) ESR spectrometer. The 334-nm line of an argon-ion

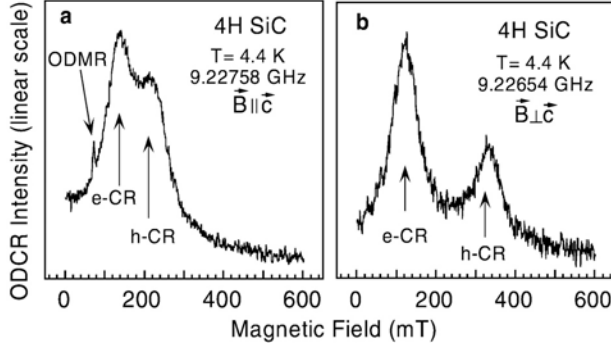


**Fig. 7.** ODCR signals observed in 4H-SiC for  $\mathbf{B}$  in the  $(11\bar{2}0)$  plane and (a) parallel and (b) perpendicular to the  $c$ -axis. A sharp peak at  $\sim 73$  mT in (a) is an optically detected magnetic resonance (ODMR) signal of an unidentified defect. The optical excitation power is 4 mW and the MW power is (a) 1.26 mW and (b) 2 mW

laser was used as the excitation source. The laser beam was defocused onto a spot area of about 3 mm in diameter to reduce the power density and the laser power was kept below 6 mW. The change of PL intensity in the visible region (400–600 nm) due to the amplitude-modulated microwave field was detected using a photomultiplier and recorded by a lock-in amplifier.

Figures 7a and b show ODCR spectra observed in 4H-SiC layers for the magnetic field  $\mathbf{B}$  parallel and perpendicular to the  $c$ -axis, respectively. The MW power was kept below 5 mW to avoid line-broadening effects. For  $\mathbf{B}$  parallel to the  $c$ -axis (Fig. 7a), two broad but well-separated ODCR peaks, labelled  $e$ -CR and  $h$ -CR, were detected in the region 140–250 mT. A sharp line at around 73 mT is an ODMR signal of an unidentified defect.

At X-band frequencies, the angular dependencies of both peaks measured in the  $(11\bar{2}0)$  and  $(\bar{1}100)$  planes are the same within experimental errors. Each peak appears to be symmetric in line shape even when measured with the lowest possible MW power (see Fig. 7b). Therefore, each peak is considered to correspond to a single cyclotron mass value  $m^*$

$$m^* = \frac{eB}{\omega}. \quad (7)$$

Here  $\omega$  is the MW frequency, and  $B$  the value of the magnetic field.

Figure 8 shows angular dependencies of the cyclotron masses corresponding to the  $e$ -CR and  $h$ -CR peaks with the magnetic field rotated in the  $(11\bar{2}0)$  plane. The angular dependencies of the cyclotron mass corresponding to both  $e$ -CR and  $h$ -CR peaks can be described by the usual relation for the case of a parabolic energy surface

$$\frac{1}{m^*} = \left( \frac{\cos^2 \theta}{m_{\perp}^2} + \frac{\sin^2 \theta}{m_{\perp} m_{\parallel}} \right)^{1/2} \quad (8)$$

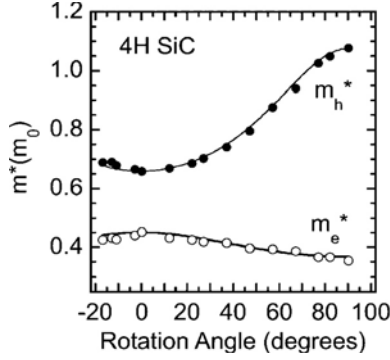


**Fig. 8.** Angular dependencies of the electron (*open circle*) and hole (*filled circle*) cyclotron masses in 4H-SiC measured in units of the free electron mass ( $m_0$ ) with  $\vec{B}$  rotated in the (11 $\bar{2}$ 0) plane. The *curves* represent the fits using (8) and the effective mass values:  $m_{e\perp} = 0.45m_0$  and  $m_{e\parallel} = 0.30m_0$  for electrons, and  $m_{h\perp} = 0.66m_0$  and  $m_{h\parallel} = 1.75m_0$  for holes. The zero angle corresponds to  $\vec{B} \parallel \vec{c}$  while 90° corresponds to  $\vec{B} \perp \vec{c}$  and  $\vec{B} \parallel [\bar{1}100]$ . Within experimental errors, the result is the same for  $\vec{B}$  rotating in the ( $\bar{1}$ 100) plane

where  $\theta$  denotes the angle between  $\vec{B}$  and the  $c$ -axis. The transverse mass,  $m_{\perp}$ , is the mass in the basal plane and the longitudinal mass,  $m_{\parallel}$ , is the mass in the direction of the  $c$ -axis. From the fit to the angular dependence of the cyclotron mass  $m^*$  corresponding to the  $e$ -CR peak, the effective mass values  $m_{e\perp} = (0.45 \pm 0.02)m_0$  and  $m_{e\parallel} = (0.30 \pm 0.02)m_0$  were obtained. Here  $m_0$  is the mass of a free electron. For the  $h$ -CR peak, the transverse and longitudinal masses  $m_{h\perp} = (0.66 \pm 0.02)m_0$  and  $m_{h\parallel} = (1.75 \pm 0.02)m_0$  were obtained.

The values  $m_{e\perp}$  and  $m_{e\parallel}$  are almost the same as those of electrons in 4H-SiC determined by ODCR also at X-band [23] and at Q-band ( $\sim 35$  GHz) [24] frequencies (here  $m_{e\perp}$  corresponds to the geometric average value of two masses in the basal plane determined in [24]). A smaller  $m_{e\perp}$  value ( $m_{e\perp} = 0.42m_0$ ) obtained in our previous work [23] was due to errors caused by a broad and asymmetric ODCR line shape with the peak position slightly shifted to lower magnetic fields, which is typical for low  $\omega\tau$  value ( $\omega\tau \sim 2.5$ ). Thus, it can be concluded that the  $e$ -CR peak corresponds to the ODCR of the electrons. From the experimental [23, 24] and theoretical [14]–[17] studies of the effective masses and energy band structure of 4H-SiC, it can be excluded that the  $h$ -CR peak is related to another component of the electron effective mass tensor. The peaks are already separately observed for  $\vec{B}$  parallel to the  $c$ -axis, and in all directions, their separation is too large compared with the splitting due to the anisotropy of the electron mass tensor. The  $h$ -CR peak can not be related to the CR of electrons occupying the second lowest CB minimum, since at the low MW frequencies (X-band) and powers used in this

case, electrons can not be excited to that band, which lies about 122 meV higher [16]. The intensity ratio between the  $e$ -CR and  $h$ -CR peaks does not change with increasing MW power. This also indicates that the  $h$ -CR peak is not related to the CR of electrons in higher bands. Otherwise the relative intensity between these two ODCR signals should change when altering the relative population of free carriers in the corresponding bands. The  $h$ -CR peak is therefore attributed to the ODCR of holes in the upper-most valence band. Since studies were performed at low temperatures (below 5 K) with low MW powers (1.26–5 mW), the obtained hole effective masses are valid only for the region very close to the valence band maximum.

Early band structure calculations by Käckell et al. [19] predicted hole effective masses, which are anisotropic in the basal plane (the longitudinal mass:  $m_{\Gamma A} = 1.73m_0$ ; on the basal plane:  $m_{\Gamma K} = 0.77m_0$  and  $m_{\Gamma M} = 0.45m_0$ ). Since the calculations neglected the spin-orbit interaction, one does not expect these values to be valid near the  $\Gamma$ -point (see previous section). In recent fully relativistic calculations, Persson and Lindefelt [15, 17] and Lambrecht et al. [14] have predicted parabolic energy surfaces for the highest valence band around the  $\Gamma$ -point of the Brillouin zone of  $4H$ -SiC. Their hole effective mass values are about 10% smaller compared to our experimental values. Including the polaron effect as described in Sect. 2, the hole effective masses calculated by Persson and Lindefelt [16, 17] become  $m_{h\perp} = 0.66m_0$  and  $m_{h\parallel} = 1.76m_0$ . These values are nicely coincident with our values. Thus, it can be concluded that in the vicinity of the maximum of the uppermost valence band, the constant energy surface can be considered as an ellipsoid with the principal axis along the  $c$ -axis and the hole effective masses:  $m_{h\perp} = (0.66 \pm 0.02)m_0$  and  $m_{h\parallel} = (1.75 \pm 0.02)m_0$ . The data are summarized in Table 4.

The MW power dependence of ODCR signals of holes and electrons was studied. Figure 9 shows ODCR spectra measured with different MW powers. As can be seen from the figure, increasing the MW power from 1.26 mW to 20 mW leads to increasing and broadening of both  $e$ -CR and  $h$ -CR peaks. In addition, a new CR peak appears at high magnetic fields ( $\sim 400$  mT). At a

**Table 4.** Effective masses of electrons,  $m_e$ , and holes,  $m_h$ , in units of  $m_0$  in  $4H$ -SiC and  $6H$ -SiC determined from ODCR. Here  $m_{e\perp} = (m_{M\Gamma} \cdot m_{MK})^{1/2}$  is the average value of the electron effective masses in the basal plane and  $m_{e\parallel} = m_{ML}$  is the longitudinal electron effective mass

Polytype	MW freq.	$m_{M\Gamma}$	$m_{MK}$	$m_{e\perp}$	$m_{e\parallel} = m_{ML}$	$m_{h\perp}$	$m_{h\parallel}$
$4H$ -SiC	X-band[50]			0.45	0.30	0.66	1.75
	Q-band[24]	0.58	0.31	0.424	0.33		
$6H$ -SiC	X-band[54]			0.48	3–5	0.66	1.85
	Q-band[53]			0.485			

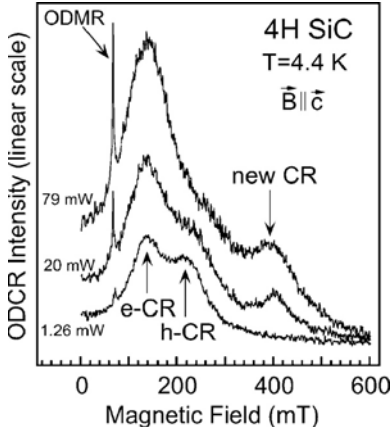
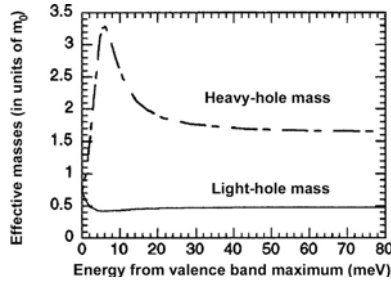


Fig. 9. X-band ODCR spectra in 4H-SiC measured for  $\vec{B} \parallel \vec{c}$  at different MW powers. A new ODCR peak near 400 mT appears at high MW powers

MW power of 79 mW, the  $e$ -CR peak becomes dominant, whereas the  $h$ -CR peak appears as a shoulder. The new CR peak gets stronger and broadened but without shifting. This new peak corresponds to a cyclotron mass of  $m^* = 1.24m_0$ . At this angle of the magnetic field, this value corresponds to the transverse effective mass.

We have repeated the experiments in other samples, in which the ODCR spectrum consists of only the  $e$ -CR peak, and could not observe this new CR signal. This suggests that the new CR peak is related to the cyclotron resonance of holes. From the structure of the valence band and the predicted hole effective masses for 4H-SiC [14]–[17] (see Table 3), it is clear that the calculated transverse masses in the two highest valence bands are the same. Therefore, one may not expect to observe a new CR peak if holes are excited into the second highest valence band. The value  $1.24m_0$  is close to the value  $m_{h\perp} = 1.49m_0$  calculated for the third highest valence band, which lies about 50 meV higher (our recent value). It is not clear if holes can be excited to the third band under the experimental conditions and we can not exclude this possibility.

Calculations of the dependence of hole effective masses in the uppermost valence band on energy [16, 51] show that the mass increases gradually to just above  $3m_0$  at energies  $\sim 6$ – $7$  meV and then decreases (Fig. 10). This dependence has also been confirmed by Lambrecht and Limpijumnong [52]. With such a dependence, one may expect to observe a broadening and shifting of the  $h$ -CR peak to high magnetic fields but not a new well-distinguished CR peak. Thus, the new CR peak may not be related to the cyclotron resonance of holes in a more flat region of the uppermost valence band. The value  $m^* = 1.24m_0$  is close to twice of the transverse hole mass ( $m_{h\perp} = 0.66m_0$ ). It is therefore possible that the new CR peak is the second harmonic of the  $h$ -CR peak. The identification of this new peak requires further CR experiments with higher resolutions.



**Fig. 10.** Spherically averaged effective heavy hole and light hole masses in units of  $m_0$  in 4H-SiC as a function of energy measured from the top of the valence band [51]

### 3.2 6H-SiC

Electron and hole effective masses in 6H-SiC are not as well determined as compared to the 4H polytype. The average of electron effective masses in the basal plane calculated by most of groups is in good agreement with the experimental value  $m_{\perp} = 0.42m_0$  determined by ODCR [26], whereas the reported calculated values for the longitudinal mass  $m_{\parallel}$  range from  $1.2m_0$  to  $2.0m_0$  [11],[12],[14]–[18],[25].

In our previous work at X-band frequency [26], it was not possible to completely characterize the angular dependence of the CR. The experiments were performed again at Q-band frequencies (36 GHz) [53], but the CR signal was only detected for some angles between 0–60 degrees from the  $c$ -axis (see Fig. 11a,b).

An average value of the electron effective masses in the basal plane,  $m_{\perp} = 0.485m_0$ , has been determined. The incomplete angular dependence of the cyclotron mass  $m^*$  shows a trend of divergence to infinity at the angle perpendicular to the  $c$ -axis (Fig. 11c).

The infinite value for the mass parallel to the  $c$ -axis can be explained by the nonparabolicity of the conduction band (Fig. 3). Lambrecht and Segall [25] predicted that the mass will increase from  $1.1m_0$  to  $2.0m_0$  (corresponding to the maximum energy at the barrier height) depending on the electron energy. Similar results were obtained by Persson and Lindefelt [16]. According to these calculations, the minimum of the conduction band is at 0.4 of the distance from the M point towards L. The barrier height is 5.3 meV. The ODCR measurement at 36 GHz used a MW power of 200 mW [53]. Depending on the quality factor of the cavity, the MW electric field can reach values up to  $2 \times 10^2$  V/cm. In such a high electric field, electrons can gain enough kinetic energy, being excited into the flat region of the band, which corresponds to an infinite effective mass. Because of this feature of the CB minimum in 6H-SiC, CR experiments using high MW frequencies can not be used to determine the electron effective mass in the direction of

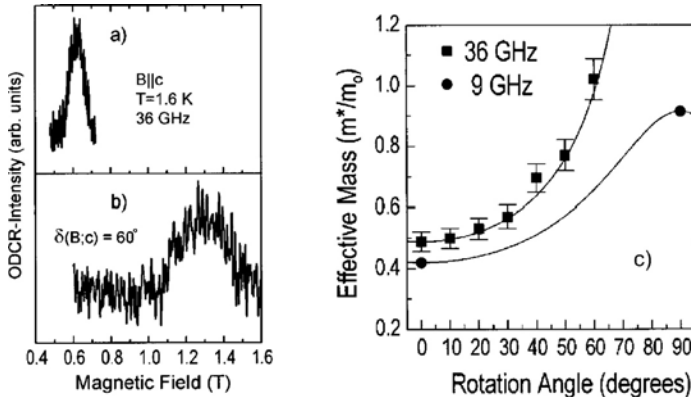


**Fig. 11.** Q-band ( $\sim 36$  GHz) ODCR spectra in 6H-SiC measured at  $T = 1.6$  K for  $B$  (a) parallel to the  $c$ -axis and (b) 60 degrees off the  $c$ -axis. (c) Angular dependence of the electron cyclotron effective mass  $m^*$  in units of  $m_0$  with  $B$  rotated in the  $(\bar{1}100)$  plane. The experimental data are shown as *filled squares* and *circles* and the curves are calculated using effective mass values:  $m_\perp = 0.42m_0$  and  $m_\parallel = 2.0m_0$  (X-band ( $\sim 9$  GHz) ODCR data) and  $m_\perp = 0.485m_0$  and  $m_\parallel = 8$  determined from Q-band ODCR experiments

the  $c$ -axis. The Q-band ODCR results also provide a direct evidence for the “camel’s back” nature of the conduction band in 6H-SiC as predicted by theory [11, 15, 16, 25].

Recently, we have performed again ODCR experiments at X-band frequency [54] using pure  $n$ -type 6H-SiC freestanding films (thickness  $\sim 80$   $\mu\text{m}$ ) grown by hot-wall CVD with the concentration of N donors and Al acceptors of  $\sim 1 \times 10^{14} \text{ cm}^{-3}$  and  $\sim 5 \times 10^{13} \text{ cm}^{-3}$ , respectively. The experimental details are similar to those for the recent ODCR experiments on 4H-SiC discussed earlier. Figure 12a shows the X-band ODCR spectrum observed for  $B$  parallel to the  $c$ -axis with the MW power of 0.1 mW and an optical-excitation power of 5.3 mW (the laser spot size is  $\sim 3$  mm in diameter). At such low MW powers, the spectrum consists of two well-separated ODCR peaks, labelled  $e$ -CR and  $h$ -CR. Both peaks are narrow with the full width at half-maximum of about 33 mT and 40 mT, respectively. From the line width or by fitting the line shape of the resonance we can estimate the scattering time to be in the range of several hundreds of picoseconds, which correspond to carrier mobilities in the  $10^5 \text{ cm}^2/\text{Vs}$  range.

Figure 12b shows the ODCR spectrum measured for  $B$  perpendicular to the  $c$ -axis and along the  $[11\bar{2}0]$  direction of the crystal and with a MW power of 3.1 mW. Because of the higher MW powers used and higher cyclotron mass values at this angle, the  $e$ -CR and  $h$ -CR peaks are broadened to a full width at half maximum values of about 150 mT and 50 mT, respectively, but are still well separated as can be seen in the figure. The  $e$ -CR and  $h$ -CR peaks observed for the direction of the magnetic field along the  $c$ -axis (Fig. 12a)

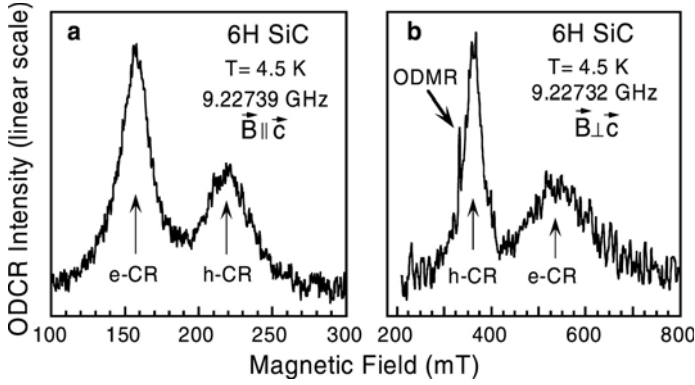


**Fig. 12.** ODCR spectra with two well-resolved peaks,  $e$ -CR and  $h$ -CR, observed in 6H-SiC for  $\mathbf{B}$  (a) parallel and (b) perpendicular to the  $c$ -axis and parallel to the  $[11\bar{2}0]$  direction. The optical excitation power is 5.3 mW and MW powers are (a) 0.1 mW and (b) 3.1 mW

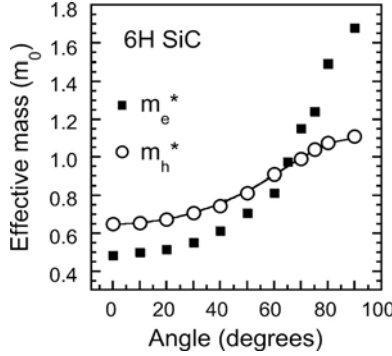


**Fig. 13.** Angular dependencies of the cyclotron masses of the electrons (*filled squares*) and holes (*open circles*) in units of  $m_0$  in 6H-SiC (from X-band ODCR data) with  $\mathbf{B}$  rotated in the  $(1\bar{1}00)$  plane. The angle  $\theta = 0$  corresponds to  $\mathbf{B} \parallel \mathbf{c}$  while  $\theta = 90^\circ$  corresponds to  $\mathbf{B} \perp \mathbf{c}$  and  $\mathbf{B} \parallel [11\bar{2}0]$ . The *solid curve* represents the fit using (8) and the hole effective masses given in Table 4

correspond to the cyclotron mass values of  $m_e^* = 0.48m_0$  and  $m_h^* = 0.66m_0$ , respectively. The corresponding values for  $\mathbf{B}$  parallel to the  $[11\bar{2}0]$  direction (Fig. 12b) are  $m_e^* = 1.68m_0$  and  $m_h^* = 1.02m_0$ .

Figure 13 shows the dependence of  $m_e^*$  and  $m_h^*$  values on the angle of the magnetic field with respect to the  $c$ -axis in the  $(1\bar{1}00)$  plane. Within experimental errors, the angular dependencies in the  $(1\bar{1}00)$  and  $(11\bar{2}0)$  planes are the same for  $m_h^*$ . Therefore, the effective mass  $m_h^*$  corresponding to the  $h$ -CR peak is considered to be isotropic in the basal plane. The angular dependencies of the  $m_h^*$  in both studied planes can be described by the effective mass relation (8) for the case of a parabolic energy surface. From the fit to

the data points shown as open circle in Fig. 13, the effective mass values  $m_{h\perp} = (0.66 \pm 0.02)m_0$  and  $m_{h\parallel} = (1.85 \pm 0.03)m_0$  were obtained. These values fit very well to the calculated values of the hole effective masses in 6H-SiC [14]–[17], taking into account the polaron effect. Arguments for the identification of the  $h$ -CR peak as due to the cyclotron resonance of holes in the uppermost valence band are similar to the case of 4H-SiC and presented in detail in [54]. Thus, similar to the 4H polytype, near the maximum of the uppermost valence band in 6H-SiC, the constant energy surface is also an ellipsoid. The hole effective masses are given in Table 4.

For the  $e$ -CR peak, we observed the angular dependence over the full range of angles in the  $(\bar{1}100)$  plane. The corresponding cyclotron masses  $m_e^*$  are shown as filled squares in Fig. 13. However, for the case of  $\mathbf{B}$  rotated in the  $(11\bar{2}0)$  plane we can only follow the  $e$ -CR peak in the region  $0 \leq \theta \leq 60$  degrees. The angular dependencies in the  $(\bar{1}100)$  and  $(11\bar{2}0)$  planes appear to be different and can not be described by one set of effective mass values using (8). This indicates that the effective mass  $m_e^*$  is anisotropic in the basal plane. Unfortunately, without observing the splitting of the angular dependence of  $m_e^*$  we can only deduce the average effective mass in the basal plane as  $m_{e\perp} = (0.48 \pm 0.02)m_0$ . This value is very close to the transverse effective mass of electrons  $m_{e\perp} = 0.485m_0$  obtained in the Q-band ODCR studies described above and the calculated values [15]–[17] including the polaron effect. Therefore it is assigned to the average value of the electron effective mass in the basal plane. The determination of the longitudinal effective mass,  $m_{e\parallel}$ , requires more experimental data, especially a complete angular dependence of the cyclotron mass in the  $(11\bar{2}0)$  plane. If the electron effective mass along the  $[11\bar{2}0]$  direction ( $m_{\text{MF}}$ ) is larger than that along the  $[\bar{1}100]$  direction ( $m_{\text{MK}}$ ) as predicted by theory (see Table 2) then it is likely that the  $e$ -CR peak overlaps with the  $h$ -CR peak in the region  $60 \leq \theta \leq 90$  degrees for the case of  $\mathbf{B}$  rotated in the  $(11\bar{2}0)$  plane. From the cyclotron mass value measured with  $\mathbf{B}$  parallel to the  $[11\bar{2}0]$  direction,  $m_e^* = 1.68m_0$ , we can estimate the longitudinal mass to be in the range 3–6  $m_0$  depending on the anisotropy of the effective mass in the basal plane.

The above result indicates that the electron effective mass along the  $c$ -direction ( $m_{e\parallel} = 2.0m_0$ ) determined in our previous work [26] must be incorrect. The studies of the MW power dependence showed that when increasing the MW power to 1.26 mW, the  $e$ -CR and  $h$ -CR peaks in Fig. 12a overlap completely with each other. In our previous experiments [26], the ODCR signal was detectable only when using a MW power level of several mW or far above (for  $\mathbf{B}$  along the  $[\bar{1}100]$  direction, a MW power of 100 mW was used). In those experiments [26], the  $h$ -CR peak might appear but completely overlap the  $e$ -CR peak, resulting in a broad CR signal. It is possible that for the magnetic field along or close to the  $[\bar{1}100]$  direction, only the hole CR signal was detected but was mistakenly identified as the CR of electrons. The value  $m_{e\parallel} = (2.0 \pm 0.2)m_0$  in [26] is indeed very closed to the value  $m_{h\parallel} = (1.85 \pm 0.03)m_0$  for holes.

### 3.3 Comparison Between Calculations and Experiments

The effective masses of electrons at the conduction band minimum of common SiC polytypes determined from CR experiments and calculations are summarized in Table 5. The electron effective masses in 3C-SiC are well determined by CR [9, 10]. The results are in good agreement with theoretical calculations [12, 15, 16]. The CB minima in 3C-SiC are predicted to be located at the zone boundaries at the X-point and the constant energy surfaces near the bottom of the CB are ellipsoids with the long axis along the  $\langle 100 \rangle$  directions [12, 15, 16] (Fig. 2). The CR experiments by Kono et al. [10] indicates that the conduction band is very parabolic up to  $\sim 53.8$  meV from the CB minimum. For 2H-SiC, no experimental data is available.

The electron effective masses in 4H-SiC are found to be fully anisotropic by both the experiments and calculations. The experimental values [24] are in excellent agreement with the theoretical calculations [15]–[17],[23] as can be seen in Table 5. The CB minima in the 4H polytype are found to be located at the M-point with no “camel’s back” structure.

As described in Sect. 2, the CB minima in 6H-SiC are located along the ML-line. The band is very flat along the ML-line and the electron effective masses are predicted to be very anisotropic. The camel’s back structure of the CB has been confirmed by ODCR experiments [53]. The anisotropy of the mass in the basal plane has not been resolved by experiments but

**Table 5.** The effective masses of electrons in the conduction band minimum for common SiC polytypes determined by cyclotron resonance experiments and by calculations.  $m_p$  denotes the polaron masses. a and b are from far-infrared CR experiments in [9] and [10], respectively. c [24] and f [53] are from our Q-band ODCR, whereas d [26] and e [54] are from our X-band ODCR experiments. Here  $m_{\perp} = (m_{M\Gamma} \cdot m_{MK})^{1/2}$  is the average value of the electron effective masses in the basal plane

Polytype	Eff. mass	Experiment	Theory [16, 17]		Theory [12]	Theory [25]
		$m(m_0)$	$m(m_0)$	$m_p(m_0)$	$m(m_0)$	$m(m_0)$
3C-SiC	$m_{\parallel}$	0.667 <sup>a</sup> , 0.68 <sup>b</sup>	0.68	0.73	0.67	
	$m_{\perp}$	0.247 <sup>a</sup> , 0.25 <sup>b</sup>	0.23	0.24	0.24	
4H-SiC	$m_{ML}$	0.33 <sup>c</sup>	0.31	0.33		0.31
	$m_{M\Gamma}$	0.58 <sup>c</sup>	0.57	0.61		0.58
	$m_{MK}$	0.31 <sup>c</sup>	0.28	0.29		0.28
6H-SiC	$m_{ML}$	2.0 <sup>d</sup> , 3–6 <sup>e</sup>	1.83	2.07		1.42
	$m_{M\Gamma}$		0.75	0.81		0.77
	$m_{MK}$		0.24	0.25		0.24
	$m_{\perp}$	0.48 <sup>e</sup> , 0.485 <sup>f</sup>	0.42	0.45		0.43

**Table 6.** Hole effective masses (in units of the free electron mass  $m_0$ ) in common SiC polytypes obtained from calculations [13]–[17] and our ODCR experiments [48, 53]. The values in parentheses are the polaron masses

Polytype	Eff. mass	Experiment	[16, 17]	[13]	[14]
3C-SiC	$m_{\Gamma X} = m_{[100]}$		0.59	0.59	
	$m_{\Gamma K} = m_{[110]}$		1.32	1.35	
	$m_{\Gamma L} = m_{[111]}$		1.64	1.68	
4H-SiC	$m_{\parallel}$	1.75	1.62(1.76)		1.60
	$m_{\perp}$	0.66	0.61(0.66)		0.62
6H-SiC	$m_{\parallel}$	1.85	1.65(1.795)		1.67
	$m_{\perp}$	0.66	0.60(0.653)		0.62

the obtained transverse mass  $m_{\perp}$  is in good agreement with the average value  $(m_{\text{M}\Gamma}m_{\text{M}\text{K}})^{1/2}$  from calculations. Due to the structure of the CB minimum, the ODCR experiments have not been able to determine the longitudinal mass. The  $m_{\parallel}$  value estimated from our ODCR studies [53] is substantially higher than that predicted by all calculations. In order to resolve the anisotropy of the electron effective masses in 6H-SiC, having samples with a very low doping level is the only alternative since using high radiation frequencies in the CR experiments does not help in this case.

The data on the hole effective masses are collected in Table 6. Experimental data are only available for 4H- and 6H-SiC. In both polytypes, the VB maximum is found to be parabolic and located at the  $\Gamma$ -point with very similar hole effective masses (Table 6). The experimental results are in excellent agreement with theoretical predictions (with inclusion of the polaron effect). In SiC, the polaron effect accounts for an increase in the effective masses of about 8–10%.

## 4 Conclusion

The band structure of 3C-, 2H-, 4H-, and 6H-SiC obtained from theoretical calculations is briefly described. In all polytypes, the calculated  $\mathbf{k}$ -space locations of the CB minima and the electron effective mass agree well with the experimental findings. The parameterization of the top of the valence bands in the vicinity of the  $\Gamma$  point shows very similar band structures for all three hexagonal polytypes. The spin-orbit interaction was found to have a strong influence on the value of the hole effective masses. ODCR experiments have been successfully determined the hole effective masses in 4H- and 6H-SiC. The result is fully consistent with the theoretical calculations. In SiC, the polaron effect induces an increase in the effective masses of about 8–10%. Q-band ODCR measurements confirm the theoretical prediction of the camel's

back structure of the conduction band in 6H-SiC. A more reliable transversal electron effective mass  $m_{e\perp} = 0.485m_0$  has been obtained for 6H-SiC. New X-band ODCR results suggest that the longitudinal electron effective mass is higher than the value  $m_{e\perp} = 2.0m_0$  determined before and can be in the range 3–6  $m_0$  depending on the anisotropy of the mass in the basal plane. We estimate that it will be possible to resolve the anisotropy of the electron effective masses in the basal plane by X-band ODCR experiments using high-purity epitaxial layers with a concentration of residual N donor slightly below  $1 \times 10^{14} \text{ cm}^{-3}$ .

## Acknowledgements

The authors thank W.R.L. Lambrecht and S. Limpijumnong for providing information prior to publication. Support for this work was provided by the SSF programs SiCEP and SiCMAT, the Swedish Research Council (VR), Swedish Defense Research Agency (FOI), and SIDA grant SRP-2000-025.

## References

1. B. Ellis and T.S. Mott: Proc. R. Soc. London A **299**, 383 (1967)
2. B. Ellis and T.S. Mott: Proc. R. Soc. London A **299**, 393 (1967)
3. L.S. Aivazova, S.N. Gorin, V.G. Sidaykin, and I.M. Shvarts: Sov. Phys. Semicond. **11**, 1069 (1978)
4. G.A. Lomakina and Yu.A. Vodakov: Sov. Phys. Solid State **15**, 83 (1973)
5. P.J. Dean, W.J. Choyke, and L. Patrick: J. Lumin. **15**, 299 (1977)
6. A.V. Melnichuk and Yu.A. Pasechnik: Sov. Phys. Solid State **34**, 227 (1993)
7. W. Suttrop, G. Pensl, W.J. Choyke, R. Stein, and S. Leibenzeder: J. Appl. Phys. **72**, 3708 (1992)
8. W. Götz, A. Schöner, G. Pensl, W. Suttrop, W.J. Choyke, R. Stein, and S. Leibenzeder: J. Appl. Phys. **73**, 3332 (1993)
9. R. Kaplan, R.J. Wagner, H.J. Kim, and R.F. Davis: Solid State Commun. **55**, 67 (1985)
10. J. Kono, S. Takeyama, H. Yokoi, N. Miura, M. Yamanaka, M. Shinohara, and K. Ikoma: Phys. Rev. B **48**, 10909 (1993)
11. K. Karch, G. Wellenhofer, P. Pavone, U. Rössler, and D. Strauch: *The Physics of Semiconductors*, ed. by D.J. Lockwood (World Scientific, Singapore, 1995), p. 401
12. B. Wenzien, P. Käckell, and F. Bechstedt: Phys. Rev. B **52**, 10897 (1995)
13. M. Willatzen, M. Cardona, and N.E. Christensen: Phys. Rev. B **51**, 13150 (1995)
14. W.R.L. Lambrecht, S. Limpijumnong, S.N. Rashkeev, and B. Segall: Phys. Stat. Sol. (b) **202**, 5 (1997)
15. C. Persson and U. Lindefelt: Phys. Rev. B **54**, 10257 (1996)
16. C. Persson and U. Lindefelt: J. Appl. Phys. **82**, 5496 (1997)
17. C. Persson and U. Lindefelt: J. Appl. Phys. **86**, 5036 (1999)
18. C. Persson, U. Lindefelt, and B.E. Sernelius: Phys. Rev. B **60**, 16479 (1999)

19. P. Käckell, B. Wenzien, and F. Bechstedt: Phys. Rev. B **50**, 10761 (1994)
20. P.G. Baranov, Yu.P. Veshchunov, R.A. Zhitnikov, N.G. Romanov, and Yu.G. Shreter: JETP Lett. **26**, 249 (1977)
21. N.T. Son, E. Sörman, W.M. Chen, J.P. Bergman, C. Hallin, O. Kordina, A.O. Konstantinov, B. Monemar, E. Janzén: J. Appl. Phys. **81**, 1929 (1997)
22. W.M. Chen, N.T. Son, E. Janzén, D.M. Hofmann, and B.K. Meyer: Phys. Stat. Sol. (a) **162**, 79 (1997)
23. N.T. Son, W.M. Chen, O. Kordina, A.O. Konstantinov, B. Monemar, E. Janzén, D.M. Hofmann, D. Volm, M. Drechsler, and B.K. Meyer: Appl. Phys. Lett. **66**, 1074 (1995)
24. D. Volm, B.K. Meyer, D.M. Hofmann, W.M. Chen, N.T. Son, C. Persson, U. Lindefelt, O. Kordina, E. Sörman, A.O. Konstantinov, B. Monemar, and E. Janzén: Phys. Rev. B **53**, 15409 (1996)
25. W.R.L. Lambrecht and B. Segall: Phys. Rev. B **52**, R2249 (1995)
26. N.T. Son, O. Kordina, A.O. Konstantinov, W.M. Chen, E. Sörman, B. Monemar, and E. Janzén: Appl. Phys. Lett. **65**, 3209 (1994)
27. W.J. Schaffer, G.H. Negley, K.G. Irvin, and J.W. Palmour: Mat. Res. Soc. Symp. Proc. **339**, 594 (1994)
28. M. Schadt, G. Pensl, R.P. Devaty, W.J. Choyke, R. Stein, and D. Stephani: Appl. Phys. Lett. **65**, 3120 (1994)
29. H.P. Iwata: Appl. Phys. Lett. **82**, 598 (2003)
30. P. Blaha, K. Schwarz, P. Dufek, and R. Augustyn: WIEN95, Technical University of Vienna 1995. (Improve from original version: P. Blaha, K. Schwarz, P. Sorantin, and S.B. Trickey, in Comput. Phys. Commun. **59**, 399, (1990))
31. G.F. Koster, J.O. Dimmock, R.G. Wheeler, and H. Statz: *Properties of the Thirty-Two Point Groups* (M.I.T., Cambridge MA, 1963)
32. F. Bechstedt and R. Del Sole: Phys. Rev. B **38**, 7710 (1988)
33. *Physics of Group IV Elements and III-V Compounds*, ed. by O. Madelung et al., Landolt-Börnstein, New Series, Group III, Vol. 17a (Springer, Berlin, 1982)
34. L. Patrick, D.R. Hamilton, and W.J. Choyke: Phys. Rev. **143**, 526 (1966)
35. W.J. Choyke, R.P. Devaty, L.L. Clemen, M.F. MacMillan, and M. Yoganathan: Inst. Phys. Conf. Ser. **142**, 257 (1996)
36. P.J. Colwell and M.V. Klein: Phys. Rev. B **6**, 498 (1972); L. Patrick, *ibid.* **5**, 2198 (1972)
37. I.S. Gorban', V.A. Gubanov, V.G. Lysenko, A.A. Pletyushkin, and V.B. Timofeev: Sov. Phys. Solid State **26**, 1385 (1984)
38. R.G. Humphreys, D. Bimberg, and W.J. Choyke: Solid State Commun. **39**, 163 (1981)
39. L. Patrick and W.J. Choyke: Phys. Rev. **186**, 775 (1969)
40. I. G. Ivanov, U. Lindefelt, A. Henry, O. Kordina, C. Hallin, A. Aroyo, T. Egilsson, and E. Janzén: Phys. Rev. B **58**, 13634 (1998)
41. C. Persson and U. Lindefelt: J. Appl. Phys. **83**, 266 (1998)
42. K. Bertilsson, H.-E. Nilsson, M. Hjelm, C.S. Petersson, P. Käckell, and C. Persson: Solid-State Electron. **45**, 645 (2001)
43. W.J. Choyke, R.P. Devaty, and S.G. Sridhara: Physica Scripta T**79**, 9 (1999)
44. S.G. Sridhara, S. Bai, O. Shigiltchoff, R.P. Devaty, and W.J. Choyke: Mater. Sci. Forum **338-342**, 567 (2001)
45. *Polarons in Ionic Crystals and Polar Semiconductors*, ed. by J.T. Devreese (North-Holland, Amsterdam, 1972)

46. G.D. Mahan: *Many-Particle Physics*, 2nd ed. (Plenum, New York, 1990) p. 497
47. R. Ahuja, A. Ferreira da Silva, C. Persson, J.M. Osorio-Guillen, I. Pepe, K. Järrendahl, O.P.A. Lindquist, N.V. Edwards, Q. Wahab, and B. Johansson: *J. Appl. Phys.* **91**, 2099 (2002)
48. F. Bechstedt, P. Käckell, A. Zywietz, K. Karch, B. Adolph, K. Tenelsen, and J. Furthmüller: *Phys. Stat. Sol. (b)* **202**, 35 (1997)
49. B. Lax and J.G. Mavroides: *Phys. Rev.* **100**, 1650 (1955)
50. N.T. Son, P.N. Hai, W.M. Chen, C. Hallin, B. Monemar, and E. Janzén: *Phys. Rev. B* **61**, R10544 (2000)
51. U. Lindefelt: *J. Appl. Phys.* **84**, 2628 (1998)
52. W.R.L. Lambrecht and S. Limpijumnong: private communication
53. B.K. Meyer, D.M. Hofmann, D. Volm, W.M. Chen, N.T. Son, and E. Janzén: *Phys. Rev. B* **61**, 4844 (2000)
54. N.T. Son, C. Hallin, and E. Janzén: *Phys. Rev. B* **66**, 045304 (2002)

# Electronic Structure of Deep Defects in SiC

N.T. Son, Mt. Wagner, C.G. Hemmingsson, L. Storasta, B. Magnusson, W.M. Chen, S. Greulich-Weber, J.-M. Spaeth, and E. Janzén

## 1 Introduction

In the early days of defect studies, electron paramagnetic resonance (EPR) was used by Woodbury and Ludwig [1] to investigate N and B impurities in 6H-SiC. Since then, different impurity-related deep centers in 4H- and 6H-SiC have been identified and studied by EPR and optically detected magnetic resonance (ODMR) [2]–[16]. Intrinsic defects have also been studied by EPR since the sixties [17]–[19] and several EPR centers observed in electron irradiated 6H- and 3C-SiC were suggested to be paired defects related to carbon and silicon vacancies. Many EPR centers with spin  $S = 1$  (W1 and G1–G8 centers) have been detected in irradiated 4H-, 6H- and 15R-SiC by Pavlov et al. [20, 21]. Some of these and other new centers (P3–P10 centers) have been observed and studied by Vainer et al. [22, 23] in heated and quenched 6H-SiC. These centers were attributed to vacancy-related complexes. The single silicon vacancy in the negative charge state ( $V_{\text{Si}}^-$ ) was first identified by Itoh et al. [24] in irradiated *n*-type 3C-SiC. The center was found to have cubic symmetry even in the hexagonal 4H and 6H polytypes [25, 26]. Its high spin configuration ( $S = 3/2$ ) has been confirmed by both experiment [25] and theoretical calculations [27]–[29]. The center was found to be annealed out in three stages at  $\sim 150$ ,  $350$ , and  $750^\circ\text{C}$  [24, 30]. In *p*-type 3C-SiC irradiated by electrons or protons, Itoh et al. [31] observed an EPR center (T5 center) with a spin  $S = 1/2$  and  $D_2$  symmetry. From the clear hyperfine (HF) structure due to the interaction with four Si atoms in the nearest neighbour (NN) shell, the spectrum was identified to originate from the single carbon vacancy in the positive charge state ( $V_{\text{C}}^+$ ) [31]. The T5 center starts to be annealed out already at  $\sim 100^\circ\text{C}$  and completely vanishes at  $\sim 400^\circ\text{C}$  [30]. Therefore, it is generally believed that  $V_{\text{C}}$  becomes mobile at lower temperatures compared to  $V_{\text{Si}}$ . Photoluminescence (PL) and annealing studies by Itoh et al. [32] suggest the ground state level of  $V_{\text{Si}}^-$  to be located at 0.5 eV above the valence band ( $E_{\text{V}}$ ) and may be related to the H3 level at ( $E_{\text{V}} + 0.54$  eV) determined by DLTS in neutron-irradiated 3C-SiC by Nagesh et al. [33, 34]. The level is close to the calculated level for  $V_{\text{Si}}$  by Talwar and Feng [35]. In as-grown and irradiated 3C-SiC, several other EPR and ODMR centers were observed [36]–[41], some of which were suggested to be related to vacancy-interstitial pairs [36] and to  $V_{\text{Si}}$ -related defects [37, 39, 40]. Different EPR centers were de-

tected in *p*-type 4*H*- and 6*H*-SiC irradiated with electrons [42]–[45] of which the PB center in 6*H*-SiC was attributed to  $V_C^+$  [42], whereas the same center in 4*H*-SiC (the EI1 center) was suggested to be a hydrogen-related defect [46]. Recently, the EI5 center in 4*H*- and 6*H*-SiC [46, 47] was identified as  $V_C^+$ . The same center in 6*H*-SiC, labelled Ky1, was also attributed to  $V_C^+$  by Bratus et al. [48, 49]. Using low-energy electron irradiation, Steeds et al. [50] were able to determine the displacement energies for C and Si atoms to be about 100 keV and 250 keV, respectively. In EPR studies of 6*H*-SiC irradiated with 350 keV electrons, von Bardeleben et al. [51] have identified the Si Frenkel pair.

Theoretical studies in 3*C*-SiC [52, 53] predicted that, although antisites have low formation energies, neither the silicon antisite ( $Si_C$ ) nor the carbon antisite ( $C_{Si}$ ) has energy levels in the band gap. Contrary to that, recent calculations in 3*C*- and 2*H*-SiC by Torpo et al. [54] predict the  $C_{Si}$  level to be resonant with the valence band and the  $Si_C$  level to be slightly above  $E_V$ . This work [54] also suggested the H1-H3 levels in 3*C*-SiC [33, 34] to originate from antisite-related defects rather than from  $V_{Si}$ . In recent EPR studies, Son et al. [46, 55] assigned the EI6 center in *p*-type 4*H*- and 6*H*-SiC irradiated with electrons to  $Si_C$  in the positive charge state ( $Si_C^+$ ). The same center in 6*H*-SiC (Ky2 center) was suggested by Bratus et al. [49] to be  $V_C^+$  at the hexagonal lattice site. The P6/P7 EPR spectra [23] and ODMR spectra *a-c* in 6*H*-SiC [56, 57], which were suggested to be the ( $V_C$ - $V_{Si}$ ) pairs, have recently been identified by Lingner et al. [58, 59] to be related to the ( $V_C$ - $C_{Si}$ ) pair in the doubly positive charge state.

Deep PL bands related to intrinsic defects have been observed in the near-infrared and visible spectral regions. The  $D_I$  and  $D_{II}$  PL centers in irradiated and annealed 3*C*-SiC were observed and studied by Choyke and Patrick [60]–[62]. The  $D_I$  center was also detected in 4*H*, 6*H*, and 21*R* polytypes by Marakov [63]. In Zeeman and PL excitation (PLE) studies by Egilsson et al. [64, 65] the center was suggested to be an exciton bound to an isoelectronic defect. Results from recent studies of these centers are reviewed by Choyke and Devaty in other chapter of this book. In 6*H*-SiC, three no-phonon (NP) lines in the near-infrared region between 1.36 eV and 1.44 eV were observed by Gorban and Slobodyanyuk [66] and were later suggested to be related to impurities. However, investigations of this PL band in 6*H*- and 15*R*-SiC samples intentionally doped with more than 30 different impurities during growth by Hagen and Kemenade [67] showed no correlation with any dopant. The same NP lines in 4*H*- and 6*H*-SiC was recently suggested to be related to  $V_{Si}^0$  at different inequivalent lattice sites [68]–[73]. Other EPR studies also suggest the center to be a single Si vacancy in neutral [74, 75] or negative charge state [76].

Different deep level centers have been observed and studied by Hall effect and deep level transient spectroscopy (DLTS) in irradiated and as-grown 4*H*- and 6*H*-SiC [77]–[90], of which some possess negative-*U* or metastable

properties [85]–[88]. DLTS studies using radioactive isotopes have made important contributions to the identification and understanding of deep level centers induced by impurities such as V, Ti, Cr, Ta, Be and W in 4H-SiC [91]–[94] and Ga, Zn, and W in 6H-SiC [94, 95] (see other review in this book). The studies of deep levels in SiC before 1999 have been reviewed by Lebedev [96].

In this paper, recent results of defect studies in SiC are reviewed with focusing on paramagnetic defect centers. Selected PL and DLTS centers are also briefly described. The description of experimental details is referred to the original works cited in the references.

## 2 Paramagnetic and Photoluminescence Centers

### 2.1 Carbon Vacancy

Figures 1a and b show EPR spectra in irradiated 4H-SiC observed at X-band ( $\sim 9.5$  GHz) and W-band ( $\sim 95$  GHz) frequencies, respectively, for the magnetic field  $\mathbf{B}$  parallel to the  $c$ -axis. Two dominant EPR lines, labelled EI5 and EI6, which overlap with each other at X-band frequencies (Fig. 1a), are well separated at W-band frequencies (Fig. 1b). Lines EI4 and EI6 will be discussed in the following sections. Four satellites (indicated by solid arrows) of the EI5 line can be identified as the HF structures due to the interaction between the electron spin and the nuclear spin of four  $^{29}\text{Si}$  atoms in the NN shell [46, 47]. Similar spectra have also been detected in the 6H polytype. The spectrum has  $C_{3v}$  symmetry at temperatures above 25 K. At temperatures below 25 K, the symmetry of the center lowered to  $C_{1h}$ . The  $g$ -values and

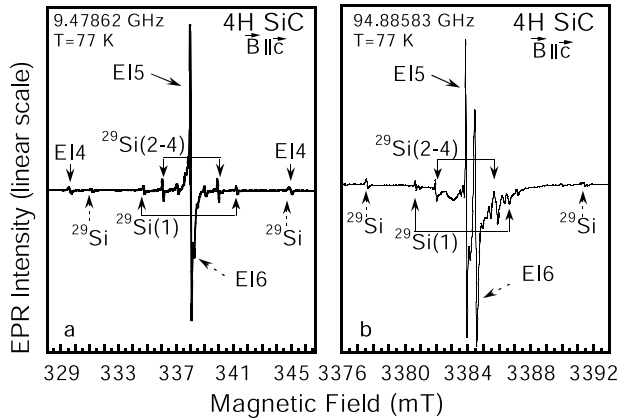


**Fig. 1.** EPR spectra observed in  $p$ -type, electron-irradiated 4H-SiC for the magnetic field  $\mathbf{B}$  parallel to the  $c$ -axis at (a) X-band and (b) W-band frequencies

**Table 1.** Spin-Hamiltonian parameters of the EI5 center in  $4H$ - and  $6H$ -SiC taken from [47] (for the  $C_{3v}$  centers) and our unpublished data (for the  $C_{1h}$  centers). Si(1) and Si(2-4) denote the nearest Si atom along the  $c$ -axis and other three Si atoms in the basal plane, respectively.  $\alpha$  and  $\beta$  are the angles between the  $c$ -axis and the principal  $z$ -axis of the  $g$ - and  $A$ -tensor for the  $C_{1h}$  symmetry, respectively

Polytype & symmetry	$g$	$A$ [MHz]
$4H, C_{3v}$	$g_{\parallel} = 2.0032, g_{\perp} = 2.0048$	Si(1): $A_{\parallel} = 181.1, A_{\perp} = 125.0$ Si(2-4): $C_{1h}, \beta = 5^{\circ}, A_x = 140.6,$ $A_y = 103.4, A_z = 106.7$
	$C_{1h}$	
	$g_x = 2.0030, g_y = 2.0047$	Si(1): $C_{1h}, \beta = 65^{\circ}, A_x = 175.6,$ $A_y = 127.4, A_z = 127.4$
	$g_z = 2.0055, \alpha = 68^{\circ}$	Si(2-4): $C_{1h}, \beta = 67^{\circ}, A_x = 103.1,$ $A_y = 102.8, A_z = 114.9$
$6H, C_{3v}$	$g_{\parallel} = 2.0031, g_{\perp} = 2.0046$	Si(1): $A_{\parallel} = 181.7, A_{\perp} = 123.2$ Si(2-4): $C_{1h}, \beta = 5^{\circ}, A_x = 140.3,$ $A_y = 103.4, A_z = 106.7$
	$C_{1h}$	
	$g_x = 2.0026, g_y = 2.0042$	Si(1): $C_{1h}, \beta = 62^{\circ}, A_x = 179.3,$ $A_y = 112.7, A_z = 128.3$
	$g_z = 2.0053, \alpha = 65^{\circ}$	Si(2-4): $C_{1h}, \beta = 64^{\circ}, A_x = 94.4,$ $A_y = 116.9, A_z = 115.7$

HF parameters of the center in  $C_{3v}$  and  $C_{1h}$  symmetry are summarized in Table 1.

Based on the ligand HF structure, the symmetry and the observation in  $p$ -type irradiated material, the EI5 center was identified as the isolated carbon vacancy in the positive charge state ( $V_C^+$ ) [46, 47]. At the same time, Bratus et al. [48] also came to the same conclusion about the Ky2 center in  $6H$ -SiC, which is identical to EI5. In a later study, Bratus et al. [49] assigned also the Ky1 and Ky3 (identical to the EI6 signal) to  $V_C^+$  at the other cubic site and hexagonal site, respectively, in  $6H$ -SiC.

Preliminary annealing studies [47] seem to indicate that the EI5 center is annealed out at  $\sim 450$ – $500^{\circ}\text{C}$  in agreement with results by Ling et al. [97]. However, our recent studies [98] show that the EI5 signal in irradiated  $4H$ -SiC can still be clearly detected after annealing at  $\sim 1600^{\circ}\text{C}$ .

The T5 center in  $3C$ -SiC has been assigned to  $V_C^+$  [31]. However, the T5 center has very different properties compared to the EI5 center in the hexagonal polytype. The EI5 center has ligand HF constants of about two times larger than that of the T5 center and is thermally stable at much higher temperatures. Son et al. [46] and Aradi et al. [99] suggested the T5 center to be a hydrogen-related defect, but no experimental evidence of the

H involvement in the center has so far been observed. Recent calculations of the ligand HF of  $V_C^+$  in 3C-SiC and at the cubic site of 4H-SiC [100]–[102] are in close agreement with the values for the EI5 center, supporting the identification of the center as  $V_C^+$  at the  $k$ -site in 4H-SiC. The calculations in [100]–[102] also predict the  $D_{2d}$  symmetry for  $V_C^+$  in 3C-SiC, which is higher than the  $D_2$  symmetry of the T5 center.

Zvanut et al. [103] have carried out photo-excitation EPR (photo-EPR) experiments in semi-insulating 4H-SiC substrates and determined the energy level of the ID center, which is identical to the EI5 center or  $V_C^+$ , at  $E_V + 1.1$  eV. Recently, high-frequency photo-EPR studies of heavily irradiated 4H-SiC revealed the (+/0) level of  $V_C$  to be at  $(1.47 \pm 0.06)$  eV above  $E_V$  [104]. We believe that the energy level determined in [102] is incorrect due to the charge transfer processes via the levels of the B acceptor and N donor as pointed out in [104]. The value of 1.47 eV is close to the ionization levels of the  $V_C$  in 4H-SiC calculated by Zywiec et al. [28] ( $E_V + 1.37$  eV and  $E_V + 1.44$  eV for the center at  $k$ - and  $h$ -site, respectively) and by Torpo et al. [29] (corresponding values: 1.41 eV and 1.53 eV). Recent calculations by Gali et al. [102] give a value of  $E_V + 1.57$  eV for the center at the  $k$ -site.

## 2.2 Silicon Antisite Related Defect

The EI6 spectra measured at X-band and W-band frequencies are shown in Figs. 1a and b, respectively (in Sect. 2.1). The main line is accompanied by two satellites, which result from the HF interaction with one  $^{29}\text{Si}$  atom (indicated by dashed arrows). Due to a severe overlapping between the EI6 and EI5 spectra, the HF structure of other close Si neighbours could not be observed. Figure 2 shows the EI6 spectra in 4H-SiC measured at 23 K. The HF structure from the interaction with four NN Si atoms can be detected

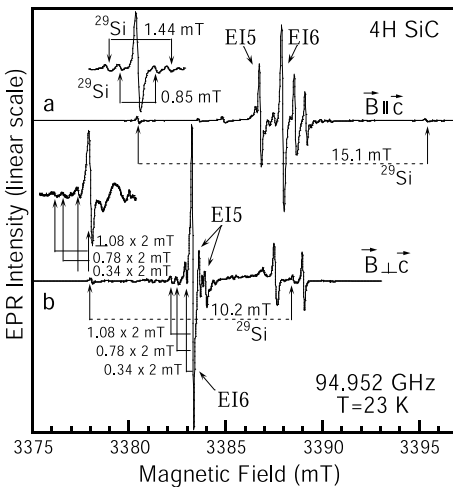


**Fig. 2.** EPR spectra of the EI6 center in 4H-SiC measured at 23 K for **(a)** along and **(b)** perpendicular to the  $c$ -axis. Two lines at high magnetic field belong to unidentified defects. The *inserts* show the  $^{29}\text{Si}$  HF structures observed at the low-field HF line for  $\mathbf{B}$  long and perpendicular to the  $c$ -axis

**Table 2.** Spin-Hamiltonian parameters for the EI6 center in 4*H*- and 6*H*-SiC (from [55] and only data of the large splitting HF of the Si with  $C_{3v}$  symmetry are given)

Polytype	$T$ [K]	$g_{\parallel}$	$g_{\perp}$	$A_{\parallel}$ [MHz]	$A_{\perp}$ [MHz]
4 <i>H</i> -SiC	138	2.0030	2.0047	370	254
	23	2.0024	2.0049	423	288
6 <i>H</i> -SiC	102	2.0029	2.0048	403	275
	23	2.0024	2.0049	440	302

at the HF line as shown in the insert of Fig. 2a. The splitting between the inner lines is 0.85 mT. At  $\mathbf{B}$  perpendicular to the  $c$ -axis, the EI5 lines appear at higher magnetic fields and therefore the low-field side of the HF structure of the EI6 line can be observed. This structure is similar to that observed at the HF line as can be seen in the insert of Fig. 2b. At this angle, the splitting of the inner lines reduces to  $\sim 0.34 \times 2 \text{ mT} = 0.68 \text{ mT}$ . In 6*H*-SiC, the corresponding splitting values are  $\sim 0.86 \text{ mT}$  and  $\sim 0.68 \text{ mT}$  for  $\mathbf{B}$  along and perpendicular to the  $c$ -axis, respectively. The splitting of the inner HF lines is anisotropic and seems to be too large for the interaction with the 12 C atoms in the NNN shell, which is usually isotropic and less than 0.4 mT (0.38 mT in the case of the EI5 center). The HF structure of the EI6 center can be identified as being due to the HF interaction with five Si atoms, of which four are the nearest neighbours. The angular dependence of the main line and large-splitting HF lines are shown to have  $C_{3v}$  symmetry at any temperature. The  $g$ -values and HF constants of the center are summarized in Table 2.

Both the  $g$ -values and HF constants are strongly temperature dependent [55] similar to the case of  $\text{Mn}^{2+}$  in MgO [105], II-VI compounds [106], and HgSe [107], and antisites in III-V compounds [108]. Based on the HF interaction with five Si atoms and the  $C_{3v}$  symmetry, Son et al. [55] proposed the model of  $\text{Si}_C^+$  for the EI6 center with a large spin density ( $\sim 46.5\%$  at 23 K) on the Si antisite. Bratus et al. [49] assigned the inner HF lines (with the splitting of 0.68 mT) to the HF interaction with 12 C in the NNN shell and suggested that the Ky3 signal in 6*H*-SiC (identical to the EI6 signal) is the  $V_C^+$  at the  $h$ -site. Later calculations [100]–[102] of  $V_C^+$  at the  $h$ -site obtained a HF constant of the interaction with one Si along the  $c$ -axis rather close to the HF value of the Si antisite EI6 center, supporting the latter identification [49]. We also observed the same HF structure at  $\sim 9 \text{ GHz}$  as in [49], but the spectrum measured at 95 GHz is different. As can be seen in Fig. 2b, there are two equal intensity satellites with splitting of  $0.78 \times 2 \text{ mT}$  and  $1.08 \times 2 \text{ mT}$ . If these lines are due to HF interaction with 3 Si atoms as suggested in [49], then the intensity of the line at  $0.78 \times 2 \text{ mT}$ , which corresponds to the interaction with two equivalent Si atoms, should be double compared to that of the outer line (corresponding to the interaction with one

Si atom in the rotating plane). The HF structure observed at  $\sim 95$  GHz is more reliable compared to that detected at  $\sim 9$  GHz, which overlaps with other EPR signals. The unusual large and anisotropic splitting attributed to the HF from 12 C atoms in the NNN shell is also difficult to understand. Recently, Bockstedte et al. [109] suggested a model of ( $V_C + Si_C$ ) pair to explain the HF structure of the EI6 center. The model gives close values of the HF constant of the EI6 center, but can not explain  $C_{3v}$  symmetry. Further detailed experimental data on the ligand HF structure of the center is required for clarifying this issue.

### 2.3 Other EPR Centers in Irradiated *p*-Type SiC

Figures 3a and b show EPR spectra observed at X-band frequencies in *p*-type 6*H*-SiC irradiated with electrons. The EI1 spectrum was first detected by Cha et al. in 6*H*-SiC and labelled as PB center [42]. The same spectra were also detected in 4*H*-SiC [43, 44, 46]. Both centers have  $C_{1h}$  symmetry. The EI1 center has spin  $S = 1/2$  and its HF structure due to the interaction with two nearest Si neighbours has been detected for 4*H*- and 6*H*-SiC [46]. The Si HF and also the HF structure of 12 C atoms in the NNN shell can be clearly observed at W-band frequencies (Fig. 3c). These HF structures indicate the EI1 to be a defect at a C site.

The EI3 center has spin  $S = 1$  and shows HF interaction with four nearest Si neighbours [43, 44]. The spin-Hamiltonian parameters of these two centers are given in Table 3. The annealing of these two centers in 6*H*-SiC is shown to be similar to that of the T5 center in 3*C*-SiC [31]. Therefore, Cha et al. [42] assigned the PB center to  $V_C^+$  although it shows a HF interaction with only two nearest Si neighbours.

Later on isochronal annealing studies in 6*H*-SiC [46] showed that the annealing of the EI1 and EI3 signals is accompanied by the appearance of

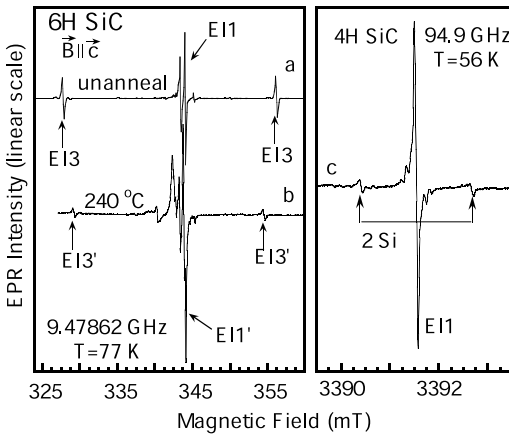


**Fig. 3.** EPR spectra observed in irradiated 6*H*-SiC (a) before and (b) after annealing at 240°C. (c) The HF structure due to interaction with two nearest Si neighbours of the EI1 spectrum in 4*H*-SiC measured at W-band frequencies

**Table 3.** Spin-Hamiltonian parameters of some EPR centers in electron-irradiated *p*-type 4*H*- and 6*H*-SiC.  $\alpha$  and  $\beta$  are the angles between the *c*-axis and the principal *z*-axis of the *g*- and *A*-tensor, respectively. Data are from [46] (for EI1, EI1', EI3, and EI3' centers) [111] (for the EI4 center) and [45] (for the I, II, and III spectra)

Center	Spin	Polytype	$g_x$	$g_y$	$g_z$	$\alpha$	$A$ [MHz] $D$ & $E$ [ $10^{-4}$ cm $^{-1}$ ]
EI1	$S=1/2$	4 <i>H</i> , 6 <i>H</i>	1.9962	2.0019	2.0015	41°	HF with 2 Si atoms, $A_x^{(1)}=57$ , $A_y^{(1)}=70$ , $A_z^{(1)}=68$ $A_x^{(2)}=70$ , $A_y^{(2)}=86$ , $A_z^{(2)}=61$ $\beta^{(1)}=\beta^{(2)}=41^\circ$
EI1'	$S=1/2$	6 <i>H</i>	1.9954	2.0013	2.0014	33°	HF with 2 Si atoms
EI3	$S=1$	4 <i>H</i> , 6 <i>H</i>	2.0063	2.0063	2.0063	46°	HF with 4 Si atoms 4 <i>H</i> : $D=552$ ; 6 <i>H</i> : $D=559$
EI3'	$S=1$	6 <i>H</i>	2.0063	2.0063	2.0063	46°	HF with 4 Si atoms $D=538$
EI4	$S=1$	4 <i>H</i> , 6 <i>H</i>	2.0051	2.0038	2.0029	54°	HF with 4 Si atoms 4 <i>H</i> : $D=344$ ; $E=67$ 6 <i>H</i> : $D=328$ ; $E=67$
I	$S=1/2$	4 <i>H</i>	2.0162	2.0035	2.0412	63°	
		6 <i>H</i>	2.0161	2.0061	2.0407	63°	
II	$S=1/2$	4 <i>H</i>	2.0144	2.0029	2.0337	50°	
		6 <i>H</i>	2.0139	2.0048	2.0323	50°	
III	$S=1/2$	6 <i>H</i>	2.0075	2.0021	2.0452	65.7°	

two new spectra, labelled EI1' and EI3' (Fig. 3b). In some samples, EI1' is already present before annealing together with the EI1 signal, but very weak. The EI3' signal only appears at annealing temperatures around 200°C. The EI1' and EI3' centers are very similar to EI1 and EI3, respectively. The principal *g*-values of the EI1' center are slightly different from that of EI1 (see Table 3) and the angle between the principal  $g_z$  and the *c*-axis is 33° (41° in the case of the EI1). Both centers have a similar HF interaction with two of the four nearest Si neighbours. The *g*-values and the direction of the principal axis of the fine-structure tensor *D* are the same for both the EI3 and EI3' centers, but the *D*-value of EI3' center is smaller (Table 3).

Based on the annealing behaviour and the similarity in the spin-Hamiltonian parameters, the EI1 and EI1' centers were assigned to two different configurations of the same defect [46]. Similarly, the EI3 and EI3' spectra are suggested to originate from different configurations of the same center. The involvement of H in the centers was suggested to explain the annealing of these centers at low temperatures [46]. Based on calculations in 3*C*- and 4*H*-SiC, Aradi et al. [99] proposed the model of *V<sub>C</sub>*-hydrogen complexes to explain the electronic structure of these centers. However, recently more accurate calculations of HF constants [102] predicted that the dipole-dipole

HF interaction between the  $p$ -lobe of Si dangling bonds and the spin of the hydrogen nuclei should be large enough to result in a HF splitting detectable by EPR. However, no H-related HF splitting has been detected (the typical line width of both the EI1 and EI3 spectra is only about 1 G). Therefore, the T5, EI1 and EI3 centers cannot be assigned to  $V_C$ -hydrogen complexes. Recently, the split-carbon interstitial model has been suggested for the centers [102, 109, 110]. The model accounts well for both the ligand HF structure and annealing behaviour of the defects (see other review on the theoretical studies in this book). So far, the HF structure of the C interstitial has not been experimentally detected.

In  $p$ -type 4H- and 6H-SiC irradiated with 2.5 MeV electrons at  $\sim 400^\circ\text{C}$  (or subsequent annealing at  $400^\circ\text{C}$  after irradiation), a weak signal, labelled EI4, is often observed besides the EI5 and EI6 spectra (see Fig. 1a and Fig. 4). The HF structure due to the interaction with four nearest Si neighbours can be seen in the insert of Fig. 4. The EI4 center has  $C_{1h}$  symmetry and a spin  $S = 1$ . The  $g$ -values and fine structure parameters  $D$  and  $E$  described the trigonal and orthorhombic crystal fields, respectively, are summarized in Table 3. The principal  $z$ -axis of the  $D$ -tensor lies in the  $(11\bar{2}0)$  plane and inclines an angle of  $54^\circ$  with the  $c$ -axis [111]. From the  $g$ -values and fine structure parameters, it is likely that the EI4 center is identical to the P4 center in  $n$ -type 6H-SiC [23]. However, the HF splitting of the P4 center is isotropic ( $\sim 1.8$  mT, corresponding to a HF constant of  $A = 6 \times 10^{-4} \text{ cm}^{-1}$ , see [23]), which is different from that observed for the EI4 center ( $\sim 1.13$  mT). The P4 center was observed in  $n$ -type material under optical excitation and attributed to the  $(V_C^- - V_C^-)$  pair with both vacancies lying in the  $(11\bar{2}0)$  or equivalent planes [23]. The EI4 signal was detected in  $p$ -type material together with the  $V_C^+$  spectrum without light illumination. This indicates that the charge state of the EI4 center is positive. The center is therefore identified as the  $(V_C^+ - V_C^+)$  pair [111].

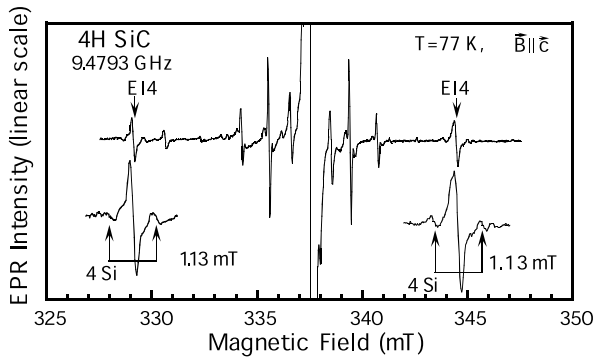


**Fig. 4.** The EI4 spectrum in  $p$ -type, electron-irradiated 4H-SiC. The *inserts* show the HF structure due to the interaction with four nearest Si neighbours

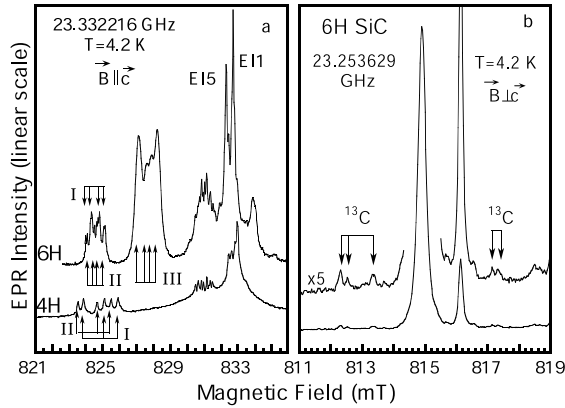


**Fig. 5.** EPR spectra observed in *p*-type, electron-irradiated 4*H*- and 6*H*-SiC (a) for  $B$  parallel to the  $c$ -axis and (b) in 6*H*-SiC for  $B$  perpendicular to the  $c$ -axis

Figure 5a shows three (I, II, and III) and two (I and II) low-symmetry spectra in *p*-type electron-irradiated 6*H*- and 4*H*-SiC, respectively. The spectra in 6*H*-SiC have been observed before by Cha et al. [42] (PC1, PC2 and PD centers). All the spectra have  $C_{1h}$  symmetry and spin  $S = 1/2$  [42, 45]. In both polytypes, the signals I and II are weak and no HF structure could be detected. Spectrum III in 6*H*-SiC appears to be more intense at some angles and the HF structure due to the interaction with four nearest C neighbours could be detected (Fig. 5b). The parameters of the centers are given in Table 3. In 4*H*- and 6*H*-SiC samples irradiated with different doses, the spectra I, II and III always appear together with similar intensity ratios and line shapes. These centers have similar temperature dependence and annealing behaviour. The parameters of the center in both polytypes are very similar. Therefore, it is suggested that these spectra belong to the same defect. The spectra I and II may correspond to the defect occupying the quasi-cubic and hexagonal sites, respectively, whereas the spectrum III originates from the same defect occupying the other cubic site of the 6*H*-SiC lattice. The spectra were found to be partially quenched after keeping the samples at room temperature for a few weeks [45]. These signals gradually decrease with increasing annealing temperature and disappear at around 700°C, which is close to the annealed-out temperature of the silicon vacancy. The observed C-ligand HF for spectrum III in 6*H*-SiC also suggests the defect to be located at a Si site. Combined with the annealing behaviour, a model of a pair defect between the Si vacancy and possibly an interstitial was suggested [45].

## 2.4 Si Vacancy Related Centers

Figure 6a shows a PL band in the near-infrared spectral region observed in electron-irradiated 4*H*- and 6*H*-SiC. At low temperatures (1.6 K), it consists

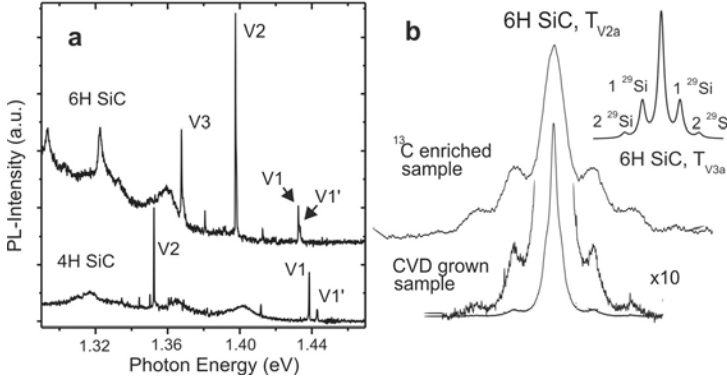


**Fig. 6.** (a) PL spectra in electron-irradiated 6H-SiC (*upper curve*,  $T = 10$  K) and 4H-SiC (*lower curve*,  $T = 34$  K). The luminescence was detected through the edge of the samples. (b) A part of the ODMR spectrum of a triplet in CVD-grown (*lower curve*) and  $^{13}\text{C}$  enriched (*upper curve*) 6H-SiC irradiated with electrons. In both samples, the HF structure due to interaction with four NN C atoms is detected. The *insert* shows the HF structure of 12 Si atoms in the next nearest neighbour shell

of 2 NP lines in 4H-SiC at 1.438 eV (labelled V1) and 1.352 eV (V2), and three NP lines in 6H-SiC at 1.433 eV (V1), 1.398 eV (V2), and 1.368 eV (V3). At elevated temperatures, additional lines, labelled V1', appear at slightly higher energies than V1 in both polytypes. This PL band has been studied in as-grown 6H- and 15R-SiC before [66, 67]. The number of NP lines corresponds to the number of inequivalent lattice sites (2, 3, and 5 in 4H-, 6H-, and 15R-SiC, respectively). Extensive doping studies [67] indicated that the center is not related to impurities. ODMR signals typical for a spin-triplet configuration (labelled  $T_{V_{ia}}$  with  $i = 1, 2, 3$  corresponding to the index of NP lines) were observed by Sörman et al. [70] upon resonant excitation of the NP lines. The defect associated with these triplet states has  $C_{3v}$  symmetry. The C-ligand HF structure of the triplet  $T_{V_{2a}}$  in  $^{13}\text{C}$  enriched and CVD-grown 6H-SiC samples irradiated with electrons observed by ODMR [73] are shown in Fig. 6b. The obtained HF structure due to the interaction with 12 Si atoms in the NNN shell (see the insert of Fig. 6b) suggests that the defect occupies a Si lattice site. HF interaction with four nearest C neighbours was detected [23, 73, 76] and the complete ligand HF tensors have been determined [73, 76]. The spin-Hamiltonian parameters for these triplets in 4H- and 6H-SiC are summarized in Table 4.

The centers have been observed by EPR before and were attributed to long-distance vacancy pairs (the P3 and P5 centers in [23]). Later, ODMR and EPR studies [69]–[76] suggested these triplets to be related to a single Si vacancy. The model of  $V_{\text{Si}}^0$  has been proposed to account for the spin  $S = 1$  of the center [70]–[73]. The triplet is suggested to be the ground state

**Table 4.** Spin-Hamiltonian parameters for the triplets of the Si vacancy in  $4H$ - and  $6H$ -SiC. The ligand hyperfine constants  $A^{(1)}$  and  $A^{(2-4)}$  given in MHz for the C atom along the  $c$ -axis and other three C atoms in the basal plane, respectively

Poly- type	Center	$g_{\parallel}$	$g_{\perp}$	$A_{\parallel}^{(1)}$	$A_{\perp}^{(1)}$	$A_{\parallel}^{(2-4)}$	$A_{\perp}^{(2-4)}$	$D$ [ $10^{-4} \text{ cm}^{-1}$ ]	Ref.
$4H$	$T_{V1a}$	2.0035	2.0037	164	71	180	72	1.4	[70, 73]
$4H$	$T_{V2a}$	2.0035	2.0038	190	80	173	67	23.2	[70, 73]
$4H$	$V_{Si}^{-}$	2.0034	2.0034	184	78	184	78		[25]
$6H$	$T_{V1a}$	2.0037	2.0038	164	73	184	69	9.2	[70, 73]
$6H$	$T_{V2a}$	2.004	2.004	184	86	184	71	42.8	[70, 73]
$6H$	P3	2.0026	2.0031	182	76	182	76	-43	[23]
$6H$	$T_{V3a}$	2.004	2.004	184	68	$A_z=171$	$A_x=86,$ $A_y=61$	9.2	[70, 73]
$6H$	P5	2.0026	2.0031	182	76	182	76	-9	[23]
$6H$	$V_{Si}^{-}$	2.0015	2.0015	184	67	184	74		[26]

for the defect [69, 70], in agreement with calculations [27, 28]. The observation of the centers by EPR at 4 K [74, 75] and the temperature dependent studies [76] also confirm the triplet ground state of the centers. Contrary to that, calculations including many-particle treatment [112] predict the singlet ground state for  $V_{Si}^0$ , and hence, the center should not be detected by EPR. In magneto-optical studies by Wagner et al. [71] no splitting of any NP lines under magnetic field (5T) could be observed, indicating that both the ground and excited state of the PL transitions are singlet states.

The observed Si-ligand HF structure seems to indicate that the triplet states are related to the single isolated Si vacancy. However, the charge state of the centers is still under debate. In recent magnetic circular dichroism absorption (MCDA) studies of neutron- and electron-irradiated  $6H$ - and  $15R$ -SiC, Lingner et al. [114] observed two lines in  $6H$ -SiC and three lines in  $15R$ -SiC. The energy positions of these lines coincide with that of the V1 and V3 lines corresponding to two cubic sites in  $6H$ -SiC and three NP lines related to cubic sites in  $15R$ -SiC. No MCDA line at the expected energy positions of the NP lines corresponding to the hexagonal lattice sites (the V2 line in  $6H$ -SiC and the two NL lines in  $15R$ -SiC) could be seen. MCDA-detected EPR (MCDA-EPR) spectra measured on each MCDA line consist of only one line, suggesting a spin  $S = 1/2$  for the ground state of the centers [113]. Based on theoretical predictions [27] the charge state  $-3$  was proposed for the ground state of the Si vacancy to explain the spin  $S = 1/2$  and the optical transition in the 1.4 eV range [113]. Using nutation method of pulse EPR technique, Mizuochi et al. [76] determine the spin  $S = 3/2$  for the center and conclude that the  $T_{V2a}$  center is  $V_{Si}^{-}$  being distorted to  $C_{3v}$  symmetry. Thus,

there are three different models with different charge states, neutral [68]–[73], single negative [76], and triple negative [113], were proposed for the center. However, none of these can explain the PL and Zeeman results [71]. A full understanding of the electronic structure of the defect calls for indepth theoretical studies.

## 2.5 ( $V_C$ - $C_{Si}$ ) Center

Neutron-irradiated 6H-SiC which was annealed at 1000°C shows intense  $S = 1$  triplet spectra in conventional EPR. Such spectra were known for a long time [23] and also partly observed in PL-EPR [57], but only recently they have been measured and analysed completely [59, 114]. They can be detected upon illumination of the samples with light of energy of about 1.1 eV as photo-EPR spectra. The spectra consist of six spin triplet systems with three having fine structure axes parallel to the  $c$ -axis (P6a, b, c) and three having their fine structure axes at about 70° off the  $c$ -axis parallel to a nearest-neighbour connection line (P7a, b, c). MCDA lines corresponding to these triplets are shown in Fig. 7. Table 2 collects the EPR spin-Hamiltonian parameters. The letters a, b, c denote three different spectra in each orientation, which are believed to arise from the defect at three inequivalent lattice sites in 6H-SiC. The P6/P7 spectra are present in irradiated samples after annealing at  $\sim 600^\circ\text{C}$  when the Si vacancy starts annealing out. The signal intensities reach a maximum at an annealing temperature of  $\sim 1100^\circ\text{C}$  and then decrease. These spectra were also observed in  $n$ -type commercial substrates [57].

At each of these MCDA lines, a single  $S = 1$  EPR spectrum from Table 5 was detectable with MCDA-EPR. Figure 8 shows, as an example, the HF structure of the low-field line of spectrum P6c for  $\mathbf{B}$  along the  $c$ -axis. The HF splitting shows the presence of one single  $^{13}\text{C}$  nucleus ( $A = 48$  MHz, intensity of one HF line  $(0.7 \pm 0.2)\%$  of the central line) and four to eight  $^{29}\text{Si}$  neighbours ( $A = 12$  MHz, intensity  $(15 \pm 5)\%$  of the central line). The  $^{29}\text{Si}$  related HF lines are broadened and may contain contributions from different

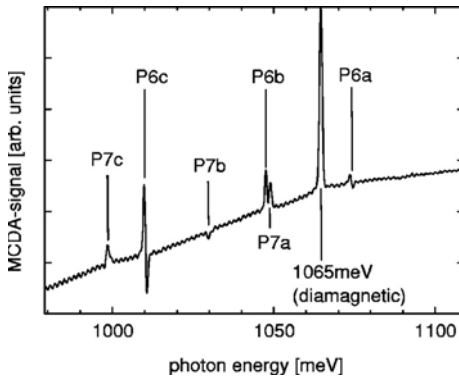


**Fig. 7.** The MCDA spectrum observed in neutron-irradiated 6H-SiC annealed at 1000°C for the magnetic field ( $B = 2$  T) directed at an angle  $\theta = 25^\circ$  off the  $c$ -axis. The sample was, in addition, excited with visible laser light

**Table 5.** EPR parameters, angle  $\theta$  between the principal axis of the fine structure tensor and the  $c$ -axis, and optical transition energies of the P6/P7 centers in 6H-SiC. The notation P6 and P7 for the axial ( $\theta = 0^\circ$ ) and the basal ( $\theta \approx 71^\circ$ ) orientations is adopted from [23]

Center	$g$	$D$ [ $10^{-4} \text{ cm}^{-1}$ ]	$E$ [ $10^{-4} \text{ cm}^{-1}$ ]	$\theta$ [deg]	$h\nu$ [meV]
P6a	2.003	456	0	0	1075
P6b	2.003	447	0	0	1048
P6c	2.003	430	0	0	1011
P7a	2.003	449	-4	71.2	1049
P7b	2.003	441	46	70.0	1030
P7c	2.003	416	-1	70.5	999

Si neighbour shells with similar HF interactions. The presence of one  $^{13}\text{C}$  nucleus with HF interaction points to a C antisite-vacancy pair defect.

Calculations [59, 115] show among different kinds of paired defects (antisite pairs, vacancy pairs and antisite-vacancy pairs) only the  $(\text{C}_{\text{Si}}-\text{V}_{\text{C}})$  pair in the +2 and the 0 charge states can explain the P6/P7 excited triplet spectra. Calculations by Rauls et al. [115] show that the formation energy of  $(\text{C}_{\text{Si}}-\text{V}_{\text{C}})$  is lower than that of the  $\text{V}_{\text{Si}}$  for most charge states. The resulting  $(\text{C}_{\text{Si}}-\text{V}_{\text{C}})$  structure is, by 1.67 eV, more favourable than the Si vacancy [116]. It turns out, in addition, that at all positions of the Fermi level the formation energy of the  $(\text{C}_{\text{Si}}-\text{V}_{\text{C}})$  pair is  $\sim 0.6$  eV lower than the sum of the formation energies of the isolated  $\text{C}_{\text{Si}}$  and the isolated  $\text{V}_{\text{C}}$ . The migration barrier for the dissociation was calculated to exceed 4.5 eV. Thus the pair is expected to be stable against dissociation into its components.

In  $C_{3v}$  symmetry, the  $(\text{C}_{\text{Si}}-\text{V}_{\text{C}})$  pair in the doubly positive charge state has a resonant  $a_1(s)$  level about 0.8 eV below the valence band maximum

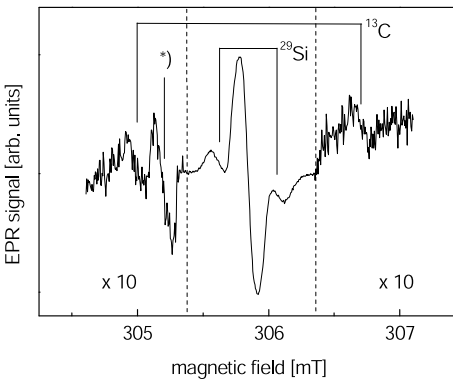


**Fig. 8.** Hyperfine structure of the P6c low-field line for  $\mathbf{B} \parallel \mathbf{c}$ . The line marked with an asterisk belongs to a different defect

(VBM) and a corresponding antibonding resonant state  $a_1^*(s)$  at 4.5 eV above VBM [59]. In addition,  $p$ -like  $a_1(p)$  level and an  $e(p)$  level are located in the band gap. The ground state of  $(C_{Si}-V_C)^{2+}$  is a singlet  $^1A_1(a_1(s) \uparrow\downarrow)$  in which two electrons with antiparallel spin occupy the  $a_1(s)$  level in the valence gap. Photon energies above 1.15 eV (1.1 eV in experiment) can excite one electron from the  $a_1(s)$  level into the  $a_1(p)$  level, forming the  $^1A_2(a_1(s) \uparrow a_1(p) \downarrow)$  state. A non-radiative transition to the energetically lower metastable triplet state  $^3A_2(a_1(s) \uparrow a_1(p) \uparrow)$  is possible with the help of phonons. This  $^3A_2$  state gives rise to the observed P6/P7 spectra. The MCDA is explained by the excitation of the  $a_1(p)$  electron into the  $e(p)$  state ( $a_1(s) \uparrow e(p) \uparrow$ ). The calculated photon energy of 1.52 eV is in reasonable agreement with the experimental value ( $\sim 1.1$  eV). A similar excitation scheme is possible for the neutral charge state of the pair, but in this case the  $e(p)$  state is occupied in the metastable triplet state  $^3E(a_1(s) \uparrow a_1(p) \downarrow e(p) \uparrow)$  and gives rise to a large HF interaction of about 180 MHz with the Si neighbours of  $V_C$  which was not observed. The calculations [59] of HF constants suggests the  $(C_{Si}-V_C)^{2+}$  model for the center.

The  $(C_{Si}-V_C)$  pair is electrically and optically active although diamagnetic in its ground state. It has a charge transfer level just above midgap. Thus at least a second anneal step is required to remove the electrical activity of silicon-vacancy-related defects.

## 2.6 Neutral $Cr^{4+}$ Center

In a series of  $4H$ - and  $6H$ -SiC epitaxial layers doped with Cr during high-temperature chemical vapour deposition (HTCVD) growth, Son et al. [117, 118] observed a near-infrared PL spectrum consisting of two and three NP lines in  $4H$ - and  $6H$ -SiC, respectively (Fig. 9). These NP lines were observed before by Gorban and Slobodyanyuk [119] in  $6H$ -SiC, but without identification. A good correlation between this PL band and the concentration of Cr measured by secondary ion mass spectrometry (SIMS) has been observed [118], confirming the involvement of Cr in the center. Three NP lines in  $6H$ -SiC labelled  $Cr_A$ ,  $Cr_B$  and  $Cr_C$ , are located at 1.1556 eV, 1.1797 eV and 1.1886 eV, respectively. In  $4H$ -SiC, the two NP lines at 1.1583 eV and 1.1898 eV are labelled  $Cr_A$  and  $Cr_C$ , respectively. In CVD layers grown on on-axis  $6H$ -SiC substrates with inclusion of  $3C$ -SiC islands, an additional NP line at 1.1752 eV corresponding to one cubic site in the  $3C$  polytype was also detected [120]. Zeeman measurements were performed on all NP lines and also some of the LP replicas [118]. In both polytypes, each of the  $Cr_A$  and  $Cr_C$  NP lines splits into a triplet for  $\mathbf{B}$  parallel to the  $c$ -axis. For  $\mathbf{B}$  perpendicular to the  $c$ -axis, an additional doublet splitting was detected for each triplet component. For the  $Cr_B$  line in  $6H$ -SiC, only triplet splitting has been detected. The triplet splitting is similar for all the lines with  $g$ -values close to 2 and small zero crystal-field splitting, whereas the doublet splitting

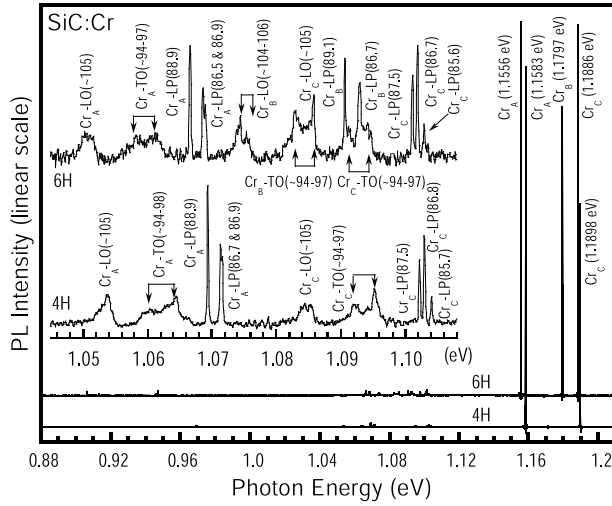


**Fig. 9.** Near-infrared Fourier-transform PL spectra observed in 4H- and 6H-SiC HTCVD layers doped with Cr. Their weak phonon bands are shown in details in the insert. The energies of the lattice (TO and LO) and local phonon (LP) replicas are given in meV in the bracket. The resolution is about 0.12 meV

is very small and anisotropic ( $g_{\perp} = 0$ ,  $g_{\parallel}$  about 0.22–0.26 and 0.62–0.64 for  $\text{Cr}_A$  and  $\text{Cr}_C$  lines, respectively, and  $g = 0$  for the  $\text{Cr}_B$  line).

Temperature dependence studies of the Zeeman components in the range (1.6–40) K suggested that the doublet splitting occurs in the excited state and the ground state is a spin-triplet ( $S = 1$ ). Spin-Hamiltonian parameters of the Cr-related center are given in Table 6. From the splitting pattern and the similarity of NP lines in the two polytypes, the  $\text{Cr}_A$  and  $\text{Cr}_C$  lines are attributed to Cr at the quasi-cubic and hexagonal site, respectively, and the  $\text{Cr}_B$  line corresponds to Cr at the other cubic site in 6H-SiC.

Among the different electronic configurations of Cr, only the  $d^2$  configuration ( $\text{Cr}^{4+}$ ) can provide such a ground-state triplet with the  $^3A_2(F)$  multiplet. According to the Tanabe-Sugano diagram of crystal field states of the  $d^2$  electronic configuration [121], the first excited state will be either the triplet  $^3T_2(F)$  or the singlet  $^1E(D)$ , depending on the crystal field strength. For  $\text{Cr}^{4+}$  in hexagonal SiC, the crystal field may reach the value, where the  $^1E(D)$  state lies below the  $^3T_2(F)$  state, being the first excited state. The Cr-related PL lines are attributed to the  $^1E(D) \rightarrow ^3A_2(F)$  transitions within the  $d$ -shell of the substitutional neutral  $\text{Cr}^{4+}$  in the  $d^2$  electronic configuration [118].

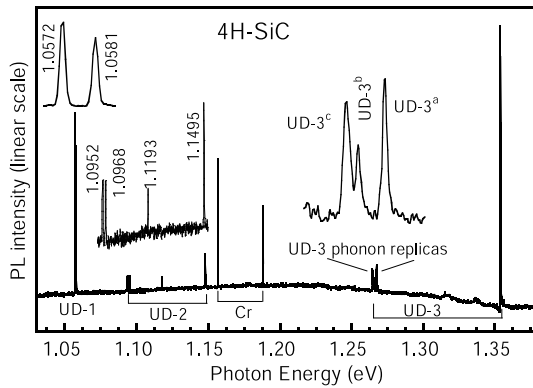
**Table 6.** Spin-Hamiltonian parameters for the triplet ground state (GS) and doublet excited state (ES) of the Cr-related NP lines in 4H and 6H-SiC. Data are from [118]

NP line [eV]	Polytype	$g_{\parallel}$	$g_{\perp}$	$D$ [cm <sup>-1</sup> ]	Remark
Cr <sub>A</sub> (1.1556)	6H	$2.01 \pm 0.02$	$2.00 \pm 0.02$	$< 0.04$	GS
	6H	$0.22 \pm 0.03$	0		ES
Cr <sub>B</sub> (1.1797)	6H	$2.00 \pm 0.02$	$2.01 \pm 0.02$	$< 0.04$	GS
	6H	0	0		ES
Cr <sub>C</sub> (1.1886)	6H	$2.02 \pm 0.02$	$1.99 \pm 0.02$	-0.18	GS
	6H	$0.62 \pm 0.03$	0		ES
Cr <sub>A</sub> (1.1583)	4H	$2.01 \pm 0.02$	$2.00 \pm 0.02$	$< 0.04$	GS
	4H	$0.26 \pm 0.03$	0		ES
Cr <sub>C</sub> (1.1898)	4H	$2.04 \pm 0.02$	$2.00 \pm 0.02$	-0.2	GS
	4H	$0.64 \pm 0.03$	0		ES

## 2.7 UD-1, UD-2 and UD-3 Centers

Many deep-level defects give rise to photoluminescence (PL) and/or absorption lines in the near infrared spectral region. In semi-insulating (SI) samples grown by HTCVD technique, traces of vanadium [3] and chromium [118] are frequently observed in PL, but there is also an additional series of lines labeled UD-1, UD-2, and UD-3 [122] as shown in Fig. 10.

The UD-1 PL band consists of two NP lines in 4H-SiC at 1.0572 eV and 1.0581 eV [123] (see Fig. 10) and three NP lines in 6H-SiC at 0.9952 eV, 1.0015 eV and 1.0020 eV [124]. The spectrum is often observed in *n*-type commercial substrates or in SI material grown by HTCVD. These NP lines can be detected at temperatures below 80 K. Zeeman studies in 6H-SiC

**Fig. 10.** Low-temperature Fourier-transform PL spectra of the UD-1, UD-2 and UD-3 center in 4H-SiC grown by HTCVD

[125] show that the low energy line corresponds to a singlet-singlet transition, whereas the other two lines are related to doublets with  $g$ -values of  $g_{\parallel} = 0$  for both and  $g_{\perp} = 1.4$  (for the 1.0015 eV line) and  $g_{\parallel} = 1.7$  (for the 1.0020 eV line). Electron irradiation reduces the signal instead of enhancing it. The signal can be recovered after annealing at high temperatures. This seems to indicate that the UD-1 center is related to impurities rather than to intrinsic defects.

The PL spectrum of the UD-2 defect in 4H-SiC is also shown in Fig. 10. It consists of four NP lines at 1.0592 eV, 1.0968 eV, 1.1193 eV and 1.1495 eV [125]. The spectrum was detected in some of the SI substrates grown by HTCVD, but the signal is usually weak. In irradiated material, the UD-2 spectrum appears after annealing at  $\sim 500^{\circ}\text{C}$  and its intensity starts increasing rapidly at  $\sim 600^{\circ}\text{C}$  when the PL band related to the neutral Si vacancy [70] begins to be annealed out. The signal keeps increasing to a maximum at  $\sim 1100^{\circ}\text{C}$  then sharply decreases and completely vanishes at  $\sim 1300^{\circ}\text{C}$  [125]. In as-grown samples, the UD-2 signal survives higher annealing temperatures but completely disappears after annealing at  $1600^{\circ}\text{C}$  for 20 minutes. A similar PL band consisting of six NP lines at 0.9983 eV, 1.0100 eV, 1.0298 eV, 1.0476 eV, 1.0484 eV and 1.0738 eV was also detected in electron-irradiated 6H-SiC after the Si vacancy has been annealed out [126]. None of the NP lines split in a magnetic field (up to 5 T). The formation conditions of the defect indicate an intrinsic origin of the center. From the annealing behaviour of the defect and the Si vacancy, the UD-2 center was suggested to be Si-vacancy related [125]. However, when the properties of the UD-2 center are compared to the recent results on MCDA and MCDA-detected EPR in 6H-SiC by Lingner et al. [58, 59], it is clear that the NP lines in 6H-SiC [126] have the same energies as the optical intracenter transitions of the P6/P7 centers. The annealing behaviour of UD-2 and the P6/P7 centers is also similar. We therefore suggest that the UD-2 PL band originated from the  $(V_{\text{C}}\text{-C}_{\text{Si}})$  pair. The transition  ${}^3E\text{-}{}^3A_2$  of the  $(V_{\text{C}}\text{-C}_{\text{Si}})$  pair [59] gives rise to the PL lines of the UD-2 center.

The UD-3 defect has a long and controversial history. When it was reported for the first time in 6H-SiC [66] it was believed to be a phonon replica of the  $a$  line in the  $abc$  defect system (now known to originate from the neutral silicon vacancy) [70] due to a sharp local phonon. Its energy difference to the  $a$  line is approximately 90 meV, therefore it was denoted as  $a_{90}$ . Hagen and Kemenade later proved that the UD-3 luminescence was not related to the  $a$  line, in their paper it is called spectrum II [67]. At the same time, Gorban and Slobodyanyuk extended their studies to the 15R polytype and found two lines there. The one line in 6H-SiC was called  $f_1$  the two lines in 15R-SiC  $f_1$  and  $f_2$ , respectively [127]. Here, we choose to adopt the most recent name UD-3 [122].

The main features of UD-3 are as follows: It gives rise to one NP line at 1.3555 eV in 4H-SiC, one line at 1.3440 eV in 6H-SiC and two NP lines

at 1.3474 eV (UD-3L) and 1.3510 eV (UD-3H) in 15*R*-SiC [128]. At the low-energy side of the NP lines, a broad phonon-assisted side band can be observed together with a series of sharp lines UD-3<sup>a</sup>, UD-3<sup>b</sup>, and UD-3<sup>c</sup> at distances between 86.6 and 89.6 meV from the NP line (Fig. 10). Similar phonon replicas can be found in PL excitation (PLE) experiments. PLE (and PL at elevated temperatures) reveals, in addition, the existence of higher-lying excited states close to the NP line of UD-3. Four such higher-lying states can be identified (UD-3<sup>I</sup>–UD-3<sup>IV</sup>). Their distances to UD-3 range from 1.9 meV for UD-3<sup>I</sup> to 8.3 meV for UD-3<sup>IV</sup> (depending only slightly on the polytype) [128].

Zeeman effect measurements indicate the symmetry of the defect is  $C_{3v}$  [128]. The ground state configuration is  $^1A_1$ , whereas the excited states have configurations  $^1E$ ,  $^1A_1$ ,  $^1A_2$ ,  $^1E$ , and  $^1A_2$ , respectively (in order of increasing energy). Such an electronic structure rules out the possibility of the luminescence originating from a bound exciton recombination. It is more likely that the emission arises from an internal transition within an inner shell of an impurity atom. The energies of the observed local phonons are remarkably similar to the ones connected with known substitutional impurities from the iron group, such as vanadium, chromium and titanium. A  $^3d_6$  configuration may explain the spin- and orbital singlet configuration of the ground state. This leaves  $[\text{Ni}]^0$ ,  $[\text{Co}]^-$ , and  $[\text{Fe}]^{2-}$  as possible candidates for UD-3. However,  $[\text{Fe}]^{2-}$  is quite unlikely, since its energetic position should be close to the conduction band edge. In the semi-insulating samples used in these studies, this charge state of the defect can hardly be populated. It should be pointed out that no direct proof has, so far, confirmed that UD-3 is indeed a simple substitutional impurity from the iron group. Therefore, other defect configurations, like a complex oriented along the *c*-axis, cannot be completely ruled out.

In 4*H*-SiC, the UD-3 defect is involved in an efficient PL up-conversion process [129]. In this process, the well-known titanium-related emission in the visible spectral region (NP lines at 2.848 eV and 2.789 eV) can efficiently be excited by resonantly tuning an IR light source (in our experiments a Ti:sapphire laser) to the energy of the NP line of UD-3 or its higher-lying excited states (Fig. 11a). PLE spectra detecting the titanium emission are identical to PLE spectra detected at UD-3 itself (Fig. 11b), proving the direct involvement of UD-3 in the up-conversion process.

There are two surprising facts about this process:

- It is a three-step process, since two times the energy of UD-3 (1.356 eV) is still (by more than 100 meV) less than the  $A_0$  line of the titanium-related emission (2.848 eV).
- This process cannot be observed in the 6*H* and 15*R* polytypes, even though they have smaller band gap energies than 4*H*-SiC, which should make the process easier to occur.

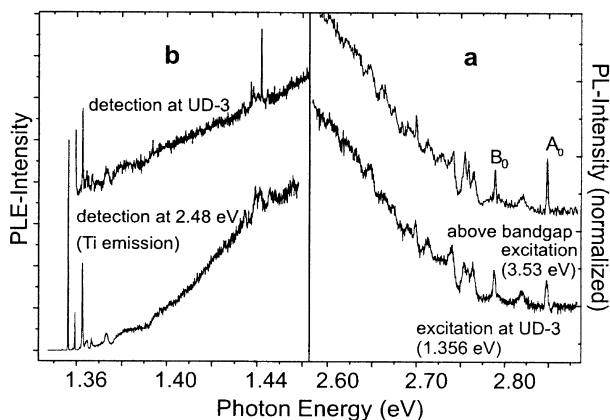


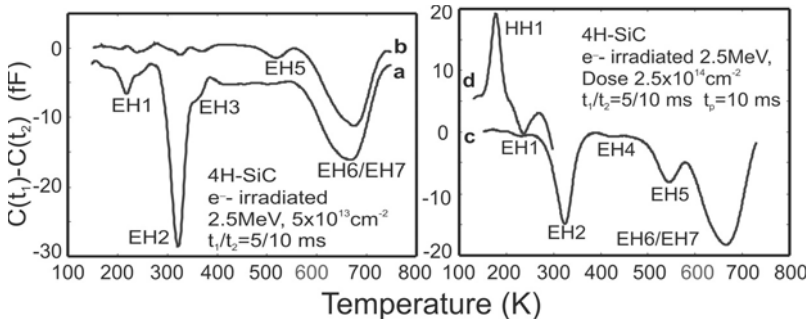
**Fig. 11.** (a) Titanium PL emission in 4H-SiC at  $T = 2$  K excited with band-gap laser light (*upper spectrum*) and excited resonantly on the NP line of UD-3 at 1.356 eV (*lower spectrum*). (b) PLE in 4H-SiC detecting the UD-3 emission at 1.356 eV ( $T = 2$  K) (*upper spectrum*) and detecting the titanium emission at 2.48 eV ( $T = 8$  K)

At this point, it is not clear whether the up-conversion process transfers electrons in three steps from the valence band to the conduction band with the titanium emission serving as the most efficient means of detecting this process or whether there is a more direct connection between the two defects, which only works in the 4H polytype. Some indications point in the latter direction.

### 3 DLTS of Intrinsic Defects

Samples used in the studies were  $n$ -type 4H- and 6H-SiC epitaxial layers grown by CVD and irradiated with 2.5 MeV electrons with doses of  $\sim 2.5 \times 10^{14} \text{ cm}^{-2}$  or higher. DLTS measurements were performed on  $p^+n$  junctions, which were made by growing an Al-doped  $p$ -type layer on top of the  $n$ -type layer [80].

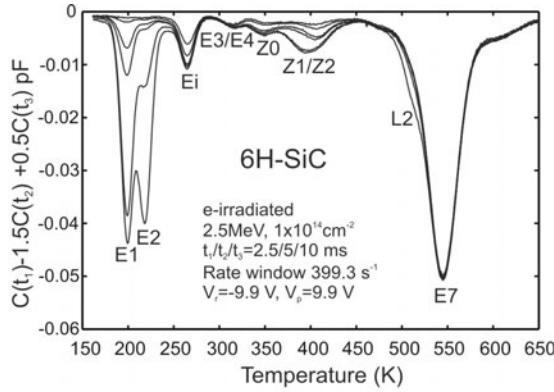
Figures 12a and b show DLTS spectra observed in 4H-SiC layers irradiated with a dose as low as  $5 \times 10^{13} \text{ cm}^{-2}$  before and after annealing. In samples irradiated with a dose of  $10^{14} \text{ cm}^{-2}$ , the weak shoulder EH3 is completely immersed in the strong EH2 signal and the EH4, EH5 peaks appear (Fig. 12c). The negative peaks indicate that the associated deep level defects are majority carrier traps, i.e. electron traps in the  $n$ -type material. In the  $p^+n$  structure, measurements with hole injection revealed a new positive peak, labelled HH1 (Fig. 12d), associated with a hole trap. The HH1 signal was observed only after the sample has been annealed during the measurement up to  $(\sim 350\text{--}400)^\circ\text{C}$  [80]. The EH2 signal was shown later to be identical to the  $Z_{1,2}$  signal. The energy position  $E_t$ , trap concentration  $N_t$ , and capture cross section  $\sigma$  for these centers are given in Table 7.



**Fig. 12.** DLTS spectrum in 4H-SiC irradiated with 2.5 MeV electrons with a dose of  $5 \times 10^{13} \text{ cm}^{-2}$  (a) before annealing and (b) after annealing at 750°C for 10 minutes, and a dose of  $2.5 \times 10^{14} \text{ cm}^{-2}$  with (c) a reverse bias of  $-9 \text{ V}$  and a pulse height of  $9 \text{ V}$ , and (d) a reverse bias of  $-9 \text{ V}$  and pulse height of  $12.5 \text{ V}$

**Table 7.** The energy position  $E_t$ , trap concentration  $N_t$ , and capture cross section  $\sigma$  for different traps observed by DLTS in 4H- and 6H-SiC irradiated with a dose of  $2.5 \times 10^{14} \text{ cm}^{-2}$ .  $\sigma_{\text{inter}}$  is estimated from the intercept of the Arrhenius plot and  $\sigma_{\text{meas}}$  is the measured value. Data for 4H and 6H polytypes are from [80] and [82], respectively

Poly-type	Trap level	$E_t$ [eV]	$N_t$ [ $\text{cm}^{-3}$ ]	$\sigma_{\text{inter}}$ [ $\text{cm}^2$ ]	$\sigma_{\text{meas}}$ [ $\text{cm}^2$ ]
4H	EH1	$E_C - 0.45$	$2.4 \times 10^{12}$	$5.0 \times 10^{-15}$	
4H	EH2( $Z_{1,2}$ )	$E_C - 0.68$	$4.1 \times 10^{13}$	$1.3 \times 10^{-14}$	$5.0 \times 10^{-17}$
4H	EH4	$E_C - 0.72$	$1.3 \times 10^{12}$	$9.3 \times 10^{-17}$	
4H	EH5	$E_C - 1.13$	$1.5 \times 10^{13}$	$3.5 \times 10^{-15}$	$1.0 \times 10^{-16}$
4H	EH6/EH7	$E_C - 1.65$	$3.9 \times 10^{13}$	$2.4 \times 10^{-13}$	
4H	HH1	$E_V + 0.35$	$1.4 \times 10^{13}$	$5.4 \times 10^{-14}$	$> 5.0 \times 10^{-15}$
6H	E1	$E_C - 0.38$	$9.5 \times 10^{13}$	$3.3 \times 10^{-15}$	$8.95 \times 10^{-16} \times \exp(-0.05/kT)$
6H	E2	$E_C - 0.44$	$8.8 \times 10^{13}$	$1.1 \times 10^{-14}$	$7.27 \times 10^{-17} \times \exp(-0.041/kT)$
6H	$E_i$	$E_C - 0.51$	$2.4 \times 10^{13}$	$3.8 \times 10^{-15}$	$2.0 \times 10^{-15}$
6H	E3/E4		$\sim 7 \times 10^{12}$		$> 1.0 \times 10^{-14}$
6H	Z0	$E_C - 0.71$	$\sim 1 \times 10^{13}$	$4.4 \times 10^{-15}$	$\sim 4 \times 10^{-16}$
6H	Z1		$\sim 9 \times 10^{12}$		$3 \times 10^{-18} < \sigma_{\text{meas}} < 3 \times 10^{-17}$
6H	Z2		$\sim 1.3 \times 10^{13}$		$\sim 4 \times 10^{-16}$
6H	E7	$E_C - 1.25$	$1.4 \times 10^{14}$	$4.7 \times 10^{-14}$	$> 9.0 \times 10^{-15}$



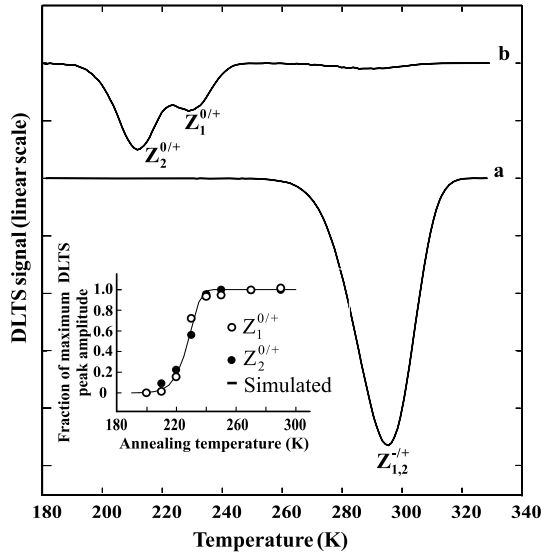
**Fig. 13.** Three-point-correlation DLTS spectra observed in electron-irradiated 6H-SiC. The pulse width was varied from 40 ns to 100  $\mu$ s

Figure 13 shows typical majority carrier DLTS spectra in  $p^+n$  junctions fabricated from  $n$ -type 6H-SiC layers irradiated with electrons measured with the pulse width varying from 40 ns to 100  $\mu$ s. The parameters for these deep levels are also given in Table 7. Some of these peaks have previously been observed [77, 81, 130, 131] but not well characterized. We will show below the negative- $U$  properties of the E1 and E2 centers in 6H-SiC and the  $Z_1$  center in 4H-SiC [78]

A defect, which has the possibility to be occupied by more than one charge carrier, has negative- $U$  properties if the binding energy of the second charge carrier is larger than that of the first one [132]. This phenomenon is observed when the gain in total energy of the defect system overcomes the Coulombic repulsion of the two charge carriers. The gain in net attraction is supplied by a local rearrangement of the lattice.

Figure 14a shows a conventional DLTS spectrum with a filling pulse width of 100  $\mu$ s measured on an as-grown sample with a high concentration of the  $Z_1$  center. Only a strong peak, labelled  $Z_{1,2}^{-/+}$ , associated with the previously reported  $Z_1$  center is observed. Using short filling pulses ( $t_p = 50$  ns) and light illumination (470 nm) before each filling pulse [85], two new peaks, labelled  $Z_1^{0/+}$  and  $Z_2^{0/+}$ , were detected (Fig. 14b). These peaks are associated with two shallower donor levels  $Z_1^0$  and  $Z_2^0$ . The relation in amplitudes of the peaks  $Z_1^{0/+}$  and  $Z_2^{0/+}$  in electron irradiated material is close to 1:1.

During each long filling pulse (100  $\mu$ s), the donor levels  $Z_1^0$  and  $Z_2^0$  may capture two electrons. The binding of the electrons is strengthened when two electrons are being captured, and consequently these centers are frozen out. With the repetitive pulses required by conventional DLTS, the one-electron emission from the donor levels will not be observed. The freeze out of the donor levels was avoided by using short filling pulse and optically emptying the levels before each filling pulse. The illumination ionizes the



**Fig. 14.** Two DLTS spectra observed in a 4H-SiC diode using pulse widths of (a) 100  $\mu$ s and (b) 50 ns with light illumination ( $\lambda \sim 470$  nm) before each filling pulse. The pulse height was 9.9 V and the reverse bias  $-9.9$  V. The reappearance of the levels  $Z_1^0$  ( $\circ$ ) and  $Z_2^0$  ( $\bullet$ ) due to annealing with bias is shown as an *inset*. The *solid curve* shows a simulation, assuming that thermal ionization of the levels  $Z_{1,2}^{0/+}$  is responsible for the reappearance of peaks  $Z_1^{0/+}$  and  $Z_2^{0/+}$ .

centers following the processes

$$Z_i^- \xrightarrow{h\nu} Z_i^0 + e^- \xrightarrow{h\nu} Z_i^+ + 2e^- \quad (i = 1, 2). \quad (1)$$

The entire optical ionization of the defects ( $Z_i^- \xrightarrow{h\nu} Z_i^+ + 2e^-$ ) was confirmed by observing the amplitude of the photo-induced capacitance transient at temperatures below the freeze out of the one-electron emission. The electron emission associated to peak  $Z_{1,2}^{-/+}$  corresponds to a two-stage ionization and the change of the net charge at the defects can be monitored via the amplitude of DLTS peaks. The sum of the amplitudes of peaks  $Z_1^{0/+}$  and  $Z_2^{0/+}$  follows closely the relation 1:2 to the amplitude of peak  $Z_{1,2}^{-/+}$ , which consists of two components corresponding to emission of two electrons from the  $Z_1^{0/+}$  and  $Z_2^{0/+}$  levels. As shown below, the  $Z_i^{-/+}$  and  $Z_i^{0/+}$  levels belong to the negative- $U$  center  $U_i$ .

Isochronal annealing with a reverse bias applied to the diode was carried out in the range (200–300) K. To assure that two electrons were captured before the annealing, the diode was heated without bias to the annealing temperature. A reverse bias of  $-9.9$  V was then applied for 5 minutes and

the sample was thereafter cooled down to 200 K with bias. The concentrations of the levels  $Z_1^0$  and  $Z_2^0$  were measured by recording the capacitance transient following a single 50 ns filling pulse and fitting two exponential transients to the biexponential transient using multiple linear regression. The reappearance of  $Z_1^0$  and  $Z_2^0$  peaks was observed at  $\sim 230$  K. A simulation assuming thermal ionization of the levels  $Z_{1,2}^-$  responsible for the reappearance gives a good agreement, as illustrated by the solid curve in the insert of Fig. 14. This confirms the relation between the  $Z_{1,2}^{-/+}$  and  $Z_1^{0/+}$  and  $Z_2^{0/+}$  levels, which belong to the centers  $U_1$  and  $U_2$ , respectively.

The thermal electron emission rates ( $e_n$ ) from the levels  $Z_1^0$  and  $Z_2^0$  were obtained from DLTS measurements. For the overlapping components  $Z_1^{-/+}$  and  $Z_2^{-/+}$  of the  $Z_{1,2}^{-/+}$  peak it was determined by fitting two exponential transients directly to the biexponential capacitance transients  $Z_{1,2}^{-/+}$  with keeping the relation in amplitudes between the two components fixed. The thermal activation energies of the electron emission processes from the levels were obtained. The values are given in Table 8.

The capturing process of the first electron to the centers seems to be very efficient since no decrease of the transient amplitudes could be detected when reducing the filling pulse width to 50 ns [85]. A large capture cross section ( $\sigma > 1 \times 10^{-14}$  cm<sup>2</sup>) was estimated for the process. The capture cross sections for capturing to the acceptor levels (i.e. of the second electron) show a weak exponential temperature dependence. Assuming a multi-phonon capturing process [133], the temperature dependent capture cross sections can be fitted

**Table 8.** The thermal activation energies  $\Delta E$ , electron binding energy  $E_i$ , and measured capture cross sections  $\sigma_{\text{meas}}$  for the different electron capturing processes. The energy range comes from the assumptions  $\sigma \propto T^{-1}$  and  $\sigma \propto T^{-3}$ , respectively. The temperature dependent capture cross sections correspond to the capture of the second electron to the centers. Data for 4H and 6H polytypes are from [85] and [86], respectively

Polytype	Level	$\Delta E$ (eV)	$E_i$ (eV)	$\sigma_{\text{meas}}$ (cm <sup>2</sup> )
4H	$Z_1^0$	0.52	0.50–0.54	$> 1 \times 10^{-14}$
4H	$Z_2^0$	0.45	0.43–0.46	$> 1 \times 10^{-14}$
4H	$Z_1^-$	0.72	0.67	$1.71 \times 10^{-15} \times \exp(-0.065/kT)$
4H	$Z_2^-$	0.76	0.71	$1.31 \times 10^{-15} \times \exp(-0.080/kT)$
6H	$E_1^0$	0.28	0.27–0.29	$> 2.4 \times 10^{-15}$
6H	$E_2^0$	0.20	0.19–0.21	$> 5.5 \times 10^{-15}$
6H	$E_1^-$	0.42	0.38	$1.1 \times 10^{-15} \times \exp(-0.048/kT)$
6H	$E_2^-$	0.47	0.44	$7.7 \times 10^{-16} \times \exp(-0.070/kT)$
6H	$E_0$	0.20		$1.2 \times 10^{-18}$

and the obtained temperature dependent capture cross sections are given in Table 8.

The fast capturing of the first electron to the positively charged center suggests a cascade capturing process [134] while the slower capturing process of the second electron is described by a multi-phonon process. Fitting the obtained thermal emission rates, assuming a cascade and multi-phonon capturing process of the first and second electron, respectively, gives the electron binding energies (Table 8). Thus, the negative- $U$  centers  $U_1$  and  $U_2$ , each gives rise to one donor and one acceptor level. The levels at  $E_C$ -(0.50–0.54) eV and  $E_C$ -(0.43–0.46) eV correspond to the donor levels  $Z_1^0$  and  $Z_2^0$ , respectively, while the acceptor levels  $Z_1^-$  and  $Z_2^-$  are located at  $E_C$ -0.67 eV and  $E_C$ -0.71 eV, respectively [85].

In 6H-SiC, there are also two similar negative- $U$  centers,  $U_1$  and  $U_2$ , giving rise to donor levels  $E_1^0$  at  $E_C$ -(0.27–0.29) eV and  $E_2^0$  at  $E_C$ -(0.19–0.21) eV, and acceptor levels  $E_1^-$  at  $E_C$ -(0.27–0.29) eV and  $E_2^-$  at  $E_C$ -(0.19–0.21) eV, respectively [86].

Figure 15 shows DLTS spectra consisting of several new peaks, labelled L1, L2, L3, and E8, measured in an irradiated 6H-SiC  $p^+n$  diode after different annealing conditions. The thermal ionization energies obtained for these peaks are:  $E_i(\text{L1}) = 0.77$  eV,  $E_i(\text{L2}) = 1.14$  eV,  $E_i(\text{L3}) = 1.78$  eV, and  $E_i(\text{E8}) = 2.30$  eV. The capture cross sections of the L1 and E8 levels were estimated as  $\sigma_n(\text{L1}) = 2.5 \times 10^{-14}$  and  $\sigma_n(\text{E8}) = 3.7 \times 10^{-12}$ , respectively. Using various junction space-charge techniques, annealing and simulation, Hemmingsson et al. [88] have shown that the L1, L2 and L3 levels belong to three different configurations,  $C_1$ ,  $C_2$  and  $C_3$ , respectively, of a metastable defect. Two of these configurations can only exist if the level is occupied by

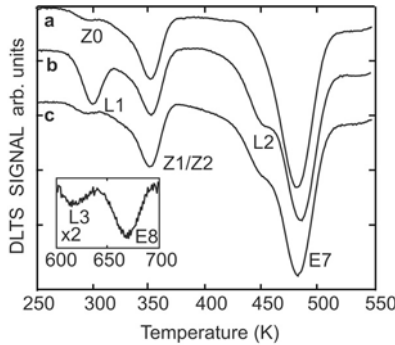


**Fig. 15.** DLTS spectra measured after three different annealing conditions on a 6H-SiC  $p^+n$ -diode irradiated with 2.5 MeV electrons and with a dose of  $2.5 \times 10^{14} \text{ cm}^{-2}$ : (a) after the defects were prepared in  $C_3$ , (b) after the defects were prepared in  $C_1$  and (c) after the defects were prepared in  $C_2$ . The high temperature part of the spectra, shown in the *inset*, is the same for (a), (b) and (c)

one or more electrons. The transformation process was found to be governed by electron capturing to the defect.

The  $Z_{1,2}$  defect in 4H-SiC was previously suggested to be related to the  $D_I$  PL center [135]. Recently, Storasta et al. [89] showed in their minority carrier transient spectroscopy (MCTS) and annealing studies that the  $D_I$  center is not correlated with the  $Z_{1,2}$  center but with a hole trap HS1 lying at  $\sim 0.35$  eV above  $E_V$ . This hole trap has been observed before by Hemmingsson et al. [80] (the HH1 peak in Fig. 12d). The annealing temperature dependence of the concentration of the  $Z_{1,2}$ , HS1, and the ratio between the L1 NP line of the  $D_I$  center and the  $Q_0$  line of the N-bound exciton ( $L_1/Q_0$ ) was studied in four sets of samples irradiated with different proton doses [89] and are shown in Fig. 16a. As can be seen in the figure, the concentration of the  $Z_{1,2}$  signal starts decreasing at ( $\sim 1100$ – $1300$ ) $^\circ\text{C}$  and reaches the level observed in as-grown samples at  $1700^\circ\text{C}$  independently of the doses of irradiation. Contrary to that, the concentration of the HS1 center keeps increasing all the way very similar to the dependence of the  $L_1/Q_0$  ratio. The correlation between the concentration of HS1 center and the intensity of the L1 NP line is also evident from Fig. 16b. The recent model of a pseudodonor [64] also predicts that the  $D_I$  defect should be associated with a hole trap at 0.34 eV above  $E_V$ . This level is remarkably close to the HS1 hole trap at  $E_V + 0.35$  eV.

Pintilie et al. [136] studied the formation of the  $Z_{1,2}$  defect in CVD samples grown with various nitrogen-doping concentrations and C/Si ratios (1.2–3). A 1:1 relation between the concentrations of  $Z_1$  and  $Z_2$  has been obtained for as-grown layers. Their DLTS results confirm the negative- $U$  properties of

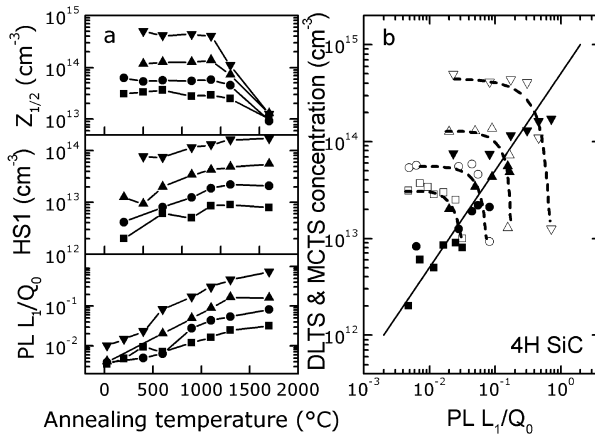


**Fig. 16.** (a) The annealing temperature dependence of  $Z_{1,2}$ , HS1 and  $L_1/Q_0$ . The proton doses used were  $\blacksquare$   $3 \times 10^{11}$ ,  $\bullet$   $1 \times 10^{12}$ ,  $\blacktriangle$   $3 \times 10^{12}$ ,  $\blacktriangledown$   $1 \times 10^{13}$  cm $^{-2}$ . (b) Concentration of DLTS  $Z_{1,2}$  (open symbols) and MCTS HS1 (solid symbols) against PL  $L_1/Q_0$  ratio. The symbols used are the same as in (a) for the different proton doses. The solid and dashed lines are only guides for the eye

the  $Z_{1,2}$  center. The concentration of the  $Z_{1,2}$  defect was observed to increase with the incorporated nitrogen concentration. The dependence was found to be linear for medium C/Si ratio (1.5–2.5). Based on this dependence a model of a complex between N and  $C_I$  or  $V_{Si}$  has been suggested for the  $Z_{1,2}$  defect. Fujihira et al. [137] studied the defect in layers grown with the C/Si of 0.6, 0.7 and 0.8 and found the  $Z_1$  concentration in the low  $10^{13} \text{ cm}^{-3}$  range in one layer with the N concentration  $\sim 1 \times 10^{16} \text{ cm}^{-3}$ . The center was suggested to be an intrinsic complex involving a Si antisite or C vacancy [137]. Thus, the defect is still not conclusively identified.

## 4 Conclusion

Recent studies of deep level defects in SiC are briefly described. The carbon vacancy in the positive charge state  $V_C^+$  is identified (the EI5 or Ky1 center). It acts as a donor center in *p*-type material and has the (+/0) level in 4*H*-SiC at  $\sim E_V + 1.47 \text{ eV}$ . The  $V_C^+$  center survives an annealing at a temperature  $\sim 1600^\circ\text{C}$ . The T5 center in 3*C*-SiC, which was attributed to  $V_C^+$  before, is now suggested by theory to be a C interstitial-related defect. The model still needs a confirmation from experiments. On the identification of the Si antisite, there is still a disagreement between experiments and also theoretical calculations. Further detailed information on the HF structure of the EI6 (or Ky3) center is needed for clarifying if the EI6 center is the  $Si_C^+$  or the  $V_C^+$  at the hexagonal site. Other important intrinsic defects, such as the ( $Si_i$ - $V_{Si}$ ) Frenkel and ( $C_{Si}$ - $V_C$ ) pairs have been identified. The ( $C_{Si}$ - $V_C$ ) pair was found to have the formation energy lower than that of  $V_{Si}$  and is a common defect in as-grown material. Detailed ligand HF structure of the so-called  $V_{Si}^0$  center has been obtained, indicating that the center is a single Si vacancy. Its charge state is under debate (three different models with the charge state of 0,  $-1$  and  $-3$  were suggested for the center). The metastable properties of the  $Z_{1,2}$  center in 4*H*-SiC, the E1 and E2 centers in 6*H*-SiC, and other deep level defects in 6*H*-SiC have been revealed. Unlike cases of the  $V^{3+}$  and  $Mo^{4+}$  PL centers, the PL of the neutral  $Cr^{4+}$  center is originated from the  $^1E(D)^{-3}A_2(F)$  transitions.

## Acknowledgements

Support for this work was provided by the SSF programs SiCEP and SiC-MAT, the Swedish Research Council (VR), Swedish Defense Research Agency (FOI), Swedish National Supercomputing Center (NSC), SIDA grant SRP-2000-025, and the Deutsche Forschungsgemeinschaft (DFG).

## References

1. H.H. Woodbury and G.W. Ludwig: Phys. Rev. **124**, 1083 (1961)
2. K.M. Lee, Si Dang Le, and G.D. Watkins: Phys. Rev. B **32**, 2273 (1985)
3. J. Schneider, H.D. Müller, K. Maier, W. Wilkening, F. Fuchs, A. Dörnen, S. Leibenzeder, and R. Stein: Appl. Phys. Lett. **56**, 1184 (1990)
4. K. Maier, H.D. Müller, and J. Schneider: Mater. Sci. Forum **83–87**, 1183 (1992)
5. M. Kunzer, H.D. Müller, and U. Kaufmann: Phys. Rev. B **48**, 10846 (1993)
6. M. Feege, S. Greulich-Weber, and J.-M. Spaeth: Semicond. Sci. Technol. **8**, 1620 (1993)
7. J. Reinke, S. Greulich-Weber, and J.-M. Spaeth: Solid State Commun. **85**, 1017 (1993)
8. P.G. Baranov, V.A. Khramtsov, and E.N. Mokhov: Semicond. Sci. Technol. **9**, 1340 (1994)
9. M. März, J. Reinke, S. Greulich-Weber, J.-M. Spaeth, H. Overhof, E.N. Mokhov, A.D. Roenkov, and E.N. Kalabukhova: Solid State Commun. **98**, 439 (1996)
10. M. Kunzer, K.F. Dombrowski, F. Fuchs, U. Kaufmann, J. Schneider, P.G. Baranov, and E.N. Mokhov: Inst. Phys. Conf. Ser. **142**, 385 (1996)
11. P.G. Baranov, I.V. Il'in, E.N. Mokhov, A.D. Roenkov, and V.A. Khramtsov: Phys. Solid State **39**, 44 (1997)
12. P.G. Baranov: Mater. Sci. Forum **264–268**, 581 (1998), and references therein
13. A.V. Duijn-Arnold, T. Ikoma, O.G. Poluektov, E.N. Mokhov, P.G. Baranov, and J. Schmidt: Phys. Rev. B **57**, 1607 (1998)
14. A.V. Duijn-Arnold, J. Schmidt, O.G. Poluektov, P.G. Baranov, and E.N. Mokhov: Phys. Rev. B **60**, 15799 (1999)
15. P.G. Baranov, I.V. Ilyin, E.N. Mokhov, and V.A. Khramtsov: Mater. Sci. Forum **353–356**, 529 (2001)
16. J. Baur, M. Kunder, and J. Schneider: Phys. Stat. Sol. (a) **162**, 153 (1997)
17. W.P. Ryneveld and J.H.N. Loubser: Brit. J. Appl. Phys. **17**, 1277 (1966)
18. J.H.N. Loubser, L.A. de S. Balona, and W.P. Ryneveld: Mat. Res. Bul. **4**, S249 (1969)
19. L.A. de S. Balona and J.H.N. Loubser: J. Phys. C **3**, 2344 (1970)
20. N.M. Pavlov, M.I. Iglitsyn, M.G. Kosaganova, V.N. Solomatin, and Y.V. Barinov: Sov. Phys. Solid State **13**, 2363 (1972)
21. N.M. Pavlov, M.I. Iglitsyn, M.G. Kosaganova, and V.N. Solomatin: Sov. Phys. Semicond. **9**, 845 (1976)
22. V.S. Vainer, V.I. Veinger, V.A. Il'in, and V.F. Tsvetkov: Sov. Phys. Solid State **22**, 2011 (1980)
23. V.S. Vainer and V.A. Il'in: Sov. Phys. Solid State **23**, 2126 (1981)
24. H. Itoh, M. Yoshikawa, I. Nashiyama, S. Misawa, H. Okumura, and S. Yoshida: IEEE Trans. Nucl. Sci. **37**, 1732 (1990)
25. T. Wimbauer, B.K. Meyer, A. Hofstaetter, A. Scharmann, and H. Overhof: Phys. Rev. B **56**, 7384 (1997)
26. J. Schneider and K. Maier: Physica B **185**, 199 (1993)
27. L. Torpo, R.M. Nieminen, K.E. Laasonen, and S. Pöykkö: Appl. Phys. Lett. **74**, 221 (1999)
28. A. Zywiets, J. Furthmüller, and F. Bechstedt: Phys. Rev. B **59**, 15166 (1999)

29. L. Torpo, M. Marlo, T.E.M. Staab, and R.M. Nieminen: *J. Phys. Condens. Matter* **13**, 6203 (2001)
30. H. Itoh, A. Kawasuso, T. Ohshima, M. Yoshikawa, I. Nashiyama, S. Tanigawa, S. Misawa, H. Okumura, and S. Yoshida: *Phys. Stat. Sol. (a)* **162**, 173 (1997)
31. H. Itoh, M. Yoshikawa, I. Nashiyama, S. Misawa, H. Okumura, and S. Yoshida: *J. Electron. Mater.* **21**, 707 (1992)
32. H. Itoh, M. Yoshikawa, I. Nashiyama, H. Okumura, S. Misawa, and S. Yoshida: *J. Appl. Phys.* **77**, 837 (1995)
33. V. Nagesh, J.W. Farmer, R.F. Davis, and H.S. Kong: *Appl. Phys. Lett.* **50**, 1138 (1987)
34. V. Nagesh, J.W. Farmer, R.F. Davis, and H.S. Kong: *Radiat. Eff. Defects Solids* **112**, 77 (1990)
35. D.N. Talwar and Z.C. Feng: *Phys. Rev. B* **44**, 3191 (1991)
36. H. Itoh, M. Yoshikawa, I. Nashiyama, S. Misawa, H. Okumura, and S. Yoshida: *Inst. Phys. Conf. Ser.* **137**, 255 (1994)
37. N.T. Son, E. Sörman, W.M. Chen, O. Kordina, B. Monemar, and E. Janzén: *Appl. Phys. Lett.* **65**, 2687 (1994)
38. N.T. Son, E. Sörman, W.M. Chen, M. Singh, C. Hallin, O. Kordina, B. Monemar, E. Janzén, and J.L. Lindström: *J. Appl. Phys.* **79**, 3784 (1996)
39. N.T. Son, E. Sörman, W.M. Chen, M. Singh, C. Hallin, O. Kordina, B. Monemar, J.L. Lindström, and E. Janzén: *Inst. Phys. Conf. Ser.* **142**, 321 (1996)
40. N.T. Son, E. Sörman, W.M. Chen, C. Hallin, O. Kordina, B. Monemar, and E. Janzén: *Diam. Relat. Mater.* **6**, 1381 (1997)
41. N.T. Son, E. Sörman, W.M. Chen, C. Hallin, O. Kordina, B. Monemar, E. Janzén, and J.L. Lindström: *Phys. Rev. B* **55**, 2863 (1997)
42. D. Cha, H. Itoh, N. Morishita, A. Kawasuso, T. Oshima, Y. Watanabe, J. Ko, K. Lee, and I. Nashiyama: *Mater. Sci. Forum* **264–268**, 615 (1998)
43. N.T. Son, W.M. Chen, B. Monemar, J.L. Lindström, and E. Janzén: *Phys. Scr. Vol. T* **79**, 46 (1999)
44. N.T. Son, W.M. Chen, B. Monemar, J.L. Lindström, and E. Janzén: *Mater. Sci. Eng. B* **61–62**, 202 (1999)
45. N.T. Son, P.N. Hai, P.T. Huy, T. Gregorkiewicz, C.A.J. Ammerlaan, J.L. Lindström, W.M. Chen, B. Monemar, and E. Janzén: *Physica B* **273–274**, 655 (1999)
46. N.T. Son, P.N. Hai, and E. Janzén: *Mater. Sci. Forum* **353–356**, 499 (2001)
47. N.T. Son, P.N. Hai, and E. Janzén: *Phys. Rev. B* **63**, R201201 (2001)
48. V.Y. Bratus, I.N. Makeeva, S.M. Okulov, T.L. Petrenko, T.T. Petrenko, and H.J. von Bardeleben: *Mater. Sci. Forum* **353–356**, 517 (2001)
49. V.Y. Bratus, I.N. Makeeva, S.M. Okulov, T.L. Petrenko, T.T. Petrenko, and H.J. von Bardeleben: *Physica B* **308–310**, 621 (2001)
50. J.W. Steeds, F. Carosella, G.A. Evans, M.M. Ismail, L.R. Danks, and W. Voegeli: *Mater. Sci. Forum* **353–356**, 381 (2001)
51. H.J. von Bardeleben, J.L. Cantin, L. Henry, and M.F. Barthe: *Phys. Rev. B* **62**, 10841 (2000)
52. Y. Li and P.J. Lin-Chung: *Phys. Rev. B* **36**, 1130 (1987)
53. C. Wang, J. Bernholc, and R.F. David: *Phys. Rev. B* **38**, 12752 (1988)
54. L. Torpo, S. Pöykkö, and R.M. Nieminen: *Phys. Rev. B* **57**, 6243 (1998)
55. N.T. Son, P.N. Hai, and E. Janzén: *Phys. Rev. Lett.* **87**, 045502 (2001)
56. N.T. Son, M. Wagner, E. Sörman, W.M. Chen, B. Monemar, and E. Janzén: *Mater. Sci. Forum* **264–268**, 599 (1998)

57. N.T. Son, Mt. Wagner, E. Sörman, W.M. Chen, B. Monemar, and E. Janzén: *Semicond. Sci. Technol.* **14**, 1141 (1999)
58. Th. Lingner, S. Greulich-Weber, and J.-M. Spaeth: *Mater. Sci. Forum* **353–356**, 505 (2001)
59. Th. Lingner, S. Greulich-Weber, J.-M. Spaeth, U. Gerstman, E. Rauls, Z. Hajnal, Th. Frauenheim, and H. Overhof: *Phys. Rev. B* **64**, 245212 (2001)
60. W.J. Choyke and L. Patrick: *Phys. Rev. B* **4**, 1843 (1971)
61. L. Patrick and W.J. Choyke: *J. Phys. Chem. Solids* **34**, 565 (1973)
62. W.J. Choyke: *Inst. Phys. Conf. Ser.* **31**, 58 (1977)
63. V.V. Marakov: *Sov. Phys. Solid State* **13**, 1974 (1972)
64. T. Egilsson, J.P. Bergman, I.G. Ivanov, A. Henry, and E. Janzén: *Phys. Rev. B* **59**, 1956 (1999)
65. T. Egilsson, J.P. Bergman, I.G. Ivanov, A. Henry, and E. Janzén: *Phys. Stat. Sol. (b)* **210**, 337 (1998)
66. I.S. Gorban and A.V. Slobodyanyuk: *Sov. Phys. Solid State* **15**, 548 (1973)
67. S.H. Hagen and A.W.C. van Kemenade: *J. Lumin.* **9**, 9 (1974)
68. E. Sörman, N.T. Son, W.M. Chen, J.L. Lindström, and E. Janzén: *Mater. Sci. Forum* **258–263**, 685 (1997)
69. E. Sörman, W.M. Chen, N.T. Son, C. Hallin, J.L. Lindström, B. Monemar, and E. Janzén: *Mater. Sci. Forum* **264–268**, 473 (1998)
70. E. Sörman, N.T. Son, W.M. Chen, O. Kordina, C. Hallin, and E. Janzén: *Phys. Rev. B* **61**, 2613 (2000)
71. Mt. Wagner, B. Magnusson, W.M. Chen, E. Janzén, E. Sörman, C. Hallin, and J.L. Lindström: *Phys. Rev. B* **62**, 16555 (2000)
72. Mt. Wagner, N.Q. Thinh, N.T. Son, W.M. Chen, E. Janzén, P.G. Baranov, E.N. Mokhov, C. Hallin, and J.L. Lindström: *Mater. Sci. Forum* **389–393**, 501 (2002)
73. Mt. Wagner, N.Q. Thinh, N.T. Son, W.M. Chen, E. Janzén, P.G. Baranov, E.N. Mokhov, C. Hallin, and J.L. Lindström: *Phys. Rev. B* **66**, 155214 (2002)
74. H.J. von Bardeleben, J.L. Cantin, I. Vickridge, and G. Battistig: *Phys. Rev. B* **62**, 10126 (2000)
75. S.B. Orlinski, J. Schmidt, E.N. Mokhov, and P.G. Baranov: *Phys. Rev. B* **67**, 125207 (2003)
76. N. Mizuochi, J. Isoya, S. Yamasaki, H. Takizawa, N. Morishita, T. Ohshima, and H. Itoh: *Phys. Rev. B* **66**, 235202 (2002)
77. G. Pensl and W.J. Choyke: *Physica B* **185**, 264 (1993)
78. T. Dalibor, G. Pensl, H. Matsunami, T. Kimoto, W.J. Choyke, A. Schöner, and N. Nordell: *Phys. Stat. Sol. (a)* **162**, 199 (1997)
79. C.G. Hemmingsson, N.T. Son, O. Kordina, E. Janzén, J.L. Lindström, S. Savage, and N. Nordell: *Mater. Sci. Eng. B* **46**, 336 (1997)
80. C.G. Hemmingsson, N.T. Son, O. Kordina, J.P. Bergman, E. Janzén, J.L. Lindström, S. Savage, and N. Nordell: *J. Appl. Phys.* **81**, 6155 (1997)
81. J.P. Doyle, A. Schöner, N. Nordell, A. Galeckas, H. Bleichner, M.K. Linnarsson, J. Linnros, and B.G. Svensson: *J. Appl. Phys.* **83**, 3649 (1998)
82. C.G. Hemmingsson, N.T. Son, O. Kordina, E. Janzén, and J.L. Lindström: *J. Appl. Phys.* **84**, 704 (1998)
83. J.P. Doyle, M.K. Linnarsson, P. PELLEGRINO, N. Keskitalo, B.G. Svensson, A. Schöner, N. Nordell, and J.L. Lindström: *J. Appl. Phys.* **84**, 1354 (1998)
84. M.O. Aboelfotoh and J.P. Doyle: *Phys. Rev. B* **59**, 10823 (1999)

85. C.G. Hemmingsson, N.T. Son, A. Ellison, J. Zhang, and E. Janzén: *Phys. Rev. B* **58**, R10119 (1998)
86. C.G. Hemmingsson, N.T. Son, and E. Janzén: *Appl. Phys. Lett.* **74**, 839 (1999)
87. C.G. Hemmingsson, N.T. Son, O. Kordina, J.L. Lindström, and E. Janzén: *Semicond. Sci. Technol.* **14**, 251 (1999)
88. C.G. Hemmingsson, N.T. Son, O. Kordina, and E. Janzén: *J. Appl. Phys.* **91**, 1324 (2002)
89. L. Storasta, F.H.C. Carlsson, S.G. Sridhara, J.P. Bergman, A. Henry, T. Egilsson, A. Hallén, and E. Janzén: *Appl. Phys. Lett.* **78**, 46 (2001)
90. T. Kimoto, T. Yamamoto, Z.Y. Chen, H. Yano, and H. Matsunami: *J. Appl. Phys.* **89**, 6105 (2001)
91. N. Achtziger and W. Witthuhn: *Appl. Phys. Lett.* **71**, 110 (1997)
92. J. Grillenberger, N. Achtziger, R. Sielmann, and W. Witthuhn: *J. Appl. Phys.* **88**, 3260 (2000)
93. F. Albrecht, J. Grillenberger, G. Pasold, W. Witthuhn, and N. Achtziger: *Appl. Phys. Lett.* **79**, 961 (2001)
94. N. Achtziger, G. Pasold, R. Sielmann, C. Hülsen, J. Grillenberger, and W. Witthuhn: *Phys. Rev. B* **62**, 12888 (2000)
95. J. Grillenberger, N. Achtziger, F. Günther, and W. Witthuhn: *Appl. Phys. Lett.* **73**, 3698 (1998)
96. A.A. Lebedev: *Semiconductors* **33**, 107 (1999)
97. C.C. Ling, C.D. Beling, and S. Fung: *Phys. Rev. B* **62**, 8016 (2000)
98. Z. Zolnai, N.T. Son, C. Hallin, and E. Janzén: to be published
99. B. Aradi, A. Gali, P. Deák, J.E. Lowther, N.T. Son, E. Janzén, and W.J. Choyke: *Phys. Rev. B* **63**, 245202 (2001)
100. M. Bockstedte, M. Heid, A. Mattausch, and O. Pankratov: *Mater. Sci. Forum* **389–393**, 471 (2002)
101. A. Gali, P. Deák, N.T. Son, E. Janzén, H.J. von Bardeleben, and J.L. Monge: *Mater. Sci. Forum* **433–436**, 511 (2003)
102. A. Gali, P. Deák, N.T. Son, and E. Janzén: to be published
103. M.E. Zvanut and V.V. Kononov: *Appl. Phys. Lett.* **80**, 410 (2002)
104. N.T. Son, B. Magnusson, and E. Janzén: *Appl. Phys. Lett.* **81**, 3945 (2002)
105. R. Orbach and P. Pincus: *Phys. Rev.* **145**, 191 (1966)
106. B.P. Koch: *Phys. Stat. Sol. (b)* **68**, 193 (1975)
107. T. Gregorkiewicz and S.W. Biernacki: *J. Phys. C* **13**, 1285 (1980)
108. A. Mauger, H.J. von Bardeleben, J.C. Bourgoin, and M. Lannoo: *Phys. Rev. B* **36**, 5982 (1987)
109. M. Bockstedte, M. Heid, A. Mattausch, and O. Pankratov: *Mater. Sci. Forum* **433–436**, 471 (2003)
110. T.T. Petrenko, T.L. Petrenko, and V.Y. Bratus, unpublished
111. N.T. Son, P.N. Hai, A. Shuja, W.M. Chen, J.L. Lindström, B. Monemar, and E. Janzén: *Mater. Sci. Forum* **338–342**, 821 (2000)
112. P. Deák, J. Miro', A. Gali, L. Udvardi, and H. Overhof: *Appl. Phys. Lett.* **75**, 2103 (1999)
113. Th. Lingner, S. Greulich-Weber, and J.-M. Spaeth: *Physica B* **308–310**, 649 (2001)
114. Th. Lingner, S. Greulich-Weber, J.-M. Spaeth, U. Gerstmann, E. Rauls, and H. Overhof: *Physica B* **308–310**, 625 (2001)
115. O. Gunnarsson, O. Jepsen, and O.K. Andersen: *Phys. Rev. B* **27**, 7144 (1983)

116. E. Rauls, Th. Lingner, Z. Hajnal, S. Greulich-Weber, Th. Frauenheim, and J.-M. Spaeth: *Phys. Stat. Sol. (b)* **217/2**, R1 (2000)
117. N.T. Son, A. Ellison, B. Magnusson, M.F. MacMillan, W.M. Chen, B. Mone-mar, and E. Janzén: *Mater. Sci. Forum* **264–268**, 603 (1998)
118. N.T. Son, A. Ellison, B. Magnusson, M.F. MacMillan, W.M. Chen, B. Mone-mar, and E. Janzén: *J. Appl. Phys.* **86**, 4348 (1999)
119. I.S. Gorban and A.V. Slobodyanyuk: *Sov. Phys. Solid State* **16**, 173 (1974)
120. O. Kordina: PhD thesis, Linköping University (1994)
121. Y. Tanabe and S. Sugano: *J. Phys. Soc. Japan* **9**, 766 (1954)
122. E. Janzén, A. Henry, J. Bergman, A. Ellison, and B. Magnusson: *Mater. Sci. Semicond. Proc.* **4**, 181 (2001)
123. B. Magnusson, A. Ellison, and E. Janzén: *Mater. Sci. Forum* **389–393**, 505 (2002)
124. B. Magnusson, A. Ellison, N.T. Son, and E. Janzén: *Mater. Res. Soc. Symp. Proc.* **640**, H7.11.1 (2001)
125. B. Magnusson, A. Ellison, F.H.C. Carlsson, N.T. Son, and E. Janzén: *Mater. Sci. Forum* **353–356**, 365 (2001)
126. N.T. Son, E. Sörman, M. Singh, W.M. Chen, C. Hallin, O. Kordina, B. Mon-emar, J.L. Lindström, and E. Janzén: *Diam. Relat. Mater.* **6**, 1378 (1997)
127. I.S. Gorban and A.V. Slobodyanyuk: *Sov. Phys. Semicond.* **10**, 668 (1976)
128. Mt. Wagner, B. Magnusson, W.M. Chen, and E. Janzén: *Phys. Rev. B* **66**, 115024 (2002)
129. Mt. Wagner, I.G. Ivanov, L. Storasta, J.P. Bergman, B. Magnusson, W.M. Chen, and E. Janzén: *Appl. Phys. Lett.* **81**, 2547 (2002)
130. V.A. Il'in and V.A. Ballandovich: *Defect Diffus. Forum* **103–105**, 633 (1993)
131. C.G. Hemmingsson, N.T. Son, O. Kordina, J.L. Lindström, and E. Janzén: *Mater. Sci. Forum* **264–268**, 561 (1998)
132. G.D. Watkins and J.R. Troxell: *Phys. Rev. Lett.* **44**, 593 (1980)
133. D.V. Lang and C.H. Henry: *Phys. Rev. Lett.* **35**, 1525 (1975)
134. V.N. Abakumov, V.I. Perel', and I.N. Yassievich: *Sov. Phys. Semicond.* **12**, 1 (1978)
135. T. Dalibor, C. Peppermüller, G. Pensl, S. Sridhara, R.P. Devaty, W.J. Choyke, A. Itoh, T. Kimoto, and H. Matsunami: *Inst. Phys. Conf. Ser.* **142**, 517 (1996)
136. I. Pintilie, L. Pintilie, K. Irmischer, and B. Thomas: *Appl. Phys. Lett.* **81**, 4841 (2002)
137. K. Fujihira, T. Kimoto, and H. Matsunami: *Appl. Phys. Lett.* **80**, 1586 (2002)

# Phosphorus-Related Centers in SiC

M. Laube, F. Schmid, K. Semmelroth, G. Pensl, R.P. Devaty, W.J. Choyke, G. Wagner, and M. Maier

## 1 Introduction

Phosphorus (P) is considered to serve alternatively to nitrogen (N) as a shallow donor in SiC. It is the aim of this paper to report the present status of our knowledge on the optical and electrical properties of P donors. We will not report on results obtained from magnetic resonance experiments in this article and refer to the relevant literature [1]–[4]. Electron paramagnetic resonance (EPR) and electron nuclear double resonance (ENDOR) investigations are predominantly taken on SiC samples, which are P-doped by neutron transmutation. These magnetic resonance experiments and also a theoretical prediction by A. Gali et al. [5] support that P donors are incorporated into the silicon (Si) sublattice. However with respect to the microscopic structure of P-related centers, there exists still a controversial discussion [1]–[4].

The electronic transitions of P donors are examined by low temperature photoluminescence (LTPL) and infrared (IR) absorption investigations, while the electrical properties of P donors are largely determined by Hall effect measurements. We will check whether P donors have any advantage compared to N donors with respect to device applications. In a first chapter, we briefly review the different methods to dope SiC with P donors. In the following chapters, the optical and electrical properties of P donors are described.

## 2 Doping of SiC with Phosphorus Donors

(a) *Neutron Transmutation Doping (NTD)*: NTD is an established method to homogeneously dope silicon with P donors [6]; this technique has been also applied to SiC [7]–[9]. It is based on the capture of thermal neutrons by  $^{30}\text{Si}$  atoms according to the reactions:  $^{30}_{14}\text{Si}(n, \gamma)^{31}_{14}\text{Si}$  and the subsequent  $\beta^-$  decay, which results in the  $^{31}_{15}\text{P}$  isotope. The capture cross-section for thermal neutrons is small enough to reach a homogeneous doping level throughout the bulk of the SiC sample. Because of the fact that the recoil energies of the  $\gamma$ -quantum and the  $\beta^-$ -particle are 780 eV and 32.3 eV [10], respectively, which is larger or comparable to the displacement energy of Si atoms of 35 eV and C atoms of 20 eV [11], it cannot automatically be concluded that P donors reside at Si lattice sites. This suspicion is supported by the observation [7]

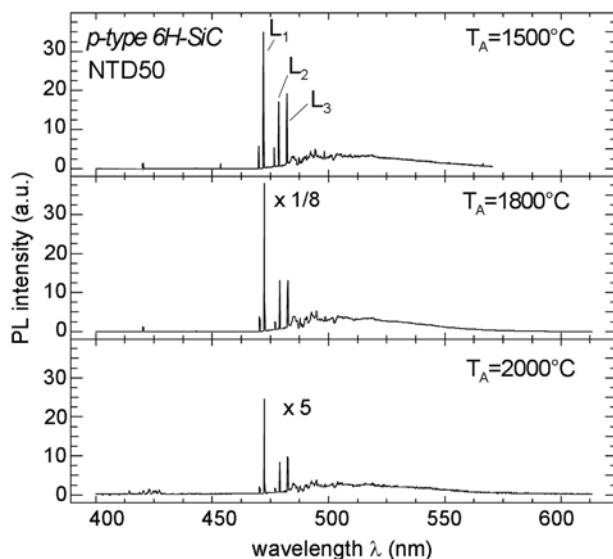


**Fig. 1.** LTPL spectra taken of 6H-SiC samples, which were irradiated with thermal neutrons (fluence =  $1.5 \times 10^{19} \text{ cm}^{-2}$ ) and subsequently annealed at different temperatures (1500°C to 2000°C) for 30 min. The  $L_\nu$ -lines ( $\nu = 1, 2, 3$ ) belonging to the intrinsic-related  $D_I$ -center are observed in all three LTPL spectra; they indicate that the lattice damage is not perfectly recovered even after annealing at such high temperatures

that subsequent to even low neutron fluences the electrical activation of P donors requires an annealing step of at least 1600°C for 30 min.

In addition, lattice damage is generated in neutron irradiated SiC samples, which is resistant even at high annealing temperatures; see e.g. the low temperature photoluminescence (LTPL) spectra ( $L_\nu$ -lines,  $\nu = 1, 2, 3$ ) in Fig. 1 [8]. With the NTD technique, P donor concentrations in the range of  $10^{16} \text{ cm}^{-3}$  are demonstrated.

*(b) Ion Implantation:* Implantation of  $P^+$  ions into SiC is a successful technique to dope SiC at high donor concentrations. Electrically active concentrations of P donors above  $10^{20} \text{ cm}^{-3}$  are demonstrated [12]. A detailed description of the implantation conditions and the electrical characterization of  $P^+$ -implanted 4H- and 6H-SiC layers are given in the following chapters.

*(c) Chemical Vapor Deposition (CVD):* The growth of P-doped epilayers is conducted at temperatures between 1500°C and 1800°C. Silane  $\text{SiH}_4$ , propane  $\text{C}_3\text{H}_8$  and phosphine  $\text{PH}_3$  are used as the sources for Si, C and P. The published growth results are controversial. While Larkin [13] reports that doping of SiC epilayers with P is consistent with the site competition effect assuming that P atoms reside at Si lattice sites, Wang et al. [14] observed the opposite trend. They have demonstrated that the incorporation of P donors

increases with decreasing C/Si-ratio. These authors also observed a decrease in the incorporation of P donors for a given precursor flow with increasing temperature. A maximum concentration of P donors of  $3.4 \times 10^{16} \text{ cm}^{-3}$  and  $3.9 \times 10^{16} \text{ cm}^{-3}$  for 4H- and 6H-SiC, respectively, is reported by these authors.

(d) *Physical Vapor Transport (PVT)*: Growth of SiC boules by the PVT method (or seeded sublimation growth) occurs at high temperatures above  $2000^\circ\text{C}$ . On the other hand, solid P sources like pure P or any P containing compound have an extremely high vapor pressure at these temperatures. In order to dope SiC during the PVT growth, the solid P source has, therefore, to be positioned at lower temperature in the sublimation furnace. Semmelroth et al. [15] have used pyrophosphate  $\text{SiP}_2\text{O}_7$  as a P source, which is industrially employed for the P-doping process of Si wafers. This solid P source has been located in the lower part of the growth furnace at about  $1300^\circ\text{C}$  and tubes drilled into the graphite walls provided diffusion channels for the P to the growth front. SIMS analyses of corresponding P-doped 6H-SiC boules result in a maximum P concentration of  $3 \times 10^{17} \text{ cm}^{-3}$ .

P-doping during CVD and sublimation growth is still an unsolved problem. It seems that the P-chemistry at high temperatures ( $T > 1600^\circ\text{C}$ ) strongly reduces the incorporation of monatomic P during the growth. The incorporation of P at the growth front may be hindered either by the formation of larger and thermally stable P molecules or C and P react chemically and form stable agglomerations. A suitable catalyst could drastically increase the incorporation of electrically active P atoms. The P-chemistry may also be responsible for the controversy between the published low solubility values for P in SiC ( $[\text{P}] = 2.8 \times 10^{18} \text{ cm}^{-3}$ ) [16] and the high electrical activity of P donors in SiC ( $[\text{P}] > 10^{20} \text{ cm}^{-3}$ ) experimentally achieved by implantation [12].

### 3 Phosphorus Neutral Donor Bound Exciton Complex in 6H-SiC

Sridhara et al. [17] observed a new LTPL spectrum in 6H-SiC homoepitaxial layers doped with phosphorus during CVD growth. They argued that the emission lines are associated with the recombination of excitons bound to neutral phosphorus donors. The samples were grown in an atmospheric pressure CVD reactor with  $\text{PH}_3$  in the flow as the source of phosphorus. Based on the dependence of the strength of the new spectra, relative to the nitrogen spectra, on the growth conditions and the mechanism of site competition epitaxy [18], Sridhara et al. proposed that P substitutes for Si. Figure 2 shows the no phonon lines of a typical spectrum taken at 2 K.

The lines labeled  $\text{Ph}^a$ ,  $\text{Ph}^b$  and  $\text{Ph}^c$  appear at the wavelengths  $4119 \text{ \AA}$ ,  $4121 \text{ \AA}$  and  $4124 \text{ \AA}$ , corresponding to binding energies of 13.8 meV, 15.2 meV

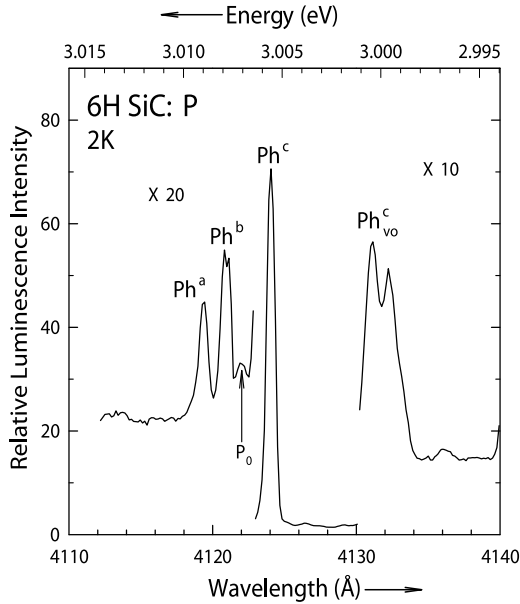


**Fig. 2.** LTPL spectrum of a 6H-SiC sample doped with phosphorus during epitaxial growth. The principal no phonon lines are labeled  $\text{Ph}^a$ ,  $\text{Ph}^b$  and  $\text{Ph}^c$  in order of increasing binding energy. The two peaks labeled  $\text{Ph}^c_{\text{vo}}$  are assigned to two-electron transitions leaving the neutral donor in excited states. The peak labeled  $\text{P}_0$  is a no-phonon line of the neutral nitrogen donor bound exciton spectrum

and 17.4 meV, respectively. Lines  $\text{Ph}^a$  and  $\text{Ph}^b$  are closely spaced and very weak compared to  $\text{Ph}^c$ . Based on their similarities, it is natural to assign  $\text{Ph}^a$  and  $\text{Ph}^b$  to the two quasicubic sites and the remaining line  $\text{Ph}^c$  to the hexagonal site of 6H-SiC. The ordering is opposite to that of the nitrogen bound exciton lines, for which excitons bind more strongly to donors on quasicubic sites. This behavior may reflect differences in the local environments on the Si versus the C sublattices. Because the no phonon lines are so closely spaced, it is not understood why the line  $\text{Ph}^c$  is so much stronger than lines  $\text{Ph}^a$  and  $\text{Ph}^b$ , although the strength of a no phonon line is expected to increase with the binding energy. With increasing temperature an excited state appears 4.3 meV above  $\text{Ph}^c$ . It is assigned to recombination of an exciton whose hole comes from the spin-orbit split  $\Gamma_7$  valence band, similar to the 4.8 meV excited state for nitrogen in 6H-SiC [19]. The feature labeled  $\text{Ph}^c_{\text{vo}}$  shows the same dependence on excitation intensity as  $\text{Ph}^c$ . It is assigned to two-electron transitions, for which exciton recombination leaves the neutral donor in an excited state, possibly a valley-orbit level. In the spectrum shown in Fig. 2, there are two  $\text{Ph}^c_{\text{vo}}$  peaks, 5.2 meV and 6 meV above the ground state, but this splitting is not observed in all samples. Figure 3 shows this phosphorus spectrum over an extended wavelength interval, which includes

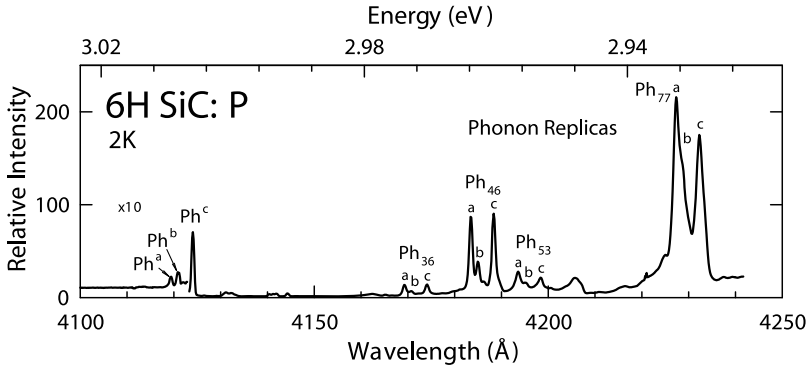


**Fig. 3.** LTPL spectrum of a 6H-SiC layer doped with phosphorus during homoepitaxial growth. The no phonon lines and a portion of the spectrum of momentum conserving phonon replicas are shown. The subscripts label the phonon energies in meV. The labels a, b and c mark three phosphorus-related spectra. The remainder of the phonon spectrum is omitted for clarity

the momentum conserving phonon replicas. Replicas of all three no phonon lines,  $\text{Ph}^a$ ,  $\text{Ph}^b$  and  $\text{Ph}^c$ , are marked. The integrated intensity of the sum of the  $\text{Ph}^a$ ,  $\text{Ph}^b$  spectra, including the no phonon lines and the phonon replicas, is only slightly greater than the corresponding sum for the deeper  $\text{Ph}^c$  spectrum. This result is contrary to the behavior of the nitrogen bound excitons in 6H-SiC, for which the integrated area of the shallow P spectrum (binding energy 16 meV) is approximately four to five times greater than that of the R and S spectra (binding energies 31 meV and 32.5 meV, respectively).

Magneto-optics provides further support for the assignment of this spectrum to neutral donor bound excitons. In the scheme of Lampert [20], a neutral donor or acceptor bound exciton is classified as a four particle complex. For example, the four particles making up the donor complex are the positively charged ion, two electrons and a hole. Radiative recombination of the exciton leaves the neutral donor, which may be in its ground state or an excited state. Thomas and Hopfield [21] developed a simple model for the behavior of neutral donor and acceptor Zeeman spectra in noncubic semiconductors, specifically those with wurtzite structure. Consider a neutral donor. The initial state is the four particle complex. The two electrons are in a spin singlet (antiparallel spins), so that the Zeeman splitting is determined by the hole. For many wurtzite semiconductors, as well as for 4H-SiC and 6H-SiC, which have the same space group,  $C_{6v}^4$ , the top valence band is labeled  $\Gamma_9$ , associated with the valence band maximum at the point  $\Gamma$  at the center of the Brillouin zone. The Zeeman splitting of a  $\Gamma_9$  hole is anisotropic, with maximum splitting for magnetic field  $\vec{H} \parallel \hat{c}$  and no splitting for  $\vec{H} \perp \hat{c}$  where  $\hat{c}$  labels the crystal  $c$ -axis. The final state electron should split essentially isotropically with a  $g$  factor of about 2. For a neutral acceptor bound exciton

complex the magneto-optical behavior is the opposite: The initial state is electron like and the final state splitting is due to the remaining hole.

Zeeman spectra were measured using a 7 T split-coil superconducting magnet with the samples at temperature 2 K [22]. Figure 4 shows Zeeman spectra for  $\vec{H} \perp \hat{c}$  and  $\vec{H} \parallel \hat{c}$  measured at 6 T. The insets illustrate the behavior predicted by Hopfield's model for a neutral donor four particle complex. The strengths of the lines are affected by thermalization of the initial state. For example, consider the strong  $\text{Ph}^c$  no phonon line. The Zeeman split lines are of equal strength for  $\vec{H} \perp \hat{c}$  but the lower energy line is stronger for  $\vec{H} \parallel \hat{c}$ . This behavior is a clear indication that the four particle complex is associated with a neutral donor, and not an acceptor. Also, the fact that the lower energy line is the stronger for the  $\vec{H} \parallel \hat{c}$  spectrum indicates that

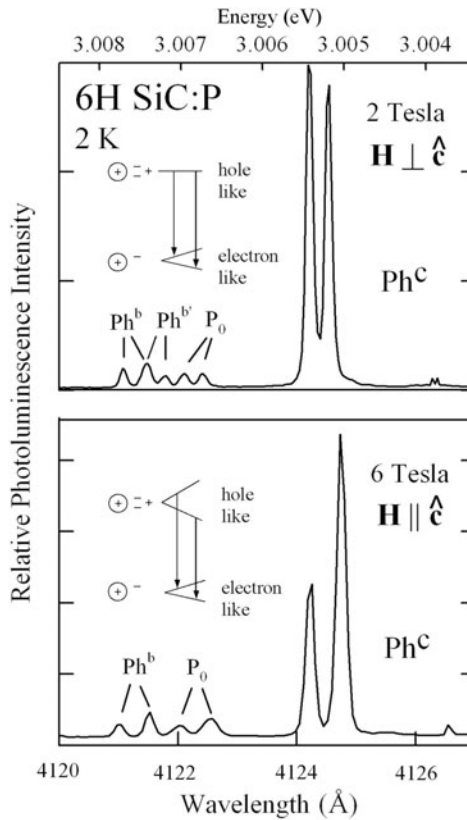


**Fig. 4.** Zeeman spectra of no phonon lines in 6H-SiC layers doped with phosphorus during epitaxial growth. The magnetic field is applied perpendicular (*top*) or parallel (*bottom*) to the crystal  $c$ -axis. The *insets* illustrate Hopfield's model for a neutral donor bound exciton.  $P_0$  labels a Zeeman split nitrogen no phonon line

$g_h > g_e$ , where  $g_h$  and  $g_e$  are the  $g$ -factors of the hole and electron, respectively. In addition, the measured values  $g_h = 3.18$  and  $g_e = 1.99$  for  $\text{Ph}^c$  are consistent with the measured spin orbit splitting of 4.3 meV, according to the model of Dang et al. [23] and Scott et al. [24]. The orbital angular momentum of the hole is quenched due to its localization in the complex. According to the model, the  $g$ -factor becomes  $g_L \approx g_L(\text{bulk}) \times \lambda(\text{Ph}^c) / \lambda(\text{bulk}) = 1 \times 4.3 \text{ meV} / 7.20 \text{ meV} = 0.60$ . Here we have used the measured value for the spin-orbit splitting of the valence bands in  $6H$ -SiC,  $\lambda(\text{bulk}) = 7.2 \text{ meV}$ , discussed elsewhere in this volume [25]. The predicted value of the  $g$ -factor for the hole is  $g_h = 2g_L + g_S = 2 \times 0.60 + 2 = 3.20$ , in good agreement with the measured value,  $g_h = 3.18$ .

#### 4 IR Transmission Measurements on Phosphorus Donors in $6H$ -SiC

IR transmission spectra are taken on samples, which are cut from  $6H$ -SiC boules with their large surfaces perpendicular to the  $c$ -axis. These crystals are P-doped during the sublimation growth [15, 26]. For the IR investigations, a Bruker IFS 66 v/S spectrometer equipped with a Mylar  $3.5 \mu\text{m}$  beam splitter and a deuterated triglycine sulphate (DGTS) detector is used.

Figure 5 shows transmission spectra taken at three different temperatures with electric field vector  $\vec{E} \perp \hat{c}$ . Besides the known absorption lines [27], which

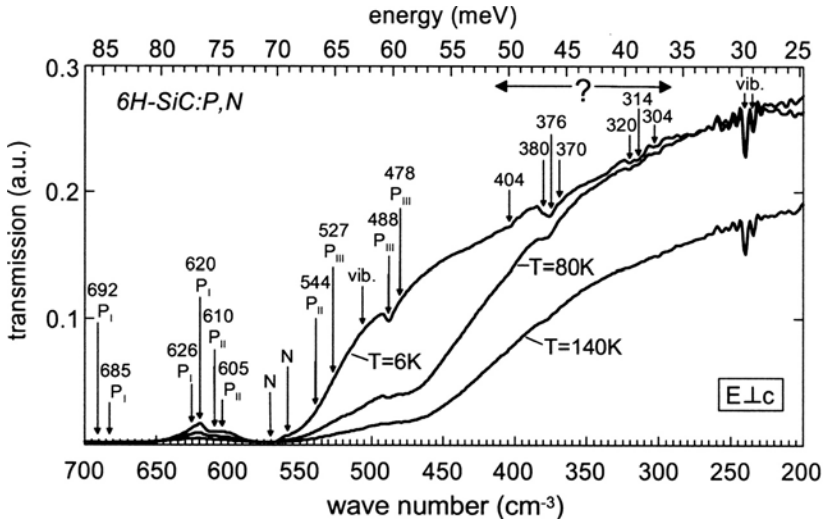


**Fig. 5.** Infrared transmission versus wave number obtained from P-doped  $6H$ -SiC samples. The spectra are taken in the wave number range from  $200 \text{ cm}^{-1}$  to  $700 \text{ cm}^{-1}$  at 6 K, 80 K and 140 K; the resolution is  $2 \text{ cm}^{-1}$

are attributed to N donors and vibrational modes, an additional pronounced absorption structure is observed. This particular structure is only observed in P-doped 6H-SiC samples and at low temperatures. It is attributed to bound-to-bound transitions of the donor electron of P donors. These absorption lines originate from excitations from the 1s ground state to  $2p/3p$  excited states; they can be not observed at temperatures  $T \geq 140$  K, where most of the P donors are already ionized.

The experimental absorption lines are discussed in the framework of Faulkner's effective mass approximation (EMA) [28]. Although Faulkner's theory considers only two independent components of the effective mass ( $m_{\parallel}$ ,  $m_{\perp}$ ), it has been demonstrated in [27] that this theory results in correct values for the ionization energy and energies of excited states of N donors in the 6H polytype, even though electrons in the lowest conduction band have three distinct effective mass components.

The measured absorption lines are ordered taking into account the following rules:

- (a) With increasing quantum number  $n$ , the line intensities decrease,
- (b) the intensity of transitions to  $np_{\pm}$ -states is larger than the intensity to  $np_0$ -states and
- (c) according to Faulkner's EMA the ordering of excited states depends on the value of the anisotropy mass factor  $1 - (m_{\perp}/m_{\parallel})^{1/3}$ .

The effective electron masses for the 6H polytype are determined by optical cyclotron resonance experiments [29]; the electron masses are:

$$m_{\perp} = 0.42m_0 \quad \text{and} \quad m_{\parallel} = 2.0m_0 .$$

With these values the anisotropy factor becomes  $1 - (m_{\perp}/m_{\parallel})^{1/3} = 0.41$ . For  $1 - (m_{\perp}/m_{\parallel})^{1/3} < 0.52$ , Faulkner's EMA predicts the following ordering:

$$E(2p_0) < E(2p_{\pm}) < E(3p_0) < E(3p_{\pm}) .$$

Based on these rules the EMA-like excited states are calculated using a simplified approximation given by Gerlach and Pollmann [30].

Three series of excited EMA states are obtained from this fit. The assignment of excited states to the experimental absorption lines is summarized in columns 1 and 2 of Table 1 for the three series; the corresponding experimental and calculated EMA transition energies are listed in columns 3 and 4, respectively. The experimental values for the ionization energies  $\Delta E(P_{\nu})$  of the three  $P_{\nu}$  donors are: 90 meV, 79.4 meV and 70.6 meV. It is assumed that the different ionization energies correspond to P atoms residing at the three inequivalent lattice sites of the 6H polytype. IR absorption measurements do not allow any identification of lattice sites; however based on EPR results [2], it may be speculated that the energetically deep P donor (opposite to the N donor) resides at the hexagonal ( $h$ ) lattice site and the energetically shallower donors reside at cubic ( $k_1$ ,  $k_2$ ) lattice sites. The straight line in Fig. 6

**Table 1.** Absorption lines and transition energies of excited P donor states in 6H-SiC obtained from a fit of the EMA after [30] to the observed absorption lines

Series I			
Final state (nlm)	Absorption lines (cm <sup>-1</sup> ) 1s → bound excited state	Transition energies $E_{\text{nlm}}$ (meV)	
		exp.	EMA
2p <sub>0</sub>	620	76.7	76.8
2p <sub>±</sub>	626	77.4	77.7
3p <sub>0</sub>	685	84.7	85.1
3p <sub>±</sub>	692	85.6	85.5
4p <sub>0</sub>	not observed	–	88.0
4p <sub>±</sub>	not observed	–	88.3
CB	728	90.0	91.8
Series II			
Final state (nlm)	Absorption lines (cm <sup>-1</sup> ) 1s → bound excited state	Transition energies $E_{\text{nlm}}$ (meV)	
		exp.	EMA
2p <sub>0</sub>	not observed	–	66.1
2p <sub>±</sub>	544	67.3	67.4
3p <sub>0</sub>	605	74.8	75.0
3p <sub>±</sub>	610	75.4	75.6
4p <sub>0</sub>	not observed	–	78.1
4p <sub>±</sub>	not observed	–	78.4
CB	642	79.4	82.1
Series III			
Final state (nlm)	Absorption lines (cm <sup>-1</sup> ) 1s → bound excited state	Transition energies $E_{\text{nlm}}$ (meV)	
		exp.	EMA
2p <sub>0</sub>	478	59.1	59.4
2p <sub>±</sub>	488	60.4	60.9
3p <sub>0</sub>	not observed	–	64.7
3p <sub>±</sub>	527	65.2	65.4
4p <sub>0</sub>	not observed	–	66.6
4p <sub>±</sub>	not observed	–	67.1
CB	571	70.6	70.9

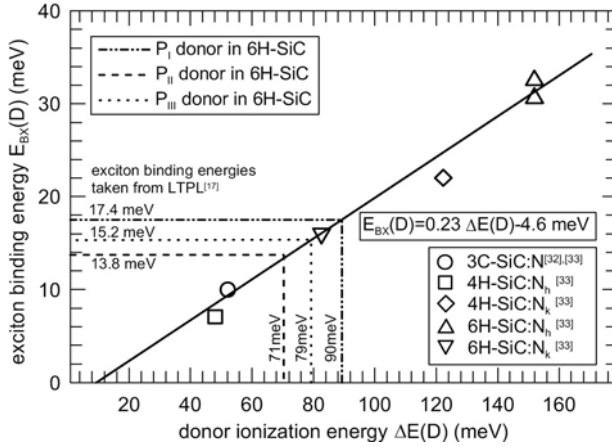


**Fig. 6.** Exciton binding energy  $E_{\text{BX}}(D)$  of nitrogen donors in different SiC polytypes residing on inequivalent lattice sites as function of the donor ionization energy  $\Delta E(D)$  (symbols). The solid straight line is a fit curve to the experimental points (Haynes rule). The exciton binding energy of P donors (see legend) obtained from LTPL spectra [17] is used to determine the corresponding ionization energies

represents a linear correlation between the exciton binding energy  $E_{\text{BX}}(D)$  of N donors incorporated in different SiC polytypes and occupying different inequivalent lattice sites and the corresponding ionization energy  $\Delta E(D)$  of these donors [31, 32]. The straight line confirms that the empirical Haynes rule is apparently valid for donors in SiC [33]. If we insert the exciton binding energies obtained from the LTPL spectra in Fig. 2 into the plot of Fig. 6, then the donor ionization energies determined by the Haynes rule result in: 71 meV, 79 meV and 90 meV. These values agree well with the ionization energies of P donors obtained from the fit of Faulkner’s effective mass theory to the observed IR absorption lines.

## 5 Electrical Properties of P Donors

Due to the limited incorporation of P into SiC during boule or epitaxial growth, it is not surprising that most of the information about the electrical properties of P donors is obtained from  $\text{P}^+$ -implanted SiC samples. In order to electrically activate the implanted P atoms and to largely reduce the implantation-induced crystal damage and intrinsic defects, an annealing step at high temperatures is required. The results of temperature dependent Hall effect measurements performed on  $\text{P}^+$ -implanted and isochronally annealed 4H-SiC layers are presented in the following section [12, 34].

In our experiments, 10  $\mu\text{m}$  thick  $p$ -type 4H-SiC:Al epitaxial layers with either [0001]- or [11-20]-oriented surface (so-called “Si-face” or “ $a$ -plane” sam-

**Table 2.** Ion energies and fluences of the eightfold P implantation used to generate a P box profile (mean P concentration  $[P] \approx 2 \times 10^{18} \text{ cm}^{-3}$ , depth  $d = 1.3 \text{ }\mu\text{m}$ )

Implantation energy $E$ [keV]	Implantation fluence $D$ [ $10^{13} \text{ cm}^{-2}$ ]
70	1.0
180	1.5
320	2
500	2.5
750	2.75
1100	2.5
1500	2.75
2000	3.5

ples) are used. The net acceptor concentration in the implanted layers  $N_A - N_D$  is  $10^{16} \text{ cm}^{-3}$  in the case of Si-face and  $3 \times 10^{15} \text{ cm}^{-3}$  in the case of  $a$ -plane samples. An eight fold P implantation has been conducted at room temperature to obtain a P box profile (mean P concentration  $[P] \approx 2 \times 10^{18} \text{ cm}^{-3}$ , depth  $d = 1.3 \text{ }\mu\text{m}$ ). The implantation parameters calculated with the TRIM.C program [35] are given in Table 2.

Subsequent to the implantation, the samples are annealed in an Ar ambient at temperature  $T_a$  for 30 minutes. The annealing temperature  $T_a$  is varied between  $1500^\circ\text{C}$  and  $1700^\circ\text{C}$  in steps of  $50^\circ\text{C}$ . In order to prevent thermal decomposition of the surface, the samples are kept in a SiC container during the annealing procedure. Ni ohmic contacts in van der Pauw configuration have been prepared by thermal evaporation of Ni and an alloying process at  $1000^\circ\text{C}$  for 5 minutes. In order to suppress leakage currents over the edges to the underlying  $p$ -type epilayer, mesa structures were prepared by reactive ion etching (RIE).

The Hall effect measurements are conducted in the temperature range from 50 K to 800 K. The free electron concentration  $n$  is obtained from the measured Hall coefficient  $R_H$  by:

$$n = -\frac{r_H}{e \cdot R_H} . \quad (1)$$

The temperature dependent Hall scattering factor  $r_H(T)$  is close to one [36] (see also special paper on the Hall scattering factor in by F. Schmid et al. at pp. 517 of this volume) and is, therefore, set to 1. The donor ionization energy  $\Delta E_{D,i}$  (index  $i$  denotes the  $i$ th donor species), the electrically active donor concentration  $N_{D,i}$  and the concentration of compensation  $N_{\text{comp}}$  are determined by a least-squares-fit of the neutrality equation (2) in Boltzmann approximation to the experimental data:

$$n + N_{\text{comp}} = \sum_{i=1,2} \frac{N_{D,i}}{1 + \frac{g_i \cdot n}{N_C} \exp\left(\frac{\Delta E_{D,i}}{kT}\right)} . \quad (2)$$

The following material parameters are used for the fit procedure:

- temperature-independent degeneracy factor  $g = 4$  ( $1s(A_1)$  and  $1s(E)$ -state are reversed after [3])
- temperature-dependent effective density of states mass  $m_n(T)$  after Wellenhofer and Rössler [37].

The free electron concentration  $n$  as a function of the reciprocal temperature for [0001]-oriented samples subsequent to P implantation and different annealing steps is displayed in Fig. 7a. An increase of the free electron concentration is observed in the whole temperature range with increasing annealing temperature  $T_a$ . The same tendency occurs in case of  $a$ -plane samples (see Fig. 7b). At temperatures below 200 K, especially after the anneal at 1700°C, the slope of the  $n(1/T)$ -curve of the Si-face sample Si5 is distinctly flatter than the corresponding slope of sample A5. This fact is attributed to a larger contribution of impurity band conduction to the carrier transport indicating the existence of a higher concentration of the compensation in Si-face samples.

In order to obtain a satisfactory fit of the neutrality equation to the measured free electron concentration, two different donor species are necessary ( $i = 1, 2$  in (2)). The two donor ionization energies determined by the fit are:

$$\Delta E_1 = (45 \pm 5) \text{ meV} \quad \text{and} \quad \Delta E_2 = (90 \pm 10) \text{ meV} .$$

These two donor species are attributed to P-donors residing at either cubic or hexagonal lattice sites. According to the identical density of cubic and

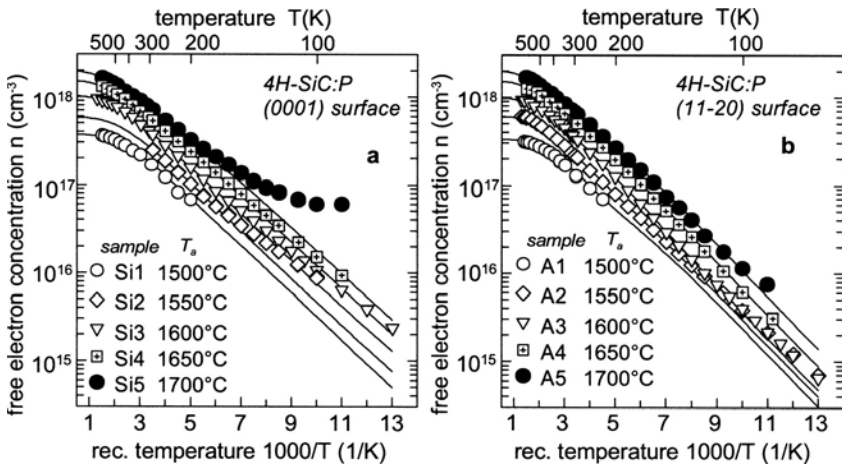


**Fig. 7.** Free electron concentration as a function of the reciprocal temperature (a) for Si-face 4H-SiC samples and (b) for  $a$ -plane 4H-SiC samples annealed at different temperatures. The annealing temperature is given in the legend. Symbols represent experimental data, solid lines show results of a least-squares-fit of the neutrality equation

**Table 3.** Total P donor concentration  $N_D = N_{D,1} + N_{D,2}$  and concentration of compensation  $N_{\text{comp}}$  obtained from least-squares fits of (2) to the experimental data (symbols) displayed in Fig. 7

Sample	Annealing temperature $T_a$ [°C]	$N_D$ [ $\times 10^{17} \text{ cm}^{-3}$ ]	$N_{\text{comp}}$ [ $\times 10^{17} \text{ cm}^{-3}$ ]
Si1	1500°C	6.1	2.4
A1	1500°C	5.3	1.7
Si2	1550°C	9.4	3.6
A2	1550°C	9.5	2.9
Si3	1600°C	16.0	5.4
A3	1600°C	15.0	3.8
Si4	1650°C	21.0	6.0
A4	1650°C	21.0	3.9
Si5	1700°C	25.0	6.1
A5	1700°C	25.0	3.6

hexagonal lattice sites in 4H-SiC, the determined concentration of cubic ( $k$ ) and hexagonal ( $h$ ) P donors is also equal demonstrating that the occupation probability is the same for both lattice sites. The maximum P donor concentration, which is identical to the implanted P concentration, is reached subsequent to an anneal at 1700°C. We point out that the applied experimental conditions result, within the measurement uncertainty, in a complete activation of the implanted P atoms. Table 3 summarizes the total electrically active P donor concentration  $N_D = N_{D,1} + N_{D,2}$  and concentration of compensation  $N_{\text{comp}}$  obtained from least-squares fits of (2) to the measurement points (symbols) in Fig. 7. In addition, no difference in the electrical activity of implanted P atoms is observed between Si-face and  $a$ -plane samples indicating that it is independent of sample orientation. Capano et al. [38, 39] reported in P<sup>+</sup>-implanted 4H-SiC two donor levels with ionization energies of 53 meV and 93 meV for an implanted P concentration of approximately  $5 \times 10^{17} \text{ cm}^{-3}$ . Troffer et al. [40] investigated P<sup>+</sup>-implanted 6H-SiC layers. These authors determined two donor levels with ionization energies of  $(80 \pm 5) \text{ meV}$  and  $(110 \pm 5) \text{ meV}$  at comparable implanted P-concentration. These results show that the ionization energies of P donors in 4H-SiC are slightly smaller than in 6H-SiC at identical donor concentrations; this trend has also been observed for N donors [41].

With the assumption that the electrical activation of P atoms can be described by first order kinetics, an activation energy  $E_A$  can be determined by the following equation [42]:

$$\ln \left( \frac{N_{D,\text{max}}}{N_{D,\text{max}} - N_D(t_a, T_a)} \right) = K \cdot t_a = K_0 \cdot \exp \left( -\frac{E_A}{k \cdot T_A} \right) \cdot t_a. \quad (3)$$

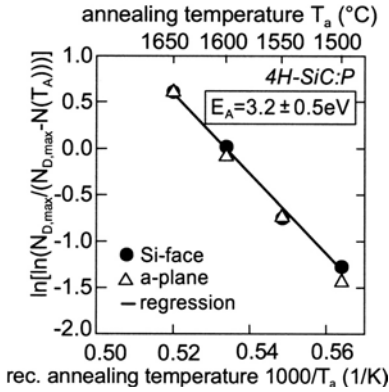


**Fig. 8.** Natural logarithm of the left hand side of the (3) as a function of reciprocal annealing temperature  $1000/T_A$  (Arrhenius plot). The *symbols* are calculated using the P concentration listed in Table 3, the *straight line* is a regression line

In (3)  $N_{D,\max}$  represents the maximum obtained P donor concentration,  $N_D(t_a, T_a)$  is the P donor concentration determined after an anneal at temperature  $T_A$  and time  $t_a$  ( $t_a = 30$  min in this experiment).  $K_0$  is a reaction constant and  $k$  the Boltzmann constant. The necessary P concentrations are listed in Table 3. The Arrhenius plot of (3) yields a straight line as demonstrated in Fig. 8. From the slope of this straight line, an activation energy of  $3.2 \pm 0.5$  eV is determined. A similar value of  $E_A = 2.5$  eV has been determined by Troffer et al. [40] for the activation of implanted P atoms in 6H-SiC. These two values agree well, taking into account the double logarithm scale of the  $y$ -axis in Fig. 8, which introduces a high sensitivity of  $E_A$  on the accuracy of the value for  $N_{D,\max}$ .

The determined concentration of compensation (see last column of Table 3) is in all the investigated Si-face/ $a$ -plane samples at least one order of magnitude higher than the background Al-doping level. It also increases with increasing annealing temperature  $T_a$  in both Si-face and  $a$ -plane samples. This observation clearly demonstrates that acceptor-like defect-centers are generated by the implantation and annealing process. This process-induced compensation is stronger in Si-face samples. The generation mechanism is not yet understood; possible explanations are discussed in Schmid et al. [34].

In Fig. 9 the electron Hall mobility determined in Si-face (Fig. 9a) and  $a$ -plane samples (Fig. 9b), respectively, is revealed. The mobility decreases with increasing annealing temperature. This effect is mainly visible at temperatures below 150 K where the mobility is dominated by scattering at charged impurities. The room temperature value for sample Si5 is  $157 \text{ cm}^2/\text{Vs}$  and for sample A5  $191 \text{ cm}^2/\text{Vs}$ . Taking into account the anisotropy of the Hall mobility parallel ( $a$ -plane samples) and perpendicular (Si-face samples) to the  $c$ -axis, a ratio of  $\mu(a\text{-plane})/\mu(\text{Si-face}) = 1.22$  is expected from the literature [43, 44]. This value agrees with the observed values at room temperature. At low temperatures, the ratio of  $\mu(a\text{-plane})/\mu(\text{Si-face})$  determined in Fig. 9 increases, however, up to a value of 8. Taking into account the anisotropy of the Hall mobility and the different concentration of compensating accep-

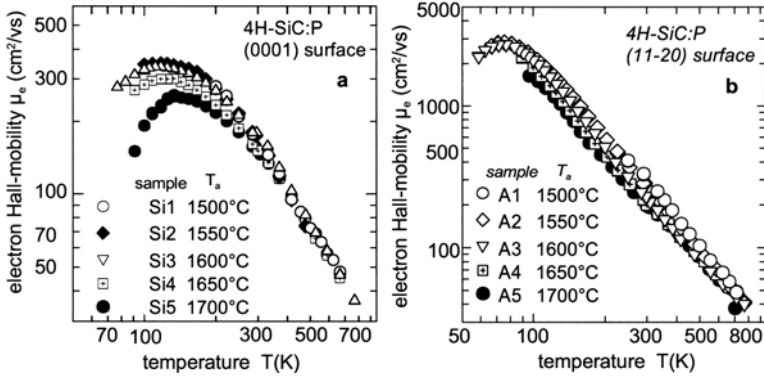


**Fig. 9.** Electron Hall mobility as a function of temperature for (a) Si-face (0001) and (b) *a*-plane (11-20) 4H-SiC samples. The samples are P<sup>+</sup>-implanted as described in Fig. 7 and annealed at different temperatures. The annealing temperature is given in the legend

tors generated by the implantation, a mobility ratio  $\mu(a\text{-plane})/\mu(\text{Si-face}) \approx 3$  is obtained, which shows the right tendency but can not quantitatively explain the experimental result. We suggest that a different concentration of extended defects (e.g. dislocations) is generated in the investigated samples with different orientation ([0001], [11-20]), which are electrically active and act as scattering barriers at low temperatures. This suggestion has to be experimentally tested e.g. by the optical beam induced current technique (OBIC).

## 6 Comparison of the Electrical Activation of Implanted P<sup>+</sup>- and N<sup>+</sup>-Ions

Depending on the device application highly *n*-type doped areas are required, e.g. for source and drain regions in *n*-channel MOSFETs or for highly conducting drift regions in the bulk of vertical devices, in order to minimize the series resistance. In all these cases, electrically active donor concentrations of  $10^{19} \text{ cm}^{-3}$  or even higher are desirable.

At the present, *n*-type doping is mainly achieved with nitrogen. This is due to the fact that N is unintentionally introduced into SiC during the sublimation growth from the residual ambient in the growth chamber. In addition, the N donor concentration can be raised by N<sub>2</sub> flow during the crystal growth. Several authors [45, 46] reported a saturation of electrically active N donors in 4H-SiC at a concentration of approximately  $4 \times 10^{19} \text{ cm}^{-3}$ , although the incorporated chemical N concentration determined by SIMS is much higher [46]. Such N-doped SiC wafers are also extremely brittle.

**Table 4.** Mean implanted N-/P- concentrations as calculated by TRIM.C [35] and partially experimentally determined by SIMS (P2, N3, P3)

Sample	N1	P1	N2	P2	N3	P3
Chemical N-/P- concentration ( $\text{cm}^{-3}$ )	$3.8 \cdot 10^{18}$	$2.6 \cdot 10^{18}$	$7.4 \cdot 10^{19}$	$5.0 \cdot 10^{19}$	$3.0 \cdot 10^{20}$	$2.0 \cdot 10^{20}$

Phosphorus is, therefore, considered to act as an alternative donor species in SiC. Due to the limited incorporation of P donors during crystal growth, implantation experiments are supposed to be suitable to study the possibility to achieve high donor concentrations.

Capano et al. [39] implanted  $\text{N}^{+}$ - and  $\text{P}^{+}$ -ions, respectively, into 4H-SiC samples at a mean concentration of  $10^{20} \text{ cm}^{-3}$  and measured the sheet resistance. These authors achieved a sheet resistance in P-implanted layers, which is lower by one order of magnitude than that one in N-implanted layers. Handy et al. [47] investigated P-implanted layers at concentrations between  $10^{17} \text{ cm}^{-3}$  and  $10^{20} \text{ cm}^{-3}$  and recommended the use of P donors when a dopant concentration above  $5 \times 10^{19} \text{ cm}^{-3}$  is required. In the following section, results of a detailed analysis [12] of the electrical activation of implanted  $\text{N}^{+}$ - or  $\text{P}^{+}$ -ions are briefly reported. The ions are implanted into *p*-type 4H-SiC epilayers, which are identically processed.

Al-doped 4H-SiC epilayers (thickness  $d = 10 \text{ }\mu\text{m}$ , net acceptor doping level  $N_{\text{A}} - N_{\text{D}} = 10^{16} \text{ cm}^{-3}$ ) are employed for the investigations. An N-/P-box profile of 800 nm in depth is generated by multiple implantation. The implantation energies used are 30, 100, 200, 330, 470 and 600 keV in the case of the N-implantation and 70, 180, 320, 500 and 750 keV in the case of the P implantation. The fluences are adjusted in such a way that three different doping levels are obtained. The mean P and N concentrations are given in Table 4.

In Fig. 10, the free electron concentration versus reciprocal temperature is displayed for three pairs of 4H-SiC epilayers, which are N- or P-implanted at different levels. Fig. 10a shows the corresponding plot for samples N1 and P1, which are implanted with the lowest fluence. Due to the slightly higher implanted N concentration (see second column of Table 3), the free electron concentration is superior in sample N1 over the whole investigated temperature range. Two donor species are necessary to achieve a satisfactory fit of (2) to the measurement points (see solid curves in Fig. 10a). The defect parameters obtained from the fit procedure are summarized in Table 5. The Hall effect analysis results in electrically active donor concentrations, which are equal to the corresponding implanted concentration within the experimental error bars demonstrating that the implanted  $\text{N}^{+}$ -/ $\text{P}^{+}$ -ions are completely activated in the low  $10^{18} \text{ cm}^{-3}$  range.

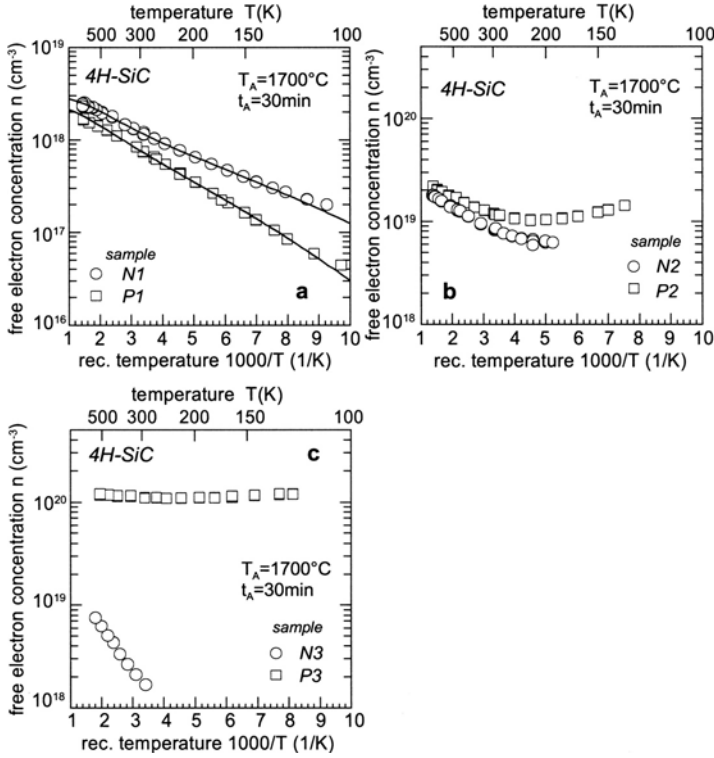


**Fig. 10.** Free electron concentration  $n$  as a function of reciprocal temperature as obtained from P- or N-implanted 4H-SiC epilayers for (a) sample P1 (*full squares*) and N1 (*open circles*), the *solid lines* represents fit curves; (b) sample P2 (*full squares*) and N2 (*open circles*), (c) sample P3 (*full squares*) and N3 (*open circles*)

In Fig. 10b, the temperature-dependence of the free electron concentration determined in samples N2 and P2 is revealed; this pair of samples is implanted at medium level (a few  $10^{19} \text{ cm}^{-3}$ ). Although the implanted N concentration in sample N2 is about 50% higher than the implanted P concentration in sample P2 (see third column in Table 4), the free electron concentration is

**Table 5.** Defect parameters obtained from the fit of (2) to the experimental data.  $\Delta E_i$  stands for the ionization energy of the  $i$ -th donor ( $i = 1, 2$ ),  $N_d$  represents the total donor concentration and  $N_{\text{comp}}$  the concentration of compensation

Sample	$\Delta E_1$ (meV)	$\Delta E_2$ (meV)	$N_d = N_{d,1} + N_{d,2}$ ( $\times 10^{18} \text{ cm}^{-3}$ )	$N_{\text{comp}}$ ( $\times 10^{17} \text{ cm}^{-3}$ )
N1	$33 \pm 5$	$89 \pm 5$	$3.5 \pm 0.3$	$4.0 \pm 1.5$
P1	$45 \pm 5$	$95 \pm 5$	$2.6 \pm 0.3$	$1.5 \pm 1.0$

superior in sample P2. This result clearly demonstrates that the electrical activation of implanted  $P^+$ -ions is more efficient than that one of implanted  $N^+$ -ions in the  $10^{19} \text{ cm}^{-3}$  doping range. Corresponding results obtained from samples P3 and N3, which are implanted at the highest concentrations in the  $10^{20} \text{ cm}^{-3}$  range, are shown in Fig. 10c. In this case, the implanted  $N^+$ - and  $P^+$ - ions have a completely different electrical activation. A free electron concentration above  $10^{20} \text{ cm}^{-3}$  is observed in the P-doped sample P3, while  $n(1/T)$  assumes a maximum value of  $8 \times 10^{18} \text{ cm}^{-3}$  in sample N3 at high temperatures; this value is even smaller than the corresponding value of about  $2 \times 10^{19} \text{ cm}^{-3}$  reached in sample N2.

In sample P3, the free electron concentration is almost independent of the temperature indicating that this sample is degenerated and the transport mechanism occurs largely in an impurity band. At high temperatures,  $n(1/T)$  reaches a value of  $1.3 \times 10^{20} \text{ cm}^{-3}$ , which unambiguously demonstrates that almost all the implanted  $P^+$ -ions are electrically activated. Contrary, the Hall effect measurement taken on sample N3 shows that the dominating portion of implanted  $N^+$ -ions forms defect complexes, which are not electrically active. The composition of these defect complexes or precipitates is not yet known. The formation of  $N_2$ -molecules has been proposed as a possible mechanism for the decrease of the N donor concentration [39].

In Fig. 11, the electron Hall mobility  $\mu_e$  determined in the N-/P-implanted  $4H$ -SiC epilayers is shown. The absolute value and temperature-dependence of  $\mu_e$  are similar in the low-implanted samples N1 and P1, no significant difference between the N- and P-implanted  $4H$ -SiC epilayer is observed (grey symbols). Because of the greater concentration of electrically active centers in samples N2 and P2, the electron Hall mobility is strongly reduced over the complete investigated temperature range by scattering at ionized impurities; the maximum value is between 30 and  $35 \text{ cm}^2/\text{Vs}$  (black symbols). The in-

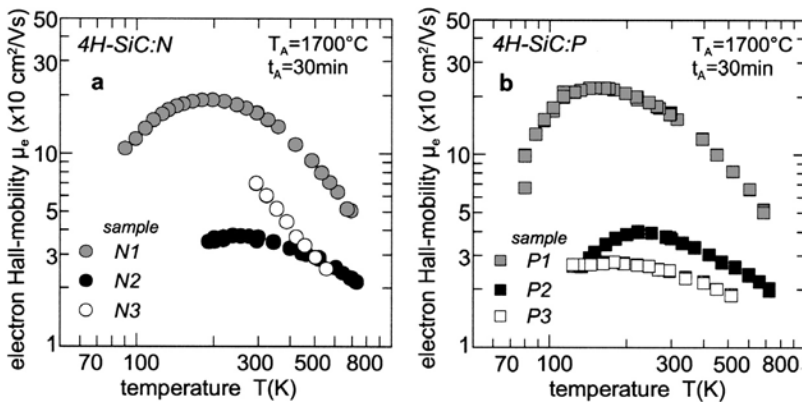


**Fig. 11.** Electron Hall mobility  $\mu_e$  as a function of temperature for the (a) N-implanted and (b) P-implanted  $4H$ -SiC epilayers introduced in Fig. 10

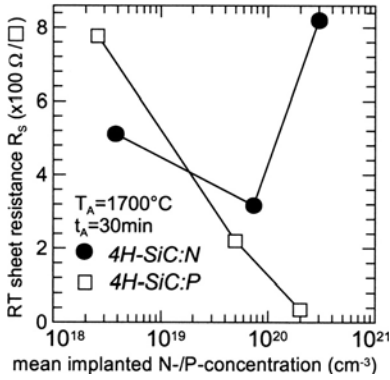


**Fig. 12.** Room temperature sheet resistance as a function of the mean implanted N-/P-concentration. The *symbols* represent experimental points, the *solid lines* serve as an eye-guide

crease of donors in sample P3 results only in a slight decrease and a weak temperature-dependence of  $\mu_e$  (see open squares in Fig. 11b), which are due to the fact that conduction in an impurity band dominates in sample P3. In sample N3, the generated N donor concentration is lower than in sample N2 (see open circles in Figs. 10b,c) leading to a smaller concentration of ionized impurities and, consequently, to the observed increase of  $\mu_e$  (compare open and black circles in Fig. 11a).

Figure 12 shows room temperature values of the sheet resistance  $R_s$  plotted as a function of the mean implanted N-/P-concentration.  $R_s$  is calculated with (4) where  $\rho$  and  $d$  are the resistivity and thickness of the conducting layer (600 nm for samples N $\nu$  and P $\nu$ ,  $\nu = 1, 2, 3$ ).

$$R_s = \frac{\rho}{d} \quad (4)$$

$R_s$  decreases monotonically with increasing mean implanted P concentration indicating that phosphorus can be electrically activated at least up to  $10^{20} \text{ cm}^{-3}$  (open squares). On the other hand,  $R_s$  passes a minimum at  $(2 - 5) \times 10^{19} \text{ cm}^{-3}$  in N-implanted 4H-SiC epilayers (full circles) and increases steeply with further enhancement of the implanted N concentration. This increase in  $R_s$  is due to the drastic reduction of the electrical activation of nitrogen. Table 6 summarizes the room temperature sheet resistances of N- or P-implanted layers as reported by different authors. The corresponding processing parameters are listed in columns 3 to 5. The lowest sheet resistances are reached by P-implantation; Negoro et al. [49] report a value of  $27\Omega/\square$  determined in a P<sup>+</sup>-implanted 4H-SiC wafer with [11-20]-orientation.

The observed saturation for N donors is independent of the doping technique. The value of  $(2 - 5) \times 10^{19} \text{ cm}^{-3}$  for the saturation concentration of N donors is obtained from the sublimation growth [45], a doping technique close to thermal equilibrium as well as from ion implantation [12], a technique far away from thermal equilibrium.

The presently available results support that doping of SiC with phosphorus is an attractive option, if high donor concentrations are required. At lower

**Table 6.** Room temperature values of sheet resistance  $R_s$  as reported by various authors

Poly-type	Implanted element	Fluence ( $\text{cm}^{-2}$ )	Implantation temperature $T_{\text{imp}}$ ( $^{\circ}\text{C}$ )	Annealing temperature/time $T_A$ ( $^{\circ}\text{C}$ )/ $t_A$ (min)	Sheet resistance $R_s(\Omega/\square)$	Ref.
4H	P	$4 \cdot 10^{15}$	600	1700/20	51	[39]
4H	P	$4.8 \cdot 10^{15}$	700	1650/15	110	[47]
4H	P	$4 \cdot 10^{15}$	600	1600/10	160	[48]
4H	P	$10^{16}$	800	1700/30	80 (Si-face) 27 ( <i>a</i> -plane)	[49]
4H	P	$1.4 \cdot 10^{16}$	800	1700/30	29 (Si-face) 29 ( <i>a</i> -plane)	[34]
6H	P	$2.7 \cdot 10^{15}$	700	1600/15	250	[50]
4H	N	$3 \cdot 10^{15}$	600	1700/20	534	[39]
6H	N	$2.7 \cdot 10^{15}$	700	1600/15	290	[50]
6H	N	$4 \cdot 10^{15}$	500	1500/30	542	[51]

donor concentrations ( $N_D < 10^{19} \text{ cm}^{-3}$ ), the electrical properties of N and P are rather similar; N offers the advantage that it can easily be incorporated during crystal growth and that it is the lighter atom permitting deeper implantation profiles at comparable implantation energies.

## 7 Conclusion

Doping of SiC with P donors during sublimation or epitaxial growth is still an unsolved problem. We suggest that P atoms form precipitates or react with carbon at temperatures above  $1600^{\circ}\text{C}$ . In this way, the incorporation of a desirable high P concentration into SiC during growth is prevented. By implantation of  $\text{P}^+$ -ions at elevated temperatures (e.g.  $500^{\circ}\text{C}$ ) and subsequent annealing at  $1700^{\circ}\text{C}$  for 30 min, P donor concentrations above  $10^{20} \text{ cm}^{-3}$  are reached. There are a few hints in the literature [2, 4, 5] that P donors reside on the Si-sublattice, however, this donor model requires a clear experimental confirmation by further magnetic resonance experiments. Reliable experiments regarding the solubility of phosphorus in SiC are still missing.

In LTPL spectra of P-doped 6H-SiC epilayers, lines labeled  $\text{Ph}^a$ ,  $\text{Ph}^b$  and  $\text{Ph}^c$  appear in the wavelength range from 4119 Å to 4124 Å; these lines are attributed to the recombination of excitons bound to neutral phosphorus donors. Zeeman investigations provide additional support for this assignment. Three series of EMA-like states are observed in the infrared absorption spectra of P-doped 6H-SiC bulk crystals. These absorption lines are attributed to transitions from ground states to excited states of P donors residing at inequivalent lattice sites. The ionization energies obtained either from LTPL

exciton binding energies in connection with the Haynes rule or from the fit of Faulkner's theory to the measured absorption lines agree well; the ionization energies determined by IR absorption are: 90 meV, 79.4 meV and 70.6 meV.

The electrical activation of implanted  $P^+$ -ions is independent of the orientation of the 4H-SiC sample surface ([0001] or [11-20]). An almost complete electrical activation of implanted  $P^+$ -ions is achieved even at a concentration of  $2 \times 10^{20} \text{ cm}^{-3}$ . At donor concentrations greater than  $(2 - 5) \times 10^{19} \text{ cm}^{-3}$ , the implantation of phosphorus is superior to the implantation of nitrogen. The lowest sheet resistances are reached by implantation of P ( $R_s = 27 \Omega/\square$  in 4H-SiC) [49].

## Acknowledgement

The support of this work by the Bundesministerium für Bildung, Wissenschaft, Forschung und Technologie (BMBF) under Contract No. 01BM974, the Bayerische Forschungsförderung (BFS) under Contract No. 362/99 and the German Science Foundation (SiC-Forschergruppe) is greatly acknowledged.

## References

1. A.I. Veinger, A.G. Zabrodskii, G.A. Lomakina, E.N. Mokhov: Soviet Phys. Solid State **28**, 917 (1986)
2. E.N. Kalabukhova, S.N. Lukin, E.N. Mokhov: Soviet Phys. – Solid State **35**, 361 (1993)
3. S. Greulich-Weber: Phys. Stat. Sol. (a) **162**, 95 (1997)
4. P.G. Baranov, I.V. Ilyin, E.N. Mokhov, H.J. von Bardeleben, J.L. Cantin: Phys. Rev. B **66**, 165206 (2002)
5. A. Gali, P. Deák, P.R. Briddon, R.P. Devaty, W.J. Choyke: Phys. Rev. B **61**, 12602 (2000)
6. J.M. Meese: *Neutron Transmutation Doping in Semiconductors* (New York, Plenum Press, 1979)
7. H. Heissenstein, C. Peppermüller, R. Helbig: J. Appl. Phys. **83**, 7542 (1998)
8. S. Tamura, T. Kimoto, H. Matsunami, M. Okada, S. Kanazawa, I. Kimura: Mater. Sci. Forum **338–342**, 849 (2000)
9. F.H.C. Carlsson, L. Storasta, B. Magnusson, J.P. Bergman, K. Sköld, E. Janzén: Mater. Sci. Forum **353–356**, 555 (2001)
10. J.M. Meese: in *Neutron Transmutation Doping in Semiconductors*, ed. by J.M. Meese (New York, Plenum Press, 1, 1979)
11. R. Devanathan, W.J. Weber, F. Gao: J. Appl. Phys. **90**, 2303 (2001)
12. M. Laube, F. Schmid, G. Pensl, G. Wagner, M. Linnarsson, M. Maier: J. Appl. Phys. **92**, 549 (2002)
13. D.J. Larkin: Phys. Stat. Sol. (b) **202**, 305 (1997)
14. R. Wang, I.B. Bhat, T.P. Chow: J. Appl. Phys. **92**, 7587 (2002)
15. K. Semmelroth, F. Schmid, D. Karg, G. Pensl, M. Maier, S. Greulich-Weber, J.-M. Spaeth: Mater. Sci. Forum, **433–436**, 63 (2003)

16. Yu.A. Vodakov, E.N. Mokhov, M.G. Ramm, A.D. Roenkov: in *Amorphous and Crystalline Silicon Carbide III*, ed. by G.L. Harris, M.G. Spencer, C.W. Yang, Springer Proceedings in Physics 56 (Berlin, Springer-Verlag, 1992) p. 329
17. S.G. Sridhara, L.L. Clemen, D.G. Nizhner, R.P. Devaty, W.J. Choyke, and D.J. Larkin: Mater. Sci. Forum **264-268**, 465 (1998)
18. D.J. Larkin, P.G. Neudeck, J.A. Powell, and L.G. Matus: Appl. Phys. Lett. **65**, 1659 (1994)
19. W.J. Choyke, L. Patrick: Phys. Rev. **127**, 1868 (1962)
20. M.A. Lampert: Phys. Rev. Lett. **1**, 450 (1958)
21. D.G. Thomas, J.J. Hopfield: Phys. Rev. **128**, 2135 (1962)
22. R.P. Devaty, W.J. Choyke, S.G. Sridhara, L.L. Clemen, D.G. Nizhner, D.J. Larkin, T. Troffer, G. Pensl, T. Kimoto, and H.S. Kong: Mater. Res. Forum **264-268**, 455 (1998)
23. L.S. Dang, K.M. Lee, G.D. Watkins, W.J. Choyke: Phys. Rev. Lett. **45**, 390 (1980)
24. J.F. Scott, D.J. Toms, L.S. Dong, K.M. Lee, G.D. Watkins, W.J. Choyke: Phys. Rev. B **23**, 2029 (1981)
25. W.J. Choyke, R.P. Devaty: pp. 607 of this volume
26. G. Pensl, F. Schmid, F. Ciobanu, M. Laube, S.A. Reshanov, N. Schulze, K. Semmelroth, H. Nagasawa, A. Schöner, G. Wagner: Mater. Sci. Forum, **433-436**, 365 (2003)
27. W. Suttrop, G. Pensl, W.J. Choyke, R. Stein, S. Leibenzeder: J. Appl. Phys. **72**, 3708 (1992)
28. R.A. Faulkner: Phys. Rev. **184**, 713 (1969)
29. W.M. Chen, N.T. Son, E. Janzén, D.M. Hofmann, B.K. Meyer: Phys. Stat. Sol. (a) **162**, 79 (1997)
30. B. Gerlach, J. Pollmann: Phys. Stat. Sol. (b) **67**, 93 (1975)
31. J.R. Haynes: Phys. Rev. Lett. **4**, 361 (1960)
32. T. Troffer: Dissertation, Erlangen (1998)
33. W.J. Choyke: in *The Physics and Chemistry of Carbides, Nitrides and Borides*, ed. by R. Freer, NATO ASI Series E (Kluwer Academic Publishers, 563, 1990)
34. F. Schmid, M. Laube, G. Pensl, G. Wagner, and M. Maier: J. Appl. Phys **91**, 9812 (2002)
35. J.P. Biersack: Fortran Monte Carlo Program TRIM CASCADE
36. G. Rutsch, R.P. Devaty, W.J. Choyke, D.W. Langer, and L.B. Rowland: J. Appl. Phys. **84**, 2062 (1998)
37. G. Wellenhofer, U. Rössler: Phys. Stat. Sol. (b) **202**, 107 (1997)
38. M. Capano, J.A. Cooper, M.R. Melloch, A. Saxler, W.C. Mitchel: J. Appl. Phys. **87**, 8773 (2000)
39. M. Capano, R. Santhakumar, R. Venugopal, M.R. Melloch, J.A. Cooper: J. Electron. Mat. **29**, 210 (2000)
40. T. Troffer, C. Peppermüller, G. Pensl, K. Rottner, A. Schöner: J. Appl. Phys. **80**, 3739 (1996)
41. W. Götz, A. Schöner, G. Pensl, W. Suttrop, W.J. Choyke, R. Stein, and S. Leibenzeder: J. Appl. Phys. **73**, 3332 (1993)
42. H. Ryssel, I. Ruge: *Ionenimplantation* (Teubner, Stuttgart, 57, 1978)
43. M. Schadt, G. Pensl, R.P. Devaty, W.J. Choyke, R. Stein, D. Stephani: Appl. Phys. Lett. **65**, 3120 (1994)
44. H. Iwata, K.M. Itoh: J. Appl. Phys **89**, 6228 (2001)

45. H.-J. Rost, D. Schulz, D. Siche: pp. 163 of this volume
46. N. Ohtani, M. Katsuno, J. Takahashi, H. Yashiro, M. Kanaya: J. Appl. Phys. **83**, 4487 (1998)
47. E.M. Handy, M.V. Rao, O.W. Holland, K.A. Jones, M.A. Derenge, N. Papanicolaou: J. Appl. Phys. **88**, 5630 (2000)
48. V. Khemka, R. Patel, N. Ramungul, T.P. Chow, M. Ghezzo, J. Kretchmer: J. Electron. Mat. **28**, 167 (1999)
49. Y. Negoro, M. Miyamoto, T. Kimoto, H. Matsunami: Appl. Phys. Lett. **80**, 240 (2002)
50. J.A. Gardner, A. Edwards, M.V. Rao, N. Papanicolaou, G. Kelner, M.A. Capano, M. Ghezzo, J. Kretchmer: J. Appl. Phys. **83**, 5118 (1999)
51. T. Kimoto, N. Inoue, H. Matsunami: Phys. Stat. Sol. (a) **162**, 263 (1997)

# Hall Scattering Factor for Electrons and Holes in SiC

F. Schmid, M. Krieger, M. Laube, G. Pensl, and G. Wagner

## Abstract

The analysis of Hall effect data taken on *n*- and *p*-type 4*H*-/6*H*-SiC is briefly described and the effect of excited states is demonstrated. The determination of the Hall scattering factor for electrons  $r_{\text{H,e}}(T, B)$  at low and high magnetic fields is introduced and temperature-dependent values taken from the literature are provided. The low field Hall scattering factor for holes  $r_{\text{H,h}}(T, B)$  is obtained from a comparison of the free hole concentration  $p(T)$  either determined by Hall effect measurement or calculated on the basis of the neutrality equation with defect parameters determined by SIMS or *C-V*. The temperature dependence of  $r_{\text{H,h}}(T, B)$  in the range from 100 K to 800 K is determined and tested for a series of Al-doped 4*H*-SiC layers.

## 1 Analysis of Hall Effect Data

Because of the wide band gap of the indirect semiconductor SiC ( $\Delta E_{\text{gap}} = 2.3 \text{ eV} - 3.3 \text{ eV}$  depending on the polytype) Hall effect measurements should be conducted in a large temperature range. The lower temperature limit is determined by the freeze out of the majority carriers (20 K to 100 K) and the upper temperature limit is due to the increasing vapor pressure of metallic connections at the sample holder and to the equipment of the Hall effect facility; in our case it is 800 K. Combined resistivity and Hall measurements result in the following experimental quantities:

resistivity  $\rho(T)$ , Hall coefficient  $R_{\text{H}}(T)$  and Hall mobility  $\mu_{\text{H}}(T)$ .

The Hall coefficient  $R_{\text{H}}(T)$  is related to the free carrier concentration  $n_{\text{f}}(T)$  by

$$R_{\text{H}}(T) = \frac{r_{\text{H}}(T)}{n_{\text{f}}(T) \cdot q}, \quad (1)$$

where  $r_{\text{H}}(T)$  and  $q$  are the Hall scattering factor and the elementary charge, respectively. The ionization energy  $\Delta E$  and concentration  $N$  of the dopants and the concentration of the compensation  $N_{\text{comp}}$  can be determined from

a least-squares-fit of the neutrality equation to the temperature-dependent free carrier concentration ( $n_f(1/T)$ -plot).

In case of one donor (e.g. nitrogen (N)) or one acceptor (e.g. aluminum (Al)) species, we obtain the following number of defect parameters  $d_p$  for the 3C-, 4H- and 6H-SiC polytype, which can be determined by the fit procedure:

$$n\text{-type } 3C\text{-SiC: } \Delta E_N, \quad N_N, \quad N_{\text{comp}}; \quad d_p = 3$$

$$p\text{-type } 3C\text{-SiC: } \Delta E_{Al}, \quad N_{Al}, \quad N_{\text{comp}}; \quad d_p = 3$$

$$n\text{-type } 4H\text{-SiC: } \Delta E_{N,h}, \quad \Delta E_{N,k}, \quad N_{N,h}, \quad N_{N,k}, \quad N_{\text{comp}}; \quad d_p = 5$$

$$p\text{-type } 4H\text{-SiC: } \Delta E_{Al}, \quad N_{Al}, \quad N_{\text{comp}}; \quad d_p = 3$$

$$n\text{-type } 6H\text{-SiC: } \Delta E_{N,h}, \quad \Delta E_{N,k1,k2}, \quad N_{N,h}, \quad N_{N,k1,k1}, \quad N_{\text{comp}}; \quad d_p = 5$$

$$p\text{-type } 6H\text{-SiC: } \Delta E_{Al}, \quad N_{Al}, \quad N_{\text{comp}}; \quad d_p = 3$$

While 3C-SiC is built up of only identical cubic lattice sites, 4H- and 6H-SiC provide 2 (one hexagonal  $h$  and one cubic  $k$ ) and 3 (one hexagonal  $h$  and two cubic  $k1$ ,  $k2$ ) inequivalent lattice sites, respectively. In  $n$ -type SiC, donors of the same species residing at inequivalent lattice sites result in distinctly different ionization energies caused by the Kohn-Luttinger interference effect [1, 2]. The difference in the ionization energy between donors residing at hexagonal and cubic lattice sites is large enough and can be resolved by means of a Hall measurement. As a consequence – although we consider only one donor species e.g. nitrogen –, we have to account for two different donors in 4H- and 6H-SiC. The difference between the ionization energy of  $k1$ - and  $k2$ -donors in 6H-SiC is only a few meV [3], therefore, they are treated as just one donor in the Hall analysis. In  $p$ -type SiC, acceptor wave functions are related to the valence band, which has its maximum at the  $\Gamma$ -point [4]. Consequently, no interference of the hole wave function according to the Kohn-Luttinger effect [1, 2] occurs and the ionization energy of acceptors of the same species differs only marginally with respect to inequivalent lattice sites [5].

Based on the Boltzmann approximation, the neutrality equation for a semiconductor with (2) one donor or (3) one acceptor species is given by [6]:

$$n + N_{\text{comp}} = \sum_i \frac{N_i}{1 + g(i) \cdot \frac{n}{N_C} \exp\left(\frac{\Delta E_i}{k_B T}\right)}, \quad (2)$$

$$p + N_{\text{comp}} = \frac{N_{\text{acc}}}{1 + g(\text{acc}) \cdot \frac{p}{N_V} \exp\left(\frac{\Delta E_{\text{acc}}}{k_B T}\right)}, \quad (3)$$

where index  $i = k$  for 3C-SiC and  $i = k, h$  for 4H- and 6H-SiC,

- $n$  = free electron concentration,
- $p$  = free hole concentration,
- $N_i$  = concentration of the  $i$ th donor(residing at  $k$  or  $h$  lattice site),
- $\Delta E_i$  = ionization energy of the  $i$ th donor,
- $N_{\text{acc}}$  = acceptor concentration,
- $\Delta E_{\text{acc}}$  = acceptor ionization energy,
- $k_B$  = Boltzmann constant,
- $N_C$  =  $2 \cdot M_C (2\pi \cdot m_{e,\text{ds}} k_B T / h^2)^{3/2}$   
= effective density-of-states (DOS) of the conduction band,
- $N_V$  =  $2 (2\pi \cdot m_{h,\text{ds}} k_B T / h^2)^{3/2}$  = DOS of the valence band,
- $M_C$  = number of conduction band minima,
- $m_{e,\text{ds}}$  = thermal DOS effective mass of electrons,
- $m_{h,\text{ds}}$  = thermal DOS effective mass of holes.

The thermal DOS effective mass of electrons  $m_{e,\text{ds}}$  and holes  $m_{h,\text{ds}}$  in 4H- and 6H-SiC is calculated by Wellenhofer and Rößler [4]. For donors and acceptors, the degeneracy factors  $g(i)$  and  $g(\text{acc})$ , respectively, are given by

$$g(i) = g_i^0 + \sum_j g_i^j \exp \left( -\Delta E_i^j / k_B T \right) , \quad (4)$$

$$g(\text{acc}) = g^0 + \sum_j g^j \exp \left( -\Delta E_j / k_B T \right) , \quad (5)$$

where  $g_i^0$ ,  $g^0$  and  $g_i^j$ ,  $g^j$  are the degeneracy factors of the ground and the  $j$ th excited state and  $\Delta E_i^j$ ,  $\Delta E_j$  is the energy separation between these two states.

The question is, in which way excited states affect the simulation of the  $n_f(1/T)$ -plot. Monovalent donors and acceptors in SiC can be treated in analogy to an isolated hydrogen atom; this system consists of an  $1s$  ground state and many possible excited states. In the following, we focus on two cases: (a) the split of donor ground states caused by the multiple minima of the conduction band and (b) higher excited states of acceptors.

(a) The ground state wave function of donors is composed of contributions of the different equivalent conduction band minima leading to a multiple degeneracy of the  $1s$  ground state (see Table 1). In the crystal field, the  $1s$  ground state splits into two levels with representation  $A_1$  and  $E$ ; the energy separation (valley-orbit-splitting) for 3C-, 4H- and 6H-SiC is listed in the fifth column of Table 1. A numerical example, which takes into account the valley-orbit-splitting, is given in Fig. 1a for the nitrogen donor in 6H-SiC.

**Table 1.** Number of equivalent conduction band minima, degeneracy of donor ground states valley-orbit-splitting for nitrogen donors in *3C*-, *4H*- and *6H*-SiC

SiC poly- type	number of equivalent conduction band minima $M_C$	degeneracy of donor ground states (including spin degeneracy)		valley-orbit-splitting of nitrogen donors	
		$1s(A_1)$	$1s(E)$		(meV)
<i>3C</i>	3	2	4	<i>k</i> -donor:	8.37 <sup>a</sup>
				<i>h</i> -donor:	7.6 <sup>b</sup>
<i>4H</i>	3	2	4	<i>k</i> -donor:	—
				<i>h</i> -donor:	13 <sup>a</sup>
<i>6H</i>	6	4	8	<i>k</i> <sub>1</sub> -donor:	60.3 <sup>a</sup>
				<i>k</i> <sub>2</sub> -donor:	62.3 <sup>a</sup>

<sup>a</sup> see [8]; <sup>b</sup> see [9]

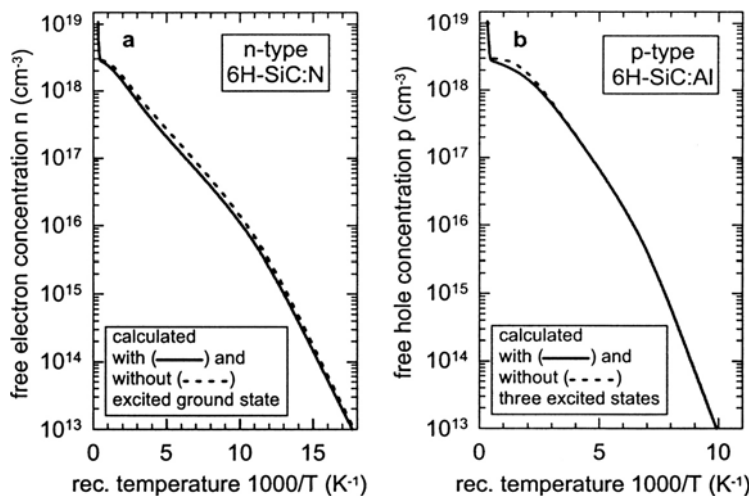


**Fig. 1.** The variation of the free carrier concentration with  $1/T$  for *n*-type/*p*-type *6H*-SiC calculated according to (2,3): (a)  $n(1/T)$ -dependence without excited state (*dashed line*) and with one excited valley-orbit-split ground state of the *h*- and *k*-donor (*solid curve*); (b)  $p(1/T)$ -dependence without excited state (*dashed line*) and for a model assuming three excited, hydrogen-like states of the Al-acceptor (*solid curve*)

The dashed curve is calculated without valley-orbit-splitting; the following defect parameters are used [7, 8]:

$$\Delta E_h = 81 \text{ meV}, \quad N_h = 1 \times 10^{18} \text{ cm}^{-3}, \quad g_h^0 = 4,$$

$$\Delta E_k = 140 \text{ meV}, \quad N_{k1,k2} = 2 \times 10^{18} \text{ cm}^{-3}, \quad g_k^0 = 4, \quad N_{\text{comp}} = 1 \times 10^{16} \text{ cm}^{-3}.$$

The solid curve in Fig. 1b is, in addition, calculated with an excited valley-orbit-split ground state for the hexagonal and cubic nitrogen donor:

$$\Delta E_h^1 = 13 \text{ meV}, \quad g_h^1 = 8,$$

$$\Delta E_k^1 = 61 \text{ meV}, \quad g_k^1 = 8.$$

At temperatures below 500 K, the split of ground states leads to a marginal reduction of the free electron concentration (see solid curve).

(b) Aluminum (Al) is the shallow acceptor in SiC. Taking into account an effective hole mass of  $1.2m_0$ , an effective-mass-like acceptor in 6H-SiC would have an ionization energy of 170 meV. The experimental value for the ionization energy of the Al acceptor in 6H-SiC is approximately 240 meV [5] demonstrating that the Al acceptor is not an “ideal” effective mass center; especially the excited states are strongly affected by the existence of the two valence bands (light- and heavy-hole band), which are degenerated at the  $\Gamma$ -point. Excited states of the Al acceptor in SiC are not yet observed. In Si, which has a similar valence band structure like SiC, optical investigations of the indium acceptor [10] indicate that the excited states of the indium acceptor clearly deviate from those of an effective mass center.

In order to demonstrate the influence of excited states, we describe the Al acceptor in 6H-SiC in a simple, non-realistic model and consider it as an effective mass-like acceptor with hydrogenic excited states. According to Shifrin [11], it is only necessary to consider the first few terms of such a series since for a finite acceptor density the wave functions for the higher excited states will overlap; these states already count to the valence band. Assuming an Al acceptor concentration of  $3 \times 10^{18} \text{ cm}^{-3}$ , the mean distance between acceptors is equal to 69 Å. On the other hand, the wave function of the fourth excited state of an effective-mass-like acceptor in 6H-SiC has an extension of 108 Å. For our illustrative numerical example in Fig. 1b, we have, therefore, employed the following data (dashed curve, without excited states):

$$\Delta E_{\text{Al}} = 170 \text{ meV}, \quad N_{\text{Al}} = 3 \times 10^{18} \text{ cm}^{-3}, \quad g^0 = 4, \quad N_{\text{comp}} = 1 \times 10^{16} \text{ cm}^{-3}.$$

In addition for the solid curve, the following excited states are taken into account:

$$\Delta E_{\text{Al}}^1 = 127.5 \text{ meV}, \quad g^1 = 16,$$

$$\Delta E_{\text{Al}}^2 = 151.1 \text{ meV}, \quad g^2 = 36,$$

$$\Delta E_{\text{Al}}^3 = 159.4 \text{ meV}, \quad g^3 = 64.$$

The solid curve in Fig. 1b shows the occupancy of excited states; it slightly reduces the free hole concentration between 300 K and the saturation region, where all the acceptors are ionized. However, we point out that the dashed and solid curve agree again at temperatures close below the onset of intrinsic conduction. This observation clearly demonstrates that excited states do not affect the determined concentration of Al acceptors as is claimed in [12]. This observation is also evident in case of Fig. 1a meaning that splitting of the ground state does also not affect the determination of donor concentrations in 6H-SiC.

## 2 Hall Scattering Factor

The motion of charge carriers in a real semiconductor under the force of crossed electric and magnetic fields depends on the scattering processes and energy distribution of the charge carriers as well as on the band structure of the semiconductor. The solutions of the equations of motion are in detail treated in textbooks (see for example [13]–[15]) or in the Monograph on *Galvanomagnetic Effects in Semiconductors* [16]. In order to describe the transport properties in the framework of the classical Boltzmann approximation, we have to assume that the energy gain or loss at each collision is small compared with the mean carrier energy. In this case, an energy-dependent relaxation time  $\tau(E)$  can be defined, where  $\tau(E)$  has to be considered as an average time over the different scattering mechanisms at a specific energy. With these assumptions the Hall scattering factor is given by [13, 14]:

$$r_H = \frac{\left\langle \frac{\tau^2}{1 + \omega_c^2 \tau^2} \right\rangle}{\left\langle \frac{\tau}{1 + \omega_c^2 \tau^2} \right\rangle^2 + \omega_c^2 \left\langle \frac{\tau^2}{1 + \omega_c^2 \tau^2} \right\rangle} . \quad (6)$$

Hall effect measurements are usually conducted at low magnetic field  $B$ , where charge carriers are scattered before they have completed one orbit. This low field limit can be defined as

$$\omega_c \tau = \mu B \ll 1 , \quad (7)$$

where  $\omega_c$  = cyclotron frequency,  
 $\mu = \mu_H / r_H$  = drift mobility,  
 $\mu_H$  = Hall mobility.

Assuming low field condition, (6) simplifies to:

$$r_H(T, B) = \frac{\langle \tau^2 \rangle}{\langle \tau \rangle^2} . \quad (8)$$

In the high field limit with  $\omega_c\tau = \mu B \gg 1$ , the Hall scattering factor  $r_H(T, B_{\text{high}})$  becomes equal one ( $r_H(T, B_{\text{high}}) = 1$ ). If the carrier mobility  $\mu$  is not sufficiently high, this condition requires experimentally extremely high magnetic fields.

The temperature-dependent measurement of the Hall coefficient  $R_H(T, B)$  in the low and high magnetic field limit allows the reliable determination of the Hall scattering factor  $r_H(T, B)$  at low magnetic fields according to:

$$r_H(T, B) = \frac{R_H(T, B)}{R_H(T, B_{\text{high}})} . \quad (9)$$

The knowledge of  $r_H(T, B)$  is necessary for the precise interpretation of Hall data.

### 3 Hall Scattering Factor for Electrons in 4H- and 6H-SiC

The Hall scattering factor for electrons  $r_{H,e}(T, B)$  has been determined by G. Rutsch et al. [17]–[19] in lightly N-doped 4H- and 6H-SiC epitaxial layers, which are grown on *p*-type SiC substrates. In this way, the epitaxial layers are junction isolated against the substrate. The Hall constant  $R_{H,e}(T, B)$  is measured in van der Pauw arrangement [20], which consists of a cloverleaf pattern – defined by reactive ion etching – and ohmic Ti/Ni contacts. The Hall effect measurements are conducted from 35 K to 290 K in magnetic fields up to 9 T (partially up to 30 T). Since high field saturation is not unambiguously observed, the normalizing factor  $R_{H,e}(T, B_{\text{high}})$  is replaced by either the value of a minimum in the measurement of  $R_{H,e}(T, B)$  versus  $B$ , if one is observed at high fields, or the value of  $R_H(T, B)$  at  $B = 9$  T. The Hall scattering factor  $r_{H,e}(T, B)$  as a function of the magnetic field  $B$  at three and two different temperatures is plotted in Figs. 2 and 3 for the 4H- and 6H-SiC polytype, respectively.

In Fig. 2, the upturn observed at the highest fields at  $T = 39.8$  K is interpreted as field-induced freeze out of conduction electrons [21]. At 109.2 K and 298.0 K,  $r_{H,e}(T, B)$  slowly rises with magnetic field. The cross-over between low and high field limits is given by  $\mu B \approx 1$ . The cross-over points for the experimental  $r_{H,e}(T, B)$ -dependences are marked by open circles; they are in good agreement with the theoretical inflection points of the corresponding curves. Figure 3 reveals results for 6H-SiC, which show a similar behavior.

Figures 4 and 5 display the low field Hall scattering factor versus temperature for a series of 4H- and 6H-SiC samples. The observed Hall scattering factor is consistently larger than unity below 50 K and smaller above 65 K for both SiC polytypes. It varies between 0.92 and 1.21 in the investigated temperature range.

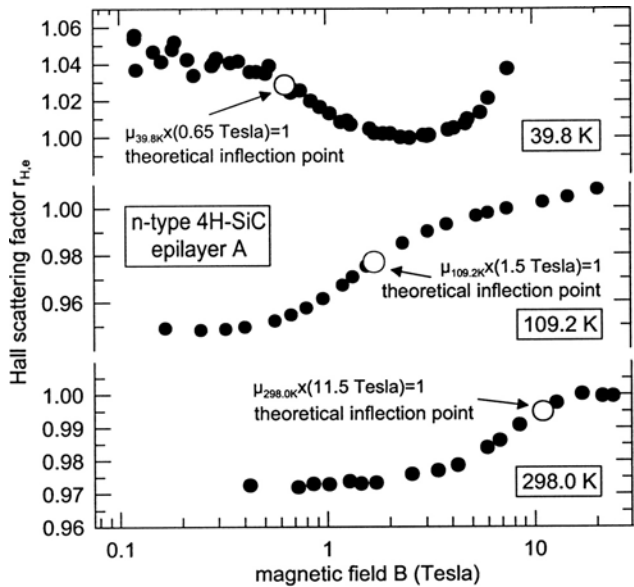


**Fig. 2.** Magnetic field dependence of the Hall scattering factor  $r_{H,e}$  of the *n*-type 4*H*-SiC homoepitaxial layer *A* grown on a *p*-type 4*H*-SiC substrate and measured at three different temperatures

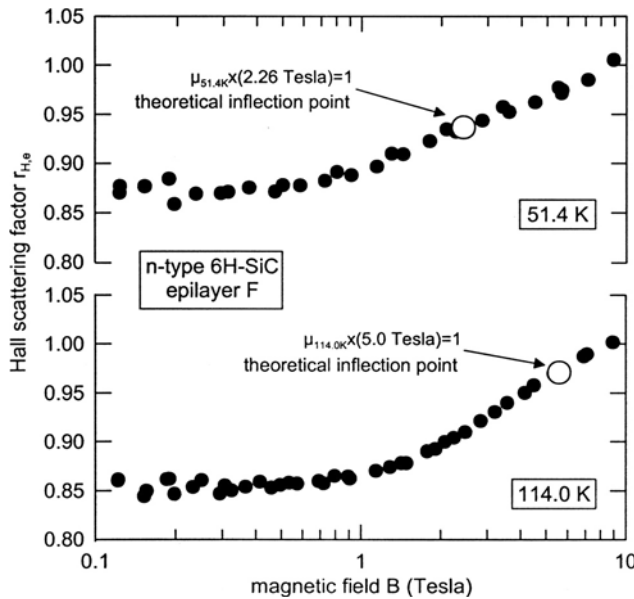


**Fig. 3.** Magnetic field dependence of the Hall scattering factor  $r_{H,e}$  of the *n*-type 6*H*-SiC homoepitaxial layer *F* grown on a *p*-type 6*H*-SiC substrate and measured at two different temperatures

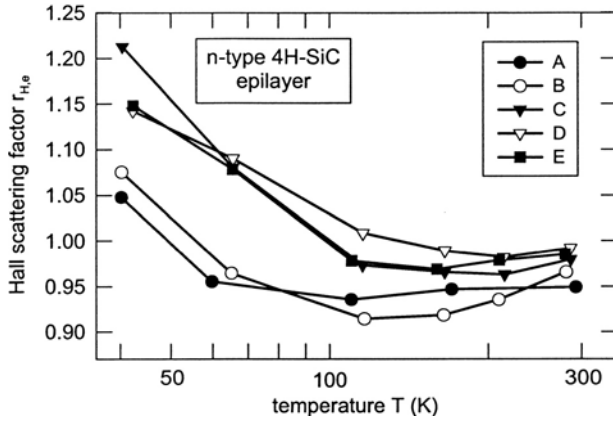


Fig. 4. Hall scattering factor  $r_{H,e}$  versus temperature of 4H-SiC epilayers A to E

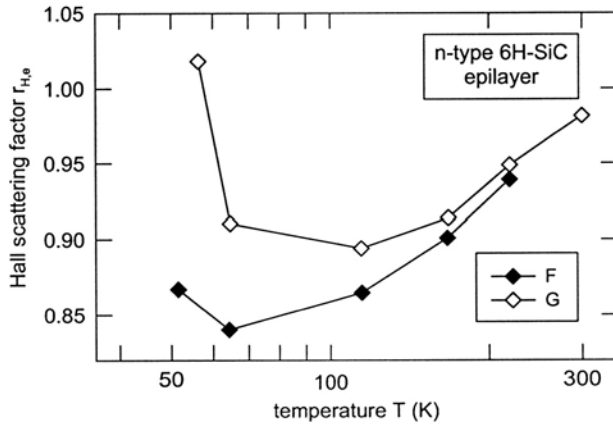


Fig. 5. Hall scattering factor  $r_{H,e}$  versus temperature of 6H-SiC epilayers F and G

#### 4 Hall Scattering Factor for Holes in 4H- and 6H-SiC

A direct determination of the hole Hall scattering factor  $r_{H,h}(T, B)$  by variation of the magnetic field as described in the previous section for the Hall scattering factor of electrons  $r_{H,e}(T, B)$  is not feasible in SiC because of the small values of the mobility of holes. The required magnetic fields to reach the high field limit  $\mu B \gg 1$  in *p*-type SiC would be extremely high. On the other hand, the assumption of  $r_{H,h} = 1$ , independent of the temperature and the magnetic field, results in a discrepancy between the Al acceptor concentration  $N_{Al}$  obtained from the Hall analysis and the chemical Al concentration  $N_{Al,SIMS}$  determined by secondary ion mass spectrometry (SIMS). It turns out that in this case the Al acceptor concentration is usually higher by a

factor between two and three than the chemical Al concentration, which is unrealistic.

We have, therefore, developed an indirect method to explore the low field Hall scattering factor of holes  $r_{\text{H,h}}(T, B)$  in a temperature range, which is of practical interest for Hall effect investigations of  $p$ -type SiC samples [22, 23]. It is determined by comparing an experimental  $p_{\text{exp}}(1/T)$ -Hall effect curve, for which  $r_{\text{H,h}} = 1$  is assumed, with a calculated  $p_{\text{theor}}(1/T)$ -curve, which is based on the neutrality equation (3) and physical quantities determined in the identical SiC sample as the Hall data by independent analysis techniques like capacitance-voltage ( $C$ - $V$ ) technique and SIMS. The calculation of  $p_{\text{theor}}(1/T)$  does not require the knowledge of  $r_{\text{H,h}}(T, B)$ .

The low field Hall scattering factor  $r_{\text{H,h}}(T, B)$  is extracted by forming the following ratio:

$$r_{\text{H,h}}(T, B) = \frac{p_{\text{theor}}(1/T)}{p_{\text{exp}}(1/T)}. \quad (10)$$

#### 4.1 Determination of the Hall Scattering Factor of Holes in 4H- and 6H-SiC

In order to minimize experimental uncertainties,  $p_{\text{exp}}(T)$  is determined by Hall effect in high quality Al-doped 4H- and 6H-SiC substrates. For the calculation of  $p_{\text{theor}}(T)$ , the following assumptions are made:

- (a) Because of the high solubility of Al in SiC (about  $10^{21} \text{ cm}^{-3}$  at  $2000^\circ\text{C}$  to  $2400^\circ\text{C}$  according to [24]) it is reasonable to assume that all the incorporated Al atoms, which are monitored by SIMS, are electrically active; it follows:  $N_{\text{Al,chem}} = N_{\text{Al,SIMS}} = N_{\text{Al}}$ .
- (b)  $C$ - $V$  measurements result in the net acceptor concentration  $N_{\text{Al,net}} = N_{\text{Al}} - N_{\text{comp}}$ ; consequently  $N_{\text{comp}}$  is given by:  $N_{\text{comp}} = N_{\text{Al,SIMS}} - N_{\text{Al,net}}$ .
- (c)  $\Delta E_{\text{Al}}$  depends on the Al acceptor concentration; for the particular concentration  $N_{\text{Al,chem}}$  is taken from a corresponding graph  $\Delta E_{\text{Al}}(N_{\text{Al}})$  published in the literature [25].

In order to determine  $p_{\text{exp}}(T)$ , Hall measurements are conducted in van der Pauw configuration on square-shaped samples with Ti/Al-contacts in the corners which are annealed at  $960^\circ\text{C}$  for 5 minutes. The free hole concentration as a function the reciprocal temperature of a 4H- and 6H-SiC substrate sample is shown in Figs. 6a,b. The open circles are calculated from the experimental  $R_{\text{H,h}}(T)$ -values with (1) assuming  $r_{\text{H,h}} = 1$  and the solid curves are least-squares-fits of the neutrality equation (3) to the open circles. The defect parameters obtained from the fit procedure for the 4H- and 6H-SiC substrate are listed in Tables 2 and 4, respectively.

In order to be able to calculate  $p_{\text{theor}}(T)$  with the neutrality equation (3), the required defect parameters ( $N_{\text{Al}}$ ,  $N_{\text{comp}}$ ) have to be determined by  $C$ - $V$  and SIMS measurements on the identical samples. In addition, the ionization

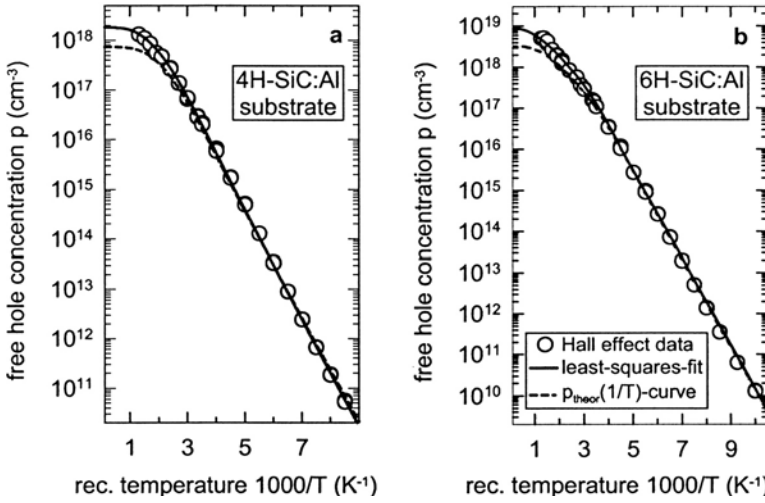


**Fig. 6.** Free hole concentration versus reciprocal temperature as obtained from Hall measurements on (a) a 4H-SiC:Al substrate and (b) a 6H-SiC:Al substrate. The *open circles* are calculated from the Hall coefficient  $R_{\text{H,h}}(T)$  according to (1) with  $r_{\text{H,h}} = 1$ . The *solid curves* are least-square-fits of (3) to the *open circles*; the *dashed curves* are calculated with (3) and parameters given in Tables 3 and 5

**Table 2.** Input and fit parameters for the Hall effect analysis of the experimental  $p_{\text{exp}}(1/T)$ -data determined in the  $p$ -type 4H-SiC substrate (see *solid curve* in Fig. 6a)

Evaluation method	Input parameter			Fit parameter		
	$r_{\text{H,h}}$	$g$	$m_{\text{h,ds}}$	$N_{\text{Al}}$ ( $\text{cm}^{-3}$ )	$N_{\text{comp}}$ ( $\text{cm}^{-3}$ )	$\Delta E_{\text{Al}}$ (meV)
Fit of (3) to Hall effect data	1	4	[4]	$2.6 \times 10^{18}$	$8 \times 10^{17}$	196

**Table 3.** Input parameters used to calculate  $p_{\text{theor}}(1/T)$  with (3) for the  $p$ -type 4H-SiC substrate (see *dashed curve* in Fig. 6a)

Evaluation method			Input parameter		
	$g$	$m_{\text{h,ds}}$ (T)	$N_{\text{Al}}$ ( $\text{cm}^{-3}$ )	$N_{\text{comp}}$ ( $\text{cm}^{-3}$ )	$\Delta E_{\text{Al}}$ (meV)
Calculation of $p_{\text{theor}}(1/T)$ -curve according to (3)	4	[4]	SIMS $1.2 \times 10^{18}$	$C$ -V/SIMS $5 \times 10^{17}$	[25] $205 \pm 10$

**Table 4.** Input and fit parameters for the Hall effect analysis of the experimental  $p_{\text{exp}}(1/T)$ -data determined in the  $p$ -type  $6H$ -SiC substrate (see *solid curve* in Fig. 6b)

Evaluation method	Input parameter			Fit parameter		
	$r_{\text{H,h}}$	$g$	$m_{\text{h,ds}}$	$N_{\text{Al}}$ ( $\text{cm}^{-3}$ )	$N_{\text{comp}}$ ( $\text{cm}^{-3}$ )	$\Delta E_{\text{Al}}$ (meV)
Fit of (3) to Hall effect data	1	4	[4]	$9 \times 10^{18}$	$4 \times 10^{17}$	197

**Table 5.** Input parameters used to calculate  $p_{\text{theor}}(1/T)$  with (3) for the  $p$ -type  $6H$ -SiC substrate (see *dashed curve* in Fig. 6b)

Evaluation method	Input parameter				
	$g$	$m_{\text{h,ds}}$ (T)	$N_{\text{Al}}$ ( $\text{cm}^{-3}$ )	$N_{\text{comp}}$ ( $\text{cm}^{-3}$ )	$\Delta E_{\text{Al}}$ (meV)
Calculation of $p_{\text{theor}}(1/T)$ -curve according to (3)	4	[4]	SIMS $4 \times 10^{18}$	$C$ - $V$ /SIMS $3 \times 10^{17}$	[25] $205 \pm 10$

energy of the Al acceptor is taken from a  $\Delta E_{\text{Al}}(N_{\text{Al}})$ -plot in [25]. The parameter values for the  $4H$ - and  $6H$ -SiC substrate are summarized in Tables 3 and 5. With both sets of parameters the dashed curves in Figs. 6a,b are calculated. The dashed and solid curves deviate especially at high temperatures in the so-called “saturation region” of the Al acceptor.

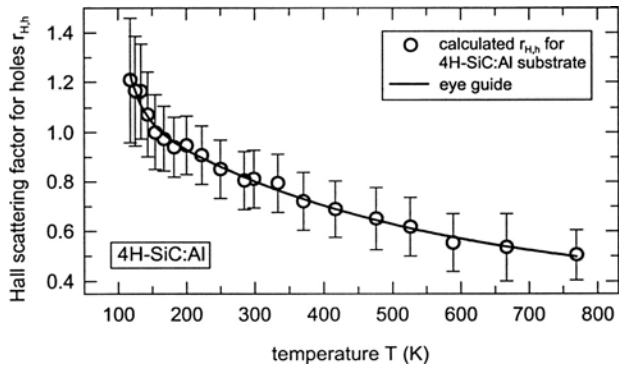


**Fig. 7.** Low field Hall scattering factor  $r_{\text{H,h}}(T, B)$  for holes in  $4H$ -SiC:Al as a function of the temperature as calculated with (10) and the data shown in Fig. 6a. The *solid curve* represents a smoothed curve connecting the calculated points (*open circles*)

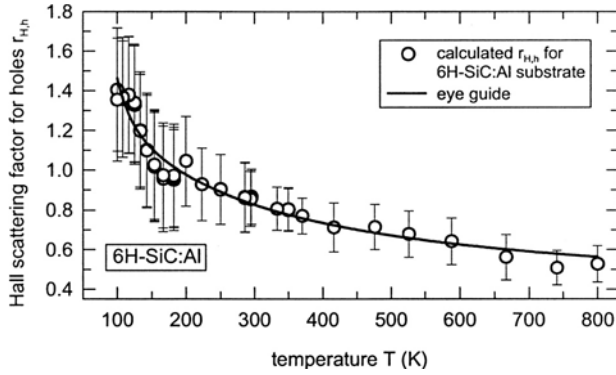


**Fig. 8.** Low field Hall scattering factor  $r_{H,h}(T, B)$  for holes in 6H-SiC:Al as a function of the temperature as calculated with (10) and the data shown in Fig. 6b. The *solid curve* represents a smoothed curve connecting the calculated points (*open circles*)

The low field Hall scattering factor of holes  $r_{H,h}(T, B)$  in 4H- and 6H-SiC is calculated with (10) in the investigated temperature range; it is depicted in Figs. 7 and 8. The uncertainty in the ionization energy of the Al acceptor, which is estimated to be equal to  $\pm 10$  meV, leads to the relatively large error bars especially at low hole concentrations in the freeze-out region. The solid curves in Figs. 7 and 8 correspond to smoothed curves connecting the calculated  $r_{H,h}(T, B)$ -values (open circles) and serving as an eye guide. The absolute values of  $r_{H,h}(T, B)$  and their temperature dependence are nearly the same for the 4H- and 6H-SiC polytype. The Hall scattering factor  $r_{H,h}(T, B)$  strongly deviates from 1 and assumes values between 1.4 at 100 K and 0.5 at 800 K.

Szmulowicz [26] calculated the temperature dependence of the Hall scattering factor of holes in *p*-type Si for low magnetic fields from solutions of the full Boltzmann equation taking into account the accurate valence band dispersions. In addition, the hole-phonon transition rates are calculated using the deformation-potential theory and one adjustable parameter for the hole-optical phonon interaction strength; this parameter is fitted to mobility data at room temperature. The solid curve in Fig. 9 reveals the result of this theory. After Szmulowicz the decrease of  $r_{H,h}(T, B)$  for temperatures  $T > 100$  K is due to the onset and the increasing strength of the hole-optical phonon interaction. The open circles and diamonds in Fig. 9 are experimental data taken on *p*-type Si [27, 28]; they are in good agreement with the theoretical prediction. The temperature dependence of  $r_{H,h}(T, B)$  for 4H- and 6H-SiC shows a similar course, particularly  $r_{H,h}(T, B)$  decreases also at temperatures above  $T > 100$  K, indicating that a distinct interaction of holes with optical phonons occurs at comparable temperatures for both the group IV-semiconductors.

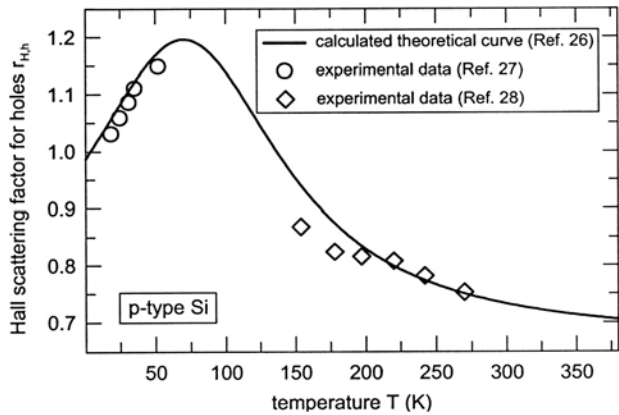


**Fig. 9.** Hall scattering factor  $r_{H,h}$  for holes in  $p$ -type Si. The *solid curve* is calculated after Szmulowicz [26], the *open circles* and *diamonds* are experimental results after [27] and [28]

**4.2 Test of the Hall Scattering Factor of Holes in 4H-SiC**

The Hall scattering factor of holes in 4H-SiC as shown in Fig. 7 is tested with help of a sample structure for which the Al concentration is well known. An Al box profile is generated in an  $n$ -type 4H-SiC epilayer ( $N_N = 5 \times 10^{15} \text{ cm}^{-3}$ ) by eightfold implantation followed by an anneal at 1700°C for 30 min. The individual Al implantation profiles based on TRIM\_C simulation after Biersack [30] (dashed curves) and the resulting Al profile determined by SIMS (solid curve) are displayed in Fig. 10 (after [29]). The results of the

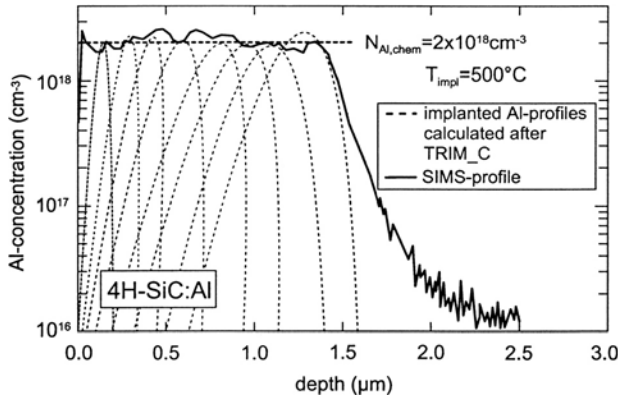


**Fig. 10.** Implanted Al concentration versus depth of sample Al(impl). The *dashed curves* correspond to the individual Al implantations calculated with the TRIM\_C simulation program; the *solid curve* is the total Al profile determined by SIMS (after [29])

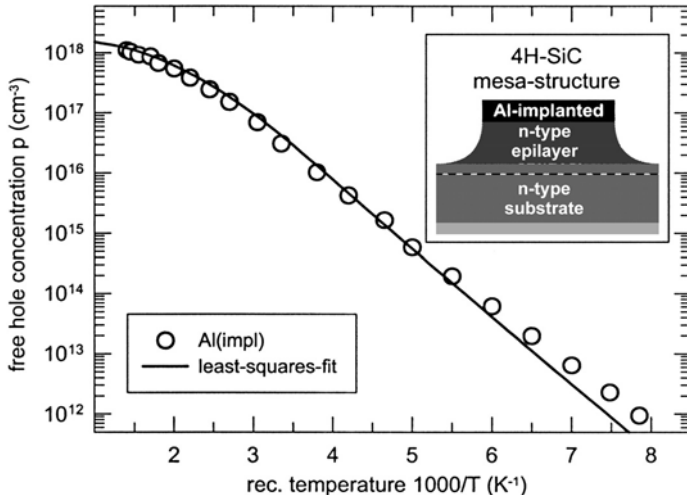


**Fig. 11.** Free hole concentration versus reciprocal temperature taken on the Al-implanted 4H-SiC sample Al(impl). *Open circles* correspond to experimental  $p_{\text{exp}}(1/T)$ -data obtained from the Hall coefficient  $R_{H,h}$  according (1) with  $R_{H,h}(T, B)$  as given in Fig. 7; the *solid curve* is a least-squares-fit of the neutrality (3) to the  $p_{\text{exp}}(1/T)$ -data. The *inset* is a scheme of the sample structure

simulation and of SIMS agree well; the mean Al concentration  $N_{\text{Al,chem}}$  and depth  $d_{\text{Al}}$  of the implanted Al profile are:

$$N_{\text{Al,chem}} = 2 \times 10^{18} \text{ cm}^{-3},$$

$$d_{\text{Al}} = 1.5 \text{ } \mu\text{m}.$$

In order to avoid leakage currents over the edges, a mesa-structure is etched by reactive ion etching (RIE) as shown in the insert of Fig. 11. The implanted  $p$ -type layer is junction isolated against the underlying  $n$ -type SiC epilayer. The  $p(1/T)$ -plot (open circles) in Fig. 11 results from a Hall measurement in van der Pauw configuration; the experimental points are obtained from (1) taking into account the low field Hall scattering factor given in Fig. 7. The solid curve in Fig. 11 corresponds to a least-squares-fit of the neutrality equation (3) to the open circles; the defect parameters obtained from the fit are summarized in Table 6. The Al acceptor concentration of  $2 \times 10^{18} \text{ cm}^{-3}$  agrees perfectly with the chemical Al concentration determined by SIMS while the Hall effect analysis with  $r_{H,h} = 1$  would result in an Al acceptor concentration of  $6.6 \times 10^{18} \text{ cm}^{-3}$ , which is about three times higher. Provided that our assumption – all the incorporated Al atoms are electrically active – is correct, then this test result is a strong hint for the validity of the low field Hall scattering factor of holes as revealed in Figs. 7 and 8.

**Table 6.** Input and fit parameters for the Hall effect analysis of the experimental  $p_{\text{exp}}(1/T)$ -data determined in the Al-implanted 4H-SiC sample (see Fig. 11)

4H-SiC sample	Input parameter				Fit parameter	
	$r_{\text{H,h}}(T, B)$	$g$	$m_{\text{h,ds}}(T)$	$N_{\text{Al}}$ ( $\text{cm}^{-3}$ )	$N_{\text{comp}}$ ( $\text{cm}^{-3}$ )	$\Delta E_{\text{Al}}$ (meV)
Al(impl)	according to Fig. 7	4	[4]	$2 \times 10^{18}$	$4 \times 10^{17}$	200

**Table 7.** Chemical concentration  $N_{\text{Al,SIMS}}$  and concentration of compensation  $N_{\text{comp}}$  together with the degree of compensation  $\eta$  for Al-doped 4H-SiC epilayers Al1(epi) to Al4(epi)

Sample #	Concentration		
	$N_{\text{Al,SIMS}}$ from SIMS ( $\text{cm}^{-3}$ )	$N_{\text{comp}}$ from kink in $p_{\text{exp}}(1/T)$ ( $\text{cm}^{-3}$ )	$\eta = \frac{N_{\text{comp}}}{N_{\text{Al,SIMS}}} \times 10^{-3}$
Al1(epi)	$1.8 \times 10^{18}$	$6 \times 10^{14}$	0.3
Al2(epi)	$3 \times 10^{17}$	$1 \times 10^{14}$	0.3
Al3(epi)	$3 \times 10^{16}$	$8 \times 10^{13}$	2.6
Al4(epi)	$1.8 \times 10^{15}$ <sup>c</sup>	$3 \times 10^{13}$	16

<sup>c</sup> taken from  $C$ - $V$  measurement;  $N_{\text{Al,SIMS}}$  of Al4(epi) is below detection limit of our SIMS system.

A second test is conducted in order to check whether the determined  $r_{\text{H,h}}(T, B)$ -values are sensitive to the Al acceptor concentration. In view of this aim, four Al-doped 4H-SiC epilayers grown by CVD on  $n$ -type 4H-SiC substrates are investigated [31]. The chemical Al concentration  $N_{\text{Al,SIMS}}$  of these epilayers is listed in the second column of Table 7; it varies over about three orders of magnitude (from  $10^{15} \text{ cm}^{-3}$  to  $10^{18} \text{ cm}^{-3}$ ). Sample preparation and Hall effect measurement are conducted in the same way as described above. The free hole concentration  $p(T)$  and the Hall mobility  $\mu_{\text{H}}(T)$  determined in the four  $p$ -type epilayers are shown in Figs. 12a and 13 (see symbols). With decreasing temperature, the slope of all four  $p(1/T)$ -dependences can be approximated by two straight lines [32]. This procedure is explicitly demonstrated in Fig.12b for the epilayer Al1(epi). The intersection point of these straight lines generates a kink, which directly indicates the concentration of the compensation. These concentrations are listed in the third column and the degree of compensation  $\eta = N_{\text{comp}}/N_{\text{Al,SIMS}}$  is given in the fourth column of Table 7. In addition, the  $p(1/T)$ -dependence of epilayer Al4(epi) shows a pronounced saturation region at high temperatures, which

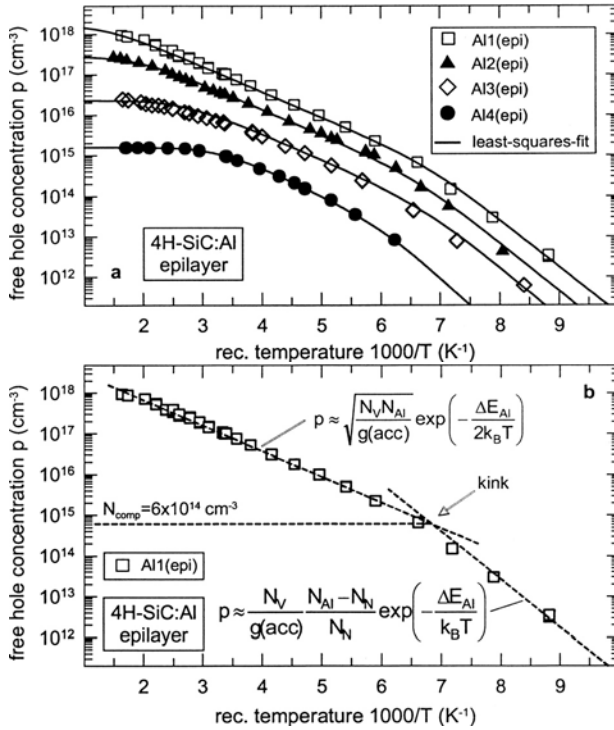


**Fig. 12.** (a) Free hole concentration versus reciprocal temperature taken on four Al-doped 4H-SiC epilayers (Al1(epi) to Al4(epi)). The *symbols* correspond to experimental  $p_{\text{ext}}(1/T)$ -data obtained from the Hall coefficient  $R_{H,h}$  according (1) with  $r_{H,h}(T)$  as given in Fig. 7. The *solid curves* are least-squares-fits of the neutrality equation (3) to the  $p_{\text{ext}}(1/T)$ -data. (b) Free hole concentration versus reciprocal temperature for epilayer Al1(epi). The slope of the  $p(1/T)$ -dependence is approximated by *two straight lines* [32] (*dashed*). The two equations given in the figure represent the analytical expressions of the *straight lines*; their slopes differ by a factor of two

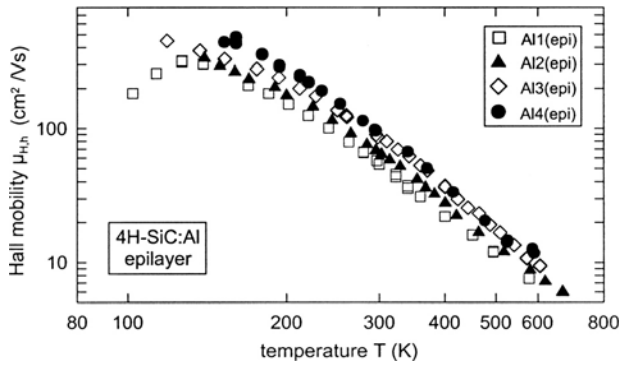
immediately defines – within the measurement accuracy – the Al acceptor concentration of  $1.8 \times 10^{15} \text{ cm}^{-3}$  (compensation is two orders of magnitude lower); this value also agrees well with the chemical Al concentration confirming our assumption that all the incorporated Al atoms are electrically active.

The solid curves in Fig. 12a are calculated by the standard fit procedure as applied above; the obtained fit parameters are listed in Table 8. The comparison of corresponding Al concentrations obtained from SIMS or  $C$ - $V$  and Hall effect analyses show an excellent agreement over several orders of magnitude.

As a consequence, we can conclude that the low field Hall scattering factor of holes  $r_{H,h}(T, B)$  in weakly compensated  $p$ -type 4H-SiC samples does not

**Table 8.** Input and fit parameters for the Hall effect analysis of the experimental  $p_{\text{exp}}(1/T)$ -data determined in Al-doped 4H-SiC epilayers Al1(epi) to Al4(epi)

Sample #	Input parameter			Fit parameter		
	$r_{\text{H,h}}(T, B)$	$g$	$m_{\text{h,ds}}(T)$	$N_{\text{Al}}$ ( $\text{cm}^{-3}$ )	$N_{\text{comp}}$ ( $\text{cm}^{-3}$ )	$\Delta E_{\text{Al}}$ (meV)
Al1(epi)	according to Fig. 7	4	[4]	$1.6 \times 10^{18}$	$7 \times 10^{14}$	216
Al2(epi)				$2.7 \times 10^{17}$	$3 \times 10^{14}$	221
Al3(epi)				$2.8 \times 10^{16}$	$7 \times 10^{13}$	227
Al4(epi)				$1.8 \times 10^{15}$	$3 \times 10^{13}$	240

**Fig. 13.** Hall mobility of holes  $\mu_{\text{H,h}}$  versus reciprocal temperature taken on the identical Al-doped 4H-SiC epilayers as displayed in Fig. 12a

critically depend on the Al acceptor concentration in the investigated concentration and temperature range. This observation is due to the fact that scattering of holes at ionized impurities dominates at temperatures below 150 K (see Fig. 13) where a strong freeze-out of Al acceptors already occurs.

## 5 Conclusion

The analysis of Hall effect data taken on 4H- and 6H-SiC is briefly described. It is demonstrated that excited states do not affect the determined concentration value of majority impurities (donors or acceptors). The determination of the low field and high field Hall scattering factor for electrons  $r_{\text{H,e}}(T, B)$  and holes  $r_{\text{H,h}}(T, B)$  is discussed.  $r_{\text{H,e}}(T, B)$  assumes values between 1.21 and 0.92 in the temperature range from 40 K to 300 K and  $r_{\text{H,h}}(T, B)$  varies between 1.4 and 0.5 in the temperature range from 100 K to 800 K. Both Hall scattering factors are nearly the same for the 4H- and 6H-SiC polytype.

## Acknowledgements

The support of this work by the Bundesministerium für Bildung, Wissenschaft, Forschung und Technologie (BMBF) under Contract No. 01BM974, the Bayerische Forschungsförderung (BFS) under Contract No. 362/99 and the German Science Foundation is greatly acknowledged.

## References

1. W. Kohn, J.M. Luttinger: Phys. Rev. **98**, 915 (1955)
2. L. Patrick: Phys. Rev. B **5**, 2198 (1972)
3. W. Suttrop, G. Pensl, W.J. Choyke, R. Stein, S. Leibenzeder: J. Appl. Phys. **72**, 3708 (1992)
4. G. Wellenhofer, U. Rößler: Phys. Stat. Sol. (b) **202**, 107 (1997)
5. M. Ikeda, H. Matsunami, T. Tanaka: Phys. Rev. B **22**, 2842 (1980)
6. J.S. Blakemore: *Semiconductor Statistics* (Dover Publications Inc., New York, 1987) pp. 117–176
7. W.J. Choyke, L. Patrick: Phys. Rev. **127**, 1868 (1962)
8. P.J. Colwell, M.V. Klein: Phys. Rev. B **6**, 498 (1972)
9. W. Götz, A. Schöner, G. Pensl, W. Suttrop, W.J. Choyke, R. Stein, S. Leibenzeder: J. Appl. Phys. **73**, 3332 (1993)
10. R. Newman: Phys. Rev. **103**, 103 (1956)
11. K. Shifrin: J. Phys. U.S.S.R. **16**, 341 (1944)
12. H. Matsuura: Mater. Sci. Forum **389–393**, 679 (2002)
13. P. Blood, J.W. Orton: *The Electrical Characterization of Semiconductors: Majority Carriers and Electron States* (Academic Press, London, 1992) pp. 93–151
14. K. Seeger: *Semiconductor Physics – An Introduction*, 7th ed. (Springer, Berlin, 1999)
15. E.H. Putley: *The Hall Effect and Related Phenomena* (Butterworths, London, 1960)
16. A.C. Beer: “Galvanomagnetic Effects in Semiconductors”, in *Solid State Physics*, Suppl. 4, ed. by F. Seitz and D. Turnbull (Academic Press, New York, 1963)
17. G. Rutsch, R.P. Devaty, D.W. Langer, L.B. Rowland, W.J. Choyke: Mater. Sci. Forum **264–268**, 317 (1998)
18. G. Rutsch, R.P. Devaty, W.J. Choyke, D.W. Langer, L.B. Rowland: J. Appl. Phys. **84**, 2062 (1998)
19. G. Rutsch, R.P. Devaty, W.J. Choyke, D.W. Langer, L.B. Rowland, E. Niemann, F. Wischmeyer: Mater. Sci. Forum **338–342**, 733 (2000)
20. L.J. van der Pauw: Philips Res. Repts. **13**, 1 (1958)
21. J. Appel: Z. Naturforsch. A **11**, 689 (1956)
22. G. Pensl, F. Schmid, F. Ciobanu, M. Laube, S.A. Reshanov, N. Schulze, K. Semmelroth, H. Nagasawa, A. Schöner, G. Wagner: Mater. Sci. Forum **433–436**, 365 (2003)
23. G. Pensl, F. Ciobanu, M. Krieger, M. Laube, S. Reshanov, F. Schmid, G. Wagner, H. Nagasawa, A. Schöner: Mat. Res. Soc. Symp. Proc. **742**, K3.2.1 (2003)

24. Yu.A. Vodakov, E.N. Mokhov: in *Silicon Carbide 1973*, ed. by R.C. Marshall, J.W. Faust, Jr., C.E. Ryan (University of South Carolina Press, Columbia, 1974) p. 508
25. A. Schöner, N. Nordell, K. Rottner, R. Helbig, G. Pensl: Inst. Phys. Conf. Ser. No. **142**, 493 (1996)
26. F. Szmulowicz: Phys. Rev. B **28**, 5943 (1983)
27. W.C. Mitchel, P.M. Hemenger: J. Appl. Phys. **53**, 6880 (1982)
28. D. Long: Phys. Rev. **107**, 672 (1957)
29. M. Schadt: Dissertation, Erlangen (1997)
30. J.P. Biersack: Fortran Monte Carlo program TRIM Cascade
31. G. Wagner, W. Leitenberger, K. Irmischer, F. Schmid, M. Laube, G. Pensl: Mater. Sci. Forum **389–393**, 207 (2002)
32. K. Seeger: *Semiconductor Physics – An Introduction*, 4th ed. (Springer, Berlin, 1989) pp. 39–44

# Radiotracer Deep Level Transient Spectroscopy

N. Achtziger and W. Witthuhn

## 1 Introduction

Basic electronic properties of semiconductors are extremely sensitive to defects and impurities. Small relative concentrations of  $10^{-10}$  or less may determine the type and magnitude of electronic conductivity or the mean life time of charge carriers. This is the case, if the impurity or defect in question gives rise to a localized electron state having an energy within the band gap of the semiconductor. Consequently, there is a general interest to reveal the correlation between a certain element or defect and its band gap states. This knowledge is the necessary basis to either identify impurities in a given material by detecting their band gap states or to adjust material properties by intentional doping with a certain element. For silicon carbide (SiC) and the impurities discussed here, both aspects are important.

Generally, spectroscopic techniques of semiconductor physics that are able to detect and characterize band gap states (including level position) do not reveal information about their microscopic origin. On the other hand, structurally or chemically sensitive methods, especially magnetic resonance techniques, generally do not reveal the energy position of a state within the band gap and quite often do not yield concentrations quantitatively. To overcome the chemical blindness of spectroscopic techniques, the present approach is using radioactive isotopes as a tracer. Because of the characteristic concentration change according to the nuclear decay law, their involvement in the formation of an electronic band gap state can be confirmed or denied definitely by several subsequent spectroscopic measurements during the elemental transmutation. Band gap states related to either the parent or the daughter isotope are uniquely identified by a decreasing or increasing concentration, respectively.

The present review presents some general aspects of this radiotracer concept, explains the possibilities for radioactive doping which are the key to such experiments, and then discusses details of the radioactive transmutation, its interpretation and specific requirements of Deep Level Transient Spectroscopy (DLTS). Finally, a survey of radiotracer DLTS experiments and results is given, including the elements Be, Zn, Cd, Ga, In, Ti, V, Cr, Ta, W, Er and Sm. Most of the data on deep levels of impurities in SiC available today result from these experiments.

## 2 Radiotracer Experiments in Semiconductors

For decades, radioactive isotopes have been used in solid state physics for nuclear probe techniques [1] or tracer diffusion. In that cases, the nuclear radiation is detected and spectroscopic or spatial information is derived. Within the last decade, a new application as a tracer for “non-nuclear” spectroscopic techniques of semiconductor physics emerged. In this case, the emitted radiation is used only to quantify the amount of isotopes present, but ignored for the spectroscopic purpose. Instead, the elemental transmutation during the decay is the key point: The known decrease or increase of the parent or daughter isotope’s concentration is correlated with the time evolution of subsequently measured spectra and element-specific properties can be identified if decreasing or increasing signals are detected on the time scale of the nuclear transmutation. The expected dependence of the relative concentrations versus time is schematically shown in Fig. 1 for a defect consisting of one radioactive probe atom and for a defect-complex containing two probe atoms.

The spectroscopic techniques used up to now on radioactive tracers in semiconductors are well-established standard techniques of semiconductor physics. For SiC, only Deep Level Transient Spectroscopy (DLTS) has been used up to now and will be described in greater detail in this article. Two further techniques, Hall effect and Low Temperature Photoluminescence (LTPL), were mainly used for radiotracer studies in silicon [9], III-V semiconductors [2, 10, 11] and II-VI compounds [12].

Some basic properties of the spectroscopic techniques have immediate consequences for radiotracer spectroscopy: DLTS requires the preparation of Schottky- or *pn*-diodes and detects “deep” levels by applying electrical

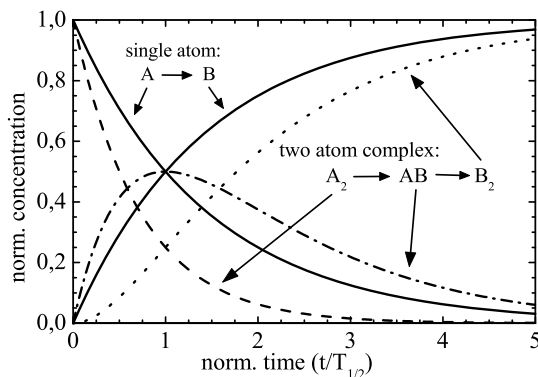


**Fig. 1.** Time dependence of the normalized concentrations of a radio-isotope  $A$ , its daughter isotope  $B$  and of pair defects originating from an initially formed  $A_2$  pair. The curve of the intermediate mixed pair  $AB$  is based on the assumption that the two atoms in the initial  $A_2$  pair are equivalent

excitation pulses and observing the subsequent relaxation of the diode's capacitance. The sensitivity is high: the minimum concentration of deep levels to be detected is typically  $10^{-4} N_S$ , where  $N_S$  is the shallow doping concentration. The Hall effect taken on an extrinsic semiconductor can be used to measure the free carrier concentration and thus to derive the dominant shallow doping concentration  $N_S$ . In PL-spectroscopy, the light emission after optical excitation is detected and specific emission lines are observed that may be related to a certain impurity. Both DLTS and PL detect band gap states in the near-surface region and are therefore well suited to ion implanted samples. Both Hall effect and DLTS are quantitative regarding the concentration of band gap states. Therefore, a direct relation between the observed concentration changes and the known nuclear half-life can be established. In contrast, the PL signal is not necessarily proportional to the concentration, i.e. the signal height versus decay time may deviate from the exponential nuclear decay law [2].

Historically, the first pioneering work on the radiotracer spectroscopy was performed on the  $^{65}\text{Zn}$  to  $^{65}\text{Cu}$  ( $T_{1/2} = 245$  d) transformation applied to ESR and PL studies of ZnO and ZnS [3, 4]. The first radiotracer experiments by DLTS came up in the beginning of the 1990's. After implantation of a precursor Hg at the "on-line" isotope separator ISOLDE/CERN, the  $^{195}\text{Au} \rightarrow ^{195}\text{Pt}$  transmutation was observed in Si by Peterson et al. [5] in order to contribute to the discussion about the Au lattice site in Si. After "off-line" implantation of  $^{111}\text{In}$ , its transmutation to Cd was observed by Lang et al. [6, 7] to establish the deep levels of Cd in Si. Additional elements in silicon were studied by DLTS, including the transition metals Sc, Ti, V, Cr, Co and the identification of  $\text{Se}_2$ -pairs [8]. In these experiments, the recoil implantation as a radioactive doping technique to be used later also for SiC has been successfully established.

### 3 Radioactive Implantation: Requirements and Techniques

The use of radioisotopes as a tracer for "non-nuclear" spectroscopy in semiconductors imposes severe requirements related to isotopic and chemical purity of the doping process. These requirements are more stringent here than for the other radioisotope applications like nuclear probe techniques or tracer diffusion. In those cases, the measurement is based on the nuclear radiation and is therefore not disturbed by any other stable isotopes. DLTS, however, is sensitive to electrically active impurities regardless of their radioactivity.

Doping via diffusion is not feasible because of severe problems related to radioactivity and impurity-contaminations. The only possibility is the implantation of radiotracers. The following implantation techniques have been used:

- (A) “off-line”, i.e. a standard ion implanter with radioactive material in the ion source,
- (B) “on line” isotope production, mass separation and implantation,
- (C) recoil implantation after a nuclear reaction.

Technique (A) generally requires chemical processing or handling of radioactive material and severe contamination problems exist. The radioactivity has to be produced in a separate preceding process. So far only the isotopes  $^{111}\text{In}$  ( $T_{1/2} = 2.83$  d) and  $^{181}\text{Hf}$  ( $T_{1/2} = 42.4$  d) have been used for tracer studies in semiconductors. Details are given in [13].

An “on-line” implantation facility (B) is operating as the ISOLDE experiment [14, 15] at CERN/Genf. A high energy proton beam (energy up to 1.4 GeV) induces nuclear spallation-reactions in a thick target. Radioisotopes diffuse into an ion source and are then accelerated, mass-separated and implanted into the sample. By varying both target and ion source, over 600 isotopes of about 70 elements are available at ISOLDE [15]. Restrictions mainly apply to non-volatile elements, e.g. transition metals and some very light isotopes.

The recoil implantation setup (C) is comparatively simple (see Fig. 2): a primary ion beam produces the desired radioisotope via a nuclear reaction when passing a thin reaction foil. The reaction products are kicked out of this foil with recoil energies up to a few MeV, depending on the nuclear reaction and the foil thickness. The recoiling atoms are directly implanted into the samples mounted off-axis to the primary beam. The recoil energy determines the range of the reaction products in the target foil. The implantation fluence is inhomogeneous and decreases with increasing distance from the beam axis. Typically a decrease by a factor of two over a sample size of a few mm is expected, which can be tolerated in most cases. The implantation is not chemically pure, because atoms of the foil (and eventually products of com-

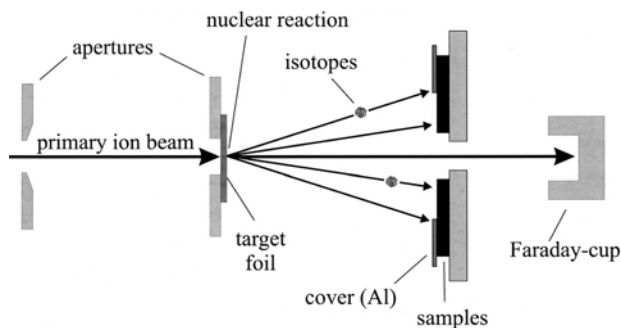


**Fig. 2.** Set up in recoil implantation experiments. The samples are mounted around the beam axis. In practice, a sequence of such target/sample arrangements is placed along the beam axis, as the energy loss of the primary ion beam in the thin target foil is negligible

**Table 1.** List of radioactive isotopes used for DLTS studies in semiconductors. In the case of heavy ion induced nuclear reactions, the recoil energies due to the nuclear decay and the co-implanted isotopes have to be discussed in detail; here one has to refer to the cited original papers. EC = electron capture

Radioactive parent isotope	Half-life	Daughter isotope	Decay	Decay induced recoil energy	Isotope production reaction/implantation	Implantation energy	Co-im- planted	Reference
$^7\text{Be}$	53.3 d	$^7\text{Li}$	EC	57 eV	$^7\text{Li}(\text{p,n})^7\text{Be} \rightarrow ^7\text{Li}$ $E_p = 6 \text{ MeV}$	1 ... 1.6 MeV	Li	18
$^{45}\text{Ti}$	3.08 h	$^{45}\text{Sc}$	86 % $\beta^+$	0 ... 22 eV	$^{45}\text{Sc}(\text{p,n})^{45}\text{Ti} \rightarrow ^{45}\text{Sc}$ $E_p = 11 \text{ MeV}$	0 ... 0.7 MeV	Ti	17
$^{48}\text{V}$	15.97 d	$^{48}\text{Ti}$	45 % EC, 45 % $\beta^+$ , + $\gamma$ cascade	33 eV 19 eV	$^{48}\text{Ti}(\text{p,n})^{48}\text{V} \rightarrow ^{48}\text{Ti}$ $E_p = 11 \text{ MeV}$ $^{45}\text{Sc}(\alpha,\text{n})^{48}\text{V} \rightarrow ^{48}\text{Ti}$ $E_\alpha = 16.5 \text{ MeV}$	0 ... 0.7 MeV 0 ... 2.5 MeV	Ti Sc, Ti	19,20 19,20
$^{51}\text{Cr}$	27.7 d	$^{51}\text{V}$	EC	6 eV	$^{51}\text{V}(\text{p,n})^{51}\text{Cr} \rightarrow ^{51}\text{V}$ $E_p = 11 \text{ MeV}$ $^{48}\text{Ti}(\alpha,\text{n})^{51}\text{Cr} \rightarrow ^{51}\text{V}$ $E_\alpha = 16.5 \text{ MeV}$	0 ... 0.7 MeV 0 ... 2.5 MeV	V Ti, V	20,21 21
$^{56}\text{Co}$	77.3 d	$^{56}\text{Fe}$	EC, $\beta^+$	30 ... 65 eV, max. 100 eV	$^{56}\text{Fe}(\text{p,n})^{56}\text{Co} \rightarrow ^{56}\text{Fe}$	0 ... 0.7 MeV	Fe	22
$^{67}\text{Ga}$	3.25 d	$^{67}\text{Zn}$	EC + $\gamma$ cascade	max. 6.6 eV	$^{67}\text{Zn}(\text{d,n})^{67}\text{Ga} \rightarrow ^{67}\text{Zn}$ $E_d = 10 \text{ MeV}$	0 ... 0.7 MeV	Zn	23
$^{71}\text{As}$	2.7 d	$^{71}\text{Ge}$	EC, $\beta^+$	25 eV	Implanter ISOLDE	260 keV		2,18
$^{73}\text{As}$	80.3 d	$^{73}\text{Ge}$	EC	0.9 eV	Implanter ISOLDE	260 keV		24

Table 1 continued

Radioactive parent isotope	Half-life	Daughter isotope	Decay	Decay induced recoil energy	Isotope production reaction/implantation	Implantation energy	Co-im- planted	Reference
<sup>75</sup> Se	120 d	<sup>75</sup> As	EC + γ-cascade	1.5 eV	<sup>72</sup> Ge(α,n) <sup>75</sup> Se → <sup>75</sup> As E <sub>α</sub> = 16.5 MeV	0 ... 1.4 MeV	As, Ge	8
<sup>111</sup> In	2.83 d	<sup>111</sup> Cd	EC	0.9 eV	Off-line implantation	400 keV		6,7,23
<sup>153</sup> Sm	46.8 h	<sup>153</sup> Eu	β- + γ-cascade	max. 3.5 eV	Implanter ISOLDE	4 ... 6 MeV		25
<sup>160</sup> Er	28.6 h	<sup>160</sup> Dy	EC		<sup>147</sup> Sm( <sup>18</sup> O,2p3n) <sup>160</sup> Er → <sup>160</sup> Ho → <sup>160</sup> Dy E <sub>180</sub> = 106 MeV T <sub>1/2</sub> ( <sup>160</sup> Ho) = 26 m			26,27
<sup>177</sup> Ta	56.6 h	<sup>177</sup> Hf	EC, β+		<sup>165</sup> Ho( <sup>16</sup> O,p3n) <sup>177</sup> W → <sup>177</sup> Ta → <sup>177</sup> Hf E <sub>160</sub> = 90 MeV T <sub>1/2</sub> ( <sup>177</sup> W) = 2.2 h			28,29
<sup>178</sup> W	21.6 d	<sup>178</sup> Hf	EC		<sup>165</sup> Ho( <sup>18</sup> O,5n) <sup>178</sup> Re → <sup>178</sup> W → <sup>178</sup> Ta → <sup>178</sup> Hf			30,31
<sup>195</sup> Au	183 d	<sup>195</sup> Pt	EC	0.05 eV	E <sub>180</sub> = 95 MeV T <sub>1/2</sub> ( <sup>178</sup> Re) = 13 m; T <sub>1/2</sub> ( <sup>178</sup> Ta) = 9 m Implanter ISOLDE	60 keV		25

peting nuclear reactions) are implanted simultaneously with fluences in the same order of magnitude (for details see [16]).

Generally, the useful half-lives are restricted towards short times by the time needed for implantation, annealing, further sample preparation (e.g. electrical contacts) and the measurement itself. The shortest time used up to now is  $T_{1/2} = 3.08$  h (recoil implanted  $^{45}\text{Ti}$ ) for a DLTS experiment [17] which is practically the lower limit. Table 1 summarizes the radioactive isotopes used for radiotracer DLTS up to now.

An essential point in the interpretation of any daughter element related phenomena refers to the question, whether the transmutation induces any other effects in addition to changing the element. Because of the emitted radiation quanta, a recoil energy is always transferred to the daughter atom. This decay induced recoil energy is included in Table 1; further details will be discussed in Sect. 4.5.

## 4 Selected Aspects of Radiotracer Deep Level Transient Spectroscopy

In this chapter, first the technique DLTS is explained shortly and some considerations specific for its application to radioactive isotopes are given. Then, the interpretation of nuclear transmutation experiments is discussed in detail.

### 4.1 Deep Level Transient Spectroscopy (DLTS)

DLTS is a versatile standard technique to characterize deep levels in the band gap of a semiconductor. In the present context, only the basic version is of interest, i.e. the measured quantity is the capacitance of a reversely biased diode (on the material of interest) and their relaxation after disturbance by an electronic filling pulse. The resulting capacitance transient is governed by the emission of charge carriers from deep traps. By varying the sample temperature and time constant of observation, the emission time constant is obtained as a function of temperature. Assuming a thermally activated emission process, a thermal activation energy for this process and a characteristic capture cross section  $\sigma$  are obtained from an Arrhenius plot of the data. For more detailed explanations, see [32]–[34].

DLTS is highly sensitive: the trap concentration  $N_T$  (“traps”) may be in the range between  $10^{-4} N_S$  and  $10^{-1} N_S$  with  $N_S$  being the concentration of shallow dopants in the sample. By choosing a material at low  $N_S$ , e.g.  $10^{14} \text{ cm}^{-3}$ , the detection limit for deep levels may thus be as low as  $10^{10} \text{ cm}^{-3}$ . The concentration of deep traps can be determined quantitatively.

In the limit  $N_T \ll N_S$ , the DLTS signal is linear in  $N_T$ . If additionally the equilibrium capacitance of the diode remains constant (expected for  $N_T \ll N_S$ , it has to be verified experimentally), it is hence justified to

form differences of subsequently measured spectra. This procedure eliminates time-independent features in radiotracer spectra and highlights the relevant changes.

There exist in general several problems and restrictions to DLTS:

- The level energy derived from DLTS is a thermal activation energy for charge carrier emission which is not necessarily identical to the “true” position of the level within the band gap. Deviations may result from an eventually temperature-dependent capture cross section  $\sigma$  or from the influence of the diode’s electric field on the emission process [32]. In favourite cases, however, these effects can be studied experimentally and both a correction of their influence as well as additional information about the band gap state become available.
- The accessible energy range within the band gap is restricted. “Shallow” levels are generally not observable. Towards high activation energies, the restriction results from the maximum operating temperature of the diode. It is not possible to express the accessible energy range quantitatively since the emission rate also depends on the capture cross section  $\sigma$ . In silicon, an interval width of about 0.5 eV (except for shallow states) starting from either valence or conduction band edge (denoted by  $E_V$  and  $E_C$ ) can be studied by using  $p$ -type or  $n$ -type material, respectively. Thus, deep levels are accessible in the whole band gap (width 1.1 eV). In the wide-gap semiconductor silicon carbide, however, a range of typically 1 eV starting from both band edges is accessible, i.e. the center of the band gap (up to 3.3 eV width) cannot be analyzed.
- The depth region probed by DLTS scales with  $N_S^{-1/2}$ . For  $N_S = 10^{15} \text{ cm}^{-3}$ , the minimum depth is in the order of 1  $\mu\text{m}$ . To gain a high sensitivity of DLTS, a material with low  $N_S$  is preferable. This implies that the sensitive depth interval of DLTS is quite deep in the crystal, i.e. the doping process has to achieve a sufficiently deep incorporation of the impurity. If this is not possible experimentally, the shallow doping level must be chosen higher and sensitivity is lost.

Because of the high sensitivity of DLTS, the absolute number of isotopes needed for a radiotracer DLTS experiment is small and, thus, the sample’s activity is very low, typically in the order of a few kBq (Bequerel =  $\text{s}^{-1}$ ) for the experiments described here. Due to this very low level of radioactivity, no severe practical restrictions regarding handling of the samples are implied.

## 4.2 Number of Isotopes Involved per Band Gap State

The microscopic origin of one band gap state may be a single defect or impurity or a complex of more than one constituent. If exactly one radioactive isotope is involved, the concentration  $c(t)$  of either parent or daughter-related band gap states will exactly follow an exponential function with a half-life identical to the nuclear half-life:

$$c(t) = c_0 e^{-t/\tau} \quad (\text{parent isotope}) , \quad (1)$$

$$c(t) = c_0(1 - e^{-t/\tau}) \quad (\text{daughter isotope}) , \quad (2)$$

with  $c_0$  being the initial concentration and  $\tau = T_{1/2}/\ln 2$  the mean life of the nuclear decay.

If two atoms are involved in one complex, the expected time dependence is different [7, 35]:

$$c(t) = c_0 e^{-2t/\tau} \quad (\text{pair of parent isotopes}) , \quad (3)$$

$$c(t) = c_0(1 - e^{-t/\tau})^2 \quad (\text{pair of daughter isotopes}) , \quad (4)$$

$$c(t) = c_0 2e^{-t/\tau}(1 - e^{-t/\tau}) \quad (\text{mixed pair}) . \quad (5)$$

Here both atoms forming the parent pair are assumed to occupy identical lattice positions, i.e. only one mixed complex exists. These functions are displayed in Fig. 1. The basic fact is that a pair complex containing two parent isotopes decreases twice as fast as compared to the nuclear decay. This has been demonstrated experimentally for  $\text{Se}_2$  pairs in silicon [8] using the transmutation of  $^{75}\text{Se}$  to  $^{75}\text{As}$ . Thus, it is possible to count the number of isotopes involved in the formation of one band gap state.

### 4.3 Stability of the Initial Configuration

The basic idea of radiotracer spectroscopy implicitly assumes that no other changes except of the radioactive decay occur in the sample. This requirement may not be fulfilled if mobile species are present in the crystal during measurement or storage. The resulting concentration curves may severely deviate from the expected exponential functions, as demonstrated by the following example, the transmutation of  $^{51}\text{Cr}$  to V in *p*-type Si [22, 36]. In Fig. 3 both the standard case, i.e. exponential concentration curves with the correct half-life (transmutation of V to Ti, Fig. 3a,b) as well as the Cr to V transmutation with deviating curve shapes (Fig. 3c,d) are shown. The deviation occurs for the following reason: the isolated Cr atom has no level in the lower part of the band gap, but a complex between boron and chromium has ( $E_V + 0.29$  eV). Its concentration first increases due to the formation of CrB pairs (Cr is the mobile species) and then decreases due to its radioactive decay with a remaining offset due to stable Cr isotopes. By chance, the pairing rate  $r$  and the nuclear decay rate  $\lambda = \tau^{-1}$  are of a similar order of magnitude ( $r = 0.64\lambda$ ) at a boron concentration of  $10^{15} \text{ cm}^{-3}$  and both processes influence the concentration of CrB pairs during storage at 290 K. The increasing peak in Fig. 3c is identical to the peak after  $^{48}\text{V}$  doping (Fig. 3a); it is due to an isolated (interstitial) V atom ( $E_V + 0.45$  eV).

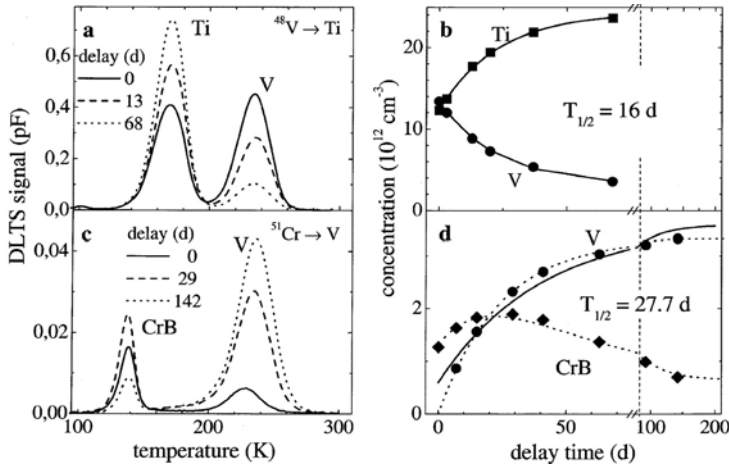


**Fig. 3.** DLTS spectra (a, c) and concentration of band gap states versus delay time (b, d) measured during the transmutation of  $^{48}\text{V}$  to  $^{48}\text{Ti}$  (a, b) or  $^{51}\text{Cr}$  to  $^{51}\text{V}$  (c, d) in *p*-type silicon. The solid lines in (b, d) are fitted exponential functions with fixed half-life of the parent isotope. The dashed lines (d) are fits of a model taking into account the CrB pair formation in addition to the nuclear decay (taken from [36])

#### 4.4 Degree of Electrical Activation

It is a very important aspect of doping studies to quantify, in addition to the position of a band gap state, how many of the incorporated atoms contribute to the formation of this specific band gap state. Normally, the “doping efficiency” is derived by comparing the concentration of gap states (known e.g. from DLTS) with the number of incorporated atoms. Though this latter number is initially well known in the case of ordinary ion implantation, a considerable loss of dopant atoms may occur by (eventually defect-enhanced) diffusion to the surface during annealing. In the case of radioactive doping, however, the activity and, thus, the number of incorporated isotopes can be monitored by  $\gamma$ -ray spectroscopy at any time during the preparation, in particular in the final state of a Schottky diode used for DLTS. Typically, the loss of the radiotracer isotopes during the preparation is between 10 and 90%. If the depth profile of the impurity is known, the fraction of dopant atoms being involved in the formation of a certain band gap state can be derived without any further assumptions (for details, see [20]: Ti, V, and Cr in SiC).

#### 4.5 Decay-Induced Defects

In contrast to results obtained for the parent isotope which are always characteristic for the specific element, the interpretation of daughter-related features may be more complicated for the following reasons [20]:

- The nuclear decay results in an excited atomic shell, especially in the case of an electron capture decay, and might thus induce non-equilibrium chemical reactions of the daughter atom.
- A nuclear decay generally imposes a recoil onto the daughter atom by emitting radiation quanta. This recoil may produce intrinsic defects by kicking-out neighbouring host atoms and the daughter atom may be displaced or be involved in complexes with such defects.

These mechanisms and the resulting configurations are collectively referred to as “decay-induced defects”. As an additional complication, the lattice site or bonding configuration of the parent isotope may be an unstable position for the daughter element, or a site which is usually not occupied by the daughter element.

The existence of recoil-induced defects, at least at low temperatures, is well established by neutrino recoil experiments [37]. To judge the relevance of the decay-induced recoil for a given experiment, the recoil energy transferred to the daughter isotopes has to be calculated. In the case of several subsequent emissions of radiation quanta, we usually specify the maximum individual recoil energy, if the life time of the intermediate level is longer than the time needed to hit a neighbouring atom due to the preceding recoil event (in the order of  $10^{-14}$  s). The recoil energies of the dominating decay mode of isotopes used up to now in radiotracer-DLTS experiments are quoted in Table 1.

Next, the recoil energy may be compared to the displacement energy of the host crystal, which is 13 eV for Si [16] and around 25 eV in SiC [59, 60], i.e. some of the recoil energies listed are well below, others are well above these numbers. This comparison, however, is a crude estimate only since the displacement energy refers to the pure crystal, whereas an impurity may act differently.

One may expect at least two possible consequences in a radiotracer experiment, either an increasing signal (starting from zero) of the decay-induced defect itself or, if this defect is not observable by the technique used, a missing fraction of the daughter element configuration. The first effect has not been detected experimentally up to now, the second case was observed for the the  $^{51}\text{Cr}$  to V transmutation in  $4H\text{-SiC}$  (for a detailed discussion see [20]).

Again, we would like to stress that the problems arising because of decay-induced defects affect the interpretation of band gap states related to the daughter element only. In this sense, it is generally advantageous to use the element of interest as the parent isotope.

## 5 Deep Levels Detected by Radiotracer DLTS

In the following sections, we summarize the deep levels identified by radio tracer DLTS so far. Only some of the radiotracer spectra are shown here, though in several cases conclusions were also drawn from additional doping

experiments with stable isotopes. In addition to the element of interest, all other levels detected in the samples (e.g. due to intrinsic defects or impurities) were characterized and compared to available data in the literature (see review by Dalibor et al. [38]). For these details as well as for the experimental procedure, we refer to the original articles. A comparison to theory is also omitted here, see [45].

Some experimental steps are common to all experiments: the samples were epitaxial layers with a shallow doping below  $10^{16} \text{ cm}^{-3}$ , radioactive doping was done by ion implantation with rather low fluences (below  $10^{11} \text{ cm}^{-2}$ , except for  $^{111}\text{In}$ ), annealing temperatures were in the range between 1600 K and 1900 K, and DLTS measurements were performed on Schottky contacts. The actual number and type of radioisotopes in each sample were monitored by  $\gamma$ -ray spectroscopy.

The level energies stated (energy differences towards the nearest band edge) are thermal activation energies as obtained by the standard DLTS procedure, assuming a temperature independent capture cross section  $\sigma$ . Alternatively, to obtain energy values for the other conventional assumption  $\sigma \propto T^{-2}$ , a correction of 2 kT has to be added where  $T$  is the peak temperature in the spectra. The influence of the electric field strength was investigated; in the case of a well identified Poole-Frenkel effect, its influence on the trap energy was corrected.

## 5.1 Deep Levels of Be, Zn, Cd

### 5.1.1 Beryllium:

The group II-element Beryllium is expected to act as a doubly charged acceptor in silicon carbide. Recently, DLTS experiments have been performed using the stable  $^9\text{Be}$  isotope [39, 40] revealing several deep band gap states. For the radiotracer experiments the radioactive isotope  $^7\text{Be}$  (decay to  $^7\text{Li}$ , half-life  $T_{1/2} = 53.3 \text{ d}$ ) was used [41]. In case of  $p$ -type  $4H$ -SiC one deep level at  $E_V + (1.06 \pm 0.05) \text{ eV}$  above the valence band is identified as Be-related. These results are in reasonable agreement with the values derived for the Be(2) level on stable Be [40]. The level is acceptor-like, but a decision whether it is a singly or doubly charged acceptor state could not be made. In  $n$ -type  $4H$ -SiC, neither Be- nor Li-correlated deep levels have been found, i.e. there are no levels in the upper part of the band gap within the detection limit of our DLTS equipment.

### 5.1.2 Zinc:

Zn related deep band gap states in  $p$ -type  $6H$ -SiC were identified using the radioactive isotope  $^{67}\text{Ga}$  (decay to  $^{67}\text{Zn}$ , half-life  $T_{1/2} = 3.25 \text{ d}$ ) [23, 42]. Since stable Zn isotopes are co-implanted, a Zn-related peak at  $E_T = E_V + (1.16 \pm 0.02) \text{ eV}$  shows up already from the beginning of the DLTS-measurements

and is then further increased by the radioactive decay of  $^{67}\text{Ga}$ . The level is formed by 20% of the transmuting atoms.

In these experiments, no indication of a Ga-related deep level has been found with a detection limit of 6% of all Ga atoms. Such a level, in addition to the well known shallow level of Ga [43], had been proposed in analogy to the known “deep boron” center [44] and has been discussed controversially.

### 5.1.3 Cadmium:

Two Cd-related deep band gap states are identified [23] in *p*-type 4*H*-SiC using the nuclear transmutation  $^{111}\text{In} \rightarrow ^{111}\text{Cd}$  ( $T_{1/2} = 2.83$  d). During the  $^{111}\text{In} \rightarrow ^{111}\text{Cd}$  decay, the DLTS spectra exhibit two strongly increasing peaks Cd1 and Cd2 with a time dependence expected for the Cd daughter element. The level energies are given in Table 2. From the magnitude of the peak height changes, a concentration ratio between Cd1 and Cd2 of 1:1 with an error of 30% is deduced. The degree of electrical activation, i.e. the concentration ratio of Cd-related gap states to Cd daughter atoms, is in the order of unity.

**Table 2.** Deep band gap states of Be, Zn, and Cd in *p*-type SiC identified by radiotracer DLTS. The capture cross sections  $\sigma$  are assumed to be independent of temperature; the error is about one order of magnitude

Isotope	Level energy (eV)	Cross section $\sigma$ ( $10^{-14}$ cm <sup>2</sup> )	Reference
$^7\text{Be}$ (4 <i>H</i> -polytype)	$E_V + (1.06 \pm 0.05)$	5	[41]
$^{67}\text{Zn}$ (6 <i>H</i> -polytype)	$E_V + (1.16 \pm 0.02)$	1	[23, 42]
$^{111}\text{Cd}$ (4 <i>H</i> -polytype)	$E_V + (0.90 \pm 0.03)$	2	[23]
	$E_V + (1.19 \pm 0.04)$	0.02	[23]

## 5.2 Deep Levels of the Transition Metals Ti, Cr, and V

In the following sections we summarize the available information with main emphasis on radiotracer experiments. The original results were published separately for different polytypes, conductivity types and are referenced individually below. The extracted level data are listed in Table 3.

**Table 3.** Energies  $E_T$  and capture cross sections  $\sigma$  (assumed to be independent of temperature) of transition-metal related deep levels in SiC-polytypes

Poly-type	Element	Peak label	Energy $E_T$ (eV)	Cross section $\sigma$ ( $10^{-14}\text{cm}^2$ )	Ref.
4H	Ti	Ti-1a	$E_C - (0.13 \pm 0.01)$	1	[19, 20]
		Ti-1b	$E_C - (0.17 \pm 0.01)$	1	[19, 20]
	V	V	$E_C - (0.97 \pm 0.03)$	1	[19, 20]
		Cr-1a	$E_C - (0.14 \pm 0.01)$	0.1	[19, 20]
		Cr-1b	$E_C - (0.18 \pm 0.01)$	0.1	[19, 20]
		Cr-2	$E_C - (0.74 \pm 0.02)$	0.2	[19, 20]
		Cr-3a	$E_V + (0.54 \pm 0.01)$	0.2	[21]
		Cr-3b	$E_V + (0.63 \pm 0.01)$	1	[21]
6H	V	V-1a	$E_C - (0.71 \pm 0.02)$	0.04	[18]
		V-2b	$E_C - (0.75 \pm 0.02)$	0.1	[18]
	Cr	Cr-2	$E_C - (0.54 \pm 0.02)$	2	[18]
15R	V	V-1a	$E_C - (0.71 \pm 0.02)$	0.2	[19, 20]
		V-1b	$E_C - (0.75 \pm 0.03)$	0.01	[19, 20]
		V-1c	$E_C - (0.80 \pm 0.02)$	0.01	[19, 20]
	Cr	Cr-2a	$E_C - (0.45 \pm 0.03)$	1	[46]
		Cr-2b	$E_C - (0.47 \pm 0.03)$	1	[46]

### 5.2.1 Titanium:

The Ti-related deep levels in  $n$ -type 4H-SiC were studied [8, 9] employing the radioactive isotope  $^{48}\text{V}$  which decays to the stable isotope  $^{48}\text{Ti}$  with a half-life of 15.97 d. The 4H samples reveal time dependent DLTS spectra (see Fig. 4): two peaks labelled with Ti-1a and Ti-1b below 100 K are present from the very beginning and are increasing with delay time (for the level data, see Table 3). A peak at 430 K decreases exponentially. Hence, it is assigned to a vanadium-related defect (level at  $E_C - 0.97$  eV) that will be discussed later.

As discussed in Sect. 4, decay-induced defects must be taken into account here. In contrast to the rather “gentle” decay modes (i.e. low recoil energy) of the isotopes discussed above, the minimum decay induced recoil energy of the daughter isotope  $^{48}\text{Ti}$  is of the same size than the lower limit of the displacement energy in SiC, around 20 eV [20]. Therefore, the formation of decay induced defects might be possible. However, a closer inspection of the doping process clarifies the situation: Both levels are present from the very beginning. This is expected for Ti atoms because of the co-implantation of stable Ti isotopes during the recoil implantation. The results could not be explained by decay induced defects, because they should have zero concentration initially.

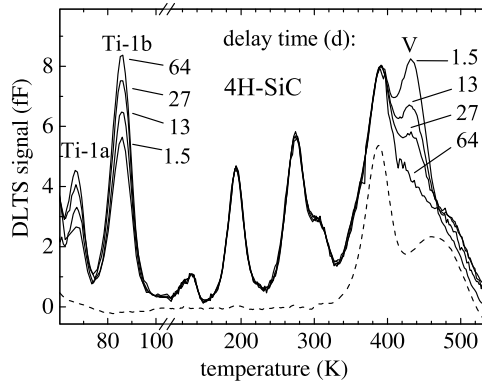


**Fig. 4.** DLTS spectra of  $^{48}\text{V}$  doped  $n$ -type  $4H$ -SiC measured after several delay times. The *dashed line* is a reference spectrum obtained from an non-implanted part of the sample

The different heights of the two Ti peaks in the spectra are caused by a partial freeze-out of the shallow nitrogen doping in the sample. A proper correction reveals that the concentration of both levels is about the same [20]. They are attributed to a Ti acceptor state that is slightly split due to the non-equivalent quasi-hexagonal and quasi-cubic lattice sites of  $4H$ -SiC. Ti is electrically active with a high efficiency in the order of 100% of the  $^{48}\text{Ti}$  daughter atoms originating from the  $^{48}\text{V}$  decay. There are no corresponding levels in  $6H$ - and  $15R$ -SiC.

The existence of such a Ti acceptor state had been predicted by electron spin resonance (ESR) studies [47]. Also, the same two DLTS peaks have been reported recently from Ti-implanted  $4H$ -SiC by Dalibor et al. [48] with trap energies of 0.11 eV and 0.15 eV.

### 5.2.2 Chromium:

Cr was studied in  $n$ -type  $4H$ - [19, 20],  $6H$ - [18],  $15R$ -SiC and in  $p$ -type  $4H$ -SiC [21] using the radiotracer isotope  $^{51}\text{Cr}$ . It decays to the stable isotope  $^{51}\text{V}$  with a half-life of 27.7 d (see Table 1). After  $^{51}\text{Cr}$  implantation in  $n$ -type  $4H$ -SiC, the four peaks dominating the spectrum are changing with delay time (see Fig. 5a). The peaks labelled Cr-1a, Cr-1b, and Cr-2 in this figure decrease exponentially in perfect agreement with the nuclear half-life of  $^{51}\text{Cr}$  (see Fig. 5b). The height of the peak V at 430 K increases with a time dependence in good agreement with the nuclear half-life. Its level data are compatible with the level observed with decreasing concentration if  $^{48}\text{V}$  is the parent atom (Fig. 4), i.e. it is due to a V-related defect.

Taking into account the inhomogeneous depth profiles (for details see appendix in [20]), the concentration ratios of the Cr levels (peak labels 1a, 1b, and 2 in Fig. 5a) are compatible with a ratio 1:1:2. Hence, the Cr levels

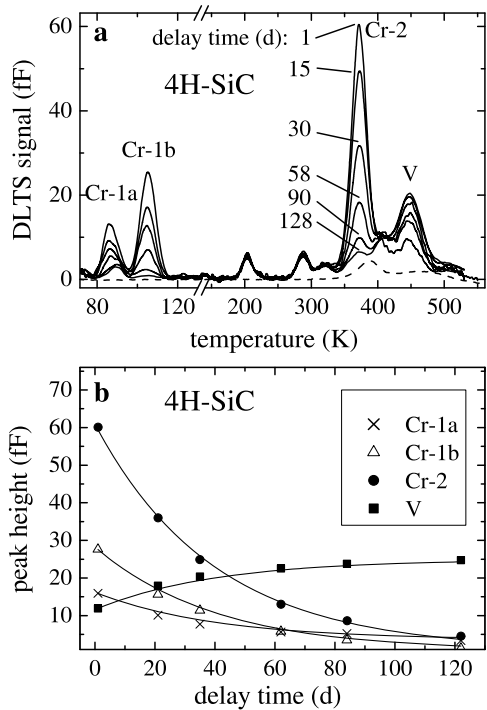


**Fig. 5.** (a) DLTS spectra of  $^{51}\text{Cr}$  doped  $n$ -type  $4H$ -SiC measured after several delay times as indicated at peak Cr-2. The *dashed line* represents a reference spectrum taken on an unimplanted part of the sample. (b) DLTS peak heights of the four peaks of (a) during the elemental transmutation of  $^{51}\text{Cr}$  to  $^{51}\text{V}$ . The *solid lines* are exponential curves with the half-life of the nuclear decay (27.7 d)

in  $4H$ -SiC are interpreted as follows: they represent two charge transitions of the same structural Cr configuration: transition 1 is sensitive to the difference between non-equivalent quasi-cubic or quasi-hexagonal sites and, therefore, has two slightly different levels 1a and 1b. The second transition (level 2) is insensitive (within DLTS accuracy) to the tiny difference between non-equivalent sites. The observed concentration fits well to a complete electrical activation of all incorporated  $^{51}\text{Cr}$  isotopes.

In  $p$ -type  $4H$ -SiC, a split Cr level (Cr-3) was established by radiotracer-DLTS [21] (spectra are shown in Fig. 6). Though the signals decreasing in the course of the transmutation are superimposed on a large background peak (probably the well known boron-related  $D$ -center), they can be clearly resolved by forming difference spectra (Fig. 6b). Here, the negative peaks reflect decreasing concentrations in good agreement with the nuclear decay half-life (27.7 d), thus proving that the levels are due to a Cr-related defect.

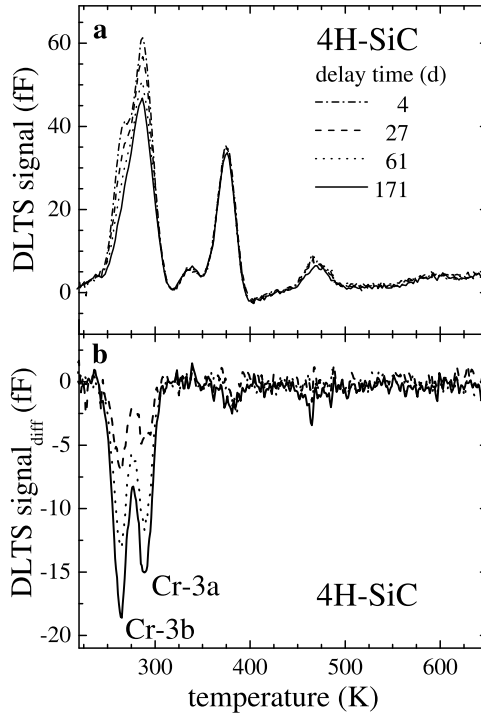


**Fig. 6.** (a) DLTS-spectra of  $p$ -type  $4H$ -SiC, recoil implanted with  $^{51}\text{Cr}$ , subsequently measured during the elemental transmutation to  $^{51}\text{V}$ . (b) DLTS-spectra obtained by subtracting the initial spectrum (measured 4 d after annealing) from the subsequently measured spectra

These levels (see Table 3) were assigned [21] to a double donor state which is slightly split due to the occupation of non-equivalent lattice sites in  $4H$ -SiC.

For the other polytypes,  $6H$  and  $15R$ , radiotracer DLTS spectra ( $n$ -type samples only) are shown in Fig. 7. The situation is quite similar to the one discussed in detail for the polytype  $4H$ , i.e. Cr peaks are uniquely labelled by their decrease and V-related peaks are appearing during the  $^{51}\text{Cr}$  decay. The level data are listed in Table 3. The relevant differences compared to  $4H$  are:

- there is no analogy to the twin Cr-peak Cr-1 detected in  $4H$ ,
- the peak positions of the Cr-2 and the V-peaks shift towards lower temperatures, i.e. the levels are closer to  $E_C$ ,
- there is a pronounced splitting of these levels into two or even three peaks for  $6H$  and  $15R$ , respectively.

The first two facts are explained completely by the polytype-dependent shift of the conduction band edge  $E_C$  (see [46]).

### 5.2.3 Vanadium:

Vanadium-related levels were studied in *n*-type 4*H*, 6*H* and 15*R*-SiC and in *p*-type 4*H*-SiC. Vanadium was used both as a parent ( $^{48}\text{V}$ ) as well as a daughter isotope ( $^{51}\text{Cr}$ ). The relevant experiments have already been described in the preceding sections on Ti and Cr.

After  $^{48}\text{V}$  as well as  $^{51}\text{Cr}$  implantation into 4*H*-SiC, peak labelled V decreases (in Fig. 4) or increases (Figs. 5 and 7) exponentially with the nuclear life-time of the parent activity. This level at  $E_C - 0.97$  eV is created by a defect which is either identical to exactly one V atom or which contains one V atom, eventually with other constituents. The same argument holds for all V-related levels in 6*H* and 15*R* (Fig. 7; for the level data see Table 3).

There is one major difference of this V-related level compared to Ti and Cr: it is formed by a non-reproducible, often small fraction (down to the detection limit) of all vanadium atoms only (for details see Fig. 8 in [20]). The results prove that vanadium is incorporated in SiC in more than one structural or atomic configuration [20]. Only one of them is detectable by DLTS on *n*-type SiC. It has to be stressed, that this lack of reproducibility of

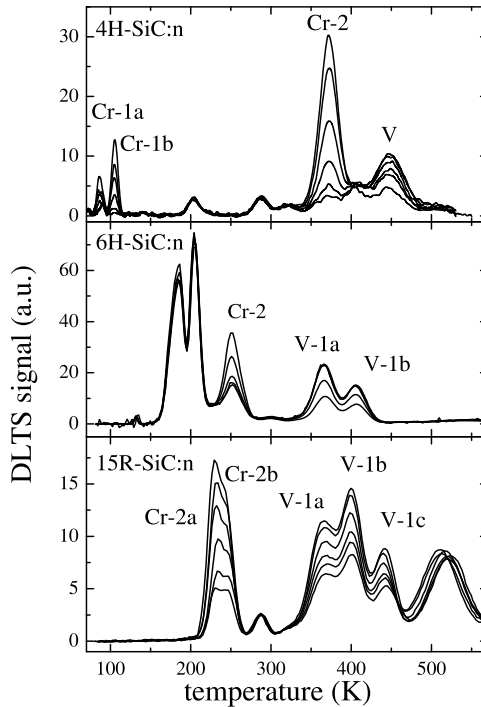


**Fig. 7.** DLTS spectra for Cr and V impurities in the polytypes 4*H*-, 6*H*-, and 15*R*-SiC indicating the level shifts and the level splittings

the concentration of the V-level does not impair its definite identification with a vanadium-related center: whenever the level is present, its concentration precisely follows the elemental transmutation.

### 5.3 Transition Metals Ta and W

Transition metals Ta or W are present in certain growth containments: recent publications about the crystal growth of SiC report the use of tantalum crucibles to avoid graphitisation during sublimation growth [51]–[53]. Due to its thermal stability the transition metal tungsten may play a similar role like Ta in the future.

#### 5.3.1 Tantalum:

Ta-related deep levels in *n*-type 4H-SiC were identified [28] by the elemental transmutation of the radiotracer isotope  $^{177}\text{Ta}$  which decays to stable  $^{177}\text{Hf}$ .

The DLTS spectra are highly reproducible except for the temperature range around 290 K (see Fig. 8a), where the DLTS signal is decreasing. The

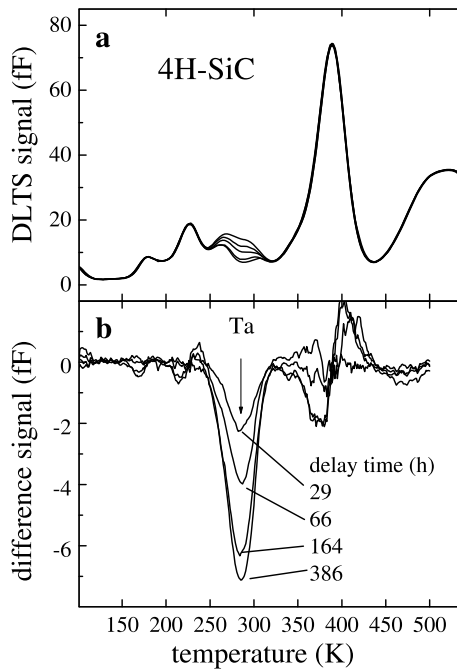


**Fig. 8.** (a) DLTS spectra of *n*-type 4H-SiC measured during the elemental transmutation of  $^{177}\text{Ta}$  to  $^{177}\text{Hf}$  ( $T_{1/2} = 56.6$  h). (b) Difference spectra obtained by subtracting the initial spectrum from subsequently measured spectra

**Table 4.** Parameters of Ta- and W-related deep levels in *n*-type SiC-polytypes detected by radiotracer DLTS

Poly-type	Element	Peak label	Energy $E_T$ (eV)	Cross section $\sigma$ ( $10^{-14}$ cm <sup>2</sup> )	Ref.
4 <i>H</i>	Ta	Ta	$E_C - (0.68 \pm 0.04)$	5	[28]
		W-1	$E_C - (0.17 \pm 0.01)$	50	[30]
		W-2	$E_C - (1.43 \pm 0.02)$	100	[30]
6 <i>H</i>	Ta	Ta-1a	$E_C - (0.46 \pm 0.03)$	10	[29, 31]
		Ta-1b	$E_C - (0.49 \pm 0.03)$	10	[29, 31]
		W-2	$E_C - (1.16 \pm 0.03)$	60	[30]
15 <i>R</i>	Ta	Ta-1a	$E_C - (0.42 \pm 0.03)$	10	[29, 31]
		Ta-1b	$E_C - (0.45 \pm 0.03)$	10	[29, 31]
	W	W-2	$E_C - (1.14 \pm 0.03)$	60	[30]

time dependent concentration can be easily deduced from the difference spectra (see Fig. 8b), which exhibit a broadened peak with a well defined temperature position. The negative height of this peak exponentially decreases with a half-life of  $(57 \pm 1)$  h, i.e. the corresponding defect contains exactly one radioactive parent isotope  $^{177}\text{Ta}$ . The level parameters are given in Table 4.

After the radiotracer identification parameters of the Ta- related deep levels in 4*H*-, 6*H*-, and 15*R*-SiC were derived from DLTS-measurements carried out on samples implanted with the stable isotope  $^{181}\text{Ta}$  [28, 29] (see Table 4). Additionally, 6*H*-SiC bulk material grown in an atmosphere containing Ta has been studied [29]. The DLTS spectrum shows a dominating peak at 200 K. Its level parameters agree within the experimental errors to the data obtained for the implanted samples.

5.3.2 Tungsten:

Tungsten was investigated in *n*-type 4*H*-, 6*H*-, and 15*R*-SiC. The isotope  $^{178}\text{W}$  used as a radioactive tracer transmutes to stable  $^{178}\text{Hf}$  in two steps. The first decay to  $^{178}\text{Ta}$  with a half-life of 22 d determines the time scale of the experiment (see Table 1). Similar to the case of Cr, tungsten exhibits one deep level, labelled W-2 in Table 4, and in the 4*H* polytype an additional level W-1 close to the conduction band (Table 4, details are given in [30]).

5.4 Deep Rare Earth Related Levels

Semiconductors doped with rare-earth elements are attractive for photonic applications. In heavily Er-doped SiC the integrated luminescence intensity remains nearly constant up to about 400 K [53, 54] whereas for moderately

**Table 5.** Parameter of Er- and Sm-related deep levels in *p*-type SiC-polytypes detected by radiotracer DLTS

Poly-type	Element	Energy $E_T$ (eV)	Cross section $\sigma$ ( $10^{-14}$ cm <sup>2</sup> )	Ref.
4H	Er	$E_V + (0.75 \pm 0.02)$	2	[27]
6H	Er	$E_V + (0.78 \pm 0.02)$	2	[27]
6H	Sm	$E_V + (0.87 \pm 0.02)$	2	[25]

Er-doped 4H- and 6H-SiC the intensity is drastically reduced at low temperatures [55]. For a detailed understanding the characterization of band gap states is of basic importance. In Table 5 we summarize the results of first radiotracer experiments of rare earth impurities Er and Sm in SiC.

Er was investigated in 4H-SiC by employing the isotope  $^{160}\text{Er}$  which decays to unstable  $^{160}\text{Ho}$  with a half-life of 28.6 h followed by a rather fast second decay of  $^{160}\text{Ho}$  ( $T_{1/2} = 0.43$  h) to the stable isotope  $^{160}\text{Dy}$ . For the present radiotracer experiment, the transmutation may simply be regarded as  $^{160}\text{Er} \rightarrow ^{160}\text{Dy}$  with a half-life of 28.6 h. In *p*-type SiC, one Er level was identified at  $E_V + (0.75 \pm 0.02)$  eV in 4H and at  $E_V + (0.78 \pm 0.02)$  eV in 6H-SiC, respectively. The latter is in good agreement with recent results obtained by Klettke et al. [54]. The degree of the electrical activation of all incorporated Er-atoms was determined to about 10%. In *n*-type SiC no Er-related level was observed.

Experiments with radioactive  $^{153}\text{Sm}$  ( $T_{1/2} = 46.8$  h) were carried out at the on-line isotope implanter ISOLDE/CERN. The  $^{153}\text{Sm}$  isotope was implanted with an energy of about 4 MeV resulting in a depth suitable for the DLTS experiments. In *p*-type 6H-SiC one level at  $E_V + (0.87 \pm 0.02)$  eV was identified to be Sm-related, in *n*-type SiC no Sm levels were detected. Also, there are no levels of the daughter element Eu.

## 6 Summary and Conclusions

The extensive reliable data set on deep states of the transition metals Ti, V, Cr, Ta, and W in the band gap of the three SiC-polytypes 4H, 6H, and 15R allows a detailed comparison of the relative energy position in the different polytypes. To draw one common level scheme for all three polytypes we align the valence bands of all SiC polytypes as postulated by Afanas'ev et al. [57]. Thus, for an intelligible comparison, all energy levels are described by their energetic distance from the valence band in each polytype as shown in Fig. 9. The deep levels of the investigated transition metals behave as expected according to the rule of Langer and Heinrich: they fairly well coincide energetically for the three polytypes. Obviously both, the statement that the

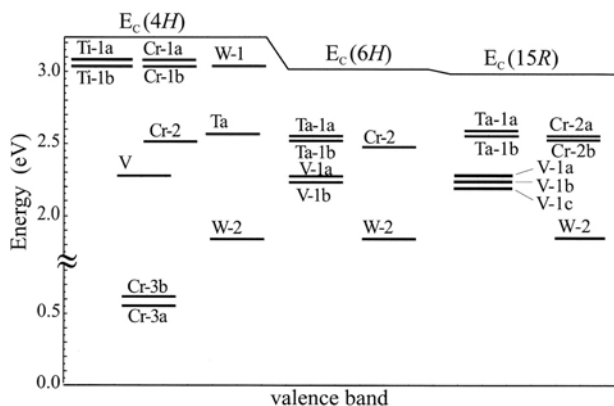


**Fig. 9.** Summary of transition metal related band gap states in SiC identified by radiotracer DLTS. The labels refer to Tables 3 and 4. To compare the three polytypes, their valence band edges were aligned

valence bands of all SiC-polytypes are energetically aligned as well as the rule of Langer-Heinrich are valid for SiC.

The radiotracer concept in combination with a classical “non-nuclear” technique of semiconductor spectroscopy, in this case DLTS, yields the definite chemical identification of an observed band gap state which is not available from the spectroscopic technique alone. In addition, the number of isotopes per electrically active center, the degree of electrical activation, and eventually, by comparison with data from other techniques, information about the lattice site occupation can be derived. In many cases, radioactive doping and ordinary doping experiments were done in parallel to overcome the disadvantages of both techniques.

There is only one essential condition on the radioactive isotope: a reasonable half-life. With a few exceptions only (essentially the first two rows of the periodic system, Al and Cl) all other elements do have at least one suitable isotope. Hence, the number of available isotopes is large and the impurities to be investigated may be chosen according to the current problems in semiconductor research. For the present case of SiC, four groups of impurities were selected:

- group II elements Be, Zn and Cd.
- Group III transition metals Ti, V, Cr: they are typical contaminations in bulk crystals and vanadium has gained high technological relevance for semi-insulating SiC substrates. For Ti and Cr, the results are well understood, whereas for vanadium, both the fraction of vanadium impurities forming the detected level as well as the polytype dependence of level splitting exhibits a complicated behaviour.

- 5 d elements Ta and W were chosen, since Ta has been used in crystal growth experiments. With the data provided here, the Ta incorporation in crystals can now be measured quantitatively with an often available, non-destructive technique like DLTS.
- Rare earth elements because of their importance for optoelectronics.

The deep level schemes identified via radiotracer DLTS as presented here form the largest available data collection of deep impurity levels in SiC. Due to the radiotracer concept, the involvement of the selected element in electrically active defects is definite, whereas in some cases open questions remain regarding the involvement of further impurities in the defect structure, the degree of electrical activation, and the existence of further levels in the unobserved part of the band gap. Compared to the long history of research on impurity levels, e.g. in silicon, with frequent controversy about the chemical identification, the radiotracer experiments presented enabled a fast progress in SiC within half a decade.

### Acknowledgements

We thank F. Albrecht, J. Grillenberger, G. Pasold, C. Hülsen, U. Grossner, and U. Reislöhner for assistance during the numerous experiments and many discussions, M. Frank and K. Rith (University Erlangen-Nürnberg) for providing beam time at the tandem accelerator of their institute and R. Sielemann (ISL of the Hahn-Meitner-Institute Berlin) for assistance with the heavy-ion-induced implantations. We thank M. Dietrich and the ISOLDE collaboration for assistance during the on-line-implantations at CERN.

The financial support of this work by the German Ministerium für Bildung und Forschung (BMBF) and by the Deutsche Forschungsgemeinschaft (DFG) is gratefully acknowledged.

### References

1. *Hyperfine Interactions of Defects in Semiconductors*, ed. by G. Langouche (Elsevier, Amsterdam, 1992)
2. R. Magerle, A. Burchard, M. Deicher, T. Kerle, W. Pfeiffer, E. Recknagel: *Phys. Rev. Lett.* **75**, 1594 (1995)
3. I. Broser, K.H. Franke: *J. Phys. Chem. Solids* **26** 1013 (1965)
4. I. Broser, G. Schulz: *Z. Physik* **254**, 35 (1972)
5. J.W. Petersen, J. Nielsen: *Appl. Phys. Lett.* **56**, 1122 (1990)
6. M. Lang, G. Pensl, M. Gebhard, N. Achziger, M. Uhrmacher: *Appl. Phys. A* **53**, 95 (1991)
7. M. Lang, G. Pensl, M. Gebhard, N. Achziger, M. Uhrmacher: *Mat. Sci. Forum* **83–87**, 1097 (1992)
8. N. Achziger, W. Witthuhn: *Phys. Rev. Lett.* **75**, 4484 (1995)
9. S.E. Daly, M.O. Henry, K. Freitag, R. Vianden: *J. Phys. Cond. Matter* **6**, L643 (1994)

10. R. Gwilliam, B.J. Sealy, R. Vianden: Nucl. Instr. and Methods B **63**, 106 (1992)
11. G. Rohrlack, K. Freitag, C.v. Nathusius, R. Vianden, R. Gwilliam, B.J. Sealy: Mat. Sci. Forum **248–249**, 119 (1997)
12. J. Hamann, A. Burchard, M. Deicher, T. Filz, V. Ostheimer, C. Schmitz, H. Wolf, Th. Wichert and the ISOLDE collaboration: Appl. Phys. Lett. **72**, 3029 (1998)
13. M. Uhrmacher, M. Neubauer, W. Bolse, L. Ziegler, K.P. Lieb: Nucl. Instr. and Methods B **139**, 306 (1998)
14. E. Kugler, D. Fiander, B. Jonson, H. Haas, A. Przwloka, H.L. Ravn, D.J. Simon, K. Zimmer: Nucl. Instr. and Methods B **70**, 41 (1992)
15. World Wide Web, <http://www.cern.ch/ISOLDE>
16. N. Achtziger, H. Gottschalk, T. Licht, J. Meier, M. Rüb, U. Reislöhner, W. Witthuhn: Appl. Phys. Lett. **66**, 2370 (1995)
17. N. Achtziger: J. Appl. Phys. **80**, 6286 (1996)
18. N. Achtziger, J. Grillenberger, W. Witthuhn: Appl. Phys. **A 65**, 329 (1997)
19. N. Achtziger, W. Witthuhn: Appl. Phys. Lett. **71**, 110 (1997)
20. N. Achtziger, W. Witthuhn: Phys. Rev. B **57**, 12181 (1998)
21. G. Pasold, N. Achtziger, J. Grillenberger, W. Witthuhn: Mat. Sci. Forum **353–356**, 471 (2001)
22. N. Achtziger, T. Licht, M. Rüb, U. Reislöhner, W. Witthuhn: in *23rd Intern. Conf. on the Physics of Semiconductors*, ed. by M. Scheffler, R. Zimmermann (World Sci Publ, Singapore, 1996) p. 2717
23. N. Achtziger, J. Grillenberger, M. Uhrmacher, W. Witthuhn: Mat. Sci. Forum **338–342**, 749 (2000)
24. F. Albrecht, N. Achtziger, M. Dietrich, G. Pasold, W. Witthuhn: J. Appl. Phys. to be published
25. G. Pasold, M. Dietrich, F. Albrecht, W. Witthuhn: Ann. report, Uni Jena (2002)
26. G. Pasold, F. Albrecht, J. Grillenberger, U. Grossner, C. Hülsen, R. Sielemann, W. Witthuhn: Mat. Sci. Forum, in press (2003)
27. G. Pasold, F. Albrecht, J. Grillenberger, U. Grossner, C. Hülsen, W. Witthuhn, R. Sielemann: J. Appl. Phys. **93**, 2289 (2003)
28. J. Grillenberger, N. Achtziger, R. Sielemann, W. Witthuhn: J. Appl. Phys. **88**, 3260 (2000)
29. J. Grillenberger, G. Pasold, W. Witthuhn, N. Achtziger: Appl. Phys. Lett. **79**, 2405 (2001)
30. N. Achtziger, G. Pasold, R. Sielemann, C. Hülsen, W. Witthuhn: Phys. Rev. **B 62**, 12888 (2000)
31. J. Grillenberger, N. Achtziger, G. Pasold, R. Sielemann, W. Witthuhn: Mat. Sci. Forum **353–356**, 475 (2001)
32. P. Blood, J.W. Orton: Academic Press, London (1992) p. 339/426
33. D.V. Lang: J. Appl. Phys. **45**, 3023 (1974)
34. G.L. Miller, D.V. Lang, L.C. Kimmerling: Annual Rev. Mat. Sci. **7**, 377 (1977)
35. N. Achtziger: Mat. Sci. Forum **248–249**, 113 (1997)
36. N. Achtziger, J. Grillenberger, W. Witthuhn: Hyperfine Interactions **120/121**, 69 (1999)
37. R. Sielemann, L. Wende, G. Weyer: Phys. Rev. Lett. **75**, 1542 (1995)
38. T. Dalibor, G. Pensl, H. Matsunami, T. Kimoto, W.J. Choyke, A. Schöner, N. Nordell: Phys. Stat. Sol. (a) **162**, 199 (1997)

39. X.D. Chen, S. Fung, C.D. Beling, M. Gong, T. Henkel, H. Tanoue, N. Kobayashi: *J. Appl. Phys.* **88**, 4558 (2000)
40. M. Krieger, M. Laube, M. Weidner, G. Pensl: *Mat. Sci. Forum* **353–356**, 467 (2001)
41. F. Albrecht, N. Achtziger, J. Grillenberger, G. Pasold, W. Witthuhn: *Appl. Phys. Lett.* **79**, 961 (2001)
42. J. Grillenberger, N. Achtziger, F. Günter, W. Witthuhn: *Appl. Phys. Lett.* **73**, 3698 (1998)
43. T. Troffer, G. Pensl, A. Schöner, A. Henry, C. Hallin, O. Kordina, E. Janzen: *Mat. Sci. Forum* **264–268**, 557 (1998)
44. P.G. Baranov: *Mat. Sci. Forum* **264–268**, 581 (1998)
45. H. Overhof: University of Paderborn, private communication (2002)
46. J. Grillenberger, N. Achtziger, G. Pasold, W. Witthuhn: *Mat. Sci. Forum* **389–393**, 573 (2002)
47. J. Schneider, K. Maier: *Physica* **B 185**, 199 (1993)
48. P.G. Baranov, V.A. Khramtsov, E.N. Mokhov: *Semicond. Sci. Technol.* **9**, 1340 (1994)
49. T. Dalibor, G. Pensl, N. Nordell, A. Schöner: *Phys. Rev.* **B 55**, 13618 (1997)
50. J. Baur, M. Kunzer, J. Schneider: *Phys. Stat. Sol. (a)* **162**, 153 (1997)
51. D. Hoffmann, S.Y. Karpov, Y.N. Makarov, E.N. Mokhov, M.G. Ramm, M.S. Ramm, A.D. Roenkov, Y. Vodakov: *Inst. Phys. Conf. Ser.* **142**, 29 (1996)
52. E.N. Mokhov, M.G. Ramm, A.D. Roenkov, Y.A. Vodakov: *J. Cryst. Growth* **181**, 254 (1997)
53. Y.A. Vodakov, A.D. Roenkov, M.G. Ramm, E.N. Mokhov, Y.N. Makarov: *Phys. Stat. Sol. (b)* **202**, 177 (1997)
54. O. Klettke, S.A. Reshanov, G. Pensl, Y. Shishkin, R.P. Devaty, W.J. Choyke: *Physica* **B 308–310**, 687 (2001)
55. Y. Shishkin, W.J. Choyke, R.P. Devaty, N. Achtziger, T. Opfermann, W. Witthuhn: *Mat. Sci. Forum* **338–342**, 639 (2000)
56. J.M. Langer, H. Heinrich: *Phys. Rev. Lett.* **55**, 1414 (1985)
57. V.V. Afanas'ev, M. Bassler, G. Pensl, M.J. Schulz, E. Stein von Kamienski: *J. Appl. Phys.* **79**, 3108 (1996)
58. W. Kohn, J.M. Luttinger: *Phys. Rev.* **98**, 915 (1955)
59. J. Wong, T. Diaz de la Rubia, M.W. Guinan, M. Tobin, J.M. Perlado, A.S. Perez, J. Sanz: *Journal of Nuclear Materials* **212–215**, 143 (1994)
60. A.L. Barry, B. Lehmann, D. Fritsch, D. Bräuning: *IEEE Transactions on Nuclear Science*, **38**, 1111 (1991)

# Vacancy Defects Detected by Positron Annihilation

A. Kawasuso, M. Weidner, F. Redmann, T. Frank, P. Sperr, G. Kögel,  
M. Yoshikawa, H. Itoh, R. Krause-Rehberg, W. Triftshäuser, and G. Pensl

## 1 Introduction

Point defects in SiC is important in connection with the technological concerns such as ion implantation, crystal growth and radiation tolerance. Among different types of point defects, vacancy defects have been frequently argued in the past studies on irradiated SiC using deep level transient spectroscopy (DLTS), electron spin resonance (ESR), photoluminescence (PL), etc. Although these conventional approaches have a capability to discriminate different defect species, even indirect for the determination of the type of defects. Consequently, the origins of important energy levels in SiC have not yet been fully understood.

Positron annihilation spectroscopy (PAS) is a useful technique to detect vacancy defects in semiconductors [1, 2]. From the positron annihilation characteristics, the presence of vacancy defects can be explicitly known. Complementary study between PAS and the other methods gives us more fruitful information than used alone. In this chapter, PAS studies of vacancy defects in SiC are described. In Sect. 2, the principle of PAS and some positron annihilation parameters in SiC are briefly described. In Sects. 3 and 4, the results on radiation-induced vacancy defects and correlations with electronic energy levels are discussed.

## 2 Principle of Positron Annihilation

Positrons implanted into crystals slow down to thermal energy within  $\sim 10$  ps. In defect free crystals, thermal positrons freely diffuse as a Bloch state and ultimately annihilate with electrons to emit two 511 keV gamma quanta per one positron-electron pair. Positrons are localized at vacancy defects because of their potential wells. Since the annihilation characteristics of positrons are different for free and vacancy-trapped-states, through positron annihilation measurements, vacancy defects can be detected. PAS is classified into positron annihilation lifetime (PAL), the Doppler broadening of annihilation radiation (DBAR) and angular correlation of annihilation radiation (ACAR) measurements [1]. In this chapter, the former two methods are used and thus they are introduced in the following.

**Table 1.** Positron lifetimes and binding energy calculated theoretically for 3C-SiC (by atomic superposition method) and 4H-SiC (by plane wave pseudopotential method). Vacancy geometry in the former case is ideal, while that in the latter case it was optimized using the lattice relaxation. Dependence of positron lifetime on equivalent lattice sites is small (1–2 ps) and therefore the listed values are averaged

	3C-SiC [11]		4H-SiC [5]	
	$\tau$ [ps]	$E_B$ [eV]	$\tau$ [ps]	$E_B$ [eV]
Bulk	141 ps		131 ps	
$V_C$	150 ps	0.28 eV	137 ps	−0.08 eV
$V_{Si}$	185 ps	1.69 eV	194 ps	1.49 eV
$V_C V_{Si}$	216 ps	2.39 eV	215 ps	2.26 eV
2- $V_C V_{Si}$	254 ps	3.48 eV		
3- $V_C V_{Si}$	286 ps	4.27 eV		
4- $V_C V_{Si}$	321 ps	4.94 eV		

Positron lifetime ( $\tau$ ) is given as an inverse of the overlap integral between electron and positron densities [3].

$$1/\tau = \pi r_e c^2 \int n_+(\mathbf{r}) n_-(\mathbf{r}) \gamma d\mathbf{r} . \quad (1)$$

Here,  $r_e$  is the classical electron radius,  $c$  the light speed,  $n_+(\mathbf{r})$  and  $n_-(\mathbf{r})$  the positron and electron densities, respectively, and  $\gamma$  the enhancement factor. Thus, the positron lifetime depends on the electron density. Theoretical positron lifetime in perfect SiC lattice (bulk lifetime:  $\tau_B$ ) is reported to be 131–142 ps irrespective to polytype [4, 5]. This is in between those of diamond (110 ps) and Si (218 ps) reflecting the order of their lattice constant [1]. Experimental bulk lifetime of SiC is 136–146 ps [6]–[10]. The small variation is probably due to residual defects. Generally,  $p$ -type materials and chemical vapor deposition (CVD) grown epitaxial layers exhibit shorter bulk lifetimes because of less positron trapping sites. Reduction of electron density at a vacancy defect gives rise to the enhancement of positron lifetime there as compared to  $\tau_B$ . Table 1 lists theoretical positron lifetimes and binding energies for various vacancy defects in SiC. It is seen that positron lifetime and binding energy increase as the size of vacancy cluster. Although positron lifetime for a silicon vacancy,  $V_{Si}$ , (185–194 ps) is well above  $\tau_B$ , that for carbon vacancies,  $V_C$ , increases only 6–9 ps. This is explained as the smaller open space of  $V_C$  because of larger ion radius of the Si atom surrounding  $V_C$ .

More than two lifetime components are observed when vacancy defects exist, i.e., bulk and defects. Assuming that only one kind of vacancy defects, the positron lifetime spectrum is decomposed into two exponential decay components:

$$L(t) = I_1 \exp(-t/\tau_1)/\tau_1 + I_2 \exp(-t/\tau_2)/\tau_2 . \quad (2)$$

Here,  $I_i$  and  $\tau_i$  ( $i = 1, 2$ ) are the intensities ( $I_1 + I_2 = 100\%$ ) and lifetimes. Based on the kinematical two-state trapping model, the second lifetime component is assigned to the positron annihilation at vacancy defects. Since the first lifetime is arising from the positron annihilation in free state, it should be equal to  $1/(1/\tau_B + \kappa)$ , where  $\kappa (= I_2(1/\tau_B - 1/\tau_2)/I_1)$  is the positron trapping rate by vacancy defects. Positron trapping rate is proportional to the specific trapping rate  $\mu$  and the defect concentration  $C$  ( $\kappa = \mu C$ ). Detectable change of  $\kappa$  is approximately  $0.1 \text{ ns}^{-1}$ . Considering that  $\mu$  varies from  $10^{15}$  to  $10^{17} \text{ s}^{-1}$  depending on the charge state of vacancy defects and materials [12], the detection limit of vacancy defects is roughly  $10^{14}$  to  $10^{16} \text{ cm}^{-3}$ . Positrons are hardly trapped by positively charged vacancy defects.

The Doppler broadening and angular correlation of annihilation radiations are required from the energy and momentum conservation laws. Momentum distribution of positron-electron pairs is given by [3]

$$\rho(\mathbf{p}) = \pi r_e^2 c \left| \int \psi_+ \psi_- \sqrt{\gamma} \exp(-i\mathbf{p} \cdot \mathbf{r}) d\mathbf{r} \right|^2. \quad (3)$$

DBAR or 2D-ACAR spectra are given by integrating this 3D momentum distribution in two or one particular direction(s). Valence and core electrons give rise to relatively smaller and larger Doppler shifts, respectively. These components are well separated in DBAR spectrum. At vacancy defects, the core annihilation probability decreases and the valence annihilation probability relatively increases. Consequently, the peak (valence electron contribution) and tail (core electron contribution) intensities of DBAR spectrum increases and decreases, respectively. The peak and tail intensities are called  $S$  and  $W$  parameters. Denoting  $S$  parameters for bulk as  $S_B$  and vacancy state as  $S_V$ ,  $S$  parameters is given by  $S = (1 - \eta)S_B + \eta S_V$ , where  $\eta = \kappa/(1/\tau_B + \kappa)$ . Similarly,  $W = (1 - \eta)W_B + \eta W_V$ .  $S$  and  $W$  parameters are usually normalized to bulk values, i.e.,  $S_B = W_B = 1$ . Thus, generally  $S > 1$  and  $W < 1$  when positrons are trapped by vacancy defects. Core electron momentum distribution can be determined using the coincidence Doppler broadening (CDB) technique, which enables to enhance the signal to noise ratio to be more than  $10^5$  [13]. From this, the elemental sensitivity of the positron method is derived.

## 3 Radiation-Induced Vacancy Defects in SiC

### 3.1 Electron Irradiation

Radiation-induced defects in 3C-SiC have been systematically studied by Itoh et al. [14]–[16] using ESR. Almost isotropic  $T1$  signal was attributed to single-negative silicon vacancies ( $V_{\text{Si}}^-$ ) in a tetrahedral symmetry. Afterward, PAL measurements have been performed [17]. Figure 1 shows the PAL spectra from a CVD grown  $n$ -type 3C-SiC before and after 1MeV  $e^-$ -irradiation.

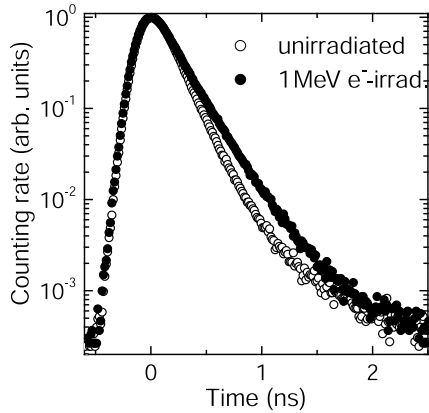


**Fig. 1.** Positron lifetime spectra obtained from CVD grown *n*-type 3C-SiC doped with nitrogen ( $[N_D] = 1 \times 10^{16} \text{ cm}^{-3}$ ) before (*open circle*) and after (*filled circle*) 1 MeV  $e^-$ -irradiation to a dose of  $6 \times 10^{17} \text{ e}^-/\text{cm}^2$  at room temperature

Apparent increase in the positron lifetime after irradiation suggests the presence of vacancy defects. Through the decomposition of spectra using (2), two lifetime components ( $\tau_1$  and  $\tau_2$ ) were obtained as a function of annealing temperature. The first lifetime ( $\tau_1$ ) was in good agreement with that expected from the two-state trapping model. The defect-related positron lifetime ( $\tau_2$ ) was approximately 190 ps. During annealing,  $\tau_2$  keeps a constant and  $I_2$  decreases at 200°C and above 800°C suggesting that the positron trapping centers do not change and the concentration decreases upon annealing. The lifetime ( $\tau_2$ ) is in good agreement with the calculated lifetime for  $V_{\text{Si}}$  (Ta-

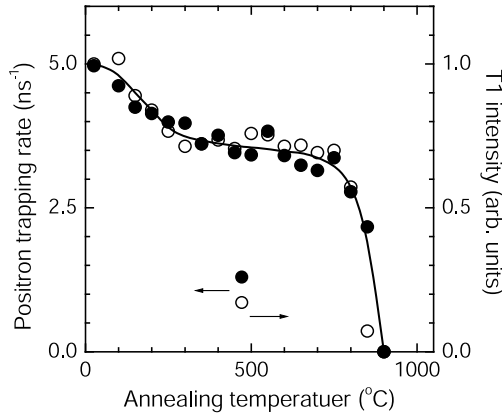


**Fig. 2.** Positron trapping rate and  $T1$ -signal intensity from CVD grown *n*-type 3C-SiC doped with nitrogen ( $[N_D] = 1 \times 10^{16} \text{ cm}^{-3}$ ) after 1 MeV  $e^-$ -irradiation to a dose of  $1.2 \times 10^{18} \text{ e}^-/\text{cm}^2$  as a function of annealing temperature

ble 1). Figure 2 shows the direct comparison of positron trapping rate and  $T1$ -signal intensity through annealing using the identical samples. Common annealing behavior between positron trapping rate and  $T1$  signal intensity gives us a confirmation that positrons are trapped at  $V_{Si}^-$ .

Two-step recovery of  $S$  and  $W$  parameters typical for  $V_{Si}$  were also observed in the DBAR study on  $3C$ -SiC (shown in Fig. 8) [18]. Normalized  $S$  and  $W$  parameters for  $V_{Si}$  in  $3C$ -SiC were determined to be  $S_V = 1.028 \sim 1.039$  and  $W_V = 0.805 - 0.834$  [18, 19]. Figure 3a shows the CDB spectra for  $n$ -type  $3C$ -SiC before and after 2 MeV  $e^-$ -irradiation to a dose of  $3 \times 10^{17} e^-/cm^2$  [18]. The change of spectrum shape after irradiation is enhanced by generating the ratio curve between unirradiated and irradiated states, i.e.,  $N_{irrad}(p)/N_{unirrad}(p)$  as shown in Fig. 3b. Low ( $p < 15 \times 10^{-3} m_0 c$ ) and high ( $p > 20 \times 10^{-3} m_0 c$ ) momentum regions of the ratio curve are dominated by valence and core electrons, respectively. In high momentum region, the intensity has a tendency to increase with momentum. When positrons annihilate at  $V_{Si}$  the intensity of the ratio curve in high momentum region increases with momentum reflecting C:1s electrons giving rise to a larger Doppler shift as compared to Si:2sp electrons. In contrast, in the case of  $V_C$ , the intensity

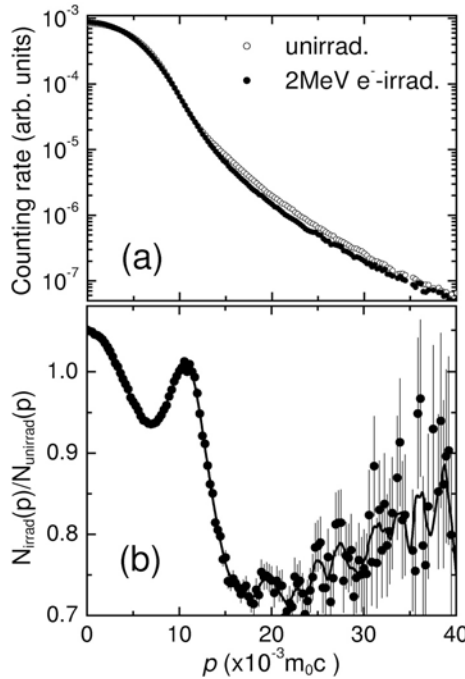


**Fig. 3.** (a) The coincidence Doppler broadening spectra and (b) the ratio curve obtained for CVD grown  $n$ -type  $3C$ -SiC doped with nitrogen ( $[N_D] = 1 \times 10^{16} cm^{-3}$ ) before and after 2 MeV  $e^-$ -irradiation to a dose of  $3 \times 10^{17} e^-/cm^2$

of the ratio curve decrease with momentum [5]. The above observation agrees with that expected for  $V_{\text{Si}}$ .

In PAS studies on 3C-SiC,  $V_{\text{C}}$ -related defects have not been detected. Considering the weak localization of positrons at  $V_{\text{C}}$  as stated in Sect. 2, the positron trapping by  $V_{\text{C}}$  may be hidden behind the strong effect of  $V_{\text{Si}}$ . If the charge state of  $V_{\text{C}}$  is positive or neutral, the positron trapping rate decreases furthermore due to the lacking of the Coulomb attraction. Then, the detection of  $V_{\text{C}}$  will be unlikely. Indeed, theoretical studies suggest that  $V_{\text{C}}$  act as donors in 3C-SiC and hence positive and neutral charge states are possible [21]–[25].

Two annealing steps of  $V_{\text{Si}}$  at around 200°C and 800°C were inferred to be due to recombination with mobile silicon interstitials ( $I_{\text{Si}}$ ) and the migration of  $V_{\text{Si}}$  to sinks [15]. The activation energy for the latter process was determined to be 2.2–3.1 eV [15, 26]. Theoretical studies predict that recombination with  $\langle 110 \rangle$  split interstitials is most likely to occur in the former process, while the transformation from  $V_{\text{Si}}$  to  $V_{\text{C}}\text{C}_{\text{Si}}$  preferentially occurs than direct migration of  $V_{\text{Si}}$  in the latter process [25], [27]–[29]. To examine the possibility of detection of  $V_{\text{C}}\text{C}_{\text{Si}}$  by PAS, theoretical calculation was carried out using the atomic superposition method [30]. The result indicates that the positron wavefunction is localized at ideal  $V_{\text{C}}\text{C}_{\text{Si}}$  much stronger than  $V_{\text{C}}$  and the positron lifetime increases approximately 26 ps from  $\tau_{\text{B}}$ . This result is a bit surprising considering the fact that  $V_{\text{C}}$  act as weak positron trapping centers. The replacement of one Si atom with one C atom surrounding  $V_{\text{C}}$  effectively enhances the binding energy and positron lifetime. The lattice relaxation around  $V_{\text{C}}\text{C}_{\text{Si}}$  [27, 29] results in an extra 20 ps increase of the lifetime. Thus,  $V_{\text{C}}\text{C}_{\text{Si}}$  complexes may be detected by positron annihilation as long as the charge state is not positive. However, after the annealing of  $V_{\text{Si}}$  no further vacancy defects were detected in positron annihilation as shown in Fig. 2. One possible explanation is that  $V_{\text{Si}}$  prefer to migrate rather than their transformation to  $V_{\text{C}}\text{C}_{\text{Si}}$  in  $n$ -type 3C-SiC. An alternative explanation is that the charge state of  $V_{\text{C}}\text{C}_{\text{Si}}$  is less negative [29] and hence the detection of  $V_{\text{C}}\text{C}_{\text{Si}}$  becomes rare.

Positively charged vacancies hardly trap positrons due to the Coulomb repulsion [12]. Positron trapping rate by negatively charged vacancies is higher than that by neutral vacancies. This effect can be used for the determination of defect charge states. Figure 4 shows  $S$  parameters obtained for  $n$ -type and  $p$ -type 3C-SiC irradiated with 2 MeV electrons to a dose of  $3 \times 10^{17} \text{ e}^-/\text{cm}^2$  as a function of incident positron energy [18]. It is found that  $S$  parameter increases in the  $n$ -type material, while it remains the same as the unirradiated state in the  $p$ -type material. The situation is almost the same even when the sample was implanted with He ions generating approximately two orders of magnitude greater number of primary knock-on atoms (see Sect. 3.2). Thus, it seems that  $V_{\text{Si}}$  have the donor state [31] and charge as positive when the Fermi level is close to the top of the valence band [21]–[24].

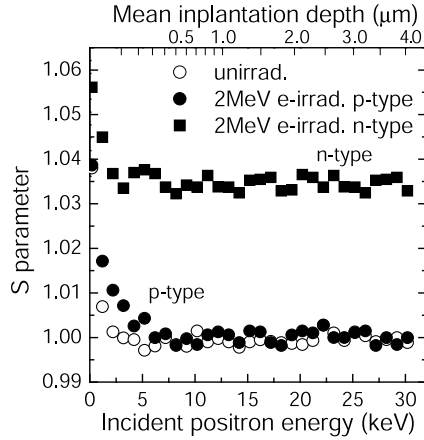


**Fig. 4.**  $S$  parameter obtained from CVD grown  $n$ -type 3C-SiC doped with nitrogen ( $[N_D] = 1 \times 10^{16} \text{ cm}^{-3}$ ) and  $p$ -type 3C-SiC doped with aluminum ( $[N_A] = 1 \times 10^{16} \text{ cm}^{-3}$ ) after 2 MeV  $e^-$ -irradiation to a dose of  $3 \times 10^{17} \text{ e}^-/\text{cm}^2$  as a function of incident positron energy

Changing energy of  $e^-$ -irradiation, the atomic displacement energy ( $E_d$ ) is evaluated [32]. Figure 5 shows the positron trapping rate per unit dose by  $V_{\text{Si}}^-$  in  $n$ -type 3C-SiC determined in the DBAR measurements [18]. The trapping rate starts to increase at a threshold energy  $E_{\text{th}} = 0.37 \pm 0.04 \text{ MeV}$ . This means that only carbon displacement occurs when electron energy is less than 0.37 MeV. From the elastic collision theory,  $E_d$  can be determined

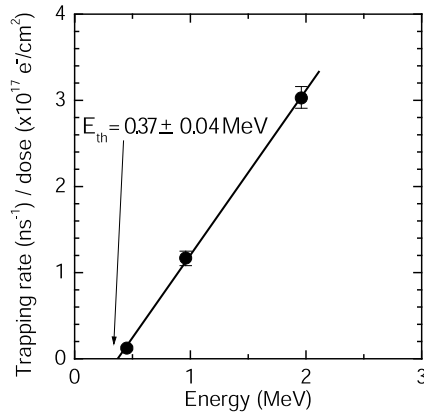


**Fig. 5.** Positron trapping rate per unit dose of  $e^-$ -irradiation obtained for CVD grown  $n$ -type 3C-SiC doped with nitrogen ( $[N_D] = 1 \times 10^{16} \text{ cm}^{-3}$ ). Doses for 0.5 MeV, 1 MeV and 2 MeV are  $1.2 \times 10^{17} \text{ e}^-/\text{cm}^2$ ,  $6 \times 10^{17} \text{ e}^-/\text{cm}^2$  and  $3 \times 10^{17} \text{ e}^-/\text{cm}^2$ , respectively

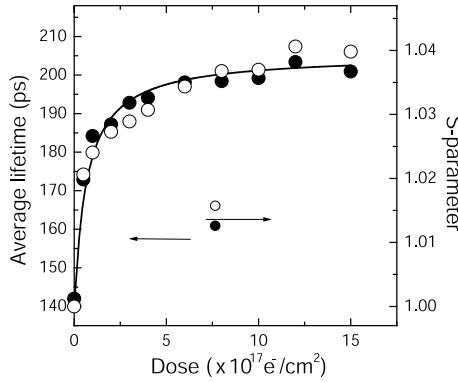


**Fig. 6.** Average lifetime and  $S$  parameter obtained from modified Lely grown  $n$ -type 6H-SiC doped with nitrogen ( $[N_D] = 5 \times 10^{17} \text{ cm}^{-3}$ ) after 3 MeV  $e^-$ -irradiation as a function of dose

by  $E_d = 2mE_{th}(E_{th} + 2mc^2)/(mc^2M)$ , where  $M$  is the mass of target atom (in the present case  $M = 28$  for Si). Thus, we obtain  $E_d = 39 \pm 5$  eV for silicon displacement. In the above experiment, electrons were irradiated from the [001] direction. The obtained  $E_d$  is in good agreement with theoretical values based on the molecular dynamics [33, 34]. The above displacement energy is also higher than that for carbon atoms (22 eV) [35].

Early PAS studies on irradiated hexagonal SiC have been carried out using bulk materials [6]–[9], [36]–[40]. Figure 6 shows the dose dependence of average positron lifetime and  $S$  parameter from modified Lely (ML) grown  $n$ -type 6H-SiC after 3 MeV  $e^-$ -irradiation [36]. Both average lifetime and  $S$  parameter increase monotonously with dose and saturate at  $\tau_{ave} \sim 200$  ps and  $S \sim 1.039$ . These values coincide with the characteristic lifetime and  $S$  parameter determined for  $V_{Si}$  in 3C-SiC. Thus,  $V_{Si}$ -related defects are responsible for positron trapping. Detailed analyses of lifetime spectra however indicated the existence of  $V_C$ -related component, which gives rise to a positron lifetime close to  $\tau_B$ , in addition to  $V_{Si}$ -related component.

Figure 7 shows the annealing behavior of positron trapping rates ( $\kappa_1$  and  $\kappa_2$ ) for  $V_C$ - and  $V_{Si}$ -related components, respectively [36]. The positron trapping rate  $\kappa_1$  for  $V_C$ -related component drastically decreases below 500°C. This annealing behavior is consistent with that observed for  $V_C^+$  in ESR studies [41, 42]. The appearance of the  $V_C$ -related component however seems to be contradictory to the result of 3C-SiC. This can be explained as an occurrence of negative charge state of  $V_C$  because of the wider band gap width of hexagonal SiC allowing the acceptor levels associated with  $V_C$  [21]–[24]. Positron lifetime for  $V_C$  was reported to be 160 ps, which is 14 ps higher than  $\tau_B$  [7, 44]. When positrons are trapped only at  $V_C$ , the CDB spectrum shows the effect of Si core electrons in the high momentum region [43]. The positron trapping rate related to  $V_C$  increases at low temperatures due to

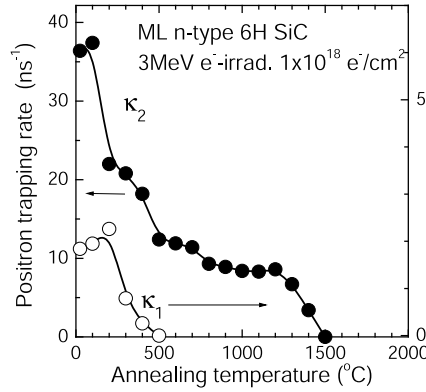


**Fig. 7.** Positron trapping rates ( $\kappa_1$  and  $\kappa_2$ ) related to  $V_C$ - and  $V_{Si}$ -related components, respectively, from ML-grown  $n$ -type 6H-SiC doped with nitrogen ( $[N_D] = 5 \times 10^{17} \text{ cm}^{-3}$ ) after 3 MeV  $e^-$ -irradiation to a dose of  $1 \times 10^{18} \text{ e}^-/\text{cm}^2$  as a function of annealing temperature. Annealing time was 5 min

the shallow potential [45]. This effect disappeared upon annealing at around 500°C. Normalized  $S$  parameter for  $V_C$  was determined to be 1.001, which is very close to  $S_B$  and hence essentially invisible in DBAR measurement [8]. Thus, in the case of  $n$ -type hexagonal SiC,  $V_C$  can be discriminated if the decomposition of the spectrum is allowed. The migration energy of  $V_C$  is estimated to be more than 3.5 eV while that of carbon interstitials ( $I_C$ ) is 0.9–1.7 eV [25, 46]. The annealing of  $V_C$  therefore may be interpreted as  $V_C$ - $I_C$  recombination through the motion of  $I_C$ .

As seen from Fig. 7, the positron trapping rate  $\kappa_2$  ( $V_{Si}$ -related) decays in four steps at around 200°C, 500°C, 800°C and 1400°C. The annealing of  $V_{Si}$  probably corresponds to the decay below 800°C. Vacancy defects still survive after the annealing at 1000°C unlike to the case of 3C-SiC. The above results indicate that more thermally stable vacancy defects than  $V_{Si}$  are created in 6H-SiC. From the analogy with the  $E$ -center in Si, the formation of complexes between  $V_{Si}$  and nitrogen is assumed [6].

Similar annealing experiments have also been carried out using high quality nitrogen doped CVD 6H and 4H-SiC. Figure 8 shows the annealing behavior of  $S$  parameters obtained after 2 MeV (dose:  $3 \times 10^{17} \text{ e}^-/\text{cm}^2$ ) and 1 MeV (dose:  $6 \times 10^{17} \text{ e}^-/\text{cm}^2$ )  $e^-$ -irradiations [47]–[49]. It is found that  $S$  parameter for 6H-SiC irradiated with 1 MeV electrons decreases at 200–400°C, 600–800°C and finally at 1200–1500°C. The annealing feature is almost the same even in the case of 2 MeV  $e^-$ -irradiation although the first two steps are observed as one overlapping decay. The final annealing step at 1200–1500°C is seen as well as the ML grown materials shown in Fig. 7. 4H-SiC also exhibits the similar recovery processes except relatively small decays at 600–800°C and maxima at around 1000°C.

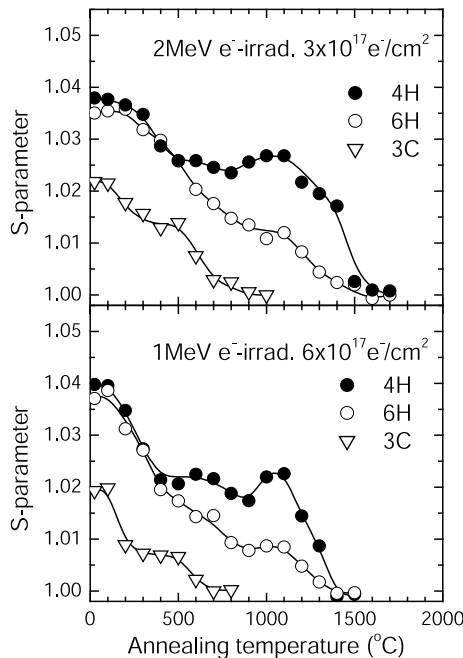


**Fig. 8.**  $S$  parameters for CVD grown  $n$ -type  $6H$  and  $4H$ -SiC doped with nitrogen ( $[N_D] = 5 \times 10^{15} \text{ cm}^{-3}$ ) and  $3C$ -SiC doped with nitrogen ( $[N_D] = 1 \times 10^{16} \text{ cm}^{-3}$ ) after 2 MeV and 1 MeV  $e^-$ -irradiations to doses of  $3 \times 10^{17} \text{ e}^-/\text{cm}^2$  and  $6 \times 10^{17} \text{ e}^-/\text{cm}^2$ , respectively, as a function of annealing temperature. Annealing time at each temperature was 30 min

From the comparison with the case of  $3C$ -SiC plotted together, the first two annealing steps ( $200\text{--}400^\circ$ ,  $600\text{--}800^\circ$ ) observed for  $4H$  and  $6H$ -SiC in Fig. 8 are interpreted as the disappearance of  $V_{Si}$ . Indeed, the positron lifetimes after 2 MeV  $e^-$ -irradiation were determined to be approximately 200 ps using a pulsed positron beam. Now the question is the origin of residual vacancy defects after the annealing at  $1000^\circ$ . As proposed by theoretical works [5, 27, 28],  $V_{Si}$  may transfer to  $V_C C_{Si}$  complexes upon heating. In the case of  $3C$ -SiC (Sect. 3.1), this possibility was not confirmed. Nevertheless, the positron lifetimes for  $V_C C_{Si}$  were calculated taking into account of a possible lattice relaxation [27]. As the charge state changes from double negative to neutral, because of the lattice relaxation, positron lifetime varies from 187 ps to 193 ps at hexagonal site and from 162 ps to 175 ps at cubic site. It is clear that positrons are localized at these complexes much stronger than at  $V_C$ . Positrons are more localized at hexagonal site. The lifetime at hexagonal sites is comparable to that for ideal  $V_{Si}$  and is in good agreement with the observation in the ML grown  $6H$ -SiC. It turns out to be difficult to exclude the possibility of positron trapping at  $V_C C_{Si}$  only from PAL measurements.

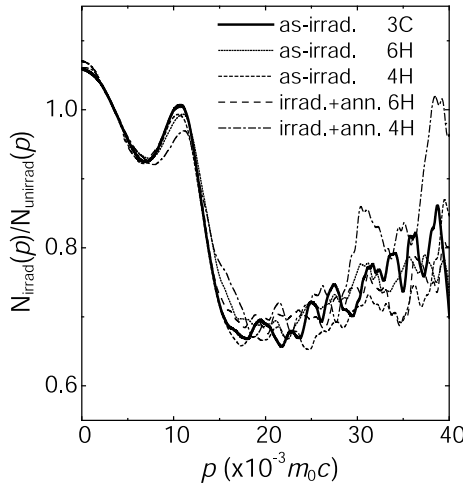


**Fig. 9.** The coincidence Doppler broadening ratio curves obtained for CVD grown *n*-type 6H and 4H-SiC doped with nitrogen ( $[N_D] = 5 \times 10^{15} \text{ cm}^{-3}$ ) after 2 MeV  $e^-$ -irradiations to a dose of  $3 \times 10^{17} e^-/\text{cm}^2$  and subsequent annealing at  $1000^\circ\text{C}$  for 30 min. For comparison, the ratio curve for 3C-SiC shown in Fig. 4b is also drawn as *solid line*. Vertical axes for 6H-SiC before and after annealing are scaled by multiplying 1.16 and 3.35, respectively. Those for 4H-SiC before and after annealing are scaled by multiplying 1.02 and 1.52, respectively

To confirm the change of defect species by annealing at  $1000^\circ\text{C}$ , i.e., from  $V_{\text{Si}}$  to  $V_{\text{C}}\text{C}_{\text{Si}}$ , CDB measurements were carried out. Figure 9 shows the CDB ratio curves (i.e.,  $N(p)/N_{\text{unirrad}}(p)$ ) for 6H and 4H-SiC after 2 MeV  $e^-$ -irradiation to a dose of  $3 \times 10^{17} e^-/\text{cm}^2$  and subsequent annealing at  $1000^\circ\text{C}$  [47]–[49]. For the direct comparison, the vertical scale for each ratio curve was appropriately adjusted. It is found that all the curves well overlap in the whole range and are quite similar to the curve obtained for  $V_{\text{Si}}$  in 3C-SiC. This indicates that the chemical surrounding of the defects is still like that for  $V_{\text{Si}}$ . Thus,  $V_{\text{Si}}$ -related complexes may be considered as the most probable candidate for the residual vacancy defects at  $1000^\circ\text{C}$ .

### 3.2 He Implantation

He implantation was examined for the study of defects [50]. Figure 10 shows  $S$  parameters obtained for various SiC samples after multiple He-implantation as a function of incident positron energy ( $S$ - $E$  plot). Here, He doses were well below the amorphous formation. The  $S$ - $E$  plots were analyzed by the one-dimensional diffusion equation of positrons [51] to obtain the depth distribution of  $S$  parameter. As expected from the SRIM simulation, the box-shaped defect profile was seen. The highest  $S$  parameters in the middle of the damaged region ( $\sim 10 \text{ keV}$ ) exceed the value for  $V_{\text{Si}}$  suggesting that

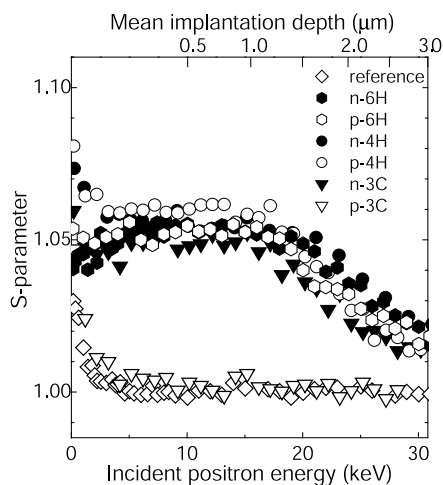


**Fig. 10.**  $S$  parameters obtained for CVD grown  $n$ -type 6H and 4H-SiC doped with nitrogen ( $[N_D] = 5 \times 10^{15} \text{ cm}^{-3}$ ),  $p$ -type 6H and 4H doped with aluminum ( $[N_D] = 5 \times 10^{15} \text{ cm}^{-3}$ ),  $n$ -type 3C-SiC doped with nitrogen ( $[N_D] = 1 \times 10^{16} \text{ cm}^{-3}$ ) and  $p$ -type 3C-SiC doped with aluminum ( $[N_A] = 1 \times 10^{16} \text{ cm}^{-3}$ ) obtained after multiple He implantation at energies (doses) of 30 keV ( $8 \times 10^{11} \text{ cm}^{-2}$ ), 100 keV ( $9.5 \times 10^{11} \text{ cm}^{-2}$ ), 210 keV ( $9.5 \times 10^{11} \text{ cm}^{-2}$ ), 350 keV ( $9.5 \times 10^{11} \text{ cm}^{-2}$ ), 500 keV ( $9.5 \times 10^{11} \text{ cm}^{-2}$ ), 650 keV ( $1 \times 10^{12} \text{ cm}^{-2}$ ), 800 keV ( $1.1 \times 10^{12} \text{ cm}^{-2}$ ) and 950 keV ( $1.3 \times 10^{12} \text{ cm}^{-2}$ ) at room temperature as a function of incident positron energy. Reference specimen is the unirradiated CVD grown  $p$ -type 6H-SiC

larger vacancy clusters are also generated. In fact the average positron lifetime measured by a pulsed positron beam was typically 220–230 ps which is higher than that in  $e^-$ -irradiated materials. Vacancy defects were detected in hexagonal SiC and  $n$ -type 3C-SiC, while not in  $p$ -type 3C-SiC. The absence of positron trapping in  $p$ -type 3C-SiC was similarly seen in the case of  $e^-$ -irradiation shown in Fig. 4. This indicates that the Fermi level of  $p$ -type hexagonal SiC shift upwards and hence the charge states of defects become more negative, while that of  $p$ -type 3C-SiC does not shift adequately.

Figure 11 shows  $S$  parameter in damage region as a function of annealing temperature. It is found that  $S$  parameter for  $n$ -type 3C-SiC first decreases drastically at 500–700°C. Two annealing steps observed in the  $e^-$ -irradiated sample (Fig. 8) probably combine together and appear as one annealing step here. The final recovery takes place at 1000°C suggesting the disappearance of residual vacancy defects. One important finding is that all the vacancy defects detected by positron vanish until 1000°C despite the greater number and size of vacancy defects than in the  $e^-$ -irradiated sample. This is an indication that vacancy-interstitial recombination is an important annealing mechanism after irradiation [52].

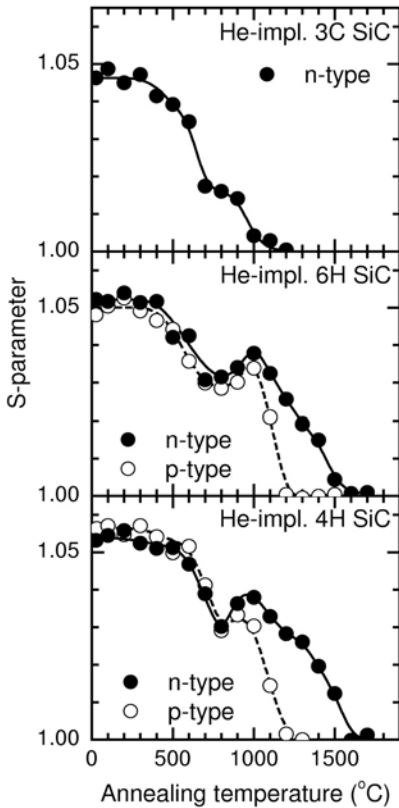


Fig. 11.  $S$  parameters obtained from the analysis of  $S$ - $E$  plots shown in Fig. 10 based on the one-dimensional diffusion equation of positrons for  $n$ -type 6H and 4H-SiC as a function of annealing temperature. Annealing time at each temperature was 30 min

$S$  parameters in 4H and 6H-SiC exhibit the common annealing features: The first annealing occurs at 500–700°C, which is similar to the 3C material. Then,  $S$  parameters increase and show maxima at 1000°C suggesting the generation of secondary defects such as vacancy clusters upon heating. Such peaks are not seen in 3C-SiC. Until these peaks, no major differences are recognized between 4H and 6H and between  $n$ - and  $p$ -type. After these peaks,  $S$  parameters of  $p$ -type materials decrease steeply and completely recover to the unimplanted states, while one more annealing steps appear in  $n$ -type materials as shoulders at 1200–1300°C. Thus, two different defect species contribute to the peaks at 1000°C and the shoulders at 1200–1300°C in both  $n$ -type 4H and 6H-SiC.  $S$  parameter of  $n$ -type materials recover to the unimplanted states up to 1700°C suggesting the disappearance of all the detectable vacancy defects. The shoulder of  $S$  parameter for the 4H-SiC is more pronounced than that for the 6H-SiC similar to  $e^-$ -irradiation (Fig. 8). Accordingly, the same defect species ( $V_{\text{Si}}$ -related defects) are responsible for the final annealing processes in both  $e^-$ -irradiated and He-implanted hexagonal SiC.

### 3.3 Polytype Dependent Vacancy Annealing

As seen above (Figs. 8 and 11), the annealing behavior of vacancy defects depends on polytype. That is, vacancy defects in 3C-SiC are no longer detected after annealing at 1000°C, while those in hexagonal SiC are still detected above 1000°C. In Fig. 8, the residual amount of vacancy defects increases in the order of  $3C < 6H < 4H$ , i.e., hexagonalities (0%, 33% and 50%) after the annealing at 1000°C. A similar trend is also seen in the case of He-implantation at 1300°C in Fig. 11. This further indicates the following two possibilities: One is that the residual vacancy defects in hexagonal SiC in the high temperature annealing process are related to hexagonal sites and hence forbidden to exist in 3C-SiC. The other is that vacancy defects detected in hexagonal SiC in the high temperature annealing process are just invisible in 3C-SiC. That is, the gap states of the vacancy defects are buried in the conduction band in 3C-SiC because of its smaller band gap width and hence the charge state become more positive in 3C-SiC. Indeed, the vacancy defects in hexagonal SiC in the high temperature annealing process are correlated to the energy levels, which are not observed in 3C-SiC. To confirm the above discussion, 2D-ACAR measurements were also performed [53].

## 4 Correlation Between Positron Annihilation Centers and Electronic Energy Levels

Many electronic energy levels have been found in SiC after irradiation as summarized in Fig. 12 [54]–[71]. Early studies show that the energy levels at  $E_C$ -0.3~0.4 eV labeled  $E_{1/2}$  (same as  $ED_{3H}/ED_4$  and  $L_{3/4}$ ) [55, 57] and at  $E_C$ -0.6~0.7 eV labeled  $Z_{1/2}$  (same as  $ED_7$  and  $L_{7/8}$ ) [55, 57] are the major products in 6H-SiC due to bombardment [60, 61, 72]. The corresponding energy levels in 4H-SiC are labeled  $Z_{1/2}$  at  $E_C$ -0.6~0.7 eV (same as  $EH_2$ ) [68] and  $RD_{1/2}$  at  $E_C$ -0.9~1.0 eV (same as  $EH_4$ ) [68] in 4H-SiC. These levels are commonly annealed at around 1500°C [56, 58, 59, 67, 73]. The  $E_{1/2}$  in 6H-SiC and the  $Z_{1/2}$  in 4H-SiC are reported to exhibit the negative- $U$  character [74]–[76].

Correlations between vacancy defects from PAS and DLTS centers were examined. Figure 13 shows the DLTS spectra for  $n$ -type 4H and 6H-SiC after 2 MeV  $e^-$ -irradiation (after the first scan, i.e., annealed at 430°C) and subsequent annealing at 1200°C [47, 48, 77]. The  $E_{1/2}$  in 6H-SiC and the  $Z_{1/2}$  in 4H-SiC are found to exist with the other small peaks labeled in the figure. The small peaks diminish by annealing up to 1200°C and thereafter the  $E_{1/2}$  in 6H-SiC and the  $Z_{1/2}$  in 4H-SiC are predominant. Figure 14 shows the annealing behavior of the densities of these levels together with the positron trapping rates obtained after increasing the dose [47, 48]. It is found that both positron trapping centers and the energy levels disappear in the same temperature range. This coincidence suggests that the energy

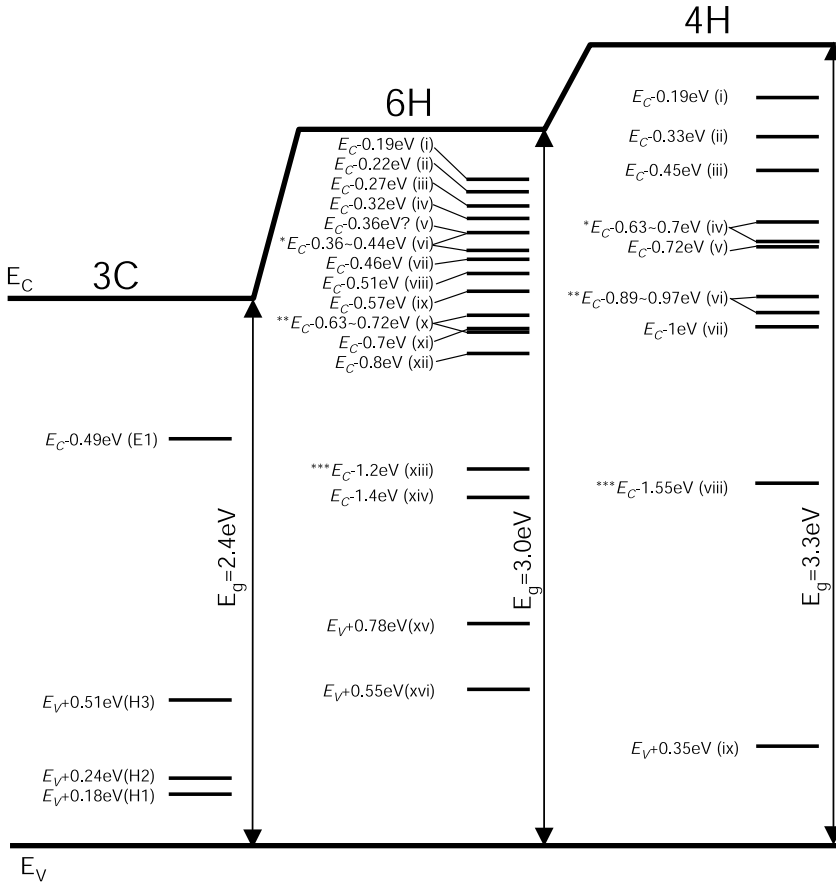


**Fig. 12.** Electronic energy levels induced by irradiation in 3C, 6H and 4H-SiC. Labels for 6H-SiC are (i) L1, (ii) L2, (iii) ED1, (iv) ED2, (v) ED3L, (vi) E1/2, ED3H/4, L3/4, (vii) L5, (viii) Ei, ED5, L6, RD5, (ix) E3/4, ED6, (x) Z1/2, L7/8, ED7, (xi) Z0, (xii) L9, (xiii) R, E7, L10, (xiv) L11, (xv) H2, (xvi) H1. Labels for 4H-SiC are (i) P1/2, (ii) P3, (iii) EH1, (iv) EH2, Z1/2, (v) EH4, (vi) RD1/2, (vii) RD3, EH5, (viii) RD4, EH6/7, (ix) HS1. \*, \*\*, \*\*\* are the levels thought to have the same defect structures in 4H and 6H-SiC

levels are composed of vacancy defects. As discussed in Sect. 3.1,  $V_{Si}$ -related complexes are annealed at 1200–1500°C. It was thus proposed that the  $E_{1/2}$  in 6H-SiC and the  $Z_{1/2}$  in 4H-SiC are originating from  $V_{Si}$ -related complexes.

In the case of He-implantation, one major deep level was observed in both 6H and 4H-SiC after annealing at 700°C as shown in Fig. 15 [50]. Individual peaks in 6H and 4H-SiC are assigned to the  $Z_{1/2}$  and  $RD_{1/2}$  levels. These peaks were found to increase at 1000°C and finally diminish above 1200°C. Accompanying the disappearance of these peaks, the  $E_{1/2}$  in 6H-SiC and the

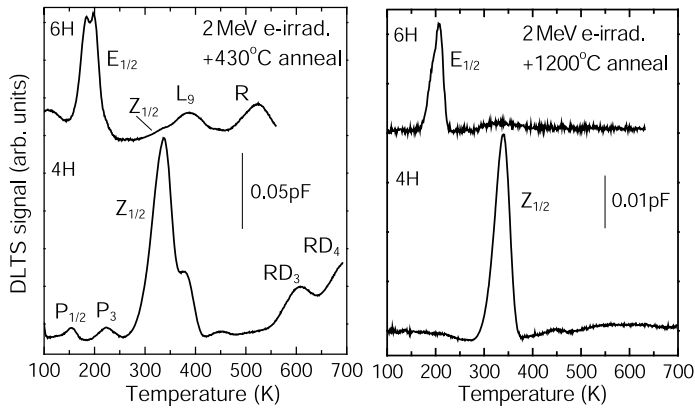


**Fig. 13.** DLTS spectra obtained for CVD grown *n*-type 6*H* and 4*H*-SiC doped with nitrogen ( $[N_D] = 5 \times 10^{15} \text{ cm}^{-3}$ ) after 2 MeV  $e^-$ -irradiation to a dose of  $1 \times 10^{15} \text{ e}^-/\text{cm}^2$  after the first scan (i.e., annealed at 430°C) and subsequent annealing at 1200°C for 30 min. The rate windows are 8 ms/16 ms and 2 ms/4 ms for 6*H* and 4*H*-SiC, respectively

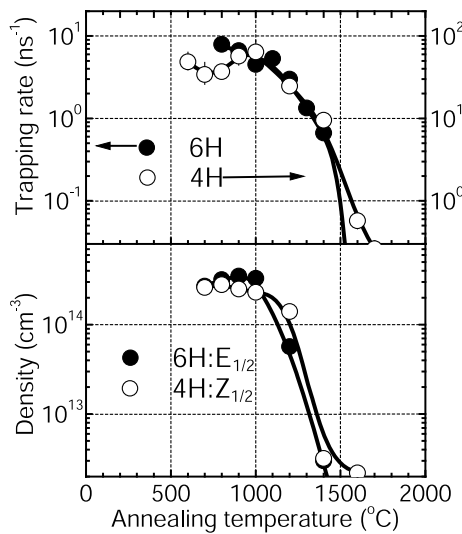


**Fig. 14.** Positron trapping rates obtained for CVD grown *n*-type 6*H* and 4*H*-SiC doped with nitrogen ( $[N_D] = 5 \times 10^{15} \text{ cm}^{-3}$ ) after 2 MeV  $e^-$ -irradiation to a dose of  $3 \times 10^{17} \text{ e}^-/\text{cm}^2$  and the densities of  $Z_{1/2}$  levels and  $E_{1/2}$  levels in CVD grown *n*-type 6*H* and 4*H*-SiC doped with nitrogen ( $[N_D] = 5 \times 10^{15} \text{ cm}^{-3}$ ) after 2 MeV  $e^-$ -irradiation to a dose of  $1 \times 10^{15} \text{ e}^-/\text{cm}^2$  as a function of annealing temperature

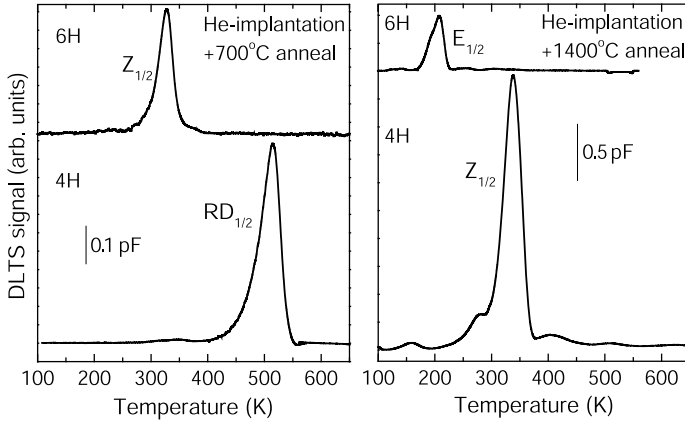


**Fig. 15.** DLTS spectra obtained for CVD grown *n*-type 6H and 4H-SiC doped with nitrogen ( $[N_D] = 5 \times 10^{15} \text{ cm}^{-3}$ ) after multiple He implantation at energies (doses) of 30 keV ( $8 \times 10^{11} \text{ cm}^{-2}$ ), 100 keV ( $9.5 \times 10^{11} \text{ cm}^{-2}$ ), 210 keV ( $9.5 \times 10^{11} \text{ cm}^{-2}$ ), 350 keV ( $9.5 \times 10^{11} \text{ cm}^{-2}$ ), 500 keV ( $9.5 \times 10^{11} \text{ cm}^{-2}$ ), 650 keV ( $1 \times 10^{12} \text{ cm}^{-2}$ ), 800 keV ( $1.1 \times 10^{12} \text{ cm}^{-2}$ ) and 950 keV ( $1.3 \times 10^{12} \text{ cm}^{-2}$ ) and subsequent annealing at 700°C and 1400°C for 30 min. The rate windows are 8 ms/16 ms and 2 ms/4 ms for 6H and 4H-SiC, respectively

$Z_{1/2}$  in 4H-SiC appear. The former and latter levels seem to be linked. The  $E_{1/2}$  in 6H-SiC and the  $Z_{1/2}$  in 4H-SiC are ultimately annealed at 1300–1500°C similarly to the case of  $e^-$ -irradiation. Figure 16 shows the annealing behavior of the above peaks and  $S$  parameters in the same implantation condition. It is readily found that the overall annealing behavior of DLTS peaks is in good agreement with that of  $S$  parameter. That is, the maxima of the densities of  $Z_{1/2}$  in 6H-SiC and  $RD_{1/2}$  in 4H-SiC coincide with those of  $S$  parameters at 1000°C. The appearance and disappearance of the  $E_{1/2}$  in 6H and the  $Z_{1/2}$  in 4H well agree with the shoulders in the annealing curves of  $S$  parameters. The density of the  $Z_{1/2}$  in 4H-SiC is higher than that of the  $E_{1/2}$  in 6H-SiC. This is also in good agreement with the larger shoulder in the annealing curve of  $S$  parameter observed in 4H-SiC. It was confirmed that the  $E_{1/2}$  and  $Z_{1/2}$  in 6H-SiC and  $Z_{1/2}$  and  $RD_{1/2}$  in 4H-SiC are related to vacancy defects.

In the previous studies,  $V_C$  was thought to be the candidate for the  $E_{1/2}$  in 6H-SiC [56, 63]. In the CVD process studies, the  $Z_{1/2}$  in 4H-SiC was correlated with the excess Si (e.g.,  $V_C$  and SiC) [78]–[80] or the excess C (e.g.,  $I_C$ ) and nitrogen doping [81]. These attributions are in conflict with the above conclusion that the  $E_{1/2}$  in 6H-SiC and the  $Z_{1/2}$  levels in 4H-SiC are coming from  $V_{Si}$ -related complexes. PAS study based on the optical illumination also suggests that the  $E_{1/2}$  in 6H-SiC are due to  $V_{Si}$ -related defects. Since the thermal stability of  $V_C$  induced by irradiation is well below than those of the  $E_{1/2}$  in 6H-SiC, it seems to be a bit difficult to attribute

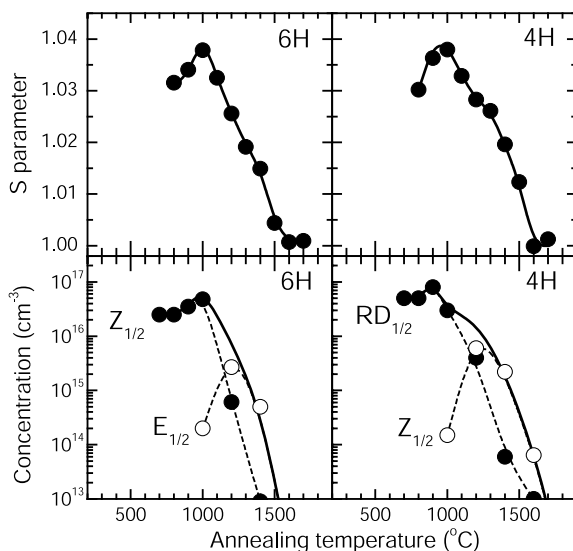


**Fig. 16.** Comparison of annealing behavior of  $S$  parameters shown in Fig. 11 after multiple He implantation and the densities of deep levels shown in Fig. 15. *Solid lines in the lower figures are the total concentrations of the deep levels*

these levels to  $V_C$ . The  $Z_{1/2}$  in 6H-SiC and  $RD_{1/2}$  in 4H-SiC were proposed to be related to either  $V_{Si}$  [56, 82] or divacancies  $V_{Si}VC$  [63]. However, the  $Z_{1/2}$  in 6H-SiC and  $RD_{1/2}$  in 4H-SiC are fully annealed above 1000°C which is well above the annealing temperature of  $V_{Si}$ . The growths of these levels at 1000°C as shown in Fig. 16 imply that they are related to complexes rather than single vacancies.

As for the other energy levels, the  $R$  levels appearing at  $E_C$ -1.1~1.3 eV in 6H-SiC (same as  $E_7$  and  $L_{10}$ ) [54, 57, 63] are attributed to  $V_{Si}$  in the PAS study [44]. The  $R$  level shown in Fig. 13 was indeed annealed at 600–1000°C [66]. This annealing temperature is in good agreement with that for  $V_{Si}$ . Hence, the  $V_{Si}$  model for the  $R$  level may be justified. The  $RD_4$  at  $E_C$ -1.5~1.6 eV (same as  $EH_{6/7}$ ) [68] in 4H-SiC corresponds to the  $R$  in 6H-SiC. An annealing study of neutron irradiated 4H-SiC using ESR and optical absorption showed that the optical transition at 780 nm (1.59 eV), which is comparable to the  $RD_4$  energy level, is originating from  $V_{Si}$  [83]. The  $RD_5$  levels at around  $E_C$ -0.5 eV in 6H-SiC (same as  $L_6$ ,  $E_i$ ) [54, 57, 58, 63, 66] are reported to show the similar annealing behavior to  $V_C$  below 500°C. This level was not seen in Fig. 13 due to heating during the first DLTS measurement. Considering the annealing temperature of  $V_C$  (Sect. 3.1), the attribution of  $RD_5$  to  $V_C$  seems to be plausible [56].

The  $D_1$  luminescence, which appears by post-irradiation annealing [84, 85], was originally attributed to vacancy defects. The correlation between  $D_1$  luminescence and DLTS centers were examined so far [65, 69, 70, 73]

although the assignments from different groups are still inconsistent. The  $D_1$  luminescence intensity increases with annealing temperature [69, 70, 86]. This luminescence is persistent even after the annealing at 1700°C. Previous PAS study could not confirm the early proposal that the luminescence is arising from vacancy defects [6].

## 5 Conclusion

PAS studies of defects in SiC were described in this chapter. In  $e^-$ -irradiated 3C-SiC, the positron trapping by  $V_{\text{Si}}^-$  was confirmed by the correlation with ESR measurements.  $V_{\text{C}}$ -related defects have not been detected. Theoretically predicted formation of  $V_{\text{C}}\text{C}_{\text{Si}}$  complexes have not been confirmed although the calculation suggested the adequate increase in positron lifetime at this complex. In  $e^-$ -irradiated 6H-SiC, in addition to  $V_{\text{Si}}$ -related defects,  $V_{\text{C}}$  have been detected through PAL measurements. After the annealing of  $V_{\text{Si}}$  at high temperatures (above 1000°C),  $V_{\text{Si}}$ -related defects were found to survive in hexagonal SiC. The amount of residual vacancy defects was found to increase with hexagonality after the high temperature annealing. PAS and DLTS measurements through annealing suggested that some levels in hexagonal SiC were related to vacancy defects.

## Acknowledgement

M.J. Puska of Helsinki University of Technology is acknowledged for permitting us to use his computer code calculating positron lifetimes. M. Bockstedt of Erlangen University is acknowledged for his valuable comments on thermodynamics of point defects in SiC. One of us (A.K.) is grateful to the Alexander von Humboldt Stiftung for the financial support.

## References

1. R. Krause-Rehberg, H.S. Leipner: *Positron Annihilation in Semiconductors*, Springer Series in Solid-State Sciences, Vol. 127 (Springer, Berlin, 1998)
2. P. Asoka-Kumar, J.K.G. Lynn, D.O. Welch: J. Appl. Phys. **76**, 4935 (1994)
3. M.J. Puska, R.M. Nieminen: Rev. Mod. Phys. **66**, 841 (1994)
4. G. Brauer, W. Anward, E.-M. Nicht, J. Kuriplach, M. Šob, N. Wagner, P.G. Coleman, M.J. Puska, T. Korhonen: Phys. Rev. B **54**, 2512 (1996)
5. T. Staab, L.M. Torpo, M.J. Puska, R.M. Nieminen: Mater. Sci. For. **353-356**, 533 (2001)
6. A. Kawasuso, H. Itoh, S. Okada, H. Okumura: J. Appl. Phys. **80**, 5639 (1996)
7. A.A. Rempel, H.-E. Schaefer: Appl. Phys. A **61**, 51 (1995)
8. S. Dannefaer, D. Craigen, D. Kerr: Phys. Rev. B **51**, 1928 (1995)
9. A. Polity, S. Huth, M. Lausmann: Phys. Rev. B **59**, 10603 (1999)

10. It is sometimes difficult to determine the bulk lifetime precisely because of the influence of the positron source components. To avoid this inconvenience, positron source material was directly deposited onto *p*-type 6H-SiC grown by the modified Lely method. Then the bulk lifetime was determined to be  $140 \pm 2$  ps for bulk lifetime.
11. G. Brauer, W. Anward, P.G. Coleman, A.P. Knight, Y. Pacaud, W. Skorupa, J. Störmer, P. Willutzki: Phys. Rev. B **54**, 3084 (1996)
12. R. Krause-Rehberg, H.S. Leipner: Appl. Phys. A **64**, 457 (1997)
13. P. Asoka-Kumar, M. Alatalo, V.J. Ghosh, A.C. Kruseman, B. Nielsen, K.G. Lynn: Phys. Rev. Lett. **77**, 2097 (1996)
14. H. Itoh, A. Kawasuso, T. Ohshima, M. Tashikawa, I. Nashiyama, S. Tanigawa, S. Misawa, H. Okumura, S. Yoshida: Phys. Stat. Sol. (a) **162**, 173 (1997)
15. H. Itoh, N. Hayakawa, I. Nashiyama, E. Sakuma: J. Appl. Phys. **66**, 4529 (1989)
16. H. Itoh, M. Yoshikawa, I. Nashiyama, S. Misawa, H. Okumura, S. Yoshida: Inst. Phys. Conf. Ser. **137**, 255 (1993)
17. A. Kawasuso, H. Itoh, N. Morishita, M. Yoshikawa, T. Ohshima, I. Nashiyama, S. Okada, H. Okumura, S. Yoshida: Appl. Phys. A **67**, 209 (1998)
18. A. Kawasuso et al.: submitted to Phys. Rev. B
19. A. Kawasuso, F. Redmann, R. Krause-Rehberg, M. Yoshikawa, K. Kojima, H. Itoh: Phys. Stat. Sol. (b) **223**, R8–10 (2001)
20. H. Itoh, M. Yoshikawa, L. Wei, S. Tanigawa, I. Nashiyama, S. Misawa, H. Okumura, S. Yoshida: Mat. Res. Soc. Symp. Proc. **262**, 331 (1992)
21. A. Zywiets, J. Furthmüller, F. Bechstedt: Phys. Rev. B **61**, 13655 (2000)
22. A. Zywiets, J. Furthmüller, F. Bechstedt: Phys. Rev. B **59**, 15166 (1999)
23. L. Torpo, R.M. Nieminen, K.E. Laasonen, S. Pöykkö: Appl. Phys. Lett. **74**, 221 (1999)
24. L. Torpo, M. Marlo, T.E.M. Staab, R.M. Nieminen: J. Phys. Condens Matter **13**, 6203 (2001)
25. A. Mattausch, M. Bockstedte, O. Pankratov: Mater. Sci. For. **353–356**, 323 (2001)
26. L.A. de S. Balona, J.H.N. Loubser: J. Phys. C **3**, 2344 (1970)
27. M. Bockstedte, O. Pankratov: Mater. Sci. For. **338–342**, 949 (2000)
28. E. Rauls, T. Linger, Z. Hajnal, S. Greulich-Weber, T. Frauenheim, J.M. Spaeth: Phys. Stat. Sol. (b) **217**, R1 (2000)
29. T. Linger, S. Greulich-Weber, J.M. Spaeth, U. Gerstmann, E. Rauls, H. Overhof: Physica, B **308–310**, 625 (2001)
30. M.J. Puska, C. Corbel: Phys. Rev. B **38**, 9874 (1988)
31. H. Itoh, M. Yoshikawa, I. Nashiyama, H. Okumura, S. Misawa, S. Yoshida: J. Appl. Phys. **77**, 837 (1995)
32. D.S. Billington, J.H. Crawford, Jr.: *Radiation Damage in Solids* (Princeton University Press, Princeton, NJ, 1961)
33. R. Devanathan, W.J. Weber and F. Gao: J. Appl. Phys. **90**, 2303 (2001)
34. R. Devanathan, W.J. Weber: J. Nucl. Mater. **278**, 258 (2000)
35. A.L. Barry, B. Lehmann, D. Fritsch, D. Bräung: IEEE Trans. Nucl. Sci. **30**, 1111 (1991)
36. A. Kawasuso, H. Itoh, N. Morishita, M. Yoshikawa, T. Ohshima, I. Nashiyama, S. Okada, H. Okumura, S. Yoshida: Appl. Phys. A **67**, 209 (1998)
37. A. Kawasuso, H. Itoh, D. Cha, S. Okada: Mater. Sci. For. **264–268**, 611 (1998)
38. A.I. Girka, V.A. Kuleshin, A.D. Mokrushin, E.N. Mokhov, S.V. Svirida, A.V. Shishkin: Sov. Phys. Semicond. **23**, 1337 (1989)

39. D. Dannefaer: Appl. Phys. A **61**, 59 (1995)
40. Y. Bodakov, E.N. Mokhov: Inst. Phys. Conf. Ser. **137**, 197(1993)
41. D. Cha, H. Itoh, N. Morishita, A. Kawasuso, T. Ohshima, Y. Watanabe, J. Ko, K. Lee, I. Nashiyama: Mater. Sci. For. **2640–268**, 615 (1998)
42. N.T. Son, P.N. Hai, E. Janzen: Phys. Rev. B **63**, 20120 (2001)
43. A.A. Rempel, K. Blaurock, K.J. Reichle, W. Sprengel, H.E. Schaefer: Mater. Sci. For. **389–393**, 485 (2002)
44. S. Arpiainen, K. Saarinen, P. Hautojärvi: Phys. Rev. B **66**, 75206 (2002)
45. C.C. Ling, C.D. Beling, S. Fung: Phys. Rev. B **62**, 8016 (2000)
46. M. Bockstedte, M. Heid, A. Mattausch, O. Pankratov: Mater. Sci. For. **389–393**, 471 (2002)
47. A. Kawasuso, F. Redmann, R. Krause-Rehberg, T. Frank, M. Weidner, G. Pensl, P. Sperr, H. Itoh: J. Appl. Phys. **90**, 3377 (2001)
48. A. Kawasuso, F. Redmann, R. Krause-Rehberg, M. Weidner, T. Frank, G. Pensl, P. Sperr, W. Triftshäuser, H. Itoh: Appl. Phys. Lett. **79**, 3950 (2001)
49. A. Kawasuso, M. Weidner, F. Redmann, T. Frank, R. Krause-Rehberg, G. Pensl, P. Sperr, W. Triftshäuser, H. Itoh: Mater. Sci. For. **389–393**, 489 (2002)
50. A. Kawasuso, M. Weidner, F. Redmann, T. Frank, P. Sperr, R. Krause-Rehberg, W. Triftshäuser, G. Pensl: Physica B **308–310** (2001)
51. A. van Veen, H. Schut, M. Clement, J.M.M. de Nijs, A. Kruseman, M.R. Ijpma: Appl. Surf. Sci. **85**, 216 (1995)
52. E. Rauls, T.E.M. Staab, Z. Hajnal, Th. Frauenheim: Physica B **308–310**, 645 (2001)
53. A. Kawasuso, M. Yoshikawa, M. Maekawa, H. Itoh, T. Chiba, F. Redmann, R. Krause-Rehberg, M. Weidner, T. Frank, G. Pensl: Mater. Sci. For., to be published
54. C. Hemmingsson, N.T. Son, O. Kordina, E. Janzén, J.L. Lindström: J. Appl. Phys. **84**, 704 (1998)
55. M. Gong, S. Fung, C.D. Beling, Z. You: J. Appl. Phys. **85**, 7604 (1999)
56. M.O. Aboelfotoh, J.P. Doyle: Phys. Rev. B **59**, 10823 (1999)
57. V.S. Ballandovich: Sov. Phys. Semicond. **33**, 1188 (1999)
58. V.S. Ballandovich, G.N. Violina: Cryst. Latt. Def. and Amorph. Mat. **13**, 189 (1987)
59. M. Gong, S. Fung, C.D. Beling, Z. You: J. Appl. Phys. **85**, 7120 (1999)
60. H. Zhang, G. Pensl, A. Dörnen, S. Leibenzeder: Electrochem. Soc. Ext. Abstracts **89-2**, 699 (1989)
61. H. Zhang, G. Pensl, P. Glasow, S. Leibenzeder: Electrochem. Soc. Ext. Abstracts **89-2**, 714 (1989)
62. G.C. Ryblik: J. Appl. Phys. **78**, 2996 (1995)
63. A.A. Lebedev, A.I. Veinger, D.V. Davydov, V.V. Kozlovski, N.S. Savkina, A.M. Strel'chuk: J. Appl. Phys. **88**, 6265 (2000)
64. J.P. Doyle, M.O. Aboelfotoh, M.K. Linnarsson, B.G. Svensson, A. Schoner, N. Nordell, C. Harris, J.L. Lindstrom, E. Janzen, C. Hemmingsson: Mat. Res. Soc. Symp. Proc. **423**, 519 (1996)
65. T. Dalibor, C. Peppermüller, G. Pensl, S. Sridhara, R.P. Devaty, W.J. Choyke, A. Itoh, T. Kimoto, H. Matsunami: Inst. Phys. Conf. Ser. **142**, 517 (1996)
66. T. Dalibor, G. Pensl, H. Matsunami, T. Kimoto, W.J. Choyke, A. Schöner, N. Nordell: Phys. Stat. Sol. (a) **162**, 199 (1997)

67. T. Dalibor, G. Pensl, T. Kimoto, H. Matsunami, S. Sridhara, R.P. Devaty, W.J. Choyke: *Diamond and Related Materials*, **6**, 1333 (1997)
68. C. Hemmingsson, N.T. Son, O. Kordina, J.P. Bergman, E. Janzen, J.L. Lindström, S. Savage, N. Nordell: *J. Appl. Phys.* **81**, 6155 (1997)
69. L. Storasta, F.H. Carlsson, S.G. Sridhara, J.P. Bergman, A. Henry, T. Egilsson, A. Hallén, E. Janzen: *Appl. Phys. Lett.* **78**, 46 (2001)
70. L. Storasta, F.H. Carlsson, S.G. Sridhara, D. Åberg, J.P. Bergman, A. Hallén, E. Janzén: *Mater. Sci. For.* **353–356**, 431 (2001)
71. V. Nagesh, J.W. Farmer, R.F. Davis, H.S. Kong: *Radiat. Effects and Defects in Solids* **112**, 77 (1990)
72. G. Pensl and W.J. Choyke: *Physica B* **185**, 264 (1993)
73. T. Frank, G. Pensl, S. Bai, R.P. Devaty, W.J. Choyke: *Mater. Sci. For.* **338–342**, 753 (2000)
74. C. Hemmingsson, N.T. Son, E. Janzén: *Appl. Phys. Lett.* **74**, 839 (1999)
75. C. Hemmingsson, N.T. Son, A. Ellison, J. Zhang, E. Janzén: *Phys. Rev. B* **58**, R10119 (1998)
76. C. Hemmingsson, N.T. Son, O. Kordina, J.L. Lindström, A. Ellison, J. Zhang, E. Janzén: *Semicond. Sci. Technol.* **14**, 251 (1999)
77. M. Weidner, T. Frank, G. Pensl, A. Kawasuso, H. Itoh, R. Krause-Rehberg: *Physica B* **308–310**, 633 (2001)
78. T. Kimoto, S. Nakazawa, K. Hashimoto, H. Matsunami: *Appl. Phys. Lett.* **79**, 2761 (2001)
79. K. Fujihira, T. Kimoto, H. Matsunami: *Appl. Phys. Lett.* **80**, 1586 (2002)
80. T. Kimoto, S. Nakazawa, K. Fujihira, T. Hirao, S. Nakamura, Y. Chen, K. Hashimoto, H. Matsunami: *Mater. Sci. For.* **389–393**, 165 (2002)
81. I. Pintille, L. Pintille, K. Irscher, B. Thomas: *Appl. Phys. Lett.* **81**, 4841 (2002)
82. H.J. von Bardeleben, J.L. Cantin, I. Vickridge, G. Battistig: *Phys. Rev. B* **62**, 10123 (2000)
83. M. Okada, K. Atobe, M. Nakagawa, S. Kanazawa, I. Kanno, I. Kimura: *Nucl. Inst. Meth. Phys. Res. B* **166–167**, 399 (2000)
84. L. Patrick and W.J. Choyke: *Phys. Rev. B* **5**, 3253 (1972)
85. W.J. Choyke: *Inst. Phys. Conf. Ser.* **31**, 58 (1977)
86. F.H.C. Carlsson, L. Storasta, B. Magnusson, J.P. Bergman, K. Sköld, E. Janzén: *Mater. Sci. For.* **353–356**, 555 (2001)

# Characterization of Defects in SiC Crystals by Raman Scattering

S. Nakashima and H. Harima

## 1 Introduction

Crystallinity of wide band-gap semiconductors such as SiC and GaN has recently been improved by reducing their defects drastically. However, these materials have lower qualities than standard Si and GaAs wafers in the sense that various defects such as micropipes, plate-like defects, stacking faults, small-angle grain boundaries, dislocations, etc., are still contained. The microstructure of these defects has been studied by various techniques using electron-, ion- and light beams, which have respective advantages and disadvantages. Since visible light penetrates deep into wide-gap semiconductors, optical spectroscopy is a promising contactless characterization technique for these bulk crystals. Among various optical characterization techniques on SiC, Raman scattering has the advantage that it can provide information on both lattice structure and electronic properties of SiC [1].

Defects in solids have been widely examined by spectroscopic techniques in the visible and infrared regions. Localized vibrational modes (LVM) arising from impurities with masses lower than the host atoms have been measured by infrared absorption and Raman scattering [2], and information about the density and the site of impurities was obtained. Photoluminescence and optical absorption yield information on the band structure as well as electronic properties of defects and impurities, but structural information on the lattice is not directly obtained. Micro-Raman spectroscopy is a non-destructive method, and furthermore can provide information on both the lattice structure and the electronic properties in local areas of  $\mu\text{m}$ - or sub  $\mu\text{m}$ -scale. Raman spectroscopy has been applied to characterization of ion-implanted semiconductors in order to evaluate the amount of damage, the dose of implanted atoms, their electrical activity, and the recovery of the crystallinity during post annealing [3]–[5].

There are various kinds of defects in SiC crystals. Typical defects are stacking faults, inclusions of different polytypes, micro- (or nano-) pipes and hexagonal plate-like defects (voids). 3C-SiC is usually grown by heteroepitaxy on Si substrates. A high density of defects is generated in the vicinity of the interface between SiC and Si owing to a large lattice mismatch between these crystals. Major defects in this case are stacking faults, twin boundaries, anti-

phase boundaries, grain boundaries and dislocations. It is anticipated that these defects influence the Raman spectrum.

Nanometer-scaled semiconductor crystallites and ion-implanted crystals show asymmetric Raman bands with a peak shifted to lower frequency with respect to the position of ideal single crystals and they are often accompanied by a low-frequency tail [6, 7]. This phenomenon has been treated by a spatial correlation model [6]–[8]. It is assumed in this model that the phonon modes in defective specimens are confined to a restricted region of size  $L$ . These confined phonons are described not by a simple plane wave but by a superposition of plane waves with various wave numbers  $q < \pi/L$ . This implies that phonons with wave vectors  $q < \pi/L$  take part in the Raman scattering process. Since the phonon dispersion is usually negative, i.e., the phonon frequency takes the maximum value at  $q = 0$  ( $\Gamma$  point), phonon bands in defective samples show peaks at frequencies lower than those at the  $\Gamma$  point and have asymmetric band shapes. Hence, in this treatment, the band shape depends on the phonon density of states and the size of the confined region.

Damage and strain at the surface of mechanically polished semiconductors have been observed by Raman scattering. Highly damaged surfaces show new Raman bands at critical points in the Brillouin zone at which the phonon density of states is high. The appearance of these new Raman bands is well known as disorder activated Raman scattering (DARS) [9, 10]. DARS has been observed in ion-implanted- and surface-lapped materials and in mixed crystals.

So far, highly damaged crystals have normally been measured at Raman-allowed geometries for phonon signals. However, intense signals of Raman-allowed bands often mask weak defect-induced signals. This difficulty was recently overcome by detecting those weak defect-induced signals using Raman-forbidden geometry [11].

This article provides an overview of recent Raman scattering studies for defects in SiC crystals. We also discuss Raman studies on electronic properties and their application to defect characterization. In Sect. 2, Raman scattering techniques for detecting defects are outlined. Section 3 focuses on the evaluation of defects in  $4H$ - and  $6H$ -polytypes. Section 4 describes recent experiments on defects in epitaxial  $3C$ -SiC films. Raman scattering studies related to impurities in SiC are discussed in Sect. 5. Section 6 is devoted to the discussion on the Raman analysis for electrical properties and its application to the influence of the defects on local electronic properties in SiC.

## 2 Detection of Defects by Raman Scattering

In this section we will describe the influence of defects on the Raman spectrum and explain how to detect defect-induced Raman signals. In single crystals only scattered light which obeys the following selection rules can contribute

to Raman scattering: (i) energy conservation;  $\hbar\omega_i = \hbar\omega_s + \hbar\Omega$ , (ii) wave-vector conservation;  $\mathbf{k}_i = \mathbf{k}_s + \mathbf{q}$ , and (iii) polarization selection rule. Here,  $(\omega_i, \mathbf{k}_i)$ , and  $(\omega_s, \mathbf{k}_s)$  are the frequency and the wave vector of incident and scattered light, respectively.  $\Omega$  and  $\mathbf{q}$  are the frequency and wave vector of the phonon, respectively. The second rule limits the wave vector of the phonons contributing to Raman scattering: When visible laser light is used, the wave vector of the phonon mode is limited to  $\mathbf{q} \cong 0$ , because the wave vectors of incident and scattered light are very small compared with those of phonons at the Brillouin zone edge. This is the reason why sharp Raman lines are observed for crystals, though there are a number of phonons with different frequencies in crystals. In ideal crystals the scattered light is usually polarized and its polarization direction is determined by the Raman tensor and the configurations of incident and scattered light relative to the crystal axes. Defects cause breakdown of the wave-vector selection rule, reduction of symmetry, and reduction of phonon lifetime. The Raman scattering is strikingly influenced by these effects. The breakdown of the selection rules provides appearance of new Raman bands, broadening and asymmetry of the Raman bands. The reduction of the phonon lifetime due to scattering at defects also results in broadening of the phonon Raman bands (lifetime broadening). In this case, however, we expect that Raman bands have a symmetric line shape in contrast to the broadening due to phonon confinement as discussed below. On the other hand, the reduction of the local crystal symmetry changes the polarization selection rule and allows observation of Raman bands at a Raman forbidden geometry. The breakdown of the wave-vector selection rule has been discussed for SiC crystals containing stacking faults [12]–[14].

The appearance of asymmetric Raman bands in nm-sized crystallites and ion-implanted semiconductors are interpreted in the framework of a spatial correlation model. The basic concept of that model is the relaxation of the wave vector selection rule. Raman bands found in highly damaged materials (DARS) also have the same origin.

So far, Raman spectra of disordered crystals have usually been observed with a Raman allowed geometry. However, the strong background signal of Raman-allowed bands often prevents detection of weak defect-induced signals. We have demonstrated that Raman measurements taken with a forbidden configuration are effective to detect a low density of defects [11]. Since in this configuration the background signal arising from allowed modes is very weak, defect-induced Raman bands can be measured with a good signal-to-noise ratio after long exposure with a CCD (charge coupled device) detector.

The folded modes observed in the Raman spectra of  $nH$ - and  $3nR$ -polytypes correspond to phonons with a wave vector of  $q = 2\pi m/(nc)$  in the basic Brillouin zone of the  $3C$ -polytype in the  $[111]$  direction, where  $n$  and  $m$  are integers ( $2m \leq n$ ) and  $c$  is the unit-cell length of the  $3C$ -polytype along the  $[111]$  direction. The Raman intensities of these folded modes in the transverse optical (FTO) and acoustic (FTA) branches can be

calculated on the basis of the bond polarizability concept [15, 16]. The  $E_1$ -type FTO (0) mode (folded transverse optical mode with a reduced wave vector of  $q = 2\pi m/(nc) = 0$ ; unfolded mode) in 4*H*- and 6*H*-SiC is forbidden in the back scattering configuration using the (0001) face. However, this mode appears in crystals containing stacking faults and its intensity increases with increasing stacking fault density [11]. The appearance of this stacking-fault-induced Raman band can be explained based on the bond Raman-polarizability model: The contributions of the bond Raman polarizabilities in one unit cell cancel out for this mode in a perfect crystal. The Raman intensity is given by the following equation:

$$I(\omega) = A \frac{n(\omega) + 1}{\omega} (\mathbf{e}_i \cdot \mathbf{R} \cdot \mathbf{e}_s)^2, \quad (1)$$

$$R_{xy} = \sum \alpha_{xy}(i) (v_i - u_i). \quad (2)$$

Here,  $\alpha_{xy}(i)$  is the bond Raman-polarizability component for the  $i$ th bond group between neighboring atomic planes of silicon and carbon atoms and  $v_i - u_i$  is the relative displacement of the relevant neighboring layers where  $v_i$  and  $u_i$  are used for Si- and C-planes, respectively. The summation is taken for the bond groups in a unit cell of periodic crystals and in a whole volume for disordered crystals. For back-scattering geometry using SiC (0001), (1) can be written in a more simple form. We will use a one dimensional force constant model with zincblende-structure approximation and bond Raman-polarizability concept, and neglect the environmental dependence of the force constant. In other words, the force constant and bond Raman-polarizability are considered to be the same for the hexagonal and cubic stackings. Under these assumptions, for the back scattering geometry using the (0001) face, (1) is reduced to the following simplified form

$$I(\omega) = A \frac{n(\omega) + 1}{\omega} \left[ \sum (\pm d) (v_i - u_i) \right]^2. \quad (3)$$

Here, the + sign is taken for positive bond sequences ( $A$ - $\beta$ ,  $B$ - $\gamma$  and  $C$ - $\alpha$  bond groups) and the - sign for negative bond sequences ( $A$ - $\gamma$ ,  $B$ - $\alpha$ , and  $C$ - $\beta$ , where  $A$ ,  $B$ , and  $C$  denote the positions of the silicon atoms, and  $\alpha$ ,  $\beta$  and  $\gamma$  denote those of the carbon atoms. For the mode with  $\mathbf{q} = 0$  (unfolded mode), the phase and amplitude of all silicon layers are the same and the same is true for all carbon layers, thus (3) is written as

$$I(\omega) = A \frac{n(\omega) + 1}{\omega} [v - u]^2 \left[ \sum (\pm d) \right]^2. \quad (4)$$

For the 4*H*- and 6*H*-SiC, the arrangement of the bond polarizabilities in the unit cell is expressed as [11]

$$\alpha(n) = (d, d, d, -d, -d, -d) \quad \text{for } 6H\text{-SiC} , \quad (5)$$

and

$$\alpha(n) = (d, d, -d, -d) \quad \text{for } 4H\text{-SiC} . \quad (6)$$

Since the numbers of positive and negative stacking sequences are the same both for  $4H$ - and  $6H$ -SiC,  $\sum(\pm d)$  becomes zero. This result is consistent with the group theory prediction that the FTO (0) mode in  $4H$ - and  $6H$ -SiC is of  $E_1$ -type and the Raman polarizability components  $\alpha'_{xy}$ ,  $\alpha'_{xx}$  and  $\alpha'_{yy}$  are zero. For crystals containing stacking faults, however, the numbers of the positive and negative stacking sequences are not the same. Therefore,  $\sum(\pm d)$  may have a finite value and as a result the Raman intensity does not vanish. This situation may occur for other modes as well. The FTO (4/6) mode in  $6H$ -SiC is Raman inactive in the backscattering geometry using the (0001) face. When the net Raman polarizability has a finite value because of incomplete cancellation of the bond Raman polarizabilities due to stacking faults as for the FTO (0) mode, the FTO (4/6) mode is also expected to be usable as a monitor of the stacking faults. In fact, this mode was observed in heavily disordered  $6H$ -SiC. However, since the FTO (4/6) mode lies on the tail of the strong FTO (2/6) mode, its observation is not easy for small densities of stacking faults.

The  $A_1$ -type LO mode is considered to be insensitive to stacking faults, because the bond Raman polarizabilities for the positive and negative sequences are the same and, as a result, the net Raman polarizability is almost independent of the stacking arrangement [15, 16]. However, as will be mentioned later, the LO-phonon-plasmon-coupled (LOPC) mode can be used for defect characterization, since it is sensitive to the electronic properties, which depends strongly on defects.

The appearance of the stacking-fault-induced FTO (0) bands in  $4H$ - and  $6H$ -SiC originates from the partial break down of the wave vector selection rule. The reduction of the local symmetry is not remarkable, because the rotational symmetry retains in these polytypes even in the presence of stacking faults. On the other hand, the reduction of the symmetry is important for  $3C$ -SiC. The stacking faults destroy the cubic symmetry, and the forbidden TO band is observed at the (100) face. The detection of the defect-induced bands is possible at a Raman forbidden configuration, when the polarization selection rule breaks down owing to the reduction of the symmetry. However, a careful treatment is necessary for polarization Raman measurements, since surface roughness and oblique incidence of the laser when using an objective lens with large numerical aperture often prevent accurate polarization measurements.

### 3 Detection of Stacking Faults in 4H- and 6H-SiC Using the (0001) Face

#### 3.1 General Description on Detection of Defects

One of the characteristic defects in SiC crystals is the stacking fault of the Si-C double atomic planes. The stacking faults are easily generated in SiC, because the difference in the formation energies of individual polytypes is small [17]. Stacking faults can be divided into three groups, (i) intrinsic and (ii) extrinsic stacking faults which accompany partial dislocations, and (iii) stacking faults without partial dislocations. Stacking faults of type (iii) may not be accompanied by the reduction of phonon lifetime. This fact is clearly seen in heavily disordered SiC crystals as shown in Fig. 5 of [1]. The stacking-fault-activated TA (transverse acoustic) phonon band drops sharply just above the frequency of the zone-edge phonon at  $265\text{ cm}^{-1}$ . This result indicates that the Raman spectral shape is mainly governed by the breakdown of the wave-vector selection rule. So far, Raman spectra of SiC crystals containing stacking faults were calculated for  $\alpha$ -type polytypes [13] and for the 3C-polytype [14, 18], and compared with experimental results.

In the following, we shall discuss the properties of phonons in SiC crystals containing stacking faults. SiC crystals with high and low densities of stacking fault were cut from 4H- and 6H-SiC ingots that were grown in the direction perpendicular or parallel to the  $c$ -axis. The stacking fault density was evaluated by etch-pit-density measurements. Figure 1 shows Raman spectra of FTO modes for these samples on a logarithmic intensity scale. The Raman

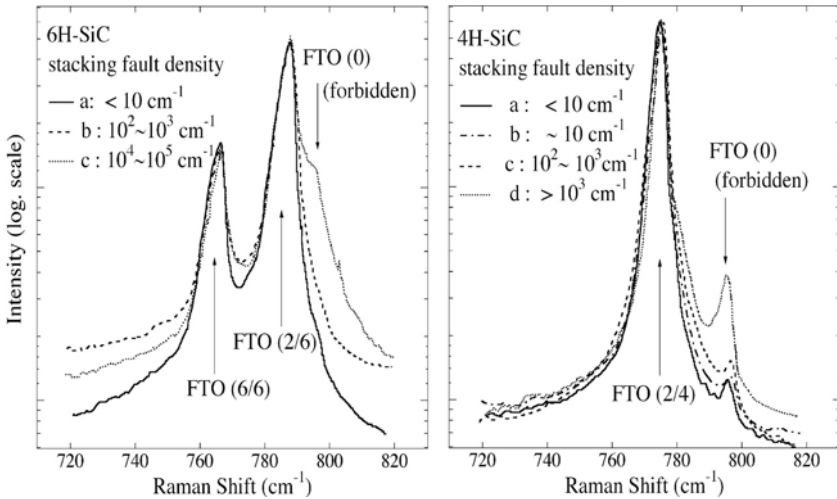


**Fig. 1.** Raman spectra of 4H-SiC (0001) crystals and 6H-SiC crystals with different stacking fault densities

spectra have been measured using the (0001) face at the back scattering geometry. A striking feature in the spectra is the growth of a Raman band at  $796\text{ cm}^{-1}$  at high densities of stacking fault in both  $4H$ - and  $6H$ -polytypes. This band corresponds to the unfolded TO, i.e., FTO (0) band. This band is an  $E_1$ -type mode and Raman-inactive in this geometry. The intensity of the FTO (0) band increases with increasing the stacking fault density, but the FTO (2/6) and FTO (6/6) bands in  $6H$ -SiC show no remarkable change for these stacking fault densities. A similar feature is also observed in  $4H$ -SiC where no remarkable change is observed for FTO (2/4). For  $6H$ -SiC the FTO (0) band is located closely to the FTO (2/6) mode at  $788\text{ cm}^{-1}$  and consequently overlap with the strong FTO (2/6) band. In  $4H$ -SiC, on the contrary, fine structures of the stacking fault activated FTO bands can be observed, since the FTO (0) mode is well separated from the FTO (2/4) mode. In samples containing a high density of stacking faults, the Raman bands are distorted and broadened. From the structure of the FTO bands, the microstructure of defective regions is inferred. As explained in Sect. 2, the forbidden FTO (0) modes are activated by stacking faults and the FTO (0) band can therefore be used as a monitor of stacking fault density.

In order to observe the FTO (0) mode which is sensitive to the stacking fault we have to use the back scattering geometry using the (0001) face of SiC crystals. When laser light is obliquely incident on the sample surface, a leakage signal of the  $E_1$ -Raman band masks the stacking fault-induced FTO (0) mode. In fact, when we used an objective lens with a large numerical aperture in the Raman micro-scope, a Raman band was distinctly observed at  $796\text{ cm}^{-1}$ , independent of the presence of stacking fault. We also mention here that the use of off-axis surfaces induces a finite  $E_1$ -type FTO (0) signal even when almost exact back scattering geometry is used. Special care is necessary to distinguish between stacking-fault-induced band and such leakage signals. For the back scattering geometry using the  $a$ -face,  $x(y,z)$ - $x$ , the FTO (0) band is strongly observed, because this mode is Raman allowed. The presence of this strong band generally prevents the detection of weak stacking-fault-induced bands.

### 3.2 Case Studies of Defects in $4H$ -SiC

Defects strongly influence the structural and electronic properties in crystals. Raman measurements of longitudinal and transverse modes in SiC crystals provide information on both properties in these crystals.

In the following, we report on a study of defective regions with a size larger than  $1\text{ }\mu\text{m}$  that were selected by taking optical microscope photographs. At such locations forbidden FTO and allowed LO phonon plasmon coupled (LOPC) modes were measured. The samples used were  $n$ -type  $4H$ -SiC wafers with the (0001) face grown by a physical vapor transport method having doping levels of  $2 \sim 7 \times 10^{18}\text{ cm}^{-3}$ . Raman spectra were measured in a back scattering geometry using a Raman microscope.

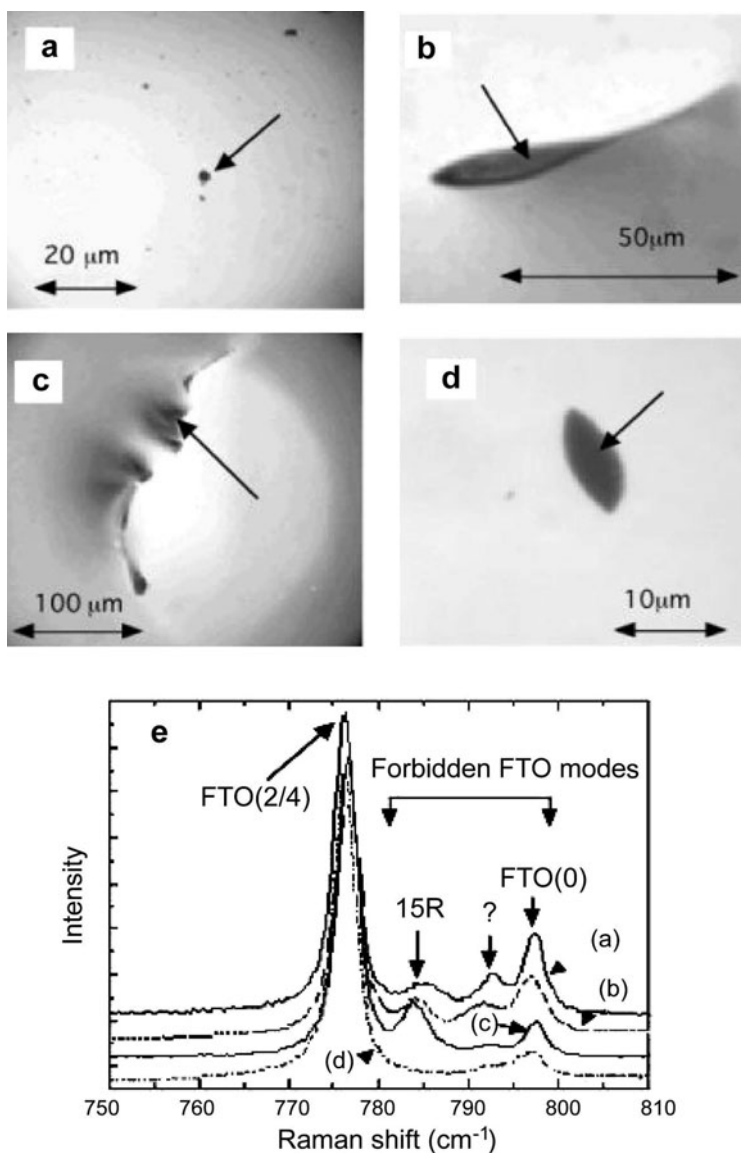


**Fig. 2.** Optical microphotograph of defects in 4H-SiC wafers showing: (a) round pit, (b) arc-shaped defect, (c) cluster of defects and (d) cusp defect. Raman spectra were measured at the *arrowed points*. (e) shows the spectra observed by the geometry in which FTO (0) is forbidden. The spectra (a–d) correspond to the positions in photographs (a–d)

Figures 2a–d show optical microphotographs of typical defective regions, and Fig. 2e shows the corresponding Raman spectra taken at the locations marked by the arrows. In the back scattering geometry using the (0001) face, only the FTO (2/4) mode is Raman active, whereas the FTO (4/4) and the FTO (0) modes are forbidden in ideal crystals. The forbidden FTO (0) mode is, however, often observed in the defective regions as mentioned above. Mostly, the observed forbidden FTO (0) bands have asymmetric line shapes and a low frequency tail as can be seen in spectrum (d) in Fig. 2e. Some of the spectra reveal new bands. The band at  $784\text{ cm}^{-1}$  of the spectra (a) and (c) corresponds to FTO (2/5) of the  $15R$  polytype and a band at  $792\text{ cm}^{-1}$  may originate from the FTO (2/8) band of a stacking sequence corresponding to the  $8H$ -polytype. The complicated spectral profiles indicate that some defective regions contain high densities of stacking faults and that the samples contain a mixture of hetero-polytype domains. Spectra that we assign to hetero-polytype domains are often observed in arc-shaped and elongated-stripe defects, which may be associated with grain boundaries. The spectrum (a) taken at the round pit suggests the presence of hetero-polytype domains. In many cases, however, small round pits have asymmetric FTO (0) bands that we ascribe to stacking faults. This asymmetry is related to a low frequency tail and usually there is no broadening towards the high frequency side as mentioned above. Furthermore, no noticeable change in the shape of the FTO (2/4) band was observed except when there were heavily disordered stacking sequences. Most of elongated stripe defects as in Fig. 2b seem to contain stacking faults as judged from the Raman spectrum. The same is true for the defect shown in Fig. 2d (see the asymmetric FTO (0) band, indicating the presence of stacking fault).

It should be noted that broadening of the FTO (0) band is also observed in the regions where the stacking fault density is high. There may be imperfections other than stacking faults that reduce the phonon lifetime. From the analysis of the Raman spectral profiles at the defective regions we conclude that stacking faults are involved with high probability in the extended defects.

## 4 Characterization of 3C-SiC Epitaxial Films on Si

### 4.1 Stacking Faults in Epitaxial 3C-SiC Layer

3C-SiC crystals are usually grown on Si substrates. Such heteroepitaxial films contain stacking faults, anti-phase boundaries and twin boundaries, etc., in the vicinity of the interface. These defects are often generated owing to the large lattice mismatch between Si and SiC. Raman scattering has been used for 3C-SiC to characterize these defects, especially stacking faults [19].

Figure 3 shows a Raman spectrum of a  $10\text{ }\mu\text{m}$ -thick epitaxial 3C-SiC film on a Si (001) substrate. Although the TO mode is forbidden in back

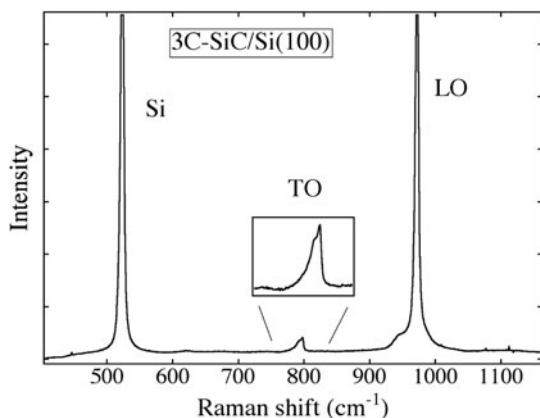


**Fig. 3.** Raman spectra of a 3C-SiC film on Si (100) with a thickness of 10  $\mu\text{m}$

scattering from the (001) face, a weak TO mode appears with intensity of only a few percent of the LO band intensity. Moreover, it was found that the intensity of the TO mode varied with the growth condition.

Using the (100) cross section of these heteroepitaxial films, we observed micro-Raman spectra at the interface region, middle region and outer surface region. The TO band as measured on the (100) face is compared with Raman bands observed for the (110) face. Since for the (110) face the TO band is Raman-allowed, it is intense, narrow and symmetric. On the contrary, the

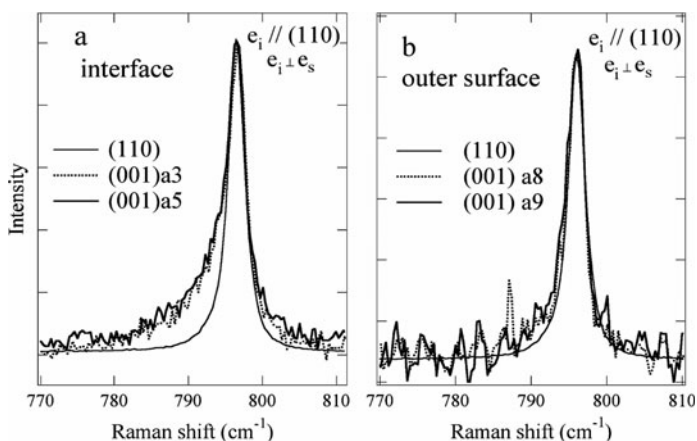


**Fig. 4.** Raman spectra of 3C-SiC film with a thickness of 79  $\mu\text{m}$  grown on (001) Si substrate which was removed by etching: (a) Raman spectra observed at the interface side, and (b) observed at the outer surface side. Raman spectra observed at the (110) cross section are shown for comparison. The TO bands are normalized by the peak height

forbidden TO band found at most places in the interface region is asymmetric and has a tail at the low frequency side. The same situation occurs when we observe the TO band using the (001) surface. As shown in Fig. 4a, an asymmetric TO band having a low frequency tail is observed at the interface side, while at the outer surface, the forbidden TO band is very weak and almost symmetric as shown in Fig. 4b. The asymmetry and the broadening of the TO band are indicative of the presence of stacking faults [3, 4] or other defects such as anti-phase boundaries and dislocations. In addition to the asymmetry observed in Fig. 4, we sometimes find a symmetric broadening of the forbidden TO band at some places. We ascribe this effect to reduction of the phonon lifetime due to the high density of defects.

## 4.2 Defects in Heteroepitaxial Films

In order to confirm that the observed forbidden TO band is defect-activated, Raman bands have been examined for various positions in several heteroepitaxial films using back scattering geometry. The films investigated were  $2.5 \sim 5 \mu\text{m}$  thick 3C-SiC films on Si with the (001) surface orientation. The intensity and the band width of the forbidden TO band vary with the position in each specimen, and we study in the following the correlation between intensity and line width.

In Fig. 5 the width (FWHM) of the forbidden TO band is plotted against the intensity. As a general trend the band width increases linearly with increasing the intensity, although the gradient is different for different samples. This result gives evidence for the fact that the forbidden TO band in the heteroepitaxial films is related to defects. We have also plotted the ratio of the widths at the low frequency side ( $\Delta W_-$ ) and at the high frequency

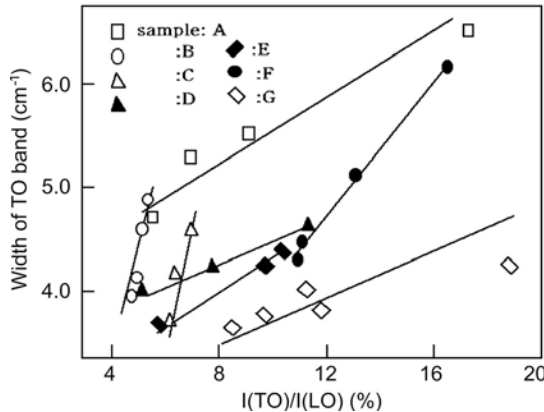


**Fig. 5.** Width of the forbidden TO band in 3C-SiC/Si plotted against the TO band intensity. The TO intensity is normalized to the LO phonon intensity. The measurements are made at various points for each specimen

side ( $\Delta W_+$ ) as a function of the intensity of the forbidden band. These data scatter and we can not observe correlations between the bandwidth ratio ( $\Delta W_-/\Delta W_+$ ) and the intensity of the forbidden band. This result suggests that the forbidden Raman band is not mainly dominated by stacking fault and that there are various other defects in the interface region of the films investigated.

### 4.3 Defects in 3C-SiC Homoepitaxial Films

We have recently observed Raman images of (100) cross sections of homoepitaxial SiC films [17]. These films ( $\sim 100\text{ }\mu\text{m}$  thick) were prepared by epitaxial growth of a 3C-SiC film on a  $100\text{ }\mu\text{m}$ -thick (001) SiC film which was heteroepitaxially grown on Si (001). The original interface between SiC and Si was used as a growth surface of the homoepitaxial film. Therefore, it is anticipated that defects are concentrated in the central region of the cross section. Again, the forbidden TO band of the sample was measured on the cross section with the (100) face cut from the epitaxial film. We found that the forbidden TO band is broad compared with the allowed Raman band of the (110) face, and the characteristic tail on the low frequency side was also observed at the central region. The asymmetry and broadening of the TO band are indicative of the presence of stacking faults [3, 4].

### 4.4 Elimination of the Phonon Polariton Mode

Some caution is necessary when we measure a defect-activated TO band in thin 3C-SiC films. Since the reflectivity of SiC is relatively high, reflected light from the reverse face of thin films and scattered light form a forward scattering geometry. The scattered light in the forward geometry for the incoming light can also be reflected at the reverse surface and is consequently recorded together with the conventional back scattering signals. Accordingly, the phonon polariton mode that is normally seen in the forward scattering only can be observed for thin films even in the back-scattering geometry. Because the polariton band lies below the TO band frequency and it is Raman active when using the (001) face, this band can mask the low frequency tail of the defect-induced forbidden Raman band. However, the polariton mode is Raman forbidden at the cross polarization geometry ( $\mathbf{e}_i \perp \mathbf{e}_s$ ,  $\mathbf{e}_i // \langle 110 \rangle$ ). Hence, using this geometry, we can eliminate the effect of the polariton.

### 4.5 Raman Intensity Profiles of SiC with Stacking Disorder

SiC crystals grown by the Acheson method often contain stacking disorder and their Raman spectra show broad and distorted bands. The Raman spectral profiles in disordered SiC crystals have been studied for  $\alpha$ -SiC [13] and 3C-SiC [14, 18]. Under the assumption of one-dimensional stacking disorder

and using the bond polarizability concept, the Raman intensity profiles have been simulated. The results of such a simulation have shown that the Raman forbidden modes appear when stacking faults exist and that the distribution of stacking faults is not completely random. The observation of various disordered SiC crystals indicated that the short-range order of the stacking sequence remains for  $\alpha$ -SiC [13]. On the other hand, Raman spectral profiles for ensembles of small grains were calculated based on the correlation model. The basic concept of this model is the relaxation of the wave-vector selection rule, which is identical to that of the calculation using the bond Raman polarization model. However, for the intensity calculation, the correlation model uses a weighting function presenting the contribution of the modes with different  $q$ -wave vectors instead of the bond polarizabilities. Hence, the bond polarizability model is suitable to treat stacking fault for which atomic layer arrangements are not completely random.

The influence of stacking faults on Raman spectra of 3C-SiC has been examined by Rohmfeld et al. [14, 18]. They calculated spectral profiles using an average distance between stacking faults,  $\Delta L$ , as a parameter. Their result showed that the TO band can extend over the entire TO branch of 3C-SiC for  $\Delta L = 7.5$  Å. The Raman spectra of as-deposited and laser-annealed 3C-SiC films have been studied by these authors by comparing observed and simulated spectra using the stacking fault model based on the bond Raman polarizability concept and the phonon confinement model [6, 7]. They concluded that the stacking fault model is more successful to account for the spectral profiles [18].

## 5 Raman Scattering Related to Damages and Impurities

Ion implantation produces high densities of defects in materials. The damaged layers in various semiconductors have been characterized by Raman spectroscopy [3, 20, 21]. Intensity and shape of the phonon Raman bands provide information on crystallinity of as-implanted and post-annealed layers. The existence of an amorphous phase has also been examined. The recovery of crystallinity by annealing has been examined as a function of the annealing temperature and also substrate temperature on hot implantation. The depth distribution of the damage has been studied by means of a confocal microscope and cross section measurement under a microscope. It was reported that a polytype conversion occurs by the annealing of implanted SiC. Micro-Raman measurements will be a useful tool for such polytype conversion. When we use visible lasers for excitation, the penetration depth of the laser light in post-annealed SiC layers often exceeds the thickness of the implanted layers. This prevents the quantitative analysis of the recovery of the crystallinity. It is desirable for the Raman measurement to use deep ul-

traviolet laser light with a penetration depth comparable to the projection range of the ion implantation.

Little work has been made on Raman scattering of impurities in SiC. Local vibrational modes were observed only for hydrogen in SiC [3]. For *6H*- and *15R*-SiC a weak Raman band was observed [22] at  $\sim 635\text{ cm}^{-1}$ . The origin of this band is unknown. A possibility might be that this band is a local vibrational mode (LVM) of nitrogen substituted on a Si site.

Nitrogen is a shallow donor in SiC. The ground state of the donors is split into a low-lying  $1s(A)$  and higher  $1s(E)$  levels by valley-orbit mechanism [22]. The electronic transitions between the ground state and excited states in *3C*, *4H* and *6H* polytypes have been observed by infrared absorption [23]–[25]. More recently the excited states of the nitrogen donor have been more accurately determined by photo-thermal ionization spectroscopy [26]. With Raman scattering the electronic transitions between  $1s(A)$ – $1s(E)$  have been observed for *4H*, *6H* and *15R* polytypes so far [22]. There are several nonequivalent configurations of N atoms on a C site, though the number of electronic Raman bands does not coincide with the reported number of the nonequivalent lattice sites.

## 6 Influence of Defects and Impurities on the Local Electronic Properties

It was shown in a recent review article [1] that Raman scattering is a powerful method to analyze local electronic properties by the LO-phonon-plasmon-coupled (LOPC) mode profiles. The carrier density and mobility can be determined from the analysis of the LOPC-mode profiles. Although this method was successfully applied to many specimens, we sometimes observe a systematic discrepancy in the carrier mobility between electrical measurements (Hall effect) and Raman characterizations, which was serious in heavily doped samples. Recently, a new approach to overcome this problem has been developed. The first part of this section describes this topic. In the second part, some recent case studies on electronic properties in the vicinity of defects in SiC are described.

### 6.1 Characterization of Electronic Properties by Raman Analysis

In polar semiconductors, the collective excitation of free carriers (plasmon) couples with the longitudinal optic (LO) phonon via the macroscopic electric field and forms the LOPC mode [27]. This mode generally consists of two branches, the upper and lower frequency branch (denoted as  $L^+$  and  $L^-$ , respectively), and the profile changes sensitively with the free carrier density and the carrier damping. Using this property, we can evaluate the carrier

density and the mobility by analyzing the LOPC mode profiles. Furthermore, when Raman microprobe is used,  $\mu\text{m}$ -order spatial resolution is easily attainable. Thus, Raman scattering is a powerful tool for non-destructive characterization of electric properties in device structures.

Various SiC samples have been examined by this method, such as 3C-SiC [28], 4H- and 6H-SiC [29]–[34]. SiC usually shows only the  $L^+$  mode, since the plasmon is over-damped. In this case, the profile is theoretically determined by two dominant contributions due to the deformation potential and electro-optic mechanisms [27]. The LOPC mode profile is then described as [35]

$$I(\omega) = A(\omega) \text{Im} \left[ -\frac{1}{\varepsilon(\omega)} \right]. \quad (7)$$

Here,  $\varepsilon(\omega)$  is a classical dielectric function with a damped harmonic oscillator for phonons combined with a Drude term for free carriers,

$$\varepsilon(\omega) = \varepsilon_\infty \left[ 1 + \frac{\omega_L^2 - \omega_T^2}{\omega_T^2 - \omega^2 - i\omega\Gamma} - \frac{\omega_P^2}{\omega(\omega + i\gamma)} \right]. \quad (8)$$

Here,  $\varepsilon_\infty$  is the optical dielectric constant,  $\omega_T(\omega_L)$  is the uncoupled TO (LO) phonon frequency,  $\omega_P$  is the plasmon frequency, and  $\gamma$  and  $\Gamma$  are the damping rates of carriers and phonon, respectively. The plasmon frequency is given by

$$\omega_P = \sqrt{\frac{4\pi n e^2}{\varepsilon_\infty m^*}}, \quad (9)$$

where  $e$ ,  $n$  and  $m^*$  are the unit charge, carrier density, and the effective mass of the electrons (here electron plasma is assumed). The carrier mobility is deduced using the following equation,

$$\mu = \frac{e}{m^* \gamma}. \quad (10)$$

The factor  $A(\omega)$  in (7) is written explicitly elsewhere [1, 28].

In previous papers [28],[30]–[35], the spectral analysis of LOPC modes in SiC was conducted by fitting the observed profiles to (7) using  $n$ ,  $\Gamma$  and  $\gamma$  as adjustable parameters. Since  $\mu$  was determined by  $\gamma$ , the resistivity  $\rho = 1/ne\mu$  was evaluated from the best fit parameters of  $n$  and  $\gamma$ .

In (8), the dielectric function  $\varepsilon(\omega)$  includes only the TO-phonon damping  $\Gamma$ . In a new approach,  $\varepsilon(\omega)$  includes also the damping of LO phonon. This dielectric function  $\varepsilon_M(\omega)$  is then given by

$$\frac{\varepsilon_M(\omega)}{\varepsilon_\infty} = \frac{\omega_L^2 - \omega^2 - i\Gamma_L\omega}{\omega_T^2 - \omega^2 - i\Gamma_T\omega} - \frac{\omega_P^2}{\omega(\omega + i\gamma_P)}, \quad (11)$$

where  $\Gamma_L$  is the damping of the LO phonon. Hereafter, we will call this equation modified classical dielectric function (m-CDF). This form of the

dielectric function was used for the analysis of infrared reflection spectra [36]–[38] and Raman spectra [39, 40]. Equation (11) reduces to (8) when  $\Gamma_L = \Gamma_T$ .

We have carried out the line shape analysis of the LOPC modes in 4H-SiC crystals with various carrier concentrations. The two models provide almost the same line shapes that are in excellent agreement with the observed spectrum, while the two models give different values for  $\gamma$ . The best-fit value of  $\gamma$  for the m-CDF is mostly smaller than that of the CDF model. For highly doped specimens, the fit to experimental spectra is better for the m-CDF than for the CDF.

## 6.2 Changes in Electrical Properties by Defects

### 6.2.1 Electronic Properties of Macro-Defects

It is well known that defects strongly influence the electrical properties in semiconductors. We have studied local electric properties in SiC containing defects by Raman scattering. Raman microprobe allows us to determine carrier density and mobility in defective regions in a contact-less manner. For this purpose Raman spectra of the LOPC mode were measured with a Raman-allowed geometry and defective regions were chosen by observing optical microphotographs.

Micro-Raman spectra have been measured for *n*-type 4H-SiC crystals that include defects. Figure 6a shows the optical micrograph of an *n*-type 4H-SiC wafer grown by a physical vapor transport (PVT) method, which has an arc shaped defect as shown in this figure. This defect is considered to be a grain boundary. Typical examples for the FTO bands observed at the back scattering geometry using the (0001) face are shown in Fig. 6b. The intensity of the FTO (0) band varies with position and the enhancement of its intensity is observed at around points G1 and G2. The intensity of the FTO (0) band at the defect free point G4 is weak. At the position G3, the FTO (0) band is weak and the FTO spectrum resembles that in the defect free region G4. The FTO band at G2 has a structure, indicating that there is a mixture of 8H and 6H domains and that there are high densities of stacking faults.

The Raman spectra of the LO-phonon-plasmon-coupled (LOPC) mode measured at these four different points (G1–G4) are shown in Fig. 6c. The local carrier density and mobility in these regions are determined from the line shape fitting of the LOPC mode using the m-CDF. The determined carrier density and mobility are depicted in Fig. 6c. The carrier density in the defective regions (e.g., G1 and G2) is in most cases lower than that of the defect free region. The carrier density at the defects shows the tendency to decrease as the intensity of the stacking-fault-induced FTO band increases. The reduction of the free carrier density at G1 and G2 may indicate that the free carriers are captured to deep traps associated with stacking faults. A

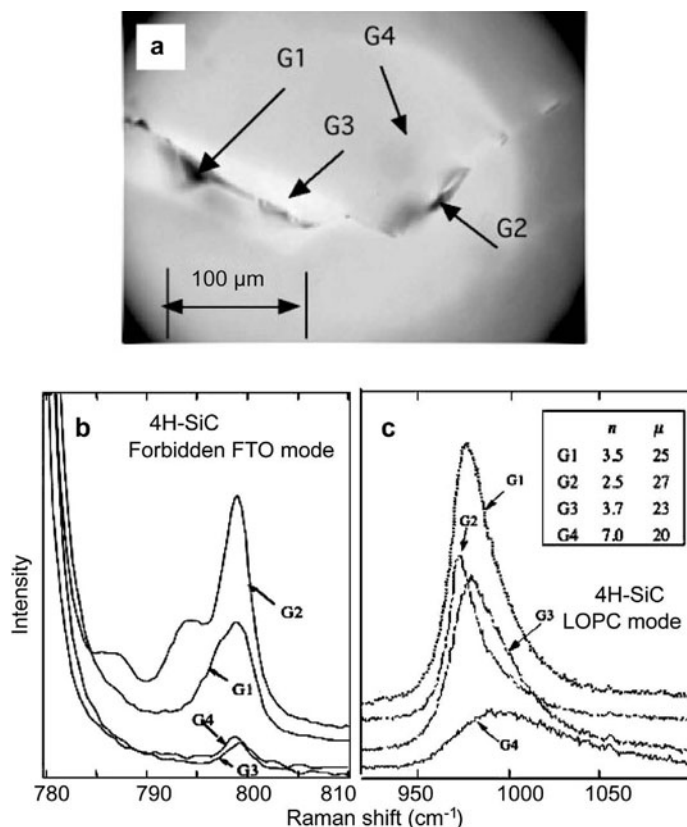


**Fig. 6.** (a) Optical microphotograph of defects in a 4H-SiC wafer with carrier concentrations of  $3 - 8 \times 10^{18} \text{ cm}^{-3}$ , (b) Raman spectra of FTO bands, and (c) LOPC mode profiles at the positions G1–G4 are depicted with the carrier concentration  $n$  ( $\times 10^{18} \text{ cm}^{-3}$ ) and mobility  $\mu$  ( $\text{cm}^2/\text{Vs}$ )

possible explanation is that partial dislocations associated with the stacking faults act as trapping centers [41].

The carrier density at G3 is lower than that of the defect free region (G4), though G3 is located in the defect-less region. The decrease of the carrier density at G3 may be due to facet growth after plate-like defects (voids) at a source side of the ingot. For heavily doped SiC wafers one often observes inhomogeneous carrier distributions. The carrier density in some cases is found to be reduced in relatively wide regions over a few hundred  $\mu\text{m}$ , even though these regions are defect less. Those regions have light color like a region around G3. The reduction of the carrier density is considered to be due to facet growth: It is known that the dopant incorporation efficiency is different for different growth facets. Surface directions of the plate-like defects are not always parallel to the (0001) face. Accordingly, when the facet growth

occurs behind the plate-like defects, different facet directions yield different dopant incorporation.

### 6.2.2 Raman Imaging Characterization of Electronic Properties of SiC Near a Micropipe

It is usually considered that threading defects or micropipes deteriorate the electrical characteristics such as the breakdown voltage of SiC devices.

Distribution of stress existing around micro pipes has been measured by Raman mapping using the TO phonon mode [42]. We describe here the results of the studies on electronic and crystalline properties in the vicinity of micropipes in an *n*-type 4H-SiC wafer using a Raman imaging technique [33].

The excitation laser beam was linearly expanded by a cylindrical lens and focused at the sample covering the cross section of the micropipe. Figure 7 shows a typical Raman image for the  $E_2$  (TO) phonon mode (left) and the  $A_1$  (LO) phonon mode (right). The position of the micropipe was taken as the origin in the vertical axis. In the Raman spectrum of an undoped standard sample [1], these modes show sharp Lorentzian peaks at about  $776\text{ cm}^{-1}$  ( $E_2$ ) and  $964\text{ cm}^{-1}$  ( $A_1$ ) with FWHM of about  $2\text{--}3\text{ cm}^{-1}$ . Let us compare the results in more detail for the point A (within  $1\text{--}2\text{ }\mu\text{m}$  from the micropipe) and point B (about  $100\text{ }\mu\text{m}$  apart from the micropipe). The  $E_2$ -mode is sharp and almost uniformly peaked throughout the probed region, which indicates that there is no noticeable anomaly in the crystallinity, such as polytype mixture, inclination of crystal axis, or lattice distortion. In contrast, the  $A_1$  (LO) mode shows a noticeable variation in the peak intensity and the frequency.

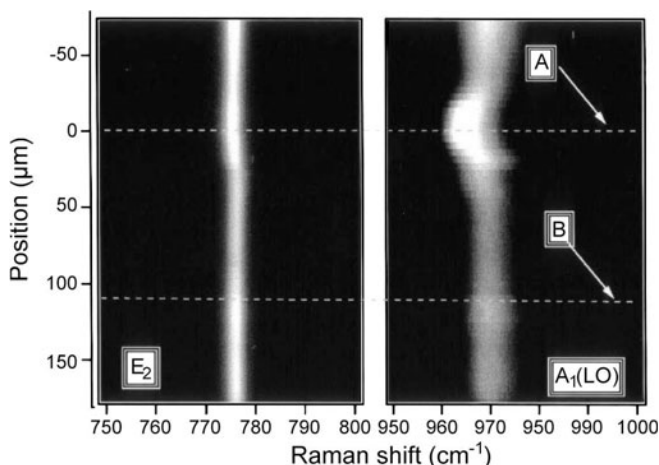


**Fig. 7.** Raman image for the  $E_2$ -phonon mode (left) and  $A_1$  (LO) phonon mode (right) observed by linear illumination of the probe laser on the (0001) plane of a 4H-SiC sample. The *vertical axis* denotes distance from a micropipe cross section [33]

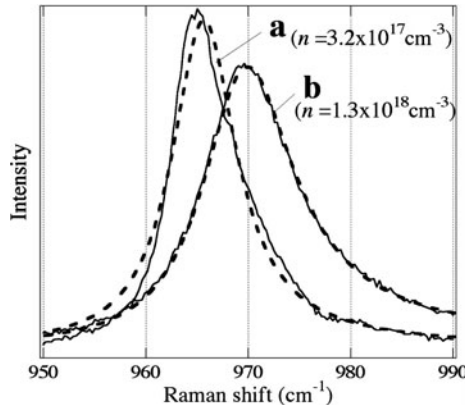


**Fig. 8.** LO-phonon spectra of a sample used in Fig. 7: (a) near a micropipe defect, and (b) far from the defect. *Solid line* denotes observed profiles and *dashed lines* give the best-fit calculations [33]

In Fig. 8, the solid lines show the observed spectra: The peak is narrower and located at lower frequency at point A than at B. As described before, LO-phonon peaks in  $n$ -type SiC broaden and shift to higher frequency with the increase of the free carrier concentration because of coupling with plasmons. Therefore, this result implies a decrease of the carrier concentration in the vicinity of a micropipe.

The carrier concentration  $n$  and the carrier mobility  $\mu$  were evaluated by the fitting to the observed profiles as described in the preceding section using the classical dielectric function, (8). The broken curves in Fig. 8 show the best-fit calculations, and their parameters yielded  $n = 3.2 \times 10^{17} \text{ cm}^{-3}$  and  $\mu = 20 \text{ cm}^2/\text{Vs}$  for point A, and  $n = 1.3 \times 10^{18} \text{ cm}^{-3}$  and  $\mu = 32 \text{ cm}^2/\text{Vs}$  for point B. At point B that carrier concentration agrees very well with Hall measurements ( $1.4 \times 10^{18} \text{ cm}^{-3}$ ), whereas at point A, a much smaller concentration is obtained and also a reduced mobility is observed. These results are interpreted as a manifestation that a high density of carrier-trap centers is distributed in the vicinity of the micropipe.

To conclude, characterization by Raman imaging in  $n$ -type SiC in the vicinity of micropipes clearly reveals the decrease in the carrier concentration and mobility. This result suggests that carrier trapping centers are densely located around micropipes.

## 7 Conclusion

In this article, recent spectroscopic studies of defects in SiC have been briefly surveyed. Micro-Raman analyses have been performed on defects that are distinguishable by optical microscopes, and both the structural and electronic properties of defects have been investigated.

Obviously, Raman microscopy has a high potential as an easy-access and non-destructive characterization technique for defects in various materials. Rapid development in Raman-imaging technique using advanced multi-channel detectors is a good example. From the material side, wide band gap semiconductors like SiC have a great advantage for Raman microscopy because of their high transparency. However, micro-Raman studies for defects have only just begun, and been limited to macro-defects of  $\mu\text{m}$ -size and their qualitative evaluations. It is therefore desirable in the future to further improve the spatial resolution as well as to deepen quantitative discussions by combining with other characterization techniques for defects.

## References

1. S. Nakashima, H. Harima: *phys. stat. sol. (a)* **162**, 39 (1997)
2. R.C. Newman: *Adv. Phys.* **18**, 545 (1969)
3. L.A. Rahn, P.J. Colwell, W.J. Choyke: in *Radiation Effects in Semiconductors* (Institute of Physics Conf. Series No.31), ed. by N.B. Urli and J.W. Corbett (IOP Publishing, Bristol, 1977) p. 515
4. T. Kimoto, A. Itoh, H. Matsunami, T. Nakata, M. Watanabe: *J. Electron. Mater.* **24**, 235 (1995)
5. Z.C. Feng, S.J. Chua, K. Tone, J.H. Zhao: *Appl. Phys. Lett.* **75**, 472 (1999)
6. H. Richter, Z.P. Wang, L. Ley: *Solid State Commun.* **39**, 625 (1981)
7. K.K. Tiong, P.M. Amirtharai, F.H. Pollak, D.E. Aspnes: *Appl. Phys. Lett.* **44**, 122 (1984)
8. I.H. Campbell, P.M. Fauchet: *Solid State Commun.* **58**, 739 (1986)
9. E. Bedel, R. Carles, A. Zwick, J. B. Renucci, M.A. Renucci: *Phys. Rev. B* **30**, 5923 (1984)
10. E. Bedel, G. Landa, R. Carles, J.B. Renucci, J.B. Roquais, P.N. Favanne: *J. Appl. Phys.* **60**, 1980 (1986)
11. S. Nakashima, Y. Nakatake, H. Harima, M. Katsuno, N. Ohtani: *Appl. Phys. Lett.* **77**, 3612 (2000)
12. S. Nakashima, Y. Nakatake, Y. Ishida, T. Takahashi, H. Okumura: *Physica B* **308–310**, 684 (2001)
13. S. Nakashima, H. Ohta, M. Hangyo, B. Palosz: *Phil. Mag. B* **70**, 971 (1994)
14. S. Rohmfeld, M. Hundhausen, L. Ley: *Phys. Rev. B* **58**, 9858 (1998)
15. S. Nakashima, H. Katahama, Y. Nakakura, A. Mitsuishi: *Phys. Rev. B* **33**, 5721 (1986)
16. S. Nakashima, K. Tahara: *Phys. Rev. B* **40**, 6339 (1989)
17. S. Nakashima, Y. Nakatake, Y. Ishida, T. Takahashi, H. Okumura: *Mater. Sci. Forum* **389–393**, 629 (2002)
18. S. Rohmfeld, M. Hundhausen, L. Ley: *phys. stat. sol. (b)* **215**, 115 (1999)
19. P. Käckell, J. Furtmüller, F. Bechstedt: *Phys. Rev. B* **58**, 1326 (1998)
20. J. Camassel, P. Vicente, L.A. Falkovski: *Mater. Sci. Forum* **353–356**, 335 (2001)
21. E. Valcheva, T. Pascova, I.G. Ivanov, R. Yakimova, Q. Wahab, S. Savage, N. Nordell, C.I. Harris: *J. Vac. Sci. Technol. B* **17**, 1040 (1999)
22. P.J. Colwell, M.V. Klein: *Phys. Rev. B* **6**, 498 (1972)

23. W.J. Moore, P.J. Lin-Chung, J.A. Freitas, Jr., Y.M. Altaiskii, V.L. Zuev, L.M. Ivanova: *Phys. Rev. B* **48**, 12289 (1993)
24. W. Götz, A. Schöner, G. Pensl, W. Suttrop, W. J. Choyke, R. Stein, S. Leibenzeder: *J. Appl. Phys.* **73**, 3332 (1993)
25. W. Suttrop, G. Pensl, W.J. Choyke, R. Stein, S. Leibenzeder: *J. Appl. Phys.* **72**, 3708 (1992)
26. C.Q. Chen, J. Zeman, F. Engelbrecht, C. Peppermüller, R. Helbig, Z.H. Chen, G. Martinez: *J. Appl. Phys.* **87**, 3800 (2000)
27. M.V. Klein: in *Light Scattering in Solids I*, ed. by M.Cardona, (Springer-Verlag, Berlin, Heidelberg, New York, 1975) p. 147
28. H. Yugami, S. Nakashima, A. Mitsuishi: *J. Appl. Phys.* **61**, 354 (1987)
29. M.V. Klein, B.N. Ganguly, P.J. Colwell: *Phys. Rev. B* **6**, 2380 (1972)
30. H. Harima, S. Nakashima, T. Uemura: *J. Appl. Phys.* **78**, 1996 (1995)
31. J.C. Burton, L. Sun, M. Pophristic, S.J. Lukacs, F.J. Long, Z.C. Feng, L.T. Ferguson: *J. Appl. Phys.* **84**, 6268 (1998)
32. H. Harima, S. Nakashima: *Mater. Sci. Forum* **264–268**, 449 (1998)
33. H. Harima, T. Hosoda, S. Nakashima: *Mater. Sci. Forum* **338–342**, 603 (2000)
34. M. Chafai, A. Jaouhari, A. Torres, R. Anton, E. Martin, J. Jimenez, W.C. Mitchell: *J. Appl. Phys.* **90**, 5211 (2001)
35. G. Irmer, V.V. Toporov, B.H. Bairamov, J. Monecke: *phys. stat. sol. (b)* **119**, 595 (1983)
36. F. Baumard, F. Gervais: *Phys. Rev. B* **15**, 2316 (1977)
37. F. Gervais: *Phys. Rev. B* **23**, 6580 (1981)
38. J.M. Miljkovic, N. Lomcovic, Z.V. Popovic, W. Konig, V.N. Nikiforov: *phys. stat. sol. (b)* **193**, 43 (1996)
39. E. Neyret, G. Ferro, S. Juillaguet, J.M. Bluet, C. Jaussaud, J. Camassel: *Mater. Sci. and Eng. B* **61–62**, 253 (1999)
40. S. Nakashima, H. Harima: unpublished
41. J. Takahashi, N. Ohtani, M. Katsuno, S. Shinoyama: *J. Cryst. Growth* **181**, 229 (1997)
42. H. Ohsato, T. Kato, T. Okuda, M. Razeghi: *SPIE* **3629**, 393 (1999)

# Characterization of Low-Dimensional Structures in SiC Using Advanced Transmission Electron Microscopy

U. Kaiser

## 1 Introduction

Quantum confinement in one, two and three dimensions has resulted in important advances in semiconductor physics. Low-dimensional structures are formed from two semiconductors that have different conduction (valence) band energies, thus giving rise to an energy barrier for electrons (holes). Examples include semiconductor superlattices and quantum dot arrays, which are formed by the periodic arrangement of layers or islands. Quantum dots can have an emission wavelength that is a pronounced function of their size, resulting in a spectral tunability over a wide energy range simply by changing their size and quantum dot lasers have already been demonstrated [1, 2] using classical III-V and II-VI semiconductors. There is strong industrial interest in the development of new low-dimensional structures. It has recently been demonstrated that Ge crystals buried in SiO<sub>2</sub> show quantum size effects and efficient, non-indirect optical transitions when they are smaller than 5 nm in size [3].

SiC is an extremely promising candidate for achieving quantum confinement as its fundamental energy gap varies by about 1 eV between the cubic polytype and the hexagonal polytypes, and heteropolytypical quantum well structures can be created from a single chemical compound [4]. Another new class of quantum structures is based on the creation of quantum dot arrays of Si or Ge in semiconducting SiC instead of in insulating SiO<sub>2</sub>, thus allowing electroluminescence, widening the field of application from optics to optoelectronics [5, 6]. Furthermore, an array of transition metal quantum dots buried in SiC may have interesting properties in the field of spintronics [7].

The number of techniques that can be used to form such nanostructures is presently restricted by the need to tune SiC polytype growth and by the low diffusion coefficient of dopant atoms in SiC [8] to non-equilibrium techniques such as molecular beam epitaxy and ion-implantation. We recently demonstrated their applicability to low-dimensional growth, (for an overview of MBE results see [9]; for recent results on ion-implantation see [10]).

In order to understand and control the fabrication of low-dimensional materials, it is essential that they be characterized at close to the atomic scale. The atomic structure of interfaces, defects and nanostructures can be investigated by atomic resolution transmission electron microscopy (TEM),

using either high resolution TEM (HRTEM) or high angle annular dark-field scanning TEM (HAADF-STEM). Just as atomic force microscopy, scanning tunneling microscopy and the atom probe have become the primary tool for studying surfaces, so TEM has become the method of choice for studying defects and low-dimensional structures within materials.

Many analytical signals are available on modern small-probe-forming TEMs. These techniques include convergent beam electron diffraction (CBED) [11]–[13], electron energy loss spectroscopy (EELS) (which gives similar information to soft X-ray absorption spectroscopy) and energy dispersive X-ray (EDX) microanalysis (similar to X-ray fluorescence microscopy). The combination of reciprocal, real space and analytical information with atomic resolution  $Z$ -contrast imaging and EELS spectroscopy offers great potential for unraveling structure-property relationships in nanostructures [14]–[16].

Theory and simulation are playing an increasing role in the interpretation of TEM image contrast. In particular, HRTEM images are difficult to interpret as a result of multiple scattering and the inability to record the phase of the electron wave that has passed through the sample [17]–[19]. Atomic resolution HAADF images are generally easier to interpret directly, however simulations are still often required [20]. The interpretation of CBED patterns requires full dynamical simulations [21]–[24], while the use of ALCHEMI (atom location of chemical enhanced microanalysis) to determine atom site locations is always accompanied by full dynamical simulations [25, 26].

The aim of this article is to show how two new types of low-dimensional structures in SiC can be characterized using advanced TEM methods. There were many questions which answering required detailed TEM analysis: What is the strain state of the  $3C$ -quantum wells within hexagonal SiC and how accurate can it be determined? And further, do nanocrystals form within SiC and can they be visualized within a defective matrix? And moreover, can the nanocrystal formation process be visualized? Which structure(s) do nanocrystals adopt and why, and finally, do nanocrystals embedded in SiC really show the quantum confinement? All these problems have been addressed by using most of the signals available for materials characterization in conventional and state of the art instruments. Thus, here an attempt is made to unravel the detailed complexity of nanometer scale structural analysis for low-dimensional structures in SiC.

## 2 Experimental

### 2.1 Lattice Parameter Determination Using TEM

There are two ways to determine lattice parameters in TEM; from direct space (HRTEM-images) and reciprocal space (CBED patterns) information. In the first case the equivalent spot distances in the Fourier Transformation (FT) pattern of a HRTEM image [27] allow crystal lattice spacings to be

measured to an accuracy of at least 0.002 nm, which is decreased in case of a distorted matrix [16]. In the second case the accuracy of the lattice parameters is about one order of magnitude worse [28]. Here lattice parameters are determined from the position of HOLZ (Higher Order Laue Zone) lines appearing in CBED patterns, which is detected using the Hough transformation [29]. It has been found that the defocus-noise in HRTEM images does not influence the accuracy of lattice parameter determination from Fourier transforms, however, noise is the limiting factor for lattice parameter determination from CBED patterns [30].

## 2.2 Z-Contrast Imaging

Nanocrystals embedded in crystalline matrices as envisaged in optoelectronics and spintronics, require routine techniques for counting precipitates and determining size distributions. As precipitates usually differ from the matrix by elemental content, *Z*-contrast imaging in a STEM [31] is suited. In the STEM a number of signals can be recorded simultaneously while a fine electron probe is scanned over the sample. An annual dark-field (ADF) detector records the electron intensity scattered to high angles (usually between 70 and 150 mrad) [31]. At these high angles the scattered intensity depends strongly on the atomic (*Z*) number in the sample [32]. An EELS spectrum, which can be recorded simultaneously, contains features that result from the excitation of phonons, plasmons, valence electrons and inner-shell electrons in the sample, and is therefore sensitive to chemical composition, electronic structure and coordination [33, 34].

By reciprocity, *Z*-contrast imaging can also be achieved in a conventional TEM using a hollow-cone aperture [35] or using dynamical hollow-cone illumination [36]. A low-cost alternative for obtaining *Z*-contrast images in a conventional TEM, albeit with a lower spatial resolution, has been suggested recently [37]. In analogy to HAADF-STEM images, these are referred to as HACDF (high-angle centered dark field) TEM images. Fixed beam tilt high-

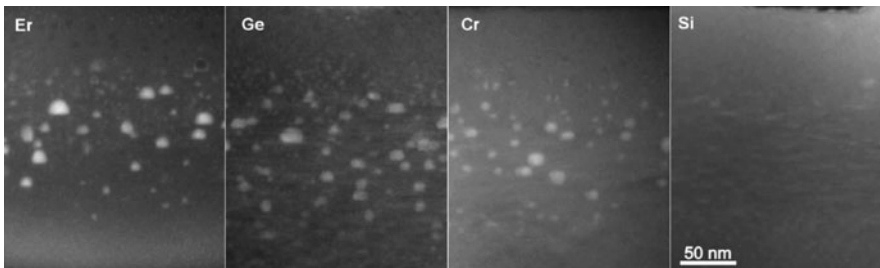


**Fig. 1.** HACDF images of precipitates in SiC after Er ( $Z = 68$ ), Ge ( $Z = 32$ ), Cr ( $Z = 24$ ) and Si ( $Z = 14$ ) ion implantation, showing a decrease in contrast with decreasing difference in *Z* between the precipitates and the matrix [37]

angle (about 70 mrad) illumination and a centered objective aperture are used [37].

Figure 1 illustrates the dependence of the content on the atomic number of the precipitates formed after Er-, Ge-, Cr- and Si implantation into SiC (formation process and structure will be described in Sect. 3.2 and 3.3).

### 2.3 ALCHEMI

The area under a peak in an EDX spectrum is proportional to the concentration of the corresponding element in the specimen. For determining elemental content, the electron-beam current is assumed to be uniform throughout the specimen and electron channeling is avoided by avoiding strong diffraction conditions. Strongly excited low-order reflections result in the electron beam current varying across each unit cell, which is advantageous for atom location by channeling enhanced microanalysis (ALCHEMI). Measurements are made at two crystal orientations, at which channeling is weak and strong [38]. As beam convergence, absorption and the smearing of the beam by inelastic scattering reduce channeling effects, care is required to use parallel beam conditions and an optimal specimen thickness [39]. It has been determined with this method that after ion beam bombardment Ge within SiC is mainly located on interstitial positions [40].

### 2.4 Computation Techniques

As a result of dynamical scattering, experimental high-resolution TEM images and convergent beam electron diffraction patterns (CBED) need to be compared with simulations, sometimes including an iterative refinement of the underlying model [41]. The total wave field in the crystal (solution of the Schrödinger equation) is described using a linear combination of Bloch waves. This concept is widely used to calculate CBED patterns and high-resolution contrast of perfect crystals with small unit cells. The computational time required to solve is proportional to the 4th power of the number of beams included in the calculation (20 to 400 beams are usually excited for a perfect crystal). Scattering from irregular or defective structure requires  $10^4$  to  $10^7$  reflections to be taken into account, which therefore is difficult to simulate using Bloch waves.

An alternative way to solve the Schrödinger equation is called the multislice method, and based on physical optics and does not require three-dimensional periodicity of the sample potential [42]. A thick specimen is subdivided into thin slices, and the scattering is calculated sequentially for each slice. The transfer of a part of the calculation to reciprocal space by Fast FT (FFT), where propagation can be calculated as a multiplication [43], reduces the calculation time. The multislice algorithm allows scattering to be calculated from irregular models, and is used widely to simulate the HRTEM con-

trast of defects, grain boundaries, particles and amorphous materials. Here, however, the problem is to get relaxed atom coordinates.

This can be solved in a full molecular dynamics (MD) calculation where the model structure is relaxed and the potential energy is minimized. MD calculations solve equations of a motion for a system of particles numerically and allow atomic processes such as the reordering of crystal interface atoms, the nucleation of particles, crystallization and melting to be investigated. Classical MD calculations can be used to simulate atomic processes in systems with up to  $10^6$  atoms within a time scale up to nanoseconds. The reliability of MD simulations depends strongly on the quality of the potential used. The Tersoff potential [44]–[46] has been found to be the most appropriate for the C-Si-Ge system [47].

The experimental HRTEM images and CBED patterns often need to be off-line processed to get experiment-near information for the start models of the simulations. To reveal information such as small strains approaches are used that involve e.g. Fourier Transformation (FT) (analyze HRTEM images) or Hough Transformation (analyze CBED patterns). Advanced Fourier analysis techniques include amplitude imaging [48] and geometrical phase analysis [49]. Amplitude imaging is used to identify a particular phase in an image [50].

In Table 1 selected data for the three different polytypes simulated are presented.

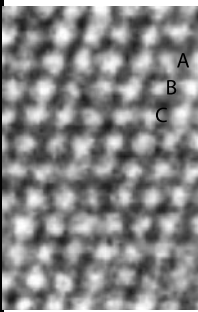
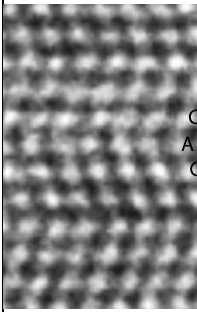
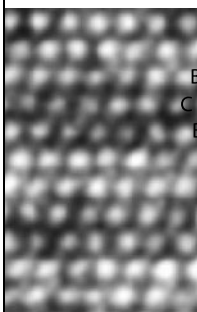
## 2.5 TEM Sample Preparation

Excellent microscopy requires an excellent TEM sample that is electron-transparent and artifact-free [51]–[53].

Many methods can be used to prepare a TEM sample. Small angle cleavage [54] results in artifact-free specimens, although the method is limited to brittle single crystals. Tripod polishing [52] involves thinning the sample mechanically to electron transparency, which results in a very thin amorphous surface layer. Ion beam milling is widely used for preparing semiconducting materials. Focused ion beam milling [55] is used when site-specific regions of a sample are required, such as for failure analysis of integrated circuits. The use of a Ga ion gun at 10–30 keV results in a short sample preparation time, and recent developments promise that the problem of ion beam damage is being reduced in such specimens and thus can be prepared for study by means of HRTEM.

Conventional Ar-ion milling at 6–10 keV is used most widely after the sample (cross-sectional or plan-view sample) has been thinned mechanically to 5–50  $\mu\text{m}$  [53, 56]. For cross-sectional samples, Ar ions are usually used to bombard both surfaces of the sample simultaneously while it is rotating. The surfaces can also be bombarded one after the other, and changes in the surface morphology can be followed using a stereo microscope or a CCD camera. Low angle thinning is advantageous for the preparation of layers with

**Table 1.** Selected data for the different polytypes studied (from: (a) Bauer et al., Phys. Rev. B **57**, 2647 (1998); (b) Kaiser and Khodos, Phil. Mag. A **82** (3), 541 (2002); (c) Maeda et al., Phil. Mag A **57**, 573 (1988), (d) Hong et al., Mater. Res. Soc. Symp. Proc. **572**, 498 (1999), (e) Limpijumngong and Lambrecht, Phys. Rev. B **57**, 12018 (1998))

	3C-SiC	6H-SiC	4H-SiC
			
Stacking sequence	ABC	ABCA <sup>T</sup> C <sup>T</sup> B <sup>T</sup>	ABCB <sup>T</sup>
Crystal system	cubic	hexagonal	hexagonal
Space group	F-43 m	P6 <sub>3</sub> mc	P6 <sub>3</sub> mc
Lattice parameter [nm] <sup>(a)</sup>	a = 0.43596 ≡ a <sub>hex</sub> = 0.30828	a = 3.08129 c = 1.51198	a = 0.308051 c = 1.008481
Atomic base	Si 0, 0, 0 C 1/4, 1/4 1/4	Si 0, 0, 0 Si 2/3, 1/3, 1/6 Si 1/3, 2/3, 1/3 C 0, 0, 1/8 C 2/3,1/3,7/24 C 1/3,2/3,11/24	Si 0, 0, 0 Si 2/3, 1/3, 1/2 C 0, 0, 3/16 C 2/3,1/3,11/16
Stacking fault energy	0.1 mJ/m <sup>2</sup> <sup>(b)</sup>	2.5 mJ/m <sup>2</sup> <sup>(c)</sup> 2.9 mJ/m <sup>2</sup> <sup>(d)</sup>	14.7 mJ/m <sup>2</sup> <sup>(d)</sup>
Hexagonality	0%	33%	50%
Bandgap E <sub>g</sub> <sup>(e)</sup>	2.4 eV	3.0 eV	3.25 eV

different sputtering yields. Sample rocking or sector speed thinning, which can be used to prevent differential milling, were used in the present study. Conventional ion milling produces an amorphised region on the surface of the TEM sample. Decreasing the ion energy to 2–3 keV decreases the damage drastically. A low voltage ( $\sim 100$  V) ion gun can sometimes produce a sample that has no detectable amorphous layer [57].

### 3 Applications of TEM Techniques to the Study of Low-Dimensional Structures

#### 3.1 Lattice Parameters of Thin Cubic MBE-SiC Films and Quantum Well Structures

Bloch wave simulations were used to determine the lattice parameters and strain states of cubic SiC layers by comparing experimental on-axis CBED patterns with simulations. The samples studied included a defect-free  $\sim 100$  nm thick cubic SiC layer on a  $6H$ -SiC substrate, a  $\sim 100$  nm thick cubic SiC film beneath a Si precipitate [28] and a 20 nm thick  $3C$ -SiC layer embedded in  $4H$ -SiC [58]. The cubic layer, which TEM investigations showed to be nearly defect-free [28], was of perfect cubic symmetry, however the lattice parameter of 0.4374 nm was  $\sim 0.4\%$  higher than X-ray data for thick cubic SiC layers ([59] and Table 1). As this layer was grown at high temperature under excess Si flow, the excess Si may have been incorporated into the  $3C$ -SiC structure. However, when growing at a lower temperature with a high Si excess in the flux, the excess Si was found to cluster on the surface in the form of hillocks [28]. Underneath the hillocks a transformation from cubic to rhombohedral symmetry was measured which can be explained by compressive stress. Such small deviation of only  $0.1^\circ$  from cubic symmetry can be already seen by the naked eye as demonstrated in Fig. 2.

As the hexagonal lattice parameter  $a$  is larger than that of the cubic polytype (see Table 1), a very thin cubic layer embedded in hexagonal SiC may be strained. From the HRTEM investigations of 20 nm thick cubic SiC layers embedded in a quantum well structure composed of  $4H$ -SiC/ $3C$ -SiC/ $4H$ -SiC, the interfaces were found to be abrupt, and no misfit dislocations were observed [58]. CBED showed that the cubic stripe was significantly rhombohedrally distorted, with a deviation from the cubic  $90^\circ$  angle by  $0.22^\circ$  ( $\alpha_{\text{rhom}} = (89.78 \pm 0.02)^\circ$  and  $a_{\text{rhom}} = (0.4360 \pm 0.0001)$  nm). Transformed to hexagonal coordinates,  $a_{\text{hex,stripe}}$  is  $(0.3078 \pm 0.0001)$  nm, which is in reasonable agreement with table values for  $4H$ -SiC (see Table 1). The measured rhombohedral distortion is interpreted as consequence of pseudomorphic growth of the  $3C$  stripe. The 2 nm thick cubic stripes in the multi-quantum well structures grown on stepped SiC are generally too thin for lattice parameter determination by CBED. The quantum confinement in thin  $3C$ -stripes has been reported recently [60].

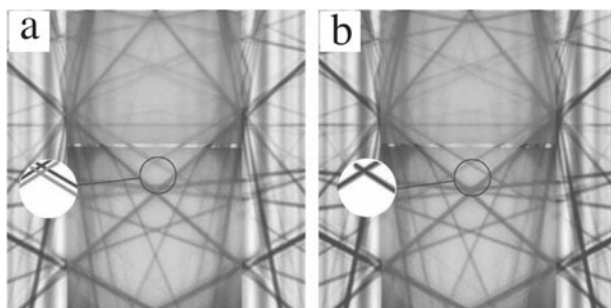


**Fig. 2.** Simulated (*dark grey*) CBED patterns at  $[320]$  incidence for (a) a cubic SiC and (b) a rhombohedral SiC cell ( $\alpha = 89.9^\circ$ ), overlaid with experimental (*light grey*) CBED patterns. As seen from the enlargements a good fit was achieved assuming rhombohedral symmetry [28]

### 3.2 The Formation Process of Embedded Nanocrystals in Hexagonal SiC Created by Ion Implantation and Annealing

For understanding of Ge nanocrystal formation within SiC, knowledge is required of whether implanted Ge atoms are located on lattice or on interstitial sites before it clusters. ALCHEMI (see Sect. 2.3) is applied to Ge implanted SiC [40, 61]. Bloch wave calculations [21] are used to determine suitable zones at which the Si, C and interstitial branches showed a different dependence of the excitation amplitude on tilt. One such zone axis is  $[01\bar{1}0]$  (see Fig. 3) where the solid curves show the calculated excitations of the Si, C and inter-

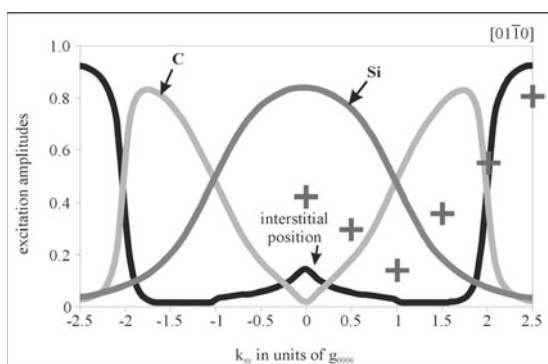


**Fig. 3.** Excitation amplitude of Bloch states as a function of the reciprocal lattice vector  $k_{xy}$  in units of  $g_{0006}$ . The *solid curves* show the result of Bloch wave calculations, while the crosses are EDX measurements indicating that Ge is preferentially distributed on interstitial sites (conditions: 250 keV  $10^{16} \text{ cm}^{-2}$  Ge ions after annealing at  $1200^\circ\text{C}$ ) [40]

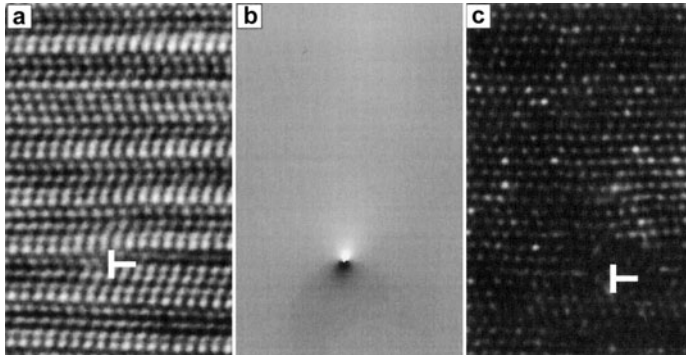


**Fig. 4.** HRTEM (a), geometrical phase analysis (b), HAADF-STEM images (c) from Er implanted SiC (dose  $10^{16} \text{ cm}^{-2}$ , energy 400 keV, implantation temperature  $700^\circ\text{C}$  before (a–c)). The edges of interstitial loops comprise strains (see the *middle image*) however cannot act as sink for the Er atoms directly after implantation; the *spotted contrast* is arising from statistically distributed Er atoms [62]

stitial branches. HRTEM, CTEM and HAADF-STEM studies showed that Ge nanocrystals did not form after high dose Ge implantation (implantation conditions:  $700^\circ\text{C}$ ,  $10^{16} \text{ cm}^{-2}$  250 keV Ge ions, annealing at  $1200^\circ\text{C}$ ). The site occupancy of Ge was studied by obtaining EDX spectra close to  $[01\text{-}10]$ .

As can be seen from the qualitative agreement between the experimental (crosses) and calculated curves in Fig. 3, a large number of Ge atoms was found to occupy interstitial positions in the  $6H$ -SiC matrix. In addi-

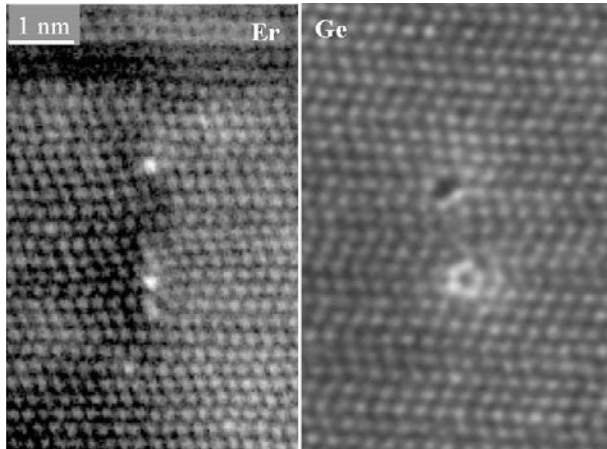


**Fig. 5.** HAADF-STEM images obtained after Er and Ge implantation into  $4H$ -SiC and annealing. Note the different configuration of the Er and Ge atom columns around the dislocation cores [63]

tion, by ALCHEMI studies, no preferred site occupancy was found in *as-implanted* specimens and preferred segregation to matrix defects (short interstitial loops) was not found as seen from Fig. 4c, where an interstitial loop is marked not acting as sink for Er atoms.

When annealing at 1600°C, atomic-resolution HAADF-STEM studies showed that, interstitial loops act as nucleation sites for Er or Ge atoms, however with strikingly different atomic configurations as demonstrated in Fig. 5.

The foreign atoms around interstitial loops were found to provide the seed of the nanocrystals [63]. From the HAADF-STEM studies moreover the nanocrystal growth process can be directly imaged as is shown for the case of ErSi<sub>2</sub> formation. Here within a single sample which we studied, different stages of the formation process were imaged, which allow the conclusion that Er gathers in atom columns, lines, planes and finally three-dimensional precipitates (Fig. 6) (for more details see [62, 63]).

A direct study of the early universe of ion implantation has been presented. It may be possible to control the dimensionality, and hence the electronic properties, of the resultant nanocrystals by matching the density of interstitial loops to the dopant atoms by co-implantation and subsequent annealing.

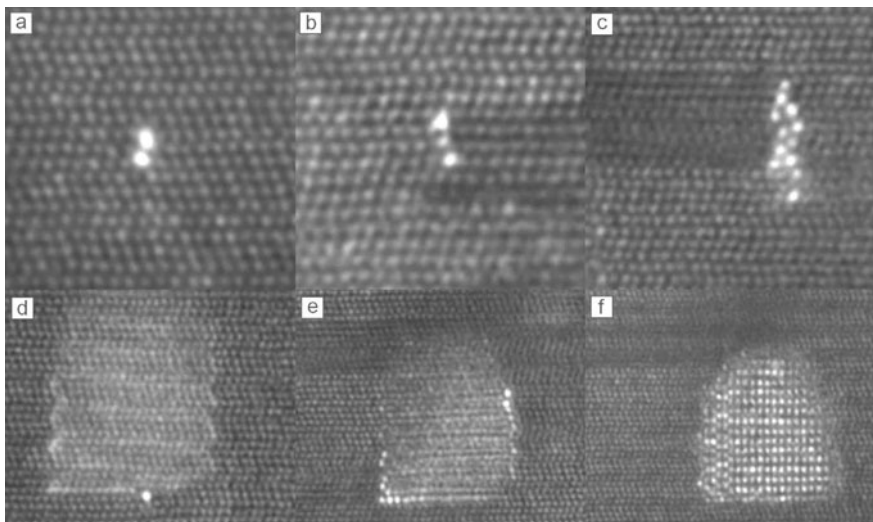


**Fig. 6.** After annealing at 1600°C; HAADF-STEM imaging shows that the Er has segregated to form precipitates of widely different size. The largest are still connected to extended defects (a) and (b) show precipitates composed of two and three columns of Er atoms (with roughly 5–10 atoms in each column); (d) is a 2D Er platelet attached to an Er rich dislocation core; (e) shows that the platelet edge are decorated first; (f) is a fully 3 dimensional unstrained erbium silicide precipitate [63]

### 3.3 Properties of Embedded Nanocrystals Created after Er, Ge or Si Implantation-Annealing

#### 3.3.1 Comparison of Nanocrystals Formed after Er and Ge Implantation

The size distribution of nanocrystals formed after Er or Ge ion implantation in SiC is very similar, as shown in Fig. 7a and b obtained from the corresponding HAADF-TEM images of Fig. 1. After Er as well as Ge implantation, many nanocrystals are  $\sim 5$  nm in size, or smaller, one representative is shown in Fig. 7c and d, respectively. It should be noted that in both cases the nanocrystals are arranged in a dipole-like configuration around interstitial loops, reminding us of their "seed configuration", which was displayed in Fig. 5.

The contrasting properties of nanocrystals formed after Er and Ge implantation are associated with the fact that Er reacts chemically with the SiC matrix atoms, whereas Si and Ge do not. ErSi<sub>2</sub>-nanocrystals (identified from HRTEM studies [63]) are always found in the same orientation relation-

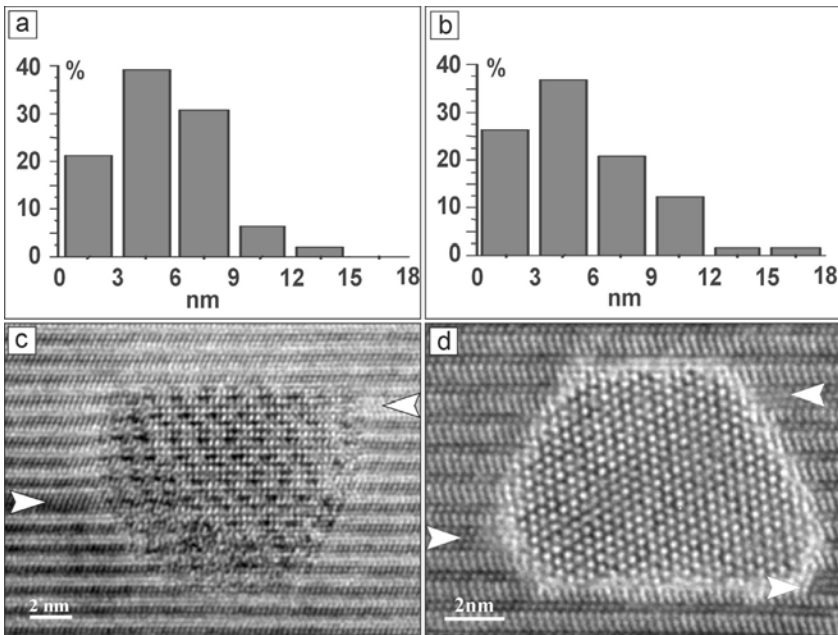


**Fig. 7.** Averaged size distribution for nanocrystals formed after (a) Er and (b) Ge ion implantation, as determined from HAADF-STEM and HAADF-TEM images. (c) and (d) show [11-20] HRTEM images of nanocrystals in 4H-SiC formed after Er and Ge implantation, respectively. Note the similar arrangement of the interstitial loops around the nanocrystal

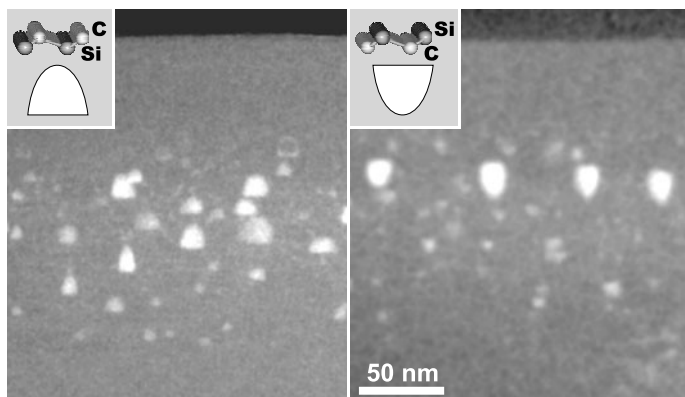


**Fig. 8.** HAADF images showing  $\text{ErSi}_2$  nanocrystals (*bright crystals*) of similar bell-like shape, which flip with the polarity of the matrix. The direction of the Si-C pair is indicated in the insert together with a scheme of the nanocrystal [62]

ship and with the same bell-like shape, which is associated with the 0004C surfaces of the SiC matrix (see Fig. 8).

In contrast, the nanocrystals created after Ge implantation, have different shapes and show different orientation relationships [40]. All nanocrystals found can be subdivided into four main orientation groups *a*, *b*, *c*, *d* as shown in Fig. 9, where always three examples of each group are presented.

The content of selected nanocrystals formed after Ge implantation had been determined by EDX and EELS point analyses in a field emission TEM where a small electron probe ( $< 1$  nm) can be realized. On average, the crystals contain  $\sim 80\%$  Ge and  $\sim 20\%$  Si [40]. Moreover, pure Si nanocrystals formed after Si implantation under comparable conditions showed lattice parameters that were  $\sim 3\%$  smaller than tabulated values [64, 65]. By analogy, a strain of  $\sim 3\%$  for the GeSi nanocrystals may be assumed. Alternatively, the nanocrystals may contain a large number of vacancies [64].

Before the question will be answered why the nanocrystals appear in the different orientation relationships to the SiC matrix, the crystallographic structure of the nanocrystals will be identified.

### 3.3.2 Identification of the Ge Structure

The nanocrystals in group *a* and *b* are in a SiC-matrix parallel orientation ( $[0001]_{\text{NC}} // [0001]_{\text{SiC}}$  and  $[11\bar{2}0]_{\text{NC}} // [11\bar{2}0]_{\text{SiC}}$ ). As can be seen from Fig. 9 all show stacking faults along  $[0001]$ , however the fault sequence is not uniform. The structure is cubic faulted GeSi or alternatively hexagonal with a irregular stacking sequence.

As can be seen from Table 2. comparing the values in the first two columns, the lattice parameter determined from the FFT pattern of the HRTEM im-

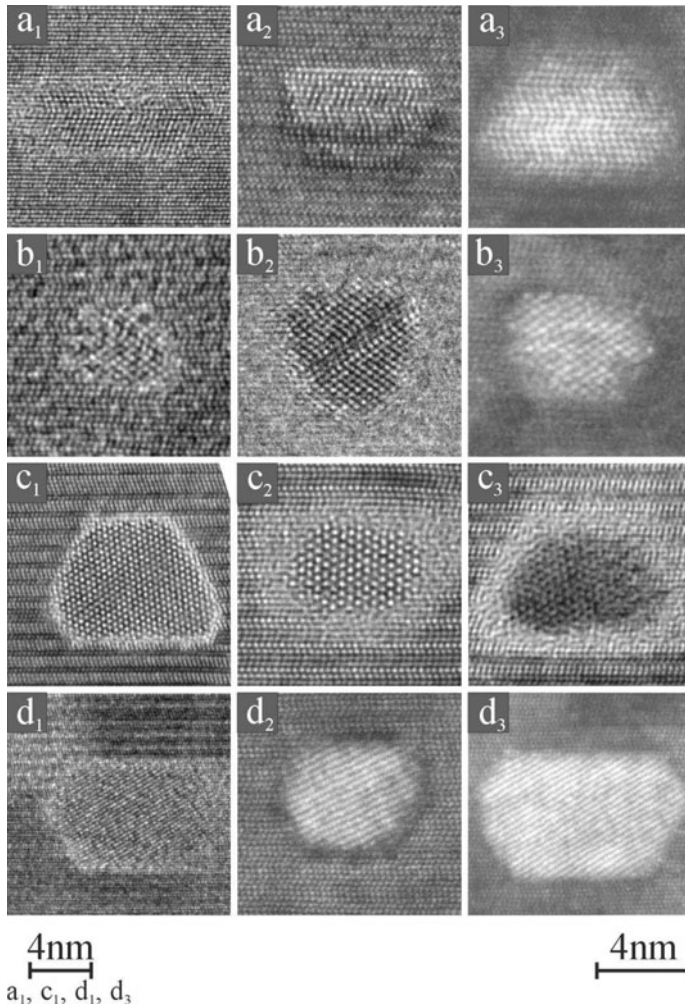


**Fig. 9.** HRTEM and HAADF-STEM ( $a_3, b_3, d_2, d_3$ ) images of four different groups  $a, b, c, d$  of nanocrystals formed after Ge implantation and annealing. Note the stacking faults in types  $a$  and  $b$ . ( $a$ :  $[0001]_{\text{NC}} // [0001]_{\text{SiC}}$  and  $[11-20]_{\text{NC}} // [11-20]_{\text{SiC}}$ ,  $b$ :  $[0001]_{\text{NC}}$  inclined to  $[0001]_{\text{SiC}}$ ,  $c$ :  $[0001]_{\text{NC}} \perp [11-20]_{\text{SiC}}$ ,  $d$ :  $[0001]_{\text{NC}}$  inclined to  $[11-20]_{\text{SiC}}$ ) [65]

ages of the nanocrystals in group  $c$  (under the assumption of a cubic structure) do not at all fit to cubic Ge.

Therefore in analogy to nanocrystals orientation group  $a$ , it was assumed that they are hexagonal as well just projected in a matrix perpendicular orientation ( $[0001]_{\text{NC}} \perp [0001]_{\text{SiC}}$ ). HR image simulations confirmed the fact that lattice fringes, which are forbidden by the structure factor in the diamond

**Table 2.** Comparison of experimental and tabulated values of lattice parameters of nanocrystals after Ge implantation

Experimental value [nm]	Table value [nm]	Experimental value [nm]	Table value [nm]
$a_{\text{NCgroupd}}$ cubic assumption	$a_{\text{Ge}}$ cubic $d_{\text{Ge01-10}}$ hex.	$d_{01-10,\text{NCgroupd}}$ hex. assumption	$d_{01-10,\text{Ge}_{0.8}\text{Si}_{0.2}}$ $d_{01-10,\text{Ge}_{0.8}\text{Si}_{0.2}+3\%\text{strain}}$ hex. assumption
0.975	0.5657 0.3460	$0.334 \pm 0.002$	0.343 0.333

structure, are present in the hexagonal structure both for an irregular and for a regular stacking sequence. Figure 10 shows calculations for 2*H*-Ge and 3*C*-Ge. The Pendellösung plot, which is simply a plot of the intensity of a reflection over the crystal thickness, demonstrates instructively that the reflection forbidden in the cubic structure is excited in the hexagonal structure. While comparing the  $d_{\text{Ge01-10}}$  value (second value in the second column) with the experimental value (third column) a strong discrepancy still remains. EDX point analysis from selected single nanocrystals showed that they contain 80% Ge and 20% Si [68]. However the experimental value still does not fit

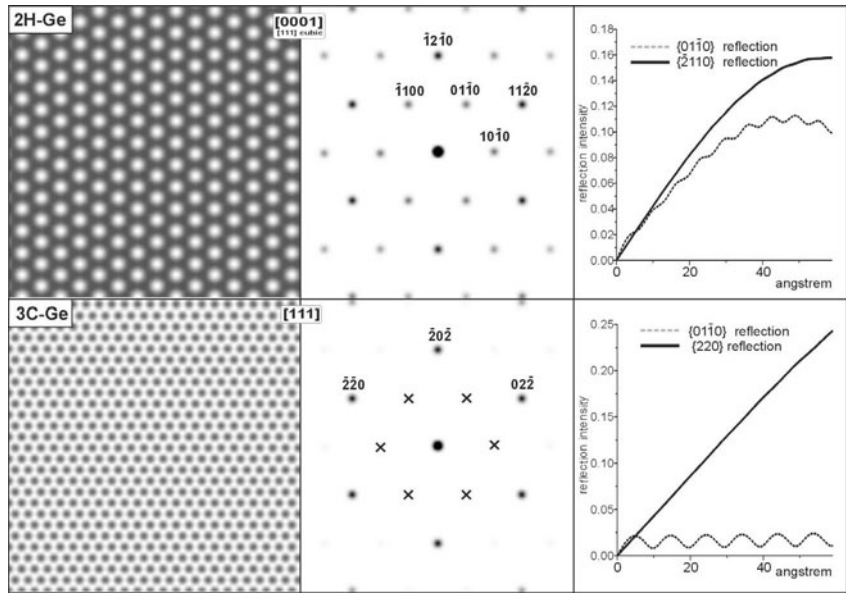


**Fig. 10.** HR image simulation of 2*H*-Ge and cubic Ge together with FFTs and Pendellösung plots for the 111 (11-20) and forbidden × (01-10) reflections

the table value (compare the value in the third column with the value in the first row, forth column). Si nanocrystals formed after Si ion implantation into SiC revealed that those pure Si nanocrystals are strained by about 3%. In analogy, such stain value has been assumed for the Ge nanocrystals. From Table 2 (see the values in the third and fourth column) it is seen that the experimental  $d$ -value fits well to those calculated for hexagonal  $\text{Ge}_{0.8}\text{Si}_{0.2}$  with 3% strain. In summary the nanocrystals presented in group  $a$ ,  $b$ ,  $c$  (see Fig. 9) are different orientations of the same strained hexagonal GeSi structure (for more details see [40, 65]). The nanocrystals presented in group  $d$  will be identified in the next chapter.

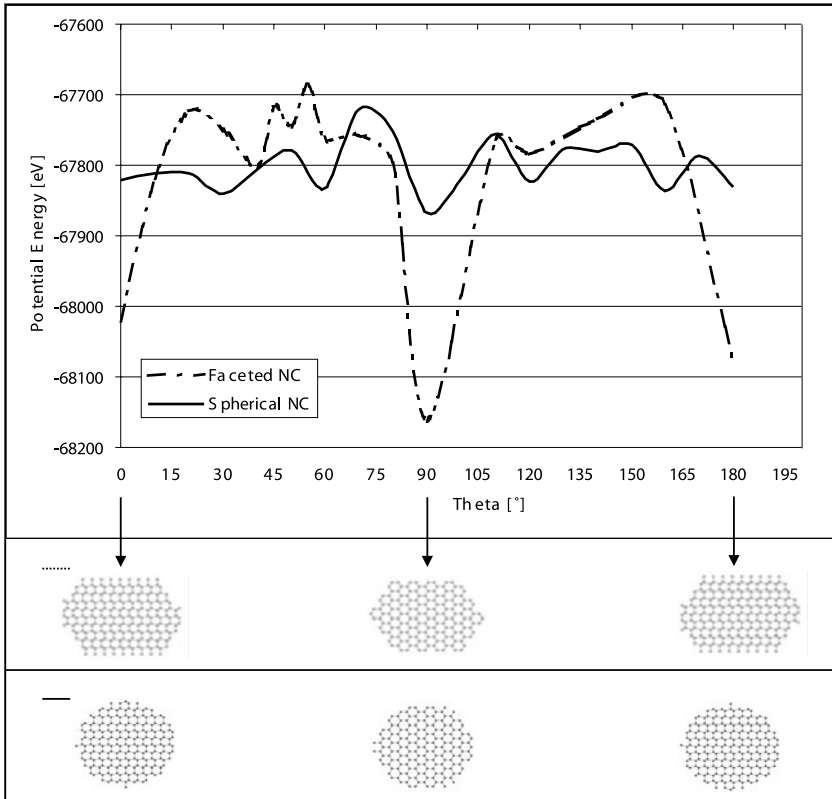


**Fig. 11.** Potential energy plots for symmetrically faceted and spherical nanocrystals as a function of the rotation angle  $\vartheta$  of the nanocrystal with respect to the SiC matrix (the model projection at  $0^\circ$  and  $180^\circ$  corresponds to group  $a$ , the model projection at  $90^\circ$  corresponds to group  $c$ ). When rotating the nanocrystals by  $180^\circ$  it is clearly seen that the faceted nanocrystal shows prominent energetic minima for orientation group  $a$  ( $0^\circ$  and  $180^\circ$ ) as well as for  $c$  ( $90^\circ$ ), however the spherical nanocrystal does not show deep energetic minima. Both nanocrystal models contain the same number of atoms (3000) [65]

### 3.3.3 Why Do GeSi Nanocrystals Appear in the Four Orientation Relationships?

To answer this question, models for differently shaped GeSi nanocrystal embedded in  $4H$ -SiC were created. Their potential energies as a function of the rotation angles of the nanocrystals in the matrix were determined using molecular dynamics calculations. It has been calculated that the four main orientation-relationships  $a$ ,  $b$ ,  $c$ ,  $d$  experimentally observed in [11-20] high-resolution TEM images of GeSi nanocrystals correlate with minima in the potential energy of the nanocrystal-matrix system [65]. For spherically shaped nanocrystals (group  $b$ ), neither group  $a$  nor group  $c$  orientation is energetically preferred as can be concluded from Fig. 11, explaining orientations observed experimentally (see Fig. 9). For symmetrically faceted nanocrystals, both group  $a$  and group  $c$  ( $90^\circ$  of group  $a$ ) orientations result in strong minima, of which the preferred orientation depends on the aspect ratio of the nanocrystal [65].

A small rotation of a nanocrystals starting from group  $c$  orientation ( $[0001]_{\text{NC}} \perp [11-20]_{\text{SiC}}$  see Fig. 9) in a fixed [11-20]  $4H$ -SiC matrix around the  $[1-100]$  direction (around rotation angle  $\vartheta$ ) and around the  $[0001]$  direction of the matrix for a symmetrically and an asymmetrically faceted nanocrystal, respectively, has been calculated to understand the orientation group  $d$ . The calculations showed that no pronounced extra minimum of the potential energy is found when the nanocrystal is symmetrically faceted. However, for the case of an asymmetrically faceted nanocrystal, a pronounced extra minimum forms at a defined small off-orientation value ( $6^\circ$  off  $[1-100]$  and  $4^\circ$  off  $[0001]$  [65]). The corresponding simulated HRTEM image results in the image shown in Fig. 12, which is in good agreement with the experiments

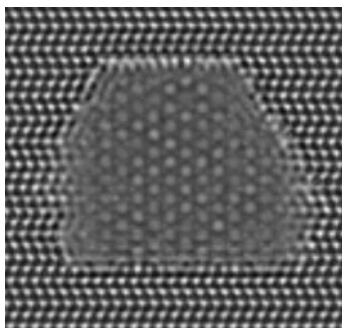


**Fig. 12.** Simulated [11-20] HRTEM image of an asymmetrically faceted nanocrystal within  $4H$ -SiC fixed at [11-20] orientation. The nanocrystal tilt coordinates used express the minimum of the potential energy of the nanocrystal-matrix system found at an orientation, which is small off oriented compared to group  $c$  nanocrystal orientations. The image shows only  $\{01-10\}$  lattice planes. See the similarity to the experimental HRTEM image shown in Fig. 9d) (for more details see [65])

(see Fig. 9d).

To summarize, hexagonal GeSi nanocrystals are formed after Ge ion implantation, which appear in different shape defined orientations. It was shown by molecular dynamics that those orientations express minima of the potential energy of corresponding simulated nanocrystal-matrix systems.

### 3.3.4 Why Are GeSi Nanocrystals Hexagonal and of Magic Size?

Molecular dynamics calculations for hexagonal and cubic Ge nanocrystals embedded in either hexagonal or cubic SiC show that the matrix structure affects the nanocrystal structure [64]. As can be seen from Fig. 13, in hexagonal SiC, hexagonal Ge nanocrystals are energetically preferred, whereas in cubic SiC, cubic Ge nanocrystals are preferred.

It may be concluded that the formation of stacking faults in the GeSi nanocrystal embedded in a hexagonal SiC matrix is energetically preferred over stacking faultfree cubic stacking. We recently experimentally confirmed that after Ge ion implantation into cubic SiC, cubic GeSi nanocrystals have been formed [66].

For elongated nanocrystals, changes in the width along the  $c$ -axis result in oscillating energy minima of the interface energy. This explains the fact that only well-defined widths, so-called magic sizes are found experimentally [64].

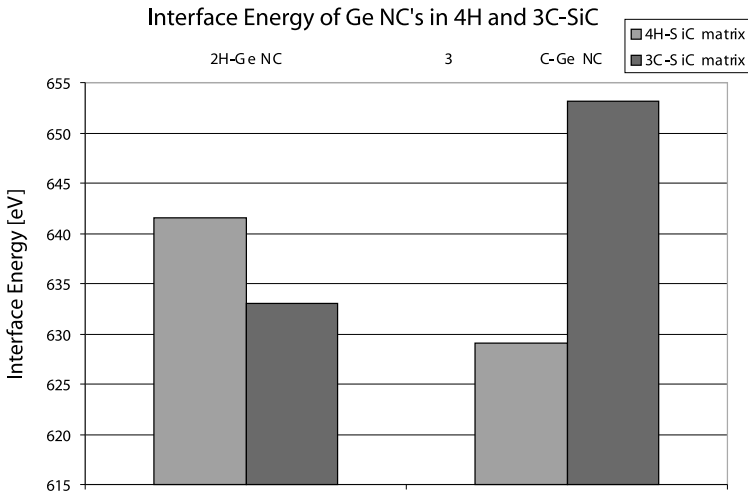


**Fig. 13.** Calculated interface energy  $E_{\text{int}}$  for different conditions.  $2H$ -Ge nanocrystals have maximum interface energy when they are embedded inside the  $4H$ -SiC matrix. In contrast,  $3C$ -Ge nanocrystals are energetically preferred inside the  $3C$ -SiC matrix [64]

### 3.3.5 Do GeSi Nanocrystals Show Quantum Confinement?

Nanocrystals that are smaller than 5 nm in size are expected to show quantum size effects [5] where quantum confinement is expected in both the conduction and valence band as demonstrated in Fig. 14 [6].

It was found from size distributions (see e.g. Fig. 9) obtained from the  $Z$ -contrast images (see e.g. Fig. 1) that many nanocrystals are measured to be smaller than  $\sim 5$  nm in size. That many are larger and that photoluminescence is an integral method, may explain that, up to now, photoluminescence from the nanocrystals has not been measured (the signal intensity from the small nanocrystals might be too low). In addition, the SiC defect luminescence may overlap that due to the nanocrystals (SiC defect luminescence: visible to near infrared spectral region, nanocrystals luminescence: expected in the red-near infrared spectral region.)

However, using a selective measurement method, as EELS in a STEM, where the EELS spectrum is obtained from a single defined nanocrystal with a one atom-wide electron probe, first evidence for quantum confinement could be shown. In Fig. 15, the Si  $L$  edges for two small GeSi nanocrystals is measured to lie at 101.8 eV and 102 eV, respectively. The nanocrystals were simultaneously imaged in atomic resolution using an annular dark-field detector (see the inserts). For comparison, the Si  $L$  edge for pure Si (99, 84 eV) and for the SiC matrix (103 eV, experiment) has been given. To interpret the shifts of the Si  $L$  edge in the nanocrystals, the Si  $L$  edge of unstrained thick  $\text{Ge}_{0.8}\text{Si}_{0.2}$  layers [67] of 100.3 eV was used as a standard value. It was checked experimentally that the shift measured is not chemical in nature, as no C was detected in the nanocrystals. In analogy to the quantum confinement measured in small Si nanocrystals [68], the shift of the Si  $L$  edge is suggestive of quantum confinement of the  $\text{Ge}_{0.8}\text{Si}_{0.2}$  nanocrystals buried in  $4H$ -SiC.

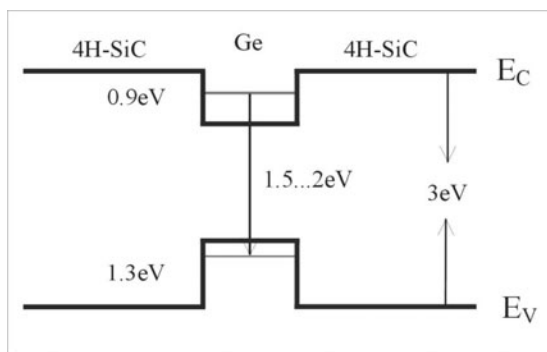


**Fig. 14.** Scheme of the band structure of a 5 nm thick Ge quantum dot inside  $4H$ -SiC [6]

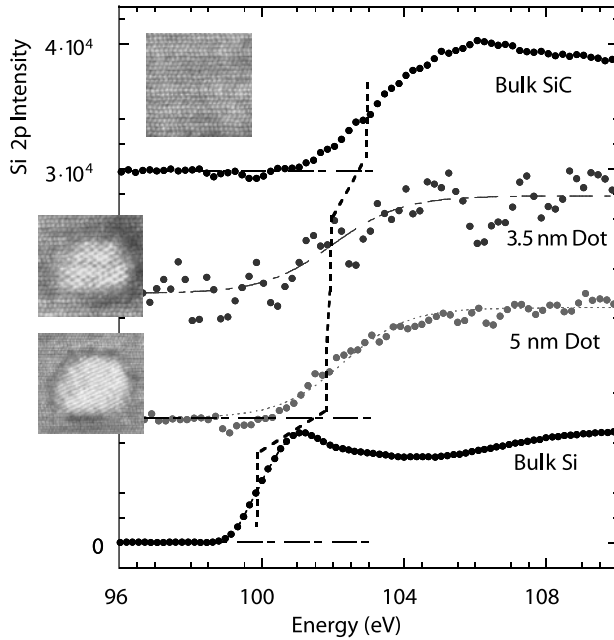


**Fig. 15.** EELS-spectra showing the intensity around the Si  $L_3$  edge in the  $4H$ -SiC matrix (*upper part*) in the GeSi nanocrystals (*middle part*) and for comparison in pure Si (*lower part*). The shift of the edge onset for the case of the nanocrystal is clearly seen. For comparison:  $SiL_{\text{bulk}} \text{ SiC}$ : 103 eV,  $SiL_{\text{bulk}} \text{ Si}$ : 99.84 eV. The 5 nm dot showed instead  $101.8 \pm 0.5$  eV and the 3.5 nm dot  $102.0 \pm 0.5$  eV [65]

## 4 Conclusion

Transmission electron microscopy and simulations have been used to characterize two types of low-dimensional structure in the wide band-gap, polytypic material SiC: i.e. quantum layers and quantum dots.

Convergent beam electron diffraction has been used to measure accurately the lattice parameters of single, about 100 nm thick cubic SiC layers, as well as of 20 nm thin cubic SiC layers periodically arranged in  $4H$ -SiC. The first case showed how the symmetry is affected by growth irregularities such as hillock formation, the second case that a rhombohedrally strained layer has been formed as a consequence of pseudomorphic growth. It demonstrates the potential of the method to determine such a small strain state from a nanosized object.

The nanocrystal formation process after high-dose ion implantation and annealing has been considered in detail. Directly after high dose and high temperature Er, Ge and Si implantation no nanocrystals have been formed and the foreign atoms are statistically distributed within the defective SiC matrix. The prevailing defects are short interstitial loops. The Ge site occu-

pancy was determined using EDX under electron channelling conditions for the as-implanted material and after annealing at 1200°C. In the latter case, diffusion is enhanced and Ge was found to be located preferentially on interstitial sites. Annealing at 1600°C results in the growth of nanocrystals whose size distributions are very similar for nanocrystals formed after Er and after Ge implantation. Atomic resolution *Z*-contrast dark-field STEM was used to visualize the nanocrystal formation, e.g. from the birth of the nanocrystals in form of single Er atom columns, trapped at the cores of dislocations, over lines, planes to fully-developed nanocrystals. Similarities and differences between the formation of nanocrystals after Er and Ge implantation were identified. Properties such as crystallographic structure and the orientation-relationship with the matrix have been determined from the high-resolution image. The result can be summarized for the Er case that ErSi<sub>2</sub> nanocrystals grow with one orientation with respect to the hexagonal SiC matrix, always showing a bell-like shape that flips with polarity. In contrast, EDX-analysis of the nanocrystals created after Ge implantation show that their content is not uniform and consists on average of 80 ( $\pm 15$ )% Ge. The structure of the GeSi nanocrystals was found to be hexagonal and they are oriented with four different shape dependent orientation relationships. Molecular dynamics simulations show that the structure and the orientation-relationships correspond to minima in the potential energy of the matrix-nanocrystal system. The electronic structure of GeSi nanocrystals was determined using atomic resolution *Z*-contrast dark-field imaging combined with electron energy loss spectroscopy. The results were indicative of quantum confinement in 5 nm and 3.5 nm Ge<sub>0.8</sub>Si<sub>0.2</sub> nanocrystals.

The new understanding of the role of interstitial loops in the formation of clusters may open the possibility of the control of the dimensionality of nanocrystals, by matching the density of the interstitial loops to the dopant atoms, thereby controlling the physical properties of the resultant nanocrystals.

## Acknowledgements

This work has been supported by the German Research Society (DFG), SFB 196 and by the BMBF-project transform 01BM804/5. The author is grateful to Dr. Andreas Fissel and Prof. Wolfgang Richter for the SiC MBE growth, and to Christian Schubert, Gunnar Pasold, Prof. Werner Wesch and Prof. Wolfgang Witthuhn for ion implantation and to all for related discussions. It is a pleasure to thank all electron microscopists who I have worked with on the fascinating SiC problems: I am very grateful to Dr. Andrey Chuvilin, Dr. David Muller, Dr. Koh Saitoh, Dr. Kenji Tsuda, Prof. Michiyoshi Tanaka, and Dr. Rafal Dunin-Borkowski. I would like to thank our PhD students Johannes Biskupek and Thomas Kups for fruitful collaboration and Dr. K. Gärtner for supervision related to molecular dynamics. Particular thanks go to Prof. Jim Choyke for initiating the work on Er implanted SiC and many encouraging discussions.

## References

1. D. Bimberg, M. Grundmann, N.N. Ledentsov: *Quantum Dot Heterostructures* (Wiley, Chichester, U.K., 1998)
2. M. Hines, P. Guyot-Sionnest: J. Phys. Chem. **100**, 468 (1996)
3. S. Takeoka: Phys. Rev. B **58**, 7921 (1998)
4. F. Bechstedt, P. Käckell: Phys. Rev. Lett. **75**, 2180 (1995)
5. G. Katula, C. Guedi, J. Kolodzy, R.G. Wilson, C. Swan, M.W. Tsao, J. Rabolt: Appl. Phys. Lett. **74**, 540 (1999)
6. H.C. Weissker, J. Furthmüller, F. Bechstedt: phys. stat. sol. B **224**, 769 (2001)
7. J. Shi, S. Gider, K. Babcock, D.D. Awschalom: Metals and Semiconductors Science **271**, 937 (1996)
8. Y.M. Tairov, Y.A. Vodakov: *Group IV Materials*, ed. by J.I. Pankove, 35 (Springer Verlag, NY, 1997)
9. A. Fissel: Habilitation Physikalisch-Astronomische Fakultät der Friedrich-Schiller-Universität Jena (2002)
10. Ch. Schubert, U. Kaiser, T. Gorelik, A. Hedler, J. Kräußlich, B. Wunderlich, G. Heß, K. Goetz, U. Glatzel, W. Wesch: J. Appl. Phys. **91**, 1520 (2002)
11. M. Kossel, G. Möllenstedt: Phys. Stat. Sol. (a) **116**, 13 (1938)
12. J.W. Steeds: *Introduction to Analytical Electron Microscopy*, ed. by J.J. Hren, J.I. Goldstein and D.C. Joy (Plenum Press, New York and London, 387, 1979)
13. M. Tanaka, R. Saito, K. Ueno, Y. Harada: J. Electron Microsc. **29**, 408 (1980)
14. N.D. Browning, I. Arslan, Y. Ito, E.M. James, R.F. Klie, P. Moeck, T. Topuria, Y. Xin: J. Electron Microsc. **50**, 208 (2001)
15. D.A. Muller, T. Sorsch, S. Moccio, F.H. Baumann, K. Evans-Lutterodt, G. Timp: Nature **399**, 758 (1999)
16. U. Kaiser: Habilitation Physikalisch-Astronomische Fakultät der Friedrich-Schiller-Universität Jena (2002)
17. A.K. Head, P. Humble, L.M. Clarebough, A.J. Morton, C.T. Forwood: *Computed electron micrographs and defect identification* (North Holland, Amsterdam, 400, 1973)
18. L. Reime: *Transmission Electron Microscopy* (Springer, 3rd ed., Berlin, 1993)
19. J.C.H. Spence: Mater. Science and Engineering R **26**, 1 (1999)
20. E.J. Kirkland: *Advanced Computing in Electron Microscopy* (Plenum Press, New York, 1998)
21. K. Tsuda and M. Tanaka: Acta Cryst. A **55**, 939 (1999)
22. J.C.H. Spence, J.M. Zuo: *Electron Microdiffraction* (Plenum Press, New York, 1992)
23. J.M. Zuo, M. Kim, R. Holmstead: J. Electron. Microsc. **47**, 121 (1998)
24. S. Krämer, J. Mayer, C. Witt, A. Weickenmeier, M. Rühle: Ultramicroscopy **81**, 245 (2000)
25. J.C.H. Spence, J. Taft: J. of Microscopy **130**, 147 (1983)
26. C.J. Rossouw, P.R. Miller: J. Electron Microsc. **48**, 849 (1999)
27. J.W. Cooley, J.W. Tukey: Mathematics Computation **19**, 297 (1965)
28. U. Kaiser, K. Saitoh, K. Tsuda, M. Tanaka: J. Electron Microscopy **48**, 221 (1999)
29. P.V.C. Hough: US Patent 3.069.654 (1962)
30. A. Chuvilin, Th. Kups, U. Kaiser: Proc. Int. Conf. Electr. Micro. **15** (Durban, South Africa, 2002)
31. A.V. Crewe, J. Wall, J.P. Langmore: Science **168**, 1338 (1970)

32. S.J. Pennycook: *Ultramicroscopy* **30**, 58 (1989)
33. R.F. Egerton: *Electron Energy Loss Spectroscopy* (Plenum, New York, 1986)
34. P. Rez: in *Physical Methods of Chemistry IV*, ed. by B.W. Rossiter and I.F. Hamilton, 2nd ed., Chap. 6 (1991)
35. F. Thon, D. Willasch: *Optik* **36**, 55 (1972)
36. W. Krakow, L.A. Howland: *Ultramicroscopy* **2**, 53–60 (1976)
37. U. Kaiser and A. Chuvilin: *J. Microscopy and Microanalysis*, in print (2003)
38. C.J. Rossouw, P.R. Miller: *J. Electron Microsc.* **48** (6), 849 (1999)
39. P.R. Busek (ed.): *Minerals and reactions at the atomic scale: Transmission Electron Microscopy*, Mineral. Soc. Am., Vol. 27, (Washington D.C., 1993)
40. U. Kaiser: *J. Electr. Microscopy* **50** (3), 251 (2001)
41. M.A. O'Keefe, P.R. Busek: *Trans. Am. Cryst. Assoc.* **15**, 27 (1979)
42. P. Goodman, A.F. Moodie: *Acta Crystallogr.* **10**, 609 (1957)
43. K. Ishizuka, N. Uyeda: *Acta Cryst. A* **33**, 740 (1977)
44. J. Tersoff: *Phys. Rev. B* **37** (12), 6991 (1988)
45. J. Tersoff: *Phys. Rev. B* **38** (14), 5002 (1988)
46. J. Tersoff: *Phys. Rev. B* **39** (8), 5566 (1989)
47. E.D. Carter, P.R. Busek: *Ultramicroscopy* **18**, 241 (1985)
48. M.J. Hytch: *Microsc. Microanal. Microstruct.* **8**, 41 (1997)
49. M.J. Hytch, E. Snoeck, R. Kilaas: *Ultramicroscopy* **74**, 131 (1998)
50. U. Kaiser, I. Khodos, P.D. Brown, A. Chuvilin, M. Albrecht, C.J. Humphreys, A. Fissel, W. Richter: *J. Mater. Res.* **14**, 3226 (1999)
51. R. Anderson (ed.): *Mat. Res. Soc. Symp. Proc. V 199*, Mat. Res. Soc. Pittsburg (1990)
52. Á. Barna: *MRS. Proc.* **254**, 3–10 (1992)
53. S.D. Walk, J.P. McCaffrey: *MRS Proc.* **480**, 149 (1997)
54. M.H.F. Overwijk, F.C. van den Heuvel, C.W.T. Bulle-Lieuwma: *J. Vac. Sci. Technol. B* **11**, 2021 (1993)
55. Á. Barna, G. Radnóczy, B. Pécz: *Handbook of Microscopy*, ed. by S. Amelinckx, D. van Dyck, J. van Landuyt, G. van Tendelo, Vol. 3, Chap. II/3, 751 (VCH Verlag, 1997)
56. Á. Barna, B. Pécz, M. Menyhard: *Ultramicroscopy* **70**, 161 (1998)
57. K. Moriguchi, A. Shintani: *Jpn. J. Appl. Phys.* **37**, 414 (1998)
58. U. Kaiser, Th. Kups, A. Fissel, W. Richter: *Crystal Res. Techn.* **37**, 466 (2002)
59. J. Kräußlich, A. Bauer, B. Wunderlich, K. Goetz: *Mater. Sci. For.* **353–356**, 319 (2000)
60. A. Fissel, U. Kaiser, B. Schröter, W. Richter, F. Bechstedt: *Appl. Surf. Sci.* **184**, 38 (2001)
61. U. Kaiser, K. Saitoh, K. Tsuda, M. Tanaka, W. Richter: *Inst. Phys. Conf. Ser.* **169**, 363 (2001)
62. U. Kaiser, D.A. Muller, A. Chuvilin, G. Pasold, W. Witthuhn: *Microscopy and Microanalysis*, accepted (2002)
63. U. Kaiser, D.A. Muller, J. Grazul, A. Chuvilin, M. Kawasaki: *Nature Materials* **1**, 182 (2002)
64. U. Kaiser, J. Biskupek, K. Gärtner: *Phil. Mag. Lett.* **83** (4), 253 (2003)
65. U. Kaiser, J. Biskupek, D.A. Muller, K. Gärtner, Ch. Schubert: *Crystal Res. and Techn.* **37**, 391 (2002)
66. U. Kaiser and J. Biskupek: 11th Ann. Meet. German Crystallo. Soc. (Berlin, 12.–15.03.03)
67. J.P. Morac, P.E. Batson, J. Tersoff: *Phys. Rev. B* **47**, 4107 (1993)
68. P.E. Batson, J.R. Heath: *Phys. Rev. Lett.* **71**, 911 (1993)

# Synchrotron White Beam X-Ray Topography and High Resolution X-Ray Diffraction Studies of Defects in SiC Substrates, Epilayers and Device Structures

M. Dudley, X. Huang, and W.M. Vetter

A general review will be presented of recent Synchrotron White Beam X-ray Topography (SWBXT) studies of defects in SiC single crystals and epitaxial layers carried out at Stony Brook and at the Stony Brook Synchrotron Topography Station at the National Synchrotron Light Source, Brookhaven National Laboratory. Results will be presented from studies of (a)  $4H$  and  $6H$ -SiC substrates growth by Physical Vapor Transport, (b) homoepitaxial layers grown on such substrates, (c) heteroepitaxial layers grown on  $4H$  substrates, and (d) SiC device structures. SWBXT results will be correlated with those from AFM, Nomarski Optical Microscopy, High Resolution X-ray Diffraction (HRXRD), SEM and TEM studies carried out on the same crystals. From (a), substrate defects observed include closed-core and hollow-core screw dislocations (micropipes) in  $6H$  and  $4H$ , deformation-induced basal plane dislocations in  $6H$  and  $4H$ ; and small angle boundaries in  $4H$ . The close correlation between simulated and observed back-reflection, grazing-incidence reflection and transmission SWBXT images of screw dislocation will be discussed. From (b) results from studies of the correlation between substrate and epilayer defects in  $6H/6H$  homoepitaxial layers will be presented. From (c) polytype mapping in  $3C/4H$ -SiC heterostructures will be described. The relationship between substrate and epilayer defects will again be explored as will the lattice mismatch between epilayer and substrate as indicated by a combination of SWBXT and HRXRD. High-precision measurements of lattice parameters by X-ray multiple-order reflections enable detailed determination of both in-plane and out-of-plane mismatch. In (d) observations of stacking fault generation during device operation will be presented.

## 1 Introduction

Silicon carbide (SiC) is a prominent material for various high-temperature and high-power electronics technologies due to its large bandgap, thermal conductivity and breakdown voltage among other outstanding properties [1, 2]. The past decade has seen rapid advances of SiC technology, mainly led by steady improvement in the quality and size of SiC crystals. Diameters of commercial boules currently approach four inches while defect densi-

ties have dropped substantially [3]. Despite these achievements, however, the overall crystalline quality of SiC is still far inferior to Si or GaAs. SiC crystals generally contain various defects, such as dislocations, stacking faults, inclusions, polytypes (with  $3C$ ,  $4H$ ,  $6H$  and  $15R$  being the most common ones among many possible polytypes), small-angle boundaries, etc, among which “micropipes” and closed-core threading screw dislocations running along the  $[0001]$  growth axis have been the most severe problem as they affect almost every aspect of SiC technology [4]–[7]. These dislocations, called “superscrew dislocations” (SSDs) in the following, are growth screw dislocations possessing Burgers vectors in integer multiples of the  $c$  lattice parameter. The Burgers vectors of hollow-core micropipes are in the range from 30 Å to over 100 Å, and Frank’s relationship between the Burgers vectors and the hollow core diameters (ranging from 0.1 to a few micrometers in general) has been experimentally confirmed [8, 9]. SSDs with smaller Burgers vectors generally have no obvious hollow cores. The Burgers vectors of closed-core SSDs are  $1c$  or  $2c$  for  $4H$ -SiC and  $1c$  for  $6H$ -SiC ( $c = 10$  Å for  $4H$  and  $= 15$  Å for  $6H$  being the lattice constant along  $[0001]$ ), which are still much larger than those in Si or GaAs.

Although the density of hollow-core SSDs has been possibly reduced to be less than  $1\text{ cm}^{-2}$  in recent years [3], the densities of closed-core SSDs are still no less than  $10^2\text{ cm}^{-2}$  for almost all commercial SiC wafers. In addition to the fact that they severely degrade the crystalline quality and can trigger the formation of other defects during growth and epitaxy, SSDs in SiC are most detrimental to devices fabricated within their wide-range strain fields [6, 7]. For this reason, crystal characterization is an indispensable step for SiC growth, epitaxy and many other processes. Synchrotron White Beam X-ray Topography (SWBXT), with its high strain sensitivity and suitable spatial resolution, is apparently the technique of choice for this aim. In fact, SWBXT has played a very strong role in the progress of SiC growth by providing a thorough understanding of the nature and origins of SSDs and other defects [5],[10]–[13]. It has been, to date, one of the most accurate and reliable methods for discerning both the distribution and character of SSDs in SiC wafers, and has been widely adopted by the SiC community as a major characterization technique.

In this paper, we present an overview of the various SWBXT imaging techniques and their basic principles for characterization of SiC crystals. These techniques include back-reflection topography, reticulography, transmission topography, and a set of section topography techniques. Apart from their particular strengths, these techniques have a common underlying principle in that the topographic contrast originating from defects (particularly SSDs) in SiC is dominated by “orientation contrast”, which may be accurately simulated with the ray-tracing method. For this reason, SSDs in SiC have been demonstrated to be a “magnified” model to quantitatively investigate the detailed contrast formation mechanisms of dislocations in X-ray topography

and to test the fundamentals of dislocation theory that have rarely been verified from experiments in the past [1]–[14]. In Sect. 4, we will also discuss the influence of SSDs on heteroepitaxial growth of 3C-SiC films on 4H and 6H-SiC and the applications of SWBXT in combination of high-resolution X-ray diffraction (HRXRD) for characterizing these heterostructures.

## 2 Back-Reflection Techniques

In applying SWBXT to characterization of SiC crystals, researchers have developed a set of special diffraction schemes, among which back-reflection topography is apparently the most efficient method for imaging SSDs in commonly (0001)-orientated SiC wafers [4, 5, 11]. In this diffraction scheme, the recording film, located at the incidence side, is set parallel to the sample surface so as to minimize projection distortion. The  $000n$  symmetric back reflections have the highest strain sensitivity for SSDs since the Burgers vectors are parallel to [0001]. In experiments, the Bragg angle of the  $000n$  harmonics is made large enough (usually around  $80^\circ$ ) to achieve high topographic resolution. As can be seen from the topograph in Fig. 1, the SSDs, either hollow-core or closed-core, are clearly revealed as circular white spots surrounded by black rings. Such white-black contrast enables us to easily discern each in-

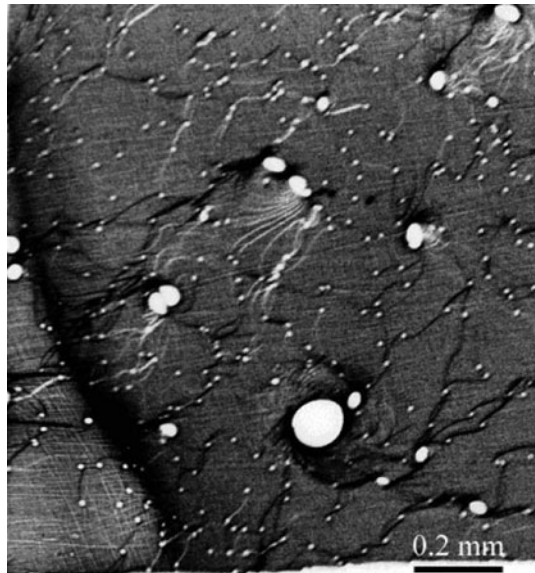


**Fig. 1.** SWBXT back-reflection image recorded from a 6H-SiC (0001) wafer thinned to around  $30\text{ }\mu\text{m}$ . The *large circular images (black rings surrounding white circles)* correspond to micropipe images and the *smallest white spots* are images of closed-core screw dislocations. Sample-to-film distance  $D_{\text{sf}} = 10\text{ cm}$

dividual SSD. By employing a scanning device, one can currently take large topographs from SiC wafers up to several inches in diameter at the Stony Brook Topography Facility [15]. Consequently, the detailed distributions of SSDs in these large wafers can be accurately mapped.

In back-reflection topography, the effective diffracting volume is of only a few micrometers in thickness beneath the crystal surface. Thus, new SSDs formed in homoepitaxial films of less than  $1\text{ }\mu\text{m}$  in thickness can still be clearly imaged. This makes back-reflection topography also suitable for characterization of SiC epilayers. Moreover, the imaging can even be performed on wafers with devices fabricated on them, further emphasizing the advantages of this technique [6, 7].

The black-white contrast of the circular SSD images in Fig. 1 mainly consists of “orientation contrast” arising from overlap or separation of the diffracted X-rays with slightly different directions. As shown in Fig. 2a, due to the helical structure of the screw dislocation, the (0001) lattice plane around a dislocation core is no longer a flat plane. According to the lattice displacement field  $u_z = b\theta/2\pi$  of a screw dislocation, the continuously varying normals ( $\mathbf{n}$ ) to the (0001) lattice plane form a series of twisted cylinders surrounding the dislocation core. Meanwhile, the Bragg law of white-beam diffraction is identical to the optical reflection principle. Thus, the (0001) plane around the core can be considered as a *curved mirror*. When a (nearly) parallel synchrotron white beam is incident on the “mirror”, it can be verified that X-rays diffracted from successive circular rings form a series of *twisted cones*. The overlap of these cones in space (Fig. 2b) results in the formation of the circular images. Based on this principle, one can actually use the ray-tracing method to simulate the SSD contrast [5, 11].

In this simulation process, the crystal surface around a dislocation core is divided into small equal-size squares. Based on the local surface normal (parallel to the local diffraction vector) that can be accurately calculated from the lattice displacement field  $u_z = b\theta/2\pi$ , the direction of the microbeam

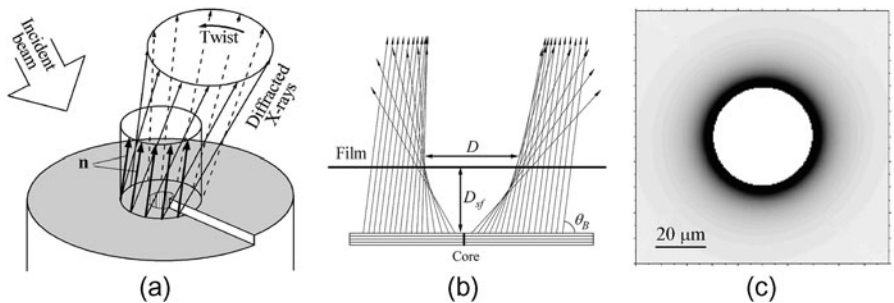


**Fig. 2.** The contrast formation mechanism of SSDs on SWBXT back-reflection topographs. (a) Formation of twisted diffraction cones. (b) Section view of the diffraction cones. (c) A simulated image of an SSD with  $b \approx 90\text{ }\text{\AA}$  and  $D_{sf} = 20\text{ cm}$

diffracted from each square can be determined. Geometrically projecting all the microbeams onto the recording film along their traces then gives the intensity distribution of the *direct dislocation image*. For example, Fig. 2c shows a simulated back-reflection image of a SSD, which is quite consistent with the recorded images in Fig. 1.

Back-reflection images of SSDs contain abundant information concerning the dislocation structures. The most important information is that the spot diameter  $D$  increases monotonically with increasing  $D_{\text{sf}}$  and  $b$  ( $D_{\text{sf}}$  and  $b$  being the sample-to-film distance and the magnitude of the Burgers vector, respectively), as can be seen from Fig. 2b. Based on the relationship between these three quantities [11], one can easily estimate the Burgers vector magnitude of each SSD from the diameter of its circular image on the topograph.

The other kind of information of the SSD predicted by the geometrical diffraction principle is the sense of the Burgers vector. As indicated in Fig. 2a, a left-handed screw dislocation gives rise to the anti-clockwise twist of the diffraction cones (viewed toward the surface). Accordingly, a right-handed screw dislocation makes the diffraction cones twist clockwise. Although it is totally hidden by the circular symmetry of SSD images on the projection topograph, this twisting effect can be readily revealed by back-reflection section topography. In this method, the incident beam is limited to be around 5–20  $\mu\text{m}$  in width and directed to cover the dislocation core. Then a partial image of the SSD is formed, which consists of two tails that clearly indicate the rotation of the diffracted X-rays [5]. Unfortunately, it is time-consuming to make the narrow beam exactly cover the dislocation core in experiments. This difficulty, however, can be easily avoided in reticulography.

Synchrotron X-ray reticulography is a new versatile method developed by Lang and his co-workers [16, 17] for mapping misorientations in single crystals. In reticulography, a fine-scale X-ray absorbing mesh is placed between the sample and the recording film such that it splits the diffracted beam into an array of individually identifiable microbeams. From the relative shifts of the distorted mesh images on the topograph, one can measure the direction differences between these microbeams and consequently the misorientations of the corresponding diffracting elements in the crystal with the angular resolution up to sub-arcsec.

Coincidentally, the principles of reticulography and the above simulation process are nearly identical if the absorbing mesh is placed very close to the sample surface. But in actual imaging processes, large sample-to-mesh distances are usually used in order to amplify the distortion of the mesh image. Figure 3 is a synchrotron back-reflection reticulograph taken from a 6H-SiC (0001) wafer that contains a large micropipe with Burgers vectors  $b \approx 309 \text{ \AA}$ , where the significant rotation of the mesh image around the micropipe image is clearly discernible. The clockwise rotation of the mesh image here unambiguously indicates that the micropipe imaged is a right-handed SSD. Thus, reticulography provides a direct and reliable way to reveal

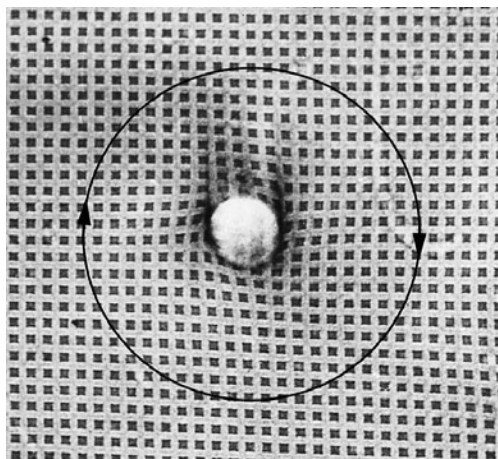


**Fig. 3.** Synchrotron back-reflection reticulograph of a micropipe taken from a  $6H$ -SiC (0001) as-grown surface. Field width 0.53 mm (mesh periodicity  $17\text{ }\mu\text{m}$ ).  $2\theta_B = 135^\circ$ . Arrow indicating the twist direction of the diffracted X-rays.  $D_{sf} = 7\text{ cm}$ . Courtesy of A.R. Lang [17]

the senses of SSDs in SiC. Meanwhile, reticulographs such as Fig. 3 directly verifies the justification of the above geometrical diffraction principle used in simulating SSD contrast on back-reflection topographs.

The determination of Burgers vector senses for SSDs has a practical significance in that it can help us understand the formation mechanism of SSDs during growth. In SWBXT studies of thin SiC Lely platelets or thin films, it has been frequently found that SSDs are formed in pairs with the same Burgers vector magnitude but with opposite senses. Based on this phenomenon, we have proposed a nucleation model that SSDs in SiC be generated at inclusions in the form of SSD pairs or groups with zero net Burgers vector [18]. This model is consistent with the conservation of Burgers vectors inside a single crystal and has been experimentally confirmed by Sanchez et al. [19].

### 3 Transmission Topography Techniques

In back-reflection geometry, the SSDs images are “magnified” by large sample-to-film distances (from 10 cm to meters). Such large imaging distances are possible only for synchrotron radiation that has high natural collimation. While back-reflection topography can only be performed with some difficulty using laboratory X-ray sources [13], conventional transmission topography is suitable for both synchrotron and laboratory sources in characterization of SiC crystals. Besides SSDs, defects that have been revealed by transmission topography in SiC include basal plane dislocations, stacking faults, partial dislocations, inclusions, voids, small-angle boundaries [4],[15],[20]–[22].

Similar to ordinary screw dislocations, SSDs in longitudinally cut SiC wafers (parallel to the  $[0001]$  axis) appear as well-defined double-contrast images in transmission topographs. Using section topography one can also readily discern the sense of the Burgers vector from the relative shifts of the two columns. These images can again be rigorously simulated with the above ray-tracing method [11, 12, 23].

However, a confusing phenomenon that has long been found in transmission topography of SiC and ZnS crystals is that when the diffraction vector is strictly perpendicular to the dislocation line, the SSD may still show strong contrast [23]–[25], as shown in Fig. 4. Such contrast was previously believed to originate either from new wavefields induced by the hollow cores or from the dense basal plane dislocations that are generally pinned at the SSDs. Nevertheless, the obvious failure of the  $\mathbf{g} \cdot \mathbf{b} = 0$  criterion made it unconvincing that SSDs in SiC and ZnS are pure screw dislocations. In fact, it has been indeed argued that micropipes in SiC could be mixed dislocations with large edge components. Based on this assumption, Heindl et al. [26] claimed that micropipes are generated from basal plane dislocations, which, however, is apparently in contradictory to the nucleation model mentioned in Sect. 2.

Our group recently demonstrated that SSD contrast formed under  $\mathbf{g} \cdot \mathbf{b} = 0$  can be quantitatively explained by the in-plane strains (parallel to the surface) induced from the dislocation image force near the crystal surface (i.e. surface relaxation effect) [14]. Consider a screw dislocation in a thin

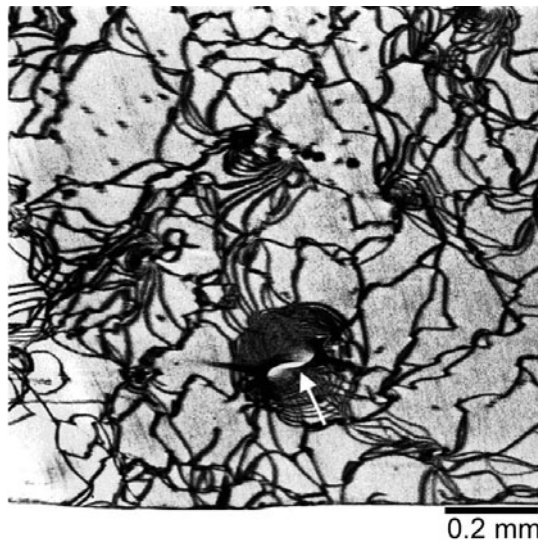


**Fig. 4.** SWBXT transmission image recorded from the same region of crystal in Fig. 1. The arrowed contrast feature is a micropipe image, and the surrounding *black rings* (as well as the *black lines* elsewhere) are basal plane dislocation images.  $\mathbf{g} = 11\bar{2}0$  (along the arrow).  $D_{sf} = 10$  cm

parallel-sided crystal plate of  $2t$  in thickness that is perpendicular to the plate surfaces. Taking into account the free surface requirement, Eshelby and Stroh have derived the additional in-plane displacement field as

$$u_\theta = -\frac{b}{2\pi} \sum_{n=0}^{\infty} (-1)^n \left\{ \frac{r}{t_{1n} + \sqrt{t_{1n}^2 + r^2}} - \frac{r}{t_{2n} + \sqrt{t_{2n}^2 + r^2}} \right\} \quad (1)$$

in the cylindrical coordinate system, where  $t_{1n} = (2n + 1)t - z$  and  $t_{2n} = (2n + 1)t + z$  [27]. This component indicates that crystal lattice around the dislocation core is rotated, and the rotation extent depends on both  $z$  and  $r$ . Based on this model, the SSD image for  $\mathbf{g} = 11\bar{2}0$  has been successfully simulated using the above ray-tracing method [14]. The good agreement between the simulated and recorded images hence *quantitatively* verifies, for the first time, the existence of dislocation image forces near crystal surfaces. Meanwhile, no edge components of the Burgers vector could be detected in such investigations, which further proves that micropipes in SiC are pure screw dislocations.

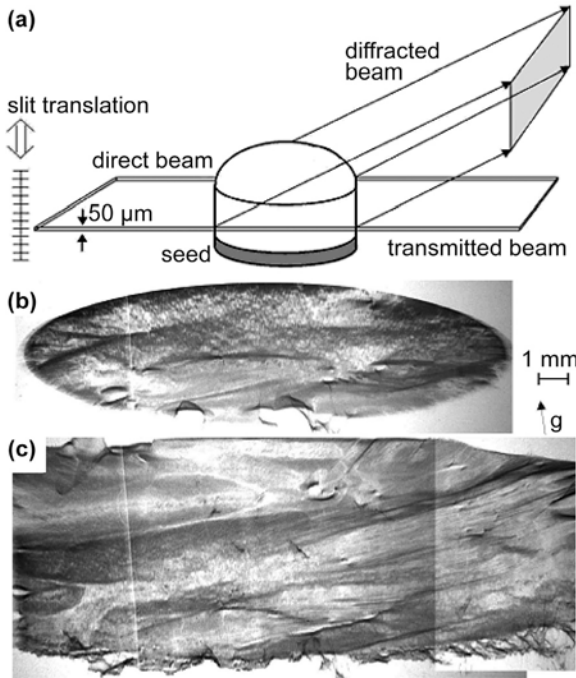


**Fig. 5.** (a) The section topography arrangement for imaging bulk SiC crystals. (b) and (c) are two section topographs recorded with the slit set at the level of the ingot dome (near the ingot end) and near the seed of a 6H-SiC crystal, respectively. The largest part of the ingot is 3.5 cm in diameter. Courtesy of E. Pernot and P. Pernot-Rejmánková [29]

In addition to the transmission projection topography technique that is suitable for thin wafers, it has been recently demonstrated by Pernot et al that synchrotron section topography in transmission geometry can be used to image defects in large SiC ingots without slicing [28, 29]. The experimental arrangement is depicted in Fig. 5a, where a synchrotron white beam of a few tens of micrometers in height is made to penetrate the whole crystal (based on the high energy and intensity of synchrotron radiation and light X-ray absorption of SiC crystals). Consequently, X-ray diffraction occurs in the entire lamella illuminated by the incident beam, while the diffracted beam can still penetrate the bulk crystal to reach the recording film.

In the diffraction process, it seems that both the dynamical diffraction effect and rescattering of the diffracted beam along its long path inside the bulk is negligible. Therefore, the contrast formed on the recording film is mainly from defects located in the thin illuminated lamella. Figures 5b,c show two such section topographs taken at different heights from a SiC ingot, where the defects are clearly revealed. The distinguishing advantage of this imaging technique is that one can quickly take a series of successive section topographs by translating the beam or sample vertically. Then it is possible to use these topographs to reconstruct the spatial distribution of defects inside the crystal. Such a three-dimensional map of the formation and propagation history of defects is invaluable feedback to the crystal grower.

A type of stacking fault, whose outline has the form of either a parallelogram or triangle, has been observed to develop in the epilayer portion of hexagonal SiC diodes during their operation under forward carrier injection [18, 19]. Its growth correlates with a degradation of electrical performance, an increase in the forward voltage drop [20].

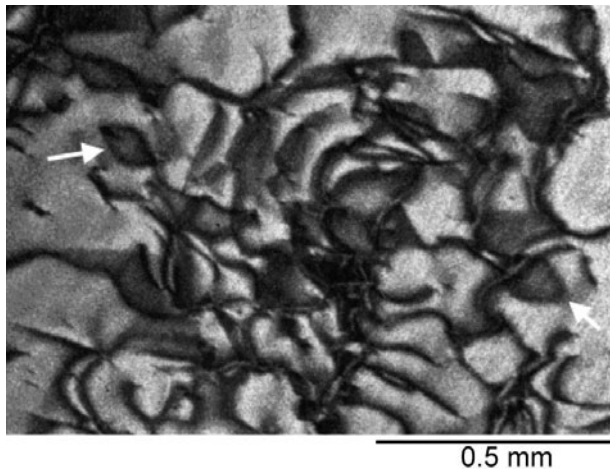


**Fig. 6.** Transmission image recorded from degraded diode. Note faults, e.g. at  $S(g = 10\bar{1}0, \lambda = 0.65 \text{ \AA})$

A transmission SWBXT of an area of a diode taken after its metallization and much of the thickness of its substrate had been removed is shown in Fig. 6. Examination of a series of topographs taken using various  $g$ -vectors showed that the bounding partials of these faults extinguished entirely in one of the  $(11\bar{2}0)$  reflections, indicating that the faults have the nature of dislocation loops of Burgers vector  $1/3\langle 10\bar{1}0 \rangle$ , a Shockley partial dislocation [21], consistent with previously reported TEM results [22].

## 4 Characterization of SiC Heterostructures

SiC is not only a promising substrate material for III-nitrides but  $4H$  and  $6H$ -SiC have also attracted much attention as substrates for epitaxial growth of  $3C$ -SiC since the in-plane lattice mismatch for such heterostructures is almost negligible in the basal planes while the bandgap differs significantly across the interfaces. Unfortunately,  $3C$  epilayers grown on  $4H$  or  $6H$  substrate generally contain high densities of defects including double-positioning boundaries and stacking faults. Threading SSDs in the substrate play a significant role in the formation of these defects. Firstly, SSDs cannot coherently propagate into the  $3C$  epilayers due to the difference in stacking sequence and periodicity. Instead, the termination of SSDs at the interfaces induces other defects to compensate the Burgers vectors. Secondly but more significantly, the self-regenerating atomic steps (spirals) of SSDs widely spread on the entire substrate surface can cause more defects in the epilayer [30].

It is worth mentioning that the existence of SSDs and small-angle boundaries in SiC substrates generally makes it difficult to solely use high-resolution X-ray diffraction (HRXRD) techniques to characterize epilayers grown on them because these defects themselves can give rise to multiple peaks in the rocking curves. Therefore, small-beam footprints are required for the HRXRD measurements. On the other hand, back-reflection topographs are of great help for one to direct the small X-ray beam to areas free of SSD and small-angle boundaries.

In characterization of  $3C/4H$  or  $3C/6H$  heterostructures, an important task is to verify the  $3C$  structure of the epilayer since homoepitaxy or formation of other polytypes may easily occur if the heteroepitaxy conditions are not well controlled. Moreover,  $3C$  epilayers grown on the  $(0001)$  surface can have two twinned variants due to the symmetry decrease from a 6-fold rotation operation along  $[0001]$  in the substrate to a 3-fold one along  $[111]$  in the epilayers. SWBXT is capable of identifying the polytype and mapping the variant distribution since each SiC polytype or variant has its unique Laue pattern. Based on such a map, small-beam HRXRD measurements can subsequently be performed for selected areas.

As an example, here we briefly introduce a study recently carried out in our group for characterization of  $3C/4H$ -SiC heterostructures using SWBXT and HRXRD [31]–[33]. In this research, the first task is to produce atomically

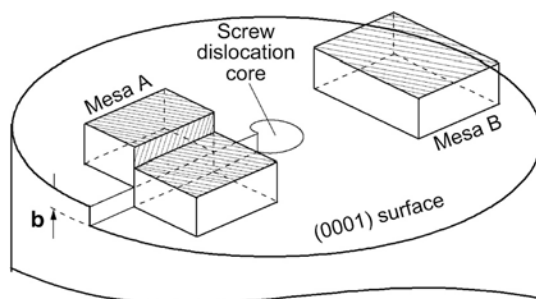


**Fig. 7.** Effects of mesas for disconnecting screw dislocation spirals on the (0001) SiC surface

flat  $4H$  (and  $6H$ ) substrate surfaces for epitaxial growth of  $3C$  films since the presence of atomic steps (resulted either from slight miscut or from the helical (0001) lattice planes around SSDs) on the surface means that different termination stacking sequences will be present side by side near a step so that if two-dimensional (2D) nucleation of  $3C$  occurs, more than one variant will nucleate on a given mesa. The steps may also induce other high-density extended defects in the films, resulting in poor film quality and degraded device performance.

In order to remove the atomic steps, the  $4H$  substrate surface was first patterned into an array of mesas by etching suitable trenches. Then if a mesa contains no SSD cores, its surface is either a flat or stepped surface, as represented by mesas A and B in Fig. 7, respectively. For stepped mesas, the step segments are isolated from the original step lines. The patterned surface was subsequently subjected to a homoepitaxial procedure designed to “grow out” all atomic steps based on the “step-flow” growth mechanism. Note that if the surface is not patterned, the homoepitaxial process can grow out only the steps arising from miscut, but not those from SSDs since the threading SSDs are continual sources of steps. Similarly, the mesas containing SSD cores are still stepped even after homoepitaxy, but the SSD core-free mesas can become atomically flat. If heteroepitaxial growth is carried out afterwards, the flat mesas will experience uniform nucleation of one of the two  $3C$  variants, resulting in high-quality  $3C$  epilayers.

SWBXT mapping of the distribution of the polytypes and their variants was carried out in grazing-incidence geometry. Due to the difference in crystal symmetry or orientation between the two  $3C$  variants and the substrate, the Laue pattern consists of three sets of diffraction spots corresponding to the three structures, respectively. Each  $3C$  variant has several unique topographs that are not overlapped by reflections from the other variant or the substrate. Figure 8 shows a small portion of the Laue pattern taken from a  $3C/4H$ -SiC heterostructure under the grazing-incidence diffraction geometry. After correcting the projection distortion, one can superimpose two such topographs

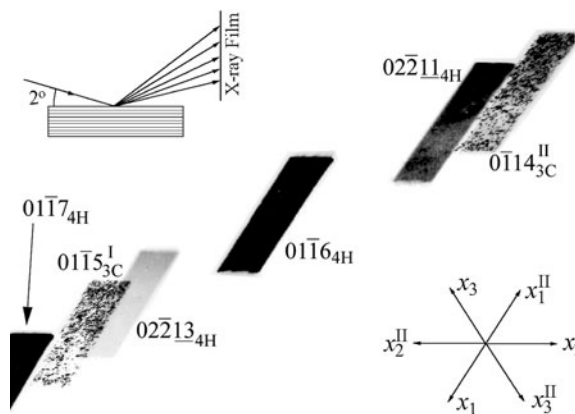


**Fig. 8.** Grazing-incidence SWBXT Laue pattern of 3C/4H-SiC heterostructure. *Upper-left inset* illustrates diffraction geometry. (0001) surface. Incidence nearly along  $[\bar{1}010]$ . *Lower-right inset* shows the hexagonal coordinates used for indexing the diffraction spots.  $x_1x_2x_3$  is the common coordinate system for 3C variant I and 4H while  $x_1^{II}x_2^{II}x_3^{II}$  is related to  $x_1x_2x_3$  by a  $180^\circ$  rotation operation for indexing 3C variant II. Here the  $01\bar{1}6_{4H}$  spot was over exposed in order to show the weak reflections

that are unique to the two 3C variants, respectively, onto the back-reflection image of the substrate to form a single topograph showing the distribution of the 3C variants and the positions of the SSDs across the sample. Figure 9a shows an image that is made up of the superimposition of such three topographs. Interestingly, 3C epilayers were formed only on atomically flat mesas while they are almost completely absent in the trenches as well as on some mesas containing SSD cores.

The detailed crystalline quality of the 3C-SiC epilayers was investigated by HRXRD. The diffractometer used was a Bede D1 system with two Si (220) channel-cut crystals as the beam conditioner in the four-bounce mode. The conditioned X-ray beam was then limited by a pinhole of 1 mm in diameter. In triple-axis diffraction, a Si (220) channel-cut analyzer was used in the symmetric four-bounce mode. By selecting areas with sparse 3C coverage, we were able to let the X-ray beam bathe only a single mesa covered by a single 3C variant.

The arrowed mesa in Fig. 9a is a  $0.4 \times 0.4 \text{ mm}^2$  terrace fully covered by a single-variant 3C epilayer, as indicated by the pure (blue) color. Figure 9b is the 0004 rocking curve taken from this mesa. The substrate peak is very sharp, with the full width at half maximum (FWHM) being 15.3 arcsec, indicating that the mesa contains no dislocation core. Obviously, the well-shaped peak at the right side of the substrate peak is from the epilayer. The FWHM value of this peak is 17.3 arcsec, from which we can estimate that the epilayer thickness is around 0.9  $\mu\text{m}$ . This peak provides further convincing

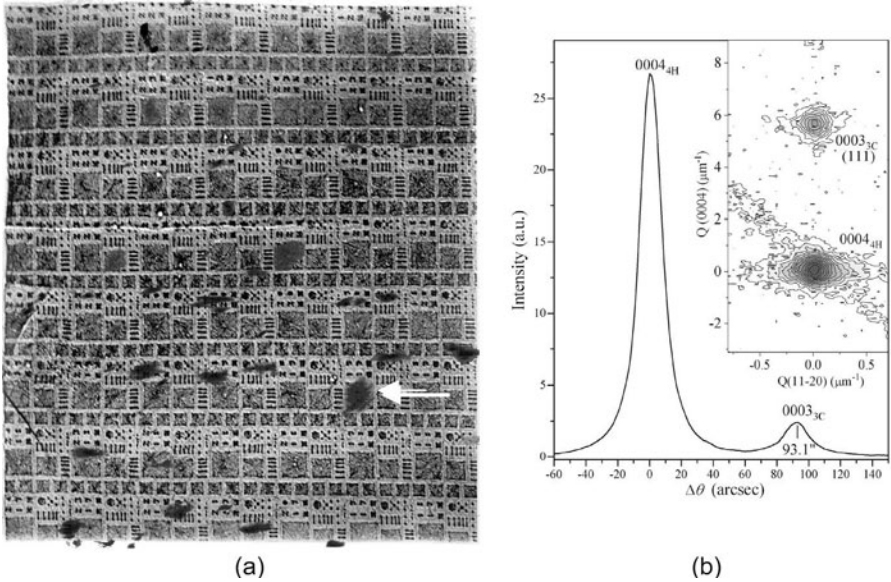


**Fig. 9.** (a) Composite image showing the distribution of 3C(I) and 3C(II) (darker regions) in the 3C/4H-SiC heteroepitaxial structure. (b) 0004 rocking curve of the arrowed mesa in (a). CuK $\alpha_1$  radiation. Inset is the triple-axis reciprocal space map, in which the inclined streak on 0004<sub>4H</sub> is the analyzer streak

proof that a high-perfection 3C epilayer with macroscopic homogeneity was indeed formed on the mesa studied. The angular separation between the two peaks indicates that the out-of-plane lattice mismatch is  $\Delta c/c = -0.14\%$ , where  $c$  should be understood as the average thickness of the Si-C bilayer ( $c_{3C} < c_{4H}$ ).

To further evaluate the crystalline quality of the 3C-SiC epilayers, we have performed triple-axis diffraction for mesas with well-defined rocking curves. The two-dimensional 0004<sub>4H</sub>/0003<sub>3C</sub> reciprocal space map corresponding to the rocking curve in Fig 9b is plotted in the inset, where the upper and lower peaks (spots) are the epilayer and substrate peaks, respectively. Note that in a reciprocal map, the peak spread along the vertical  $Q(0004)$ <sub>4H</sub> direction indicates statistically the extent of the out-of-plane  $d$ -spacing variation while lattice tilt is reflected by the spread along the horizontal  $Q(11\bar{2}0)$  direction. Therefore, the fact that the centers of the two peaks are well aligned on a vertical line shows that there is no misorientation between the epilayer and substrate (i.e. the (0001)<sub>3C</sub> and (0001)<sub>4H</sub> lattice planes are parallel to each other).

Although the out-of-plane mismatch can be readily calculated as  $\Delta c/c \approx -0.14\%$  ( $c_{4H} > c_{3C}$ ) from the symmetric-reflection rocking curve in Fig. 9b, the measurement of the in-plane mismatch for 3C/4H heterostructure is difficult. A full examination of reciprocal space shows that  $11\bar{2}8_{4H}$  and  $11\bar{2}6_{3C}$

(cubic index  $402_{3C}$ ) are the only two asymmetric reflections with closely matched Bragg angles. However, in the glancing-exit geometry, it was found that these two peaks are so close to each other that it is difficult to separate them. This makes it difficult to use the conventional asymmetric reflection scheme [34] to measure the in-plane mismatch.

In fact, HRXRD is a comparative method mainly used to measure lattice mismatch in heterostructures. In this method, only when the lattice parameter of one component, usually the substrate, is known can one derive the parameters of other components. This limitation arises from the uncertainty in the zero setting, i.e., the absolute value of the measured diffraction angle is inaccurate while the only reliable quantity measured is the angular difference. Therefore, in conventional HRXRD studies of heterostructures, we are in general unable to measure the absolute angular positions of the Bragg peaks. By assuming that the precise values of the substrate lattice constants are known, one can calculate the absolute Bragg angle of the substrate. Consequently, the absolute position of the epilayer peak may be obtained from its deviation from that of the substrate peak. For largely mismatched heterostructures, or when the epilayer(s) and substrate differ significantly in orientation or crystal symmetry, however, this method usually fails.

Here we present a very simple method that is based on multiple-order reflections for solving the uncertainty of the zero setting. The basic principle can be illustrated using the 0004 and 0008 symmetric Bragg reflections of  $4H$ -SiC in the inset of Fig. 10. Let  $\theta_1$  and  $\theta_2$  be the Bragg angles of these two reflections. Then the two Bragg equations are

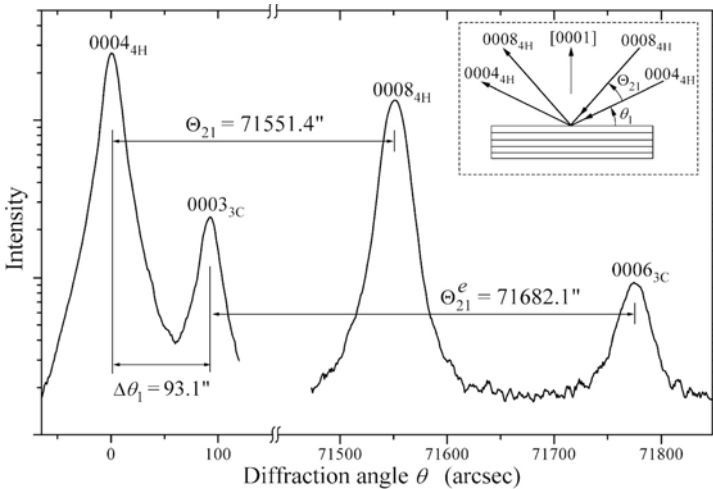


**Fig. 10.** Rocking curves and peak positions of  $0004_{4H}$  ( $0003_{3C}$ ) and  $0008_{4H}$  ( $0006_{3C}$ ) reflections measured from a wide-range  $\theta - 2\theta$  scan. *Inset* schematically shows the relationship between  $0004_{4H}$  and  $0008_{4H}$  Bragg reflections

$$2d \sin \theta_1 = \lambda, \quad (2)$$

$$2(d/2) \sin \theta_2 = \lambda, \quad (3)$$

where  $d$  is the spacing of the (0004) lattice planes and  $\lambda$  the X-ray wavelength. In a wide-range  $\theta - 2\theta$  scan that covers both Bragg peaks, the measured  $\theta_1$  and  $\theta_2$  are generally not accurate, but their difference,  $\Theta_{21} = \theta_2 - \theta_1$ , is an accurate quantity independent of the zero setting. Surprisingly, (2) and (3) indicate a very simple relationship between  $\Theta_{21}$  and  $\theta_1$ :

$$2 \sin \theta_1 = \sin(\theta_1 + \Theta_{21}). \quad (4)$$

Obviously,  $\theta_1$  can be numerically solved from (4) to any precision based on the measured  $\Theta_{21}$ . Then the true zero point is determined to be  $-\theta_1$  relative to 0004 peak. Inserting the calculated  $\theta_1$  into (2) immediately gives the absolute value of  $d$ , provided that  $\lambda$  is known.

From (2) and (4) the measurement precision can be derived as

$$\frac{\Delta d}{d} = \frac{\cot \theta_1 \cos(\theta_1 + \Theta_{21})}{\cos(\theta_1 + \Theta_{21}) - 2 \cos \theta_1} \Delta \Theta_{21}. \quad (5)$$

As an example, the  $c$  lattice constant of 4H-SiC is roughly 10.08 Å, which gives  $\theta_1 = 17.80^\circ$  and  $\Theta_{21} = 37.69^\circ$ , respectively for CuK $\alpha$ 1 radiation ( $\lambda = 1.540562$  Å). The precision of  $\Theta_{21}$  measured by double-crystal diffractometer is usually in the order of sub-arcsec. If we choose  $\Delta \Theta_{21} = 0.2''$ , (5) gives  $|\Delta d/d| = 2 \times 10^{-6}$ . This is in fact a high precision (comparable to that of the Bond method) adequate for most applications, and it can be further improved using high-angle reflections (e.g.  $|\Delta d/d| = 2 \times 10^{-7}$  for Si 333 and 444).

The specimen alignment is almost the same as that in other single-crystal diffraction procedures. In the preferred symmetric Bragg reflection geometry, only the tilt angle  $\chi$  of the specimen should be carefully adjusted so that the misalignment is minimized within  $0.02^\circ$ . A simple way to achieve this is to adjust  $\chi$  to make the measured  $\theta_2$  angle smallest. When this condition is satisfied, both  $\theta_1$  and  $\Omega_{21}$  are spontaneously minimized.

In order to make the lattice parameter measurement reach a precision of  $10^{-6} \sim 10^{-7}$ , the goniometer is required to have a calibrated angular accuracy of sub-arcsec for rotation ranges of several tens of degrees. Such calibration is generally a very difficult task, but it can be easily realized with multiple-order reflections.

In addition to the 0004 and 0008 reflections of 4H-SiC considered above, let us include a third reflection, 00012 with a Bragg angle  $\theta_3$ . Combining the corresponding Bragg equation  $2(d/3) \sin \theta_3 = \lambda$  with (2) gives another equation

$$3 \sin \theta_1 = \sin(\theta_1 + \Theta_{31}), \quad (6)$$

where  $\Theta_{31} = \theta_3 - \theta_1$ . Again  $\Theta_{31}$  can be precisely measured in the  $\theta - 2\theta$  scan. On the other hand, using the value of  $\theta_1$  obtained from the above measure

$\Theta_{21}$ , one can actually calculate  $\Theta_{31}$  from (6). If the goniometer is accurate, the measured and calculated values of  $\Theta_{31}$  must be identical (in other words, the zero points determined by the 0004/0008 and 0004/0001 $\bar{2}$  reflection pairs should be identical since they both refer to the unique zero point of the (0001) planes). Otherwise, adjusting the related instrumental parameters (usually of the angular encoder) to make these two values equal can lead to precise calibration. The unique advantage of this calibration procedure is that it only involves (4) and (6) and is independent of the detailed values of  $d$  and  $\lambda$ . Therefore, the calibration is based on a pure geometric effect.

We have used the novel multiple-order-reflection method to measure the lattice parameter of the high-quality 3C-SiC epilayer studied in Fig. 9. Only the 0004 $_{4H}$ /0003 $_{3C}$  (cubic index of 0003 $_{3C}$  is 111 $_{3C}$ ) and 0008 $_{4H}$ /0006 $_{3C}$  reflection pairs were chosen for the  $c$  lattice parameter measurements (since the 0009 $_{3C}$  reflection is extremely weak). During the measurements, the second channel-cut crystal of the monochromator (in the dispersive setting) was carefully adjusted to the  $\text{CuK}\alpha 1$  peak position. Figure 10 shows parts of the  $\theta-2\theta$  scan intensity profile covering these four reflections. After the refractive-index corrections, the angular distance between 0004 $_{4H}$  and 0008 $_{4H}$  peaks is  $\Theta_{21} = 71554.5''$ . Then (4) and (2) gives  $d = c_{4H} = 2.521119 \text{ \AA}$ . Here  $c_{4H}$  represents the average thickness of the Si-C bilayer for 4H-SiC (1/4 the lattice parameter along [0001]). The corrected angular difference between 0003 $_{3C}$  and 0006 $_{3C}$  is  $\Theta_{21}^e = 71685.2''$ , corresponding to  $c_{3C} = 2.517586 \text{ \AA}$  for the 3C epilayer. Thus, the out-of-plane mismatch is  $(c_{3C} - c_{4H})/c_{4H} = 1.401 \times 10^{-3}$ , which is consistent with the result in Fig. 9.

In calculating  $c_{4H}$  and  $c_{3C}$ , we have considered the epilayer and substrate as two independent crystals. Their orientation relationship is actually indicated by the relative positions of the two sets of peaks. In Fig. 10, because the 0004 $_{4H}$  peak is set at  $\theta = 0$ , the zero points of the epilayer and substrate are  $\theta = -\theta_1$  and  $\theta = -\Delta\theta_1 - \theta_1^e$ , respectively, where  $\theta_1^e$  is the 0003 $_{3C}$  Bragg angle and  $\Delta\theta_1$  is the splitting between the 0004 $_{4H}$  and 0003 $_{3C}$  peaks. The difference,  $\theta_1 - \theta_1^e + \Delta\theta_1$ , obviously represents the misorientation of the epilayer against the substrate. However, the value of this calculated here is less than  $0.5''$ , which is negligible, indicating that the 0001 $_{3C}$  and 0001 $_{4H}$  planes are exactly parallel. This directly confirms an important feature of the growth mechanism designed for the current heteroepitaxy technique, i.e., the 3C-SiC epilayer is formed through a two-dimensional layer-by-layer nucleation process on the flat (0001) basal planes rather than the step-flow model commonly dominating SiC growth.

After the zero point of the (0001) planes has been determined, the a lattice parameters can be measured with the aid of 11 $\bar{2}$ 8 $_{4H}$ /11 $\bar{2}$ 6 $_{3C}$  asymmetric reflections in the glancing-incidence geometry [35]. The relationship between 11 $\bar{2}$ 8 $_{4H}$  and 0004 $_{4H}$  reflections is illustrated in the inset of Fig. 11, where the incidence angle of 11 $\bar{2}$ 8 $_{4H}$  reflection is  $\theta_A = \theta_1 - \Theta_{1A}$ . It can be easily proved that the lattice parameter  $a_{4H}$  is a function of  $c_{4H}$  and  $\theta_A$ :

$$a_{4H} = \frac{-C_2 + \sqrt{C_2^2 - 4C_1C_3}}{2C_1}, \quad (7)$$

where  $C_1 = c_{4H} \sin \theta_A - \lambda$ ,  $C_2 = c_{4H}^2 \cos \theta_A$ , and  $C_3 = \lambda c_{4H}^2$ .

The rocking curves of  $11\bar{2}8_{4H}$  and  $11\bar{2}6_{3C}$  asymmetric reflections are plotted in Fig. 11. As the  $0004_{4H}$  peak is located at  $\theta = 0$ , we have  $\Theta_{1A} = 17782.1''$  (after refraction correction), which gives  $\theta_A = 46271.3''$ . The lattice parameter  $a_{4H}$  calculated from (7) is then  $3.07950 \text{ \AA}$ . Meanwhile, the angular difference between the  $0003_{3C}$  and  $11\bar{2}6_{3C}$  peaks is  $\Theta_{1A}^e = 17511.6''$  (corresponding to  $\theta_A^e = 46634.8''$ ). Based on the same principle, the basal-plane lattice parameter of the epilayer is calculated as  $a_{3C} = 3.08039 \text{ \AA}$ . The in-plane mismatch is, hence,  $(a_{3C} - a_{4H})/a_{4H} = 2.89 \times 10^{-4}$ . Although very small, the finite in-plane mismatch clearly shows that the interface of the heterostructure is not perfectly coherent. The cubic lattice of unstrained  $3C$ -SiC requires an  $a/c$  ratio of  $\sqrt{1,5}$  ( $\approx 1.22474$ ) while the measured ratio is  $a_{3C}/c_{3C} = 1.22355$ . The difference clearly reveals that the epilayer lattice is compressed in directions parallel to the interface but has a tensile strain along the interface normal. Overall, the epilayer is *partially* relaxed.

Using the multiple-order-reflection method, we have obtained simultaneously but independently two sets of lattice parameters for the two components of the  $3C/4H$ -SiC heterostructure. The lattice parameters of  $4H$ -SiC measured here are in fact very close to those reported in [36] and [37].

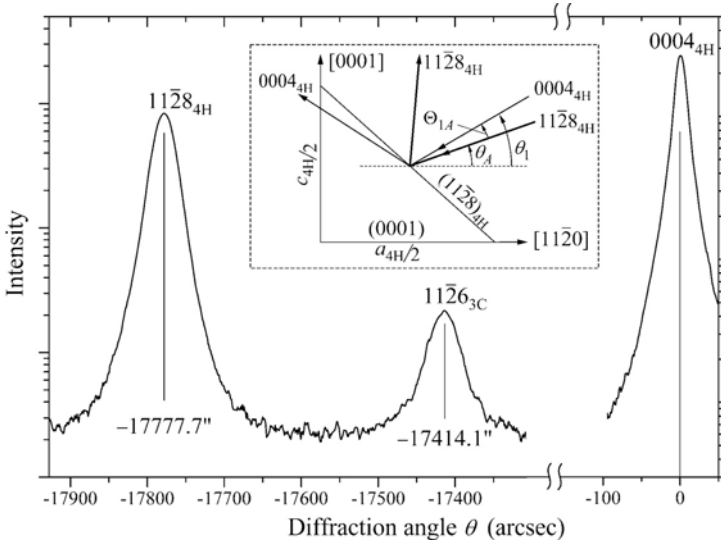


**Fig. 11.**  $\theta$ -scan rocking curves of  $11\bar{2}8_{4H}$  and  $11\bar{2}6_{3C}$  asymmetric reflections relative to the  $0004_{4H}$  Bragg peak. *Inset* shows the diffraction position of  $11\bar{2}8_{4H}$  reflection with respect to that of  $0004_{4H}$

## 5 Conclusions

SWBXT is an extremely powerful technique for nondestructive characterization of defects in SiC crystals. Based on the simple geometrical diffraction principle underlying the various imaging processes, it has, to date, provided complete quantitative characterization of both closed-core and hollow-core SSDs as well as other defects, and has provided essential insight into the formation mechanisms of these defects. Being capable of imaging defects in wafers with devices fabricated on them, it has enabled much light to be shed on the influence of the various defects on device performance.

SWBXT is also a simple and efficient technique for complete polytype determination and variant mapping in  $3C/4H$  and  $3C/6H$  heterostructures, which has significantly facilitated optimization of the growth conditions. In general, SWBXT is an invaluable aid to HRXRD characterization of SiC-based heterostructures that are usually inhomogeneous due to the existence of SSDs and small-angle boundaries in the substrate. SWBXT makes it possible to perform selected area HRXRD measurements, or it can help discern the diffraction contributions of substrate defects in the rocking curves or reciprocal space maps. The combination of SWBXT and HRXRD thus enables us to fully characterize such heterostructures. Combining these two techniques, we have studied in detail  $3C$ -SiC films heteroepitaxially grown on atomically flat mesas on  $4H$  and  $6H$ -SiC substrates. These techniques reveal extremely high crystalline perfection and homogeneity of the ideally grown  $3C$ -SiC epilayers on isolated mesas. In particular, the multiple-order-reflection method is successfully applied to measure the absolute lattice parameters of  $3C$  epilayers and  $4H$  and  $6H$  substrates, from which the small strain relaxation effect involved in the heteroepitaxy process is demonstrated. The 2D nucleation mechanism of the  $3C$  epilayer from a flat coherent interface is clearly revealed from the fact the (0001) lattice planes across the  $4H/3C$  or  $6H/3C$  interface are exactly parallel. These results demonstrate that the "step-free surface heteroepitaxy" growth process is an effective technique for high-quality single-crystal SiC heteroepitaxy.

## Acknowledgements

The authors gratefully acknowledge the assistance of P.G. Neudeck and his colleagues at NASA Glenn Research Center. Support is also acknowledged from the U.S. Army Research Office under contract number DAAG 559810392, partially funded by the DARPA Electronics Technology Office and NASA Glenn Research Center, from NSF grant DMR 9903702 (subcontract 54406855242), and from ONR grants N000140010348 and N000140110302. Topography was carried out at the Stony Brook Topography Facility (Beamline X-19C) at the NSL, BNL, supported by the U.S. DoE, Division of Materials Sciences and Chemical Sciences.

## References

1. H. Morkoç, S. Strite, G.B. Gao, M.E. Lin, B. Sverdlov, and M. Burns: *J. Appl. Phys.* **76**, 1363 (1994)
2. P.G. Neudeck: in *The VLSI Handbook, The Electrical Engineering Handbook Series*, ed. by W.K. Chen (CRC Press and IEEE Press, 2000), pp. 6.1–6.24
3. D. Hobgood, M. Brady, W. Brixius, G. Fechko, R. Glass, D. Henshall, J. Jenny, R. Leonard, D. Malta, S.G. Müller, V. Tsvetkov, and C. Carter Jr.: *Mater. Sci. Forum* **338–342**, 3 (2000)
4. M. Dudley, S. Wang, W. Huang, C.H. Carter, and C. Fazi: *J. Phys. D, Appl. Phys.* **28**, A63 (1995)
5. X.R. Huang, M. Dudley, W.M. Vetter, W. Huang, S. Huang, and C.H. Carter: *Appl. Phys. Lett.* **74**, 353 (1999)
6. P.G. Neudeck, W. Huang, and M. Dudley: *Mat. Res. Soc. Symp. Proc.* **483**, 285 (1998)
7. P.G. Neudeck, W. Huang, and M. Dudley: *IEEE Trans. Electron. Devices* **46**, 478 (1999)
8. M. Dudley, W. Si, S. Wang, C.H. Carter, R. Glass, and V.F. Tsvetkov: *Nuovo Cimento* **19D**, 153 (1995)
9. W. Si, M. Dudley, R. Glass, V. Tsvetkov, and C.H. Carter: *Mater. Sci. Forum* **264–268**, 429 (1998)
10. M. Dudley and X. Huang: *Mater. Sci. Forum* **338–342**, 431 (2000)
11. X.R. Huang, M. Dudley, W.M. Vetter, W. Huang, W. Si, and C.H. Carter: *J. Appl. Cryst.* **32**, 516 (1999)
12. M. Dudley, X.R. Huang, and W. Huang: *J. Phys. D, Appl. Phys.* **32**, A139 (1999)
13. X.R. Huang, M. Dudley, J.Y. Zhao, and B. Raghothamachar: *Phil. Trans. R. Soc. Lond. A* **357**, 2659 (1999)
14. W.M. Vetter and M. Dudley: *J. Appl. Cryst.* **35**, 689 (2002)
15. T.A. Kuhr, W.M. Vetter, M. Dudley, and M. Skowronski: *Mater. Sci. Forum* **338–342**, 473 (2000)
16. A.R. Lang and A.P.W. Makepeace: *J. Synchrotron Rad.* **3**, 313 (1996)
17. A.R. Lang and A.P.W. Makepeace: *J. Phys. D, Appl. Phys.* **32**, A97 (1999)
18. M. Dudley, X.R. Huang, W. Huang, A. Powell, S. Wang, P.G. Neudeck, and M. Skowronski: *Appl. Phys. Lett.* **75**, 784 (1999)
19. E.K. Sanchez, J.Q. Liu, M.D. Graef, M. Skowronski, W.M. Vetter, and M. Dudley: *J. Appl. Phys.* **91**, 1143 (2002)
20. W.M. Vetter and M. Dudley: *Mat. Sci. Eng. B* **87**, 173 (2001)
21. T.A. Kuhr, E.K. Sanchez, M. Skowronski, W.M. Vetter, and M. Dudley: *J. Appl. Phys.* **89**, 4625 (2001)
22. W. Si, M. Dudley, H.-S. Kong, J. Sumakeris, and C. Carter: *J. Electronic Materials* **26**, 151 (1997)
23. S. Mardix and A.R. Lang: *Phil. Mag.* **24**, 683 (1971)
24. P. Krishina, S.S. Jiang, and A.R. Lang: *J. Cryst. Growth* **71**, 41 (1985)
25. W.M. Vetter and M. Dudley: *J. Appl. Cryst.* **34**, 20 (2001)
26. J. Heindl, W. Dorsch, H.P. Strunk, S.G. Müller, R. Eckstein, D. Hofmann, and A. Winnacker: *Phys. Rev. Lett.* **89**, 740 (1998)
27. J.D. Eshelby and A.N. Stroh: *Phil. Mag.* **42**, 1401 (1951)

28. E. Pernot, P. Pernot-Rejmánková, M. Anikin, B. Pelissier, C. Moulin, and R. Madar: *J. Phys D, Appl. Phys.* **34**, A136 (2001)
29. J. Baruchel, J. Härtwig, and P. Pernot-Rejmankova: *J. Synchrotron Rad.* **9**, 107 (2002)
30. J.A. Powell, P.G. Neudeck, A.J. Trunek, G.M. Beheim, L.G. Matus, R.W. Hoffman, and L.J. Keys, *Appl. Phys. Lett.* **77**, 1449 (2000)
31. P.G. Neudeck, J.A. Powell, A.J. Trunek, X.R. Huang, and M. Dudley: *Mater. Sci. Forum* **389–393**, 311 (2002)
32. M. Dudley, W.M. Vetter, and P.G. Neudeck: *J. Cryst. Growth* **240**, 22 (2002)
33. M. Dudley, W.M. Vetter, X.R. Huang, P.G. Neudeck, and J.A. Powell: *Mater. Sci. Forum* **389–393**, 391 (2002)
34. D.K. Bowen and B.K. Tanner: *High Resolution X-ray Diffractometry and Topography* (Taylor & Francis, London, 1998)
35. M. Fatemi: *Appl. Phys. Lett.* **80**, 936 (2002)
36. Y.M. Tairov and V.F. Tsvetkov: in *Crystal Growth and Characterization of Polytype Structures*, ed. by P. Krishna (Pergamon Press, Oxford, 1983) pp. 111
37. A. Bauer, J. Kräußlich, L. Dressler, P. Kuschnerus, J. Wolf, K. Goetz, P. Käckell, J. Furthmüller, and F. Bechstedt: *Phys. Rev. B* **57**, 2647 (1998)

## Part V

## Processing

# Ohmic Contacts for Power Devices on SiC

S. Tanimoto, H. Okushi, and K. Arai

## 1 Introduction

An ohmic contact in semiconductor devices consists of an electrode (metal) and a semiconductor, and it plays an important role in current injection and ejection. Because a voltage drop at the contact increases the power loss and deteriorates the device performance, the contact resistance must be negligible relative to the total resistance of the device (its on-resistance) [1]. Contacts through which a high-density current flows horizontally must have the lowest resistivity possible because their effective contact area is very small due to current crowding at the contact edges [2]. Source contacts in vertical DMOS-FETs are one example of such contacts. Increasing the size of the contact area to make it larger than that of the effective area does not reduce contact resistance. The only way to minimize contact resistance is to reduce the specific contact resistivity,  $\rho_C$ , itself. High-power and high-frequency SiC devices need horizontal contacts with a  $\rho_C$  in the range of  $10^{-6} \Omega\text{cm}^2$  or lower [3].

A great deal of effort has been made to obtain low-resistivity contacts on SiC. Results for contacts on 3C-SiC ( $E_g = 2.2$  eV) and 6H-SiC ( $E_g = 2.9$  eV) were critically reviewed by Porter and Davis [4] and by Crofton and colleagues [5]. A common technique to form ohmic contacts on SiC is to deposit a suitable material (typically, metal) in a heavily doped  $n$ - or  $p$ -type region, followed by post-deposition annealing (PDA or contact annealing), typically at 950°C. PDA creates a metallic reaction layer with a low Schottky barrier between the contact material and the SiC surface. As a result, the contact has a reaction layer/SiC structure. Heavy doping makes the Schottky barrier thinner and significantly facilitates field emission conduction, eventually leading to a decrease in  $\rho_C$ . In contact materials incorporating  $n$ - or  $p$ -type impurities, trace elements migrating into the substrate during PDA may promote bulk doping. Naturally, the  $\rho_C$  strongly depends on the contact material, the doping level, and the PDA conditions. However, it is also markedly affected by the surface preparation condition just before metal deposition [4, 5]. Factors that may affect the  $\rho_C$  include: surface roughness [6], organic and metal contamination [7], natural oxide formation [7]–[9], graphitized skin [10]–[12], photoresist residue [13], and a deformed or plasma-damaged surface [14].

A variety of contact materials have been investigated in the past decade. The most promising material is Ni for  $n$ -type regions and Al-Ti for  $p$ -type re-

gions [5]. Also, Co/Si-based material may be used for  $p$ -type regions [15]. The best results ever reported on  $6H$ -SiC are  $\rho_C$  values of  $7 \times 10^{-7} \Omega\text{cm}^2$  [16] and  $2.8 \times 10^{-6} \Omega\text{cm}^2$  [17] in  $n$ - and  $p$ -type regions, respectively. These results were achieved using Ni and alloyed Al-Ti, and they meet the  $\rho_C$  level required in actual SiC devices. Recently, excellent long-term stability has been obtained for contacts made of these materials at temperatures up to  $500^\circ\text{C}$  [18, 19]. Nevertheless, conventional techniques for contact formation on SiC are still imperfect, and problems with structural and fabrication-process compatibility remain in practical SiC devices. In addition, low contact resistivity has never been demonstrated for practical power devices.

This paper describes a technology for fabricating the contacts of practical power devices on  $4H$ -SiC ( $E_g = 3.2 \text{ eV}$ ) with superior electron mobility. The technology described here is in fact not limited to the fabrication of contacts in  $4H$ -SiC devices, but can also be used to fabricate contacts on  $6H$ - and  $3C$ -SiC.

First, we briefly review some existing techniques for the fabrication of low-resistivity contacts on  $4H$ -SiC. Then, we describe the optimal contact structure, which can solve many problems that occur with conventional techniques. Two basic contacts fabricated on  $4H$ -SiC with this new technology are examined: one is a low-resistivity contact for the  $n$ -type region, and the other is a single-material contact with an ohmic property for both the  $n$ - and  $p$ -type regions. The reliability of these contacts is evaluated. Finally, the proposed technology is applied to a poly-Si gate  $n$ -channel vertical power MOSFET fabricated on  $4H$ -SiC [20]–[22], which looks like a DMOSFET in Si devices.

## 2 Critical Review of Ohmic Contacts on $4H$ -SiC

### 2.1 Contacts in the $n$ -Type Region

Table 1 shows the results of contact fabrication in the  $n$ -type region.  $\rho_C$  values in the range of  $10^{-7} \Omega\text{cm}^2$  have already been demonstrated on heavy N-doped epilayers using contacts made of Nb [28] and Ni [29, 32]. These  $\rho_C$  values are lower than the best values obtained for  $n$ -type  $6H$ -SiC [16]. This success probably resulted from the recent improvement of the in situ heavy doping technique during homo-epitaxy and the refinement of PDA and surface preparation before contact annealing. Nickel is a major material for the fabrication of contacts on  $n$ -type SiC, and it has been investigated extensively. Better results have been obtained for Ni-based contacts subjected to PDA at temperatures ranging from  $900$  to  $1000^\circ\text{C}$  for an interval of  $1$  to  $5$  min. A significant reduction in  $\rho_C$  necessitates heavy doping at a donor concentration of more than  $N_D = 10^{19} \text{ cm}^{-3}$ . The doping technique involving ion implantation followed by activation annealing is relatively less effective for the reduction of  $\rho_C$  than in situ doping during epitaxy. The same tendency

**Table 1.** Ohmic contacts on *n*-type 4H-SiC. The layered contact materials are shown with slashes to separate the distinct layers; the material on the left-hand side touches the SiC surface. The doping level indicates either the carrier density or the donor concentration in the SiC. During surface preparation, the material to the left of the slash was cleaned first, followed by cleaning of the material to the right of the slash. Photolithography performed during surface preparation is indicated by <Ph>

Contact mat.	Depos. meth.	PDA conditions	Electrical property		Doping		Surface prep.	Ref.
			$\rho_C$ [ $\Omega\text{cm}^2$ ]	Method of meas.	Level [ $\text{cm}^{-3}$ ]	Method		
Ni	t	950–1000°C, 5min.	$1 \times 10^{-6}$	TLM	$2 \times 10^{19}$	epi.	HF/ Ar ion	[23]
Mo	t	1000–6000°C	$2 \times 10^{-5}$	TLM	$5 \times 10^{18}$	epi.	HF/ Ar ion	[23]
Ni	eb	950°C, 10min., N <sub>2</sub>	$2.8 \times 10^{-6}$	TLM	$1 \times 10^{19}$	epi.	HF(1%)/ Ar ion	[24], [25]
Ni/Cr/W	sp	1000–1050°C, 5–10min., Ar	$5 \times 10^{-6}$	TLM	$1 \times 10^{17}$ – $1 \times 10^{18}$	bulk sub.	org./Sac <Ph>	[26]
Al/Ni/Al	t	1000°C, 5min., N <sub>2</sub>	$1.8 \times 10^{-5}$	4P	$1 \times 10^{19}$	epi.	SPM/ HPM/HF	[27]
Nb	sp	1100°C, 3–10min, vac.	$3.1 \times 10^{-7}$	TLM	$1.3 \times 10^{19}$	epi.	N.R.	[28]
Ni	eb	1000°C, 2min, Ar	$3.3 \times 10^{-7}$	TLM	$1.5 \times 10^{19}$	epi.	RCA/ Sac/HF	[29]
Ti/Ni	eb	no anneal.	$\sim 1 \times 10^{-6}$	TLM	$2 \times 10^{20}$	P-impla	RCA/ Sac/HF	[30]
Ni	sp	1050°C, 10min Ar-H <sub>2</sub> (5%)	$6 \times 10^{-6}$	TLM	$1 \times 10^{19}$	N-impla	(ICP etch or Sac) <Ph>	[31]
Ni	eb	1000°C, 2min, Ar	$6 \times 10^{-6}$	TLM	$2 \times 10^{20}$	p-impla	RCA/ Sac/HF	[32]
Si/Ni	eb	900°C, 10min, Ar-H <sub>2</sub> (5%)	$1.9 \times 10^{-6}$	TLM	$2 \times 10^{19}$ (N)	epi.	Sac/HF	[33]
Ni	t	900°C, 1min, Ar-H <sub>2</sub> (15%)	$6 \times 10^{-5}$	TLM	$1 \times 10^{20}$ (N)	epi+Ge- impla	N.R.	[34]
TiW	sp	650°C, 30min, 950°C, 30min vac.	$3.8 \times 10^{-5}$	TLM	$1.1 \times 10^{19}$	epi.	SPM/ HF/Sac	[35]

Notations: t = thermal evaporation, eb = electron beam evaporation, sp = sputtering, N.R. = not reported, 4P = four-point probe method, epi = in situ doping during epitaxial growth, and Sac = sacrificial oxidization followed by oxide removal

is also observed for contacts in the *p*-type region, which will be described later. This ineffectiveness may be caused by crystalline imperfections such as lattice damage, surface step-bunching and secondary defects that remain or are formed after activation annealing. Further investigation and improvement are required for heavy doping using ion implantation. The drawbacks of Ni-based contacts are an excessive amount of carbon precipitate and thicker reaction layers resulting from the reaction between the contact material and the SiC substrate [5, 23, 28]. These problems can be solved by using one of the following contact materials: thinner Ni [29, 32], nickel silicide [25, 33], or a refractory material causing the formation of a thin reaction layer such as that of Nb [28]. The fabrication of Nb-based contacts involves PDA at a temperature of more than 1100°C, which may significantly affect thermal oxides such as gate oxides.

## 2.2 Contacts in the *p*-Type Region

The results of contact fabrication on *p*-type 4*H*-SiC are listed in Table 2. A variety of contact materials, including Ti, Pd, Al, Ni, Si, and Co, have been investigated. A widely used approach is to use Al in conjunction with Ti to form Ti/Al, Al/Ti, and Al-Ti. These materials were originally used for anode contacts of light-emitting diodes fabricated on 6*H*-SiC [36]. Crofton and colleagues significantly improved these materials and obtained a very low  $\rho_C$  on 6*H*-SiC [17]. A  $\rho_C$  value in the range of  $10^{-6} \Omega\text{cm}^2$  or lower was obtained on *p*-type 4*H*-SiC with these materials [29, 53], but the  $\rho_C$  values obtained by different researchers differ by as much as two orders of magnitude, as shown in Table 2. This difference is too large to be explained only by the difference in the doping level and/or PDA conditions. The  $\rho_C$  may also be significantly dependent on the surface preparation condition before the deposition of contact material. Unfortunately, surface preparation has not been systematically studied. Al-based contacts can be significantly damaged during PDA; that is, there may be aluminum spill-over on neighboring areas [48], they may become strongly oxidized and change into  $\text{Al}_2\text{O}_3$  [13, 48, 58, 59], or the contact surface may be “pitted” [5, 13, 32]. These problems have not been resolved. It is possible that the use of Ti-based contacts accompanied by very heavy doping can be effective in overcoming these difficulties [37].

## 3 Contact Design for Practical Devices

### 3.1 Problems with Conventional Techniques

If there were a material, just like aluminum in Si devices, which could be used to fabricate both interconnects and contacts, the contact structure could then be simplified as shown in Fig. 1a, where  $n^+$  ( $p^+$ ) signifies a heavily doped *n*-type (*p*-type) region. Such a two-way material should also be resistant

**Table 2.** Ohmic contacts on *p*-type 4H-SiC. The layered contact materials are shown with slashes to separate the distinct layers; the material on the left-hand side touches the SiC surface. The doping level indicates either the carrier density or the acceptor concentration in the SiC. During surface preparation, the material to the left of the slash was cleaned first, followed by cleaning of the material to the right of the slash. Photolithography performed during the surface preparation is indicated by ⟨Ph⟩

Cont. mat.	Dep. meth.	PDA cond.	Electric. property		Doping		Surface prep.	Ref.
			$\rho_C$ [ $\Omega\text{cm}^2$ ]	Meth. of meas.	Level [ $\text{cm}^{-3}$ ]	Meth.		
Ti	sp	800°C, 1min or no anneal	$5 \times 10^{-6}?$	TLM	$4 \times 10^{20}$	Al-C- co- impla	N.R.	[37]
Al/Ni/ W etc.	sp	850°C, 2min	$4 \times 10^{-5}$	TLM	$1 \times 10^{19}$	bulk sub.	org/Acid/ HF	[38]
Al-Si, Si/Al	sp	700°C, 20min, N <sub>2</sub>	$3.8 \times 10^{-5}$	TLM	$5 \times 10^{19}$ (Al)	epi.	Acid/Ar dis- charge ⟨Ph⟩	[39], [40]
Pd	eb	700°C, 15min, N <sub>2</sub>	$5.5 \times 10^{-5}$	TLM	$5 \times 10^{19}$ (Al)	epi.	org/HF:HNO <sub>3</sub> ⟨Ph⟩HF/Ar discharge	[41], [42], [43]
Pd	t	600°C, in situ	$4 \times 10^{-4}$	CTLM	$4 \times 10^{18}$ (Al)	epi.	HNO <sub>3</sub> :HF	[44]
(Ti/Al/ Ti/Pd/ Ni	eb	1150°C, 50sec, H <sub>2</sub>	$6 \times 10^{-5}$	CTLM	$1.5 \times 10^{20}$ (Al)	LPE	Chem/HF ⟨Ph⟩	[45], [46]
Al	t	950°C, 5min, Ar	$6.1 \times 10^{-5}$	TLM	$6 \times 10^{20}$ (Al)	Al-C- co- impla	RCA	[47]
Ti/Al etc.	N.R.	1050°C, 5min, Ar+H <sub>2</sub>	$1.4 \times 10^{-4}$	TLM	$\sim 1 \times 10^{20}$ (Al)	Al-C- co- impla	Sac⟨Ph⟩ (ICP or BHF), or Sac/BHF/ (ICP or BHF) ⟨Ph⟩	[48]
Al	N.R.	950°C, 5min, Ar+H <sub>2</sub>	$4.7 \times 10^{-5}$	TLM	$\sim 1 \times 10^{20}$ (Al)	Al-C- co- impla	Sac⟨Ph⟩ (ICP or BHF), or Sac/BHF/ (ICP or BHF) ⟨Ph⟩	[48]
Ti/Al	eb	1000°C, 2min, Ar	$9.7 \times 10^{-7}$	TLM	$1.2 \times 10^{19}$ (Al)	epi.	RCA/Sac/ CVD⟨Ph⟩ HF	[29]
Al/Ni	t	1100°C, 20sec, vac. or 950°C, 5min, Ar	$1.5 \times 10^{-4}$	(C)TLM	$1 \times 10^{19}$	Al-diff.	RCA/HF	[49]

Notations: t = thermal evaporation, eb = electron beam evaporation, sp = sputtering, N.R. = not reported, 4P = four-point probe method, epi = in situ doping during epitaxial growth, and Sac = sacrificial oxidization followed by oxide removal

Table 2 continued

Cont. mat.	Dep. meth.	PDA cond.	Electric. property		Doping		Surface prep.	Ref.
			$\rho_C$ [ $\Omega\text{cm}^2$ ]	Meth. of meas.	Level [ $\text{cm}^{-3}$ ]	Meth.		
Al/Ti	t	1100°C, 20sec, vac./ 950°C, 5min, Ar	$1.3\times 10^{-4}$	(C)TLM	$1\times 10^{19}$	Al-diff.	RCA/HF	[49]
Al-Ti	sp	1000°C, 2min, vac.	$1.5\times 10^{-4}$	TLM	$7\times 10^{18}$	epi.	Org/BHF	[50]
Ti/Al/ Ti/Al/ Ti	sp	1050°C, 2min, Ar	$4\times 10^{-4}$	TLM	$7\times 10^{18}$	epi.	Org/BHF	[50]
Ni	sp	1050°C, 10min, Ar-H <sub>2</sub> (5%)	$1.5\times 10^{-4}$	TLM	$1\times 10^{21}$ (Al)	Al-C- co- impla	(ICP etch or Sac) ⟨Ph⟩	[31]
Al/Ti/ Pt/Ni	eb	1000°C, 2min, vac.	$9\times 10^{-5}$	TLM	$6-8\times 10^{18}$	epi.	RCA/HF ⟨Ph⟩HF	[51]
Al: Si,Ti	eb	950°C, 7min, Ar	$9.6\times 10^{-6}$	TLM	$3-5\times 10^{19}$	LPE	NH <sub>4</sub> OH/HCl/ H <sub>2</sub> SO <sub>4</sub> / HNO <sub>3</sub> /HF/Ar discharge	[52]
multi- Ti/Al	eb or t	500°C, 30min, vac./1000°C, 2min, vac.	$6\times 10^{-6}$	CTLM	$1\times 10^{19}$	epi.	RCA	[53]
Ni	eb	1000°C, 2min, Ar	$7\times 10^{-3}$	TLM	$2\times 10^{20}$	Al- impla	RCA/Sac/ CVD⟨Ph⟩ HF	[32]
Al/Co	eb	900°C, 5min, vac.	$4\times 10^{-4}$	CTLM	$9\times 10^{18}$ (Al)	epi.	RCA/Sac/ HF	[54]
Ni(100)	t	900°C, 1min, Ar+H <sub>2</sub> (15%)	$8.3\times 10^{-5}$	TLM	$5\times 10^{16}$ (Al)	N-Ge- co- impla	N.R.	[55]
Ti/Si/ Co	sp	500°C, 5min, vac./850°C, 1min, vac.	$4\times 10^{-4}$	TLM	$3.9\times 10^{18}$ (Al)	epi.	RCA/BHF ⟨Ph⟩	[56]
Al/Ti/ Au	ep or sp	900°C, 15min, Ar	$1.42\times 10^{-5}$	TLM	$3-5\times 10^{19}$	epi.	APM/HF: HNO <sub>3</sub> /HF ⟨Ph⟩Ar discharge	[57]
Al/Pd/ Au	eb or sp	900°C, 5min, Ar	$4.08\times 10^{-5}$	TLM	$3-5\times 10^{19}$	epi.	APM/HF: HNO <sub>3</sub> /HF ⟨Ph⟩Ar discharge	[57]

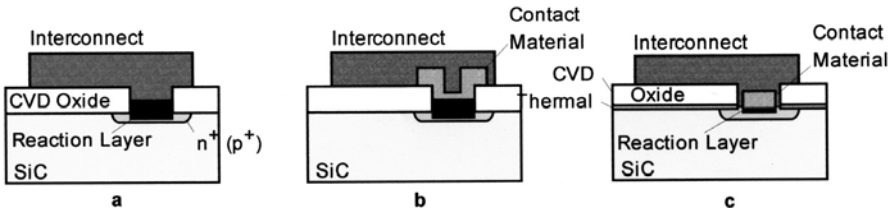


**Fig. 1.** Contact structures on SiC: (a) ideal, (b) conventional, and (c) proposed

to PDA at temperatures as low as 1000°C and must not affect the oxide layer underneath during contact annealing. However, such a material has yet to be discovered. Figure 1b shows a conventional contact structure that is often referred to in articles on SiC devices [60]. The contact material and the interconnect material are structurally divided, with the former extending over the CVD oxide. The interconnect is formed after PDA to avoid damaging it in the annealing process. However, such contacts have a number of problems. For example, contact material with strong tensile stress, such as Ni and Co, often peels off in handling [61]. Also, during PDA, the reaction layer may penetrate the thin, heavily doped region [13, 23, 32], and the contact material may attack or spill over the oxide [48, 62]. In addition, the surface morphology of such contacts is poor [29, 50] and it is difficult to form both *n*- and *p*-type contacts with a very low  $\rho_C$  on the same surface.

### 3.2 Preferred Contact Structure

Figure 1c shows the contact structure that we recommend [29]. There is a contact window in the thick oxide, which is sequentially grown by thermal oxidization or other deposition techniques. This oxide corresponds to the field oxide and insulating interlayer in an actual device. The bottom thermal oxide acts as a sacrificial oxide layer in the contact region and as a stabilizer of surface states in the regions outside the contact. This oxide may be thin, but it must be present. It should be noted that the contact material is defined precisely in the contact window, leaving a constant and fine clearance to the sidewall of the oxide. This configuration solves one of the above-mentioned problems associated with the contact material attacking or spilling over the oxide during PDA. The optimal contact material is determined experimentally from a number of materials with a low  $\rho_C$  and one of the following attributes: thin texture, deposited silicide, and low reactivity with SiC during PDA. Such a contact material enables formation of a reaction layer that is relatively thinner than the junction depth,  $X_j$ . This solves the aforementioned problems associated with the peeling off of the contact material during handling, the penetration of the reaction layer in the thin doped region, and the poor surface morphology of the contacts. The effectiveness of such a contact

material will be demonstrated later by using a contact with a 50-nm-thick Ni layer. Interconnect metal such as an Al-Si-Cu alloy or TiW is overlaid on the contact. The fabrication process for this contact structure has been detailed in [32].

## 4 Integration of Contacts into Vertical Power MOSFETs

### 4.1 Preliminary Study

All the contacts reported in this section were fabricated by the authors on (0001)Si 8°-off 4H-SiC epitaxial substrates, using the contact structure in Fig. 1c and the same process as described in [32]. A mirror projection aligner (UTS-1500, ULTRA-Tech.) and a photoresist (OFPR8600, Tokyo Ooka) were used in all the photolithography processes: the mesa-based isolation of the heavily doped region, the opening of the contact window, and the patterning of the interconnect material. This facilitates precise and reproducible photolithography. Many L-TLM (linear transfer length method) contacts were formed on the substrates in order to determine their  $\rho_C$  and transfer length,  $L_T$ , accurately. The contacts had the following size:  $W = 200\text{ }\mu\text{m}$  and  $D = 100\text{ }\mu\text{m}$ , and the contact spacing was  $L = 6, 10, 15, 20, 25$ , and  $30\text{ }\mu\text{m}$ . The limit for evaluating  $\rho_C$  seems to be around  $10^{-7}\text{ }\Omega\text{cm}^2$ . The  $\rho_C$  values were determined on the basis of at least five TLM measurements. The reproducibility of the  $\rho_C$  data was within 20%. Reactive ion etching (RIE) of the mesa electrically isolated the heavily doped region. A 420-nm-thick oxide was sequentially grown around the contacts by dry  $\text{O}_2$  oxidization at  $1100^\circ\text{C}$  and by CVD (chemical vapor deposition) at  $300^\circ\text{C}$  using  $\text{SiH}_4$  and  $\text{O}_2$ . The total thickness included the 20-nm-thick thermal oxide layer. All the contact materials were deposited by using an electron beam evaporator. Unless stated otherwise, PDA was performed at  $1000^\circ\text{C}$  for 2 min in an Ar ambient. The Al interconnect overlayer was about 500 nm thick.

#### 4.1.1 Low-Resistivity Contacts in the $n^+$ Region

The contact material was a thin layer of Ni ranging in thickness from 20 to 200 nm. An 800-nm-thick epilayer in which nitrogen was in situ doped at a level of  $1.5 \times 10^{19}\text{ cm}^{-3}$  was used as the  $n^+$  region. All the  $\rho_C$  values were normalized by the  $\rho_{C0}$  measured at room temperature for a 50-nm-thick Ni-based contact subjected to PDA at  $1000^\circ\text{C}$ .

Figure 2a shows the  $\rho_C$  as a function of the Ni thickness,  $t_{\text{Ni}}$ . The  $\rho_C$  is independent of the Ni thickness, except at 20 nm. The smallest  $\rho_C$  of  $3.3 \times 10^{-7}\text{ }\Omega\text{cm}^2$  was obtained at a thickness of 50 nm. The electrode surface morphology improved noticeably when the thickness was reduced, and it was fairly smooth at a thickness of no more than 50 nm (see [32]). Figure 2b

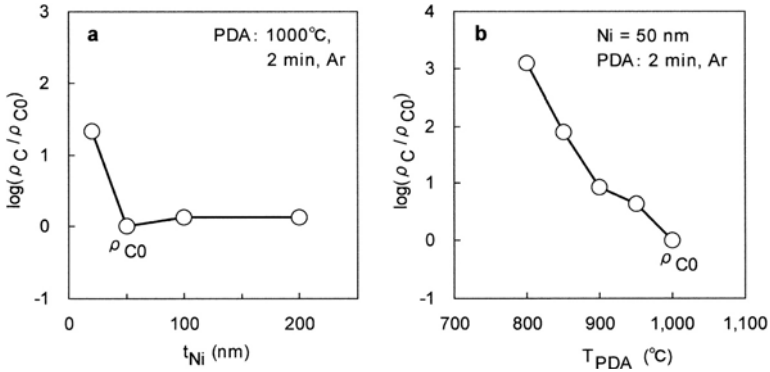


**Fig. 2.** Relationship between fabrication conditions and specific contact resistance,  $\rho_C$ , of the Ni contact formed in the  $n^+$  region (epilayer) in situ N-doped with  $N_D = 1.5 \times 10^{19} \text{ cm}^{-3}$ : (a) Ni film thickness ( $t_{\text{Ni}}$ ) dependence and (b) PDA temperature ( $T_{\text{PDA}}$ ) dependence.  $\rho_{C0} = 3.3 \times 10^{-7} \Omega\text{cm}^2$  is the specific contact resistivity for  $t_{\text{Ni}} = 50 \text{ nm}$  and  $T_{\text{PDA}} = 1000^\circ\text{C}$

shows the PDA temperature ( $T_{\text{PDA}}$ ) dependence of the  $\rho_C$  on the 50-nm-thick Ni contact. Although the contact exhibited an ohmic property at all  $T_{\text{PDA}}$  values, the  $\rho_C$  increased exponentially with a decrease in  $T_{\text{PDA}}$ . We can see from this result that the  $T_{\text{PDA}}$  should be as high as possible.

Rutherford back-scattering (RBS) analysis revealed that even the 200-nm-thick Ni contact completely reacted with the SiC substrate, resulting in the formation of a reaction layer consisting of nickel silicide and carbon. A cross-sectional transmission electron micrograph (X-TEM) for the 50-nm-thick Ni contact is shown in Fig. 3. This micrograph indicates that the Ni reaction layer varied between 100 and 180 nm in thickness, but was still much thinner than the typical junction depth of 300 nm in the  $n^+$  region of

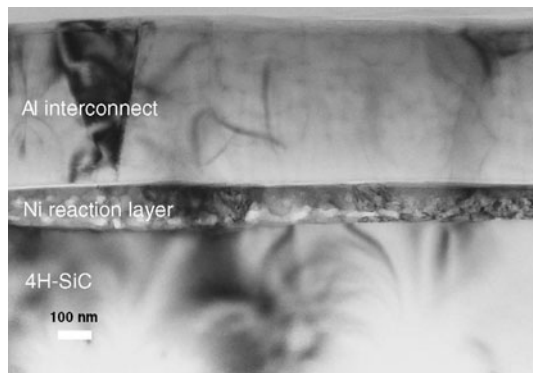


**Fig. 3.** Cross-section of a 50-nm-thick Ni contact on the in situ N-doped  $n^+$  4H-SiC epilayer observed by transmission electron spectroscopy

actual devices. The figure also shows that the layer was studded with lots of white islands. High-resolution X-TEM and electron energy loss spectroscopy (EELS) techniques revealed that the white islands were carbon precipitate with a curl structure.

A 50-nm-thick Ni contact was also fabricated in the  $n^+$  region doped by ion implantation, and the results obtained are described in the following section concerning single-material contacts.

#### 4.1.2 Single-Material Contacts for the $p$ -Base and $n$ -Source Regions

Practical power MOSFETs require a contact fabrication technique that would enable simultaneous fabrication of contacts with a single material both in the  $n^+$ -source and  $p$ -base regions. This technique would have a direct impact on the miniaturization of cells. It could also shorten the device fabrication process by eliminating the contact fabrication step for the  $p$ -base region. Downsizing and short-cut processing in turn can result in a reduction of specific on-resistance and significant cost savings. A very low  $\rho_C$  is needed for source contacts through which high-density currents flow. A moderately low  $\rho_C$  is acceptable for  $p$ -base contacts. The most crucial aspect in forming such contacts, therefore, is to obtain an ohmic property in the  $p$ -type region using a contact material that shows very low contact resistivity in the  $n$ -type region. The most promising materials are obviously Ni-based ones. Several studies have investigated these materials [31, 32, 37, 63, 64]. The results of one such study conducted by the authors [32, 64] are briefly described below.

50-nm-thick Ni-based TLM contacts were fabricated in the  $n^+$  and  $p^+$  regions formed by multiple-energy  $P^+$  and  $Al^+$  ion implantation at 500°C and 750°C, respectively, followed by activation annealing at 1700°C for 1 min in an Ar ambient. The substrates were (0001)Si 8°-off 4H-SiC substrates with lightly Al- and N-doped epitaxial layers, respectively. The doping level and the junction depth were  $N_D = 2 \times 10^{20} \text{ cm}^{-3}$  and  $X_{Dj} = 350 \text{ nm}$  for the  $n^+$  region, and  $N_A = 2 \times 10^{20} \text{ cm}^{-3}$  and  $X_{Aj} = 270 \text{ nm}$  for the  $p^+$  region.

Figure 4a shows the  $I$ - $V$  characteristics between two adjacent contacts in the  $p^+$  region of a TLM test structure where the parameter  $L$  is the contact spacing. As can be seen from this figure, all the contacts had ohmic properties. Although the results for the  $n^+$  region are omitted here, the contacts in that region showed superior ohmic properties. The total resistance,  $R_T$ , between the adjacent contacts is plotted in Fig. 4b as a function of the contact spacing. Note that the range of the total resistance is different between the  $n$ - and  $p$ -type contacts. This is because the sheet resistance under the contacts in the  $p$ -type region is several orders of magnitude higher than that in the  $n$ -type region. The plots have an excellent linear relationship, indicating that the  $\rho_C$  and sheet resistance in the  $n^+$  and  $p^+$  regions are rather uniform. TLM analysis of the contacts revealed that  $\rho_C = 5.8 \times 10^{-6} \text{ } \Omega\text{cm}^2$  and  $L_T = 1.3 \text{ } \mu\text{m}$

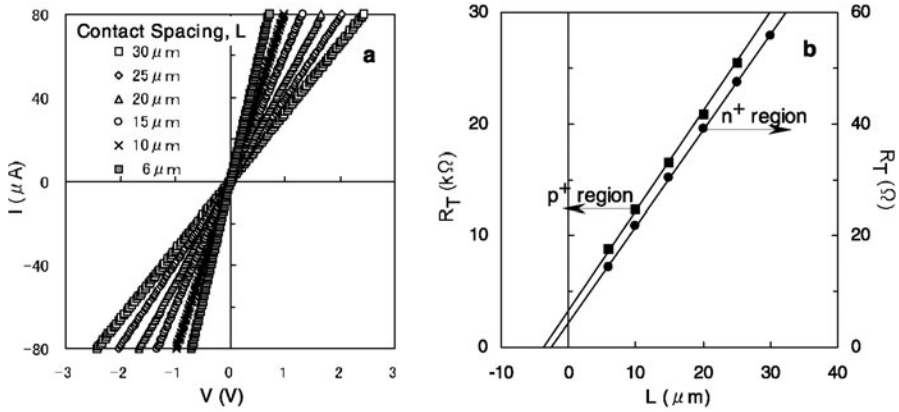


**Fig. 4.** Electrical properties for single-material 50-nm-thick Ni contacts (TLM) in the heavily-doped  $p^+$  and  $n^+$  regions on 4H-SiC formed by Al and P ion hot-implantation followed by activation annealing: (a) current-voltage ( $I$ - $V$ ) characteristics between adjacent contacts in the  $p^+$  region with contact spacing,  $L$ , as a parameter, and (b) total resistance plotted as a function of  $L$  between adjacent contacts in the  $n^+$  and  $p^+$  regions. Here,  $N_A(\text{Al}) = 2 \times 10^{20} \text{ cm}^{-3}$  and  $N_D(\text{P}) = 2 \times 10^{20} \text{ cm}^{-3}$

in the  $n^+$  region, and  $\rho_C = 6.2 \times 10^{-3} \Omega\text{cm}^2$  and  $L_T = 1.9 \mu\text{m}$  in the  $p^+$  region. The contacts had fairly smooth surfaces, similar to the surface of the 50-nm-thick Ni contact in the epitaxy in situ doped  $n^+$  region (N) described above.

## 4.2 Reliability of Contacts

The reliability of the contacts for power MOSFETs was examined in terms of the  $\rho_C$  variation at elevated temperatures, their thermal resistance to the device fabrication process, and their long-term reliability. The samples were two 50-nm-thick Ni contacts prepared and used in the above-mentioned preliminary study: one was a low-resistivity contact ( $\sim 10^{-7} \Omega\text{cm}^2$ ) in the epitaxy in situ-doped  $n^+$  region (N), and the other was a single-material contact ( $\sim 10^{-3} \Omega\text{cm}^2$ ) in the Al<sup>+</sup> implanted/activated  $p^+$  region. Prior to the first test, their Al overlayer was removed with a wet etchant in order to rule out the possibility of a chemical reaction between the contacts and the interconnect layer.

### 4.2.1 Properties at Elevated Temperatures

Figure 5a shows the  $\rho_C$  of the two Ni contacts as a function of the operation temperature,  $T_{\text{op}}$ , ranging from room temperature to 300°C. The  $\rho_C$  values were normalized by the specific contact resistivity at room temperature,  $\rho_{C0}$ .

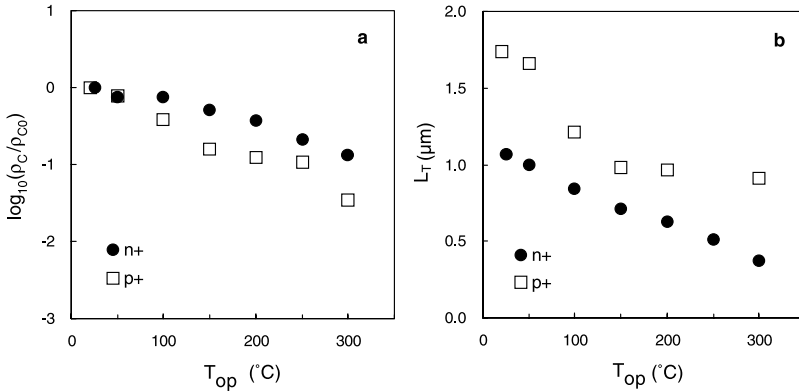


**Fig. 5.** Operation temperature ( $T_{op}$ ) dependence of: (a)  $\rho_C$  and (b) transfer length ( $L_T$ ) for 50-nm-thick Ni contacts in the  $n^+$  and  $p^+$  regions formed by epitaxy in situ N-doping and by Al ion implantation followed by activation annealing, respectively, where  $N_D(N) = 1.5 \times 10^{19} \text{ cm}^{-3}$  and  $N_A(Al) = 2 \times 10^{20} \text{ cm}^{-3}$ .  $\rho_{C0}$  is the specific contact resistivity at room temperature. Data for the  $n^+$  region obtained at temperatures higher than 250°C include large error since they reached the limit of our TLM measurement capability

We can see from this figure that the  $\rho_C$  monotonically decreased as the operation temperature increased and that its variation was approximately one order of magnitude for the contact in the  $n^+$  region and one-and-a-half orders of magnitude for the contact in the  $p^+$  region.

The transfer length,  $L_T$ , is an important yardstick for determining the length of the “lateral” contact in power devices. Figure 5b plots the operation temperature dependence of  $L_T$  for the two Ni contacts. Though the data are a little scattered, the results clearly indicate that  $L_T$  gradually dropped to a sub-micrometer level and reached 0.4 μm and 0.9 μm for the  $n^+$  and  $p^+$  regions at 300°C. The values of  $\rho_C$  and  $L_T$  plotted as a function of reverse  $T_{op}$  [K] do not show a linear relationship for either the  $n^+$  region or the  $p^+$  region.

#### 4.2.2 Resistance to Thermal Budgets in the Device Fabrication Process

Before the completion of the device fabrication process, contacts usually receive additional thermal budgets from subsequent fabrication steps such as  $H_2$  sintering (PMA), passivation film deposition, and packaging. Some of the samples were subjected to a heat cycle test, which simulated such additional thermal budgets in a typical power MOSFET fabrication process. The change in  $\rho_C$  was monitored at room temperature after each step.

The results of the heat cycle test are plotted in Fig. 6. The vertical axis is the logarithmic  $\rho_C$  normalized by the specific contact resistance before the

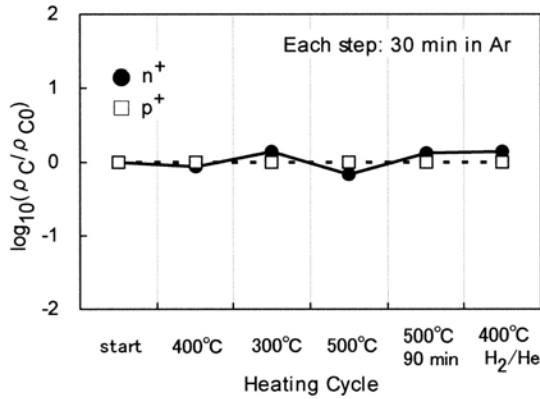


**Fig. 6.** Change in  $\rho_C$  of 50-nm-thick Ni contacts in the  $n^+$  and  $p^+$  regions subjected to a heat cycle test simulating the additional thermal budgets in a typical power MOSFET fabrication process. The samples are identical to those in Fig. 5.  $\rho_{C0}$  is the specific contact resistivity that the contacts showed before the cycle test

test,  $\rho_{C0}$ . As can be seen in this figure, for both the contacts in the  $n^+$  and  $p^+$  regions, the  $\rho_C$  did not change significantly during and after the test. It is concluded that both Ni contacts can withstand additional thermal budgets in the device fabrication process.

#### 4.2.3 Long-Term Reliability

When contacts are subjected to a high temperature (e.g., 300°C) for a long period of time, the  $\rho_C$  may increase. This is a very serious problem because it results in an increase in the specific on-resistance of power devices [24]. The long-term reliability of the two Ni-based contacts was examined at 500°C for 1 000 hours in an Ar ( $t < 10$  hours) and N<sub>2</sub> ( $t > 10$  hours) ambient. The samples were the TLM contacts used in the experiment in Fig. 6. The 500°C heating process was occasionally stopped in line with the time schedule, and the  $\rho_C$  was measured at room temperature.

The changes in the  $\rho_C$  for the two contacts are shown in Fig. 7, where  $\rho_{C0}$  is the specific contact resistivity of the contacts before they were heated to 500°C. The horizontal axis is the logarithmic heating time in hours. This figure clearly shows that the contact in the  $p^+$  region was extremely stable even at 500°C and that its  $\rho_C$  did not vary at all for 1 000 hours. In contrast, the contact in the  $n^+$  region behaved differently. The  $\rho_C$  decreased in the first few hours, then gradually returned to the initial level, and eventually became stable after 100 hours. The mechanism that caused such behavior is not yet clear. However, it is evident that low-resistivity Ni contacts in the  $n^+$  region can potentially withstand 1 000 hours of heating at 500°C in the sense that the  $\rho_C$  during and after the heating test does not exceed the initial  $\rho_C$  value.

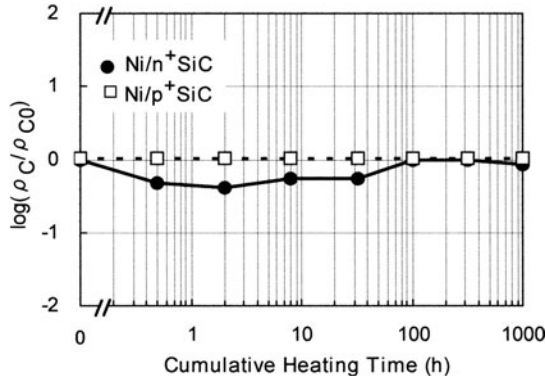


**Fig. 7.** Change in  $\rho_C$  of 50-nm-thick Ni contacts in the  $n^+$  and  $p^+$  regions subjected to a thermal test at 500°C for 1000 hours, where  $\rho_{C0}$  is the specific contact resistivity that the contacts showed before the cycle test. The samples are identical to those in Figs. 5 and 6

### 4.3 Process Design and Fabrication of Power MOSFETs

We propose poly-Si gate  $n$ -channel vertical power MOSFETs on 4H-SiC, successfully assembling the single-material Ni contacts as explained above and describe their fabrication process. Figure 8f shows the cross-sectional structure of a unit cell in the proposed vertical MOSFETs. As shown in this figure, a single Ni contact is commonly used in both the  $n^+$ -source and  $p^+$  regions in the  $p$ -base region. This contact structure is identical to that in Fig. 1c.

Figures 8a through f show the fabrication process. Figure 8a shows the cell structure after the  $p$ -base,  $p^+$  in the  $p$ -base,  $n^+$ -source, and doped-channel regions are selectively formed in the  $n$ -epilayer on the heavily N-doped 4H-SiC substrate. After sacrificial oxidization followed by the removal of the resultant oxide, a thick field oxide is formed on the substrate surface by thermal oxidization and APCVD. The bottom oxide of the field oxide may be as thick as 10 nm. The field oxide over the active area is then removed by photolithography using BHF-based wet etching. As a result, although the cell returns to the structure in Fig. 8a, the field oxide still remains over the gate-pad area, which is not shown in the figure. The substrate is subjected to a surface-cleaning procedure consisting of RCA cleaning followed by slight etching with a diluted hydrofluoric solution. A gate oxide is then thermally grown in the active region followed by the deposition of a poly-Si layer by LPCVD. After phosphorus doping using  $\text{POCl}_3$ , the  $n^+$  poly-Si gate is defined by photolithography using dry etching. The cell structure thus obtained is depicted in Fig. 8b. It should be noted that part of the gate oxide remains on the  $n^+$ -source and  $p^+$ -base regions and that a thermal oxide and a poly-Si layer are also formed on the back side of the substrate. Then, after the top

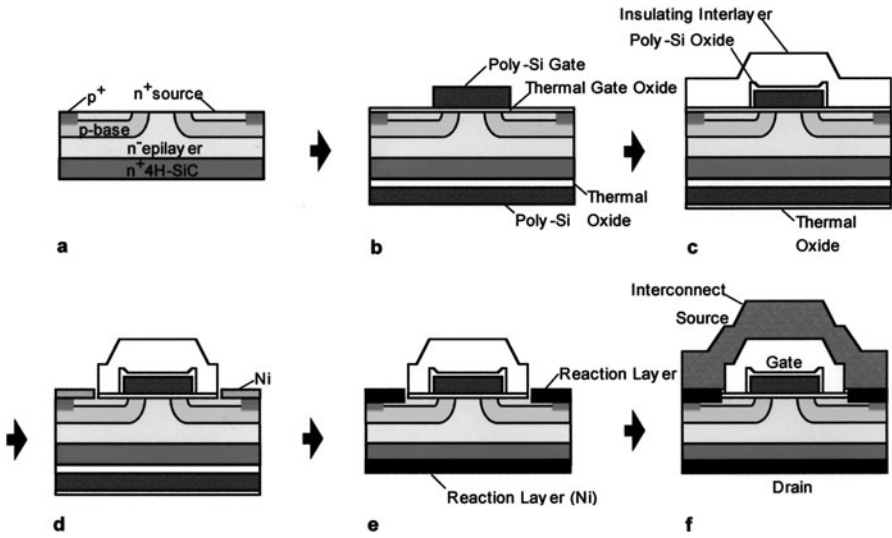


**Fig. 8.** Fabrication process of poly-Si gate vertical power MOSFETs by assembling the single-material Ni contacts in both the  $n^+$ -source and  $p^+$  regions in the  $p$ -base region

and side surfaces of the poly-Si gate are thermally oxidized, a thick insulating interlayer, (in this case, PSG) is deposited on the surface by APCVD, as shown in Fig. 8c, and it is then densified by annealing in an inert ambient. Next, two windows for the  $n^+$  source/ $p^+$  base and poly-Si gate contacts are opened in the insulating interlayer by photo-lithography with RIE followed by BHF-based wet etching, and a 50-nm-thick Ni film is quickly deposited on the entire surface of the substrate, which still has the photoresist. When the photoresist is removed, the Ni film remains at the bottom of the windows (Fig. 8d). After protecting the front surface with the photoresist, both the poly-Si and the thick thermal oxide layers are removed from the back surface by dry and BHF-based wet etching, respectively, and then a blanket Ni film is deposited on the “clean” back surface. After the removal of the protective photoresist, the substrate is rapid-thermally annealed at 1000°C for 2 min in Ar to simultaneously form ohmic contacts in the  $n^+$ -source/ $p^+$ -base,  $n^+$ -poly gate (pad), and  $n^+$ -drain (back surface) regions. Figure 8e shows the cell structure after this PDA. A thick Al overlayer is finally deposited on the surface by DC magnetron sputtering and patterned by photolithography using RIE (Fig. 8f).

Based on the fabrication process described above, vertical  $n$ -channel power MOSFETs with a variety of cell pitches have been fabricated on low-resistivity (0001)<sub>Si</sub> 8°-off 4H-SiC substrates. The substrates had a 10-μm-thick epilayer with a donor concentration of less than  $10^{16}$  cm<sup>-3</sup>. One of the fabricated normally “off” power MOSFETs showed a specific on-resistance

**Table 3.** Doping level and specific contact resistivity ( $\rho_C$ ) for each region in the fabricated vertical power MOSFETs

Region	Doping [ $\text{cm}^{-3}$ ]	$\rho_C$ [ $\Omega\text{cm}^{-2}$ ]
$n^+$ source	$2.0 \times 10^{20}$ (P)	$6.0 \times 10^{-6}$
$p^+$ body	$7.0 \times 10^{20}$ (Al)	$2.0 \times 10^{-3}$
$n^+$ poly-Si	not measured (P)	$4.8 \times 10^{-7}$

of  $17 \text{ m}\Omega\text{cm}^2$  at a gate voltage of 23 V and a blocking voltage of more than 600 V. The electrical characteristics of the MOSFETs are reported in detail elsewhere [65]. Only the results for the Ni-based contacts in the  $n^+$  source and  $p^+$  base regions and the  $n^+$  poly-Si gate are described here [64].

The  $\rho_C$  of each contact except for the drain (back-side) contact of the power MOS structures was accurately measured by a transfer length method. TLM test structures were formed on a substrate identical to that on which the MOSFETs were fabricated. Table 3 lists the doping levels and the  $\rho_C$  values for each region. The source contact showed a  $\rho_C$  of  $6 \times 10^{-6} \Omega\text{cm}^2$ . This  $\rho_C$  value meets the requirements for wide power-MOS applications using  $4H$ -SiC. The single-material (Ni)  $p^+$  base contact had a  $\rho_C$  lower than that given in the preliminary investigation. This slightly better  $\rho_C$  may have resulted from a higher Al-doping level. The  $\rho_C$  for the  $n^+$  poly-Si contact was sufficiently small to drive the gate of the power MOS structures.

## 5 Conclusion

A contact fabrication technology for practical power devices on  $4H$ -SiC was described. An optimal contact structure was proposed, which can overcome the drawbacks of conventional techniques. Specific contact resistances in the range of  $10^{-7} \Omega\text{cm}^2$  were demonstrated using a Ni-based contact in an epitaxially grown  $n^+$  region on  $(0001)_{\text{Si}}$   $4H$ -SiC substrates. A single-material Ni contact showing an ohmic property for both the  $n$ - and  $p$ -type regions was also fabricated on  $4H$ -SiC, and it had a specific contact resistivity in the range of  $10^{-6} \Omega\text{cm}^2$  and  $10^{-3} \Omega\text{cm}^2$  in the ion implanted  $n^+$  and  $p^+$  regions, respectively. The fabricated contacts were able to withstand a thermal stress of  $500^\circ\text{C}$  for 1 000 hours. Finally, our contact structure was applied to a vertically structured  $n$ -channel poly-Si-gate power MOSFET fabricated on a  $4H$ -SiC substrate. We found that low-resistivity and single-material contacts could be made in real vertical power MOSFETs.

## Acknowledgements

This work was performed with the collaboration of the R&D Association for Future Electron Devices (FED) and the National Institute of Advanced Industrial Science and Technology (AIST) as part of a Ministry of Economy, Technology and Industry (METI) project concerning the research and development of ultra-low-loss power device technologies, supported by The New Energy Development Organization (NEDO). The authors wish to thank Mr. T. Mihara (NRC) for allowing us to use a Si-device fabrication line, Ms. Y. Hirose (NRC) for the design of the photomask, Mr. T. Mori (NRC) for helping us perform thermal oxidization and CVD processes, Dr. S. Kanemaru (AIST) for the use of a projection aligner, and Mr. S. Kaneko (NRC), Mr. N. Kiritani (FED), and Mr. M. Hoshi (FED) for their help in this research.

## References

1. B.J. Baliga: *Modern Power Devices* (Krieger, Malabar 1987) p. 263
2. H. Murrmann, D. Widmann: IEEE Trans. Electron Devices **ED-16**, 1022 (1969)
3. R.J. Trew: phys. stat. sol. (a) **162**, 409 (1997)
4. L.M. Porter, R.F. Davis: Mater. Sci. Eng. B **34**, 83 (1995)
5. J. Crofton, L.M. Porter, J.R. Williams: phys. stat. sol. (a) **202**, 581 (1997)
6. M.J. Bozack: phys. stat. sol. (a) **202**, 549 (1997)
7. S.W. King, R.J. Nemanich and R.F. Davis: J. Electrochem. Soc. **146**, 2648 (1999)
8. J.R. Waldrop, R.W. Grant: Appl. Phys. Lett. **62**, 2685 (1993)
9. R.K. Kaplan: Surf. Sci. **215**, 111 (1989)
10. A.J. van Bommel, J.E. Crombeen, A. van Tooren: Surf. Sci. **48**, 463 (1975)
11. F. Bozso, L. Muehlhoff, W.J. Chouke and J.T. Yates, Jr.: J. Vac. Sci. Tech. A **2**, 1271 (1984)
12. L. Muehlhoff, W.J. Choike, M.J. Bozack, J.T. Yates, Jr.: J. Appl. Phys. **60**, 2842 (1986)
13. J. Crofton, J.M. Ferrero, P.A. Barnes, J.R. Williams, M.J. Bozack, C.C. Tin, C.D. Ellis, J.A. Spitznagel, P.G. McMullin: "Amorphous and Crystalline Silicon Carbide IV," Springer Proceedings in Physics **71**, 176 (1992)
14. J. Pezoldt, B. Stottko, G. Kupris, G. Eche: Mater. Sci. Eng. B **29**, 95 (1995)
15. N. Lundberg, M. Östling: Solid-State Electron. **39**, 1559 (1996)
16. J. Crofton, P.G. McMullin, J.R. Williams, M.J. Bozack: J. Appl. Phys. **77**, 1317 (1995)
17. J. Crofton, L. Beyer, J.R. Williams, E.D. Luckowski, S.E. Mohny, J.M. Deluca: Solid-State Electron. **41**, 1725 (1997)
18. Ts. Marinova, A. Kakanakova-Geotgieva, V. Krastev, R. Kakanakov, M. Neshchev, L. Kassamakova, O. Noblanc, C. Arnodo, S. Cassette, C. Brylinski, B. Pécz, G. Radnóczy, G. Vincze: Mater. Sci. Eng. B **46**, 223 (1997)
19. T. Toda, Y. Ueda, M. Sawada: Mater. Sci. Forum **338-342**, 989 (2000)
20. S. Onda, R. Kumar, K. Hara: phys. stat. sol. (a) **162**, 369 (1997)

21. S.H. Ryu, A. Agarwal, J. Richmond, M. Das, L. Lipkin, J. Palmour, N. Saks, J. Williams: *Mater. Sci. Forum* **389–393**, 1195 (2002)
22. D. Planson, M.L. Locatelli, F. Lanois and J.P. Chante: *Mater. Sci. Eng. B* **61–62**, 497 (1999)
23. C. Arnode, S. Tye, F. Wyezisk, C. Brylinski: *Inst. Phys. Conf. Ser.* **142**, 577 (1996)
24. O. Noblanc, C. Arnodo, C. Brylinski, S. Cassette, R. Kakanakov, L. Kassamakova, M. Neshev, A. Kakanakova-Georgieva, V. Krastev, Ts. Marinova: *Inst. Phys. Conf. Ser.* **155**, 609 (1997)
25. B. Pécz, G. Radnóczy, S. Cassette, C. Brylinski, A. Arnodo, O. Noblanc: *Diamond and Related Materials* **6**, 1428 (1997)
26. S. Liu, K. Reinhardt, C. Severt and J. Scofield: *Inst. Phys. Conf. Ser.* **142**, 589 (1996)
27. Ts. Marinova, A. Kakanakova-Georgieva, C. Hallin, R. Yakimova, R. Kakanakov, L. Kassamakova, E. Janzén: *ECASIA 97*, 659 (1997)
28. T.N. Oder, J.R. Williams, K.W. Bryant, M.J. Bozack, J. Crofton: *Mater. Sci. Forum* **338–342**, 997 (2000)
29. S. Tanimoto, Y. Hayami, H. Okishi: *Extended Abstracts of the Symposium on Future Electron Devices 2000 (Tokyo, Japan)* **FED-172**, 107 (2000)
30. S. Tanimoto, J. Senzaki, Y. Hayami, H. Hoshi, H. Okushi: *Extended Abstracts of 1st International Workshop on Ultra-Low-Loss Power Devices Technology (UPD2000, Nara, Japan)* **FED-171**, 187 (2000)
31. L.G. Fursin, L.H. Zhao, M. Weiner: *Electron. Lett.* **37**, 1092 (2001)
32. S. Tanimoto, N. Kiritani, M. Hoshi, H. Okushi: *Mater. Sci. Forum* **389–393**, 879 (2002)
33. T. Nakamura, M. Satoh: *Mater. Sci. Forum* **389–393**, 889 (2002)
34. G. Katulka, K.J. Roe, J. Kolodzey, C.P. Swann, G. Desalvo, R.C. Clarke, G. Eldridge, R. Messham: *J. Electron. Mater.* **31**, 346 (2002)
35. S.-K. Lee, S.-M. Koo, C.-M. Zettering, M. Östling: *J. Electron. Mater.* **31**, 340 (2002)
36. T. Nakata, K. Koga, T. Matsushita, Y. Ueda, T. Niina: “Amorphous and Crystalline Silicon Carbide II (Santa Clara, 1988),” *Springer Proceedings in Physics* **43**, 26 (1989)
37. J. Crofton, L. Beyer, T. Hogue, R.R. Siegiej, S. Mami, J.B. Casady, V.R. Iyer, S.E. Mohney: *Proceedings of 4th International High Temperature Electronics Conference (Albuquerque, NM, June 14–18, 1998)*, p. 84
38. S. Liu, J. Scofield: *Proceedings of 4th International High Temperature Electronics Conference (Albuquerque, NM, June 14–18, 1998)*, p. 88
39. L. Kassamakova, R. Kakanakov, N. Nordell and S. Savage: *Mater. Sci. Forum* **264–268**, 787 (1998)
40. L. Kassamakova, R. Kakanakov, I. Kassamakov, N. Nordell, S. Savage, E.B. Svehberg, L.D. Madsen: *Mater. Sci. Forum* **338–342**, 1009 (2000)
41. L. Kassamakova, R.D. Kakanakov, N. Nodell, S. Savage: *Mater. Sci. Forum* **264–268**, 787 (1998)
42. L. Kassamakova, R.D. Kakanakov, I.V. Kassamakov, N. Nordell, S. Savage, B. Hjörvarssö, E.B. Svedberg, L. Åbom, D. Madsen: *IEEE Transact. Electron Devices* **46**, 605 (1999)
43. L. Kassamakova, R. Kakanakov, N. Nordell, S. Savage, A. Kakanakova-Georgieva, T. Marinova: *Mater. Sci. Eng. B* **61–62**, 291 (1999)

44. E.V. Kalinina, G.F. Kholuyanov, A.V. Shchukarev, N.S. Savkina, A.I. Babanin, M.A. Yagovkina, N.I. Kuznetsov: *Diamond and Related Materials* **8**, 1114 (1999)
45. K.V. Vaslevski, S.V. Rendakova, I.P. Nikitina, A.I. Babanin, A.N. Andreev, K. Zekentes: *SEMICONDUCTORS* **33**, 1206 (1999)
46. K.V. Vaslevski, G. Cconstantinidis, N. Papanicolaou, N. Martin, K. Zekentes: *Mater. Sci. Eng. B* **61–62**, 296 (1999)
47. K. Tone, J.H. Zhao: *IEEE Tansact. Electron Devices* **46**, 612 (1999)
48. Y. Luo, F. Yan, J.H. Zhao: *J. Crofton, Mater. Sci. Forum* **338–342**, 1013 (2000)
49. X. Wang, S. Soloviev, Y. Gao, G. Straty, T. Sudarshan, J.R. Williams, J. Crofton: *Mat. Res. Symp. Proc.* **640**, H5.19.1 (2001)
50. J.Y. Lin, S.E. Mohny, M. Smalley, J. Crofton, J.R. Williams, T. Izaacs-Smirh: *Mat. Res. Symp. Proc.* **640**, H7.3.1 (2001)
51. K. Vasilevski, K. Zekentes, K. Tsagaraki, G. Cconstantinidis, I. Nikitana: *Mater. Sci. Eng. B* **80**, 370 (2001)
52. R. Kakanakov, L. Kassamakova, I. Kassamakov, K. Zekentes, N. Kuzenetsov: *Mater. Sci. Eng. B* **80**, 374 (2001)
53. O. Nakatsuka, T. Takei, T. Koide, M. Murakami: *Mater. Trans.* **43**, 1684 (2002)
54. O. Nakatsuka, Y. Koide, M. Mirakami: *Mater. Sci. Forum* **389–393**, 885 (2002)
55. G. Katulka, K.J. Roe, J. Kolodzey, C.P. Swann, G. Desalvo, R.C. Clarke, G. Eldridge, R. Messham: *J. Electron. Mater.* **31**, 346 (2002)
56. K.H. Jung, N.I. Cho, J.H. Lee, S.J. Yang, C.K. Kim, B.-T. Lee, K.H. Rim, N.K. Kim, E.D. Kim: *Mater. Sci. Forum* **389–393**, 913 (2002)
57. R. Kakanakov, L. Kassamakova, N. Hristeva, N. Kuznetsov, K. Zetentes: *Mater. Sci. Forum* **389–393**, 917 (2002)
58. S. Liu, J.D. Scofield: *Mater. Sci. Forum* **264–268**, 791 (1998)
59. F.V. Vassilevski, K. Zekentes, G. Constantinidis, N. Papanicolau, I.P. Nikitina, A.I. Babanin: *Mater. Sci. Forum* **338–342**, 1017 (2000)
60. D. Alok, E. Arnold, R. Egloff, J. Barone, J. Murphy, R. Conrad, J. Burke: *IEEE Electron Devices Lett.* **22**, 577 (2001)
61. M. Kataoka, T. Suzuki: *Japanese Patent Application First Publication No. Hei-sei 10-125620*, 1998 (in Japanese)
62. K. Ueno: *Japanese Patent Application First Publication No. Heisei 8-64801*, 1998 (in Japanese)
63. A.K. Agarwal, J.B. Casady, L.B. Rowland, W.F. Valek, C.V. Brant: *Mater. Sci. Forum* **264–268**, 989 (1998)
64. N. Kiritani, M. Hoshi, S. Tanimoto, K. Adachi, S. Nishizawa, T. Yatsuo, H. Okushi, K. Arai: *Mater. Sci. Forum*, to be published
65. S. Kaneko, M. Hoshi, S. Tanimoto, T. Hayashi, H. Tanaka: presented as a paper at the 2003 Electronic Material Conference (Salt Lake City, Utah, USA, 2003)

# Micromachining of SiC

C.A. Zorman and M. Mehregany

## 1 Introduction

MEMS, short for microelectromechanical systems, is an enabling technology with the potential to impact nearly all fields of science and engineering. In a general sense, MEMS consists of an integrated set of microfabricated sensors, actuators and electronics designed to perceive and act on its local environment in order to achieve a desired function. To make such systems possible, materials or material systems that have favorable mechanical and electrical properties are required. When researchers discovered that Si had favorable mechanical properties and could be machined into micromechanical structures, the field advanced rapidly by leveraging the know-how, techniques and infrastructure of the silicon IC industry. Si pressure sensors were among the first devices in this new field. These devices consisted of micromachined Si membranes and doped Si piezoresistors fabricated using relatively simple and straightforward bulk micromachining processes. With significant advancements in polycrystalline silicon (polysilicon) deposition and etch technologies, more complex Si mechanical elements, such as tethered membranes, micromotors, laterally actuated resonators, hinged plates and the like could be fabricated from thin films using surface micromachining techniques. The heavy dependence on IC materials and processing techniques opened the possibility for integrating microelectronics with microsensors and microactuators, thus differentiating MEMS from discrete sensor technologies. Development of micromolding and wafer bonding techniques advanced the field even further by enabling the fabrication of three dimensional structures that could not be realized by bulk and surface micromachining. This repertoire of micromachining techniques (bulk and surface micromachining, micromolding, and wafer bonding) became, in many respects, a micro-scale analog to the conventional machining techniques of the macro-scale world.

Micromachining of Si has advanced to the point that MEMS technology is being used in a number of commercial applications, including inkjet printing, projection displays, pressure sensing, collision safety, and inertial sensing, with new applications emerging with each major advancement in the field. And while there is little doubt that Si-based MEMS will continue to make a significant impact in application areas that can benefit from miniaturization and batch fabrication, use of Si restricts new applications to those in

benign temperature, chemical, and erosive environments due to the physical properties of Si. This is not to say that Si MEMS devices cannot be used in harsh environments, but deployment often requires extensive packaging that can limit or negate the benefit of miniaturization. To extend the benefits of MEMS technology to harsh environments (e.g., combustion and flow control) with a minimum of packaging, alternatives to Si are needed. Durable semiconductors such as SiC and diamond are excellent candidates, because they are largely chemically inert, wear resistant, radiation hard, and electrically stable at high temperatures. Comparatively, SiC is more advanced as a result of the diversity of production techniques available for amorphous, polycrystalline and single crystal films, the commercial availability of high quality single crystal substrates, and a host of processing techniques developed to support the SiC electronic device industry. And while SiC is most noted for harsh environment applications, it has recently been recognized for its potential in mainstream applications where Si currently dominates. For instance SiC is particularly well suited for biomedical MEMS where materials that are both biocompatible and resistant to the damaging effects of sterilization are needed [1]. SiC is also a leading material for high frequency/high force electrostatic microactuators due to its high Young's modulus-to-density ratio, fracture strength, and electrical conductivity [2]. Of course to fabricate MEMS devices from SiC requires techniques to produce and micromachine material suitable for the devices of interest. This chapter presents a review of the major techniques currently being used to micromachine SiC, including deposition techniques for thin films, bulk micromachining techniques for SiC substrates, surface micromachining techniques for SiC thin films, molding techniques for micro-scale SiC components and production methods for SiC-on-insulator substrates. While not the main focus of this chapter, examples of structures and devices created using the various techniques will be presented where appropriate. To learn more about the specifics of micromachined SiC devices, several thorough reviews have recently been published in main-line journals and should be consulted by those interested in the technology [3]–[5].

## 2 Thin Film Growth Processes for SiC MEMS

Silicon carbide has long been known for its outstanding electrical properties, especially those that enable SiC microelectronics to function at temperatures, voltages and frequencies that are not easily sustained in Si. The demand for such devices has pushed the development of techniques for the production of electronic-grade SiC substrates and thin films that are sufficient for high performance devices. Along different lines, SiC is equally well known as a robust mechanical and chemical material, and consequently has been used extensively in industrial applications requiring durable bulk components, resistant thin film coatings and heavy-duty abrasives. In both situations the material is chemically the same, however the requirements for electronic applications

differ so much from those for industrial applications that, until recently, there has been little need to develop versatile SiC production processes designed to capitalize on the full set of its physical properties.

MEMS, by its very nature, requires materials that have favorable electrical, mechanical and chemical properties. Where possible, MEMS technology favors materials that have advantageous characteristics in all three categories, hence the growing interest in SiC. Early work in SiC MEMS utilized thin film growth techniques developed specifically for SiC electronics, since such techniques were the state-of-the-art at the time. As interest in SiC MEMS began to grow, techniques to produce SiC specifically for MEMS began to emerge. These techniques are designed to produce SiC with the desired physical traits on a wide variety of substrates. In essence, SiC MEMS seeks to capitalize on the properties that make the material attractive for both industrial applications and electronic applications. The following section presents a review of deposition techniques designed and developed specifically for SiC MEMS.

## 2.1 Single Crystal SiC

In wafer form, SiC currently exists in the *4H*- and *6H*-SiC polytypes and both are well suited for homoepitaxial growth of *4H*- and *6H*-SiC films. As the cost of these wafers continues to decrease and the size continues to increase, use of *4H*- and *6H*-SiC polytypes in micromachined devices becomes more attractive. Several examples are beginning to appear in the literature and are detailed later in this chapter. To the best of our knowledge, the processes used to fabricate the substrates and epitaxial thin films in the few cases where the hexagonal polytypes are used in micromachining are the same as those for SiC electronics and thus will not be reviewed here.

In contrast to the hexagonal polytypes, *3C*-SiC is formed at lower temperatures and has a crystalline structure similar to silicon, enabling *3C*-SiC films to be heteroepitaxially grown on Si substrates. The typical process involves conversion of Si by carbonization in a hydrocarbon gas, followed by *3C*-SiC film growth. The carbonization process results in a carbonized layer thickness of 10 to 20 nm. The bulk of the film is then grown by homoepitaxy using carbon and silicon containing precursors. This process was first developed for electronic applications in hopes that a low cost, larger area alternative to *6H*-SiC could be found. The high defect density resulting from the lattice mismatch between *3C*-SiC and Si and continued improvements in the quality and size of *6H*-SiC substrates eventually led most development efforts away from *3C*-SiC for SiC electronics, although work does continue and recent advancements are beginning to show promise.

Interest in *3C*-SiC began to grow not long after MEMS technology entered a rapid phase of development (mid 1990's) for much the same reasons as mentioned previously. Much of this early work utilized *3C*-SiC films grown using the aforementioned two step heteroepitaxial process. Zorman et al.,

were among the first to report on 3C-SiC heteroepitaxy for MEMS applications, using propane, silane, and hydrogen to grow 3C-SiC films on 100 mm-diameter (100) Si wafers by atmospheric pressure chemical vapor deposition (APCVD) at temperatures around 1360°C [6]. This group was the first to report the growth of 3C-SiC films on large area substrates absent of interfacial voids, a characteristic that is particularly important for micromechanical device structures that are attached to the substrate using small anchor pads. The growth process remains essentially unchanged to this day and has been used in 3C-SiC based pressure sensors, lateral resonators and nanomechanical systems, all of which are detailed later in this chapter.

Growth of heteroepitaxial 3C-SiC films on Si substrates is not limited to APCVD and numerous low pressure CVD (LPCVD) processes using both single and dual source precursors have been reported. Single source precursors are becoming increasingly more common as Si- and C-containing compounds that decompose at low temperatures become commercially available. LPCVD offers several advantages over APCVD, including improved film thickness uniformity over large areas, potentially lower impurity concentrations due to generally better vacuum systems, and lower processing temperatures. In a notable example pertaining to SiC MEMS, Krotz et al., reported a LPCVD process using mono-methylsilane ( $\text{H}_3\text{Si-CH}_3$ ) that yielded 3C-SiC films on Si substrates at temperature as low as 1000°C [7]. The films proved particularly useful as free standing membranes, tethered plates and other structures micromachined from the Si wafers. The authors were able to show the utility of 3C-SiC at high temperature by demonstrating that a 3C-SiC membrane pressurized to 1 bar and heated to 850°C did not suffer plastic deformation. In contrast, an identical Si membrane tested in the same manner was permanently deformed.

Production of 3C-SiC films for use in MEMS is not restricted to CVD processes. Serre, et al., reported on a novel process to form 3C-SiC by  $\text{C}^+$  implantation into Si [8]. The process involves high temperature (500°C) ion implantation at moderate doses followed by a high temperature anneal (1150°C) for 6 hr to form the 3C-SiC layer. For improved conductivity, doped Si wafers are used. The films are suitable for surface micromachining, either by selective removal of the underlying Si substrate, or by bonding and etch back to form 3C-SiC-on-insulator substrates that can be micromachined by selective removal of a buried oxide [9]. Membranes, cantilever beams and other thin, single layer structures can be made in this manner. Details about SiC-on-insulator substrates will be provided later in this chapter.

## 2.2 Polycrystalline SiC

Many micromechanical devices and a large number of microsensor structures do not require the high crystal quality needed to fabricate SiC electronics, and thus can be fabricated from polycrystalline material. The freedom to use polycrystalline material lifts many restrictions on the deposition processes,

especially with regards to deposition temperatures and substrate materials. As such, polycrystalline SiC films can be deposited on substrate layers such as polysilicon,  $\text{SiO}_2$ , and  $\text{Si}_3\text{N}_4$ , enabling the fabrication of more complex structures than could be realized from single SiC layers.

As with 3C-SiC, early work in polycrystalline SiC MEMS utilized polycrystalline 3C-SiC (poly-SiC) films deposited by APCVD using modifications to the heteroepitaxial growth process described earlier [10]. And while research using APCVD poly-SiC films continues [11], the trend is to use LPCVD for the reasons mentioned earlier. With the restrictions related to epitaxy completely lifted, a wide variety of single and dual precursors can be used. Dual precursor processes specifically for SiC MEMS include dichlorosilane ( $\text{SiH}_2\text{Cl}_2$ ) and acetylene ( $\text{C}_2\text{H}_2$ ) at  $900^\circ\text{C}$  [12] and silane ( $\text{SiH}_4$ ) and carbon tetrabromide ( $\text{CBr}_4$ ) at  $940^\circ\text{C}$  [13]. The process used by Zorman et al., is noteworthy for the size of the furnace, which can accommodate up to one-hundred, 100 mm-diameter wafers in a single run [12]. Single precursors have also been used, with temperatures ranging from  $1200^\circ\text{C}$  for compounds such as silacyclobutane (SCB) and trimethylsilane (3MS) [14] to  $800^\circ\text{C}$  for disilabutane (DSB) [15]. It should be noted that while the deposition temperature for SCB and 3MS is high, the deposition rates were nearly  $1\text{ }\mu\text{m}/\text{min}$ , which significantly reduces the overall thermal budget of the process.

As in the case of 3C-SiC growth, poly-SiC processes for SiC MEMS are not restricted to CVD techniques. If fact,  $\text{C}^+$  implantation into polysilicon films on oxidized Si substrates enables the creation of poly-SiC films on  $\text{SiO}_2$  sacrificial layers, as reported by Serre, et al. [16]. The process is essentially the same as detailed previously except that the post implant annealing step is not required. Other methods, such as reactive and magnetron sputtering, can also be used to produce poly-SiC films, but to the best of our knowledge, use of these films is not widespread in MEMS, although the potential is high for applications such as protective coatings.

### 2.3 Amorphous SiC

Amorphous SiC is attractive from a MEMS fabrication point-of-view because it can be deposited at very low substrate temperatures ( $\sim 200^\circ\text{C}$ ) on a wide variety of substrates using processes such as plasma enhanced chemical vapor deposition (PECVD). Due to its chemical inertness, PECVD SiC is commonly used as a masking material in Si bulk micromachining applications. Amorphous SiC films are especially resistant to KOH and HF if annealed prior to use [17], although films deposited at moderate temperatures ( $400^\circ\text{C}$ ) exhibit excellent resistance to KOH, HF and TMAH [18]. PECVD offers the opportunity to control the residual stress in as-deposit SiC films, with stresses ranging from moderately compressive to moderately tensile [19], enabling the films to be used in a variety of micromechanical applications.

PECVD is not the only means to produce amorphous SiC films for MEMS applications. Ledermann, et al., recently showed that magnetron sputtering

of a SiC target could be used to produce stress-controlled SiC films on planar and non-planar Si surfaces [20]. Film thicknesses up to 2  $\mu\text{m}$  were produced by this method. And unlike conventional PECVD, amorphous, non-hydrogenated SiC could be deposited at a substrate temperature of 25°C. Pinhole-free, low stress films resistant to KOH etchants were produced when the oxygen content was held below 3 at. %.

### 3 SiC Bulk Micromachining

In general terms, bulk micromachining is a process used to create micro-scale mechanical structures by sculpting them directly from the substrate. Bulk micromachining was one of the first techniques used in MEMS, and is still commonly employed to fabricate MEMS devices from Si, GaAs, quartz and other high quality substrate materials. Bulk micromachining is typically performed using wet and dry etching techniques, with laser and ion beam milling becoming increasingly popular as these techniques become refined and applications require materials that cannot easily be etched. Bulk micromachining of Si is extremely common, owing to the availability of high quality single crystalline substrates, anisotropic wet etchants and appropriate etch mask and etch-stop materials. Anisotropic wet etchants such as ethylene-diamine pyrocatechol (EDP) and potassium hydroxide (KOH) etch the (100) and (110) planes of Si much faster than the (111) planes, which enables the fabrication of deep rectangular and square cavities in (100) Si wafers. Other crystalline materials, namely quartz and III-V materials (e.g., GaAs) also exhibit an anisotropic etching behavior to particular crystal planes. A significant advantage of wet anisotropic etching of Si and GaAs is that mechanical structures can be machined out of electronic-grade material, thus facilitating integration with electronic devices for sensing and signal processing. A drawback of this technique, however, is that the geometry of the micromachined structure is ultimately restricted by the crystal orientation of the substrate. Consequently, fabricating micromechanical structures with complex, free form geometry is difficult. Nevertheless, it is relatively straightforward to bulk micromachine structures such as suspended cantilevers and square membranes from Si wafers for use in high performance devices, such as micromachined pressure sensors and accelerometers. To address the geometric restrictions of wet anisotropic Si etching, deep reactive ion etching (DRIE) processes have been developed and are now widely used. These processes anisotropically etch Si with respect to the overlying etch masks, therefore columnar structures with circular cross-sections can easily be etched. This technology allows the patterning of high-aspect-ratio (e.g.,  $> 20 : 1$ ) features directly into a Si wafer using photoresists or  $\text{SiO}_2$  as etch masks. Etch depths of a few hundred microns are possible while maintaining smooth, vertical sidewall profiles. When silicon-on-insulator (SOI) wafers are used as substrates, device

structures such as accelerometers, gyroscopes, and mechanical resonators can be made.

Due to its extreme chemical inertness, fabrication of micromachined structures in SiC using the aforementioned conventional bulk micromachining techniques has proven to be impossible in most cases and very difficult in the few that have shown promise. With the exception of a phosphoric acid etch at about 200°C, SiC is not known to etch in any wet chemicals at reasonable temperatures. As a result, anisotropic wet chemical etching of SiC along select crystal planes has not been demonstrated despite the availability of very high quality, single crystal substrates. Some common molten salts, such as Na<sub>2</sub>CO<sub>3</sub>, Na<sub>2</sub>B<sub>4</sub>O<sub>7</sub>, NaOH, Na<sub>2</sub>O<sub>2</sub>, and KOH, have been used to decorate crystalline defects in SiC substrates, but these etchants lack the selectivity necessary to produce device structures by bulk micromachining.

The chemical inertness of SiC requires that alternative methods be used for bulk micromachining. Despite its inertness, SiC can be selectively etched using electrochemical processes recently reviewed in detail by Okojie [21]. In general, SiC electrochemical etching is performed in an aqueous HF solution using a basic three-electrode configuration consisting of an ohmic contact to the SiC substrate, a reference electrode, and a Pt counter electrode. For etching to occur, holes (of the electronic type) must be present in the SiC crystal at the SiC/electrolyte interface, which can be generated by an external energy source. Etching occurs by the oxidation of SiC, which is promoted by the large concentration of holes at the surface of the SiC/electrolyte interface. SiO<sub>2</sub> is removed by the HF solution, while carbon evolves in gaseous form as CO<sub>2</sub> and CO.

For *n*-type SiC, the generation of a sufficient number of holes is achieved by the use of an external light source in the 250 nm to 400 nm wavelength range in conjunction with an anodic potential applied to the SiC substrate. For etching selected regions of the SiC substrate, laser-assisted photoelectrochemical (PEC) etching has been performed by simply scanning a laser across the surface of the region to be etched. For broad area etching, HF resistant masks can be used in conjunction with flood exposures. Electrochemical etching has been primarily used to etch 6*H*-SiC, however, *n*-type 3*C*-SiC films grown on Si wafers have also been etched. *p*-type SiC has an excess of holes; hence the etching process can be performed without illumination and thus is referred to as dark electrochemical etching.

Due to differences in electrochemical etching of *n*- and *p*-type SiC, bulk micromachining processes that incorporate etch stop layers can be performed, especially in 6*H*-SiC substrates where epitaxial growth of high quality doped layers is now routine. A PEC process utilizing an epitaxially grown etch stop has been developed to fabricate bulk micromachined piezoresistive 6*H*-SiC pressure sensors for high temperature applications [22]. The process starts with an *n*-type 6*H*-SiC substrate on which epitaxial *p*- and *n*-type 6*H*-SiC films are successively grown. Using the *p*-type epilayer as an etch stop, the

overlying *n*-type epilayer is patterned and etched by PEC into *n*-type piezoresistors. A timed photoelectrochemical etch is then used to form a circular cavity into the backside of the *n*-type substrate, resulting in the creation of a 50  $\mu\text{m}$ -thick, *n*-type diaphragm underneath the piezoresistors. The *p*-type epilayer serves both as an etch stop and as a junction isolation layer. Upon testing, this sensor demonstrated stable output at temperatures up to 500°C and 69 bar, showing the potential for 6H-SiC in specialized MEMS applications.

The chemical inertness of all SiC polytypes makes physical processes such as laser micromachining particularly attractive for generating micromachined structures. Unlike plasma processes, laser micromachining is a maskless, direct-write process, meaning that patterns are generated by a focussed beam only in the illuminated area and at a depth determined largely by the power density of the beam. Lasers are commonly used in macroscopic machining to create well-defined holes in substrate materials such as SiC. Laser micromachining is significantly more challenging because in most cases, structures with a higher degree of geometric complexity than holes and cavities are desired. Nevertheless, several recent efforts have explored laser techniques specifically for micromachining applications. For instance, Jandeleit et al. detail a study investigating the removal process of SiC and other notable materials using pico- and nanosecond pulsed Nd:YAG laser irradiation [23]. As the authors report, pulsed laser radiation has potential in micromachining applications because the laser irradiation can be focussed to micron-sized spot diameters and the thermal load can be controlled by the duration of the laser pulse. Using nano and picosecond pulse lengths allow for very high power densities to be used while minimizing the adverse effects of melt pool resolidification on the substrate, a problem that can significantly alter the shape and size of the final structure. With removal rates of 75 nm to 1.1  $\mu\text{m}$  per laser pulse, the authors report the ability to produce holes in SiC with diameters as small as 4  $\mu\text{m}$  with sharp edges and steep sidewalls.

For Si bulk micromachining, DRIE is becoming an extremely popular technique, since the selective nature of the process with respect to convenient etch mask and etch stop materials (photoresist and  $\text{SiO}_2$ ) enables the fabrication of complex structures that cannot be realized using other methods. In general terms, DRIE utilizes high-density plasmas to anisotropically etch features deep into the substrate without regard to crystal orientation. In some Si processes, the etching step is not continuous, but rather is interrupted periodically so that a thin protective film can be applied to the sidewalls of the newly created structure. In this manner, deep structures ( $> 100 \mu\text{m}$ ) with nearly vertical sidewalls can be created.

Fortunately, SiC is not so chemically inert that it resists all types of energetic plasmas. Quite the contrary, SiC can be etched in fluorinated plasmas, many of which are commonly used in Si microfabrication, albeit at slower etch rates. For a comprehensive review of SiC plasma etching processes, the reader

is directed to [24]. While there are numerous dry etching techniques suitable for SiC patterning, most of these were developed for thin film monolithic 6H- and 4H-SiC electronic devices. Consequently, etch rate, while important, was a secondary parameter to etch profiles and etch field characteristics. With the rapid rise in the development of SiC-based high power and high frequency devices, interest in using ultra-thick ( $> 50 \mu\text{m}$ ) SiC layers has given rise to RIE processes for etching such thick layers. Naturally, these processes will have utility in SiC bulk micromachining, since many of the requirements are similar.

Deep plasma etching of SiC is similar to Si in that etching is performed using a high density plasma consisting of fluorinated chemistries. To achieve etch rates comparable to Si DRIE, SiC DRIE requires plasmas that include highly energetic ion bombardment to damage the exposed SiC surface, making it more susceptible to chemical reactions with fluorine radicals. This necessitates the use of hardened, non volatile etch masks such as Ni and indium-tin-oxide (ITO) as opposed to less durable photoresists and  $\text{SiO}_2$  masking materials [25]. The inertness of SiC does, however, provide one significant advantage over Si in that the sidewall passivation step that is crucial for high aspect ratio Si DRIE, is not required for SiC DRIE, especially since the SiC DRIE plasmas are highly directional.

Several recent publications have detailed the development and applications of SiC DRIE for microelectronics and MEMS applications. Cho et al., describe a process to produce via hole etching in 4H-SiC substrates by inductively coupled plasma (ICP) etching with  $\text{SF}_6$  and  $\text{O}_2$  [26]. Etch rates of  $0.6 \mu\text{m}/\text{min}$  were achieved and selectivities of greater than 50 were realized when Al was used as an etch mask. Columnar via holes etched both partially and completely through  $100 \mu\text{m}$ -thick wafers were formed, thus demonstrating the utility of the process for at least relatively simple structures. Along similar lines, Chabert reported the deep etching of 4H-SiC using  $\text{SF}_6$  and  $\text{O}_2$  in helicon generated plasmas [27]. The authors report via hole etch depths of  $330 \mu\text{m}$ , etch rates of  $1.35 \mu\text{m}/\text{min}$  and a selectivity to Ni etch masks of 50 for helicon-based plasmas. In what is likely the first use of SiC DRIE to produce an active bulk micromachined MEMS device, Beheim reports the fabrication of a 6H-SiC piezoresistive pressure sensor from 6H-SiC wafers [25]. The sensor consists of four piezoresistors patterned on top of a  $60 \mu\text{m}$ -thick, 1 mm-diameter 6H-SiC membrane etched from a  $120 \mu\text{m}$ -thick, commercial grade 6H-SiC wafer. With the appropriate metalization and packaging, the sensor was successfully tested in the compressor discharge of a gas turbine engine, reaching temperatures as high as  $520^\circ\text{C}$ .

Bulk micromachining of Si substrates using SiC is straightforward since SiC thin films can be readily deposited on Si wafers and is an ideal etch stop for Si etchants such as KOH, TMAH, and EDP. This fact enables the fabrication of single and polycrystalline 3C-SiC thin film structures suspended from micromachined Si substrates, such as the membranes shown in Fig. 1.

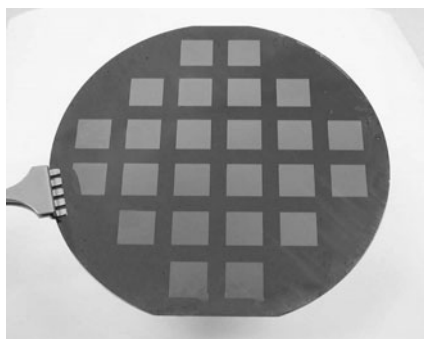


**Fig. 1.** Poly-SiC thin film membranes on a 100 mm-diameter Si wafer fabricated by wet Si anisotropic etching (courtesy FLXMicro, Cleveland, Ohio USA)

A cross section and plan-view of the structure are shown schematically in Fig. 2.

The process begins with the deposition of a 3C-SiC film on a (100) Si substrate. Following SiC growth, the wafer is placed in a thermal oxidation furnace, where a 1.5  $\mu\text{m}$ -thick  $\text{SiO}_2$  film is grown on the backside of the Si wafer. Etch windows are photolithographically patterned in the backside oxide using HF as an etchant. The wafer is then submerged in an anisotropic Si etchant such as KOH to remove the unmasked regions of the Si substrate. As mentioned previously, the etch preferentially removes (100) and (110) Si planes, forming a cavity beneath the SiC membrane bound on four sides with (111) Si planes angled at 54.7 degrees to the wafer surface. Due to the preferential nature of the anisotropic etch, only square or rectangular membranes can be formed. Overetching is of no concern, since the anisotropic Si etchants do not attack SiC. Essentially the same process can be used to form more complex structures such as cantilevers and tethered plates by simply patterning the SiC film by reactive ion etching prior to the Si micromachining steps.

The Si bulk micromachining methods described here can be used to fabricate test structures to evaluate the mechanical properties of single and polycrystalline forms of 3C-SiC, as well as amorphous SiC. Suspended SiC

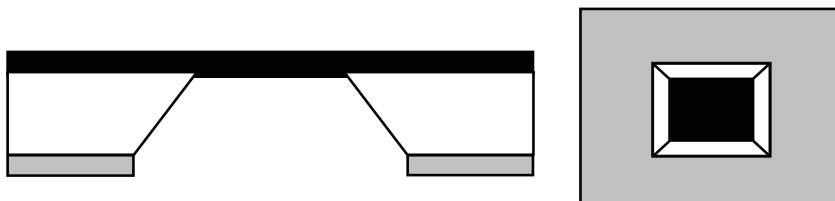


**Fig. 2.** Cross-sectional and plan-view schematics of a SiC membrane fabricated by Si bulk micromachining of a (100) Si wafer. The angled sidewalls are the (111) Si planes that terminate at the SiC film (*black*) and the edges of the  $\text{SiO}_2$  etch mask (*grey*)

membranes are particularly useful since the Young's modulus and residual stress can be determined from the deflection behavior of membranes subjected to pressure loads [28]. As determined using such structures, (100) 3C-SiC films grown by APCVD typically have Young's modulus values of about 350 GPa and residual stress values in the range of 200 to 300 MPa. Likewise, typical values of Young's modulus and residual stress for poly-SiC range from 350 GPa to 450 GPa and 100 MPa to 500 MPa, respectively. In contrast, amorphous SiC has a much lower Young's modulus (180 GPa) and widely varying residual stress (−400 to 490 MPa) [29]. As with other thin film materials, the Young's modulus of a particular crystal form (i.e., poly-SiC) is relatively insensitive to small differences in processing conditions, while the residual stress varies widely depending on process parameters, the main parameter being substrate temperature. It should be noted that for epitaxial films, only (100) 3C-SiC membranes are fabricated by this method, due to the anisotropic behavior of the wet Si etchants.

As mentioned previously, SiC cantilever beams can easily be fabricated by simply patterning the SiC films by RIE prior to the backside Si anisotropic etching step. Alternatively, a small region of Si beneath the patterned SiC structures can be removed from the front side of the substrate by isotropic etching techniques. Several groups have used cantilever structures to evaluate the mechanical properties of 3C-SiC films [8, 30, 31]. Using 10  $\mu\text{m}$ -thick cantilever beams made from 3C-SiC films grown by LPCVD, Su et al., found that the Young's modulus varies significantly for doped and undoped films, with the Young's modulus of undoped films being 694 GPa while that for Al doped films being 474 GPa [30]. By studying the behavior of bending cantilever structures, Serre, et al., found that the Young's modulus of 0.3  $\mu\text{m}$ -thick 3C-SiC films fabricated by  $\text{C}^+$  ion implantation is 470 GPa, which is in fairly close agreement with the doped films in the previous example [31].

The evaluation of mechanical properties using bulk micromachined 3C-SiC structures is not limited to membranes and singly clamped cantilever beams. In fact, doubly anchored beams offer the opportunity to use conventional tensile testing methods to determine the Young's modulus and strength of the material under test. Jackson et al., recently reported the results of such a study using epitaxial 3C-SiC films and bulk poly-SiC specimens [32]. For both specimen types, the test structures consisted of micromachined dog-bone structures. The 3C-SiC specimens were fabricated using the method outlined above for the cantilever beams, while the poly-SiC dog-bone structures were created using a molding process described in the micromolding section of this chapter. From the load-displacement data, the authors found that the Young's modulus for the 3C-SiC films was 420 GPa with a strength of 1.2 GPa, while the poly-SiC samples had a Young's modulus of 430 GPa with a strength of 0.49 GPa.

In addition to mechanical characterization structures, Si bulk micromachining offers many opportunities to fabricate 3C-SiC MEMS devices. Ar-

guably the most common 3C-SiC MEMS device is the bulk micromachined piezoresistive pressure sensor. For such sensors, 3C-SiC is attractive for both its electrical and mechanical properties, especially at operating temperatures too high for Si sensors. For pressure sensing, 3C-SiC films can be used for both membranes and piezoresistors, but unlike the 6H-SiC pressure sensors, no successful design has both the piezoresistors and membranes made from 3C-SiC. This is because  $p$ - $n$  junction isolation in 3C-SiC is significantly hampered by junction leakage in the heteroepitaxially grown films, which only gets worse with increasing temperature. Successful pressure sensor designs use 3C-SiC only for the piezoresistors and use silicon-on-insulator wafers [33, 34] or 3C-SiC on insulator wafers [35] as substrates. An example of such a sensor is shown in Fig. 3. In each of these examples, the membrane is made of (100) Si and is fabricated using Si bulk micromachining either by Si DRIE [33, 34] or wet chemical etching [35]. As a result, the sensors are suitable for high temperature operation (up to 400°C) but are limited to chemical environments favorable to Si unless protective packaging is employed.

3C-SiC is particularly well suited for applications requiring robust mechanical membranes to support active or passive structures made from materials other than 3C-SiC. For instance, Sugiyama et al., fabricated X-ray lithography masks made of 8  $\mu\text{m}$ -thick Au gold absorber structures supported by thin (2  $\mu\text{m}$ ) bulk micromachined 3C-SiC membranes [36]. 3C-SiC is well suited for such applications due to its superior mechanical properties, radiation hardness, and its compatibility with Si bulk micromachining.

Several groups have capitalized on the favorable thermal properties of 3C-SiC to create suspended microbridge heaters for gas sensing applications. Each of the following sensor designs is based on the same basic platform, namely a bulk micromachined poly-SiC microbridge that can be used either as a thermally-isolated mechanical support or a suspended microheater. Ho et

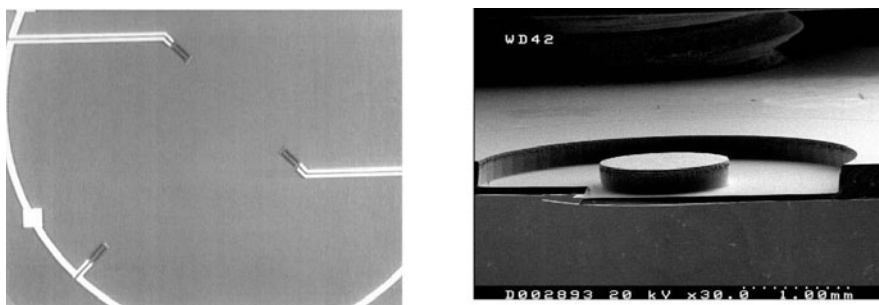


**Fig. 3.** Micrographs of a 3C-SiC piezoresistive pressure sensor fabricated on SOI substrates by Si DRIE: (*left*) top view of the circular membrane showing the position of the piezoresistors, and (*right*) cross-sectional view of the pressure sensor cavity formed by Si DRIE. The sensor incorporates a center boss (courtesy of M. Eickhoff, Walter Schottky Institute, Germany)

al., describe an ethanol gas sensor that utilizes such SiC microbridges [37]. In their design, poly-SiC films deposited on Si substrates by rapid thermal CVD using  $\text{SiH}_4$  and  $\text{C}_3\text{H}_8$  at  $1150^\circ\text{C}$  were fabricated into cantilevered bridges using Si bulk micromachining. The SiC bridges served as resistively heated microheaters. Au and Ni thin films were used as electrodes and an ethanol-sensitive  $\text{SnO}_2$  thin film was used for sensing. The poly-SiC microheaters allowed the device to reach an operating temperature of  $300^\circ\text{C}$ , enabling the sensor to detect an ethanol concentration of 1000 ppm in air. In three separate papers, Solzbacher et al., describe various  $\text{NO}_2$  sensor designs that incorporate bulk micromachined poly-SiC microbridges [38]–[40]. In their design, poly-SiC films deposited by CVD at  $1200^\circ\text{C}$  on oxidized Si wafers were fashioned into microbridge hotplates using Si bulk micromachining. The poly-SiC films were utilized in one of two ways depending on the application. For low voltage applications, the poly-SiC microbridges provided mechanical support and thermal isolation for  $\text{HfB}_2$  thin film heaters. For high voltage applications, selected regions of the poly-SiC bridge were doped with nitrogen by ion implantation to create resistive SiC microheaters imbedded into the poly-SiC bridge.  $\text{In}_2\text{O}_3$  thin films were used for sensing  $\text{NO}_2$ . The authors report that the packaged sensors require only 20 mW for stable operation at  $250^\circ\text{C}$  and can sense  $\text{NO}_2$  at concentrations as low as 5 ppm. The authors noted that while the operating temperature need not exceed  $300^\circ\text{C}$  for detection purposes, the poly-SiC microheaters could easily reach temperatures of  $650^\circ\text{C}$ .

## 4 SiC Micromolding

Micromolding refers to the fabrication of microstructures using disposable molds to define the device structure. In general, micromolding is an additive process where the structural material is deposited only in areas constituting the microdevice structure; in contrast, subtractive micromachining processes (i.e., bulk and surface micromachining) feature blanket deposition of the structural material followed by etching to realize the final device geometry. A molding-based processing approach has been developed to fabricate high aspect ratio MEMS devices from polycrystalline 3C-SiC, such as a SiC fuel atomizer shown in Fig. 4 [41]. This approach uses molds fabricated by Si DRIE to provide for controlled depth variations in the thickness direction. SiC structures are fabricated by the deposition of SiC material into the molds followed by mold removal in a Si etchant. Molding techniques have long been used to fabricate macro-scale SiC structures; however, these processes use graphite molds that cannot be micromachined to the dimensions required for MEMS. DRIE, on the other hand, can be used to create Si molds with the requisite dimensions.

The process begins with the fabrication of the Si mold, which is created by two Si DRIE steps. The molds are first coated with a thin film of 3C-SiC to protect the Si surfaces from pitting during a high deposition rate poly-SiC

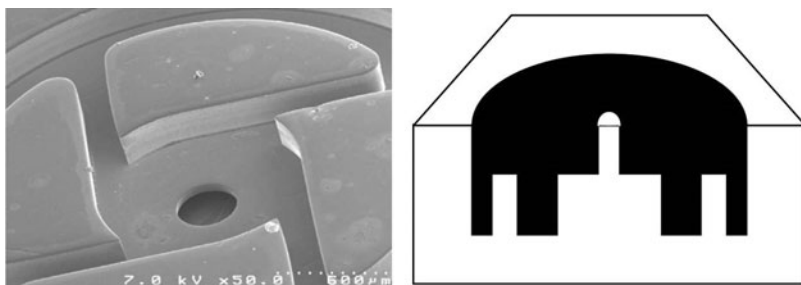


**Fig. 4.** Fabrication of micromachined SiC components by micromolding: (*left*) a SEM micrograph of a SiC fuel atomizer, and (*right*) cross sectional schematic of a Si mold (*white*) filled with poly-SiC (*black*) after polishing [41]

process that is used to fill the 400  $\mu\text{m}$ -thick molds. Since deposition occurs on all critical surfaces of the mold, mechanical polishing is used to remove excess SiC. Once the top surface of the Si mold is exposed, the device is released by dissolving the Si mold in a KOH solution. Structures, such as components for micro-gas turbine engines [42] and tensile testing structures [32] have been fabricated from poly-SiC films deposited into Si molds.

The micromolding process is not limited to CVD SiC, and in fact works for sintered SiC components as well. Tanaka et al., report on a process to create microturbine components by hot isostatic pressing of SiC and graphite sintering powders into DRIE fabricated Si molds [43]. The hot isostatic pressing process involves cold pressing the SiC and graphite powders into the molds, followed by hot isostatic pressing at temperatures in excess of the melting point of Si. As the Si begins to melt, it infiltrates the pressed powder and reacts with graphite to form SiC on the pre-existing SiC powder, resulting in a dense SiC structure. The remaining Si mold is then dissolved in a mixture of HF and  $\text{HNO}_3$  to reveal the micromolded SiC structure. The authors report that the sintered material has a bending strength and hardness that is roughly 70 to 80% of commercially available sintered SiC fabricated by conventional means. Moreover, the pressing process results in dimensional shrinkage of less than 3%.

While use of Si as a material for microfabricated molds works well for the fabrication of SiC components, geometric restrictions related to Si DRIE ultimately limit the complexity of SiC components made by this method. Alternative molding techniques utilizing thick, photodefinable polymer films such as SU-8 have proven to be very useful in the fabrication of electroplated metal structures that are thicker than Si structures patterned by DRIE and have much higher height-to-width aspect ratios. For bulk SiC created using conventional means, polymer molds could not be used because the SiC processing temperatures are simply much too high. However a new class of material, polymer-derived SiCN ceramics that retain many of the properties of stoichiometric SiC, such as temperature stability, oxidation resistance, thermal

shock resistance, and can be patterned using polymer molds show promise for harsh environment MEMS. The first to report on the development of polymer-derived SiCN for MEMS was Liew et al. [44]. In this paper, the authors detail a polymer-based micromolding process to cast SiCN ceramics into components for micromachined devices. Unlike the aforementioned examples, the molds in this case were fabricated using photodefinable SU-8 deposited onto Si wafers and patterned using a standard UV-based photolithographic process. After patterning the SU-8 molds, liquid phase SiCN was injected into the molds and converted to a solid ceramic by heating first to 250°C then to 400°C and finally to 1000°C, at which temperature the SU-8 thermally decomposes, leaving behind the SiCN part. Structures such as tensile testing specimens and micromotor gears have been successfully fabricated in SiCN.

## 5 SiC Surface Micromachining

Surface micromachining, in its simplest form, is a process where a thin film comprising the structural layer of a device is deposited and patterned onto a second film that serves as a temporary, or sacrificial, substrate. The sacrificial layer is then selectively dissolved using a chemical etchant that does not attack the structural layer, thus releasing the device in select regions and allowing it to move with at least one degree of freedom. In contrast to bulk micromachining, the wafer is used as the mechanical support on which surface micromachining is performed. With the proper materials, multiple, alternating layers of structural and sacrificial material can be deposited, patterned, and selectively etched to realize multilayer micromechanical structures that would be very difficult if not impossible to fabricate using traditional bulk micromachining.

Surface micromachining is a versatile technology because the patterning of the structural and sacrificial layers is typically accomplished by etching processes that are insensitive to the crystalline structure of the films. Moreover, surface micromachining enables integrated, multilevel structures using multiple layers of structural and sacrificial material. There is no inherent restriction on the structural-sacrificial material system as long as the compatibility between the two materials is maintained.

The most widely used group of materials in surface micromachining today is the polysilicon-SiO<sub>2</sub>-Si material system, with polysilicon serving as the structural material, SiO<sub>2</sub> as the sacrificial material, and single crystal Si as the substrate. When needed, Si<sub>3</sub>N<sub>4</sub> can be included for electrical isolation and etch masking. To pattern the polysilicon films, reactive ion etching in fluorinated plasmas is commonly performed. Use of SiO<sub>2</sub> as the sacrificial layer facilitates the use of hydrofluoric acid (HF) for release. In general, polysilicon surface micromachining is limited to structural layers of about 10 μm due to residual stresses in the thicker films as well as process practicalities.

For single crystal Si surface micromachining, silicon-on-insulator substrates are used.

In principle, surface micromachining of SiC can be performed in the same manner as Si surface micromachining. As reported by Fleischman et al., the first SiC surface micromachining processes utilized poly-SiC films deposited on polysilicon sacrificial layers [10]. This simple one-structural-layer process begins with the growth of a thermal SiO<sub>2</sub> layer on a Si substrate to provide electrical isolation for the device and chemical protection for the substrate. A sacrificial polysilicon film is then deposited by LPCVD on the thermal oxide, after which a structural poly-SiC film is then grown on the polysilicon sacrificial layer and patterned using a fluorine-based RIE and a metal hard mask. After removing the RIE mask, the free-standing sections of the device are released by dissolving select regions of the sacrificial polysilicon in KOH. The anchor pads of the device structure are sized such that the free-standing sections are completely undercut long before the anchors. Schematics and an SEM micrograph of a lateral resonant structure made by this method are shown in Fig. 5 [11].

For the devices reported in [10], 2  $\mu\text{m}$ -thick poly-SiC films were grown using a heteroepitaxial 3C-SiC growth recipe. In a follow-up study, Fleischman et al., reported that this process could be simplified by using SiO<sub>2</sub> as both an electrical isolation and sacrificial substrate layer [45]. In both cases, single layer, electrostatically actuated lateral resonators were fabricated using these processes. Roy et al., later showed that the mechanical quality factor for such devices can be quite high, with values in excess of 150 000 measured under high vacuum conditions [11]. As with Si, single layer 3C-SiC structures can be surface micromachined from heteroepitaxial films grown directly on SOI wafers or transferred to oxide coated Si wafer using wafer bonding techniques. Alternatively, SiC structures can be surface micromachined by first growing and patterning a 3C-SiC film, then converting a thin region of Si beneath

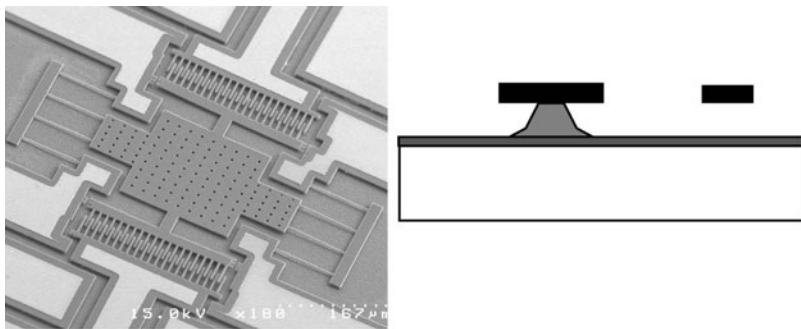


**Fig. 5.** Single layer poly-SiC surface micromachining on Si substrates: (*left*) SEM micrograph; (*right*) cross sectional schematic showing the poly-SiC, polysilicon and SiO<sub>2</sub> layers as *black*, *shaded*, and *grey*, respectively

the film to porous Si, then dissolving the porous Si chemically to release the structure. In this manner, microbridge structures for mass flow sensors [46] can be fabricated without much difficulty.

Single layer SiC surface micromachining is relatively straightforward with respect to the etch recipes used to pattern the SiC films, since any damage that might occur to the sacrificial underlayer will have no long-term impact since the layer will be dissolved during the release step. For multilayer SiC surface micromachining, however, the same is not true, since any damage created during a particular SiC patterning step will be manifest in some way in the sacrificial and structural layers that follow in the process. In essence, the single most important characteristic of an RIE step in multilayer surface micromachining is the selectivity between the structural layer and underlying sacrificial layer. For polysilicon surface micromachining, the selectivities between polysilicon and  $\text{SiO}_2$  are quite high, but unfortunately the same is not true for SiC. To address this limiting issue, Yasseen et al., has developed a technique designed specifically for multilevel SiC surface micromachining using thin film molds fabricated on sacrificial substrates to pattern SiC films [47]. To illustrate the process, a two-layer surface micromachining process to produce SiC micromotors is shown in Fig. 6. The process begins with the growth of a sacrificial  $\text{SiO}_2$  layer on a Si wafer. A polysilicon layer is then deposited by LPCVD and patterned to form a thin film mold. Poly-SiC is then deposited into the mold. SiC deposited on the top surfaces of the mold is removed by polishing with a diamond polishing slurry. As seen in Fig. 6b, the polishing step also serves to planarize the substrate, an important attribute of the process. A second mold pattern is then fabricated by etching the polysilicon in select regions, and followed by a timed etch of the exposed  $\text{SiO}_2$  sacrificial layer. The etched cavity is then coated with a thin  $\text{SiO}_2$  layer to complete the creation of the second mold. Poly-SiC is then deposited to

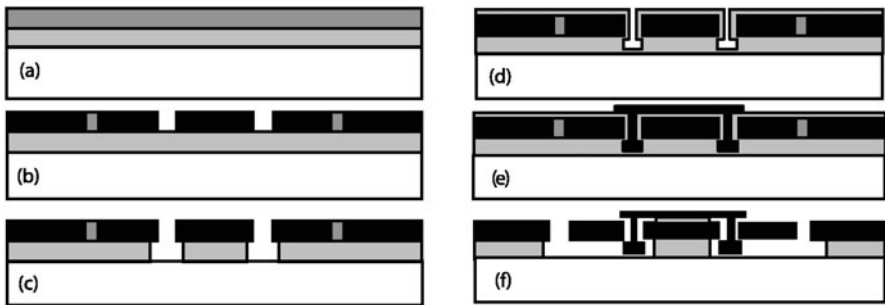


**Fig. 6.** Cross-sectional schematics of the two-SiC-layer SiC micromotor fabrication process: (a) after sacrificial oxide (*grey*) and polysilicon mold (*dark grey*) depositions; (b) after poly-SiC deposition (*black*) and planarization; (c) after second mold patterning; (d) after second molding oxide deposition; (e) after second poly-SiC deposition and patterning; and (f) after mold and sacrificial layer release

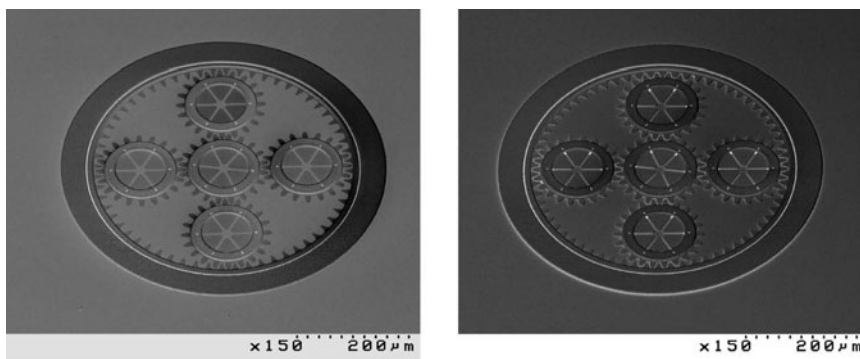


**Fig. 7.** SEM micrographs of a series of interlocked poly-SiC micromotors fabricated using the micromolding method: (*left*) before mold removal; and (*right*) after mold removal and release

fill the second mold. This layer is then patterned by RIE. In this case, the release process involves the removal of both the molding and sacrificial layers. The device can be released by sequential etching in KOH and HF. The selectivity issues associated with SiC RIE are completely bypassed by using polysilicon and SiO<sub>2</sub> as molding materials since the processes used to pattern these materials are highly selective to each other and SiC. Issues related to polishing selectivity require further research. SEM micrographs of poly-SiC micromotors fabricated using the micromolding technique are shown in Fig. 7.

The micromolding-based surface micromachining concept has recently been extended to a four-SiC-layer process called MUSiC<sup>TM</sup>. Short for MultiUser Silicon Carbide Process, MUSiC<sup>TM</sup> is modeled after the MUMPs<sup>TM</sup> (MultiUser MEMS Process) process for polysilicon and is the first large-scale process for micromachined SiC devices. And like MUMPs, the multi-user approach offers opportunities for those who do not have access to SiC processing tools.

SiC surface micromachining is not restricted to polycrystalline and single crystalline 3C-SiC, although these materials appear to be the most versatile. In an effort to extend the usefulness of amorphous SiC in MEMS beyond etch masks, simple membranes, and protective coatings, Bagolini et al., has recently reported on a novel technique using polyimide sacrificial layers to surface micromachine amorphous SiC films [48]. Polyimide is an attractive polymeric material for MEMS, since it can easily be deposited by spin casting, is chemically and thermally durable, and is compatible with Si IC processing. The surface micromachining process described in [48] is relatively straightforward. First, a polyimide thin film is deposited on Si wafers by spin casting and cured at temperatures up to 400°C. If desired, the polyimide sacrificial layer can be patterned using O<sub>2</sub> or CF<sub>4</sub>/O<sub>2</sub> plasmas. After patterning, an amorphous SiC structural layer is deposited by PECVD at 400°C. The SiC

layer is patterned using an anisotropic  $\text{CF}_4/\text{SF}_6/\text{O}_2$  plasma, and the resulting structure is released by etching the underlying polyimide using an isotropic  $\text{O}_2$  plasma etch. Using this process, single layer SiC structures such as tethered membranes can readily be fabricated. This process shows promise for application areas that would benefit from SiC but cannot tolerate the high deposition temperatures needed for thin film growth.

With the recent popularity in all things “nano” has come a growing interest in developing SiC structures on the nano-scale in hopes that the attractive properties on the micro-scale are retained or enhanced as sizes move toward nanometer dimensions. Along these lines, two groups have recently reported successes in fabricating 3C-SiC nanorods and nanowires on Si substrates. Lai et al., reported the ability to grow straight, 1  $\mu\text{m}$ -long 3C-SiC nanorods by hot filament CVD [49], while Kim et al., reported the successful large scale synthesis of 500  $\mu\text{m}$ -long, 40 nm diameter (111) 3C-SiC nanowires on Si substrates [50]. And while these approaches do not presently utilize surface micromachining in the creation of the nanostructures, it is likely that some sort of surface micromachining technique will eventually be used if these structures are to be employed in nano- or micro-scale devices, and thus merit mentioning here.

SiC nanorods and nanowires notwithstanding, recent developments in SiC surface nanomachining have epitaxial 3C-SiC at the forefront of a new family of devices collectively called nanoelectromechanical systems (NEMS). In the first ever attempt to create a nanoelectromechanical structure from SiC, Yang et al., have described a process to fabricate nanomechanical beams from 3C-SiC [51]. The process is relatively simple in concept, starting with the heteroepitaxial growth of ultra thin ( $< 200$  nm) 3C-SiC on Si wafers. Etch masks are then patterned into beams on the 3C-SiC surfaces by conventional electron beam lithography techniques, and the 3C-SiC films are anisotropically etched down to the Si substrate in an ECR plasma using  $\text{NF}_3$  and  $\text{O}_2$ . The 3C-SiC beams are then released by isotropically etching the exposed Si using a  $\text{NF}_3/\text{Ar}$  plasma. The first sets of structures were nominally 260 nm thick, 150 nm wide and 8 to 17  $\mu\text{m}$  long. In a follow-up study, the same group fabricated beams that were 75 nm thick, 120 nm wide and 1.1  $\mu\text{m}$  long. Beams with these dimensions have fundamental resonant frequencies in excess of 1 GHz, a first for mechanical oscillators [52]. Such an achievement was made possible, in part, by the high Young's modulus-to-density ratio of 3C-SiC and its chemical inertness, which makes such small structures less challenging to fabricate than similar structures made from Si.

An important issue that has hampered the development of SiC for MEMS is the presence of residual stresses in SiC thin films. SiC films deposited for micromachining applications are, with few exceptions, in a state of residual stress. Although not fully characterized in SiC, the stress is believed to result from the thermal and lattice mismatches between the SiC thin film and the various substrates used in device fabrication. For devices made from

6H-SiC epilayers, residual stress is not an issue since 6H-SiC wafers are used as substrates. For 3C-SiC and poly-SiC devices, however, the stress issue is significant, since Si, SiO<sub>2</sub>, Si<sub>3</sub>N<sub>4</sub> and other non-SiC materials are used for substrates, and relatively high temperatures (800°C to 1300°C) are used to grow the films. Typically, the stress in 3C-SiC and poly-SiC films is tensile and is generally in the range of several hundred MPa depending on microstructure and processing conditions. For free standing structures such as micromachined bridges and membranes, a moderate tensile stress is desirable, as it keeps the structures from buckling. For structures anchored in only one location, a uniform residual tensile stress is also not problematic, since the stress will simply cause the structure to contract uniformly along its length upon release. From a device perspective the main issue with respect to stress is that of a stress gradient through the thickness of the film. A stress gradient will cause free-standing cantilevers to bend as the stress is relieved upon release, and the bending becomes more severe as the beam length increases. This effect is problematic for many MEMS designs, especially electrostatic devices such as mechanical resonators, since these devices rely on well-formed capacitive gaps for sensing and actuation. 3C-SiC and poly-SiC films suffer in varying degrees from residual stress gradients. The mechanisms responsible for residual stress gradients are not fully understood, but likely sources include a gradient in defect density as a function of film thickness for 3C-SiC films, and a gradient in microstructure (grain size) and orientation in poly-SiC films. Nevertheless, work is underway to identify the proper processing conditions to significantly reduce, if not eliminate, residual stresses and stress gradients in SiC films.

## 6 Wafer Bonding Techniques

Wafer bonding is a relatively new micromachining technique that involves the joining of two substrates to create a structure that otherwise could not readily be made using deposition techniques. As with bulk and surface micromachining, the most commonly used substrate material in wafer bonding is Si. A single crystal Si wafer can be joined to another Si wafer by a process called fusion bonding to quartz or glass substrates by anodic bonding. Si fusion bonding is generally performed with the wafers under pressure at temperatures of 500 to 1000°C, while anodic bonding utilizes much lower temperatures (~200°C) and high voltages (400 to 1000 V). Thermally oxidized Si wafers can also be bonded together. In all cases, extremely smooth (< 0.5 nm roughness), flat, and chemically clean surfaces are required for bonding to be successful. Wafer bonding is a key step in the fabrication of commercially available silicon on insulator (SOI) wafers. By combining bulk micromachining and wafer bonding techniques, highly complex three-dimensional microstructures, such as microvalves, micropumps, and sealed channels, can readily be fabricated from Si substrates.

As in the case of bulk micromachining, bonding of SiC wafers is extremely challenging. The stability of SiC surfaces at temperatures typical for fusion bonding makes direct SiC-to-SiC bonding nearly impossible even under ideal conditions. Moreover, achieving a level of surface roughness typical for large area Si bonding is also very difficult because the hardness and inertness of SiC renders most chemical and chemical-mechanical polishing processes ineffective. As a consequence, SiO<sub>2</sub> bonding layers which can easily be polished to a roughness level that is satisfactory for bonding are almost always used to join SiC wafers to SiC and other substrate materials.

Interest in SiC wafer bonding is primarily motivated toward the production of single crystalline SiC-on-Insulator (SiCOI) substrates for electronic device applications. Like SOI wafers, SiCOI wafers generally consist of a single crystal SiC substrate, a buried SiO<sub>2</sub> layer, and a thin single crystal SiC top layer. In the most common configuration, the substrate is a 6H-SiC wafer, the buried oxide is several microns thick, and the top SiC layer is 6H-SiC that also is several microns thick. The production of such substrates faces two significant challenges; (1) bonding the two 6H-SiC wafers, and (2) removing all but a thin layer of one wafer. The challenges associated with bonding notwithstanding, removal of the unwanted 6H-SiC substrate is not straightforward, since chemical etching is not possible and mechanical grinding is impractical and economically not feasible, as too much valuable material would be wasted. To address these challenges, a substrate splitting method has been developed [53, 54]. This method was first developed as an alternative to Si etch back techniques for the production of SOI substrates, but since has been used to create 6H-SiC-on-insulator wafers. The process begins with the thermal oxidation of two wafers; hereafter called the implant wafer and the handle wafer. The implant wafer is made of 6H-SiC, whereas the handle wafer can be 6H-SiC, polycrystalline SiC, or Si. Hydrogen ions are implanted completely through the thermal oxide and a thin portion of the 6H-SiC implant wafer. The two wafers are then bonded at the SiO<sub>2</sub> surfaces using standard oxide bonding conditions (i.e., 1100°C). The bonding temperature causes the implanted hydrogen to coalesce, resulting in the formation of a well-defined void layer in the 6H-SiC implant wafer. This layer serves as a cleavage seam; allowing for the majority of the implant wafer to be separated from the handle wafer, leaving behind a thin 6H-SiC layer atop the SiO<sub>2</sub> coated substrate. The newly created 6H-SiC-on-insulator substrate is then polished and readied for device fabrication. Since only a thin (several micron) region of the implant wafer was removed in the process, the remaining wafer can be reused. While the aforementioned process employs SiO<sub>2</sub> fusion bonding techniques, anodic bonding has also been used to extend the process to insulating quartz wafers [55]. As with SOI wafers that quickly found uses in Si micromachining, the 6H-SiC-on-Insulator substrates are likely to find applications in MEMS where single crystal SiC is needed.

Unlike 6H-SiC-on-insulator substrates, fabrication of 3C-SiC-on-insulator substrates is greatly enhanced by the fact that 3C-SiC films can be heteroepitaxially grown on Si wafers. To date, three general methods that leverage heavily on this capability have been developed to create 3C-SiC-on-insulator substrates. These methods include direct heteroepitaxial growth of 3C-SiC on SOI wafers [56]–[58], conventional wafer bonding techniques [59, 60], and 3C-SiC film transfer on deposited polycrystalline substrates [61].

Without question the most straightforward technique to create a 3C-SiC-on-insulator structure is by direct heteroepitaxial growth on commercially available SOI wafers. Because the Si top layer in an SOI substrate was produced from a high quality wafer, it too is of high crystal quality. As a result, the heteroepitaxial 3C-SiC films are of comparable crystal quality to films grown directly on Si substrates. SOI wafers are typically produced either by oxygen ion implantation (SIMOX) or by wafer bonding and etchback. The main difference between these two substrates (other than the production method) is the thickness of the buried oxide layer, with the maximum thickness of the buried oxide for SIMOX wafers being a few thousand angstroms as compared to several microns for the bonded wafers. This difference makes bonded SOI substrates generally more attractive for Si MEMS, since the thicker oxides provide greater electrical isolation (important for electrostatic devices) and thicker substrate-to-device gaps when the oxides are used as sacrificial layers. For surface micromachined SiC MEMS, this difference is less important since the top Si layer could serve as the sacrificial layer.

As stated previously, 3C-SiC-on-insulator wafers have successfully been fabricated by direct heteroepitaxial growth on SOI wafers. The process works very well except in cases where complete conversion of the Si top layer is desired. Recalling that heteroepitaxial growth of 3C-SiC on Si involves the growth of a thin carbonization layer, complete conversion of the Si top layer requires that the layer be relatively thin compared with typical SOI substrates. When using such substrates, care must be taken to avoid the formation of pits and voids at the 3C-SiC/Si interface. For thin Si layers, the voids can actually penetrate deep into the buried oxide layer. These voids, at the very least, can compromise device fabrication by altering the geometry of the microfabricated structure. But in the extreme case where the voids completely penetrate the buried oxide layer, they can either compromise the adhesion of the device anchor layers, or, if they become filled with SiC, can lead to electrical shorting of device structures. To counter this effect, Zappe et al., report on the use of an intermediate  $\text{Si}_3\text{N}_4$  layer sandwiched between the top Si layer and the buried oxide film [62]. The nitride layer was formed by N ion implantation and the authors showed that its presence significantly reduced the size of voids without compromising the quality of the 3C-SiC film. Despite potential problems with voids, 3C-SiC-on-SOI wafers have been successfully used as substrates in bulk micromachined pressure sensors [33, 34]. These sensors utilize SOI substrates to fabricate electrically isolated 3C-SiC piezoresistors

on top of a bulk micromachined Si diaphragm. For the sensor reported in [34], Si DRIE was used to fashion the Si membrane and selective epitaxial growth using SiO<sub>2</sub> molds was used to pattern the 3C-SiC piezoresistors. The sensor was successfully tested at temperatures to 200°C, and the authors expect the sensor to have satisfactory performance up to 450°C. The pressure sensor reported in [33] was also constructed on a Si membrane machined by DRIE, but the 3C-SiC piezoresistors were patterned by RIE in a SF<sub>6</sub>/O<sub>2</sub> plasma. To compensate for a known temperature dependence of sensitivity and offset voltage, the sensor also incorporated a poly-SiC thermistor. The buried oxide layer provided reliable electrical isolation for temperatures up to 400°C, and the sensor provided satisfactory output at temperatures up to 300°C. These examples demonstrate the potential as well as the challenges of using SOI substrates and Si bulk micromachining to fabricate 3C-SiC based pressure sensors. For a short, yet informative review of the topic, a paper written by Krotz et al., is highly recommended [63].

Conventional Si wafer bonding techniques are another relatively straightforward, albeit challenging way to produce SiC-on-insulator substrates. As stated previously, the 3C-SiC surface is not well suited for bonding, therefore SiO<sub>2</sub> bonding layers are commonly used. The first reported attempt at wafer-scale SiC bonding utilized thermally-grown SiO<sub>2</sub> layers on 3C-SiC films that were heteroepitaxially grown on Si transfer wafers [59]. The transfer wafers were fusion bonded to thermally oxidized handle wafers and then removed in a Si etchant. The results proved the feasibility of the approach, but unfortunately, the 3C-SiC transfer yield was quite low (about 30%). Although the authors did not report the reason for the low transfer yield, it is likely due to a combination of oxide surface roughness and wafer curvature that results from high tensile stresses characteristic of epitaxial 3C-SiC films.

Silicon dioxide is not the only material that can be used as a bonding layer for SiC wafer bonding, in fact polysilicon works well also, as shown by Vinod et al. [60]. This process bypasses any dependence on the quality of the 3C-SiC surface by using a series of polysilicon depositions and thermal oxidations to create a polysilicon/SiO<sub>2</sub> multilayer stack atop a heteroepitaxially-grown 3C-SiC film. The multilayer stack not only provides a surface that is chemically well suited for bonding, but also a surface that can readily be polished to a finish that closely resembles standard Si wafers. The basic process begins with heteroepitaxial growth of 3C-SiC on a (100) Si transfer wafer. After 3C-SiC growth, a LPCVD polysilicon film is deposited on the 3C-SiC surface. This film is then completely converted to SiO<sub>2</sub> by thermal oxidation. A thermal oxide is simultaneously created on a single crystal Si handle wafer. A second LPCVD polysilicon film is then deposited on both the transfer and handle wafers. The polysilicon surfaces are polished by CMP, chemically cleaned and then joined together by fusion bonding. After bonding, the Si transfer wafer is chemically dissolved leaving behind a 3C-SiC-on-insulator wafer. It was reported that the highest transfer yields were obtained using 3C-SiC film

thicknesses of around 300 nm, which is too thin for most MEMS applications. To thicken the 3C-SiC film, the wafer surface is mechanically polished, lightly oxidized, etched in HF and additional 3C-SiC is grown using a homoepitaxial process. The polishing, oxidation and etching steps are performed to remove the near surface region of the 3C-SiC-on-insulator wafer. The transfer process flips the transferred film upside down. For heteroepitaxially grown 3C-SiC, this serves to expose the region of highest defect density, which is located just inside the original 3C-SiC/Si interface. By removing this layer, the homoepitaxial film has a better starting substrate than would otherwise be present, thus resulting in a higher quality film. Transfer yields nearing 80% on 100 mm diameter substrates and a significant reduction in the overall density of defects in the homoepitaxial 3C-SiC films were reported [60]. Improvements to the process resulting in the elimination of the polysilicon bonding layers, relying instead on SiO<sub>2</sub> films created by the complete thermal oxidation of polysilicon have led to the creation of 3C-SiC-on-insulator wafers without buried Si layers [64]. The resulting substrate consists of a 2  $\mu\text{m}$ -thick 3C-SiC film on a 2.5  $\mu\text{m}$ -thick SiO<sub>2</sub> layer on a Si wafer. These substrates are well suited for both single crystal surface and bulk micromachining, as evidenced by the single crystal 3C-SiC lateral resonant structures reported by Stefanescu et al. [64], and the piezoresistive pressure sensor shown in Fig. 8 [35]. At present, the only major drawback to this approach is that warpage in the Si handle wafers keeps transfer yields below 100%. Not only are yields lower than desired, the regions where bonding fails tend to be random, therefore additional improvements are required for such processes to demonstrate commercial viability.

In addition to the aforementioned bond and etch back approaches to wafer bonding with 3C-SiC, the hydrogen implant-induced layer splitting technique has also been applied to 3C-SiC films in a manner very similar to that detailed for 6H-SiC and thus will not be presented here.

In order to achieve 100% transfer yields in a 3C-SiC-on-insulator fabrication process, an approach that utilizes a deposited “substrate” has recently

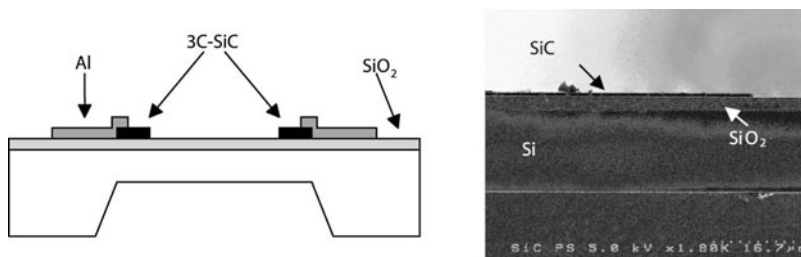


**Fig. 8.** Bulk micromachined, 3C-SiC pressure sensor fabricated on SiC-on-insulator substrates made by wafer bonding: (*left*) schematic cross section; and (*right*) SEM micrograph showing the various layers

been reported [61]. Like the other 3C-SiC-on-insulator fabrication processes, this process begins with the heteroepitaxial growth of a 3C-SiC film on a 100 mm-diameter Si transfer wafer, after which an LPCVD polysilicon film is deposited and completely converted to SiO<sub>2</sub> by thermal oxidation. A thick (750  $\mu\text{m}$ ) polysilicon handle “substrate” is then deposited on the SiO<sub>2</sub> surface, a thickness that far exceeds the single crystal Si wafer thickness (500  $\mu\text{m}$ ). After the polysilicon deposition, the Si transfer wafer is dissolved, creating a 3C-SiC-on-insulator wafer that is ready for processing. The polysilicon deposition process is conformal to the substrate, and as a result, wafer warpage and surface roughness does not affect film transfer yields, which are 100%. Moreover, since bonding is not required, insulating layers such as Si<sub>3</sub>N<sub>4</sub>, which are highly inert and thus much more difficult to bond, can easily be incorporated as the insulating layer. In addition the overall thickness of the 3C-SiC film is not restricted by the process. For applications where the substrate serves only as a mechanical support for the device, these wafers appear to be particularly well suited.

## 7 Concluding Remarks

Interest in developing MEMS for use in applications where conventional materials are not well suited has pushed researchers to develop micromachining techniques for SiC. In comparison with other potential materials, SiC is particularly attractive because it is highly compatible with Si fabrication processes. The long and fruitful effort to develop SiC for specialized electronic devices puts SiC in a favorable position for those harsh environment applications that require micromachined devices with on-chip electronics. And while many of the basic techniques necessary to realize SiC MEMS have been established, much work remains to bring SiC to a level comparable with Si, the benchmark material for MEMS. But with an attractive complement of material properties that is difficult to ignore, it is just a matter of time and, of course, effort before SiC takes its place alongside Si in the micro- (and nano) machinists’ toolbox.

## References

1. G. Kotzar, M. Freas, P. Abel, A. Fleischman, S. Roy, C.A. Zorman, J.M. Moran, J. Melzak: *Biomaterials* **23**, 2737 (2002)
2. V.T. Srikar, S.M. Spearing: *Sens. Actuators A* **102**, 279 (2003)
3. G.H. Kroetz, M.H. Eickhoff, H. Moeller: *Sens. Actuators* **74**, 182 (1999)
4. G. Muller, G. Krotz, J. Schalk: *Phys. Stat. Sol. A* **185**, 1 (2001)
5. M. Werner, G. Krotz, H. Moller, M. Eickhoff, P. Gluche, M. Adamschik, C. Johnston, P.R. Chalker: *Sensors Update* **5**, 141 (1999)
6. C.A. Zorman, A.J. Fleischman, A.S. Dewa, M. Mehregany, C. Jacob, S. Nishino, P. Pirouz: *J. Appl. Phys.* **78**, 5136 (1995)

7. G. Krotz, W. Legner, C. Wagner, H. Moller, G. Muller: in *Proc. 8th Int. Conf. Solid-State Sens. Actuators* (IEEE, Piscataway, NJ, 1995) pp. 186–189
8. C. Serre, A. Perez-Rodriguez, A. Romano-Rodriguez, J.R. Morante, J. Esteve, M.C. Acero: *J. Micromech. Microeng.* **9**, 190 (1999)
9. C. Serre, A. Romano-Rodriguez, A. Perez-Rodriguez, J.R. Morante, L. Fonseca, M.C. Acero, A. Kogler, W. Skorupa: *Sens. Actuators* **74**, 169 (1999)
10. A.J. Fleischman, S. Roy, C.A. Zorman, M. Mehregany: in *Proc. 9th Int. Workshop Microelectromech. Sys.* (IEEE, Piscataway, NJ, 1996), pp. 234–238
11. S. Roy, R.G. DeAnna, C.A. Zorman, M. Mehregany: *Trans. Electron. Dev.* **49**, 2323 (2002)
12. C.A. Zorman, S. Rajgopal, X.A. Fu, R. Jezeski, J. Melzak, M. Mehregany: *Electrochem. Sol. State Lett.* **5**, G99 (2002)
13. I. Behrens, E. Peiner, A.S. Bakin, A. Schlachetzki: *J. Micromech. Microeng.* **12**, 380 (2002)
14. J. Chen, J. Scofield, A.J. Steckl: *J. Electrochem. Soc.* **147**, 3845 (2000)
15. C.R. Stoldt, C. Carraro, W.R. Ashurst, D. Gao, R.T. Howe, R. Maboudian: *Sens. Actuators A* **97–98**, 410 (2002)
16. C. Serre, A. Perez-Rodriguez, J.R. Morante, J. Esteve, M.C. Acero, R. Kogler, W. Skorupa: *J. Micromech. Microeng.* **10**, 152 (2000)
17. A. Klumpp, U. Schaber, H.L. Offereins, K. Kuhl, H. Sanmaier: *Sens. Actuators A* **41–42**, 310 (1994)
18. P.M. Sarro, C.R. Deboer, E. Korkmaz, J.M.W. Laros: *Sens. Actuators A* **67**, 175 (1998)
19. P.M. Sarro: *Sens. Actuators* **82**, 210 (2000)
20. N. Ledermann, J. Baborowski, P. Muralt, N. Xantopoulos, J.M. Tellenbach: *Surf. Coat. Tech.* **125**, 246 (2000)
21. R. Okojie: in *The MEMS Handbook*, ed. by M. Gad-el-Hak (CRC Press, Boca Raton, FL, 2002), pp. 20.1–20.31
22. R.S. Okojie, A.A. Ned, A.D. Kurtz: *Sens. Actuators A* **66**, 200 (1998)
23. J. Jandeleit, A. Horn, R. Weichenhaim, E.W. Kreutz, R. Poprawe: *Appl. Surf. Sci.* **127–129**, 885 (1998)
24. P.H. Yih, V. Saxena, A.J. Steckl: *Phys. Stat. Sol. B* **202**, 605 (1997)
25. G. Beheim: “Deep reactive ion etching of silicon carbide.” in *The MEMS Handbook*, ed. by M. Gad-el-Hak (CRC Press, Boca Raton, FL, 2002), pp. 21.1–21.12
26. H. Cho, K.P. Lee, P. Leerungnawarat, S.N.G. Chu, F. Ren, S.J. Pearton, C.M. Zetterling: *J. Vac. Sci. Tech. A* **19**, 1878 (2001)
27. P. Chabert: *J. Vac. Sci. Tech. B* **19**, 1339 (2001)
28. M. Mehregany, L. Tong, L.G. Matus, D.J. Larkin: *IEEE Trans. Elec. Dev.* **44**, 74 (1997)
29. U. Schmid, M. Eickhoff, C. Richter, G. Krotz, D. Schmitt-Landsiedel: *Sens. Actuators A* **94**, 87 (2001)
30. C.M. Su, M. Wuttig, A. Fekade, M. Spencer: *J. App. Phys* **77**, 5611 (1995)
31. C. Serre, A. Perez-Rodriguez, J.R. Morante, P. Gorostiza, J. Esteve: *Sens. Actuators* **74**, 134 (1999)
32. K.M. Jackson, R.L. Edwards, G.F. Dirras, W.N. Sharpe Jr.: *Mat. Res. Soc. Symp. Proc.* **687**, 217 (2002)
33. R. Ziermann, J. von Berg, E. Obermeier, F. Wischmeyer, E. Niemann, H. Moller, M. Eickhoff, G. Krotz: *Mat. Sci. Eng. B* **61–62**, 576 (1999)
34. M. Eickhoff, H. Moller, G. Kroetz, J. von Berg, R. Ziermann: *Sens. Actuators* **74**, 56 (1999)

35. C.H. Wu, S. Stefanescu, H.-I. Kuo, C.A. Zorman, M. Mehregany: in *Tech. Dig. 11th Inter. Conf. Solid State Sen. Actuators* (IEEE, Piscataway, NJ, 2001) pp. 514–518.
36. S. Sugiyama, Y. Zhang, M. Hosaka, H. Ueno, O. Tabata, S. Konishi, R. Maeda: *Microsys. Tech.* **4**, 61 (1998)
37. J.J. Ho, Y.K. Fang, K.H. Wu, W.T. Hsieh, C.H. Chen, G.S. Chen, M.S. Ju, J.J. Lin, S.B. Hwang: *Sens. Actuators B* **50**, 227 (1998)
38. F. Solzbacher, C. Imawan, H. Steffes, E. Obermeier, H. Moller: *Sens. Actuators B* **64**, 95 (2000)
39. F. Solzbacher, C. Imawan, H. Steffes, E. Obermeier, M. Eickhoff: *Sens. Actuators B* **78**, 216 (2001)
40. F. Solzbacher, C. Imawan, H. Steffes, E. Obermeier, M. Eickhoff: *Sens. Actuators B* **77**, 111 (2001)
41. N. Rajan, M. Mehregany, C.A. Zorman, S. Stefanescu, T.P. Kicher: *J. Microelectromech. Sys.* **8**, 251 (1999)
42. K.A. Lohner, K.-S. Chen, A.A. Ayon, S.M. Spearing: *Mat. Sci. Symp. Proc.* **546**, 85 (1999)
43. S. Tanaka, S. Sugimoto, J.-F. Li, R. Watanabe, M. Esashi: *J. Microelectromech. Sys.* **10**, 55 (2001)
44. L.A. Liew, W. Zhang, V. Bright, L. An, M.L. Dunn, R. Raj: *Sens. Actuators A* **89**, 64 (2001)
45. A.J. Fleischman, X. Wei, C.A. Zorman, M. Mehregany: *Mat. Sci. Forum* **264–268**, 885 (1998)
46. C. Lyons, A. Friedberger, W. Welser, G. Muller, G. Krotz, R. Kassing: in *Proc. 11th Int. Wrkshp. Microelectromech. Sys.* (IEEE, Piscataway, NJ, 1997) pp. 356–360
47. A.A. Yasseen, C.H. Wu, C.A. Zorman, M. Mehregany: *Elec. Dev. Lett.* **21**, 164 (2000)
48. A. Bagolini, L. Pakula, T.L.M. Scholtes, H.T.M. Pham, P.J. French, P.M. Sarro: *J. Micromech. Microeng.* **12**, 385 (2002)
49. H.L. Lai, N.B. Wong, X.T. Zhou, H.Y. Peng, F.C.K. Au, N. Wang, I. Bello, C.S. Lee, S.T. Lee, X.F. Duan: *Appl. Phys. Lett.* **76**, 294 (2000)
50. H.Y. Kim, J. Park, H. Yang: *Chem. Commun.* **256** (2003)
51. Y.T. Yang, K.L. Ekinici, X.M.H. Huang, L.M. Schiavone, M.L. Roukes, C.A. Zorman, M. Mehregany: *Appl. Phys. Lett.* **78**, 162 (2001)
52. X.M.H. Huang, C.A. Zorman, M. Mehregany, M. Roukes: *Nature* **421**, 496 (2003)
53. L. Di Cioccio, Y. Le Tiec, F. Letertre, C. Jaussaud, M. Bruel: *Electronics Lett.* **32** 1144 (1996)
54. L. Di Cioccio, Y. Le Tiec, C. Jaussaud, F. Hugonnard-Bruyere, M. Bruel: *Mat. Sci. Forum* **264–268**, 765 (1998)
55. Q.-Y. Tong, T.-H. Lee, P. Werner, U. Gosele, R.B. Bergmann, J.H. Werner: *J. Electrochem. Soc.* **144**, L111 (1997)
56. A.J. Steckl, C. Yuan, Q.-T. Tong, U. Gosele, M.J. Loboda: *J. Electrochem. Soc.* **141**, L66 (1994)
57. W. Reichert, E. Obermeier, J. Stoemenos: *Dia. Rel. Mat.* **6**, 1448 (1997)
58. J.M. Bluett, S. Contreras-Azema, J. Camassel, J.L. Robert, L. Dicioccio, W. Reichert, R. Lossy, E. Obermeier, J. Stoemenos: *Mat. Sci. Eng. B* **46**, 145 (1997)
59. Q.-Y. Tong, U. Gosele, C. Yuan, A.J. Steckl, M. Reiche: *J. Electrochem. Soc.* **142**, 232 (1995)

60. K.N. Vinod, C.A. Zorman, A.A. Yasseen, M. Mehregany: *J. Electron. Mat.* **27**, L17 (1998)
61. H.I. Kuo, C.A. Zorman, M. Mehregany: *Mat. Res. Soc. Symp. Proc.* **681E**, I5.16.1 (2001)
62. S. Zappe, E. Obermeier, J. Stoemenos, H. Moller, G. Krotz, H. Wirth, W. Skorupa: *Mat. Sci. Eng. B* **61–62**, 522 (1999)
63. G. Krotz, H. Moller, M. Eickhoff, S. Zappe, R. Ziermann, E. Obermeier, J. Stoemenos: *Mat. Sci. Eng. B* **61–62**, 516 (1999)
64. S. Stefanescu, A.A. Yasseen, C.A. Zorman, M. Mehregany: in *Proc. 10th Int. Conf. on Solid State Sens. Actuators* (IEEE, Piscataway, NJ, 1999), pp. 194-198

# Surface Preparation Techniques for SiC Wafers

S. Monnoye, D. Turover, and P. Vicente

## 1 Introduction

The excellent chemical and mechanical properties of SiC make, paradoxically, damage free surface preparation a real challenge. The preparation of SiC wafers can be described in four successive stages corresponding to different objectives:

- Grinding/lapping gives good geometrical parameters to the wafer.
- Mechanical polishing enables a decrease in roughness and improves the geometrical characteristics of the wafer.
- The chemical mechanical polishing is the best way to produce surface without any scratches or subsurface damage.
- The cleaning step is essential to remove the contaminants on the surface.

Alternative preparation methods based on etching have been used to replace the second and third steps. The results are not fully satisfactory in terms of roughness, damage and geometrical wafer characteristics.

In this paper, recent results on surface preparation are described with a detailed review of the published work. A description of each step of the preparation is detailed in Sect. 2. We present in Sect. 3 the state of the art results and the influence of surface preparation on epitaxial growth and device performance. A summary will be given in the final section.

## 2 Preparation Techniques

### 2.1 Grinding/Lapping and Mechanical Polishing

The main objective of this stage is to produce from as-cut wafers, flat and parallel surfaces with a minimum of bow, warp and total thickness variation (TTV). Silicon carbide is one of the hardest materials. Only diamond (C), cubic boron nitride (BN) and boron carbide ( $B_4C$ ) are comparable or harder than SiC [1]. Therefore, only these materials can be used as abrasive for mechanical polishing. By using abrasive slurries of decreasing grit size it is possible to obtain a very low roughness but scratches and subsurface damage are still generated. Of course, not only abrasives do influence polishing but

also other parameters like the down pressure, the slurry feed composition and temperature, the rotation speed of the plate or carrier and the polishing pad characteristics [2]–[4]. An interesting attempt combines mechanical lapping/polishing and chemical etching with 600°C KOH flux for less than 3 minutes [5]. The surfaces obtained are similar or better to those obtained by commercial suppliers but have to be controlled carefully to avoid revealing bulk defects.

Slicing and even more grinding and mechanical polishing generate subsurface damage. The subsurface damage thickness is critical information at each step of the preparation for successful polishing. To assess the subsurface damage thickness, different methods have been used. Depending on the analysed thickness, simple edge Normarski observation [6], transmission electron microscopy [7]–[9], Rutherford backscattering [9], photon backscattering [10]–[12], KOH etching [12] and more recently Raman spectroscopy [13, 14] or positron annihilation [15] have been used. A qualitative measure of subsurface damage has been done using high resolution X-ray measurement [16]. However, there is no simple answer to the question “how deep is the subsurface damage in a given wafer?” Depending on the observation method, it has been found to extend from 1/2 to 1/75 of the abrasive slurry size. Rapid thermal annealing has been used in conjunction with Raman scattering to estimate the effect of mechanical and chemical mechanical polishing on the carrier traps showing that the free carrier density decreases with polishing [17].

## 2.2 Chemical Mechanical Polishing and Etching

### 2.2.1 Chemical Mechanical Polishing

In the past decade chemical-mechanical polishing (CMP) has emerged as the fastest growing operation in silicon semiconductor manufacturing industry. The same treatment is now compulsory for “exotic” semiconductors, such as silicon carbide [7],[12],[18]–[20]. In a typical CMP process, the chemicals interact with the material to form a chemically modified surface. Simultaneously, the abrasives in the slurry mechanically interact with the chemically modified surface layers, resulting in material removal. Of course, the same parameters that control the mechanical polishing, pressure, slurry temperature, pad etc are still important [20].

The difficulty with the CMP process on SiC is built on the low chemical reactivity of silicon carbide. Moreover the removal rate and homogeneity depend on the orientation, the doping level and polytype of the wafer. As a result it is necessary to adapt all these parameters for each kind of substrate.

### 2.2.2 Hydrogen Etching

For many years high temperature  $H_2$  etching has been investigated [16],[21]–[34]. Alternative etching techniques utilize etch mixtures of  $H_2/HCl$ ,  $H_2/C_3H_8$ ,

$\text{H}_2/\text{C}_2\text{H}_4$  in order to limit the formation of Si droplets above  $1410^\circ\text{C}$  [23]–[25],[32],[35]–[37]. The mechanism for all  $\text{H}_2$  type etching process is based on producing at high temperature ( $1400$ – $1700^\circ\text{C}$ ) volatile hydrocarbons and free silicon.

Up to now hydrogen-based etching processes are the best alternatives to CMP for surface preparation. These techniques appear to remove to some extent scratches but quite often remnant scratches are visible after epitaxy. The combination of  $\text{H}_2/\text{HCl}$  seems to be the most effective etching to remove scratches.

A major problem with hydrogen etching is the relatively high roughness of the surface [16]. The RMS surface roughness is larger than  $4\text{ \AA}$  and depends strongly on the initial surface quality [28, 33].

### 2.2.3 Reactive Ion Etching

This third surface preparation technique leads to mixed results [38]. RHEED shows that Wet  $\text{O}_2$  oxidation at  $1100^\circ\text{C}$  followed by reactive ion-assisted plasma etching improves the surface. But in order to achieve the best results concerning surface structure quality the aforementioned procedure is followed by 10 successive iterations of oxidation and removal via etching in 10% HF. One should also notice that the micropipes lead to the formation of large area surface defects under ion plasma etching.

The surface roughness obtained with reactive ion etching is clearly too high for epitaxial growth [39]–[41]. The situation is better using a combination of ion implantation and wet chemical etching [42, 43] but the roughness is still high with RMS of about  $9\text{ \AA}$  over a  $10 \times 10\text{ }\mu\text{m}$  area [41].

### 2.2.4 Tribochemical Polishing

Tribochemical polishing of ceramics (including SiC) has been demonstrated and consists of dissolution of material by friction using hard pad at contacting asperities and a solution free of abrasive particles [3, 44]. On ceramics the surface quality is quite comparable to CMP techniques. On monocrystalline substrates the situation is sensibly different because the efficiency of this technique is proportional to the friction coefficient (which is quite high for ceramics); and therefore efficiency becomes poor. In order to increase the efficiency load has to be higher and so self scratching (SiC particles removed from the surface) limits the surface quality.

### 2.2.5 Electrochemical Mechanical Polishing

This technique is based on electrochemical oxidation and simultaneous removal of the oxide by polishing [45, 46]. Regulating the current density can control the oxidation rate. The polishing abrasive hardness should be higher

than the oxide hardness but much lower than the SiC hardness. Authors did not show quantitative results but claim that following this process no more scratches were revealed in etching in an alkaline melt, which usually decorates such defects. A limitation of this technique arises for low-doped samples, which slows down the oxidation and for non-uniformly doped samples where non-homogeneity can be revealed.

2.3 Cleaning

The objective of this stage is to remove all possible contaminants like particles, organics, and metallics from the substrate surface. Wafers are usually cleaned using the following steps: degreasing; deoxidizing; rinsing in high-purity de-ionized water and blowing dry with nitrogen.

Deoxidizing is the critical step to achieve a hydrophobic surface to ease the removal of all the surface contaminants in the later steps [47]–[49]. Subsequent ultraviolet ozone cleaning has been mainly used in order to prepare the surface for SiO<sub>2</sub> layer deposition by improving the interfacial characteristics of SiO<sub>2</sub>/SiC [50].

Xue et al. [28] have presented an interesting method using 10 cycles of ultrahigh vacuum (UHV) Si molecular beam etching. During each cycle Si layers are deposited and then annealed at about 1000°C. The principle of this technique is to desorb silicon oxides and avoid graphitization due to the presence of Si. However, to clearly assess this technique, a quantitative

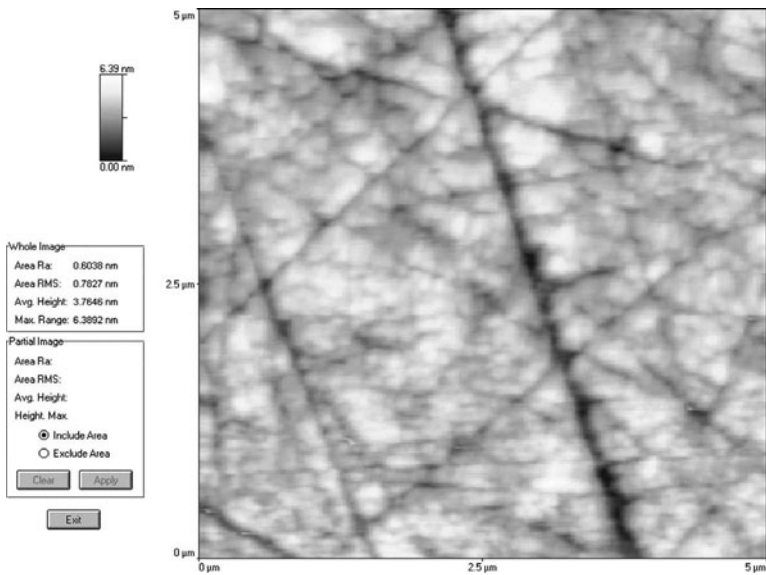


**Fig. 1.** AFM micrograph of standard as-delivered surface of a 4H-SiC “on axis” wafer. Here the RMS surface roughness is 7.8 Å

measure of the residual contaminants must be done. It is worth to mention that when this technique is combined with hydrogen etching, the measured RMS surface roughness is still quite high with about 15 Å.

To assess the level of contamination different methods can be used. The silicon industry has validated the following techniques: time of flight SIMS (ToFSIMS) [51] as well as vapor/liquid phase decomposition to inductively coupled plasma mass spectroscopy (VPD/LPD-ICPMS) [52]–[54]. Including synchrotron radiation total reflection X-ray fluorescence spectroscopy (SR-TXRF) [55, 56], these techniques are the most relevant for true surface contamination analysis. In the SiC industry almost no work on contamination analysis has been reported until now. For instance, it would be very fruitful to correlate surface contaminants with defects appearing after homo or heteroepitaxy to find out the possible sources of defect killers (causing catastrophic failure of the device).

3 Results

3.1 Polishing Results

It is well known that the substrate surface quality prior to epitaxial growth is a key parameter to achieve high quality epilayers. In this section we will present the most recent SiC polishing processes which produce surfaces free of scratches with no subsurface damage and for on-axis wafers lead to the formation of atomic steps: StepSiC® [57]. The process based on CMP cannot

**Table 1.** Standard and state of the art surface preparation results on 4H- and 6H-SiC wafers

Poly-type	Orien-tation	Face	Standard Roughness	State of the art results (CMP) Roughness	Comments
4H	On axis	Si	5–2.5 Å	1 Å	Atomic steps
		C	Optical	4 Å	
	8° off	Si	10–5 Å	1 Å	
		C	Optical	4 Å	
6H	On axis	Si	5–2.5 Å	< 1.5 Å	Atomic steps
		C	Lapped	2 Å	

be the same for each polytype, orientation and doping levels and has to be tuned to reach similar surface quality.

Table 1 shows the standard results of surface preparation on the two commercial polytypes of SiC. The Root Mean Square (RMS) surface roughness was obtained using Atomic Force Microscopy (AFM) images collected using an Autoprobe M5 or a Nanoscope III apparatus in the so-called tapping mode with a field of  $5 \times 5 \mu\text{m}$ .

One should notice the final result of these preparation processes is not jeopardize by the manufacturer origin or carrier density of the wafer, but more by the intrinsic crystallographic quality of the material.

Similar results are obtained with  $6H$ -SiC wafers. The appearance of steps with “on-axis” wafers is in fact due to the residual off-axis angle of the surface. These steps are a good illustration of the high quality surface preparation.

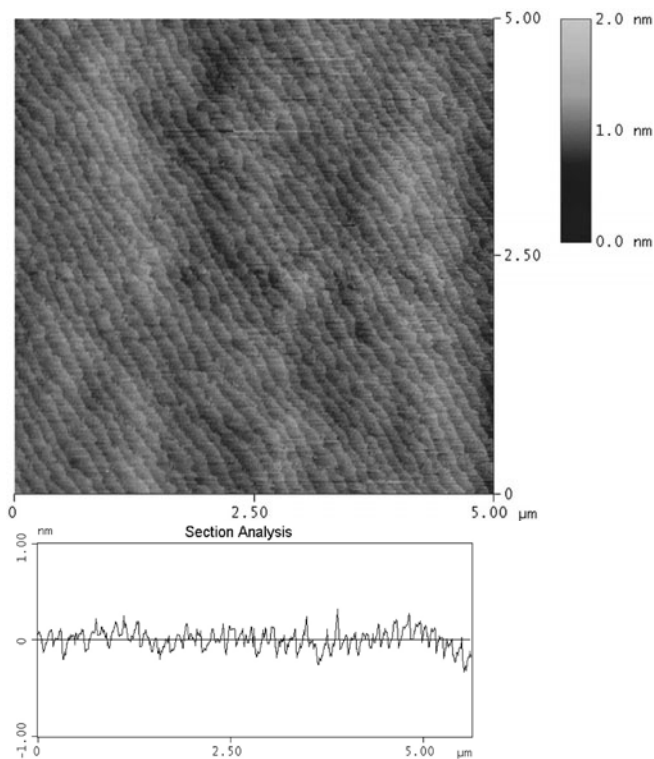


**Fig. 2.** Atomic steps (StepSiC<sup>®</sup>) after a CMP process on  $4H$ -SiC “on axis” wafer and the corresponding height section across the steps. The RMS surface roughness is  $0.9 \text{ \AA}$

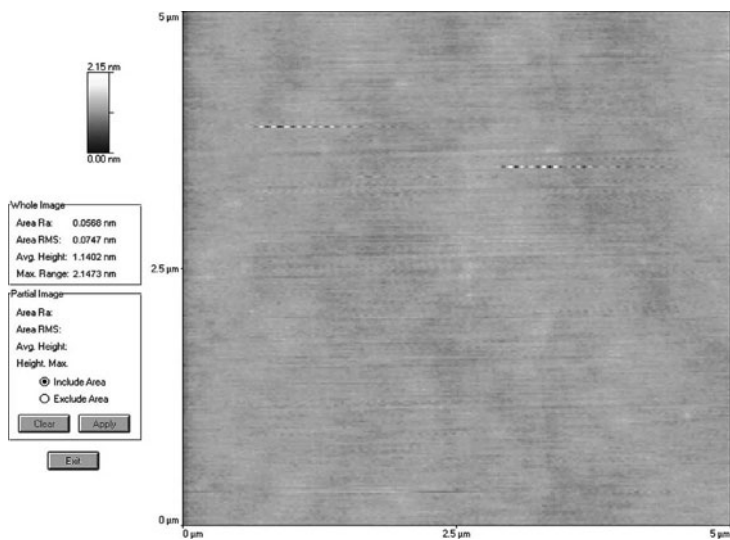


**Fig. 3.** AFM image of the typical surface obtained after CMP process on 4H-SiC “8° off” wafer. The RMS surface roughness is 0.75 Å

**3.1.1 Surface Reconstruction**

A very interesting characteristic of this CMP surface preparation has been observed using reflection high-energy electron diffraction (RHEED). B. Daudin at Grenoble and F. Semond at Valbonne have collected these results independently. Without any annealing or etching they find that the surface exhibits a clear  $3 \times 1$  reconstruction pattern.

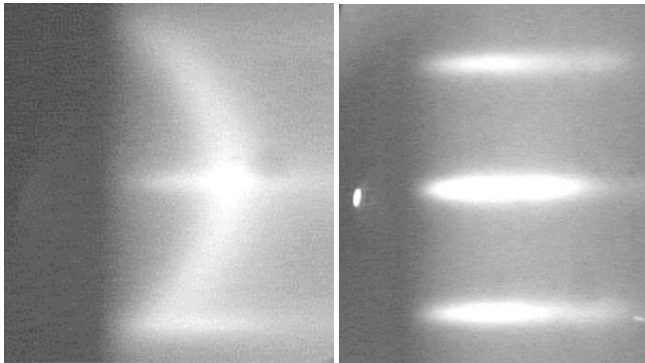


**Fig. 4.** RHEED surface reconstruction observed on a 6H-SiC on-axis wafer before (*left pattern*) and after CMP (*right pattern*) surface preparation (unpublished data)

3.1.2 Wafer Reclaim

Due to the high price and the scarce availability of the material a real need for reclaiming (recycling) wafers has recently emerged. Polishing or “strip and etch” process, which consists of dipping the wafers into successive baths, can remove defective homo-epitaxy, hetero-epitaxy and surface technology. After this step the wafers are polished by CMP processes. Using these processing steps, the surface quality is similar to the ones obtained by CMP on bare wafers.

3.2 Contamination Results

Almost no published work has been performed on surface contamination analysis. In Table 2 we present results obtained on 2'' wafers after epi-ready surface preparation.

LPD-ICPMS has been performed at the center of the wafer (9 cm<sup>2</sup>) after that surface was covered with HF 2% solution for 2 minutes and then analyzed. All the contaminant levels are lower than 2·10<sup>11</sup> atom/cm<sup>2</sup> (see Table 2). The ‘S’ value corresponds to the maximum error for the detection technique. The amount of iron is below the white noise (W.N.) of the apparatus. These levels are equivalent to a silicon standard surface. This confirms the excellent cleanliness (and packaging) of the surface.

These results have been confirmed by ToFSIMS analysis where only Ca and Na metallics are detected with level close to the detection limit.

**Table 2.** Typical surface contamination levels on epi-ready wafers

	Na	Ca	Fe	Zn	Al
C At/cm <sup>2</sup>	7.0·10 <sup>10</sup>	1.8·10 <sup>11</sup>	W.N	1.7·10 <sup>10</sup>	1.6·10 <sup>10</sup>
S %	9.2	7.7	–	7.7	31.0

3.3 Impact of Surface Preparation on the Epitaxy and the Device Performances

Recently several groups have published results of epitaxy on wafers processed using special surface preparation techniques.

Di Forte-Poisson et al. [58] have shown a clear improvement of the quality of a GaN layer grown on 6H-SiC treated with a damage free surface preparation process. HR-XRD full-line widths at half-maximum (FWHM) of the GaN epitaxy on 6H-SiC without polishing is typically 100 arcsec and after

polishing the layer is much better with a decrease of FWHM down to 50 arc-sec. TEM measurements have evidenced an improved crystallinity quality in the first GaN layers at the GaN/SiC interface.

Weimann et al. [59] found that a surface treatment is crucial to the reproducible production of high 2DEG mobility of AlGaN/GaN heterostructures for High Electron Mobility Transistors (HEMT).

Wan et al. [60] have fabricated 3C-SiC MOSFETs (3C-SiC on Si) which exhibit after adequate polishing and sacrificial oxidation of the 3C-SiC layer an improved mobility of  $165 \text{ cm}^2/\text{Vs}$  with a gate oxide breakdown field of  $3.5 \text{ MV/cm}$ .

### 3.4 Prospective

New orientations, such as  $(11\bar{2}0)$ ,  $(1\bar{1}00)$ ,  $(03\bar{3}8)$  for hexagonal polytypes are available on the market. In order to benefit from their expected qualities it is necessary to develop adapted surface preparation techniques but their surface properties are not fully studied.

3C-SiC on Si and stand-alone 3C-SiC are not yet mature in terms of crystalline quality but surface preparation techniques has recently started to be developed [3, 60].

New interests, such as C-face preparation or preparation for wafer bonding are emerging. The chemistry of C-face is completely different with an oxidation rate much higher than the Si-face.

Also among the new challenging developments, the evolution of processes to larger diameters (4 inch) and high volume/lower costs is on the way.

## 4 Conclusion

Initial work on surface preparation began in the mid-sixties but only recently real breakthroughs have emerged. Reproducibility of processes depends strongly on the material quality, which has been greatly improved in the last five years. CMP process in combination with adapted cleaning has allowed the preparation of epi-ready surfaces.

Now the surface preparation is mature for 4H- and 6H-SiC polytypes for the common crystal orientations. New challenges concern exotic orientations, cubic phase, C-side preparation and wafer thinning. Improving processes on such multi-form material is a never-ending work.

### Acknowledgements

The authors wish to thank J. Camassel at GES Montpellier University, J. Kronwasser and C. Jacques for their critical reading. They also thank B. Daudin at DRFMC-CEA Grenoble and F. Semond at CHREA Valbonne for the surface reconstruction results and M.F. Manfra at Lucent Bell Lab. for the results on HEMTs structures.

## References

1. H. Kitahara, Y. Noda, F. Yoshida, H. Nakashima, N. Shinohara and H. Abe: J. Ceramic Society Japan **109**, 602 (2001)
2. K. Li and T.W. Liao: J. of Mater. Processing Technology **57**, 207 (1996)
3. A.A. Yasseen, C.A. Zorman and M. Mehregany: Journal of the Electrochemical Society **146** (1), 327, (1999)
4. Z. Zhu, V. Muratov and T. Fisher: Wear **225**, 848 (1999)
5. T.C. Chandler, M.B. Lari and T.S. Sudarshan: Mater. Sci. Forum **338**, 845 (2000)
6. H.H.K. Xu and S. Jahanmir: J. of American Soc. **77**, 1388 (1999)
7. M. Kikuchi, Y. Takahashi, T. Suga, S. Suzuki and Y. Bando: J. American Soc. **75**, 189 (1992)
8. W. Qian, M. Skowronski, G. Augustine, R.C. Glass, H.McD. Hobgood and R.H. Hopkins: J. Electrochem. Soc. **142**, 4290 (1995)
9. M. Kanaya, H. Yashiro, N. Ohtani, M. Katsuno, J. Takahashi and S. Shinoyama: Materials Science Forum **264–268**, 359 (1998)
10. R.M. Silva, F.D. Orazio, J.M. Bennett: Optics News **12**, 2 (1986)
11. W.C. Mitchel, J. Brown, K. Malalingham, F.D. Orazio, Jr., P. Pirouz, H.J.R. Tseng, U. Ramabadran and B. Roughani: Materials Science Forum **338–342**, 841 (2000)
12. W.J. Everson, D.W. Sydney and V.D. Heydemann: Mater. Sci. Forum **338**, 837 (2000)
13. J. Camassel, P. Vicente and L. Falkovski: Silicon Carbide and Related Materials, Materials Science Forum **353–356**, 335 (2000)
14. P. Vicente, D. David, J. Camassel: Materials Science and Engineering B **80**, 348 (2001)
15. M.F. Barthe, P. Desgardin, L. Henry, C. Corbel, D.T. Britton, A. Hempel, W. Kugelmann, G. Kögel, P. Sperr, W. Triftshäuser, P. Vicente and L. di Cioccio: Material Science Forum **389**, 493 (2001)
16. E.K. Sanchez, S. Ha, J. Grim, M. Skowronski, W.M. Vetter, M. Dudley, R. Bertke and W.C. Mitchel: J. Electrochem. Soc. **149**, G131 (2002)
17. B. Roughani, U. Ramabadran, D. Phillips, W.C. Mitchel, and C.L. Neslen: Mater. Res. Soc. Symp. **640**, H5.40, (2001)
18. L. Zhou, V. Audurier, P. Pirouz, J.A. Powell: Electrochem. Soc. **144**, L161 (1997)
19. S. Sundararajan and B. Bushan: Wear **217**, 251 (1998)
20. C.L. Neslen, W.C. Mitchel and R.L. Hengehold: J. Electron. Mater. **30** (10) 1271 (2001)
21. T.L. Chu and R.B. Campbell: J. Electrochemical Society **112**, 955 (1965)
22. M.A. Kulakov, P. Heuell, V.L. Svetkov and B. Bullemer: Surface Sci. **315**, 248 (1994)
23. C. Hallin, A.S. Bakin, F. Owman, P. Martensson, O. Kordina and E. Janzen: Inst. Phys. Conf. Ser. **142**, 613 (1996)
24. F. Owman, C. Hallin, P. Martensson and E. Janzen: J. Crystal Growth **167**, 391 (1996)
25. J.A. Powell and D.J. Larkin, P.B. Abel: J. of Elect. Mater. **24**, 295 (1995)
26. J.A. Powell and D.J. Larkin: Phys. Stat. Sol. b **202**, 529 (1997)

27. V. Ramachandran, M.F. Brady, A.R. Smith, R.M. Feenstra, D.W. Greve: *J. Electron. Mater.* **27** (4), 308 (1998)
28. Q. Xue, Q.K. Xue, Y. Hasegawa, I.S.T. Tsong and T. Sakurai: *Applied Phys. Lett.* **74**, 2468 (1999)
29. Z.Y. Xie, C.H. Wei, L.Y. Li, Q.M. Yu, J.H. Edgar, J. Chaudhari, C. Ignatiev: *MRS Internet J. Nitride Semicond. Res.* **4S1**, G3.39 (1999)
30. Z.Y. Xie, C.H. Wei, L.Y. Li, Q.M. Yu and J.H. Edgar: *J. Crystal Growth* **217**, 115 (2000)
31. Z.Y. Xie, C.H. Wei, L.Y. Li, Q.M. Yu and J.H. Edgar: *J. of Electron. Mater.* **29**, 411 (2000)
32. Z.Y. Xie, J.H. Edgar, B.K. Burkland, J.T. George and J. Chaudhuri: *J. Crystal Growth* **224**, 235 (2001)
33. R. Wang, I. Bhat and P. Chow: *Mater. Res. Soc. Symp.* **640**, H2.6, (2001)
34. F. Dulot, L. Mansour, A. Leycuras, W. Wulfhekel, D. Sander, F.A. d' Avitaya and M. Hanbücken: *Applied Surface Science* **187**, 319 (2002)
35. E. Neyret, L. Di Ciccio, E. Blanquet, C. Raffy, C. Pudda, T. Billon and J. Camassel: *Mater. Sci. Forum* **338–342**, 1041 (2000)
36. A.A. Burk Jr., L.B. Rowland: *J. Crystal Growth* **167**, 586 (1996)
37. T. Kimoto, Z.Y. Chen, S. Tamura, S. Nakamura, N. Onojima and H. Matsumami: *Jpn. J. Appl. Phys.* **40**, 3315 (2001)
38. A.S. Bakin, S.I. Dorozhkin, S.V. Bogachov, A.Z. Kazak-Kazakevich, I.G. Lyutetskaja and A.P. Sazanov: *Mater. Sci. and Engineering B* **46**, 370 (1997)
39. D. Alok, B.J. Baliga: *J. Electron. Mater.* **24**, 311 (1995)
40. D. Alok, B.J. Baliga: *J. Electrochem. Soc.* **144**, 1135 (1997)
41. T. Henkel, G. Ferro, S. Nishizawa, H. Presler, Y. Tanaka, H. Tanove, N. Kobayashi: *Mater. Sci. Forum* **338–342**, 599 (2000)
42. J.A. Edmond, J.W. Palmour, and R.F. Davis: *J. Electrochem. Soc.* **133**, 20 (1986)
43. R. Menzel, T. Bachmann, F. Machalet, W. Wesch, U. Lang, M. Wendt, C. Musil and R. Muhle: *Appl. Surf. Sci.* **136**, 1 (1998)
44. V.A. Muratov and T.E. Fisher: *Annual Rev. Mater. Sci.* **30**, 27 (2000)
45. V.J. Jennings: *Mater. Res. Bull.* **4**, S199 (1969)
46. E.I. Radovanova: *Semiconductors* **30**, 527 (1996)
47. S.W. King, R.J. Nemanich and R.F. Davis: *J. Electrochemical Soc.* **146**, 1910 (1999)
48. S.W. King, R.J. Nemanich and R.F. Davis: *J. Electrochemical Soc.* **146**, 2648 (1999)
49. S.W. King, R.S. Kern, M.C. Benjamin, J.P. Barnak, Robert, J. Nemanich and R.F. Davis: *J. Electrochemical Soc.* **146**, 3448 (1999)
50. R. Kosugi, S. Ichimura, A. Kurokawa, K. Koike, K. Fukuda, S. Suzuki, H. Okushi, S. Yoshida, and K. Arai: *Appl. Surf. Sci.* **159–160**, 550 (2000)
51. S. Verhaverbeke, S. Kuppurao, C. Beaudry and J. Kelly Truman: *Applied Materials Inc., Santa Clara, Calif., Semiconductor International* (2002)
52. F. Meyer, J. White and M. Radle: *Semiconductor International* (1999)
53. H.Y. Chung, Y.H. Kim, H.Y. Cho, B.Y. Lee, H.D. Yoo and S.H. Lee: *Analytical Science* **17**, 653 (2001)
54. *Semi C10-94 Guide for Determination of Method Detection Limits for Trace Metal analysis by plasma spectroscopy*

55. K. Baur, S. Brennan, P. Pianetta, R. Opila: *Anal. Chem.* **74**, 609 (2002)
56. P. Pianetta, K. Baur, A. Singh, S. Brennan, J. Kerner, D. Werho, J. Wang: *Thin Solid Films* **373**, 222 (2000)
57. P. Vicente, E. Pernot, D. Chaussende, J. Camassel: *Mater. Sci. Forum* **389–393**, 729 (2001)
58. M.A. Di Forte Poisson, A. Romann, M. Tordjman, M. Magis, J. Di Persio, C. Jacques, P. Vicente: *J. Crystal Growth* **248**, 533 (2003)
59. N. Weimann, M.J. Manfra and T. Wächtler: to be published in *IEEE Electron Device Letters* (2003)
60. J. Wan, M.A. Campano, M.R. Melloch and J.A. Cooper, Jr.: *IEEE Electron. Device Letters* **23**, 482 (2002)

# Epitaxial Growth and Device Processing of SiC on Non-Basal Planes

T. Kimoto, H. Yano, Y. Negoro, K. Hashimoto, and H. Matsunami

## 1 Introduction

Recent progress in silicon carbide (SiC) crystal growth and device processing technologies has enabled the fabrication of prototype high-power and high-frequency devices which outperform the conventional Si or GaAs counterparts. Since the development of step-controlled epitaxy [1], 4*H*- and 6*H*-SiC(0001) wafers with several-degree off-angles have exclusively been employed for SiC homoepitaxy and device development except a few reports [2]–[5]. However, SiC metal-oxide-semiconductor field effect transistors (MOSFETs) have suffered from unacceptably low channel mobility, especially in 4*H*-SiC. Although significant improvements in channel mobility have been reported [6, 7], the maximum inversion-channel mobility of 4*H*-SiC(0001) MOSFETs is still below 30–50 cm<sup>2</sup>/Vs. From our demonstration of high channel mobility in MOSFETs using the (11-20) face [8], bulk and epitaxial growth, characterization, and device processing on this face have attracted attention from both scientific and industrial viewpoints. The authors have also proposed 4*H*-SiC(03-38), which is tilted by 54.7° from (0001) toward [01-10], as a novel face with potentially superior quality of MOS interface [9].

Another drawback of the SiC(0001) face is the threading micropipes (hollow cores associated with “superscrew” dislocations), which severely affect blocking performance of high-voltage SiC devices [10]. To scale up the current handling capability of SiC power devices, micropipes must be eliminated. In this respect, 4*H*-SiC(11-20), parallel to the *c*-axis, is expected to be micropipe-free [11]. Sublimation growth of micropipe-free 4*H*-SiC(03-38) ingots has also been suggested [12]. It is well known that growth behavior, impurity incorporation, and device performance strongly depend on the crystal face employed in Si and most III-V semiconductors. Thus, the investigation on non-basal planes, 4*H*-SiC (11-20) and (03-38), is of fundamental interest.

In this paper, we review the homoepitaxial growth and fundamental device processing of 4*H*-SiC(11-20) and 4*H*-SiC(03-38). After describing the crystallographic features of these non-basal planes, homoepitaxy by chemical vapor deposition (CVD) is presented. Surface morphology, crystalline quality, impurity doping, structural defects, and the fabrication of Schottky barrier diodes to assess the quality of the grown materials and the effect of structural defects on the device performance are discussed for these non-basal

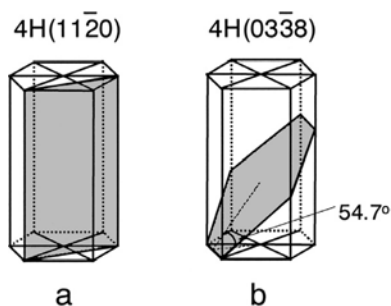
planes. The ion implantation process and the implant damage anneal, as well as the performance of MOSFETs and the quality of the MOS interface on  $4H$ -SiC(11-20) are also reviewed.

## 2 Non-Basal Planes in $4H$ -SiC

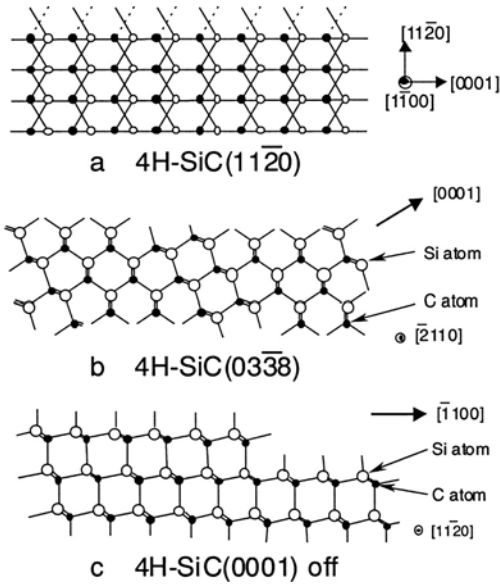
Figure 1 illustrates the location of the (a)  $4H$ -SiC(11-20) and (b) (03-38) faces in the unit cell of  $4H$ -SiC. The  $4H$ -SiC(0001) and (11-20) faces are crystallographically equivalent to (111) and (110) in the cubic structure, respectively. The  $4H$ -SiC(03-38) is semi-equivalent (though not identical) to (100).

Figure 2 schematically illustrates surface bond configurations for (a)  $4H$ -SiC(11-20), (b)  $4H$ -SiC(03-38), and (c) off-axis  $4H$ -SiC(0001). In the figure, open and closed circles denote Si and C atoms, respectively. Surface reconstruction and adsorbed species are neglected for simplicity. At least, 50% of bond configuration on the  $4H$ -SiC(03-38) surface is identical to that on  $3C$ -SiC(001) [13].

Although the sublimation growth of  $4H$ -SiC(11-20) and (03-38) ingots has been reported [11, 12], no wafers sliced from those ingots are commercially available at present. In this experiment,  $4H$ -SiC(11-20) and (03-38) substrates were prepared by cutting [000-1]-grown ingots. The typical substrate size was about 25 mm  $\times$  8 mm for  $4H$ -SiC(11-20) and 40 mm  $\times$  20 mm for  $4H$ -SiC(03-38). The substrates were  $n$ -type, doped with nitrogen to the  $10^{18}$  cm $^{-3}$  range. It should be noted that the (11-20) face is non-polar but the {03-38} exhibits polarity: (03-38) and (0-33-8). The authors mainly employed the (03-38) face, because of the superior surface morphology and lower background doping level.



**Fig. 1.** (a)  $4H$ -SiC(11-20) and (b)  $4H$ -SiC(03-38) faces in the unit cell of  $4H$ -SiC



**Fig. 2.** Surface bond configurations for (a) 4H-SiC(11-20), (b) 4H-SiC(03-38), and (c) off-axis 4H-SiC(0001)

### 3 Chemical Vapor Deposition for Non-Basal Planes

#### 3.1 Homoepitaxial Growth Process

Epitaxial growth was carried out by either cold-wall or hot-wall CVD at 1500–1550°C [1, 14]. The source gases were SiH<sub>4</sub> and C<sub>3</sub>H<sub>8</sub> with carrier gas H<sub>2</sub> purified by a Ag-Pd cell. The growth process consists of in-situ HCl or C<sub>3</sub>H<sub>8</sub>+H<sub>2</sub> etching and CVD growth. The typical flow rates of SiH<sub>4</sub>, C<sub>3</sub>H<sub>8</sub>, and H<sub>2</sub> were 0.50 sccm, 0.33 sccm, and 3 slm for cold-wall CVD, and 1.5 sccm, 0.75 sccm, and 10 slm for hot-wall CVD, respectively. The growth rate was 3.5 μm/h for cold-wall and 5 μm/h for hot-wall CVD. When CVD growth was performed on non-basal planes, 8° off-axis 4H-SiC(0001) substrates were placed for comparison side by side on the susceptor.

The epilayer thickness was determined from cross-sectional observation of cleaved samples with a scanning electron microscope or from depth analyses in secondary ion mass spectroscopy (SIMS) measurements. Epilayers were characterized by Nomarski microscopy, photoluminescence (PL), capacitance-voltage (*C-V*) measurements, and deep level transient spectroscopy (DLTS). Within the authors' experience, no essential differences were observed in 4H-SiC(11-20) and (03-38) growth itself by either cold-wall or hot-wall CVD systems, as far as surface morphology, shapes of surface defects, and tendency of impurity doping are concerned. Thus, results obtained by hot-wall CVD are mainly described in this paper.

It is noteworthy that no intentional off-angles are required for these non-basal planes to realize homoepitaxy of  $4H$ -SiC. This fact may be readily predictable from the appearance of stacking information on the surface, as shown in Fig. 2. Even if the growth proceeds through two-dimensional nucleation and subsequent layer-by-layer growth, instead of step-flow, the replication of substrate polytype is ensured on these faces. The growth rate on the non-basal planes was almost the same as that on off-axis (0001) under the same condition, indicating that growth is controlled by mass transport.

The  $4H$ -SiC(11-20) and (03-38) epilayers exhibited very good morphology and a small surface roughness of 0.18–0.24 nm in a  $10\text{ }\mu\text{m} \times 10\text{ }\mu\text{m}$  area [13, 15], without any triangular defects and “carrot-like” grooves which occasionally appear on off-axis SiC(0001) epilayers. No signs of “step-flow” growth such as step bunching have been observed for these epilayers, suggesting layer-by-layer growth. The typical surface defect density was approximately  $100\text{ cm}^{-2}$  on off-axis (0001),  $30\text{ cm}^{-2}$  on (11-20), and  $300\text{ cm}^{-2}$  on (03-38). In the present hot-wall CVD on off-axis (0001), the optimum window of C/Si ratio, where specular morphology is obtained, was 0.7–3.0: Pits caused by Si droplets are observed at lower C/Si ratios, while triangular stacking faults appeared at higher C/Si ratios. On the (11-20) face, hillocks with a density of  $10^2\text{ cm}^{-2}$  were formed when the C/Si ratio was below 1.5. The optimum C/Si ratio seems to depend on the crystal face, being 1.5–5.0 on (11-20) and 0.7–5.0 on (03-38).

### 3.2 Unintentionally Doped Epilayers

Figure 3 shows the  $C$ - $V$  characteristics ( $1/C^2$ - $V$ ) measured for 1.5 mm diameter Ni/ $4H$ -SiC Schottky structure on various crystal faces [13]. The epilayers were approximately  $30\text{ }\mu\text{m}$  thick, and were simultaneously grown in the same run without intentional doping at a C/Si ratio of 1.5 by horizontal hot-wall CVD. The net donor concentration determined from  $C$ - $V$

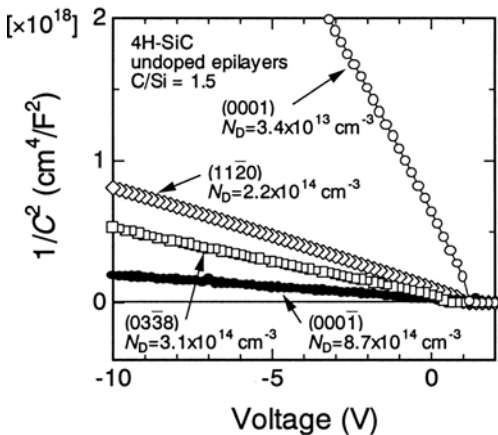


**Fig. 3.** Capacitance-voltage ( $1/C^2$ - $V$ ) characteristics measured for 1.5 mm diameter Ni/ $4H$ -SiC Schottky structure on various crystal faces

measurements was  $2.2 \times 10^{14} \text{ cm}^{-3}$  for (11-20) and  $3.1 \times 10^{14} \text{ cm}^{-3}$  for (03-38) epilayers. These doping levels are in between those on off-axis (0001)Si ( $3.4 \times 10^{13} \text{ cm}^{-3}$ ) and (000-1)C ( $8.7 \times 10^{14} \text{ cm}^{-3}$ ) faces. Since a donor concentration well below  $5 \times 10^{13} \text{ cm}^{-3}$  has been routinely obtained on off-axis (0001) in the present growth system, the higher background doping levels in 4H-SiC (11-20) and (03-38) growth might be one issue to be improved. Nevertheless, the purity in the low  $10^{14} \text{ cm}^{-3}$  range is sufficiently low for most device applications. A lower doping concentration may be expected by increasing C/Si ratio.

Figure 4 shows typical PL spectra at 4.2 K obtained from (a) 4H-SiC(11-20), (b) 4H-SiC(03-38), and (c) off-axis 4H-SiC(0001) epilayers grown in the same CVD run. A He-Cd laser ( $\lambda = 325 \text{ nm}$ ) was used as an excitation source. The 60  $\mu\text{m}$ -thick epilayers were grown, so that PL signals from substrates are negligibly small even for lightly-doped 4H-SiC epilayers. The PL spectra are dominated by peaks of excitons bound to neutral-nitrogen donors labeled by the *P* (nitrogen at the hexagonal site) or *Q* (nitrogen at the cubic site) series and by free exciton peaks denoted by the *I* series. Phonons involved in the recombination are represented as the subscripts of labels. The donor concentration determined by *C-V* measurements was  $8 \times 10^{14} \text{ cm}^{-3}$  for 4H-SiC(11-20),  $1 \times 10^{15} \text{ cm}^{-3}$  for 4H-SiC(03-38), and  $5 \times 10^{13} \text{ cm}^{-3}$  for 4H-SiC(0001) epilayers. The relative intensity of free exciton peaks ( $I_{\text{TA}}$ ,  $I_{\text{LA}}$ ,  $I_{\text{TO}}$ ) for the 4H-SiC(11-20) and (03-38) epilayers are smaller than those for the 4H-SiC(0001) epilayer, due to the higher donor concentration. The PL spectrum for the 4H-SiC(11-20) epilayer is very similar to that for the 4H-SiC(03-38) epilayer, because of the similar doping level. PL peaks related with

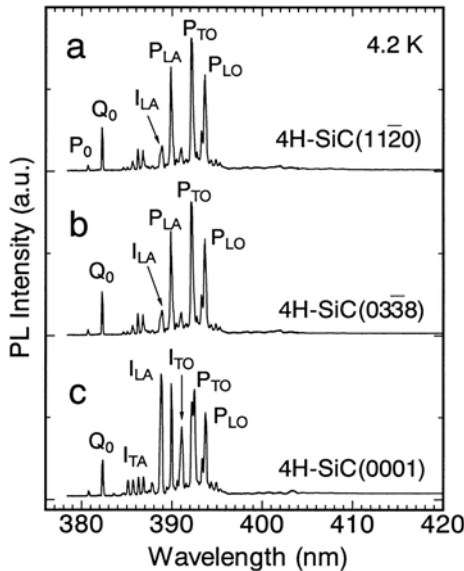


**Fig. 4.** Typical PL spectra at 4.2 K obtained from (a) 4H-SiC(11-20), (b) 4H-SiC(03-38), and (c) off-axis 4H-SiC(0001) epilayers

unwanted impurities, such as aluminum-bound exciton ( $4Al_0$  at 381–382 nm), Ti ( $C_0$  at 444 nm), and nitrogen-aluminum (or boron) donor-acceptor pair luminescence, were not observed for all the epilayers (not shown in the figure). The  $L_1$  peak at 427 nm due to the  $D_I$  center was also not observed.

In DLTS spectra measured on Ni/4H-SiC(11-20), Ni/4H-SiC(03-38), and Ni/off-axis 4H-SiC(0001) Schottky contacts, two peaks were observed at 300–320 K and 620–650 K. From the Arrhenius plots of emission time constant, the dominant peak at 300–320 K could be assigned to the  $Z_{1/2}$  center, located at  $E_c - 0.65 \pm 0.3$  eV ( $E_c$ : the conduction-band edge) [16]. The high-temperature peak at 620–650 K originates from the  $EH_{6/7}$  center with an activation energy of  $1.5 \pm 0.6$  eV [17]. Except these defect centers, no DLTS peaks due to unwanted impurities such as Ti and V are observed. The C/Si ratio dependence of  $Z_{1/2}$  center concentration for 4H-SiC(0001), (11-20) and (03-38) epilayers is shown in Fig. 5. On the off-axis (0001) face, the  $Z_{1/2}$  center concentration could be reduced to  $1 \times 10^{11}$  cm $^{-3}$  or less by increasing C/Si ratio. Although the trap concentration is higher for (11-20) and (03-38) epilayers, a high C/Si ratio during CVD is also effective to suppress the formation of the  $Z_{1/2}$  center. The  $Z_{1/2}$  center concentrations of  $3 \times 10^{11}$  cm $^{-3}$  for (11-20) and  $8 \times 10^{11}$  cm $^{-3}$  for (03-38) could be obtained, which are low enough to fabricate, at least, majority-carrier devices. The authors found that the formation of  $EH_{6/7}$  center can be also suppressed under C-rich condition. It is, however, not easy to provide clear explanation on these C/Si ratio dependencies, because the exact microscopic structures of  $Z_{1/2}$  and  $EH_{6/7}$  centers have not been identified. Note that the growth rate showed very little change in the C/Si ratio-range investigated. The formation of intrinsic defects, such as Si vacancy, C vacancy and antisite, may be influenced by the C/Si ratio during growth, leading to different appearance of the defect centers.

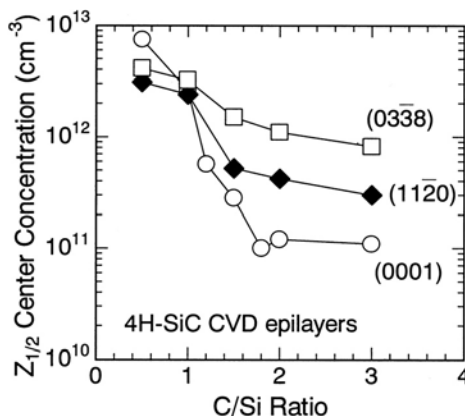


**Fig. 5.** C/Si ratio dependence of  $Z_{1/2}$  center concentration for 4H-SiC(0001), (11-20) and (03-38) epilayers

### 3.3 Nitrogen and Boron Doping

Intentional nitrogen (N) or boron (B) doping was investigated for different faces by *C-V* and SIMS measurements. When the  $N_2$  gas was introduced, the epilayers grown on (11-20) and (03-38) always showed higher donor concentration than on off-axis (0001), being consistent with Fig. 3. Figure 6 shows the C/Si ratio dependence of nitrogen concentration determined by SIMS for 4H-SiC epilayers on (11-20), (03-38), and off-axis (0001) and (000-1) faces grown by hot-wall CVD. In this experiment, four SiC substrates of different faces were loaded in the same run. Growth conditions were changed during the CVD run, and the doping characteristic of nitrogen was determined through depth profiling of nitrogen atoms by SIMS measurements. The detection limit of nitrogen atoms in the SIMS measurement was  $5 \times 10^{16} \text{ cm}^{-3}$ . The growth was performed by keeping constant flow rates of  $SiH_4$ ,  $N_2$ , and  $H_2$  but changing only the  $C_3H_8$  flow rate. The flow rate of  $N_2$  and reactor pressure were 10 sccm and 100 Torr, respectively. The nitrogen incorporation is significantly reduced by increasing the C/Si ratio on (11-20), (03-38), and off-axis (0001), following the site competition concept [18]. The C/Si ratio dependence is the largest on (0001), while (11-20) and (03-38) faces show smaller changes in nitrogen incorporation. On the (000-1) face, however, the higher C/Si ratio does not always lead to the lower nitrogen concentration. As suggested in the undoped growth experiments, the doping efficiency of nitrogen on 4H-SiC(11-20) and (03-38) is located in between that on off-axis (0001) and (000-1) faces.

Figure 7 represents the doping characteristics of boron by cold-wall CVD using  $B_2H_6$  as a dopant source. The flow rates of  $SiH_4$  and  $C_3H_8$  were fixed at 0.30 and 0.40 sccm (C/Si ratio = 4), respectively. In this experiment, the boron concentration was determined by *C-V* measurements. SIMS measurements on several samples indicated that the doping concentration determined by *C-V* measurements agreed with the boron concentration obtained by SIMS

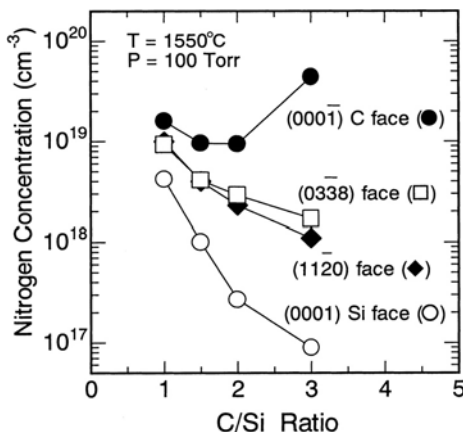


**Fig. 6.** C/Si ratio dependence of nitrogen concentration determined by SIMS for 4H-SiC epilayers on (11-20), (03-38), and off-axis (0001) and (000-1) faces

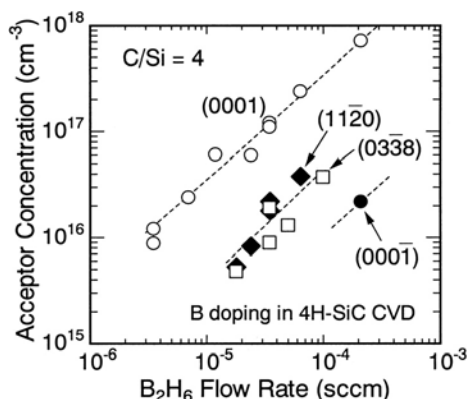


**Fig. 7.** Doping characteristics of boron by cold-wall CVD using  $B_2H_6$  as a dopant source. The flow rates of  $SiH_4$  and  $C_3H_8$  were fixed at 0.30 and 0.40 sccm ( $C/Si$  ratio = 4), respectively

within the error ( $\pm 10\text{--}20\%$ ) of SIMS measurements. In contrast to the nitrogen doping, the acceptor concentration of (11-20) and (03-38) epilayers was lower than that of off-axis (0001) epilayers at a given  $B_2H_6$  flow rate. The authors have reported that the doping efficiencies of nitrogen and aluminum (Al) on (11-20) are located in between off-axis (0001) and (000-1) at any  $C/Si$  ratio [19, 20]. The present study indicates that the crystal-face dependence of B doping is similar to that of Al doping. The doping characteristics on (03-38) are very similar to those on (11-20). When  $B_2H_6$  was introduced during CVD, the growth rate was always decreased by 10–30%, depending on the  $B_2H_6$  flow rate. The mechanism of the growth-rate reduction has not been clarified yet.

It is known that less nitrogen and more aluminum or boron atoms are incorporated on (0001), compared to (000-1), both in CVD [19] and sublimation growth [21]. The authors speculate that the impurity incorporation in SiC growth may be dominated mainly by surface bond configuration and surface stoichiometry. Reminding that N atoms substitute at the C lattice site, N atoms adsorbed on the growing surface should form chemical bonds with the outermost Si atoms to occupy the “C site” and thereby to be incorporated into the crystal. On the (0001) face, only one bond is available from one Si atom on the surface, whereas the (11-20) and (03-38) faces may provide two bonds and the (000-1) face three bonds from one Si atom on the surface. Since nitrogen-related species may be easily vaporized, rather than condensed, higher desorption rate of nitrogen is expected on the (0001) face, on which a nitrogen atom is bound by only one chemical bond. This may lead to a lower doping efficiency of nitrogen on (0001). The desorption of nitrogen species may be suppressed on (11-20) and (03-38), and may be the slowest on (000-1), because of the increased number (or density) of available bonds from Si atoms on the surface. This may be the reason why the doping efficiency of nitrogen on (11-20) and (03-38) is located in between (0001) and (000-1) faces. In a similar manner, the Al and B doping may be

strongly influenced by the number (or density) of chemical bonds from the surface C atoms, because Al and B atoms substitute at the Si site to form shallow acceptors in SiC [22]. Thus, the Al and B incorporation on (11-20) and (03-38) is less efficient than on (0001) and more efficient than on (000-1). These crystal-orientation dependencies of impurity doping must be observed in SiC growth by any growth techniques. However, the mechanism of impurity incorporation should be much more complicated, since surface migration of impurity atoms and reaction at step sites are involved.

### 3.4 Structural Defects in 4H-SiC(11-20) Epilayers

Structural defects in 4H-SiC epilayers were investigated by molten KOH etching experiments. Etching was performed at 470°C for 1–3 min. Figure 8a shows the typical surface of a 4H-SiC(11-20) epilayer after KOH etching. The (11-20) epilayers were micropipe-free, as expected. Instead, triangular-shaped and elliptic etch pits were observed with a density of  $6-8 \times 10^4 \text{ cm}^{-2}$ . The origin and structural nature of these etch pits are not clear at present. According to the bulk growth study on 4H-SiC(11-20) [11], major structural defects existing in the (11-20) substrates must be slip dislocations in the basal planes and {0001} stacking faults. In particular, stacking faults are crucial in (11-20) growth. KOH etching of the (1-100) cross-section obtained by cleavage of (11-20) samples indicated that all the stacking faults in the substrates are replicated in the epilayers. The typical stacking fault density was  $1-10 \text{ cm}^{-1}$ . Recently, it has been reported that stacking faults in 4H-SiC(11-20) epilayers severely degrade reverse characteristics of Schottky barrier diodes [23]. The elimination of stacking faults is a next challenge in 4H-SiC(11-20) bulk and epitaxial growth.

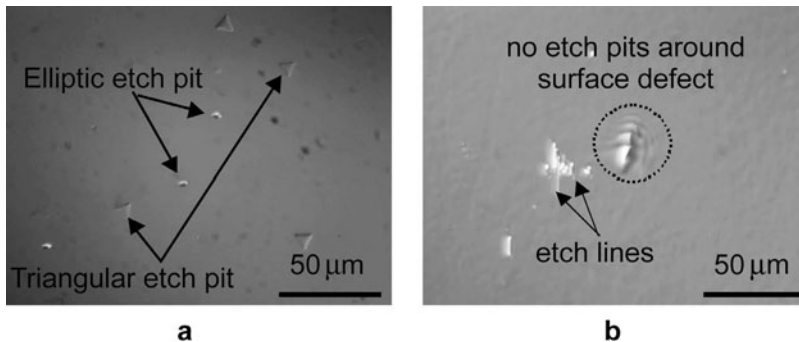


**Fig. 8.** Typical surface after molten KOH etching. (a) 4H-SiC(11-20) and (b) 4H-SiC(03-38) epilayers

### 3.5 Structural Defects in 4H-SiC(03-38) Epilayers

The authors have found that micropipes are dissociated in epitaxial growth of 4H-SiC(03-38) [24]. Figure 8b shows the typical surface of a (03-38) epilayer after KOH etching at 470°C for 3 min. As shown in the picture, localized “etch lines” were observed near a surface defect, in addition to randomly-distributed small etch pits. The total etch pit density was in the range from high  $10^4$  to low  $10^5$  cm<sup>-2</sup>. Careful observation of Nomarski and transmission images at the same location revealed that one surface defect is formed above the region where a micropipe exists in the (03-38) substrate. However, molten KOH etching did not yield any micropipe-etch pits (dark holes) around the surface defects. Instead, the [-2110]-aligned “etch lines” were detected, the position of which is shifted from the surface defect. Observation with a transmission optical microscope and successive etching experiments elucidated that micropipes in substrates were dissociated near the epilayer/substrate interface [24].

Micropipe dissociation has been investigated for totally 236 micropipes observed in four samples. Micropipe closing (complete dissociation) is influenced by the size of micropipes. Figure 9 shows the percentage of micropipe closing for a 60 μm-thick epilayer grown by hot-wall CVD, as a function of the micropipe diameter. The numbers above each bar mean “the number of closed micropipes/the number of micropipes existing in substrates”. The micropipe closing is perfect (100%) except for abnormally large ( $> 3$  μm) micropipes. Si et al. have clarified that hollow cores (micropipes) are created when the Burgers vector ( $\mathbf{b}$ ) of a screw dislocation equals to  $3\mathbf{c}$  or larger in 4H-SiC ( $\mathbf{c}$ : unit vector along the  $c$ -axis) [25]. According to their study, the diameter of micropipes is proportional to the square of Burgers vectors ( $|\mathbf{b}|^2$ ), following the Frank’s theory. Therefore, the smaller micropipes, which have smaller Burgers vectors, should be more easily closed, if the dissociation process ( $n\mathbf{c} \rightarrow (n-1)\mathbf{c} + \mathbf{c}$ ) takes place during epitaxial growth.

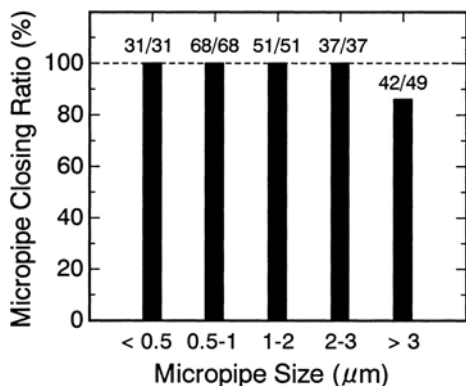


**Fig. 9.** Percentage of micropipe closing for a 60 μm-thick epilayer grown by hot-wall CVD, as a function of the micropipe diameter

Successive etching experiments indicated that the position of etch lines moved toward the [0-33-16] direction, as the epilayer thickness decreased by polishing. A quantitative analysis on this movement of etch lines suggested that the dislocations responsible for the etch lines lie in the {0001} basal plane. Since the Burgers vector of these dislocations in the basal plane should be mainly  $m\mathbf{c}$  ( $m = 1$  or less), the dislocations are of “edge” nature. The experimental details and mechanism of micropipe dissociation will be described in a subsequent publication.

Recently, Kamata et al. reported that a micropipe could be dissociated into several closed-core screw dislocations in CVD growth on off-axis 4H-SiC(0001) [26]. In the present study on 4H-SiC(03-38), however, “screw dislocations” propagating along the  $c$ -axis were not observed near the locations of micropipe closing. The authors found that even closed-core screw dislocations in substrates do not thread into 4H-SiC(03-38) epilayers but change the direction of dislocation lines.

### 3.6 Effect of Structural Defects on Performance of Schottky Diodes

In order to assess the epilayer quality and the influence of structural defects on the device performance, Schottky barrier diodes were processed. Ni/4H-SiC(11-20) and Ni/4H-SiC(03-38) Schottky barrier diodes were fabricated on 60  $\mu\text{m}$ -thick epilayers with a donor concentration of  $0.8 - 2 \times 10^{15} \text{ cm}^{-3}$ . The net donor concentration of substrates was estimated to be  $4 - 7 \times 10^{18} \text{ cm}^{-3}$  from  $C$ - $V$  measurements. Back-side ohmic contacts were formed by evaporation of Ni followed by annealing at 1000°C for 10 min. The diameter of as-deposited Ni Schottky contacts was 300  $\mu\text{m}$ . Neither edge termination nor surface passivation was employed.

The highest breakdown voltage obtained for diodes fabricated on 4H-SiC(11-20) was 3.36 kV. The on-resistance was not fluctuated among fabricated diodes, being 24  $\text{m}\Omega\text{cm}^2$ . On the other hand, the performance of 3.28 kV–22  $\text{m}\Omega\text{cm}^2$  was obtained for the 4H-SiC(03-38) diode. In the forward characteristics, both (11-20) and (03-38) diodes showed a small ideality factor of 1.04–1.08, and the barrier height was estimated to be 1.63–1.67 eV. The measured on-resistances (22–24  $\text{m}\Omega\text{cm}^2$ ) agree with the resistance of the  $n^-$  drift layer (20  $\text{m}\Omega\text{cm}^2$ ), assuming an electron mobility of 1000  $\text{cm}^2/\text{Vs}$ .

The authors investigated the effects of micropipe closing on the reverse characteristics of 4H-SiC(03-38) diodes. The current-voltage ( $I$ - $V$ ) characteristics were measured for 52 micropipe-free diodes and 43 diodes which contain “closed” micropipes. Figure 10 demonstrates the  $I$ - $V$  characteristics for typical three (03-38) diodes without micropipes and three (03-38) diodes with closed micropipes. The maximum breakdown voltage was 3.28 kV for diodes without micropipes and 2.97 kV for those with closed micropipes. These values are about 75–80% of the parallel-plane breakdown voltage (4 kV) calculated for this epilayer structure. It should be noted that the breakdown field

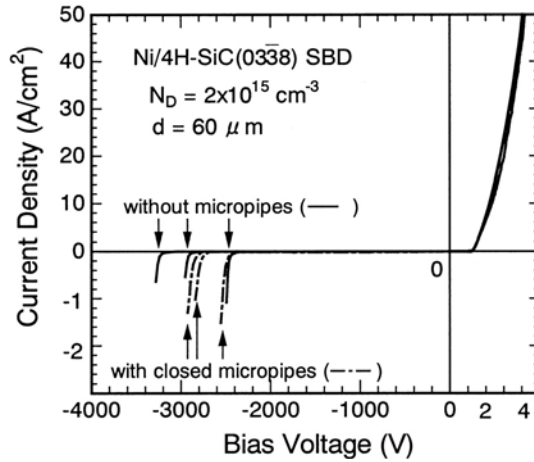


**Fig. 10.** Current-voltage characteristics for typical Ni/4H-SiC(03-38) Schottky barrier diodes without micropipes and diodes with closed micropipes

along 4H-SiC  $\langle 03\bar{3}8 \rangle$  is approximately 75% of that along 4H-SiC  $\langle 0001 \rangle$  [27], and is estimated to be about 1.58 MV/cm at the doping concentration used. Although the breakdown voltage for diodes with closed micropipes was slightly reduced by 5–10%, compared to micropipe-free diodes, the present result indicates that 4H-SiC(03-38) devices processed on closed-micropipe regions can withstand high electric field, at least, close to 1.5 MV/cm. The authors also measured five diodes with a threading micropipe, which was not closed because of its large diameter. All these diodes exhibited an excessive leakage current of 0.2–1 A/cm<sup>2</sup> at –1 kV and catastrophic breakdown at 1.0–1.2 kV. Thus, micropipe closing is very effective in improving the high-voltage blocking capability of SiC devices. Recently, Kamata et al. demonstrated that the breakdown voltage of 4H-SiC(0001) Schottky barrier diodes was significantly improved by micropipe closing [28]. Thus, the present work on 4H-SiC(03-38) is in agreement with the work on off-axis 4H-SiC(0001).

## 4 Device Processing

### 4.1 Phosphorus Ion Implantation and Implantation Damage Reduction

In high-dose ion implantation to form heavily-doped SiC, implantation at an elevated temperature followed by annealing at a high temperature above 1500–1600°C has been employed, because recrystallization of SiC is rather difficult. However, a recent report has shown that when activation annealing is performed at a high temperature in Ar, considerable roughening and

macrostep formation are observed, which may adversely affect the mobility of MOSFETs [29]. In this section, high-dose phosphorus ion implantation into 4H-SiC(11-20) and 4H-SiC(0001) is described. The electrical properties, implantation-induced damage, and surface roughness of implanted layers are discussed.

To form selective  $n^+$  regions in SiC, phosphorus ion ( $P^+$ ) [30] or nitrogen ion ( $N^+$ ) [31] implantations is commonly employed. Recently  $P^+$  implantation has attracted increasing attention to obtain lower sheet resistances [32, 33], probably due to its higher solubility limit in SiC. In this experiment, both  $8^\circ$  off-axis 4H-SiC(0001) and on-axis 4H-SiC (11-20) epilayers doped with boron to the net acceptor concentrations of  $0.8 - 6 \times 10^{16} \text{ cm}^{-3}$  were used as a starting material. Multiple energy (10–360 keV) implantation of  $P^+$  was carried out at either room temperature ( $RT$ ) or  $800^\circ\text{C}$  to form a  $0.45 \text{ }\mu\text{m}$ -deep box profile of P atoms. The total implant dose was  $1 \times 10^{16} \text{ cm}^{-2}$ , which resulted in the average P concentration of  $2 \times 10^{20} \text{ cm}^{-3}$ . Post-implantation annealing was performed in a CVD reactor at  $800\text{--}1700^\circ\text{C}$  for 30 min in pure Ar ambience. The electrical properties of the implanted regions were characterized by Hall effect measurements using the van der Pauw configuration. Ohmic contacts were formed by evaporation of either Al/Ti or Ni followed by annealing at  $900^\circ\text{C}$  in Ar. Mesa structures were fabricated by reactive ion etching.

Figure 11 shows the measured sheet resistance of  $P^+$ -implanted layers as a function of annealing temperature [34]. In the case of implantation at  $800^\circ\text{C}$  into 4H-SiC(0001), the sheet resistance takes a minimum value of  $80 \text{ }\Omega/\square$  after  $1700^\circ\text{C}$ -annealing, which agrees with recent reports [32, 33]. The sheet resistance for the (0001) samples implanted at  $RT$  was higher, compared to those implanted at  $800^\circ\text{C}$ . On the other hand, when 4H-SiC(11-20) epilayers were employed, a low sheet resistance of  $110 \text{ }\Omega/\square$  has been achieved by  $RT$ -implantation followed by annealing at  $1700^\circ\text{C}$ . The low-temperature an-

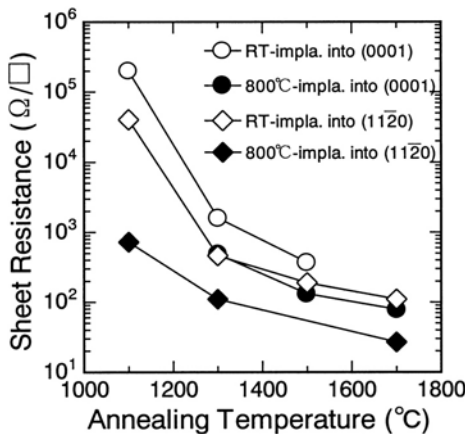


**Fig. 11.** Sheet resistance of  $P^+$ -implanted 4H-SiC(11-20) and (0001) layers as a function of annealing temperature

nealing even at 1300°C resulted in a reasonable sheet resistance of 460  $\Omega/\square$ . The sheet resistance could be further reduced to 27  $\Omega/\square$  by employing 800°C-implantation and subsequent annealing at 1700°C. Recently, Schmid et al. reported the Hall effect study on P<sup>+</sup>-implanted 4H-SiC(0001) and (11-20) [35]. They observed significantly higher electron mobility in 4H-SiC(11-20) samples, owing to a lower carrier compensation than (0001) samples.

It is important to understand, from a viewpoint of lattice damages, the reason why *RT*-implantation of P<sup>+</sup> into 4H-SiC(11-20) brings a low sheet resistance while hot implantation is generally required in the case of 4H-SiC(0001). Implantation-induced damages were analyzed by Rutherford backscattering spectroscopy (RBS)-channeling measurements with a 2.0 MeV He<sup>2+</sup> primary beam and a scattering angle of 170°. Figure 12a shows the aligned spectra of as-implanted and 1700°C-annealed 4H-SiC(0001) samples. The aligned yields of the damaged region (channel number: 230–280) are close to the random yields in the case of *RT*-implantation without annealing. Although the yields decrease by annealing at 1700°C, severe damages near the surface still remain (normalized yield:  $\chi = 18\%$ ) as reported previously. In contrast, the damage is considerably decreased for the 800°C-implanted and 1700°C-annealed sample. Figure 12b depicts the aligned spectra of *RT*-implanted 4H-SiC(11-20) samples followed by annealing at 1300°C or 1700°C. Implantation-induced damages are considerably decreased ( $\chi = 4.7\%$ ) even by annealing at 1300°C. The damages are reduced down to the virgin (epilayer) level ( $\chi = 1.2\%$ ) by 1700°C-annealing. This indicates that remarkable lattice recovery is realized in 4H-SiC(11-20), owing to a much faster recrystallization rate along the  $\langle 11\bar{2}0 \rangle$  direction [36]. Further investigation is required to understand the crystal face dependence of damage generation and annealing.

Although a relatively low sheet resistance of 180  $\Omega/\square$  was obtained for the (0001) samples implanted at *RT* followed by 1700°C-annealing, as shown in

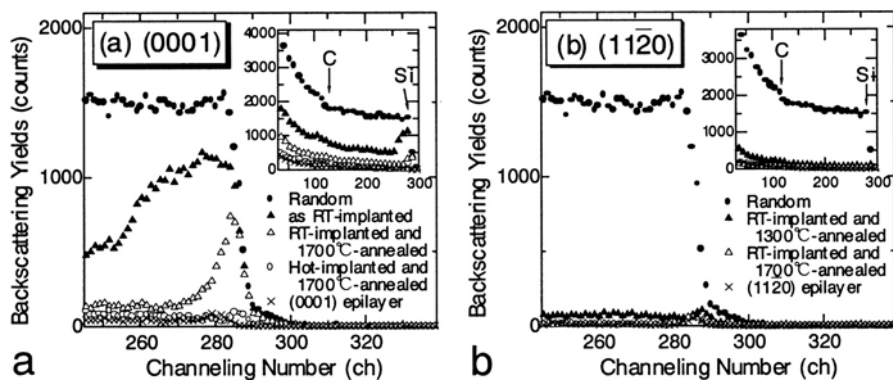


**Fig. 12.** RBS channeling spectra of as-implanted and annealed 4H-SiC for (a) off-axis (0001) and (b) (11-20) samples

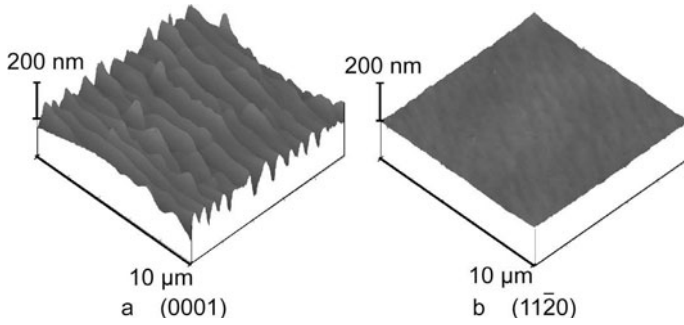


**Fig. 13.** AFM image of the 4H-SiC samples implanted at 800°C followed by annealing at 1700°C for (a) off-axis (0001) and (b) (11-20)

Fig. 11, a recent transmission electron microscopy (TEM) analysis revealed that the implanted region contains high density of 3C-SiC islands [37]. No 3C-SiC inclusions were, however, detected in TEM analyses of the 4H-SiC(11-20) samples implanted at *RT* [37]. As in CVD growth, the availability of stacking information on the (11-20) plane may suppress the appearance of 3C-SiC inclusions.

Figure 13a shows an atomic force microscopy (AFM) image of the 800°C-implanted 4H-SiC(0001) sample annealed at 1700°C. Considerable macrostep formation is observed. The surface roughness defined as root-mean-square (rms) is 13.7 nm in the  $10 \times 10 \mu\text{m}^2$  scan area. An AFM image of the 4H-SiC(11-20) sample implanted at 800°C followed by annealing at 1700°C is shown in Fig. 13b. The surface is mirror-like, and the value of rms roughness is as low as 1.5 nm. The absence of an off-angle orientation for 4H-SiC(11-20) samples may be the reason for the good surface morphology after high-temperature annealing.

Thus, the electrical properties, lattice damage and surface roughness can be improved by utilizing 4H-SiC(11-20). In addition, hot implantation may be unnecessary for 4H-SiC(11-20), which is attractive for improvement in SiC device processing technology. The advantages of *RT*-implantation include the much higher throughput and the use of a photoresist as an implantation mask.

#### 4.2 Performance of MOSFETs Fabricated on 4H-SiC(11-20)

Planar *n*-channel MOSFETs were fabricated on B-doped *p*-type 4H-SiC(11-20) and off-axis 4H-SiC(0001) epilayers. The thickness and the acceptor concentration of epilayers were  $4 \mu\text{m}$  and  $5 - 10 \times 10^{15} \text{ cm}^{-3}$ , respectively. The source and drain regions were formed by  $\text{N}^+$  implantation at *RT* followed by annealing at 1550°C for 30 min in Ar. The total implant dose was  $8 \times 10^{14} \text{ cm}^{-2}$ . Then, the samples were cleaned by the RCA process prior to the gate oxidation. About 40 nm-thick gate oxides were formed by wet

oxidation at 1100°C for 60 min on (11-20) or at 1150°C for 120 min on 4H-SiC(0001), taking into account of the 3–6 times faster oxidation rate for 4H-SiC(11-20). Both samples were annealed in Ar at the oxidation temperature for 30 min. Ohmic contacts for source and drain were formed by evaporation of Al/Ti and subsequent alloy at 600°C. Al was employed as the gate electrode. The channel length and width were 30 and 200  $\mu\text{m}$ , respectively.

From the MOSFET characteristics on (11-20) with two different current directions, the anisotropy of inversion channel mobility at room temperature was determined [38]. The anisotropy, defined as  $\mu_{\langle 1-100 \rangle} / \mu_{\langle 0001 \rangle}$ , is 0.85 for 4H-SiC, showing almost the same anisotropy as bulk mobility [39]. From the  $I_D / g_m^{1/2} - V_G$  plots ( $I_D$ : drain current,  $g_m$ : transconductance,  $V_G$ : gate voltage), the low-field mobility ( $\mu_0$ ) was determined to be 81.7  $\text{cm}^2/\text{Vs}$  and 5.59  $\text{cm}^2/\text{Vs}$  along the  $\langle 1-100 \rangle$  current direction for the 4H-SiC(11-20) and off-axis (0001) MOSFETs, respectively. The low-field mobility along the  $\langle 0001 \rangle$  current direction of the 4H-SiC(11-20) MOSFET is even higher, 95.9  $\text{cm}^2/\text{Vs}$ . In the case of 6H-SiC MOSFETs, the channel mobility on (11-20) along the  $\langle 1-100 \rangle$  was also much higher (116  $\text{cm}^2/\text{Vs}$ ) than that on (0001) (44.8  $\text{cm}^2/\text{Vs}$ ) [38].

Recently, Senzaki et al. have reported that the channel mobility can be further increased by decreasing the temperature of the wet oxidation process [40]. By combining low-temperature wet oxidation at 950°C and post-oxidation annealing in  $\text{H}_2$  at 800°C, a very high mobility of 198  $\text{cm}^2/\text{Vs}$  in inversion channel has been achieved [40]. The (11-20) face is also effective to obtain high channel mobility even in buried-channel MOSFETs [40, 41]. Although the technology of 4H-SiC(11-20) bulk growth is still not mature, fabrication of trench *U*-shaped MOSFETs on (0001) wafers with the side-wall channel exactly aligned on (11-20) may be one solution to realize SiC power MOSFETs with low on-resistance.

The temperature dependencies of the low-field channel mobility for 4H-SiC MOSFETs on (11-20) and (0001) are shown in Fig. 14a. Regarding the 4H-SiC(0001) MOSFET, the channel mobility is thermally activated, increasing with temperature. This abnormal dependence may be caused by Coulomb scattering and/or the trapping of mobile electrons in the inversion layer at a high density of interface states [42]. In contrast, the 4H-SiC MOSFET on (11-20) exhibits a high channel mobility at room temperature and decreases with increasing temperature above 200 K, according to the  $T^{-2.2}$  dependence, due to phonon scattering. Figure 14b depicts the temperature dependence of threshold voltage for 4H-SiC (11-20) and (0001) MOSFETs. The threshold voltage of 4H-SiC(0001) MOSFET is very high, 7.8 V at room temperature. It decreases to 2.7 V at 500 K, which is accompanied by the increased channel mobility, indicating a reduced number of negative charges near the MOS interface. However, the threshold voltage of 4H-SiC(11-20) MOSFET is lower, 4.0 V, and is not very much dependent on the temperature.

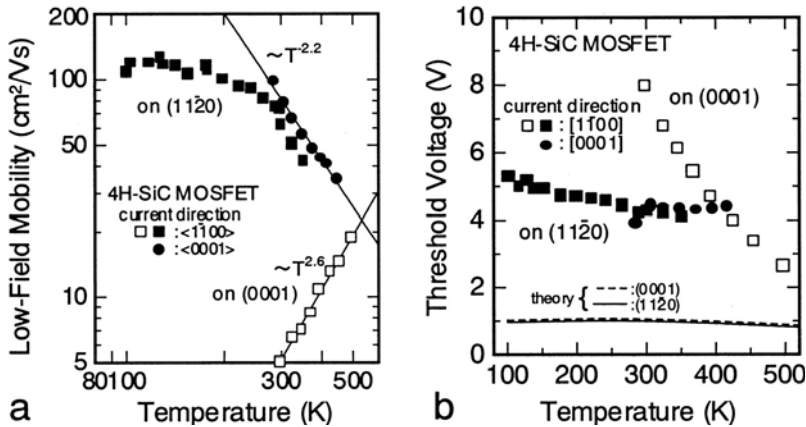
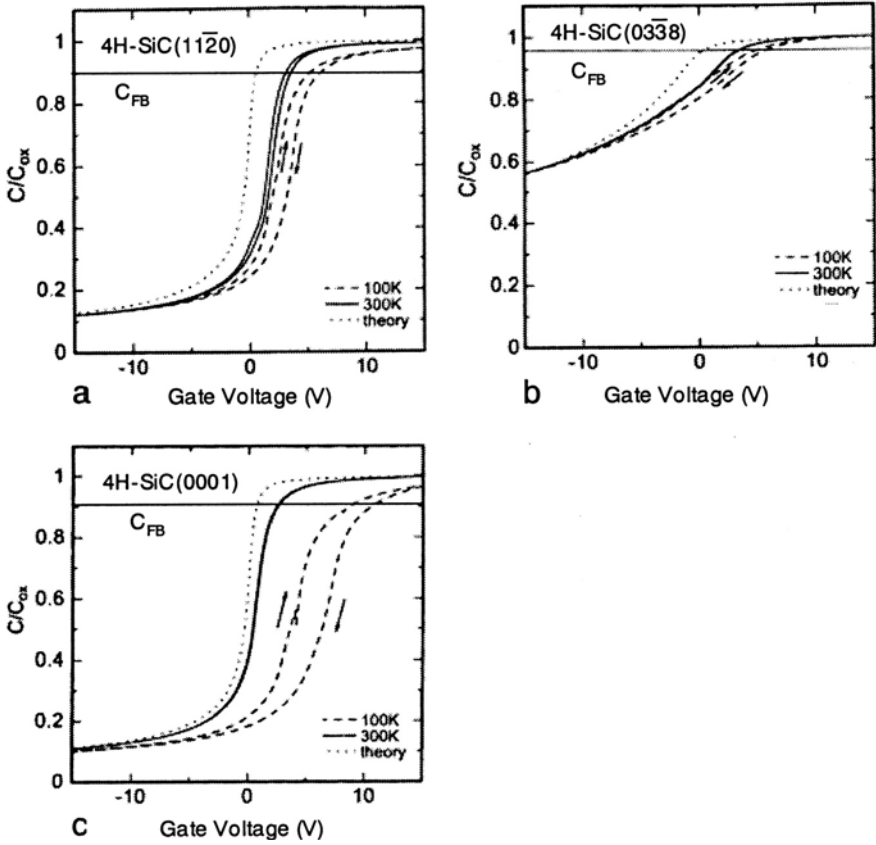


Fig. 14. Temperature dependencies of (a) low-field channel mobility and (b) threshold voltage for 4H-SiC MOSFETs on (11-20) and (0001)

### 4.3 MOS Interface Properties

To investigate the MOS interface, MOS capacitors with an oxide thickness of 40–60 nm were fabricated on *N*-doped *n*-type 4H-SiC epilayers grown on (11-20), (03-38), and off-axis (0001) substrates. The oxides were grown by wet oxidation at 1150°C followed by annealing at the same temperature in Ar. The MOS interface quality on 4H-SiC(11-20) and 4H-SiC(03-38) was always deteriorated when oxides were formed by dry oxidation, though the reason is not clear at present [43, 44]. The interfaces of the MOS capacitors were characterized by high-frequency (1 kHz, 1 MHz) *C-V* measurements at room temperature (300 K) and 100 K with a bias sweep rate of 0.1 V/s.

*C-V* measurements on *n*-type 4H-SiC MOS capacitors at 300 K have revealed that (11-20) and (03-38) MOS capacitors exhibit much smaller frequency dispersion in the accumulation region [9, 45]. This result suggests a higher density of interface states near the conduction band edge for MOS structure on (0001). This speculation was confirmed by *C-V* measurements at low temperature. Figure 15 shows *C-V* curves at 1 MHz for 4H-SiC MOS capacitors on the (a) (11-20), (b) (03-38), and (c) off-axis (0001) substrates measured at 300 K and 100 K. The donor concentration of (11-20), (03-38), and (0001) epilayers was  $2 \times 10^{16} \text{ cm}^{-3}$ ,  $3 \times 10^{17} \text{ cm}^{-3}$ , and  $2 \times 10^{16} \text{ cm}^{-3}$ , respectively. The larger stretch-out in *C-V* curve for the (03-38) MOS capacitor is ascribed to the higher doping level in the semiconductor. The 4H-SiC(11-20) MOS capacitor exhibited a carrier-injection type hysteresis of 0.4 V at 300 K and increased to 0.9 V at 100 K. The *C-V* curve for the (03-38) MOS capacitor showed a similar hysteresis. On the other hand, a very large hysteresis of 2.4 V was observed at 100 K for the 4H-SiC(0001) MOS capacitor, in spite of a small hysteresis of 0.1 V at 300 K, which agrees with a previous work on 4H-SiC(0001) MOS capacitors [46].



**Fig. 15.** Capacitance-voltage curves at 1 MHz for 4H-SiC MOS capacitors on the (a) (11-20), (b) (03-38), and (c) off-axis (0001) substrates measured at 300 K and 100 K

At low temperatures, the Fermi level at the flatband condition shifts toward the conduction band edge, and the time constant for electron emission from interface states significantly increases with cooling. Thus, a high density of acceptor-like interface states in the upper half of the bandgap causes a large positive flatband voltage shift because more electrons are trapped at these interface states. In addition, at low temperatures, electrons trapped at shallow interface states or at traps very close to the conduction band edge are gradually emitted to the band during voltage sweep, resulting in a carrier-injection type hysteresis [46]. From the hysteresis at 100 K, the density of shallow interface states was estimated to be  $4.7 \times 10^{11} \text{ cm}^{-2}$  for (11-20),  $4.9 \times 10^{11} \text{ cm}^{-2}$  for (03-38), and  $1.3 \times 10^{12} \text{ cm}^{-2}$  for (0001), respectively. From the flat-band shift, the “effective” fixed charge density at 100 K was  $2.4 \times 10^{12} \text{ cm}^{-2}$  for (11-20),  $1.4 \times 10^{12} \text{ cm}^{-2}$  for (03-38), and  $4.3 \times 10^{12} \text{ cm}^{-2}$

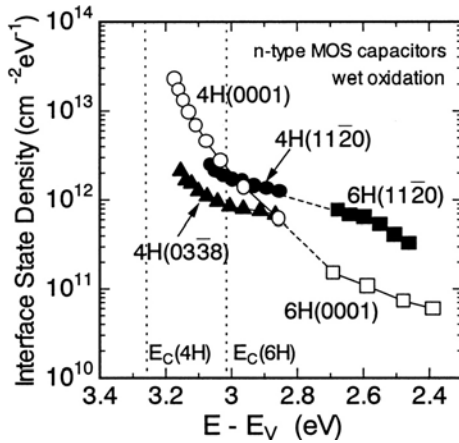


**Fig. 16.** Distribution of interface state density for 4H-SiC(0001), (11-20) and (03-38) together with 6H-SiC(0001) and (11-20)

for (0001), respectively. These results indicate that the interface state density near the conduction band edge is significantly lower on (11-20) and (03-38) than on (0001).

From the parallel conductance measured in the frequency range from 1 kHz to 1 MHz at room temperature, the interface state density was determined by a conductance method. Figure 16 shows the distribution of interface state density for 4H-SiC(0001), (11-20) and (03-38) together with 6H-SiC(0001) and (11-20). Since 4H- and 6H-SiC have the same energy position of the valence band edge ( $E_v$ ), which is 6.0 eV below the conduction band edge of SiO<sub>2</sub> [47], the distribution of the interface state density for two different polytypes can be plotted against the valence band edge. The interface state density of 6H-SiC(11-20) MOS structure is higher than that of 6H-SiC(0001), in good agreement with a previous report [48]. The 4H-SiC MOS structures show a higher interface state density near the conduction band edge, due to the larger bandgap. At the deep energy region ( $E - E_v < 2.9$  eV), the interface state density for (11-20) and (03-38) are even higher than that for (0001). However, the interface state density of 4H-SiC(0001) exhibits a sharp increase to above  $10^{13}$  cm<sup>-2</sup>eV<sup>-1</sup> near the band edge ( $E - E_v > 3.0$  eV). On the other hand, the interface state density of 4H-SiC(11-20) and (03-38) MOS structures stays in the low  $10^{12}$  cm<sup>-2</sup>eV<sup>-1</sup> range near the band edge ( $E - E_v > 3.0$  eV).

Regarding the correlation between the interface state density and channel mobility in inversion-type SiC MOSFETs, the authors have suggested that negative charges near the MOS interface may limit the channel mobility [49]. Schörner et al. have proposed that the mobility is mainly affected by the acceptor-like interface states near the conduction band edge [50]. Saks et al. demonstrated that most of electrons in the inversion layers, especially for 4H-SiC(0001) MOSFETs, are trapped and immobile based on MOS-Hall effect measurements [42]. Afanas'ev et al. reported that near interface traps

existing either in  $\text{SiO}_2$  or the interface at  $E_c(\text{SiO}_2) - 2.77 \text{ eV}$ , which is located between  $E_c(4H\text{-SiC})$  and  $E_c(6H\text{-SiC})$ , may be responsible for the low channel mobility of  $4H\text{-SiC}(0001)$  MOSFETs [47]. These models are consistent with each other: Electron trapping at shallow acceptor-like interface states or traps leads to the reduced concentration of mobile inversion electrons as well as to the enhanced Coulomb scattering. Since the shallow interface state density in the  $10^{12} \text{ cm}^{-2}$  range for the  $4H\text{-SiC}(0001)$  MOS structure is of the same order as the surface charges in the inversion layer induced by gate bias, most of induced electrons may be trapped at these interface states and become immobile [42, 51]. Thus, the lower interface state density near the band edge on (11-20) brings about the higher concentration of mobile electrons in the inversion layer together with the higher channel mobility. Concerning the  $4H\text{-SiC}(03\text{-}38)$  MOSFETs, a relatively high channel mobility of  $36 \text{ cm}^2/\text{Vs}$  has been obtained. The mobility may be improved by process optimization.

In Si MOSFETs, the (001) face is the best choice which exhibits the lowest interface state density and the highest channel mobility, the (111) face the worst, and the (110) in between. From a simple crystallographical analogy,  $4H\text{-SiC}(03\text{-}38)$ , semi-equivalent to (001), is expected to be the best, and (0001), equivalent to (111), the worst, and (11-20), equivalent to (110), in between. However, this assumption may not be valid in SiC MOS structures, because the major origin of high interface state density may be not caused as in Si by the  $\text{P}_b$  center, related with Si dangling bonds, but by C-clusters or complexes [47]. Different bond configurations on non-basal surfaces might lead to a different removal process of C-related materials from the interface during oxidation and to the reduced number of electrically active states near the band edge. Further investigations are required to clarify the origin of interface states and the crystal-orientation dependence.

## 5 Conclusions

Chemical vapor deposition and device processing technologies on  $4H\text{-SiC}(11\text{-}20)$  and  $(03\text{-}38)$  have been reviewed. A low background doping concentration of  $2 - 3 \times 10^{14} \text{ cm}^{-3}$  ( $n$ -type) could be achieved. The efficiency of N incorporation was higher but that of B and Al was lower on these non-basal planes than on (0001).  $4H\text{-SiC}(11\text{-}20)$  epilayers are micropipe-free, as expected. Almost complete closing of micropipes was realized in  $4H\text{-SiC}(03\text{-}38)$  epitaxial growth, although some of very large ( $> 3 \mu\text{m}$ ) micropipes were threading into epilayers. Ni/ $4H\text{-SiC}(11\text{-}20)$  and  $(03\text{-}38)$  Schottky barrier diodes showed good characteristics of  $3.36 \text{ kV}\text{-}24 \text{ m}\Omega\text{cm}^2$  and  $3.28 \text{ kV}\text{-}22 \text{ m}\Omega\text{cm}^2$ , respectively. The breakdown voltage of  $4H\text{-SiC}(03\text{-}38)$  Schottky barrier diodes was significantly improved from 1 kV to above 2.5 kV by micropipe closing.

In high-dose  $\text{P}^+$  implantation, lower sheet resistances and very little surface roughening were obtained by utilizing (11-20). Even though severe damage is introduced by  $RT$ -implantation, solid state recrystallization without

3C-SiC inclusion is realized on (11-20). A high channel mobility of  $96 \text{ cm}^2/\text{Vs}$  has been achieved for inversion-type 4H-SiC MOSFETs fabricated on (11-20). The channel mobility of 4H-SiC(11-20) MOSFET decreased according to the  $T^{-2.2}$  dependence above 200 K, whereas the mobility on (0001) increased at elevated temperatures. These properties can be ascribed to the much lower interface state density near the conduction band edge on (11-20). 4H-SiC(03-38) also possesses much potential to achieve high channel mobility in MOSFETs.

## Acknowledgements

The authors greatly thank Dr. S. Nakamura, T. Hirao, and S. Nakazawa in the authors' group for their experimental contributions. Kyoto University Venture Business Laboratory is acknowledged for the use of characterization systems. This work was partially supported by Grant-in Aids and the 21st Century Center-Of-Excellence Program (No. 14 213 201) from the Ministry of Education, Culture, Sports, Science and Technology of Japan, and also by TEPCO Research Foundation.

## References

1. H. Matsunami, T. Kimoto: *Mat. Sci. & Eng. R* **20**, 125 (1997)
2. J.A. Powell, H.A. Will: *J. Appl. Phys.* **44**, 5177 (1973)
3. A.A. Burk, Jr., D.L. Barrett, H.M. Hobgood, R.R. Siegiej, T.T. Braggins, R.C. Clarke, G.W. Eldridge, C.D. Brandt, D.J. Larkin, J.A. Powell, W.J. Choyke: *Silicon Carbide and Related Materials* (IOP, Bristol, 1994), p. 29
4. A. Yamashita, W.S. Yoo, T. Kimoto, H. Matsunami: *Jpn. J. Appl. Phys.* **31**, 3655 (1992)
5. C. Hallin, C. Hallin, A. Ellison, I.G. Ivanov, A. Henry, N.T. Son, E. Janzén: *Mat. Sci. Forum* **264–268**, 123(1998)
6. G.Y. Chung, C.C. Tin, J.R. Williams, K. McDonald, R.K. Chanana, R.A. Weller, S.T. Pantelides, L.C. Feldman, O.W. Holland, M.K. Das, J.W. Palmour: *IEEE Electron Device Lett.* **22**, 176 (2001)
7. R. Kosugi, S. Suzuki, M. Okamoto, S. Harada, J. Senzaki, K. Fukuda: *IEEE Electron Device Lett.* **23**, 136 (2002)
8. H. Yano, T. Hirao, T. Kimoto, H. Matsunami, K. Asano, Y. Sugawara: *IEEE Electron Device Lett.* **20**, 611 (1999)
9. H. Yano, T. Hirao, T. Kimoto, H. Matsunami, H. Shiomi: *Appl. Phys. Lett.* **81**, 4772 (2002)
10. P.G. Neudeck, J.A. Powell: *IEEE Electron Device Lett.* **15**, 63 (1994)
11. J. Takahashi, N. Ohtani, M. Kanaya: *J. Crystal Growth* **167**, 596 (1996)
12. K. Nakayama, Y. Miyagi, H. Shiomi, S. Nishino, T. Kimoto, H. Matsunami: *Mater. Sci. Forum* **389–393**, 123 (2002)
13. T. Kimoto, T. Hirao, S. Nakazawa, H. Shiomi, H. Matsunami: *J. Crystal Growth* **249**, 208 (2003)

14. T. Kimoto, S. Nakazawa, K. Hashimoto, H. Matsunami: Appl. Phys. Lett. **79**, 2761 (2001)
15. T. Kimoto, T. Yamamoto, Z.Y. Chen, H. Yano, H. Matsunami: Mat. Sci. Forum **338-342**, 189 (2000)
16. T. Dalibor, G. Pensl, H. Matsunami, T. Kimoto, W.J. Choyke, A. Schöner, N. Nordell: phys. stat. sol. (a) **162**, 199 (1997)
17. C. Hemmingsson, N.T. Son, O. Kordina, J.P. Bergman, E. Janzén, J.L. Lindström, S. Savage, N. Nordell: J. Appl. Phys. **81**, 6155 (1997)
18. D.J. Larkin, P.G. Neudeck, J.A. Powell, L.G. Matus: Appl. Phys. Lett. **65**, 1659 (1994)
19. T. Yamamoto, T. Kimoto, H. Matsunami: Mat. Sci. Forum **264-268**, 111 (1998)
20. H. Matsunami, T. Kimoto, H. Yano: Mat. Res. Soc. Symp. Proc. **640**, H3.4.1 (2001)
21. J. Takahashi, N. Ohtani, M. Kanaya: Jpn. J. Appl. Phys. **34**, 4694 (1995)
22. S. Greulich-Weber: phys. stat. sol. (a) **162**, 95 (1997)
23. K. Kojima, T. Ohno, T. Fujimoto, M. Katsuno, N. Ohtani, J. Nishio, T. Suzuki, T. Tanaka, Y. Ishida, T. Takahashi, K. Arai: Appl. Phys. Lett. **81**, 2974 (2002)
24. T. Kimoto, K. Danno, K. Fujihira, H. Shiomi, H. Matsunami: *Ext. Abstr. of European Conference on Silicon Carbide and Related Materials 2002* (Linköping, 2002), TuP1-23
25. W. Si, M. Dudley, R. Glass, V. Tsvetkov, C.H. Carter, Jr.: Mat. Sci. Forum **264-268**, 429 (1998)
26. I. Kamata, H. Tsuchida, T. Jikimoto, K. Izumi: Jpn. J. Appl. Phys. **39**, 6496 (2000)
27. S. Nakamura, H. Kumagai, T. Kimoto, H. Matsunami: Appl. Phys. Lett. **80**, 3355 (2002)
28. I. Kamata, H. Tsuchida, T. Jikimoto, K. Izumi: Jpn. J. Appl. Phys. **40**, L1012 (2001)
29. M.A. Capano, S. Ryu, J.A. Cooper, Jr., M.R. Melloch, K. Rottner, S. Karlsson, N. Nordell, A. Powell, D.E. Walker, Jr.: J. Electron. Mater. **28**, 214 (1999)
30. T. Troffer, C. Peppermüller, G. Pensl, K. Rottner, A. Schöner: J. Appl. Phys. **80**, 3739 (1996)
31. T. Kimoto, N. Inoue, H. Matsunami: phys. stat. sol. (a) **162**, 263 (1997)
32. V. Khemka, R. Patel, N. Ramungul, T. P. Chow, M. Ghezzo, J. Kretchmer: J. Electron. Mater. **28**, 167 (1999)
33. M.A. Capano, R. Santhakumar, R. Venugopal, M.R. Melloch, J.A. Cooper, Jr.: J. Electron. Mater. **29**, 210 (2000)
34. Y. Negoro, N. Miyamoto, T. Kimoto, H. Matsunami: Appl. Phys. Lett. **80**, 240 (2002)
35. F. Schmid, M. Laube, G. Pensl, G. Wagner, M. Maier: J. Appl. Phys. **91**, 9182 (2002)
36. M. Satoh, Y. Nakaike, K. Kuriyama: J. Appl. Phys. **89**, 61 (2001)
37. T. Okada, T. Kimoto: unpublished
38. H. Yano, T. Hirao, T. Kimoto, H. Matsunami, K. Asano, Y. Sugawara: Mat. Sci. Forum **338-342**, 1105 (2000)
39. W.J. Schaffer, G.H. Negley, K.G. Irvine, J.W. Palmour: Mat. Res. Soc. Symp. Proc. **339**, 595 (1994)
40. J. Senzaki, K. Kojima, S. Harada, R. Kosugi, S. Suzuki, T. Suzuki, K. Fukuda: IEEE Electron Device Lett. **23**, 13 (2002)

41. S. Harada, S. Suzuki, J. Senzaki, R. Kosugi, K. Adachi, K. Fukuda, K. Arai: IEEE Electron Device Lett. **22**, 272 (2001)
42. N.S. Saks, A.K. Agarwal: Appl. Phys. Lett. **77**, 3281 (2000)
43. H. Yano, T. Kimoto, H. Matsunami: Mat. Sci. Forum **353–356**, 627 (2001)
44. T. Hirao, H. Yano, T. Kimoto, H. Matsunami, H. Shiomi: Mat. Sci. Forum **389–393**, 1065 (2002)
45. H. Yano, T. Kimoto, H. Matsunami: Appl. Phys. Lett. **81**, 301 (2002)
46. M. Bassler, V.V. Afanas'ev, G. Pensl, M. Schulz: Mat. Sci. Forum **338–342**, 1065 (2000)
47. V.V. Afanas'ev, M. Bassler, G. Pensl, M. Schulz: phys. stat. sol. (a) **162**, 321 (1997)
48. J.N. Shenoy, M.K. Das, J.A. Cooper, Jr., M.R. Melloch, J.W. Palmour: J. Appl. Phys. **79**, 3042 (1996)
49. H. Yano, F. Katafuchi, T. Kimoto, H. Matsunami: IEEE Trans. Electron Devices **46**, 504 (1999)
50. R. Schörner, P. Friedrichs, D. Peters, D. Stephani: IEEE Electron Device Lett. **20**, 241 (1999)
51. E. Arnold, D. Alok: IEEE Trans. Electron Devices **48**, 1870 (2001)

## Part VI

## Devices

# SiC Power Bipolar Transistors and Thyristors

T.P. Chow, N. Ramungul, J. Fedison, and Y. Tang

## 1 Introduction

Silicon has long been the dominant semiconductor of choice for high-voltage power electronics applications [1, 2]. However, recently, wide bandgap semiconductors, particularly SiC and GaN, have attracted much attention because they are projected to have much better performance than silicon [3]–[8] and the epi/substrate technology has matured to make device commercialization possible. SiC offers a lower intrinsic carrier concentration, a higher electric breakdown field, a higher thermal conductivity and a larger saturated electron drift velocity, when compared to silicon (see Table 1). The experimental impact ionization coefficients, usually extracted from breakdown character-

**Table 1.** Physical properties of important semiconductors for high-voltage power devices

Mate- rial	$E_g$ (eV)	$n_i$ ( $\text{cm}^{-3}$ )	$\varepsilon_r$	$\mu_n$ ( $\text{cm}^2/\text{V}\cdot\text{s}$ )	$E_c$ (MV/cm)	$v_{\text{sat}}$ ( $10^7 \text{ cm/s}$ )	$\lambda$ (W/c mK)	Direct/ Indirect
Si	1.1	$1.5 \times 10^{10}$	11.8	1350	0.3	1.0	1.5	I
Ge	0.66	$2.4 \times 10^{13}$	16.0	3900	0.1	0.5	0.6	I
GaAs	1.4	$1.8 \times 10^6$	12.8	8500	0.4	2.0	0.5	D
GaP	2.3	$7.7 \times 10^{-1}$	11.1	350	1.3	1.4	0.8	I
2H-InN	0.7	$\sim 10^3$	9.6	3000	1.0	2.5	–	D
2H-GaN	3.44	$1.9 \times 10^{10}$	9.5	900	3.3	2.5	1.3	D
3C-SiC	2.2	6.9	9.6	900	1.2	2.0	4.5	I
4H-SiC	3.26	$8.2 \times 10^{-9}$	10.0	720 <sup>a</sup> 650 <sup>c</sup>	2.0	2.0	4.5	I
6H-SiC	3.0	$2.3 \times 10^{-6}$	9.7	370 <sup>a</sup> 50 <sup>c</sup>	2.4	2.0	4.5	I
Diam.	5.45	$1.6 \times 10^{-27}$	5.5	1900	5.6	2.7	20	I
BN	6.0	$1.5 \times 10^{-31}$	7.1	5	10	1.0*	13	I
2H-AlN	6.2	$\sim 10^{-31}$	8.5	300	11.7	1.7	2.85	D

<sup>a</sup> mobility along *a*-axis, <sup>c</sup> mobility along *c*-axis, \* estimate

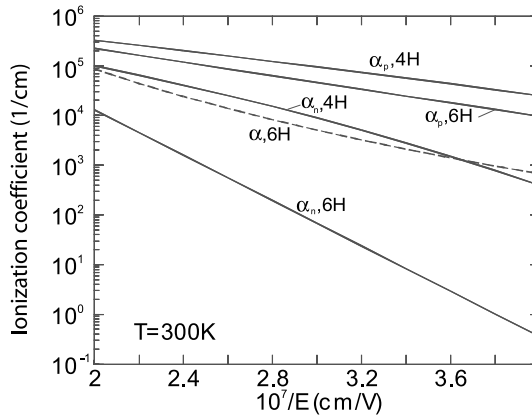


**Fig. 1.** Experimental impact ionization coefficients of electron and hole in 6H- and 4H-SiC [9,10]

istics of reverse-biased *pn* or Schottky junctions, are shown in Fig. 1 for both 6H- and 4H-SiC [9]–[11]. Also included in the figure is the average ionization coefficient for 6H-SiC. Such an average ionization coefficient, allows one to estimate analytically the breakdown voltage and depletion width at breakdown. (See [12] for the silicon case and [13] for 6H-SiC.) Theoretically calculated coefficients for 3C-SiC have also been performed [14]. Unlike in silicon, the hole ionization coefficient is higher than the electron coefficient in both 4H-SiC and 6H-SiC. Such trends have significant impact on bipolar transistor structure (*nnp* vs. *pn**p*) considerations, as will be discussed later. Also, SiC, like silicon, is an indirect semiconductor, hence SiC can have relatively long minority carrier lifetimes. Experimentally, recombination lifetimes  $> 1 \mu\text{s}$  have been extracted in 4H-SiC [15].

In this chapter, the figures of merit of bipolar power switching devices will be first briefly reviewed to demonstrate the potential performance improvement using wide bandgap semiconductors. Then, the basic physics of operation and key device design parameters of three-terminal power bipolar transistors and thyristors will be presented. Recent experimental highlights on high-voltage SiC devices are summarized. Also, the outstanding material and processing issues that need to be overcome for device commercialization will be pointed out.

## 2 Figures of Merit

To quantify the potential performance enhancement possible with SiC, several unipolar and bipolar figures of merit have been proposed [3]–[8]. Bipolar transistors, such as BJT, IGBT and HBT, need to use bipolar figures of merit [5, 6]. Among the bipolar transistors, we can classify them into two

**Table 2.** A bipolar figure of merit applied to the power *npn* BJT (calculated at  $J_F = 100 \text{ A/cm}^2$ ,  $BV = 1000 \text{ V}$ ,  $\beta = 10$ ) [6]

Name	$N_d$ ( $\text{cm}^{-3}$ )	$W_{N-}$ ( $\mu\text{m}$ )	$V_F$ (V)	$J_{\text{off}}$ ( $\frac{\text{A}}{\text{cm}^2}$ )	$t_s$ ( $\mu\text{s}$ )	$t_f$ ( $\mu\text{s}$ )	$E_{\text{off}}$ (mJ)	$P_1^*$ ( $\frac{\text{KW}}{\text{cm}^2}$ )	$P_{100}^*$ ( $\frac{\text{KW}}{\text{cm}^2}$ )
Si	$1.3 \times 10^{14}$	100	22.9	$2.0 \times 10^{-5}$	1.0	0.02	3.3	1.15	1.48
Ge	$4.4 \times 10^{13}$	200	50.6	$6.8 \times 10^{-2}$	1.0	$1.4 \times 10^{-2}$	6.4	2.57	3.20
3C-SiC	$3.8 \times 10^{15}$	16.7	0.067	$2.0 \times 10^{-15}$	$6.3 \times 10^{-4}$	$9.6 \times 10^{-2}$	13	0.016	1.3
6H-SiC	$1.6 \times 10^{16}$	8.33	0.086	$2.8 \times 10^{-21}$	$1.9 \times 10^{-3}$	0.196	27	0.031	2.7
4H-SiC	$1.1 \times 10^{16}$	10	0.073	$1.2 \times 10^{-24}$	$1.3 \times 10^{-3}$	0.135	19	0.021	1.9
Diam.	$1.2 \times 10^{17}$	2.3	0.094	$5.5 \times 10^{-44}$	$1.7 \times 10^{-4}$	0.42	5.8	0.011	0.58

\* $P_1$  and  $P_{100}$  is the power density dissipated at a switching frequency of 1 and 100 kHz, respectively

**Table 3.** A bipolar figure of merit applied to *n*-channel IGBT (calculated at  $J_F = 100 \text{ A/cm}^2$ ,  $BV = 1000 \text{ V}$ ,  $\alpha_{npn} = 0.14$ ) [6]

Name	$N_d$ ( $\text{cm}^{-3}$ )	$W_{N-}$ ( $\mu\text{m}$ )	$\tau_{n0}$ ( $\mu\text{s}$ )	$V_F$ (V)	$W_R$ ( $\mu\text{m}$ )	$J_{\text{off}}$ ( $\text{A/cm}^2$ )	$\tau_B$ ( $\mu\text{s}$ )	$E_{\text{off}}$ (mJ)	$f_{\text{min}}$ (kHz)
Si	$1.3 \times 10^{14}$	100	1.0	1.2	6.0	$2.0 \times 10^{-5}$	0.285	2.55	–
Ge	$4.4 \times 10^{13}$	200	0.95	0.63	12.0	$8.5 \times 10^{-2}$	0.302	2.70	<190
3C-SiC	$3.8 \times 10^{15}$	16.7	0.37	2.74	1.0	$5.4 \times 10^{-15}$	0.058	0.55	38.4
4H-SiC	$1.1 \times 10^{16}$	10	0.19	3.12	0.60	$1.2 \times 10^{-24}$	0.02	0.18	37.1
6H-SiC	$1.6 \times 10^{16}$	8.33	0.15	2.97	0.5	$1.8 \times 10^{-20}$	0.016	0.15	36.9
Diam.	$1.2 \times 10^{17}$	2.3	0.0011	5.04	0.14	$5.0 \times 10^{-41}$	$0.6 \times 10^{-4}$	$5.0 \times 10^{-4}$	75.3

groups, those with odd number and those with even number of junctions. The BJT has an even number of junctions and hence its on-state voltage can be minimized through cancellation of junction voltages when it is in saturation. In this case, SiC clearly excels over Si and the power dissipation is clearly smaller in SiC transistors, as shown in Table 2. By contrast, the Insulated-Gate Bipolar Transistor (IGBT) [2], which is the dominant silicon power transistor structure, has an odd number of junctions in its structure and its forward drop cannot be reduced to less than a diode drop. Since SiC has a large diode turn-on voltage due to its larger bandgap, its conduction loss cannot be less than the silicon device at low to medium current density and only yields a lower total power loss when the switching frequency exceeds a certain frequency,  $f_{\text{min}}$  [5, 6]. This  $f_{\text{min}}$ , at which the conduction loss is equal to the switching loss (at 50% duty cycle), has been considered as the bipolar figure of merit, and, in the case of a 1000 V IGBT, is about 20 kHz for SiC when compared to silicon, as illustrated in Table 3. Similarly, this bipolar

**Table 4.** A bipolar figure of merit applied to gate turn-off (GTO) thyristor (calculated at  $J_F = 100 \text{ A/cm}^2$ ,  $BV = 1000 \text{ V}$ , turn-off gain of 4) [6]

Name	$N_d$ ( $\text{cm}^{-3}$ )	$W_N$ ( $\mu\text{m}$ )	$V_F$ (V)	$J_{\text{off}}$ ( $\text{A/cm}^2$ )	$\beta_{\text{max}}$	$J_{\text{ATO}}$ ( $\text{A/cm}^2$ )	$t_s$ ( $\mu\text{s}$ )	$t_{\text{fl}}$ ( $\mu\text{s}$ )	$E_{\text{tfl}}$ (mJ)	$E_{\text{tail}}$ (mJ)	$f_{\text{min}}$ (kHz)
Si	$1.3 \times 10^{14}$	144	0.99	$2.9 \times 10^{-5}$	5.8	$1.1 \times 10^3$	0.3	0.58	9.6	24	–
Ge	$4.4 \times 10^{13}$	285	0.60	$1.1 \times 10^{-1}$	5.5	$3.0 \times 10^3$	0.26	0.62	10	24	<53.7
3C-SiC	$3.8 \times 10^{15}$	33	2.00	$3.9 \times 10^{-13}$	25.1	$2.6 \times 10^3$	0.014	0.29	4.8	24	10.5
4H-SiC	$1.1 \times 10^{16}$	26	3.04	$3.4 \times 10^{-22}$	63	$1.1 \times 10^4$	0.007	0.16	2.7	24	14.8
6H-SiC	$1.6 \times 10^{16}$	24	2.65	$7.9 \times 10^{-19}$	88	$1.8 \times 10^4$	0.011	0.19	3.1	24	12.6
Diam.	$1.2 \times 10^{17}$	72	5.21	$1.7 \times 10^{-41}$	$2.3 \times 10^4$	$8.0 \times 10^8$	$4.1 \times 10^{-5}$	0.03	0.5	24	23.2

figure of merit can be applied to thyristors, as shown in Table 4.

There are basically two families of two- and three-terminal power semiconductor switching devices – the Schottky rectifier and the power FET representing the unipolar family and the junction rectifier, the bipolar junction transistor and the thyristor belonging to the bipolar family. As will be shown below, at a system dc voltage of 5000 V or higher and a device operating temperature higher than  $150^\circ\text{C}$ , we expect MOS-gated bipolar transistors and thyristors to be superior to unipolar transistors and are the devices of choice for electrical vehicle applications.

For each semiconductor, dependent on its bandgap, there is a crossover in voltage rating above which bipolar devices are preferred over unipolar ones due to the reduced drift-layer resistance from conductivity modulation of bipolar carrier injection. For silicon, this voltage is about 300 V whereas, for SiC, it is above 3000 V [16]. Also, with increasing operating temperature, this crossover voltage is expected to decrease since the ON-resistance of unipolar devices varies inversely as the second power of temperature while the turn-on voltage decreases and carrier lifetime increases. Recent calculations [17, 18] on SiC power transistors have confirmed our observation.

Besides device type,  $n$ -channel or  $npn$  type devices are chosen over  $p$ -channel or  $pnp$  counterparts in silicon. The reason for this is the higher electron mobility and lifetimes. On the other hand, the higher impact ionization of electrons leads to a poorer SOA. In SiC, the electron also has a higher mobility but has a lower impact ionization capability than holes. These considerations lead to the inclusion of  $p$ -channel IGBT in SiC.

As mentioned earlier, we have approximated the electron and hole ionization coefficients using a power law. Then, we obtain the ideal breakdown voltage ( $BV_{pp}$ ) and depletion layer width at breakdown ( $W_{pp}$ ) as a function of background doping, as shown in Fig. 2 for 6H- and 4H-SiC. These analytical calculations have been corroborated well with numerical simulations and experimental results. It can be seen that, for the same background dop-

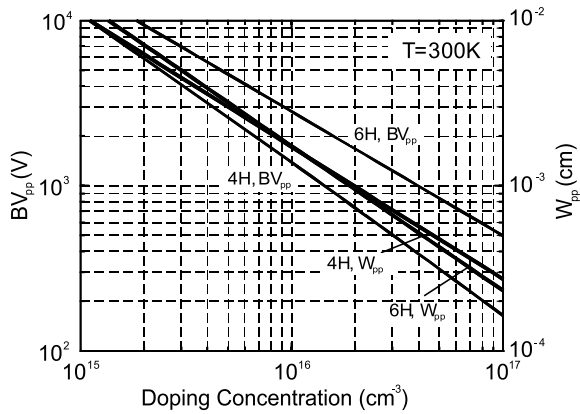


**Fig. 2.** Breakdown voltage of parallel-plane, one-sided abrupt junction ( $BV_{pp}$ ) and its depletion layer width at breakdown ( $W_{pp}$ ) for 6H- and 4H-SiC at 300 K

ing and along the  $c$ -axis, 6H-SiC has a 10–15% higher  $BV$  than 4H-SiC, despite the larger bandgap of the latter. Also, the effective avalanche field estimated for doping concentration of  $10^{15}$  to  $10^{17} \text{ cm}^{-3}$  is the range  $2.5$  to  $5 \times 10^6 \text{ V/cm}$ , close to the experimental value of  $2$  to  $3 \times 10^6 \text{ V/cm}$ . Like silicon, the breakdown voltage of SiC has been established to increase when temperature increases, or, in other words, has been shown to have a positive temperature coefficient [19].

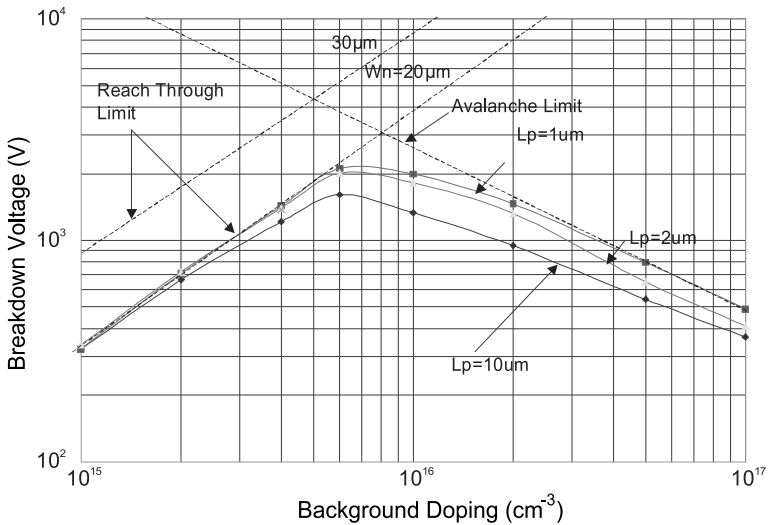


**Fig. 3.** Breakdown voltage of open base bipolar transistors in 4H-SiC

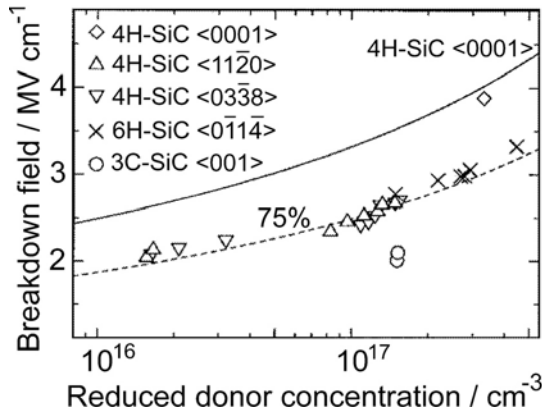


**Fig. 4.** Breakdown field along various crystal orientations in three SiC polytypes at room temperature [20]

The breakdown voltages of bipolar transistor structures are generally lower than those of  $pn$  junctions due to current gain. Figure 3 shows the breakdown voltage of open base transistor in 4H-SiC for several carrier diffusion lengths. High voltage open-base  $pnp$  bipolar transistor  $BV$  ( $BV_{CEO}$ ) design depends primarily on minority carrier lifetime and  $BV_{CEO} \propto (1 - \alpha_0)^{1/n}$ , where  $\alpha_0$  is the common-base current gain,  $n$  is 4 for  $nnp$  and 6 for  $pnp$  transistors in silicon. For 4H-SiC, we have found that  $n$  is 13 for  $nnp$  and 3 for  $pnp$ , implying the  $nnp$  is more rugged than the  $pnp$  [18]. Since no orientation dependence on the ionization coefficients has been measured on 6H- and 4H-SiC, our discussions above ignore any anisotropy in the avalanche process. While this approximation is indefensible for 6H-SiC, it is acceptable for 4H-SiC since its anisotropy in material properties are generally within 15%. Recent measurements of mesa  $p^+n$  diodes indicated that the breakdown fields along various crystal orientations in 4H-SiC, 6H-SiC and 3C-SiC is about 75% that of 4H-SiC (0001) (Fig. 4) [20].

### 3 Power Bipolar Transistors

In general, the power transistors can be classified as the unipolar and bipolar transistor families. Within each family, they can be further divided into current- and voltage-controlled devices. A voltage-controlled transistor is often preferred for ease of integrating IC-based gate driving circuitry. A review of recent advances in the power unipolar transistors can be found in another chapter in this book. Table 5 summarizes the recent experimental results on bipolar power transistor structures in 6H- and 4H-SiC.

Shown in Figs. 5 and 6 are the schematic cross-sections of several three terminal power bipolar transistors and thyristors that can be implemented

**Table 5.** A list of SiC power bipolar transistors that have been experimentally demonstrated

Device type	Poly-type	Power ratings	Features	Researcher	Ref.
SIAFET	4H	4500 V, 10 mA	Bipolar mode, $83 \text{ m}\Omega\text{cm}^2$	KEPCO/Cree, 2000	[38]
		6100 V	$732 \text{ m}\Omega\text{cm}^2$	KEPCO/Cree, 2001	[76]
		5050 V	Bipolar mode $80 \text{ m}\Omega\text{cm}^2$	KEPCO/Cree, 2001	[75]
BJT	6H	200 V	Epi emitter	Cree, 1993	[23]
	4H	60 V	Implanted emitter	RPI, 2000	[26]
		1800 V, 3.8 A	Epi emitter, $10.8 \text{ m}\Omega\text{cm}^2$	Cree, 2000	[27, 29]
		900 V	Epi emitter	Rutgers, 2000	[25]
		500 V	Implanted emitter	RPI, 2001	[28]
		3200 V	Epi emitter, $69 \text{ m}\Omega\text{cm}^2$ $\beta \sim 15$	Purdue, 2002	[32]
		1300 V, 17 A	Epi emitter, $8 \text{ m}\Omega\text{cm}^2$ , $\beta \sim 11$	Cree/RPI, 2003	[33]
Darlington	4H	200–400 V	Implanted emitter $\beta \sim 80$	RPI, 2002	[34]
		200–400 V	Implanted emitter $\beta \sim 450$ , $V_{F100} \sim 7 \text{ V}$	RPI, 2003	[35]
IGBT	6H	300 V, 1 mA	<i>n</i> -channel, self-aligned UMOS	RPI/GE, 1996	[39]
	4H		<i>p</i> -channel, self-aligned UMOS	RPI/GE, 1997	[40]
		600 V, 1 mA	<i>p</i> -channel	Cree, 1999	[41]

in SiC [18]. Besides the BJT and GTO, the UMOS devices include the power MOSFET, IGBT and MOS-Controlled Thyristor (MCT). A lesser-known MOS-controlled bipolar transistor, called the MOS-Gated Transistor (MGT), is also shown in its UMOS version (Fig. 6e). The DMOS version of the MGT has been previously demonstrated in silicon [21] but has not been widely used. However, the MGT deserves considerations in SiC due to the use of an  $n^+$  substrate, which can be doped heavier than the  $p^+$  substrate for the *n*-channel IGBT, as well as a larger safe operating area (SOA).

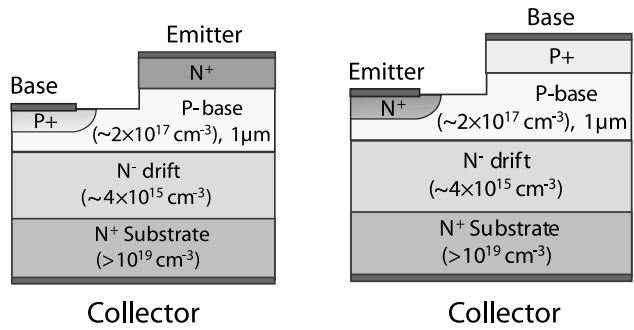


**Fig. 5.** Schematic cross-sections of (left) an epitaxial and (right) implanted emitter SiC bipolar junction transistor

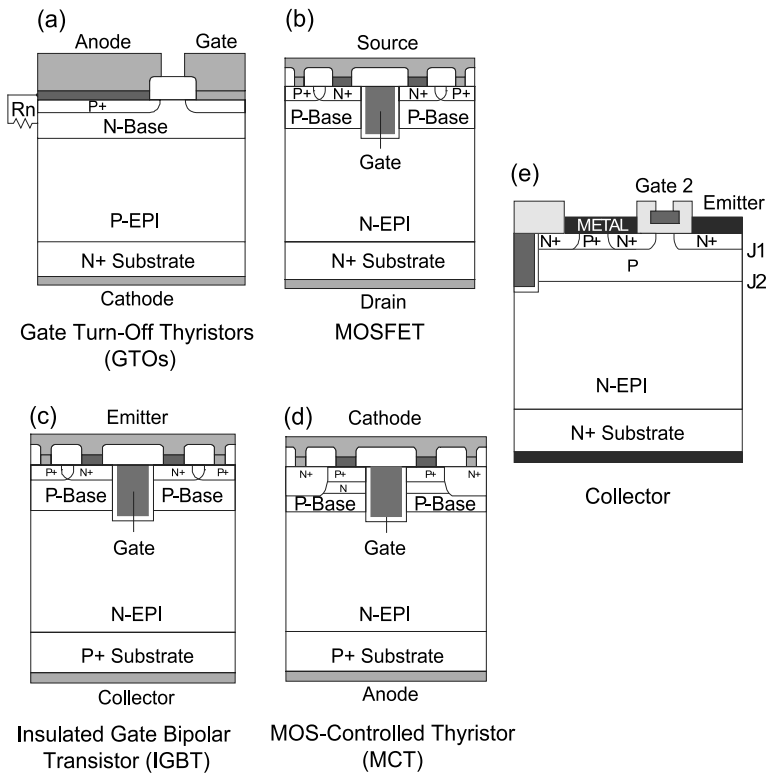


**Fig. 6.** Schematic cross-sections of several three-terminal vertical power semiconductor devices: (a) GTO thyristor, (b) MOSFET, (c) IGBT, (d) (5-layer) MCT and (e) MGT

### 3.1 Bipolar Junction Transistor (BJT)/Darlington Configuration

The Bipolar Junction Transistor (BJT) uses a base current to control the on-off conditions of the transistor. To design it to support high voltage, a lightly doped collector region is used. Also, the base thickness and doping must be sufficient to prevent punch-through breakdown. The details of the basic operation of the power BJT can be found in [1, 2].

The major distinguishing feature of the forward  $I$ - $V$  characteristics of the power BJT is the quasi-saturation region, which is a direct consequence of the lightly doped collector and is not present in low-voltage BJT's. This region reduces the output current and slows down the switching speed. At high current densities, part or the entire  $n^-$  collector region is flooded with an  $e^-/h^+$  plasma and is conductivity modulated and hence the voltage drop across it decreases [2]. Once the  $n^-$  region is no longer highly resistive, the conventional saturation region commences and the base collector junction is forward biased, leading to a junction voltage cancellation and a low forward voltage drop. However, with increasing level of carrier injection, the recombination rate in the base/collector region increases, decreasing the current gain and requiring a larger base current drive. Other second order effects such as emitter crowding and Kirk effect, tend to lower the current gain and degrade the conduction performance of the BJT. To enhance the current gain, a two-stage, Darlington configuration can be realized by cascading two BJT's with a common collector [2]. This Darlington configuration has a current gain,  $\beta_D$ ,

$$\beta_D \sim \beta^2, \quad (1)$$

where  $\beta$  is the current gain of each BJT stage, and the base current required is significantly reduced.

During turn-off, the BJT undergoes several carrier removal stages. Also, besides the open base turn-off during which the carriers are removed with recombination, one can use the base drive circuitry to extract the excess carriers from the device via the base terminal. Due to the  $10\times$  reduced collector drift region to support the blocking voltage, the SiC BJT has less stored charge and can have a switching frequency up to at least 200 kHz.

Several reports on 6H-SiC and 4H-SiC npn BJT's have been presented [22]–[33]. Many of the emitter regions are epitaxially grown and the base contacts are made by trench etching through the emitter region, resulting in a non-planar structure. Some of the emitters were implanted, but even in this case, the device is often non-planar to avoid the use of  $p^+$  implantation and subsequent high-temperature anneal (see Fig. 5). In 6H-SiC, the best device has a breakdown voltage of 200 V and an on-resistance of  $126 \text{ m}\Omega\text{-cm}^2$  [23].

Recently, there are significant advances on 4H-SiC BJTs [25]–[33]. An 1800 V, 3.8 A epitaxial emitter BJT in 4H-SiC has been reported [24]. Its forward  $I$ - $V$  and blocking characteristics are shown in Fig. 7. A maximum

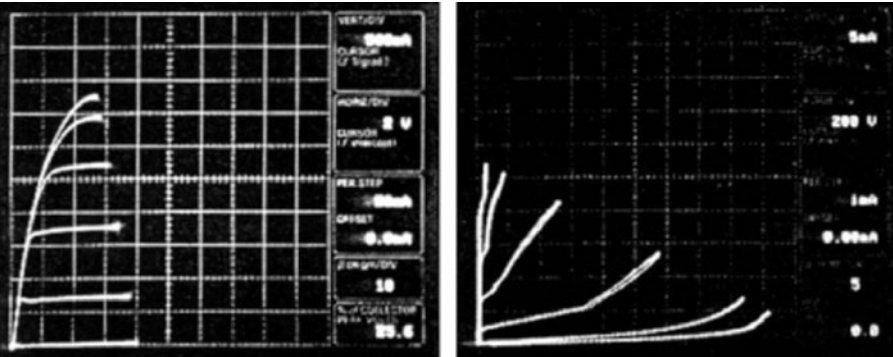


**Fig. 7.** (left) Forward  $I$ - $V$  and (right) blocking characteristics of an epitaxial-emitter 4H-SiC BJT [27]

current gain of 20 has been measured together with a  $BV_{\text{CEO}}$  of 1800 V for devices with an emitter pitch of 23  $\mu\text{m}$ . At  $V_{\text{CE}} = 2$  V, it has a specific on-resistance of 10.8  $\text{m}\Omega\text{-cm}^2$  at room temperature and 19.7  $\text{m}\Omega\text{-cm}^2$  at 250°C. These specific on-resistances are better than those reported for power MOSFETs (15–50  $\text{m}\Omega\text{-cm}^2$  at room temperature) of the same blocking voltage because of the lack of conductivity modulation and low channel mobility in the latter. The switching characteristics have also been measured [29]. As expected, due to minority carrier storage, the turn-off time is slower than that of a power MOSFET and the storage time is about 0.1  $\mu\text{s}$  and the fall time is 0.4  $\mu\text{s}$  with a reverse base current for a collector current density of 50  $\text{A/cm}^2$  and switching to a collector voltage of 300 V. By increasing the  $n^-$  collector region, an epitaxial emitter BJT with a current gain of 20 and  $BV_{\text{CEO}} > 3200$  V, which is the highest  $BV$  reported to date, has been achieved [32]. The largest current of any BJT is 17 A with 1300 V of breakdown voltage [33]. 400 V, 22 A power inverter circuits based on epi-emitter BJTs have also been constructed and demonstrated [31].

Probably due to residual implantation damage in the base region, the implanted-emitter BJTs have inferior current gain vs.  $BV_{\text{CEO}}$  tradeoffs when

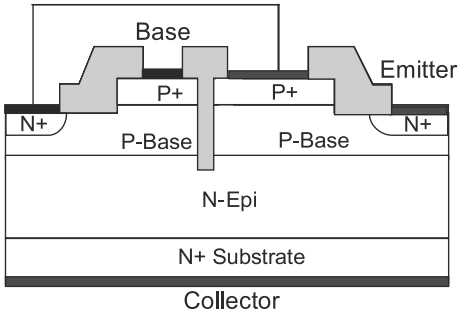


**Fig. 8.** Schematic cross-section of SiC Darlington transistor with oxide trench interstage isolation [34, 35]

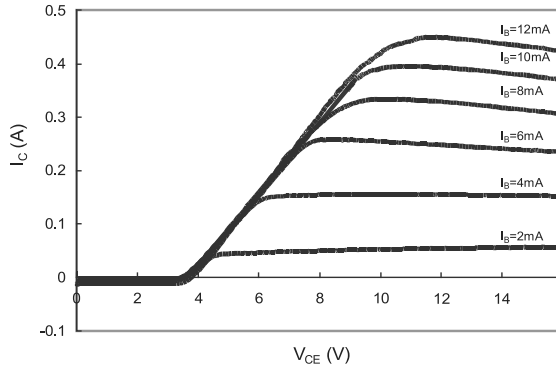


**Fig. 9.** Forward  $I$ - $V$  characteristics of an implanted-emitter Darlington in  $4H$ -SiC [34]

compared to the epi-emitter BJTs. The first implanted-emitter has a high ( $\sim 40$ ) current gain but low  $BV$  ( $\sim 60$  V) [26]. To improve the  $BV_{CEO}$ , a refined process has been adopted and its implementation has resulted in  $BV_{CEO}$  as high as 500 V. Unfortunately, the current gain has also decreased to 10 or less [28, 30]. Nevertheless, the implanted-emitter process is more flexible than the epi-emitter process and further optimization in implantation anneal is needed and desirable.

Recently, monolithic Darlington transistors, based on the implanted-emitter technology and oxide trench interstage isolation, have been experimentally demonstrated in  $4H$ -SiC. The schematic cross-section of these Darlingtons are shown in Fig. 8 and the forward  $I$ - $V$  characteristics are shown in Fig. 9 [34, 35]. The current gain dependence on  $V_{BE}$  is shown in Fig. 10, indicating a current gain as high as 450 [34, 35]. Compared to the BJTs, these Darlingtons can significantly reduce the base drive current needed.

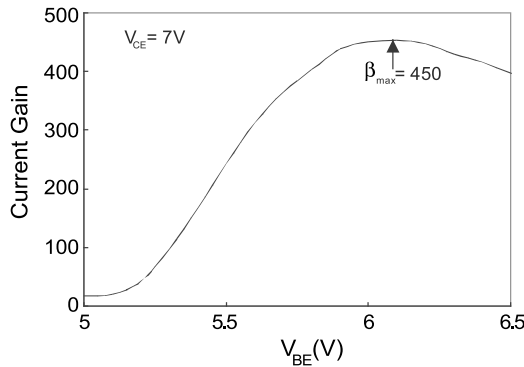


**Fig. 10.** Current gain plot of a  $4H$ -SiC Darlington [34]

### 3.2 Bipolar-Mode JFET/ Static Induction Injected Accumulated FET (SIAFET)

The Junction Field-Effect Transistor (JFET) is usually a unipolar field effect transistor. However, if the gate/drift junction is forward biased, minority injection from the gate into the channel and drift regions will conductivity modulate these regions, resulting in a much lower specific on-resistance (see, for example, [36]). For SiC, the gate/drift junction will be forward biased when the gate voltage exceeds 3 V. Since this bipolar mode operation involves current injection from the junction gate, the proper device performance parameter for this mode is the current gain, which is defined as

$$\beta = I_{DS}/I_{GP} \quad (2)$$

where  $I_{DS}$  is the drain-to-source current and  $I_{GP}$  is the gate current. Several reports have utilized the high-voltage SiC JFETs close to the bipolar mode (to as much as 1 A/cm<sup>2</sup> of gate current [37]) but no true bipolar mode operation has been studied.

The SIAFET is an integrated JFET/MOSFET structure that has recently been experimentally demonstrated up to 4.5 kV [38]. In its normal operation, it is a unipolar field effect transistor that consists of a lateral accumulation MOS channel and a vertical JFET channel (Fig. 11). However, the junction gate can be forward-biased to beyond the turn-on voltage so as to inject minority carriers (holes in this case), very similar to the case of JFET operating in the bipolar mode [36].

The dependence of the current gain,  $\beta$ , on the buried gate bias  $V_{GP}$  for a SIAFET with a blocking voltage of 2030 V, is shown in Fig. 12 [38]. With a forward drop of 1 V and a MOS gate of 40 V, a current gain of  $\sim 1500$  at  $V_{GP}$  of 7 V was measured. The corresponding specific on-resistance (at  $V_{DS} = 0.5$  V) was reduced from 1200 m $\Omega$ -cm<sup>2</sup> in the unipolar mode to

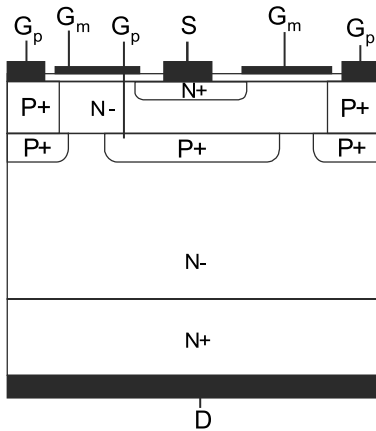


**Fig. 11.** Schematic cross-section of a 4H-SiC SIAFET [75]

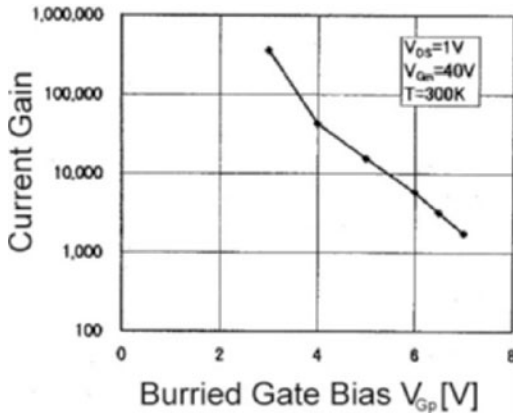


**Fig. 12.**  $\beta$  vs. buried-gate bias for SIAFET [75]

172 m $\Omega$ -cm<sup>2</sup> in the bipolar mode. 4–6 kV SIAFETs have also been reported with a specific on-resistance of 732 m $\Omega$ -cm<sup>2</sup> for the 6.1 kV devices [76]. Another 5 kV merged MOSFET/JFET (called SEMOSFET) operating in the bipolar SIAFET mode has yielded a  $R_{on,sp}$  of 80 m $\Omega$ -cm<sup>2</sup> [75]. The dynamic characteristics of 4–6 kV SIAFETs have been performed, demonstrating a high switching time (30–40 ns) despite minority carrier injection from the gate [76].

### 3.3 Insulated-Gate Bipolar Transistor (IGBT)

We have previously indicated that the most popular silicon power bipolar transistor is the IGBT, in which a MOSFET is connected to the base of a bipolar transistor in a Darlington configuration, as shown in Fig. 6c for an *n*-channel, UMOS device. In parallel with the MOSFET is a parasitic narrow-base *nnp* transistor, which is usually emitter-base shorted and, together with the wide-base *pnp*, forms a parasitic thyristor. The *n*-channel MOSFET has a better transconductance than the *p*-channel one due to higher electron mobility but the *nnp* has a higher current gain than the *pnp*. Compared to silicon IGBTs, *n*- and *p*-channel SiC IGBT's have similar forward drops because SiC has similar asymmetric electron and hole mobility's and lifetimes. However, the *pnp* is more rugged and less susceptible to second breakdown than the *nnp* in SiC due to a larger electron ionization coefficient (Fig. 1). Hence, the *p*-channel SiC IGBT has a larger safe-operating area than and is preferred over the *n*-channel one.

In the IGBT, the lower wide-base bipolar transistor in the open-base configuration supports the forward blocking voltage. Hence, we can use Fig. 3 to design the base doping and thickness. There are two designs. The first approach (called non-punch-through design) is to have a uniform base doping and maximize the base width so that some undepleted base width is left at the maximum blocking voltage. In the second, we put a buffer layer of a higher

doping than the base between the substrate and base so that we can thin down the base and use the buffer layer to prevent the depletion layer from reaching the substrate. The latter (called the punch-through case) needs to be used for SiC devices because lightly doped ingots are so far not achievable and the drift layer is epitaxially grown and is limited in thickness. In the punch-through design, the electric field must reduce to zero within the buffer layer so the minimum net space charge needs to be

$$Q_B = d_B N_B \geq \epsilon_S E_C \text{ (Gauss' Law)} \approx 2 \times 10^{13} \text{ q/cm}^2$$

for 6H- and 4H-SiC (3)

where  $d_B$  and  $N_B$  are the buffer layer thickness and doping respectively. The buffer layer can also be used to control the emitter injection efficiency of the bipolar transistor in the on state.

To compare the performance of the IGBT with the power MOSFET and MCT, the forward  $I$ - $V$  characteristics of 5000 V  $n$ - and  $p$ -channel IGBT's and an  $n$ -channel MGT at 400°C are compared in Fig. 13. The  $n$ -channel IGBT is superior over  $p$ -IGBT and  $n$ -MGT at room temperature but at elevated temperatures, the higher gain of the  $nnp$  over  $pn$ p makes  $p$ -IGBT and  $n$ -MGT very competitive in terms of forward drop. Also, the material parameters, such as lifetime and substrate resistivity, can significantly impact the on-state characteristics.

Besides on-state performance, the switching characteristics of these bipolar transistors need to be optimized so as to minimize the switching energy loss. Due to the reduced drift layer and higher background doping possible with SiC, the turn-off time is substantially faster in SiC than silicon devices. The turn-off time for an IGBT is primarily determined by the open base

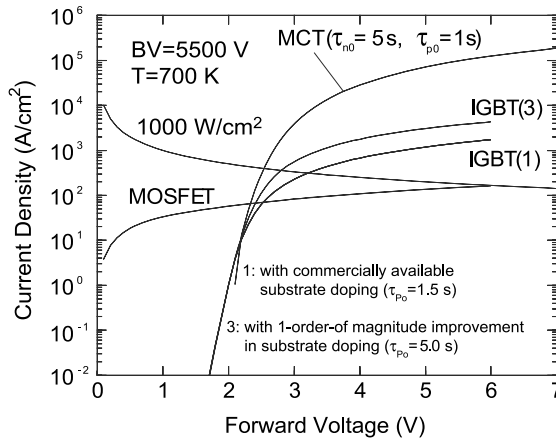


**Fig. 13.** Calculated forward  $I$ - $V$  characteristics of 5000 V 4H-SiC UMOS FET, IGBT and MCT at 400°C. All devices have punch-through epi structures [16]

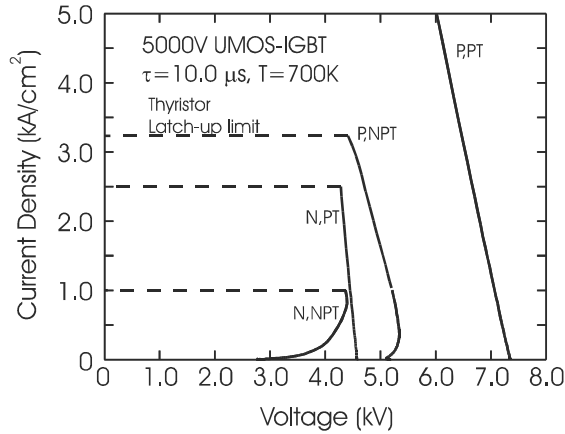


**Fig. 14.** Reverse-biased safe-operating-area (RBSOA) of 5000 V UMOS *n*- and *p*-channel IGBT's with punch-through and non-punch-through structures. That of the UMOS MCT is also included for comparison [16]

turn-off of the constituent wide-base *pnp* and hence dependent on ambipolar recombination lifetime. To minimize the power transistor for total power loss, a forward drop vs. turn-off time analysis is usually performed (see [16] for the 5 kV case).

To quantify the ruggedness of the power transistor under high-voltage switching, safe-operating-areas are often defined. The most demanding switching condition imposed on the transistor is the high-current turn off under high-voltage inductive loads, and the transistor capability can be assessed by the reverse-biased SOA (RBSOA). The reverse-biased SOA's of *n*- and *p*-channel IGBT's with non-punch-through and punch-through designs are shown in Fig. 14 [16]. Unlike silicon, the *p*-channel IGBT's have larger RBSOA's than those of the *n*-IGBT's in SiC, due to the larger hole ionization coefficient.

Experimentally, only three reports on SiC IGBT's have been reported. The first IGBT is a *n*-channel planarized UMOS IGBT on 6H-SiC. Due to the large unit cell size, the *BV* is limited by the trench corner breakdown to 300 V. Also, the channel inversion mobility along the trench sidewalls is low so that only a small current (<1 mA) has been measured [39]. A *p*-channel 4H-SiC UMOS IGBT with a smaller unit cell yielded a *BV* as high as 700 V but the output current is still limited by the channel mobility [40]. A *p*-channel 4H-SiC UMOS IGBT with higher current (up to 1.5 A or 75 A/cm<sup>2</sup>) was reported [41]. The experimental *I*-*V* characteristics are shown in Fig. 15. The higher-than-expected turn-on voltage (~8 V) is attributed to the non-Ohmic contact to the top *p*<sup>+</sup> emitter. Also, the IGBT *BV* is only 85 V while a high *BV* has been observed on a diode fabricated along side, inferring that the IGBT breakdown is caused by the high gain of the constituent open-base

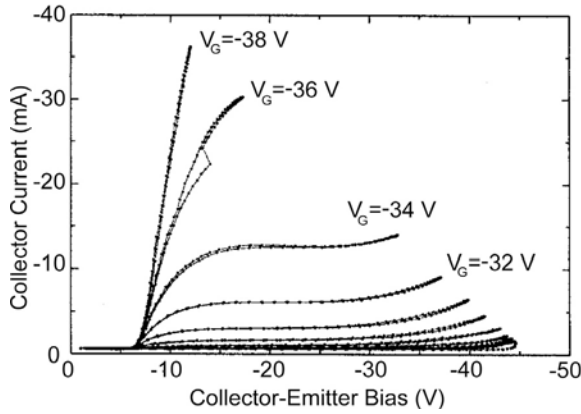


**Fig. 15.** Experimental blocking characteristics of a planarized UMOs *p*-channel IGBT [41]

*npn* transistor [41]. The breakdown problem can be suppressed by using a heavier *p*-type buffer layer and the contact problem can be alleviated by a more optimized anneal cycle or re-grown  $p^+$  contact as demonstrated in pin rectifiers [42].

### 3.4 MOS-Gated Bipolar Transistor (MGT)

Structurally, the *n*-channel MOS-Gated Transistor (MGT) (Fig. 6e), which can be fabricated in the same IGBT process, has an *n*-channel MOSFET driving a narrow-base high-voltage *npn* transistor with an optional turn-off MOSFET [8, 21]. A 600 V, DMOS version of the MGT has previously been demonstrated in silicon [21]. For SiC, the MGT has the optimum device structure because the *n*-channel MOSFET provides a higher transconductance than a *p*-channel MOSFET and the *npn* bipolar transistor has a higher current gain and  $BV_{CEO}$  than the *pn*p counterpart. Also, when compared to the IGBT, it does not have a four-layer parasitic thyristor and thus has a better forward-biased SOA and has an optional *n*-channel turn-off MOSFET. In addition, the hole ionization coefficient is larger than the electron coefficient in SiC and, thus, the *npn* is now more rugged than the *pn*p. Furthermore, the MGT uses a  $n^+$  substrate, which can be doped heavier than the  $p^+$  substrate for the *n*-channel IGBT in SiC. Considering the drawbacks of the MGT, we note that this device has more current non-uniformity and less conductivity modulation in the drift layer in the on-state when compared to the IGBT. Also, the inclusion of the turn-off gate increases the unit cell size and the device layout is less straightforward than the IGBT. In light of these considerations, it is worth considering the MGT together with IGBT in SiC.

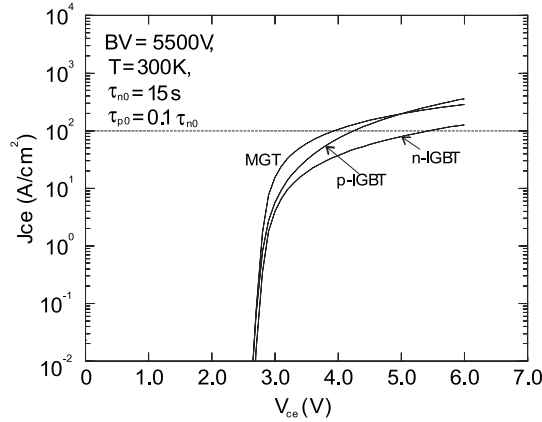


**Fig. 16.** Calculated forward  $I$ - $V$  characteristics of 5000 V SiC UMOS  $n$ - and  $p$ -channel IGBT and MGT at room temperature [16]

The simulated forward  $I$ - $V$  characteristic of a 5000 V  $4H$ -SiC  $n$ -channel MGT is shown in Fig. 16. At room temperature, it is similar to both that of the  $n$ - and  $p$ -IGBT, mainly due to a larger device unit cell size. An analytical  $I$ - $V$  model, like the ones shown for the IGBT, has not been developed. Nevertheless, the forward voltage drop can be estimated, to the first order, by combining the standard analytical models for the power BJT and MOSFET [2].

Unlike the IGBT, the turn-off characteristics are not necessarily open base and can be controlled by the turn-off MOSFET ( $M_2$ ). The active turn-off case is to short the gate of the MGT to ground through  $M_2$  and the minority carriers that are stored in the base region can be extracted out of the device, similar to the BJT. In this mode, the turn-off time is much faster

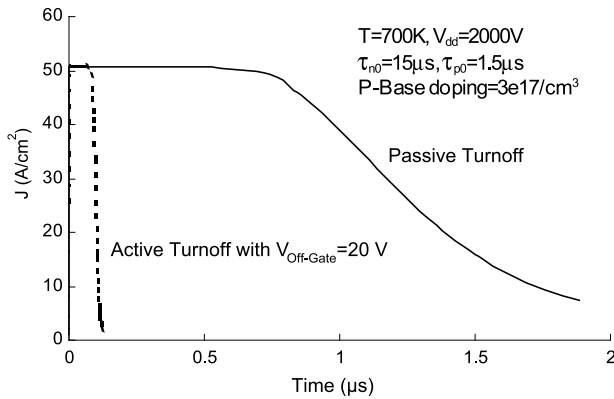


**Fig. 17.** Passive and active turn-off characteristics of a 5000 V  $4H$ -SiC MGT [8]

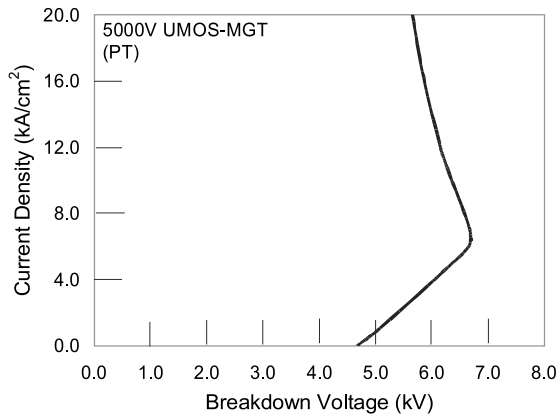


**Fig. 18.** Reverse-biased safe-operating-area (RBSOA) of 5000 V UMOS *n*-channel MGT [8]

( $\sim 0.2 \mu\text{s}$ ) and almost independent of carrier lifetime. By comparison, the turn-on time in the passive (open base) mode is larger, as shown in Fig. 17.

The main bipolar transistor of the MGT has a narrow-base, lightly doped collector structure. At high current densities with high-level injection, the base region will extend into the collector region and the peak electric field at the *p* base/*n*<sup>-</sup> collector junction will shift to the *n*<sup>-</sup>/*n*<sup>+</sup> collector junction (the Kirk Effect). As a result, the reverse-biased SOA of the MGT, as shown in Fig. 18, is unusual in that when the collector current increase, the maximum sustainable collector voltage actually increases. Eventually, the MGT still fails with the formation of current filaments and second breakdown commences. Nevertheless, because of the Kirk effect, the *n*-channel 4*H*-SiC MGT has been projected to have a larger RBSOA than those of *n*- or *p*-channel IGBT's.

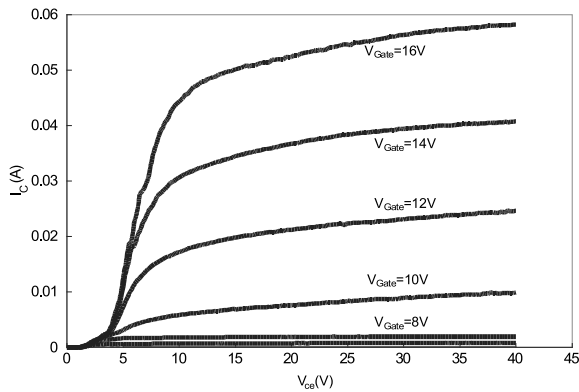


**Fig. 19.** Experimental forward *I*-*V* characteristics of an all-SiC hybrid MGT [44]

The development of the SiC MGT is still in its early stage so that no monolithic experimental device has been demonstrated. However, hybrid MGTs using either a Si MOSFET or a SiC MOSFET driving a 4H-SiC BJT have been experimentally demonstrated [43, 44]. The forward  $I$ - $V$  characteristics of 500 V implanted-emitter 4H-SiC BJT driven by a 6H-SiC lateral MOSFET are shown in Fig. 19 [44].

Also, we can observe that the MOSFET in the structure can be replaced with a JFET or MESFET, particularly if one is concerned with the gate oxide reliability.

### 3.5 Heterojunction Bipolar Transistor (HBT)

No HBT in the SiC system with varying polytypes has been realized. However, an HBT with heteroepitaxially grown GaN emitter on 6H-SiC substrate has been reported [45]. An extraordinarily high common-base current gain of  $>10^6$  has been reported but no common-emitter characteristic was shown. A high leakage current across the collector-base junction is attributed.

## 4 Power Thyristors

Thyristors belong to a family of switching devices that have been specifically developed for power electronics applications.

### 4.1 Silicon Controlled Rectifier (SCR)

The silicon controlled rectifier (SCR) is a 4-layer,  $pnpn$  thyristor that utilizes a gate current for triggering into the conduction state [1, 2]. In silicon, the SCR consists of a lower, wide-base  $pnp$  and an upper, narrow-base  $nnp$  because the higher gain  $nnp$  can be more easily controlled with the gate terminal and the wide-base  $pnp$  has a larger SOA than the  $nnp$ . To prevent the thyristor from inadvertent firing, cathode shorts are usually placed on the top cathode surface [1, 2]. An involute gate pattern is adopted to ensure an equi-distance between the cathode and the gate edge. With a cathode short, the gate triggering current is (for a linear stripe geometry)

$$I_{GT} = (V_{bi}/\rho_{SB})(Z/L) \quad (4)$$

where  $V_{bi}$  is the built-in potential,  $\rho_{SB}$  is the base sheet resistance,  $Z$  is the emitter width and  $L$  is the emitter length between cathode shorts. It should be noted that the gate triggering current is strongly controlled by the surface geometry design. Another important parameter is the holding current, which is the minimum current needed to sustain the thyristor in the on-state and is given by

$$I_{HA} = 2V_{bi}Z/[(1 - \alpha_{nnp})\rho_{SB}L] \quad (5)$$

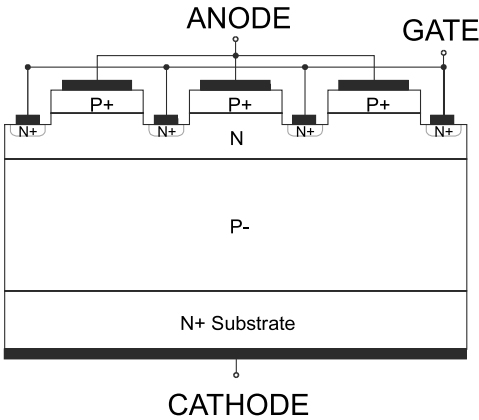


**Fig. 20.** Schematic cross-section of a SiC thyristor [46]

It can be seen that the holding current can be minimized by increasing the sheet resistance of the upper base region and the distance between cathode shorts.

For SiC, due to the difficulties in heavy  $p$ -type doping in the substrate, a  $n^+$  substrate is usually used. Consequently, the actual thyristor structure studied is complementary to that of conventional silicon SCR'sSilicon Controlled Rectifier (SCR). Figure 20 shows the schematic cross-section of a SiC thyristor [46]. From device considerations, the lower transistor being  $nnp$  improves the  $BV_{CEO}$  and safe-operating area but the upper  $pnp$  transistor requires a larger gate current to turn on due to lower  $n$ -base sheet resistance and current gain. To quantify the performance between  $pnpn$  and  $nnpn$  SCR'sSilicon Controlled Rectifier (SCR), we have calculated their respective holding currents and found that the SCR'sSilicon Controlled Rectifier (SCR) with the cathode as substrate is favored.

Once triggered on, the thyristor on-state characteristics strongly resemble that of a pin junction rectifier [1, 2]. With both the upper and low base conductivities modulated with carriers injected from the anode and cathode, the forward drop approaches that of the pin diode. With SiC, a much higher table operating temperature is possible in thyristors. The first SiC SCR'sSilicon Controlled Rectifier (SCR), demonstrated in  $6H$ -SiC, already can operate as high as  $400^\circ\text{C}$  [46].

## 4.2 Gate Turn-Off Thyristor (GTO)

To facilitate turn-off, the thyristors can be designed so that a gate current (in opposite direction to the gate triggering current) is used without device commutation (or anode-cathode voltage reversal). Since SiC thyristors is desired to have a complementary structure to those for silicon thyristors, the condition for gate turn-off in SiC Gate Turn-Off Thyristors (GTO's), unlike that in the silicon case [1, 2], is

$$I_G > (\alpha_{npn} + \alpha_{pnp} - 1) I_A / \alpha_{pnp} \quad (6)$$

and the maximum turn-on gain is

$$\beta_{\max} = \alpha_{pnp} / (\alpha_{npn} + \alpha_{pnp} - 1) . \quad (7)$$

It can be noted that, the current gain of the upper narrow base *pnp* transistor controls the gate current for turn-off and maximum turn-off gain. However, similar to silicon, since 4H-SiC has the same asymmetric mobilities ( $\mu_n > \mu_p$ ) and lifetimes ( $\tau_{n0} > \tau_{p0}$ ),  $\alpha_{npn}$  tends to be larger than  $\alpha_{pnp}$ . Consequently,

**Table 6.** A list of SiC power thyristors that have been experimentally demonstrated

Device type	Poly-type	Power ratings	Features	Developer	Ref.
SCRs	6H	100 V, 20 mA	Gate Triggered	Cree, 1993	[46]
	4H	900 V, 2 A	Gate Triggered, 0.82 mΩ-cm <sup>2</sup>	Cree, 1996	[48]
GTOs	6H	100 V, 1.8 A	Epi $p^+$ emitter, $V_{F100} = 2.9$ V, $J_{\max} = 5200$ A/cm <sup>2</sup>	ARL, 1995	[52]
	4H	600 V, 4.2 A	Epi $p^+$ emitter, Involute Gate (1600 A/cm <sup>2</sup> , $V_{F100} = 4.5$ V)	Northrop-Grumman, 1997	[49]
	4H	600 V,	Implanted $p^+$ emitter	RPI, 1997	[60]
	4H	1100 V	Gate Turn-Off (GTO), $V_{F100} \sim 5$ V	GE/RPI, 1999	[54]
	4H	600 V	Implanted $n$ Base	RPI, 2000	[61]
	4H	2800 V	Gate Turn-Off (GTO)	Cree, 2000	[56]
	4H	3000 V	Gate Turn-Off (GTO)	GE/RPI, 2000	[61]
	4H	3100 V	Gate Turn-Off (GTO) Turn-off gain 12.5 at 300 A/cm <sup>2</sup> Assymetrical	Cree, 2001	[63]
	4H	7 kV	Gate Turn-Off (GTO) $V_{F100} \sim 4$ V	Northrop-Grumman, 2002	[64]
FCTs	4H	305 V	Buried gate, 4.5 V at 1 A ( $\sim 525$ A/cm <sup>2</sup> ), Blocking gain 7.6	Cree, 1997	[66]

---

$V_{F100}$  is defined as the forward voltage drop at  $J_F = 100$  A/cm<sup>2</sup>

the current gain asymmetry is much less pronounced in SiC thyristors than in that found in silicon counterparts and suppresses the maximum turn-off current gain achievable. This trend has been pointed out and measured experimentally [54].

Besides controlling the current gain of the constituent transistors, the surface geometry design, such as the emitter stripe width, plays a critical role in determining the maximum gate controllable current with device failure due to second breakdown [1, 2].

Shown in Table 6 are the experimental thyristors that have been demonstrated to date. Symmetric and asymmetric 6H- and 4H-SiC gate-controlled thyristors reported have  $BV$  up to 7000 V and 6 A at present [47]–[64]. It has been demonstrated early that SiC thyristors can operate at much higher temperatures than silicon ones [46, 47]. Most of the published thyristor structures use epi  $p^+$  emitter and  $n^+$  substrates. In Fig. 21, the forward  $I$ - $V$  characteristics of 1 and 3 kV gate-turn-off thyristors are shown [54]. The lower forward drop of the 3 kV devices is due to a lower anode contact resistivity from an improved annealing process. The effect of the parasitic contact resistance on the thyristor forward drop was first pointed out and quantified in [52]. Interestingly, unlike silicon devices, the SiC thyristor turns on faster with increasing temperature (Fig. 22) because an increase in acceptor activation improves hole injection from the  $p^+$  emitters [54]. The turn-off characteristics are shown in Fig. 23 and the turn off time increases with temperature because of an increase in recombination lifetime. A maximum turn-off current density of over 100 A/cm<sup>2</sup> is possible at 190°C. The dependence of turn-on and turn-off characteristics on device geometries (such as stripe vs. involute cell geometries) has also been studied [59].

Probably due to reduced injection emitter from residual implant defects, most of the GTO's reported so far have utilized epi-grown emitters. We have tried an implanted  $p^+$  emitter process with Al/C/B on a symmetric thyristor

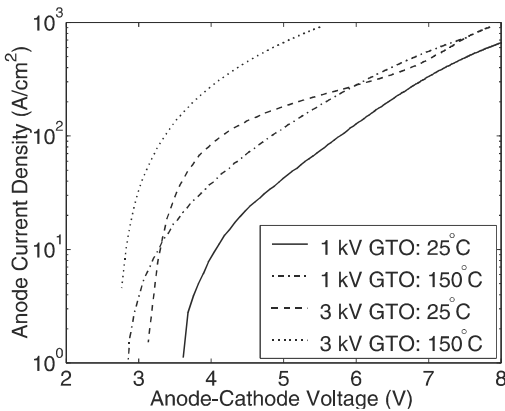


**Fig. 21.** Experimental forward  $I$ - $V$  characteristics of 1 and 3 kV 4H-SiC GTOs [54]

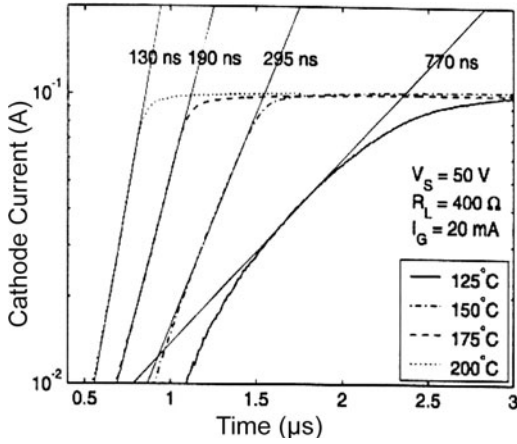


**Fig. 22.** Turn-on characteristics of an 1100 V 4H-SiC GTO with increasing temperature [54]

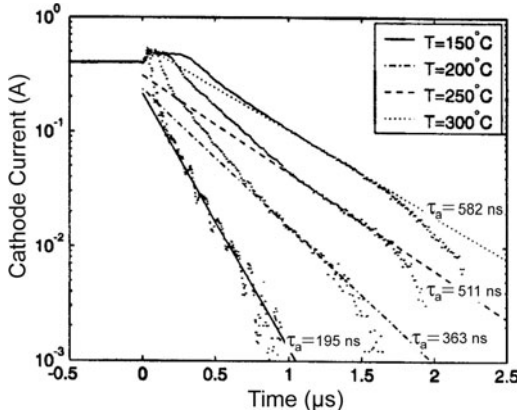


**Fig. 23.** Unity gain turn-off characteristics of an 1100 V 4H-SiC GTO with increasing temperature [54]

structure with a drift layer of 10  $\mu\text{m}$  and have obtained  $BV$  of 600 V [60] but the forward drop (5–20 V) is higher than expected. The sheet resistance of the implanted  $p^+$  emitter needs to be further improved to enhance the injection efficiency and lower the contact resistance. More promisingly, the use of nitrogen or phosphorus implantation to form the upper  $n$ -base has been recently demonstrated in a 600 V 4H-SiC GTO [61]. However, the forward drop of this GTO is still relatively high at high current densities ( $>10 \text{ A/cm}^2$ ) so that the implantation process needs to be further optimized. Nevertheless, this is the first SiC GTO that has been formed with an implantation process.

The turn-off gain of SiC GTO is expected to be less than the silicon counterpart since a complementary structure is usually adopted. The reason is that the upper transistor is now  $pnp$  in the SiC case and hence it has less current gain. According to (7),  $\beta_{\text{max}}$  is thus smaller. Experimentally, turn-off gains between 3 and 7 have been measured on 700 V 4H-SiC GTO's (see for example [57]–[59]). However, a unity gain turn-off is also possible (this mode

of GTO operation is called the IGCT mode). Typical unity gain turn-off characteristics of 4H-SiC GTOs are shown in Fig. 23 [54]. Furthermore, due to the reduced base widths, SiC thyristors can switch at a higher frequency than Si devices of the same blocking voltage rating. For example, 700 V 4H-SiC GTO's with a switching frequency up to 250 kHz have been reported [47].

### 4.3 Light Triggered Thyristor

Light-triggered thyristors are commonly used in applications where electrical isolation is important. The turn-on of a thyristor by optical means is an especially important approach for devices that are to be used in extremely high voltage circuits, such as those found in dc transmission systems in which each of the serially connected switches must be triggered on command. Optical firing in this application is ideal for providing the electrical isolation for trigger circuits required for these devices.

Often, these light-triggered thyristors are used to provide gate current for larger thyristors, in other words, in an externally connected amplifying gate configuration, with the light-activated device serving as a pilot thyristor. The turn-on process in these devices is quite analogous to that in conventional gate-controlled thyristors, with the excess carriers now generated with optical absorption. The delay in the turn-on process is directly related the amount of excess carriers and hence to the optical power and the efficiency of photon absorption. The wavelength of the optical source also needs to be larger than the semiconductor bandgap. Recently, light triggering in SiC thyristors was demonstrated for the first time with an UV laser with an energy of 3.68 eV turn on a 2.6 kV 4H-SiC device at room temperature [65]. It was observed that, with sufficient optical power, the turn-on process can be very rapid and the current rise is only 3 ns, about 30 times faster than with the conventional current-triggered mode.

### 4.4 Field-Controlled Thyristor

The Field-Controlled Thyristor (FCT) (or Field-Controlled Diode) is a pin diode that utilizes voltage-control through a reverse-biased *pn* (gate-channel) junction to modulate the main current flow between the anode and cathode terminals [2]. The gate region can be accessible from the top surface or buried. The schematic cross-section of a SiC buried-gate FCT is shown in Fig. 24 [66]. In the on-state, the FCT closely resembles that of a pin junction rectifier, with electrons and holes injecting from the cathode and anode, respectively, and hence has a high level of conductivity modulation and a very low forward drop. During turn-off, the excess minority carriers can be extracted through the gate terminal and a high switching speed can be attained. The forward blocking state is achieved by the merging of the depletion layers from the gate junctions and the formation of a potential barrier in the drift layer,

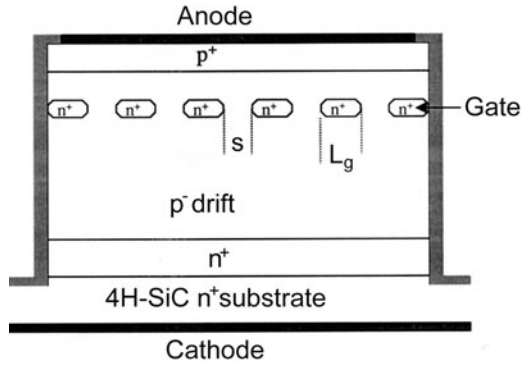


**Fig. 24.** Schematic cross-section of a 4H-SiC Field-Controlled Thyristor [66]

thus preventing current flow from the anode to the cathode. Consequently, the blocking voltage is determined by the gate voltage and a key device performance parameter is the blocking voltage gain, which is defined as

$$G = V_{AK}/V_{GK} . \quad (8)$$

The critical device design parameter is the channel width  $s$  and the gate width  $L_G$ . Also, the channel geometry determines the depletion layer profile and the peak electric field at the blocking gate-channel junctions. One of the main drawback of the FCT is the normally-on characteristics. Even though it can be designed to be normally off, it requires very fine feature sizes and it may turn on at elevated temperatures.

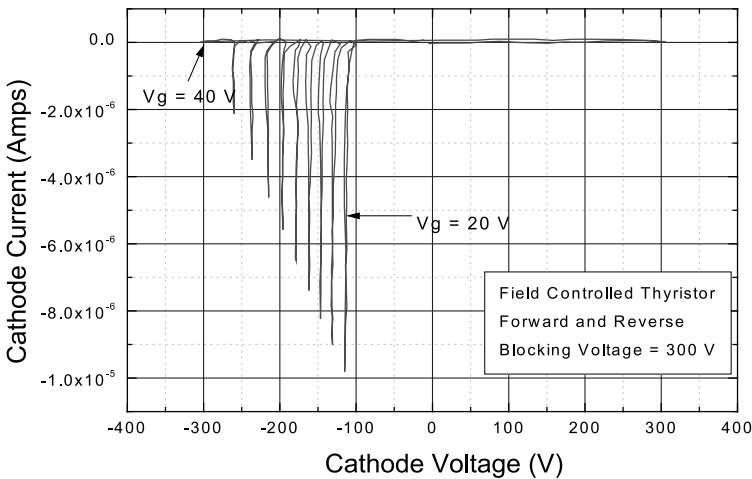


**Fig. 25.** Forward and reverse blocking characteristics of a 4H-SiC Field-Controlled Thyristor with a linear gate width of 1  $\mu\text{m}$  and channel width of 3  $\mu\text{m}$  [66]

A buried-gate FCT in 4H-SiC with a blocking voltage up to 335 V has been reported [66]. The basic FCT here employs a  $p^-$  drift layer so that an  $n^+$  gate junction can be used. Both linear and honeycomb cell geometries have been designed and examined with channel spacing between 3 and 5  $\mu\text{m}$  and gate widths between 0.5 and 2  $\mu\text{m}$ . The forward and reverse blocking characteristics of a linear gate FCT with channel width of 3  $\mu\text{m}$  and gate width of 1  $\mu\text{m}$  are shown in Fig. 25. A FCT with good on-state and blocking characteristics has a maximum forward blocking voltage of 305 V and blocking gain of 7.6 [48]. An on-state forward drop of 4.5 V at 525 A/cm<sup>2</sup> has also been obtained. While the forward drop improves with increasing temperature, both the leakage current and blocking gain degrade. The  $V_F$  decreased from 5 to 3.4 V with the corresponding increase in  $I_{\text{leakage}}$  from 0.8 to 450 A/cm<sup>2</sup> and decrease in blocking gain from 6.7 to 5.3 when the temperature increased from room temperature to 350°C.

#### 4.5 MOS-Gated Thyristors

MOS-gate thyristors use a gate voltage for turn-on and turn-off and they have been actively studied in silicon. Examples of these are the MOS-Controlled Thyristor (MCT) and Emitter Switched Thyristor (EST) [2]. Usually, a MOSFET is connected in series with the emitter terminal like the EST or connected in parallel across the emitter-base junction like the MCT. Due to the process complexities, 4-layer MOS-gated thyristor structures are preferable to 5-layer ones. The MCT, usually implemented with 5 layers, has a 4-layer version though the turn-off performance is not as good as the 5-layer counterpart.

No monolithic functional MOS-gated thyristor in SiC has been reported so far. However, recently, 4H-SiC GTOs have been turned off with Si MOSFETs as base-emitter shunts [56, 57]. It has been demonstrated that the maximum gate controllable current is higher with a MOS-gate control than conventional gating [57]. Also, the turn-off waveform can be used to extract recombination lifetimes in the base regions [56].

### 5 Materials and Process Challenges

At present, commercial 4H-SiC substrates of up to 3 inches in diameter are available and custom  $n$ - and  $p$ -type epitaxial layers up to over 100  $\mu\text{m}$  can be ordered. For high-voltage devices, total epitaxial layer thickness of at least up to 50  $\mu\text{m}$  with acceptable surface flatness and doping uniformity and minimum compensation is needed. To minimize parasitic substrate resistance and maximum carrier concentration, a doping of  $10^{19} \text{ cm}^{-3}$  would be desired. Such a high doping level seems to be difficult with  $p^+$  substrates. The most severe structural defect is the micropipe but its density has been substantially improved (to a recently reported value of less than 1 micropipes/cm<sup>2</sup>).

A micropipe density of less than  $1/\text{cm}^{-2}$  is needed to realize devices of current ratings larger than 100 A with reasonable yield. Other structural defects, such as screw dislocations, appear to correlate with excessive leakage current in 4H-SiC *pn* junctions [67] and must be suppressed now that the micropipe problem is largely under control. For bipolar devices, the minority carrier lifetime is a very critical parameter and needs to be maximized to ensure a high level of important conductivity modulation in the drift region. Despite the continuing improvement of SiC MOS interfacial parameters (to, at present, a fixed oxide charge density close to  $5 \times 10^{11}/\text{cm}^{-2}$  and an interface state density less than  $3 \times 10^{10}/\text{cm}^{-2}$ ), the correlation between surface state densities with inversion layer mobility is still weak. Recently, with high-temperature NO anneal, a DMOS inversion layer mobility of  $\sim 50 \text{ cm}^2/\text{V-s}$  has been achieved in 4H-SiC [68] but it still needs to be further optimized and correlated to surface process conditions. Moreover, gate oxide reliability at elevated temperatures still needs to be ascertained. *n*-type phosphorus implantation [69]–[71] has yielded sheet resistance values approaching those in silicon ( $< 50 \text{ } \Omega/\text{square}$ ) but *p*-type implanted layers still have a too high sheet resistance ( $> 1 \text{ k}\Omega/\text{square}$ ) [72, 73]. Ohmic contacts of reasonable contact resistivities ( $10^{-6}$  to  $10^{-4} \text{ } \Omega\text{-cm}^2$ ) have been made to SiC [74]. Usually, Ni is used on *n*-type contacts and Al is used for *p*-type contacts. A relatively high (around  $1000^\circ\text{C}$ ) sintering step is performed for contact formation. Formation of *p*-type contacts is more difficult because a high surface hole concentration is often hard to achieve due to the deepness of the acceptor levels ( $> 180 \text{ meV}$ ).

## 6 Conclusion

We have reviewed the progress in SiC bipolar power switching devices in the last few years. Besides the figures of merit, we have discussed the physics of operation of three-terminal homojunction devices that are applicable to SiC. The performance potential, tradeoffs, and limitations of these SiC devices are discussed, together with their recent experimental demonstrations. We expect continuing technological improvement and imminent device commercialization in this area in the near future.

## Acknowledgement

We would like to acknowledge support from Office of Naval Research under Grant # N00014-95-1-1302, DARPA under Contract # MDA 972-98-C-0001, the ERC Program of the National Science Foundation under Award Number EEC-9731677 and ARL Collaborative Technology Alliance in Power and Energy, Cooperative Agreement No. DAAD19-01-2-0010.

## References

1. S.K. Ghandhi: *Semiconductor Power Devices* (Wiley, 1977, republished 1998)
2. B.J. Baliga: *Physics of Semiconductor Power Devices* (JWS Publishing, 1996)
3. K. Shenai, R.S. Scott, and B.J. Baliga: IEEE Trans. Electron Devices **36**, 1811 (1989)
4. B.J. Baliga: IEEE Electron Device Letters **10**, 455 (1989)
5. A. Bhalla and T.P. Chow: "Examination of semiconductors for bipolar power devices," Inst. Phys. Conf. Ser. No. 137, 621 (IOP Publishing Ltd., 1994)
6. A. Bhalla and T.P. Chow: Proc. 6th International Symp. Power Semiconductor Devices and ICs, 287–292 (1994)
7. T.P. Chow and R. Tyagi: IEEE Trans. Electron Devices **41**, 1481 (1994)
8. T.P. Chow: *Handbook of Thin Film Devices, Vol. 1, Hetero-Structures for High Performance Devices*, Chap. 7, "Silicon Carbide Power Devices," (Academic Press, 2000)
9. A.S. Kyuregyan and S.N. Yurkov: Sov. Phys. Semicond. **23**, 1126 (1989)
10. A.O. Konstantinov, Q. Wahab, N. Nordell, and U. Lindefelt: Appl. Phys. Lett. **71**, 90 (1997)
11. R. Raghunathan and B.J. Baliga: "Measurement of electron and hole impact ionization coefficients for SiC," Proc. 9th IEEE International Symposium on Power Semiconductor Devices and ICs, 173–176, (1997)
12. W. Fulop: Solid-State Electronics **10**, 39 (1967)
13. N. Ramungul, R. Tyagi, A. Bhalla, T.P. Chow, M. Ghezzi, J. Kretchmer, W. Hennessy: "Design and Simulation of 6H-SiC UMOS FET and IGBT for High-Temperature Power Electronics Applications," Inst. Phys. Conf. Ser. No. 142, 773–776, (1995)
14. J. Kolnik, I.H. Oguzman, K.F. Brennan, R. Wang, and P.P. Ruden: "Theoretical prediction of zinc blende phase GaN avalanche photodiode performance based on numerically calculated electron and hole impact ionization rate ratio" Mat. Res. Soc. Symp. Proc. **423**, 45 (1996)
15. See, for example, R. Singh, K.G. Irvine, O. Kordina, J.W. Palmour, M.E. Levinshstein, S.L. Rumyanetsev: "4H-SiC bipolar P-i-N Diodes with 5.5 kV blocking voltage," 56th Annual Device Research Conference Digest, 86–87 (1998)
16. T.P. Chow: Electrochemical Society Proc. **98–12**, 16 (1998)
17. J. Wang and B.W. Williams: IEEE Trans. Electron Devices **46**, 589 (1999)
18. A.Q. Huang and B. Zhang: IEEE Trans. Electron Devices **48**, 2535 (2001)
19. P. Neudeck and C. Fazi: Electron Device Letters **18**, 96 (1997)
20. S. Nakamura, H. Kumagai, T. Kimoto, and H. Matsunami: Mat. Sci. Forum **389–393**, 651 (2002)
21. T. Tanaka, Y. Yasuda, and M. Ohayashi: IEEE Trans. Electron Devices **ED-33**, 2041 (1986)
22. W. von Munch and P. Hoeck: Solid-State Electronics **21**, 479 (1978)
23. J.W. Palmour, J.A. Edmond, and C.H. Carter: presented at the 51st Device Research Conference, (1993)
24. Y. Wang, W. Xie, J.A. Cooper, Jr., M.R. Melloch, and J.W. Palmour: "Mechanisms limiting current gain in SiC bipolar junction transistors," Proceedings of the 6th International Conference on Silicon Carbide and Related Materials, 809–812, (1996)
25. Y. Luo, L. Fursin, and J.H. Zhao: Electronics Letters **36**, 1496 (2000)

26. Y. Tang, J.B. Fedison, and T.P. Chow: *Electron Device Letters* **22**, 119 (2001)
27. S.-H. Ryu, A.K. Agarwal, R. Singh, and J.W. Palmour: *Electron Device Letters* **22**, 124 (2001)
28. Y. Tang, J.B. Fedison, and T.P. Chow: *Electron Device Letters* **23**, 16 (2002)
29. S.-H. Ryu, A.K. Agarwal, R. Singh, and J.W. Palmour and M.E. Levinshstein: "1.8 kV, 3.8 A bipolar junction transistors in 4H-SiC" *Proc. International Symp. Power Semiconductor Devices and ICs*, 37–40 (2001)
30. Y. Tang, J.B. Fedison, and T.P. Chow: *Mat. Sci. Forum* **389–393**, 1329 (2002)
31. Y. Luo, L. Fursin, J.H. Zhao, P. Alexandrov, B. Wright, and M. Weiner: *Mat. Sci. Forum* **389–393**, 1325 (2002)
32. C.-F. Huang and J.A. Cooper: "4H-SiC npn bipolar junction transistors with  $BV_{CEO} > 3200$  V" *Proc. International Symp. Power Semiconductor Devices and ICs*, 57–60 (2002)
33. A. Agarwal, S.-H. Ryu, J. Richmond, C. Capell, J.W. Palmour, Y. Tang, S. Balachandran and T.P. Chow: "Large area, 1.3 kV, 17 A, bipolar junction transistors in 4H-SiC" *Proc. International Symp. Power Semiconductor Devices and ICs*, 135–138 (2003)
34. Y. Tang and T.P. Chow: "Demonstration of monolithic Darlington transistors in 4H-SiC" *European Conf. Silicon Carbide and Related Materials*, Late News Paper (2002)
35. Y. Tang and T.P. Chow: "High gain monolithic 4H-SiC Darlington transistors" *Proc. International Symp. Power Semiconductor Devices and ICs*, 383–387 (2003)
36. B.J. Baliga: *Modern Power Devices* (Wiley, 1987)
37. X. Li, L. Fursin, J.H. Zhao, P. Alexandrov, M. Pan, M. Weiner, T. Burke, and G. Khalil: *Mat. Sci. Forum* **389–393**, 1345 (2002)
38. Y. Sugawara, K. Asano, R. Singh, J. Palmour, and D. Takayama: "4.5 kV Novel high Voltage High Performance SiC-FET 'SIAFET'" *Proc. 12th International Symp. Power Semiconductor Devices and ICs*, 105–108 (2000)
39. N. Ramungul, T.P. Chow, M. Ghezzi, J. Kretchmer, and W. Hennessy: "A Fully Planarized, 6H-SiC UMOS Insulated-Gate Bipolar Transistor" *54th Annual Device Research Conference Digest*, 56–58 (1996)
40. T.P. Chow and M. Ghezzi: *Materials Research Society Fall Meeting* (1997)
41. R. Singh, S.-H. Ryu, and J.W. Palmour: "High Temperature, High Current, *p*-Channel UMOS 4H-SiC IGBT" *Device Research Conference*, Paper II.B.-4 (1999)
42. H. Lendenmann, A. Mukhitdinov, F. Dahlquist, H. Bleichner, M. Irwin, R. Soderholm, and P. Skytt: "4.5 kV 4H-SiC diodes with ideal forward characteristics" *Proc. International Symp. Power Semiconductor Devices and ICs*, 31–34 (2001)
43. Y. Tang, T.P. Chow, A.K. Agarwal, S.-H. Ryu, and J.W. Palmour: *Mat. Sci. Forum*, **389–393**, 1341 (2002)
44. Y. Tang, S. Banerjee, and T.P. Chow: "Hybrid all-SiC MOS-gated Bipolar Transistor (MGT)" *Proc. International Symp. Power Semiconductor Devices and ICs*, 53–56 (2002)
45. J.I. Pankove, M. Leksono, S.S. Chang, C. Walker, and B. Van Zeghbroeck: *MRS Internet Journal of Nitride Semiconductor Research* **1**, 1092 (1996)
46. J.W. Palmour et al.: *Mat. Research Soc. Spring Meeting* (1994)

47. J.W. Palmour, R. Singh, R.C. Glass, O. Kordina, C.H. Carter, Jr.: "Silicon carbide for power devices" Proc. International Symp. Power Semiconductor Devices and ICs, 25–30 (1997)
48. J.W. Palmour, R. Singh, and D.G. Waltz: "High power 4H-SiC thyristors" 54th Annual Device Research Conference Digest, 54–55 (1996)
49. A.K. Agarwal, J.B. Casady, L.B. Rowland, S. Seshadri, R.R. Siergiej, W.F. Valek, C.D. Brandt: Electron Device Letters **18**, 518 (1997)
50. R.R. Siergiej, J.B. Casady, A.K. Agarwal, L.B. Rowland, S. Seshadri, S. Mani, P.A. Sanger, and C.D. Brandt: "1000 V 4H-SiC Gate Turn Off (GTO) Thyristor" Proc. International Symp. Comp. Semicond., San Diego, CA (Sept. 1997)
51. S. Seshadri, J.B. Casady, R.R. Siergiej, L.B. Rowland, P.A. Sanger, C.D. Brandt, J. Barrow, D. Piccone, R. Rodrigues, and T. Hansen: "Turn-Off Characteristics of 1000 V SiC Gate-Turn-Off Thyristors" Proc. International Symp. Power Semiconductor Devices and ICs, 25 (1998)
52. K. Xie and J.H. Zhao: Electron Device Letters **17**, 142 (1996)
53. M.E. Levinshstein, J.W. Palmour, S.L. Rumyantsev, and R. Singh: "Turn-on process in 4H-SiC thyristors" Proceedings of the 23d International Symposium on Compound Semiconductors, 601–603 (1996)
54. J. Fedison, T.P. Chow, M. Ghezzi, J.W. Kretchmer, and M.C. Nelissen: Materials Science Forum **338–342**, 1391 (2000)
55. J. Fedison and T.P. Chow: to be published
56. J. Fedison, T.P. Chow, A.K. Agarwal, and J.W. Palmour: Device Research Conference (June 2000)
57. P.A. Ivanov, M.E. Levinshstein, S.L. Rumyantsev, A.K. Agarwal, and J.W. Palmour: Solid-State Electronics **44**, 2155 (2000)
58. S.H. Ryu, A.K. Agarwal, R. Singh, and J.W. Palmour: Electron Device Letters **22**, 127 (2001)
59. J. Fedison, T.P. Chow: "Dependence of turn-on and turn-off characteristics on anode/gate geometry of high-voltage 4H-SiC thyristors" Proc. International Symp. Power Semiconductor Devices and ICs, 175–178 (2001)
60. J. Fedison and T.P. Chow: unpublished
61. J. Fedison and T.P. Chow: Mat. Sci. Forum **353–356**, 739 (2001)
62. A.K. Agarwal, P.A. Ivanov, M.E. Levinshstein, J.W. Palmour, S.L. Rumyantsev, S.H. Ryu, and M.S. Shur: Mat. Sci. Forum **353–356**, 743 (2001)
63. A.K. Agarwal, P.A. Ivanov, M.E. Levinshstein, J.W. Palmour, and S.L. Rumyantsev: Mat. Sci. Forum **389–393**, 1349 (2002)
64. S. VanCampen et al.: MRS Fall Meeting, Paper K7.7 (2002)
65. M.E. Levinshstein et al.: Electronics Letters **38** (June 2002)
66. R. Singh, K.G. Irvine, and J.W. Palmour: "4H-SiC buried gate field controlled thyristor" 55th Annual Device Research Conference Digest, 34–35 (1997)
67. P. Neudeck, W. Huang, and M. Dudley: Solid-State Electronics **42**, 2157 (1998)
68. A. Agarwal: to be published
69. V. Khemka, R. Patel, N. Ramungul, T.P. Chow, M. Ghezzi, and J. Kretchmer: J. Electron. Mat. **28**, 161 (1999)
70. M. Capano et al.: J. Electron. Mat. (2000)
71. L. Zhu, Z. Li, and T.P. Chow: J. Electron. Mat. **30**, 891 (2001)
72. H. Itoh, T. Troffer, and G. Pensl: Materials Science Forum **264–268**, 685 (1998)
73. S. Seshadri, G.W. Eldridge, and A.K. Agarwal: Appl. Phys. Lett. **72**, 2026 (1998)

74. See, for example, J. Crofton, L. Beyer, J.R. Williams, E.D. Luckowski, S.E. Mohny, J.M. Delucca: *Solid-State Electronics* **41**, 1725 (1997)
75. Y. Sugawara, K. Asano, D. Takayama, S. Ryu, R. Singh, J. Palmour, and T. Hayashi: *Mat. Sci. Forum* **389–393**, 1199 (2002)
76. D. Takayama, Y. Sugawara, T. Hayashi, R. Singh, J. Palmour, S. Ryu, K. Asano: “Static and dynamic characteristics of 4–6 kV 4H-SiC SIAFETs” *Proceedings of the 13th International Symposium on Power Semiconductor Devices & ICs*, 41–44 (2001)

# High Voltage SiC Devices

Y. Sugawara

## 1 Introduction

High voltage SiC devices are expected to have big impacts for some large electric power converters in the electric application field, which has been simulated and is shown in Table 1 [1]. In these simulations, the valve of the SiC converters and the valve used for the comparison are composed of a pair of SiC MOSFET and SiC diode of 5 kV, 3 kA ratings and a pair of Si GTO and Si-diode of 6 kV, 6 kA ratings, respectively. The reason why the voltage and current rating of the devices are different is explained as follows: since an anode reactor is not needed for a MOSFET, the voltage surge is reduced during turning on, therefore, MOSFET with the low rated voltage of 5 kV can be used in place of 6 kV GTO. While the average on-state current of MOSFET is the same as its controllable on-state current, average on-state current of a GTO is approximately half of its controllable on-state current. Consequently, the current rating of a MOSFET can be half that of GTO. The free-wheeling diodes should have the same voltage and current rating as those of switching devices used in conjunction with them.

From Table 1, it is shown that SiC power devices will have a considerable impact when they are applied to large electric power conversion equipment used for power transmission and distribution. Therefore, high voltage SiC FETs and SiC fly wheeling diodes with blocking voltage of 5 kV class have been developed for the equipment.

**Table 1.** Impact of SiC power semiconductor devices for electric power conversion equipment

Equipment	Capacity	Impact	Power loss*	Valve volume*
Self-commutated BTB or HVDC	300 MW	Low loss Small size	~0.26	~0.16
SVG	50 MW	High efficiency Small size	~0.3	~0.2
Active filter	10 MW	Air-cooled	<0.2	–

\* Relative value in case that the power loss and volume of the valve using Si GTO is 1



The blocking voltage is 4.5 kV and the leakage current is 0.3 A/cm<sup>2</sup> at 4.4 kV, which is lower than that of a previously reported SBD, about 2 A/cm<sup>2</sup> [3]. The figure of merit,  $[(BV)^2/R_{\text{ons}}]$ , is 841 MW/cm<sup>2</sup>, which is the highest value among the reported SBDs.

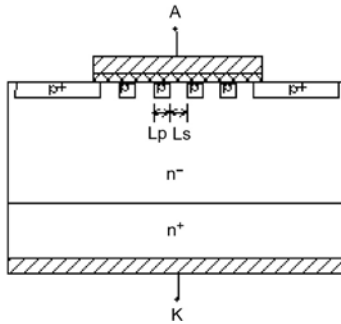
## 2.2 3.7 kV 4H-SiC JBS Diode [4, 5]

Figure 3 shows a cross-sectional structure of the JBS diode. Under the Schottky barrier metal, *p*-type regions are formed with a specified spacing. These regions reduce the electric field of the Schottky barrier by using static induction phenomena in the reverse blocking state and therefore reduce the leakage current. Thus, a JBS diode can be expected to realize high *BV* similar to that of the *pn* diode with a high yield. In the on-state, the forward current flows through the Schottky junction among the spacings between *p* regions. Therefore, the JBS diode can be expected to have a low  $V_F$  similar to that of SBD and the same fast recovery characteristics as that of SBD.

In order to realize high *BV*,  $p^+$  JTE layer formed by  $B^+$  implantation is adopted as the edge-termination and Ni is employed as the Schottky barrier metal also. *BV* and  $V_F$  depend on  $R_p \equiv L_p/(L_p + L_s)$ .  $L_p$  is a *p* region width and  $L_s$  is a distance between *p* regions. In case of  $R_p$  of 0.5, similar good forward characteristic and lower leakage current can be realized as compared with that of SBD.

Figure 4 shows the forward and reverse characteristics of the 4H-SiC JBS diode with  $R_p = 0.5$ , which has an *n*-epitaxial layer thickness of 50 μm and a doping of  $1.5 \times 10^{15}$  cm<sup>-3</sup>. The shape of the JBS diode is circle and its diameter is 300 μm also. The *BV* of 3.6 kV is achieved. The leakage current of the JBS diode is  $6 \times 10^{-3}$  A/cm<sup>2</sup> at 3.6 kV and is very low as compared with that of SBD. Its  $V_F$  at 100 A/cm<sup>2</sup> is 6.0 V. The ideality factor of the JBS diode is 1.24 and the excellent low  $R_{\text{ons}}$  of 31 mΩcm<sup>2</sup> is obtained.

Furthermore, JBS diode can offer excellent high speed turn-off performances compared with a commercialized Si high speed diode of 400 V class.



**Fig. 3.** Cross-sectional structure of of 3.7 kV 4H-SiC JBS diode

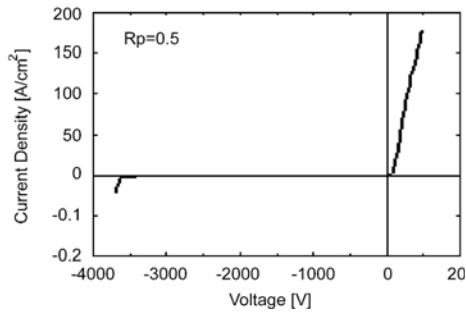


Fig. 4. Forward and reverse characteristics of 3.7 kV 4H-SiC JBS

The recovery time ( $t_{rr}$ ) and reverse recovered charge ( $Q_{rr}$ ) of the 3.6 kV JBS are 9.7 ns and 0.18 nC, respectively, which are about 1/10 and 1/150 of those of the Si high speed diode respectively, in spite of high  $BV$ . The  $t_{rr}$  and  $Q_{rr}$  of JBS diode are independent of temperature although those of the Si diode become remarkably large with increase in operating temperature [4]. Therefore, in the case of JBS diode, snubber loss does not become large even at high operating temperature.

Figure 5 shows the trade-off relationships between  $R_{onS}$  and  $BV$  of the main reported SBDs and JBS diodes with  $BV$  of more than 1 kV. The developed SBD has the best trade-off.  $R_{onS}$  of the developed SBD and JBS diode are about 1/420 and 1/190 of the Si theoretically limited value, which is only about 2 times and 4.5 times of 4H-SiC theoretically limited  $R_{onS}$ .

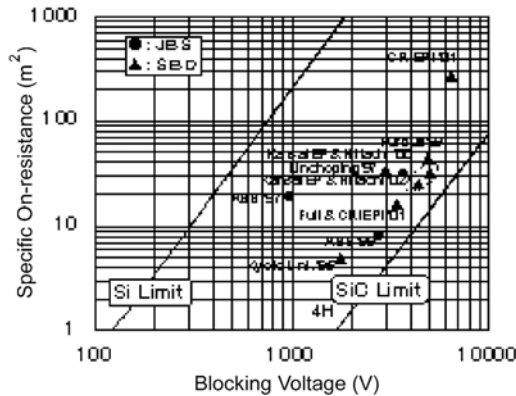


Fig. 5. Trade-off relationships between  $R_{onS}$  and  $BV$  of the main SBDs and JBS diodes

## 2.3 6.2–19.3 kV 4H-SiC *pn* Diode [5, 6]

### 2.3.1 Device Structure

Figure 6 shows the cross-sectional structure of the developed high voltage diode. A main *pn* junction is formed with an epitaxial deposition and a shallow mesa JTE [5] is formed with ion implantations after a shallow dry etching of the epitaxial layer around the main junction. By using this structure, the main junction with good performance and the termination with proper impurity concentration for electric field reduction can be formed, and excellent forward and reverse characteristics can be realized at the same time.

The dopant for the *p* epitaxial layer is aluminum and that of the termination is boron. The impurity concentration of the former is about  $5 \times 10^{19} \text{ cm}^{-3}$ . The depth of the shallow mesa is about  $1 \mu\text{m}$ . An  $n^-$  drift layer is also formed with epitaxial deposition and its dopant is nitrogen. The shape of the diodes is circular and its diameter is  $200 \mu\text{m}$ .

Figure 7 shows a packaged high voltage *pn* diode. The package is developed for high voltage transistors, therefore, it has three terminals. In the case of this packaged high voltage diode, the center terminal is used as the cathode terminal and one of the other terminals is used as the anode terminal.

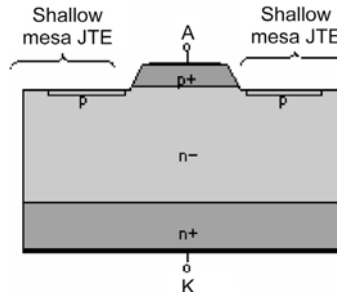


**Fig. 6.** Cross-sectional structure of 4H-SiC high voltage *pn* diode with shallow mesa JTE

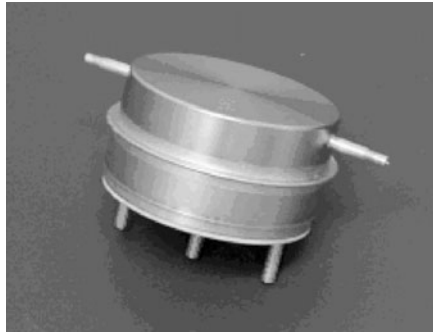


**Fig. 7.** Packaged high voltage *pn* 4H-SiC diode

The diameter of the package is about 5 cm and its height is about 2.5 cm. In the package,  $N_2$  or  $SF_6$  gas is filled through the two pipes of the cap. The blocking voltage of the package without a diode is designed to be 25 kV and is confirmed to be more than 20 kV in air at room temperature.

### 2.3.2 Electrical Characteristics

Diodes with four kinds of drift layer thickness are fabricated : 60  $\mu m$ , 120  $\mu m$ , 150  $\mu m$  and 200  $\mu m$ . The typical JTE length for the former is 250  $\mu m$  and it is 500  $\mu m$  for the latter three. Each diode shows the  $BV$  of about 6 kV, 12 kV, 15 kV and 19 kV, respectively.

Figure 8 shows the  $I$ - $V$  characteristics of the high voltage diodes with the drift layers of 150  $\mu m$  and 200  $\mu m$ . The former diode, type A, has  $BV$  of 14.9 kV and  $V_F$  of 4.4 V at 100 A/cm<sup>2</sup>. The latter diode, type B, has  $BV$  of 19.5 kV and  $V_F$  of 6.5 V at 100 A/cm<sup>2</sup>, whose  $BV$  is the highest among all developed semiconductor devices presently. The reverse leakage current density of the type A diode is less than  $1.0 \times 10^{-3}$  A/cm<sup>2</sup> even at the voltage near  $BV$ . Although the reverse leakage current density of the type B diode is less than  $1.0 \times 10^{-3}$  A/cm<sup>2</sup> at less than 6 kV, it increases around 6 kV and becomes to  $2.5 \times 10^{-3}$  A/cm<sup>2</sup> at more than 10 kV. An increase tendency of the reverse leakage current density like this is observed in all type B diodes, but is not observed at higher temperature.

Figure 9 shows the turn-off waveforms for these diodes.  $t_{rrs}$  are very small and are about 34 ns and 43 ns for type A and B diodes respectively, which are less than 1/30 that of commercially available Si free wheeling diodes in the 6 kV class.  $Q_{rrs}$  are also very small and are about 3.6 nQ and 3.8 nQ for type A and B diodes, respectively. The 6 kV Si diode is used for the comparison because it is the highest voltage available for commercialized Si

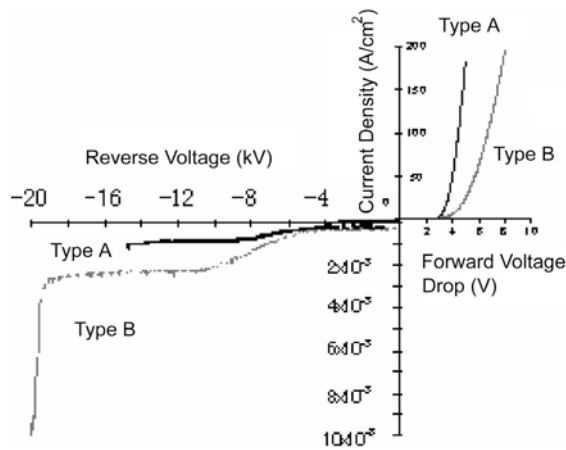
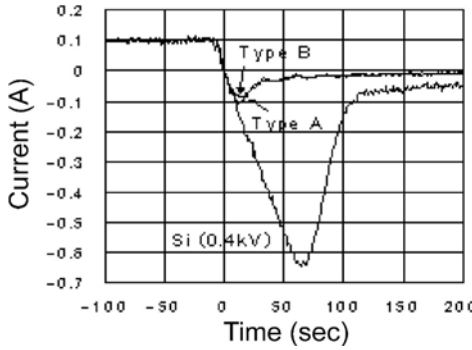


Fig. 8.  $I$ - $V$  characteristics of high voltage 4H-SiC  $pn$  diodes



**Fig. 9.** Turn-off waveforms for high voltage 4H-SiC *pn* diodes

diodes. In Fig. 9, the waveform of the commercialized 0.4 kV Si high speed diode is also included, whose  $t_{rr}$  is about 4 times larger than the developed diodes in spite of the lower  $BV$ .

Figure 10 shows the trade-off relationships between  $BV$  and  $V_F$  for the main reported SiC *pn* diodes. In the figure, the relationship curves of the commercialized Si *pn* diodes are shown. The tendency of the curve is explained as follows: since the built-in potential of the *pn* junction is more dominant under  $BV$  of 3 kV, the slope of the curve increases with increasing  $BV$  slightly, but it becomes steep above 3 kV because the resistance of  $n^-$  drift layer becomes dominant. In case of SiC *pn* diodes, the slope is gradual because increase of  $R_{onS}$  with increasing  $BV$  is small even above 5 kV.

The SiC *pn* diodes with  $BV$  of 6–19 kV has not only the excellent trade-off between  $BV$  and  $V_F$  but also the extremely fast switching characteristics as compared with Si *pn* diodes, therefore, its power loss can be reduced to 1/2–1/6 drastically.

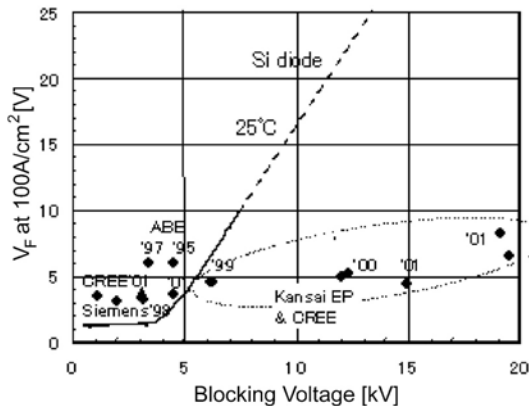


**Fig. 10.** Trade-off relationships between  $BV$  and  $V_F$  for main reported SiC *pn* diodes

3 High Voltage 4H-SiC FETs

Recently, several high voltage SiC FETs with high performance over the theoretical limit of Si FETs have been developed [7]–[12]. Hereinafter, our developed 4H-SiC FETs are introduced [7]–[10].

3.1 4.5 kV SIAFET [7] and 5.0 kV SEMOSFET [8]

Figure 11 shows a cross-sectional structure of the SiC-SIAFET (Static induction carrier Injected Accumulated FET) [7], which has two gates, a  $p^+$  buried gate  $Gp$  and an accumulated MOS gate  $Gm$ . The SIAFET acts as an accumulated MOSFET under zero  $p^+$  buried gate signal, but offers superior blocking characteristics due to a more effective channel pinch-off operation by  $Gp$  under a negative  $p^+$  buried gate bias,  $-V_{Gp}$ . Furthermore, SIAFET acts similar to the ACCUFET under a positive MOS gate bias  $+V_{Gm}$ , but under a positive  $p^+$  buried gate bias  $+V_{Gp}$ , SIAFET achieves a lower  $R_{onS}$  by using two effects: (a) a reduction of a depletion layer around the  $p^+$  buried gate in the channel; and (b) conductive modulation by minority carriers injected

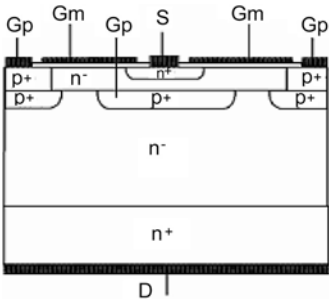


Fig. 11. Cross-sectional structure of 4.5 kV 4H-SiC SIAFET

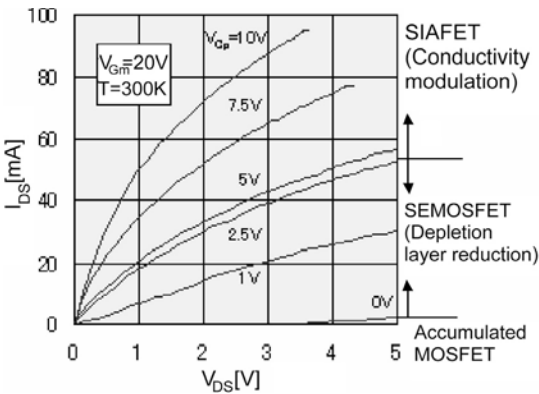


Fig. 12. Typical output characteristics of 4.5 kV 4H-SiC SIAFET

from  $Gp$ . Although SIAFET has two gates, it can operate as a three terminal device by connecting  $Gp$  and  $Gm$  with diodes between the terminals.

Figure 12 shows the output characteristics of the fabricated SIAFET with an  $n^-$  epitaxial layer thickness of  $75\text{ }\mu\text{m}$  and a doping of  $5 \times 10^{14}\text{ cm}^{-3}$ , which is a normally-off type device and has  $BV$  of 4580 V and the leakage current density is  $5 \times 10^{-4}\text{ A/cm}^2$ . The typical three operation modes are observed in the figure like described above, such as the accumulated FET mode, the depletion layer reduction FET mode and the conductivity modulation mode. A channel mobility is  $11\text{ cm}^2/\text{Vs}$  and  $V_{th}$  is 6 V for the accumulated MOSFET. By the conductivity modulation for  $V_{Gp}$  of greater than 2.7 V,  $I_{DS}$  becomes more than 6 times that of the depletion layer reduction mode FET (namely  $I_{DS}$  at  $V_{Gp}$  of 1 V and  $V_{Gm}$  of 20 V). Thus,  $R_{onS}$  is reduced remarkably, and becomes  $387\text{ m}\Omega\text{cm}^2$  (at  $V_{DS}$  of 0.5 V,  $V_{Gp}$  of 10 V and  $V_{Gm}$  of 20 V) in the case of 4580 V SIAFET.

The FET structure is improved and SEMOSFET (Static channel expansion MOSFET) is developed [8], which has the similar device structure like shown in Fig. 11, but is different from SIAFET [7], since an  $n^+$  buried channel is formed on the  $p^+$  buried gate to increase channel impurity concentration and reduce  $R_{onS}$  and its gate voltage of  $Gp$  is limited under the built-in potential of the buried  $p^+$  gate junction. The fabricated SEMOSFET has an  $n^-$  epitaxial layer of  $60\text{ }\mu\text{m}$  in thickness, a doping density of about  $7 \times 10^{14}\text{ cm}^{-3}$ ,  $n^-$  channel layer with a dose of about  $3 \times 10^{16}\text{ cm}^{-3}$  and the gate oxide layer with 80 nm in thickness. Its chip size is  $1.1\text{ mm} \times 1.1\text{ mm}$  and active area is  $3.66 \times 10^{-3}\text{ cm}^2$ . It has a square cell pattern and the cell size is  $28\text{ }\mu\text{m} \times 28\text{ }\mu\text{m}$ . When the same design rule with the minimum pattern width of  $2\text{ }\mu\text{m}$  is used, the channel resistance of the square cell is estimated to be about 51% of that of the stripe cell. The developed SEMOSFET has  $R_{onS}$  of  $87\text{ m}\Omega\text{cm}^2$  and  $BV$  of 5.0 kV, which has excellent switching characteristics also. Its turn-on time is 36 ns and the turn-off time is 47 ns, which are measured at  $V_{DS}$  of 30 V,  $I_{DS}$  of 60 mA,  $V_{Gm}$  of 20 V,  $V_{Gp}$  of 2 V and room temperature. Since these switching speeds are less than 1/50 of the 4.5 kV Si-IGBT, SEMOSFET has drastically lower switching power loss as compared with the Si-IGBT.

### 3.2 5.3 kV SEJFET [9, 10]

The SEJFET (Static Expansion Junction FET) is developed by using the similar device concept with SEMOSFET except the gate structure. Figure 13 shows its cross-sectional structure, whose  $n^-$  epitaxial layer thickness is  $45\text{ }\mu\text{m}$ , and a doping density is about  $9 \times 10^{14}\text{ cm}^{-3}$ . Figure 14 shows a top view of the developed SEJFET. A chip size is  $1.7\text{ mm} \times 1.7\text{ mm}$  and an active area is  $4.45 \times 10^{-3}\text{ cm}^2$ . SEJFET has a square cell pattern which has the channel width of about 1.3 times greater than that of a stripe cell pattern.

The developed SEJFET has the shallow mesa JTE as the termination also and has  $BV$  of greater than 5.3 kV. At less than 5.3 kV, the leakage current

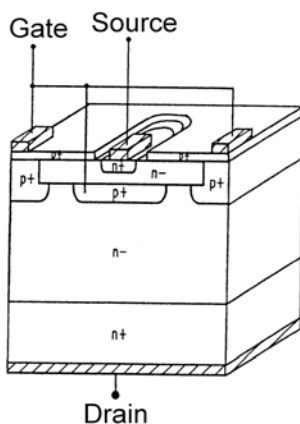


**Fig. 13.** Cross-sectional structure of 5.3 kV 4H-SiC SEJFET

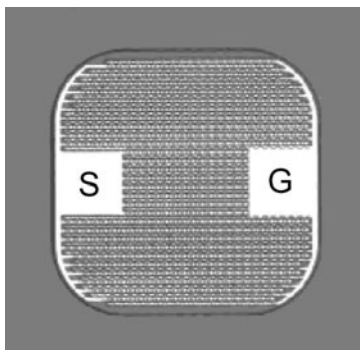


**Fig. 14.** Top view of 5.3 kV 4H-SiC SEJFET

is very low, being less than  $3.4 \times 10^{-5}$  A/cm<sup>2</sup>. Figure 15 shows its output characteristics. The threshold voltage is 1.0 V. The expansion of the channel region appears at a positive gate bias of greater than 1.5 V and reduces both the lateral and vertical channel resistances remarkably. At a positive gate bias of 5 V, its  $R_{\text{onS}}$  at  $V_{\text{DS}}$  of 1 V becomes only 69 mΩcm<sup>2</sup>. The figure of merit  $BV^2/R_{\text{onS}}$  is 407 MW/cm<sup>2</sup>. This value is the largest among reported normally-off FETs.

SEJFET has excellent switching characteristics, which are measured at  $V_{\text{DS}}$  of 30 V,  $I_{\text{DS}}$  of 60 mA,  $V_{\text{GS}}$  of 5 V and the room temperature. Its turn-on time is 20 ns. The turn-on delay time and the rise time are 7 ns and 13 ns respectively. The turn-off time is 47 ns. The turn-off delay time is 7 ns and the fall time is 40 ns, respectively.

Figure 16 shows the trade-off relationships between  $BV$  and  $R_{\text{onS}}$  of the main reported FET. SEMOSFET and SEJFET have the excellent relation-

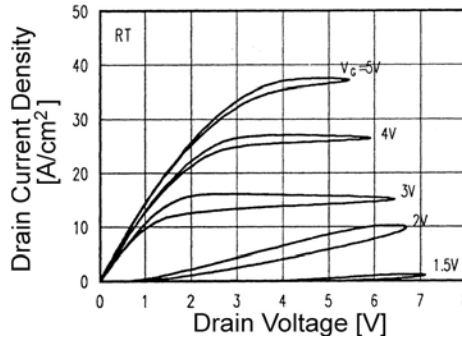


Fig. 15. Output characteristics of 5.3 kV 4H-SiC SEJFET

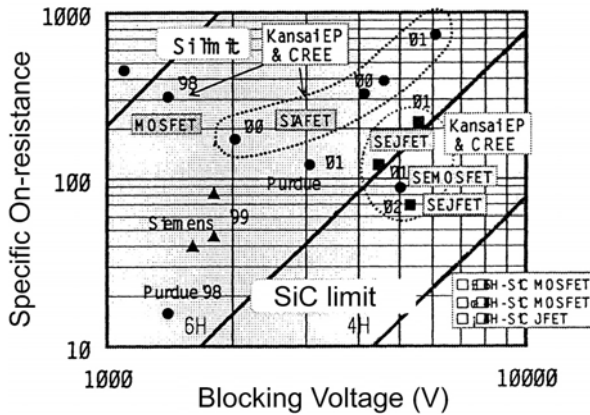


Fig. 16. Trade-off relationships between  $BV$  and  $R_{ons}$  of main reported FETs

ships and have  $R_{ons}$  of less than  $1/140$  and  $1/230$  of the theoretical  $R_{ons}$  limit of Si-MOSFET for their blocking voltage respectively.

## 4 High Voltage High Current SiC Module

Because of many SiC crystal defects such as micropipes and stacking faults, the chip of SiC devices is limited to very small size and its current capability becomes very small for practical applications. To increase the current capability, the SiC modules are effective. A few modules such as SiC pressure contact flat package module [13], Si-IGBT & SiC-diode combination module [14] and a direct bonding copper substrate module [15] have been developed. Hereinafter, our approaches for electric power applications are introduced, which are aimed at using under high temperature of more than  $250^{\circ}\text{C}$  in order to make heat sink simple and compact.

#### 4.1 Module Design and Fabrication

Figure 17 shows a top and a cross-sectional structure of a designed pressure contact flat package diode module, which includes 5 diode chips [13]. Both cathode and anode electrodes are composed of copper, and intermediate electrodes are composed of molybdenum which acts for reduction of the thermal expansion coefficient difference between SiC and copper electrodes. Spacers are for accurate chip arrangement and are composed of ceramics.

Figure 18 shows the developed diode module, which has 105 mm in diameter and 36 mm in height. Since the module is developed for high voltage SiC transistor modules, it has five gate terminals. The module is designed to be used at temperatures of higher than 300°C in an air atmosphere, therefore, the surfaces of the copper electrodes are coated to reduce their oxidation. Furthermore, the module structure is optimized to avoid the destruction by the thermal expansion and the mounting force needed for good electrical contact.

The fabricated modules has been tested under the high temperature and high mounting force, and has been confirmed that the module does not get oxidized even at 500°C in the air and is not warped at the mounting force of 2 ton.

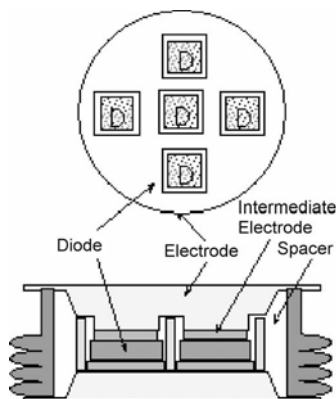


**Fig. 17.** Cross-sectional structure of high temperature pressure contact flat package module



**Fig. 18.** Developed 3 kV 600 A 4H-SiC diode module

## 4.2 Diode Module Characteristics [13]

Figure 19 shows forward output characteristics of a module with 5 diode chips. The size of the diode chip is  $6\text{ mm} \times 6\text{ mm}$  and its  $V_F$  is  $5.67\text{ V}$  at  $100\text{ A}$  and its  $BV$  is  $5.0\text{ kV}$  typically. The developed module has  $V_F$  of  $4.43\text{ V}$  at  $600\text{ A}$  and  $150^\circ\text{C}$ . Its  $T_j$  is estimated to be more than  $300^\circ\text{C}$ .  $V_F$  measurements over  $150^\circ\text{C}$  are impossible due to limitations of our measurement tools. The blocking voltage of the module is  $3.1\text{ kV}$ .

Figure 20 shows the temperature dependence of its reverse characteristics. The leakage current increases with increasing temperature. The leakage current density at room temperature and  $300^\circ\text{C}$  are  $2 \times 10^{-4}\text{ A/cm}^2$  and  $3 \times 10^{-3}\text{ A/cm}^2$  at  $3\text{ kV}$ , respectively.

Figure 21 shows turn-off waveforms of the module at  $500\text{ V}$ ,  $600\text{ A}$ ,  $1200\text{ A}/\mu\text{s}$  and  $150^\circ\text{C}$ .  $t_{rr}$ , and  $Q_{rr}$  are  $330\text{ ns}$  and  $33\text{ }\mu\text{C}$ , respectively, which are about  $1/10$  of those of  $4.5\text{ kV}$   $200\text{--}600\text{ A}$  Si diodes. Hence, this SiC diode module can reduce the switching loss drastically.

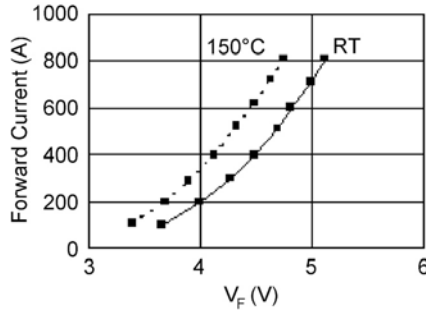


Fig. 19. Forward output characteristics of 3 kV 600 A diode module

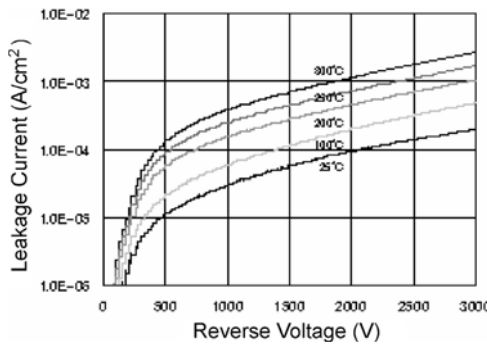
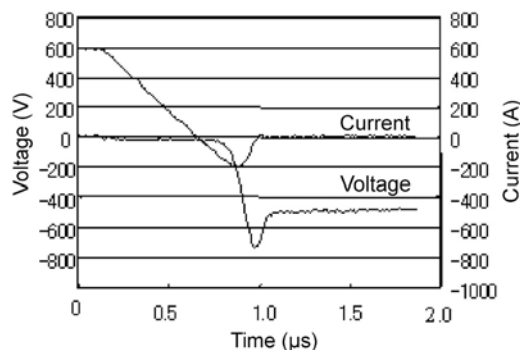


Fig. 20. Temperature dependence of reverse output



**Fig. 21.** Turn-off waveforms of 3 kV, 600 A 4H-SiC diode module at 150°C

## 5 Conclusion

High voltage 4H-SiC devices have big impacts for the reduction of both power loss and valve volume in many kinds of large electric power conversion equipment. As the fly-wheeling diodes, high voltage diodes such as 4.5 kV SBD, 3.7 kV JBS and 6.2–19.3 kV *pn* diodes were developed. The developed SiC SBD and JBS diodes have low  $R_{\text{onS}}$  of less than 1/420 and 1/190 as compared with the Si SBDs with the same  $BV$ , therefore, their power loss can be reduced drastically. Since the developed SiC *pn* diodes have short  $t_{\text{tr}}$  of less than 1/10 and small  $Q_{\text{tr}}$  of less than 1/100 as compared with the Si high speed diodes with the same  $BV$ , their switching loss can be reduced drastically. As the switching devices, 4.5 kV 387 mΩcm<sup>2</sup> SIAFET, 5 kV 87 mΩcm<sup>2</sup> SEMOSFET and 5.3 kV 69 mΩcm<sup>2</sup> SEJFET were developed, which have low  $R_{\text{onS}}$  of less than 1/25, 1/140 and 1/230 as compared with Si-MOSFETs with same  $BV$  respectively. The current capabilities of these developed devices are limited to small value because of many crystal defects. In order to increase the current capability, high temperature pressure contact flat package module technology was developed and 3 kV 600 A SiC *pn* diode module was demonstrated, which can operate in the air atmosphere of 300°C.

## References

1. Y. Sugawara: Trans. of Electronics, Information and Communication Engineers Japan, Vol. J81-C-II, p. 8 (1998); Electronics and Communications in Japan by John Wiley & Sons, Vol. 82, p. 36 (1999)
2. T. Hayashi, K. Asano, D. Takayama, Y. Kobayashi, R. Saitou, Y. Sugawara: Annual Meeting of Japan Soc. of Appl. Phys., 29a-ZR-10, p. 430 (2002)
3. R. Singh, J.A. Cooper, M.R. Mellon, T.P. Chow, J.W. Palmour: IEEE Trans. Electron Devices **49**, 665 (2002)
4. K. Asano, T. Hayasdhi, R. Saito, Y. Sugawara: Proc. of 12th ISPSD, p. 97 (2000)

5. Y. Sugawara , K. Asano, R. Singh, J.W. Palmour: Proc. ICSCRM, p. 1371 (1999)
6. Y. Sugawara, D. Takayama, K. Asano. R. Singh, J.W .Palmour, T. Hayasdhi: Proc. of 13th ISPSD, p. 27 (2001)
7. Y. Sugawara, K. Asano, R. Singh, J.W. Palmour, D. Takayama: Proc. of 12th ISPSD, p. 105 (2000)
8. Y. Sugawara, K. Asano, R. Singh, J.W. Palmour, D. Takayama: Proc. ICSCRM, p. 1199 (2001)
9. K. Asano, Y. Sugawara, S.H. Ryu, R. Singh, J.W. Palmour, T. Hayashi, D. Takayama: Proc. of 13th ISPSD, p. 23 (2001)
10. K. Asano, Y. Sugawara, T. Hayashi, S.H. Ryu, R. Singh, J.W. Palmour, D. Takayama: Proc.of 14th ISPSD, p. 61 (2002)
11. S.H. Ryu, A.K. Agarwal, J.W. Palmour, M.E. Levinshtein: Proc. of 13th ISPSD, p. 37 (2001)
12. I.A. Khan, J.A. Cooper, M.A. Capano, T.I. Smith, J.R. Williams: Proc. of 14th ISPSD, p. 157 (2002)
13. Y. Sugawara, D. Takayama, K. Asano. R. Singh, H. Kodama, S. Ogata, T. Hayasdhi: Proc. of 14th ISPSD, p. 245 (2002)
14. H. Lendenmann, A. Mukhitdinov, F. Dahlquist, H. Bleichner, M. Irwin: Proc. of 13th ISPSD, p. 31 (2001)
15. S. Seahadri, W.B. Hall, J.C. Kotvas, P.A. Sanger: Proc. ICSCRM, p. 1403 (1999)

# Power MOSFETs in 4H-SiC: Device Design and Technology

A. Agarwal, S.-H. Ryu, and J. Palmour

## 1 Introduction

Silicon (Si) power metal-oxide-semiconductor field-effect transistors (MOSFETs) are widely used in audio and radio frequency (rf) amplifiers, switch mode power supplies (SMPS), power factor correction (PFC) circuits, lamp ballasts and many types of control circuits. Power MOSFETs have several desirable characteristics such as (a) high switching speed due to the absence of minority carrier storage, (b) voltage controlled input, and (c) ease of paralleling due to the negative temperature coefficient of the on-state current. Power MOSFETs have largely replaced bipolar junction transistors (BJTs) in medium power (<20 kW) applications requiring high switching speeds (>10 kHz). In contrast to a power MOSFET, a power BJT requires a large continuous base current to turn it on and keep it on. The base current requirement can be as high as 25% of the collector current. It is difficult to parallel power BJTs due to the fact that the on-state current increases with temperature making the current sharing between different transistors unequal. Furthermore, the switching speed of BJTs is much slower than power MOSFETs due to the storage of minority carriers in the base and collector regions. Thus, the switching losses become prohibitively high at switching frequencies higher than 10–20 kHz.

Si power MOSFETs are available up to about 1200 V. However, for ratings above 200–300 V, the specific on-resistance becomes very high and a very large chip area is required to obtain an adequate current rating. For example, 200 V Si MOSFETs can be purchased as a single unit up to about 100 A whereas a 1200 V device is generally available for <10 A current rating. Therefore, above 600 V, it is customary to use Si insulated gate bipolar transistors (IGBTs), which are available in large current ratings but are extremely slow due to the minority carrier storage. In contrast, SiC power MOSFETs can be developed with voltage ratings up to 3000 V with a specific on-resistance similar to that of a 300 V Si MOSFET. Therefore, it will be advantageous to replace a Si IGBT with a SiC power MOSFET up to about 3 kV in applications requiring faster switching speed and lower switching losses.

## 2 Device Structures and Operation of Power MOSFETs

Figure 1 illustrates the two basic designs used for power MOSFETs in SiC. The UMOS structure was the first one to be realized by Palmour et al. in SiC [1]. Subsequently, it was developed by a number of groups [2]–[7] culminating in the first report of a 1600 V UMOSFET in 1997 by Agarwal et al. [8]. However, the UMOSFET suffers from several practical problems. First, the quality of the SiC/SiO<sub>2</sub> interface along the reactive ion-etched sidewalls of the trench is extremely poor due to the surface roughness and the damage done by the reactive ion etch (RIE). These factors contribute to a lower inversion layer mobility on the sidewalls.

The sharp corners of the trench result in electric field crowding under a high voltage on the drain with source and gate terminals at ground potential. The electric field at the corners can exceed 2 MV/cm which results in  $>5$  MV/cm field in the gate oxide – significantly higher than the 2–3 MV/cm recommended for longterm reliable operation. Furthermore, the thermal oxide tends to grow approximately 5 times faster on the sidewalls as compared to the Si-face which results in a very thin oxide at the bottom surface of the trench and at the top surface of the  $n^+$  source. This is of great concern under the on-state when a gate voltage of 15–20 V is applied on the gate *wrt.* the source terminal. The electric field in the thin regions of the gate oxide can easily exceed 2 MV/cm which is the maximum recommended value in the oxide under positive gate bias (on-state). This problem can be avoided with a deposited oxide layer provided an adequate inversion layer electron mobility can be achieved.

The first two problems were solved by Tan et al. in 1998 [9] with a very elegant structure shown in Fig. 2. The first feature of this structure is a self-aligned  $p$ -type implant in the bottom of the gate trench. The  $p$ -type layer is grounded (not shown) and shields the trench corners and the trench oxide from high fields in the blocking state. The second feature is a thin  $n$ -type

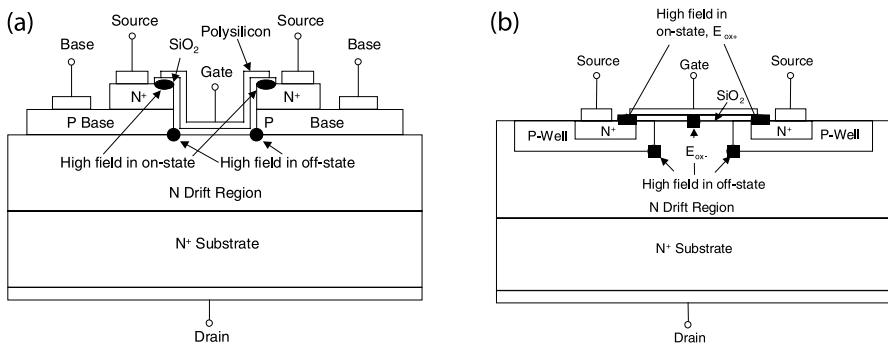


**Fig. 1.** Cross-sections of (a) UMOS and (b) DMOS power transistors in SiC

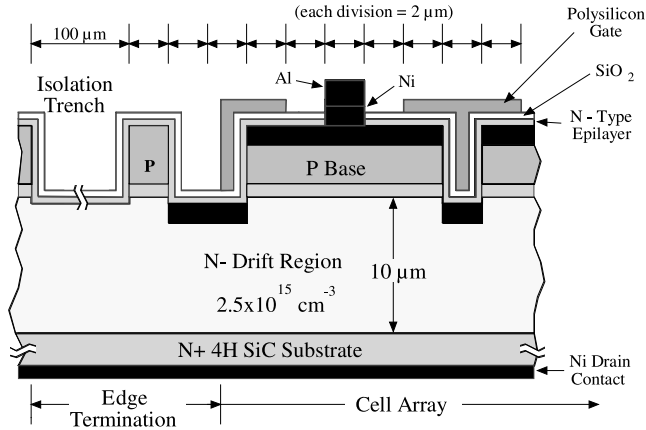


**Fig. 2.** Cross-section of the trench-oxide protected UMOFET introduced in 1998 [9]

current spreading layer formed between the blocking layer and the  $p$ -type base during the epilayer growth. This layer is designed such that it fully depletes in the blocking state and thus has negligible effect on the blocking voltage. In the on-state, it provides current spreading, thereby reducing current crowding at the trench corners. The third feature is an  $n$ -type epilayer formed by epi-growth after the trench etch. This provides the counter-doping and enhances the effective channel electron mobility while reducing the threshold voltage [7, 10, 11]. With this structure, it was possible to obtain a blocking voltage of 1400 V, which is approximately 72% of the theoretical parallel plate voltage for the 10  $\mu\text{m}$  drift layer, and a record low on-resistance of  $15.7 \text{ m}\Omega\text{-cm}^2$ .

Although the basic UMOFET in SiC has evolved into an advanced structure with a successful resolution of many problems, several issues still remain: (1) The electric field in the gate oxide over the source and bottom trench corners is very high when the transistor is in the on-state leading to oxide reliability concerns as discussed later, and (2) it is very difficult to manufacture these devices with any useful yield due to the poor doping control during epi-regrowth of very thin films used for  $n$ -type current spreading layer and the counter-doped channel layer. The main advantage is of course that the cells can be packed very tightly in a given area resulting in a reduction of the overall on-resistance.

The second type of the structure, called a DMOSFET, has also been developed with some success [12]–[21]. In Si, the  $p$ -type channel and  $n^+$  source regions of DMOSFET are formed by double diffusion of  $p$  and  $n$ -type dopants through a single oxide window. This process is difficult in SiC due to the small diffusion coefficients of impurities in SiC. However, Suvorov et al. have succeeded in making the DMOS structure by diffusing Boron (B) at  $1600^\circ\text{C}$  [16]. Nevertheless, separate implants for  $p$ -well and  $n^+$  source seem more practical.

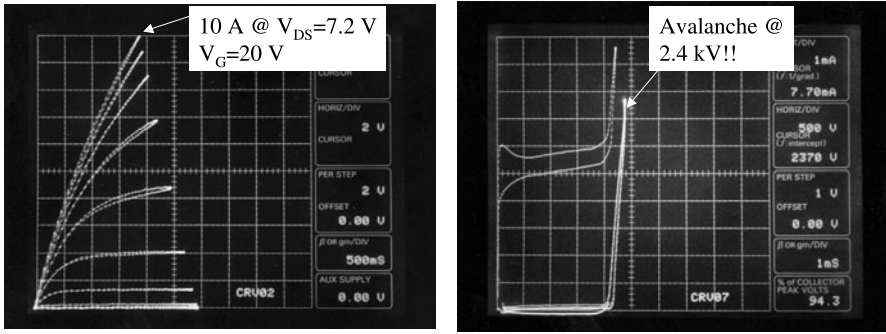


**Fig. 3.**  $I$ - $V$  characteristics of the 2.4 kV, 10 A 4H-SiC DMOSFET [21]

In the DMOSFET structure, the inversion layer electrons flow along the Si plane, a surface that has not been roughened by RIE. However, the DMOS structure has its own problems. The  $p$ -well,  $n^+$  and  $p^+$  body contacts have to be implanted at elevated temperature and annealed at 1600°C or higher to achieve electrical activation. During the high temperature anneal, the Si leaves the surface leaving it carbon rich and somewhat rough. This higher implant anneal temperature has been shown to result in lower inversion layer mobility [22]. The second problem with this structure has to do with the quality of the gate oxide on the implanted  $n^+$  region. The high electric field in this region, due to positive gate bias, can lead to oxide failure.

Agarwal et al. demonstrated a counter-doped 4H-SiC DMOSFET [20]. In this device, a thin  $n$ -type surface layer is introduced by ion-implantation to improve the surface mobility and reduce the threshold voltage. This is similar to the threshold adjust implant done in Si devices. The on-state  $I$ - $V$  characteristics demonstrated a maximum drain current of 10 A in an active area of 0.105 cm<sup>2</sup>. This represents a specific on-resistance of approximately 45 mΩ-cm<sup>2</sup>. This device had a threshold voltage of -2 V (normally on, accumulation mode) and showed a maximum effective channel electron mobility of 195 cm<sup>2</sup>/V-s at a gate bias of 2.5 V. This device blocked only about 350 V. Subsequently, Ryu et al. improved on this design and demonstrated a normally off device with a blocking voltage of 2.4 kV, and a specific on-resistance of 42 mΩ-cm<sup>2</sup> with 10 A capability as shown in Fig. 3 [21].

Since, of the two structures, the DMOSFET seems to be a more practical structure at this time, we will focus exclusively on this structure in the rest of this chapter.

### 3 Design of the Drift Layer

The drift layer resistance in SiC power MOSFETs can be significant depending upon the blocking voltage. The goal of the design process is to minimize the drift layer resistance for a given blocking voltage. This is gener-

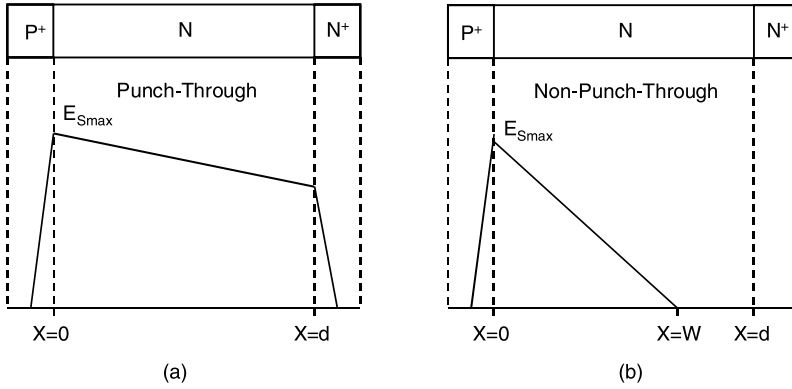


**Fig. 4.** Electric field vs. distance profile for (a) the punch-through, and (b) the non-punch-through cases

ally achieved by the “punch-through” design in which, the depletion region reaches through the  $n$ -type drift layer before the breakdown occurs. The “non-punch-through” design is the one in which the breakdown occurs before the entire drift layer is depleted. The two cases are shown in Fig. 4.

### 3.1 Punch-Through Design

In this case, the breakdown voltage,  $V_B$ , is calculated as an area under the  $E$  vs.  $x$  plot and is given by

$$V_B = E_{smax} \cdot d - \frac{qN_D d^2}{2\epsilon_s}, \quad (1)$$

where,  $E_{smax}$  is the maximum surface field in SiC, which is not to be exceeded for reliability considerations of the gate oxide,  $d$  is the drift layer thickness,  $N_D$  is the doping density in the drift layer, and  $\epsilon_s$  is the permittivity of SiC. It should be noted that  $E_{smax}$  is not the breakdown field strength,  $E_C$ , of SiC. In fact  $E_{smax}$  is much less than  $E_C$  as discussed later.

The specific on-resistance of the drift layer is simply given by

$$R_{drift} = \frac{d}{q\mu_n N_D}, \quad (2)$$

where,  $\mu_n$ , is the bulk electron mobility in the drift layer. Eliminating  $N_D$  from equations (1) and (2), we get

$$R_{drift} = \frac{d^3}{2\mu_n \epsilon_s (E_{smax} d - V_B)}. \quad (3)$$

It can be shown from equation (3) that  $R_{drift}$  is minimum when,

$$d_{\text{optimum}} = \left(\frac{3}{2}\right) \frac{V_B}{E_{s \max}} . \quad (4)$$

Thus, the minimum value of  $R_{\text{drift}}$  is given by

$$R_{\text{drift, optimum}} = \left(\frac{27}{8}\right) \frac{V_B^2}{\mu_n \epsilon_s E_{s \max}^3} . \quad (5)$$

### 3.2 Non-Punch-Through Design

In this case, the doping density in the drift layer is higher than the punch-through design. In an optimum design, the doping density and thickness of the drift layer are chosen in such a way that the electric field drops to zero at the epilayer/substrate interface when the surface electric field reaches the maximum allowed value of  $E_{s \max}$  ( $W = d$  in Fig. 4b). The optimum values of  $d$  and  $N_D$  are given by

$$d = \frac{2V_B}{E_{s \max}} , N_D = \frac{\epsilon_s E_{s \max}}{qd} . \quad (6)$$

Using equations (2) and (6), we can get an expression for  $R_{\text{drift}}$  as follows

$$R_{\text{drift}} = \frac{4V_B^2}{\mu_n \epsilon_s E_{s \max}^3} . \quad (7)$$

Comparing equations (5) and (7), we see that the  $R_{\text{drift}}$  in the punch-through design is approximately 15% smaller than the non-punch-through design. The parameters for the punch-through design have been plotted against

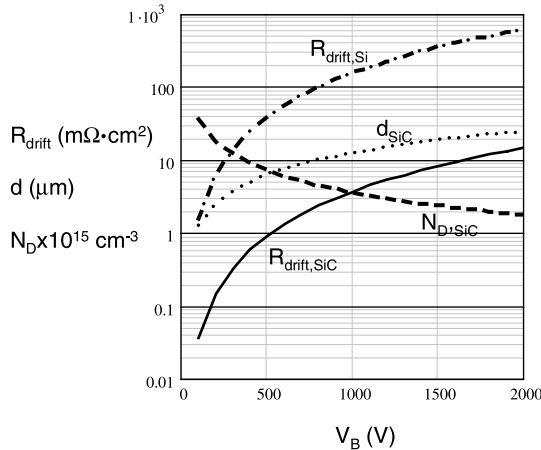


**Fig. 5.** Design curves for a punch-through design of the drift layer for 4H-SiC and Si as a function of the breakdown voltage. The following values for 4H-SiC were used:  $E_{s \max} = 1.2$  MV/cm,  $\mu_n = 600$  cm²/V·s. The values used for Si were  $E_{s \max} = 0.3$  MV/cm,  $\mu_n = 800$  cm²/V·s

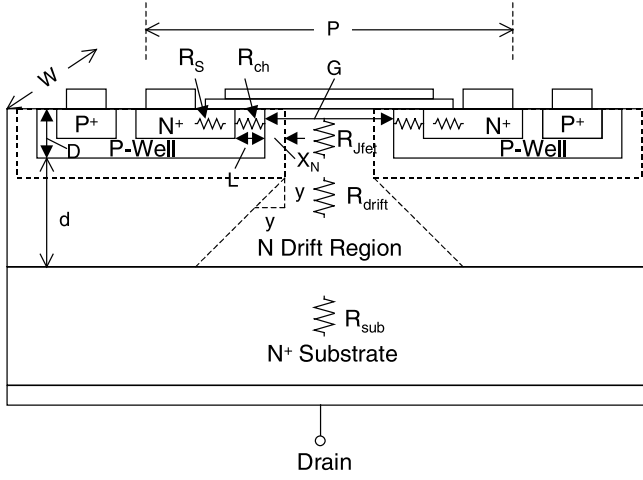


**Fig. 6.** Various contributions to the on-resistance in the DMOSFET structure

$V_B$  in Fig. 5. The maximum surface field for SiC has been assumed to be 1.2 MV/cm. The reason for assuming such a low value of  $E_{s\max}$  is the fact that the field in the oxide is approximately  $2.5E_{s\max}$  ( $\epsilon_{\text{SiC}}/\epsilon_{\text{oxide}} \approx 2.5$ ), which needs to be limited to about 3 MV/cm for long-term reliability of the gate oxide (discussed later). The plots in Fig. 6 can be used as design curves for designing the drift layer of a SiC power MOSFET. They also show that the advantage of using SiC over Si improves with breakdown voltage. For example, the drift layer resistance for 4H-SiC at 1200 V is  $\sim 6.0 \text{ m}\Omega\text{-cm}^2$  compared to  $\sim 200 \text{ m}\Omega\text{-cm}^2$  for Si.

## 4 On-Resistance

The overall on-resistance is determined by various contributions to the on-resistance as shown in Fig. 6.

### 4.1 Channel Resistance, $R_{\text{ch}}$

The channel resistance,  $R_{\text{ch}}$ , represents the resistance in the inversion layer of the MOSFET. In the linear region of operation,  $R_{\text{ch}}$  is given by

$$R_{\text{ch}} = \left( \frac{LP}{2\mu_n C_{\text{ox}}(V_g - V_T)} \right) \Omega \cdot \text{cm}^2, \quad (8)$$

where,  $L$  is the channel length,  $P$  is the cell pitch,  $\mu_n$  is the effective inversion layer electron mobility,  $C_{\text{ox}} = \epsilon_{\text{ox}}/d_{\text{ox}}$  is the oxide capacitance per unit area, and  $V_T$  is the threshold voltage. Using  $L = 2 \text{ }\mu\text{m}$ ,  $\mu_n = 30 \text{ cm}^2/\text{V}\cdot\text{s}$ ,  $\epsilon_{\text{ox}} =$

$3.9 \times 8.86 \times 10^{-14}$  F/cm,  $d_{\text{ox}} = 750$  Å,  $V_G - V_T = 10$  V, and  $P = 20$  μm, we obtain  $R_{\text{ch}} = 14.5$  mΩ-cm<sup>2</sup>. This value of  $R_{\text{ch}}$  is rather high in comparison to the drift layer resistance and should be minimized. From an inspection of (8), it is clear that the channel resistance can be decreased in a number of ways:

- a. Reduction of channel length to about 0.5 μm. This is more easily achieved in a UMOSFET structure because the channel length is defined by the epilayer thickness. It will require extremely flat wafers to consistently achieve a channel length of 0.5 μm.
- b. Increase in the channel mobility (discussed later).

## 4.2 JFET Region Resistance

The JFET region is shown in Fig. 6 for the DMOSFET structure. This region is not present in the UMOSFET structure. The JFET resistance depends on the gap between the  $p$ -wells,  $G$ , thickness of the  $p$ -well,  $D$ , doping density,  $N_D$ , of the  $n$ -type JFET region and depletion width,  $X_N$ . The forward drop,  $V_F$ , reverse biases the  $p$ -well *wrt.* the  $n$ -type JFET region and results in the depletion width,  $X_N$ , which restricts the current flow through a narrow neutral part of the JFET gap,  $G$ . Therefore, the JFET region resistance increases with the forward drop.  $X_N$  may be calculated by using the following expression:

$$X_N = \sqrt{\frac{2(V_{\text{bi}} - V_F)\epsilon_s}{qN_D}}, \quad (9)$$

where,  $V_{\text{bi}}$  is the built-in voltage of about 3 V. The JFET resistance is given by

$$R_{\text{JFET}} = \left[ \frac{1}{q\mu_n N_D} \left( \frac{D + X_N}{G - 2X_N} \right) \right] P, \quad (10)$$

where,  $\mu_n$  is the bulk electron mobility in the JFET region.

Assuming,  $\mu_n = 600$  cm<sup>2</sup>/V-s,  $N_D = 3 \times 10^{15}$  cm<sup>-3</sup> for a 1200 V design,  $D = 0.5 \times 10^{-4}$  cm,  $G = 5 \times 10^{-4}$  cm, pitch ( $P$ ) =  $20 \times 10^{-4}$  cm,  $V_{\text{bi}} = 3$  V and  $V_F = 2$  V, we get  $X_N = 1.36 \times 10^{-4}$  cm and  $R_{\text{JFET}} = 5.7$  mΩ-cm<sup>2</sup>. This value of  $R_{\text{JFET}}$  is quite significant in comparison to the drift layer resistance and the channel resistance. One possible way to reduce the JFET resistance would be to increase the doping density in the JFET region through ion-implantation by about a factor of 2 to 3. However, one should be careful about not increasing the doping too much otherwise, the breakdown voltage would reduce. Another possibility would be to increase the JFET gap,  $G$ . However, as shown later, the electric field in the gate oxide increases with an increase in  $G$ . The maximum value of  $G$  should be selected consistent with a maximum permissible electric field in the gate oxide.

### 4.3 Drift Layer Resistance

The drift layer resistance calculated in the previous section represents an ideal value. In practice, the current spreads from the JFET region into the drift layer at about  $45^\circ$  angle as shown in Fig. 6. The current spreads from a cross-section of  $W(G - 2X_N)$ , where  $W$  is the width of the cell normal to the plane of the paper. At a depth  $y$  below the  $p$ -well, the cross-section is given by  $W(G - 2X_N + 2y)$ . Therefore, the drift region resistance is given by:

$$R_D = PW \int_0^d \frac{1}{q\mu_n N_D} \frac{dy}{W(G - 2X_N + 2y)}$$

$$= \frac{P}{2q\mu_n N_D} \ln \left( \frac{G - 2X_N + 2d}{G - 2X_N} \right) \Omega \cdot \text{cm}^2. \quad (11)$$

Using  $\mu_n = 600 \text{ cm}^2/\text{V-s}$ ,  $P = 20 \text{ } \mu\text{m}$ ,  $N_D = 3 \times 10^{15} \text{ cm}^{-3}$  (for a 1200 V design),  $d = 14 \text{ } \mu\text{m}$ ,  $G = 5 \text{ } \mu\text{m}$ ,  $X_N = 1.36 \text{ } \mu\text{m}$ , we get  $R_D = 9 \text{ m}\Omega\text{-cm}^2$ .

Comparing the above number with the ideal drift layer resistance,  $R_{D,\text{ideal}} = d/q\mu_n N_D = 4.86 \text{ m}\Omega\text{-cm}^2$ , we see that the actual drift layer resistance is almost twice the ideal value due to the spreading effect. The above equation applies as long as the spreading cones from two adjacent cells do not touch each other. If they do (as in the numerical example above), then the actual value of the resistance will be higher than what is predicted by the above equation.

### 4.4 Optimization of the JFET Region

Once the drift layer doping and thickness have been selected for a given breakdown voltage, the next task is to choose an appropriate JFET gap.

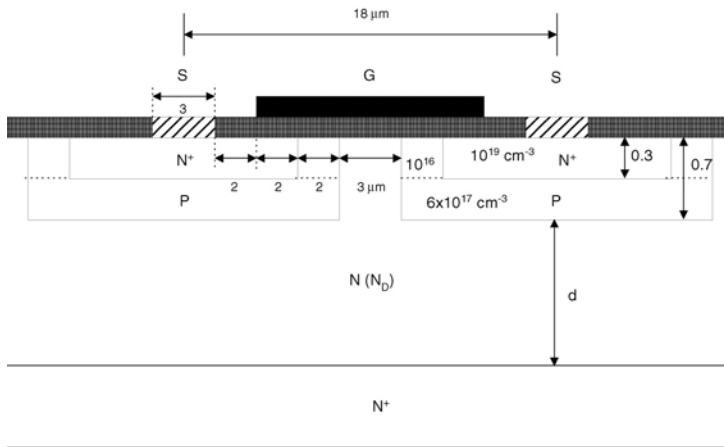


**Fig. 7.** Cross-section of the DMOS structure used for 2D-device simulation

An example is shown in Fig. 7, which illustrates a device cross-section for a 2000 V, 4H-SiC MOSFET. The doping density is chosen as  $3 \times 10^{15} \text{ cm}^{-3}$  and drift layer thickness as 25  $\mu\text{m}$ .

The 2D-Simulations were done to optimize the  $p$ -well spacing in the vertical DMOSFET structure shown in Fig. 9. The cell pitch of the structure is 18  $\mu\text{m}$ . For the sake of clarity, we have not shown the  $p^+$  contacts to the  $p$ -well. In the real structure, the  $p^+$  contacts are placed within the  $n^+$  implants along the  $z$ -axis (width of the cell) at regular intervals and are shorted to the source by a common contact. The  $p$ -well is designed with a retrograde profile with higher doping near the bottom to block the voltage and lower doping near the surface to reduce the threshold voltage.

The results of the 2-D simulations are summarized in Figs. 8–9 for the 2000 V, 4H-SiC MOSFET. The relevant parameters are listed in the figure captions. The electric field in the oxide is maximum in the center of the JFET gap. Figure 8 shows the variation of the oxide field vs. the gap between the  $p$ -wells. The oxide field increases with an increase in the gap and reaches  $\sim 3 \text{ MV/cm}$  for a gap of 4  $\mu\text{m}$ . In view of the long-term reliability issues with the oxide, the gap dimension should not exceed 5  $\mu\text{m}$ . Figure 9 shows the variation of current density vs. the gap. Again, the current density increases rapidly up to a gap of 3  $\mu\text{m}$  and then saturates. Thus, from current density considerations, the gap dimension of 4 to 5  $\mu\text{m}$  is appropriate.

The key question which needs to be answered before we can decide on the JFET gap dimension relates to the maximum electric field the gate oxide can tolerate at a given operating temperature under blocking state (negative gate bias) for a reliable operation. Similarly, before we decide the gate oxide thickness and the maximum gate voltage, we must decide the maximum electric field the gate oxide can withstand at a given temperature under on-state (positive gate bias) for longterm reliability. Therefore, we turn to the question of reliability next.

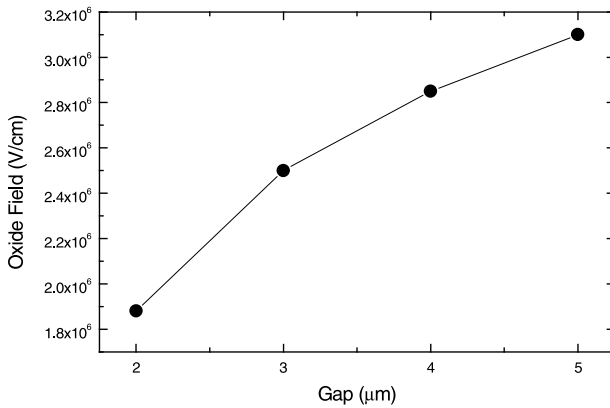


**Fig. 8.** Oxide field vs.  $p$ -well spacing for the 2000 V, 4H-SiC MOSFET biased in the off-state with  $V_G = 0 \text{ V}$  and  $V_D = 2000 \text{ V}$

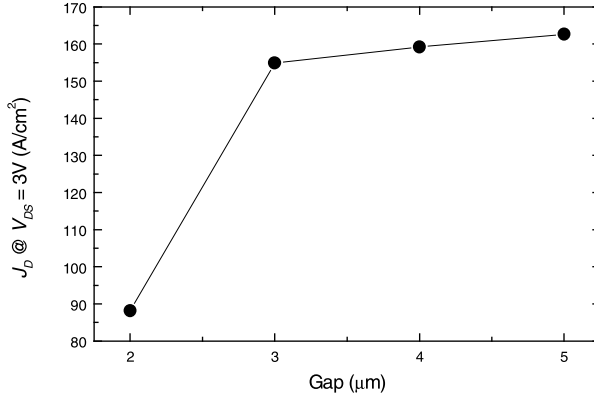


**Fig. 9.** Current density vs.  $p$ -well spacing for the 2000 V, 4H-SiC MOSFET biased in the on-state with  $V_G = 10$  V and  $V_D = 3$  V.  $\mu_{neff} = 25$  cm<sup>2</sup>/V-s and  $\mu_{bulk} = 600$  cm<sup>2</sup>/V-s along the vertical direction have been assumed

## 5 Reliability of the Gate Dielectric

Long-term reliability of the gate oxide in a 4H-SiC MOSFET is crucial for it to be a useful commercial device. This becomes even more important for applications where the oxide is subject to high electric field at high temperatures. A comprehensive study of MOS reliability has not been conducted in SiC. However, some initial studies have been conducted which point to some important considerations in the design of the power MOSFET which are not present in the Si technology [23]. Basically, the maximum electric field in the gate oxide, in a 4H-SiC/SiO<sub>2</sub> system, must be kept below some critical value to insure long-term device reliability. This critical value of electric field is temperature dependent and different for on and off conditions of the MOSFET.

### 5.1 On-State Under Positive Gate Bias

As shown in Fig. 1, the electric field under positive gate bias,  $E_{ox+}$ , in the gate insulator overlapping the  $n^+$  source regions can be very high as source is grounded and +15 V is applied to the gate. Under on-state, the drain is at a relatively low voltage of 1–2 V. This field is also enhanced by the presence of sharp corners in the UMOSFET or any topology in the oxide over the source since the oxide grows at a faster rate in heavily implanted regions. The presence of high electric field induces Fowler-Nordheim (F-N) injection of electrons from the conduction band of  $n^+$  SiC into the gate oxide. The energy band diagram showing the conduction and valence band line-up for Si, 6H-, 4H-SiC, and SiO<sub>2</sub> is shown in Fig. 10 [23]. The barrier determining the F-N injection of electrons is measured from the conduction band edge

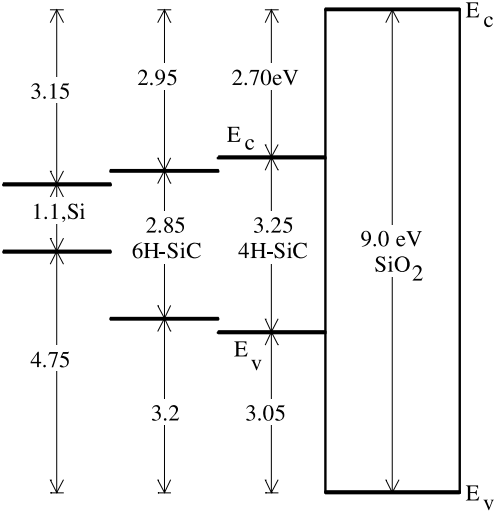


**Fig. 10.** Energy band diagram of Si, 6H-SiC, 4H-SiC, and SiO<sub>2</sub> illustrating barrier heights for F-N electron injection from semiconductor into the gate oxide

of SiC to the conduction band edge of SiO<sub>2</sub>. This barrier was measured by F-N and internal photo-emission studies [23]–[25]. It is evident that the 4H-SiC/SiO<sub>2</sub> system has the lowest barrier height and is therefore expected to have the highest F-N injection at a given electric field. This is unfortunate as 4H-SiC is the material of choice because of its four to five times higher electron mobility along the *c*-axis as compared to 6H-SiC.

The energy band diagram under positive gate bias is shown in Fig. 11. Since the barrier for electrons in the conduction band of *n*<sup>+</sup> 4H-SiC is only 2.7 eV compared to 3.15 eV for Si, the F-N tunneling distance is only 135 Å

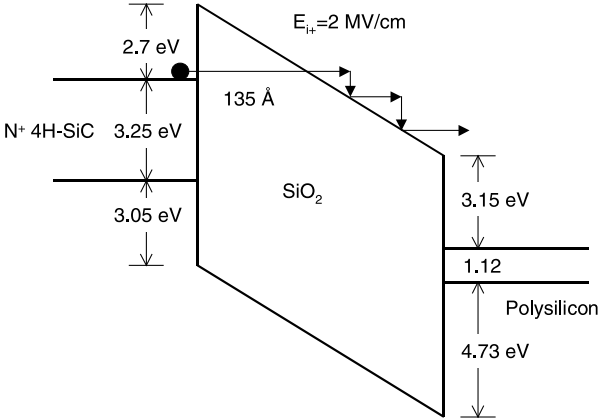


**Fig. 11.** Energy band diagram of *n*<sup>+</sup> 4H-SiC/SiO<sub>2</sub>/polysilicon system under positive gate bias (on-state of the power MOSFET)

**Table 1.** The effective barrier heights, extracted from F-N measurements, for Si, 6H-SiC and 4H-SiC at different temperatures [23]

$T$ ( $^{\circ}\text{C}$ )	$\Phi_{\text{eff}}$ (V)		
	Si	6H-SiC	4H-SiC
25	3.10	2.69	2.43
150	3.07	2.38	2.11
325	3.02	2.03	1.76

at  $E_{\text{ox}+} = 2$  MV/cm. At elevated temperature, the F-N current increases due to temperature induced statistical spreading of energy of electrons in the conduction band. The broadening of the electron distribution allows a larger fraction of electrons to tunnel through the thinner (upper) part of the triangular barrier. This phenomenon is well understood in Si MOS devices [26]. The effective barrier heights, extracted from F-N measurements, for Si, 6H-SiC and 4H-SiC at different temperatures are given in Table 1 [23]. It should be noted that the effective barrier height, extracted from F-N measurements at high electric fields, is lower than the barrier height extracted from internal photo-emission studies shown in Fig. 11. From data in Table 1, it can be concluded that the effective barrier height at elevated temperature is much lower than the room temperature value for both 6H-SiC, and 4H-SiC whereas the effective barrier height in Si remains relatively constant up to  $350^{\circ}\text{C}$ . The reduction of effective barrier height at higher operating temperatures raises serious concerns about the long-term reliability of SiC MOS devices. Thus, a maximum limit on the electric field under the on-condition of the power MOSFET structures should be established for a given junction temperature and given projected life of the device. This maximum electric field will limit the inversion layer charge density and hence the resistance of the inversion layer,  $R_{\text{ch}}$ .

In order to determine a maximum limit on the electric field across the gate oxide, Time Dependent Dielectric Breakdown (TDDB) measurements are needed. However, it is clear that the maximum electric field in the 4H-SiC MOS system should be lower than that in 6H-SiC, which in turn, should be lower than the maximum value allowed in a Si MOS system. It should be further reduced for operation at higher junction temperature.

The TDDB measurements were done by Maranowski et al. [27] on 6H-SiC and Das et al. [28] on 4H-SiC. A sample data from [28] on 4H-SiC is shown in Fig. 14. Here, the mean-time-to-failure (MTTF) is plotted as a function of the electric field in the gate oxide for different temperatures. The data is actually taken at high fields and is extrapolated to lower fields. A MOS capacitor is considered failed when the leakage current exceeds  $10\text{ }\mu\text{A}$ . If we consider an MTTF of 1000 years as a reasonable insurance for reliability, then the data in Fig. 12 gives us the maximum positive electric field,  $E_{\text{ox}+}$

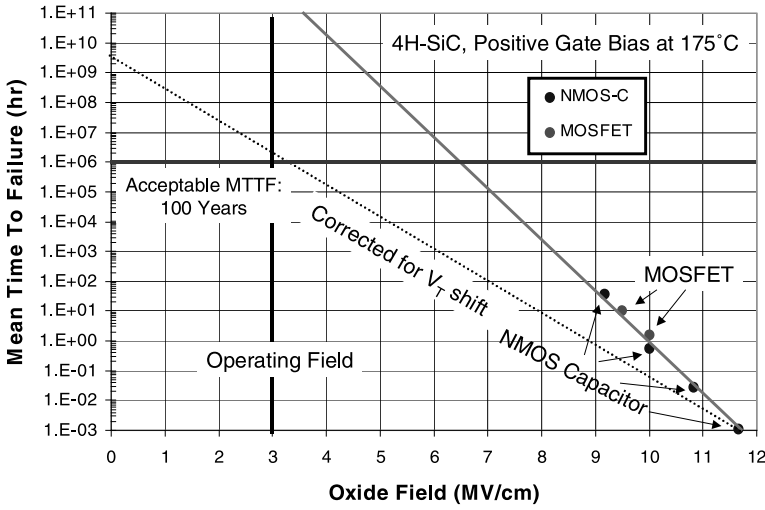


**Fig. 12.** TDDDB data for  $n$  4H-SiC/SiO<sub>2</sub> system from [28]

for each temperature which should not be exceeded during the on-state of the MOSFET. The electric field in the oxide can be related to the gate voltage by the following expression:

$$E_{\text{ox}+} = (V_G - \phi_{\text{ms}})/t_{\text{ox}} , \quad (12)$$

where,  $\phi_{\text{ms}}$  is the metal-semiconductor work-function difference and  $t_{\text{ox}}$  is the oxide thickness. Considering  $\phi_{\text{ms}} = 0.45$  V for  $n^+$  polysilicon and  $n^+$  4H-SiC and  $E_{\text{ox}+} = 2$  MV/cm and  $V_G = 15$  V, the oxide thickness should be about 725 Å.

## 5.2 Off-State Under Negative Gate Bias

Under off-state, both the source and gate terminals are kept at ground potential while a large voltage is applied at the drain terminal. As shown in Fig. 1, the electric field,  $E_{\text{ox}-}$ , is highest in the gate insulator around the bottom corner of the trench in a UMOS structure or between the two  $p$ -wells at the SiC/SiO<sub>2</sub> interface. Under this condition, F-N injection of electrons may occur from the gate electrode, into the oxide film as shown in Fig. 13. The barrier for electron injection from  $n^+$  polysilicon is around 3.15 eV. Again, the TDDDB studies are needed to establish the temperature dependent maximum electric field in the oxide,  $E_{\text{ox}-}$ . It has been suggested that for a given junction temperature of 175°C,  $E_{\text{ox}-}$ , should not exceed 3 MV/cm to ensure >100 years of life-time [28]. The field in the SiC is given by

$$E_{\text{SiC}} = E_{\text{ox}-} \frac{\varepsilon_{\text{r,ox}}}{\varepsilon_{\text{r,SiC}}} = 3 \times \frac{3.9}{10} \text{ MV/cm} \approx 1.2 \text{ MV/cm} . \quad (13)$$

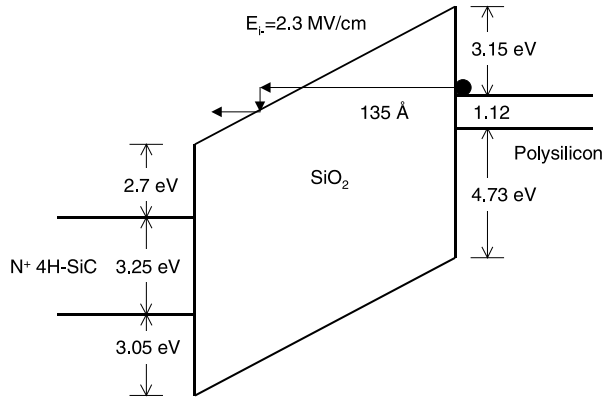


**Fig. 13.** Energy band diagram of  $n^+$  4H-SiC/SiO<sub>2</sub>/polysilicon system under negative gate bias (off-state of the power MOSFET)

The above value of 1.2 MV/cm is well below the breakdown field strength of SiC ( $\sim 3$  MV/cm). Such a low value of field will drastically increase the drift layer resistance for a given blocking voltage. The value of  $E_{ox-}$  should be appropriately reduced for higher temperature operation. It is clear that the performance is limited by the insulator reliability rather than the intrinsic SiC properties. The reliability issues become more severe at elevated temperatures and thus it is difficult to take advantage of low leakage currents in SiC at high operating temperatures.

## 6 Design of the MOSFET Structure: Various Considerations

We have already examined the design of the drift layer, the JFET gap and the selection of gate oxide thickness in previous sections. The next step is to design the  $p$ -well doping and the cell layout. In order to decide on the  $p$ -well doping, we need to consider the bipolar second breakdown [29].

The bipolar second breakdown effects determine the Safe Operating Area (SOA) of the device. When the device is operating under high voltage and high current at the same time, it is susceptible to destructive failure due to excessive thermal dissipation and the phenomena of second breakdown.

The bipolar second breakdown originates from the parasitic  $npn$  bipolar transistor shown in Fig. 14. Normally, the breakdown voltage,  $BV$ , is supported by the  $p$ -well/ $n$ -drift layer  $pn$  junction and is equal to the common base breakdown voltage,  $BV_{CBO}$ , of the bipolar transistor. As discussed before, the electric field is highest at and around point “y” in the  $p$ -well where the avalanche process is initiated. As a result, electron-hole pairs are generated. The generated electrons are collected by the drain whereas the holes

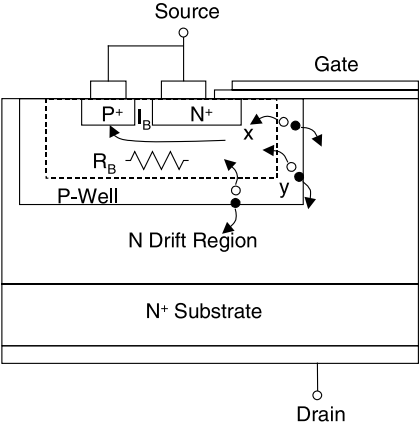


**Fig. 14.** The origin of bipolar second breakdown from the parasitic *npn* bipolar transistor

flow towards the  $p^+$  contact through the base resistance,  $R_B$ , of the undepleted base region. If the base resistance is high, then the voltage drop along the  $p$ -well forward biases the  $n^+$  emitter at and around point “x”. When the forward bias at point “x” exceeds 2.7 V, the  $n^+$  emitter begins to inject electrons which transport through the thin neutral base and are collected by the  $n$ -drift layer acting like a collector. Thus the breakdown voltage of the device reduces to the common emitter breakdown voltage,  $BV_{CEO}$ , which is normally less than the  $BV_{CBO}$  depending upon the current gain of the parasitic bipolar transistor. An example of this effect is shown in Fig. 15 (left), where the breakdown characteristics of a 4H-SiC power MOSFET are shown. The manner in which the subsequent traces curl up at lower drain voltages

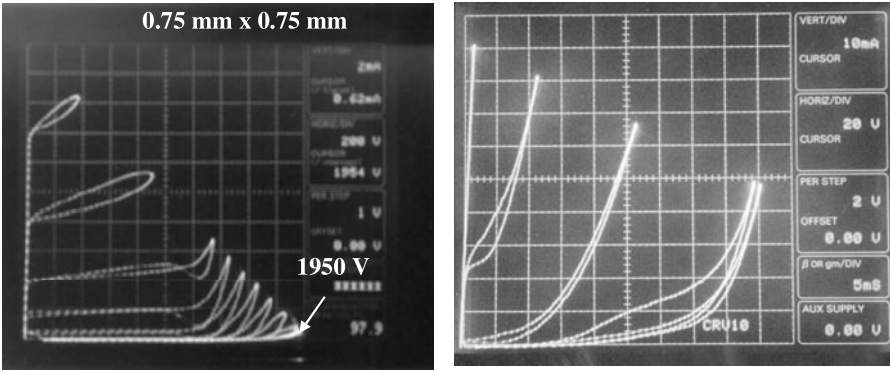


**Fig. 15.** (left) The breakdown characteristics of a 4H-SiC power MOSFET showing bipolar second breakdown. The  $p$ -well dose was  $3 \times 10^{13} \text{ cm}^{-2}$ . (right) Blocking characteristics of a 4H-SiC MOSFET with a box-type  $p$ -well profile ( $p$ -well charge  $\sim 3 \times 10^{13} \text{ cm}^{-2}$ ). Reduction in blocking voltage was observed with an increasingly positive gate bias

is a tell-tale sign of bipolar second breakdown. An extreme example of the second breakdown is shown in Fig. 15 (right)). The  $p$ -type charge under the implanted  $n^+$  source regions was about  $1 \times 10^{13} \text{ cm}^{-2}$ , which was enough to block the voltage,  $BV_{\text{CBO}} \sim 2000 \text{ V}$  as measured on the  $p$ -well/ $n$ -drift layer diode on the same wafer. However, the resistance of the  $p$ -well was sufficiently high to cause the open base bipolar breakdown.

### 6.1 P-Well Design

Both of these effects can be suppressed by reducing the lateral resistance of the  $p$ -well by increasing the  $p$ -well doping and placing the  $p^+$  contact in the center of the  $p$ -well. However, increasing the  $p$ -well doping everywhere would lead to very high threshold voltage of the MOS transistor. An ideal combination is shown in Fig. 16, where the  $p$ -well is divided into two regions – A and B. The doping in region B,  $P_B$ , is kept below  $1 \times 10^{16} \text{ cm}^{-3}$  to keep the threshold voltage low. At the same time, the doping in region A,  $P_A$ , is kept as high as possible without adversely affecting the doping in region B. The total charge in region A should be about  $0.5 - 1.0 \times 10^{15} \text{ cm}^{-2}$  to reduce the lateral base resistance and keep the depletion in the  $p$ -well as small as possible under high drain bias.

The next question is which acceptor impurity should be used: Al or B? Al has a shallower acceptor level than B and therefore its ionization is much higher and the resistance much lower than B at any given temperature. Furthermore, Al does not diffuse in SiC whereas B is known to diffuse in SiC during the implant activation anneal [16], which can close up the JFET gap. For these reasons, it is preferred to use Al for  $p$ -well doping and  $p^+$  contact implant. With an increase in temperature, the avalanche current reduces which tends to increase the second breakdown voltage. The  $p$ -well resistance,  $R_B$ ,

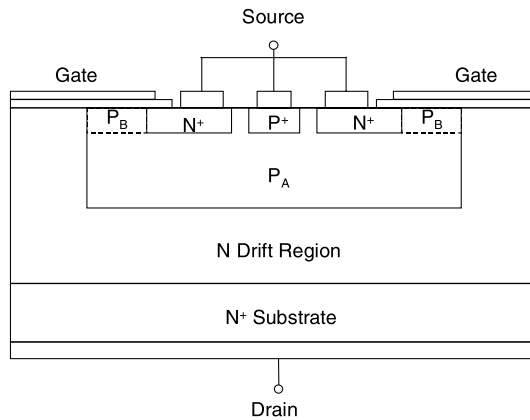


**Fig. 16.** The doping in part B is chosen to set the threshold voltage whereas the doping in region B is made as high as possible to reduce the base resistance

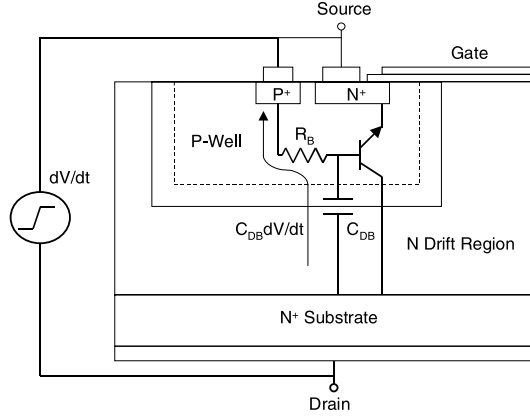


**Fig. 17.** A cross-section of the 4H-SiC DMOSFET showing the turn-on of the parasitic BJT by high  $dV/dt$  induced capacitive current flowing through the base resistance,  $R_B$

will remain relatively constant with temperature due to the cancellation of reduction in the hole mobility with an increase in the hole density due to the increased ionization of deep acceptors.

Another advantage of reducing  $R_B$  is that it improves the  $dV/dt$  capability of the device [29]. As shown in Fig. 17, a high  $dV/dt$  across the capacitance  $C_{DB}$ , causes a current flow of approximately  $C_{DB}(dV/dt)$  through the base resistance,  $R_B$ , which can forward bias the base emitter junction enough ( $>2.7$  V) to turn on the parasitic BJT and collapse the breakdown voltage from  $BV_{CBO}$  to  $BV_{CEO}$ . A low value of  $R_B$  will prevent the  $dV/dt$  turn on of the parasitic BJT.

## 6.2 Threshold Voltage

The doping in region B (Fig. 16),  $P_B$ , is solely determined by threshold voltage considerations. The threshold voltage is given by,

$$\begin{aligned}
 V_T &= \frac{\sqrt{4\varepsilon_{SiC}kTP_B \ln(P_B/n_i)}}{\varepsilon_{ox}/t_{ox}} + 2\frac{kT}{q} \ln\left(\frac{P_B}{n_i}\right) + V_{FB} \\
 V_{FB} &= \phi_{ms} - \frac{Q_{ox}}{\varepsilon_{ox}/t_{ox}} - \frac{Q_{st}}{\varepsilon_{ox}/t_{ox}} \\
 \phi_{ms} &= 3.15 - \left[ 2.70 + \frac{kT}{q} \ln\left(\frac{P_B}{n_i}\right) + \frac{3.25}{2} \right], \\
 &\quad (n^+ \text{ polysilicon to } p\text{-type } 4H\text{-SiC})
 \end{aligned} \tag{14}$$

where,

$\varepsilon_{\text{SiC}} = 8.86 \times 10^{-13}$  F/cm, permittivity of SiC,

$kT = 0.026 \times 1.6 \times 10^{-19}$  eV,

$kT/q = 0.026$  V,

$P_B$  = doping density in the  $p$ -well in  $\text{cm}^{-3}$ ,

$n_i = 5 \times 10^{-9} \text{ cm}^{-3}$ , intrinsic carrier concentration at room temp. in 4H-SiC,

$\varepsilon_{\text{SiO}_2} = 3.46 \times 10^{-13}$  F/cm, permittivity of SiO<sub>2</sub>,

$t_{\text{ox}}$  = gate oxide thickness in cm,

$\phi_{\text{ms}}$  = metal-semiconductor work function difference in Volt,

$Q_{\text{ox}}$  = fixed oxide charge in  $\text{C}/\text{cm}^2$ ,

$Q_{\text{st}}$  = interface state charge in  $\text{C}/\text{cm}^2$ .

In the above equations,  $Q_{\text{ox}}$  is generally positive and is of the order of  $q \times 10^{12} \text{ C}/\text{cm}^2$  whereas  $Q_{\text{st}}$  is negative due to high density of interface traps and can be as high as  $-q \times 10^{12} \text{ C}/\text{cm}^2$ . Thus the two terms generally cancel

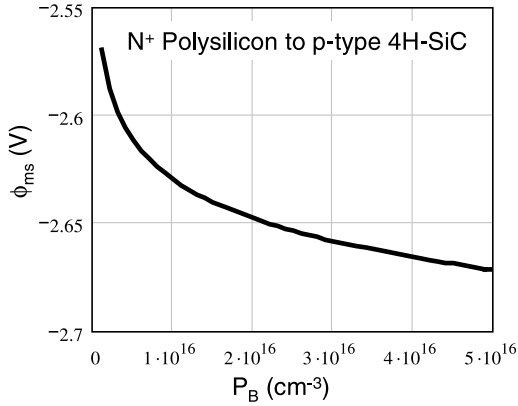


**Fig. 18.**  $\phi_{\text{ms}}$  vs.  $P_B$  for  $n^+$  polysilicon/4H-SiC MOS system

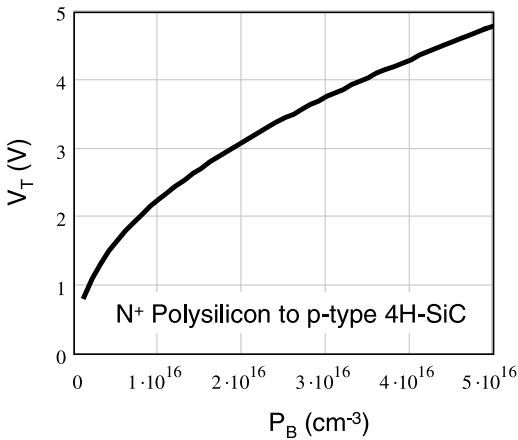


**Fig. 19.**  $V_T$  vs.  $P_B$  for different values of oxide thickness assuming  $Q_{\text{ox}} = -Q_{\text{st}}$

out leaving  $V_{FB} \sim \phi_{ms}$ , a small negative number.  $\phi_{ms}$  vs.  $P_B$  is plotted for  $n^+$  polysilicon/ $4H$ -SiC MOS system in Fig. 18. The threshold voltage,  $V_T$  vs.  $P_B$  is plotted for different values of oxide thickness in Fig. 19 assuming  $Q_{ox} = -Q_{st}$ . In order to keep the threshold voltage at a reasonable value of 2 to 3 V, we note that  $P_B$  should be kept between  $10^{16} \text{ cm}^{-3}$  to  $10^{17} \text{ cm}^{-3}$  for an oxide thickness of 750–1000 Å.

### 6.3 Cell Design

Figure 20 shows a schematic cross-section and a layout of the basic cell. The cell pitch is  $16 \mu\text{m}$ . All the  $p$ -wells are connected to each other with  $p^+$  contacts placed at the four corners and the center of the cell. The JFET gap, as drawn is  $4.0 \mu\text{m}$ . It should be remembered that the actual JFET gap will shrink to about  $3.0 \mu\text{m}$  due to the process bias and implant straggle. The gate length, as designed, is  $1.5 \mu\text{m}$ . The most critical dimension is the spacing between the gate and the  $n^+$  ohmic contact, designed to be  $1.5 \mu\text{m}$ . Any misalignment will result in a direct short between the gate and source electrodes. This spacing is selected after taking into account the relative lack of flatness in SiC wafers. While the state of the art projection aligners can achieve alignment tolerances of less than  $0.2 \mu\text{m}$ , they do require absolutely flat wafers. Typical bow in SiC wafers is about  $20\text{--}40 \mu\text{m}$  which can change shape during the process, especially after the high temperature implant activation anneal and the oxidation process. Therefore, the design with absolute minimum design rules is not recommended for SiC unless one is using a direct-write ebeam lithography with die by die alignment.

The source overlayer connects the  $n^+$  and  $p^+$  ohmic contacts and covers most of the active area of the chip. The gates which are connected to each other are fed from a single pad, generally at the center of the chip.

Many cell designs are possible. Some designs may have disconnected  $p$ -wells which are inter-connected by the overlayer. The  $p$ -wells shield each other under high drain bias and the entire device acts like a single  $p$ - $n$  junction

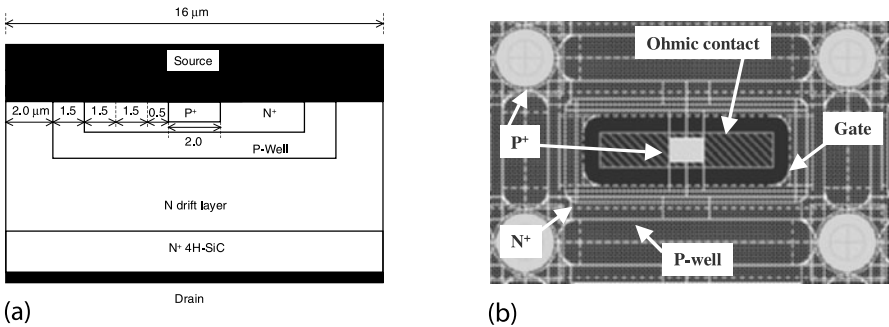


**Fig. 20.** (a) The cross-section of a DMOSFET cell, (b) design of a single DMOSFET cell

diode under reverse bias to achieve the blocking voltage. However, if any of the  $p$ -well contacts is missing due to any reason, then the potential of that particular  $p$ -well will float resulting in a high local electric field and loss of the blocking voltage. Therefore, the design with disconnected  $p$ -wells is not desirable in SiC because it is very likely to have unopened vias in a large area chip due to the bow in wafers. Due to the relatively poor inversion layer mobility, it is desirable to select the design which maximizes the gate periphery for a given area.

## 7 Process Integration

### 7.1 Fabrication Process Sequence

Figure 21 shows a simplified fabrication process sequence of DMOSFETs. Starting material is lightly doped  $n$ -type epilayer grown on Si-face of a  $n^+$  SiC substrate, preferably 4H- polytype. Since this  $n$ - epilayer serves as the drift layer of the power DMOSFET, the doping and the thickness of this layer is selected so that the peak field in SiC is approximately 1.5 MV/cm (see Sect. 3). First, alignment marks are etched into SiC epilayer using dry etching techniques. Then,  $p$ -wells are formed by implanting aluminum (Al) or B ions into the  $n^-$  epilayer (Fig. 21a). Al is the preferred species for this step because it is a relatively shallower level acceptor in 4H-SiC when compared to B, and therefore the use of Al implants will result in lower  $p$ -well resistance. This alleviates the problem with open base breakdown of the parasitic bipolar transistor, as discussed in Sect. 6. The other advantage of Al over B is that it has negligible diffusion coefficient in SiC. Therefore, it is much easier to implement tight pitch designs if Al implants are used.  $n^+$  source regions are then formed by heavy-dose nitrogen or phosphorus implantation (Fig. 21b). The MOS channel length is defined by the distance between the edges of the  $n^+$  source implants and the  $p$ -well implants. The contact regions for  $p$ -wells are formed by heavy dose Al implants (Fig. 21c). If the device uses the floating guard rings for its edge termination, the guard rings are formed at this time. All implants are done at elevated temperatures ( $>650^\circ\text{C}$ ) to reduce implant damages. All implants are then activated together at a temperature greater than  $1550^\circ\text{C}$ . During the high temperature implant activation, a Si overpressure [30] must be provided in the ambient to suppress surface roughening.

A thick ( $>1\ \mu\text{m}$ ) field oxide layer is formed after the implant activation. The field oxide is generally deposited using LPCVD or PECVD because Si-face SiC has very low oxidation rate, and because consumption of implanted layer must be minimized. The field oxide layer is then patterned by selectively etching to open active areas, then a pad oxide, which is approximately 5000 Å thick, is deposited and patterned. The pad oxide provides a mechanical support for bonding pads, and reduces input capacitance. Gate oxide

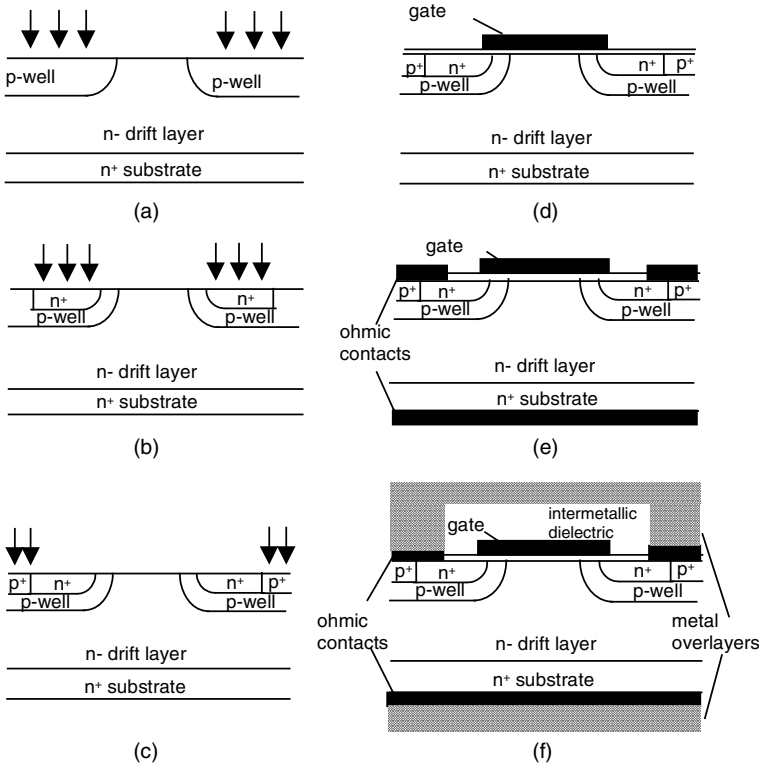


**Fig. 21.** Cross-sectional view of the SiC DMOSFET fabrication. (a) Selective implantation for  $p$ -wells. (b)  $n^+$  source implantation. (c)  $p^+$  implantation for contacts to  $p$ -wells. (d) Gate oxidation followed by gate metal deposition. (e) Formation of ohmic contacts. (f) Deposition and patterning of metal overlayers

layer with a thickness ranging from 400 Å to 1200 Å is then formed by either thermal oxidation or LPCVD deposition and densification. The gate oxide is then nitrided in NO [31, 32] or  $N_2O$  [33] to achieve higher effective channel mobility. The gate electrode is then formed by depositing and patterning of a heavily doped polysilicon layer or a refractory metal layer, such as Molybdenum (Fig. 21d). The ohmic contacts are formed by removing oxide layer from the contact regions (both  $n^+$  and  $p^+$ ) and the backside of the wafer and depositing metal (Fig. 21e). Ni is the most commonly used metal for ohmic contacts in SiC, and other metal stacks, such as Ti/Al [17] and Al/Ni/Al [34], can also be used. The gate then can be metallized to reduce gate resistance, which results in a very high switching speed of the device. The structure is then covered with intermetallic dielectric. Via holes are then opened, and finally, a thick metal layer, such as Al or Ti/Pt/Au stack, is deposited and patterned as the final metal layer (Fig. 21f).

## 7.2 Processing Considerations

The  $p$ -wells in SiC DMOSFETs must meet three requirements. First, the  $p$ -type doping density at the surface must be low, so that a reasonable threshold voltage and MOS effective channel mobility can be achieved. Second, the  $p$ -wells should have enough  $p$ -type charge to prevent punch-through in blocking state. The critical field in SiC is generally believed to be around 2 MV/cm. Therefore, the  $p$ -well should have a  $p$ -type charge density of at least  $1 \times 10^{13} \text{ cm}^{-2}$ . Third, the  $p$ -wells must have low resistance to prevent the open base breakdown phenomenon in the parasitic bipolar transistor and MOS second breakdown, as discussed in Sect. 6. Retrograde  $p$ -well implants are used to meet these requirements in a planar structure. Figure 22 shows an implant depth profile created by an Al implantation with an energy of 360 keV and a dose of  $4 \times 10^{13} \text{ cm}^{-2}$ . The doping concentration at the surface is approximately  $7 \times 10^{15} \text{ cm}^{-3}$  and a peak concentration of  $1.5 \times 10^{18} \text{ cm}^{-3}$  is at a depth of around 3800 Å. This implant profile meets the first two requirements. In most cases, the contacts to  $p$ -wells are placed at the center of the  $n^+$  source regions, which are generally formed by ion implantations. Therefore, the outside parts of the  $p$ -well are connected to the ground contact only through the thin  $p$ -type regions sandwiched between  $n^+$  source regions and the  $n$ -drift layer (Fig. 23a). The resistance of this  $p$ -region increases when high drain biases are applied due to depletion of holes, and eventually results in open base breakdown in the parasitic bipolar transistor and MOS second breakdown.

Implanting a buried  $p^+$  layer the  $n^+$  source regions can alleviate this problem (Fig. 23b) [35]. In Si devices, deep  $p^+$  diffusion regions are placed under the  $n^+$  regions [29]. In SiC devices, the depth of the  $p^+$  regions are limited due to lack of controlled diffusion processes. Instead of using deep  $p^+$

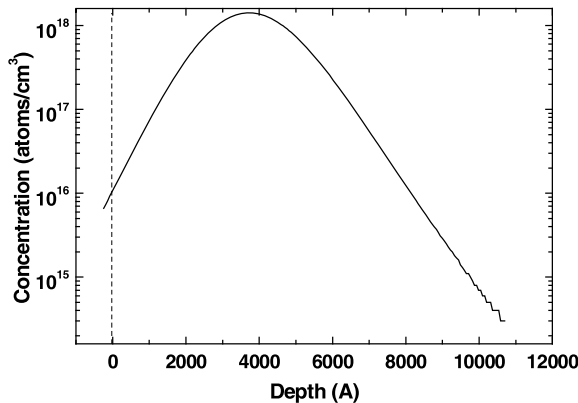


**Fig. 22.** Simulated dopant depth profile for a  $p$ -well formed by Al ion implantation. The dose of the implant is  $4 \times 10^{13} \text{ cm}^{-2}$  at an energy of 360 keV

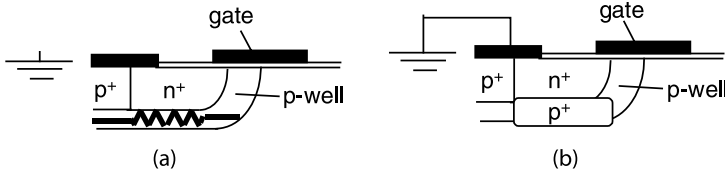


**Fig. 23.** Planar SiC DMOSFET structure with retrograde  $p$ -well implants. (a)  $n^+$  source implants pinch  $p$ -well regions, results in increased  $p$ -well resistance. The structure is susceptible to open base bipolar breakdown and MOS second breakdown. (b) Buried  $p^+$  layer reduces  $p$ -well resistance. This structure has improved resistance to open base bipolar breakdown and MOS second breakdown

regions, thin  $p^+$  layers with higher impurity concentration should be used in SiC devices. This layer can be easily implemented by implanting Al ions at a very high energy using same implant mask that were used for implanting  $n$ -type species to form source regions. In this case, the depth of the  $n^+$  source should be limited. If nitrogen implants are used, the implant energy should be limited to less than 130 keV.

## 8 Results on 2.4 kV Design

4H-SiC DMOSFETs with blocking voltage rating of 2.4 kV were fabricated following the sequence described in Sect. 7 [21]. A 20  $\mu\text{m}$  thick drift region with a doping concentration of  $2.5 \times 10^{15} \text{ cm}^{-3}$  was used for a 2.4 kV blocking voltage design. The MOS channel length, defined by the  $p$ -well and  $n^+$  implants, is 1.5  $\mu\text{m}$ . Electrons flow from  $n^+$  source through an MOS channel on the implanted  $p$ -well, then through the 4  $\mu\text{m}$  wide JFET region formed by two adjacent  $p$ -well regions, and then through lightly doped  $n^-$  drift region into the drain. A rectangular cell design was used. The cell pitch is 16  $\mu\text{m}$ , and packing density of the gate periphery is 1250  $\text{cm}/\text{cm}^2$ . The contacts to the  $p$ -wells are placed at the center of the  $n^+$  source regions and at the four corners (Fig. 20b) of the  $p$ -wells for higher resistance to open base bipolar and MOS second breakdown. Multiple floating guard ring structure was used as edge termination, and a 2  $\mu\text{m}$  thick PECVD oxide was used as field oxide. A 500  $\text{\AA}$  thick gate oxide was formed by thermal oxidation, and the oxide layer was later nitrided in NO ambient. 2500  $\text{\AA}$  thick sputtered molybdenum layer was deposited and patterned as gate metal, which was later reinforced with 2500  $\text{\AA}$  thick Ni/Au layer to achieve lower gate resistance.

Figure 3 shows the on-state and blocking characteristics of a 3.3 mm  $\times$  3.3 mm DMOSFET at room temperature. The active area, excluding pad area, of this device is 0.103  $\text{cm}^2$ . The device is normally off, and shows an on-current of 10 A (97  $\text{A}/\text{cm}^2$ ) at a forward drop of 7.2 V. Specific on-resistance,  $R_{\text{on,sp}}$ , measured with  $V_{\text{GS}} = 20 \text{ V}$  is 42  $\text{m}\Omega\cdot\text{cm}^2$  at room temperature. The specific on-resistance is very dependent on the gate bias, and moderately high

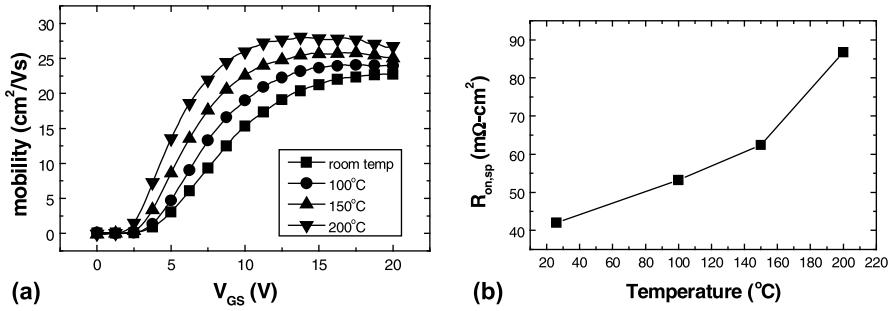


**Fig. 24.** Temperature dependent characteristics of the 4H-SiC DMOSFETs. (a) Effective channel mobility, and (b) specific on-resistance

gate voltages were required to turn the devices fully on, indicating that the on-resistance is dominated by the MOS channel resistance at room temperature. The measurement was done in Fluorinert<sup>TM</sup> oil to prevent arcing. The device starts showing some leakage current at a  $V_{\text{DS}}$  of 2100 V, then avalanches at a  $V_{\text{DS}}$  of 2370 V. This blocking voltage is approximately 75% of the ideal parallel plate blocking voltage of the drift layer.

Figure 24a shows the effective MOS channel mobility ( $\mu_{\text{eff}}$ ) and threshold voltage measured on a 200  $\mu\text{m}/200 \mu\text{m}$  lateral test MOSFET. A peak mobility of 22  $\text{cm}^2/\text{Vs}$  was measured at room temperature. At 200°C, the peak mobility increases to 27  $\text{cm}^2/\text{Vs}$ . This suggests that the MOS channel is still severely affected by interface traps. Figure 24b shows  $R_{\text{on,sp}}$  as a function of temperature. The  $R_{\text{on,sp}}$  value increases with temperature due to decrease in electron mobility in the drift layer, which enables easy paralleling of these devices.

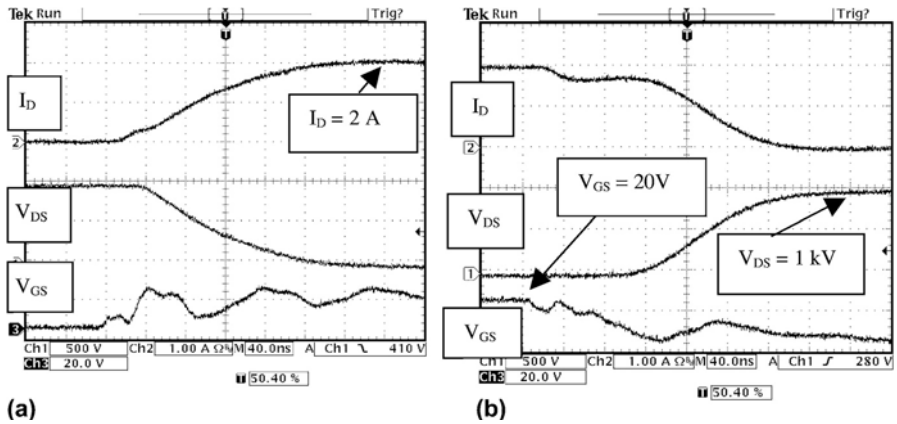


**Fig. 25.** Switching characteristics of a 0.0387  $\text{cm}^2$  4H-SiC DMOSFET at room temperature. (a) Turn on characteristics, and (b) turn off characteristics

Figure 25 shows dynamic characteristics of a  $0.0387\text{ cm}^2$  device at room temperature. A supply voltage of 1000 V, a  $500\ \Omega$  resistive load, a  $50\ \Omega$  gate resistor, and a 100 kHz gate pulse were used for this measurement. The device switches 2 A of drain current (about  $52\text{ A/cm}^2$ ) with a turn-on delay,  $t_{d(\text{on})}$ , of 40 ns, a rise time,  $t_r$ , of 140 ns, a turn-off delay,  $t_{d(\text{off})}$ , of 100 ns, and a fall time,  $t_f$ , of 120 ns. This shows that these DMOSFETs are ideal for low loss, high speed power switching applications.

## References

1. J.W. Palmour, J.A. Edmond, H.S. Kong and C.H. Carter, Jr.: Proc. 28th Inter-Society Energy Conversion Conference, 1249 (1993)
2. N. Tokura, K. Hara, T. Miyajima, H. Fuma and K. Hara: Jpn. J. Appl. Phys. **34**, 5567 (1995)
3. J.W. Palmour, R. Singh, L.A. Lipkin, and D.G. Waltz: Trans. 3rd Int'l Conf. on High Temperature Electronics (HiTEC), Albuquerque, NM, 2, XVI-9, June 9–14 (1996).
4. A.K. Agarwal, R.R. Siergiej, S. Seshadri, M.H. White, P.G. McMullin, A.A. Burk, L.B. Rowland, C.D. Brandt and R.H. Hopkins: ISPSD, (1996)
5. A.K. Agarwal, R.R. Siergiej, S. Seshadri, M.H. White, P.G. McMullin, A.A. Burk, L.B. Rowland, C.D. Brandt and R.H. Hopkins: Mat. Res. Soc. Symp. Proc. **423**, 92 (1996)
6. A.K. Agarwal, J.B. Casady, L.B. Rowland, W.F. Valek, M.H. White, C.D. Brandt: IEEE Electron Device Lett. **18**, 586 (1997)
7. K. Hara: Mat'l. Sci. Forum, Trans. Tech Publications, Sweden **264–268**, 901 (1997)
8. A.K. Agarwal, J.B. Casady, L.B. Rowland, W.F. Valek, and C.D. Brandt: *Proceed. of the 7th Int. Conf. on Silicon Carbide, III-Nitrides and Related Materials ICSCIII-N'97* (Stockholm, Sweden, 1997) 989
9. J. Tan, J.A. Cooper, Jr., and M.R. Melloch: IEEE Electron Device Lett. **19**, 487 (1998)
10. N.S. Saks, A.K. Agarwal, S.S. Mani, and V.S. Hedge: Appl. Phys. Letts. **76**, 1896 (2000)
11. K. Ueno and T. Oikawa: IEEE Electron Device Letters **20**, 624 (1999)
12. J.N. Shenoy, J.A. Cooper and M.R. Melloch: IEEE Electron Device Letters **18**, 93 (1997)
13. J.B. Casady, A.K. Agarwal, L.B. Rowland, W.F. Valek, and C.D. Brandt: IEEE Device Research Conference, Ft. Collins, CO, June 23–25 (1997)
14. R. Schörner, P. Friedrichs, D. Peters, H. Mitlehner, B. Weis and D. Stephani: Materials Science Forum, **338–342**, 1295 (2000)
15. V.R. Vathulya and M.H. White: Electronic Materials Conference, Santa Barbara, CA, June 30–July 2, (1999)
16. A.V. Suvorov, L.A. Lipkin, G.M. Johnson, R. Singh and J.W. Palmour: Materials Science Forum **338–342**, 1275 (2000)
17. P.M. Shenoy and B.J. Baliga: IEEE Electron Device Letters **18**, 589 (1997)
18. R. Singh, S.-H. Ryu and J.W. Palmour: Materials Science Forum **338–342**, 1271 (2000)

19. Y. Wang, C. Weitzel and M. Bhatnagar: Materials Science Forum **338-342**, 1287 (2000)
20. A. Agarwal, S.-H. Ryu, M. Das, L.A. Lipkin, J.W. Palmour, and N. Saks: Int'l. Symp. on Power Semiconductor Devices & ICs, **183** (2001)
21. S.-H. Ryu, A. Agarwal, J. Richmond, J. Palmour, N. Saks and J. Williams: IEEE Electron Device Letters **23**, 321 (2002)
22. M.K. Das, J.A. Cooper, Jr., M.R. Melloch, and M.A. Capano: IEEE Semiconductor Interface Specialists Conference, San Diego, CA, December 3-5 (1998)
23. A.K. Agarwal, S. Seshadri and L.B. Rowland: IEEE Electron Device Letters **18**, 592 (1997)
24. P. Friedrichs and E.P. Burte: Appl. Phys. Lett. **65**, 1665 (1994)
25. V.V. Afanas'ev, M. Bassler, G. Pensl, and M.J. Schulz: J. Appl. Phys. **79**, 3108 (1996)
26. G. Pananakakis, G. Ghibaudo, R. Kies, and C. Papadas: J. Appl. Phys. **78**, 2635 (1995)
27. M.M. Maranowski and J.A. Cooper, Jr.: IEEE Trans. Electron Devices **46**, 520 (1999)
28. M. Das: private communication
29. B.J. Baliga: PWS Publishing Company, **395** (1996)
30. M.A. Capano, S. Ryu, J.A. Cooper, Jr., M.R. Melloch, K. Rottner, S. Karlsson, N. Nordell, A. Powell, and D.E. Walker, Jr.: Journal of Electronic Materials **28**, 214 (1999)
31. H.-F. Li, S. Dimitrijevic, D. Sweatman, H.B. Harrison: Journal of Electronic Materials **29**, 1027 (2000)
32. G.Y. Chung, C.C. Tin, J.R. Williams, K. McDonald, M. Di Ventra, S.T. Pantelides, L.C. Feldman, and R.A. Weller: Applied Physics Letters **76**, 1713 (2000)
33. L.A. Lipkin, M.K. Das, and J.W. Palmour: Materials Science Forum **389-393**, 985 (2002)
34. D. Alok, E. Arnold, R. Egloff, J. Barone, J. Murphy, R. Conrad, J. Burke: IEEE Electron Device Letters **22**, 577 (2001)
35. D. Peters, R. Schorner, P. Friedrichs, J. Volkl, H. Mitlehner, D. Stephani: IEEE Transactions on Electron Devices **46**, 542 (1999)

# Normally-Off Accumulation-Mode Epi-Channel Field Effect Transistor

R.K. Malhan

## 1 Introduction

The MOSFETs have been one of the most versatile devices in Si and is the building block for most VLSI application. SiC power MOSFET can revolutionize the high voltage switching applications in the blocking voltage ( $V_B$ )  $< 5.0$  kV. For such a high voltage range, typically Si power devices utilize conductivity modulation in the drift region to reduce the forward drop, however, compromising with the switching speed of the device. SiC MOSFETs are currently being developed because of exceptional electrical and physical properties. SiC power devices has the capability for high temperature operations in the range  $\sim 200^\circ\text{C}$  for MOS based and  $\sim 400^\circ\text{C}$  or higher for non-MOS based devices. Today about 15% of the electric power produced undergoes some form of electronic conversion that mostly occurs at the consumer end. Therefore, there is strong demand for the improvement of the following critical parameters of the power inverter systems viz., (a) cost (low device and circuit cost, modularity), (b) size (weight, volume, and foot-print), (c) efficiency (low conduction and switching losses, fast switching capabilities), and (d) reliability (rugged high temperature operations, high blocking stability, and low random failure).

SiC is unique among compound semiconductor in the sense that its native oxide is  $\text{SiO}_2$ , the same oxide as Si. The GaN and AlGaN have high breakdown field and high carrier mobility, and would appear to be ideally suited for power device implementation. However, these III-V nitride compounds do not possess a native oxide similar to  $\text{SiO}_2$ , so true MOS devices will not be feasible. In addition, the nitrides suffer from the lack of a suitable lattice-matched substrate for crystal growth, and hence the material is in a more primitive state of development than SiC. Various figure-of merits were calculated in order to quantify the advantage of SiC over the Si viz., Johnsons Figure-of-Merit, Keys Figure-of-Merit, and Baliga Figure-of-Merit. The Baliga Figure-of-Merit (BFM) is for power devices in general defined by Baliga in 1989 [1]. BFM ( $V_B^2/AR_{ON}$ ) is a single quantity that represents how closely the device approaches the theoretical limits for the semiconductor material. The theoretical maximum BFM for Si unipolar devices is about  $5 \text{ MW}/\text{cm}^2$ , whereas the theoretical limit for  $4H$ -SiC unipolar device like MOSFET is about  $2000 \text{ MW}/\text{cm}^2$ . Compared to bipolar Si-IGBTs,

considerable reduction in static and dynamic losses can be achieved for the unipolar power MOSFETs. However, the inversion-mode  $4H$ -SiC MOSFET performance is still hampered by the problem of low channel mobility due to the high interface trap density near the conduction band edge ( $D_{\text{NIT}}$ ). Refined oxidation techniques have improved the  $\text{SiO}_2/\text{SiC}$  MOS interface quality, but producing reliable devices still require a process innovation. Recently, there has been significant progress in producing SiC devices for high power and high frequency applications [2, 3]. From the HEV application point of view, inverter system power module requires high-efficiency, high-functionality, and high-reliability [4, 5]. Existing HEV inverter systems use Si-IGBT based power modules. Being a unipolar switching device, SiC MOSFETs are the ideal replacement for Si-IGBTs. This paper provides an overview of the normally-off Accumulation-mode Epi-Channel Field Effect Transistor (ECFET) design concept. The challenges for power device development beginning from SiC wafer quality to key device processes of thermal oxidation and ion-implantation are also discussed. Finally, the applicability of these ideal SiC switches in HEV propulsion application is reviewed.

## 2 Design of SiC Power MOSFETs

Until DENSO's ECFET reported in ICSCRM'97 [6, 7], SiC power MOSFETs had not significantly exceeded the Si theoretical limits. ECFET is basically a trench type accumulation-mode MOSFET in which a thin  $n$ -type epi-channel layer was grown on the trench sidewalls to form an accumulation-mode power device. The use of an accumulation-mode channel improved the MOSFET channel mobility significantly, resulting in the lowest specific on-resistance ( $R_{\text{ON}}$ ) of about  $10.9 \text{ m}\Omega\text{cm}^2$  at room temperature with controlled avalanche breakdown of about 450 V, the first Si-limit breaking performance by any SiC power switching device. The SiC MOS based power device design is evolving mainly on the accumulation-mode MOSFET design concept in efforts to utilize the maximum potentials of SiC material.

### 2.1 Accumulation-Mode SiC ECFET

The main feature of ECFET is that the  $n$ -type channel-forming region is epitaxially grown on the  $p$ -base region to form the MOS structure. This epilayer provides an independent control of the impurity concentration of the channel and the  $p$ -base region. Therefore, a power MOSFET with high blocking voltage, low specific on-state resistance and low threshold voltage can be designed such as to allow independent control of the dopant concentration of the different regions. Since, the concentration in the  $p$ -base region can be raised independently, therefore, the thickness of the  $p$ -base region can be reduced. This helps in trimming the JFET component of  $R_{\text{ON}}$ , compared to the inversion-mode structure. Moreover, in the accumulation-mode conduction,

the channel depth is about  $5 \sim 10\times$  larger than that of the inversion-mode channel, thereby the current conduction is less affected by the MOS interface conditions. The accumulation-mode channel mobility is expected to be higher than the inversion-mode channel mobility due to relaxation of electric field. The epitaxially grown  $n$ -type epi-layer that defines the channel region can be completely depleted by the potentials created by the work function difference between the  $p$ -base region and the epi-channel layer, and the work function difference between the epi-channel layer and the poly-Si gate electrode. ECFET can be turned-on by applying the positive bias to the gate electrode. This design concept can withstand up to the avalanche breakdown conditions. We reported the fabrication of first accumulation-mode  $4H$ -SiC trench ECFET on (0001) plane  $4H$ -SiC epi-wafers [6, 7]. On the similar accumulation-mode channel design, a blocking voltage of about 1400 V was reported for the  $4H$ -SiC IOP-ACCUFET [8]. IOP effectively eliminated oxide breakdown in the trench corner, allowing the device to reach 87% of the theoretical value. The  $R_{ON}$  was  $15.7 \text{ m}\Omega\text{cm}^2$  with Figure-of-Merit of  $125 \text{ MW/cm}^2$ , a value  $25\times$  higher than the theoretical limit for Si-MOSFET. In trench MOSFET design, practically it's difficult to realize the high blocking voltages due to the poor gate oxide reliability, as the electric field is higher near the bottom of the trench corners.

Chilukuri et al. [9] reported the fabrication of planar accumulation-mode MOSFET, called ACCUFET on (0001) plane  $6H$ -SiC  $n$ -type epi-wafers. Accumulation-mode mobility as high as  $120 \text{ cm}^2/\text{V.s}$  was reported for the fabricated device. However, they reported the problem related to the  $p$ -type dopant B diffusion from the  $p$ -base region. Usually, high power applications require a high level of unit-cell integration, which can be achieved by reducing the pitch of unit-cell. The B diffusion can limit the reduction of  $p$ -base spacing due to increasing JFET pinch resistance. We reported a novel C/B sequential implantation process to control the B lateral and vertical diffusion from the  $p$ -base region of the planar ECFET [10]. The schematic cross-section structure of our proposed accumulation-mode planar ECFET is shown in Fig. 1. The B vertical and lateral diffusion as shown in figure can lead to serious design problems and electrical performance degradation of fabricated device. The B lateral diffusion into the JFET region results in high on-state resistance or even completely blocks the current conduction due to pinch effect phenomenon. We performed the 2D numerical device simulations using ISE DESIS simulator to access the (a) Effect of electric field relaxation on the channel mobility in the accumulation-mode of current conduction, and (b) Effect of B lateral diffusion on the ECFET on-state characteristics. Figure 2 shows the simulated correlation between electric field and electron mobility as a function of distance from the MOS interface for the both, inversion-mode and the accumulation-mode conduction. The channel doping levels and the biasing conditions are marked in the inset of the figure. It is clearly evident from the simulation results that the channel mobility in the accumulation-

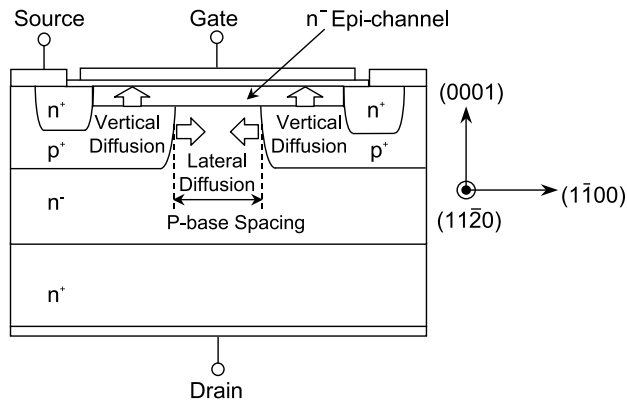


**Fig. 1.** Schematic cross-sectional structure of accumulation-mode planar ECFET

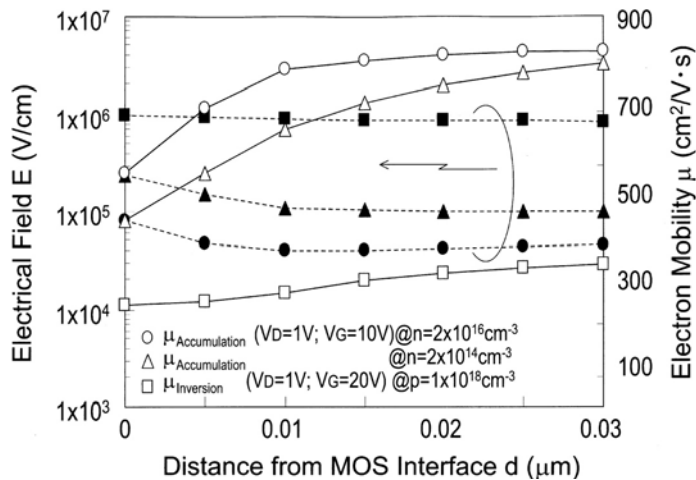


**Fig. 2.** Correlation between electric field strength and electron mobility as a function of distance from the MOS interface for both, the inversion-mode and the accumulation-mode conduction

mode of conduction is  $2\times$  higher than that for the inversion-mode under a given condition. In addition, the higher doping levels of the epi-channel layer further leads to further increase in the channel mobility due to the relaxation in the electric field.

To access the effect of B lateral diffusion on the ECFET on-state characteristics, three ECFET models with different B lateral diffusion length were considered viz., diffusion length = 0  $\mu\text{m}$  (without diffusion), 0.5  $\mu\text{m}$ , and 1  $\mu\text{m}$ . The B lateral diffusion simply translates a decrease in the  $p$ -base spacing of the ECFET unit-cell. The simulated potential contours for the 26  $\mu\text{m}$  unit-cell ECFET with (diffusion length = 1  $\mu\text{m}$ ) and without B lat-

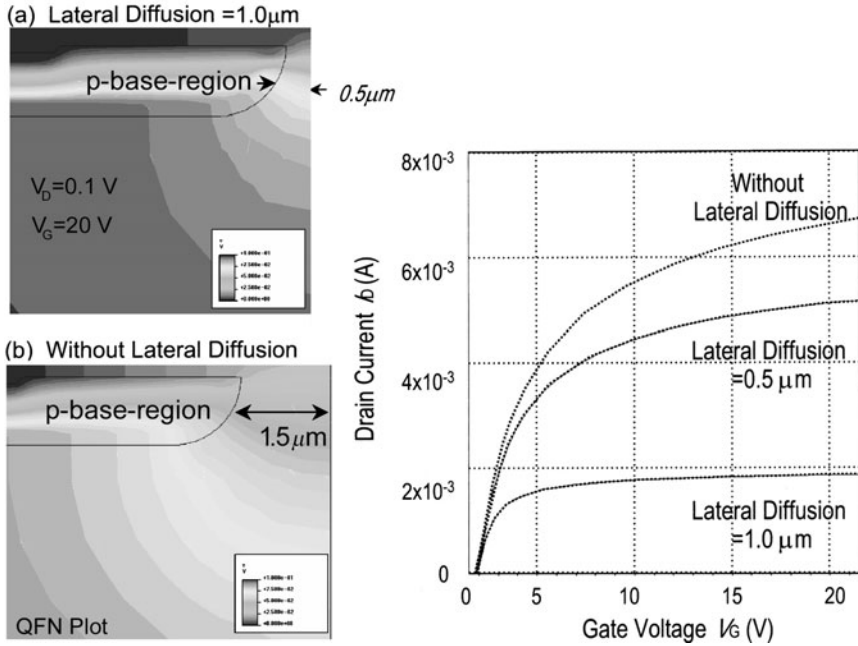


**Fig. 3.** Simulated potential contours in the planar accumulation-mode ECFET (Half cell model). The simulated output characteristics of ECFET with and without B lateral diffusion are also shown in the figure

eral diffusion are shown in Fig. 3. The contours gradient in the JFET region indicates the voltage drop in that region. The voltage drop is higher in the JFET region for the case where B diffusion was considered. The simulated on-state characteristics of ECFET indicates the strong affect of B diffusion on the  $R_{ON}$  due to JFET pinch effect as the drain current is reduced by a factor of 1/3 for lateral diffusion length of 1 μm for a given drain and gate bias conditions. Therefore, it is vital to suppress the lateral as well as vertical diffusion of B to fabricate the accumulation-mode ECFET. Al is another *p*-type dopant for selective implantation process, however, requires the relatively high temperature activation annealing and also yields more residual defects in comparison with B dopant.

The planar 4H-SiC ECFETs were fabricated using (0001) plane  $n/n^+$  4H-SiC single epi-wafer. The planar ECFET device fabrication details are given elsewhere [11]. Typical on-state output characteristics of the fabricated 4H-SiC planar ECFET with and without the B lateral diffusion at room temperature are shown in Fig. 4. Excellent  $I_D$ - $V_D$  characteristics were obtained for the planar ECFET without B lateral diffusion as the device shows good current saturation and gate control. The threshold voltage measured at  $V_G = V_D$  was about 2.0 V. The effectiveness of C/B sequential implantation

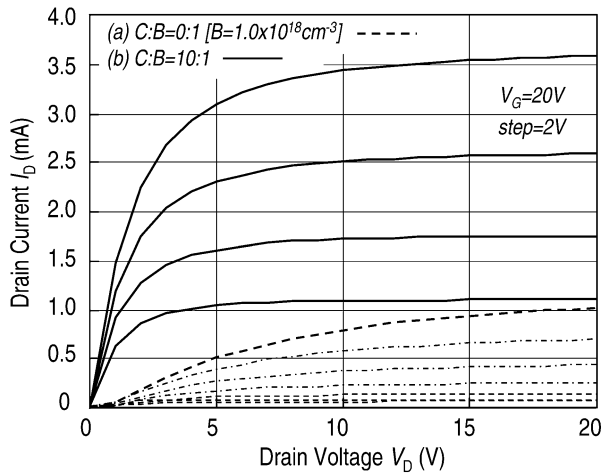


**Fig. 4.** Typical on-state output characteristics of the fabricated planar 4H-SiC ECFET with (a) B implanted and (b) C/B sequentially implanted *p*-base region

process in suppressing the JFET pinch effect is clearly visible from the 3 ~ 4 fold increase in drain current of ECFET for *p*-base spacing which was scaled down to about 3  $\mu\text{m}$ . Therefore, this technique opens door for the larger packing densities through unit-cell pitch reduction for power device applications by suppressing the B diffusion to match the design requirements. Typical

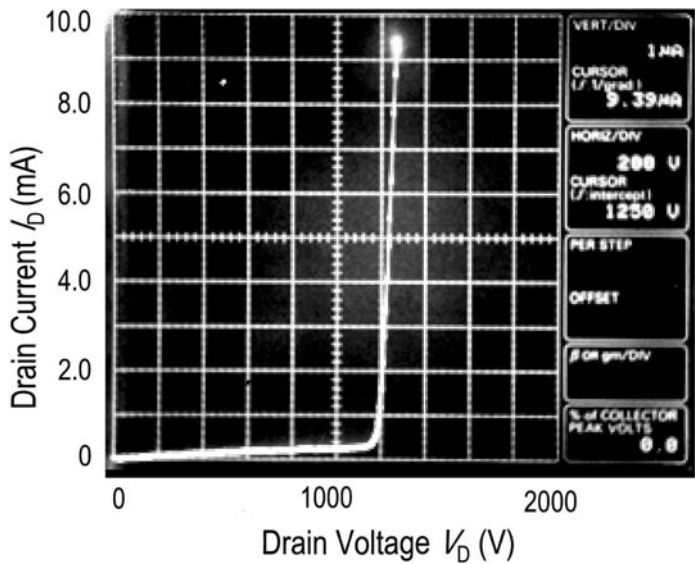


**Fig. 5.** Typical off-state characteristics of the 4H-SiC ECFET

off-state output characteristics of the fabricated 4H-SiC planar ECFET at room temperature are shown in Fig. 5. The fabricated device features the controlled avalanche  $V_B$  of about 1200 V.

The 1st SiC trench MOSFET was reported by Cree Inc. in 1993 [12] and the 1st accumulation-mode SiC ECFET with  $R_{ON}$  lower than that of Si-limits was reported by DENSO CORPORATION in 1997 [6]. The  $V_B$  as high as 5.0 kV for SEMOSFET has been reported by KEPCO and Cree [13]. The  $R_{ON}$  was  $88 \text{ m}\Omega\text{cm}^2$  with Figure-of-Merit of  $284 \text{ MW}/\text{cm}^2$ , a value about  $50\times$  higher than the theoretical limit for Si-MOSFET. The power MOSFETs reported to date [14, 15] indicate that although the  $V_B$  has increased steadily over the past 10 years, there has been slow reduction in  $R_{ON}$ . This is because the specific on-resistance of 4H-SiC MOSFETs is still dominated by the channel resistance, rather than by the drift region resistance. The relatively high channel resistance is due to relatively low channel mobility, particularly in the 4H-SiC polytype. The reduction of channel resistance is vital for any further improvement in the performance of MOS based SiC power devices. For an insight of the future trends of SiC power devices, relations between blocking voltage and specific on-resistance of conventional unipolar and super junction devices is shown in Fig. 6. The specific on-resistance of conventional SiC power devices will be trimmed further by one or two orders of magnitude, depending on the targeted blocking voltage using the RESURF technology [16] in the future.

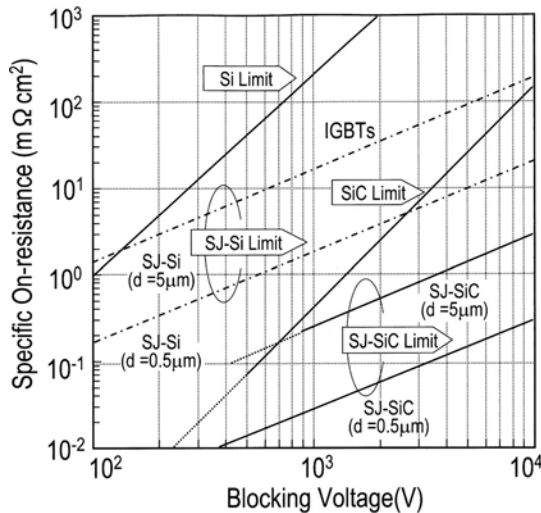


**Fig. 6.** Specific on-resistance and blocking voltage plot for conventional unipolar and super-junction Si and SiC power devices

## 2.2 Selection of SiC Polytype: Bulk Electron Mobility Anisotropy

4*H*-SiC polytype is the material of choice for power device applications because of (a) nearly isotropic high bulk electron mobility in comparison to 6*H*-SiC, (b) availability of relatively high quality wafer, and (c) advanced processing technologies including epitaxial growth. Earlier, Schörner et al. [17] had reported a comparison for inversion-mode channel mobility of 4*H*-, 6*H*- and 15*R*-SiC MOSFETs under the identical processing conditions. They observed low inversion-mode channel mobility for 4*H*-SiC MOSFETs and attributed it to the high density of interface states located at approximately 2.9 eV above the valence band edge or just below the conduction band edge of 4*H*-SiC. More of these states lie in the band gap for 4*H*-SiC ( $E_G = 3.3$  eV) compared to 6*H*-SiC ( $E_G = 3.0$  eV) where they affect the channel mobility via carrier trapping and Coulomb scattering. Afanasev et al. [18] originally reported the existence of near interface trap states between the conduction band edge of 4*H*- and 6*H*-SiC, which act as the scattering centers at the MOS interface. They proposed that interface states in SiC/SiO<sub>2</sub> structures result from C-clusters at the interface and defects in a near-interface sub-oxide. 6*H*-SiC MOSFETs have shown moderate inversion-mode channel mobility, however, the performance of 6*H*-SiC vertical power MOSFETs are limited by lower bulk mobility in the direction parallel to the *c*-axis, which is about 1/10 of 4*H*-SiC. Alternatively, the 15*R*-SiC is another attractive solution as the band gap of this polytype is smaller than that of 4*H*-SiC, therefore, the inversion-mode channel mobility is less influenced by near interface trap states. In addition, the bulk mobility of 15*R*-SiC is less anisotropic in nature. Therefore, 15*R*-SiC is a promising polytype for power device applications, however, the large size high quality wafers are not yet available.

## 2.3 Selection of Crystal Plane: Channel Mobility Anisotropy

As mentioned earlier, anisotropic nature of the bulk electron mobility is an important parameter for power device design. The channel mobility anisotropy is another important design parameter that determines the device performance. The step controlled epitaxial growth on the conventional (0001) plane requires off-axis 6*H*-SiC (3.5 deg. off) or 4*H*-SiC (8.0 deg. off) substrates to inherit the polytype information from the substrate. The surface roughness introduced by the use of off-axis wafers may affects the MOS interface properties and thereby channel mobility. Yano et al. [19] reported a dramatic improvement in the inversion-mode channel mobility of 6*H*- and 4*H*-SiC MOSFETs fabricated on (11-20) plane by using on-axis substrates. The planar SiC MOSFETs on (11-20) plane have also shown the negative temperature dependence of channel mobility that was observed for the first time. These results indicate that the (11-20) plane may be the best selection for SiC MOSFETs, however, the maximum breakdown electric field in (11-20) plane is only 75% of that for the (0001) plane and that limits the

use of this plane for the power MOSFETs with  $V_B < 2$  kV. The best reported inversion-mode mobility values are typically  $\sim 50$  cm<sup>2</sup>/V.s and  $\sim 150$  cm<sup>2</sup>/V.s for the planar MOSFETs fabricated on (0001) and (11-20) oriented 4H-SiC wafers, respectively [20]. The oxide reliability issues are yet to be addressed.

### 3 Key Device Processing Technologies

In SiC device fabrication process, various high temperature conflicting processes influence strongly the SiC MOSFETs channel mobility. Fabrication process steps like thermal oxidation, *p*-type dopant activation, and ohmic contact annealing collectively degrade the channel mobility. The process dependent channel mobility degradation of SiC MOSFET is still poorly understood to date. The key device processing technologies include (a) True  $\mu$ -pipe defect and dislocation free large size ( $\sim 4''$  size) off-axis  $\langle 0001 \rangle$  oriented Si-face and on-axis  $\langle 11-20 \rangle$  oriented *a*-face SiC wafers (Recently, higher channel mobilities are reported with MOSFETs fabricated on  $\langle 11-20 \rangle$  oriented *a*-face wafers), (b) High quality SiO<sub>2</sub>/SiC MOS interface and its high temperature reliability (this is the most critical factor for MOSFET practical applications), and (c) High dopant activation process for selective ion-implantation. The main challenge in ion-implantation process is to develop a technology for *p*-type low temperature dopant activation annealing process that can cap the surface morphology degradation.

#### 3.1 Quality of 4H-SiC Large Size Wafers

Recently, 600 V class SBDs and MESFET are available commercially from Infineon Technologies [2] and Cree Inc. [3], respectively. Infineon Technologies has announced the market introduction of cascode switching (normally-on SiC-JFET with Si-MOSFET) devices. However, the high quality and large diameter wafer is a prerequisite for industrial-scale fabrication of power devices which to date lacks for SiC. The greatest challenge is the quality of the material, which limits both current capability and yield of such devices with respect to the chip area. Development of SiC wafers has been very successful over the past years in achieving major improvements in quality and yield. However, there are particular areas where SiC wafers are still significantly behind state of the art Si wafers technology viz., (a) SiC wafer size which is currently available in 2'' and 3'' diameters (research level: 4'' diameter), (b) Lack of high quality material as SiC wafers still contains various type of defects, and (c) SiC wafer process technology (Warp, total thickness variation (TTV), local thickness variation (LTV), etc.) is still demanding. The crystal defects such as  $\mu$ -pipe defect, comet-tail defect, dislocations, and impurities within the active region of large area devices affect both on- and off-state characteristic adversely. At present, the dislocation density in the commercially available wafer is in the range of  $10^4 \sim 10^5$  cm<sup>-2</sup>. The secondary effects

of dislocation centers on leakage current or breakdown phenomenon are not clear at present. There are several thermodynamic, kinetic, and technological mechanisms, which causes  $\mu$ -pipe formation in SiC wafer. The  $\mu$ -pipe defects generally propagate into the LPCVD grown epitaxial layers, which leads to premature junction breakdown below the maximum permissible electric field. The  $\mu$ -pipe density of less than  $1 \text{ cm}^{-2}$  is needed to realize devices of current ratings  $>100 \text{ A}$  with reasonable yield. Recently,  $\langle 11\text{-}20 \rangle$  oriented  $a$ -face SiC wafers are commercially available from Cree. The key epitaxial growth and selective ion-implantation technologies appear very feasible on  $\langle 11\text{-}20 \rangle$  oriented  $a$ -face SiC wafers.

### 3.1.1 4H-SiC Wafer Quality Versus Bipolar Forward Degradation

As we will discuss later, in the HEV inverter power module, 600 V class Si-IGBTs are generally used in parallel with and Si-PiN free wheel diode (FWD) to conduct the reverse current for IGBTs. Bipolar power devices stand to benefit greatly in high voltage and high temperature applications. The MOSFETs can be used as a bi-directional switch and the internal  $pn$  body diode can eliminate the needs of the external FWDs. Recently, the bipolar forward degradation phenomenon [21] characterized by an increase of the forward voltage caused by forward operation has been reported. Such an electrical degradation of bipolar  $pn$  diode can limit the use of the internal body diode of SiC MOSFETs. The suppression of the bipolar forward degradation is vital for the future development of such an ideal switch.

Earlier, we reported the impact of SiC structural defects on the forward current degradation of  $pn$  diodes fabricated on in-house developed high quality 4H-SiC wafers [22]. The  $pn$  diodes were fabricated on in-house developed (1-100) off oriented 4H-SiC standard (STD), (11-20) off oriented 4H-SiC high quality (HQ), and (11-20) off oriented 4H-SiC reference wafer to evaluate the impact of SiC structural crystal defects. The etch pit density, especially the slip/stacking faults of DENSO HQ wafer is about 1 ~ 2 order of magnitude lower than that of other wafers. Moreover, these wafers are free from the  $\mu$ -pipe defects. The electroluminescence (EL) images of  $pn$  diodes fabricated on DENSO STD, HQ, and reference 4H-SiC wafers, before and after the forward current degradation are shown in Fig. 7. EL images reveal the formation of triangular type structural defects after the current degradation. Bright lines observed at low current densities were formed as a result of high current density stress effect. Whereas, these bright lines are viewed as dark features at high current densities and are attributed to a localized reduction of carrier lifetime caused by the creation of extended defects viz., the stacking faults. The propagated defect looks like a single layer Shockley type stacking fault bounded by partial dislocations with Burgers vector of  $a/3\langle 1\text{-}100 \rangle$  type. These created extended defects degrade the device performance due to large recombination leakage current. The defect grows in the direction perpendicular to the off-axis direction and often grows until it spans over the

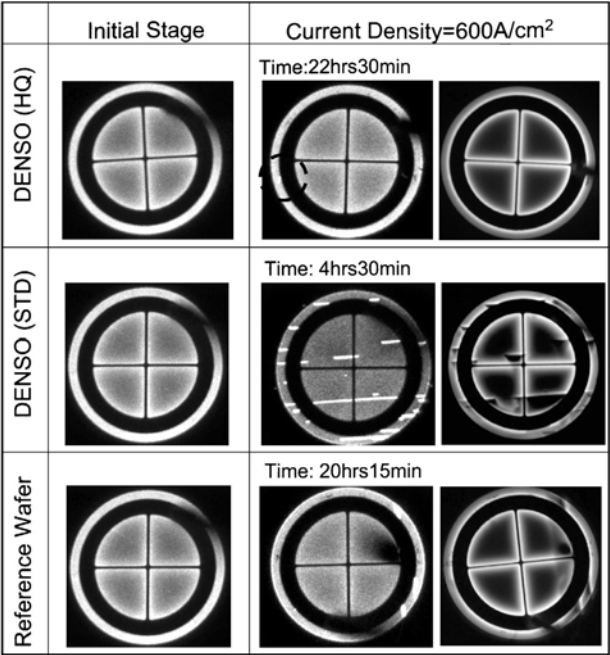


**Fig. 7.** Electroluminescence images of *pn* diodes before and after the forward current stress degradation

whole device area. The nucleation and propagation velocity of defect seems to be different, depending on the quality of the wafers. We observed that defect generation rate is relatively higher for *pn* diodes fabricated on 4H-SiC wafer with higher defect densities. It is shown that the in-house developed DENSO HQ 4H-SiC wafer is less susceptible to the forward current degradation, which we attributed to comparatively much lower EPD values. These results demonstrate that the degradation phenomenon of bipolar *pn* diodes is strongly related to the SiC structural crystal defects of the starting material. The continuous SiC material development will eventually lead to the robust bipolar device in the future.

**3.2 Thermally Oxidized SiO<sub>2</sub>/SiC MOS Interface**

The thermal oxidation kinetics and the MOS interface of SiC are poorly understood as they still lacks the critical know how. Afanasev et al. [18] originally proposed that interface states in SiC/SiO<sub>2</sub> structures result from C-clusters at the interface and defects in a near-interface sub-oxide that is produced when the oxidation process is terminated. The reported low MOS-FET channel mobility is due to high interface trap density that increases exponentially near the conduction band edge. Schörner et al. [17] reported

the relatively one-order higher channel mobility values for 6H- and 15R-SiC MOSFETs, compared to 4H-SiC MOSFET. The microstructure of transient-SiO<sub>2</sub> region in the SiO<sub>2</sub>/SiC system is very much different from that of SiO<sub>2</sub>/Si system [23]. The C-related compounds such as Si<sub>4</sub>C<sub>4-x</sub>O<sub>2</sub> complex and SiO<sub>1.5</sub> sub-oxide interspersed in C-matrix were reported to exist in the transient region. These residual complexes can form clusters or interact with H<sup>+</sup> or OH<sup>-</sup> ions under pyrogenic oxidation condition. Therefore, the control over the C in the transient region is vital for improving the quality of MOS interface. Electrical characteristics of MOS interface have shown strong dependence on the pre- and post-oxidation conditions. The re-oxidation and O<sub>2</sub>-annealing post-oxidation treatments were found to be effective in reducing the C-content near the MOS interface, which was attributed to the reduction of C concentration near or at the MOS interface. The maximum electric breakdown fields above 10 MV/cm and interface trap density value below  $1 \times 10^{12} \text{ eV}^{-1} \text{ cm}^{-2}$  have been reported for thermally grown SiO<sub>2</sub> on (0001) oriented Si-face *n*-type 4H-SiC.

We investigated the  $D_{\text{NIT}}$  using the thermal admittance (TAS) spectroscopy on 4H-SiC MOS capacitors fabricated under the wet oxidation ambient. *n*-type 4H-SiC (0001) Si face off-oriented epi-wafers were used in the present investigation. The thickness and nitrogen doping concentration of the epi-layer was 10  $\mu\text{m}$  and  $1 \times 10^{16} \text{ cm}^{-3}$ , respectively. Figure 8 shows a series of admittance spectra for 4H-SiC MOS capacitor under various accumulation bias conditions in the range of 0  $\sim$  15 V. The conductance was measured over the temperature range of 80–380 K. The admittance spectroscopy can provide the information related to the trap centers in MOS capacitor. It can be seen from the figure that even for 0 V bias, tail of peak-A was detected in the measured temperature range that corresponds to the deep traps near the midgap. When the accumulation bias voltage is increased in steps from 0 V to 8 V, a broad peak was observed for each biasing condition. Under the accumulation condition, the electrons are available near the MOS interface that can be trapped by the interface traps, which are close to the Fermi-level. The admittance signal arises from these charged interface traps. The shift in the peak position towards the lower temperature range indicates lowering of ionization energy or capture cross-section of the corresponding trap states. For 8 V bias, two peaks (peak-A and peak-B) appear as a result of response from interface traps of different microstructures. The intensity of the broad peak was also decreased with increasing accumulation bias voltage due to bias effect on the TAS signal. At this point, we think that the  $D_{\text{NIT}}$  is contributing to the peak-B. Finally, in the strong accumulation region i.e., 15 V bias, only peak-B appears which supports the above stated statement. The Arrhenius plots of electron emission rate  $e_p T^{-2}$  for the trap state calculated from the admittance spectra is shown in Fig. 9. The estimated density of traps from the admittance data for peak-A and peak-B are shown in the figure. The ionization energy of broad peak-A shows a strong bias dependence

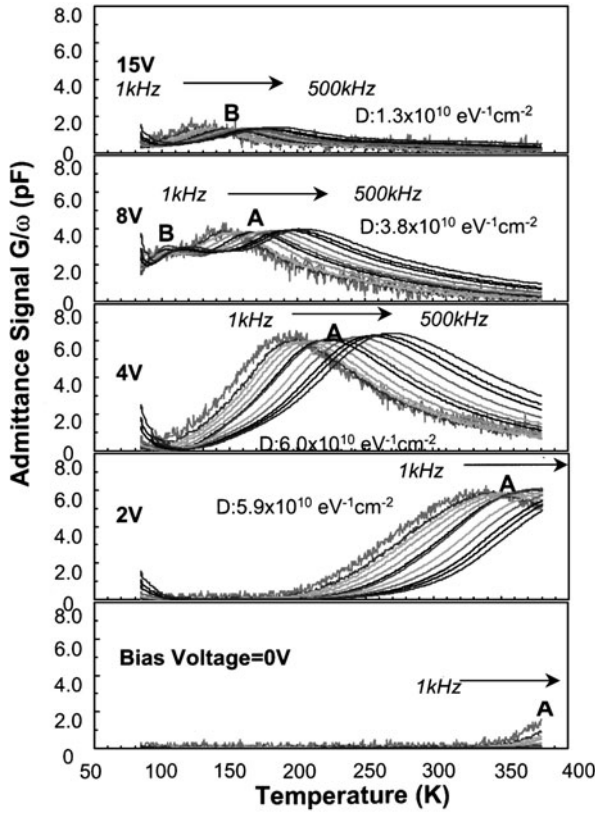


**Fig. 8.** The admittance spectra for 4H-SiC MOS capacitor under various accumulation bias conditions

and indicates a broad distribution of these traps below the conduction band down to midgap region. The peak-B corresponds to the traps in the near SiO<sub>2</sub> region and lies very close to the conduction band edge that was first reported by Afanasev et al. [18]. The  $D_{\text{NIT}}$  has strong influence on the channel mobility of 4H-SiC MOSFETs because their ionization energy ( $\Delta E = 180$  meV) lies between the conduction band edge of 4H- and 6H-SiC polytype. However, the  $D_{\text{NIT}}$  values estimated from the admittance data is in the range of  $10^{10} \sim 10^{11} \text{ eV}^{-1}\text{cm}^{-2}$ , which is about 1-order lower than that estimated by the capacitance-voltage ( $C$ - $V$ ) measurements. Earlier, Bassler et al. [24] reported the presence of high value of  $D_{\text{NIT}}$  at 4H-SiC/SiO<sub>2</sub> interface located close to the conduction band edge of MOS capacitors fabricated under the dry oxidation ambient. Novel innovations are needed to bring the  $D_{\text{NIT}}$  value down to about  $\sim 1 \times 10^{11} \text{ eV}^{-1}\text{cm}^{-2}$ .

Recently, the NO and N<sub>2</sub>O annealing at high temperatures has revealed to improve SiO<sub>2</sub>/SiC MOS interface properties. Fabrication of 10–20 A class

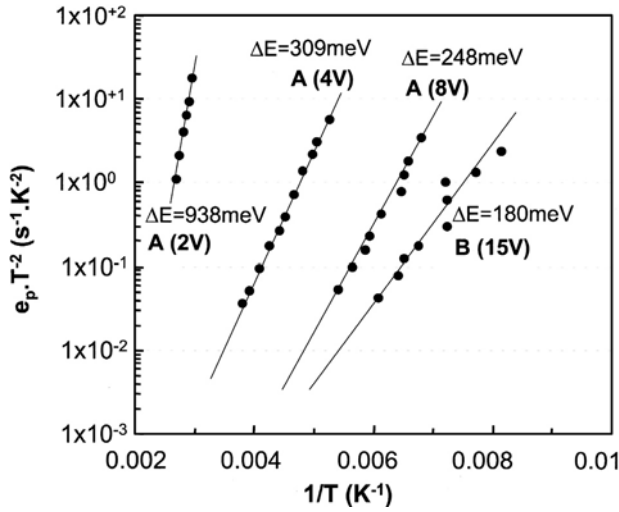


**Fig. 9.** Arrhenius plots of electron emission rate  $e_p T^{-2}$  vs. reciprocal temperature

power DMOSFETs were reported by Cree Inc. [25, 26]. Remarkable improvements of the 4H-SiC MOSFET inversion layer mobility were reported by using the oxide nitridation [27]–[29]. The oxide is usually thermally grown in nitrous oxide atmosphere at 1250°C. Inversion layer mobility values up to  $\sim 50 \text{ cm}^2/\text{Vs}$  for lateral 4H-SiC MOSFETs which were prepared on low doped *p*-type epilayers and the oxide was thermally grown in nitrous oxide atmosphere at 1250°C [30]. This annealing process is considered to have two effects, one is formation of stable Si-N bonds and the other is removal of C-related sub-oxides. However, it is not yet understood which effect brings the improvement of MOS interface properties. Main reason for the improvement should be an increase of channel mobility. The channel mobility increase may be due to the reduction of the  $D_{\text{NIT}}$ . The N introduced into the SiO<sub>2</sub>/SiC interface can passivate interface states, however, it does not remove the residual-C in the oxide as C was detected by XPS measurements [31]. The high inversion-mode channel mobility and high temperature reliability using deposited ONO (silicon oxide/silicon nitride/silicon oxide) are also quite encouraging for MOS based devices. The innovations in the SiC oxidation process have improved the SiO<sub>2</sub>/SiC MOS interface quality, but producing reliable devices will require additional improvements.

### 3.3 Selective Ion-Implantation Doping in SiC

For SiC selective doping process, the thermal diffusion commonly used for Si devices is not available because of the extreme stability of SiC [32]. One of the key issues for realizing the SiC planar devices is to eliminate the ion-implantation process induced damages as well as to achieve the high electrical

activation for dopants to match the design requirements. However, the high temperature activation annealing process of SiC usually deteriorates the important chemical and morphological surface that eventually leads to poor electrical properties. Donor (N, P, As) and acceptor (Al, B, Ga) atoms are required for the tailored *n*- and *p*-type doping profiles. Recent reports on *n*-type SiC doping indicate that P is a potential candidate for power device applications, which require low source/drain contact resistance. Capano et al. [33] reported that P is the better choice for the high doses due to higher electron mobility, however, N is preferred for the moderate doping levels. Khan et al. [34] reported about four times lower dielectric strength of thermal oxide grown over a P implanted region than a non-implanted region and about two times lower than the N implanted region under the identical conditions. However, the average ionization energies (*h*- and *k*-lattice sites) of the P donor are relatively higher than that of the N donor in 4H-SiC. Recently, Laube et al. [35] reported that below the critical implantation donor concentration of about  $3 \times 10^{19} \text{ cm}^{-3}$ , the N is superior below and P above this critical value. We have shown that the co-doping with N and P is better for higher activation at low annealing temperatures [36]. The lower activation of N for higher concentration was attributed to the formation of deep electrically inactive complexes.

On the other hand, the efficient electrical activation for *p*-type dopant in SiC is difficult, a common feature in wide band gap semiconductors. The Al shallow acceptor energy level is located at  $191 \sim 230 \text{ meV}$ . The B-related shallow and deep levels are located at  $285 \sim 390 \text{ meV}$  and  $540 \sim 720 \text{ meV}$ , respectively. The B dopant provides an advantage that it can be implanted deeper into the SiC than the other group-IIIa impurities for a given implantation energy and causes less implantation damage to the SiC crystal lattice. Magnetic resonance studies by Adrian et al. [37] confirmed that the shallow acceptor level consists of B residing at Si-lattice site. The microscopic structure of second deep levels, known as *D* center is still an open issue and needs to be addressed theoretically as well as experimentally. Based on EPR/ENDOR investigations, Baranov et al. [38] speculated a complex microstructure in which B on Si-lattice site is paired with a C-lattice vacancy i.e.,  $B_{\text{Si}}-V_{\text{C}}$  configuration. These *D* centers can lead to the degradation of the device electrical characteristics in long term, therefore, a suitable process is needed to suppress these centers. Moreover, long B diffusion tail has been observed in SiC polytypes [39]. The B has the large diffusion constant at elevated temperatures compared to most of the other *p*- or *n*-type doping species. As we discussed earlier, the high power applications require a high level of unit-cell integration. However, B lateral diffusion can limit the reduction of unit-cell due to increasing JFET pinch resistance.

### 3.3.1 Control Over B Diffusion

Considering that B has middle values between Si and C both in atomic covalent radius and electronegativity, and also that both Al and B form shallow level in Si. It is expected that B substituted on a Si-lattice site in SiC will have low formation energy and will form a shallow level. This implies that a suitable process is needed to increase the probability for B to occupy the favored Si-lattice site for high electrical activation. The B on a Si-lattice site is favorable under the C-rich conditions to achieve high electrical activation, based on a site-competition effect [40, 41]. Earlier, we reported that B on a Si-lattice site is favorable under the C-rich conditions to achieve high electrical activation, based on first principle calculations [42]. Therefore, the C/B sequential implantation can increase the probability for B to occupy Si-lattice site and this way also suppresses the formation of  $D$  centers. Troffer et al. [39] have demonstrated that the C/B co-implantation can suppress the formation of  $D$  centers. Laube et al. [43] recently reported the suppression of B out-diffusion and correlated it to the mechanism based on an analogy to the B diffusion in Si.

We have systematically investigated the effect of C/B sequential implantation on the formation B-related  $D$  center and the transit enhanced diffusion (TED). The (0001)-oriented 4H-SiC epitaxial wafers consisting of a LPCVD grown 5  $\mu\text{m}$  thick  $p$ -type epitaxial layers on  $p$ -type substrates were used. The background Al dopant concentration of the epitaxial layer was  $1 \times 10^{16} \text{ cm}^{-3}$ . Multiple 8-fold implantations with suitable ion energies were performed to create a box profile of C and B with a mean B concentration of  $1 \times 10^{18} \text{ cm}^{-3}$  and a depth of 0.8  $\mu\text{m}$ . The C concentration was varied from  $1 \times 10^{17} \text{ cm}^{-3}$  to  $1 \times 10^{20} \text{ cm}^{-3}$ . The C/B implanted samples were furnace annealed at 1650°C for 30 min in Ar to activate the dopants. The B implantation was performed at 1000°C to prevent amorphization in (0001), (1-100), and (11-20) oriented 4H-SiC wafers to determine the anisotropic nature of vertical and lateral diffusion of B dopant. The single step B implantation doping concentration and energy were  $1 \times 10^{18} \text{ cm}^{-3}$  and 400 keV, respectively. The (0001) oriented wafer represent the vertical diffusion and the (1-100), and (11-20) oriented wafers represent the lateral diffusion. As evident from the SIMS data in Fig. 10, we found that the lateral diffusion of B is more dominant compared to the vertical diffusion for a given set of implantation conditions. This was the first confirmation report on the anisotropic nature of B diffusion in 4H-SiC. Also, compared to (1-100) orientation, the B tends to diffuse even at lower temperature in the (11-20) orientation. The SIMS data of the as-implanted (11-20) oriented wafer shows the B diffusion during the implantation at 1000°C. Therefore, the suppression of B enhanced lateral diffusion is vital for fabricating the SiC power devices with high cell packing density. Planar circular Schottky diodes were fabricated on the C/B sequentially implanted 4H-SiC, forming Ni Schottky contacts with  $\phi = 500 \mu\text{m}$  and large area Al/Ni Ohmic backside contacts. The  $i$ -DLTS measurements setup used

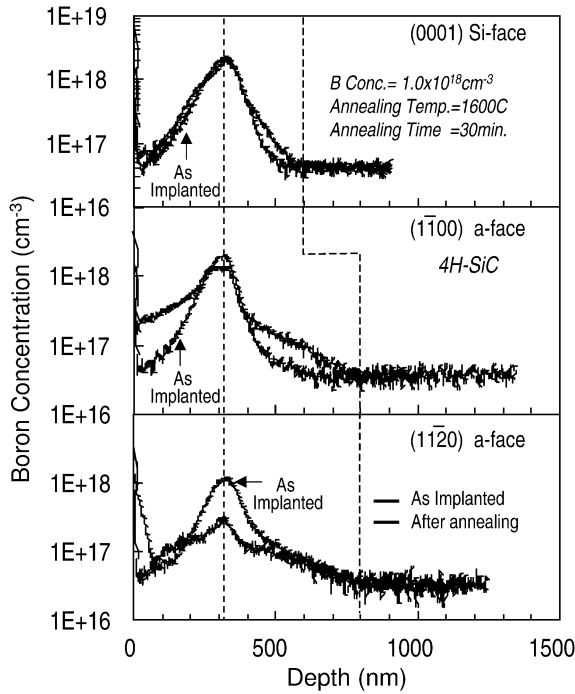


**Fig. 10.** SIMS profile of implanted B impurity in 4H-SiC along the (0001), (1-100), and (11-20) orientations showing a long diffusion tail after annealing at 1600°C for 30 min

to monitor the electrically active deep defects in C/B sequentially implanted 4H-SiC. The measured typical *i*-DLTS spectra for the B implanted 4H-SiC sample #1 are shown in Fig. 11a. The mean implantation concentration was  $1 \times 10^{18} \text{ cm}^{-3}$ .

The *i*-DLTS spectra can provide information on the deep levels undergoing charge transfer at higher temperatures. The spectra for different time windows exhibit a sharp peak due to the B-related *D* centers. The calculated ionization energy and the density of *D* center were  $E_V + 529 \text{ meV}$  and  $9.4 \times 10^{18} \text{ cm}^{-3}$ , respectively. The identical *i*-DLTS spectra were observed for the C/B sequentially implanted sample #2 as shown in Fig. 11b. It can be seen that there is no visible changes in the *i*-DLTS spectra of sample #2 from that of sample #1. However, the ionization energy of the *D* center has shifted towards the higher side i.e.,  $E_V + 566 \text{ meV}$ . The *D* center spectrum for sample #2 shows a decrease in the peak intensity, which is directly related to the density of defect centers. This indicates that the introduction of C leads to the suppression of *D* centers. Sample #3 was prepared under the identical process parameters except that the C concentrations raised by one order of magnitude. This time as evident from the *i*-DLTS spectra of sample #3 that

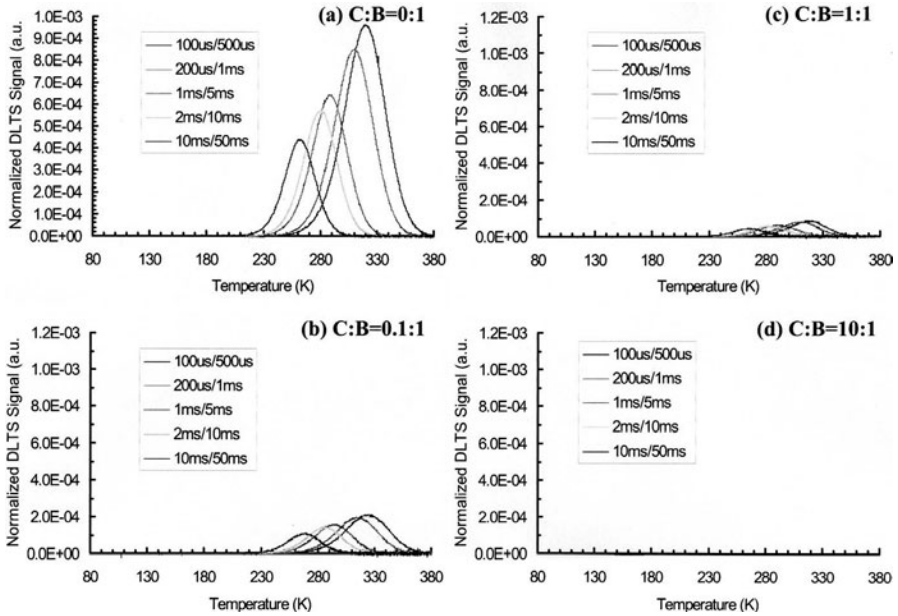


**Fig. 11.** The *i*-DLTS spectra of C/B sequentially implanted 4H-SiC. There is no visible change from that of typical *i*-DLTS spectra of B implanted 4H-SiC, except for the decrease in the intensity of *D* center with increasing C content

the *D* center is suppressed further in this C/B sequential implanted sample with C and B ratio of 1:1 as shown in Fig. 11c. Again, the ionization energy of the *D* center shifted towards the higher side i.e.,  $E_V + 586$  meV. We further raised the C concentration by one order of magnitude in sample #4. It was found that the *D* center peak completely disappeared for C and B ratio of 10:1 as shown in Fig. 11d. The free hole concentration calculated from the *C-V* analysis also shows an increase for C/B sequentially implanted samples as the density of *D* center start decreasing with increasing C concentration. These results demonstrate that the C/B sequential implantation, a site-competition effect, is effective in suppressing the formation of *D* center. The above results of the C/B sequential implantation process lead to the speculation that the *D* center microstructure configuration is more likely a complex in which B on Si-lattice site is paired with a C-lattice vacancy i.e.,  $B_{Si}-V_C$  configuration. The *D* center is located at about  $E_V + 529 \sim 586$  meV.

In this C/B sequential implantation process, another striking results were observed from the SIMS profiles of the annealed samples as shown in Fig. 12. Two main noticeable points are as follows:

- (a) Long B diffusion tail of more than  $1\text{ }\mu\text{m}$  was observed in the implanted  $4H\text{-SiC}$  sample, and
- (b) The B diffusion tail is suppressed to as-implanted SIMS profile when the C concentration reaches about  $1 \times 10^{19}\text{ cm}^{-3}$  (C and B ratio of 10:1) for sample #4 for a given ion-implantation and activation annealing conditions.

This suppression of B diffusion tail can be attributed to the following phenomenon. First, as evident from the *i*-DLTS data that for this particular composition of C/B the deep defects are less than the detection limit of the measurement system. This indicates that the elimination of defect is one of the phenomena, which is responsible for the suppression of the B transit enhanced diffusion. Based on the *i*-DLTS analysis of the B implanted *pn* junction, Gong et al. [44] reported the high density of *D* centers in the extended B diffusion tail. These results clearly correlate the B transit enhanced diffusion to the formation of *D* centers, a B-vacancy complex. Secondly, the implanted C may out number the C vacancies with increasing C concentration in C/B sequential implantation. This phenomenon can also explain the observed suppression of B diffusion tail. According to our first principle calculations, it is more likely that the C vacancy concentration control the B diffusion. On the other hand, it may be possible that the B out-diffusion is somewhat related to the kick out mechanism [45] as the RBS data of C/B sequentially implanted samples indicate the creation of a Si-rich subsurface region. In summary, by implanting the electrically inactive C into the *p*-base region and/or epi-channel layer and/or the JFET region between the *p*-base regions, a B diffusion resistant region can be formed to match the ECFET design requirements.

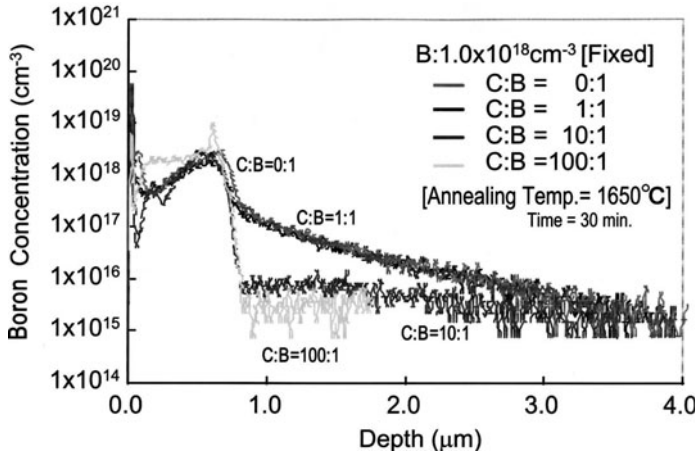


**Fig. 12.** SIMS profile of implanted B in  $4H\text{-SiC}$  along the (0001) orientation showing a long diffusion tail after annealing at  $1650^\circ\text{C}$  for 30 min in Ar ambient

## 4 Application of MOS Based Power Devices in HEV Inverters

MOS based SiC power switches, with their superior features compared with Si-based switches, can substantially improve the performance of hybrid electric vehicle (HEV) inverter systems. Today's most advanced electric vehicle still suffers from the insufficiency of the energy storage because of the limited battery capabilities. Compared to fuel tanks, they are inferior in terms of mobility at high costs. The commercial production of HEVs using a combination of electric motors and internal-combustion engines (ICE) for power-train became feasible. HEVs eliminate the limited mobility of electric vehicles. The various technical solutions for hybrid drive systems can be categorized into series and parallel hybrid system. In simplified terms, a series hybrid transfers the power electrically i.e., the electric power produced by an ICE-generator unit is transformed into mechanical power via electric drive motors. The parallel hybrid transfers the power mechanically to the wheels. The power and torque of the ICE and electric motor can be added by running both at the same time. However, the potential to reduce emissions is greater for a series hybrid drive system than of a parallel hybrid. For the inverter of HEV traction motor control system, vital requirements are compactness, light-weight, highly efficient, and high reliability. Existing HEV inverter systems generally use intelligent power modules in an attempt to achieve compact and efficient designs. One of the basic building blocks of power module is the half bridge pulse width modulation (PWM) circuit in which pairs IGBT switch and anti-parallel PiN FWD are connected in series in a Totem-pole configuration. For the IGBT power module (18-chips in 6-arms) of a rated voltage of 600 V and a rated current of 600 A, each chip is connected in parallel to each other for each phase arm. The IGBT power module contains within a package the protective functions against over-current, short-circuit, voltage drop, and overheat. Required characteristics for the IGBTs are low losses, high ruggedness, and easy drivability. However, there is a trade-off relation between the power loss and ruggedness. The controller produces gate-driving signal into each phase arm based on the PWM signal from the engine control unit (ECU). The performance of the inverter systems generally depends on the quality of its power chips.

In these IGBT inverters, the circulating current flows through FWDs because these devices can't conduct reversely. In this configuration, when the gate voltage turns the IGBT on, the PiN diode attempts to turn off. The PiN diode drift region is conductivity modulated by minority carrier injection, and there is a substantial minority charge storage that must be removed each time when the diode turns off. Therefore, the transient reverse current in the FWD adds to the motor current flowing through the IGBT, causing the collector current to overshoot. This high current flows while the collector voltage of the IGBT begins to fall, and the IGBT dissipates considerable instantaneous power. Therefore, the turn-on energy loss is given by

the integral of the current-voltage product during the overshoot spike. The turn-off losses are mainly dominated by the turn-off characteristics of bipolar Si-IGBT alone. The total switching loss can be roughly classified into two categories: (a) the conduction loss, determined mainly by the product of the voltage and current, when the element is turned-on, and (b) the switching loss, caused in the transient state of switching. When the carrier frequency reaches or exceeds 10 kHz, the switching loss accounts for nearly 50% of all the total inverter loss. The high switching losses lead to high heat dissipation from the power switching devices. Therefore, to increase the efficiency and decrease the cost, weight, and volume of power inverter systems, it is important to reduce this heat dissipation. The higher destruction immunity is required for automobile applications. 600 V class (Current rating = 200 A) planar or trench Si-IGBTs and soft recovery PiN FWDs are being used in the existing inverter systems. FWDs soft recovery characteristics are desired in order to reduce the EMI noise occurring with IGBT switching operations. FWD power loss reduction is particularly important for HEV systems because of the frequent regenerative operations and stall modes. To reduce these switching losses or heat dissipation, both software as well as hardware approaches are available. One of the hardware solutions is to use the unipolar SiC power switching devices. Majority carrier devices like the MOSFETs and JFETs offer extremely low switching power losses. Therefore, the application of SiC unipolar devices can drastically reduce both the conduction loss and the switching power dissipation of power inverter systems. The soft switching characteristics also guarantee good electromagnetic compatibility (EMC) behavior. It is expected that SiC MOSFETs will replace the Si-IGBT for the future generation inverter system for medium class power applications in the blocking voltage range below 5 kV. The bipolar devices like IGBTs, and GTOs offer low forward voltage drops at high current densities but have higher switching losses than majority carrier devices. Since a built-in junction potential of SiC is higher than that of Si due to larger band gap, therefore bipolar power devices are attractive with a blocking voltage above 5 kV. There exists a design trade-off between the switching speed and the on-state voltage drop in a switching power device. There are also other considerations that may be of paramount importance for the circuit designer while making the choice of the switching device for a particular application viz., high temperature capability, radiation hardness, easy current control ability, simple protection under abnormal modes of operation, and operation-mode of device (normally-on or -off type). In addition, the high value of thermal conductivity for SiC allows dissipated heat to be readily extracted from the device. This, in turn, allows a corresponding increase in power to be applied to the device for a given junction temperature, while maintaining the power chip destruction immunity. The other advantages of using the SiC MOSFETs are their reverse conduction characteristics and the availability of internal pn body diode that can be used as a FWD to achieve a FWD-less inverter system. Figure 13

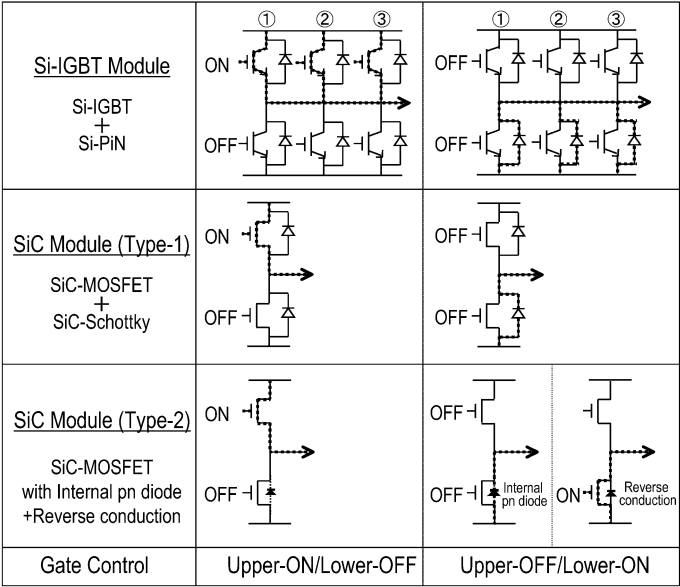


**Fig. 13.** A comparison of existing Si-IGBT power module basic half-bridge circuit with the possible SiC unipolar device based power modules

shows a comparison of existing Si-IGBT power module configuration with the SiC power modules. The SiC module type-1 utilizes the Schottky FWD, while module type-2 is using the internal *pn* diode and reverse conduction mechanism. The SiC power devices will reduce the conduction losses and the switching losses drastically by 1~2 order of magnitudes depending on the applications. These features allow the construction of power module using fewer power device chips e.g., three Si-IGBT chips in each phase arm can be replaced by a single SiC unipolar MOSFET chip. The FWD-less SiC power module will further helps in the downsizing of inverter system. Cost reduction is one of the most important problems to overcome for the popularization of HEV vehicles. The SiC unipolar power devices have various advantages compared with Si-IGBT, provided the following issues that are limiting the wide-spread use would find the reasonable solutions. Some of these key issues are (a) size of the SiC wafer and low processing yield because of high density of defects, (b) high cost and limited availability of SiC power devices, and (c) unavailability of high-temperature packaging technology.

## 5 Conclusions

Accumulation-mode ECFET design concept that is particularly applicable to wide band gap SiC and the device processing technologies that face the hard challenges for high power switching applications have been reviewed. The challenges for power device development beginning from SiC wafer quality to key device processes of thermal oxidation and ion-implantation are also discussed. The outstanding material issue demands the reduction in the  $\mu$ -pipe defects and the dislocation density to allow higher yields and larger devices to become practical. We demonstrated that the degradation phenomenon of bipolar devices is strongly related to the SiC structural crystal defects of the starting material. SiO<sub>2</sub>/SiC MOS interface fabrication process calls for the novel innovations to improve the MOS interface quality. The  $D_{\text{NIT}}$  close to the conduction band edge remains high in the range of  $\sim 10^{12} \text{ eV}^{-1}\text{cm}^{-2}$ . The near interface traps in SiO<sub>2</sub> were observed below the conduction band edge that severely degrade the channel mobility. High temperature nitric oxide annealing techniques have shown reduction in the  $D_{\text{NIT}}$  values as well as improvement in the MOSFET channel mobility. We found that C/B sequential implantation process can control the B transit enhanced diffusion. This vital process can match the design requirements, especially for the high blocking voltage power device design. Finally, the applicability of ideal SiC switches in HEV propulsion application is reviewed. These systems with SiC power devices have the qualities of being more compact, lighter, and efficient.

## Acknowledgements

The author would like to thank Dr. K. Hara, for his encouragement. The research engineers at DENSO Research Laboratories and Toyota Central R&D Labs., Inc. are acknowledged for their invaluable assistance.

## References

1. B.J. Baliga: IEEE Elec. Dev. Lett. **10**, 455 (1989)
2. SiC Schottky Diode SDP10S30, Data Sheet, Infineon Technologies, Germany
3. 10 W SiC RF MESFET CRF-20010-001, Data Sheet, Cree Inc., USA
4. F. Profumo, A. Tenconi, G. Brusaglino, V. Ravello: Intern. Power Electronics Conference (Tokyo, 2000) p. 1953
5. L.M. Tolbert, B. Ozpineci, S.K. Islam, F.Z. Peng: SAE World Congress, Detroit, 02FCC-37 (2000)
6. K. Hara: 7th Int. Conf. on Silicon Carbide, III-Nitrides and Related Materials (Stockholm, 1997) p. 901
7. S. Onda, R. Kumar, K. Hara: phys. stat. sol. (a) **162**, 369 (1997)
8. J. Tan, J.A. Cooper, Jr., M.R. Melloch: IEEE Elec. Dev. Lett. **19**, 487 (1998)
9. R.K. Chilukuri, P.M. Shenoy, B.J. Baliga: Proc. of 10th Intern. Symp. on Power Semiconductor Devices & ICs (Kyoto, 1998), p. 115

10. R. Kumar, J. Kozima, T. Yamamoto: Intern. Conf. on Solid State Devices and Materials (Tokyo, 1999) p. 146
11. R. Kumar, J. Kozima, T. Yamamoto: Jpn. J. of Appl. Phys. **39**, 2001 (2000)
12. J.W. Palmour, J.A. Edmond, H.S. Kong, C.H. Carter, Jr.: Proc. 28th InterSociety Energy Conversion Conf. (1993) p. 1249
13. Y. Sugawara, K. Asano, D. Takayama, S.-H. Ryu, R. Singh, J.W. Palmour, T. Hayashi: Mater. Sci. Forum **389–393**, 1199 (2002)
14. R. Schörner, P. Friedrichs, D. Peters, H. Mitlerhner, B. Weis, D. Stephani: Materials Science Forum **338–342**, 1295 (2000)
15. D. Takayama, Y. Sugawara, T. Hayashi, R. Singh, S.-H. Ryu, J.W. Palmour, K. Asano: Proc. of 13th Intern. Symp. on Power Semiconductor Devices & ICs (Osaka, 2001) p. 41
16. *Technology Roadmap of Power Devices/ICs*, 13th Intern. Symp. on Power Semiconductor Devices & ICs (Osaka, 2001)
17. R. Schörner, P. Friedrichs, D. Peters, D. Stephani: IEEE Elec. Dev. Lett. **20**, 241 (1999)
18. V.V. Afanasev, M. Bassler, G. Pensl, M. Schulz: phys. stat. sol. (a) **162**, 321 (1997)
19. H. Yano, T. Hirao, T. Kimoto, H. Matsunami, K. Asano, Y. Sugawara: Mater. Sci. Forum **338–342**, 1105 (2000)
20. K. Fukuda, S. Suzuki, J. Senzaki, R. Kosugi, S. Harada, M. Okamoto, M. Kato, K. Suzuki, K. Kojima, T. Suzuki, K. Takao, T. Mori, T. Yatsuo: 11th SiC and Relation Wide Gap Semiconductor Society Meeting (Tokyo, 2002) p. 12
21. H. Lendenmann, F. Dahlquist, J.P. Bergman, H. Bleichner, C. Hallin: Mater. Sci. Forum **389–393**, 1259 (2002)
22. R.K. Malhan, H. Nakamura, S. Onda, D. Nakamura, K. Hara: European Conf. on Silicon Carbide and Related Materials (Linköping, Sweden, 2002)
23. R. Kumar: Annual Meeting of Jpn. Society of Appl. Phys. 29p-YH-8 (1999)
24. M. Bassler, V.V. Afanas'ev, G. Pensl, M. Schulz: Mater. Sci. Forum **338–342**, 831 (2000)
25. S.-H. Ryu, A. Agarwal, J. Richmond, J. Palmour, N. Saks, J. Williams: IEEE Elec. Dev. Lett. **23**, 321 (2002)
26. S.-H. Ryu, A. Agarwal, J. Richmond, J. Palmour, N. Saks, J. Williams: Proc. of 14th Intern. Symp. on Power Semiconductor Devices & ICs (Santa Fe, 2002) p. 65
27. H. Li, S. Dimitrijević, H.B. Harrison, D. Sweatman: Appl. Phys. Lett. **70**, 2028 (1997)
28. G.Y. Chung, C.C. Tin, J.R. Williams, K. McDonald, M.D. Ventra, S.T. Pantelides, L.C. Feldman, R.A. Weller: Appl. Phys. Lett. **76**, 1713 (2000)
29. S. Ogino, T. Oikawa, K. Ueno: Mater. Sci. Forum **338–342**, 1101 (2000)
30. D. Peters, R. Schörner, P. Friedrichs, D. Stephani: European Conf. on Silicon Carbide and Related Materials (Linköping, Sweden, 2002)
31. Y. Maeyama, H. Yano, T. Hatayama, Y. Uraoka, T. Fuyuki, T. Shirafuji: Mater. Sci. Forum **389–393**, 997 (2002)
32. M. Ikeda, H. Matsunami, T. Tanaka: Phys. Rev. B **22**, 2842 (1980)
33. M.A. Capano, J.A. Cooper, Jr., M.R. Melloch, A. Saxler, W.C. Mitchel: Mater. Sci. Forum **338–342**, 703 (2000)
34. I.A. Khan, B. Um, M. Matin, M.A. Capano, J.A. Cooper, Jr.: MRS Fall Meeting (Boston, 2000)

35. M. Laube, F. Schmid, G. Pensl, G. Wagner: Mater. Sci. Form **389–393**, 791 (2002)
36. R.K. Malhan, J. Kozima, T. Yamamoto, A. Fukumoto: Mater. Sci. Form **389–393**, 541 (2002)
37. F.J. Adrian, S.G. Weber, J.M. Spaeth: Solid State Commun. **94**, 41 (1995)
38. P.G. Baranov: Mater. Sci. Forum **264–268**, 581 (1998)
39. T. Troffer, M. Schadt, T. Frank, H. Itoh, G. Pensl, J. Heindl, H.P. Strunk, M. Maier: phys. stat. sol. (a) **162**, 277 (1997)
40. T. Miyajima, N. Tokura, A. Fukumoto, H. Hayashi: Jpn. Patent 9-63968 (1995)
41. D.J. Larkin, P.G. Neudeck, J.A. Powell, L.G. Matus: Appl. Phys. Lett. **65**, 1659 (1994)
42. R. Kumar, K. Hara, A. Fukumoto, H. Hayashi: Intern. Workshop on Hard Electronics (Tsukuba, 1998) p. 16
43. M. Laube, G. Pensl, H. Itoh: Appl. Phys. Lett. **74**, 2292 (1999)
44. M. Gong, C.V. Reddy, C.D. Beling, S. Fung, G. Brauer, H. Wirth, W. Skorupa: Appl. Phys. Lett **72**, 2739 (1998)
45. N.E.B. Cower, K.T.F. Jandden, G.F.A. van de Walle, D.J. Gravensteijn: Phys. Rev. Lett. **65**, 2434 (1990)

# Development of SiC Devices for Microwave and *RF* Power Amplifiers

E. Morvan, A. Kerlain, C. Dua, and C. Brylinski

## 1 Introduction: At the End of the Feasibility Period

### 1.1 *RF* and Microwave Power: Switching vs. Analog

*RF* and microwave power is a specific world in the universe of electronics. For a given power level, the frequency spectrum is divided in two territories: the digital lowland and the analog highland. On the low frequency side, digital electronics is installed, seemingly for ever. The primary power signal is made of short pulses with variable duration and/or amplitude. Passive filters reject the higher parasitic harmonics. In contrast, the high frequency side still belongs to analog electronics, a world of high complexity, a world in which electronics is still to some extent an art, and not yet a science.

Let's take the example of radio and TV transmitters, systems in which power is measured in kilowatts. Up to 1 MHz, they actually operate in a switching mode using silicon switching transistors. Solid state switching solutions are available for power levels up to almost one Megawatt. Switching modules and electric lines are the main visible elements. At higher frequency, the shape and the content of the electronics is changed. Heat sinks, fans and cooling pipes dominate the landscape. Rise and fall transition delays and the related heat dissipation are stressing the system architecture. Heat starts to appear as a major threat and concern. Very few kinds of active components can achieve the job: vacuum grid tubes for the higher power levels, over 10 kW, and solid state analog transistors for the lower power amplifiers.

Of course, the high frequency limit of switching power electronics is continuously pushed upwards by the progress of solid state devices. However, for the past ten years, some kind of saturation has been observed. The next revolution will happen through the use of wide bandgap semiconductors. Electrically speaking, the figure of merit in this area is that of Baliga, a few hundred times higher for the wide bandgap materials and devices. Since switching electronics has high energy conversion efficiency, heat is not the major issue and thermal management will not set the limit. The new semiconductors can actually bring a steep increase of performance by one or two orders of magnitude. However, the wide band gap revolution for switching transistors has not yet happened. A few reasons can be found for the de-

lay. First, the switching devices are big devices driving large currents. They require large chip area and substrates with low defect density.

Second, the MOS structures on SiC still do not work fast enough. Finally, bipolar transistors have not yet been developed; significant research on them has only started a few years ago. Today, the wide bandgap devices are absent in the area they would bring the most tremendous change. The *RF* switching market is rather small, but the *RF* switching device specifications are not far away from that of the huge industry of high frequency switching power supplies. We are confident that wide bandgap transistors will be developed for switching power supplies and then applied to *RF* switching amplifiers, probably by 2010–2015.

## 1.2 Wide Bandgap Semiconductors for Analog RF Power Applications: The Challenge of Thermal Management

The area in which SiC and GaN devices are emerging is that of the analog *RF* power amplifiers. The relevant electrical figure of merit is that of Johnson [1], the value of which is again hundred times higher for the wide bandgap semiconductors as compared to Si or GaAs based semiconductors.

Analog power amplifiers are circuits based on devices for which switching times from ON and OFF state and back are not significantly less than the signal period. The devices permanently operate in a “lag” regime that is considered as transition for switching devices. In this regime, there is a period of the electrical cycle for which there is simultaneous presence of both voltage and current in the device. As a consequence, part of the energy from the power supply is dissipated as heat, often half or more. The heat power level is comparable to the *RF* power delivered to the load. It has to be evacuated. Here lies a major challenge. SiC or GaN are electrically 100 times or more better than silicon, but, for the thermal conductivity, SiC is only 3 times better, and the present hetero-epitaxial GaN is comparable to silicon.

For the present SiC devices, such as MESFETs and SITs, the dissipated heat density is at least twice that for silicon devices [2]. For GaN it is further twice higher and it will be even more in the future. There is a chance to manage the heat problem for SiC devices with the classical thermal management technology, but for the full exploitation of GaN, and later of AlN, diamond, BN based devices, it is expected that the development of a new technology for more efficient heat transport will be mandatory. For many years, the US defense agencies have understood the importance of thermal management and today, they support several projects aimed at providing this kind of breakthrough.

Thermal management can be complicated because of the specific hardware it requires. It often involves “dirty technology” such as liquids, gases, or mixed fluids, and a whole set of mechanical pipes, seals, vents, valves together with awkward thermo-mechanical design optimization. This side of

the development is not usually considered as the “noble” side. Nevertheless, it can be expected to account for the major part of the actual business value in future systems.

### 1.3 The Small World of Analog Microwave Power

“Cleaner” hardware is required for the design of microwave power amplifiers. Built around the power transistors, such an amplifier includes passive input and output circuits, which are assemblies of lines and localized passive elements. The core of the effort for the designer can be described as “impedance matching”. The impedance levels of the load and the source are dictated by the application. Those required by the transistor on input and output are measured by “Load – Pull” and “Source – Pull” techniques. The designer has to provide networks which will “transform” each of the source and the load impedance values into the optimum impedance required by the transistor. This transformation must be realized over the whole frequency range of operation, sometimes including harmonics in order to get maximum energy conversion efficiency. Additionally, the amplifier must be stable over the whole spectrum. A heavy batch of constraints.

#### 1.3.1 *RF* Power Designer’s Obsession: The Impedance Issue

The impedance issue is the obsession of the microwave amplifier designer. Let us consider how it affects the design of the power stage of a typical base station for mobile communications. Around year 2000, the base stations are working around 1 or 2 GHz. The typical power requirement is 100 watt according to the base stations urban density. For building the power amplifier, the designer has very little choice in terms of devices. Although GaAs FET and HBT are proposed as alternative solutions, silicon LD-MOS has been retained by most of the system manufacturers, at least in Europe.

No commercial LD-MOS product could be operated safely at more than 28–32 V drain voltage bias. Those who have tried to operate a few volts over the specs sheet limit have experienced a dramatic reduction of the device lifetime, by about one order of magnitude. This lifetime issue has even led to industrial breakdown of one of the major device manufacturers, due to reliability problems.

In order to get 100 W *RF* power at 30 V bias supply supposing 40% efficiency, a good figure, the real part of the impedance to be set at the intrinsic transistor outlet is ideally 5 ohms, it is actually around 1 Ohm, due to the reactive part of the transistor admittance. This is a major problem, since the impedance of antennas and access lines cannot be moved away from 50 ohms by more than a factor 2.

By applying their art and science, the microwave power designers have been able to cope with the existing devices and build amplifiers good enough

for the first and second generations of mobile communications. They have found their ways to get together: high power, high gain, the required bandwidth without too much distortion, good enough linearity, and stability over the whole spectrum. However, they often have failed to get good efficiency and they have had to implement device pre-matching in the transistor case. As a result, one packaged device generally offers very limited bandwidth. A typical 1 GHz catalogue transistor offers poor performance at 900 MHz.

### **1.3.2 New Standards Bring Next Challenge: The Wide Band Gap Opportunity**

Meeting all these amplifier specifications together has been a real challenge for the GSM standard. It has become a nightmare for the next generation of modulation standards. With the new signal modulation modes, constraint on linearity has become a hundred times more stringent.

With higher voltage handling and higher output impedance, impedance matching becomes considerably simpler. A wide bandgap transistor is to be considered as a piece of paradise by all microwave power designers. To them, at the end of years 1980s, we, the wide bandgap semiconductor community, have promised this paradise. It took us more than 10 years to demonstrate on real experimental devices and circuits the existence of the high voltage and high impedance capability we had initially promised [3, 4]. The SiC Schottky gated FET devices (SIT and Mesfet) have been the first wide bandgap transistors available as prototypes for trying to make prototype amplifiers. The use of SIT has been restricted so far to one company and its customers. SiC Mesfet power devices have been available so far at two places or more in the USA, and at least in one place in Europe.

### **1.4 Troubles with Traps: The Importance of Getting “Clean” Material**

Indeed, what  $RF$  power amplifier designers do not like is a device which breaks too easily. And what they really hate is a device the properties of which are not stable with time or vary with bias history.

Even the first SiC devices have been rather robust as compared to early silicon or GaAs ones. Unfortunately, the early SiC Mesfet devices on semi-insulating substrates were very unstable. The qualitative explanation is simple. In wide bandgap semiconductors, the deep levels induced by metals or defects or interface states have higher energy and much longer charging and discharging time constants, orders of magnitude longer. The same kind of deep levels which generate temporary effects in the millisecond range or less in silicon or GaAs, produces effects in the range from minutes to weeks in the case of wide bandgap materials, precisely the worst possible time-scale range for microwave power designers. Furthermore, the new devices operate

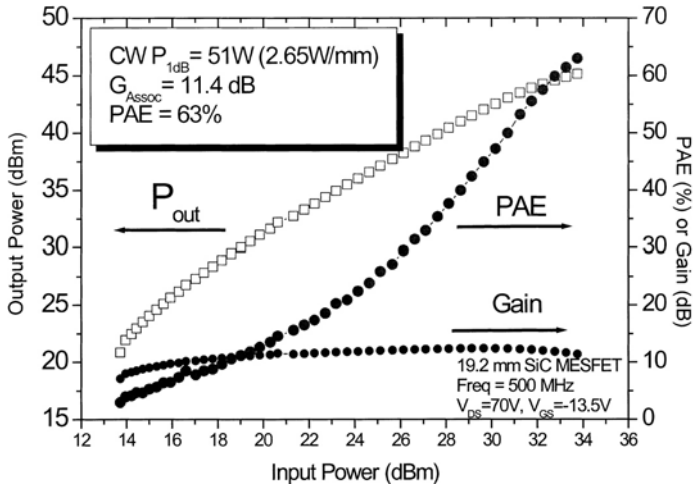


**Fig. 1.** 19.2 mm Thales SiC UHF MESFET prototype provides  $P(1dB) = 51$  W *RF* output power (2.65 W/mm) at 500 MHz for  $V_{ds} = 70$  V

with very large voltage sweep. This large voltage makes it possible for a small but significant part of the electron population to get enough energy to reach almost any trap present in the device structure.

Consequently, wide bandgap *RF* power device technology requires “clean” material and interface structures in terms of traps, even cleaner than for previous materials. Regrettably, in the starting period, not any new material is clean, there are plenty of traps everywhere. At Thales we have obtained our first 30 W *stable* power SiC MESFET devices only in the year 2001, reaching 50 W *CW* in year 2002 (see Fig. 1). At the beginning of year 2003, stable III-N compounds based devices have still to be demonstrated. At present, III-N compounds layers are made by hetero-epitaxy with very high mismatch.

They contain many crystal defects which can induce traps. And passivation too is far from perfect. Reducing the trap density in III-N devices is still a major challenge for the years 2000–2010.

### 1.5 Approaching the Market

Now, the feasibility of a first wide bandgap *RF* power technology has been established. The present Thales 50 W SiC Mesfet prototype exhibits a 40 ohms input and output optimum impedance (both imaginary and real part) in UHF (500 MHz) without any pre-matching in the package, only simple wire bonding without any special optimization. Such packaged devices have been successfully operated and measured from 1 MHz up to 2 GHz. We have also measured real part of output impedance around 25 ohms on a 50 W transistor working at 1.5 GHz with 50 V bias. Future devices from more mature technology are expected to deliver *RF* power over 100 W *CW* with output

impedance close to the 50 ohm ideal. In a few places in the world, including ours, good amplifiers have now been demonstrated with performance level never achieved before with silicon devices. As an example, at Thales, for a very wide band *RF* to UHF amplifier prototype for military communications, we can now reproducibly achieve power levels over 60 W over the whole band, while 5 W has been the maximum power ever obtained with silicon devices.

The whole community of solid state *RF* and microwave power is convinced that wide bandgap semiconductors are the right materials for the applications requiring the top possible performance. There is no more doubt. Wide bandgap *RF* and microwave power semiconductor devices will appear on the market. The main issues are time and cost.

## 2 Key Issues on the Way to SiC *RF* Power Device Industry

### 2.1 Device Topology

It is noticeable that none of the popular device structures for silicon has found its way so far for silicon carbide. No SiC MOS has achieved high frequency power operation [5]. Device development on Bipolar Junction Transistor has just started recently in the USA [6], and in Sweden. It could have been started before, but it requires a high degree of control on the epitaxy.

#### 2.1.1 Missing the MOS

Great initial enthusiasm was born from the fact that silicon carbide can be oxidized in a way somewhat similar to silicon, creating a silicon dioxide layer with good insulating properties. The disappointment came from the low electron mobility in the inversion layer. To date, it is still at least 5 times lower than on silicon MOS [7, 8]. On standard  $\langle 0001 \rangle$  Si-face *4H* substrate surface, it is often much lower. The result is that no *RF* or microwave SiC MOS transistor has been demonstrated yet. Terrible oxide reliability problems are also predicted if the mobility problem could be solved, in relation with the very high field in SiC transistors [9]. It is already very difficult to master the oxide reliability problem for 50 V silicon LD-MOS. It seems that nobody knows how it can be solved for a 100 V SiC transistor.

#### 2.1.2 Vertical Structures Static Induction Transistor (SIT) and Bipolar Junction Transistor (BJT)

Probably the most successful SiC transistor structure today is the Static Induction Transistor (SIT) [10, 11], with kW power achieved in pulse regime from UHF to *L*-band, and several hundred watts in *CW* operation. The SIT

device structure had never really found its way on the silicon device market, despite of repeated attempts, especially in Japan. It seems that the *RF* power SiC SIT is being developed exclusively for some defense applications and not aiming at any open commercial activity at the device level. The BJT devices can be seen as possible competitors to SIT, with the advantage of simpler process but with the drawback of lower input impedance, and also the need of excellent control on the epitaxial material and the etching process. The process of optimal vertical *RF* power devices is difficult. There are many problems arising from the trench configuration: (1) the ohmic contacts on the top of narrow trenches, (2) the gate contacts on the side or at the bottom of the trenches, (3) passivation and peripheral protection on the trench edges, in combination with (4) planarisation for interconnect.

It is even more difficult to make high voltage vertical devices with anode electrode (or drain, or collector) on top. In this configuration, the high voltage between drain and gate enhances the problems related to passivation, peripheral protection, and interconnect. We have seen so far no publication on such device configuration, although it would be the simplest for device packaging and thermal management. In all the published realizations of vertical SiC devices, the anode electrode is down and connected to a conductive  $N^+$  substrate.

### 2.1.3 HBT Early Attempts

Early attempts to make GaN/SiC Heterojunction Bipolar Transistors at Astralux, Thomson-CSF (now Thales), and The Royal Institute of Technology (Sweden) have not led to any viable *RF* power demonstration. The GaN/SiC heterojunctions measured so far exhibit a strange behavior, somewhat similar to the old results on GaAs/Ge. In most cases, the bipolar transistors have a current gain far below unity. Early better results could not be reproduced [12].

### 2.1.4 The Dream of Heterojunctions Between SiC Polytypes

Using heterojunction between polytypes to make some kind of HEMT device is still a dream. Quasi valence band alignment is predicted by almost all theoreticians, potentially leading to very high conduction band offset, 0.5 to 1 eV, ideal for HEMT structures, higher than for any heterojunction on GaAs substrate. The problem is that the material is extremely difficult to fabricate. Some people at Jena University, NASA, and also at Cornell have managed to demonstrate *3C/6H* heterojunction on *6H* substrate, but no heterojunction transistor has been shown. One reason is that the useful heterojunction for HEMTs would be the “reverse” heterostructure made of *6H* or *4H* layer on *3C* substrate, never obtained so far.

### 2.1.5 SiC MESFET

The SiC MESFET is probably the simplest structure which can be proposed for SiC microwave power devices. Indeed, transistor-like characteristics can be obtained on simple test devices fabricated with only 4 lithography steps using the geometry of any good old GaAs MESFET and some basic process adaptation to SiC material. This is one reason why SiC MESFET has been chosen for the first demonstrations of wide bandgap microwave devices.

On the other hand, for making large power *RF* and microwave devices, fully exploiting the capability of the wide bandgap material and fulfilling the tough requirements of the device consumers, the work is as hard as for any other kind of sophisticated device [13, 20].

## 2.2 The Substrate Issue

The SiC material in use today is expensive, and the substrates are too small for being used in existing foundries of silicon or GaAs *RF* and microwave products [21]. The SiC crystal still contains a high density of structural defects. In addition, there are only one or two sources in the world for the preferred kind of material: semi-insulating SiC. However, some competition has started to appear. As a result, the purity of the material available on the market has improved dramatically. Still, the price has not decreased, staying around 4000 \$EUR for one piece, two inch diameter. Two reasons for the high price. One is the low fabrication yield of the sublimation technique used today for growing the semi-insulating crystals. This may change soon. High Temperature-Chemical Vapor Deposition (HT-CVD) growth techniques are expected to provide higher yield. The other reason comes from a starting market issue: “egg and chicken”. For the present substrate price range, the customer basis is very narrow. A small decrease on the price is not expected to result in any substantial increase on the volume. Most of the device manufacturing units and the future customers are not ready yet to use the new substrates. Only a big change on the substrates can break the circle. This can only be achieved by incentive coming from applications with high added value. Military market can be one type. National programs on advanced technology is another possible way. Investment from the high added value product manufacturers is a third possibility. All those are presently at work for SiC in different places in the world. We expect the critical mass to be gathered before year 2005.

### 2.2.1 Polytype

No good quality and large substrates are available in cubic *3C*, *15R* or other rhombohedral polytypes. It seems that nobody has ever succeeded in growing any kind of *2H*-SiC crystal with size over a few mm. Up to now, the only SiC

material polytypes that can be used for *RF* power device development are *6H* and *4H*. For SiC MESFETs, as for the “vertical” devices such as Bipolar Junction Transistor (BJT) or Static Induction Transistor (SIT), the use of *6H* results in lower *RF* power gain devices as compared to *4H*. The *4H* polytype is therefore needed, although good *3C* would be welcome if it was to become available one day. For III-N HEMTs, no difference has been identified on the basic device performance between *4H* and *6H* substrates. It seems that people can use both. The actual choice is more based on other criteria such as substrate diameter, availability, cost, and crystal defect density.

### 2.2.2 Orientation and Surface Polarity

All the SiC *RF* power devices demonstrated so far have been fabricated on the Si face of *4H*  $\langle 0001 \rangle$  substrate. It seems that going to C-face would only provide additional problems, and no improvement. Polishing is more difficult, the surface has more microscopic defects, epitaxy also is more difficult, especially doping. For optimum epitaxy, the substrate surface is mis-oriented, typically by  $8^\circ$  for *4H* polytype. This high angle should decrease as the crystal quality improves, to reach probably around  $2^\circ$  or even less, as for the most of the III-V or silicon misoriented substrates in use today.

### 2.2.3 Electrical Conductivity

Doped substrates are used for vertical devices.  $N^+$  is preferred, because of the *n*-type channel of the device, a choice resulting from the higher mobility of electrons as compared to holes. For lateral devices, electrically isolating substrate is preferred. A key advantage for SiC is that it can be made semi-insulating by incorporating deep centers in the crystal lattice, as for GaAs and InP.

### 2.2.4 SiC Semi-Insulating Substrates (SI-SiC)

SiC Semi-Insulating Substrates (SI-SiC) are surely today the best kind of substrates available for making *RF* and microwave power devices. SI-SiC offers high thermal conductivity, around 4 W/K.cm and very high electrical resistivity, typically over 10 G $\Omega$ .cm at 300 K and 1 M $\Omega$ .cm at 500 K. Only diamond substrates will be better, but today they are still small and much too expensive. Today, there exist three kinds of *4H* semi-insulating substrates available on the market. The oldest is PVT grown and vanadium doped, with [V] between the low  $10^{16}$  and the mid  $10^{17}$  cm $^{-3}$ . The two others are “vanadium free”, PVT or HT-CVD grown, with [V] much below  $10^{16}$  cm $^{-3}$ .

### 2.2.5 Vanadium Doped SI-SiC

Vanadium is known to create both a deep donor level and a deep acceptor level in  $4H$  and  $6H$ -SiC crystals, with the deep donor level located below the deep acceptor. It has therefore the unique capability to confer semi-insulating properties to both  $p$ -type and  $n$ -type SiC, whatever  $4H$  or  $6H$  polytype [22].

For SiC without intentional doping, the main impurity limiting the residual doping level is the nitrogen donor. It seems that the following approach has been used for making the vanadium doped SI-SiC crystals from which the commercial V-doped SI substrates are extracted: (1) aluminum is added with quantity adjusted in such a way that the average Al shallow acceptor density compensates the average shallow nitrogen donor density as exactly as possible, (2) vanadium is added in density large enough so that it can compensate for the largest difference between nitrogen density and aluminum density in the whole volume of the useful crystal. Since none of the impurities has any kind of uniform distribution in the crystal, the peak density of vanadium in some places of a V-doped semi-insulating substrate today can be very high (from low to high  $10^{17} \text{ cm}^{-3}$ ).

This approach is very clever. The problem for SiC MESFET is that the starting nitrogen residual level for PVT grown SiC crystal is usually around  $10^{17} \text{ cm}^{-3}$ . Therefore, the minimum average vanadium density required in the crystal is in the range from mid  $10^{16} \text{ cm}^{-3}$  to mid  $10^{17} \text{ cm}^{-3}$ , about the same range as the doping level of active layer in almost all the SiC MESFET transistors developed today. Since each vanadium element in excess can act as a trapping center, the SiC MESFET devices made on such V-doped PVT grown material generally exhibit strong trapping effects leading to  $DC$  and  $RF$  instability, and lower efficiency in  $RF$  power regime. On such substrates, we do not know any European research group that has ever obtained SiC MESFET which could be used to build amplifiers with any kind of stable performance. The amplifier prototypes we have built at Thales from such devices on such substrates had very short lifetime (a few minutes) due to drift of the device characteristics. The failure was partly reversible under light, and/or long rest (days to weeks) and/or elevated temperature storage (typically  $300^\circ\text{C} - 1 \text{ hour}$ ). However, the behavior depends on epitaxial structure. None of the 6 types of buffer (undoped,  $n^-$ ,  $n^+$ ,  $p^+$ ,  $p$ ,  $p^-$ , thicker or thinner, some of them in combination), obtained from 4 different epitaxy sources could ever solve the stability problem we have met using commercial V-doped substrates for SiC MESFET power devices.

Moreover, it seems that the vanadium solubility limit is low, typically in the  $E16 \text{ cm}^{-3}$  range, and that high density of vanadium results in the creation of vanadium-rich precipitates or aggregates.

For III-N HEMT transistors, it is still not clear whether the deep level density in the substrate has significant importance. There are still too many other possible sources of trapping effect which can mask the effect of the substrate. Traps can originate from passivation, buffer layer, cladding layer,

structural defects. Also, since the channel carrier density is very high, around  $10^{13} \text{ cm}^{-2}$ , it is more difficult for trapped charges to deplete the channel. The heterojunctions in the epitaxial buffer can also make it difficult for electrons to be injected into the substrate.

4H polytype off-axis (for SiC MESFET) and on-axis (for III-N HEMTs epitaxy) vanadium doped SI-SiC substrates are commercially available from Cree in the USA. A few other suppliers like Sixxon and possibly Sterling and Okmetic may be sampling 6H on-axis material soon.

In conclusion, we believe vanadium has not necessarily to be prohibited as a deep level for the doping of semi-insulating SiC material. The problem is most probably quantitative, not qualitative. The vanadium density should simply stay much below the doping density in the active layer of the device. Typically, for the SiC MESFET devices under development today, that have channel doping density in the low to medium  $10^{17} \text{ cm}^{-3}$ , vanadium density should be kept well below  $10^{16} \text{ cm}^{-3}$ .

### 2.2.6 High Purity SI-SiC Substrates from PVT Grown Crystals

According to the literature [23, 24], it seems that the Westinghouse semi-insulating material has reached rapidly high purity and low vanadium doping level, in such a way that Westinghouse probably never met on their substrates the problems we have encountered on the highly V-doped substrates [25]. Therefore, in the USA, it is almost sure that pure SI-SiC has been available in limited quantity since 1995 as a result of the Westinghouse SiC research activity, transferred later into the Northrop Grumman group, and seemingly to the “Litton Airtron” and “II-VI” companies. The material resulting from this work has not reached the open market so far. A new quality of PVT grown substrates called “Vanadium Free High Purity Semi-Insulating” is now commercially available [26]. Only Cree has published the results of extensive tests on this material [20]. The Cree results show impressive improvements of MESFET performance in terms of energy conversion efficiency. A few other groups are presently testing this new material.

Initial commercial samples had nitrogen density in the mid  $10^{16} \text{ cm}^{-3}$ , only about twice as low as the usual vanadium doped substrates. This is still rather high value and it brings a risk. The crystal may contain a too high density of deep levels for most MESFET structures to deliver optimum performance.

### 2.2.7 High Purity SI-SiC Substrates from HT-CVD Grown Crystals

The first SI-SiC substrates made from HT-CVD grown crystals were demonstrated in the year 2000 from the work of the Swedish groups at Linköping. The use of High-Temperature Chemical Vapor Deposition technique (HT-CVD) allows to achieve very low residual density for almost all impurities.

Therefore, a low density of deep levels in the crystal is sufficient to get the semi-insulating properties. Those substrates have allowed us to demonstrate devices stable enough for building a prototype for *RF* to *L* band amplifier at Thales Com.

The amplifier performance has stayed unchanged upon the whole test duration, typically 10 to 20 hours, which has never been obtained using commercial vanadium doped substrates.

### 2.2.8 Structural Crystal Quality of SiC Substrates

More than ten years after the first release of commercial SiC substrates (6H N<sup>+</sup>, PVT grown, one inch diameter), the quality has improved considerably [27], but it is still far from the level required for *RF* power device manufacturing with acceptable yield. The optical image obtained by transmission of polarized light through SI-SiC substrates, reveals many sub-structures even in the best SI SiC substrates accessible on the open market, with evidence that the crystal is not uniform at the macroscopic level.

X-ray diffraction on a 1 mm<sup>2</sup> round spot reveals several peaks at almost every place on the substrate surface. This is the sign of persistent mosaicity, related to the presence of domains or grains with small but significant mis-orientation from one to the neighbors [28]. The mosaicity on SI substrates seems to be much worse as compared to N<sup>+</sup> substrates. Probably the growth conditions for SI crystals have to be different, away from the optimum conditions for getting the best crystal quality. At the border between domains, dislocations appear, and also micropipes.

It also seems that the diameter-increasing crystal growth process, necessary for the substrate manufacturer to maintain or enlarge the crystal diameter from one growth run to the next one, is deleterious to the crystal quality. It induces high strain resulting in crystal relaxation through the creation of extended defects.

The quality improvement process for SI crystals started a long time ago. Looking at the present results and the relative stagnation, we believe that some special effort should be devoted by the manufacturers to improve the crystal quality. There will be no large expansion of SiC device market as long as the crystal quality remains at the present level. We will insist again on this aspect at the end of this chapter. Approaching substrate customer satisfaction and the opening of new markets will require larger substrates, larger defect-free zones, and higher process yield.

### 2.2.9 Homo-Epitaxy

The epitaxy of the SiC and III-N compounds has been dramatically improved, and the main phenomena understood [29]. Uniform epitaxy of both 4H-SiC and III-N compounds has become a reality. Multi-wafer epitaxy reactors for both can be found on the market for substrate diameter up to 100 mm

### 2.3 Schottky Contacts for SiC Mesfet Gate

The quality of the Schottky barrier is one of the most important issue for the performance and reliability of SiC MESFET devices, as it is for MESFETs on other materials, including all kind of HEMT devices. The role of this barrier is to prevent electron flooding from the gate into the drift region of the device towards the drain. The state of the art of making Schottky contact and the state of the understanding of the Schottky contacts on SiC are now as good as on any other semiconductor possibly including silicon [30, 31].

It is, however, still very poor on most III-N compounds, including GaN. For the realization of MESFETs, the highest possible barrier height seems to be the preferable, simply because a higher barrier height brings a lower gate leakage current, and also a higher breakdown voltage through the shift of the impact ionization threshold field. In normal device operation, MESFET gate contacts operate very seldom in the direct regime. The on-state voltage is not an issue as it is for the Schottky rectifiers, for which lower Schottky barrier height may be preferred.

#### 2.3.1 Surface Preparation

Efficient cleaning of the surface is necessary prior to metallisation. In principle, cleaning is easier for SiC than it is for almost all the other semiconductors, since SiC can accept any kind of chemical cleaning. It has now been checked that the classical cleaning procedures in use for silicon, such as CARO and RCA procedures, can be successfully used for the cleaning of virgin SiC surface. However, the choice for chemical is completely free only if the cleaning step happens at the very beginning of the process. If metal or insulator has already been deposited before, some limitations appear. This is the case for the usual fabrication processes. We will not enter in depth into the description of all the possible gate process schedules, but we will emphasize two key issue for the Schottky gates of MESFET transistors. One is related to ohmic contacts processing, and the other to the lift-off processing technique generally used for gate patterning.

In principle, the ohmic contact can be realized before or after the gates. The standard way to process those contacts involves annealing of the nickel metal around 950°C for a few minutes. If tungsten is chosen, the temperature is even higher, around 1300°C [30].

Therefore, if the ohmic contact are realized before the gates, the surface cleaning process prior to gate metallization must preserve ohmic contact metal, which is often nickel silicide. This discards the use of many aggressive chemicals. This also brings a risk for pollution of the surface by nickel compounds before gate metal deposition.

On the other hand, if the gates are realized before, the gate Schottky contact, and the whole gate metal stack, have to withstand the 950°C anneal of

the ohmic contacts. This requires the use of refractory metals for the Schottky contact metal and the whole metal stack, including very efficient metal diffusion barrier layer between the Schottky contact metal and the highly conductive top metal layer, often gold or even copper. This generally brings too many constraints. In practice, ohmic contacts are actually realized before the gates and the cleaning procedure before gate contact must accommodate with the presence of nickel on the wafer.

In the lift-off process, often used for gate patterning, resist is deposited on the whole wafer, exposed, and locally dissolved inside the patterns defining the metal deposition zones. Therefore, most of the SiC surface is covered by resist polymer during the gate Schottky metal evaporation. In consequence, the chemical treatment prior to evaporation must preserve the resist. Many classical chemicals for cleaning silicon surface cannot be used, especially those designed to eliminate organic molecules. Only soft cleaning and some plasma or ion gun cleaning/etching can be applied because resist is present on the wafer.

This is probably the main explanation why the Schottky contact quality on processed MESFET wafers is generally lower as compared to Schottky contact on test diodes made on test wafer. The cleaning is not as good, and the metal is evaporated, and not sputtered. In silicon and III-V technology, sputtering of metal is known to yield better contact as compared to metal evaporation.

### 2.3.2 Choice of Metal

Many different metals provide good Schottky barrier behavior on SiC. One family of metals which seem especially suited for Schottky contact on SiC is that of the nine “most classical refractory” chemical elements of the columns IVb, Vb, VIb of the periodic table. At least the following metals have been tested : Ti, Hf, Ta, Cr, Mo, W and it is almost sure that the three other Zr, V, Nb could also be used successfully. All the nine metals also form both metallic silicides and carbides. There seems to be a general trend for Schottky barrier height. The carbides would yield barrier height higher than the silicides. We have checked this trend for TiC and studies on WC can be found in the literature. The same metals also form nitrides and borides. The nitrides we have tested yield barrier height lower than the pure metal, but higher than the silicide. We have checked the case of TiN and  $WN_x$  ( $x$  around 0.15) [32]. The borides may give higher barrier height than the pure metals, but very few have been tested so far as Schottky contacts on SiC.

Other metals could also be used. Platinum could be a good candidate, but its evaporation results in highly strained layer. Iridium and Osmium could be good candidates too, but they are really exotic for most process lines. Nickel yields high barrier height just after deposition. However, at high temperature it attacks SiC to form  $Ni_2Si$  silicide ohmic contact. It forms no carbide that would stop the reaction process. Therefore, nickel gates are suspected as

possible troublemakers for the reliability of SiC MESFETs and they are not used for this purpose. Palladium, gold, and silver may cause the same kind of troubles. Additionally, it seems that gold does not stick well on SiC surface.

### 2.3.3 Thermal Stability

For most of the nine classical refractory pure metals, the Schottky behavior of the contact is probably maintained even after thermal annealing in clean atmosphere (primary 1 mtorr vacuum in our case) at temperature over 1000°C. We have checked that it works for W, Ti (protected with TiN), Mo, and TiW.

Most of the nine metals are sensitive to oxidation. They can be protected by a layer made of nitride or carbide of the same metal. When the metal is deposited by sputtering, the nitride is easily obtained by adding nitrogen into the plasma. However, when heated at high temperature without protective atmosphere, the metal nitride tends to dissociate and form a layer of the pure metal. For TiN, nitrogen evaporates after a few minutes at 800°C under vacuum, for TaN, at 600°C, and for WN, around 1000°C. Carbides are extremely stable.

The upper temperature limit of the SiC/metal carbide systems seem to be even higher than that for pure metal on SiC.

### 2.3.4 Barrier Height of “Pure Metals”

The barrier height of pure metals is variable. It is generally around 1 eV on 4H-SiC. It depends on the metal work function and on the chemistry of one or a few atomic layers at the interface between the metal and the semiconductor. Depending on the surface preparation, the metal atoms may bond with silicon or with carbon, or both. The barrier height will depend on the proportion. This proportion can change after thermal treatment. Generally, the carbides have higher bonding energy as compared to the silicides. For titanium contacts, barrier height between 0.75 and 1.25 eV can be actually obtained, just by changing the surface preparation. On diodes with areas around 0.01 mm<sup>2</sup>, the behavior of the diodes in direct regime is nearly perfectly described using thermo-ionic model with 2 nm interfacial layer. In reverse mode, at low electric field, the model also applies when corrections are applied for barrier lowering through image effect [33].

### 2.3.5 Metallisation Process

For diodes, sputtering metallisation process is generally preferred to evaporation, as it is for silicon technology. It is considered to yield better bonding of metal onto SiC. It also allows simpler manipulation of the wafers.

For transistors, the realization of short gates is simpler using lift-off process. As we already pointed out, lift-off with fine geometry is generally not

possible using classical sputtering tools for metallisation, since the energetic ions present in the plasma deteriorate the mask resist. Therefore, when lift-off is applied, evaporation metallisation process has to be used. The evaporation of refractory metals is difficult, even using e-beam surface heating, because of the very high temperature needed to get high enough deposition rate. This brings limitation to the actual choice of metals available for fabricating the gate Schottky contact of SiC MESFETs.

Ti, Nb, Cr, Mo can be evaporated using “normal” machines from the silicon industry. Silicide layers can be obtained after annealing of multilayer deposition of metal and silicium with the right thickness ratio for optimum silicide stoichiometry. However, the silicide option is generally not chosen because it tends to yield lower barrier height.

### 2.3.6 In-Situ Surface Cleaning

In a sputtering machine, it is easy to clean the surface prior to metallisation by ion etching using a temporary reverse of the electric field. In an evaporation machine, a separate ion gun has to be used. It generally provides argon ions with energy from a few ten eV up to a few hundred eV. We never could get good Schottky contact behavior from evaporated metal without in-situ ion gun etching prior to gate metal deposition.

### 2.3.7 Ideality Factor

On an ideal Schottky barrier, this factor should be equal to 1. It is really easy to make Schottky contact on SiC with almost ideal behavior in the direct regime. On diodes with areas around  $0.01 \text{ mm}^2$ , almost all of the diodes have an ideality factor below 1.05 for at least 5 different metals we have tried. On larger diodes and FET gates, ideality factor increases and effective barrier height decreases. Using the classical Werner theory, a model can be built for interpreting those deviations as consequences of microscopic barrier height dispersion within the diode area [33].

### 2.3.8 Reverse Leakage Current

In reverse mode at low electric field, the same thermo-ionic model also applies when corrections are included for barrier lowering through image force effect and tunnel assisted process (see Fig. 3). At high field, however, even with optimum peripheral protection, there is always much higher reverse current as compared to what is predicted by the available models, often by a few orders of magnitude. From evaluation of geometrical effect on diodes with different diameters, it seems that this excess current does not come from the periphery but from the bulk part of the contact. The role of the defects induced by the substrate or the epitaxy on the leakage current have been studied by several groups [34]–[36].

From our experience and the dozens of trials with different metals and surface preparation, we can conclude that the leakage phenomenon is present for all kinds of metals we have tried and for all surface preparation schemes. Therefore, we tend to incriminate possibly an influence of the steps due to the surface misorientation. We have not been able so far to check the validity of this hypothesis on epitaxy with lower misorientation angle.

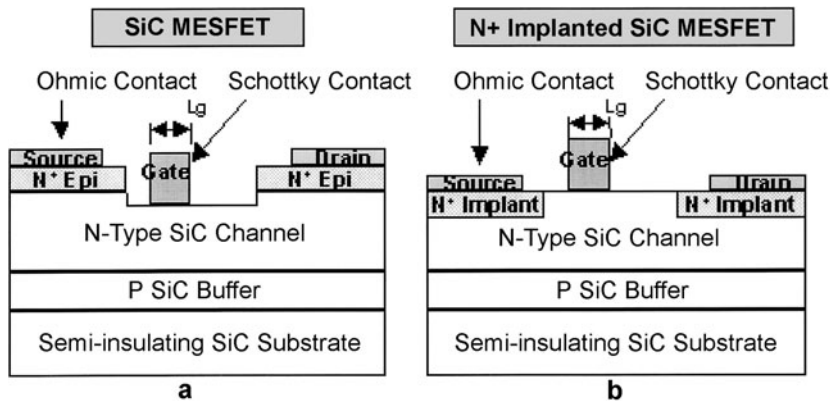


**Fig. 2.** Two examples of SiC MESFET device topology: (a) Recessed MESFET, (b)  $N^+$  implanted MESFET

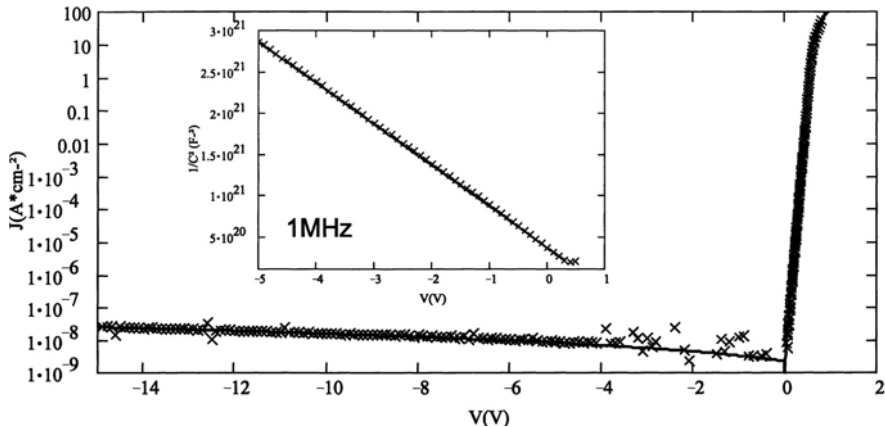


**Fig. 3.** Experimental low field  $J(V)$  and  $C(V)$  characteristics of Ti/SiC Schottky contact (*crosses*) fitted with a thermo-ionic model [33]. The fit is remarkable, almost ideal

## 2.4 Transistor Design and Fabrication Process

The transistor design proceeds in two steps: (1) The elementary transistor or “finger”, and (2) the finger assembling or “chip layout”.

### 2.4.1 The Elementary Transistor Design

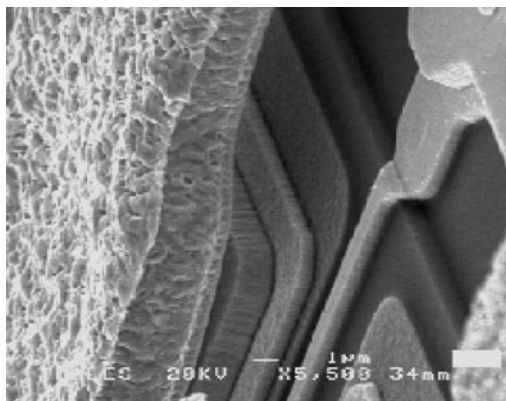


**Fig. 4.** SEM image of an elementary SiC MESFET device (recess topology) with mesa, and with air bridge on source pads

#### *Channel Characteristics*

*Channel Material.* The preferred channel SiC material is 4H. The use of 6H leads to devices with much lower gain, due to much lower electron mobility. This was published by Westinghouse around year 1995 [24], and, at Thales, we have got the same kind of results later. Cubic 3C-SiC could be used in principle, but no good 3C-SiC layer has been ever available yet from any source in the world.

*Channel Doping Level.* Preferred channel material conductivity is *n*-type, (1) because the mobility of the electrons is higher than that of the holes, and (2) because the donor levels, (mainly those of nitrogen, possibly in the future those of phosphorus too) are much shallower as compared to the known acceptor levels (essentially aluminum and boron). Over 90% activation of nitrogen donors in 4H-SiC is obtained at temperature of operation for doping level up to  $10^{17} \text{ cm}^{-3}$ , and slow decrease above. Channel doping level is usually chosen between 1 and  $3 \times 10^{17} \text{ cm}^{-3}$ . The lowest end is chosen for devices requiring breakdown of 200 V or higher. The highest is chosen for maximum power gain at high frequency, but the breakdown voltage can be twice lower. It degrades rapidly with increasing doping level.

*Channel Thickness.* Thick channel provides maximum current density and output power density, but lower transconductance and power gain. As an example, for  $2 \times 10^{17} \text{ cm}^{-3}$  channel doping level, 300 nm effective channel thickness yields 300 mA/mm drain current at  $V_{gs} = 0 \text{ V}$  and  $V_{ds} = 20 \text{ V}$  for  $1 \times 100 \text{ } \mu\text{m}^2$  device measured in *DC* regime directly on-wafer without special cooling of the device or the wafer. Transistor pinch off voltage in such device is around  $-15 \text{ V}$  at  $V_{ds} = 20 \text{ V}$ .

#### *Sub-Channel Buffer Issues*

What lies under the channel has a tremendous influence on the device behavior. In our experience, even the most sophisticated buffer structure cannot provide safe electrical separation between the device channel and a substrate with high density of traps. We have previously developed this point in greater details in Sect. 2.2.5.

#### *The Lateral MESFET Approach*

ACREO and AMDS (Sweden) has developed the concept of a “lateral MESFET” for nearly ideal configuration of the underchannel structure [36]. Like for the silicon LD-MOS, there is a vertical *p*-type confinement layer underneath the part of the channel located just under the gate. This almost eliminates the reverse transconductance effect, improves the voltage handling, and allows to use much shorter gates. In principle, the gain can be increased and the maximum frequency of use may be extended, probably up to 10 GHz. The associated fabrication process is, however, more complex than for the other SiC MESFET structures developed so far.

### **2.4.2 Source and Drain Electrodes**

Current has to be injected in and collected out of the semiconductor through ohmic contacts located at source and drain electrodes. Ohmic contacts with specific resistance below  $10^{-5} \text{ ohm.cm}^2$  are needed to get no significant disturbance on the device behavior. The realization of such Ohmic contacts requires high  $\text{N}^+$  doping level of the SiC zones and an adequate metal structure.

#### *$\text{N}^+$ Doping for Source and Drain*

Doping level must be over  $3 \times 10^{18} \text{ cm}^{-3}$ , and much preferably higher, in the range  $1\text{--}3 \times 10^{19} \text{ cm}^{-3}$ . There are mainly two ways of getting the  $\text{N}^+$  zones under the source and drain (Fig. 2). One is to use localized ion implantation (Fig. 2b), the second is to use either  $\text{N}^+$  epitaxy, or blanket ion implant, together with “recess” etching between source and drain (Fig. 2a).

*N<sup>+</sup> Ion Implant*

There has been many studies on N<sup>+</sup> ion implant in SiC [38, 39]. What can be practically used is somewhat different from the peak results of the best publications in the literature. For getting those best results, high temperature implantation is necessary. It requires special implantation machines. It also excludes the use of a resist mask for localization. We have preferred to use standard ion implanters working at room temperature for the substrate and providing maximum ion energy around 200 keV. For nitrogen, a maximum depth of 150–200 nm can be obtained, with an additional 200 nm deeper tail. For phosphorus, the maximum ion penetration is shallower, typically 100–150 nm, also with an additional tail. In both cases, multiple energy implantation is used to achieve a flat plateau, followed by an exponential decrease over a distance twice the length of the plateau for a level decrease by two or three orders of magnitude. Activation of the implanted ions requires annealing at high temperature. The minimum temperature to get any significant activation is 1300°C, but 1400–1500°C is highly preferable [38]–[40]. For annealing in this temperature range and higher, the SiC surface must be protected to prevent departure of silicon, carbon, or both, depending on the annealing atmosphere [41]. Using a reproducible process with standard tools, a sheet resistance around 1500 ohm can be obtained with both nitrogen and phosphorus (see Fig. 5).

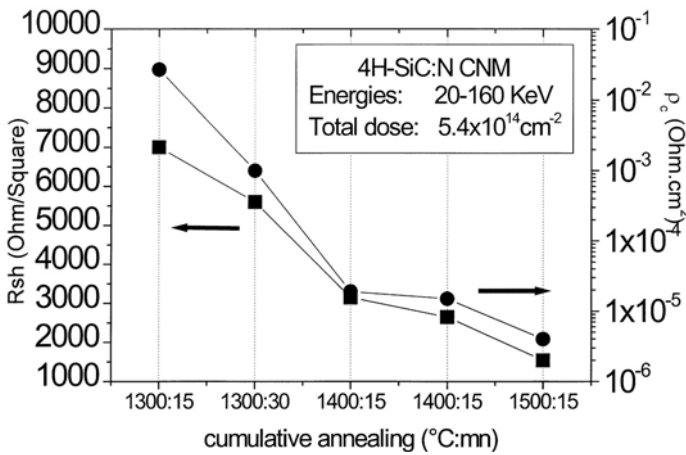


**Fig. 5.** Cumulative annealing dependence of N<sup>+</sup> sheet resistance (*square*) and Ni Ohmic contact specific resistance (*circle*) for Nitrogen *RT* multiple energy implanted 4H-SiC

### 2.4.3 Gate Length

Reducing gate length brings an increase of drain current and a decrease of input capacitance. It also brings increased reverse transconductance, except in the case of the lateral MESFET.

Gate length around 1 micrometer is probably short enough for UHF power amplifiers. Going down to half micrometer has allowed Cree to get excellent results in *S*-band at 3 GHz [42].

## 2.5 Passivation

One key limitation for the passivation resides in the fact that the very same insulator materials optimised for the previous silicon and GaAs technologies have to be used for passivating the new wide bandgap devices. After years of work, they now work rather well for the previous technologies, but in the new wide bandgap devices, they will have to accept five to tenfold higher electric field. The insulator reliability may suffer dramatically from long time high field exposure. One other issue is that the interface between SiC and insulators is still the location of many parasitic charges and traps. Those charges have electrostatic influence on the device channel.

### 2.5.1 The Case of No Passivation or Thin Insulator (50 nm)

When there is no passivation or only thin insulator film (50 nm) on the device active zone, the net charge density seems to be negative at normal operation bias voltage. Higher breakdown voltage is observed by some spontaneous effect of gate periphery protection, analog to the  $P^+$  guard ring configuration for high voltage devices. However, those charges also bring problems. They are not stable. They can move away under light, or after long rest. They are also responsible for parasitic pinching of the device gate to drain zone (see Fig. 6a). The on-state resistance increases dramatically as the drain voltage is increased and recovers very slowly. When such high charge density is present, the device can present good *DC* characteristics, but does not operate properly in *RF* power mode. The drain efficiency and the power density are low, typically <30% and 1 W/mm.

### 2.5.2 The Case of PECVD Deposited Silicon Oxide or Nitride

Device with stable characteristics can be obtained using PECVD deposition of either silicon oxide or silicon nitride with thickness in the range 200–500 nm. The presence of the thick insulator brings increased leakage of the gate/channel Schottky barrier and reduced breakdown voltage, as compared to the situation before insulator deposition (see Fig. 6b).

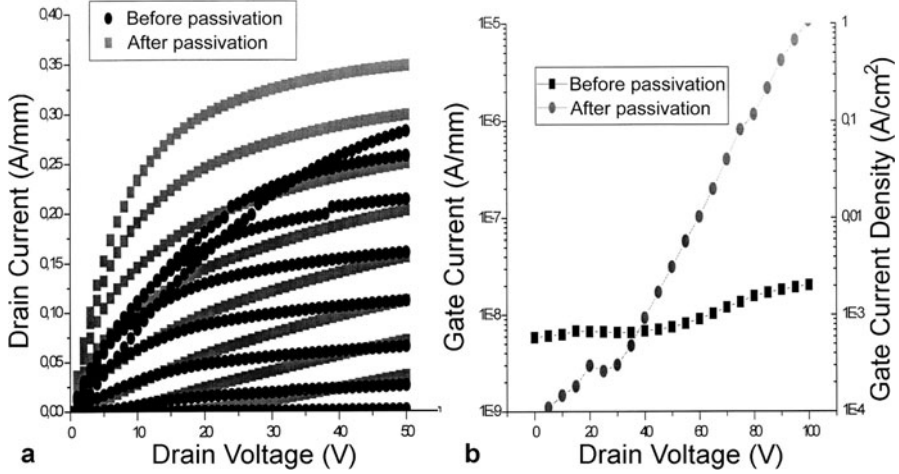


**Fig. 6.** DC 100 μm periphery SiC MESFET characteristics before and after passivation (400 nm PECVD SiO<sub>2</sub>). (a) Parasite pinching induced by  $V_{dg}$  stress for a device without passivation as compared to a stable device behavior after deposition of the PECVD insulator. (b) increase of gate leakage current after passivation

## 2.6 Chip Lay-Out

The initial SiC MESFET designs were directly translated from the GaAs MESFET experience.

### 2.6.1 Thermal Management

It appears now that the thermal management of SiC devices indeed requires even more care and effort than that of silicon or GaAs devices. The main reasons are the following. At first, it is true that at 300 K and for pure SiC, the thermal conductivity is more or less that of copper. But that of copper is only 3 times that of silicon and stays unchanged up to temperatures above 400°C, while that of SiC goes down as  $T^{-1.5}$ . Increasing channel temperature to 300°C, the local thermal conductivity drops by a factor 3. Moreover, the early semi-insulating substrates, with high vanadium doping level, had thermal conductivity in the range 2.5–3 W/K.cm [43]. Only the recent high purity semi-insulating materials have the “normal” conductivity, around or above 4 W/K.cm at 300 K.

Another fact was not clear enough for early SiC device designers: the rapid decrease of mobility with temperature, which was later confirmed to follow a  $T^{-\alpha}$  rule ( $\alpha \sim 2$ –2.4) [43]–[45]. The global result is a saturation of power vs. periphery for a given chip size and for a single set of parallel fingers (see Fig. 7). Thermal simulations and temperature measurements have allowed to correct the designs in order to take the actual materials limitations into account.

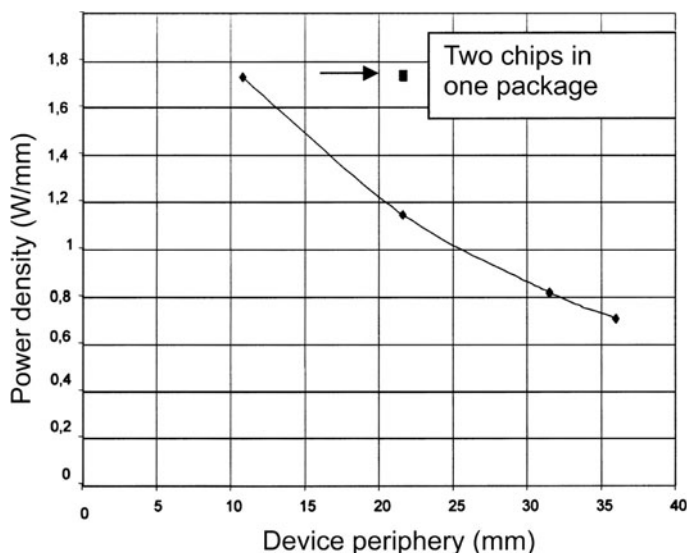


**Fig. 7.** Output power density versus the device periphery on chips from the same wafer for 4H-SiC MESFET with short pitch (11  $\mu\text{m}$ )

### 2.6.2 Chip Size

Large chips have large cost, both for material and processing. Also, brazing of large chips can lead to too large stress and the appearance of cracks in the brazing area. Finally, large chips means large device periphery and higher probability of failure, hence lower fabrication yield, limited essentially by the defect density in the material. With the material quality available today, chip size between 1 and 3  $\text{mm}^2$  is probably the best choice for devices with 20–30  $\text{W}/\text{mm}^2$  dissipated power density. Parallel operation of several chips in the same package is possible, and simpler as for silicon and GaAs because of the higher impedance levels.

### 2.7 Packaging

The packaging is also an issue for the wide bandgap *RF* power devices. For silicon carbide devices with dissipated power density in the range 2–5  $\text{W}/\text{mm}$ , or 20–30  $\text{W}/\text{mm}^2$ , the existing packaging technology used for silicon or GaAs devices can be used, but it works close to its hard limits. Temperature will generally be 100°C higher at the chip bottom as it is at the case bottom. For III-N devices, a new packaging technology is required. For both, the actual device performance of the device in operation will heavily depend on the channel local temperature.

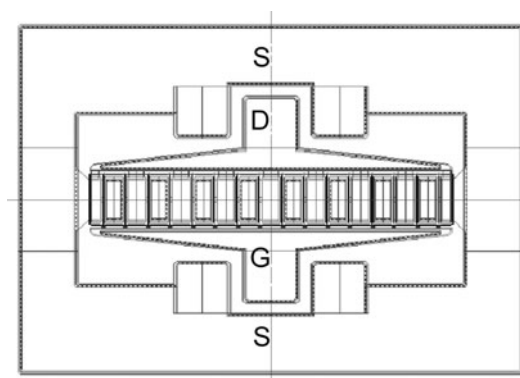


**Fig. 8.** Example of medium power MESFET device layout:  $16 \times 100 \mu\text{m}$  width fingers with a  $50 \mu\text{m}$  pitch

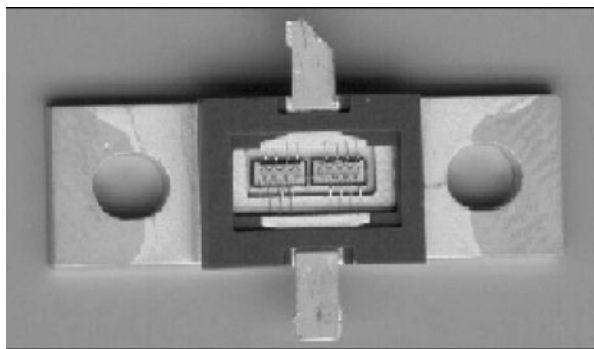


**Fig. 9.** Example of dual chip 50 W SiC MESFET packaged using conventional approach

### 2.7.1 Necessary Adaptation for SiC Devices

Silicon and GaAs devices have very low input and output impedance level. Therefore, it is interesting to have connection lids to the outside with low characteristic impedance, hence, geometrically speaking, as large as possible. This is why most packages in the catalogues have large lids. For SiC FET devices, the level of impedance is much higher and low characteristic impedance of connecting lines is no more a requirement. New variants of packages with different geometry in the same technology are required. It brings additional initial cost but nothing severe in the long term for the competitiveness of the new SiC devices.

For devices without via-holes, another adaptation is necessary to provide surface connection for the source electrode. One solution is to perform wire bonding directly from the chip surface to the ground on the metal base plate. This is simple but it brings very high source inductance and a decrease of

power gain. It is certainly not acceptable for devices working over 1 GHz. A better solution for high frequency operation is to organize source connection lift from the base plate up to the front face of the chip. This can be done either by adding a metal bar on the base plate along the chip, or by adding via holes in the ceramic frame of the package. Both solutions increase the package cost and probably cannot be used for operation at frequency over 2–3 GHz.

For the players who have not yet developed via hole technology on SiC substrate, a choice will have to be made. Either to develop the via-hole technology and use more standard packaging, or to accept more expensive packaging solutions. For those who are also developing III-N HEMT technology for higher frequency up to millimeter waves, as we do, via-hole or flip-chip solutions are the only known solutions.

### 2.7.2 Economical Trade Off:

#### Chip Area vs. Temperature/Performance

For SiC devices working in *CW* mode, the usual packaging technology will be used at the upper limit of its capability in terms of heat power density. For 100°C ambience and 25 W/mm<sup>2</sup> heat flow, the chip back side temperature will probably reach 180–200°C, and the channel temperature will stay around 300°C for optimum chip lay out. Some of the performance capability will be lost. The actual compromise will depend more on economical choice. Either accept larger chips and packages in order to get lower temperature and better performance, or restrict both chip and packaging areas, together with performance. Since the price of the SiC substrate will stay an issue for a long time, the compromise will have to be continuously managed all along the development and during the starting phase of the volume production for this technology.

### 2.7.3 Substrate Thinning

Without via holes, there is no need for substrate thinning in SiC MESFET technology. SiC substrate thinning can only be justified in the case the chip is placed on diamond tab in the aim to reduce device thermal resistance. In the other cases, it does not bring any significant thermal advantage while it adds some complex steps in the fabrication process. When via holes are used, substrate thinning can be of interest to reduce hole digging duration. The digging is usually performed by plasma etching which is a slow process. Etching rate is often limited to 1 µm/mn, even with the dense plasma techniques available today. This means many hours duration process for each wafer batch. Thinning the substrate from typically 300–400 micrometers down to 100 micrometers can bring dramatic savings on the device fabrication cost. Today, SiC substrate thinning process is under control and can be considered as a normal fabrication step. It can even be purchased as a commercial service.

### 2.7.4 Via Holes

Via holes bring minimum source inductance and possibly simpler device interconnect scheme. However, very few groups in the world have the complete technology for processing via holes in SiC. Only Cree is known to have it readily available for SiC MESFET. Thales has shown probably the first via holes in SiC in 1997 [46], but this process is not incorporated yet in the Thales SiC MESFET process.

Apart from the digging process, there is a problem for finding an appropriate mask for defining the hole geometry. Nickel has been used with success, but it has to be removed after the digging process, which is complex. Other approaches for masking involve thick resist or spin on glass (SOG).

## 3 Perspectives

### 3.1 Need for Better *RF* and Microwave Power Devices

There is definitely a need and a place for better *RF* and microwave power devices. None of the designers of the most advanced high power *RF* amplifiers based on solid state devices are satisfied with the exiting products. They sometimes manage to live with them, but they will surely warmly welcome new and better devices. What they want is a device with higher impedance and accepting higher temperature of operation. The present situation for amplifiers for UMTS base stations seemed to be somewhat desperate at the beginning of year 2002. From two sources, we have got the information that the prototypes could hardly or not meet the new specifications for linearity, and that the final stage of the amplifier had to be operated in conditions in which the energy conversion efficiency was lower than 10%. This is not acceptable. Whatever silicon LD-MOS or GaAs transistors, it seems that none of them has brought any viable solution. Designers hope that III-N or SiC devices will bring better behavior. A first market niche is there. It is not sure that the SiC or III-N devices are ready to catch it.

In addition, there are many other new potential applications of *RF* and microwave power waiting for better devices. Some of them are small niches. Some could become large volume industry. Microwave heating is one example. It is limited today by the rather clumsy magnetron tubes used as microwave sources. Adjusting power and/or frequency is not possible with this technology. Plasma applications is one other area in which more friendly microwaves sources can pave the way to new markets, some related to lighting industry. Ignition is a particular case of plasma applications. Improving ignition control is surely a way to get energy savings, lower pollution release, and enhance safety.

### 3.2 Si and III-V Technologies Close to the Limit

The progress of silicon bipolar transistors is more or less stopped. There is still some progress on the LD-MOS<sup>2</sup>, but it is slow and it seems to reach some kind of saturation, which is easily explained by the Johnson's limit. The situation is similar for GaAs HBT and FET technologies. Getting higher voltage brings new problems. There is also some kind of saturation along the Johnson's limit for the GaAs based power devices.

### 3.3 Long Term Is Diamond and Related, for Sure

In the long term (10–15 years), it is almost sure that the technology for *RF* and microwave power transistors will switch to diamond and related materials such as BN based compounds. For diamond, the breakdown field is higher, the carrier velocity is higher, and it seems that the carrier mobility is also higher. However, working with these extreme electric fields will be a new challenge. Working on SiC and the III-N is a helpful training.

### 3.4 Minimum Time to Market for SiC and III-N Devices

In the short term, it will take time for SiC and GaN devices to find some place on the market. No III-N product can be found today and very little SiC, and only at the 10 watts level. Maybe the large recent funding from US defense to wide bandgap industrial players will result in the acceleration of product release. It is not sure however, since defense administration has also to maintain a technology gap. What we fear most is the reliability issue. Because of the higher field and voltage, we think that problems won't be the same as for previous technologies. Reliability studies have started on the SiC MESFET. From preliminary limited storage and ageing tests under DC bias on our devices without macroscopic crystal defects, we find no special degradation, out of the transformations in the metal phases at high temperature and some long term trapping effects inducing current lag, which can be compensated by 10% gate voltage bias shift. It will still take us a few more years to get the complete results needed for acceptance by the most demanding users such as space embarked applications.

### 3.5 III-N Devices Will Take It All... When They Arrive on the Market

For the frequency range extending over 3 GHz, the existing device products are so expensive and difficult to use that there is strong appeal from the market for device products based on wide bandgap semiconductors. This is why III-N device research receives so much support at present. III-N HEMT devices have more gain, and there is strong hope to get devices working up to

30 or even 40 GHz, as illustrated by recent press release from several groups. If III-N device development was easy and straightforward, there would be no place for SiC based devices like SiC MESFET. The question arises because III-N device research is everything but easy and straightforward. Today, we don't know anybody who can tell with confidence how long it will take to get the first reliable microwave power device product based on III-N compounds. Maybe the most advanced groups in the USA have a more precise idea, but almost surely no group in Europe or Japan.

### **3.6 To Go or Not to Go into the Industry of SiC *RF* Power Devices**

Despite some release of SiC MESFET devices initiated several years ago to selected customers, there seems to be today no volume on this kind of product on the open market. At the beginning of year 2003, in Europe, people have to decide whether it is worth building the infrastructure to launch SiC based product for *RF* and microwaves. This is a complex debate.

Those who push towards have the feeling that III-N products will not appear before year 2006–2008. This is our opinion. It cannot be based only on objective computation. There are too many influencing factors. Some of them are completely out of our control like those related to politic issues. Some other are more or less subjective, like the market admittance. However, such a SiC MESFET project is vulnerable. It can be destroyed by the arrival of good III-N products on the market or even by any rumor about it. On the other hand, we can also try to compare to what happened for GaAs MESFET. For ten years, in principle, GaAs HBT and GaAs HEMTs have better peak performance as compared to any GaAs MESFET. Still there has been so far good market places for GaAs MESFETs and the development of new GaAs MESFET products has not been stopped yet. The same could happen for the SiC MESFET. Since there are people really pressed by the need for better devices, we are convinced that there is a market place for SiC MESFET, today and for the next coming ten years. To be honest, there are also a few open technical questions. One issue is about the surface passivation, in relation with gate periphery protection. The transition zone between SiC and the atmosphere is still a mess. How to manage it is not clear cut today. One other issue is about the process yield. It used to be severely limited by epitaxial uniformity. This problem is solved with the new epitaxy systems already on the market. More of a problem is the substrate crystal quality. It is still much too far from any kind of stable satisfactory state for commercial semi-insulating material. For crystal quality improvement, a real effort is still necessary. When the quality is better, the consumption will increase and the price will decrease, not before.

Organizing manufacturing is also a necessity. No industry can be built on device prototypes. The manufacturing of *RF* and microwave power devices based on wide bandgap semiconductors is still far from maturity in terms of

yield and fabrication cost. Because of the small substrates, it cannot use the silicon or GaAs “mainstream” processing tools, and it is not sure it can be made competitive in the short term without public money support.

## Acknowledgements

The SiC project at Thales has received support from French MoD DGA/DSP/STTC, European Community through the Esprit “TELSiC” and the Brite Euram “JESiC” projects, and from the French Ministry of research through the “Saut Technologique SiC” and RNRT “PHYSiC” projects.

## References

1. E.O. Johnson: RCA Rev **163** (1965)
2. J. Olsson, N. Rorsman, L. Vestling, C. Fager, J. Ankarcrona, H. Zirath, K.-H. Eklund: IEEE Electron Devices Lett. **23**, 206 (2002)
3. M. Bhatnagar, B.J. Baliga: IEEE Electron Devices. **40**, 645 (1993)
4. C.E. Weitzel: IEEE Electron Devices Lett. **16**, 451 (1995)
5. J.A. Cooper Jr., M.R. Melloch, R. Singh, A. Agarwal, J.W. Palmour: IEEE Trans. Electron Devices **49**, 658 (2002)
6. S.-H. Ryu, A.K. Agarwal, R. Singh, and J.W. Palmour: IEEE Electron Device Lett. **22**, 124 (2001)
7. G. Pensl, M. Bassler, F. Ciobanu, V. Afanas'ev, H. Yano, T. Kimoto, H. Matsunami: Mat. Res. Soc. Symp. **640**, H.3.2.1 (2001)
8. L. Lipkin, M. Das, J. Palmour: Mat. Res. Soc. Symp. **640**, H.3.1.1 (2001)
9. L. Lipkin, and J. Palmour: IEEE Trans. Electron Devices **46**, 525 (1999)
10. Y.M. Sung, J.B. Casady, J.B. Dufrene, A.K. Agarwal: Solid-State Electronics **46**, 605 (2002)
11. A.A. Burk, M.J. O'Loughlin, R.R. Siergiej, A.K. Agarwal, S. Sriram, R.C. Clarke, M.F. MacMillan, V. Balakrishna, C.D. Brandt: Solid-State Electronics **43**, 1459 (1999)
12. J.I. Pankove et al.: IEDM Tech. Dig. **389** (1994)
13. A. Konstantinov, A.-M. Saroukhan, S. Karlsson, C. Harris, A. Litwin: Mat. Res. Soc. Symp. **640**, H.4.6.1 (2001)
14. A. Konstantinov, P. Ericsson, C. Harris: Mat. Sci. Forum **389–393**, ICSCRM 2001
15. H.R. Chang, E. Hanna, R. Hackett, R. Gupta: Mat. Sci. Forum **389–393**, ICSCRM 2001
16. J. Eriksson, N. Rorsman, H. Zirath: Mat. Sci. Forum **338–342**, 1259, ICSCRM 1999
17. H. Cha, C.I. Thomas, G. Koley, L.F. Eastma, M.G. Spencer: IEEE Lester Eastman Conference 2002
18. M.G. Walden, M. Knight: IEEE EDMO Conference 2002
19. H. Honda, M. Ogata, H. Sawazaki, S. Ono, M. Arai: ECSCRM 2002, to be published
20. S. Allen, T. Alcorn, H. Hagleitner, J. Henning, C. Janke, Z. Ring, S. Srinam, A. Ward, J. Palmour: ECSCRM 2002, to be published
21. M.G. Spencer, J.W. Palmour, C. Carter: Trans. Electron Devices **49**, 940 (2002)

22. H.M. Hobgood, R.C. Glass, G. Augustine, R.H. Augustine, R.H. Hopkins, J.R. Jenny, M. Skowronski, W.C. Michel, M. Roth: *Appl. Phys. Lett.* **66**, 1965 (1995)
23. R.C. Glass, G. Augustine, V. Balakrishna, H.M. Hobgood, R.H. Hopkins, J. Jenny, M. Skowronski, W.J. Choyke: *Inst. Phys. Conf. Ser.* **142**, 37, IC-SCRM 1995
24. R.R. Siergiej, S. Sriram, R.C. Clarke, A.K. Agarwal, C.D. Brandt, A.A. Burk, T.J. Smith, A. Morse, P.A. Orphanos: *Inst. Phys. Conf. Ser.* **142**, 769, ICSCRM 1995
25. E. Morvan, O. Noblanc, C. Dua, C. Brylinski: *Mat. Sci. Forum* **353–356**, 669, ICSCRM 2000
26. J.R. Jenny, St.G. Müller, A. Powell, V.F. Tsvetkov, H.M. Hobgood, R.C. Glass, C.H. Carter Jr.: *J. Electron. Mat.* **31**, 366 (2002)
27. S.G. Müller, M.F. Brady, W.H. Brixius, G. Fechko, R.C. Glass, D. Henshall, H.M. Hobgood, J.R. Jenny, R. Leonard, D. Malta, A. Powell, V.F. Tsvetkov, S. Allen, J. Palmour, C.H. Carter Jr.: *Mat. Sci. Forum* **389–393**, 23, ICSCRM 2001
28. T. Tuominen, R. Yakimova, M. Syväjärvi, E. Janzén: *Mat. Sci. And Eng. B* **61–62**, 168 (1999)
29. U. Forsberg: CVD Growth of Silicon Carbide for High Frequency Applications, PhD thesis, Linköping Universitet
30. L.M. Porter, R.F. Davis: *Materials Science and Engineering, B* **34**, 83 (1995)
31. A. Itoh, H. Matsunami: *Phys. Stat. Sol. (b)* **202**, 389 (1997)
32. D. Defives, O. Durand, F. Wyczisk, O. Noblanc, C. Brylinski, F. Meyer: *Microelectronic Engineering* **55**, 369 (2001)
33. D. Defives: Etude du contact Schottky Metal/SiC, Application aux redresseurs Schottky de puissance et aux transistors MESFET hyperfréquence, PhD thesis, Paris Sud University (2000)
34. R. Raghunathan, B.J. Baliga: *Appl. Phys. Lett.* **72**, 3196 (1998)
35. Q. Wahad, A. Ellison, A. Henry, E. Janzén, C. Hallin, J. Di Persio, R. Martinez: *Appl. Phys. Lett.* **76**, 2725 (2000)
36. U. Zimmermann, J. Österman, D. Kuylenstierna, A. Hallén, A.O. Konstantinov, W.M. Vetter, M. Dudley: *J. Appl. Phys.* **93**, 611 (2003)
37. A.O. Konstantinov, C.I. Harris, P. Ericsson: *Mat. Sci. Forum* **389–393**, IC-SCRM 2001
38. M.A. Capano, J.A. Cooper, Jr., M.R. Melloch, A. Saxler, W.C. Mitchel: *J. Appl. Phys.* **87**, 8773 (2000)
39. Y. Negoro, N. Miyamoto, T. Kimoto, H. Matsunami: *Appl. Phys. Lett.* **80**, 240 (2002)
40. T. Kimoto, H. Yano, S. Tamura, N. Miyamoto, K. Fujihira, Y. Negoro, H. Matsunami: *Mat. Sci. Forum* **353–356**, 1259, ICSCRM 2000
41. W. Handy, M. Rao, K.A. Jones, M.A. Derenge, P.H. Chi, R.D. Vispute, T. Venkatesen, N.A. Papanicolaou, J. Mittereder: *J. Appl. Phys.* **86**, 746 (1999)
42. R.C. Clark, J.W. Palmour: *Proc. IEEE* **90**, 987 (2002)
43. A.S. Royet, T. Ouisse, B. Cabon, O. Noblanc, C. Arnodo, C. Brylinski: *IEEE Trans. Electron Devices* **47**, 2221 (2000)
44. P. Terziyska, C. Blanc, J. Pernot, S. Contreras, J.L. Robert, J. Camassel, E. Morvan, C. Dua, C. Brylinski: EXMATEC conference (2002)
45. M. Roschke, and F. Schwierz: *IEEE Trans. Electron Devices* **48**, 1442 (2001)
46. P. Chabert: Study of an SF<sub>6</sub> helicon plasma devoted to high rate etching of Silicon Carbide, Ph. D. thesis, Paris Sud University (1999)

# Advances in SiC Field Effect Gas Sensors

A. Lloyd Spetz and S. Savage

## 1 Introduction

Constraints around environmental issues continue to increase in severity. This causes a demand for increasing control of emissions and reduction of energy consumption in vehicles and in industry, which necessitates the development and production of faster and more efficient sensors for on-line control. Gas sensors that can function in extreme environments have the potential to provide this control. Those based on wide band-gap materials such as SiC, AlN, GaN, AlGaIn and diamond have the potential to function in these extreme environments such as corrosive atmospheres and at high temperatures. Through the employment of a catalytic material on the device surface, chemical gas sensors based on a variety of field effect devices have been realised. The capability for operation at elevated temperatures considerably increases the speed of response to a change of gas atmosphere, providing the potential for the production of very fast sensors. The possibility to measure directly on-line in extreme atmospheres, for example in car exhausts or flue gases, makes it possible to quickly detect unwanted emissions, which allows immediate adjustment of the system and permits the requirements of low emission levels and fuel consumption to be met.

The wide band-gap of silicon carbide, 3.2 eV for 4H-SiC, permits an operation temperature up to 1000°C [1, 2], with time constants for the gas response of a few milliseconds [3, 4]. An electronic device based on silicon carbide can function as a chemical sensor by the deposition of a catalytic material on a thin insulating layer on its surface [5]–[15]. The catalytic material can be for example a metal such as platinum, iridium or palladium, or combinations of these. Metal oxides can also be used as catalytic layers on devices where the material does not need to conduct large currents.

Other wide band-gap materials, such as GaN, AlN and diamond, with bandgaps of 3.4, 6.3 and 5.5 eV respectively, have also been explored. These have higher band-gaps than SiC, and so have the potential to function at even higher temperatures. Several groups have started to develop chemical gas sensors based on these materials, but the film growth and process technology of these materials is currently not so mature as for SiC. Therefore, commercialisation of these devices cannot be expected until the technology has matured somewhat.

The high quality of the SiC material available today and the maturity of the processing technology has allowed commercialisation of SiC devices to begin. This includes Schottky diodes as commercialised by Infineon [16] and UV flame detectors as commercialised by General Electric [17]. It has also permitted the demonstration of high quality prototypes of other devices, such as large-area SiC X-ray detectors based on Schottky diodes which function at 100°C [18]. Therefore, if commercialisation is to be realised in the near future, SiC is the preferred material for the development of gas sensors that can function in extreme environments.

In this chapter, the state of the art concerning the development of field effect chemical gas sensors based on SiC is described, together with a review of other wide band gap materials. The detection principle and gas response is explained, and the various devices that have been developed are described together with a number of applications in which they have been tested.

## 2 Detection Mechanism of Field Effect Gas Sensors

It is important to have a clear picture of the gas detection mechanism when considering the results obtained from the field-effect chemical gas sensors. Therefore, we include this section about the detection mechanism as well as the gas sensing properties at this point. The sensing mechanism is largely independent of the device type, since the chemical reactions responsible for the gas response are defined by the type of catalytic material processed onto the device and the operation temperature [1, 2, 19, 20]. Even at a temperature of 600°C, the rate at which these chemical reactions occur in the catalytic material is slower than the response time of the device.

### 2.1 Gas Sensing Principle

The detection principle of field-effect sensors with catalytic metal contacts is based on the formation of an electric field in the underlying insulator due to a change of the electric charge at the insulator surface. Gas molecules adsorb, dissociate and react on the catalytic material. The so formed gas species diffuse from the metal onto the insulator and, through adsorption and/or complex formation, create a polarized layer at the metal-insulator interface. This gives rise to an electric field in the insulator, which causes the concentration of mobile carriers in the semiconductor to change.

In the case of thick, dense catalytic metals, hydrogen or hydrogen-containing molecules such as hydrocarbons dissociate on the surface of the metal and react with for example adsorbed oxygen forming H<sub>2</sub>O and CO<sub>2</sub>. These leave the surface and the resulting hydrogen atoms diffuse through the metal within microseconds to the insulator surface (see Fig. 1a). This occurs at temperatures as low as 150°C, and the speed at which it occurs increases

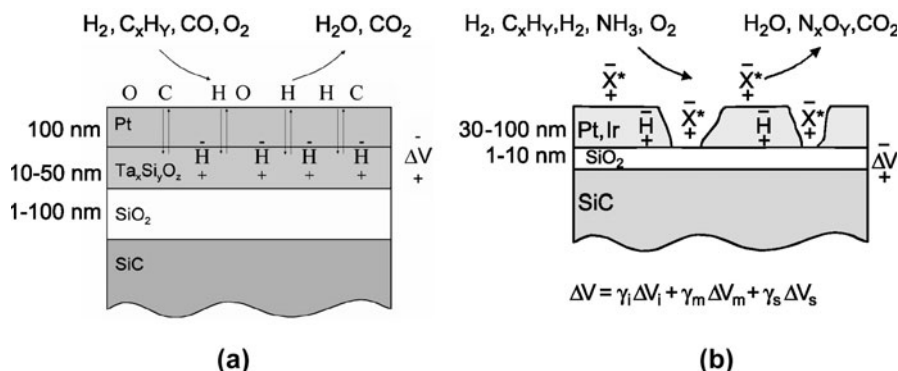


**Fig. 1.** (a) Schematic picture of a MISiC device with a dense catalytic metal contact and (b) a porous catalytic metal contact. The total gas response is a combination of response at metal-insulator interface (i), metal in contact with insulator (m) and exposed insulator surface (s). The constant  $\gamma$  is a function of e.g. metal coverage and temperature

with increasing temperature. Recent experimental results on Si sensors indicate that the polarized layer is indeed located on the insulator surface [19, 20]. This is further supported by results from ion selective field-effect sensors (IS-FETs), where it is shown that hydrogen introduces  $\text{SiO}^-$ ,  $\text{SiOH}$  and  $\text{SiOH}_2^+$  groups on the  $\text{SiO}_2$  surface in a liquid environment [21].

GaN Schottky diodes have been shown to produce a similar gas response to their SiC counterparts, irrespective of whether the Schottky contact is formed on the Ga or N surface. This indicates that the interface properties which are responsible for the gas response are similar for SiC and GaN and on both faces of the GaN [22, 23]. Indeed, a similar model to that for SiC has been suggested for the hydrogen response of thick Pt films on GaN Schottky diodes. This is supported by results from elastic-recoil detection (ERD) experiments, which lead to a model where the hydrogen-induced polarized layer is formed at an oxidic interfacial layer [9].

The gas detection mechanism of FET devices is very complicated and not all details are well understood. A very interesting experiment was performed by Neuberger et al. using AlGaIn/GaN high electron mobility transistors (HEMTs) that do not include metal or insulator on the gate region [22]. These devices also showed modulation of the channel current when Ga or N face surfaces were exposed to fluxes of negative or positive ions generated by an ion spray technique [22]. The channel current was amplified by as much as 1000. The mechanism here was explained by electrostatic interaction and accumulation of negative or positive charges respectively on the GaN surface.

The detection of other molecules, such as ammonia, requires the use of a porous catalytic metal. It is believed that triple points are required in these cases, where gas molecules interact with both the metal and insulator in order

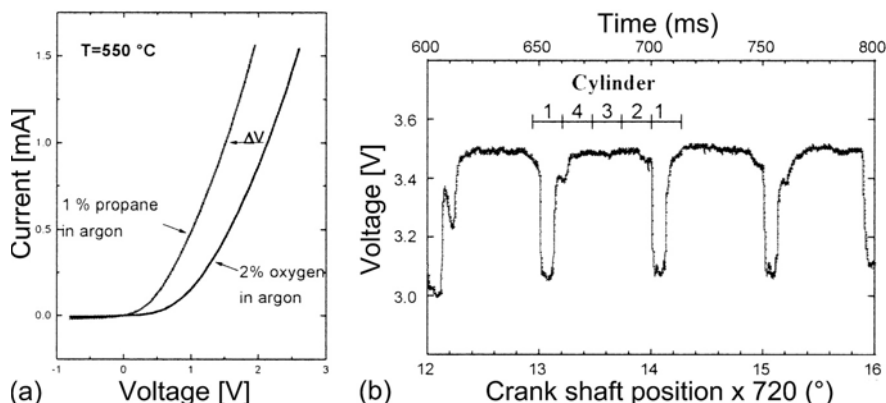


**Fig. 2.** (a) When the MISiC sensor is exposed to a test gas, such as propane, its *IV* curve shifts. The voltage at a constant current is the sensor signal. (b) The sensor signal during cylinder-specific monitoring of a petrol engine, when one cylinder is purposely driven under rich conditions. When cylinder 1 ignites, the sensor signal changes to a lower voltage

to obtain a response. Gas species such as hydrogen atoms or protons will diffuse out onto the exposed oxide surface in-between the metal grains, (see Fig. 1b) [24]–[26]. It has been suggested by several groups that oxygen may be involved in the detection mechanism [27, 28]. For example, the removal of adsorbed negative oxygen ions will give the same electrical effect as adsorption of positive hydrogen ions, protons.

The polarization introduced by the gases at the insulator interface will change the current voltage (*IV*) curve of a Schottky diode (see Fig. 2a) or a transistor, and will change the flat band voltage of a capacitor. A time resolved gas response can therefore be measured as the voltage shift at a constant current or constant capacitance level (see Fig. 2b).

Since chemical reactions on the catalytic metal surface are responsible for the detection of gases, the sensor response is highly temperature dependent. In general, an increased temperature gives a faster gas response, see Sect. 4.1 [4]. Thus, both the catalytic metal type and the temperature influence the gas response [29, 30].

Further details of the detection mechanism may be obtained by spectroscopy studies such as DRIFT, Diffuse Reflectance Transform Infrared Spectroscopy, which can be performed under realistic conditions [31, 32] and theoretical modelling [33].

## 2.2 Selectivity at Different Temperatures

The metal-insulator-SiC (MISiC) sensors function over a large temperature range, 100–700°C. Their gas response can be divided into two different temperature regimes with the break-over point around 600°C.

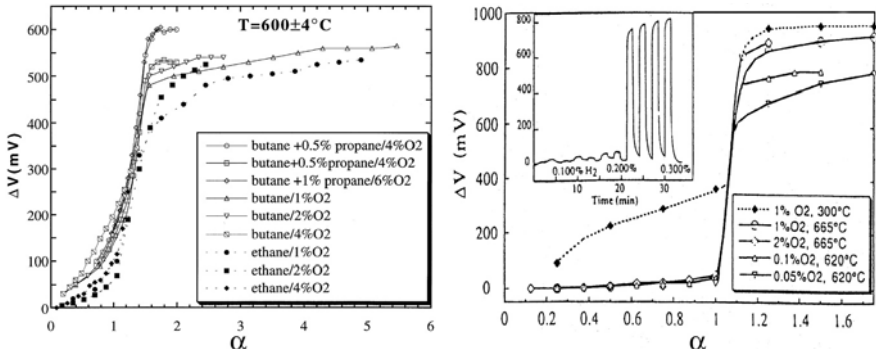


**Fig. 3.** The response of a MISiC sensor (a) at  $600^\circ\text{C}$  to gas mixtures containing different hydrocarbon concentrations (buthane, propene, ethane) (b) to hydrogen in different oxygen concentrations at  $300^\circ\text{C}$  and  $>600^\circ\text{C}$ . Inset: the pulse response at  $620^\circ\text{C}$  to 0.1, 0.2 and 0.3% H<sub>2</sub> in 0.1% O<sub>2</sub>/Ar.  $\alpha$  = as defined in (1) (from [35, 36])

Above  $600^\circ\text{C}$  the gas response of MISiC sensors, for example to hydrocarbons, shows a binary behaviour. This means that the signal has basically only two voltage levels and changes rapidly from a low level in excess hydrocarbons to a high level in excess oxygen, see Fig. 3.

Due to the large reaction rates that occur at temperatures around and above  $600^\circ\text{C}$ , exposure to hydrogen or hydrocarbon gases causes the platinum surface to go rapidly through a transition from a surface covered with adsorbed oxygen atoms to a surface covered with adsorbed hydrogen and hydrocarbon species [34]. This causes the sensor signal to change quickly from the base-line level in oxygen to the saturated hydrogen response level. In excess oxygen, it is assumed that total combustion of the hydrocarbon molecules on the metal surface occurs at these high temperatures. This causes the hydrocarbons to convert to water and carbon dioxide, which leave the surface, causing the sensor to register the baseline signal level. A model for this binary response has been suggested by Baranzahi et al. based on kinetic phase transitions [35]. This explains that the signal depends on the total ratio of oxidizing and reducing species,  $\alpha$  as defined in (1), but is largely independent of the gas composition.

$$\alpha = \sum_{i=1}^n \frac{\left(2x + \frac{y}{2}\right) [C_xH_y]_i}{2[O_2]} \quad (1)$$

In the temperature regime below  $600^\circ\text{C}$ , a more linear response is obtained. This is demonstrated in the response to hydrogen at  $300^\circ\text{C}$  as shown in Fig. 3b [36]. In this lower temperature regime it is postulated that only partial combustion of the gas molecules occurs on the metal surface. This means that at these lower temperatures, the various hydrocarbons are disso-

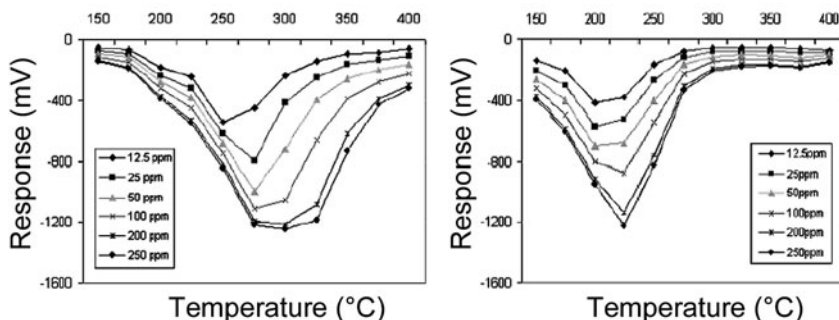


**Fig. 4.** The ammonia response versus temperature for a MISiCFET sensor with (a) 60 nm Ir and (b) 25 nm Pt as the gate contact metal.  $\text{NH}_3$  concentration: 12.5, 25, 50, 100, 200, 250 ppm in 10%  $\text{O}_2/\text{N}_2$  (from [37])

ciated to different degrees and give substantially different responses at critical temperatures. This gives the possibility to differentiate between different hydrocarbons at these lower temperatures.

Other gas molecules such as ammonia and CO also show a strong temperature dependence. The response to ammonia as a function of temperature is shown in Fig. 4 for the case of two different catalytic metals. It is seen that the temperature profile of the response is dependent upon both the type of catalytic metal and the concentration of  $\text{NH}_3$  [37]. This provides the opportunity to tailor-make the sensor to fit the application by choosing an appropriate catalytic metal and measurement temperature.

The fact that the sensing of different gases can be controlled by the correct choice of catalytic metal and measurement temperature opens the possibility to use arrays of these sensors together with pattern recognition techniques in order to provide detailed information about the composition of ambient gases. This has been tested in flue gases by Unéus [38] et al. and is described in Sect. 6.4. Hunter et al. have also suggested the use of their SiC-based Schottky diodes in arrays at different temperatures to enhance the versatility of their sensors [10].

### 3 Field Effect Chemical Gas Sensor Devices

The hydrogen sensitivity of Palladium-Oxide-Semiconductor, Pd-MOS, structures was first reported by Lundström et al. in 1975 [39]. In the past decade, various groups have demonstrated a variety of field effect devices during efforts to develop sturdy chemical gas sensors for use at elevated temperatures (see Fig. 5) [40]–[45].

Since the capacitor, Schottky diode and transistor all contain an insulating layer under the catalytic metal, they are all referred to in this chapter as

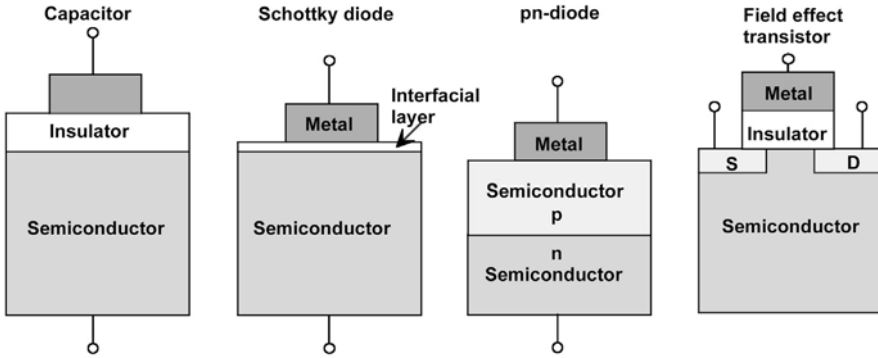


**Fig. 5.** Schematic diagrams of the different field effect devices described in this chapter

field-effect devices. In published literature, the capacitor and diode SiC devices are often referred to as MISiC (metal-insulator-silicon carbide) devices, and the transistor as a MISiCFET (metal-insulator-silicon carbide-field effect transistor) device. Examples of measurements on the various devices will be given here, and their advantages and disadvantages will be discussed.

### 3.1 Capacitor Sensors

SiC capacitor sensors were first published in 1992 [40] and have demonstrated gas-sensitivity to gases such as hydrogen and hydrocarbons [2, 6, 28] up to a maximum temperature of 1000°C [2, 46, 47]. These devices are easy to fabricate and especially suitable for basic research studies in the laboratory. Devices that can be operated both as MOS capacitors (reverse bias) and as Schottky diodes at temperatures greater than 490°C have also been demonstrated (see Sect. 3.2 [6]). These devices showed sensitivity to combustible gases such as propane, propylene and CO and were tested at temperatures up to 640°C.

Ghosh et al. investigated Pt/SiO<sub>2</sub>/SiC capacitors at high temperature (527°C) in oxygen or hydrogen atmosphere [13]. Baranzahi et al. investigated Pt/TaSi<sub>x</sub>/SiO<sub>2</sub>/6H-SiC capacitors [48] at temperatures above 650°C and Tobias et al. the same device types made on 4H-SiC [49]. In addition to the polarization effects at the metal-insulator interface (Fig. 1a), these researchers found phenomena related to the diffusion of hydrogen through SiO<sub>2</sub>, which occurs at a considerable speed at these temperatures. It was proposed [50] that hydrogen reversibly occupies and vacates surface states at the insulator-SiC interface at temperatures above 427°C. This has implications for the operation of a MOS capacitor sensor in the constant capacitance mode, especially *n*-type devices biased in the upper part of the *CV*-curve [13, 50]. A response time in the order of 30 minutes when switching from hydrogen to oxygen was observed and attributed to a slow emptying of interface states

[50]. The inversion capacitance was seen to decrease in the presence of hydrogen at 750°C by about 50 pF, and this was attributed to a reduction in the minority carrier generation at the oxide-SiC interface and/or at the surface of the SiC in the presence of hydrogen [48, 49]. The reversible hydrogen-induced shift in the inversion capacitance value also took place in the 4H-SiC devices, but at a somewhat higher temperature, which was attributed to the higher band gap of the 4H polytype [49].

## 3.2 Schottky Sensors

The development of SiC Schottky diode sensors was of interest due to their simple associated electronic circuitry. These devices were pioneered by Hunter et al. [41], and several research groups have subsequently contributed to the development effort. For a review see [51].

In the first Schottky diode sensors produced by the authors, the catalytic metal contact was deposited directly onto the semiconductor surface using HF to remove the native oxide. These devices showed poor stability and reproducibility. This was attributed to the presence of surface states, caused by dangling bonds for example, which are known to introduce pinning of the Fermi level. In the worst case, changes in the metal work function caused by the ambient gas would not cause a change in the barrier height [52], thus preventing a gas response.

Tobias et al. also investigated Pt-contact 6H-SiC Schottky diodes with an interfacial layer of 1 nm Ta or 10 nm TaSi<sub>x</sub> [53]. Both *n*-type and *p*-type diodes showed a gas response to hydrogen at 400–600°C. It was postulated that the gas response observed in the forward direction was mainly due to a change in the resistance of the metal contact [53].

It was demonstrated that reproducible gas-sensitive silicon Schottky sensors could be produced after terminating the silicon surface with an oxide layer [54, 55]. Therefore, this technique was also tested on SiC. An ozone treatment (10 min at room temperature) was carried out on the HF-etched SiC surface before the metallisation step [56]. The use of spectroscopic ellipsometry analysis and also photoelectron spectroscopy utilizing synchrotron radiation showed that an oxide, 1 nm in thickness, was formed by this ozone exposure [56, 57]. The oxide was also found to be close to stoichiometric SiO<sub>2</sub> in composition. This thin oxide increased the stability of the SiC Schottky diodes considerably, without the need for any further interfacial layer such as the Ta and TaSi<sub>x</sub> mentioned above. Schottky diodes employing a porous Pt gate electrode and the ozone-produced interfacial layer were subsequently operated successfully in both flue gases and diesel exhausts [38, 58].

Several groups have investigated the use of Pd as a catalytic contact to Schottky sensors. Hunter et al. experienced a drift when their sensors were operated at 350°C for a period of several weeks [5], which they attributed to a reaction between Pd and SiC. They subsequently reported a substantial

improvement in the long term stability, and an increase in the hydrogen sensitivity, after testing an alloy of Pd/Cr and the use of SnO<sub>2</sub> as an interfacial layer under the Pd contact [5]. Kim et al. [12] compared the response of Pt- and Pd-SiC Schottky diodes to hydrogen and methane at 400–600°C. The Pd-SiC Schottky diodes were found to have a higher sensitivity, as well as faster speed of response to both gases. Both types of sensor used in this work showed excellent stability when the hydrogen response was tested for 30 days at 500°C. However, those investigated by Chen et al. [59] did not show such good stability. Chen et al. investigated the effect of a high temperature anneal (425°C for 140 h) on Pd-contact Schottky diodes both with and without an interfacial oxide layer. In both cases, sensitivity to hydrogen was reduced and Pd<sub>x</sub>Si formed on the surface of the diode.

AlN exhibits both a wide band gap (6.3 eV) and also a high dielectric constant. It is capable of being used either as a substrate or as an insulator in SiC-based sensors. AlN has the potential to form an excellent insulating layer on SiC, as the crystalline materials are latticed-matched and so can be expected to be an advantageous substitute for the interfacial oxide layer. Crystalline AlN can be formed on SiC by epitaxial growth [60, 7].

Sarina et al. have demonstrated the use of Pt/AlN/SiC devices as highly selective hydrogen sensors, where the AlN was deposited by plasma source molecular beam epitaxy [7]. Samman et al. have tested Pt/AlN/SiC devices, where both the Pt and AlN were deposited by a laser ablation technique [6]. The latter devices could be used as both a MOS capacitor (in reverse bias) and as a Schottky diode (in forward bias) [6]. In the capacitive mode the maximum response was caused by hydrogen, while in the forward-bias mode at 5 µA, propane, propylene and CO produced the largest responses. The device could be operated in the Schottky diode mode in the temperature range of 250–650°C. These results led to the conclusion that the normal diode equation for thermionic emissions should be adjusted with a resistance term:

$$V = \varphi + nkT(\ln I)/q + RI . \quad (2)$$

Nakagomi has suggested a similar relationship, involving a barrier height change in series with a resistance change, for the hydrogen response of Schottky sensors based on Pt/TiO<sub>x</sub>/SiC devices. The hydrogen response of Pt/SiC diodes could be accounted for by considering only changes in the barrier height [61]. The response of the latter device was found to be constant, while the response of the former devices was dependent on the current level and increased with increasing current level. The varying gas response was attributed to a change in the resistance of the device.

A mixed ion conductor, BaSnO<sub>3</sub>, has also been tested as a catalytic contact layer on a Schottky sensor [62]. The BaSnO<sub>3</sub>/SiC sensor showed a response to oxygen and this was most pronounced at 400°C. The sensor was tested from 200°C to 700°C. Operated at 700°C the sensor showed a negative resistance peak at a bias of 2 V, see Fig. 6. This peak was accounted for by

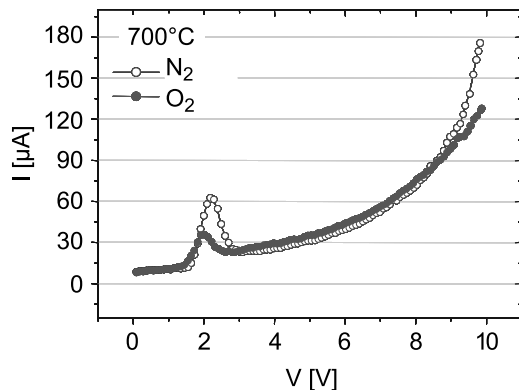


**Fig. 6.** *IV*-curves at 700°C in different gas atmosphere, N<sub>2</sub> and 21% O<sub>2</sub>/N<sub>2</sub> [62]

the tunnel or Esaki effect [63]. Up to an operation temperature of 400°C, thermionic emission was proposed to explain its behaviour. At higher temperatures, a resistance connected in series with a Schottky diode can model the device [6, 61]. At temperatures of 500–600°C, the BaSnO<sub>3</sub> shows a mixed behaviour of electronic and ion conduction, and the Nernst potential [64] can be added to the model. The complete proposed model is given in equation (3):

$$I = SA * T^2 \exp[-q\phi_{Bn}/kT] * (\exp[q(V - IR_s - V_{NERNST})/nkT] - 1) . \quad (3)$$

The first part of the equation relates to the well known thermionic emission equation [65]. At low temperatures (up to 400°C), the term  $IR_s$  is more significant than  $V_{NERNST}$ , and vice versa at high temperatures (above 400°C).

The BaSnO<sub>3</sub>/SiC device has the potential to be used as an oxygen sensor without the need for the reference electrode and reference air required during use of the regular lambda sensor based on zirconia [66]. Sensitivity to oxygen has also been achieved in SiC-based capacitor or Schottky diode devices through the introduction of a metal oxide, for example zirconia [67], CeO<sub>2</sub> [68] or LaF<sub>3</sub> [8], on top of the SiO<sub>2</sub>.

Schottky diode sensors based on other wide band-gap materials have also been investigated. GaN Schottky diodes processed on both the Ga and N face have been examined by Schalwig et al., as mentioned in Sect. 2.1 [9, 69]. A Pt Schottky contact to GaN with a barrier height of 1 eV has been shown to reversibly transform into an ohmic contact through exposure to H<sub>2</sub> [70]. Nakagomi et al. have also investigated the use of Pt/GaN Schottky diodes as hydrogen sensors up to 600°C [71].

Pt/SnO<sub>x</sub>/diamond diode gas sensors have been investigated by Gurbuz et al. [72]. This sensor responded in seconds to small concentrations of O<sub>2</sub>, CO and H<sub>2</sub> at operation temperatures up to 450°C.

### 3.3 Transistor Sensors

Both capacitor and Schottky sensors have disadvantages. Capacitors require complex surrounding circuitry in order to measure the gas response. Schottky sensors require extremely thin insulating layers under the catalytic metal through which current must constantly flow, which can degrade at high temperatures and during long term operation. The use of a thick interfacial layer in a Schottky sensor has been shown to lead to low repeatability due to a current dependent gas response [61]. The best characteristics of these two devices can be combined in a MOS transistor device, where simple circuitry can be combined with the use of a thick gate insulator through which no current flows.

A silicon carbide transistor chemical gas sensor has been developed in a cooperative effort between S-SENCE and Acreo AB [42, 43, 73]. The sensor is based on a silicon carbide field-effect transistor, with buried source, drain and channel regions in order to improve high temperature performance [37]. The transistor functions as a gas sensor by the application of a catalytic gate material, such as Pt or Ir, on the device surface over the channel region. The device design is shown in Fig. 7. The source and gate of the device are connected together in order to create a convenient two-terminal device. A voltage applied between the source and drain contacts causes a current to flow between these contacts through the buried channel region. This device has shown stable gas sensitivity to hydrogen, hydrocarbons, ammonia and CO up to temperatures of 500°C. Detection of hydrocarbons up to a temperature of 775°C has been demonstrated [43], but a slow drift was detected in the response at temperatures above 600°C.

GaN MODFETs, modulation-doping-field effect transistors, have been developed by Pyke [74]. These are operated in a constant drain current mode. Pt and Rh catalytic metal gates are used to detect and distinguish between hydrogen and carbon monoxide. This device shows the best high temperature

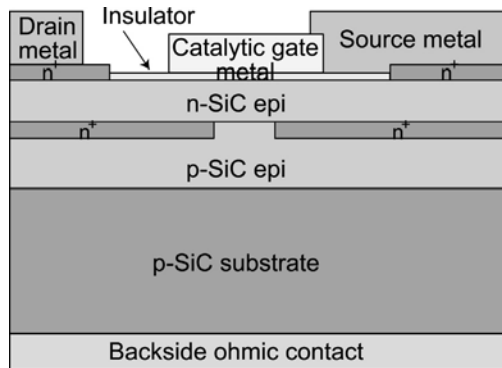


**Fig. 7.** A schematic drawing of the design of the MISiCFET sensor (from [42])

performance of the GaN and AlGaIn-based devices reported so far. It performs at temperatures as high as 600°C for some time, and it is not clear if the failure at higher temperatures is due to the device itself or due to packaging, which is a critical issue at these high temperatures.

Schalwig et al. [69] and Stutzmann et al. [70] have processed HEMTs, high electron mobility transistors, with the structure Pt/GaN/AlGaIn/GaN or Pt/AlGaIn/GaN and tested their sensor performance. The devices were processed onto sapphire substrates by plasma induced molecular beam epitaxy at 800° and showed a gas response to H<sub>2</sub>, hydrocarbons and CO up to a temperature of 400°C. Some baseline drift indicated that improvements in the material quality are needed [69, 70].

GaAs JFET devices have also been tested as gas sensors. A *n*-type SnO<sub>2</sub> layer was used to form a hetero-junction to the *p*-type channel region. Palladium on top of the SnO<sub>2</sub> caused the device to detect NO<sub>2</sub> at a device temperature around 200°C [75].

### 3.4 *p-n* Junction Diodes

*p-n* junction diodes with catalytic metal contacts have recently been tested for their gas sensing abilities, as described below. In general the sensor response tended to be lower than for the devices described previously in this chapter.

Nakshima et al. fabricated *p-n* junction devices by the use of Al implantation into *n*-type 6H-SiC [44]. A Pt layer on top of the *p*-type ohmic contact (PtSi) provided both protection and a catalytic metal contact in order to create a chemical gas sensor device. A response of 30 and 60 mV respectively was obtained to 50 ppm and 100 ppm of ammonia in nitrogen at 500°C.

Another *p-n* junction based gas sensor has been produced by the implantation of palladium ions into 6H *n*-type SiC material [45]. The gas response to hydrogen was measured as (small) changes in current as the gas ambient was varied between air and 4% H<sub>2</sub> in argon in the temperature range 23–240°C. However, at absolute voltages above 1.2 V the *p-n* junction tended to break down.

## 4 Sensor Properties

### 4.1 Speed of Response

The speed of response is normally determined by the adsorption, desorption, chemical reactions and diffusion of the gas molecules on the sensor surface. The time constants involved are in the second to millisecond time range. This means that the speed of response is defined by the type and structure of the catalytic metal and insulator in combination with the operation temperature of the device. It is normally not dependent on the choice of the semiconductor material. Device properties such as the carrier mobility, which are normally

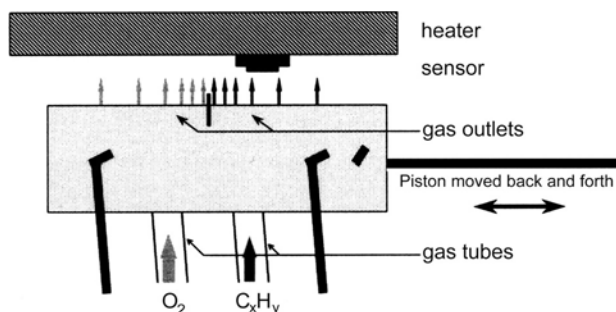


**Fig. 8.** The gas outlets of the MGO equipment move back and forth under the sensors, powered by a small electrical engine attached to the piston, thereby exchanging the gas in the sensor's immediate environment at a high frequency (from [3])

of great importance in electronic devices, are in general not important for chemical gas sensor devices.

In order to be able to measure the time constants for the gas response, it must be possible to change the gas atmosphere surrounding the sensor surface at a frequency of 1–20 Hz. This challenging experimental problem was elegantly solved by Tobias et al. through the development of moving gas outlets, MGOs, which vibrate under the sensor surface, powered by a small electrical engine [3]. A diagram of the construction is shown in Fig. 8. Another solution was the use of a very small cavity, a 6 ml chamber in this case, around the sensor and high speed injection of the gases through automotive injection valves [76]. In this way, the response time of  $\text{SrTiO}_3$  sensors was estimated to be below 10 ms.

In SiC-based capacitor devices with a contact of 40 nm  $\text{TaSi}_x$ /40 nm Pt, response time constants to hydrogen in the millisecond range have been measured at 200°C with an MGO system by Schalwig et al. [77]. Response time constants to CO, ethylene and propane have been measured as less than 50 ms at a temperature of 500°C, while the time constant of the NO response was found to be several seconds [77].

The largest influence on the speed of response is found to be the temperature. Wingbrant et al. has investigated the temperature dependence of the speed of response for a large number of different MISiCFET devices used as both hydrogen and ammonia sensors [4]. Gate metals of 100 nm Pt/10 nm  $\text{TaSi}_x$ , porous Pt and porous Ir of different thickness were used.

The hydrogen sensor can be used as a lambda sensor, where lambda is defined as follows:

$$\lambda = \frac{\left(\frac{\text{air}}{\text{fuel}}\right)_{\text{real}}}{\left(\frac{\text{air}}{\text{fuel}}\right)_{\text{stoich}}} \quad (4)$$

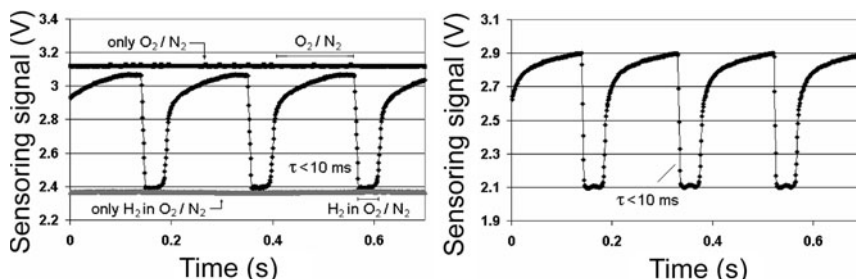


**Fig. 9.** The sensor response to 1% H<sub>2</sub> for a 10 nm TaSi<sub>x</sub>/100 nm Pt sensor at (a) 500°C and (b) 600°C. The steady state values at constant gas concentrations are indicated in (a). The sensor is switched at a frequency of 5 Hz between 0.4% O<sub>2</sub> and 1% H<sub>2</sub> in 0.4% O<sub>2</sub>. The current between source and drain is 0.1 mA. Sampling is performed each ms (from [4])

In automotive applications such as the cold-start application described in Sect. 6.2, a sensor response time of the lambda sensor is required to be less than 10 ms.

In Fig. 9, it is shown that sensors with this response time have been demonstrated [4]. To make the measurement, the sensor signal was sampled by the MGO equipment every millisecond over a period of 10 s at an exposure frequency of 5 Hz. The sensors shown here were operated at 500°C and 600°C and employed TaSi<sub>x</sub>/Pt catalytic layers. In Figure 9, two sequences of responses are shown where the gas mixture from one of the outlets was chosen as 1% H<sub>2</sub> in 0.4% O<sub>2</sub>/N<sub>2</sub> and from the other outlet as 0.4% O<sub>2</sub>/N<sub>2</sub>. It is seen in Fig. 9 that after exposure to the hydrogen-containing gas mixture, the sensor signal reaches its lowest level in less than 10 ms, and that the sensor signal switches between values that are close to the constant levels. This shows that 10 ms at 500°C is sufficient to bring the sensor close to a steady state condition and indicates that these sensors can achieve the 10 ms switching speed required for this application. It also shows that the MGO equipment is capable of measuring time constants of this magnitude.

An ammonia sensor has been developed for another automotive application, the selective catalytic reduction (SCR) of NO<sub>x</sub> gases in diesel exhaust. A response speed of 1 s is required for use in this application, see Sect. 6.3.

The response in the MGO from sensors with two different catalytic layers is shown in Fig. 10 [4]. The ammonia sensors were exposed to pulses of 500 ppm NH<sub>3</sub> in 20% O<sub>2</sub>. The sensor signals were sampled every millisecond for 10 s periods at an exposure frequency of 3 Hz. The sensor response measured at 300°C, which is the temperature normally encountered in the SCR system, is shown in Fig. 10a. As can be seen in the figure, the sensor signal reaches its lowest level in less than 100 ms for both types of sensor. However, in this case, neither the highest or lowest signal level reaches the steady-state value, indicating that the gas exposure frequency is too high for

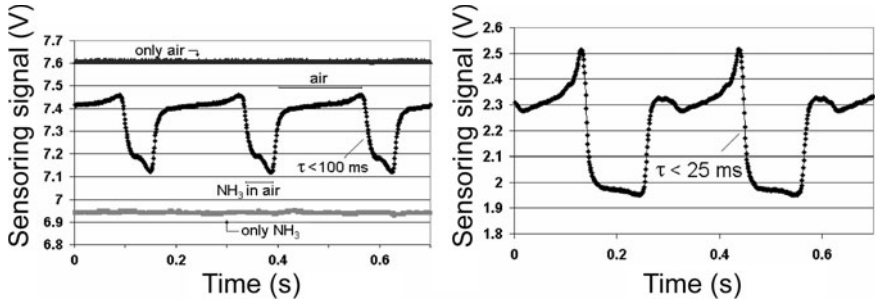


**Fig. 10.** (a) The sensor response to 500 ppm NH<sub>3</sub> for a 25 nm porous Pt sensor at 300°C. The steady state values at constant gas concentrations are also shown. (b) The sensor response to 500 ppm NH<sub>3</sub> for a 60 nm porous Ir sensor at 350°C (from [4])

the reactions on the sensor surface to reach a steady state. This means that the response time, traditionally defined as the time required for the response to change from 10% to 90% of its final value, would have been longer if a slower exposure frequency had been used. However, if the frequency is too low, mixing of the gases by diffusion can occur, and this defines the limit at which the MGO can be used.

In Figure 10b, the response at 350°C is shown. At this temperature, the gas surface reactions can be expected to occur at a faster rate, and indeed it is seen that the response now reaches a steady-state value after exposure to the ammonia atmosphere. The extra dip in the response curve in the oxygen environment is attributed to the slow diffusion of ammonia which leads to some ammonia molecules still remaining under the sensor surface when the oxygen gas outlet arrives. Due to the discovery of a capacitance-level-dependent response time in capacitor sensors, as reported in Sect. 3.1, the authors looked into the influence of the current level on the response time of MISiCFET sensors at 500°C. Current levels of 0.67, 100, 500 mA were investigated, but no influence on the speed of response was observed.

## 4.2 Long-Term Stability

The long-term stability of a sensor that is to be used at high temperatures and in corrosive atmospheres can be affected by many parameters. An overview of these is presented below.

The quality of the insulator under the catalytic material is an important parameter for high temperature operation. The formation of good quality insulators is especially difficult on wide band-gap materials, since the barrier height at the interface decreases as the band-gap of the semiconductor increases. Many techniques have been developed to improve insulator quality, especially for the case of SiC, but the technology is still not so mature

as that for silicon. However, a  $\text{SiO}_2/\text{Si}_3\text{N}_4/\text{SiO}_x$  (densified  $\text{Si}_3\text{N}_4$ ) insulator stack, as used in MISiCFET devices, see Sect. 3.3, has shown good stability at temperatures up to  $500^\circ\text{C}$  [37].

The effect of hydrogen annealing on the passivation of insulator-semiconductor interface states is well-known. This is often carried out at temperatures around  $500^\circ\text{C}$ , and normally improves the electrical characteristics of devices operated below this temperature. However, during operation at higher temperatures, the complexes formed by hydrogen with interface states at the insulator-semiconductor interface may dissociate, see Sect. 3.1. An investigation has been carried out on Schottky sensors into the effect of annealing the devices in either  $\text{H}_2$  or  $\text{O}_2$  at 500 or  $600^\circ\text{C}$  [78]. *IV* characteristics were measured at  $300^\circ\text{C}$  in an oxygen atmosphere after the anneal. The *IV* curves differed by up to 200 mV due to the different anneal cycles. Although it is possible that hydrogen may penetrate the SiC and interact with impurities such as dopant atoms, the shift was mainly attributed to a change in the occupancy of surface states.

Mixing and reaction between adjacent layers in the sensor device has also been observed to be a problem at elevated temperatures. Capacitor sensors with a platinum contact layer, a buffer layer of tantalum silicide and thermal  $\text{SiO}_2$  as an interfacial layer were investigated by XPS and AES after heat treatment at  $550^\circ\text{C}$  in oxygen and hydrogen atmospheres for 1 hour. It was concluded that considerable mixing of layers and some consumption of the oxide had occurred during this time [79]. Other researchers have also found inter-diffusion of metals and insulators as well as silicide formation after treatment or use at elevated temperatures [80, 81]. Therefore, the use of diffusion barriers, such as the  $\text{Si}_3\text{N}_4$  used in the insulator stack mentioned above, will probably be necessary for the operation of sensors at  $600^\circ\text{C}$  and above.

Ohmic contacts that are unaffected by corrosive environments at high temperatures are not yet fully developed, although several groups have addressed this problem. It has been shown, for example, that TiW contacts covered by  $\text{TaSi}_x + \text{Pt}$  as corrosion protection showed better performance at high temperatures in an environment of  $\text{H}_2/\text{O}_2$  pulses than standard alloyed Ni contacts also with  $\text{TaSi}_x + \text{Pt}$  protection [82].

During high temperature sensor operation, the use of catalytic metal contacts such as Pt can be the cause of hydrogen incorporation into the active regions of the device, causing associated stability problems. It was shown by Linnarsson et al. using secondary ion mass spectroscopy, SIMS, that hydrogen (deuterium) is introduced into SiC at temperatures  $\geq 600^\circ\text{C}$  through contacts of Pt and Ni, although not through Au contacts or non-contacted surfaces [83]. The penetration depth was  $3\text{ }\mu\text{m}$  at  $600^\circ\text{C}$  after a 4 h anneal in deuterium (5%  $\text{D}_2$  in  $\text{N}_2$ ). The presence of Ti contacts caused a large concentration of deuterium to pile up in the contact material, but no deuterium diffused into the SiC.

## 5 Experimental

### 5.1 Sample Preparation

The SiC Schottky and capacitor sensors produced by the authors were processed on either 6H- or 4H-SiC substrates ( $n$ -type, about  $1 \times 10^{19} \text{ cm}^{-3}$ ) with a 5–10  $\mu\text{m}$   $n$ -type epi-layer ( $2 - 6 \times 10^{15} \text{ cm}^{-3}$ ) [46, 84]. A thermal oxide was grown and holes were etched for the metal contacts. In the case of the Schottky sensors, the SiC surface was exposed to ozone for 10 minutes before deposition of the catalytic contact metal. This ozone treatment produced an extremely thin silicon dioxide layer,  $10 \pm 1 \text{ \AA}$  as measured by ellipsometry [56, 57]. The MISiCFET sensors were processed on 4H-SiC as described in detail elsewhere [85]. The catalytic metal contacts consisted of 10 nm TaSi<sub>x</sub> plus 100 nm Pt, porous Pt or porous Ir deposited by sputtering or by e-beam evaporation.

The layout of the MISiCFET device connects the gate and source together. This creates a “two terminal” device, which produces diode-like  $IV$  characteristics. For more details of sample preparation, see [85, 1].

The sensor signal was measured as the change in voltage at a constant current of 0.1 mA.

### 5.2 Mounting

For testing in both laboratory and industrial applications, the sensor chip produced by the authors is mounted by gluing onto a ceramic heater, which is attached to a 16-pin holder while maintaining an air gap underneath, see Fig. 11b. This allows the sensor chip to be heated to 600°C, while the holder stays below 200°C. A Pt-100 element is also glued to the heater and used for temperature control. In order to carry out measurements in exhaust gases,

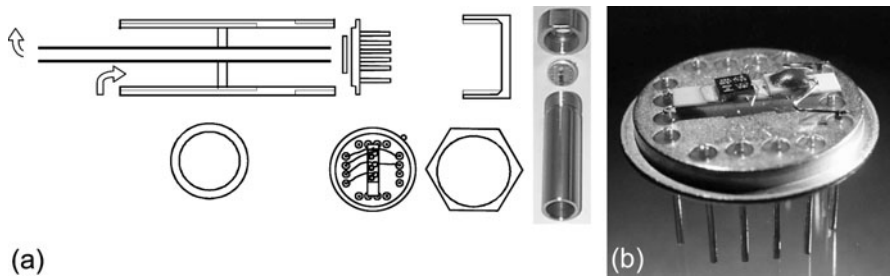


**Fig. 11.** (a) The tube mounting used for engine exhaust measurements by the authors. The flow direction of the gas is indicated by the arrows. To the left a schematic drawing of the device without the inner tube. (b) A sensor chip mounted together with a ceramic heater and a Pt-100 element on a 16-pin holder (from [86])

the 16-pin holder is mounted in a specially-designed tube, see Fig. 11a [86]. Exhaust gases are cooled while passing through the tube, which makes it possible to make measurements with the sensor chip at a constant temperature that is somewhat below the exhaust gas temperature.

Hunter et al. have mounted their sensors by gluing the SiC sensor chip onto a thin membrane realized by spin-on glass, with a heater and temperature detector underneath. This mounting technique has enabled operation of the sensor at 600°C with a heater power of close to 1 W [10].

Solzbacher et al. have constructed a micro-hotplate based on a SiC-membrane and a  $\text{HfB}_2$  thin film heater, where the active part of the membrane is separated from the surrounding structures by six SiC micro-bridges. The heater is designed for operation temperatures up to 700°C and can be operated at 380°C with a power of 35 mW [87, 88].

### 5.3 Device Operation

It is advantageous to operate the FET devices in a constant current mode using a feed back system to compensate for the voltage change caused by the gas molecules. It is considered to be more relevant to measure the voltage change, and it has been proposed that this will promote a greater base line stability since the electric field over the sensor remains constant [74, 89].

Testing of the basic properties of the SiC sensors is often performed in intermittent pulses of oxygen and hydrogen (1%  $\text{O}_2/\text{N}_2$ , 60 s, and 1%  $\text{H}_2/1\% \text{O}_2/\text{N}_2$ , 30 s) in the laboratory. This treatment is chosen since the corrosive oxygen atmosphere combined with the hydrogen/oxygen atmosphere can be regarded as being very tough for the catalytic metals. For example, catalytic etching can take place in  $\text{O}_2/\text{H}_2$  at temperatures above 450°C [90]. This treatment has been used by the authors to speed up aging phenomena in the sensors. In this way, improvement of the stability and reproducibility of the gas response can be promoted.

## 6 Applications

The authors have identified several areas in automotive and industrial applications where the excellent properties of SiC can be exploited. The MISiC and MISiCFET sensors have been tested in a variety of applications, both in simulated environments in the laboratory [77] and in real applications in the field [15, 37, 38, 58, 86, 91]. This section will describe the evaluation of sensor signals by chemometric methods during cylinder specific monitoring in exhaust gases, a cold start sensor,  $\text{NH}_3$  monitoring during the selective catalytic reduction (SCR) of diesel exhausts, and the possibility for combustion control in boilers.

## 6.1 Cylinder Specific Monitoring

The SiC-based MISiC sensors have been used to demonstrate cylinder-specific control of the burning process in petrol engines [15, 86, 91]. Gas responses in the order of a few milliseconds [3, 4] and a sensitivity to the change between oxidizing and reducing gases at very high temperatures [16] are prerequisites for this application. Tests have been performed in an engine test bench using both MISiCFET transistor sensors and MISiC Schottky sensors operated at about 600°C with a catalytic gate metal of 100 nm Pt with a 10 nm layer of TaSi<sub>x</sub> underneath [15, 86, 91]. During field tests, the SiC sensor is placed in the exhaust system at the point where the four outlet pipes from the cylinders join together. The signal from a Schottky diode sensor is shown in Fig. 2b, when it is operated at 600°C in the exhaust of a four-cylinder engine where the air to fuel ratio to one cylinder is deliberately run fuel rich. The deviating cylinder is immediately identified by a sharp dip in the sensor signal. Also MISiCFETs have been successfully operated in a similar experiment [15].

It has also been shown by Larsson et al. that the MISiCFET sensor behaves as a linear lambda sensor when operated at 500°C [15], which is further described in the next section.

## 6.2 Cold Start

During cold start of a car engine, as much as 95–98% of the total emission during an entire test driving cycle is emitted [92]. This is partly due to the fact that the zirconia-based lambda sensor [66], which is currently used to control the air-to-fuel ratio of the engine, cannot be heated to its operating temperature and therefore does not function until the engine is sufficiently warm. This is because water droplets, which form on the cold walls of the exhaust pipe during cold start, can be subsequently carried downstream by the gas flow, and can cause the brittle heated zirconia sensor to break. Therefore vehicle manufacturers currently choose to prevent the sensor from functioning until the engine is warm and water droplets do not form. The lambda value of the gas mixture, defined according to (4), needs to be close to a value of 1.0 for the catalytic converter to work efficiently. If the lambda sensor does not function, the lambda value cannot be controlled effectively, and so even if the catalytic converter has reached its optimum operation temperature, it will not combust the exhaust gases efficiently.

One way to solve this problem, and thereby control emissions directly from the start, is to use a sensor based on a material more resistant to thermal shock as a cold start sensor. Silicon carbide is such a material and has been tested by the authors for its suitability in such an application. Very encouraging results have been obtained to date, although it cannot yet be stated that the water splash resistance of SiC has been verified, since these experiments are complicated and difficult to perform in a laboratory engine test bench.

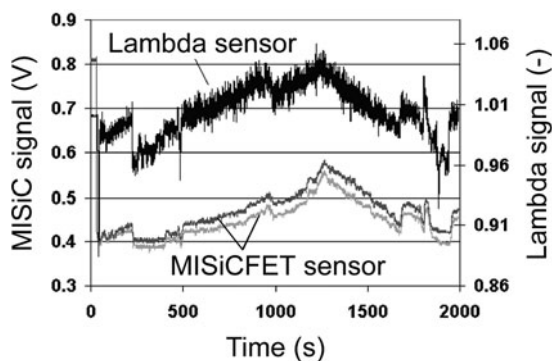


**Fig. 12.** Lambda stair in a computer-controlled engine. Lambda varies between 0.94 and 1.07. The operating temperature of the MISiCFET device is 500°C, and the current between source and drain is 0.1 mA (from [86])

The cold start sensor should also be capable of selective response to  $\lambda$ , (defined in 4), in the vicinity of  $\lambda = 1$ . The sensitivity of the MISiC sensors to  $\lambda$  was tested in a 5-cylinder 2.5-liter turbo engine in a test bench at Volvo Cars in Gothenburg, Sweden [86]. The sensor holder was placed in a tube mounting, see Fig. 11a, and plugged into the exhaust pipe of the engine between the manifold and the catalytic converter. The tube mounting was used in order to cool the gases since the exhaust is at a temperature of 700–900°C and the 16-pin holder, see Fig. 11b, cannot withstand this temperature. It is also important to be able to control the temperature of the sensors during operation. The lambda value in the engine was varied during idle running [86]. The signal from the  $\text{ZrO}_2$  linear lambda sensor together with the signals from the MISiCFET sensors can be found in Fig. 12. As can be seen in the figure, the MISiCFET sensor signals follow the lambda sensor signal very closely in the range 0.98–1.06, thus demonstrating its potential for this application.

### 6.3 $\text{NH}_3$ Sensor for Use in Selective Catalytic Reduction of Diesel Exhausts

Selective catalytic reduction (SCR) is a process by which  $\text{NO}_x$  gases in diesel exhausts can be reduced to levels that will meet future legislation. SCR is based upon the reduction of  $\text{NO}_x$  in the catalytic converter. Ammonia is injected into the exhaust gases before they enter the catalytic converter where  $\text{NO}_x$  and  $\text{NH}_3$  react to form  $\text{N}_2$  and  $\text{H}_2\text{O}$ . The ammonia injection process may be controlled by measuring either the ammonia or nitric oxide slip after the gases have passed through the catalytic converter.

Such an ammonia sensor should be able to tolerate contaminants such as particles in the exhaust gases and should show very low cross sensitivity to  $\text{NO}_x$  and HC. Typical diesel exhaust contains 3–9%  $\text{CO}_2$ , 50–250 ppm

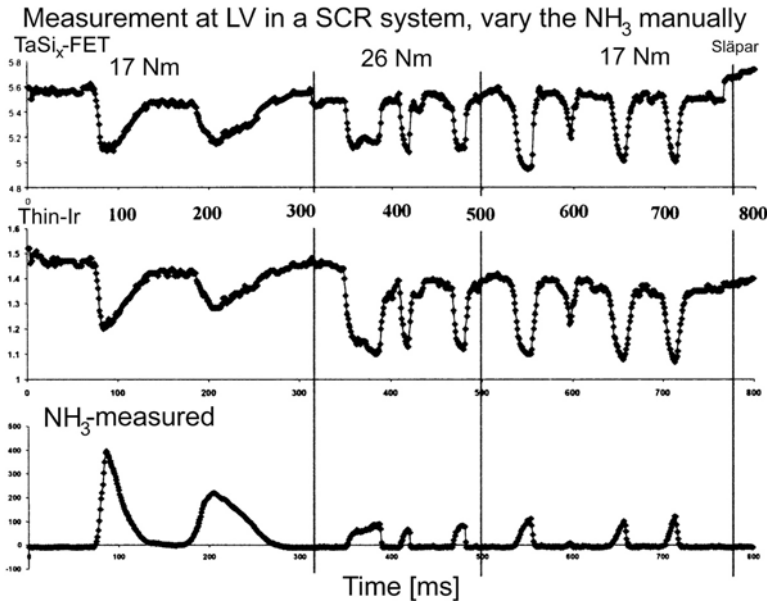


**Fig. 13.** The sensor signal from two MISiCFET sensors (*upper curves*) and the optical reference instrument (*lower curve*) during injection of  $\text{NH}_3$  into the exhaust pipe of a diesel engine. *y*-axis (*upper two curves*) shows the signal in volts; *first curve*: step 0.2 V, starting level 5.6 V; *second curve*: step 0.1 V, starting level 1.6 V; *third curve*: step 100 ppm, starting level 0 ppm (from [37])

$\text{CO}$ , 6–12%  $\text{O}_2$ , 200–1000 ppm  $\text{NO}_x$  and 130–260 ppm HC. Furthermore, the response to  $\text{NH}_3$  should have a time constant in the order of 1 s.

The MISiCFET sensor operated at 300°C has demonstrated very promising results in this application, as reported by Svenningstorp et al. [58]. In Fig. 13, the sensor response to  $\text{NH}_3$  obtained from two MISiCFET sensors with porous Pt and Ir gates respectively is compared to the  $\text{NH}_3$  concentration as measured by an optical instrument [37]. It is seen that the MISiCFET sensors follow the optical signal very closely. It can also be noted that even very small concentrations of ammonia produce a significant response in the MISiCFET sensors, which is an important factor if the sensor is to detect small amounts of ammonia that slip through the catalytic converter. At a device temperature of 300°C, the time constant for the sensor response is estimated to be 50 ms (see Fig. 10a) in Sect. 4.1, which falls well within the required limit.

Although the response to  $\text{NH}_3$  of a MISiCFET with a porous Pt gate shows an optimum at around 250°C, an operation temperature of 300°C is chosen since it has been observed that this ensures a clean sensor surface even in diesel exhaust [58]. The choice of Ir as the gate material produces a high  $\text{NH}_3$  sensitivity over a broader temperature range and at a somewhat

higher temperature, see Fig. 4a [37]. The temperature at which maximum sensitivity occurs increases as the  $\text{NH}_3$  concentration increases.

Schalwig et al. have tested the feasibility of using a SiC MOS capacitor sensor containing a contact metal of 40 nm  $\text{TaSi}_x$  plus 45 nm Pt to detect  $\text{NO}_x$  and HC after the catalytic converter. This was carried out by simulating lean burn engine exhausts [77]. It was observed that the sensor signal increased for  $\text{NO}_x$  detection and decreased for HC detection. This could permit this sensor to be used in a sensor array in order to differentiate these two gases.

## 6.4 Flue Gas Monitoring

In flue gases MISiC sensors can be used to either monitor the gas components, such as carbon monoxide (CO), nitric oxide (NO) and oxygen, or to identify different modes of combustion in the boilers (small power plants). In this way, it is possible to optimise the combustion in boilers of capacity 0.5–5 MW in which optical techniques such as Fourier Transform Infrared (FTIR) are too expensive and complex. The authors have performed measurements in a larger boiler of 100 MW, since this boiler is equipped with the necessary reference instruments. This boiler has been used for the remote heating of industrial and residential buildings and for the generation of electricity in Nyköping, Sweden. It is fuelled by wood pellets, and there was a natural randomisation of the flue gases, which were used to stimulate the sensors [93]. MISiCFET sensors containing Pt or Ir gates, metal oxide sensors and a lambda sensor were used in the measurements, together with signals from the reference instruments.

It was found that the CO concentration in the flue gases varied substantially within the range 80 to 500 ppm, while the NO concentration varied within a smaller range, 60–100 ppm. The oxygen level also varied a little and seemed to be correlated to the NO level. These relative variations are advantageous for the measurement and prediction of CO since  $\Delta\text{CO}/\text{CO}_{\text{max}}$  is large.

Data was collected over several months. The data from the sensors was evaluated using PCA (principal component analysis) [94]. Figure 14b shows that it is possible to separate different operation modes of the boiler, as defined in Fig. 14a [93]. It was also possible to use partial least square algorithms to build models of the sensor signals representing the CO concentration. Here it is important to use data containing enough variation for the calibration model.

The results in this investigation showed that it should be possible to use an array of these sensors together with chemometric data evaluation to control the operation mode of the boiler. Also, fine-tuning of the combustion should be possible, by measuring the CO concentration in the preferred boiler mode for example.

The MISiC sensors have been operated in the flue gas environment at 300°C for a total of 6 months without failure.

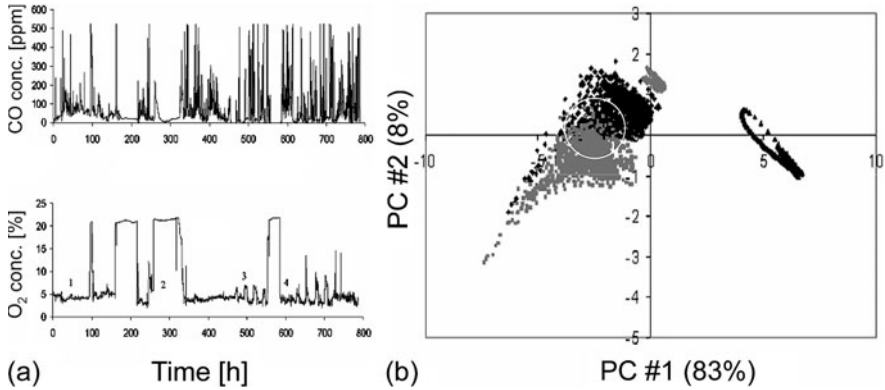


**Fig. 14.** (a) The CO (*above*, in ppm) and O<sub>2</sub> (*below*, in percentage) concentrations versus time in the flue gases from a boiler. Different boiler modes of operation (1–4) could be identified according to different combinations of the CO and O<sub>2</sub> concentrations. (b) The different modes of operation could be identified in a score plot. Measurement points from the most advantageous mode of operation (low emissions and good combustion) are found within the *white circle* (from [93])

## 7 Outlook and Conclusions

Field effect devices based on high band-gap materials are under rapid development, since the robustness of the materials and their tolerance of extreme environments makes them very attractive for use in high temperature and corrosive environments. GaN, AlN and diamond have wider band-gaps than SiC and will probably be important as sensor materials in the future. However their production and processing technology is not so mature as that of SiC, and so commercialisation of devices produced on these materials will occur at a later date than those produced on SiC.

A number of field effect devices such as capacitors, Schottky diodes, *p-n* junctions and transistors have been explored for use as chemical gas sensors. Advanced transistor sensors have been demonstrated in both SiC and GaN. The use of transistor devices has many advantages, such as greater stability and simple electronic circuitry. It also permits the use of more resistive catalytic materials, enabling the use of a greater range of materials, and causing a corresponding increase in the range of gases that can be selectively detected. MISiCFETs can be operated over a large temperature range, from 100°C to 700°C. This enables these sensors to be used in a large number of applications, such as control of exhaust gases in vehicle engines and for flue gas monitoring. The small size and versatility of these sensors also permits sensor arrays to be used in sensor systems such as the electronic nose.

The gas response of the field effect devices is determined by the catalytic properties of the contact material, which includes both the catalytic layer and the underlying material. The temperature plays a dominant role in the

detection process, since the origin of the gas response is found in the chemical reactions that take place on the sensor surface, together with the mass transport properties of the gas molecules. This permits sensors of a common design to be tailor-made for detection of a range of gases, for use in a range of applications.

SiC material and processing technology is rapidly reaching maturity as described in other chapters of this book. Wafers of 3" diameter are already available and 4" is expected to follow soon. SiC also offers the possibility to integrate electronics on the sensor chip in the future, which makes this technology very attractive. Free-standing chips of SiC can, in the future, include arrays of chemical sensors, a heater, temperature control and signal processing circuitry. The high thermal conductivity of SiC will permit heating of these chips up to 600°C within a few seconds and also rapid cooling should be possible.

SiC technology provides the opportunity for the exploitation of chemical gas sensors in the near future, in environments and applications that are problematic today. The extension of this technology to these areas will enable the reduction of unwanted emissions and will promote reductions in the use of fuel and energy, resulting in positive implications for natural resources and the environment.

## Acknowledgement

Our research on high temperature chemical sensors based on silicon carbide is supported by grants from the Swedish Agency for Innovation Systems, and Swedish Industry through the Center of Excellence, S-SENCE, the Swedish Research Council, and the SSF-SiCEP program. Measurements have been carried out together with the Laboratory of Applied Physics at AB Volvo Technology Corporation in Göteborg, Sweden, Vattenfall Development, Älvkarleby, Sweden, AppliedSensor, Mjärdevi Science Park, Linköping, Sweden, Ford Research Laboratory, Dearborn, Michigan, USA and Mecel AB, Åmål, Sweden. The MISiCFET devices were designed and processed at Acreo AB in Kista, Sweden. The skillful metal gate deposition and mounting of the sensor chips was performed by Jeanette Nilsson and Evald Mild, respectively, at Linköping University, Sweden.

## References

1. A. Lloyd Spetz, L. Unéus, H. Svenningstorp, P. Tobias, L.-G. Ekedahl, O. Larsson, A. Göras, S. Savage, C. Harris, P. Mårtensson, R. Wigren, P. Salomonsson, B. Häggendahl, P. Ljung, M. Mattsson, and I. Lundström: *phys. stat. sol. (a)* **185**, 15 (2001)
2. A. Lloyd Spetz, A. Baranzahi, P. Tobias, and I. Lundström: *physica status solidi (a)* **162**, 493 (1997)
3. P. Tobias, P. Mårtensson, A. Göras, I. Lundström and A. Lloyd Spetz: *Sens. Actuators B* **58**, 389 (1999)
4. H. Wingbrant, I. Lundström and A. Lloyd Spetz: *Sens. Actuators B*, **93**, 1–3. 286 (2003)
5. G.W. Hunter, P.G. Neudeck, L.-Y. Chen, D. Knight, C.C. Liu, and Q.H. Wu: *Mat. Sci. Forum* **264–268**, 2, 1093 (1998)
6. A. Samman, S. Gebremariam, L. Rimai, X. Zhang, J. Hangan, G.W. Auner: *J. Appl. Phys.* **87**, 6, 3101 (2000)
7. F. Serina, K.Y.S. Ng, C. Huang, G.W. Auner, L. Rimai, R. Naik: *Appl. Phys. Lett.* **79**, 20, 3350 (2001)
8. A. Vasiliev, W. Moritz, V. Fillipov, L. Bartholomäus, A. Terentjev, T. Gabusjan: *Sensors and Actuators B* **49**, 133 (1998)
9. J. Schallwig, G. Müller, U. Karrer, M. Eickhoff, O. Ambacher, M. Stutzmann, L. Görgens, G. Dollinger: *Appl. Phys. Lett.* **80**, 7, 1222 (2002)
10. G.W. Hunter, P.G. Neudeck, M. Gray, D. Androjna, L.-Y. Chen, R.W. Hoffman Jr., C.C. Liu, Q.H. Wu: *Mat. Sci. Forum* **338–342**, 1439 (2000)
11. C.K. Kim, J.H. Lee, Y.H. Lee, N.I. Cho, D.J. Kim, W.P. Kang: *J. Electr. Mat.* **28**, 3, 202 (1998)
12. C.K. Kim, J.H. Lee, S.M. Choi, I.H. Noh, H.R. Kim, N.I. Cho, C. Hong, G.E. Jang: *Sens. Actuators B* **77**, 455 (2001)
13. R.N. Ghosh, P. Tobias and B. Golding: *Mat. Res. Symp.* **742**, 363 (2003)
14. S. Nakagomi, T. Azuma, and Y. Kokubun: *Electrochemistry*, **3**, 174 (2002)
15. O. Larsson, A. Göras, J. Nytomt, C. Carlsson, A. Lloyd Spetz, T. Artursson, M. Holmberg, I. Lundström, L.-G. Ekedahl, and P. Tobias: *SAE Technical Paper Series*, 2002-01-0847
16. [http://www.infineon.com/cgi/ecrm.dll/ecrm/scripts/prod\\_cat.jsp?oid=-8681](http://www.infineon.com/cgi/ecrm.dll/ecrm/scripts/prod_cat.jsp?oid=-8681)
17. D.M. Brown, J. Kretchmer, J. Fedison, T. Dean: *Electrochem. Soc. Proc.* **3**, 83 (2002)
18. G. Bertuccio, R. Casiraghi, E. Gatti, D. Maiocchi, F. Nava, C. Canali, A. Cetrone, C. Lanzieri: *Mat. Sci. Forum*, **433–436**, 941 (2003)
19. J. Fogelberg, M. Eriksson, H. Dannetun, and L.-G. Petersson: *J. Appl. Phys.* **78**, 2, 988 (1995)
20. L.-G. Ekedahl, M. Eriksson, and I. Lundström: *Acc. Chem. Res.* **31**, 5, 249 (1998)
21. D.E. Yates, S. Levine, T.W. Healy: *J. Chem. Soc., Faraday Trans.* **70**, 1807 (1974)
22. R. Neuberger, G. Müller, M. Eickhoff, O. Ambacher, M. Stutzmann: *Mat. Sci. Eng. B* **93**, 143 (2002)
23. J. Schallwig, G. Müller, M. Eickhoff, O. Ambacher, M. Stutzmann: *Mat. Sci. Eng. B* **93**, 207 (2002)
24. M. Holmberg, and I. Lundström: *Appl. Surf. Sci.* **93**, 67 (1996)

25. M. Eriksson, and L.-G. Petersson: *Surf. Sci.* **311**, 139 (1994)
26. E. Hedborg, F. Winquist, H. Sundgren, I. Lundström: *Thin Sol. Films* **340**, 250 (1999)
27. S. Nakagomi, P. Tobias, A. Baranzahi, I. Lundström, P. Mårtensson, and A. Lloyd Spetz: *Sens. Actuators B* **45**, 183 (1997)
28. J. Schallwig, P. Kreisl, S. Ahlers, C. Bosch-v. Braunmühl, and G. Müller: Response mechanism, submitted
29. A. Spetz, M. Armgarth, I. Lundström: *Sens. Materials*, **4**, 187 (1988)
30. L. Unéus, P. Tobias, P. Salomonsson, I. Lundström, A. Lloyd Spetz: *Sensors and Materials*, **11**, **5**, 305 (1999)
31. E. Fridell, H. Persson, L. Olsson, B. Westerberg, A. Amberntsson and M. Skoglundh: *Topics in Catalysis*, **16/17**, **1–4**, 133 (2001)
32. P.D. Holmes, G.S. McDougall, I.C. Wilcock, K.C. Waugh: *Catalysis Today*, **9**, 15 (1991)
33. J. Olander and K. Larsson: *J. Phys. Chem.* **103**, 9604 (1999)
34. M. Rinnemo, D. Kulginov, S. Johansson, K.L. Wong, V.P. Zhdanov, and B. Kasemo: *Surf. Sci.* **376**, 297 (1997)
35. A. Baranzahi, P. Tobias, A. Lloyd Spetz, P. Mårtensson, L.-G. Ekedahl, and I. Lundström: *J. Electrochem. Soc.* **145**, **10**, 3401 (1988)
36. A. Baranzahi, A. Lloyd Spetz, M. Glavmo, C. Carlsson, J. Nytomt, P. Salomonsson, E. Jobson, B. Häggendahl, P. Mårtensson, I. Lundström: *Sens. Actuators, B* **43**, 52 (1997)
37. H. Wingbrant, L. Unéus, M. Andersson, J. Cerdá, S. Savage, H. Svenningstorp, P. Salomonsson, P. Ljung, M. Mattsson, J. H. Visser, D. Kubinski, R. Soltis, S.G. Ejakov, D. Moldin, M. Löfdahl, M. Einehag, M. Persson, and A. Lloyd Spetz: *Mat. Sci. Forum*, **433–436**, 953 (2003)
38. L. Unéus, M. Mattsson, P. Ljung, R. Wigren, P. Mårtensson, L.G. Ekedahl, I. Lundström, A. Lloyd Spetz: *Proc. ISOEN'2000*, Brighton, England, July 24–26, 291 (2000)
39. K.I. Lundström, M.S. Shivaraman, and C.M. Svensson: *J. Appl. Phys.* **46**, **9**, 3876 (1975)
40. A. Spetz, A. Arbab, and I. Lundström: *Proc. Eurosensors VI*, San Sebastian, Spain, 5–7 October, 9, 1992
41. G.W. Hunter, P.G. Nuedeck, G.D. Jefferson, G.C. Madzsar, C.C. Liu, and Q.H. Wu: *NASA Technical Memorandum*, 106141, 1993
42. S.M. Savage, A. Konstantinov, A.M. Saroukan, C. Harris: *Mater. Sci. Forum* **338–342**, 1431 (2000)
43. H. Svenningstorp, P. Tobias, P. Salomonsson, I. Lundström, P. Mårtensson, and A. Lloyd Spetz, *Mat. Sci. Forum* **338–342**, 1435 (2000)
44. K. Nakashima, Y. Okuyama, S. Ando, O. Eryu, K. Abe, H. Yokoi, and T. Oshima: *Mat. Sci. Forum*, **389–393**, 1427 (2002)
45. C.I. Muntele, D. Ila, E.K. Williams, D.B. Poker, D.K. Hensley, D.J. Larkin, and I. Muntele: *Mat. Sci. Forum*, **338–342**, 1443 (2000)
46. Cree Research Inc, 4600 Silicon Drive, Durham, NC 27703, USA
47. E. Janzén, O. Kordina: *Inst. Phys. Conf. Ser.* **142**, 653 (1996)
48. A. Baranzahi, A. Lloyd Spetz and I. Lundström: *Appl. Phys. Lett.* **67**, 21, 3203 (1995)
49. P. Tobias, A. Baranzahi, I. Lundström, A. Schöner, K. Rottner, S. Karlsson, P. Mårtensson and A. Lloyd Spetz: *Mat. Sci. Forum* **264–268**, 1089 (1998)

50. P. Tobias, B. Golding and R.N. Ghosh: IEEE Sensors Journal, October 2003
51. A. Lloyd Spetz, P. Tobias, A. Baranzahi, P. Mårtensson, I. Lundström: IEEE Trans. Electr. Dev. **46**, **3**, 561 (1999)
52. L.L. Tongson, B.E. Knox, T.E. Sullivan, and S.J. Fonash: J. Appl. Phys. **50**, 1535 (1979)
53. P. Tobias, A. Baranzahi, I. Lundström, A. Schöner, K. Rottner, S. Karlsson, P. Mårtensson and A. Lloyd Spetz: Mat. Sci. Forum **264–268**, 1097 (1998)
54. M.S. Shivaraman, I. Lundström, C. Svensson, and H. Hammarsten: Electron. Lett. **12**, 483 (1976)
55. J.N. Zemel, B. Keramati, C.W. Spivak, and A.D'Amico: Sensors and Actuators **1**, 427 (1981)
56. S. Zangoie, H. Arwin, P. Tobias, I. Lundström and A. Lloyd Spetz: Mat. Sci. Forum **338–342**, 1085 (2000)
57. R.P. Mikalo, P. Hoffman, D.R. Batchelor, A. Lloyd Spetz, I. Lundström, and D. Schmeisser: Mat. Sci. Forum **353–356**, 219 (2001)
58. H. Svenningstorp, P. Tobias, P. Salomonsson, B. Häggendal, I. Lundström, L.-G. Ekedahl, and A. Lloyd Spetz: Proc. Eurosensors XIV, Copenhagen, Denmark, August 27–30, (2000) p. 933 (W3E5)
59. L.-Y. Chen, G.W. Hunter, P.G. Neudeck, and G. Basal: J. Vac. Sci. Technol. A **15**, 1228 (1997)
60. C.-M. Zetterling, M. Östling, K. Wongchotigul, M.G. Spencer, X. Tang, C.I. Harris, N. Nordell, and S.S. Wong: J. Appl. Phys., **82**, 2990 (1997)
61. S. Nakagomi, H. Watanabe, Y. Kokubun: Chemical Sensors 17, Supplement B **50** (2001) 2A09
62. J. Cerdá, J.R. Morante, and A. Lloyd Spetz: Mat. Sci. Forum, **433–436**, 949 (2003)
63. E.S. Yang: in *Microelectronic Devices*, Chap. 4 (McGraw-Hill Series in Electrical Engineering, 1988) p. 106
64. D.C. Harris: in *Quantitative Chemical Analysis*, (Freeman and Company, 1987) p. 312
65. S.S. Cohen, G.S. Gildenblat: in *VLSI Electronics Microstructure Science*, ed. by N.G. Einspruch (Academic Press, Inc., Orlando, 1986) 13
66. J.H. Visser and R.E. Soltis: IEEE Trans. Instr. and Meas. **50** 1543 (2001)
67. P. Tobias, K. Macak, U. Helmersson, I. Lundström, and A. Lloyd Spetz: Proc. 8IMCS, Basel Switzerland, 149 (2000)
68. S. Jacobsén, U. Helmersson, L.G. Ekedahl, I. Lundström, P. Mårtensson, and A. Lloyd Spetz: Proc. Transducers'01 and Eurosensors XV 832 (2001)
69. J. Schalwig, G. Müller, O. Ambacher, M. Stutzmann: phys. stat. sol. (a) **185**, **1**, 39 (2001)
70. M. Stutzmann, G. Steinhoff, M. Eickhoff, O. Ambacher, C.E. Nebel, J. Schalwig, R. Neuberger, G. Müller: Diamond and Related Mat. **11**, 886 (2002)
71. Y. Kokobun, T. Seto, S. Nakagomi: Jpn. J. Appl. Phys. **40**, L663 (2001)
72. Y. Gurbuz, W.P. Kang, J.L. Davidson, D.V. Kerns: IEEE Trans. Electr. Dev. **46**, **5**, 914 (1999)
73. S. Savage, and A. Lloyd Spetz: Compound Semiconductor, **6**, **3**, 76 (2000)
74. <http://www.eere.energy.gov/> search button: Stephen C. Pyke
75. J. Wöllenstein, F. Ihlenfeld, M. Jaegle, G. Kühner, H. Böttner, W.J. Becker: Sensors and Actuators B **68**, 22 (2000)
76. J. Gerblinger, U. Lampe, and H. Meixner: Sens. Actuators B **24–25**, 639 (1995)

77. J. Schallwig, C. Bosch-v. Braunmühl, G. Müller, and A. Lee: SAE Technical Paper Series, 2002-01-1095
78. L. Unéus, S. Nakagomi, M. Linnarsson, M. Jansson, B. Svensson, R. Yakimova, M. Syväjärvi, A. Henry, E. Janzén, L.-G. Ekedahl, I. Lundström, and A. Lloyd Spetz: *Mat. Sci. Forum*, **389–393**, 1419 (2002)
79. A. Lloyd Spetz, D. Schmeisser, A. Baranzahi, B. Wälivaara, W. Göpel, and I. Lundström: *Thin Solid Films*, **299**, 183 (1997)
80. E. Danielsson, C. I. Harris, C.-M. Zetterling, and M. Östling: *Mat. Sci. Forum*, **264–268**, **2**, 805 (1997)
81. L.-Y. Chen, G.W. Hunter, P.G. Neudeck, G. Bansal, J.B. Petit, D. Knight: *J. Vac. Sci. Technol. A* **15**, **3**, 1228 (1997)
82. L. Unéus, S.-K. Lee, C.-M. Zetterling, L.-G. Ekedahl, I. Lundström, M. Östling, and A. Lloyd Spetz: *Proc. ICSCRM2001*, Tsukuba, Japan, Oct. 28–Nov. 2, 410 (2001)
83. M.K. Linnarsson, A. Lloyd Spetz, M.S. Janson, L.G. Ekedahl, S. Karlsson, A. Schöner, I. Lundström and B.G. Svensson, *Mat. Sci. Forum*, **338–342**, 937 (2000)
84. Okmetic Oyj, Piitie 2, Koivuhaka, FIN-01301, Vantaa, Finland
85. S. Savage, H. Svenningstorp, L. Unéus, A. Kroutchinine, P. Tobias, L.-G. Ekedahl, I. Lundström, C. Harris, and A. Lloyd Spetz: *Mat. Sci. Forum*, **353–356**, 747 (2001)
86. H. Wingbrant, H. Svenningstorp, P. Salomonsson, P. Tengström, I. Lundström and A. Lloyd Spetz: *Sens. Actuators B*, **93**, **1–3**, 295 (2003)
87. F. Solzbacher, C. Imawan, H. Steffes, E. Obermeier, H. Möller: *Sens. Actuators B* **64**, 95 (2000)
88. F. Solzbacher, C. Imawan, H. Steffes, E. Obermeier, M. Eickhoff: *Sens. Actuators B* **78**, 216 (2001)
89. I. Lundström, M. Armgarth, and L.G. Petersson: *CRC Critical Rev. Solid State and Mat. Sci.* **15**, 201 (1989)
90. V.W. Dean, M. Frenklach, and J. Phillips: *J. Phys. Chem.* **92**, 5731 (1988)
91. A. Baranzahi, A. Lloyd Spetz, P. Tobias, I. Lundström, P. Mårtensson, M. Glavmo, A. Göras, J. Nytomt, P. Salomonsson, and H. Larsson: SAE Technical Paper Series 972940, p. 231 (1997) (SP-1300)
92. Federation Internationale de L'Automobile, 8 Place de la Concorde, 75008 Paris, France, <http://www.fia.com/tourisme/enviro-a/cleana.htm>, 1999
93. L. Unéus, T. Artursson, M. Mattsson, P. Ljung, R. Wigren, P. Mårtensson, M. Holmberg, I. Lundström and A. Lloyd Spetz: submitted to *IEEE Sensors Journal*
94. G.E.P. Box, W.G. Hunter, J.S. Hunter: *Statistics for experimenters*

# Index

- 3C-SiC 179–186, 188, 193–201, 207–227
- Absorption 413–420, 422
- Accumulation-mode ECFET 814, 817, 835
- Activation of acceptors 57
- Advanced transmission electron microscopy 607
- Annealing mechanisms 26, 29, 42, 47, 50, 53
- Anti-phase boundary 208
- Antisites 3, 5, 7, 10, 22, 462, 466
- Band lineup at semiconductor interfaces 317
- Band offsets of heterostructures 317, 318, 327, 328, 330, 333–335, 337–339
- Band structure 437, 439, 440, 447, 449, 450, 457
- Barrier heights of Schottky contacts 317, 318, 320, 321, 324, 326, 331–334, 337, 339
- Bipolar figures of merit 738–740
- Bipolar junction transistor 738, 744–747
- Breakdown field 742
- Bulk crystal growth 137, 153
- Bulk growth 163
- Cantilevers 179, 188–193, 198, 200
- Catalytic material 869, 870, 883, 891
- Channel mobility 814, 815, 819–821, 823, 825, 826, 835
- Chemical gas sensors 869, 870, 874, 891, 892
- Contact 651–655, 657–666
- Contact resistance 651, 666
- Crystal defects 179, 181, 182, 193, 201
- Crystal mosaicity 137, 149, 152–154
- Cubic inclusions 89, 90, 94, 95, 109–113
- Cyclotron resonance 437–439, 451, 455, 456
- Deep level transient spectroscopy 537, 543
- Defects 585–587, 589–593, 595–598, 600–604, 629, 630, 634, 637–639, 646
- Degeneracy factor 519
- Dislocations 137–152, 154–156, 160
- DMOSFET 787, 788, 791, 792, 794, 802, 804–810
- Dopant diffusion 27, 29, 31, 43, 46, 47, 53
- Doping uniformity 236, 244, 246
- Effective mass 437–439, 443, 444, 446, 447, 449–457
- Effective mobility 387, 388, 392, 393, 408
- Electrical activation 494, 505, 507, 508, 510, 511, 513
- Electron trapping 387, 390–393, 396–399, 402
- Electronic properties of defects 585, 603
- Elemental transmutation 537, 538, 552, 553, 555
- Epi-ready surface 706, 707
- Epitaxial 3C-SiC 251, 259, 262
- Epitaxial growth 711, 713, 719, 720, 730
- Erbium 420, 421

- Excited states 517, 519, 521, 522, 534  
 Extreme environments 869, 870, 891
- Field effect devices 869, 874, 875, 891
- Gate oxide 373, 375, 381, 383–385  
 Grain boundaries 4, 5  
 Growth 122–127, 130–134
- H-diffusion 57  
 H-passivation 57  
 Hall mobility 388, 390, 391, 393, 397, 407  
 Hall scattering factor for electrons 517, 523  
 Hall scattering factor for holes 517, 525  
 Heteroepitaxy 179, 193, 198, 201, 207  
 HEV inverter 814, 822, 832  
 High resolution X-ray diffraction 629, 631, 638  
 High voltage SiC devices 769  
 High-dose implantation 251, 252  
 Homoepitaxial growth of SiC 229, 230  
 Horizontal hot wall reactor 230–232, 235, 239–241, 243, 244  
 Hydrogen solubility 57
- IFIGS-and-electronegativity theory 318, 329, 331, 332, 337, 338  
 Image simulation 619, 620  
 Impact ionization coefficient 738  
 Impurities 461–463, 471, 478, 479, 537, 539, 548, 554, 557–559  
 Infrared absorption 493, 512  
 Insulated-gate bipolar transistor (IGBT) 740, 749–752  
 Interface defect 343, 366, 378  
 Interface traps 401, 406  
 Interface-induced gap states 317, 329, 338  
 Interstitial migration 30, 37, 43, 46, 47, 51, 53  
 Intrinsic defects 421, 461, 462, 478, 480, 487  
 Ion beam synthesis 251, 252, 267, 273  
 Ion implantation 712, 722  
 IR transmission 499
- JBS 770–772, 782
- Kohn-Luttinger effect 518
- Low temperature photoluminescence 493, 494  
 Low-dimensional structures in SiC 607, 608
- MEMS 671–676, 678, 679, 681, 683, 685, 688–692, 694, 695  
 Micromachining 671–683, 685–691, 694, 695  
 Micromolding 671, 681, 683–685, 688  
 Micropipe 137–142, 144–147, 150, 154, 156, 160, 711, 719–722, 730  
 Modeling 121–125, 130, 131, 134  
 Molecular dynamics 611, 622, 623, 626  
 MOS capacitors 379, 383, 384  
 MOS interface 711, 712, 726, 727, 729  
 MOS-gated bipolar transistor (MGT) 752–755  
 MOSFETs 374, 375, 378, 381, 383
- Nano-polytypes 427, 428, 430, 431  
 Nanocrystal formation process 608, 625  
 Nitridation 373–375, 377, 378, 380–383, 385  
 Nitrogen doping 163, 164, 169, 170, 174, 176  
 Non-basal planes 711–714, 730
- One-dimensional localization 100, 103, 104  
 Oxidized SiC 343, 356
- Phosphorus 493, 495–499, 508, 511–513  
 Photoluminescence 413, 415, 422, 424–428, 431, 432  
*pn* diode 770, 771, 773–775, 782  
 Polaron effect 443, 450, 455, 457  
 Polishing 699–701, 703, 706, 707  
 Poly-SiC 675, 680–684, 686–688, 690, 693  
 Polytypism 3, 4, 17  
 Power bipolar transistors 742–744, 749, 751, 753  
 Power devices 651, 652, 662, 663, 666

- Power MOSFET 785, 786, 788, 791, 796, 797, 799, 800
- Power thyristors 755, 757
- Quantum-well 104–106, 110, 112, 114–117
- Radiotracer 537–539, 543–549, 551–553, 555–559
- Raman scattering 585, 586, 593, 597–600
- Reconstruction 283, 286–289, 291–293, 295, 298–300, 302, 305, 307–310
- Reliability 652, 661, 663
- Resistivities 163, 164, 170, 171, 176
- SBD 770–772, 782
- Screw dislocations 629–631, 635, 636
- SEJFET 777–779, 782
- Self diffusion 27, 28, 43–46, 53
- SEMOSFET 776, 777, 779, 782
- Shallow donor 493
- Sheet resistance 508, 511, 512
- Si-IGBTs 813, 814, 833
- SIAFET 776, 777, 782
- SiC 121–126, 130, 131, 133, 134, 629–646, 651–655, 657, 659, 699–704, 707, 785–789, 791, 795–799, 801, 804–808
- SiC crystal growth 121
- SiC module 779
- SiC MOS 387, 388, 390, 391, 399, 400, 402, 408
- SiC MOS technology 343–345
- SiC MOSFETs 813, 814, 820–822, 833
- SiC/SiO<sub>2</sub> interface state 343–346, 350–352, 355–359, 365
- Silicate 294, 296, 300, 301, 305, 306, 309, 310
- Silicon controlled rectifier 755
- Simulation 121–124, 128–130, 132–134
- Solubility limit 166, 176
- Spin-orbit interaction 439, 444–447, 450
- Stacking fault energies 107, 113
- Stacking fault formation 171, 174, 176
- Stacking faults 4, 5, 21, 89–117, 138, 146, 156–160, 208, 211, 226, 227, 585, 587–591, 593, 595, 597, 600
- Step-free 179, 184–189, 191–199, 201
- Structure 281–289, 291–305, 307–310
- Surface 281–283, 285–297, 299–310
- Surface preparation 699, 701, 704–707
- Surface stacking 297, 304, 310
- Synchrotron white beam X-ray topography 629, 630
- Theory 57, 61, 63, 78, 80
- Thermal oxidation 343, 349, 353, 361
- Thickness uniformity 239, 243, 244, 247, 248
- Thin films 251, 266
- Thyristor
  - field-controlled 760–762
  - gate turn-off 740, 744, 756–760
  - light triggered 760
- UMOSFET 786, 787, 792, 795
- Undulant-Si 207, 210–217, 219, 220, 222–224, 226, 227
- Vacancies 3, 5, 7–9, 11–14, 22, 461–464, 470–475, 478, 487
- Vacancy migration 28, 29, 31, 41–43, 45, 52
- Vapor phase epitaxy 229
- Wafer bonding 671, 686, 690–694
- Wide band-gap materials 869, 878, 883